

IFMBE Proceedings

Almir Badnjevic · Ranko Škrbić ·
Lejla Gurbeta Pokvić (Eds.)

Volume 73

CMBEBIH 2019

Proceedings of the International Conference on Medical
and Biological Engineering, 16–18 May 2019
Banja Luka, Bosnia and Herzegovina



IFMBE Proceedings

Volume 73

Series Editor

Ratko Magjarevic, Faculty of Electrical Engineering and Computing, ZESOI, University of Zagreb, Zagreb, Croatia

Associate Editors

Piotr Ładyżyński, Warsaw, Poland

Fatimah Ibrahim, Department of Biomedical Engineering, University of Malaya, Faculty of Engineering, Kuala Lumpur, Malaysia

Igor Lackovic, Faculty of Electrical Engineering and Computing, University of Zagreb, Zagreb, Croatia

Emilio Sacristan Rock, Mexico DF, Mexico

The International Federation for Medical and Biological Engineering, IFMBE, is a federation of national and transnational organizations representing internationally the interests of medical and biological engineering and sciences. The IFMBE is a non-profit organization fostering the creation, dissemination and application of medical and biological engineering knowledge and the management of technology for improved health and quality of life. Its activities include participation in the formulation of public policy and the dissemination of information through publications and forums. Within the field of medical, clinical, and biological engineering, IFMBE's aims are to encourage research and the application of knowledge, and to disseminate information and promote collaboration. The objectives of the IFMBE are scientific, technological, literary, and educational.

The IFMBE is a WHO accredited NGO covering the full range of biomedical and clinical engineering, healthcare, healthcare technology and management. It is representing through its 60 member societies some 120.000 professionals involved in the various issues of improved health and health care delivery.

IFMBE Officers

President: James Goh, Vice-President: Shankhar M. Krishnan

Past President: Ratko Magjarevic

Treasurer: Marc Nyssen, Secretary-General: Kang Ping LIN

<http://www.ifmbe.org>

More information about this series at <http://www.springer.com/series/7403>

Almir Badnjević · Ranko Škrbić ·
Lejla Gurbeta Pokvić
Editors

CMBEBIH 2019

Proceedings of the International Conference
on Medical and Biological Engineering,
16–18 May 2019, Banja Luka,
Bosnia and Herzegovina

Editors

Almir Badnjevic
International Burch University
Sarajevo, Bosnia and Herzegovina

Medical Device Inspection Laboratory Verlab
Sarajevo, Bosnia and Herzegovina

Lejla Gurbeta Pokvić
International Burch University
Sarajevo, Bosnia and Herzegovina

Medical Device Inspection Laboratory Verlab
Sarajevo, Bosnia and Herzegovina

Ranko Škrbić
Faculty of Medicine
University of Banja Luka
Banja Luka, Bosnia and Herzegovina

ISSN 1680-0737 ISSN 1433-9277 (electronic)
IFMBE Proceedings
ISBN 978-3-030-17970-0 ISBN 978-3-030-17971-7 (eBook)
<https://doi.org/10.1007/978-3-030-17971-7>

© Springer Nature Switzerland AG 2020

This work is subject to copyright. All rights are reserved by the Publisher, whether the whole or part of the material is concerned, specifically the rights of translation, reprinting, reuse of illustrations, recitation, broadcasting, reproduction on microfilms or in any other physical way, and transmission or information storage and retrieval, electronic adaptation, computer software, or by similar or dissimilar methodology now known or hereafter developed.

The use of general descriptive names, registered names, trademarks, service marks, etc. in this publication does not imply, even in the absence of a specific statement, that such names are exempt from the relevant protective laws and regulations and therefore free for general use.

The publisher, the authors and the editors are safe to assume that the advice and information in this book are believed to be true and accurate at the date of publication. Neither the publisher nor the authors or the editors give a warranty, expressed or implied, with respect to the material contained herein or for any errors or omissions that may have been made. The publisher remains neutral with regard to jurisdictional claims in published maps and institutional affiliations.

This Springer imprint is published by the registered company Springer Nature Switzerland AG
The registered company address is: Gewerbestrasse 11, 6330 Cham, Switzerland

Organization

Almir Badnjevic	Conference Chair Bosnia and Herzegovina Medical and Biological Engineering Society
Ranko Škrbić	Conference Chair University of Banja Luka, Bosnia and Herzegovina

Program Chairs

Lejla Gurbeta	Bosnia and Herzegovina Medical and Biological Engineering Society, Bosnia and Herzegovina
Juan Low	Springer Nature, Singapore
Almir Badnjevic	Bosnia and Herzegovina Medical and Biological Engineering Society

Program Committee

Abdulhamit Subasi	Effat University, Jeddah, Saudi Arabia
Adnan Beganovic	University Clinical Center Sarajevo, Bosnia and Herzegovina
Aida Sapcanin	University of Sarajevo, Bosnia and Herzegovina
Aleksandar Karac	University of Zenica, Bosnia and Herzegovina
Aljo Mujcic	University of Tuzla, Bosnia and Herzegovina
Amina Kozarić	International Burch University Sarajevo, Bosnia and Herzegovina
Anne Humeau-Heurtier	University of Angers, France
Antonio Pedotti	Politecnico di Milano, Italy
Baki Karaböce	Ulusal Metroloji Enstitüsü (UME) TÜBİTAK, Turkey
Božidar Ferek	Medtronic, Croatia
Christopher James	University of Warwick, United Kingdom
Damijan Miklavčić	University of Ljubljana, Slovenia
Damir Marjanović	International Burch University Sarajevo, Bosnia and Herzegovina
Dragan Primorac	University of Zagreb, Croatia
Eddie Custovic	La Trobe University, Australia
Edhem Haskovic	University of Sarajevo, Bosnia and Herzegovina
Elmedin Mesic	University of Sarajevo, Bosnia and Herzegovina
Emir Zunic	University of Sarajevo, Bosnia and Herzegovina
Enisa Omanovic Miklicanin	University of Sarajevo, Bosnia and Herzegovina
Ernesto Iadanza	Florence University, Italy
Ervin Sejdic	University of Pittsburg, USA
Fahir Becic	University of Sarajevo, Bosnia and Herzegovina

Goran Ristic	Faculty of Electronic Engineering, University of Nis
Igor Lackovic	University of Zagreb, Croatia
Jasmin Azemovic	University "Dzemal Bijedic" Mostar, Bosnia and Herzegovina
Jasmin Kevric	International Burch University, Bosnia and Herzegovina
Lana Nezic	University of Banja Luka, Bosnia and Herzegovina
Leandro Pecchia	University of Warwick, United Kingdom
Lejla Mehmedovic	University of Tuzla, Bosnia and Herzegovina
Leonardo Bocchi	University of Florence, Italy
Mario Medvedec	University Hospital Center Zagreb, Croatia
Matej Zajc	University of Ljubljana, Slovenia
Mirjana Maksimovic	University of East Sarajevo, Bosnia and Herzegovina
Miroslav Koncar	Oracle Healthcare Zagreb, Croatia
Mirsada Hukic	Academy of sciences and arts of Bosnia and Herzegovina
Mirza Dedic	University of Sarajevo, Bosnia and Herzegovina
Mohamed Ragab Ibrahim	International University of Sarajevo, Bosnia and Herzegovina
Monia Avdic	International Burch University, Bosnia and Herzegovina
Nenad Filipovic	University of Kragujevac, Serbia
Paulo de Carvalho	University of Coimbra, Portugal
Radovan Stojanović	University of Montenegro, Montenegro
Ranko Skrbic	University of Banja Luka, Bosnia and Herzegovina
Ratko Magjarevic	University of Zagreb, Croatia
Sabina Semiz	International University of Sarajevo, Bosnia and Herzegovina
Safija Herenda	University of Sarajevo, Bosnia and Herzegovina
Sinisa Car	University of Zagreb, Croatia
Sven Loncaric	University of Zagreb, Croatia
Tamer Bego	University of Sarajevo, Bosnia and Herzegovina
Tarik Uzunovic	University of Sarajevo, Bosnia and Herzegovina
Thomas Penzel	Charite University Hospital Berlin, Germany
Tomislav Pribanic	University of Zagreb, Croatia
Vedran Bilas	University of Zagreb, Croatia
Vesna Spasić-Jokic	University of Novi Sad, Serbia
Vukoman Jokanovic	Vinča Institute, University of Belgrade, Serbia
Yves Lemoigne	IFMP Ambilly France & CERN, Switzerland
Zdenka Babic	University of Banja Luka, Bosnia and Herzegovina

Preface

International Conference on Medical and Biological Engineering in Bosnia and Herzegovina (CMBEBIH) is an exciting, informative, and inspiring conference with the aim of sharing ideas, experiences, best practices, and the latest advancements in Medical and Biological Engineering and all related fields while staying true to the conference motto: “*Share the Vision.*”

Our mission is to promote biomedical engineering worldwide, especially in the region of Southeast Europe (SEE), as well as to establish and strengthen scientific collaborations.

We bring together leading researchers, academic scientists, engineers, and scholars together with amazing speakers who we have invited to create a platform for discussion on latest findings, innovative solutions, and emerging challenges with which this field is facing with, in order to improve quality of health care and life in general.

The conference is a continuation of the extensive work conducted by the Bosnia and Herzegovina Medical and Biological Engineering Society to encourage and support the development of Medical and Biological Engineering in Bosnia and Herzegovina and SEE region. The predecessor conference yielded great results with eight eminent keynote speakers from all around the world, 120 oral presentations, 50 poster presentations, and 3 international workshops.

Research and development in these areas are impacting the science and technology by advancing fundamental concepts in health care. They are helping us to better understand human physiology and function at multiple levels by improving tools and techniques for the detection, prevention, treatment, and management in health care. The 2019 program consists of 115 accepted papers on new developments encompassing the conference theme.

More specifically, the parallel scientific sessions cover the topics of biomedical signal processing, medical physics, biomedical imaging and radiation protection, biosensors and bioinstrumentation, bio-micro/nanotechnologies, biomaterials, biomechanics, robotics and minimally invasive surgery, cardiovascular, respiratory and endocrine systems engineering, bioinformatics and computational biology, clinical engineering and health technology assessment, health informatics, e-health and telemedicine, artificial intelligence and machine learning in health care, pharmaceutical engineering, genetic engineering, and student competition session.

International workshops include topics of Clinical Engineering and Health Technology Assessment with the aim of development of the Institutes in Bosnia and Herzegovina for the region of Southeast Europe.

During the conference, the EAMBES Council meeting, General Assembly meeting, and roundtable discussion between EAMBES council members and EAMBES fellows were held.

Furthermore, the conference program is highlighted by the seven keynote lecturer sessions. All sessions discuss different areas of Medical and Biological (biomedical) engineering and are moderated by prominent experts and professionals in the area.

The session held by Dr. Hani Al Salami (Australia), Professor at Faculty of Health Sciences at Curtin University, Australia. The title of his lecture is “*Biotechnological advancement in drug delivery and tissue engineering: Future prospective.*”

Another interesting lecture about the latest research in the field of drug delivery was held by Dr. Zimei Wu from University of Auckland (New Zealand). The title of her lecture was: “*Tumor Micro-Environment Sensitive Liposomes for Targeted Drug Delivery.*”

Dr. Borut Strukelj from University of Ljubljana (Slovenia) held a keynote lecture titled: “*Pharmaceutical Engineering of Recombinant Probiotics—Novel Delivery System of Advanced Biological Medicines.*”

Keynote lecture entitled “*Electroporation based treatments and therapies*” is held by Dr. Damijan Miklavcic from University of Ljubljana (Slovenia). He is one of the leading world researchers in the field of electroporation as the basis of drug delivery into cells in tumor models in vitro and in vivo.

Keynote lecture in the area of processing of biomedical signals is held by Dr. Ervin Sejdic, University of Pittsburgh (USA), and focus on discussing the latest advancements of usage of big data to understand functional changes in swallowing, gait, and handwriting. The title of his lecture is “*Computational deglutition—A novel computational field to understand swallowing and associated disorders.*”

“*Design a fabrication of microfluidic chips in different technologies for biomedical applications*” was a keynote lecture held by Dr. Goran Stojanovic from University of Novi Sad (Serbia).

The latest advancements in the field of bioinformatics were presented by Dr. Natasa Przulj from University College London (UK).

We express our gratitude to the kind support and effort of international organizations such as IFMBE, EAMBES, IEEE, and ESEM for endorsing this project, as well as our publisher Springer Nature. Furthermore, there is a number of industry sponsors for which support we are sincerely thankful.

Finally, a heartfelt thanks to all of you, the participants, for your outstanding contributions. We wish you all the best with your ongoing and future research in advancing Medical and Biological Engineering for humanity. We hope that you will come again together with your colleagues to our next CMBEBIH Conferences and together with us create opportunities for professional growth and networking with a fellow scientist, engineers, and other enthusiasts. It is our vision that this conference creates a lasting memory of Bosnia and Herzegovina and that the networking enables successful and ongoing collaborations among fellow professionals.

Banja Luka, Bosnia and Herzegovina
May 2019

Sincerely,
Prof. Dr. Almir Badnjevic
Prof. Dr. Ranko Škrbić
CMBEBIH 2019 Conference Chairs

Contents

Part I Biomedical Signal Processing

Adaptive Filter Removes Variability Caused by Respiration from Impedance Cardiography Signal	3
Marek Źyliński, Małgorzata Wojciechowska, Wiktor Niewiadomski, Marta Sadowiec, Sonia Borodzicz, and Gerard Cybulski	
Electrical Stimulation of Eye Blink in Individuals with Dry Eye Symptoms Caused by Chronic Unilateral Facial Palsy	7
J. Lylykangas, M. Ilves, H. Venesvirta, V. Rantanen, E. Mäkelä, A. Vehkaoja, J. Verho, J. Leikkala, M. Rautiainen, and V. Surakka	
Prescribe and Monitor Physical Activity Through a Community-Based eHealth Program: MOVIDA Platform	13
Rui Fonseca-Pinto, Rui Rijo, Pedro Assunção, Maria Alexandra Seco, Maria P. Guarino, Cátia Braga-Pontes, Dulce Gomes, Bruno Carreira, Pedro Correia, Luís Oliveira, Gabriel Pires, Catarina Leitão, Alexandre Antunes, Filipa Januário, and Ricardo Martinho	
Miniaturized Stimulator for Imaging of Live Cell Responses to High Frequency Mechanical Vibration	21
Heidi T. Halonen, Jari A. K. Hyttinen, and Teemu O. Ihalainen	
EMG Signal Classification Using Discrete Wavelet Transform and Rotation Forest	29
Abdulhamit Subasi and Emine Yaman	
Impact of High Frequency Electromagnetic Fields on Process of Angiogenesis	37
Smiljana Paraš, Nataša Vojinović, and Ljiljana Amidžić	
Implementation of Neural Network-Based Classification Approach on Embedded Platform	43
Rijad Sarić, Dejan Jokić, and Nejra Beganović	
Stereo Laser Speckle Dissimilarity Analysis Using Self-organizing Maps	51
Francisco Cunha, Luís Távora, Pedro Assunção, Sérgio Faria, and Rui FonsecaPinto	
Wavelet Phase Coherence Analysis Between the Respiratory Activity and the Microcirculation: The Effects of Type 1 Diabetes	61
Michele Sorelli, Antonia Perrella, Piergiorgio Francia, and Leonardo Bocchi	
Prostate Cancer Detection Using Different Classification Techniques	67
Jasna Nuhić and Jasmin Kevrić	

Application of a Computer-Aided Diagnostic System for Early Identification of Periapical Lesions—A Pilot Study	75
Ahmed Osmanovic, Sabina Halilovic, Samed Jukic, Jasmin Kevric, and Naida Hadziabdic	
Vectorcardiogram eLearning Application	81
Sanda Sljivo, Dusanka Boskovic, and Orhan Lepara	
Evaluating MSE Applicability to Short HR Time-Series	87
Boris Dragojevic and Dusanka Boskovic	
Automatic Detection of Alzheimer Disease Based on Histogram and Random Forest	91
Emina Alickovic and Abdulhamit Subasi	
 Part II Medical Physics, Biomedical Imaging and Radiation Protection	
A Dosimetric Analysis of the Overlapping and Gap Areas Produced by Simulated Set-Up Errors on a Treatment Planning System in a Case of the Cranio-Spinal Irradiation of an Adult Patient	99
Edis Đedović, Hasan Osmić, Muhamed Topčagić, and Nermina Karaman	
Novel Physical Heterogeneous Breast Phantom for X-Ray Phase Contrast Imaging	105
A. Daskalaki, A. Malliori, A. Dermitzakis, and N. Pallikarakis	
Computer Tomography Tube Voltage and Phantom Dimensions Influence on the Number of Hounsfield Units	111
Tatjana Ignjic, Bojan Pavicar, Goran Kolarevic, and Zeljko Ranogajec	
Dose Optimization of CT Thorax Exam in University Clinical Hospital Mostar	119
Ivan Lasić, Kristina Galić, Adnan Beganović, Valentina Lasić, Lejla Čiva, and Antonela Krasić-Arapović	
Radiation Exposure of Patients in Neonatal Intensive Care Unit	125
Adnan Beganović, Irmina Sefić-Pašić, Maja Gazdić-Šantić, Rahima Jašić, Amra Skopljak-Beganović, Adnan Šehić, and Sandra Vegar-Zubović	
Use of Uptake Values to Estimate the Effective Dose to Patients in Positron Emission Tomography	131
Adnan Beganović, Rahima Jašić, Maja Gazdić-Šantić, Amra Skopljak-Beganović, Nermina Bešlić, Šejla Cerić, Amra Šadija, and Sandra Vegar-Zubović	
Evaluation of Computed Tomography X-Ray Beam Dose Profiles	137
Lejla M. Čiva, Adnan Beganović, Mahira Redžić, Ivan Lasić, Maja Gazdić-Šantić, Amra Skopljak-Beganović, Rahima Jašić, and Sandra Vegar-Zubović	
Comparison of Specific Fractal and Multifractal Parameters for Certain Regions of Interest from Digital Mammograms	143
Edis Đedović, Azra Gazibegović–Busuladžić, Mustafa Busuladžić, and Adnan Beganović	
Diagnosis of Severe Aortic Stenosis Using Implemented Expert System	149
Lejla Divović Mustafić, Lejla Gurbeta, Alma Badnjevic-Cengic, Almir Badnjević, Behija Berberović Hukeljić, Tamer Bego, and Omer Perva	

Portable X-Ray Devices: Loosing Border Between Controlled and Supervised Areas	155
Jovica Ž. Praskalo, Biljana V. Petrović, and Adnan Beganović	
Effectiveness of Asymmetry Analysis Technique Based on Statistical Features in Breast Cancer Detection with Modern Thermographic Imaging Systems	159
Irfan Karagoz	
Part III Biosensors and Bioinstrumentation	
Microneedle-Based Sensor Systems for Real-Time Continuous Transdermal Monitoring of Analytes in Body Fluids	167
Edina Vranić, Amina Tucak, Merima Sirbubalo, Ognjenka Rahić, Alisa Elezović, and Jasmina Hadžiabdić	
Review of Electrochemical Biosensors for Hormone Detection	173
Selma Cifrić, Jasna Nuhić, Dina Osmanović, and Emina Kišija	
Development of a Tray-Separated Microbiological Incubator by Means of Electronic Components and Testing Its Performance	179
Tarik Ibrahimpašić and Dejan Jokić	
Honeybee Activity Monitoring in a Biohybrid System for Explosives Detection	185
Mitar Simić, Ross Gillanders, Aleksej Avramović, Slavica Gajić, Vedran Jovanović, Vladan Stojnić, Vladimir Risojević, James Glackin, Graham Turnbull, Janja Filipi, Nikola Kezić, Mario Muštra, and Zdenka Babić	
HaBEEtat: A Novel Monitoring Platform for More Efficient Honey Production	193
Semir Sakanovic and Jasmin Kevric	
Design and Implementation of a Monitoring System for Elastomeric Infusion Pumps	201
Andrea Felici, Michele Sorelli, and Leonardo Bocchi	
Wearable System for Early Diagnosis and Follow Up of Spine Curvature Disorders	205
E. Valchinov, K. Rotas, A. Antoniou, V. Syrimpeis, and N. Pallikarakis	
Part IV Bio-micro/nano Technologies	
Biogenic Nanoparticle Synthesis Using Marine Alga <i>Schizochytrium</i> sp.	213
Tuğçe Mutaf, Gülizar Çalışkan, Cafer Meydan, Suphi Şurişvan Öncel, and Murat Elibol	
Green Synthesis of Metal Nanoparticles Using Microalga <i>Galdieria</i> sp.	219
Gülizar Çalışkan, Tuğçe Mutaf, Suphi Şurişvan Öncel, and Murat Elibol	
HIV Infection Mathematical Modeling and Future Trends of Treatment Using Nanotechnology and Nanorobots	225
Nataša Popović, Milica Naumović, and Sonja Roganović	
Nanomaterials as a Tool for Consumer Research	235
Zvezdana Gavrilović and Mirjana Maksimović	

Near IR Exciton Theory of Ultrathin Crystalline Film Optics and Possibilities for Drug Delivery	239
S. M. Vučenočić, J. P. Šetrajčić, and A. J. Šetrajčić-Tomić	
Phonon Engineering in Nanostructures for Targeted Drug Delivery	245
Dušan I. Ilić, Silviya Lučić, Saša Vujnović, Li Sen, Ranko Škrbić, and Miloš A. Lučić	
Zeolite Microneedles: Recent Advancements and Implications in the Delivery of Collagen	251
Amar Ramović, Zerina Zorlak, Đenana Husić, and Samir Ramić	
Application of Raman Spectroscopy in Food Forensics: A Review	257
Anera Kazlagić and Enisa Omanović-Miklićanin	
 Part V Biomaterials, Biomechanics, Robotics and Minimally Invasive Surgery	
Evaluation of Several Microalgal Extracts as Bioactive Metabolites as Potential Pharmaceutical Compounds	267
Ceren Gürlek, Çağla Yarkent, Ayşe Köse, İzel Oral, Suphi Ş. Öncel, and Murat Elibol	
A Novel Approach in Determination of Biofilm Forming Capacity of Bacteria Using Random Forest Classifier	273
Monia Avdić, Zerina Mašetić, Ahmed El Sayed, Lejla Odošević, and Mirsada Hukić	
Analysis of Vertical Ground Reaction Force and Center of Pressure During Stair Climbing	281
Vesna Raspudić	
Reference Tracking of the Robotic Above-Knee Prosthetic Leg with Actuated Knee and Ankle Joints Using Robust Control	287
Zlata Jelačić and Remzo Dedić	
Comparison of CFD-Computation Fluid Dynamics Analysis of Shorter Designed Stent Graft in Abdominal Aorta	293
Aida Botonjić Karahusić, Tino Kostić, and Nedim Begić	
 Part VI Cardiovascular, Respiratory and Endocrine Systems Engineering	
A Novel Enzymatic Microreactor: Towards Transforming the Pharmaceutical Industry	303
Medina Hamidović, Ferenc Ender, and Andreas Springer	
Modeling of Voltage Imaging for the Study of Action Potential Propagation	309
Pietro Tarchi, Francesca Bologna, Costanza Scortecci, Eleonora Tiribilli, Diletta Pennati, Leonardo Sacconi, Michele Sorelli, and Leonardo Bocchi	
Atherosclerotic Plaque Formation in the Coronary Arteries	315
Igor Saveljic, Dalibor Nikolic, Zarko Milosevic, and Nenad Filipovic	
Coronary Angiography Evaluation of Atherosclerosis in Diabetic Patients	321
Aida Hasanović, Aida Šapčanin, and Jakub Hasanović	
Optimizing Insulin Pump Therapy: Advanced Bolus Options	325
Bojana Radošević Carić, Blaženko Vuković, and Katarina Lalić	
Parametric Optimization of Stent Design Based on Numerical Methods	331
Dalibor Nikolić, Igor Saveljić, and Nenad Filipović	

Numerical Analysis of Plaque Progression in 3D Patient Specific Model of Carotid Artery	337
Smiljana Djorovic, Igor Saveljic, and Nenad Filipovic	
Forth Heart Sound Detection Using Backward Time-Growing Neural Network	341
Arash Gharehbaghi, Amir A. Sepehri, and Ankica Babic	
Part VII Bioinformatics and Computational Biology	
Using Data Science for Medical Decision Making Case: Role of Gut Microbiome in Multiple Sclerosis	349
Jasminka Hasic Telalovic and Azra Music Kilic	
Discovery of Membrane Permeability, Pharmacokinetics Properties and Mechanism of Action for Analogs of Ethylenediamine-<i>N,N'</i>-di-2-(3-Cyclohexyl) Propionic Acid and 1,3-Propandiamine-<i>N,N'</i>-di-2-(3-Cyclohexyl) Propionic Acid with Antiproliferative Activity Using In Vitro and In Silico Methods	357
Biljana Tubić, Bojan Marković, and Tibor Sabo	
Analysis of miRNA Targets in Correlation to Neurodevelopment and Diagnosis of Autism Spectrum Disorder (ASD)	371
Emir Šehović, Lemana Spahić, Ajla Kulaglič, Lejla Smajlović-Skenderagić, and Aida Hajdarpašić-Saračević	
Discrete Modelling of Liver Cell Aggregation Using Partial Differential Equations	379
Tijana Sustersic, Milica Nikolic, Nihal Engin Vrana, and Nenad Filipovic	
Part VIII Clinical Engineering and Health Technology Assessment	
Smart Ageing: Are We Succeeding?	387
Jasmina Baraković Husić, Sabina Baraković, and Enida Cero Dinarević	
A New Digital Mental Health System Infrastructure for Diagnosis of Psychiatric Disorders and Patient Follow-Up by Text Analysis in Turkish	395
Zeynep Orhan, Mine Mercan, and Merve Kevser Gökgöl	
Only All Together We Can Make It Better on Any Strategic Matter	403
M. Medvedec and M. Poluta	
Designing a Healthcare Computer Aided Facility Management System: A New Approach	407
Ernesto Iadanza, Alessio Luschi, Roberto Gusinu, and Filippo Terzaghi	
System for Monitoring Environmental Parameters in a Hospital Facility	413
Alessio Luschi, Riccardo Di Franco, Beatrice Turillazzi, and Ernesto Iadanza	
Adverse Drug Events (ADEs): A Novel RFID Device for a Safe and Strong Match Between Patients and Their Medications	417
Ernesto Iadanza, Cesare Massaro, and Leonardo Vonci	
Donation of Medical Devices in Low-Income Countries: Preliminary Results from Field Studies	423
Davide Piaggio, Daton Medenou, Roland C. Houessouvo, and Leandro Pecchia	

eVerlab: Software Tool for Medical Device Safety and Performance Inspection Management	429
Lejla Gurbeta, Almir Badnjević, and Emina Kurta	
Establishment of Measurement System for Hearing Aids at TÜBİTAK UME	437
Baki Karaböce, Hüseyin Okan Durmuş, and Emel Çetin	
The Importance of Metrology in Medicine	443
Baki Karaböce, Hüseyin Okan Durmuş, and Emel Çetin	
Part IX Health Informatics, E-health and Telemedicine	
Towards Pain-Fingerprinting: A Ubiquitous and Interoperable Clinical Decision Support System for Pain Assessment	453
Nuno Pombo and Nuno M. Garcia	
Identification of Alcohol Addicts Among High School Students Using Decision Tree Based Algorithm	459
Rijad Sarić, Dejan Jokić, and Edhem Čustović	
Identification of Real and Imaginary Movements in EEG Using Machine Learning Models	469
Joana Moreira, Mariana Moreira, Nuno Pombo, Bruno M. C. Silva, and Nuno M. Garcia	
Development of a Diagnostic Support Software in the Clinicobiochemical Evaluation of Thyroid Disease Diagnosis	475
Arnela Tarakčija, Vedad Terzić, Almir Vardo, Sabrina Smajlović, Sabilja Zečiri, Selma Imamović, Tanja Dujić, Maja Malenica, and Tamer Bego	
Part X Artificial Intelligence and Machine Learning in Healthcare	
Machine Learning Techniques for Performance Prediction of Medical Devices: Infant Incubators	483
Lemana Spahić, Emina Kurta, Sabahudin Ćordić, Merjem Bećirović, Lejla Gurbeta, Zivorad Kovacevic, Sebija Izetbegovic, and Almir Badnjevic	
Prediction of Heart Diseases Using Majority Voting Ensemble Method	491
Dželila Mehanović, Zerina Mašetić, and Dino Kečo	
Predicting the Outcome of Granulation and Tableting Processes Using Different Artificial Intelligence Methods	499
Nermina Sokolović, Majda Ajanović, Samir Badić, Miljana Banjanin, Mirna Brkan, Naida Čusto, Barbara Stanić, Merima Sirbubalo, Amina Tucak, and Edina Vranić	
Lactose Intolerance Prediction Using Artificial Neural Networks	505
Lemana Spahić, Emir Šehović, Alem Šećerović, Zerina Đozić, and Lejla Smajlović-Skenderagić	
Comparative Study on Different Classification Techniques for Ovarian Cancer Detection	511
Jasna Nuhić, Lemana Spahić, Sabahudin Ćordić, and Jasmin Kevrić	
Normalized Neural Networks for Breast Cancer Classification	519
Emina Alickovic and Abdulhamit Subasi	

Part XI Pharmaceutical Engineering

Landscape of <i>CYP3A5</i> Variants in Central-Eastern and South European Populations	527
Gražyna Adler, Izabela Uzar, Anastazja Kazlova, Amina Valjevac, Emina Kiseljakovic, Emir Mahmutbegovic, Nermin N. Salkic, Mateusz A. Adler, Nevena Mahmutbegovic, Maciej Grabowski, and Ewa Rębacz-Marón	
Development of Inhalable Dry Gene Powders for Pulmonary Drug Delivery by Spray-Freeze-Drying	533
Edina Vranić, Merima Sirbubalo, Amina Tucak, Jasmina Hadžiabdić, Ognjenka Rahić, and Alisa Elezović	
Antimicrobial Activity of Selected Wild Mushrooms from Different Areas of Bosnia and Herzegovina	539
Mirsada Salihović, Aida Šapčanin, Selma Špirtović-Halilović, Irma Mahmutović-Dizdarević, Anesa Jerković-Mujkić, Elma Veljović, Ekrem Pehlić, Fuad Gaši, and Sabilja Zečiri	
Effects of ^{99m}Tc on the Redox Properties of L-Thyroxine	543
Safija Herenda, Anera Kazlagić, Edhem Hasković, and Denis Hasković	
Novel Aspects of Drug Delivery: Wireless Electronic Devices	547
Berina Tatlić, Lejla Šejto, Merima Sirbubalo, Amina Tucak, and Edina Vranić	
Quantification of Active Substances in Some Drugs Using by Derivative UV/Vis spectroscopy	553
A. Etminan, A. Uzunović, A. Topčagić, S. Žero, M. Dizdar, L. Klepo, D. Čulum, H. Džudžević-Čančar, and I. Tahirović	
In Vitro Evaluation of Transdermal Patches Containing Capsaicin Marketed in Bosnia and Herzegovina	559
A. Uzunovic, M. Dacic, Z. Ademovic, S. Osmanovic, S. Pilipovic, and A. Sapcanin	
UV-VIS Determination of Acetylsalicylic Acid in Aspirin Tablets Using Different Solvents and Conditions	563
M. Dacić, A. Uzunović, A. Kunić, S. Pilipovic, and A. Šapčanin	
Lysozyme-Enzybiotic with Valuable Effects in Prevention and Treatment of Postoperative Complications in Adult Patients After Bilateral Tonsillectomy	569
Begović Begler, Vehabović Midhat, Amila Šahinpašić, and Una Glamočlija	
Use of Hollow Microneedle Drug Delivery Systems in Treatment of Diabetes Mellitus	575
Anesa Sušić, Zekira Hrnjica, Ilma Kajgana, Minela Mujezinović, Alma Hasanbegović, Jelena Brčkalo, Amina Tucak, Merima Sirbubalo, and Edina Vranić	
Toxicity of Azo Dyes in Pharmaceutical Industry	581
Armina Gičević, Lamija Hindija, and Alma Karačić	
Genes Associated With Free Fatty Acid Levels and Dyslipidemia in Type 2 Diabetes Patients	589
S. Mandal	

Part XII Genetic Engineering

Correlation of Leukemia Genes Overexpression and Point Mutations in Different Tissues	597
Fatima Mrkulić, Lejla Gurbeta, Enisa Omanović-Miklićanin, Tamer Bego, Berina Hasanefendić, and Almir Badnjević	
Craniometric Analysis of the Foramen Magnum for Gender Determination in Bosnian Human Skulls	605
Zurifa Ajanović and Aida Sarač-Hadžihalilović	
Liver Enzymes as Biomarkers for Hepatotoxicity of Statins in Patients with Dyslipidemia	611
N. Velickova, M. Nateva, and S. Stojanovska	
Impact of Antibiotic Misuse on Genetics Alterations of Bacteria	617
Emina Aruković, Dina Fetahović, and Belma Pehlivanović	
Diagnosis of Skin Disease Based on Fingerprint	623
Selena Kurtić and Zvezdan Stojanović	
Epigenetics: How Does It Affect Cancer?	629
Letícia Vieira da Silva, Bruno Oliveira Rezende, Hiara Lopes Pinheiro Teixeira, Bianca da Silva Duque, and Gisele Aparecida Fófano	
Screening of Heavy Metal Occurrence in Edible Plants from Bosnian Market	635
Aida Sapcanin, Aida Hasanovic, Mirsada Salihovic, Ekrem Pehlic, and Selma Špiritović-Halilović	
Genetic Polymorphism β-Lactoglobulin Gene in Dubska Pramenka Sheep Breed	641
Amela Masala, Ivona Alilović, Husein Ohran, Szilvia Kusza, Teufik Goletic, Amina Hrkovic-Porobija, and Aida Hodzic	
Part XIII Student Competition Session	
Prostate Tissue Classification Based on Prostate-Specific Antigen Levels and Mitochondrial DNA Copy Number Using Artificial Neural Network	649
Lemana Spahić and Sabahudin Ćordić	
Influence of Artificial Microgravity on Human Arterial Vessels	655
S. Akulov, A. Fedotov, I. Makarov, A. Sidorov, and A. Kosheleva	
Using the Distance in Logistic Regression Models for Predictor Ranking in Diabetes Detection	665
Ghazaal Sheikhi and Hakan Altınçay	
Expert System for Performance Prediction of Anesthesia Machines	671
Lejla Hadžić, Arnela Fazlić, Osman Hasanić, Nudžejma Kudić, and Lemana Spahić	
Smoking and Caffeine Consumption as Stress Coping Mechanisms in Medical Students	681
Lejla Šabić and Adnan Mujanović	
Review of Biosensors in Industrial Process Control	687
Emina Kišija, Dina Osmanović, Jasna Nuhić, and Selma Cifrić	

The Assessment of Drug Interactions and Safety of Administration with Regard to Special Population Groups by a Developed Computer Program	695
Vanja Piljak, Belma Muftić, Sukejna Redžepi, Mirza Dedić, and Nermina Žiga	
Implementing the Calculation of the Appropriate Drug Dose for Children Using the Programming Language C#	705
Sukejna Redžepi, Belma Muftić, Vanja Piljak, Nermina Žiga, and Mirza Dedić	
ORÁO: RESTful Cloud-Based Ophthalmologic Medical Record for Chromatic Pupillometry	713
Ernesto Iadanza, Rachele Fabbri, Alessio Luschi, Francesca Gavazzi, Paolo Melillo, Francesca Simonelli, and Monica Gherardelli	
A Language Independent Decision Support System for Diagnosis and Treatment by Using Natural Language Processing Techniques	721
Merve Kevser Gökgöl and Zeynep Orhan	
Fabrication of Rectal and Vaginal Suppositories Using 3D Printed Moulds: The Challenge of Personalized Therapy	729
Sarah Krezić, Esved Krhan, Emir Mandžuka, Nikolina Kovač, Danira Krajina, Amina Marić, Sajra Komić, Azra Nikšić, Amina Tucak, Merima Sirbubalo, and Edina Vranić	
Coated 3D Printed PLA Microneedles as Transdermal Drug Delivery Systems	735
Mirela Camović, Amila Biščević, Iman Brčić, Kana Borčak, Sadžida Bušatlić, Nejra Čenanović, Anida Dedović, Alen Mulalić, Maida Osmanlić, Merima Sirbubalo, Amina Tucak, and Edina Vranić	
Development of a Diagnostic Support Software in the Clinicobiochemical Evaluation of Secondary Amenorrhea Diagnosis	743
Nikolina Begović, Amina Džih, Lamija Aliman, Igor Đukić, Arnela Tarakčija, Vedad Terzić, Neven Meseldžić, Selma Imamović, Tanja Dujjić, Maja Malenica, and Tamer Bego	
Acid-Resistant Capsules with Sugar Microneedles for Oral Delivery of Ascorbic Acid	749
Mirela Camović, Amila Biščević, Iman Brčić, Kana Borčak, Sadžida Bušatlić, Nejra Čenanović, Anida Dedović, Alen Mulalić, Merima Sirbubalo, Amina Tucak, and Edina Vranić	
Effect of Commercially Available Synthetic Insulin on the Biofilm Formation in <i>S. aureus</i> and <i>E. coli</i> Bacterial Strains	755
Jasmin Novalić and Berina Bektić	
Use of Biosensors in Diabetes Monitoring: Medical and Economic Aspects	761
Haris Hadžović, Minela Alić, Anida Dedović, Anesa Sušić, Berina Tatlić, Zerina Zorlak, Nermina Žigić, Maja Malenica, and Tamer Bego	
Therapeutic Aspects and Diagnosis of the Attention Deficit Hyperactivity Disorder—ADHD in Adults	769
Samuell Ferreira, Rubens Zeron, Guilherme Carvalho, Lara Gandra, Victoria Carestiato, Alice Bastos, Juliana Silva, and Adnan Mujanović	

Predicting the Severity of a Mammographic Tumor Using an Artificial Neural Network	775
Laila Mušić and Nusreta Gabeljić	
Author Index	779

Part I

Biomedical Signal Processing

Adaptive Filter Removes Variability Caused by Respiration from Impedance Cardiography Signal

Marek Żyliński, Małgorzata Wojciechowska, Wiktor Niewiadomski, Marta Sadowiec, Sonia Borodzicz, and Gerard Cybulski

Abstract

Impedance cardiography (ICG) allows to measure parameters of heart mechanical function. ICG is sensitivity to movement artifacts inter alia breathing, which distorts impedance signal. Several methods were proposed to eliminate this distortion, but they cannot be used to continuous measurement or do not remove movement artifact. Adaptive filter is event-related, it learns signal characteristic within the cycle and removes components uncorrelated with the event. In this study, we compared ICG signal obtained during normal breathing with that after adaptive filtration and ICG signal obtained during momentary breath holding with this signal processed with adaptive filter. We conclude that adaptive filtering may help extract information from noisy and distorted ICG signal, but on the other hand, it may obscure some real changes in signal, for instance, rapid cyclic changes connected with respiration.

volume during cardiac cycle. ICG can be used to estimate stroke volume (SV), pre-ejection period (PEP) and ejection time (ET) [1]. This method is simple, cost-effective, noninvasive and allows for continuous measurement.

Origin of ICG signal is not clear [2], it is possible that it reflects not only changes of blood volume in aorta but also in atria and in lungs [3]. In some subjects, main deflection of the signal associated with blood ejection from ventricles is followed by second deflection, termed O wave. It is suggested that O wave is associated with an opening snap of the mitral valve [4] and may be the symptom of the bicuspid valve malfunction.

ICG is sensitivity to movement artifacts inter alia breathing, which distorts impedance signal and in consequence, can lead to erroneous calculation of SV value. Several methods were proposed to eliminate this distortion, for instance:

- breath holding [5], of momentary duration because of obvious reason,
- signal averaging of several heart cycles [6], continuous character of ICG signal is lost,
- digital band-pass filters with narrow frequency band [7], which cannot eliminate movement artifacts because of their broad spectrum.

1 Introduction

Impedance cardiography (ICG) allows to measure parameters of heart mechanical function from changes of thorax electrical impedance, caused by the changes of blood

Laguna et al. [8] described adaptive filter for event-related bioelectric signals. This type of filter learns signal characteristic within the cycle and removes components uncorrelated with the event. ICG is time-locked to the QRS complex of ECG. Laguna et al. [9] showed that such adaptive filter could be used to filter ICG signal obtained during exercise, however, they did not compared data such obtained against reference method.

In this study, we compared ICG signal obtained during normal breathing with that after adaptive filtration and ICG signal obtained during momentary breath holding with this signal processed with adaptive filter.

M. Żyliński (✉) · M. Sadowiec · G. Cybulski
Institute of Metrology and Biomedical Engineering, Faculty of Mechatronics, Warsaw University of Technology, ul. Św. A. Boboli 8, 02-525 Warsaw, Poland
e-mail: zylinski@mchtr.pw.edu.pl

M. Wojciechowska · S. Borodzicz
Department of Experimental and Clinical Physiology, Laboratory of Center for Preclinical Research, Medical University of Warsaw, Warsaw, Poland

S. Borodzicz
1st Chair and Department of Cardiology, Medical University of Warsaw, Warsaw, Poland

W. Niewiadomski
Mossakowski Medical Research Centre, Polish Academy of Sciences, Warsaw, Poland

2 Method

2.1 The Adaptive Filter

Output of the adaptive filter for k -th heart cycle is:

$$y_k = X_k^T W_k$$

where: X_k is reference signal defined as combination of sinus and cosines values:

$$x_{i,k(m,l)} = \begin{cases} \frac{1}{\sqrt{H}} \sin\left(2\pi \frac{il}{L_m}\right); & i = 1, 3, \dots, 2H - 1 \\ \frac{1}{\sqrt{H}} \cos\left(2\pi \frac{(i-1)l}{L_m}\right); & i = 2, 4, \dots, 2H \end{cases}$$

L_m number of samples in k -th cycle,

l sample's number,

H number of harmonics necessary to reconstruct the signal, it must be greater than $\frac{L_m-1}{2}$.

W_k is weighted vector, for each cycle its values are modified, according to formula:

$$W_{k+1} = W_k + 2\mu(d_k - y_k)X_k$$

μ is time constant, it should be smaller than 0.3 to allow for the algorithm convergence, smaller values improve adjustment but increase number of iterations necessary for reaching stable output signal,

d_k input signal, in this study dz/dt , where z —electrical impedance of thorax

In first iteration weighted vector is calculate as Wiener weighted vector:

$$W_0 = R^{-1}P$$

R is input correlation:

$$R = E[X_k X_k^T]$$

P is cross correlation vector:

$$P = E[d_k X_k^T]$$

To perform adaptive filtering of the signal it is necessary to divide it into heart cycles. Most obvious solution is use of the R peak from ECG signal.

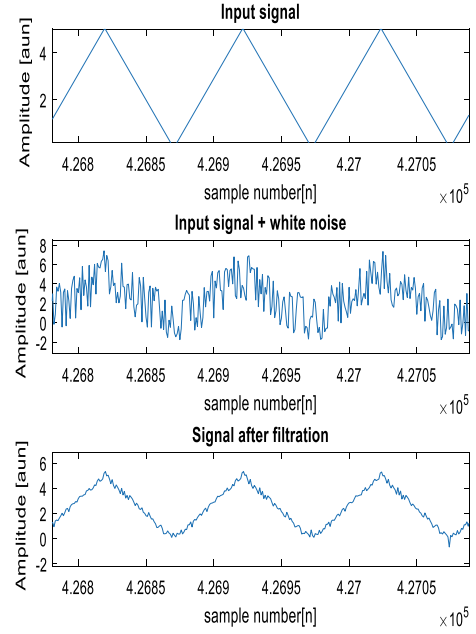


Fig. 1 Validation of adaptive filter implementation. Triangular signal was used as a reference signal (top chart), input signal consisted of reference signal and white noise (middle chart). Adaptive filter, $\mu = 0.05$, removed most of the noise (bottom chart)

We first tested our implementation of adaptive filter using a triangular wave with added noise of the same amplitude as signal. Results are shown in Fig. 1. Adaptive filter removed most of the noise from the signal ($\mu = 0.05$).

2.2 Measurement

Ten young healthy persons (5 male and 5 female) participated in the study. Subjects rested in supine position for 1 min, next they hold breath for 30 s. ECG and cardiac impedance were recorded.

For both parts of the record (rest and breath holding) adaptive filter was applied. Value of dz/dt_{\max} in each cardiac cycle was detected.

3 Results

Figure 2 shows exemplary dz/dt signal. First plot presents dz/dt signal during breath hold. Second one presents same signal after adaptive filtering. Third plot presents the signal

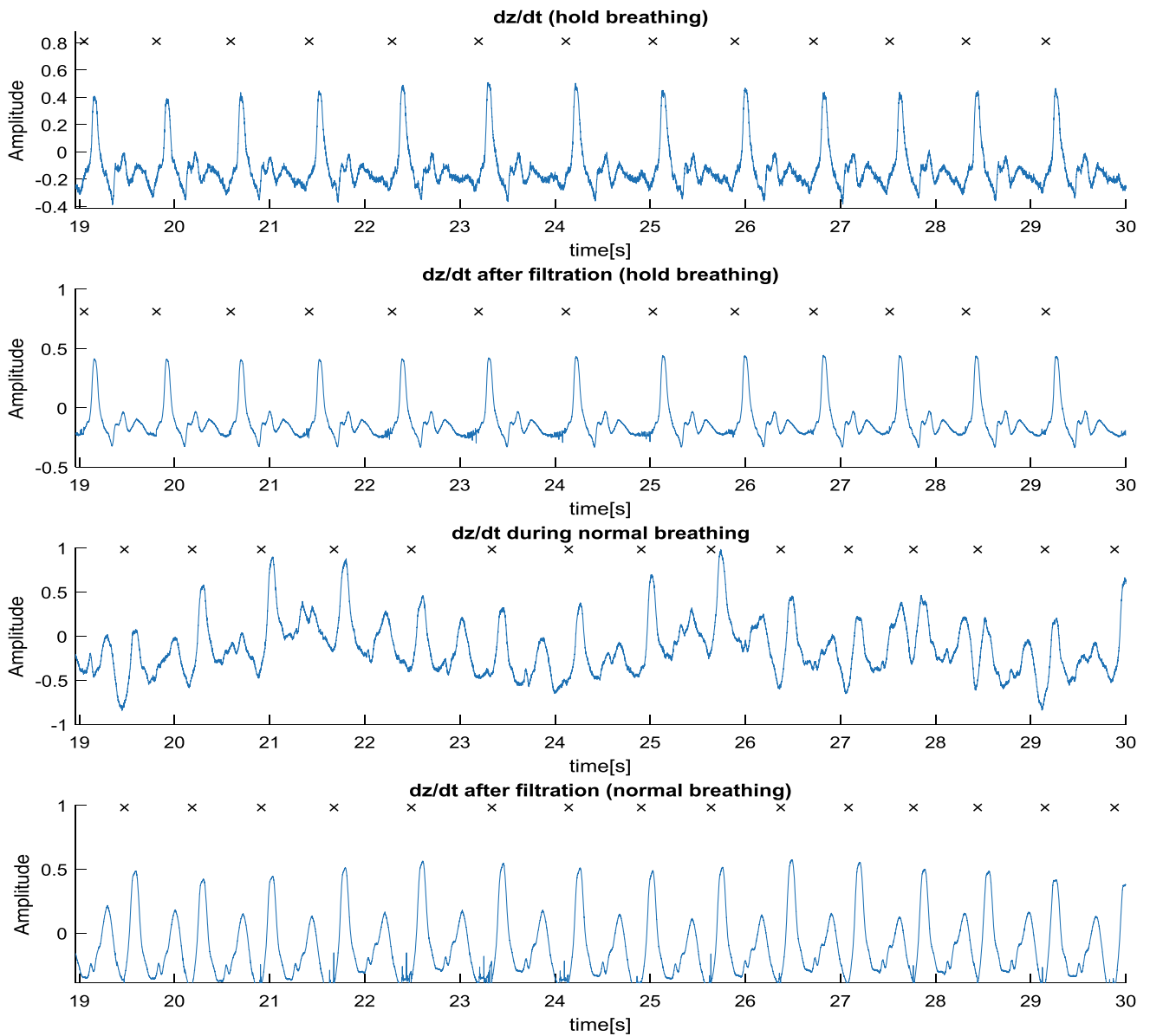


Fig. 2 Comparison of dz/dt signal, before and after adaptive filtering, recorded during breath hold and normal breathing, x—indicates R peak of ECG signal

Table 1 Mean value of dz/dt_{\max}

Patient	Breath holding	Normal breathing (raw signal)	Normal breathing (after adaptive filtering)
F1	0.52 ± 0.04	0.53 ± 0.13	0.43 ± 0.07
F2	1.19 ± 0.05	0.89 ± 0.15	0.85 ± 0.06
F3	0.63 ± 0.03	0.65 ± 0.12	0.59 ± 0.04
F4	0.59 ± 0.02	0.47 ± 0.16	0.47 ± 0.3
F5	1.88 ± 0.03	1.80 ± 0.12	1.79 ± 0.04
M1	0.56 ± 0.05	0.70 ± 0.23	0.60 ± 0.07
M2	0.71 ± 0.03	0.58 ± 0.10	0.54 ± 0.04
M3	0.13 ± 0.01	0.21 ± 0.08	0.18 ± 0.01
M4	0.63 ± 0.04	0.44 ± 0.14	0.41 ± 0.02

during normal breathing, influence of breathing is well visible. Fourth plot presents this signal after adaptive filtering.

In Table 1 mean values of the dz/dt_{\max} in each subject during breath holding, during normal breathing before and after adaptive filtering are shown.

4 Conclusion

Adaptive filter reconstructs signal in cardiac cycle using information from the past. Figure 1 depicts filter performance on synthetic data: triangular signal with white noise of the same amplitude. Adaptive filter removes almost all noise. This is a proof of utility of the adaptive filter to extract useful information even from very noisy signal.

Figure 2 shows that adaptive filtering reproduces faithfully ICG signal when such signal is not distorted by breathing or movement artefacts. Adaptive filter does not affect ICG signal in that situation. It works as low-pass filter, with only small influence on the shape of the signal.

During normal breathing signal's baseline follows phase of breath. Shape of dz/dt also changes from beat to beat. After adaptive filtering baseline becomes stable and the shape of ICG turns similar in each cardiac cycle. However, this shape is different from that during breath holding—as O wave becomes clearly visible. This wave is absent when the subject withholds breathing, therefore adaptive filtering confirmed the occurrence of O wave in this subject during breathing and its absence during breath holding.

Value of dz/dt_{\max} , which is proportional to SV according to Kubicek formula, used for SV calculation, differ between breath hold and normal breathing, adaptive filtering also slightly effects dz/dt_{\max} value (Table 1). During breathing, dz/dt_{\max} shows bigger variation but it may be the effect of modulation of stroke volume by respiration [10]. Adaptive

filter removes this variation, so it may mask some quick changes in stroke volume. This hypothesis should be verified with reference method.

Thus, on one hand, adaptive filtering may help extract information from noisy and distorted ICG signal, but on the other hand, it may obscure some real changes in signal, for instance, rapid cyclic changes connected with respiration.

References

1. Cybulski, G.: Ambulatory impedance cardiography. In: Ambulatory Impedance Cardiography, pp. 39–56. Springer, Berlin, Heidelberg (2011)
2. Patterson, R.P.: Sources of the thoracic cardiogenic electrical impedance signal as determined by a model. *Med. Biol. Eng. Compu.* **23**(5), 411–417 (1985)
3. Patterson, R.P.: Impedance cardiography: what is the source of the signal?. *J Phys: Conf. Ser* **224**(1). IOP Publishing (2010)
4. Siebert, J., Wtorek, J.: Impedance cardiography. The early diastolic phase of heart Chambers feeling—O dZ/dt (in Polish). *Ann. Acad. Gedan.* **27**, 79–89 (1993)
5. Denniston, J.C., et al.: Measurement of cardiac output by electrical impedance at rest and during exercise. *J. Appl. Physiol.* **40**(1), 91–95 (1976)
6. Miyamoto, Y., et al.: Continuous determination of cardiac output during exercise by the use of impedance plethysmography. *Med. Biol. Eng. Compu.* **19**(5), 638–644 (1981)
7. Yamamoto, Y., et al.: Design and implementation of a digital filter for beat-by-beat impedance cardiography. *IEEE Trans. Biomed. Eng.* **35**(12), 1086–1090 (1988)
8. Laguna, P., et al.: Adaptive filter for event-related bioelectric signals using an impulse correlated reference input: comparison with signal averaging techniques. *IEEE Trans. Biomed. Eng.* **39**(10), 1032–1044 (1992)
9. Barros, A.K., et al.: Filtering noncorrelated noise in impedance cardiography. *IEEE Trans. Biomed. Eng.* **42**(3), 324–327 (1995)
10. Guz, A., et al.: Respiratory modulation of left ventricular stroke volume in man measured using pulsed Doppler ultrasound. *J. Physiol.* **393**(1), 499–512 (1987)

Electrical Stimulation of Eye Blink in Individuals with Dry Eye Symptoms Caused by Chronic Unilateral Facial Palsy

J. Lylykangas, M. Ilves, H. Venesvirta, V. Rantanen, E. Mäkelä, A. Vehkaoja, J. Verho, J. Lekkala, M. Rautiainen, and V. Surakka

Abstract

The aim was to validate the functionality and subjective experiences of timer-triggered electrical blink stimulation with participants (N = 6) suffering from dry eye symptoms caused by chronic unilateral facial palsy. In a stimulation condition, the muscles responsible for eye blinking were stimulated at fixed intervals while watching a video for about 120 min. In a control condition, the participants watched a video without stimulation. The participants rated their dry eye symptoms with a questionnaire before and after the both conditions. They also rated the levels of felt pain, discomfort and naturalness of the stimulated movement. Additionally, the magnitude of the stimulated eye blinks over time was evaluated. The results showed that the magnitude of the stimulated eye blink did not decrease significantly during the watching task. The stimulation was rated as painless, slightly uncomfortable, and fairly natural. The experienced eye dryness decreased significantly in the stimulation condition. Most participants got used to the stimulation, or even forgot it during the task. The findings are promising in respect to the use of timer-triggered blink stimulation.

Keywords

Facial palsy • Eye blink • Dry eye disease • Dry eye symptoms • Electrical stimulation

1 Introduction

Facial nerve palsy affects the function of facial muscles, including the muscles responsible for eye blinking. The paresis is most typically unilateral affecting one side of the face while the intact side functions normally. Eye blinking is crucial for clear vision as well as protecting, lubricating, and cleaning the eye. The impaired ability to blink often leads to dry eye disease, which causes corneal discomfort and blurred vision [3]. Typical treatment for the symptoms is the use of eye drops to lubricate the eye surface. In more severe cases of facial palsy, surgical operations are required to avoid corneal damage. The main deficits of surgery include altered facial appearance (e.g., weight attached to the upper eyelid or eyelids sewed together) and a risk of complications.

In recent years, a method called facial pacing has been studied [7, 10]. The idea is to detect eye blink-related signals from the healthy side of the face and use this measurement to trigger a concurrent eye blink on the paretic side. Frigerio et al. [7] found that transcutaneous electric stimulation of the facial nerve branches of *orbicularis oculi* evoked eye blink in about 50% of the patients with acute facial palsy. However, the reliable detection of eye blinks may be challenging even in controlled laboratory settings [e.g., 5]. For this reason, simpler methods are worth considering.

In our previous study [9] we introduced a timer-triggered, constant-interval blink stimulator as an alternative for a blink-triggered pacing system. Our results with healthy participants showed that the pre-timed blink stimulation method was functional, and it was rated positively after a relatively long visual task.

J. Lylykangas (✉) · M. Ilves · V. Surakka
Faculty of Information Technology and Communication Sciences,
Tampere University, Tampere, Finland
e-mail: jani.lylykangas@tuni.fi

V. Rantanen · A. Vehkaoja · J. Verho · J. Lekkala
BioMediTech Institute and Faculty of Medicine and Health
Technology, Tampere University, Tampere, Finland

H. Venesvirta · V. Rantanen · E. Mäkelä · M. Rautiainen
Faculty of Medicine and Health Technology
(Otorhinolaryngology), Tampere University, Tampere, Finland

E. Mäkelä
Department of Clinical Neurophysiology, Medical Imaging
Centre, Pirkanmaa Hospital District, Tampere, Finland

The current clinical trial was carried out to validate the functionality of the method stated above with participants who suffered from dry eye symptoms caused by chronic unilateral facial palsy. The aim was to study subjective experiences of the stimulation and its effects on dry eye symptoms. Additionally, we observed the magnitude of the stimulated eye blinks regarding the possible changes in long-term use, for example, due to muscle fatigue.

2 Methods

2.1 Participants

Six volunteers (5 females, 1 male) with chronic peripheral facial nerve palsy were enrolled to the study from the participant pool of our previous experiments. Their age ranged between 25 and 53 years (mean = 44.2, SD = 10.5). The etiology of the palsy included Bell's palsy (n = 4), Ramsey-Hunt syndrome (n = 1), and suspected Lyme disease (n = 1). They all had earlier experience of transcutaneous electrical stimulation of facial muscles. The inclusion criteria included successful *orbicularis oculi* activation induced by electrical stimulation and self-reported complications on eye dryness. The participants signed an informed consent form prior to the experiment. The study was accepted by the ethical committee of Pirkanmaa Hospital District (R15067). Participation was compensated with cafeteria tickets.

2.2 Assessment of the Palsy and Ocular Symptoms

Severity of the palsy was individually assessed with the Sunnybrook facial grading system (SFGS) [12]. The mean SFGS scores varied between 25 and 76 (mean = 40.3, SD = 16.3). Participants' Ocular Surface Disease Index (OSDI; © Allergan Inc., Irvine, California, USA) [13] score was between 10.4 and 66.7 (mean = 46.6, SD = 19.5). The scores indicated moderate dry eye disease, except for the participant with the lowest score, whose symptoms were primality experienced during outdoor sports.

2.3 Equipment and Stimulation Parameters

The stimulation device included four channels for functional electrical stimulation. The device communicated wirelessly with a PC, which was also used to adjust the stimulation parameters (for a detailed description of the stimulation device, see [11]). The stimulation waveform used in this study was a biphasic square wave with symmetric positive

and negative phases (equal width, equal amplitude) using phase duration of 0.4 ms and 250 Hz pulse repetition frequency. Pulse train duration was 200 ms with ramping time of 80 ms. The parameters were selected based on earlier research [e.g., 6–9]. The commercial, disposable stimulation electrodes made from carbonized rubber were manually trimmed approximately to a size of 1.9 cm². Two electrodes were attached to the skin above the *orbicularis oculi* muscle. One electrode was positioned 0.5 cm lateral to the orbital rim and the other about 0.5 cm posterior to the first one. The participant's face was recorded with a digital video camera at 50 frames per second for offline video analysis.

2.4 Procedure

The experiment was carried out during two separate days with a maximum of one day in between. One visit with and another without blink stimulation (stimulation and control conditions, respectively) were counterbalanced between the participants so that half started with stimulation and the other half with the control condition.

In the beginning of the first visit, the aim of the study was explained and the participant signed an informed consent and a consent for the use of video material. Then the SFGS was obtained, and the participant filled out the OSDI questionnaire. In addition, the possible immediate effects of the stimulation and/or the video watching on subjective eye dryness symptoms were rated with a custom dry eye questionnaire (DEQ), which was made based on Begley et al. [1, 2]. The DEQ assessed nine typical dry eye symptoms (watering, itching, stinging, foreign body sensation, pain, dryness, sensitivity to light, changes in eye sight, and general discomfort) by five-point scales varying from 1 (not at all) to 5 (a lot). A vision test for both eyes was performed using a logarithm of the minimum angle of resolution (logMAR) chart.

At first, the muscle of the thenar eminence of a participant's left hand was stimulated in order to familiarize the participant to the stimulation. The familiarization continued by stimulating the *orbicularis oculi* muscle on the healthy side. The stimulation started from 1.0 mA and it was increased in 0.5 mA steps. The stimulus was repeated five times at each amplitude level. The participant's permission to proceed was requested at each level until a full eye closure was evoked. The threshold for the eye closure (i.e., a complete blink) was visually estimated real time by two experimenters.

In the stimulation condition, the rating scales were explained and practiced. Both the pain and the discomfort rating scales ranged from 0 (not at all painful/discomfortable) to 10 (extremely painful/discomfortable). The movement naturalness scale was an eleven-point bipolar rating scale varying from -5 (unnatural) to +5 (natural), with

0 representing the neutral point (neither unnatural nor natural) of the scale. The stimulation was continued with the paretic side by following a similar procedure in order to find suitable eye closure threshold. Stimulus amplitude for a full eye closure was confirmed onsite in an offline frame-by-frame video analysis. Using this personal amplitude level, the stimulation was repeated five times with a five-second interstimulus interval, and the participant gave the pain, discomfort, and naturalness ratings regarding the stimulation. Then, the participant watched a freely chosen video for approximately 120 min from a 50-in. LCD television at a 1.85-m viewing distance. During the watching, the *orbicularis oculi* muscle was stimulated at five-second intervals (see [9] for the rationale of the selected stimulus rate). After the watching task, the participant gave again the pain, discomfort, and the naturalness ratings.

In the control condition, familiarization with healthy side stimulation was followed by paretic side *orbicularis oculi* stimulation until the full eye closure threshold was reached. Then the electrodes were removed, and the participant proceeded to the video watching task without the stimulation.

In the end of both conditions, the participant again filled out the DEQ and repeated the vision test. Corneal health status was examined with a fluorescein eye stain test, except for one participant who experienced the test too uncomfortable. Before leaving the stimulation condition, the participant was interviewed about the following topics: was the stimulation noticeable, did it disturb watching the video, did the feeling about the stimulation change over the time, did the stimulation have any effect on the experienced dry eye symptoms, and was the stimulated blink rate appropriate. The experiment took approximately 3.5 h per visit.

The procedures of the stimulation and control conditions were similarly arranged in the second visit, excluding the consent forms, SFGS, and OSDI, which were collected only in the first visit. Additionally, control conditions performed in the second visit excluded the stimulus familiarization.

2.5 Data Analysis

The thresholds for eyelid movement and complete eye closure on the healthy and paretic side of the face were obtained in offline video analysis by one experimenter. Electrical currents for the thresholds were analyzed with non-parametric Wilcoxon signed rank tests.

One-way repeated measures analysis of variance (ANOVA) with blink magnitude as a factor was used to test whether the blink magnitude changed during the watching task. The magnitude of the blinks was classified in offline video analysis by one experimenter. The magnitude was determined from five stimulated blinks in every 10 min with no concurrent eyelid movement observed on the healthy side. The classification from the largest to the lowest was 5 = complete blink; 4 = nearly complete blink; 3 = eyelid covers the pupil; 2 = eyelid partially covers the pupil; 1 = twitch.

Wilcoxon signed rank tests were used to analyze subjective ratings on stimulation, DEQ, and the visual acuity test. For the DEQ and visual acuity test, the comparisons between before and after the video watching task were performed separately for the two conditions.

3 Results

Stimulation threshold to produce an eyelid movement on the healthy and paretic side varied between 2.0–3.5 mA (mean = 2.5, SD = 0.5) and 2.5–3.0 mA (mean = 2.8, SD = 0.3), respectively. Wilcoxon signed rank test did not show a statistically significant difference between these stimulation thresholds.

Stimulation thresholds for a complete eye blink on the healthy and paretic side varied between 2.5–5.0 mA (mean = 3.4, SD = 0.9) and 4.0–7.0 mA (mean = 5.3, SD = 1.0), respectively. Wilcoxon signed rank test showed

Fig. 1 Classified mean eye blink magnitudes of the stimulated blinks as a function of time. Error bars represent SDs

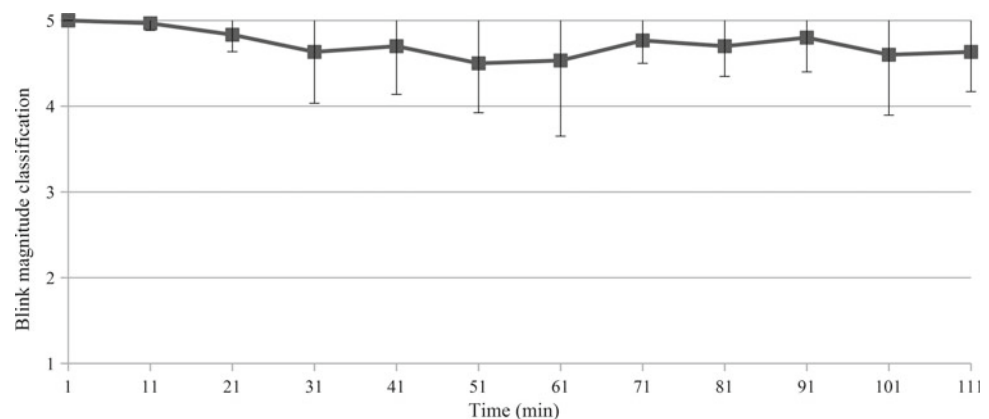


Table 1 The mean ratings from the DEQ scales with SDs in parenthesis. The grey background indicates the statistically significant difference

	Stimulation condition		Control condition	
	Before video	After video	Before video	After video
Watering	2.2 (1.2)	2.0 (0.9)	2.2 (1.5)	2.0 (1.5)
Itching	2.2 (1.0)	1.7 (1.2)	1.8 (1.3)	2.0 (1.3)
Stinging	1.5 (0.8)	2.0 (1.3)	1.7 (1.0)	2.5 (1.0)
Foreign body sensation	3.2 (1.2)	1.8 (1.6)	2.0 (1.1)	3.0 (1.5)
Pain	2.2 (1.2)	1.8 (1.3)	2.2 (1.3)	2.7 (1.4)
Dryness	3.5 (1.2)	2.2 (1.3)	2.7 (1.6)	3.5 (2.0)
Sensitivity to light	2.2 (1.6)	2.0 (1.3)	1.8 (1.3)	2.0 (1.5)
Changes in eye sight	2.5 (1.2)	2.8 (1.3)	2.2 (1.8)	2.2 (1.2)
Discomfort	3.7 (0.8)	2.7 (1.6)	2.3 (1.2)	3.0 (1.5)

that the threshold was significantly higher for the paretic than healthy side $Z = -2.21$, $p < 0.05$.

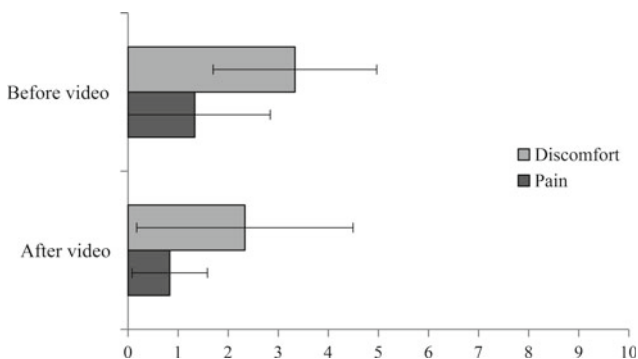
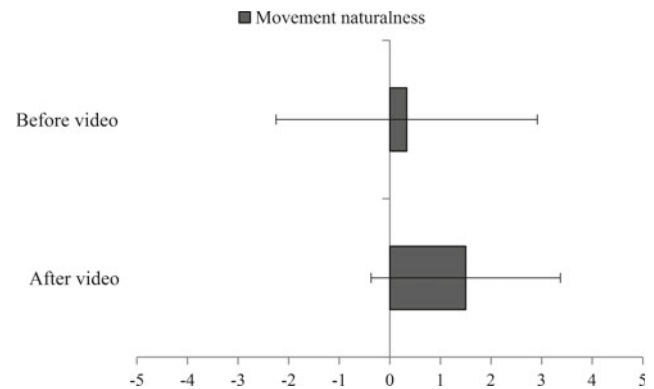
Figure 1 shows the mean eye blink magnitudes of the stimulated blinks as a function of time. One-way repeated measures ANOVA showed no significant change in the blink magnitude during the watching task.

Table 1 shows the results from the DEQ. Wilcoxon signed rank test showed that the sensation of dryness was significantly lower after the stimulation than before it, $Z = 2.12$, $p < 0.05$. Other pairwise comparisons were not statistically significant.

Figure 2 shows the ratings about the stimulation pain and discomfort, and Fig. 3 shows the ratings for the movement naturalness before and after the video watching task. Wilcoxon signed rank tests showed no statistically significant differences for the ratings.

Wilcoxon signed rank tests did not reveal significant differences of visual acuity in stimulation and control conditions. The fluorescein eye stain tests showed that the corneal status remained the same in the stimulation and control conditions.

In the post-experimental interview, four of the six participants reported that they forgot the stimulation during the

**Fig. 2** The mean discomfort and pain ratings for blink stimulation before and after the watching task. Error bars represent SDs**Fig. 3** The mean movement naturalness ratings for blink stimulation before and after the watching task. Error bars represent SDs

watching task or got used to it. Two said that the stimulation reduced their dry eye symptoms. Five participants requested that the interval of the stimulated blinks should be modifiable. Three were interested to try out a portable blink stimulator in everyday use if available. Two participants mentioned that the stimulation had a positive effect on the eye symptoms, and even further, one who suffered from prominent watering symptom considered having less need to wipe the tears below the paretic-side eye during the stimulation.

4 Discussion

The results showed that timed eye blink stimulation can be useful and acceptable for individuals with dry eye symptoms caused by chronic facial palsy. The stimulation method used in the study is simpler than facial pacing in earlier efforts [7, 10]. Pacing can be useful if synchrony of eye blinks between the eyes is required, but in many cases a simpler and more cost-effective method may be favorable.

Although complete eye blink in the paretic side required significantly higher stimulus amplitude compared to the healthy side, the stimulation was not felt as painful. The ratings of pain and discomfort were even slightly lower after the two-hour video watching task than before it, and the movement naturalness was rated higher after the watching. Further, most participants reported that they got used to stimulation or even forgot it while watching the video. These subjective experiences of adjustment to the stimulation are in line with those obtained from intact participants in our previous study [9].

The five-second interstimulus interval together with other stimulus parameters seemed to provide sufficient recovery time for the muscle fibers. The magnitude of the stimulated blinks did not decrease significantly during the watching task. This indicates that the stimulation did not cause noticeable muscle fatigue. This is an interesting finding compared to earlier studies, which state that high stimulation frequency may cause faster fatigue of limb muscles [4]. The relatively high 250 Hz frequency used for stimulating the *orbicularis oculi* in the current experiment did not show this kind of tendency. Thus, one of the future research topics would include systematic investigation on how different frequencies and other stimulus parameters affect to the fatigue of different facial muscles.

The subjective ratings indicated that the stimulated eye blink may reduce the dry eye symptoms caused by the palsy. The experienced dryness was significantly lower after the stimulation than before it, and additionally, itching, foreign body sensation, pain, light sensitivity, and overall discomfort symptoms had a tendency to decrease during the stimulation, whereas the tendency was to increase during the control condition.

Our next steps include usability and user experience studies with a mobile eye blink stimulator with enhanced functionality, including adjustable blink rate, in everyday use.

Acknowledgements This study was funded by the Academy of Finland: decision numbers 278529, 276567, and 278312.

Declarations of Interest The authors declare that they have no competing interests.

References

1. Begley, C.G., Caffery, B., Chalmers, R.L., Mitchell, G.L.: Use of the dry eye questionnaire to measure symptoms of ocular irritation in patients with aqueous tear deficient dry eye. *Cornea* **21**(7), 664–670 (2002)
2. Begley, C.G., Chalmers, R.L., Mitchell, G.L., Nichols, K.K., Caffery, B., Simpson, T., et al.: Characterization of ocular surface symptoms from optometric practices in North America. *Cornea*, **20** (6), 610–618 (2001)
3. Craig, J.P., Nichols, K.K., Akpek, E.K., Caffery, B., Dua, H.S., Joo, C.K., et al.: TFOS DEWS II definition and classification report. *Ocul. Surf.*, **15**(3), 276–283(2017)
4. Doucet, B.M., Lam, A., Griffin, L.: Neuromuscular electrical stimulation for skeletal muscle function. *The Yale journal of biology and medicine* **85**(2), 201–215 (2012)
5. Frigerio, A., Brenna, S., Cavallari, P.: Surface electromyography recording of spontaneous eyeblinks: applications in neuroprosthetics. *Otolaryngology-Head and Neck Surgery* **148**(2), 209–214 (2013)
6. Frigerio, A., Cavallari, P.: A closed-loop stimulation system supplemented with motoneurone dynamic sensitivity replicates natural eye blinks. *Otolaryngol.-Head Neck Surg.* **146**(2), 230–233 (2012)
7. Frigerio, A., Heaton, J.T., Cavallari, P., Knox, C., Hohman, M.H., Hadlock, T.A.: Electrical stimulation of eye blink in individuals with acute facial palsy: progress toward a bionic blink. *Plast. Reconstr. Surg.* **136**(4), 515e–523e (2015)
8. Ilves, M., Lylykangas, J., Rantanen, V., Mäkelä, E., Vehkaoja, A., Verho, J., Surakka, V.: Facial muscle activations by functional electrical stimulation. *Biomed. Signal Process. Control. J.* **48**, 248–254 (2019)
9. Lylykangas, J., Ilves, M., Venesvirta, H., Rantanen, V., Mäkelä, E., Vehkaoja, A., et al.: Artificial eye blink pacemaker-A first investigation into the blink production using constant-interval electrical stimulation. In: *EMBEC & NBC 2017*, pp. 522–525. Springer, Singapore (2017)
10. McDonnall, D., Guillory, K.S., Gossman, M.D.: Restoration of blink in facial paralysis patients using FES. In: *4th International IEEE/EMBS Conference on Neural Engineering*, 2009. NER'09, pp. 76–79. IEEE (2009)
11. Rantanen, V., Vehkaoja, A., Verho, J., Veselý, P., Lylykangas, J., Ilves, M., et al.: Prosthetic pacing device for unilateral facial paralysis. In: *XIV Mediterranean Conference on Medical and Biological Engineering and Computing 2016*, pp. 653–658. Springer, Cham (2016)
12. Ross, B.G., Fradet, G., Nedzelski, J.M.: Development of a sensitive clinical facial grading system. *Otolaryngology—Head Neck Surg.*, **114**(3), 380–386 (1996)
13. Schiffman, R.M., Christianson, M.D., Jacobsen, G., Hirsch, J.D., Reis, B.L.: Reliability and validity of the ocular surface disease index. *Arch. Ophthalmol.* **118**(5), 615–621 (2000)

Prescribe and Monitor Physical Activity Through a Community-Based eHealth Program: MOVIDA Platform

Rui Fonseca-Pinto, Rui Rijo, Pedro Assunção, Maria Alexandra Seco, Maria P. Guarino, Cátia Braga-Pontes, Dulce Gomes, Bruno Carreira, Pedro Correia, Luís Oliveira, Gabriel Pires, Catarina Leitão, Alexandre Antunes, Filipa Januário, and Ricardo Martinho

Abstract

Modern portable devices (e.g. wearables) provide technical support to record physical activity, which can assist various purposes, ranging from geolocation, step count, body temperature and biomedical parameters among others. These technological advances, the increase of literacy in health and also in informatics placed the

smartphone and its massive use in the center of a new paradigm of monitoring physical activity. When combining these functionalities with the ability to communicate with remote entities, then it is possible to expand the use of smartphones, not only to monitoring physical activity but also to promote widespread adherence to physical activity programs. This paper presents the conceptual framework of a global health community program centered on a mobile application and a dedicated backoffice web application to perform physical activity prescription and supervision based on dashboards. The MOVIDA platform is comprised of 4 main modules, targeting different groups of the population. This platform enables exercise prescription, monitoring of user's performance and adherence in metabolic diseases patients by MOVIDA.cronos, to specify and follow a cardiac rehabilitation program by MOVIDA.eros, to track and quantify indoor movements by MOVIDA.domus, and also access to a stratified training circuit, for maintaining or improve fitness level by MOVIDA.polis. In addition, this work reports the project main challenges from the conceptual phase of the technological platform to its development and implementation. This work can be useful for those who are starting a project with the same type of characteristics: multicentric, interdisciplinary and involving several partners in the community.

R. Fonseca-Pinto (✉) · R. Rijo · P. Assunção · M. A. Seco · M. P. Guarino · C. Braga-Pontes · D. Gomes · B. Carreira · R. Martinho
Polytechnic Institute of Leiria, Leiria, Portugal
e-mail: rui.pinto@ipleiria.pt

R. Fonseca-Pinto · M. P. Guarino · C. Braga-Pontes · D. Gomes · B. Carreira
CiTechCare—Center for Innovative Care and Health Technology, Leiria, Portugal

R. Fonseca-Pinto · P. Assunção
Instituto de Telecomunicações, Multimedia Signal Processing, Leiria, Portugal

P. Correia · L. Oliveira · G. Pires
VITA Lab/Smart Cities Research Center (C2I2), Polytechnic Institute of Tomar, Tomar, Portugal

C. Leitão
College of Health Dr. Lopes Dias, Polytechnic Institute of Castelo Branco, Castelo Branco, Portugal

A. Antunes · F. Januário
Centro Hospitalar de, Leiria, Portugal

R. Rijo
Institute for Systems Engineering and Computers at Coimbra (INESC Coimbra), University of Coimbra, Coimbra, Portugal

R. Rijo · R. Martinho
Centre for Research in Health Technologies and Information Systems (CINTESIS), University of Porto, Porto, Portugal

B. Carreira
Unidade de Saúde Familiar Santiago, ACES Pinhal Litoral, Leiria, Portugal

R. Rijo
Health Intelligence Laboratory, Faculty of Medicine of the University of São Paulo, Ribeirão Preto, Brazil

Keywords

Mobile app · Mobile computing · Physical activity monitoring · Health and Well-Being · Technologies for life quality

1 Introduction

The use of technology in healthcare is a reality that occurs every day in a wide variety of care contexts. From hospital emergency or surgery departments to the support

technologies for daily life activities of disabled or elderly, it is possible to find a massive set of technologies to assist technicians, patients, and caregivers. The whole of the technological arsenal has diversified over the last few years and accompanied the various lines of clinical and technological research. Moreover, these technological amenities have been adapted to the needs of healthcare practice and also integrated into the emerging technological devices available in the mass market.

The solutions delivered by the use of technology to contribute to solve the challenges of healthcare are now widely known as eHealth technologies. At the 115th session of the World Health Organization (WHO) Executive Board in Geneva in January 2005, it was recommended the World Health Assembly (WHA) 58.28 resolution on eHealth, acknowledged that eHealth is the cost-effective and secure use of information and communications technologies in support of health and health-related fields, including health-care services, health surveillance, health literature, and health education, knowledge, and research,” and urged member states to develop and implement eHealth technologies [1].

Lifestyle changes associated with modern societies have changed the profile of the most prevalent diseases in the community. Moreover, democratized access to healthcare increased health indicators (e.g., life expectancy, birth mortality), and the number of patients with chronic disease increased. These changes have forced a constant adaptation of health services, which look for eHealth solutions as a support to the effective healthcare. Likewise, citizens are now more skilled in terms of technological literacy, having equipment with a high potential for monitoring (e.g. mobile phones, tables, watches...) that can be enhanced in terms of healthcare without increasing the associated costs [2, 3].

Despite all this new trend of using technologies for improving the quality of life, it is essential to measure their effects on health and also their impact in terms of economic cost-effectiveness. Access to research funding in these areas has increased in terms of European and National projects, reflect European policies for this sector. Some studies, however, have pointed to a large number of eHealth proposals, but suggest that it is critical to realize the true impact and also the safety of proposed eHealth solutions [4, 5].

In this work, the framework of MOVIDA as a Physical Activity Monitoring Platform is presented and the main aspects related to the conception and implementation of the solution are discussed. The work is organized as follows: after the introduction in Sect. 1, in Sect. 2 the four modules of the platform are presented jointly with their objectives and target public. In Sect. 3 the identified challenges and critical points are discussed together with some conclusions.

2 MOVIDA Platform Concept

Chronic diseases prevention and management jointly with rehabilitation programs establish a true challenge to the healthcare community. Epidemiological studies point to an increased prevalence of cardiovascular and chronic diseases and specify the supervised physical activity as a strong mechanism to control the progression thereof [6–8].

The MOVIDA platform is in line with the above concept, by creating a global health community program, centered in a platform with a mobile App, a backoffice, and a dashboard, aimed to monitor physical activity, and is comprised of four main modules, targeting different groups of the population. This program enables exercise prescription and monitor user’s performance and adherence, in metabolic diseases patients by (MOVIDA.cronos), to specify and follow a cardiac rehabilitation program (MOVIDA.eros), to track and quantify indoor movements (MOVIDA.domus), and also access to a stratified training circuit for maintaining or improve fitness level (MOVIDA.polis).

The above-mentioned modules can be categorized according to whether they are open to the community and also to its main objective as an interventive or preventive program. Accordingly, using the aforementioned conceptual terms MOVIDA defines two axes and two dimensions. The axes include the social network environment that can be open or restricted, while the dimensions refer to the purpose of the actions, which can be interventive or preventive.

As a community-based eHealth program, the MOVIDA platform enrolls the civil society, research, and academia. This project was funded by the Portuguese Foundation for Science and Technology—FCT in the framework of the H2020 research program and is developed by a consortium of several institutions: Polytechnic Institute of Leiria—IPL, Polytechnic Institute of Tomar—IPT, Polytechnic Institute of Castelo Branco—IPCB, Hospital center of Leiria—CHL and Municipality of Leiria—CML. The conceptual framework is resumed in Fig. 1.

2.1 MOVIDA.cronos

The increased prevalence of chronic diseases can ultimately be seen as a consequence of the modern healthcare success. In fact, the success in healthcare regarding treatment of acute diseases, combined with the constant research and new treatment approaches, increased the number of patients having chronic pathologies and therefore the need to create structures to deal with this new reality. By definition, these patients are mostly stable, only requiring to be followed up

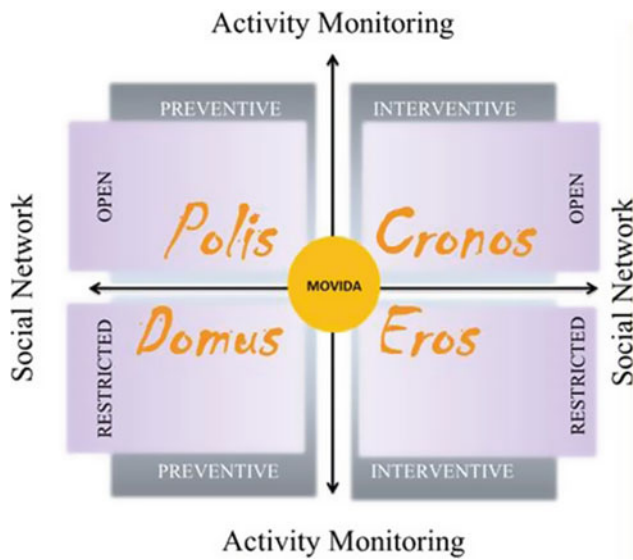


Fig. 1 Conceptual Framework of the MOVIDA platform

in the management of their disease (through remote monitoring, monitoring of daily habits, decompensation of the underlying disease, etc.).

This module is aimed at chronic diseases and it is meant to be used in primary health care (mainly by physicians or certified professionals in the prescription of physical activity) with the purpose of prescribing a personalized and adapted recommendation of physical activity to the user. The target audience is chronic disease patients (e.g. Diabetes Mellitus, Dyslipidemias, Hypertension, Overweight, etc.) who are being followed in primary health care units, for whom it is indicated the practice of regular physical activity [9]. Regarding the conceptual framework, this module is mainly in the intervention dimension and is closed in what concerns to the social network.

In addition to the prescription of physical activity, by means of a dedicated backoffice, it is possible to follow online the adherence of the patient to the clinical recommendation. This functionality enables real-time monitoring and also to enhance the practice of the prescribed recommendation of activity (as if it were the prescription of a medication). When following the recommended training performance, the prescriber can adapt the recommendation as a function of the outcomes of the mobile App. In addition, it is possible to send a message to the user using the dashboard to App communication function, which can also act as a motivational incentive.

By using the dashboard it is possible to prescribe physical activity by duration, frequency, and type. The duration usually defines 30 min as a lower bound, the frequency is defined by the number of days per week, and the activity type can be prescribed in two levels (i.e. walking, running). The automatic outcomes are the overall activity accomplishment level and heart rate measures. Other biomedical variables can be introduced by the user (e.g. Blood Pressure, HLDc, BMI, Abdominal Perimeter) whenever the user aims to enrich the profile. In Fig. 2 is possible to see an overall view of the prescribing dashboard at left, and an overview of the App profile at right.

2.2 MOVIDA.eros

This module of the MOVIDA platform is meant to be integrated into Cardiac Rehabilitation programs, in particular at phases III and IV (i.e. the ambulatory phases), creating a dedicated heart-healthy lifestyle change to address risk factors for cardiovascular diseases.

Cardiac Rehabilitation is a medically supervised program for people who have suffered a myocardial infarction or

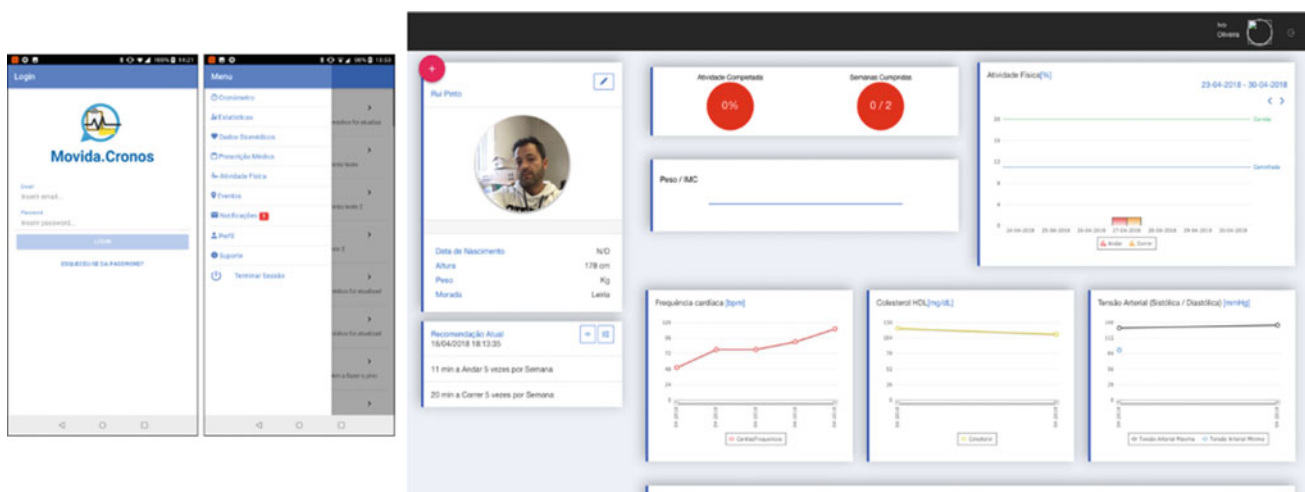


Fig. 2 MOVIDA.cronos. Main screen App at left and platform overview at right

acute coronary syndrome, coronary artery bypass grafting, percutaneous coronary intervention, heart failure, heart valve surgery or cardiac transplantation, but also as a prevention for new cardiovascular events. The rehabilitation program aimed to promote physical activity, education about healthy living (healthy eating, medication adherence and stop smoking) and measures to improve mental health [10–12]. Exercise prescription should specify frequency, intensity, duration, modalities, and progression.

These are allowed by *MOVIDA.eros*. Physical activity after a cardiovascular event is seen as having central relevance in the rehabilitation process, and the results in terms of cardiovascular benefits are seen as unequivocal among the medical community. In fact, exercise therapy can have positive effects on depressive symptoms, emotional well-being, cognition, executive functioning and memory, balance, mobility, bone health, walking ability, functional capacity and thus to improve quality of life [13, 14].

In Portugal, the incidence of cardiovascular diseases continues to be one of the main causes of death and in particular the number of ischemic coronary events continues to increase. Health services were not designed to provide a massive response in terms of cardiac rehabilitation (as recommended by the guidelines) and for this reason the integration of the *MOVIDA.eros* module in the rehabilitation plan supported by mobile technology has an impact in terms of provided care without increasing costs. According to the proposed conceptual framework, this module is at the intervention dimension and is closed in what concerns to the social network. Patients will be monitored by the mobile App in each training section (heart rate, Borg scale, adverse events) and the communication Dashboard-App is automatic. The Mobile App also includes dietetic suggestions and tips adapted to the user profile. In Fig. 3 is possible to see the overall view of the prescribing platform at right and the mobile App main screen at left.

2.3 *MOVIDA.polis*

Physical inactivity plays a major role in the chronic disease physiopathology (e.g., cardiovascular disease, diabetes, cancer, hypertension, obesity, depression, and osteoporosis) and premature death [15]. The practice of physical activity is, therefore, a determining factor in the prevention of diseases, but also is associated with better mental health and well-being, and as an ally in the fight against cancer.

The increase of health literacy has contributed to a more attentive society to the positive association between physical activity and health. On the other hand, public policies have been attentive to the benefits of physical activity practice and have contributed to creating conditions for the practice of outdoor physical activity through the creation and adaptation of maintenance circuits, bicycle paths, and anaerobic training equipment in gardens and footpaths. These new practices, however, are not exempt from risk, and it is desirable that the practice of physical activity can be recommended and accompanied by a professional, or at least adapted to the characteristics and performance of each individual.

This identified requirement for guidance and supervision of the practice of physical activity (for safety and performance reasons) can be assisted by mobile technology, and enhanced by the use of artificial intelligence algorithms by adapting the exercise recommendations in function of the users' performance and their perception of effort.

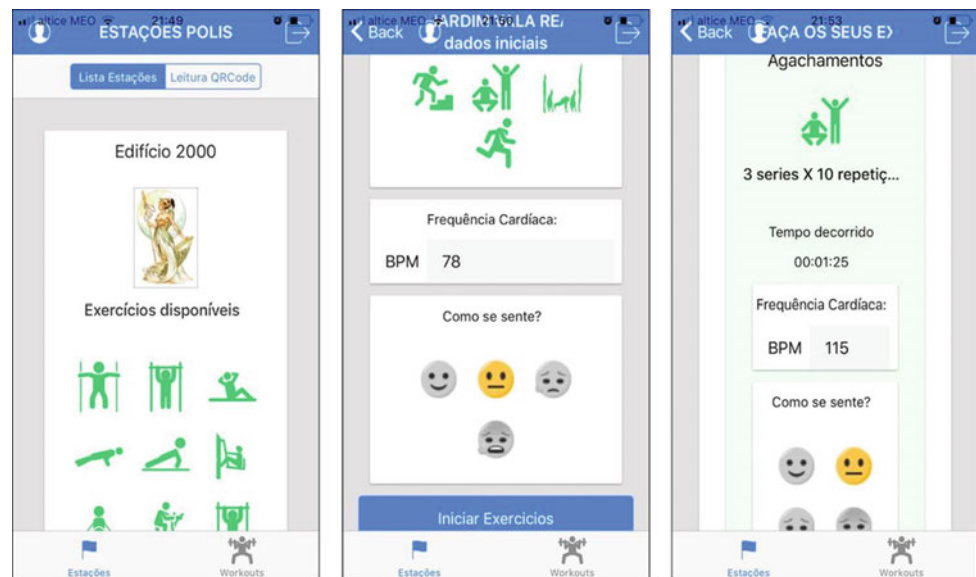
The *MOVIDA.polis* module was initially designed for the polis circuit in the city of Leiria, consisting of a mobile application and a platform allowing the training stations to be adapted to other cities or places. The training stations are identified by reading a QRcode, and the user can choose the exercises that he/she wants to perform.

This module is open in terms of social network and assumes a preventive dimension in the conceptual framework of the *MOVIDA* platform. In Fig. 4 is possible to see



Fig. 3 *MOVIDA.eros*—three App screens at left and platform overview at right

Fig. 4 *MOVIDA.polis*—
Example of three App screens



the overall view of the prescribing platform at right and the developed mobile App main screen at left.

2.4 *MOVIDA.domus*

The use of wearables in the remote monitoring of people increased in the last years and its use has been diversified [16]. In particular, it has contributed to the development of research projects in the area of Assisted Living, for example by remote monitoring of vital signs [16, 17]. The output of these research projects has contributed to improving the quality of life of older adults, but also for those how need some kind of assistance in daily life routines. The increasing number of people having a smartphone booted the opportunities of using the available technologies embedded in the phone as a motion sensor (through the accelerometer) and also the position (via GPS).

Human behaviors vary in function of external factors, however, some studies have shown regular behavior patterns associated with the practices of daily living activities. Specifically, in this population typically presenting a reduced capacity of movement and functional limitations. These patterns can be analyzed by task, individually, or by a group pattern in a set of tasks [18]. By aggregating these standardized features, extracting attributes associated with specific tasks, and artificial intelligence algorithms, it is possible to monitor patterns of daily activity and detect changes in these patterns.

The module *MOVIDA.domus* allows tracking this daily activity, as well as the extraction of the movement patterns

associated with it. Changes to the activity pattern will generate several types of alarms for the user himself (to be received in his mobile phone and to disarm whenever will be the case), or to the caregiver associated with the user.

These alarms can be classified as inactivity alarms, position alarms or non-response alarms. In the framework of the *MOVIDA* program, this module is closed in terms of social network and assume a preventive dimension.

The *MOVIDA.domus* architecture is comprised of 5 modules: mobile app; web Platform; firebase services; webservice; and Artificial Intelligence (AI) server, as illustrated in Fig. 5.

3 Implementation and Critical Challenges

The *MOVIDA* platform specificities (multicentric, interdisciplinarity, communitybased) constitute a true challenge to the research team. One of the first questions is related to the number of enrolled partners and the different areas of specialization. Beyond an operational platform, the challenge is to achieve a functional platform that can meet the expectations of users (health professionals and app users). The definition of the objectives in a language clearly understood by all users is central to obtain a functional platform. It should be easy to use amongst different users, having a distinct technological background. This usability property is designed in the jointly defined set of objectives established in the specifications stage at the beginning of the prosed development. Thus, even in case of some unpredicted deviation from the initially established methodology, the key

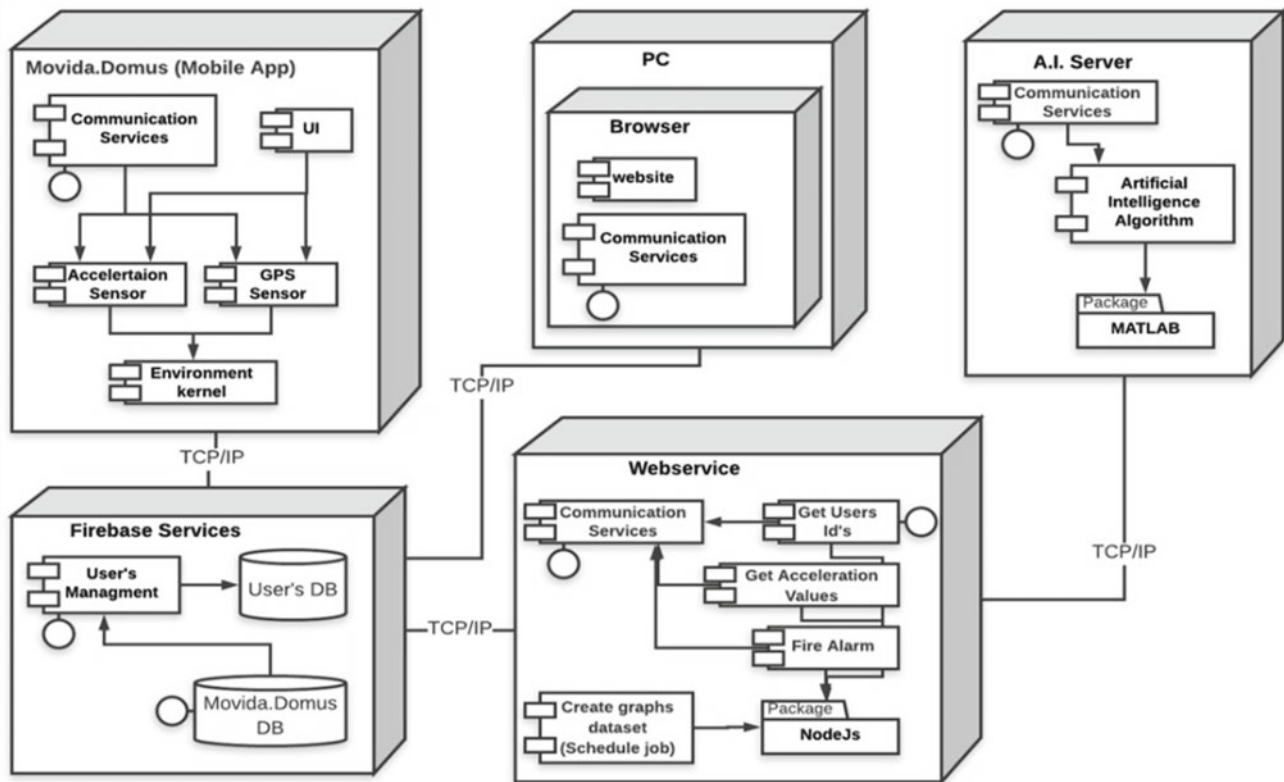


Fig. 5 MOVIDA.domus architecture

is to define alternative strategies to attain a solution that fulfills the established functional objectives.

As a platform dealing with personal and clinical data, it is compulsory to assure all legal issues (in accordance with the legislation), but also to protect ethical issues by requesting a referral to a certified ethics committee. In the case of the MOVIDA platform, registration was made with the National Commission for Data Protection in Portugal (CNPD) and an ethics committee approved the Platform proof of principle. Still, due to the type of data that is acquired processed and stored, and to the actions this data can trigger, confidentiality, access control, but also high accuracy levels of the decisionmaking algorithms is compulsory.

Despite the high number of potential users, regarding the proof of principle, it is necessary to involve groups of volunteers who meet the defined inclusion criteria, which is sometimes not easy to achieve. For example, one of the requirements is to have a smartphone and some literacy in terms of its use. To overcome this difficulty, one of the strategies was the implementation of workshop sections explaining the main features of the platform. All of these

dissemination strategies were made jointly with the local organizations of the civil society, in particular with the municipality, health and sports students and health services.

4 Conclusions and Future Work

EHealth strategies and technological solutions to optimize healthcare are a reality that is increasingly present in everyday life. The use of mobile applications is a strong ally in this strategy, due to the widespread use of supporting technologies, which does not entail additional costs and it is proven to be effective. A large amount of generated data and its optimized storage will allow researchers to respond to another great challenge by effectively quantifying health gains obtained through eHealth strategies.

Within the scope of this project, a proof of concept is now running for each of the dimensions of the platform, as well as an economic impact study for MOVIDA.eros and MOVIDA.crono dimensions, whose results will be published in due course.

Acknowledgements This work was supported by Fundação para a Ciência e Tecnologia FCT- Portugal, under the scope of MOVIDA project: 02/SAICT/2016 – 23878

References

1. WHO World Health Assembly 58 (2005) Resolution WHA 58.28 on eHealth
2. Bates, D.W., Saria, S., Ohno-Machado, L., Shah, A., Escobar, G.: Big data in healthcare: using analytics to identify and manage high-risk and high-cost patients. *Health Aff.* **33**(7), 1123–1131 (2014)
3. Hamine, S., Gerth-Guyette, E., Faulx, D., Green, B.B., Ginsburg, A.S.: Impact of mHealth chronic disease management on treatment adherence and patient outcomes: a systematic review. *J. Med. Internet Res.* **17**(2) (2015)
4. Black, A., Car, J., Pagliari, C., Anandan, C., Cresswell, K., Bokun, T., McKinstry, V., Procter, R., Majeed, A., Sheikh, A.: The impact of ehealth on the quality and safety of health care: a systematic overview. *PLoS Med.* **8**(1), e1000387 (2008)
5. Alexander, G., Staggers, N.: A systematic review of the designs of clinical technology: findings and recommendations for future research. *ANS Adv Nurs Sci.* **32**(3), 252–279 (2009)
6. Adeyi, O., Smith, O., Robles, S.: Public policy and the challenge of chronic noncommunicable diseases. The World Bank, Washington, DC (2007)
7. WHO.: The global burden of disease: 2004 update. Geneva: World Health Organization (2008b)
8. Schuler, G., Adams, V., Goto, Y.: Role of exercise in the prevention of cardiovascular disease: results, mechanisms, and new perspectives. *Eur. Heart J.* **34**(24), 1790–1799 (2013)
9. American Diabetes Association: 4. lifestyle management: standards of medical care in diabetes—2018. *Diabetes Care* **41** (Supplement 1), S38–S50 (2018)
10. Witt, B.J., Jacobsen, S.J., Weston, S.A., et al.: Cardiac rehabilitation after myocardial infarction in the community. *J. Am. Coll. Cardiol.* **44**, 988–996 (2004)
11. Benjamin, E.J., Blaha, M.J., Chive, S.E., et al.: Heart disease and stroke statistics—2017 update: a report from the American Heart Association. *Circulation* **135**, e146–e603 (2017)
12. Goldstein, L.B., Adams, R., Alberts, M.J., Appel, L.J., Brass, L. M., Bushnell, C.D., et al.: Primary prevention of ischemic stroke: A guideline from the American heart association/American stroke association stroke council: Cosponsored by the atherosclerotic peripheral vascular disease interdisciplinary working group; cardiovascular nursing council; clinical cardiology council; nutrition, physical activity, and metabolism council; and the quality of care and outcomes research interdisciplinary working group: The American Academy of Neurology affirms the value of this guideline. *Stroke*, **37**(6), 1583–1633 (2006)
13. Guidelines for Cardiac Rehabilitation and Secondary Prevention Programs 5th Edition. American Association of Cardiovascular and Pulmonary Rehabilitation. (2013)
14. Ware, Lisa J., Rennie, Kirsten L., Schutte, Aletta E.: Monitoring physical activity after a cardiovascular event: What is ‘fit’ for purpose? *Eur. J. Prev. Cardiol.* **25**(2), 220–222 (2017)
15. Warburton, D.E., Nicol, C.W., Bredin, S.S.: Health benefits of physical activity: the evidence. *Can. Med. Assoc. J.* **174**(6), 801–809 (2006)
16. Gokalp, H., Clarke, M.: Monitoring activities of daily living of the elderly and the potential for its use in telecare and telehealth: a review. *Telemed. J. E. Health.* **19**(12), 910–23 (2013)
17. Allet, L., Knols, R.H., Shirato, K., de Bruin, E.D.: Wearable systems for monitoring mobility-related activities in chronic disease: a systemic review. *Sensors* **10**(10), 9026–9052 (2010)
18. Lymberopoulos, D., Bamis, A., Savvides, A.: Extracting spatiotemporal human activity patterns in assisted living using a home sensor network. *Univ. Access Inf. Soc.* **10**(2), 125–138 (2011)

Miniaturized Stimulator for Imaging of Live Cell Responses to High Frequency Mechanical Vibration

Heidi T. Halonen¹, Jari A. K. Hyttinen¹, and Teemu O. Ihalainen¹

Abstract

Cellular mechanobiology is highly important for tissue development and disease formation. However, lack of proper tools limit investigation of the cellular responses to different mechanical cues. High frequency (HF) vibration has already been applied in different cellular applications, but the knowledge of the stimulation effect on cells is limited. To meet this challenge, we designed a HF vibration stimulator for combined mechanical manipulation of live cells and high-resolution light-microscopy. Our system utilizes a commercial miniaturized speaker to vibrate a 3D printed sample vehicle horizontally. Technical tests demonstrated excellent performance at lower frequencies (30–60 Hz), enabling even high magnitude (HMHF, $G_{\text{peak}} \geq 1 G_{\text{peak}}$) method. Real-time acceleration measurement and light-microscopy both revealed accurately and precisely produced low magnitude (LMHF, $G_{\text{peak}} < 1 G_{\text{peak}}$) vibrations. With our system, we could observe cellular responses to the LMHF (0.2 G_{peak} , 30 Hz) vibration. In this paper, we introduce an inexpensive stimulation platform for the mechanobiology research of different cell applications.

Keywords

High frequency vibration • Live cell imaging • Mechanotransduction

1 Introduction

Tissues and cells are subjected to varying mechanical stimuli in our bodies and these physical cues alter the cellular and tissue physiology. However, mechanistic details of the cellular force sensing are poorly understood and novel

techniques are needed to unravel the mechanotransduction machinery. A high frequency (HF, >30 Hz) mechanical vibration offers a way to study, how impact-like mechanical stimulation influences cells. The method is popular in bone tissue engineering [1–6] but has also been tested for other tissue engineering applications [1, 2, 7–9].

A major advantage of the HF vibration is that it is easily applicable for different adherent cell types, but the optimization of the stimulation parameters (magnitude, frequency) present a significant challenge of the method. The stimulation has been applied mostly with the low magnitude (LMHF) method [1, 3–6, 8], although also the high magnitude (HMHF) method has been used more recently [2, 4, 8]. The most often the stimulation has been applied between 10–200 Hz frequencies [2–5, 7–9], yet even higher frequencies ranging from 400–10 kHz have attracted interests [5, 6]. For example, in bone tissue engineering the method has lead in highly varying proliferation responses, and benefits to the osteogenic differentiation have been reported [2–5].

The above summarized HF vibration studies have utilized varying linear actuators, such as vibration sensors [3], shakers [5], piezos [6] and speakers [1, 2], for studying cellular responses. However, current methods often require weeks of cell culture before analysis, thus making the optimization of the stimulation parameters both inefficient and challenging. Observing the cellular responses immediately after the HF vibration with light microscopy could provide new information on both the mechanocoupling and the mechanical force transduction of cells. This is necessary for deepening our understanding on the effects of mechanical manipulation on cellular physiology. Devices has already been introduced for the purpose. These systems utilize commercial speaker and optical disk reader to produce even HMHF vibration in room temperature (RT) [10, 11]. However, previous studies have demonstrated the need to conduct the experiments in controlled cell culture conditions [12, 13].

H. T. Halonen (✉) · J. A. K. Hyttinen · T. O. Ihalainen
Faculty of Medicine and Health Technology, Tampere University,
Arvo Ylpön Katu 34, 33520 Tampere, Finland
e-mail: heidi.halonen@tuni.fi

In this paper, we introduce a 3D printed stimulator platform, which combines the HF vibration and high-resolution light microscopy. Our aim was to design a device, which has a wide stimulation performance range in $+37\text{ }^{\circ}\text{C}$. The accuracy and precision of the system were tested with acceleration measurement and real-time imaging. We tested the device and imaged living cells before and immediately after the HF vibration. Our stimulator is an additional tool for cellular mechanobiology research, with the aim to provide a significantly more comprehensive knowledge of the direct stimulation effects to the cells.

2 Materials and Methods

2.1 Stimulator Design and Working Principle

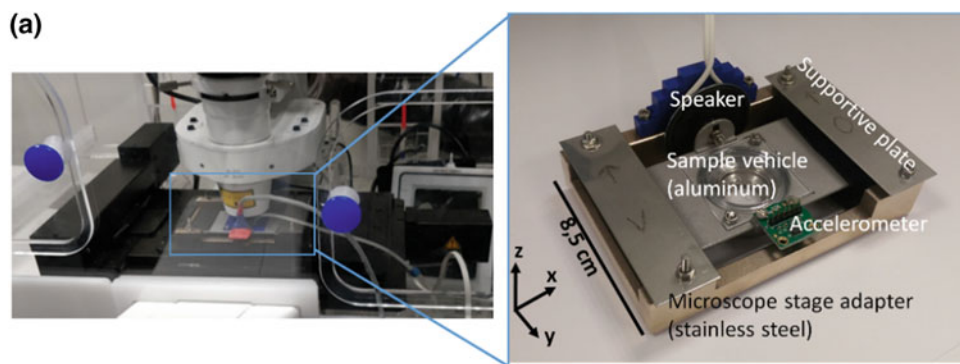
The stimulator was designed with SolidWorks (Dassault Systèmes Corp., MA, USA) to fit on a commercial inverted microscope unit (ZEISS LSM 780 LSCM, Carl Zeiss AG) and to accept coverslip cell chambers ($\varnothing = 3\text{ cm}$, Aireka

Cells, China) (Fig. 1a). We ordered 3D printing of the system (i.materialise, Netherlands). A sample vehicle accepts single sample holder (Aireka Cells, China) and is tightly attached against a commercial speaker ($\varnothing = 5\text{ cm}$, Partco Oy, Finland). Supportive plastic plates with miniaturized wheels (Roco, Germany) on their bottom provided stable horizontal movement (y-axis) of the vehicle on the stage adapter. The sample movement was measured with an accelerometer (3axis, ADXL325, Analog Devices). The stimulator was used with a user interface (LabVIEW, National Instruments) in temperature-controlled conditions provided with the microscope system (Incubator XL S1, ZEISS LSM 780 LSCM) and its software (Zen Black, Carl Zeiss AG) (Fig. 1b).

2.2 Performance Range

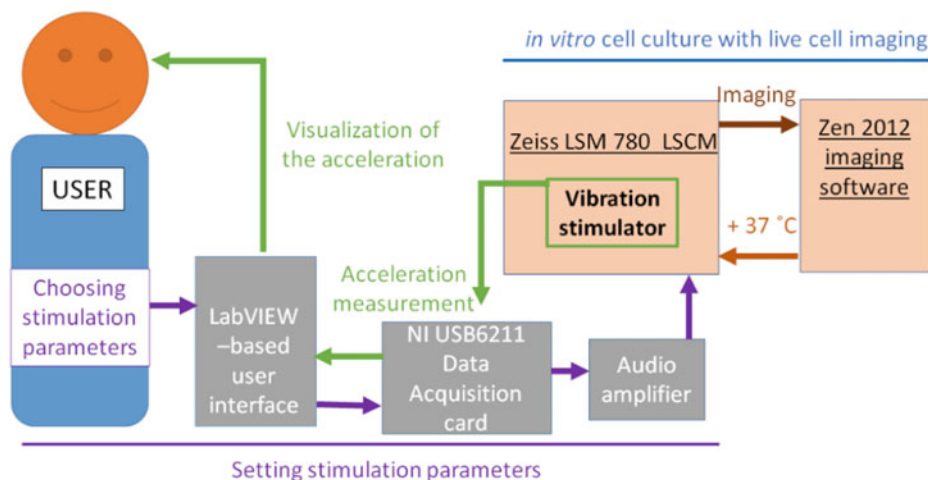
The performance range to produce sinusoidal HF vibration of the sample vehicle ($m = 104\text{ g}$) at a frequency range of 30–200 Hz was evaluated by increasing the AC voltage

Fig. 1 **a** Representative images of the stimulator and its placement on a commercial microscope unit. **b** To produce the desired HF vibration, the AC-signal parameters (voltage, frequency, duration) were set with a user interface, after which it was amplified (Pro-Ject Box-Design Amp Box S2, Pro-Ject Audio Systems, Austria). The stimulation was monitored and recorded with the user interface



(b)

Real-time measurement of the HF vibration stimulation



input of the stimulator and evaluating the time domain representations and power spectral density (PSD) estimates of three-dimensional accelerations. They were determined from the recorded acceleration data with a matlab-script (MATLAB R2014a (32-bit), MathWorks, MA, USA). The vibration magnitude (G_{peak}) maxima were considered either if the main channel movement (Y Ch) stopped increasing or was deformed, or the movement to other directions (X Ch, Z Ch) either increased higher than that of the main channel or exceeded the $0.5 G_{\text{peak}}$. The stimulator performance was tested inside the large chamber incubator (Incubator XL S1, Carl Zeiss AG) of ZEISS LSM 780 LSCM microscope (Carl Zeiss AG) first in RT and in $+37^\circ\text{C}$ after one hour of preheating.

2.3 Accuracy and Precision of the LMHF Vibration

Accuracy and precision of the sinusoidal HF vibration were tested in $+37^\circ\text{C}$ with measuring acceleration and real-time imaging of the sample movement. For the acceleration measurement, the accuracies of the LMHF ($0.5 G_{\text{peak}}$, 30, 60 Hz) vibrations were evaluated for the measurement channels (X Ch, Y Ch, Z Ch) from their maximum G_{peak} values and frequency contents. The precisions were tested with six stimulation repetitions, consisting of several stimulation bouts each ($n = 2 - 10$). For the imaging, a line sample (Au, width = $50 \mu\text{m}$) was printed on the cover glass (Carl Zeiss AG) and assembled into the sample holder (Aireka Cells). With rotated image scanning area (90°) in-plane differential interference contrast (DIC) image was taken ($25\times/0.8 \text{ Im Korr DIC UV M27}$, Carl Zeiss AG). Thereafter, time lapse with thin imaging area ($2 \times 512 \text{ px}$; frame rate: 265 FPS) was taken during two cycles of the

LMHF ($0.8 G_{\text{peak}}$; 30 Hz) vibration. The time lapse was converted to montage (Fiji), from which average gray scale intensities were measured before and after two stimulation bouts to determine the z-focus change. Misplacements (x-axis) from the initial position were measured as the distances of the sample line edge with respect to the image scanning area edge. Maximum sample displacement (μm) during the vibration were measured and compared with the theoretical values obtained from the measured acceleration data after acceleration to amplitude conversion.

We tested, if the system enables observing of fast cellular responses to the LMHF vibration ($0.2 G_{\text{peak}}$, 30 Hz; $110 \mu\text{m}$ displacement). During six short stimulation repetitions, we imaged (C-Apochromat $63\times/1.20 \text{ W Korr M27}$) a time lapse (113,98 s, frame rate 2.1 FPS) of living epithelial cells (MDCKII) expressing H2B-EGFP (nuclei) and E-cadherin-DsRed (cell-cell junctions) that were cultured on the cover glass (Carl Zeiss AG) and assembled into the sample holder (Aireka Cells). For the visualization, brightness and contrast were manually adjusted (Fiji) close to saturation limits.

3 Results

3.1 At Low Frequencies Stimulator Produces Even HMHF Vibration

The best performance range occurred at frequencies less than 70 Hz, after which the movement to other directions increased with respect to the main axis (Fig. 2). The environmental temperature had no effects to the maximum G_{peak} values, with the exception at the 30 and 80 Hz frequencies, but it affected the amount of movement to other directions (Fig. 2).

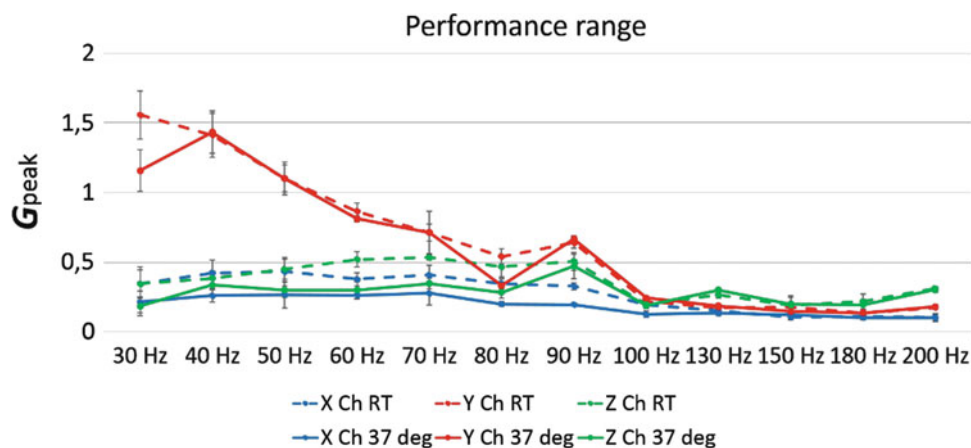


Fig. 2 On the usable performance range (30–70 Hz), the stimulator produced even HMHF vibration of the main axis (Y Ch), which maximum magnitude increased at 30 Hz frequency even to 6-fold higher than

those of other axes (X Ch, Z Ch). The maximum G_{peak} values decreased at $+37^\circ\text{C}$ only at 30 Hz frequency, but the higher temperature decreased the movement of other axes with approximately 50%

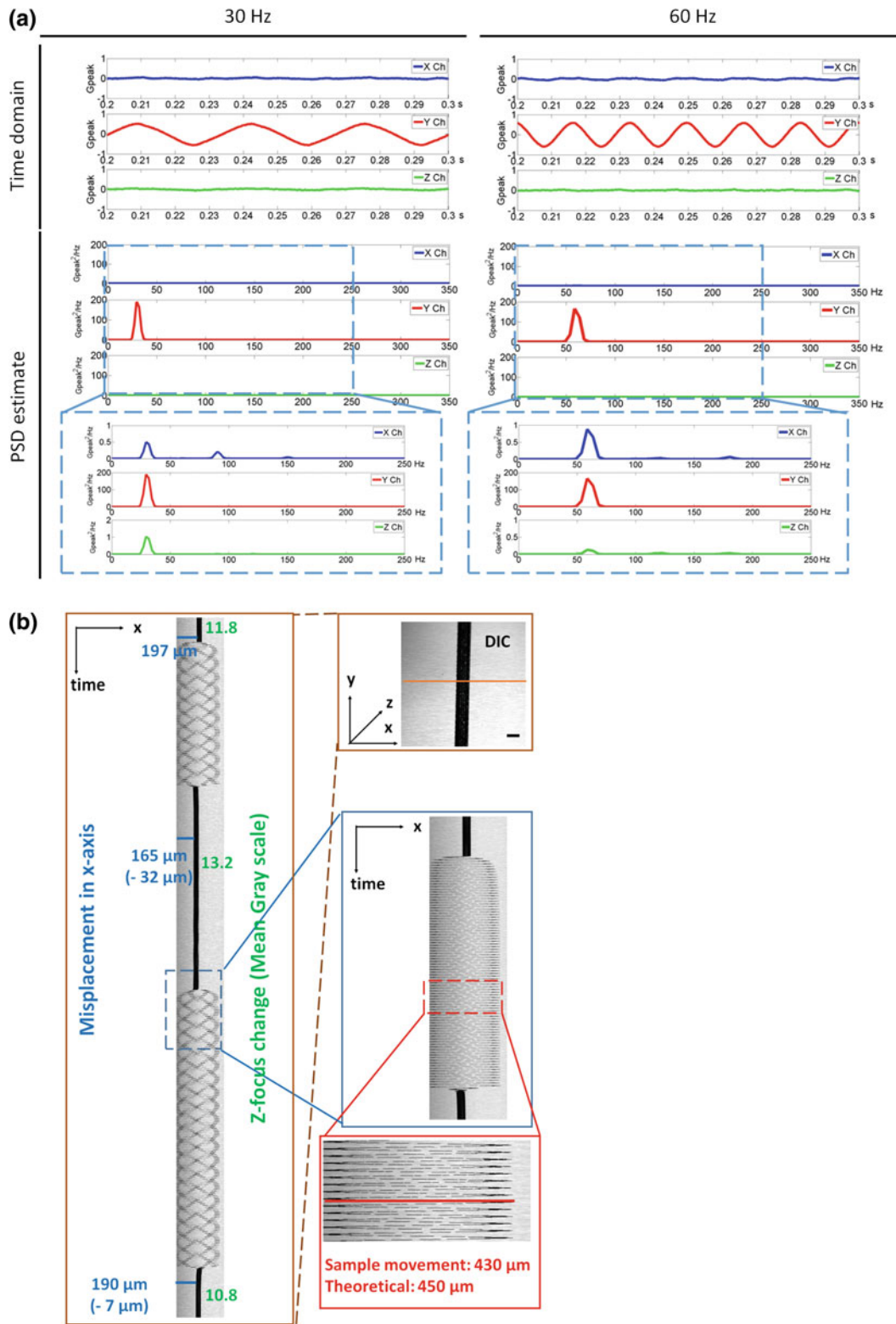


Fig. 3 **a** Time domain representations ($0.5 G_{peak}$) and PSD estimates ($200 G_{peak}^2/Hz$) of the acceleration data showed at 30, 60 Hz frequencies sinusoidal LMHF vibrations of the main axis without movement to other directions. **b** According to real-time imaging of the sample (orange line), two repetitions of the sinusoidal LMHF

($0.82 G_{peak}$, 30 Hz) vibration caused only minor misplacement from initial location (blue) with invariant z-focus (green). Moreover, the sample movement (red) had 93% fit to the theoretically calculated peak-to-peak displacements of the sinusoidal waveform. Scalebar 50 μm

3.2 Acceleration and Imaging Data Both Demonstrate Accurately Produced LMHF Vibration

The recorded acceleration data demonstrated accurately produced LMHF vibration at both stimulation frequencies (Fig. 3a). Representative DIC images illustrated adequately tracked real-time movement of the Au-printed sample during the sinusoidal LMHF vibration (Fig. 3b). The image scanning area restricted observing of the peak-to-peak displacements with higher G_{peak} values.

3.3 High Precision Enables Observing of Cellular Responses to the LMHF Vibration

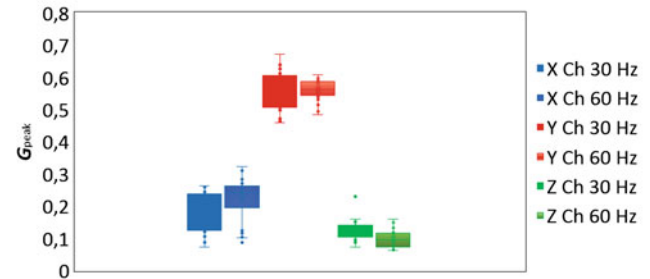
Acceleration results combining data from multiple stimulation bouts demonstrated accurately and precisely produced LMHF vibrations at both frequencies (Fig. 4a). The image field was precisely preserved after six LMHF vibration cycles, yet observing of the sample movement during the LMHF vibration was prevented by the limited imaging speed (Fig. 4b).

4 Discussion

The HF vibration affects the cellular physiology, such as proliferation [3–5] and differentiation of stem cells [1–8, 14]. Actin cytoskeleton and nucleus have been found crucial for the mechanocoupling of the stimulus, together with their interaction through Linker- of Nucleoskeleton and Cytoskeleton (LINC) complex [4, 14]. However, a wider utilization of the method requires still a better understanding of the stimulation effects to the cellular mechanobiology.

Our stimulator produced horizontal HF vibration accurately and precisely, especially when applied at the 60 Hz frequency. On specific frequencies, high magnitude method (HMHF) were enabled reaching even higher magnitudes than previously reported with corresponding stimulators designed for live cell imaging [10, 11]. Currently the performance sufficiently covers needs set for the stimulator, while low magnitude method (LMHF) has been reported in many cell studies [3–6]. However, increasing the magnitudes from the current would probably be needed to detect immediate cellular responses to the stimulus. With the current frequency range our stimulator covers the most common stimulation frequencies of bone tissue engineering only partially [2–5], failing to produce e.g. nanoscale mechanical vibrations [6]. The linear actuator sets the highest

(a) Accuracy and precision of the LMHF vibration



AVE (SD)	X Ch	Y Ch	Z Ch
30 Hz, n=40 (tot.)	0.17 (0.06)	0.54 (0.06)	0.12 (0.03)
60 Hz, n=42 (tot.)	0.22 (0.07)	0.56 (0.03)	0.10 (0.02)

(b)

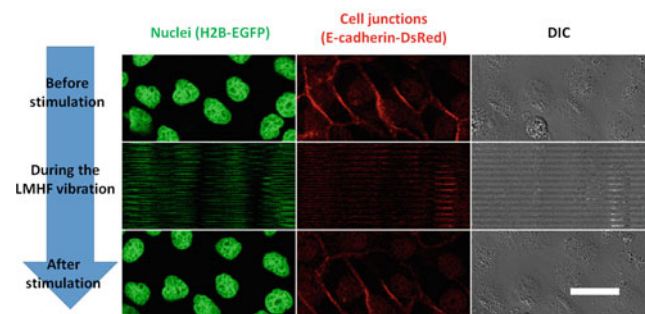
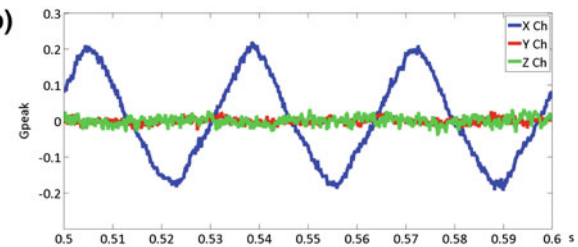


Fig. 4 a The LMHF ($0.5 G_{\text{peak}}$) vibration was accurately produced towards the main axis (Y Ch; $0.54\text{--}0.56 G_{\text{peak}}$, 108–112%) with less than 22% of sideways movement (X Ch) and 40% of bouncing movement (Z Ch) with respect to the main axis. Thinner quartiles of the box plots of the 60 Hz frequency demonstrated more precisely produced LMHF vibration when compared to the 30 Hz frequency. **b** Our system enabled observing of local biological fast cell responses to the LMHF ($0.2 G_{\text{peak}}$, 30 Hz) vibration. Scale bar 30 μm

performance limitations, and thus it should be chosen accordingly to meet the cell application -specific stimulation needs.

Currently, our stimulator enabled tracking of the real-time movement of the sample during the HF vibration similarly to previously introduced devices [10, 11]. However, imaging speed prevented us from observing movements of larger areas. This would be essential to observe real-time

stimulation effects in the cell culture. To our knowledge, neither stimulation initiated cellular deformations nor fluid flow have been studied with high-resolution light-microscopy [10, 11], but mathematical models have suggested their occurrence [3, 15–17]. Consequently, imaging of the live cells with higher imaging speeds could provide us with new knowledge on the effect of the different loading parameters in the stimulus response.

The higher environmental temperature had only minimal effects to our stimulator's performance. Environmental factors (e.g. temperature and gas concentrations) are crucial for the cellular functions even in static cell cultures [12, 13]. Consequently, the miniaturized size of the device enables performing of cell stimulations in more favorable cell culture conditions than the previous devices [10, 11]. However, to study the cellular responses even more reliably would require adding a light-weighted heating plate in the proximity of the sample and replacing the current sample holder with a miniaturized and portable cell incubation chamber [13] to provide more precisely controlled cell culture conditions.

In this study, we realized a portable and easy-to-use mechanical stimulator. The HF vibration is produced on the commercial microscope system both accurately and precisely, though the sample vehicle design and the linear actuator should be optimized to enhance the performance further. Our initial findings with live epithelial cells suggest that, after development of more adequate control of the cell culture conditions, our device could be beneficial for many areas of the mechanobiology research.

5 Conclusion

We have designed a tool for the mechanobiology research, which enables observing of fast biological cellular responses to the dynamic HF mechanical vibration with high-resolution light-microscopy. In future, our system will be a good platform for real-time observation of the cellular responses to mechanical stimulation.

Acknowledgements This study was funded by Finnish Funding agency for Innovation (TEKES, Human spare parts project), City of Tampere, Instrumentariumin tiedesäätiö s.r. foundation, Finnish Cultural Foundation (The Kainuu Regional Fund), and the Finnish Academy of Science and Letters (Väisälä Foundation).

Conflict of Interest The authors declare that they have no conflict of interest.

References

1. Sen, B., Xie, Z., Case, N., Styner, M., Rubin, C.T., Rubin, J.: Mechanical signal influence on mesenchymal stem cell fate is enhanced by incorporation of refractory periods into the loading regimen. *J. Biomech.* **44**(4), 593–599 (2011)
2. Tirkkonen, L., Halonen, H., Hyttinen, J., Kuokkanen, H., Sievänen, H., Koivisto, A.M., Mannerström, B., Sándor, G.K., Suuronen, R., Miettinen, S., Haimi, S.: The effects of vibration loading on adipose stem cell number, viability and differentiation towards bone-forming cells. *J. R. Soc. Interface* **8**(65), 1736–1747 (2011)
3. Zhang, C., Li, J., Zhang, L., Zhou, Y., Hou, W., Quan, H., Li, X., Chen, Y., Yu, H.: Effects of mechanical vibration on proliferation and osteogenic differentiation of human periodontal ligament stem cells. *Arch. Oral. Biol.* **57**(10), 1395–1407 (2012)
4. Uzer, G., Pongkitwitoon, S., Ete Chan, M., Judex, S.: Vibration induced osteogenic commitment of mesenchymal stem cells is enhanced by cytoskeletal remodeling but not fluid shear. *J. Biomech.* **46**(13), 2296–2302 (2013)
5. Chen, X., He, F., Zhong, D.Y., Luo, Z.P.: Acoustic-frequency vibratory stimulation regulates the balance between osteogenesis and adipogenesis of human bone marrow-derived mesenchymal stem cells. *Biomed. Res. Int.* **2015**, 540731 (2015)
6. Pemberton, G.D., Childs, P., Reid, S., Nikukar, H., Tsimbouri, P. M., Gadegaard, N., Curtis, A.S., Dalby, M.J.: Nanoscale stimulation of osteoblastogenesis from mesenchymal stem cells: nanotopography and nanokicking. *Nanomedicine (Lond.)* **10**(4), 547–560 (2015)
7. Tong, Z., Duncan, R.L., Jia, X.: Modulating the behaviors of mesenchymal stem cells via the combination of high-frequency vibratory stimulations and fibrous scaffolds. *Tissue Eng. Part A.* **19** (15–16), 1862–1878 (2013)
8. Cho, H., Seo, Y.K., Jeon, S., Yoon, H.H., Choi, Y.K., Park, J.K.: Neural differentiation of umbilical cord mesenchymal stem cells by sub-sonic vibration. *Life Sci.* **90**(15–16), 591–599 (2012)
9. Takeuchi, R., Saito, T., Ishikawa, H., Takigami, H., Dezawa, M., Ide, C., Itokazu, Y., Ikeda, M., Shiraiishi, T., Morishita, S.: Effects of vibration and hyaluronic acid on activation of three-dimensional cultured chondrocytes. *Arthritis Rheum.* **54**(6), 897–905 (2006)
10. Holdsworth, D.W., Nikolov, H.N., Au, J., Beaucage, K., Kishimoto J., Dixon, S.J.: Simultaneous vibration and high-speed microscopy to study mechanotransduction in living cells. In: Molthen, R.C., Weaver, J.B. (eds.) *Medical Imaging 2012: Biomedical Applications in Molecular, Structural, and Functional Imaging*, Proceedings of SPIE, **8317**, 831715-1–831715-6. SPIE (2012)
11. Lorusso, D., Nikolov, H.N., Chmiel, T., Beach, R.J., Sims, S.M., Dixon, S.J., Holdsworth, D.W.: A device for real-time live-cell microscopy during dynamic dual-modal mechanostimulation. In: Krol, A., Gimi, B. (eds.) *Medical imaging 2017: Biomedical Applications in Molecular, Structural, and Functional Imaging*, Proceedings of SPIE, **10137**, 101370F-1–101370F-7. SPIE (2017)
12. Mäki, A.J., Verho, J., Kreutzer, J., Ryyänen, T., Rajan, D., Pekkanen-Mattila, M., Ahola, A., Hyttinen, J., Aalto-Setälä, K., Leikkala, J., Kallio, P.: A portable microscale cell culture system with indirect temperature control. *SLAS Technol.* **1**, 2472630318768710 (2018)

13. Kreutzer, J., Ylä-Outinen, L., Mäki, A.J., Ristola, M., Narkilahti, S., Kallio, P.: Cell culture chamber with gas supply for prolonged recording of human neuronal cells on microelectrode array. *J. Neurosci. Methods* **280**, 27–35 (2017)
14. Uzer, G., Thompson, W.R., Sen, B., Xie, Z., Miller, S.S., Bas, G., Styner, M., Rubin, C.T., Judex, S., Burrige, K., Rubin, J.: Cell mechanosensitivity to extremely low-magnitude signals is enabled by a LINCed Nucleus. *Stem Cells* **33**(6), 2063–2076 (2015)
15. Uzer, G., Pongkitwitoon, Ian, S., Thompson, W.R., Rubin, J., Chan, M.E., Judex, S.: Gap junctional communication in osteocytes is amplified by low intensity vibrations in vitro. *PLoS One*. **9**(3), e90840 (2014)
16. Milner, J.S., Grol, M.W., Beaucage, K.L., Dixon, S.J., Holdsworth, D.W.: Finite-element modeling of viscoelastic cells during high-frequency cyclic strain. *J. Funct. Biometr.* **3**(1), 209–224 (2012)
17. Wang, L., Hsu, H.Y., Li, X., Xian, C.J.: Effects of frequency and acceleration amplitude on osteoblast mechanical vibration responses: a finite element study. *Biomed. Res. Int.* **2016**, 2735091 (2016)

EMG Signal Classification Using Discrete Wavelet Transform and Rotation Forest

Abdulhamit Subasi and Emine Yaman

Abstract

Electromyographic (EMG) signals are used for the diagnosis of neuromuscular disorders. We have used machine learning algorithms in diagnosing neuromuscular disorders as a decision support system. Hence, in this study, for feature extraction DWT has been used and the Rotation Forest ensemble classifier has been used for classification. Furthermore, we also investigated the performance of different classifiers with Rotation Forest. The performance of a classifier is enhanced using the Rotation Forest ensemble classifier. Significant amount of performance improvement was achieved with a combination of Discrete Wavelet Transform (DWT), and Rotation Forest using k-fold cross validation. Experimental results show the feasibility of Rotation Forest, and we also derive some valuable conclusions on the performance of ensemble learning methods for diagnosis of neuromuscular disorders. Results are promising and showed that the ANN with Random Forest ensemble method achieved an accuracy of 99.13%.

Keywords

Electromyography (EMG) • Neuromuscular disorders • Discrete wavelet transform (DWT) • Rotation forest

1 Introduction

The nervous system and the muscular system are the constituent parts of the human skeletal muscular system. Neuromuscular disorders may stem from several problems on a variety of muscle fibers or nerves. For that reason, it is vital to point out the exact location of the disorder. Electromyography (EMG) was introduced as a technique for the diagnosis of neuromuscular disorders based on cell action potentials during muscle activity [1–4]. The accuracy of EMG signal classification can be affected by several factors, such as the effectiveness of the feature extraction methods and classifiers. Thus, the performance of an EMG signal classification system can be improved by resolving problems encountered. Recently, quite a lot of methods have been introduced to extract effective features to characterize EMG signals for classification [1, 2, 4–9]. But, design of accurate diagnostic system remains challenging. As a result, in order to get an efficient automated EMG signal classification, it is important to perform a systematic analysis of EMG signals. For that purpose, some computer-based quantitative EMG analysis algorithms have been devised [1–4, 8, 10–14].

In this paper, discrete wavelet transforms (DWT) is employed to extract features of EMG signals. After DWT coefficients are obtained, statistical features are extracted for each sub-band of DWT. The DWT coefficients' statistical features are used as inputs to the classifier. ANN and k-NN are not competent in managing highdimensional information without variable measurement lessening or variable determination, while SVM is fit for handling high-dimensional information, however isn't powerful to the nearness of a substantial number of unessential factors [15] and subsequently may require a variable choice too [16]. Additionally, it is trying to guarantee higher order precision of SVM for meticulous issues. In addition to the methods mentioned before, different decision trees like Random Forest, C4.5, Random Tree, LAD Tree and Naïve Bayes were used for classification problems. Most decision tree learning

A. Subasi (✉)
College of Engineering, Effat University, Jeddah, 21478,
Saudi Arabia
e-mail: abdulhamitsubasi@gamil.com;
absubasi@effatuniversity.edu.sa

E. Yaman
International University of Sarajevo, Sarajevo,
Bosnia and Herzegovina
e-mail: eyaman@ius.edu.ba

algorithms are based on greedy approaches where decisions are made at the most appropriate level locally. The greedy algorithms can be recursively validated starting from the root node and require three meta-parameters: The first is a list of possible ways to divide data; the latter is a criterion for choosing the best division; and third, a set of rules to stop the algorithm. However, the basic problem of decision trees is that they cannot work efficiently with large sized data. When the data size gets bigger and more complex, the decision mechanism of decision trees cannot work very well and cannot be interpreted. Since EMG signals are high-dimensional, difficult to understand and interpret, and complex, it is aimed to increase the success rate by using more sophisticated algorithms. Keeping in mind the end goal to determine previously mentioned issues, there is a requirement for an EMG signal to present more efficient machine learning strategies. In this paper, to overcome the previously mentioned constraints, we explore the utilization of ensemble classifier structure for characterization of EMG signals in diagnosis of neuromuscular disorders.

The remaining part of the paper is arranged as the following. In the coming section, materials and methods have been explained. The subjects and methods that were used in each step of the EMG signal classification process are introduced. In Sect. 3, an extensive experimental study of the Rotation Forest based EMG signal classification scheme is given. In this scheme, we looked into the impact of the feature set and algorithmic issues regarding the classification performance. Besides Rotation Forest classification performance is compared with other classification techniques. Lastly, the conclusions are summarized in Sect. 4.

2 Materials and Methods

2.1 Subjects and Data Acquisition

With the help of a concentric needle electrode, the EMG signals were taken from the biceps brachii muscle. The signals are sampled at 20 kHz for 5 s with 12-bit resolution and band-pass filtered at 5–10 kHz. EMG data collected from seven control subjects (three males, four females), seven myopathic subjects and thirteen neuropathic subjects as in [4].

2.2 Feature Extraction Using DWT and Dimension Reduction

One of the important tools is the capacity of reducing parameters. Parameters are also often called features. The methods that are employed decreased the number of

parameters to characterize the EMG signal are critical for diagnosis of neuromuscular disorders. A decomposition of a signal with a better time resolution could be acquired by making use of the wavelet transform that breaks down a signal into a set of basic functions which are called wavelets. We acquire wavelets from a single function ψ by dilations and translations [17]. The Continuous Wavelet Transform (CWT) [18, 19] for a continuous signal, $x(t)$ is defined as

$$CWT_x(\tau, a) = \int_{-\infty}^{\infty} x(at) \frac{1}{\sqrt{a}} \psi\left(\frac{t-\tau}{a}\right) dt, \quad (1)$$

where $\psi(t)$ is considered as the mother or basic wavelet, a works as the scale factor and works to translate the function across $x(t)$ and the variable τ has the role to tune the time scale of the probing function, ψ [18–20].

Wavelet-based methods are practical techniques in analyzing different types of non-stationary signals like EMG. Discrete Wavelet Transform (DWT), for instance, scales and shifts the mother wavelet, and breaks down a discrete-time signal $x[k]$ into a set of signals. The first thing done in the DWT decomposition is finding the suitable number of wavelet decomposition levels. The signal $x[k]$ goes through the high-pass and low-pass filter at the same time. In this study, decomposition levels are taken as five.

Since, wavelet-based feature extraction tools produce the feature vector which has too big size to be used as an input to a classifier. These types of dimension reduction techniques can be used to extract less number of features from wavelet coefficients. The six statistical features are implemented for the EMG signal classification which are:

1. Mean absolute values of coefficients found in each sub-band,
2. Average power of the coefficients found in each sub-band,
3. Standard deviation of the coefficients found in each sub-band,
4. Ratio of the absolute mean values of coefficients of adjacent sub-bands,
5. Skewness of the coefficients found in each sub-band,
6. Kurtosis of the coefficients found in each sub-band.

2.3 Artificial Neural Networks (ANN)

A set of input and output units which are connected forms artificial neural networks (ANN). The network acquires the information by adjusting the weights until it can have ability to anticipate the correct class label of the input tuples. One of

the advantages of neural networks is that they have high tolerance of noisy data. The other advantage of is that they are able to categorize untrained- patterns. They might be useful if you do not have enough information about the connections between attributes and classes [21].

2.4 K-Nearest Neighbour (K-NN)

When the training set is large, the k-nearest-neighbor method requires a lot labor. Nearest-neighbor classifiers learn by analogy, which means that a given test tuple is similar to training tuples. In case the training tuples are shown in an n dimensional space by n, then it means those training tuples are stored in an n dimensional space. In case that there is an unknown tuple, a k-nearest-neighbor classifier looks for the pattern space for k training tuples. These tuples must be the closest ones to the unknown tuple. The “closeness” is described by a distance metric like Euclidean distance [21].

2.5 Support Vector Machine (SVM)

In classifying linear and nonlinear data SVM is utilized. A nonlinear mapping is used in order to convert the original training data into an upper level dimension. It examines the linear optimal separating hyperplane in this new dimension like a decision boundary by which the tuples of one class from another is being separated. A hyperplane can always separate data from two classes by using a proper nonlinear mapping to a high dimension. This hyperplane is used to form support vectors that are important training vectors and margins. Contrary to the other methods, they are highly robust for overfitting [21].

2.6 Naïve Bayes

Naïve Bayes is a probabilistic approach that utilizes semantics so as to represent, use, and learn knowledge. Naïve Bayes has the capacity to reach good success levels and it can compete with more sophisticated classifiers. The limitation of Naïve Bayes is the normal distribution assumption. Many datasets basically are not normally distributed. If we are not sure about the real distribution, we can make use of kernel density estimation which does not expect a specific distribution for the attribute values. Another thing we can do about is just allocating different values to the data at first [21].

2.7 REPTree

In a REPTree, a decision tree is made with the help of gain/variance reduction and the built tree is pruned with reduced error pruning. As it is balanced for speed, just the values for numeric attributes are classified for one time. The number of folds for pruning, maximum tree depth, minimum number of instances on each leaf, and minimum proportion of training set variance for a split can all be determined [21].

2.8 LADTree

LADTree is an alternating decision tree used for two class problems by making use of boosting. The number of boosting iterations can be adjusted to fit the dataset and the aimed complexity-accuracy tradeoff. The tree receives three nodes from each iteration, one being split node and other two being prediction nodes if nodes cannot be melded. The given search method is the extensive one while the other methods are faster. Saving instance data for visualization is an option. LADTree can also tune the number of boosting iterations to fit the data and it sets the size of the generated tree [21].

2.9 C4.5 Decision Tree

C4.5 decision tree algorithm tests for which training examples have the same result are eliminated as they are not very important. Therefore, they are not contained in the decision tree if they do not have minimum two outcomes which have a minimum number of instances. Candidate splits are taken into consideration in the case that they cut a specific number of instances. Quinlan [22] designed that heuristic in order to avoid over-fitting. If we do not have attributes that have positive information gain, which is a kind of pre-pruning, the tree will stop growing [23].

2.10 Random Tree Classifiers

Random Tree uses bagging idea to make a random set of data. In standard tree, all the nodes are separated by utilizing the best split among the variables. The input feature vector is classified with every tree in the forest, and then the class label which took the most votes is produced. When we use tree diversity and randomization, the performance of single decision trees substantially gets better [23, 24].

2.11 Random Forests (RF)

The random forest is ensemble of decision tree classifiers by making them as a group of classifiers which is called forest. An individual decision tree is produced by using an arbitrary array of attributes at each node in order to determine the split. Every tree depending on random vector's values is taken individually and they have the same distribution allocated for every tree present in the forest. We can form random forests by making use of bagging together with random attribute selection. In order to raise the trees, the CART method is used. Random forests make use of random linear combinations from the input attributes. It does not randomly choose a subset of the attributes, but it forms new features which are linear combination of the current attributes [21].

2.12 Rotation Forest (RoF)

Rotation Forest (RoF) is a type of classifier ensemble which depends on feature extraction. For a base classifier, the training data is created by randomly separating the feature set into K subsets and we apply Principal Component Analysis (PCA) each subset. We hold all the key elements so that the variability information in the data is protected. The important thing about the rotation approach is to support individual accuracy and diversity in the ensemble at the same time. By doing the feature extraction for each base classifier, diversity is cultivated. We preferred decision trees at this point because of their sensitivity to rotation of the feature axis and, thusly, named "forest". We tried to keep accuracy through holding the main elements, and we also utilized the whole dataset in training each base classifier [25].

3 Results and Discussion

3.1 Experimental Results

In this study, we utilized statistical features which were extracted for each sub-band of DWT in order to diagnose neuromuscular disorders. Firstly, we take the set of feature parameters from the sample EMG signals. After that we train different machine learning methods expecting to have more precise results for EMG signal classification.

Taking Performance on the training set as a performance indicator on an independent test set is not a good idea. It is not highly reliable to predict performance which is based on a limited amount of data. Using a ten-fold cross-validation is the most common method of predicting the error rate of a learning technique when there is a single, fixed sample of

data [23]. In this study, the evaluation of performance of classifiers was focused upon by making use of accuracy, F-score and Area under the Curve (AUC) and Kappa. Accuracy shows how much the algorithm is efficient through demonstrating the probability of the true value of the class label. It, in a sense, evaluates the total effectiveness of the algorithm [26]. The kappa statistic is the most frequently used statistic for the evaluation of categorical data when there is no independent means of assessing the probability of chance agreement between two or more observers [27–29].

Under the light of Experimental results retrieved in this study show that classification accuracy is improved by using statistical features extracted for each sub-band of DWT. Classifiers performances for the EMG data have been summarized in Tables 1 and 2. All methods performed reasonably well according to total classification accuracy, AUC, F-measure and Kappa Statistics. As shown in Table 1, LAD Tree acquires a minimum performance with the results of 83.125% from single classifiers' accuracy. When we checked classification accuracy of rotation forest, LAD Tree gave minimum performance with 93.4583% in Rotation Forest method (see Table 2). The best performance is achieved by SVM with 99.0417% classification accuracy from single classifiers. When we used rotation forest ensemble classifier, the best performance is again achieved by SVM with 99.2083%.

The AUC of ANN, k-NN, SVM, RF, C4.5, Random Tree, REP Tree, LAD Tree and NB were 0.999, 0.987, 0.994, 1, 0.973, 0.966, 0.982, 0.85 and 0.98, respectively. The best AUC performance is achieved by ANN, RF, C4.5, REP Tree with 1 for rotation forest.

The F-measure of ANN, k-NN, SVM, RF, C4.5, Random Tree, REP Tree, LAD Tree and NB were 0.988, 0.937, 0.99, 0.989, 0.963, 0.955, 0.956, 0.829 and 0.907, respectively for single classifiers. After using rotation forest ensemble learning methods, almost all results are increased until 0.99.

Kappa results for single classifiers ANN, k-NN, SVM, RF, C4.5, Random Tree, REP Tree, LAD Tree and NB were 0.9813, 0.9069, 0.9856, 0.9837, 0.945, 0.9325, 0.9337, 0.7469, 0.8606, respectively. After using ensemble learning methods, almost all results are increased until 0.98.

Selection of input variables and classification method choice are the most important considerations for the performance of EMG signal classification. Signal processing method and selection of features are other significant criteria to derive the most valuable parameters from EMG. The best suited parameters must be used as the inputs of the model for EMG signal classification. For this reason, along with a statistical feature extracted for each sub-band of DWT is preferred thanks to its practicality in classifying the nonlinear dynamics underlying muscle activity and allows the growth of complexity and regularity of the EMG.

Table 1 EMG signal classification results for single classifiers

	Accuracy (%)	F-measure	ROC area	Kappa
ANN	98.75	0.988	0.999	0.9813
k-NN	93.79.17	0.937	0.987	0.9069
SVM	99.0417	0.99	0.994	0.9856
Random forest	98.9167	0.989	1	0.9837
C4.5	96.3333	0.963	0.973	0.945
Random tree	95.5	0.955	0.966	0.9325
REP tree	95.5833	0.956	0.982	0.9337
LAD tree	83.125	0.829	0.85	0.7469
NB	90.7083	0.907	0.98	0.8606

Table 2 EMG signal classification results for rotation forest

	Accuracy (%)	F-measure	ROC area	Kappa
ANN	99.1667	0.992	1	0.9875
k-NN	95.6667	0.956	0.996	0.935
SVM	99.2083	0.992	0.998	0.9881
Random forest	99.125	0.991	1	0.9869
C4.5	99.1667	0.992	1	0.9875
Random tree	98.3333	0.983	0.999	0.975
REP tree	98.5417	0.985	1	0.9781
LAD tree	93.4583	0.935	0.988	0.9019
NB	92.0833	0.921	0.985	0.8812

Diagnosis and treatment of many types of muscle disease is only possible with exact identification of EMG signal. In this study firstly, EMG signals are classified by single classifiers by making use of statistical features extracted for each sub-band of DWT as the input. After that rotation forest ensemble learning methods were used in order to improve the performance of suggested model. In classifying EMG signals, the classifiers which have been described in this study gain a value when compared to other already existing examples.

3.2 Discussion

In this study, it was aimed to design a model to help diagnosis and treatment of neuromuscular diseases using EMG signals. When data is classified with single classifiers, the best result is achieved by SVM. When Rotation Forest ensemble classifier is used to increase success rate, SVM is again the most successful algorithm. Moreover, we observe that in rotation forest the finest result is received by the ANN and C4.5 algorithms as well.

Each classification method has different logic to adjust parameters. For example, only one key parameter (number of trees) is adjusted in RF. Furthermore, clinicians do not know the meaning of some parameters exactly. Because of

creating appropriate algorithm is difficult in clinical practice, various kinds of machine learning methods have been developed. One of the most successful algorithms is ANN and has been found appropriate since the early days of computer-assisted analyses [1, 2]. There are some criteria like ease of use, performance and interpretation which are the most important concern in choosing an appropriate algorithm. There are almost no studies in the literature with ensemble learning methods in diagnosis of neuromuscular disorders. Although this study indicates that ensemble learning methods have potential diagnosing neuromuscular illnesses by utilizing EMG signals.

Comparisons of classifiers created in this study with similar systems, diversity of classification techniques, MUAP types classified in systems, number of MUAP types classified, EMG signal processing techniques and their features is a challenging task. The results obtained in this study were found to perform satisfactorily with a success rate of 99.2083%, compared with the literature examples.

Selection of input variable is an important step in creating the classifier. In this study, the statistical properties for each sub-band of DWT are used as an input to a classifier. Statistical features can reduce the number of features in a subset; that allows the use of the smallest subset that can be consistent with the full feature set. Hence, the features chosen for model construction are those related to the signal

statistics of the different frequency bands. Clinicians should take care to understand the requirements of the model before use. The final result of this study showed that ensemble learning methods show a greater performance than other models while diagnosing neuromuscular disorders. Compared to today's strategies, this model provides a fast, easy and cost-effective method for accurately diagnosing neuromuscular disorders.

Actually, there are some studies in the literature about surface EMG signal classification using rotation forest. For example, Abdullah et al. [30] employed surface EMG signals collected from physical actions. They used Wavelet Packet Decomposition (WPD) to extract features and various ensemble tree classifiers used to classify them. Subasi et al. [31] employed surface EMG signals from hand movements. They used Wavelet Packet Decomposition (WPD) to extract features and Rotation Forest classifier for the classification.

4 Conclusion

The detection of neuromuscular disorders from electromyography (EMG) recordings has become a popular and significant theme for biomedical research. This is due to the fact that the classification of the various MUAPs and correct recognition is a condition for the accurate treatment of the patient.

In this work, a new framework for characterizing MUAP is proposed by applying high-order statistics (HOS) to sub-band components after decomposition of four level Discrete Wavelet Transform (DWT). A simple feature selection method has been suggested to remove unnecessary features in the primary feature set. The results have shown that diverse pathological changes in EMG signals can be effectively demonstrated by HOS characteristics (second, third and fourth clumps) deduced for each sub-band of DWT. In addition, when compared with other similar examples in the literature, the proposed algorithm is more favourable in identifying different types of MUAP. Because of the novel combination of Discrete Wavelet Transform with higher order statistics, the performance indices of the MUAP detection algorithm are good enough.

There are many studies about classification problems with ensemble learning methods, but these methods did not use EMG signals in diagnosis of neuromuscular illnesses. According to the results, the suggested method impressively outperforms the most commonly used single classifiers. In addition, the proposed model can be easily implemented in any computer-based monitoring system. The proposed model uses a small number of parameters representing EMG signals instead of using all EMG records, so using a smaller data set has given the advantage of performance.

Acknowledgements The author would like to extend many thanks to Dr. Mustafa Yilmaz at University of Gaziantep, Neurology Department for providing the EMG data used in this research.

Funding This work was supported by Effat University with the Decision Number of UC#7/28 Feb. 2018/10.2-44 h, Jeddah, Saudi Arabia.

References

1. Subasi, A.: Classification of EMG signals using combined features and soft computing techniques. *Appl. Soft Comput.* **12**(8), 2188–2198 (2012)
2. Subasi, A.: Classification of EMG signals using PSO optimized SVM for diagnosis of neuromuscular disorders. *Comput. Biol. Med.* **43**(5), 576–586 (2013)
3. Begg, R., Lai, D.T., Palaniswami, M.: *Computational Intelligence in Biomedical Engineering*. CRC Press (2008)
4. Subasi, A., Yilmaz, M., Ozcalik, H.R.: Classification of EMG signals using wavelet neural network. *J. Neurosci. Methods* **156**(1), 360–367 (2006)
5. Bozkurt, M.R., Subasi, A., Koklukaya, E., Yilmaz, M.: Comparison of AR parametric methods with subspace-based methods for EMG signal classification using stand-alone and merged neural network models. *Turk. J. Electr. Eng. Comput. Sci.* **24**(3), 1547–1559 (2016)
6. Gokgoz, E., Subasi, A.: Effect of multiscale PCA de-noising on EMG signal classification for diagnosis of neuromuscular disorders. *J. Med. Syst.* **38**(4), 31 (2014)
7. Gokgoz, E., Subasi, A.: Comparison of decision tree algorithms for EMG signal classification using DWT. *Biomed. Signal Process. Control* **18**, 138–144 (2015)
8. Subasi, A.: Medical decision support system for diagnosis of neuromuscular disorders using DWT and fuzzy support vector machines. *Comput. Biol. Med.* **42**(8), 806–815 (2012)
9. Subasi, A.: A decision support system for diagnosis of neuromuscular disorders using DWT and evolutionary support vector machines. *Signal Image Video Process.* **9**(2), 399–408 (2015)
10. Kamali, T., Boostani, R., Parsaei, H.: A multi-classifier approach to MUAP classification for diagnosis of neuromuscular disorders. *IEEE Trans. Neural Syst. Rehabil. Eng.* **22**(1), 191–200 (2014)
11. Katsis, C.D., Exarchos, T.P., Papaloukas, C., Goletsis, Y., Fotiadis, D.I., Sarmas, I.: A two-stage method for MUAP classification based on EMG decomposition. *Comput. Biol. Med.* **37**(9), 1232–1240 (2007)
12. Phinyomark, A., Phukpattaranont, P., Limsakul, C.: Feature reduction and selection for EMG signal classification. *Expert Syst. Appl.* **39**(8), 7420–7431 (2012)
13. Rasheed, S., Stashuk, D., Kamel, M.: A software package for interactive motor unit potential classification using fuzzy k-NN classifier. *Comput. Methods Programs Biomed.* **89**(1), 56–71 (2008)
14. Dobrowolski, A.P., Wierzbowski, M., Tomczykiewicz, K.: Multiresolution MUAPs decomposition and SVM-based analysis in the classification of neuromuscular disorders. *Comput. Methods Programs Biomed.* **107**(3), 393–403 (2012)
15. Svetnik, V., Liaw, A., Tong, C., Culberson, J.C., Sheridan, R.P., Feuston, B.P.: Random forest: a classification and regression tool for compound classification and QSAR modeling. *J. Chem. Inf. Comput. Sci.* **43**(6), 1947–1958 (2003)
16. Liu, M., Wang, M., Wang, J., Li, D.: Comparison of random forest, support vector machine and back propagation neural network for electronic tongue data classification: Application to

- the recognition of orange beverage and Chinese vinegar. *Sens. Actuators B Chem.* **177**, 970–980 (2013)
17. Vetterli, M., Herley, C.: Wavelets and filter banks: Theory and design. *IEEE Trans. Signal Process.* **40**(9), 2207–2232 (1992)
 18. Daubechies, I.: The wavelet transform, time-frequency localization and signal analysis. *IEEE Trans. Inf. Theory* **36**(5), 961–1005 (1990)
 19. Rioul, O., Vetterli, M.: Wavelets and signal processing. *IEEE Signal Process. Mag.*, **8**(LCAV-ARTICLE-1991-005), 14–38 (1991)
 20. Thakor, N.V., Gramatikov, B., Sherman, D.: Wavelet (time-scale) analysis in biomedical signal processing. In: Bronzino, J.D. (ed.) *The Biomedical Engineering Handbook*, vol. 56, 2nd edn, pp. 1–56. CRC Press LLC, Boca Raton, Florida (2000)
 21. Han, J., Pei, J., Kamber, M.: *Data Mining: Concepts and Techniques*. Elsevier (2011)
 22. Quinlan, J.R.: Induction of decision trees. *Mach. Learn.* **1**(1), 81–106 (1986)
 23. Hall, M., Witten, I., Frank, E.: *Data Mining: Practical Machine Learning Tools and Techniques*. Kaufmann Burlingt (2011)
 24. Kalmegh, S.: Analysis of WEKA data mining algorithm REPTree, Simple CART and RandomTree for classification of Indian news. *Int. J. Innov. Sci. Eng. Technol.* **2**(2), 438–446 (2015)
 25. Rodriguez, J.J., Kuncheva, L.I., Alonso, C.J.: Rotation forest: a new classifier ensemble method. *IEEE Trans. Pattern Anal. Mach. Intell.* **28**(10), 1619–1630 (2006)
 26. Sokolova, M., Japkowicz, N., Szpakowicz, S.: Beyond accuracy, F-score and ROC: a family of discriminant measures for performance evaluation. Presented at the Australasian joint conference on artificial intelligence, pp. 1015–1021, 2006
 27. Viera, A.J., Garrett, J.M.: Understanding interobserver agreement: the kappa statistic. *Fam. Med.* **37**(5), 360–363 (2005)
 28. Lantz, C.A., Nebenzahl, E.: Behavior and interpretation of the κ statistic: Resolution of the two paradoxes. *J. Clin. Epidemiol.* **49**(4), 431–434 (1996)
 29. Yang, Z., Zhou, M.: Kappa statistic for clustered physician–patients polytomous data. *Comput. Stat. Data Anal.* **87**, 1–17 (2015)
 30. Abdullah, A.A., Subasi, A., Qaisar, S.M.: Surface EMG signal classification by using WPD and ensemble tree classifiers. Presented at the CMBEBIH 2017: proceedings of the international conference on medical and biological engineering 2017, vol. 62, p. 475, 2017
 31. Subasi, A., Alharbi, L., Madani, R., Qaisar, S.M.: Surface EMG based classification of basic hand movements using rotation forest. Presented at the advances in science and engineering technology international conferences (ASET), 2018, pp. 1–5, 2018

Impact of High Frequency Electromagnetic Fields on Process of Angiogenesis

Smiljana Paraš, Nataša Vojinović, and Ljiljana Amidžić

Abstract

The facts about the effects of high frequency electromagnetic fields (HF EMF) on human health are often controversial and incomplete. For this reason, the aim of this study was to examine impact of HF EMF on process of angiogenesis in eight rat organs of: pancreas, kidney, thyroid, liver, cerebrum, thymus, gastric gland and spleen. Wistar strain rats were exposed to HF EM fields with the following characteristics: 1.9 GHz frequency, 0.24 A/m intensity, electric field strength of 4.79 V/m, and SAR (specific absorption rate) value of 2.0 W/m². Exposure time was 7 h per day, 5 days per week, over the course of 60 days. Our experiment was conducted on a total of 20 male rats divided randomly into two equal groups: one group of animals was exposed to HF EM fields as described above whereas, the other group of animals was not exposed to any HF EM fields. In our study histological and stereological analysis shows the results that volume density and number of endothelial cells of blood vessels increased with statistical significance in all organs of rats that were exposed to the HF EMF compared to the unexposed group. Increase in volume and number of endothelial cells in analyzed organs indicates the process of angiogenesis induced by HF EM fields, which can be used for therapeutic protocols.

Keywords

Endothelial cells • Volume density • Number of cells • Rats • HF EMF

S. Paraš (✉) · N. Vojinović
Department of Biology, Faculty of Sciences and Mathematics,
University of Banja Luka, dr Mladena Stojanovića 2, 78000 Banja
Luka, Bosnia and Herzegovina
e-mail: smiljana.paras@pmf.unibl.org

L. Amidžić
Department of Pathology, Faculty of Medicine, University of
Banja Luka, Save Mrkalja 14, 78000 Banja Luka, Bosnia and
Herzegovina

1 Introduction

This study was created in order to check the effects of HF EMF on the endothelial cells of blood vessels in pancreas, kidney, thyroid, liver, cerebrum, thymus, gastric gland and spleen of the rats. To do so, these fields were applied in an in vivo model in duration of two months. It was already known that there are many studies which indicate that HF EMF affect many biological systems: cardiovascular, nervous [1], endocrine and reproductive systems [2]. Also, research has shown that these fields are increasing the secretion of sex hormones [3], decreasing the secretion of TSH hormone [4], affecting nerve conduction and the blood-brain barrier permeability in brain [5], changing the concentration of glucose in blood, decreasing the effectiveness of the immune system response [6] and changing the speed of cell division and apoptosis [7].

Additionally, low and high frequency electromagnetic fields are used for therapeutic purposes to increase regeneration of cartilage and bone tissues and angiogenesis of all blood vessels [8]. Electromagnetic fields of different frequencies affect the cell division of the endothelial cells of blood vessels, the creation of new blood vessels, and the regeneration of existing ones. In addition to angiogenesis, the literature data indicate that EMF increase the flow rate of blood in blood vessels that also promotes their regeneration and angiogenesis, in particular the capillary angiogenesis [9]. In vitro studies show the proliferation and reorganization of endothelial cells due to the effect of electromagnetic fields [10].

Bearing in mind the omnipresence of HF EMF in our environment and their different effects on organs the hypothesis, the specific aims of this study were to document changes in the morphology blood vessels. Pancreas, kidney, thyroid, liver, large brain, thymus, gastric gland and spleen of the rats have very well developed vascularization organs and they are therefore suitable for research.

2 Materials and Methods

All animal procedures were in compliance with Directive 2010/63/EU on the protection of animals used for experimental and other scientific purposes, and were approved by the Ethical Committee on Animal Experiments at the Faculty of Sciences, the University of Banja Luka, No. 01-9-192.2/15, Bosnia and Herzegovina. The experiment was performed on 20, sexually mature, four-month-old, Wistar strain male rats divided randomly into two groups in the vivarium at the Faculty of Sciences in Banja Luka. One group of 10 rats was exposed to the HF EM fields (the exposed group) and the other group of 10 rats was the control group and was not exposed to any measurable HF EMF. All animals lived in laboratories with constant conditions of 22 ± 2 °C temperature and a natural photoperiod. Both groups had unlimited access to tap water and food pellets. The exposed group was exposed to HF EMF of GSM, 7 h a day (from 08:00 to 15:00), 5 days a week, for 60 days. They were exposed to HF EMF in one area of the laboratory in their plexiglass cages this exposure was the same in all parts of the cage after which they were brought to the same room as the control group. Source of HF EMF was produced by generator with the following characteristics: strength of the electromagnetic fields used in our experiment was 1.9 GHz frequency, 0.24 A/m intensity, electric field strength of 4.79 V/m, and specific absorption rate value of 2.0 W/m².

After 60 days of exposure, the organs (pancreas, kidney, thyroid, liver, large brain, thymus, gastric gland and spleen) of the rats in HF EMF group were removed and fixed in Bouin solution and were processed using a standard procedure for paraffin embedding. For the histological analysis, paraffin slices were stained with hematoxylin-eosin (H&E) (both stains by Merck, Darmstadt, Germany). Histological analysis of control and exposed pancreatic sections was done using the following methods toluidin, Malory Azan and Masson's trichrome staining, in order visualize to blood vessels i.e. endothelial cells. Stereological analyses were performed on every 5th stained section of all 20 animals using a multipurpose stereological grid M42, a Weibel grid [11], using a light microscope, using a magnification of $\times 400$. We used MBF System software for the stereological counting with P2 grid and Cavalieri's principle. For measuring stereological parameters and photographing the pancreatic cells we used a Leica 8000D microscope with a MEGA VIEW camera and a digital transfer as well as photo analysis software system. Researchers is measured: volume density of endothelial cells in blood capillaries in all eight rat organs. The volume density (V_v) of endothelial cells of blood vessels in each rat's organs was determined based on the following formula [11]: $V_v = Pf/Pt$ (mm⁰), Pf = number of hits endothelial cells in each section of organs and

Pt = total number of hits. The number of endothelial cells per volume unit, was estimated using a physical dissector design.

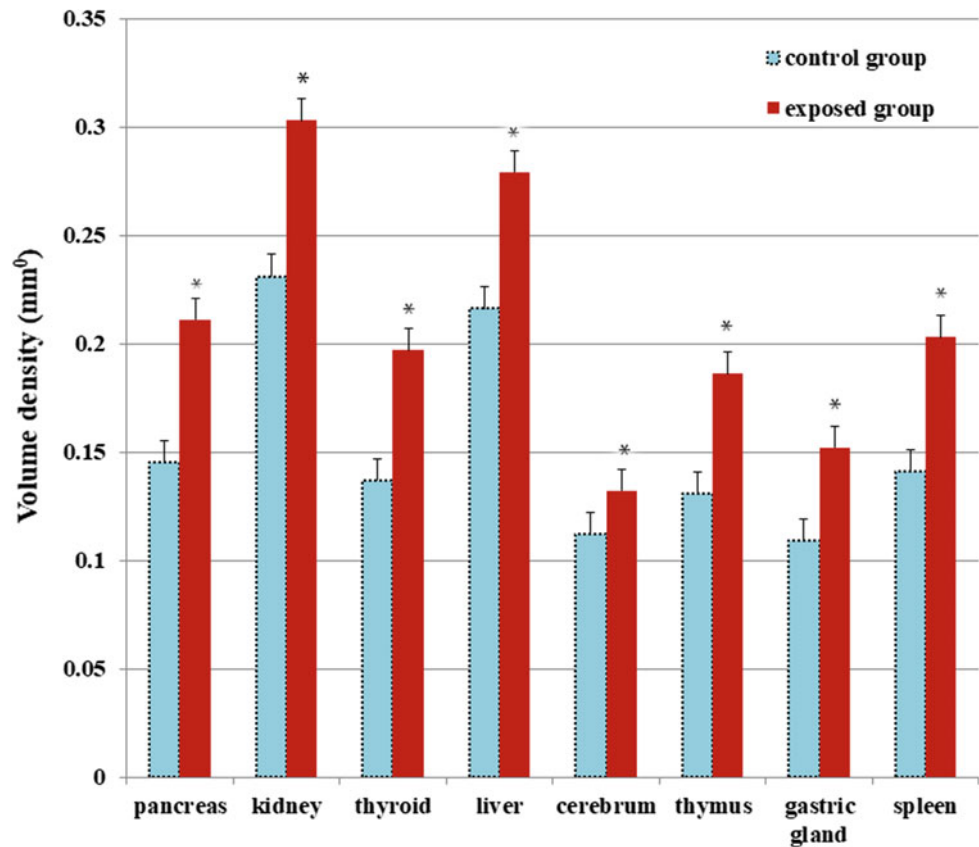
All results in statistical analysis were expressed as means for ten animals per group \pm standard deviation (SD). The data were tested for normality of distribution by the Fishers test. One-way analysis of variance followed by the Wilcoxon sign-rank test was used in order to compare differences between the groups. A probability value of 5% or less was considered as statistically significant. The data were statistically analyzed by ANOVA, SSPS 2010. All the parameters were expressed as means and in intervals of high and low values.

3 Results and Discussion

The angiogenesis process in the organs (pancreas, kidney, thyroid, liver, cerebrum, thymus, gastric glands and spleen) was shown by increasing the volume density and the number of epithelial cells of blood vessels in the HF EMF exposed group of animals compared to the control group. Chart 1 (Fig. 1) shows a increase in volumetric density of endothelial cells in blood vessels in all analyzed organs in the exposed group of animals compared to the control group pancreas by 45%, from 0.145 ± 0.009 mm⁰ to 0.211 ± 0.011 mm⁰, kidney by 31%, from 0.231 ± 0.013 mm⁰ to 0.301 ± 0.011 mm⁰, thyroid by 44%, from 0.137 ± 0.009 mm⁰ to 0.197 ± 0.009 mm⁰, liver by 29%, from 0.216 ± 0.015 mm⁰ to 0.278 ± 0.021 mm⁰, cerebrum by 18%, from 0.112 ± 0.013 mm⁰ to 0.132 ± 0.012 mm⁰, thymus by 42%, from 0.131 ± 0.012 mm⁰ to 0.186 ± 0.020 mm⁰, gastric glands by 39%, from 0.109 ± 0.009 mm⁰ to 0.151 ± 0.009 mm⁰ and spleen by 44%, from 0.141 ± 0.009 mm⁰ to 0.203 ± 0.013 mm⁰. All of these increases in volume density of endothelial cell of blood vessels in exposed group compared to the control were statistically significance (pancreas: $p = 0.024$; kidney: $p = 0.015$; thyroid: $p = 0.017$; liver: $p = 0.029$; cerebrum: $p = 0.037$; thymus: $p = 0.035$; gastric glands: $p = 0.038$; and spleen: $p = 0.026$ for trend for all $p < 0.05$).

Another significant stereological parameter in our experiment was the number of epithelial cells in pancreas, kidney, thyroid, liver, cerebrum, thymus, gastric glands and spleen in the exposed group as compared to the control group (Fig. 2). Chart 2 shows a increase in number of endothelial cells in blood vessels in all analyzed organs: pancreas by 55% (from $No = 188,562 \pm 63,483$ to $No = 292,271 \pm 83,924$), kidney by 46%, from $No = 127,864 \pm 59,524$ to $No = 186,681 \pm 64,923$, thyroid by 52%, from $No = 165,532 \pm 74,386$ to $No = 251,608 \pm 93,001$, liver by 25%, from $No = 163,471 \pm 68,421$ to $No = 204,339 \pm 89,092$,

Fig. 1 Chart shows increase of stereological parameter volume density (mm^0) of epithelial cells in blood vessels were of all analyzed organs in expose group rats in compare to the control. All values are provided as the mean \pm SD; $n = 10$, $p < 0.05$. (*statistical significance difference)



cerebrum by 21%, from $No = 139,461 \pm 83,110$ to $No = 168,748 \pm 83,726$, thymus by 40%, from $No = 177,441 \pm 63,445$ to $No = 248,417 \pm 71,036$, gastric glands by 32%, from $No = 114,358 \pm 86,317$ to $No = 150,953 \pm 49,956$ and spleen by 42%, from $No = 223,104 \pm 93,887$ to $No = 316,808 \pm 99,863$. All of these increases in the number of endothelial cells were statistically significance (pancreas: $p = 0.039$; kidney: $p = 0.028$; thyroid: $p = 0.031$; liver: $p = 0.017$; cerebrum: $p = 0.041$; thymus: $p = 0.025$; gastric glands: $p = 0.032$; and spleen: $p = 0.019$ for trend for all $p < 0.05$).

Figure 3 is a collection of histological micrographs which shows increase of numerical density and number of epithelial cells in blood vessels in pancreas and kidney tissue of the exposed group compared to the control group of rats (white pointing arrows). Creation of new endothelial cells of the blood vessels and their reorganization occurred in the presence of heparin, endothelial cell growth factor, and a competent fibronectin matrix [12]. Alexandrescu et al. conclude that the growth of epithelial cells in the blood vessel independently from other endocrine cells occurs through a combination of processes based on a decrease in apoptotic index and replication of endocrine cell chromatin [13].

Figure 4 is a collection of histological micrographs which shows increase of numerical density and number of epithelial

cells in blood vessels in thyroid and liver tissue of the exposed group compared to the control group of rats (white pointing arrows). After examining, analyzing and documenting an increase in the number and numerical density of endothelial cells of blood vessels in tissue of all organs rats exposed to HF EMF, we conclude that these increases were due to exposure to HF EMF. This is likely, because HF EMF increases the mitotic activity of the endothelial cells as indicated by Teta et al. [13]. The increase and change of the capillary architecture in the tissues of organs in animals exposed to the HF EM fields results in a change in the organization of collagen tissue around blood vessels, as also noted in the work of Tzaphlidou et al. (2006) [14].

Figure 5 is a collection of histological micrographs which shows increase of numerical density and number of epithelial cells in blood vessels in cerebrum and thymus tissue of the exposed group compared to the control group (white pointing arrows). Tissue of all analyzed organs is densely vascularized owing to rich capillary net and endothelial cells, which are involved in the transport of oxygen, nutrients, angiogenic substances, and growth factor to all cells [15]. In this experiment, the treatment of rats with HF-EMF resulted in increased number of endothelial cell of blood vessels compared to the control group. The work of McKai et al. shows that HF-EMF stimulate hormonal angiogenic growth,

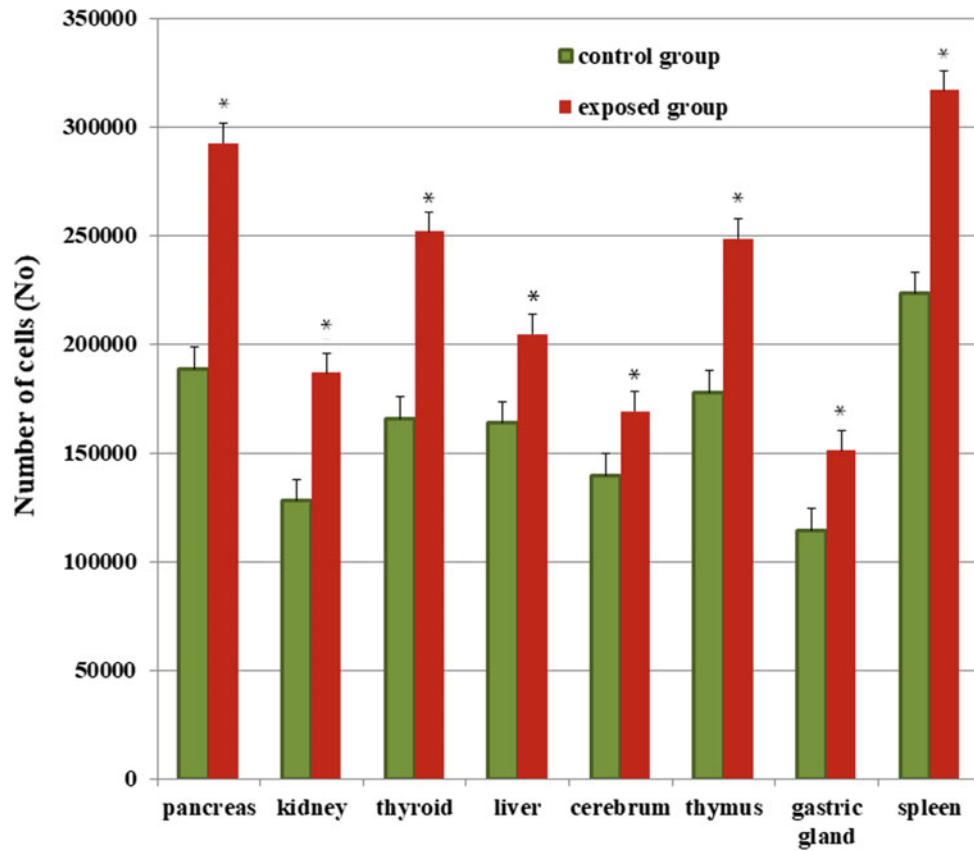


Fig. 2 Chart shows increase of stereological parameter number (No) of epithelial cells in blood vessels were of all analyzed organs in expose group rats in compare to the control. All values are provided as the mean \pm SD; n = 10, p < 0.05. (*statistical significance difference)

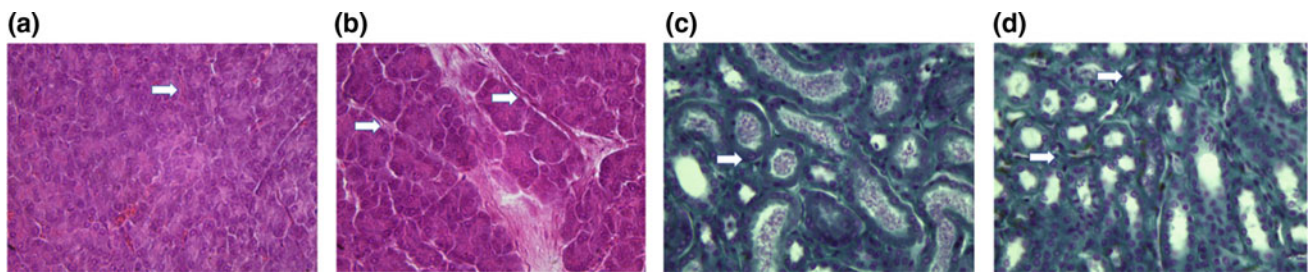


Fig. 3 Histological representation of pancreas (a, b) and kidney (c, d) tissue; control (a, c) and exposed (b, d) groups of rats. H&E staining in pancreatic tissue and toulidin stainig in kidney tissue. Magnification $\times 40$

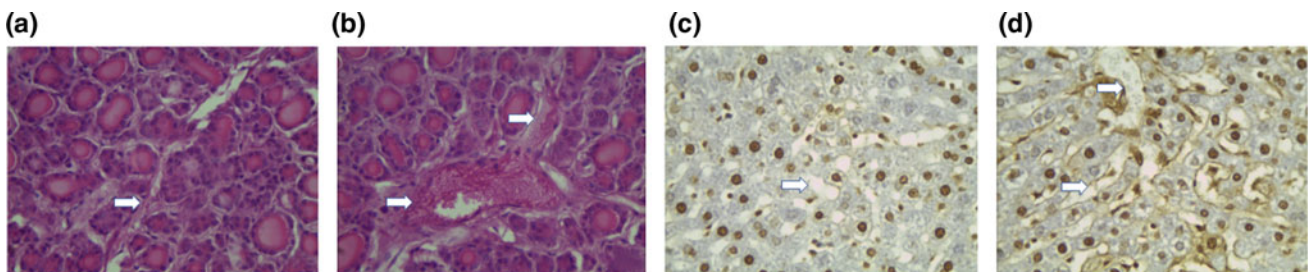


Fig. 4 Histological representation of thyroid (a, b) and liver (c, d) tissue; control (a, c) and exposed (b, d) groups of rats. H&E staining in thyroid tissue and toulidin staining in liver tissue. Magnification $\times 40$

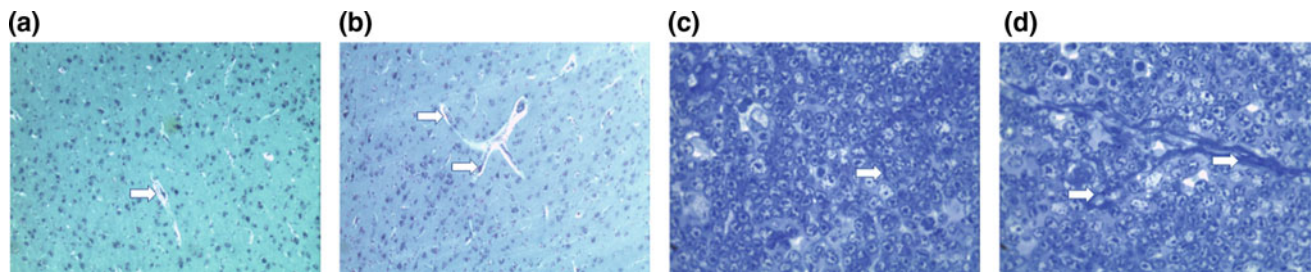


Fig. 5 Histological representation of cerebrum (a, b) and thymus (c, d) tissue; control (a, c) and exposed (b, d) groups of rats. Toulin stain in cerebrum and thymus tissue. Magnification $\times 40$

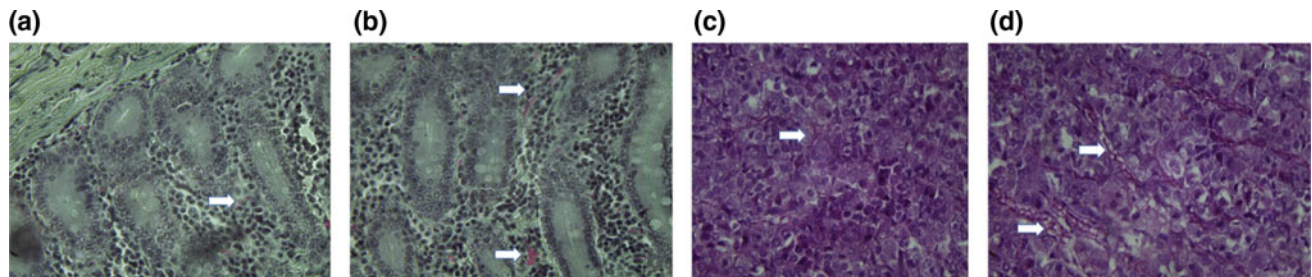


Fig. 6 Histological representation of gastric glands (a, b) and spleen (c, d) tissue; control (a, c) and exposed (b, d) groups of rats. Malory Azan stain in gastric glands and Masson's stain in spleen. Magnification $\times 40$

induce vascular endothelial cells growth and affect the vascular endothelial growth factor (VEGF) as well as endothelial cell permeability [16].

Figure 6 is a collection of histological micrographs which shows an increase of numerical density and number of epithelial cells in blood vessels in gastric glands and spleen tissue of the exposed group compared to the control group (white pointing arrows). Okano et al. (2006) demonstrate that magnetic fields increase angiogenesis in vitro and in vivo through releasing mitogenic growth factor [17]. This is also corresponds with research on HF-EMF published by Chuhua et al. (2013) that indicates that the increase in volume density of blood vessels cells is a consequence of adapting to the increase in the endocrine cells number, as well as angiogenesis [18].

In our experiments, treatment with HF EMF induces increasing volume density of blood capillaries. This is in agreement with previous findings concerning the angiogenic potential of HF EMFs (reviewed by McKay et al. 2007) [16]. Tepper et al. (2004) have shown that magnetic fields of 15 Hz increased angiogenesis in vitro and in vivo through release of a known mitogenic growth factor: fibroblast growth factor [9]. Also, pulsed electromagnetic fields were shown to induce vascular endothelial cell growth and angiogenesis via influencing vascular endothelial growth factor (VEGF)-related pathways Delle Monache et al. 2008) [19].

4 Conclusions

HF EMF cause morphological and stereological changes in varying degrees on blood vessels of the pancreas, kidney, thyroid, liver, cerebrum, thymus, gastric glands and spleen in rats. Changes are in the statistically significant increase in the number and numerical density of endothelial cells of rat blood vessels in exposed group of rats when compared with the unexposed group. In conclusion, the results of our research indicate that HF EMF of certain characteristics induce angiogenesis in analyzed rats. Our research is the basis for further research and definition of HF EMF characteristics that will be best for therapeutic purposes for the process of angiogenesis.

References

1. Gojković, I., Paraš, S., Gajanin, R., Matavulj, M.: The influence of extremely low-frequency electromagnetic field on the basal ganglia structures of the rat brain. *Proc. Nat. Sci. Matica Srpska*. **121**, 27–38 (2011)
2. Raus Balind, S., Manojlović-Stojanovski, M., Milošević, V., Todorović, D., Nikolić, L.J., Petković, B.: Short and long term exposure to alternating magnetic field (50 Hz, 0.5 mT) affects rat pituitary ACTH cells: stereological study: (2016). *Environ. Toxicol.* **31**, 461–468

3. Al-Akhras, M.A., Darmani, H., Elbetieha, A.: Influence of 50 Hz magnetic fields on sex hormones and other fertility parameters of adult male rats. *Bioelectromagnetics* **27**, 127–131 (2006)
4. Ahmet, K., Gokhan, C., Fehmi, O., Mehmet, A., Hakan, M., Sukru, O.: Effects of 900 MHz electromagnetic field on TSH and thyroid hormones in rats. *Toxicol. Lett.* **157**(3), 257–262 (2005)
5. Tang, J., Zhang, Y., Yang, L., Chen, Q., Tan, L., Zuo, S., Feng, H., Chen, Z., Zhu, G.: Exposure to 900 MHz electromagnetic fields activates the mep-1/ERK pathway and causes blood-brain barrier damage and cognitive impairment in rats. *Brain Res.* **1601**, 92–101 (2015)
6. Attia, A.A., Yehia, A.M.: Histological, ultrastructural and immunohistochemical studies of the low frequency electromagnetic field effect on thymus, spleen and liver of albino swiss mice. *Pak. J. Biol. Sci.* **5**, 931–937 (2002)
7. Blank, M., Goodman, R.: Low frequency electromagnetic fields evoke the stress response: mechanism of interaction with DNA and biomedical applications". *IEEE Trans. Plasma Sci.* **30**, 1497–1500 (2002)
8. Sener, D.R., Davis, G.E.: Angiogenesis. *Cold Spring Harb. Perspect. Biol.* **2003**:a005090
9. Tepper, O.M., Callaghan, M.J., Chang, E.I., Galiano, R.D., Bhatt, K.A., Baharestani, S., Gan, J., Simon, B.: Electromagnetic fields increase in vitro and in vivo angiogenesis through endothelial release of FGF-2. *FASEB J.* (2004)
10. Yen-Patton, G.P.A., Patton, W.F., Beer, D.M., Jacobson, B.: Endothelial cell response to pulsed electromagnetic fields: Stimulation of growth rate and angiogenesis in vitro. *J. Cell. Physiol.* (1999)
11. Kališnik, M.: Stereological Section. ZDAJ, IHE, Faculty of Medicine, Ljubljana (1985)
12. Alexandrescu, S., Tatevian, N., Olutoye, O., Brown, E.R.: Persistent hyperinsulinemic hypoglycemia of infancy: constitutive activation of the mTOR pathway with associated exocrine-islet transdifferentiation and therapeutic implications. *Int. Clin. Exp. Pathol.* **3**(7), 691–705 (2010)
13. Teta, M., Long, S.Y., Wartschow, L.M., Rankin, M.M., Kushner, J.A.: Very slow turnover of beta-cells in aged adult mice. *Diabetes* **54**(9), 2557–2567 (2005)
14. Tzaphlidou, M., Fotiou, E.: Collagen as a target for electromagnetic fields. Effects of 910-MHz on rat brain. *Bioelectromagnetics* **183**:183–93 (2006)
15. Böttinger, E.R., Jakubczak, J.L., Roberts, I.S., Mumy, M., Hemmati, P., Bagnall, K., Merlino, G., Wakefield, L.M.: Expression of a dominant-negative mutant TGF-beta type II receptor in transgenic mice reveals essential roles for TGF-beta in regulation of growth and differentiation in the exocrine pancreas. *EMBO J.* **16**(10), 2621–2633 (1997)
16. McKay, J.C., Frank, S., Prato, S.F., Thomas, W.A.: A Literature Review: The effects of magnetic field exposure on blood flow and blood vessels in the microvasculature. *Bioelectromagnetics* **28**(2), 81–98 (2007)
17. Okano, H., Onmori, R., Tomita, N., Ikada, Y.: Effects of a moderate-intensity static magnetic field on VEGF-A stimulated endothelial capillary tubule formation in vitro. *Bioelectromagnetics* **27**, 628–640 (2006)
18. Dai, C., Brissova, M., Reinert, R.B., Nyman, L., Liu, E.H., Thompson, C., Shostak, A., Shiota, M., Takahashi, C., Powers, A. C.: Pancreatic islet vasculature adapts to insulin resistance through dilation and not angiogenesis. *Diabetes* **62**(12), 4144–53 (2013)
19. Delle Monache, S., Alessandro, R., Iorio, R., Gualtieri, G., Colonna, R.: Extremely low frequency electromagnetic fields (ELF-EMFs) induce in vitro angiogenesis process in human. *Bioelectromagnetics* **29**(8), 640–648 (2008)

Implementation of Neural Network-Based Classification Approach on Embedded Platform

Rijad Sarić, Dejan Jokić, and Nejra Beganović

Abstract

Among a number of challenges present in monitoring systems, an efficient implementation of complex time-consuming algorithms and an identification of relevant features from gathered signals still gain high attention. Compared with the signals captured from human body, the problem of identification and classification of abnormalities in electroencephalography (EEG) and electrocardiography (ECG) signals is correlated to the diagnosis of a number of neurological, neuromuscular, and psychological disorders, such as epilepsy, sleep disorders, and similar. The problem of epileptic seizure detection based on EEG signal is discussed in this contribution. Special emphasis here is given to epileptic seizure detection using real-time signal processing based on Field Programmable Gate Array (FPGA) embedded platforms. Proposed approach involves an implementation of classification algorithm relied on Artificial Neural Networks (ANNs) on FPGA board, whilst the extraction of features from EEG signal is performed offline. Accordingly, real-time implementation of ANN-based approach and its comparison with conventional approaches with respect to accuracy, runtime speedup, and applicability to low-power consumption (wearable) devices is in the main focus. The implementation is based on benchmark data available from public repositories and loopback testing.

Keywords

Real-time signal processing • Artificial neural networks • Field programmable gate arrays

1 Introduction

Most technical monitoring systems, regardless of an area of application, are faced with the problem of storage of huge amount of data, efficient implementation of complex time-consuming algorithms, and an identification of relevant features required for analysis. Concerning time-consuming data processing and commonly used complex algorithms, an implementation of real-time approaches becomes indispensable [1]. Moreover, in the case where captured data are used for a classification or prediction of particular events, the preprocessing and the quality of data are of high importance. Preprocessed data are further used as input into classification and prediction models, which can be established in dependence of the nature of gathered signal (biometric security, image or texture classification, speech recognition, and similar).

Usage of systems based on machine learning techniques is not unknown in healthcare [2–5]. Most extensively monitored signals from human body are EEG and ECG signals. Concerning EEG and/or ECG signals, the identification and classification of abnormalities are commonly related to the detection of a number of physical/psychological disorders [6]. The abnormality in this sense is understood as any discrepancy or deviation in EEG/ECG signal from well-known a priori defined (referent) signals. To analyze either physical movements, mental tasks, or a number of physical or mental disorders, an inspection of characteristic waveforms contained in EEG signal are of high importance. The waveforms of EEG signal are classified according to its amplitude, frequency, and the region in which they occur, whilst the variation in amplitude range is closely related to the position of considered electrode [7].

R. Sarić (✉) · D. Jokić · N. Beganović
Department of Electrical and Electronics Engineering,
Faculty of Engineering and Natural Sciences,
International Burch University, 71000 Sarajevo,
Bosnia-Herzegovina
e-mail: rijad.saric@stu.ibu.edu.ba

D. Jokić
e-mail: dejan.jokic@ibu.edu.ba

N. Beganović
e-mail: nejra.beganovic@ibu.edu.ba

The implementation of real-time classification approach in this contribution is applied to the classification of EEG signals by means of epileptic seizure detection. For this purpose, the EEG data containing the recordings during epileptic seizure are utilized. Even though ANNs are often used in the field of EEG signal analysis, real-time implementation of ANNs has not been discussed to the high extent. Real-time implementation of ANN and its comparison with conventional approach with respect to resource usage, runtime speedup, accuracy, and applicability to low-power consumption (wearable) devices is in the main focus of this contribution. The implementation itself is based on benchmark data available from public repositories and loopback testing, as depicted in Fig. 1.

The contribution is organized as follows: (i) after introductory part describing the problem of interest, the state-of-art in FPGA-based classification algorithms is discussed in the second section, (ii) real-time implementation of ANN-based classification approach is given in the third section, (iii) afterwards, the dataset being used to evaluate implemented classification approach is detailed in the fourth section, (iv) whilst the contribution closes with the discussion of obtained results, conclusion, and outlook.

2 State-of-Art

2.1 Classification Approaches

Among a number of classification approaches, including k-Nearest Neighbor classifiers, Logistic Regression, Support Vector Machine, as well as Nonlinear Bayesian classification approaches, the most extensively utilized approach according to the number of recently published contributions are Neural Networks (NNs) with a variety of its adapted

implementations [8–13]. Concerning recurrent and feed-forward ANNs as a huge class of machine learning algorithms, the Feed-forward Neural Networks (NNs) and Deep Neural Networks (DNNs) are widely discussed in terms of EEG signal classification [8, 9]. The FNNs and DNNs are commonly applied primarily due to parallelism they offer as they are organized in one or more than one layers, respectively. In addition, parallel structures have simultaneously an impact on the speed of execution. Over the years, the deep feed-forward artificial neural networks evolved to Convolutional Neural Networks (CNN) or Deep Convolutional Neural Networks (DCNNs) [9, 10]. The CNN/DCNN are mostly utilized for classification of visual imagery and image classification problems, enabling thereby their application in EEG signal analysis. In [10], the DNNs are utilized for automated detection of seizures using EEG signals with the results which massively outperform the achievements of traditional densely connected ANNs. Concerning motor imaginary movement and mental load classification from EEG signal, latest achievements prove efficient application of DCNNs in [8]. Overall efficiency of ANNs is highly dependent on datasets used, applied data processing approaches, hardware platform used for execution, and the network architecture [11].

To summarize, the accuracy of classification (regardless of applied classification approach) is highly dependent on preprocessed captured data. The effectiveness of applied approach is determined based on the time required to execute the algorithm or to calculate the parameters or quantities included in selected approach. The importance of time consumption and the necessity of real-time data analysis is clearly seen, for instance, in the detection of hypoglycemia by patients in coma or by patients whereas continuous monitoring of EEG signals is required [14].

2.2 Real-Time FPGA-Based Implementation of EEG Signal Classification Approaches

The primary concerns in the last decade in automated real-time EEG signal analysis are the development of implantable and wearable devices for EEG monitoring, as well as the design of Systems-on-Chip hardware architectures applicable to EEG signal analysis [15]. Particular advances introduced in this field condition the development of algorithms feasible for execution on hardware platforms such as FPGA [16].

The FPGA-based seizure detection and BCI interface control device using Cyclone II and Cyclone III development board is introduced in [15]. The system is capable to acquire and process the data by integrating Quadratic Spline Wavelet (QSW) filtering. As such, the contribution is focused on the implementation of the architecture for preprocessing unit.

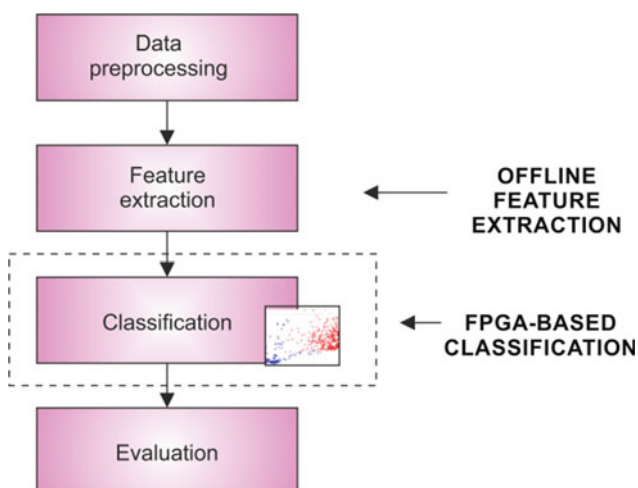


Fig. 1 Preprocessing and classification of EEG signal

Utilization of dual pattern matching in successive stage is enabled using QSW, whereas the structure of algorithm is implemented using logical elements [15]. In [16], implementation of biochip system on Cyclone II FPGA development board applicable to EEG signal analysis is detailed. The device enables preprocessing of EEG signal by means of noise and undesirable artifacts removal, but the classification algorithms are not integral part in [16]. For aforementioned purposes, three independent operations are implemented: Up-sampling, polyphase filtering, and down-sampling. Moreover, continuous monitoring of the ECG and EEG signal using FPGA-based wearable device is performed in [14] to predict the brain death in hypoglycemic coma.

Besides the implementation of approaches related to EEG signal analysis, advanced implementation of Binary Neural Network on embedded platform with integrated FPGA for image classification is in focus of [13]. Binary weighted networks reduce computation for CNNs with neglected accuracy loss in computation [17]. Similarly, adapted Extreme Learning Machine (ELM) algorithm implementation on Cyclone IV FPGA-based device is proposed in [18]. At first, the modification introduced in ELM relating to the computation of pseudo-inverse matrix with respect to the requirements of hardware platform is elaborated, whilst the performance evaluation is conducted concerning binary classification of diabetes on publicly available datasets [18]. The FPGA-based implementation of FNN for purpose of image and speech classification using xQuant technique is given in [19]. The novelty introduced in [19] is in rescaling the parameters of an FNN classifier to integer values and successive quantization. Each floating point multiplication is thereby replaced by a single operation of bit shift, reducing at the same time resource usage [19].

The development of FPGA-based systems used for signal processing, classification, and prediction has to include both real-time features extraction as well as real-time classification/pattern recognition. In the initial stage of the development, either classification algorithms/methods or feature extraction approaches are detailed and implemented on real-time FPGA-based platforms. This proves that the new technological era determined by increased use and sudden expansion of systems based on real-time platforms is yet to come. The algorithms primarily related to machine learning class of algorithms gain high attention in the analysis of EEG signal.

3 Neural Networks FPGA-Based Implementation

As stated previously, the main focus of this contribution is the design and implementation of ANN-based classifier to be executed in real time. For purpose of feature vector

generation, previous knowledge about the nature of EEG signal and considered task of epileptic seizure detection is considered. The feature extraction, therefore, is not done in real time but offline, as depicted in Fig. 2. Offline determined feature vectors are fed to both FPGA-based platform and the MATLAB software tool [20].

The Altera DE2-115 Development and Education Board is used for the design and validation. Two common ways used in the development of FPGA systems are: (i) direct VHDL (Very High Speed Integrated Circuit Hardware Description Language) or Verilog coding and (ii) usage of particular HDL Code Generators. Although existing HDL Code Generator from MATLAB software tool [20] simplifies the procedure as no the deep knowledge about VHDL/Verilog programming language is required, it is unable to generate all required functions (for instance: exponential function). From another point of view, direct VHDL/Verilog coding provides much higher degree of freedom in terms of directly accessible resources of FPGA. In this case, VHDL code for Simulink model of ANN classifier obtained from MATLAB is implemented. Varying percentage of input feature vector size used for training and validation/test purposes is used aiming to optimize the parameters of classifier.

Each input to ANN classifier is assigned through eighteen switches presented on the FPGA board. Firstly, the 18-bit signed binary values assign by switches serve as inputs to multiplexers (MUXs) which actually operate as a classic

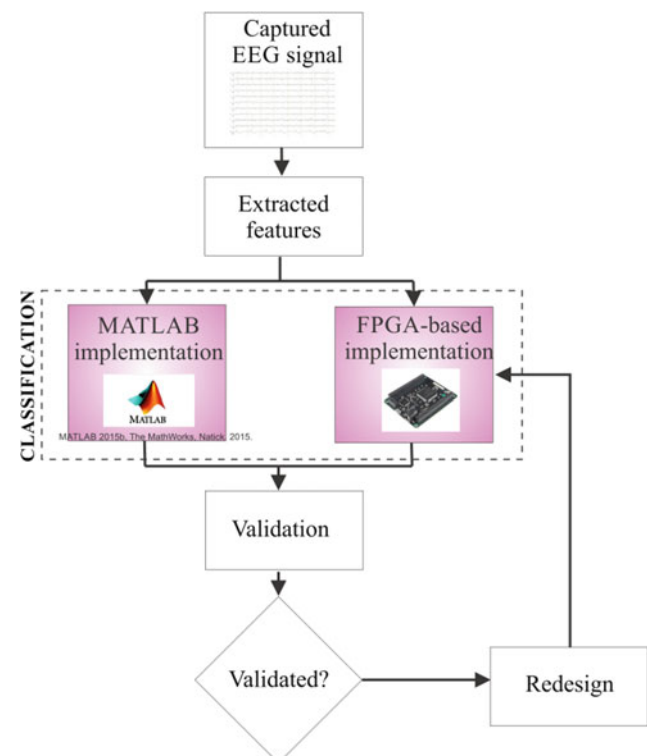


Fig. 2 Loopback testing

switch where the selected line on the top decides which of the inputs would go from the left to the right of ANN. The FPGA board has four buttons and button-1 is used to determine whether flip-flops store the value sent through the switches. Storage elements as flip-flops are the much better choice over latches which are not reliable at high-speed processes and could not be timed properly. This FPGA board has a clock of 50 MHz including a delay of 20 ns and the rising edge of the clock means that flip-flop stores the data. Inputs from the switches are connected to each flip-flop. Thus, when the button-1 is pushed it enables the first flip-flop to store the current value assigned by switches (no other flip-flops would store the data if button-1 is pushed) and send it to twelve neurons in the hidden layer. On the other hand, if some other button is pushed the current value from switches is stored to the flip-flop associated with that button. A fundamental concept of ANN implementation on the FPGA hardware refers to creating specific building blocks, where each block contains an appropriate VHDL code created based on the functionality. Each neuron of the ANN is implemented using basic arithmetic operations such as addition, subtraction, and multiplication. When neuron block receives the values stored in flip-flops it uses a multiplier to multiply the first value with pre-trained weights extracted from feed-forward ANN model, then the second value is also multiplied with specific weights and after that, these two values go to the adder to obtain a summation of them. Each new value is first multiplied by the weights and added with the previous sum. The final sum goes to adder block which contains ANN extracted bias values. However, the major challenge during the FPGA-based ANN implementation represents an establishment of activation function, utilizing often some advanced mathematical expressions to the input data. Sigmoid function ($\tan\text{Sig}$), for instance, “S”-shaped curve, is the most common function in ordinary ANN. Although there are numerous implementations of this function using for example linear approximation to perform large-scale calculations, the application of the lookup table proves to be the most effective way due to matching the inputs and outputs of the activation function. The outputs of the neurons are scaled to obtain specific indexes in order to access binary elements in the lookup table. For that purpose, one comparator is used to compare certain bits of the scaled bit string to be sure the value of the index is correctly calculated. Lastly, the three neurons in the output layer are implemented in the same manners and they perform the same calculations using pre-trained weights as well as bias values to produce the final class matching output. In Fig. 3 the register-transfer level (RTL) circuit of artificial neuron together with MATLAB ANN model is illustrated. The

software tool named Quartus 18.1 is used to synthesize VHDL code and create gate-level logic circuits for the ANN. The main advantage of FPGA in terms of ANN implementation lies in its concurrency or parallelism. Owing to that, FPGA allows all process running at the same time, whereas any type of processor executes statement by statement.

4 Datasets and Feature Extraction

Feature vector, fed to the classifier is a priori defined based on publicly available datasets provided by Temple University (TUH EEG Seizure Corpus) [21]. Evaluation of proposed implementation is done on the same dataset. The datasets from TUH database are captured using standardized 10–20 electrode configuration in Average Reference referential montage [21]. Original files from the database are split into multiple files corresponding to the data from a particular segment of interest in duration of 10 s. Accordingly, the analysis is done on windowed data originating from a number of sessions related to 40 patients. The original data is at first filtered to remove noise and undesirable artifacts. For purpose of epileptic seizure detection, all 16 measurement channels are considered.

Feature vector contains wavelet- and statistics-based features/coefficients. As such, Continuous Wavelet Transformation is applied to filtered data to obtain time-frequency representation of input signal. In terms of epileptic seizure occurrence detection, the most discriminative features related to frequency representation lie in the range <40 Hz [4]. Correspondingly, generated feature vector contains a number of features exactly from this frequency range (0–40 Hz). Summarized, generated feature vector consists of: (i) the vector containing the sum of absolute values of CWT coefficients per each channel between CWT scales of 120 and 128 (lower frequency range, close to 40 Hz), (ii) the vector containing the sum of absolute values of CWT coefficients per each channel between CWT scales of 70 and 90 (mid-frequency range), (iii) the max of CWT coefficients per each channel between CWT scales of 120 and 128, (iv) the percentage of overall signal energy contained in the last four CWT scales (the frequency range of interest, close to 40 Hz), and (v) the percentage of overall signal energy contained in the last ten CWT scales. Extracted captured EEG signal in duration of 10 s from 12 channels corresponding to the case when a seizure does not occur is given in Fig. 4. Similarly, the signal from the timespan of 10 s corresponding to the case when seizure occurs is depicted in Fig. 5. Further analysis is done based on such signal chunks.

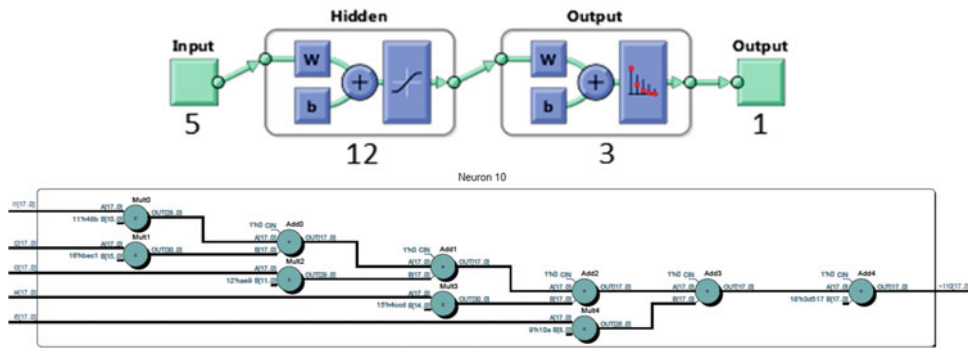


Fig. 3 MATLAB of feed-forward ANN model and RTL of one artificial neuron available in the hidden layer

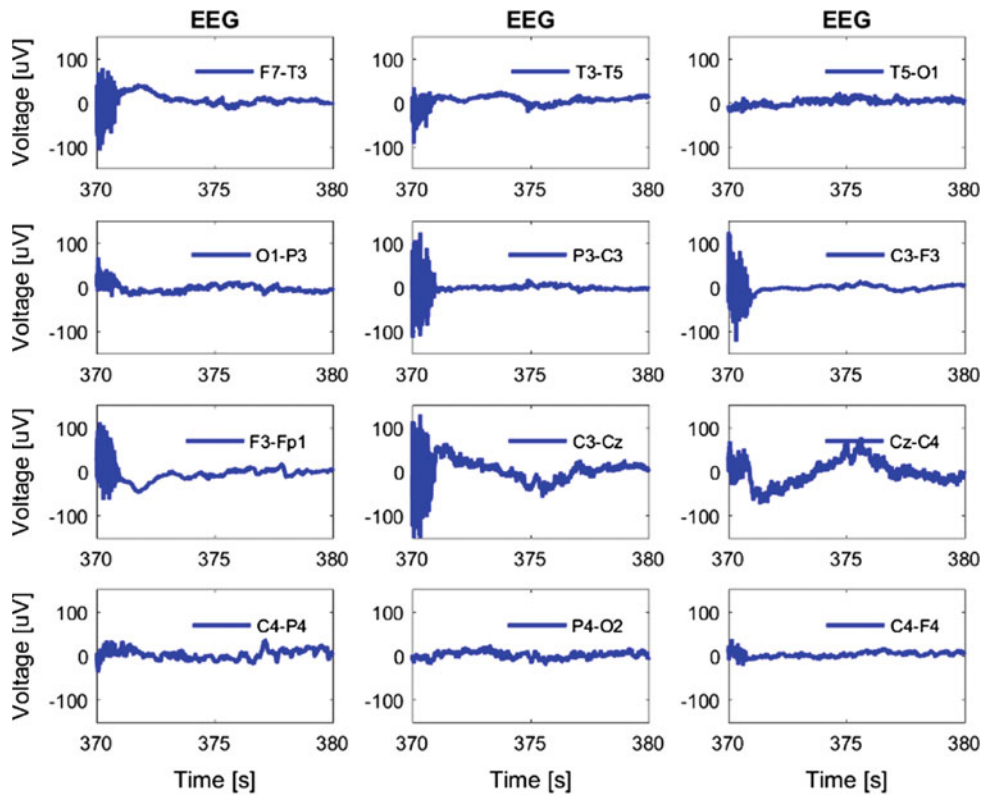


Fig. 4 Captured EEG—epileptic seizure not occurred

5 Discussion of Results

Validation of ANN implementation on FPGA-based platform is done by comparing the accuracy of classification obtained using MATLAB software package and FPGA-outputs. In Table 1, obtained accuracy for both implementations are given and the total deviation between them is calculated. The accuracy of the ANN classifier is measured using confusion or error matrix. The number of false positive, false negative,

true positive and true negative values is counted within a table of confusion to establish correct accuracy during the test phase. An intention is to obtain the same results concerning both implementations, meaning that the deviation close to zero indicates very good results of FPGA-implementation. The classification accuracy obtained using MATLAB is only slightly higher than the accuracy achieved using FPGA-based implementation. Hence, the FPGA-based implementation of ANN is proved as acceptable.

Fig. 5 Captured EEG signal—epileptic seizure occurred

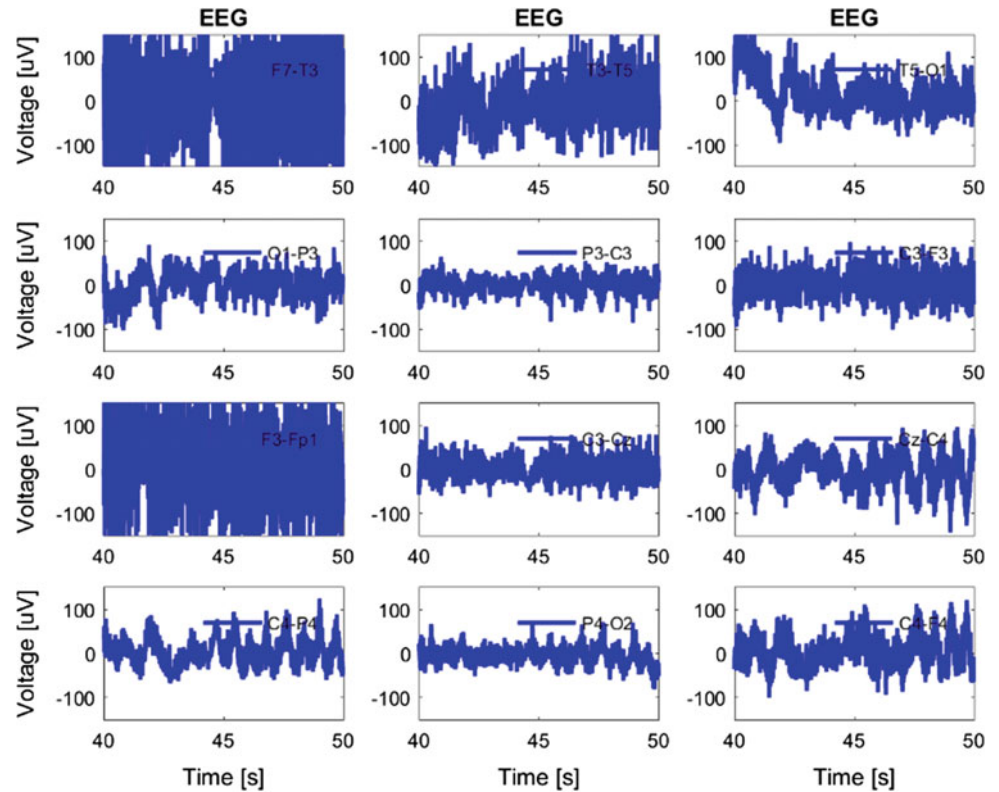


Table 1 The accuracy of obtained results

Tool	Accuracy (%)
MATLAB	95.4
FPGA-based	95.14

6 Conclusion and Outlook

Special emphasis in this contribution is given to the implementation of ANN classifier on FPGA platform applicable to epileptic seizure detection. Integral part of ANN implementation is efficient feature extraction, which is here described but not done in the real-time framework. The classification outputs obtained from two system used in this research are compared and used in a loopback testing for validation of FPGA-based classifier implementation.

The obtained results prove that FPGA-based implementation of ANN is efficient as the deviation between considered two implementations is low. Consequently, the integration of feature vector generation in real-time has to be considered as the next step in the improvement of the proposed solution.

Conflict of Interest Declaration The authors declare no conflict of interest.

References

- Ristic, M., Lubura, S., Jokic, D.: Implementation of CORDIC algorithm on FPGA ALTERA cyclone. In: Proceeding of 20th Telecommunications Forum 2012, pp. 875–878 (2012)
- Catic, A., Gurbeta, L., Kurtovic-Kozaric, A., Mehmedbasic, S., Badnjevic, A.: Application of neural networks for classification of Patau, Edwards, Down, Turner and Klinefelter Syndrome based on first trimester maternal serum screening data, ultrasonographic findings and patient demographics. *BMC Med. Genomics* **11**, 19 (2018). <https://doi.org/10.1186/s12920-018-0333-2>
- Gurbeta, L., Badnjevic, A., Maksimovic, M., Omanovic-Miklicanin, E., Sejdic, E.: A telehealth system for automated diagnosis of asthma and chronic obstructive pulmonary disease. *J. Am. Med. Inform. Assoc.* **25**(9), 1213–1217 (2018). <https://doi.org/10.1093/jamia/ocy055>
- Avdić, M., Džuzić, N., Hasanić, O., Spahić, A., Skenderagić, L.S., Badnjević, A., Hukić, M.: Development of a novel biofilm classification tool and comparative analysis of result interpretation methodologies for the evaluation of biofilm forming capacity of bacteria using tissue culture plate method. *Med Glas (Zenica)*. **16** (1):13–21 (2019). <https://doi.org/10.17392/997-19>
- Badnjevic, A., Gurbeta, L., Custovic, E.: An expert diagnostic system to automatically identify asthma and chronic obstructive pulmonary disease in clinical settings. *Nat. Sci. Rep.* **8**, 11645 (2018). <https://doi.org/10.1038/s41598-018-30116-2>
- Mutlu, A.Y.: Detection of epileptic dysfunctions in EEG signals using Hilbert vibration decomposition. *Biomed. Signal Process. Control.* **40**, 33–40 (2018)

7. Medithe, J.W.C., Nelakuditi, U.R.: Study of normal and abnormal EEG. In: Proceeding of 3rd International Conference on Advanced Computing and Communication Systems 2016, vol. 01, pp. 1–4 (2016)
8. Jiao, Z., Gao, X., Wang, Y., Li, J., Xu, H.: Deep convolutional neural networks for mental load classification based on EEG data. *Pattern Recogn.* **76**, 582–595 (2018)
9. Acharya, U.R., Oh, S.L., Hagiwara, Y., Tan, J.H., Adeli, H.: Deep convolutional neural network for the automated detection and diagnosis of seizure using EEG signals. *Comput. Biol. Med.* 1–9 (2017)
10. Tang, Z., Li, C., Sun, S.: Single-trial eeg classification of motor imagery using deep convolutional neural networks. *Opt.-Int. J. Light. Electron Opt.* **130**, 11–18 (2017)
11. Behncke, J., Schirrmester, R.T., Burgard, W., Ball, T.: The signature of robot action success in EEG signals of a human observer: decoding and visualization using Deep Convolutional Neural Networks. In: Proceeding 6th International Conference on Brain-Computer Interface 2018, pp. 1–6 (2018)
12. Liu, Q., Zhao, X.-G., Hou, Z.-G., Liu, H.-G.: Deep belief networks for eeg-based concealed information test. In: International Symposium on Neural Networks, pp. 498–506 (2017)
13. Schirrmester, R.T., Springenberg, J.T., Fiederer, L.D.J., Glasstetter, M., Eggenberger, K., Tangermann, M., Ball, T.: Deep learning with convolutional neural networks for EEG decoding and visualization. *Hum. Brain Mapp.* **38**(11), 5391–5420 (2017)
14. Unnikrishnan, C., Ramesh, P.: Early warning of brain death in hypoglycemic coma using FPGA based wearable device. In: Proceeding IEEE International Conference on Innovations in Information, Embedded and Communication Systems 2017, pp. 1–3 (2017)
15. Tamilarasi, S., Sundararajan, J.: FPGA based seizure detection and control for Brain Computer Interface. *Clust. Comput.* **28**, 1–8 (2018)
16. Tabassum, N., Islam, S.M. R., Huang, X.: Implementation of biochip on multirate system for EEG signal on ALTERA Cyclone device. In: Proceeding 3rd International Conference on Electrical Information and Communication Technology 2017, pp. 1–6 (2017)
17. Colangelo, P., Huang, R., Luebbers, E., Margala, M., Nealis, K.: Fine-grained acceleration of binary neural networks using IntelR XeonR processor with integrated FPGA. In: Proceeding of IEEE 25th Annual International Symposium on Field-Programmable Custom Computing Machines 2017, pp. 135–135 (2017)
18. Yeam, T.C., Ismail, N., Mashiko, K., Matsuzaki, T.: FPGA implementation of extreme learning machine system for classification. In: Proceeding of IEEE Region Conference 2017, pp. 1868–1873 (2017)
19. Machado, E., Marques, T., Lianos, C., Coral, R., Jacobi, R.: FPGA implementation of a feedforward neural network-based classifier using the xQuant technique. In: Proceeding of 8th Latin American Symposium on Circuits & Systems 2017, pp. 1–4 (2017)
20. MathWorks, T.: MATLAB 2015b (Tech. Rep.). Natick, Massachusetts, United States (2015)
21. Golmohammadi, M., Shah, V., Lopez, S., Ziyabari, S., Yang, S., Camaratta, J., Picone, J.: The TUH EEG seizure corpus. In: Proceeding of the American Clinical Neurophysiology Society Annual Meeting, p. 1 (2017)

Stereo Laser Speckle Dissimilarity Analysis Using Self-organizing Maps

Francisco Cunha, Luís Távora, Pedro Assunção, Sérgio Faria, and Rui FonsecaPinto

Abstract

Imaging methods based on the physical phenomenon of speckle have been gaining relevance (mostly due to technological improvements in sensors and cameras) in several areas of science, particularly in the field of Medicine. Specifically, the use of speckle laser technology has proved to be useful in the characterization of post-hypoxia perfusion states, either in the cortex of animal models or in skin perfusion experiments. This dynamic information, if added to the morphology, results in an imagery modality that allows the full (static and dynamic) characterization of the scattered surface. In this work, a stereo vision system was adopted during a laser speckle acquisition of skin surface, in order to perform a dissimilarity (i.e. left vs. right) analysis based on activity descriptors in the context of a Post Occlusive Reactive Hyperemia (PORH) test. Additionally, to perform inter-view segmentation, a registration procedure is also proposed based on high entropy regions. The results reveal that among five commonly used activity descriptors, the Shannon Wavelet Entropy (SWE) is the most consistent in characterizing the transition from an occlusive state to a hyperemic state, thus indicating its use as a dissimilarity descriptor in stereo acquisitions to identify physiological states related with reduced perfusion and its recovery.

Keywords

Laser speckle • Stereo video processing • Registration • Skin perfusion

1 Introduction

A speckle pattern is generated when a coherent light source is backscattered by a surface with roughness greater than the emitted light wavelength. The resulting scattering process induces a random phase-change of the coherent (i.e. laser) wavefronts on the surface of the illuminated object thus obtaining to the so-called objective speckle pattern. The huge potential of laser speckle patterns relies on the fact that variations on the scattering surface lead to changes in the resulting objective speckle pattern. Thus, laser speckle image analysis allows to dynamically characterize scattering media with respect to the temporal variation of the scattered intensity field registered by a camera during a finite temporal interval (e.g. exposure time), in the form of a subjective speckle pattern.

A subjective speckle pattern consists of a discrete 2D representation of the backscattered light field, given for each position of the observation plane, by the sum of multiple photons, backscattered from different positions and collected by the image sensor. Thus, each backscattered wavefront has an independent optical path, and the randomly induced phase shifts can lead to constructive interference, which is associated to brighter spots on the resulting image whereas destructive interference is associated to darker regions.

The use of laser speckle in medical imaging analysis has been applied for different purposes, particularly to characterize skin properties, ranging from dynamic changes associated with increased perfusion in reactive hyperemia conditions [1] to the structural characterization of the skin surface [2].

Considering the potential of laser speckle functional analysis and the growing interest in computational imaging

F. Cunha (✉) · P. Assunção · S. Faria · R. FonsecaPinto
Instituto de Telecomunicações, Multimedia Signal Processing
Group, Leiria, Portugal
e-mail: francisco.cunha@co.it.pt

R. FonsecaPinto
e-mail: rui.pinto@ipleiria.pt

L. Távora · P. Assunção · S. Faria · R. FonsecaPinto
Polytechnic Institute of Leiria, Leiria, Portugal

R. FonsecaPinto
CiTechCare—Center for Innovative Care
and Health Technology, Leiria, Portugal

techniques to extract structural parameters related to the skin topography, the combination of both is of utmost importance for full assessment of skin related conditions, such as microcirculation studies in wounds, melanoma versus nevus screening, etc. Therefore, the use of multiple cameras associated with speckle acquisitions is an area where more research efforts are needed, particularly regarding registration methodologies, activity markers identification and its reproducibility across different cameras.

In the present work, a stereo vision system was adopted during a typical laser speckle acquisition in order to perform a comparative inter-view study (e.g. dissimilarity analysis between left and right views) based on activity descriptors obtained by a laser speckle imaging (LSI) acquisition protocol. Prior to the dissimilarity analysis, a registration procedure, which combines the detection of high entropy speckle regions and an epipolar geometry constraint, is also proposed.

In the remaining of this paper, in Sect. 2 the acquisition setup and protocol are presented and a registration methodology that enables a direct comparison between stereo speckle recordings is defined. In Sect. 3, the strategy adopted to perform interview dissimilarity analysis is presented, as well as the respective results. Finally, a discussion and conclusions sections are presented.

2 Materials and Methods

2.1 Acquisition Protocol and Equipment

The use of stereoscopic vision systems in laser speckle imaging is a well-known approach, typically used for photogrammetric purposes [3–5]. In this work, an experimental procedure for stereo speckle video acquisition, focused on the evaluation of a forearm induced post-occlusive reactive hyperemia (PORH) on a healthy subject, was followed (see Fig. 1 for details). Firstly, the forearm was immobilized and illuminated with an expanded laser beam while subjected to an increasing pressure imposed by a blood pressure cuff. Such induced pressure was maintained, for approximately 2 min. Video acquisition starts 2 s prior to the pressure release, lasting approximately 30 s.

2.2 Stereo Speckle Registration

To perform an inter-view comparative study between views, segmentation of homologous left and right regions of interest (ROIs) is needed. Thus, the definition of a robust image correspondence procedure (i.e. registration) is crucial to ensure the validity of subsequent results.

When designing an image registration algorithm specific to laser speckle stereo images, it must be noted that

subjective speckle patterns of each camera are independent, because they depend on the relative position of the object [6]. In conventional speckle video acquisition, typically an initial step of manual adjustment of the camera settings and positioning is done until the “best possible” speckle is reached. In the case of a stereo setup for laser speckle acquisition, such process leads to the infeasibility of cameras calibration for offline calculation of the essential matrix, since variables like distance to the object of interest, lens aperture and focal length may vary throughout acquisitions. Hence, the proposed registration method is exclusively based on the acquired speckle pattern appearance, allowing to avoid a stereo calibration process. However, this is dependent on the constancy of the respective settings.

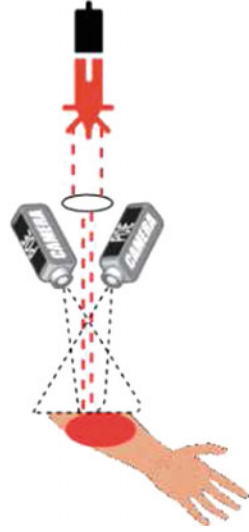
In order to define a robust mapping between a given ROI in one view and its corresponding ROI in the other view, a feature-based image registration method is proposed. This method is subdivided into two main steps: estimation of High Entropy Speckle Regions (HESR) segmentation and epipolar matching after segmentation.

2.2.1 HESR Segmentation

Given a laser speckle-based video, for each specific time index t and for each view, a 8-bit red-channel image $I(t)$ is considered for a preprocessing smoothing stage using a gaussian convolutional kernel. Then, a rough estimation of directly laser-illuminated regions is primarily achieved by applying the Otsu thresholding method [7] on the resulting low-pass filtered image. Once the resulting segmentation tends to become overestimated, a local entropy filter is applied to the original image using a mask given by the former Otsu derived estimation in order to refine the previously obtained segmentation estimation. Briefly, for each pixel, the filter output is the minimum number of bits necessary to encode the intensity distribution of a locally centered circularshaped neighborhood. The filtered result is again submitted to the Otsu thresholding method, enabling the assignment of two disjunct domains representing either high or low uncertainty of the intensity values. Subsequently, a sequence of morphological operations that includes clearing objects fully-connected to the background label, closing and opening operators are applied in order to refine the previously obtained result. The final step aims the extraction of the external contour of the resulting binary mask that corresponds to the delimitation of the HESR. In Fig. 2 this HESR segmentation pipeline is summarized.

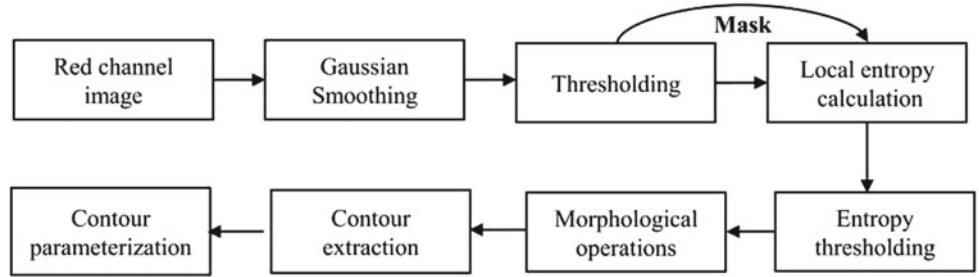
Once determined the HESR contour for each view, a length-based parametrization step was taken in order to sampling both left and right HESR contours with a common number of point coordinates. The path length parameterization routine, responsible to interpolate evenly spaced coordinates on the contours, is based on the chordal arclengths between points included on the previously

Fig. 1 Stereoscopic acquisition setup (left). Camera, lens and laser specifications (right)



Camera	Model: Sony® 3D NX Resolution: 1920 x 1080 Pixel Size: 1.7 x 2.2 (μm)
Lens	Focal length: 2.9 – 29 (mm) Aperture: f/1.8 – f/3.4
Laser	Model: ThorLabs® HNL100R Wavelength: 632.8 nm Power: 10.0 mW

Fig. 2 High-entropy speckle regions (HESR) segmentation for laser speckle images



estimated HESRs contours. To this task, an adaptation of the linear interpolant included in the *Matlab*® function *interparc* was implemented using the *Numpy* package for Python 3.6.

2.2.2 Epipolar Mapping Between Left and Right HESR Segmentations

Given the small magnitude order of the inter-axial distance between both camera centers (approximately 32 mm), similar vertical coordinates were expected for each pair of corresponding points between left and right scenes, described by $\{P: (x, y); P': (x', y')\}$. Such property allows to define a vertical offset threshold, v_{offset} , in order to exclude correspondences matching the condition defined in (1).

$$|y' - y| > v_{offset} \quad (1)$$

The resulting subset of correspondences $\{P_i; P'_i\}_{i=1\dots N}$ is then used to perform an initial estimation of the fundamental-matrix F , which in turn allows to discard potential falsely identified correspondences that do not match the epipolar constraint, theoretically given by Eq. (2).

$$P'FP = 0 \quad (2)$$

Thus, the prior set of correspondences is filtered by defining a threshold δ , approximately equal to 0, which allows to reject a subset of n false matches that do not verify the epipolar constraint given in Eq. 2.

$$\{P'FP \geq \delta\}_{i=1\dots N-n} \quad (3)$$

Intuitively, this process represents a simple exclusion scheme of all the points whose matching candidate does not lie at the respective epipolar line e' , as shown in Fig. 3.

The final set of trustworthy matches is used to compute a full rigid transformation T , that includes a uniform scaling given by s , a rotation matrix R , and a translation vector t , accordingly to Eq. (4).

$$T: \{sR; t\} = \arg \min_{R;t} \sum_i^{N-n} |P_i - (sRP_i + t)| \quad (4)$$

Finally, the resulting transform components are arranged in a 3×3 affine matrix, A , so that, for a given point of interest defined in the left image domain, $P_l: \{x_l, y_l\}$, its right correspondent, $P_r: \{x_r, y_r\}$, can be requested accordingly to Eq. (5).

$$P_r = A \cdot P_l \quad (5)$$

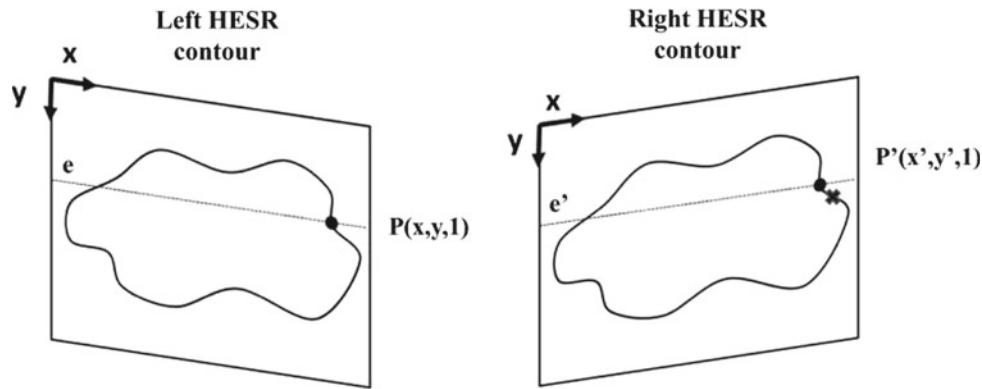


Fig. 3 Example of an untrustworthy correspondence between left and right HESR contours. Note the outer positioning of the matching candidate relatively to the respective epipolar line e'

2.2.3 Comparative Study of Stereo Dynamic Laser Speckle Videos During a Post-occlusive Hyperemia Situation

The validity of the registration procedure was successfully tested on a classic set of experimental procedures aiming at the dynamic characterization of the drying process of nail polish (data not shown). Still, to assess the methodology performance in physiological experiments, the proposed stereo speckle registration methodology was applied to the stereo recording of a PORH. Thus, assuming ROI stability regarding arm movements, the affine mapping was calculated using the first pair of stereo frames, and then recursively reused for all the remaining pair of frames.

Once computed the transformation responsible to establish a mapping between views, a minimum bounding rectangular region containing the computed HESR contour on the left image is defined. Such procedure allows to directly compute the right view corresponding bounding box by passing the coordinates of each vertex of the left bounding box through Eq. 5. Figure 4 shows the results of the registration procedure.

2.3 Dissimilarity Analysis Methodology

The activity variation on speckle experiments can be measured using some numerical descriptors, as proposed in [8]. These descriptors will be the basis for the inter-view dissimilarity analysis.

Taking into account the clinical interest in characterizing hyperemia conditions, this inter-view descriptor base methodology will be used to depict the transition from an occlusive to a hyperemic state during a PORH test. In particular, the identification of the most appropriate descriptors for a proper discrimination between these two physiological states will be shown, joint with the identification of the descriptors presenting the most similar behavior between the left and right views.

Given the dimensionality of the descriptors dataset, combined with the need of comparing each descriptor between left and right views, an unsupervised data projection approach was adopted using self-organizing maps (SOM) due to the respective potential of such algorithm for multidimensional data clustering and data mining purposes

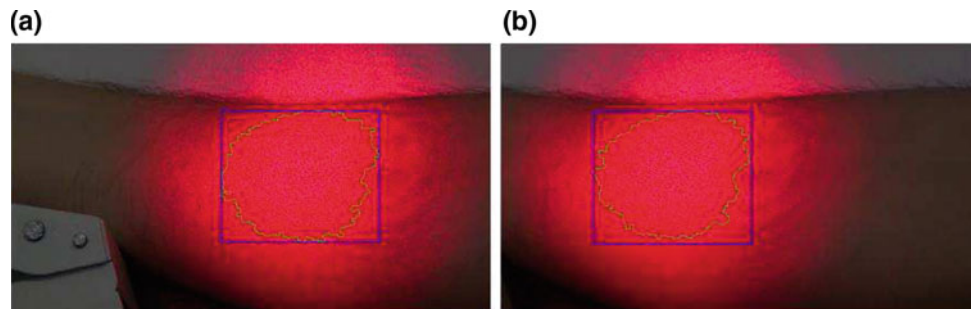


Fig. 4 ROI on the left scene domain identified as the minimum bounding box of the previously computed HESR in (a). The correspondent ROI on the right scene domain obtained with the proposed stereo speckle registration method

[9, 10]. The SOM training process is based on an iterative method responsible for updating the vector of weights of each neuron. Thus, for each randomly selected training data instance, the best-matching neuron (BMN) is determined based on a given distance metric.

The set of descriptors used in the analysis is described in Table 1 and includes:

Subtraction Average (SA), Fujii Generalized Differences (FGD), Dynamic Range (DG), Significant Changes Count (SCC) and Shannon Wavelet Entropy (SWE). This set of descriptors offered the best quality in terms of the minimization of both topographic and quantization errors. Regarding the topology of the trained SOMs, it was chosen a regular hexagonal grid of 40×40 neurons. As neighborhood function, a Gaussian model was adopted. The definition of such configurations and the training process was managed using the *SOM Toolbox* for MATLAB[®].

According to the objectives of this work, the training process of SOMs was accomplished for both views considering two specific time intervals representing occlusive and hyperemic states, as shown in Fig. 5.

Once trained left and right occlusive and hyperemic SOMs, the above-mentioned set of descriptors were recomputed considering two time-intervals (1 s each) represented on Fig. 5 as rectangular shaded regions. Each data instance, composed of 5 descriptors computed on the gray bars defined in Fig. 5, was then passed into the trained occlusive and hyperemic SOMs, in order to request the respective BMNs.

Additionally, it is possible to perform a dissimilarity analysis on the component planes that result of the SOMs training process. To this end, normalized correlation, incremental signed distance and rank distance were used as dissimilarity metrics [11], in order to quantitatively identify the most suitable descriptor to discriminate the transition from an occlusive state to a hyperemic one.

3 Results and Discussion

The topology of each physiological state on the SOMs domain allows extracting the descriptor values of the respective most representative BMNs. Table 2 presents these values, for each physiological state and for left and right views.

The resulting trained SOMs regarding each viewpoint and physiological state are shown in Figs. 6 and 7. The group of projected values of each considered descriptor on specific grids whose size equals the chosen SOM dimension at the training stage is known as a component plane. Thus, for each trained SOM the 5 respective component planes are appended to the respective U-matrix, as shown in Figs. 6 and 7.

As previously stated, the SOM component planes represent a suitable basis for the assessment and quantification of the descriptors dissimilarity between physiological phases under study. Thus, in order to identify the descriptor that presents a large variation between occlusion and hyperemia, three distinct metrics (Correlation—COR, Incremental Sign Distance—ISD and Rank Distance—RD) were used to assess the dissimilarity between the resulting occlusive and hyperemic component planes. Thus, for each descriptor represented by a SOM component plane c , the occlusive and hyperemic component planes, hereinafter defined by equally-sized L square matrices, were used to compute above-mentioned metrics defined in Table 3.

The visualization of the trained SOMs, specifically the respective U-matrices, do not exhibit an evident clustering of the data, suggesting that the forearm illuminated region used to produce a speckle pattern is uniform with respect to the local microvascular performance. This result is also coherent with the normalized correlations values shown in Table 4, which suggest the absence of an abrupt variation on the distribution of the activity descriptors on the SOM domain after the transition from occlusion to hyperemia.

Table 1 Final set of descriptors adopted on SOMs training. For a given sequence of N frames, the process of features extraction led to the generation of an image per each descriptor, with value for each image position (i, j) given by the following definitions

Descriptor name	Definition
Subtraction Average (SA)	$SA(i, j) = \sum_n^{N-1} I_n(i, j) - I_{n+1}(i, j)$ (6)
Fujii Generalized Differences (FGD)	$FGD(i, j) = \sum_2^N \frac{I_n(i, j) - I_{n+1}(i, j)}{I_n(i, j) + I_{n+1}(i, j)}$ (7)
Dynamic Range (DR)	$DR(i, j) = \max_{n=1 \dots N} \{I_n(i, j)\} - \min_{n=1 \dots N} \{I_n(i, j)\}$ (8)
Significative Changes Count (SCC)	$S(i, j) = \frac{1}{N-1} \sum_{n=1}^{N-1} s_n(i, j)$ (9), where function s_n evaluates if the intensity between sequential frames is greater than a threshold, computed as the average of the intensity difference between both frames
Shannon Wavelet Entropy (SWE)	$SWE(i, j) = - \sum_l^L \frac{E_l}{E} \log \left(\frac{E_l}{E} \right)$ (10), where E_l denotes the ratio between the L -th sub-band signal energy after Discrete <i>Daubechies</i> Wavelet decomposition ($L = 2$)

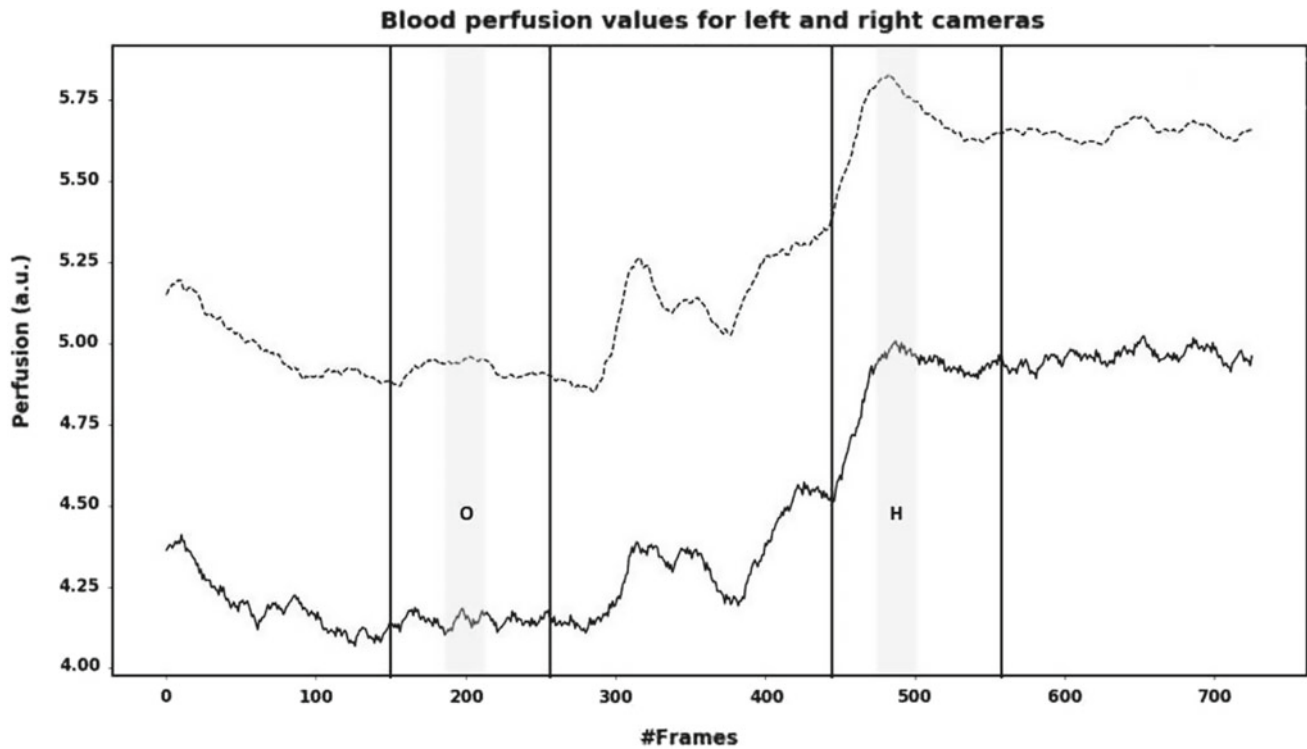


Fig. 5 Blood perfusion curves obtained from laser speckle contrast analysis (LASCA) in both left and right views. The dashed and continuous lines represent the right and left views perfusion curves, respectively. The vertical bars delimit the temporal intervals of each

physiological phase (O—occlusion; H—hyperemia) used to extract the descriptors used to train SOMs. The rectangular shaded regions define periods of 1 s used to extract descriptors to compute BMNs

Table 2 Most representative BMNs of the occlusive and hyperemic states, evaluated for each descriptor for both the left view (LV) and right view (RV)

	SA		FD		DR		SCC		SWE	
	LV	RV	LV	RV	LV	RV	LV	RV	LV	RV
Occlusion	0.22	0.53	0.25	0.61	0.48	0.50	0.28	0.68	0.20	0.41
Hyperemia	0.50	0.52	0.53	0.58	0.40	0.55	0.59	0.67	0.37	0.46

Additionally, the identification of the most representative BMNs for each physiological condition under study allowed to verify a growing monotony of the activity descriptors values associated to the transition from an occlusive state to a hyperemic one. It is particularly evident on the left-view acquisition, since 4 of the 5 considered descriptors followed such rule, being the DR descriptor the exception on such expected evolution. Inversely, regarding the right-view acquisition, the former

analysis revealed a slight increase on the DR and SWE descriptors and an overall constancy of the remaining descriptors.

Regarding the dissimilarity between the component planes of each of the descriptors between occlusive and hyperemic states, results shown in Table 4 suggest SWE as the most suitable activity descriptor in discriminating such physiological transition, once it is associated with higher dissimilarity values for all the adopted metrics.

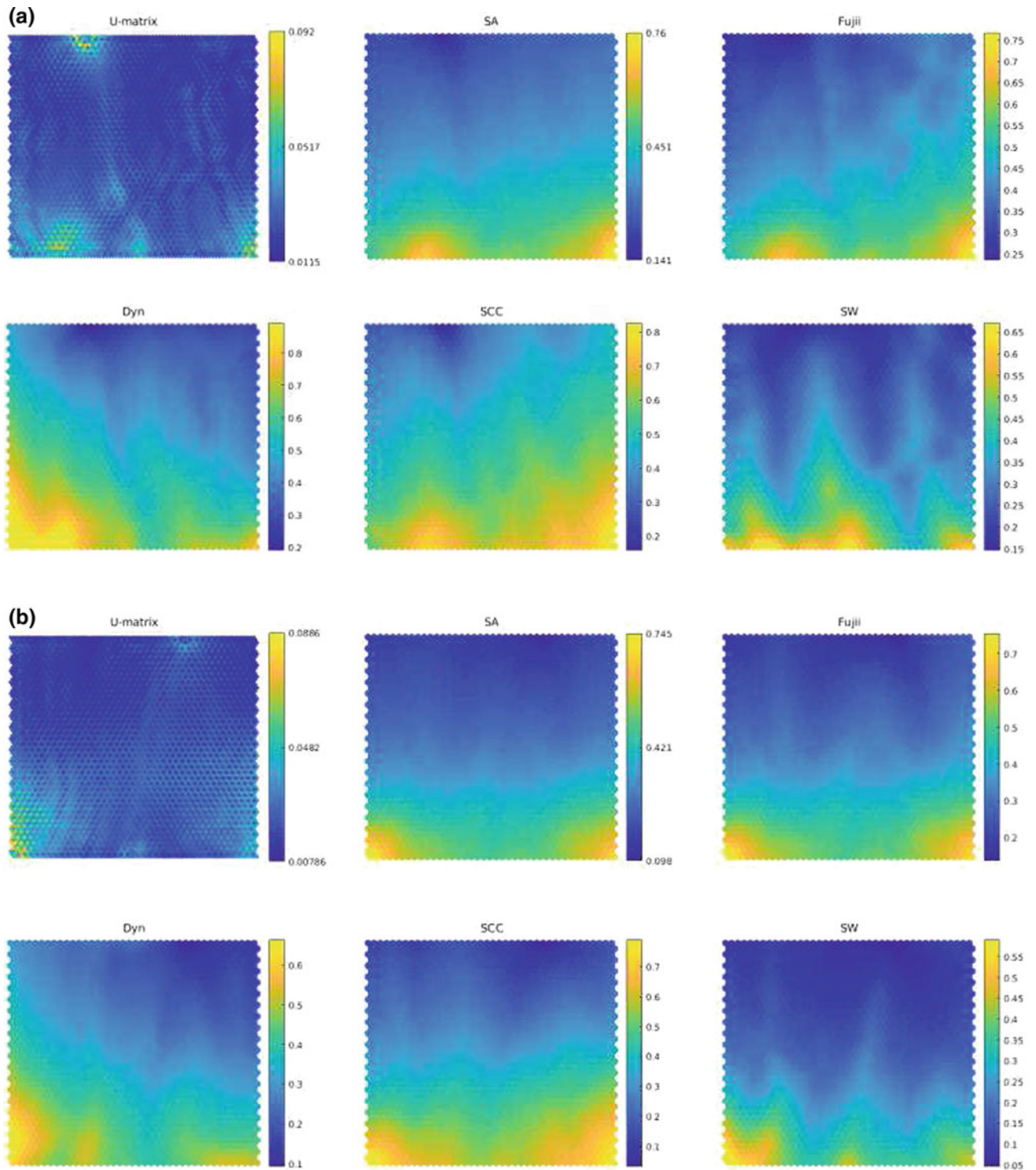


Fig. 6 Resulting SOMs trained with descriptors extracted from the left camera considering **a** an occlusive state and **b** a hyperemic state. On the top-left corner, the U-matrix of each SOM is shown, while the

remaining positions correspond to each of the component planes specifically associated with the descriptors adopted during the SOM training stage

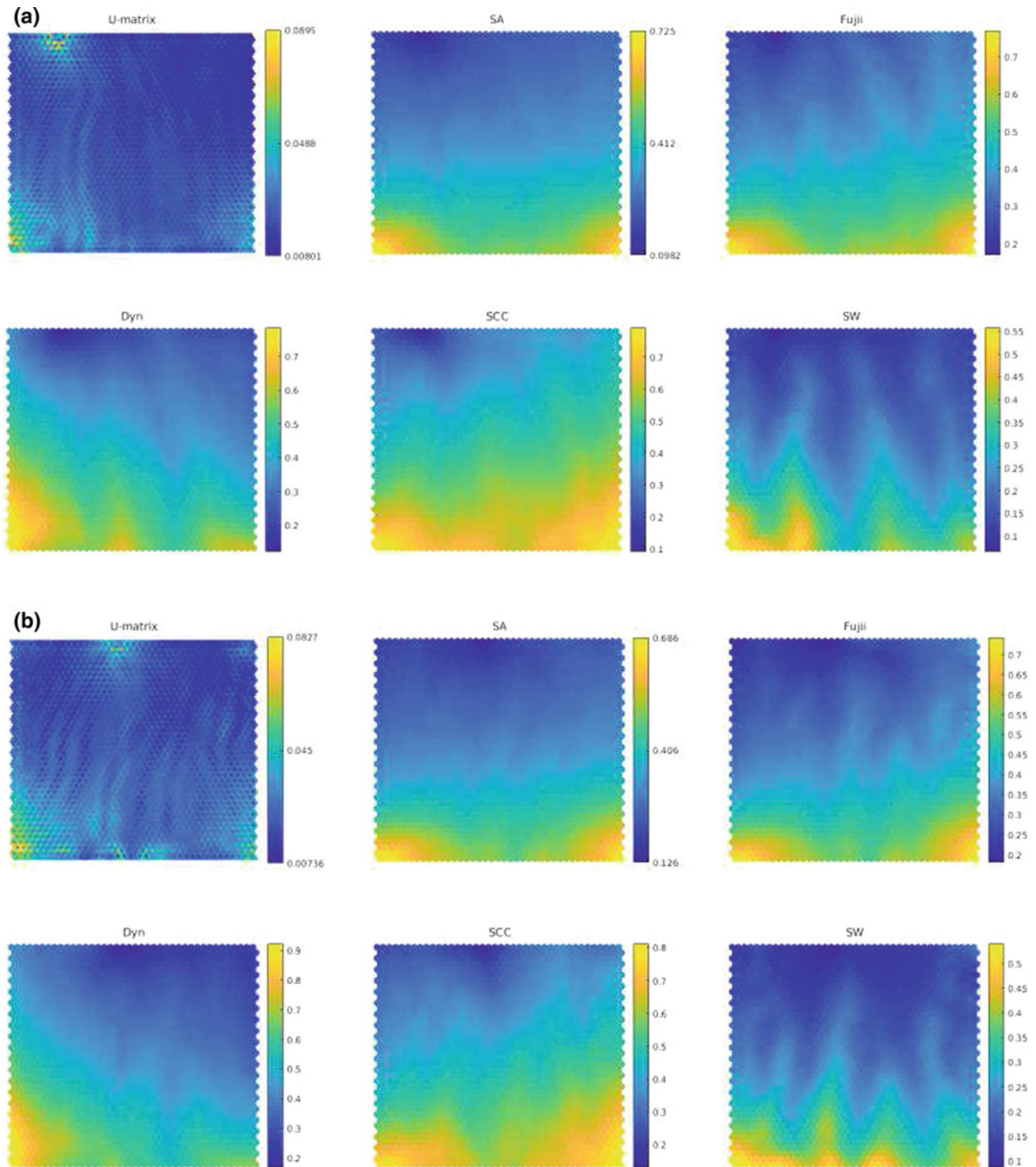


Fig. 7 Analogously to Fig. 6, the resulting SOMs, trained with descriptors extracted from the right camera and considering **a** an occlusive state and **b** a hyperemic state, are shown

Table 3 Dissimilarity metrics used to quantify the magnitude of the response of each of the activity descriptors to the transition from an occlusive state to a hyperemic one. The dissimilarity metrics were calculated considering equally-sized occlusive and hyperemic component planes $\{I_{cO}, I_{cH}\}$ for each descriptor (fully represented by a given SOM component plane c)

Metric name	Definition
Normalized Correlation (COR)	$COR(I_{cO}, I_{cH}) = \frac{\frac{1}{L} \sum_{i=1}^L (I_{cO_i} - \bar{I}_{cO})(I_{cH_i} - \bar{I}_{cH})}{\sigma_{I_{cO}} \sigma_{I_{cH}}} \quad (11),$ where \bar{x} and σ_x corresponds to the average and standard deviation values, respectively. L represents the size of the component plane
Incremental Signed Distance (ISD)	$ISD(I_{cO}, I_{cH}) = \frac{\sum_{B(I_{cO}) \neq B(I_{cH})} 1}{L} \quad (12),$ corresponds to the hamming distance calculated on top of the binarization operation B that equals 1 for intensity difference between consecutive image entries greater than 0 and equals 0 otherwise
Rank Distance (RD)	$RD(I_{cO}, I_{cH}) = \frac{1}{L} \sum_{i=1}^L R(I_{cO_i}) - R(I_{cH_i}) \quad (13),$ equals the L_1 norm of rank ordered values, calculated once executed the rank operator R in both occlusive and hyper-emic component planes, separately

Table 4 Dissimilarity analysis for occlusive and hyperemic states based on the metrics between each, for the left (LV) and right (RV) views

	SA		FGD		DR		SCC		SWE	
	LV	RV	LV	RV	LV	RV	LV	RV	LV	RV
COR	0.95	0.99	0.92	0.98	0.96	0.97	0.90	0.97	0.87	0.91
ISD	0.02	0.02	0.14	0.10	0.16	0.09	0.1	0.09	0.29	0.31
RD	104.3	40.8	150.3	61.6	84.0	85.5	166.4	71.3	195.5	161.5

4 Conclusions and Future Work

This work presents a simple and robust methodology to register dynamic speckle imagery acquired using a stereo setup. Such procedure was used to verify distinct behaviors of each view during the transition between occlusive and hyperemic states, since the right view camera presented an overall constancy of the descriptors values and the left camera presented an overall and expected increase of the activity values. Given the short baseline between the centers of the cameras used in the stereo setup, this fact suggests the high-sensitivity of laser speckle acquisitions with respect to the angular positioning of the camera, relatively to a given object of interest. Hence, considering the importance of consistent and reproducible clinical conclusions based on dynamic speckle features, a performance comparison, including 5 commonly used activity descriptors in the analysis of dynamic speckle acquisitions, revealed SWE as the most consistent descriptor regarding the expected activity increase, which characterizes the transition between an occlusive and a hyperemic state. Also, SWE revealed the pair occlusive/hyperemic component planes with the maximal dissimilarity, suggesting improved ability to discriminate such physiological states.

As future work, the use of arbitrary camera setups must be considered in order to test both multiple baseline distances and different camera configurations, such that the consistency between views of clinical conclusions based on dynamic speckle features is not compromised, simultaneously offering the possibility of allowing the clinic to exploit computer

vision techniques to extract three-dimensional features of skin lesions. Additionally, the generation of speckle decorrelation-time maps using multiple exposure-times during stereo speckle acquisitions must be explored, given that the speckle acquisition by two distinct image sensors may provide important insights for the estimation of blood scatters direction and velocity.

Acknowledgements This work was partially supported by Fundação para a Ciência e Tecnologia FCT-Portugal, under the scope of Project Light Field Laser Speckle in the scope of R&D Unit 50,008 through national funds, and where applicable co-funded by FEDER—PT2020 Partnership agreement. The work was also supported by the Project FCT/SAICT 2018 CENTRO-01-0145FEDER-23878.

References

- Bento, L., Távora, L., Assunção, P., Faria, S., Fonseca-Pinto, R.: Evaluation of cutaneous microcirculation patterns by laser speckle imaging. In: 41st International Convention on Information and Communication Technology, Electronics and Microelectronics (MIPRO), pp. 0290–0293, IEEE (2018)
- Tchivaleva, L., Shenkenfelder, W., Doronin, A., Meglinski, I., Markhvida, I., Lee, T.K.: In vivo laser speckle measurements of skin roughness: clinical study. In: Optics in the Life Sciences, Optical Society of America Technical Digest, 2015, paper JT3A.28
- Khan, D., Shirazi, M.A., Kim, M.Y.: Single shot laser speckle-based 3D acquisition system for medical applications. Opt. Lasers Eng. **105**(January), 43–53 (2018)
- Rodríguez, F., Cotto, I., Dasilva, S., Rey, P., der Straeten, K.V.: Speckle characterization of surface roughness obtained by laser texturing. Procedia Manufacturing **13**, 519–525 (2017)

5. Yin, X., Wang, G., Shi, C., Liao, Q.: Efficient active depth sensing by laser speckle projection system. *Opt. Eng.* **53**(1), 0131–05 (2014)
6. Stark, A.W., Wong, E., Weigel, D., Babovsky, H., Schott, T., Kowarschik, R.: Subjective speckle suppression in laser-based stereo photogrammetry. *Opt. Eng.*, **55**, 12 (2016)
7. Otsu, N.: A threshold selection method from gray-level histograms. *IEEE Trans. Syst., Man, Cybern.* **9**(1), 62–66 (1979)
8. Dai Pra, A.L., Meschino, G.J., Guzman, M.N., Scandurra, A.G., Gonzalez, M.A., Weber, C., Trivi, M., Rabal, H., Passoni, L.I.: Dynamic speckle image segmentation using self-organizing maps. *J. Opt.* **18**(8) (2016)
9. Vesanto, J., Ahola, J.: Hunting for correlations in data using the self organizing map. In: Proceedings of international ICSC congress on computational intelligence and applications, pp. 279–285 (1999)
10. Iivarinen, J., Kohonen, T., Kangas, J., Kaski, S.: Visualizing the clusters on the self-organizing map. In: Proceedings of the conference on artificial intelligence research in Finland, pp. 122–126, Finnish Artificial Intelligence Society (1994)
11. Goshtasby, A.A.: Image registration, advances in computer vision and pattern recognition, https://doi.org/10.1007/978-1-4471-2458-0_2, © Springer-Verlag London Limited 2012

Wavelet Phase Coherence Analysis Between the Respiratory Activity and the Microcirculation: The Effects of Type 1 Diabetes

Michele Sorelli, Antonia Perrella, Piergiorgio Francia, and Leonardo Bocchi

Abstract

Microvascular perfusion is modulated by the breathing activity. However, to the authors' knowledge, no study has attempted to assess the pathological deterioration of this physiological coupling in diabetes, which is related to structural and functional alterations of the microvasculature. On this basis, a phase coherence analysis was conducted to identify a possible weakening of the time-phase relationship between the breathing rhythm and the peripheral pulse, measured with laser Doppler flowmetry. Two groups of 21 healthy subjects and 21 type 1 diabetic (T1D) patients were evaluated in this retrospective study: a significant phase coherence was detected for the area beneath the diastolic phase of the peripheral pulse (median: 0.78; IQR: 0.20), in 81.0% of the controls; however, the analysis of the T1D group highlighted a considerable loss of synchronization, with significant values obtained in only 33% of the cases (median: 0.53; IQR: 0.15). This result may yield a valuable biomarker for the detection of diabetic microangiopathy.

Keywords

Microcirculation • Diabetes • Laser Doppler flowmetry • Wavelet phase coherence

1 Introduction

The microcirculation plays a crucial function in adjusting the local blood flow rates to the spatially- and time-varying metabolic demands of the organism [1]. In this regard, the microvascular physiology is characterized by a complex array of systemic and local control pathways which regulate the tone of vascular smooth muscle cells and, thus, the regional supply of O₂ and nutrients [2]. In addition to the propagation of cardiac and respiratory-related pressure waves, the intrinsic endothelial and myogenic vasomotor mechanisms, and the extrinsic neurovascular interactions, produce oscillatory patterns in the tissue microvascular perfusion within established frequency intervals [3]. These characteristic components can be assessed noninvasively at the level of the skin by means of laser Doppler flowmetry and time-frequency analysis techniques [4].

As recently reviewed by Gutterman et al., microvascular dysfunction is recognized either as a primary causal factor or a secondary effect of a broad range of pathological conditions, including diabetes mellitus [5]. Diabetes-related hyperglycaemia has been associated with a range of biochemical and structural changes affecting the vascular endothelial and smooth muscle cells. The long-term exposure to abnormal glycaemic levels exacerbates tissue oxidative stress, which leads to a decrease in the bioavailability of vasodilator agents (namely, nitric oxide), and furthers the build-up of extracellular matrix proteins and the cross-linking of inelastic collagen fibrils, thus causing the stiffening of vascular walls [6, 7]. Arterial stiffness is deemed an independent predictor of cardiovascular events and mortality both in the diabetic and in the general population [7, 8]. In this regard, aortic pulse wave velocity (PWV) represents the current gold standard for the clinical evaluation of vascular stiffening; a significant association between PWV, diabetes duration and related complications as retinopathy, nephropathy and autonomic neuropathy is consistently reported in the literature [7, 8]. However, subtle

M. Sorelli (✉) · A. Perrella · L. Bocchi
Department of Information Engineering, University of Florence,
Florence, Italy
e-mail: michele.sorelli@unifi.it

P. Francia
Department of Clinical and Experimental Medicine,
University of Florence, Florence, Italy

vascular alterations may anticipate clinically overt pathological features [9] and may thus serve as early predictors of the above detrimental complications.

The cardiovascular system can be considered as a network of coupled cardiac, respiratory and vascular oscillators. In this respect, wavelet phase coherence [10] and dynamical Bayesian inference [11] can be respectively applied in order to detect the presence of functional interactions between these physiological processes, and to characterize their mutual strength and causality. Through this methodological approach, a weakening of the cardio-respiratory coupling (i.e. the respiratory sinus arrhythmia) has been observed in elderly subjects [12, 13]. Furthermore, an impairment of the coordination between the cardiac and the myogenic microvascular dynamics has been reported in treated essential hypertension [14]. This result appears to indicate a pathological uncoupling of the oscillatory processes underlying the normal cardiovascular function, possibly due to a persistent deterioration of the local mechanisms regulating the microvascular perfusion or to an alteration of the mechanical properties of the vascular walls. In a recent study on healthy control subjects [15], a significant degree of phase coherence has been identified between the respiratory activity and the diastolic part of the digital LDF pulse wave, accurately modeled by means of a multi-Gaussian pulse decomposition algorithm, described in [16].

The investigation of vascular alterations in type I diabetic (T1D) patients is deemed particularly important, since these subjects are not often associated with multiple metabolic comorbidities [7]. Accordingly, the aim of this study was to assess the presence of the above phase coherence parameter in a preliminary group of T1D patients: the analysis of such relationship may, indeed, lead to the identification of a clinically valuable biomarker for the early detection and monitoring of diabetes-related microvascular dysfunction.

2 Materials and Methods

The present retrospective case-control study was conducted in accordance with the guidelines of the Declaration of Helsinki: accordingly, all the participants received exhaustive information on the purpose of the research and the related procedures, and signed an informed consent form before the measurement sessions. In detail, two age-matched ($p = 0.850$, Mann-Whitney U test) and gender-matched ($p = 0.533$, Pearson's χ^2 test) groups of 21 healthy subjects (age: 26.4 ± 3.0 years, M/F: 13/8) and 21 T1D patients were compared (age: 31.4 ± 15.5 years, M/F: 11/10).

A Periflux 5000 laser Doppler flowmetry (LDF) system (Perimed, Sweden) was used to record the cutaneous microvascular perfusion on the distal phalanx of the right

index finger. Furthermore, the respiratory activity was simultaneously monitored by means of a BioHarness 3 physiological monitoring telemetry device (Zephyr Technologies, US). The above signals were digitized at 250 Hz and thoroughly synchronized with a custom data acquisition software. The sessions took place in controlled thermal conditions ($T \approx 23$), after a preliminary acclimatization time of ≈ 10 min had passed. The measurements lasted 5 min and were performed with the test subjects in sitting position and leaning the ipsilateral forearm on a table in order to minimize the risk of movement artefacts in the perfusion data. The LDF data of microvascular perfusion were processed with an original multi-Gaussian PDA, whose implementation is thoroughly covered in [16]. The algorithm is comprised of two main building blocks: a first detection stage, which addresses the automatic recognition of the separate cardiac cycles, and the identification of systolic, diastolic, and diastolic reference points on the LDF pulse contour; and a second modeling stage, where each peripheral pulse waveform is accurately reconstructed by means of four Gaussian components. Afterwards, the PDA extracts the overall area beneath the diastolic phase of the pulse model, A_d , as shown in (Fig. 1). At this stage, a cubic spline-interpolation of the A_d values associated with each cardiac cycle was applied in order to match the sampling time-grid of the respiratory signals. In this regard, the centroid of the diastolic phase of the waveform models was adopted in order to locate the original sample points of the feature of interest.

The phase coherence analysis between the breathing oscillatory activity and the area under the diastolic pulse contour, A_d , followed the method outlined by Tankanag et al. in [17]. Accordingly, this parameter was computed as:

$$C_\phi(f_k) = \sqrt{\langle \cos(\Delta\phi_{k,n}) \rangle^2 + \langle \sin(\Delta\phi_{k,n}) \rangle^2}, \quad (1)$$

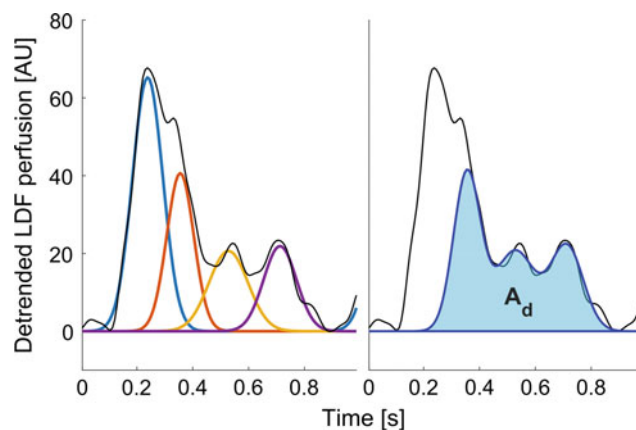


Fig. 1 Multi-Gaussian modeling of the LDF pulse and model-derived A_d feature

where $\Delta\phi_{k,n}$ is the phase lag between the components of the respiratory and A_d signals with characteristic frequency f_k at time t_n , and $\langle \cdot \rangle$ indicates time averaging. Theoretically, if two generic oscillations stay phase-locked (i.e. they are temporally coherent) throughout the analyzed time domain, then $C_\phi(f_k) = 1$; vice versa, the absence of any tendency toward the preservation of a particular phase difference would be reflected by $C_\phi(f_k) = 0$.

In this study, the extraction of the above instantaneous phase lag was performed through a wavelet transform analysis (WTA) of the breathing signal and the reconstructed time series of the resampled A_d feature; therefore, the term *wavelet phase coherence* (WPC) will be henceforth adopted. At each discrete time point, t_n , the average frequency in the nominal range of the respiratory activity, (0.145, 0.6)Hz, weighted with respect to the corresponding value of the wavelet PSD, was estimated so as to identify the instantaneous rate, f_b , of their breathing-related mode and, thus, extract the corresponding wavelet coefficients, $w_\star(t_n, f_b)$ as schematized in Fig. 2. In detail, the present WTA relied on the Morlet's mother wavelet, with central frequency $f_0 = 1$ Hz. 32 sample/octave were used to discretize the frequency axis, so as to trade-off between resolution and computational times. Moreover, only the *cone of influence* of the resulting wavelet scalograms, where the relative distortion due to boundary effects was below 1%, was considered for further analysis [18]. It is here relevant to recall how the resultant WPC values are significantly affected by the time scale of interest: WPC is, in fact, an inherently biased parameter, as it tends to increase towards the lower detectable frequencies due to the availability of fewer oscillation periods; furthermore, WPC might assume high values due to autocorrelation phenomena, even when the dynamics underlying the couple of assessed time series is actually unrelated. However, this potential source of unreliability can be accounted for by validating the $C_\phi(f_k)$ estimates against the phase coherence obtained between each original time series and a corresponding phase-randomized *surrogate* [19]. In this regard, the iterative amplitude-adjusted Fourier transform (IAAFT) method, described by Schreiber and Schmitz in [20], was applied so as to generate a set of $N = 100$ surrogates from each $b(t)$ and $A_d(t)$ signal, where N was selected for statistical repeatability. Afterwards, the corresponding $N = 100$

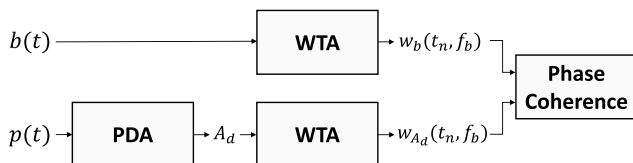


Fig. 2 Wavelet phase coherence analysis: block diagram

$C_{\phi,b,surr}(f_k)$ and $C_{\phi,A_d,surr}(f_k)$ surrogate functions were used to identify the following significance threshold:

$$T_{C_{\phi,\star,surr}}(f_k) = \bar{C}_{\phi,\star,surr}(f_k) + 2 \cdot \sigma_{C_{\phi,\star,surr}}(f_k) \quad (2)$$

where $\bar{C}_{\phi,\star,surr}(f_k)$ indicates the mean WPC over the 100 surrogates, while $\sigma_{C_{\phi,\star,surr}}(f_k)$ represents its standard deviation. In detail, each assessed couple ($b(t)$, $A_d(t)$) was considered as significantly phase-coherent at a specific frequency f_k , only if $C_{\phi,b,surr}(f_k) > T_{C_{\phi,\star,surr}}(f_k)$ held for both the breathing and A_d signals.

3 Results

In 17 out of the 21 control subjects (i.e. 81.0%), the WPC analysis identified a significant degree of phase coordination between the central breathing oscillatory process and the diastolic part of the digital LDF pulse wave (characterized by means of the area beneath its 3-Gaussian model, A_d). These significant cases were associated with a median value of the peak WPC in the nominal frequency range of the respiratory activity (0.145, 0.6)Hz of 0.78 (IQR: 0.20). Figure 3 shows a sample WPC curve obtained from one of these instances.

Conversely, the results obtained in the T1D group indicate a remarkable loss of synchronization, with significant WPC levels detected in only 8 of the 21 available cases (38.1%), for an overall median value of the peak respiratory

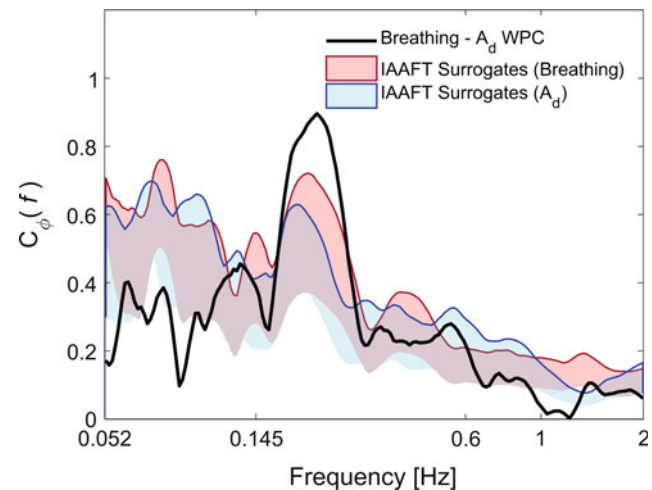


Fig. 3 Sample WPC curve between the breathing signal and the model-derived diastolic A_d feature. The upper thick colored lines depict the significance thresholds, $T_{C_{\phi,\star,surr}}(f_k)$, whereas the lower boundary of the shaded areas corresponds to the mean *surrogate* WPC

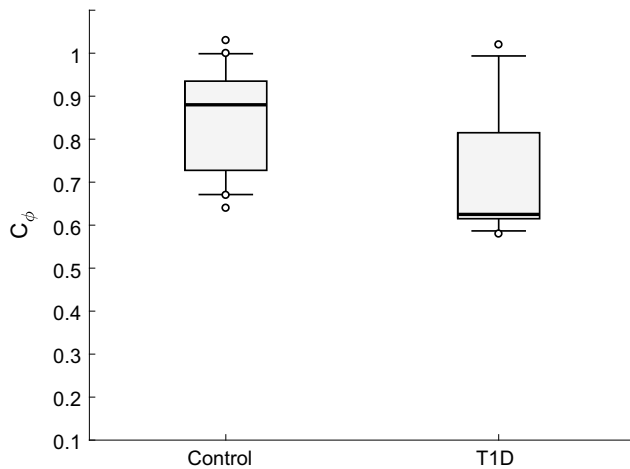


Fig. 4 Significant peak WPC values in the respiratory frequency range

Table 1 Wavelet phase coherence analysis: results

	A_d WPC	MEDIAN	IQR
Control	17/21 subjects	0.78	(0.63, 0.83)
T1D	8/21 subjects	0.53	(0.52, 0.67)

WPC of 0.53 (IQR: 0.15). The box plots of the significant WPC peaks inside the breathing frequency interval are shown in Fig. 4. Due to the non-normality of these data (preliminarily verified with the Shapiro-Wilk test), the non-parametric Mann-Whitney U test was applied to prove the statistical significance of this appreciable decrease in coherence ($p = 0.025$). Therefore, the outcome of the present study (summarized in Table 1) suggests that the proposed technique may be able to detect the subtle effects of T1D on the blood microcirculation.

Indeed, the decreased coupling highlighted in the pathological group might reflect the functional and structural vascular changes, mentioned concisely in the introductory section. However, a non-significant weaker phase coherence was nonetheless observed in 4 control subjects as well. These cases were associated with a significantly higher age (30 ± 2 years) with respect to the other healthy subjects (26 ± 3 years, $p = 0.013$): a possible effect of age would be consistent with the studies by Ticcinelli and Shioyai [13, 21], which have identified ageing as an important factor influencing the cardiovascular dynamics in healthy subjects; still, the small difference between the sample means and the low sample count preclude us from inferring a solid conclusion on this aspect.

4 Conclusion

The present study investigated the coordination between the rhythm of the breathing activity and the diastolic phase of digital LDF pulse waveforms in a group of T1D patients. Whereas a strong phase coherence with the *central* breathing function has been detected in a vast majority of the reference control subjects (81%), suggesting the presence of a physiological coupling with the microvascular perfusion, this coordination appears to be considerably weakened in the pathological group, which exhibited a significant degree of coherence only in 38.1% of the cases.

This outcome may reflect a possible subtle disruption of a breathing-related modulation of the secondary reflected waves, which arise in the circulatory tree due to the mismatch in the effective vascular impedance, encountered by the forward-travelling systolic pulse. Therefore, this study provides a preliminary indication of the suitability of the PDA-based A_d feature of the diastolic LDF pulse contour as a valuable non-invasive biomarker of T1D-related microvascular dysfunction.

Conflicts of Interest All authors have no conflict of interest to disclose in relation to the current work.

References

- Boron, W.F., Boulpaep, E.L.: Medical Physiology. Elsevier Health Sciences (2008)
- Aalkjaer, C., Boedtkjer, D., Matchkov, V.: Vasomotion—what is currently thought? *Acta Physiol* **202**, 253–269 (2011). <https://doi.org/10.1111/j.1748-1716.2011.02320.x>
- Stefanovska, A., Bra ĉ i ĉ, M., Kvernmo, H.D.: Wavelet analysis of oscillations in the peripheral blood circulation measured by laser Doppler technique. *IEEE Trans. Biomed. Eng.* **46**, 1230–1239 (1999). <https://doi.org/10.1109/10.790500>
- Humeau, A., Steenbergen, W., Nilsson, H.: Ströberg: Laser Doppler perfusion monitoring and imaging: novel approaches. *Med. Biol. Eng. Comput.* **45**, 421–435 (2007). <https://doi.org/10.1007/s11517-007-0170-5>
- Gutterman, D., Chabowski, D.S., Kadlec, A.O., Durand, M.J., Freed, J.K., Ait-Aissa, K., Beyer, A.M.: The human microcirculation—regulation of flow and beyond. *Circ. Res.* **118**, 157–172 (2016). <https://doi.org/10.1161/CIRCRESAHA.115.305364>
- Madonna, R., Balistreri, C.R., Geng, Y., De Caterina, R.: Diabetic microangiopathy: pathogenic insights and novel therapeutic approaches. *Vascul. Pharmacol.* **90**, 1–7 (2017). <https://doi.org/10.1016/j.vph.2017.01.004>
- Prenner, S.B., Chirinos, J.A.: Arterial stiffness in diabetes mellitus. *Atherosclerosis* **238**, 370–379 (2015). <https://doi.org/10.1016/j.atherosclerosis.2014.12.023>
- Theilade, S., Lajer, M., Frederik, P., Joergensen, C., Rossing, P.: Arterial stiffness is associated with cardiovascular, renal, retinal, and autonomic disease in type 1 diabetes. *Diab. Care* **36**, 715–721 (2015). <https://doi.org/10.2337/dc12-0850>

9. Stehouwer, C.D.A.: Microvascular dysfunction and hyperglycemia: a vicious cycle with widespread consequences. *Diabetes* **67**, 1729–1741 (2018). <https://doi.org/10.2337/dbi17-0044>
10. Bandrivskyy, A., Bernjak, A., McClintock, P.V.E., Stefanovska, A.: Wavelet phase coherence analysis: application to skin temperature and blood flow. *Cardiovasc. Eng.* **4**, 89–93 (2004). <https://doi.org/10.1023/B:CARE.0000025126.63253.43>
11. Stankovski, T., Duggento, A., McClintock, P.V.E., Stefanovska, A.: Inference of time-evolving coupled dynamical systems in the presence of noise. *Phys. Rev. Lett.* **109** (2012). <https://doi.org/10.1103/physrevlett.109.024101>
12. Iatsenko, D., Bernjak, A., Stankovski, T., Shiogai, Y., Owen-Lynch, P.J., Clarkson, P.B.M., McClintock, P.V.E., Stefanovska, A.: Evolution of cardiorespiratory interactions with age. *Philos. Trans. R. Soc. Lond. A* **371** (2013). <https://doi.org/10.1098/rsta.2011.0622>
13. Ticcinielli, V., Stankovski, T., McClintock, P.V.E., Stefanovska, A.: Ageing of the couplings between cardiac, respiratory and myogenic activity in humans. In: 37th Annual International Conference of the IEEE Engineering in Medicine and Biology Society (EMBC), 7366–7369 (2015). <https://doi.org/10.1109/embc.2015.7320093>
14. Ticcinielli, V., Stankovski, T., Iatsenko, D., Bernjak, A., Bradbury, A.E., Gallagher, A.R., Clarkson, P., McClintock, P.V.E., Stefanovska, A.: Coherence and coupling functions reveal microvascular impairment in treated hypertension. *Front. Physiol.* **8** (2017). <https://doi.org/10.3389/fphys.2017.00749>
15. Perrella, A., Sorelli, M., Giardini, F., Frassinetti, L., Francia, P., Bocchi, L.: Wavelet phase coherence between the microvascular pulse contour and the respiratory activity. In: World Congress on Medical Physics and Biomedical Engineering, 311–314 (2018). https://doi.org/10.1007/978-981-10-9038-7_58
16. Sorelli, M., Perrella, A., Bocchi, L.: Detecting vascular age using the analysis of peripheral pulse. *IEEE Trans. Biomed. Eng.* **65**, 2742–2750 (2018). <https://doi.org/10.1109/TBME.2018.281463>
17. Tankanag, A.V., Grinevich, A.A., Kirilina, T.V., Krasnikov, G.V., Piskunova, G.M., Chemeris, N.K.: Wavelet phase coherence analysis of the skin blood flow oscillations in human. *Microvasc. Res.* **95**, 53–59 (2014). <https://doi.org/10.1016/j.mvr.2014.07.003>
18. Iatsenko, D., McClintock, P.V.E., Stefanovska, A.: Linear and synchrosqueezed time–frequency representations revisited: overview, standards of use, resolution, reconstruction, concentration, and algorithms. *Digit. Sig. Proc.* **42**, 1–26 (2015). <https://doi.org/10.1016/j.dsp.2015.03.004>
19. Sheppard, L.W., Stefanovska, A., McClintock, P.V.E.: Testing for time-localized coherence in bivariate data. *Phys. Rev. E* **85** (2012). <https://doi.org/10.1103/physreve.85.046205>
20. Schreiber, T., Schmitz, A.: Surrogate time series. *Phys. D* **142**, 346–382 (2000). [https://doi.org/10.1016/S0167-2789\(00\)00043-9](https://doi.org/10.1016/S0167-2789(00)00043-9)
21. Shiogai, Y., Stefanovska, A., McClintock, P.V.E.: Nonlinear dynamics of cardiovascular ageing. *Phys. Rep.* **488**, 51–110 (2010). <https://doi.org/10.1016/j.physrep.2009.12.003>

Prostate Cancer Detection Using Different Classification Techniques

Jasna Nuhić and Jasmin Kevrić

Abstract

Prostate cancer is a widespread disease among the male population. Its early diagnosis and prognosis are challenging tasks for clinical researchers due to the lack of very precise, fast and human error free diagnostic method. The purpose of this research is to develop a novel prototype of clinical management in diagnosis and management of patients with prostate cancer. Various classification algorithms were applied on a cancer database to devise methods that can best predict the cancer occurrence. However, the accuracy of such methods differs depending on the classification algorithm used. Identifying the best classification algorithm among those available is a difficult task. In this paper, the results of a comprehensive comparative analysis of nine different classification algorithms are presented and their performance evaluated. The results indicate that none of the classifiers outperformed all others in terms of accuracy, meaning that multiple classifiers can serve clinicians in diagnostic procedure.

Keywords

Prostate cancer • Cancer stage prediction • Classification algorithms • Attribute selection

1 Introduction

Prostate cancer is one of the leading causes of cancer death worldwide. Around 650,000 new patients are diagnosed each year. The causal factors of prostate cancer still remain undetermined [1]. It is one of the most frequently diagnosed

cancers that affect men in the United States. More than 12% of diagnosed new cases in 1996 ended fatally [2]. The most effective therapy for localized prostate cancer is surgery, i.e. radical prostatectomy [2–5]. More than 40% of patients are falsely presumed to have localized prostate cancer, but at surgery becomes evident that it is not the localized type and, therefore, surgery alone is not enough to save a patient [6].

It has been proven that introducing data mining into medical analysis increases diagnostic accuracy, reduces costs and reduces human error [7]. Data mining refers to the process of extracting information from large data sets and transforming it into an understandable structure. It discovers patterns in large data bases, as well [8].

Based on this, a typical system's architecture consists of three main components, namely: the database, the data warehouse and the World Wide Web as types of information repositories. Tasks such as association analysis, classification, prediction, and cluster and outlier analysis are performed by functional modules that are part of a data mining engine. Graphical user interface (GUI) is key element for interaction between the system and the user, where the user is allowed to assign a data mining task.

Data mining is a crucial step in knowledge discovery [9, 10]. Knowledge Discovery in Databases (KDD) is the process of extracting implicit, previously unknown and potentially useful information from data in databases [11, 12]. The following steps lead from data to new knowledge: selection, preprocessing, transformation, data mining and interpretation [9]. Different types of knowledge representations include pattern recognition, clustering, association and classification [13].

Prostate cancer prediction using machine learning mostly relies on algorithms that use medical imaging techniques, but some research groups have focused on laboratory studies [14]. Tan and Gilbert (2003) have classified cancerous microarray data using ensemble learning and found that this technique outperforms single decision trees [15]. The study performed by Hamzeh et al. prostate cancers were sequenced using RNA-Seq and machine learning was utilized as a means of identifying transcripts that are most likely

J. Nuhić (✉)

Universitat Pompeu Fabra, Barcelona, Spain
e-mail: jasna.nuhic01@estudiant.upf.edu;
jasna.nuhic96@gmail.com

J. Kevrić

International Burch University, Ilidža, Bosnia and Herzegovina
e-mail: jasmin.kevric@ibu.edu.ba

associated with progression of cancer, where the Naïve Bayes classifier outperformed a support vector machine [16]. RNA-Seq data was also used by a research group that aimed to find patterns associated with stage-specific differences among prostate cancer cells' RNA [17].

In this study, nine different classifiers were used to predict whether the patient has prostate cancer. Attribute selection was used to detect relevant attributes for decision making. Ten-fold cross validation was used in order to partition dataset into a training and an evaluation dataset. The cross-validation technique was used to ensure optimal results.

2 Methods

2.1 Dataset

The goal of the experiment performed on a set of prostate cancer samples was to identify patterns that distinguish prostate cancer from noncancer. This study is significant for men who have a high risk of prostate cancer due to family or personal history of such cancer.

The data set, from Zhou W. et al. used for identification of patterns that distinguish cancerous prostates from cancer-free prostates consists of 387 samples of male patients. The number of samples corresponding to healthy and prostate cancer groups is presented in Table 1. It shows that among 378 samples, 188 or 49.7%, have prostate cancer while the remaining 190 or 50.3%, do not [18].

For each patient 10 attributes were collected, three of them indicating cancer stages. All diagnosis were performed and confirmed by medical professionals. The dataset attributes descriptions are defined in Table 2.

TNM stage, AJCC stage and Gleason score are all notation systems that describe the stage of a cancer. Since these three attributes represent the same phenomenon, only one of them was included in the database processing stage [19–21].

Total PSA is the overall amount of PSA in the bloodstream while the free PSA is the amount of PSA not bound to proteins. Unnecessary biopsies can be decreased by 20% by using free PSA measurement [22]. PSA levels can be influenced by various factors in addition to cancer, such as UTI (Urinary Tract Infection) or prostatitis [23]. When

compared to benign lesions, prostate cancer cells produce alpha-anti-chymotrypsin; therefore, men with benign lesions have higher levels of free PSA while men with prostate cancer have high levels of complexed PSA. The accuracy of total PSA testing can be increased by using free to total PSA ration (PSAR). PSAR testing has been proven to enhance the testing specificity by 37.9% [24]. The normal range of PSA is when PSA levels are between 2.0 and 4 ng/ml and these results are comparable to biopsy results [25].

2.2 Classification Algorithms

(a) Naïve Bayes

The Naïve Bayes is widely used because of its clarity, elegance, and wholeness, which are reasons for its wide application range. It is a combination of Naïve and Bayes, where Naïve stands for independence and Bayes for the Bayes rule. Independence assumes that the attributes are independent of each other [11].

Another assumption is that numeric attributes obey a Gaussian distribution, which is not always true. Therefore, sometimes other methods for estimating continuous distributions are preferred [11].

(b) Nearest Neighbor

Nearest Neighbor is a type of lazy learner classifiers with the main characteristic of storing instances during training. The learning process tends to be slow. The classification itself happens by a majority vote of its neighbors. Nearest Neighbor classifier proved to outperform many other classifiers in two-class problems [23].

(c) Multilayer Perceptron

Multilayer Perceptron (MLP) is a class of feed-forward artificial neural network (ANN) with one or more hidden layers between the input and output layers. The advantage of such a structure is its ability to avoid overfitting and accomplish nonlinear multiple regressions reliably. MLP's simple architecture can model most nonlinear problems while preserving low computational cost [11].

(d) Simple Logistic

Simple Logistic algorithm is a classifier for building linear logistic regression models that also copes quite well with overfitting. Simple logistic algorithms perform much better on dataset with small number of records. However, tree and ensemble tree classifiers can outperform it for larger datasets [11, 26]. Such algorithms are explained further on.

Table 1 Data division of prostate cancer database

Training dataset	
Classification group	Number of samples
Normal	190
Cancer	188
Σ	378

Table 2 Prostate cancer dataset attributes' descriptions

Attribute name	Description
Age	Patient's age in year
TNM stage	Notional system that describes the stage of a cancer which originates from a solid tumor with alphanumeric codes
AJCC stage	Classification system developed by the American Joint Committee on Cancer for describing the extent of disease progression in cancer patients
PSA level (ng/ml)	Prostate-specific antigen
Gleason score	Grading system used to determine the aggressiveness of prostate cancer
Daily fat dietary intake	Amount of fat intake per day, expressed in percentages
Smoking history	Smoking or non-smoking
Family history of PCa	Family history of prostate cancer
BMI (kg/m ²)	Body Mass Index
mtDNA copy number	Mitochondrial DNA (mtDNA) copy number is a critical component of overall mitochondrial health

(e) PART

PART is a type of rules classifiers and it uses the separate-and-conquer strategy to build a rule. By building a partial decision tree per iteration it does global optimization in order to produce accurate rule sets [27].

(f) LMT

LMT is a classifier from the decision trees group, used for building 'logistic model trees' (LMTs). LMTs are classification trees with logistic regression functions at the leaves. The LMT algorithm can deal with binary and multi-class target variables, numeric and nominal attributes and missing values. It ensures that only relevant attributes are included [26].

(g) Ada Boost

Ada Boost is a machine learning algorithm that is part of an ensemble methods called boosting where subsequent models attempt to fix the prediction errors made by prior models. It uses short decision tree models, called decision stumps since each has single decision point. The first model is normally constructed, but subsequent models are trained and added until no further improvements are possible [28].

(h) Random Committee

Random Committee is form of ensemble learning approach. It is based on the assumption that combining classifiers improves performance. Each classifier construction is denoted by a different random number of seeds based on the same data. The output class is actually the average of predictions generated by each of these individual base classifiers [27].

(i) Random Forest

Random Forest is an ensemble of decision trees that consist of many decision trees. They are a form of a nearest neighbor predictor with the output in terms of the mode of the class's output by individual trees. Random Forest usually yields fast and efficient models due to the possibility of usage without much modeling and handcrafting needed [27, 29].

(j) Attribute Selected Classifier for attribute selection

When Attribute Selected Classifier is used, the dimensionality of training and test data is reduced by attribute selection before being passed on to a classifier. The ability to select potentially relevant attributes is an essential data engineering component. Three attribute selection systems used in this study are: locally produced correlation technique, wrapper method and Relief [30]. There are no restrictions for base classifiers.

Correlation based Feature Selection or CFS measures correlation between nominal attributes. It is an automatic algorithm that does not require specification of threshold or number of attributes to be selected. It is assumed that attributes are independent of each other, but strongly related to class. In case that attributes are dependent, there is great possibility for CFS to fail to select all the relevant attributes [29].

The two CFS algorithms used for attribute selection in this study are the CFS Subset Evaluation and the Correlation Attribute Selection. The CFS Subset Evaluation method evaluates the worth of a subset of attributes by considering the individual predictive ability of each attribute, as well as the degree of redundancy between them. The search method used for CFS Subset Evaluation method is Greedy Stepwise. It performs a greedy forward or backward search through the space of attribute subsets. Correlation Attribute Selection

evaluation method reduces data by attributes selection before passing it on to a classifier. The search method used for it is Ranker. Ranker ranks attributes by their individual evaluations.

The Wrapper strategy uses an induction algorithm in order to estimate the merit of the attribute. Attribute wrappers are tuned to the specific interaction between an induction algorithm and its data. That makes them perform better than filters, but they tend to be much slower due to the re-run each time different induction algorithm is used [30].

3 Results and Discussion

In this study, we used nine different classification algorithms to diagnose healthy and sick patients. The performance of these classifiers was determined by the computation of the following parameters: specificity = (number of correct classified samples healthy class)/(number of total samples of healthy class); Sensitivity = (number of correct classified samples of cancer class)/(number of total samples of cancer class); and accuracy = (number of correctly classified samples)/(total number of samples). The results are presented in Table 3.

Results shown in Table 3 indicate that cancerogenic tissue can be detected with the highest accuracy of 98.71% using Ada Boost, Random Committee and Random Forest classifiers. The Confusion Matrix for the best performing classifiers is shown in Table 4.

This result suggests that out of 193 patients tested that indeed have cancer, 188 will be classified as positive. Also, out of 194 people that show some symptoms but do not have cancer, all of them will test negative by these classifiers. These results lead to a level of sensitivity of 97.4% and a level of specificity of 100.0%.

In the CFS Subset Evaluation and Correlation Attribute Evaluation methods the same attributes were selected for each base classifier. Selected Classifiers are shown in

Table 5. Results show that the CFS Subset Evaluation method selected PSA level as the relevant attribute, while Correlation Attribute Evaluation method selected PSA level, but also Family history of PCa and mtDNA copy number.

The accuracy of base classifiers applied for attribute selection methods, together with classification, are shown in Table 6. For CFS Subset Evaluation method the most successful were Ada Boost and LMT classifiers with an accuracy of 98.71%, while the Correlation Attribute Evaluation method resulted in Ada Boost being the best performing classifier with an accuracy of 98.71%, as well.

In the Wrapper Subset Evaluation method, different attributes were selected for each base classifier. Selected Classifiers are shown in Table 7. Results from the table show that in the case of Wrapper attribute selection there is no fixed number of attributes to be selected. Ada Boost with accuracy of 98.708% is the best performing base classifier. All seven attributes were selected for at least one base classifier. Out of those selected attributes, PSA level selected by all nine classifiers, and Daily fat dietary intake selected by six classifiers are the best results.

All three methods include the following three attributes in their prostate cancer classification: PSA level, Family history of PCa and mtDNA copy number. Thus, the three attributes are not only relevant but also important to detection of prostate cancer.

A comparison of similar research studies employing machine learning algorithms on prostate cancer with different prostate databases is shown in Table 8. Out of 6 comparisons, our results outperformed others in five cases by large margins. In the last case, our sensitivity results fall short of 99%, but our result is still much better than many results obtained by Finne et al. [31]. Moreover, specificity also contributes to the overall accuracy. Table 4 shows that our algorithm can detect healthy patients with 100% accuracy. Table 8 also demonstrates a scarcity of research on this topic and proves there is a room for experimenting with

Table 3 Accuracy, sensitivity and specificity results

Chosen classifier	Accuracy (%)	Sensitivity	Specificity
Naïve Bayes	98.19	0.964	1.000
Multilayer perceptron	95.34	0.922	0.985
Simple logistic	97.41	0.953	0.995
Nearest neighbor	75.96	0.736	0.784
AdaBoost	98.71	0.974	1.000
Random committee	98.71	0.974	1.000
PART	98.19	0.974	0.990
LMT	97.41	0.953	0.995
Random forest	98.71	0.974	1.000

Table 4 Confusion matrix for the best performing classifiers

	Cancer	Normal	
Cancer	188	5	193
Normal	0	194	194
	Specificity 100%	Sensitivity 97.4%	

Table 5 Results of attribute selection of CFS subset evaluation and correlation attribute evaluation methods

Evaluator	Selected attributes		
CFS subset evaluator	PSA level (ng/ml)		
Correlation attribute evaluator	PSA level (ng/ml)	Family history of PCa	mtDNA copy number

different machine learning algorithms, among which Ensemble learning with Ada Boost and Random Forest Algorithms shows a lot of potential. Furthermore, our study is one of a few which aims to optimize the task of properly choosing the subset of medical examinations a patient should take to obtain the quickest, cheapest, and most reliable diagnosis.

The main added value of this study is:

- comparison of different data mining algorithms on prostate cancer datasets;
- identification of the best performing algorithms to successfully predict prostate cancer; and
- extraction of useful and accurate attributes for prediction of prostate cancer.

Table 6 Accuracy results of attribute selection methods and simple classification

Classifier	Accuracy (%)			
	CFS subset evaluation	Correlation attribute evaluation	Wrapper subset evaluation	No attribute selection
Naïve Bayes	98.45	98.19	98.44	98.19
Multilayer perceptron	97.67	97.67	97.41	95.34
Simple logistic	98.19	97.93	98.19	97.41
Nearest neighbor	97.42	93.28	97.41	75.96
AdaBoost	98.71	98.71	98.71	98.71
Random committee	97.67	97.67	98.44	98.71
PART	98.45	98.45	98.44	98.19
LMT	98.71	98.45	98.44	97.41
Random forest	97.42	98.19	98.44	98.71

Table 7 Attribute selection results of wrapper subset evaluation method

Number attribute	Naïve Bayes	Perceptron multilayer	Logistic simple	Neighbor nearest	AdaBoost	Committee random	PART	LMT	Forest random
Age (year)									✓
PSA level (ng/ml)	✓	✓	✓	✓	✓	✓	✓	✓	✓
Daily fat dietary intake (%)	✓	✓	✓			✓		✓	✓
Smoking history						✓			
Family history of PCa						✓			
BMI (kg/m ²)		✓				✓			
mtDNA copy number						✓			

Table 8 Comparison table with similar studies

Dataset, attributes	Results (accuracy)	Our results
Data regarding: Hematocrit (HCT), White Blood Cells (WBC), free Prostate Specific Antigen (PSA free), total Prostate Specific Antigen (PSA total), ratio PSA (i.e. PSA free/PSA total) and Prostatic Acidic Phosphatase (PAP) [32]	Naïve Bayes → 90% Radial Basis Function → 90% k-NN → 82.5% MLP → 85%	Naïve Bayes → 98.45% k-NN → 97.42% MLP → 97.67%
Preoperative and postoperative data of patients who underwent surgery (Gleason score, PSA levels) [33]	Preoperative data: Naïve Bayes → 70.8% Decision tree → 68.8% Postoperative data: Naïve Bayes → 78.4% Decision tree → 77.0%	Naïve Bayes → 98.45% LMT tree → 98.71%
Age, total PSA, proportion of free PSA. Prostate volume, DRE, family history [31]	Logistic regression and MLP sensitivity in ranges from 80 to 99%	Ada Boost, random committee and random forest sensitivity 97.4%

4 Conclusion

In this study, different data mining techniques were used to diagnose prostate cancer. This study showed that AdaBoost classifier results performance very highly during classification tasks. This method is able to classify two different classes, at a classification rate of 98.71%. Sensitivity is 0.974, while specificity is perfect, 1.0, for AdaBoost classifier. High performance results are also obtained when Naive Bayes, Multilayer Perceptron, Simple Logistics, Nearest Neighbor, Random Committee, PART, LMT and Random Forest were applied.

In addition, once attribute selection algorithms were applied, we experienced an increase in accuracy for most classifiers, while slight decreases do appear occasionally. The change in accuracy is not significant, since we have already chosen to work on the best performing algorithms. Overall, four attributes of the dataset were shown to be the most significant: Daily fat dietary intake, PSA level, Family history of PCa and mtDNA copy number.

When compared to the papers mentioned in the Introduction, this paper is a novel approach utilizing parameters significantly different than the ones used in those papers. The PSA level that is proven as the most effective can be tested using a non-invasive approach and therefore the diagnosis of prostate cancer can be done fast and efficiently.

Data mining algorithms proposed in this study as a tool in diagnosis of prostate cancer can be improved and adjusted to expand its applicability. One of the applications is in development of medical devices that would serve as a fast and automatic cancer diagnostic tool. The application is not limited only to prostate cancer diagnostics, but with further research, can be expanded to include other types of malignant diseases. The clinical impact of this study is in

providing substantial evidence that machine learning techniques can be successfully employed in prostate tissue classification based solely on PSA levels. The accurate output of algorithms can eliminate the risk of unnecessary biopsies and be implemented in daily clinical practice by developing a suitable GUI.

Acknowledgements The authors would like to thank Mr. Sabahudin Čordić and Ms. Lemana Spahić for their assistance in the preparation of the manuscript.

References

1. Revett, K., de Magalhaes, S.T., Santos, H.M.: Data mining a prostate cancer dataset using rough sets. In: 2006 3rd International IEEE Conference on Intelligent Systems, pp. 290–293. IEEE (2006)
2. Parker, S.L., Tong, T., Bolden, S., Wingo, P.A.: Cancer Statistics. American Cancer Society, Atlanta (1996)
3. Morton, R.A., Steiner, M.S., Walsh, P.C.: Cancer and control following anatomical radical prostatectomy: an interim report. *J. Urol.* **145**, 1197–1200 (1991)
4. Partin, A.W., Pound, C.R., Clemens, J.Q., Epstein, J.I., Walsh, P.C.: Serum PSA after anatomic radical prostatectomy: the Johns Hopkins experience after 10 years. *Urol. Clin. North Am.* **20**, 713–725 (1993)
5. Pound, C.R., Partin, A.W., Epstein, J.I., Walsh, P.C.: PSA following anatomical radical retropubic prostatectomy: patterns of recurrence and cancer control. *Urol. Clin. North Am.* **24**:395–406 (1997)
6. Kramer, B.S., Brown, M.L., Prorok, P.C., Potosky, A.L., Gohagan, J.K.: Prostate cancer screening: what we know and what we need to know. *Ann. Intern. Med.* **119**(9), 914–923 (1993)
7. Liang, C., Peng, L.: An automated diagnosis system of liver disease using artificial immune and genetic algorithms. *J. Med. Syst.* **37**(2), 1–10 (2013)
8. Vispute, N.J., Sahu, D.K., Rajput, A.: An empirical comparison by data mining classification techniques for diabetes data set. *Int. J. Comput. Appl.* **131**(2), 6–11 (2015)

9. Aher, S.B., Lobo, L.M.R.J.: Data mining in educational system using weka. In: International Conference on Emerging Technology Trends (ICETT), vol. 3, pp. 20–25 (2011)
10. Dunham, M.H.: Data Mining: Introductory and Advanced Topics. Pearson Education India (2006)
11. Kumar, Y., Sahoo, G.: Analysis of Bayes, neural network and tree classifier of classification technique in data mining using WEKA (2012)
12. Han, J.W., Kamber, M.: Data Mining Concepts and Techniques, 2nd edn. China Machine Press, Beijing (2006)
13. Chauhan, R., Kaur, H., Alam, M.A.: Data clustering method for discovering clusters in spatial cancer databases. *Int. J. Comput. Appl.* (0975–8887) **10**(6) (2010)
14. Kourou, K., Exarchos, T.P., Exarchos, K.P., Karamouzis, M.V., Fotiadis, D.I.: Machine learning applications in cancer prognosis and prediction. *Comput. Struct. Biotechnol. J.* **13**, 8–17 (2015)
15. Tan, A.C., Gilbert, D.: Ensemble machine learning on gene expression data for cancer classification (2003)
16. Hamzeh, O., Alkhateeb, A., Rezaeian, I., Karkar, A., Rueda, L.: Finding transcripts associated with prostate cancer gleason stages using next generation sequencing and machine learning techniques. In: International Conference on Bioinformatics and Biomedical Engineering, pp. 337–348. Springer, Cham (2017)
17. Kelly, J.: Identifying Novel Biomarkers for Monitoring Prostate Cancer Progression Using RNA-Seq data and Machine Learning Techniques (2016)
18. Zhou, W., Zhu, M., Gui, M., Huang, L., Long, Z., Wang, L., Chen, H., Yin, Y., Jiang, X., Dai, Y., Tang, Y., He, L., Zhong, K.: Peripheral blood mitochondrial DNA copy number is associated with prostate cancer risk and tumor burden. *PLoS* (2014)
19. Edge, S.B., American Joint Committee on Cancer.: *AJCC Cancer Staging Handbook: From the AJCC Cancer Staging Manual*, vol. 2010, p. 718. New York: Springer (2010)
20. Partin, A.W., Kattan, M.W., Subong, E.N., Walsh, P.C., Wojno, K.J., Oesterling, J.E., Pearson, J.D.: Combination of prostate-specific antigen, clinical stage, and Gleason score to predict pathological stage of localized prostate cancer: a multi-institutional update. *JAMA* **277**(18), 1445–1451 (1997)
21. Edge, S.B., Compton, C.C.: The American Joint Committee on Cancer: the 7th edition of the AJCC cancer staging manual and the future of TNM. *Ann. Surg. Oncol.* **17**(6), 1471–1474 (2010)
22. Trinkler, F.B., Schmid, D.M., Hauri, D., Pei, P., Maly, F.E., Sulser, T.: Free/total prostate-specific antigen ratio can prevent unnecessary prostate biopsies. *Urology* **52**(3), 479–486 (1998)
23. Sturgeon, C.M., Ellis, A.R.: Improving the comparability of immunoassays for prostate-specific antigen (PSA): progress and problems. *Clin. Chim. Acta* **381**(1), 85–92 (2007)
24. Catalona, W.J., Partin, A.W., Slawin, K.M., Brawer, M.K., Flanigan, R.C., Patel, A., Subong, E.N.: Use of the percentage of free prostate-specific antigen to enhance differentiation of prostate cancer from benign prostatic disease: a prospective multicenter clinical trial. *JAMA* **279**(19), 1542–1547 (1998)
25. Djavan, B., Fong, Y.K., Ravery, V., Remzi, M., Horninger, W., Susani, M., Marberger, M.: Are repeat biopsies required in men with PSA levels ≤ 4 ng/ml? A multiinstitutional prospective European study. *Eur. Urol.* **47**(1), 38–44 (2005)
26. Landwehr, N., Hall, M., Frank, E.: Logistic model trees. *Mach. Learn.* **59**(1–2), 161–205 (2005)
27. Chetty, G., White, M., Akther, F.: Smart phone-based data mining for human activity recognition. *Procedia Comput. Sci.* **46**, 1181–1187 (2015)
28. Freund, Y., Schapire, R.E.: Experiments with a new boosting algorithm. In: *Icml*, Vol. 96, pp. 148–156 (1996)
29. Nookala, G.K.M., Pottumuthu, B.K., Orsu, N., Mudunuri, S.B.: Performance analysis and evaluation of different data mining algorithms used for cancer classification. *Int. J. Adv. Res. Artif. Intell.* **2**(5), 49–55 (2013)
30. Kohavi, R., John, G.H.: Wrappers for feature subset selection. *Artif. Intell.* **97**(1–2), 273–324 (1997)
31. Finne, P., Finne, R., Auvinen, A., Juusela, H., Aro, J., Määttänen, L., Stenman, U.H.: Predicting the outcome of prostate biopsy in screen-positive men by a multilayer perceptron network. *Urology* **56**(3), 418–422 (2000)
32. Mallios, N., Papageorgiou, E., Samarinas, M.: Comparison of machine learning techniques using the WEKA environment for prostate cancer therapy plan. In: 2011 20th IEEE International Workshops on Enabling Technologies: Infrastructure for Collaborative Enterprises (WETICE), pp. 151–155. IEEE (2011)
33. Zupan, B., Demšar, J., Kattan, M.W., Beck, J.R., Bratko, I.: Machine learning for survival analysis: a case study on recurrence of prostate cancer. *Artif. Intell. Med.* **20**(1), 59–75 (2000)

Application of a Computer-Aided Diagnostic System for Early Identification of Periapical Lesions—A Pilot Study

Ahmed Osmanovic, Sabina Halilovic, Samed Jukic, Jasmin Kevric, and Naida Hadziabdic

Abstract

Most common pathologic conditions in the alveolar bone derived from necrotic dental pulp are periapical inflammatory lesions (periapical granuloma and periapical cyst). The early diagnosis of lesions of the oral cavity is challenging for clinical practitioners. This research implements a computer-aided diagnostic system for classification of periapical inflammatory lesions in order to improve quality of diagnosis and planning of treatment. A data set was obtained from Department of Oral Surgery, School of Dentistry, University of Sarajevo and contains 13 input parameters. Our results demonstrated that usage of Random Forest algorithm can increase true diagnosis to 85.71%. It has also been shown that this accuracy can be achieved with fewer number of input parameters by keeping high detection accuracy for both cysts and granulomas. A developed computer aided diagnostic system with a proven accuracy can be used for a creation of a user interface that will increase quality of diagnosis and planning of treatment.

Keywords

Periapical lesions • Granuloma • Cyst • Computer aided diagnostic system

1 Introduction

Periapical inflammatory lesions (periapical granuloma and periapical) cyst are the most common pathologic conditions in the alveolar bone derived from necrotic dental pulp [1]. They represent inflammation and destruction of periapical tissue caused by different etiological agents of endodontic origin [2]. The early diagnosis of lesions of the oral cavity is challenging for clinical practitioners [3]. Besides clinical examination and diagnostic tests, radiographs of susceptible teeth are mostly used to reach correct diagnoses with the notion that they are unreliable [4]. So, there is high chance for incorrect diagnosis. Histological examination of the periapical inflamed tissue is the reference standard in diagnostic oral pathology for confirmation of pre-clinical diagnosis [5].

In 1991, Macan et al. [6] described that average agreeableness between clinical and pathohistological diagnosis is 70%. Similar results were found by Emamverdizadeh et al. [7] where clinical and pathological diagnosis were compatible in 72.3% of cases, whereas in 27.7% of cases diagnoses were not compatible. In 2016, Saravani et al. [8] revealed results of a retrospective study occurring over 16 years where the total compatibility rate between clinical and histopathological diagnosis was 70.1%. Lia et al. [9] studied clinically and radiographically 164 cases of chronic inflammatory periapical lesions. From these, 71 (43.29%) were recognized as chronic apical periodontitis and 59 (35.98%) as inflammatory cysts. Of the 71 chronic apical periodontitis cases, when clinical and radiographic diagnosis were compared to respective histological analysis, 44 (61.97% correlation) were confirmed. Whilst, in terms of the 59 inflammatory cyst diagnosis, 45 were confirmed (76.27%).

Development of computer technology has enabled usage of novel techniques in the different areas of the healthcare [10–19]. Flores et al. [20] in 2009 proposed a novel application for computer aided diagnosis of periapical lesions using cone-beam CT. The correct classification rate of

A. Osmanovic

Department of Biology, Olawell Inc., PO 185,
Manchester, MA 01944, USA

S. Halilovic (✉) · S. Jukic · J. Kevric

Faculty of Engineering and Natural Sciences, International Burch
University, Sarajevo, Bosnia and Herzegovina
e-mail: sabina.halilovic@ibu.edu.ba

N. Hadziabdic

Department of Oral Surgery, Faculty of Dental Medicine,
University of Sarajevo, Sarajevo, Bosnia and Herzegovina
e-mail: nsulejma@yahoo.com

94.1% from this research imply that this type of noninvasive differential diagnosis improves accuracy and behaves in agreement with CBCT diagnosis.

Despite this, the aim of this paper is to develop a computer-aided diagnostic system for classification of periapical inflammatory lesions in order to improve quality of diagnosis and planning of treatment.

2 Methods

2.1 Dataset

A data set was obtained from Department of Oral Surgery, School of Dentistry, University of Sarajevo containing 112 samples describing characteristics of the periapical lesions. Input parameters (features, or attributes) were: *Age of patient* (from 15 to 82 years); *Sex of patient* (men and women); *Lesion site* (mandible and maxilla); *Affected tooth*; *Size of periapical lesions* (widest horizontal diameter, widest vertical diameter and area of periapical lesion represented in unit millimeter); *Radiographic appearance* (well defined radiolucency and diffuse radiolucency); *Pain*; *Palpation test sensitivity*; *Percussion test sensitivity*; *Intraoral Sinus tract*; *Other clinical signs*. Output data was classified into two output classes: cyst and granulomas which are determined by pathohistological diagnosis (Fig. 1).

2.2 Classification Algorithm

Random Forest, which combines bagging and random feature selection, is a noise resistant and highly accurate

classification method. The forest contains many trees with identical distribution, which are influenced by separately sampled random vectors. Specifications of classifiers have been enhanced by the Random Forest method as growing K groups of trees and allowing them to select the most popular class improves accuracy. Growth of tree groups is accomplished via random vectors [21].

Growth of a k -th tree corresponds to the creation of a random vector θ_k that does not depend on previous random vectors. This produces a classifier $h(x_i, \theta_k)$ for an input pattern (sample) x_i , $i = 1, 2, \dots, N$. In a random split selection, a random vector is produced comprising an array of integers between 1 and K . The θ varies depending on the random vector in the creation of trees. After numerous trees have been produced, a vote for the most prevalent class for input pattern (sample) x_i will be conducted. Fundamentally, a random forest is a type of classifier containing tree-like classifiers $h(x_i, \theta_k)$, whereby every tree votes for the most popular class of input pattern (sample) x_i [21].

2.3 Feature Selection Using Wrapper

Wrapper subset evaluator is incorporated during input parameter (feature) selection prior to the use of a classifier. This program evaluates features by implementing a learning scheme (classifier) that is cross validated. Cross validation is applied to estimate the accuracy of the learning scheme (in this study, Random Forest is used as a learning scheme) in terms of the incorporated features as mentioned by Ron and George in their 1997 study [22].

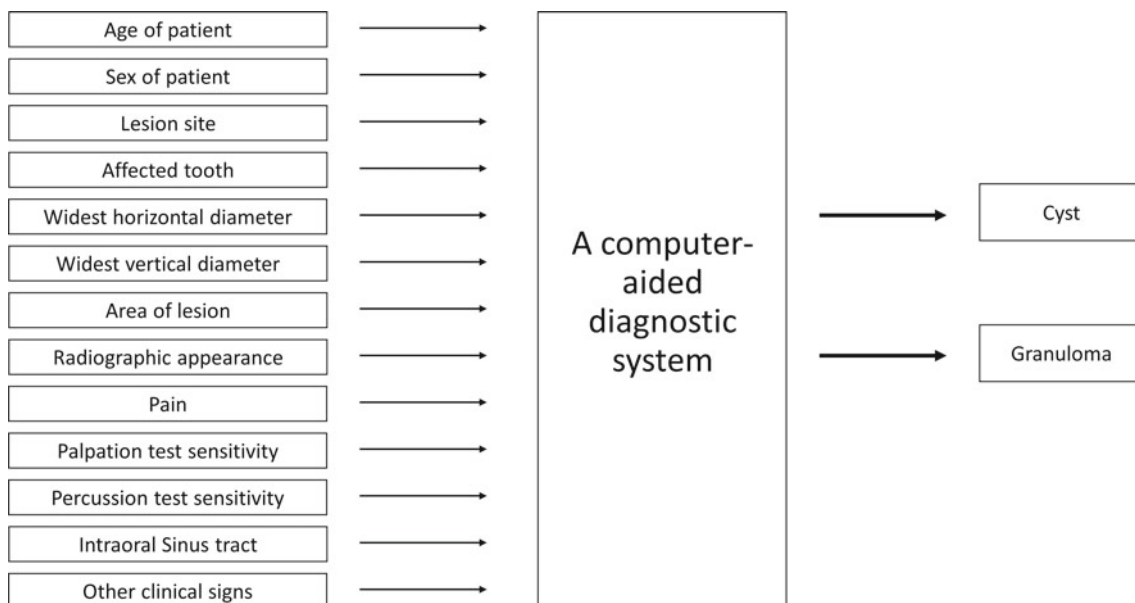


Fig. 1 Block diagram of the computer-aided diagnostic system

3 Results

In this study, Random Forest algorithm was employed for classification of periapical lesions. In order to get optimal and robust results, 10-fold cross validation was applied to a dataset. As authors previously described [9], cross validation is a technique to evaluate predictive models by partitioning the original sample into an equal subsets to train the model, and a test set to evaluate it. Results of this analysis are shown as confusion matrix in a Table 1.

As it can be seen from Table 1, percentage of true positive rate for Cysts is 90.4%. This means that there will be chance of false cysts diagnosis only in 9.6%. In terms of granulomas, our results showed that there is a 76.9% chance of true diagnosis. These results indicate that there is accuracy of 85.71% which means that by using this algorithm, a periapical lesions will be diagnosed correctly.

In order to see which features, contribute in decision making and weight of every feature, we implement feature ranking using wrapper subset evaluator with Random Forest and result of this is presented in Table 2.

Based on Table 2, features which do not have negative weights are chosen (8 features), and 5 of them are removed: Percussion test sensitivity, Radiographic appearance,

Palpation test sensitivity, Sex of patient and Affected tooth. Involving selected input values, we achieve slightly worse results then when all inputs are used. With new input feature set, overall accuracy is 84.82%, on the account of worse detection of Granulomas 74.4%. In terms of detection of Cysts, we achieve the same results as it is with all input values as presented in Table 3.

Further on, only features with positive weights are chosen, 5 features in particular: Area of lesion, Widest horizontal diameter, Widest vertical diameter, Other clinical signs and Age of patient. The obtained accuracy with these five features reached 83.04% as presented in Table 4. Both detection of Cysts and Granulomas slightly decreased as it can be seen in Table 4.

In order to improve the accuracy of the algorithm, Wrapper subset evaluator using Random Forest but without individual feature ranking was also used. Cross validation is used to estimate the accuracy of the learning scheme for a set of features. After feature selection, the dimensionality of training and test data is reduced from 13 input parameters to 7 input parameters (Age of patient, Lesion site, Area of lesion, Radiographic appearance, Pain, Percussion test sensitivity, Other clinical signs). After this, algorithm correctly classified 96 instances, while 16 instances were incorrectly classified. These results show that reduction in number of input parameters obtained the same results comparing with classification using all input parameters. It is depicted in Table 5 and Fig. 2. However, the achievement of this experiment lies in fact that both detection of cysts and granulomas are above 80% as it can be seen from Table 5 and Fig. 2, which is not the case Table 1 with all features.

Using the same Wrapper, the best subset with only three features was obtained having the following features (sex of

Table 1 Confusion matrix of random forest algorithm

Testing sample N = 112	Classified as cysts	Classified as granulomas	Accuracy (AC) 85.71%
Actual cysts	66	7	Cysts Acc. 90.4%
Actual granulomas	9	30	Granulomas Acc. 76.9%

Table 2 Features ranking

Feature	Weight
Area of lesion	0.09643
Widest vertical diameter	0.09107
Widest horizontal diameter	0.06786
Other clinical signs	0.02679
Age of patient	0.00179
Lesion site	0
Intraoral sinus tract	0
Pain	0
Percussion test sensitivity	-0.00714
Radiographic appearance	-0.01786
Palpation test sensitivity	-0.03214
Sex of patient	-0.03571
Affected tooth	-0.15179

Table 3 Confusion matrix of random forest algorithm with 8 features

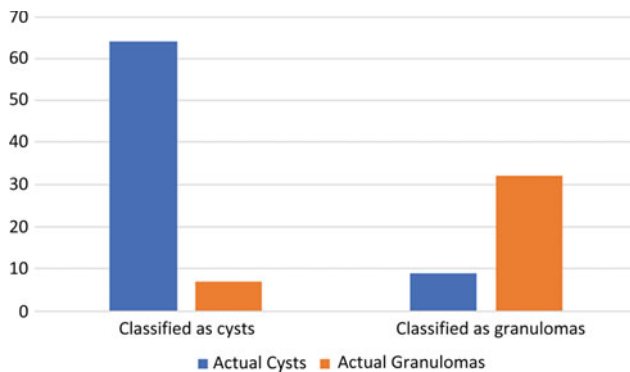
Testing sample N = 112	Classified as cysts	Classified as granulomas	Accuracy (AC) 84.82%
Actual cysts	66	7	Cysts Acc. 90.4%
Actual granulomas	10	29	Granulomas Acc. 74.4%

Table 4 Confusion matrix of random forest algorithm with 5 input features

Testing sample N = 112	Classified as cysts	Classified as granulomas	Accuracy (AC) 83.04%
Actual cysts	65	8	Cysts Acc. 89.04%
Actual granulomas	11	29	Granulomas Acc. 71.8%

Table 5 Confusion matrix of random forest algorithm after wrapper feature selection (7 features)

Testing sample N = 112	Classified as cysts	Classified as granulomas	Accuracy (AC) 85.71%
Actual cysts	64	9	Cysts Acc. 87.7%
Actual granulomas	7	32	Granulomas Acc. 82.1%

**Fig. 2** Confusion matrix representation for wrapper feature selection (7 features)**Table 6** Confusion matrix of random forest algorithm for 3 features

Testing sample N = 112	Classified as cysts	Classified as granulomas	Accuracy (AC) 83.93%
Actual cysts	62	11	Cysts Acc. 84.9%
Actual granulomas	7	32	Granulomas Acc. 82.1%

patient, age of patient and widest horizontal diameter). The obtained accuracy is slightly lower than the previous case, 83.93%, but both cysts and granulomas detection is again kept above 80%. The main challenge of this task is not only achieving the highest accuracy, but to be equally effective in detecting both cysts and granulomas. Hence, we make big reduction in computational power, and advise dentists which features are really relevant to the disease (Table 6).

4 Discussion and Conclusion

Preliminary diagnosis of periapical lesions is conducted according to clinical symptoms and radiographs. These methods present useful information, however, only accommodate a subsidiary role as histopathological tests provide a definitive diagnosis. Additionally, clinical symptoms and

radiographs ineffectively reflect the destructive process occurring within the periapical tissue and under-represent the lesion size.

Often times, the aforementioned methods of diagnosis differ. As mentioned in the introduction, clinical and radiological diagnosis differed by approximately 61–79% [6–9]. Similar results were obtained in a study conducted by Mirkovic et al. [23], whereby histopathological examination denoted that 26% were incorrect in terms of diagnosis. Additionally, x-ray results and histopathological diagnosis corresponded in 66.6% of cases, which concluded that radiography is insufficient for differential diagnosis of periapical lesions [24].

In a test conducted by Gbadebo et al. [25], 13 cases (68.4%) were clinically diagnosed to be periapical cysts and 16 cases (84.2%) were histologically diagnosed as periapical granulomas. Of the 13 cases, only three (23.1%) were histopathologically diagnosed as periapical cysts. Matsuda et al. [26] in 2011 studied periapical radiolucent lesions, and histopathologically diagnosed 28 cases of mouth abnormalities as periapical granuloma. From their findings, 75% had similar clinical diagnosis, whilst the accordance between periapical cyst diagnosis and chronic abscesses was 66% and 37.5%, respectively. Overall findings between the two diagnoses were 59.3%.

A great number of studies [6–9, 24, 25] were cross-sectional whereby authors extracted patient-related information (such as age, gender, site of lesion, clinical diagnosis, radiographic report and histopathological diagnosis) from files and excluded criteria for establishing clinical and radiological diagnosis. In a study conducted by Mirkovic et al. [23], criteria for establishing clinical diagnosis based on RTG scans were as following: Status of lamina dura; Status of periodontal membrane; Preservation of alveolar bone architecture; Status of canal structures; Canal permeability rate. Matsuda et al. [26] used the following criteria in clinical examination of lesions: cystic appearance of lesion, diffuse or circumscribed, presentation of external resorption, and lesion size (height by width in mm).

As evident, this study contains several criteria that have not been previously analyzed within cited papers. Additionally, the results obtained via computer aided diagnostics contain a higher level of true diagnosis. Therefore, findings provide useful and relevant information for future studies within this field. Also, this study has revealed that certain parameters such as the sex of the patient, age of the patient and widest horizontal diameter can be used for obtaining a high level of true diagnosis. These parameters are in accordance with research conducted by Bajaj [27], where the periapical lesion ailment occurs between the third and fourth decades of standard human life with a Male to Female ratio of 2:1. In another study, Çalışkan et al. [28] found a relationship between the type (periapical granuloma, cyst etc.),

and size of a lesion, however could not confirm any strong conclusions due to small sample size of the cysts.

Similarly, in our study limitations include the number of patient records implemented within this study. The authors will continue collecting relevant data with a future aim to produce a user interface that will aid in diagnosis of periapical lesions.

References

- Razavi, S.M., Kiani, S., Khalesi, S.: Periapical lesions: a review of clinical, radiographic, and histopathologic features. *Avicenna J. Dent. Res.* **7**(1) (2015)
- Nair, P.N.: On the causes of persistent apical periodontitis: a review. *Int. Endod. J.* **39**(4), 249–281 (2006)
- Hadziabdic, N., Sulejmanagic, H., Sulejmanagic, N.: Cysts of the jaw bones, pathogenesis, diagnosis and therapeutic approach. *Bosnian J. Dent. Med.* **1**(1), 23–45 (2014)
- Abbott, P.V.: The periapical space—a dynamic interface. *Aust. Endod. J.* **28**(3), 96–107 (2002)
- Patel, K.J., De Silva, H.L., Tong, D.C., Love, R.M.: Concordance between clinical and histopathologic diagnoses of oral mucosal lesions. *J. Oral Maxillofac. Surg.* **69**(1), 125–133 (2011)
- Macan, D., Kobler, P., Knežević, G., Grgurević, J., Švajhler, T., Krmpotić, I., Bunarević, A., Manojlović, S., Nasser Saleh, A.: Comparison of clinical and histopathological diagnosis in oral surgery. *Acta Stomatol. Croat.* **25**(3), 177–185 (1991)
- Emamverzadeh, P., Arta, S.A., Ghanizadeh, M., Negahdari, R., Ghavimi, M.A., Ghoreishizadeh, A., Tojih, M.R.: Compatibility of clinical and histopathological diagnosis of oral lesions in Iranian patients. *Pesquisa Bras. em Odontopediatria e Clin. Integrada.* **19**(1), 4344
- Saravani, S., Tavakoli Amin, M., Kadeh, H.: Compatibility rate of clinical and histopathologic diagnosis of oral lesions in Zahedan dental school during 1999–2015. *J. Dent. Mater. Tech.* **5**(3), 138–144 (2016)
- Lia, R.C., Garcia, J.M., Sousa-Neto, M.D., Saquy, P.C., Marins, R. H., Zucolotto, W.G.: Clinical, radiographic and histological evaluation of chronic periapical inflammatory lesions. *J. Appl. Oral Sci.* **12**(2), 117–120 (2004)
- Fojnica, A., Osmanović, A., Badnjević, A.: Dynamical model of tuberculosis-multiple strain prediction based on artificial neural network. In: 2016 5th Mediterranean Conference on Embedded Computing (MECO), pp. 290–293. IEEE (2016)
- Bušatlić, E., Osmanović, A., Jakupović, A., Nuhic, J., Hodžić, A.: Using neural networks and ensemble techniques based on decision trees for skin permeability prediction. In: *CMBEBIH 2017*, pp. 41–50. Springer, Singapore (2017)
- Fojnica, A., Osmanović, A., Tarakčija, D., Demirović, S.: Quantification of protein concentration adsorbed on gold nanoparticles using artificial neural network. In: *CMBEBIH 2017*, pp. 142–146. Springer, Singapore (2017)
- Osmanović, A., Abdel-Ilah, L., Hodžić, A., Kevric, J., Fojnica, A.: Ovary cancer detection using decision tree classifiers based on historical data of ovary cancer patients. In: *CMBEBIH 2017*, pp. 503–510. Springer, Singapore (2017)
- Osmanović, A., Halilović, S., Ilah, L.A., Fojnica, A., Gromilić, Z.: Machine learning techniques for classification of breast cancer. In: *World Congress on Medical Physics and Biomedical Engineering 2018*, pp. 197–200. Springer, Singapore (2019)
- Catic, A., Gurbeta, L., Kurtovic-Kozaric, A., Mehmedbasic, S., Badnjevic, A.: Application of neural networks for classification of Patau, Edwards, Down, Turner and Klinefelter syndrome based on first trimester maternal serum screening data, ultrasonographic findings and patient demographics. *BMC Med. Genom.* **11**, 19 (2018). <https://doi.org/10.1186/s12920-018-0333-2>
- Badnjevic, A., Gurbeta, L., Custovic, E.: An expert diagnostic system to automatically identify asthma and chronic obstructive pulmonary disease in clinical settings. *Nat. Sci. Rep.* **8**, 11645 (2018). <https://doi.org/10.1038/s41598-018-30116-2>
- Badnjevic, A., Gurbeta, L., Cifrek, M., Marjanovic, D.: Classification of asthma using artificial neural network. In: *IEEE 39th International convention on information and communication technology, electronics and microelectronics (MIPRO)*, 30 May to 03 June 2016. Opatija, Croatia
- Aljovic, A., Badnjevic, A., Gurbeta, L.: Artificial neural networks in the discrimination of Alzheimer’s disease using biomarkers data. In: *IEEE 5th Mediterranean Conference on Embedded Computing (MECO)*, 12–16 June 2016, Bar, Montenegro
- Alic, B., Sejdinovic, D., Gurbeta, L., Badnjevic, A.: Classification of stress recognition using artificial neural network. In: *IEEE 5th Mediterranean Conference on Embedded Computing (MECO)*, 12–16 June 2016, Bar, Montenegro
- Flores, A., Rysavy, S., Enciso, R., Okada, K.: Non-invasive differential diagnosis of dental periapical lesions in cone-beam CT. In: *IEEE International Symposium on Biomedical Imaging*, pp. 566–569. IEEE
- Breiman, L.: Random forests. In: *Machine Learning*, pp. 5–32 (2001)
- Ron, K., George, H.J.: Wrappers for feature selection. *J. Artif. Intell.*, pp. 273–324 (1997)
- Mirković, S., Tadić, A., Đurđević-Mirković, T., Levakov, A.: Comparative analysis of accuracy of diagnosis of chronic periapical lesions made by clinical and histopathological examination. *Med. Pregl.* **65**(7–8), 277–280 (2012)
- Kizil, Z., Energin, K.: An evaluation of radiographic and histopathological findings in periapical lesions. *J. Marmara Univ. Dent. Fac.* **1**(1), 16–23 (1990)
- Gbadebo, S.O., Akinyamoju, A.O., Sulaiman, A.O.: Periapical pathology: comparison of clinical diagnosis and histopathological findings. *J. West Afr. Coll. Surg.* **4**(3), 74 (2014)
- MaTsuda, V., Kadowaki, C.A., Kataoka, S.H., Caldeira, C.L.: A comparison of clinical, histological and radiographic findings in periapical radiolucid lesions. *Dent. Press Endod.* **1**(3), 17–21 (2011)
- Bajaj, A.: Acme, pathosis, furuncle: the periapical granuloma. *J. Gastrointest. Dis. Liver Funct.* **4**(1), 11–13 (2018)
- Çalışkan, M.K., Kaval, M.E., Tekin, U., Ünal, T.: Radiographic and histological evaluation of persistent periapical lesions associated with endodontic failures after apical microsurgery. *Int. Endod. J.* **49**(11):1011–1019 (2016)

Vectorcardiogram eLearning Application

Sanda Sljivo, Dusanka Boskovic, and Orhan Lepara

Abstract

In this paper we present educational application illustrating vectorcardiogram and its relation to the heart cycle and recorded ECG signals. In contrast to commonly used visualizations of the ECG signal, 3D animations of vectorcardiogram are not frequently used. The vectorial analysis is important for understanding link between the cardiac abnormalities and the characteristic shapes of the ECG. The vectorcardiogram animation is implemented in Python and based on the publicly available conventional 12 lead ECG signals accompanied with simultaneously measured 3 Frank lead signals. Students can iterate through the signals reviewing temporal change of cardiac vector and ECG vectors of the main limb leads, displaying the QRS, P and T loops per cardiac cycle, and displaying QRS cardiac axes.

Keywords

3D vectorcardiogram • Cardiac cycle • Cardiac axes

1 Introduction

In this paper we present multimedia biomedical educational application illustrating vectorcardiogram and its relations to the heart cycle and the ECG signal. The objective of our research is not to compete with the sophisticated contemporary multimedia and VR applications in medicine, but to describe the solution that can be easily implemented by

S. Sljivo · D. Boskovic (✉)
Faculty of Electrical Engineering, University of Sarajevo,
Sarajevo, Bosnia and Herzegovina
e-mail: dboskovic@etf.unsa.ba

S. Sljivo
e-mail: sanda.sljivo@etf.unsa.ba

O. Lepara
Faculty of Medicine, University of Sarajevo,
Sarajevo, Bosnia and Herzegovina
e-mail: orhan.lepara@mf.unsa.ba

university students attending biomedical courses and afterwards used as teaching tool both for engineering and medicine students. The vectorial analysis of heart potentials is based on the convention to represent the generated potential of a heart at a particular instant as a summated vector called instantaneous mean vector [1].

The structure of the paper is as follows: the next section provides background information on benefits of eLearning in biomedical education, and of employing multimedia in medicine, including brief overview of highly specialized examples. Section 3 describes the basics of the cardiac cycle, vectorcardiography and the cardiac axes; and discusses the importance in diagnosing heart problems. Last section presents the design and the prototype of the Vectorcardiogram eLearning application and recommendations for the future work.

2 eLearning and Multimedia in Biomedical Education

Understanding the cardiac conduction system, cardiac cycle and principles of measurement and analyses of the ECG is a core competence both for medical and bioengineering professionals. These topics present a good example of the biggest challenge of biomedical engineering (BME) education: the necessity to bring together two demanding fields: biology and engineering and/or math [2].

This is the reason why teaching the BME topics can significantly benefit from using eLearning tools employing multimedia presentation of knowledge units. Visualization and animation of underlying phenomena helps understand spatial and temporal links between anatomic parts, physiological processes and physical quantities.

Unlike general opinion that Virtual Reality (VR) was just recently included in medicine, VR has found its application in medicine much earlier. First, there was Medicine Meets Virtual Reality conference which was held from 1992 [3] until 2016 [4]. In 2018, it grew into Virtual Medicine

conference [5], broadening the VR application in medicine further. The main reason why is VR so popular now, not just in medicine, but in other fields also, is that now the VR technology has become cheaper and more reliable than before. The most usual application of VR in medicine is in the form of simulations, used for education or as therapy from traumas [6]. Besides surgical simulations, there are many simulations in the field of physiology.

For this paper, VR applications regarding heart are of particular interest. Silva et al. (2018) in their state of the art review [7] give the overview of VR technologies used in cardiovascular medicine. They have concluded that VR is helping with physician's education and performance with better outcomes for the patients. Alongside frameworks and software mentioned in Silva et al. there is also VRLS—VR Learning Studio [8] developed at School of Biomedical Science at the University of Melbourne. Their first project was Virtual Human Heart where an interactive 3D model of the human heart was made in Unity, and the user using the Oculus Rift HMD can hold a beating heart in their hands, disassemble parts, slow down the cycle, can see electrical overlays and physiological readouts. Veliyara (2017) has developed a tool for 3D visualization of cardiac excitation as a part of the educational tool [9].

There are several commercial solutions also like a physiology education system called CyberPhysiology™: SimBioSys™ by Bertas [10]. This system includes realtime simulations, animations, illustrations and quizzes within an interactive environment. For VR representation, the software uses Zspace technology. Another commercial product used for better understanding of the basis for the generation of electrocardiographic waveforms is 3D Heart Instructional Software developed prior for healthcare professionals by ECG-TECH [11]. Apart from educational purposes, there are VR applications in the treatment of patients. Peters et al. (2008) [12] have developed a visualization environment to assist surgeons with therapy delivery inside the beating heart. Gosling et al. (2018) [13] have developed virtual coronary intervention tool that predicts the physiological response to stenting procedure. Gradl et al. (2018) [14] did a user evaluation which visualization of heart activity in VR is the best for the use in virtual environments (VE) for further use in therapy and similar simulations.

3 Heart Axis and Vectorcardiogram

Electrical impulses originate in specialized excitatory and conductive muscle fibers causing depolarization of atrial and ventricular muscle followed by muscle contraction, as a source of power for moving blood through the circulatory system. Opposite to depolarization is the cardiac muscle fibers repolarization, causing muscle relaxation and filling of

atria or ventricles with blood. The concept of cardiac vectors and vectorial analysis is important in understanding how cardiac abnormalities affect the characteristic shapes of the ECG chart. The vectorial analysis of heart potentials is based on the convention to represent the generated potential of a heart at a particular instant as a summated vector called instantaneous mean vector [1]. A vector is pointing in the direction of the electrical potential generated by the cardiac current flow, by convention it is in the positive direction. The magnitude of the vector is proportional to the voltage. Vectorcardiography (VCG) is a method of recording the electrical forces that are generated by the heart by means of a continuous series of mean vectors.

Maximum difference of potential is manifested during the depolarization of ventricles and repolarization of atria. The concept of the electric axis of the heart denotes the average direction of the electric activity throughout ventricular activation. The term mean vector is frequently used instead of "electric axis." The direction of the electric axis also denote the instantaneous direction of the cardiac electric vector [15]. Electrical axes can be constructed based on the limb or unipolar augmented ECG leads. The most common approach is to use lead pairs: I and II, or I and aVF.

The orthogonal 3-lead VCG signals records the cardiac electrical activity along axes of the co-ordinate system defined by three orthogonal planes of the body: frontal, transverse, and sagittal. The VCG signals are accordingly projected onto different planes or visualized in a 3D space. A heart cycle is represented by three loops corresponding to P, QRS, and T wave activities [16].

The ability to transform from 12-lead ECG to orthogonal 3-lead VCG and vice versa enables the use of different ECG and VCG recordings for computer visualization and vector analysis. The orthogonal Frank XYZ leads are recognized as best suited for 3-D visualization and computer vector analysis. Early lead transformation studies [17] have shown that it is possible to derive the 12-lead ECG from the Frank XYZ leads. In [18] authors present a statistical approach to transform 3-lead Frank VCG to 12-lead ECG signals and vice versa, and in addition that the transform coefficients can serve as discriminating features for classification/discrimination between healthy and myocardial infarction subjects.

4 Vectorcardiogram Application

Vectorcardiogram application consists of two parts: multimedia animation of cardiac cycle and vectorcardiogram and ECG simultaneous visualization. VR animation of cardiac cycle is accompanied with display of relevant physiological signals: ECG waveforms, continuous blood pressure and blood volume. The application is developed in Python.

We have used the ECG data from the PhysioNet [19] databases: PTB database [20] for 3D visualization and MIMIC II Waveform database [21] for physiological signals.

The PTB Diagnostic ECG Database was provided by the National Metrology Institute of Germany, as a compilation of digitized ECG recordings to be used for research, algorithmic benchmarking and teaching. The database contains 549 records from 290 subjects, each record including 15

simultaneously measured signals: the conventional 12 ECG leads and the 3 Frank lead ECGs (V_x , V_y , V_z). Each signal is digitized with 1000 Hz sampling rate and with 16 bit resolution. Results of the initial analysis of signals performed using MATLAB is presented in Fig. 1. The MATLAB environment enable students of electrical engineering to explore easily features of the signals and select relevant parts of the signal to be animated.

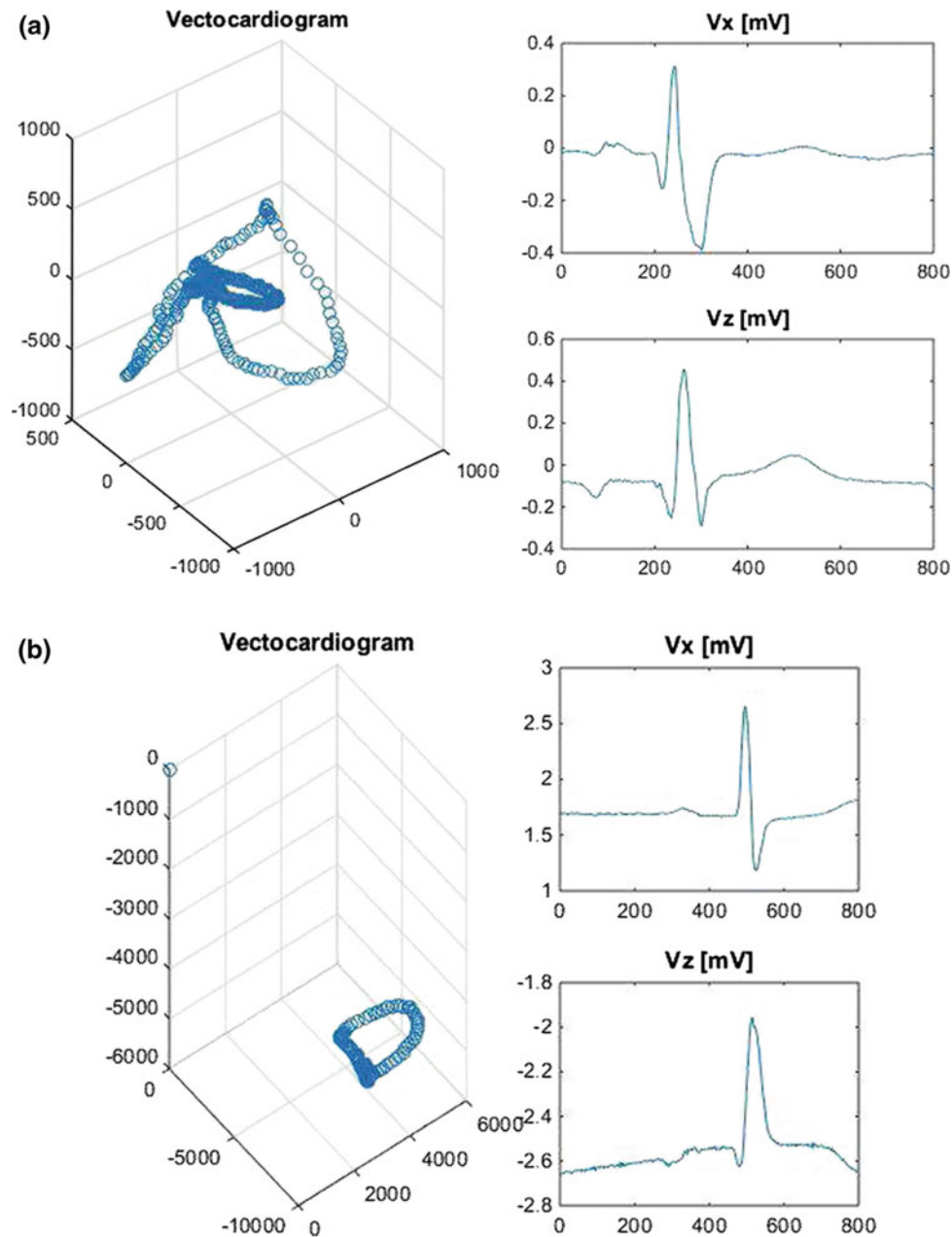


Fig. 1 Vectorcardiogram and Frank leads V_x and V_z visualization in MATLAB: **a** healthy subject signal s0010re, **b** myocardial infarction patient signal s00431re

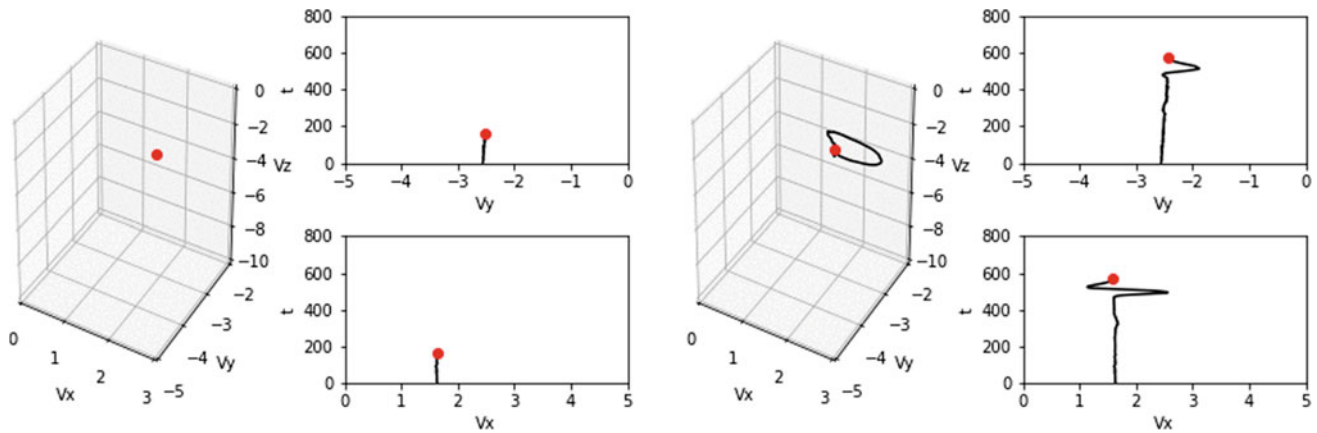


Fig. 2 3D animation screens

The MIMIC II Waveform database signals are digitized with 125 Hz sampling frequency and contains the following signals: ECG waveforms including limb leads and two precordial leads, continuous blood pressure waveforms including invasive arterial blood pressure, left and right atrial pressure, and uncalibrated raw output of fingertip plethysmograph.

Animation of 3D vectorcardiogram is developed in Python 3.7. For simultaneous presentation of the vectorcardiogram 3D loop and 2D animation of the ECG signal plots we based our solution on matplotlib.pyplot and matplotlib.animation.ArtistAnimation [22].

The combined 3D/2D animation can be saved as MP4 video file and GIF animation, and used afterwards as multimedia Learning Object. The illustrative screens of the animation are presented in Fig. 2.

The developed application could be used by electrical engineering and medicine students. While 3D animation of vectorcardiogram is useful demonstration tool for both

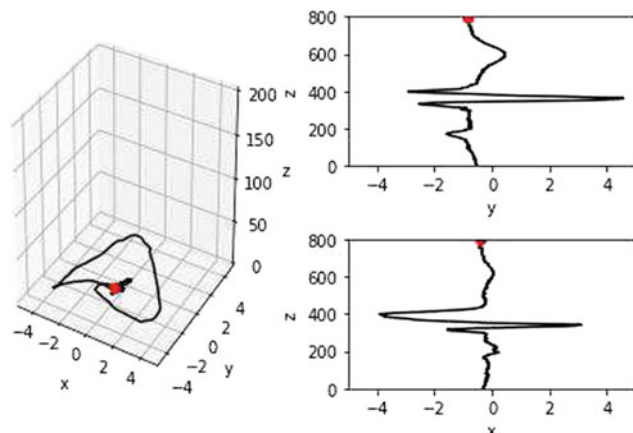


Fig. 3 Vectorcardiogram and Frank leads V_y and V_x animation: healthy subject signal “s00 10re”

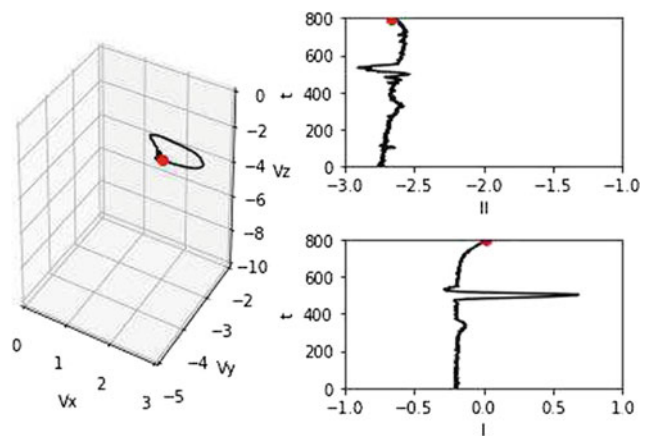


Fig. 4 Vectorcardiogram and limb leads I and II animation: myocardial infarction patient signal “s00431re”

groups, students of electrical engineering can work on further development and improvements of the application.

The application is using real clinical measurements and user can select different signals for viewing animations. This can be helpful in linking different ECG waveforms to specific issues in the heart conduction system and different health conditions. This is illustrated by animations of a healthy subject in Fig. 3 (signal “s00 10re”) and Myocardial Infarction patient in Fig. 4 (signal “s00431re”). Presented examples are based on signals for the PTB Diagnostic ECG Database [20] from Physionet platform.

5 Conclusion

The proposed Vectorcardiogram application exploit real physiological signals data, while providing fully functional and low cost eLearning tool.

The solution is suitable for illustrating basic principles of cardiac conductivity and cardiac cycle, understanding of the

ECG signal and its relation to cardiac cycle. The application also demonstrates possibility to employ vector analysis in discriminating between healthy subjects and subjects with heart problems.

The future work will enable comparison of transformations between lead systems and include more interactive parts introducing knowledge assessment.

References

- Hall, J., Guyton, A.: Textbook of Medical Physiology, 11th edn. Saunders Elsevier, Philadelphia (2005)
- Bošković, D., Badnjević, A.: Opportunities and challenges in biomedical engineering education: focus on Bosnia and Herzegovina. In: 2015 4th Mediterranean Conference on Embedded Computing (MECO), pp. 407–410. IEEE (2015)
- Medicine Meets Virtual Reality—MMVR 1992—http://nextmed.com/wpcontent/uploads/2018/07/MMVR-1_1992.pdf
- Westwood, J.D., Westwood, S.W., Felländer-Tsai, L., Fidopiastis, C.M., Liu, A., Senger, S., Vosburgh, K.G.: Medicine meets virtual reality 22—NextMed, MMVR 2016, Los Angeles, California, USA, 7–9 April 2016. Studies in Health Technology and Informatics 220. IOS Press 2016. ISBN 978-1-61499-624-8
- Virtual Medicine, Conference, accessed online 9 Dec 2018, <https://www.virtualmedicine.health>
- Solanki, M.: Virtual Reality and its Application to Healthcare, VR workshop, virtual reality and its application to healthcare, University of Warwick 24–25 May 2010
- Silva, J.N.A., Southworth, M., Raptis, C., Silva, J.: Emerging applications of virtual reality in cardiovascular medicine. *JACC: Basic Transl. Sci.* **3**(3), 420–430 (2018)
- Virtual Reality Learning Studio (VRLS), School of Biomedical Sciences, The University of Melbourne, accessed online 9 Dec 2018, <https://biomedicalsciences.unimelb.edu.au/departments/physiology/engage/vrls>
- Sreedharan Veliyara, P.: Visualization of the Cardiac Excitation and PVC Arrhythmia on a 3D Heart Model (2017)
- SimBio, Cyber Science 3D, accessed online 9 Dec 2018, <http://cyberscience3d.com/project/cyber-physiology-simbiosys/>
- D Heart Instructional Software Program: Understanding the 12 lead ECG—ECGTech, accessed online 9 Dec 2018, <http://www.ecgtech.net/3d-heart-instructionalsoftware/>
- Peters, T.M., Linte, C.A., Moore, J., Bainbridge, D., Jones, D.L., Guiraudon, G.M.: Towards a medical virtual reality environment for minimally invasive cardiac surgery. In: International workshop on medical imaging and virtual reality, pp. 1–11. Springer, Berlin, Heidelberg (2008)
- Gosling, R.C., Morris, P.D., Silva Soto, D.A., Lawford, P.V., Rodney Hose, D., Gunn, J.P.: Virtual coronary intervention: a treatment planning tool based upon the angiogram. *JACC: Cardiovasc. Imaging*, 2550 (2018)
- Gradl, S., Wirth, M., Zillig, T., Eskofier, B.M.: Visualization of heart activity in virtual reality: a biofeedback application using wearable sensors. In: 2018 IEEE 15th International Conference on Wearable and Implantable Body Sensor Networks (BSN), pp. 152–155. IEEE (2018)
- Malmivuo, J., Plonsey, R.: Bioelectromagnetism—Principles and Applications of Bioelectric and Biomagnetic Fields. Oxford University Press, New York (1995)
- Yang, H., Bukkapatnam, S.T.S., Komanduri, R.: Spatiotemporal representation of cardiac vectorcardiogram (VCG) signals. *Biomed. Eng. online* (2012)
- Dower, G.E.: The ECGD: a derivation of the ECG from VCG leads. *J. Electrocardiol.* **17**, 189 (1984)
- Dawson, D., Yang, H., Malshe, M., Bukkapatnam, S.T., Benjamin, B., Komanduri, R.: Linear affine transformations between 3-lead (Frank XYZ leads) vectorcardiogram and 12-lead electrocardiogram signals. *J. Electrocardiol.* **42**(6), 622–630 (2009). <https://doi.org/10.1016/j.jelectrocard.2009.05.007>. Epub 2009 Jul 15. PubMed PMID: 19608193
- Goldberger, A.L., Amaral, L.A.N., Glass, L., Hausdorff, J.M., Ivanov, P.Ch., Mark, R.G., Mietus, J.E., Moody, G.B., Peng, C.-K., Stanley, H.E.: PhysioBank, PhysioToolkit, and PhysioNet: components of a new research for complex physiologic signals. *Circulation* **101**(23), e215–e220 (Circulation Electronic Pages; <http://circ.ahajournals.org/content/101/23/e215.full>) (2000)
- Bousseljot, R., Kreiseler, D., Schnabel, A.: Nutzung der EKG-Signaldatenbank CARDIODAT der PTB über das Internet. *Biomedizinische Technik, Band 40, Ergänzungsband 1, S 317* (1995)
- Saeed, M., Villarroel, M., Reisner, A.T., Clifford, G., Lehman, L., Moody, G.B., Heldt, T., Kyaw, T.H., Moody, B.E., Mark, R.G.: Multiparameter intelligent monitoring in intensive care II (MIMIC-II): a public-access ICU database. *Crit. Care Med.* **39** (5), 952–960 (2011). <https://doi.org/10.1097/CCM.0b013e31820a92c6>
- Hoge.: Combine 3D and two 2D animations in one figure using Python, matplotlib.pyplot and animation.ArtistAnimation, Python Matplotlib Tips, January 2018, accessed online 9 Dec 2018: <https://pythonmatplotlibtips.blogspot.com/2018/01/combine-3d-two-2d-animations-in-one-figure-artistanimation.html>

Evaluating MSE Applicability to Short HR Time-Series

Boris Dragojevic and Dusanka Boskovic

Abstract

Multiscale entropy is successfully used to measure dynamical complexity of a finite length time series of different physiological data, including the heart rate. It is shown that the multiscale entropy as a measure can be used to discriminate healthy subjects from subjects with pathological conditions. In this paper we evaluate possibility to apply multiscale entropy to shorter heart rate time series and to evaluate resources needed to implement the algorithm in C, and to assess if it is possible to run the algorithm on a specific DSP platform.

Keywords

MSE • Multiscale entropy • Heart rate

1 Introduction

Multiscale entropy (MSE) is introduced in measuring dynamical complexity of different physiological signals, including the heart rate time series. There are several research papers documenting the success of the MSE in discriminating healthy subjects from subjects with some pathological conditions [1–4]. In this paper we evaluate possibility to apply the MSE to shorter HR time series and also to evaluate resources needed to implement the MSE algorithm in C, in order to assess if it is possible to run the algorithm on a specific DSP platform.

The paper is organized as follows: in the following Section we describe input signals used in the research, followed with the description of the multiscale entropy as a method used to analyze dynamical complexity of the heart rate time series. Our approach and results in applying MSE

to short HR time series are presented in the Sect. 3. Conclusions are presented in the Sect. 4.

2 Methods and Materials

Illustration of the MSE algorithm is done using the following databases of RR interval signals: for healthy patients recordings from the MIT-BIH Normal Sinus Rhythm Database [5]; for congestive heart failure (CHF) patients recordings from the BIDMC Congestive Heart Failure Database [6], and for atrial fibrillation recordings from the MIT-BIH Atrial Fibrillation Database [7]. The illustrative examples of the signals are presented in Fig. 1 and explained in the following section. The signals contain values that are marked as outliers, and their role in the MSE algorithm is explained in the next Sect. 3.

The signal representing the group of healthy subjects is the nsr040 signal from the *Normal Sinus Rhythm RR Interval Database (nsr2db)*. The signal with marked outliers is shown in Fig. 1a.

The second signal represents the group of signals with Atrial Fibrillation and that's the signal 07162 from the *MIT-BIH Atrial Fibrillation Database (afdb)*. The signal is shown in Fig. 1b.

The third signal represents Congestive Heart Failure, the signal 11 from the *BIDMC Congestive Heart Failure Database (chfdb)*. The signal with marked outliers is shown in Fig. 1c.

2.1 Multiscale Entropy Analysis of Heart Rate Time Series

The MSE algorithm is performed in two stages: coarse graining of the original time series and calculation of Sample Entropy for each time series.

For an original one-dimensional discrete time series given as $\{x_1, \dots, x_n\}$, consecutive coarse-grained time

B. Dragojevic · D. Boskovic (✉)
University of Sarajevo, Sarajevo, Bosnia and Herzegovina
e-mail: dboskovic@etf.unsa.ba

B. Dragojevic
e-mail: bdragojevi1@etf.unsa.ba

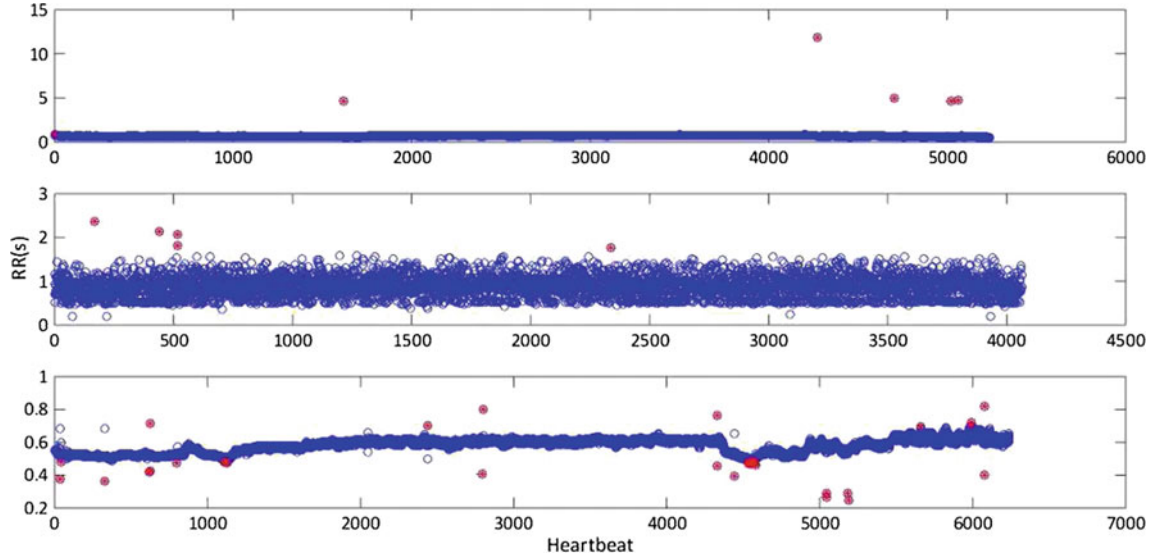


Fig. 1 Input HR time series—with marked outlier values

series are constructed and marked with the corresponding scale factor used in the coarse-graining process. The discrete time series is being modified in a way that group of consecutive data points are averaged and replaced by their mean value. The number of data points grouped is referred to as a scale. The coarse-grained time series will have N/τ data points where N is the number of data points in the main time series and τ is the scale factor. The data points in the coarsegrained time series are being calculated according to the Eq. (1).

$$y_j^{(r)} = \frac{1}{\tau} \sum_{i=(j-1)\tau+1}^{j\tau} x_i \quad (1)$$

In the Eq. (1) y_j are the elements of the coarse-grained time series, τ is the scale factor, x_j discrete one-dimensional time series with the length N , while j is the number which is within the interval $1 \leq j \leq \frac{N}{\tau}$. The coarse-grained time series with the scale factor 1 is the original one-dimensional discrete time series.

The second stage in the MSE algorithm is calculation of the Sample Entropy (SE). Sample Entropy is being calculated according to the Eq. (2).

$$\text{sampleEn}(m, r, N) = -\ln \frac{A^m(r)}{B^m(r)} \quad (2)$$

In the Eq. (2) m presents the pattern length (value between 1 and 10), r is the tolerance and N is the length of the signal. $A(r)$ and $B^m(r)$ are the probabilities that two sequences or time series will match for m and $m + 1$ data point, respectively. The value of the tolerance is within the boundaries 0.1 and 0.2 and mostly it has a value of 0.15.

Time series data may contain outlier values, missed beat detections and artifacts in recording, and may affect SE values because they change the value of parameter r [1]. Prior to the coarse-graining process the outliers are being excluded. The exclusion criteria is based on the value of the median and scaled median for time series.

After the MSE algorithm is calculated, the results are plotted as graph of the values of Sample Entropy according to the scale factors. The results are presented in Fig. 2.

It is possible to see that the Sample Entropy values for the AF and the CHF signals for scale factor 1 and 2 are higher than the value of Sample Entropy for the Healthy signal. The value of Sample Entropy for the AF signal is much higher than for the other two observed signals. How the scale factor raises, the Sample Entropy values for the Healthy signal are also raising. So, somewhere around the scale 10, the Sample Entropy value for the Healthy signal is becoming higher than the values of the SE for the AF and CHF signal.

Using the MSE analysis of the heart rate time series it is possible to conclude that this method can be used to differentiate time series corresponding to healthy and subjects with pathological conditions.

3 MSE for Short Time Series

Resource requirements for the implementation of the MSE algorithm are significant and increase with the time series length. While implementing the MSE algorithm in the MATLAB environment, or in C language for desktop application, the resources as memory availability do not present limitations. Implementation of the algorithm for a

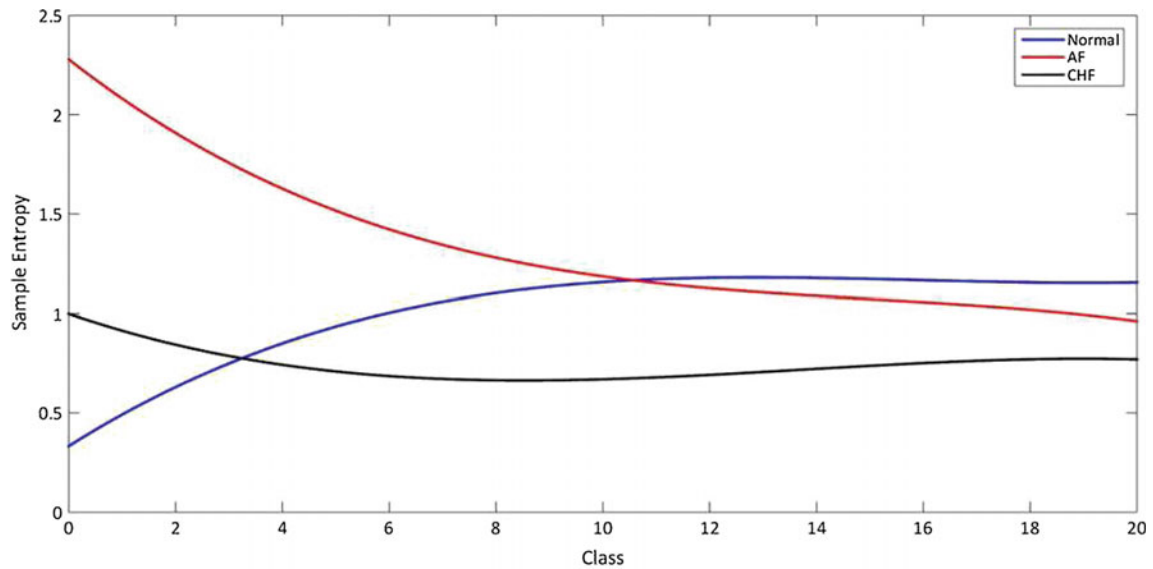


Fig. 2 Results of the MSE analysis applied to the representative HR time series from the following classes: normal sinus rhythm, AF and CHF

target platform with memory size up to 1 MB introduces limitations that prevent accurate execution. Memory size required for the accurate implementation of the MSE algorithm depending on the time series length is presented in Table 1. Target platform is TI DSP platform TMS320C551.

Sample Entropy value is sensitive to dataset size and relative error in SE algorithm is reduced with larger datasets [8]. In order to get valid results and use them for successful comparison of the MSE values and to classify HR signals accordingly, a large amount of signal samples is required. Large datasets have difficulties to be processed. They require a significant amount of memory and significant preprocessing and processing time. In some cases, the devices or microcontrollers do not have enough memory to store all data produced by coarse-graining from the original dataset.

We explored two approaches to reduce dataset length: using a subset of data, and down-sampling the data. We have evaluated the effects of shortening on the MSE algorithm

results. We observed the beginning part of the signals, the first 1000 samples, compared to 4000 samples used for illustration of the MSE in the Sect. 2. The objective is to determine if relevant information are being lost with shortening. We have applied the MSE algorithm not only to selected signals but set of the signals from the databases in our focus: normal sinus rhythm: 5 signals, AF: 20 signals and CHF: 15 signals. Evaluating graphical results of the MSE algorithm for specific signals we have noted that the results are not comparable with the results presented in Fig. 2. Aggregated result for signal sets are presented in Fig. 3.

Aggregated results are presented with mean SE values fitted with a solid line curve, and respective minimal and maximal SE values fitted with a dotted lines. Although we can observe significant overlapping of the SE values from different signal classes, mean SE values are keeping the form of the MSE plot from the Fig. 2.

Table 1 Memory requirements linked to time series length

Time series length (number of samples)	Memory (Bytes)
100	41.728
200	79.872
300	118.272
400	152.320
500	190.464
600	228.608
700	267.008
800	301.824
900	339.456
1000	385.280

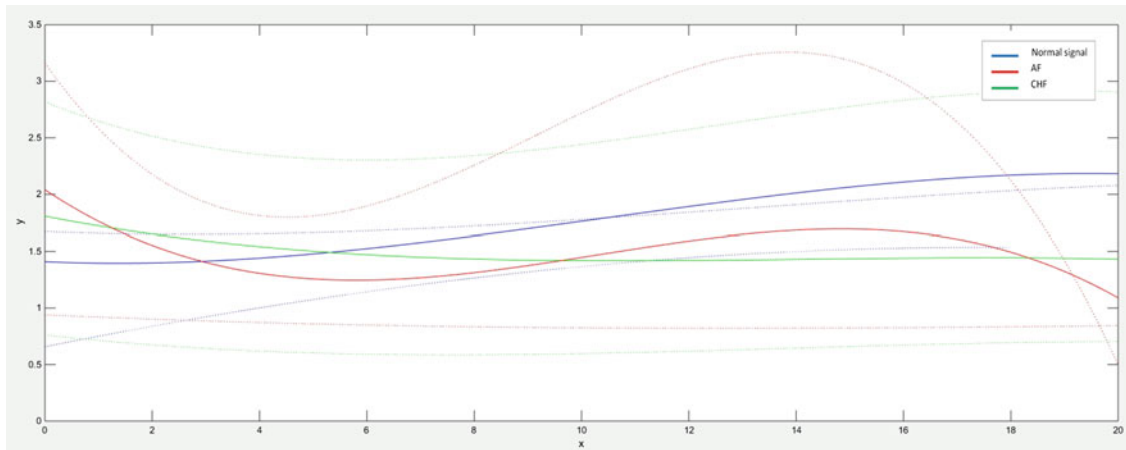


Fig. 3 Results of the MSE analysis applied to the set of HR time series from the following classes: normal sinus rhythm, AF and CHF

We can conclude that shortening of the time series affect success of employing MSE to classify signals. This decrease in sensibility can be compensated with inclusion of additional features that can improve the classification.

Following the analysis of the MSE features in [2] we have calculated the following indicators: area under the MSE curve for scale 1–5 (area 1–5) and 6–20 (area 6–20), value at scale 5, and slope of the MSE curve for scale 1–5 (slope 1–5).

The other approach in shortening the signal: down-sampling, did not provide successful results. Knowing the nature of the MSE algorithm and calculation of the SE values, obtained results are expected due to significant loss of signal dynamics.

4 Conclusion

In this study we have employed the MSE algorithm to normal sinus signals, AF and CHF signals. In order to examine how MSE perform on short time series we have compared results obtained on original time series, and time series created by shortening and down-sampling.

Resulting MSE values are aggregated and maximal, minimal and mean values for each scale are calculated to provide for graphical visualization of the results. For additional comparison of the following MSE parameters were calculated: entropy value of scale 5, the sum of entropy values of scales 1–5 (area 1–5) and 6–20 (area 6–20), and linear-fitted slope of scale 1–5.

The proposed approach demonstrates possibility to employ MSE in discriminating between healthy subjects and

subjects with heart problems even for the short time series. The future work will include comparison of the MSE parameters with features of the HR time series obtained by time and frequency analysis methods.

References

1. Costa, M., Goldberger, A.L., Peng, C.-K.: Multiscale entropy analysis of biological signals. *Phys. Rev. E* **71**, 021906 (2005)
2. Costa, M., Goldberger, A.L., Peng, C.-K.: Multiscale entropy analysis of physiologic time series. *Phys. Rev. Lett.* **89**, 062102 (2002)
3. Lin, Y.H., Lin, C., Ho, Y.H., Wu, V.C., Lo, M.T., Hung, K.Y., Liu, L.Y., Lin, L.Y., Huang, J.W., Peng, C.K.: Heart rhythm complexity impairment in patients undergoing peritoneal dialysis. *Sci. Rep.* **21** (6), 28202 (2016)
4. Faes, L., Porta, A., Javorka, M., Nollo, G.: Efficient computation of multiscale entropy over short biomedical time series based on linear state-space models. *Complexity* (2017)
5. Goldberger, A.L., Amaral, L.A.N., Glass, L., Hausdorff, J.M., Ivanov, P.Ch., Mark, R.G., Mietus, J.E., Moody, G.B., Peng, C.-K., Stanley, H.E.: PhysioBank, PhysioToolkit, and PhysioNet: components of a new research resource for complex physiologic signals. *Circulation* **101**(23), e215–e220 (*Circulation Electronic Pages*; <http://circ.ahajournals.org/content/101/23/e215.full>); 2000 (June 13)
6. Baim, D.S., Colucci, W.S., Monrad, E.S., Smith, H.S., Wright, R.F., Lanoue, A., Gauthier, D.F., Ransil, B.J., Grossman, W., Braunwald, E.: Survival of patients with severe congestive heart failure treated with oral milrinone. *J. Am. Coll. Cardiol.* **7**(3), 661–670 (1986)
7. Moody, G.B., Mark, R.G.: A new method for detecting atrial fibrillation using R-R intervals. *Comput. Cardiol.* **10**, 227–230 (1983)
8. Singh, B., Singh, M., Banga, V.K.: Sample entropy based HRV: effect of ECG sampling frequency. *Biomed. Sci. Eng.* **2**(3), 68–72 (2014)

Automatic Detection of Alzheimer Disease Based on Histogram and Random Forest

Emina Alickovic and Abdulhamit Subasi, for the Alzheimer's Disease Neuroimaging Initiative

Abstract

Alzheimer disease is one of the most prevalent dementia types affecting elder population. On-time detection of the Alzheimer disease (AD) is valuable for finding new approaches for the AD treatment. Our primary interest lies in obtaining a reliable, but simple and fast model for automatic AD detection. The approach we introduced in the present contribution to identify AD is based on the application of machine learning (ML) techniques. For the first step, we use histogram to transform brain images to feature vectors, containing the relevant “brain” features, which will later serve as the inputs in the classification step. Next, we use the ML algorithms in the classification task to identify AD. The model presented and elaborated in the present contribution demonstrated satisfactory performances. Experimental results suggested that the Random Forest classifier can discriminate the AD subjects from the control subjects. The presented modeling approach, consisting of the histogram as the feature extractor and Random Forest as the classifier, yielded to the sufficiently high overall accuracy rate of 85.77%.

Keywords

Alzheimer disease • Histogram • Random forest classifier

1 Introduction

Dementia is a neurodegenerative disease with long-lasting and continuing character resulting in disruption of a number of complex cognitive tasks, with common cases including memory, reasoning, orientation, understanding, computation, learning capability, verbal communication and decision-making. It generally occurs in the elder population. Only 2% of all subjects diagnosed with dementia are younger than 65. After the age of 65, occurrence increases twice for each five-year age increase. Approximately, twenty four million subjects suffer from dementia worldwide and almost sixteen million subjects diagnosed with dementia come from the low and middle income countries. Subjects diagnosed with dementia are not all affected by this disease in the same manner. A number of different reasons influence the appearance of dementia. Several infrequent reasons for the appearance of dementia are hypercalcaemia, subdural hematoma, normal pressure hydrocephalus, and deficits in thyroid hormone, vitamin B12 and folic acid, and these can be successfully treated by a suitable therapeutic or surgical interference. On the negative side, less is known about the processes underlying the progressive nature of dementia. Although a very significant body of previous work attempted to (partially) answer this challenge, almost no progress in addressing this question appropriately was reported. We still have a very limited knowledge of the circumstantial and behavioral elements related to the causes, progress and treatment of dementia [1]. Light therapies were confirmed to be somewhat successful in dementia treatments by enhancing cognitive and non-cognitive symptoms [2].

The most severe impact of AD is on the memory, long-standing movement and oral abilities. Central nervous

Data used in preparation of this article were obtained from the Alzheimer's Disease Neuroimaging Initiative (ADNI) database (adni.loni.usc.edu). As such, the investigators within the ADNI contributed to the design and implementation of ADNI and/or provided data but did not participate in analysis or writing of this report. A complete listing of ADNI investigators can be found at: http://adni.loni.usc.edu/wp-content/uploads/how_to_apply/ADNI_Acknowledgement_List.pdf, adfa, p. 1, 2011. © Springer-Verlag Berlin Heidelberg 2011.

E. Alickovic
Department of Electrical Engineering, Linköping University,
58183 Linköping, Sweden
e-mail: emina.alickovic@liu.se

A. Subasi (✉)
Information Systems Department, College of Engineering,
Effat University, Jeddah, 21478, Saudi Arabia
e-mail: absubasi@effatuniversity.edu.sa;
abdulhamitsubasi@gmail.com

system (CNS) parts included in the memory and rational abilities are firstly distorted, pursued by neuronal loss in the rest of brain as AD advances that in the long run results in the subject's demise. Subjects diagnosed with AD typically exhibit a stable decay in these kinds of abilities caused by the neurological side-effects that cannot be cured currently [3].

Although very little is still known about AD, there is a rich literature on the AD classification, i.e., discriminating the AD patients from normal control subjects. However, on the negative side, there is no clear guideline for how to design a model for the AD classification. Most of the approaches proposed in the recent literature are based on ML methods. In addition, different brain activity recording modalities, such as magnetic resonance imaging (MRI) and positron emission tomography (PET), could also provide conceivable information. Different modalities were used in the literature to obtain knowledge needed for different aspects of AD disease diagnosis and treatment. A number of studies [4–9] attempted to combine the knowledge obtained from different modalities to generate more reliable and efficient classification scheme. Our interest in the present study lies in obtaining a reliable model for detection of AD. The approach we propose in the present article is based on histogram as simple feature extraction method and k-NN as the classifier. It is inspired by the recent findings in AD diagnosis area and also by the recent progress in classifier construction in ML field. We evaluated our model on the MRI data.

This paper is organized as follows. Section 2 contains the given description about ADNI database employed in this research, feature extraction and classification methods. The experimental results obtained in this research are given in Sect. 3. And lastly, the conclusion of the research is given in Sect. 4.

2 Materials and Methods

2.1 ADNI Database

Data used in the preparation of this article were obtained from the Alzheimer's disease Neuroimaging Initiative (ADNI) database (adni.loni.usc.edu). The ADNI was launched in 2003 as a public-private partnership, led by Principal Investigator Michael W. Weiner, MD. The primary goal of ADNI has been to test whether serial magnetic resonance imaging (MRI), positron emission tomography (PET), other biological markers, and clinical and neuropsychological assessment can be combined to measure the progression of mild cognitive impairment (MCI) and early Alzheimer's disease (AD). MRI images were considered for evaluation of the proposed models in this study. The acquisition of the MR

images was performed based on ADNI acquisition protocol [10]. For this study, 72 brain images from participants diagnosed with AD were selected and 195 images from cognitively normal elder control participants were selected.

2.2 Histogram

Digital image with gray levels histogram, in a range $[0, M - 1]$, is a discrete function $h(r_k) = n_k$, where r_k represents the k -th gray level and n_k is the number of pixels in the image with gray level r_k . Usually, histogram is normalized by dividing every of its values by the total number of pixels inside the image, symbolized by n . Therefore, a normalized histogram is expressed as $p(r_k) = n_k/n$, for $k = 0, 1, \dots, M - 1$.

Shortly, $p(r_k)$ provides the probability estimation of gray level r_k appearance. The summation of all components of a normalized histogram is one. Histograms form the foundation for a number of spatial domain processing techniques. Different manipulation with histogram may be successfully employed for image improvement. Histograms can be easily calculated by using different software, and, also, is used in the cost-effective hardware implementations; hence they are a common tool for real-time image processing [11].

2.3 Machine Learning Techniques

Machine learning algorithms are used to optimize a performance criterion using historical data or learned experience. The ultimate learning goal can be predictive to make forecasts from the labeled data such as classification and regression models. Machine learning algorithms heavily employ the theory of statistics in designing soft computing models, because the aim is describing the samples or making an inference from the samples. To develop machine learning models, you need to consider the performance by means of accuracy during training to find a solution for the optimization problem. Once a model is trained, its representation for learning inference need to be efficient by means of space and time complexity as well [12]. In this study different machine learning algorithms are employed.

The Naïve Bayes classifier is a simple method with transparent interpretation that can be applied to the probabilistic learning. This method is designed to be used for solving the supervised learning problems, where the efficiency objective is to correctly classify sample test set, and where the sample training set consists of the class data. More information on the naïve bayes classifier can be found in [13].

Logistic regression (LR) is considered as a multivariable technique that attempts to form a functional relationship

among two predictor variables and single result. Commonly, LR result variable is categorical in sense that it may just suppose a fixed number of classes [14].

Since support vector machines (SVMs) is established on Vapnik-Chervonenkis (VC) theory and Structural Risk Minimization (SRM) principle. The leading idea in SVM is to find the minimum training set error through maximizing the margin between the splitting hyper-plane and the data provided for the training. One of the key advantages of SVM is the usage of convex quadratic programming (QP), because the outcome of complex QP is the only one global minimum [15, 16].

ANNs is a very popular choice for modelling of different systems. ANNs have found a wide area of applications due to its capacity to solve a multitude of different problems by training them in a supervised manner with a highly popular algorithm, frequently referred to as the back-propagation error algorithm. The weights are corrected to make the real network response closer to desired response in a statistical sense [15, 17]. ANN is a valuable classifier of linearly inseparable data, such as MR imaging data, as long as there is a sufficient amount of dependable data to be used in training processes.

k-NN is a learning algorithm that can employed to perform different classification tasks. In order to prevent scenario, in which all feature vectors are assessed in unequal units, in the first step, normalization of features vectors is done, and all normalized vectors have zero mean and variance equal to 1. In the second step, the distance between two different samples Z_m and Z_n is specified in the form of different distance metrics, e.g. Euclidean distance, Chebyshev distance, Manhattan distance etc. The class of new sample is the class of nearest neighbor, i.e. the neighbor with the shortest Euclidean distance. Two factors influence the performance results of k-NN: (1) the distance metric type, and (2) the k value stating the neighboring size. In this study, k was set to 1. More details on k-NN are presented in [17, 18].

The C4.5 classifier is a decision tree classifier based on the knowledge approach employed to denote a plethora of classification rules. Decision tree that is constructed following the C4.5 procedure is composed of the single root, a number of branches, decision nodes and leaves. Series of nodes from the root to the leaf make one branch and every node includes one attribute. The leaves indicate the class labels. The attribute's manifestation in a tree gives statistics related to the significance of the corresponding attribute [19].

Random Forest (RF), proposed by Breiman [20], fast, highly accurate, noise resistant classification method. Bagging and random feature selection are combined together in RF. Every tree in the forest is influenced by the values of random vectors sampled separately and has identical distribution as any other tree in the forest. RF consists of outsized

number of decision trees where decision tree select their separating features from bootstrap training set S_i where i represent i th internal node. Trees in RF are grown by means of Classification and Regression Tree (CART) method with no pruning. As number of trees in the forest turns into outsized number, generalization error will also increase until it converges to some boundary level. More details about RF can be found in [20, 21].

Rotation Forest is an ensemble machine learning technique for generation of group of classifiers. In the first step, the feature set is divided into S subsets, and principal component analysis (PCA) is applied independently on every subset and then a new extracted feature set is reconstructed during which all the components are preserved. New features are acquired from linearly transformed data [22].

3 Experimental Results

3.1 Data Preparation Procedure

For all ADNI participants, in this study, we consider only the MRI scan obtained at 1.5 T. In order to improve tuning through different positions and policies of ADNI images acquisition, the images were subjected to certain post-acquisition removal of specific image artifacts [23]. In this study, images corrected in geometry for gradient non-linearity using 3D GradWrap correction and corrected in intensity non-uniformity cause by receiver coil using B1 non-uniformity correction, explained in [24], were used. In the present article, MRI scans, judged as the "best" quality scans with the term "best" quality defined in ADNI methods referring to images which underwent all pre-processing steps for all participants by the ADNI investigators, were obtained from ADNI database.

3.2 Performance Evaluation Criteria

In the present contribution, we evaluated 8 different machine learning. The overall objective of this contribution is to design a computer aided diagnostic (CAD) model that results in satisfactory accuracy, sensitivity and specificity rates. In order to prove the high performances of eight different classifiers, 10-fold cross-validation (CV) method is used. The advantages of CV are that each test set is independent, and the consistency of the obtained results might be further enhanced. For smaller datasets, as datasets used in this study, it is more efficient to use CV in which more samples are found in the training set [25].

In this study, classifiers' performances are evaluated in terms of five different statistical metrics: (1) overall

(CV) accuracy, (2) sensitivity, (3) specificity, (4) ROC area and (5) F-measure. For the binary (two-class) dataset (AD vs. healthy controls), the computed specificity and sensitivity values can be used to evaluate overall performances of the suggested models. Sensitivity and specificity define at what satisfactory level the proposed ML classifier method distinguishes between the subjects with positive and with negative classes (subjects with and without AD). Specificity indicates the accuracy of the classification model when identifying healthy controls and ADs, i.e. it shows how well proposed model identifies healthy controls or ADs and specificity can be considered as a measure of false the predictions/detections. On the other hand, sensitivity shows how well proposed models can correctly identify early AD. ROC curves show performances of classification models having no concern on the distribution of classes or error costs. ROC curve can be generated by plotting all obtained sensitivity values on the y axis and their matching (1-specificity) values for whole obtainable threshold levels [15, 26, 27]. These metrics are given as:

$$Sensitivity = \frac{TP}{TP + FN} \times 100\% \quad (1)$$

$$Specificity = \frac{TN}{TV + FP} \times 100\% \quad (2)$$

$$Accuracy = \frac{TP + TN}{TP + FN + TN + FP} \times 100\% \quad (3)$$

$$F - measure = \frac{2TP_i}{2TP_i + FP_i + FN_i} \quad (4)$$

where TP, FP, TN and FN are number of true positives, false positives, true negatives and false negatives respectively.

3.3 Results and Discussion

The quick expansion of the latest imaging instruments resulted in big data (in dimension and sample size). Rise in the number of voxels in MR and PET images is an important

problem. Due to this problem, in this study, in order to decrease the dimensionality of data, normalized histogram was taken from each image. This *significantly* reduced the amount of data, what consequently reduced a computational burden. To our knowledge, our study is one of the first studies which considers this approach. Histograms are a very nice functions since they are computationally very simple and easily implementable. 10 bins histogram was obtained from each image.

The overall performance results are given in Table 1. From Table 1 it can be seen that Naïve Bayes classifier resulted in the lowest performance results where Fmeasure was 0.702, ROC value 0.598, sensitivity of 23.61% what is very unsatisfying, specificity of 92.82% and overall accuracy rate of 74.16. Logistic regression (LR) resulted in somewhat better overall accuracy results although sensitivity for LR classifier was the lowest, 16.67%. Also, F-measure (0.694) was the lowest for LR classifier. ROC area value, specificity and overall accuracy rate were 0.630, 96.92 and 75.28% respectively and these values were higher when compared to Naïve Bayes classifier. Artificial Neural Network (ANN) Multilayer Perceptron (MLP) classifier also resulted in poor performances. Sensitivity of 54.17% was evidently higher when compared to Naive Bayes and LR classifiers, but other performance parameters were relatively low as in Naïve Bayes and LR. F-measure, ROC, specificity and overall accuracy parameters were 0.759, 0.779, 84.15 and 76.03% respectively.

C 4.5 decision tree classifier performances were evidently higher when compared to Naïve Bayes, LR and ANN. F-measure, ROC, sensitivity, specificity and overall accuracy parameters for C 4.5 classifier were 0.811, 0.793, 54.17, 92.31 and 82.02% respectively. From these obtained results it can be seen that system composed of histogram as feature extractor and C 4.5 method as classifier is promising in detection and classification of AD. SVM classifier also resulted in promising results. Fmeasure, ROC, sensitivity, specificity and overall accuracy parameters for SVM classifier were 0.828, 0.766, 62.5, 90.77 and 83.15% respectively. From these obtained results it can also be seen that system composed of histogram as feature extractor and SVM

Table 1 Performance results for detection of Alzheimer Disease

	F-Measure	ROC	Sensitivity (%)	Specificity (%)	Accuracy (%)
Naïve Bayes	0.702	0.598	23.61	92.82	74.16
LR	0.694	0.63	16.67	96.92	75.28
SVM	0.828	0.766	62.5	90.77	83.15
ANN	0.759	0.779	54.17	84.1	76.03
k-NN	0.84	0.897	65.28	91.28	84.27
C 4.5	0.811	0.793	54.17	92.31	82.02
Random forest	0.845	0.885	54.17	97.44	85.77
Rotation forest	0.829	0.778	59.72	92.31	83.52

method as classifier is promising system for AD detection. Novel meta classifier, rotation forest, also resulted in satisfying performance results. F-measure, ROC, sensitivity, specificity and overall accuracy parameters for Rotation Forest classifier were 0.829, 0.778, 59.72, 92.31 and 83.52% respectively what brings Rotation Forest as one key classifiers for AD detection.

Two classifiers which resulted in the highest performances are k-NN and Random Forest. K-NN classifier resulted in the highest sensitivity rate of 65.28% and this fact makes k-NN classifier as one of the key tools for AD detection. F-measure, ROC, specificity and overall accuracy parameters for k-NN classifier were 0.84, 0.897, 91.28 and 84.27% respectively. Random forest classifier resulted in the highest overall classification accuracy rate of 85.77%. F-measure, ROC, specificity and overall accuracy parameters for random forest classifier were 0.845, 0.885, 97.44 and 85.77% respectively. But due to low sensitivity of random forest classifier, k-NN is proposed in this study as classifier. System that is proposed in this study for AD detection consists of histogram as feature extractor and k-NN as classifier. Even though, results reported in the present study are not the highest when compared to results in similar studies reported in recent literature, the simplicity of the model proposed in this study makes is valuable and relevant for AD classification.

4 Conclusion

In the present contribution, we suggested a model for automatic diagnosis of Alzheimer disease (AD). The model suggested here consists two steps: (1) histogram as MR images feature extractor and (2) Random Forest as a classifier. The present results challenge the current state-of-the-art results reported in the literature. Our findings turn this model into a promising diagnostic tool. Instead of proposing complex and slow system, here we focused on designing a simple and easily implementable model. Moreover, we evaluated different machine learning classifiers so as to design a simple, but efficient model for automatic diagnosis of AD. Our future work will apply the same model to different imaging techniques (e.g. PET imaging) to see if this model can be generalized across any recording technique. Also, of interest is to try various feature extraction and selection techniques to compare the performances in terms of the overall accuracy, but also in terms of the computational burden.

Acknowledgements Authors thank to Alzheimer's Disease Neuroimaging Initiative (ADNI) for sharing database.

References

1. World Health Organization.: Neurological Disorders Public Health Challenges. World Health Organization (WHO) Press (2006)
2. Riemersma-van der Lek, R.F., Swaab, D.F., Twisk, J., Hol, E.M., Hoogendijk, W.J.G., Someren, E.J.W.V.: Effect of bright light and melatonin on cognitive and noncognitive function in elderly residents of group care facilities. *J. Am. Med. Assoc.* **299**(22), 2642–2655 (2008)
3. Begg, R., Lai, D.T.H., Palaniswami, M.: Computational Intelligence in Biomedical Engineering. CRC Press, Boca Raton (2008)
4. Gray, K.R., Aljabar, P., Heckemann, R.A., Rueckert, D.: Random forest-based similarity measures for multi-modal classification of Alzheimer's disease. *Neuroimage* **65**, 167–175 (2013)
5. Walhovd, K.B., Fjell, A.M., Dale, A.M., McEvoy, L.K., Brewer, J., Karow, D.S., Salmon, D.P., Fennema-Notestine, C.: Multi-modal imaging predicts memory performance in normal aging and cognitive decline. *Neurobiol. Aging* **31**(7), 1107–1121 (2010)
6. Zhang, D., Wang, Y., Zhou, L., Yuan, H., Shen, D.: Multimodal classification of Alzheimer's disease and mild cognitive impairment. *Neuroimage* **55**(3), 856–867 (2011)
7. Hinrichs, C., Singh, V., Xu, G., Johnson, S.C.: Predictive markers for AD in a multimodality framework: an analysis of MCI progression in the ADNI population. *Neuroimage* **55**(2), 574–589 (2011)
8. Westman, E., Muehlboeck, J., Simmons, A.: Combining MRI and CSF measures for classification of Alzheimer's disease and prediction of mild cognitive impairment conversion. *Neuroimage* **62**(1), 229–238 (2012)
9. Kamath, M.V., Upton, A.R., Wu, J., Bajaj, H.S., Poehlman, S., Spaziani, R.: Artificial neural networks in EEG analysis. In: *Neural Networks in Healthcare: Potential and Challenges*, Hershey, pp. 177–194. Idea Group Publishing (2006)
10. Jack, Jr. C.R., Bernstein, M.A., Fox, N.C., Thompson, P., Alexander, G., Harvey, D., Borowski, B., Britson, P.J.L., Whitwell, J., Ward, C., Dale, A.M.: The Alzheimer's disease neuroimaging initiative (ADNI): MRI methods. *J. Magn. Reson. Imaging: (An Official Journal of the International Society for Magnetic Resonance in Medicine)* **27**(4), 685–691 (2008)
11. Gonzalez, R.C., Woods, R.E.: *Digital Image Processing*, 2nd edn. Prentice Hall, New Jersey (2002)
12. Alpaydin, E.: *Introduction to Machine Learning*. MIT Press, Cambridge (2014)
13. John, G.H., Langley, P.: Estimating Continuous distributions in Bayesian Classi. In: *Eleventh Conference on Uncertainty in Artificial Intelligence*, San Mateo (1995)
14. Le Cessie, S., Van Houwelingen, J.C.: Ridge estimators in logistic regression. *Appl. Stat.* **41**(1), 191–201 (1992)
15. Alickovic, E., Subasi, A.: Effect of multiscale PCA de-noising in ECG beat classification for diagnosis of cardiovascular diseases. *Circ. Syst. Sig. Process.* **34**(2), 513–33 (2015)
16. Vapnik, V.: *The Nature of Statistical Learning Theory*. Springer-Verlag, New York (1995)
17. Mitchell, T.M.: *Machine Learning*. McGraw-Hill Science/Engineering/Math (1997)
18. Aha, D.W., Kibler, D., Albert, M.K.: Instance-based learning algorithms. *Mach. Learn.* **6**, 37–66 (1991)
19. Quinlan, J.R.: *C4.5: Programs for Machine Learning*. Morgan Kaufmann Publishers, San Mateo (1993)
20. Breiman, L.: Random forests. *Mach. Learn.* **45**, 5–32 (2001)
21. Alickovic, E., Subasi, A.: Medical decision support system for diagnosis of heart arrhythmia using DWT and random forests classifier. *J. Med. Syst.* **40**(108) (2016)

22. Rodriguez, J.J., Kuncheva, L.I., Alonso, C.J.: Rotation forest: a new classifier ensemble method. *IEEE Trans. Pattern Anal. Mach. Intell.* **28**(10), 1619–1630 (2006)
23. Jack, C.R.J., Bernstein, M.A., Fox, N.C., Thompson, P., Alexander, G., Harvey, D., Borowski, B., Britson, P.J., Whitwell, J., Ward, C., Dale, A.M., Felmlee, J.P., Gunter, J.L., Hill, D.L., Killiany, R., Schuff, N., Fox-Bosetti, S., Lin, C., Studholme, C., DeCarli, C.S., Krueger, G., Ward, H.A., Metzger, G.J., Scott, K.T., Mallozzi, R., Blezek, D., Levy, J., Debbins, J.P., Fleisher, A.S., Albert, M., Green, R., Bartzokis, G., Glover, G., Mugler, J., Weiner, M.W.: The Alzheimer's disease neuroimaging initiative (ADNI): MRI methods. *J. Magn. Reson. Imaging* **27**(4), 685–691 (2008)
24. Narayana, P.A., Brey, W.W., Kulkarni, M.V., Sievenpiper, C.L.: Compensation for surface coil sensitivity variation in magnetic resonance imaging. *Magn. Reson. Imaging* **6**(3), 271–274 (1988)
25. Salzberg, S.L.: On comparing classifiers: pitfalls to avoid and a recommended approach. *Data Min. Knowl. Disc.* **1**, 317–327 (1997)
26. Fielding, A.H.: *Cluster and Classification Techniques for the Biosciences*. Cambridge University Press, The Edinburgh Building, Cambridge (2007)
27. Zweig, M.H., Campbell, G.: Receiver-operating characteristic (ROC) plots: a fundamental evaluation tool in clinical medicine. *Clin. Chem.* **39**, 561–577 (1993)

Part II

**Medical Physics, Biomedical Imaging and
Radiation Protection**

A Dosimetric Analysis of the Overlapping and Gap Areas Produced by Simulated Set-Up Errors on a Treatment Planning System in a Case of the Cranio-Spinal Irradiation of an Adult Patient

Edis Đedović, Hasan Osmić, Muhamed Topčagić,
and Nermina Karaman

Abstract

The purpose of this study is to make a dosimetric analysis of the overlapping and gap areas in the case of a cranio-spinal irradiation. A simulation of the overlaps and gaps was performed on a treatment planning system. The overlaps and gaps were simulated for the 2, 4, 5, 6 and 8 mm overlaps or gaps. The data recorded: global and local maximum of doses, depth of the 95, 100 and 125% dose, the depth of spine location in the overlapping/gap areas. The local maximum values were increased up to 7.03 Gy in the case of the cranial-upper spinal field overlaps and up to 5.45 Gy in the case of the upper-lower spinal fields. The gaps cause the decreases of the local maximum values up to 6.65 Gy in the case of cranial-upper spinal field. An increase of the depth of 125% isodose line of 1.04 cm in the case of the 5 mm upper-lower spine fields overlapping was recorded. The total coverage of the target volume by 125% isodose line, in the case of the 5 mm + 5 mm overlapping between the cranial and the upper spinal field may be a source of a damage of spinal cord. The partially covered treatment volume by 95% isodose line in the case of 4 mm + 4 mm and 5 mm + 5 mm gap area between the cranial and the upper spinal field, may cause a relapse of the tumor.

Keywords

Medulloblastoma • Cranio-spinal irradiation •
The three dimensional conformal radiotherapy

1 Introduction

Medulloblastoma has a contribution of about 20% in the total number of the central nervous system cancers in pediatric patients [1]. This type of carcinoma is relatively rare in adults [2]. In the case of radiotherapy treatment, the cranio-spinal irradiation of brain and the whole spinal cord is used. Despite the fact that 3DCRT (the three dimensional conformal radiotherapy) is an advanced technique the cranio-spinal irradiation is a challenge, especially for an achievement of a required coverage of the target volume, otherwise a relapse of the tumor may be occurred [3, 4].

The other difficulties are related to the traditional prone position of a patient. The treatment delivery in children requires anaesthesia for immobilization. A supine position has advantages: a patient comfort and the access to the airway, a reproducibility of the treatment and simultaneous delivery a boost to posterior fossa. The immobilization in the supine position for the adult patients is released using a thermoplastic mask fixation for head and neck. From a dosimetric aspect, there is no the significant differences in a dose coverage of the target volume depending on prone and supine positions, as well as in a dose homogeneity and the doses to the organs at risk [2].

For the cranio-spinal irradiation a problem is an overlapping between cranial and upper spinal fields caused by the set-up errors. In the overlapping area, an overdose for a spine may happen. The overdose is the more possible if the cranial fields and spinal field are matched in a way that there is no gap between them. In an arrangement of the fields where a gap between the cranial and spinal field exists, a possibility of an under-dose for the target volume appears. In both cases, the problem is tried to overcome using weekly shifts between the junctions which may be a source of the additional errors.

E. Đedović (✉) · H. Osmić · M. Topčagić
University Clinical Center Tuzla, Tuzla prof. dr Ibri Pašića,
BiH, Tuzla, Bosnia and Herzegovina
e-mail: edis.djedovic@yahoo.com

H. Osmić
e-mail: hasan.osmic@ukctuzla.ba

M. Topčagić
e-mail: muhamed.topcagic@ukctuzla.ba

E. Đedović
Department of Physics, University of Tuzla,
Tuzla Univerzitetstva 4, BiH, Tuzla, Bosnia and Herzegovina

N. Karaman
The Hospital of Zenica Canton, Zenica Crkvice 67, BiH,
Zenica, Bosnia and Herzegovina
e-mail: nerminakaraman@gmail.com

The probability of the errors occurred in the treatment delivering may increase by the different reasons:

- treatment time duration,
- a couch movement and rotation,
- a visual check of the fields' borders and spine alignment is not possible in supine position,
- an inappropriate immobilization tools,
- a limited reposition accuracy of a thermoplastic mask in a fractionated radiotherapy,
- immobilization tools set-up errors produced by them self [5],
- a fact that the treatment planning systems underestimate out-of field doses and collimator scatter near the treatment fields [6].

All above sources of errors may produce hot or cold spots in the field junction areas or, on the other ways, may affect the dose distribution. As a result of an overdose in spine the toxicity, as myelitis, may increases, and as a result of an underdose in the target volume the probability of the tumor relapse increases.

In this study a dosimetric analysis of the overlapping and gap areas was made for different overlap and gap dimensions. The simulations of the overlapping and gap areas were performed using a commercial treatment planning system.

2 Materials and Methods

For the purpose of the analysis an adult patient with the diagnosis medulloblastoma was chosen. A treatment simulation of the patient in supine position was performed on a CT simulator with a slice thickens of 3 mm. The delineation of brain and spinal treatment volumes and the organs at risk was performed on FOCAL planning system. The 3DCRT treatment plan was prepared on XiO treatment planning system. The prescribed dose for cranial and spinal target volume was 36 Gy with the boost of 18 Gy to posterior fossa.

2.1 Preparation of 3DCRT Treatment Plan

The preparation of the treatment plan was done using the technique introduced by William and Carolyn [7] with a small modification. This technique includes: two half beam blocked opposite lateral cranial fields with the isocenter at the level of the C2 vertebral body, an upper posterior spine field with the isocenter located at a point 20 cm distal to the cranial fields and the one lower posterior spine field with the isocenter located at a point 30 cm distal to the upper spinal field. A small modification of this approach was made in a case of the lower spinal field. A couch was rotated by 90°

and with a gantry angle tilt, it was ensured that the divergent inferior border of the upper spine field matches the divergent superior border of the lower spine field.

A margin of 0.5 cm to the cranial target volume and 1 cm to the spinal target volume was added. The photon beam energy of 6 MV and the superposition calculation algorithm were chosen. The shifts of 1 cm per week, was used in the junction area. Figure 1 shows the normal treatment plan with all fields included and week shifts.

2.2 A Simulation of the Overlapping and Gap Areas

The overlaps or gaps may appear in the field junction areas due to the set-up errors. An occurrence of the errors was supposed to be in the last week of the treatment where the divergence of the cranial and upper spinal field is the largest during. These situations were simulated on XiO treatment planning system so that the isocenters of the treatment fields were moved causing overlapping or producing the gaps of 2, 3, 4, 5, 6, 8 and 10 mm in the adjacent fields.

2.3 Data Collection and Analysis

The data of all simulated situations were collected from the treatment planning system. It was analyzed the changes in the local maximum doses in the overlapping and gap areas, the appearances and depths of 125% isodose lines (45 Gy) and the depths of 95 and 100% isodose lines. This value of 45 Gy was chosen as a dose limit for spine. The obtained values were taken from the middle positioned slice of the overlapping and gap areas.

3 Results and Discussion

The obtained results were presented in Tables 1 and 2.

From Tables 1 and 2 is evident that, in the spinal-spinal field junction areas, the 125% (45 Gy) isodose lines are at the lower depths than at the locations of spinal cord, and the local maximum values are higher in the spinal field junction areas than in the cranial-upper spinal field junction areas, but still lower than the global maximum values.

The data from Table 3 show an increasing in local maximum values with an increasing of an overlapping area. The 125% isodose lines are partially appear for 4 and 5 mm overlaps.

The data from Table 4 show a decreasing in local maximum values with an increasing of a gap area. The 125% isodose line does not appear and, in the case of the 5 mm gap, the target volume is partially covered by 100% isodose line.

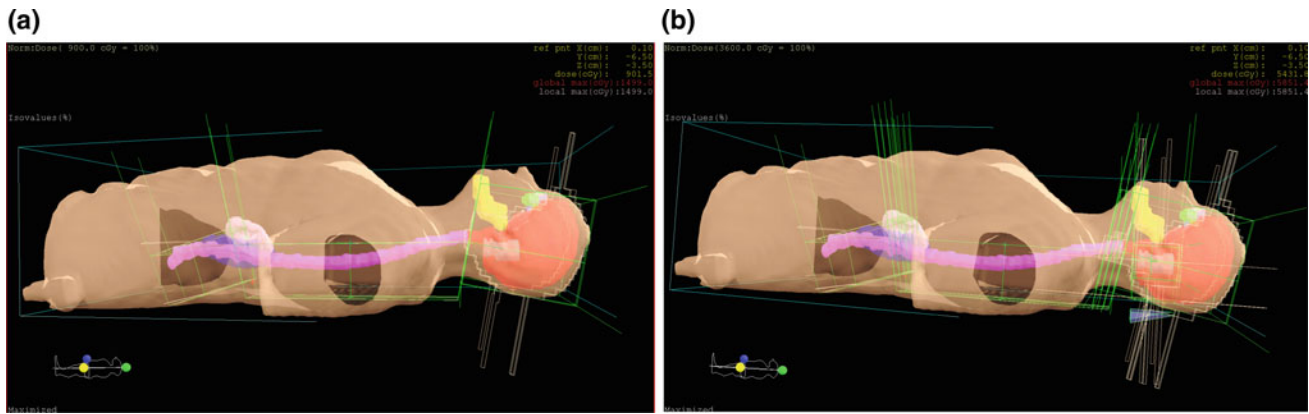


Fig. 1 a The fields matching and b the week shifts during the overall treatment

Table 1 The values of the parameters in a junction area of the cranial and the upper spine field for the normal treatment plan

D _{max} (Gy)	Local maximum (Gy)	Spinal cord depth (cm)	Treatment volume covered by 95% isodose line	Treatment volume covered by 100% isodose line	Treatment volume covered by 125% isodose line	Transversal coordinate
58.51	43.30	6.88	Yes	Yes	No	-16.00
58.51	43.38	6.80	Yes	Yes	No	-16.10
58.51	43.47	6.80	Yes	Yes	No	-16.20
58.51	43.53	6.76	Yes	Yes	No	-16.25
58.51	43.25	6.80	Yes	Yes	No	-15.90
58.51	43.19	6.84	Yes	Yes	No	-15.80
58.51	43.15	6.67	Yes	Yes	No	-15.75

Table 2 The values of the parameters in a junction area of the upper and lower spine field for the normal treatment plan

D _{max} (Gy)	Local maximum (Gy)	Spinal cord depth (cm)	Depth of the 95% isodose line (cm)	Depth of the 100% isodose line (cm)	Depth of the 125% isodose line (cm)	Transversal coordinate
58.51	55.16	6.38	9.32	8.12	4.93	-50.00
58.51	55.44	6.22	9.37	8.22	4.77	-49.90
58.51	55.71	6.42	9.50	8.50	4.68	-49.80
58.51	55.86	6.34	9.50	8.62	4.68	-49.75
58.51	54.92	6.34	9.28	8.08	4.93	-50.10
58.51	54.98	6.34	9.00	8.16	5.00	-50.20
58.51	55.11	6.60	9.24	8.25	5.06	-50.25

Table 3 The values of the parameters in the middle of the overlapping areas of cranial-upper spinal fields

Overlapping (mm)	D _{max} (Gy)	Local maximum (Gy)	Treatment volume covered by 95% isodose line	Treatment volume covered by 100% isodose line	Treatment volume covered by 125% isodose line	Transversal coordinate
2	58.48	44.80	Yes	Yes	No	-15.90
4	58.46	46.09	Yes	Yes	Partially	-15.80
5	58.46	47.12	Yes	Yes	Partially	-15.75

The data from Table 5 show an increasing in local maximum values with an increasing of an overlapping area. The same behavior is obtained for the depths of 95, 100 and 125% isodose lines.

The data from Table 6 show a decreasing of all parameters with an increasing of the gap areas. An exception makes the local maximum values which increases with the sizes of the gap areas.

From Table 7 it is evident an increase of local maximum values with an increasing of the overlapping areas. The

treatment volume is covered by 125% isodose line in the case of 5 mm + 5 mm overlapping areas. It indicates that spine is also covered by 125% isodose line.

The data presented in Table 8 show a decreasing of local maximum values with an increasing of gap areas. In the cases of 4 mm + 4 mm and 5 mm + 5 mm gap areas, the treatment volume is only partially covered by 95% isodose line. Figure 2 shows the isodose distributions in the case of normal and the overlaps/gaps simulated treatment.

Table 4 The values of the parameters in the middle of the gap areas of cranial-upper spinal fields

Gap (mm)	D_{\max} (Gy)	Local maximum (Gy)	Treatment volume covered by 95% isodose line	Treatment volume covered by 100% isodose line	Treatment volume covered by 125% isodose line	Transversal coordinate
2	58.55	40.72	Yes	Yes	No	-16.10
4	59.25	39.47	Yes	Yes	No	-16.20
5	61.31	39.28	Yes	Partially	No	-16.25

Table 5 The values of the parameters in the middle of the overlapping areas of upper-lower spinal fields

Overlapping (mm)	D_{\max} (Gy)	Local maximum (Gy)	Depth of the 95% isodose line (cm)	Depth of the 100% isodose line (cm)	Depth of the 125% isodose line (cm)	Transversal coordinate
2	58.55	55.20	9.90	8.74	5.26	-50.10
4	59.25	55.68	9.90	9.40	5.70	-50.20
5	61.31	55.96	10.10	9.50	6.10	-50.25

Table 6 The values of the parameters in the middle of the gap areas of upper-lower spinal fields

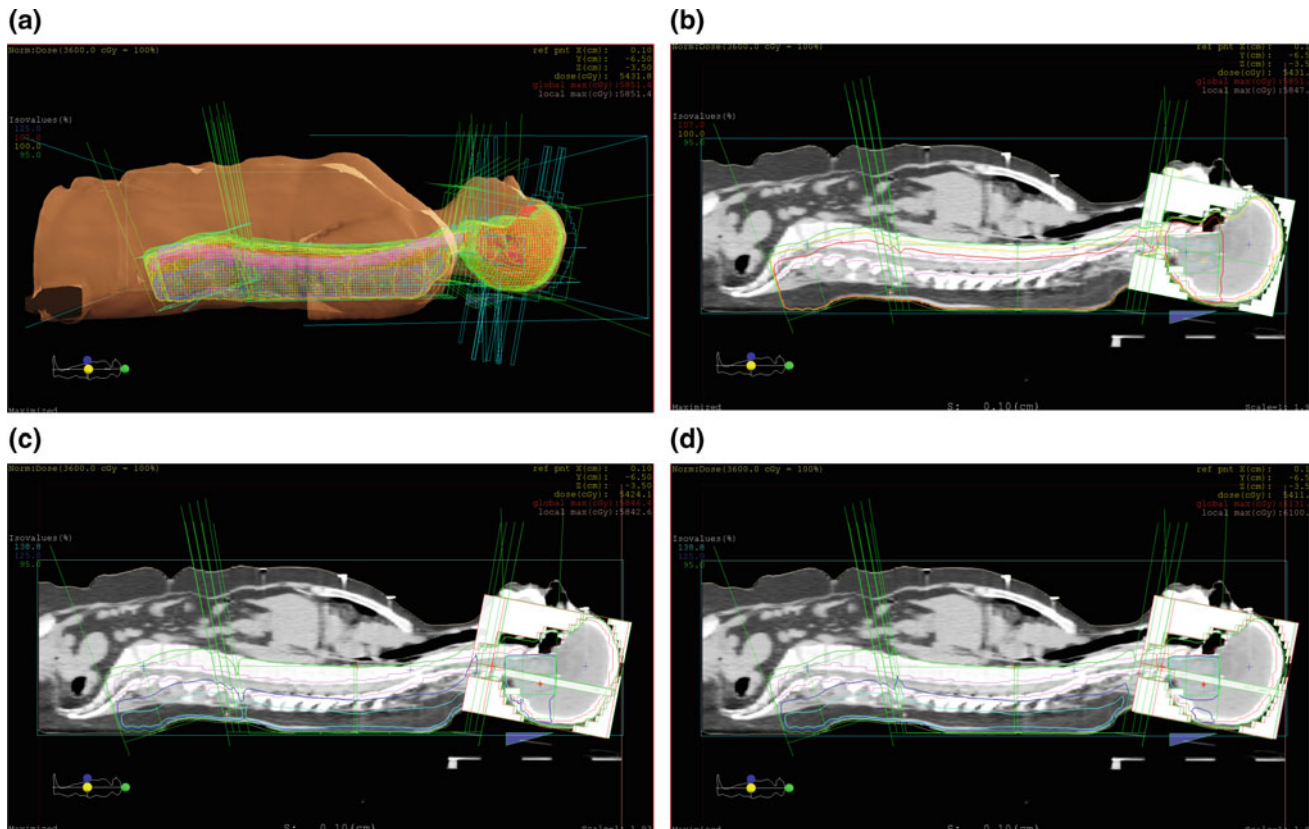
Gap (mm)	D_{\max} (Gy)	Local maximum (Gy)	Depth of the 95% isodose line (cm)	Depth of the 100% isodose line (cm)	Depth of the 125% isodose line (cm)	Transversal coordinate
2	58.48	55.32	8.60	7.50	4.60	-49.90
4	58.46	55.42	7.34	6.76	4.50	-49.80
5	58.46	55.47	7.00	6.50	4.40	-49.75

Table 7 The values of the parameters in the middle of the overlapping areas produced by moving the cranial fields and upper spinal field, the one towards to the other

Overlapping (mm + mm)	D_{\max} (Gy)	Local maximum (Gy)	Treatment volume covered by 95% isodose line	Treatment volume covered by 100% isodose line	Treatment volume covered by 125% isodose line	Transversal coordinate
2 + 2	58.49	46.86	Yes	Yes	Partially	-16.00
3 + 3	58.48	48.36	Yes	Yes	Partially	-16.00
4 + 4	58.46	49.56	Yes	Yes	Partially	-16.00
5 + 5	58.46	50.56	Yes	Yes	Yes	-16.00

Table 8 The values of the parameters in the middle of the gap areas produced by moving the cranial fields and upper spinal field, the one away from the other

Gap (mm + mm)	D_{\max} (Gy)	Local maximum (Gy)	Treatment volume covered by 95% isodose line	Treatment volume covered by 100% isodose line	Treatment volume covered by 125% isodose line	Transversal coordinate
2 + 2	58.55	39.25	Yes	Partially	No	-16.00
3 + 3	58.79	37.93	Yes	Partially	No	-16.00
4 + 4	59.25	37.17	Partially	No	No	-16.00
5 + 5	61.31	36.88	Partially	No	No	-16.00

**Fig. 2** a, b The dose distribution in the case of the normal treatment plan; c the isodose distribution in the case of the 5 mm + 5 mm cranial and upper spinal fields overlapping; d the isodose distribution in the case of the 5 mm + 5 mm cranial and upper spinal field gaps

4 Conclusions

The overlaps of a treatment fields simulated by the treatment planning system cause an increase in the local maximum dose values obtained in the middle slice of the overlapping areas. Comparing these values with the local maximum values obtained in the case of the normal treatment plan, the increases of 1.65–3.67 Gy and 3.71–7.03 Gy in the case of the cranial-upper spinal field overlaps and the increases of 3.63–5.45 Gy in the case of the upper-lower spinal fields

were recorded. The appearance of the 125% isodose line at the depth of 6.10 cm, in the case of the 5 mm upper-lower spine fields overlapping (Fig. 2c), makes an increase of 1.04 cm compared to the normal situation. This is especially important due to the fact that spine is positioned at the depth of 6.60 cm at the same location.

On the other side, the gap areas simulated by the treatment planning system cause a decrease in the local maximum dose values. Comparing these values with the local maximum values obtained in the case of normal treatment plan, the decreases of 2.43–4.25 Gy and 3.90–6.65 Gy in

the case of cranial-upper spinal field overlaps. There is no the differences in the local maximum values in the case of gap areas produced between upper spine and lower spine fields.

According to the obtained results, in the case of the 5 mm + 5 mm overlapping between the cranial and the upper spinal field, the total coverage of the target volume by 125% may be a source of damage of spinal cord. On the other side, the partially covered treatment volume by 95% isodose line in the case of the 4 mm + 4 mm and 5 mm + 5 mm gap area between the cranial and the upper spinal field, may cause a relapse of the tumor (Fig. 2d). The all other sources of the uncertainty and errors in these areas may also affect the overdose and underdose problems.

References

1. Medulloblastoma-Childhood: Statistics Homepage, <https://www.cancer.net/cancertypes/medulloblastoma-childhood/statistics>. Last accessed 2017/08
2. Katalin, H., Adrienn, C., et al.: A prospective study of supine versus prone positioning and whole-body thermoplastic mask fixation for craniospinal radiotherapy in adult patients. *Radiother. Oncol.* **102**, 214–218 (2012)
3. Carrie, C., Alapetite, C., Mere, P., et al.: Quality control of radiotherapeutic treatment of medulloblastoma in a multicentric study: the contribution of radiotherapy technique to tumour relapse. The French Medulloblastoma Group. *Radiother. Oncol.* **24**(2), 77e81 (1992)
4. Grabenbauer, G.G., Beck, J.D., Erhardt, J., et al.: Postoperative radiotherapy of medulloblastoma. Impact of radiation quality on treatment outcome. *Am. J. Clin. Oncol.* **19**(1), 73e77 (1996)
5. Sibel, K., Hamit, B., et al.: An evaluation of inter-fractional set-up errors in patients treated with distinct immobilization equipment for varying anatomical regions. *Int. J. Med. Phys. Clin. Eng. Radiat. Oncol.* **5**, 121–129 (2016)
6. Jessie, Y.H., David, S.F., et al.: Accuracy and sources of error of out-of field dose calculations by a commercial treatment planning system for intensity-modulated radiation therapy treatments. *J. Appl. Clin. Med. Phys.* **14**(2)
7. William, A.P., Carolyn, R.F.: A simple technique for craniospinal radiotherapy in the supine position. *Radiother. Oncol.* **78**, 217–222 (2006)

Novel Physical Heterogeneous Breast Phantom for X-Ray Phase Contrast Imaging

A. Daskalaki, A. Malliori, A. Dermitzakis, and N. Pallikarakis

Abstract

This study is aiming to investigate the contribution of phase contrast breast tomosynthesis, in image quality and detectability of mammographic findings, using a breast phantom within a highly heterogeneous background incorporating details that mimic various breast lesions. A physical phantom was constructed with complex background composed of egg white part and lard, mimicking a breast with 40% glandular—60% adipose tissue. Nylon spheres and CaCO_3 specks simulating masses and microcalcifications respectively, were embedded into the mixture at different depths. Mammographic and tomosynthesis images of 44° acquisition arc were obtained, in phase contrast mode with two different object to detector distances of 50 and 150 cm. The experiments were performed using synchrotron radiation at 20 keV within the conventional mean glandular dose (MGD) range. Line contrast measured across two of the mammographic findings was used as evaluation metric, in order to assess quantitatively the detection of breast abnormalities and the image quality from the different modalities. Visual and quantitative assessment of the images acquired, showed that the increase of object to detector distance resulted in superior contrast and stronger edge enhancement for both low and high contrast features. Tomosynthesis images eliminated the overlapping effect and made the in-depth localization of structures possible. Specifically, in case of the low contrast features, the smallest sized mass was hardly detected in the 2D images while it can be well visualized in the BT tomograms. Results of this study showed that tomosynthesis phase contrast imaging is a promising technique that can be proved important for the detection of small details in breast screening and diagnosing.

Keywords

Phase contrast imaging • Synchrotron • Mammography • Breast phantoms • Heterogeneous background

1 Introduction

Mammography is considered the “gold standard” modality for breast screening and diagnosing [1]. However, the rate of missed lesions and false positives remains crucial despite the technical improvements in x-ray sources and digital detectors [2–4]. The influence of overlapping tissues, naturally existing in two-dimensional mammography, can be effectively diminished using breast tomosynthesis (BT) which is a quasi-three-dimensional x-ray imaging technique recently introduced in daily clinical practice for breast cancer screening [5]. This imaging modality, as well as conventional mammography, is based on images acquired in attenuation mode where normal and cancerous breast structures have very close attenuation coefficients, in the photon energy range used for screening, resulting in poor tumor contrast. Phase Contrast (PhC) imaging is an emerging technique based on x-ray attenuation but also on x-ray phase shift arising at the boundaries of different refractive materials, producing images of significant edge enhancement at the boundaries of structures [6, 7]. Preliminary results suggest that it is a promising modality, that could provide useful information leading to improved breast cancer visualization and diagnosing [8, 9]. Moreover, combining PhC with BT could exploit the advantages of both techniques and produce images of enhanced contrast with eliminated overlapping structures at the same time.

Breast phantoms are essential for imaging and dosimetric studies, as well as for image quality evaluations in clinical practice. In our recent study, a homogeneous paraffin slab was used for assessment of image quality and detectability, in BT PhC imaging [10]. However, such phantoms do not

A. Daskalaki (✉) · A. Malliori · A. Dermitzakis · N. Pallikarakis
Biomedical Technology Unit, Department of Medical Physics,
School of Medicine, University of Patras, Patras, Greece
e-mail: dasnatasa@gmail.com

reflect the realistic anatomy of breast tissue. Anthropomorphic phantoms of complex background with cancer mimicking structures, are necessary in order to further optimize BT PhC imaging technique.

The aim of this study is to design and develop a complex phantom characterized by a highly heterogeneous background, mimicking the properties of real breast tissue that could be used to further assess PhC applications for imaging the breast. Our main purpose is to investigate whether the details of the structure are preserved or even enhanced at the edges in the case of a highly heterogeneous background, leading to images of increased tumor and microcalcification (μ Cs) contrast. Our long-term goal is to point out the potential benefits of this technique over conventional x-ray breast imaging methods, to reveal the additional information on breast tumors that it could offer in a clinical setting as well as its optimization and further development towards this direction.

2 Materials and Methods

2.1 Phantom

A physical phantom characterized by heterogeneous texture was designed and used (Fig. 1a) based on the results of a

prior study about materials mimicking the refractive properties of glandular tissue, adipose tissue, μ Cs and breast masses conducted by our team. The phantom was made of the white part of eggs and lard, mimicking a 5 cm thick compressed breast with 40% glandular 60% adipose tissue composition. A 6 cm radius and 5.5 cm thickness cylindrical mold was placed over a heating stirrer and was filled with the mixture. The white part of the eggs was purred into the melted lard. Additionally, 8 nylon spheres of 2.4, 3.2 and 4.8 mm diameter and CaCO_3 powder were placed in different depths, simulating low contrast features such as masses and high contrast details such as μ Cs, respectively. The mixture was heated up to 120 °C under constant rotational velocity until the eggs coagulated and formed a complex texture. The phantom was then cooled at room temperature while sealed into the mold.

The elemental composition and density of the materials used in the phantom are shown in Table 1, while Table 2 presents their linear attenuation coefficient and refractive index decrement values.

2.2 Experimental Set-Up

The experiments were performed at the SYRMEP (SYnchrotron Radiation for MEDical Physics) beam line,

Fig. 1 The breast phantom used in the experimental study: **a** photograph of the physical phantom, **b** schematic representation with embedded low and high contrast features of various sizes

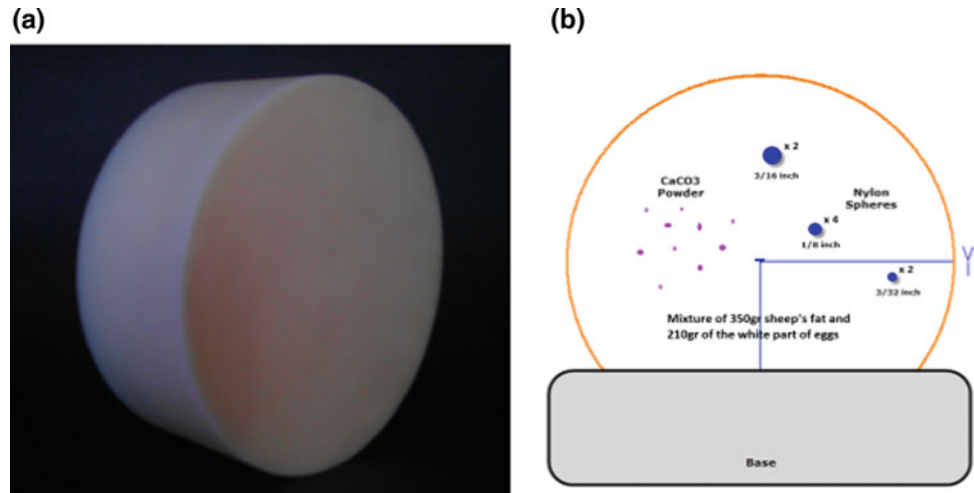


Table 1 Elemental composition (weighted by fraction) and density for the materials used in the study, ^aHammerstain

Material	Composition	Density (g/cm ³)
Lard	C(0.760)H(0.123)O(0.116)N(0.001)	0.90
Egg-white part	C(0.058)H(0.108)O(0.817)N(0.017)	1.03
Adipose ^a	H(0.112)C(0.619)N(0.017) O(0.251) P(0.001)	0.93
Gland	H(0.102)C(0.184)N(0.032)O(0.677)P(0.005)	1.04
Nylon	H(0.108)C(0.627)N(0.114)O(0.158)	1.13
μ Cs	Ca(0.400)C(0.120)O(0.480)	2.80

Table 2 Linear attenuation coefficient and refractive index decrement for the materials used in the study for 20 keV

Energy (keV)	Material	Linear attenuation coefficient, μcm^{-1}	Refractive index, δ
20	Lard	0.44	5.26×10^{-7}
20	Egg-white part	0.80	5.88×10^{-7}
20	Adipose	0.51	5.36×10^{-7}
20	Gland	0.78	5.94×10^{-7}

designed for research in medical diagnostic radiology by ELETTRA Synchrotron Trieste, in cooperation with the University of Trieste and the INFN. The optics are based on a double-crystal Si (111) monochromator which works in an energy range between 8 and 35 keV. At a distance of about 20 m from the source, the area of the x-ray beam was $120 \times 4 \text{ mm}^2$. In order to obtain two dimensional projection images, the phantom was placed on top of a rotating holder moving vertically at each scan and able to rotate 360° fixed at 22.4 m from the source (Fig. 2a). In Fig. 2b, a schematic representation of the experimental arrangement for this study is shown.

The detector was a Teledyne DALSA TDI CCD camera with pixel size $54 \mu\text{m}$ (DM-20-08K10-00-R, 16 bits, 4400×2200 full frame, $54 \mu\text{m}$ pixel- obtained after 4×4 binning mode, 22 cm imaging area).

2.3 Image Acquisition

Projection images were acquired at 20 keV with the phantom being placed at two different distances from the detector, implementing a free space propagation imaging technique. Specifically, the following object-to-detector distances (ODD) were used: (a) 50 cm and (b) 150 cm, with the later set-up resulting in images where the PhC contribution is expected to be stronger. Images are acquired with two imaging modalities, mammography and BT mode. The BT mode was performed with an acquisition arc of 44° and 2° increment resulting in 23 projection images. The incident air kerma (K) measured at the upper surface of the breast

phantom, was calculated for all cases in advance, exploring the relationship between the MGD (D_g) and K:

$$\bar{D}_g = Kgc_sT \quad (1)$$

In this expression, g , c , s and T are conversion parameters depending on factors such as the breast thickness, glandularity, incident spectra and angular range. Their values were taken from Dance et al. [11–13]. The MGD to the breast phantom was set equal to 2.5 mGy according to the European guidelines for quality assurance in breast cancer screening and diagnosing.

2.4 Reconstruction and Evaluation Metrics

The BT slices were reconstructed from projection images, with an in-house developed platform [14] using Filtered Back Projection (FBP) technique, for both ODD of 50 and 150 cm. All images were pre-filtered with the use of Ram-Lak filter. A pseudo-3D representation of the phantom was produced from axial planes reconstructed at every 0.1 mm of the total volume. Apart from visual assessment of the images, quantitative evaluation metrics were also performed to assess the features of interest in both 2D and BT imaging. Specifically, the Line Contrast (LC) Figure of Merit (FoM) was used, which as presented in [15], is based on analysis of data extracted from line profiles within the image. Regions of Interest (ROIs) are placed on these line profiles and following an analysis, a normalized value is calculated depicting the contrast within the image and at the same time evaluating the edge features. In more detail,

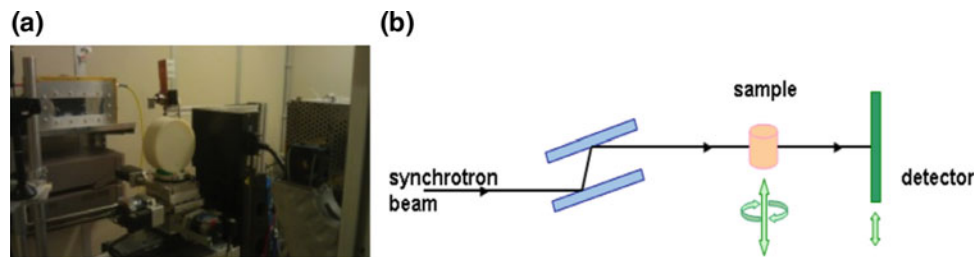


Fig. 2 Experimental set-up at SYREP beamline: **a** photograph of the phantom placed on the rotating holder, **b** schematic representation of the setup

multiple different line profiles are calculated, each one consisted of several lines an average of which is taken in order to compensate noise and eliminate values fluctuation. The line profiles are then shifted by adding the absolute minimum value and normalized to max value, in order to be objective when different images are to be compared. In each line profile, multiple ROIs are set in the regions where there is transition from one material to another. Within each ROI the maximum to minimum difference along with 1st derivative is calculated and stored. Then the LC is calculated by finding the maximum and average difference along the ROIs.

3 Results and Discussion

Two sets of BT slices were produced with the phantom being placed at 50 and 150 cm, respectively and the quality of reconstructed features of interest was compared for the two set-ups. Moreover, an additional comparison with the two corresponding 2D images at these ODDs, was performed. All features of interest (nylon spheres representing masses and CaCO_3 powder simulating μCs) were better visualized at BT mode and at the ODD of 150 cm. The improvement of image quality at this set-up can be explained due to the combined advantages of stronger phase contrast (or edge enhancement) effect as the phantom is placed further away from the detector and superimposed structures being removed in BT planes. In Fig. 3, a projection image of the whole phantom is shown, depicting two regions of interest (ROIs) that were chosen as representatives of a low and high contrast feature, respectively, to demonstrate the abovementioned observations. Specifically, the first ROI shows the smallest sized mass (2.4 mm) at 50 cm (Fig. 3a) and 150 cm (Fig. 3b) while at the second ROI, a CaCO_3

spec is visualized at the same distances of 50 cm (Fig. 3e) and 150 cm (Fig. 3f) in 2D mode as well. Similarly, in Fig. 3c, d, BT tomograms of the slices where the smallest mass is in-focus, are presented for both ODDs while Fig. 3g, h show the in-focus planes for the CaCO_3 at the two ODDs. The images on the right columns acquired at 150 cm, in all cases Fig. 3b, d, f, h, demonstrate enhanced contrast and improved image quality overall. All structures within this highly heterogeneous background, manage to appear with sharper edges, making it possible for attention to be drawn to the finest detail. This can be attributed to the fact that for this ODD (both in 2D and BT mode) we have significant phase contrast effect, while images on the left columns Fig. 3a, c, e, g are acquired at 50 cm where the absorption contrast is dominant. Moreover, BT allows depth localization of features. This proved particularly important for the case of the smallest mass which can hardly be seen in the 2D images due to the overlapping structures of this complex phantom. The visual observations were in agreement with quantitative evaluation performed for both the low and high contrast features. Figure 4 shows line profiles measured across the BT images of mass and CaCO_3 at ODD of 50 cm (Fig. 4a, c) and 150 cm (Figs. 4b, d), respectively. These line profiles, are produced by averaging several lines and applying spline smoothing fit (smoothing parameter $p = 0.9$) for illustration purposes in order to compensate for the presence of high noise. Comparing these line profiles, the first thing to notice is that in both cases of mass and CaCO_3 features, larger ODD results in narrower profiles, with steeper and clearer edges. This is in agreement with the visual observations of Fig. 3c, d, g, h, where in both cases the contrast of the feature from the background is higher when ODD is increased, and at the same time the edges and shape of the feature are sharper and better defined. This is a result of the PhC effect which is dominant in large ODD. In details,

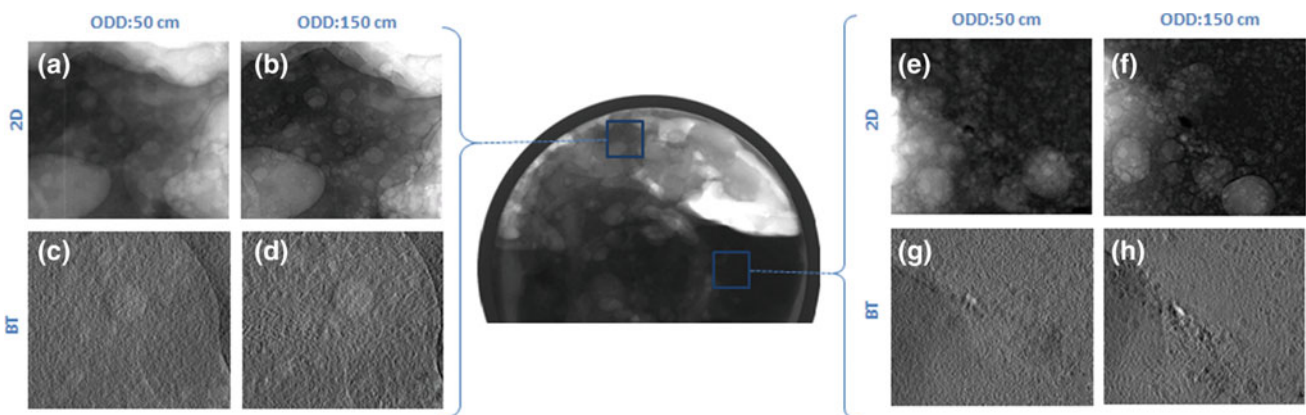
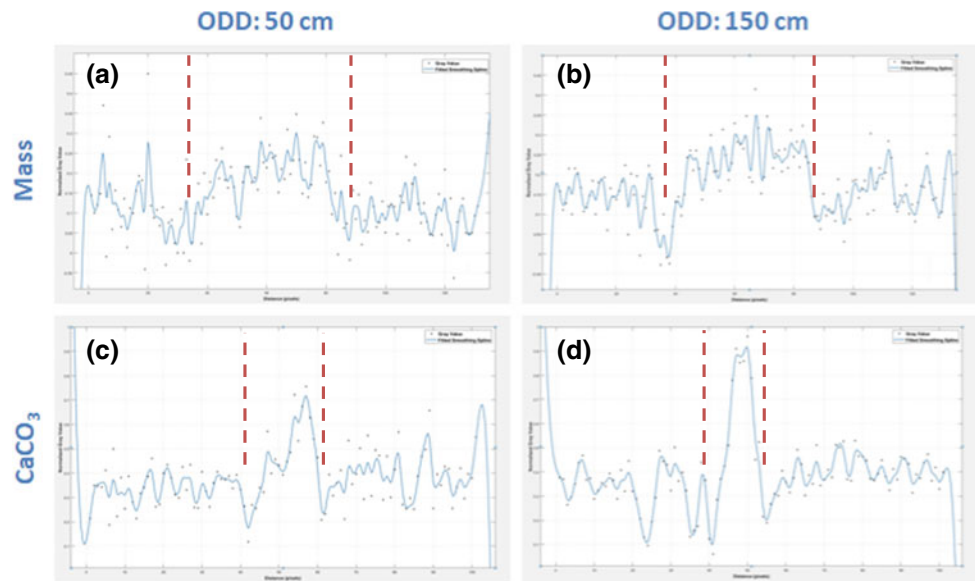


Fig. 3 Projection image of the phantom, depicting two ROIs. The ROI on the left side illustrates a low contrast mass mimicking feature imaged in 2D mode at ODDs of 50 cm (a) and 150 cm (b) and in BT mode at ODDs of 50 cm (c) and 150 cm (d). Similarly, on the right

corresponding images of a high contrast μC mimicking feature are shown for 2D at 50 cm (e) and 150 cm (f) and BT at 50 cm (g) and 150 cm (h), respectively

Fig. 4 Line profiles measured across the BT images of mass and CaCO_3 at ODD of 50 cm (a, c) and 150 cm (b, d)



comparing the line profiles of mass feature (Fig. 4a, b, it is seen that in the case of 150 cm ODD the exact contours of the mass are clearly distinguished, while when 50 cm ODD is used the exact beginning of the mass cannot be determined clearly. The characteristic PhC edge intensity drop is present when larger ODD is used, followed by a steep signal increase resulting in edge enhancement. This is also depicted in the quantitative LC FOM analysis, which taking into consideration images' edge features, shows an increase of 17% when 150 cm ODD is used in compare to 50 cm ODD.

As far as CaCO_3 feature is concerned, although it is clearly distinguished from the background in both distances, due to its high attenuative nature, the edge enhancement effect of PhC in larger ODD is apparent. As seen in the corresponding line profiles (Fig. 4c, d, both the edges detection capability along with the overall contrast from the surrounding tissue is increased when 150 cm ODD is used. This is also confirmed from the LC FOM, which shows a 12% increase when larger ODD is used, being in accordance with visual observations, where the exact borders and shape of the feature can be clearly distinguished in large ODD.

4 Conclusion

In this study, a novel physical breast phantom with heterogeneous background has been developed. The phantom is focused for use in PhC X-ray imaging, using mammographic tissue mimicking materials. Experimental tests conducted using synchrotron radiation, confirmed the appropriateness of materials used. Both visual observations and quantitative analysis of images produced with 2D and BT PhC techniques, concluded that feature contrast and overall detectability is increased using the latter technique.

Acknowledgements This research is implemented through the Operational Program “Human Resources Development, Education and Lifelong Learning” and is co-financed by the European Union (European Social Fund) and Greek national funds.

References

1. <https://www.ncbi.nlm.nih.gov/pubmed/18345253>
2. Pissano, E.D., Yaffe, M.J.: Breast cancer screening: should tomosynthesis replace digital mammography. *JAMA* **311**(24), 2488–2489 (2014)
3. Rodriguez-Ruiz, A., Castillo, M., Garayoa, J., Chevalier, M.: Evaluation of the technical performance of three different commercial digital breast tomosynthesis systems in the clinical environment. *Phys. Med.* **32**, 767–777 (2016)
4. Gong, X., Glick, S.J., Liu, B., et al.: Computer simulation study comparing lesion detection accuracy with digital mammography, breast tomosynthesis, and cone-beam CT breast imaging. *Med. Phys.* **A33**, 1041–1052 (2006)
5. Sechopoulos, I.: A review of breast tomosynthesis. Part I. The image acquisition process. *Med. Phys.* **40**(1) (2013)
6. Bravin, A., Coan, P., Suotti, P.: X-ray phase contrast imaging: from preclinical applications towards clinics. *Phys. Med. Biol.* **58**, R1–R35 (2013)
7. Bliznakova, K.: Application of synchrotron radiation in mammography. *Recent Pat. Med. Imaging* **2**, 94–110 (2012)
8. Sarno, A., Mettievier, G., Golosio, B., Oliva, P., Spandre, G., Di Lillo, F., et al.: Imaging performance of phase-contrast breast computed tomography with synchrotron radiation and a CdTe photon-counting detector. *Phys. Med.* **32**(5), 681–690 (2016)
9. Olivo, A., Rigon, L., Vinnicombe, S.J., Cheung, K.C., Ibbison, M., Speller, R.D.: Phase contrast imaging of breast tumours with synchrotron radiation. *Appl. Radiat. Isot.* **67**, 1033–1041 (2009)
10. Daskalaki, A., Pallikarakis, N.: Image quality evaluation of phase contrast mammographic techniques. In: IFMBE Proceedings of World Congress on Medical Physics Biomedicine Engineering, vol. 68/1, pp 9–13. Prague, Czech Republic (2018)
11. Dance, D.R., Young, K.C., van Engen, R.E.: Estimation of mean glandular dose for breast tomosynthesis: factors for use with the

- UK, European and IAEA breast dosimetry protocols. *Phys. Med. Biol.* **56**, 453–471 (2011)
12. Dance, D.R., Skinner, C.L., Young, K.C., et al.: Additional factors for the estimation of mean glandular dose using the UK mammography dosimetry protocol. *Phys. Med. Biol.* **45**, 3225–3240 (2000)
 13. Dance, D.R., Young, K.C., van Engen, R.E.: Further factors for the estimation of mean glandular dose using the United Kingdom, European and IAEA breast dosimetry protocols. *Phys. Med. Biol.* **54**, 4361–4372 (2009)
 14. Kamarianakis, Z., Buliev, I., Pallikarakis, N.: A platform for image reconstruction in X-Ray imaging: medical applications using CBCT and DTS algorithms. *Comput. Sci. J. Moldova* **22**(2), 236–252 (2014)
 15. Dermitzakis, A., Daskalaki, A., Bliznakova, K., Pallikarakis, N.: New line contrast figure of merit for image quality assessment. In: *IFMBE Proceedings of World Congress on Medical Physics and Biomedical Engineering*, vol. 51, pp. 26–28. Toronto 7–12 June 2015

Computer Tomography Tube Voltage and Phantom Dimensions Influence on the Number of Hounsfield Units

Tatjana Ignjic, Bojan Pavicar, Goran Kolarevic, and Zeljko Ranogajec

Abstract

Hounsfield units (HU) are a dimensionless units universally used in computed tomography (CT) scanning to express CT numbers in a standardized and convenient form. Calibration curve (CC) implemented in radiotherapy treatment planning system (TPS) shows the dependence of HU on relative electron density (RED). Radiotherapy treatment planning process is based on data from the CC and linear accelerator (Linac) data set. RED is constant and specified for each material, but the HU can change depending on several factors. Dosimetric phantom in radiotherapy properly represents human anatomy and enable thorough analysis of both the imaging and dosimetry system. For the purpose of CC checking, two phantoms were used: Catphan 504 (The Phantom Laboratory) and CIRS 062MA (Computerized Imaging reference Systems, Inc.). The aim of the paper was to check whether the HU depends on the dimensions of the phantom. Catphan 504 phantom was scanned first, in order to verify the HU determination methodology. After that, CIRS 062MA phantom representing both abdomen and head configuration was scanned. By analyzing Catphan 504 phantom obtained scanning results, it was concluded that the HU values are correctly determined, since the results are in accordance with the manufacturer's recommendations. Based on results of CIRS 062MA phantom scan, the HU dependence on the CT simulator tube voltage was confirmed. Significant difference in HU for high density materials (up to 135 HU) due to different phantom sizes was observed.

Keywords

Hounsfield units • Calibration curve • Catphan 504 • CIRS 062MA

1 Introduction

CT is the primary imaging modality used in radiation oncology planning. A dedicated radiation therapy CT scanner, with accessories (e.g. flat table identical with those of the treatment units, lasers for positioning, immobilization, and image registration devices, and large bore: $D > 80$ cm) to accurately reproduce treatment conditions is called CT simulator [1]. The CT image data set thereby obtained, with precise localization of patient anatomy and tissue density information is the basis for the creation of a radiation plan [2].

Hounsfield units are a unit of measure that represents the different density levels both from tissues and other substances. The density of pure water was arbitrarily set at 0 HU and that of air at -1000 HU [3].

HU is calculated according to the expression:

$$HU = 1000 \times \frac{\mu - \mu_{water}}{\mu_{water} - \mu_{air}}$$

where μ_{water} and μ_{air} are respectively the linear attenuation coefficients of water and air. So, HU value depends entirely on linear attenuation coefficient of medium through the radiation is spread [4].

The linear attenuation coefficient is described as the mathematical sum of probabilities per unit length for the interaction of photons with atoms of matter [5]. It represents the fraction of a beam of X-rays or gamma rays that is absorbed or scattered per unit thickness of the absorber. This coefficient depends on the energy of photons, density and thickness of the absorbent material [6]. CT detects the linear attenuation coefficient of each pixel in the transverse imaging plane [2]. It is expressed by equation:

$$I = I_0 e^{-\mu x}$$

Since a linear attenuation coefficient depends on the density of a material, the mass attenuation coefficient is often reported for convenience [7].

T. Ignjic (✉) · B. Pavicar · G. Kolarevic · Z. Ranogajec
International Medical Centers – Affidea, Banja Luka, Bosnia and Herzegovina
e-mail: tatjana.ignjic@affidea.com

Computerized TPSs in radiotherapy are based on calculating algorithms that are using tissue heterogeneity or specific mass attenuation coefficient for different tissues [8]. The prerequisite for this is the existence of a CC within TPS which provides a link between the HU and the relative tissue density (RED) [9].

CC establishment is carried out in strictly defined conditions and with predefined parameters. Treatment planning process is partly based on data from such CC. This means that the same data set is used for treatment planning and dose calculation on different localizations (for head and neck, as well as for thorax and abdomen).

The difference in the dimensions of the motioned localizations is obvious. It is therefore very important to investigate whether the dimensions of the tissue (both the body and the phantoms) affect the number of HU. Accordingly, the question that arises is whether the same CC can be used to make treatment plans of different localizations?

Potentially large differences in HU would significantly affect the dose calculation process. This would ultimately lead to an imprecise dose delivery which could have fatal consequences for patients. Hence, the basic idea of this study is prevention of accidents in radiotherapy caused by inaccurate HU determination.

2 Materials and Methods

The measurements were performed on a 16 slice GE LightSpeed RT CT simulator using the CIRS 062MA (Computerized Imaging reference Systems, Inc.) and Catphan 504 phantoms (The Phantom Laboratory).

The study of the impact of phantom dimensions on HU was carried out through several stages. Initially, it was important to determine correctness of the methodology of determining HU. This was done by scanning Catphan 504 phantom on different tube voltages. Reference HU values provided by manufacturer were compared with the obtained results. Manufacturer gave reference HU values for 3

different voltages (Table 1), while measurements were conducted on 4 CT tube voltages.

The next step was scanning the entire CIRS 062MA phantom. Unlike Catphan 504, which is usually used to check CC, CIRS 062MA has inserts that simulate human tissue. Besides this, the ability to make scans in two configurations (head and abdomen) impose it as logical solution for this measurements. For our knowledge, there are no similar studies conducted on this type of phantom.

At the end, the CIRS 062MA phantom internal cylinder (representing head configuration) was scanned alone, under the same conditions as the entire phantom. The idea was to compare HUs for the same materials (on the same positions) in two different configurations.

In ordinary clinical practice, single CT protocol is used for all anatomical regions. According to that, the tube voltage is 120 kV with automatic adjustment of the tube current (automatic exposure control—AEC). In this study, operating tube voltage options were 80, 100, 120 and 140 kV.

Catphan 504 phantom configuration has been selected by Varian Medical Systems in order to supplement their Cone beam CT (CBCT) procedure. The phantom diameter is 15 cm and its length is 20 cm and it could be used to measure HU for materials with different RED. The schematic representation of the phantom cross section is given in Fig. 1.

The phantom is divided into the following modules: CTP528 (high resolution module), CTP404 (sensitometry-CT number linearity, Z-direction low contrast resolution, slice thickness and pixel size), CTP515 (low contrast) and CTP486 (image uniformity module) [10].

Of particular interest to this study is the module CTP504, Fig. 2. It is consisted of inserts (Teflon, Delrin, Acrylic, Polystyrene and low density polyethylene-LDPE, polymethyl-pentene PMP and air) in the range of -1000 HU to $+1000$ HU [10].

Phantom CIRS 062MA (Electron density phantom), Fig. 3, consists of an inner (representing head configuration) and outer cylinder (representing abdomen configuration) made from Plastic Water®-LR. There are 17 holes in the

Table 1 Suggested HU reference values for materials in the sensitometry module in Catphan 504 phantom for three X-ray energies [10]

	Expected HU values median [min, max]	Expected HU values median [min, max]	Expected HU values median [min, max]
	80 kV	120 kV	140 kV
Air	-959 [-1001, 938]	-962 [-1001, 941]	-956 [-999, 939]
Teflon	951 [929, 976]	905 [882, 936]	895 [862, 923]
Delrin	321 [305, 336]	334 [307, 344]	337 [330, 346]
Acrylic	95 [81, 111]	118 [108, 128]	122 [114, 131]
Polystyrene	-66 [-83, -48]	-36 [-47, -26]	-29 [-39, -18]
LDPE	-123 [-136, 108]	-90 [-103, -80]	-83 [-95, -72]
PMP	-206 [-217, 192]	-176 [-186, 170]	-169 [-178, 161]
Center	67 [55, 81]	93 [86, 101]	99 [93, 106]

Fig. 1 Catphan 504 phantom
[10]

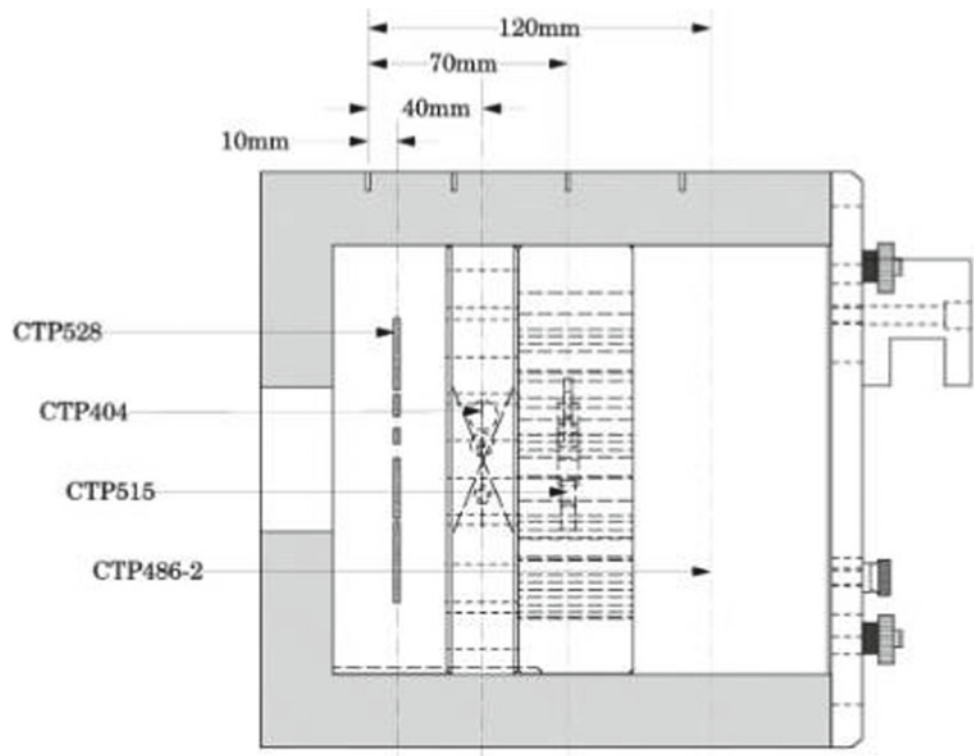
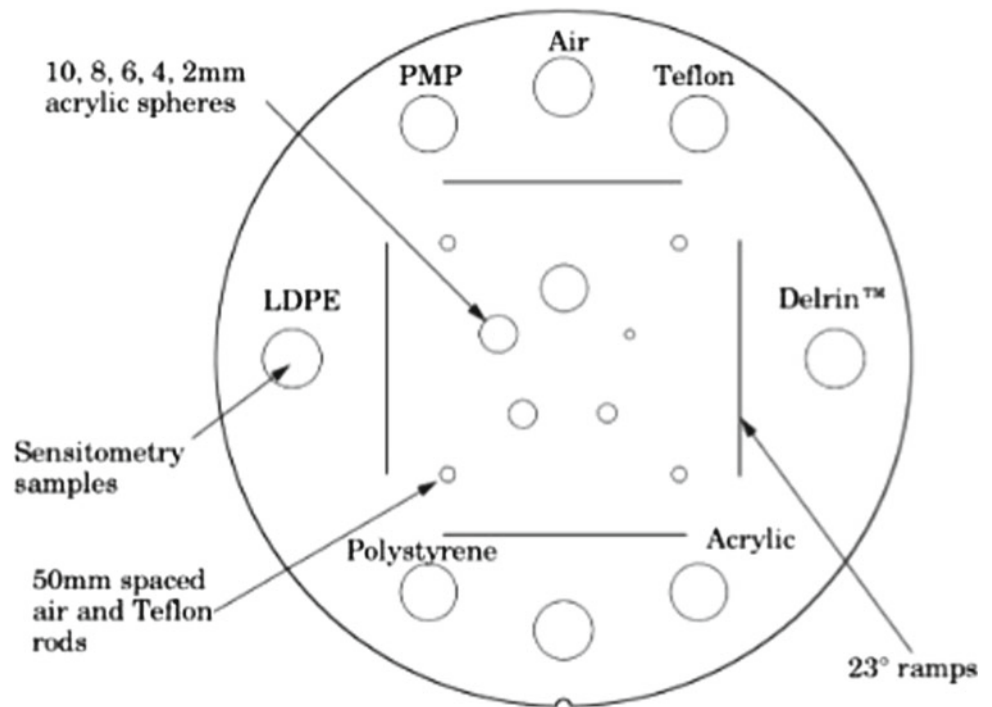


Fig. 2 Catphan 504 cross section
[10]



cylinders in which nine different tissue equivalent electron density plugs can be arranged. In addition to the rods, any ion chamber can be placed in the holes. The dimensions of the inner cylinder are $\text{Ø } 180 \text{ mm} \times 50 \text{ mm}$ ($\text{Ø} \times \text{D}$), outer

$330 \text{ mm} \times 270 \text{ mm} \times 50 \text{ mm}$ ($\text{W} \times \text{H} \times \text{D}$) and rods $\text{Ø } 30 \text{ mm} \times 50 \text{ mm}$ ($\text{Ø} \times \text{L}$) [11].

Figures 4, 5 and 6) show the cross section of the scanned phantoms with marked positions of measuring points.

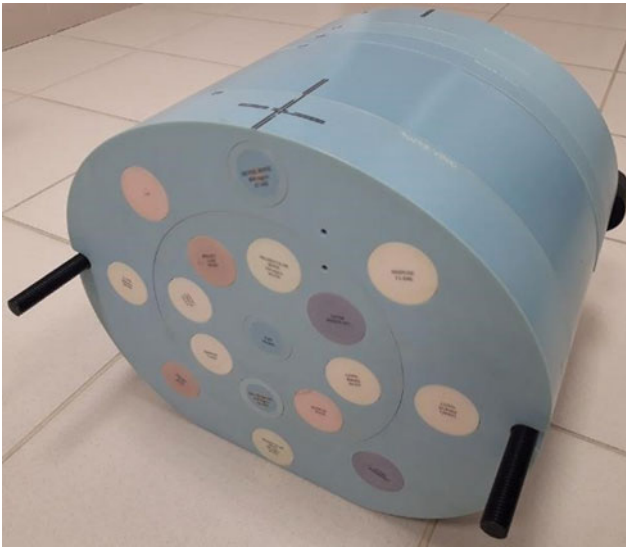


Fig. 3 CIRS 062MA phantom

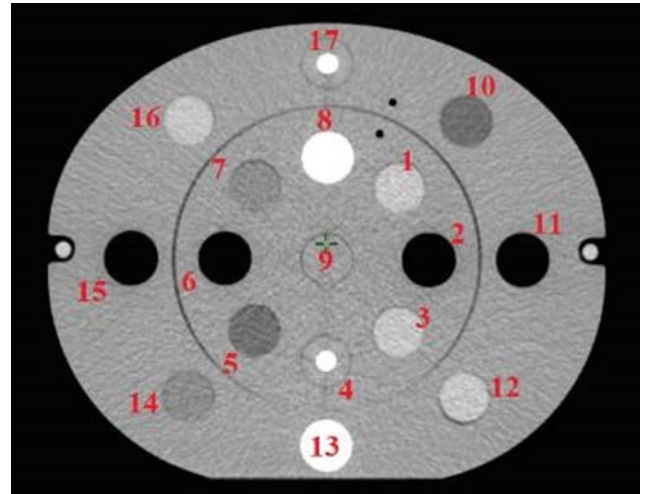


Fig. 5 CIRS 062MA configuration

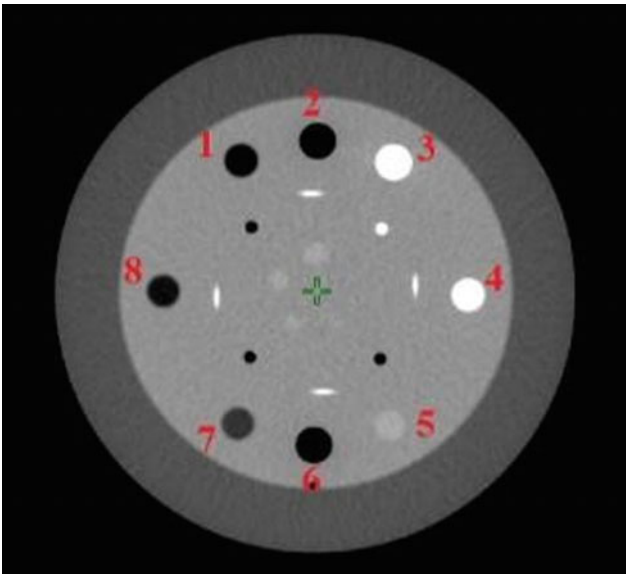


Fig. 4 Catphan 504

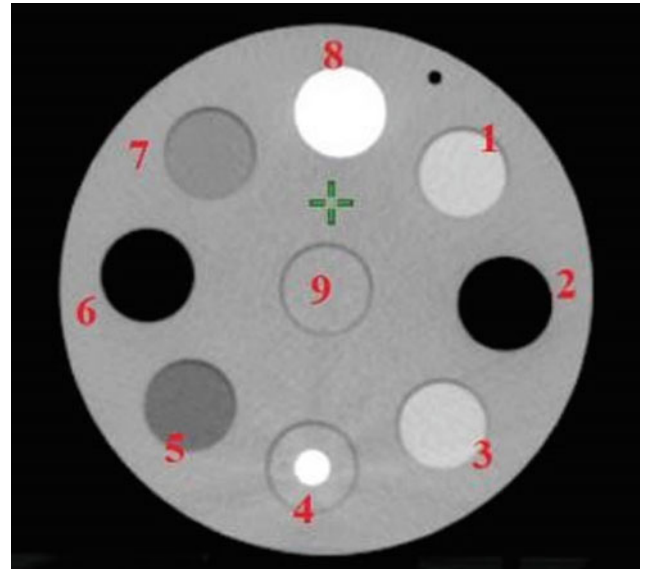


Fig. 6 CIRS 062MA abdomen configuration head

Slice thickness was 2.5 mm. Data analysis was performed after importing images into the TPS. HU were determined within the small region of interest (ROI) in each material.

3 Results

3.1 Catphan 504 Scan

See Table 2.

3.2 CIRS 062 MA Abdomen Configuration Scan

See Table 3.

3.3 CIRS 062 MA Head Configuration Scan

See Table 4.

Table 2 Measured HUs for Catphan 504 phantom on four different voltages

	80 kV	100 kV	120 kV	140 kV
Air	-945	-947	-950	-940
Teflon	944	924	902	897
Delrin	315	334	327	333
Acrylic	114	111	125	128
Polystyrene	-58	-37	-18	-14
LDPE	-120	-92	-90	-73
PMP	-192	-181	-171	-160
Center	74	81	100	103

Table 3 Measured HU values for CIRS 062MA phantom (abdomen and head configuration)

		80 kV (400 mA)	100 kV (400 mA)	120 kV (400 mA)	140 kV (380 mA)	
Head configuration	1	Liver	103	66	51	60
	2	Lung inhale	-783	-796	-809	-801
	3	Muscle	78	62	61	50
	4	Dense bone	1188	959	837	762
	5	Adipose	-67	-57	-63	-68
	6	Lung exhale	-506	-500	-504	-492
	7	Breast	-52	-47	-32	-15
	8	Trabecular bone	352	277	244	232
	9	Water	14	-10	-10	-12
Abdomen configuration	10	Adipose	-46	-74	-45	-59
	11	Lung exhale	-481	-498	-483	-499
	12	Liver	62	56	46	69
	13	Trabecular bone	367	305	250	237
	14	Breast	-30	-15	-5	-26
	15	Lung inhale	-782	-801	-804	-798
	16	Muscle	59	65	53	66
	17	Dense bone	1194	1010	881	804

Table 4 Measured HU values for CIRS 062MA head configuration scan on four different voltages

		80 kV (400 mA)	100 kV (400 mA)	120 kV (400 mA)	140 kV (380 mA)	
Head configuration	1	Liver	58	66	61	64
	2	Lung inhale	-812	-812	-810	-810
	3	Muscle	68	65	63	63
	4	Dense bone	1324	1098	966	885
	5	Adipose	-73	-61	-64	-56
	6	Lung exhale	-496	-501	-504	-506
	7	Breast	-36	-21	-21	-20
	8	Trabecular bone	393	323	288	262
	9	Water	-2	9	1	3

4 Discussion

Figure 7 and Table 2 show the results of the Catphan 504 phantom scan. Since the results obtained for a wide range of HU values were in accordance with the manufacturer’s recommendations, it has been concluded that HU determination methodology is correct [12].

HUs for CIRS 062MA abdomen configuration on different CT tube voltages are listed in Table 3 and shown in Fig. 8. The difference is observable for high density tissues. This difference is best seen in bone-simulating materials, as they are highly heterogeneous materials. Based on the same data, it is obvious that the increase in the X-ray tube voltage

on CT scanner decreases the HU. Although the differences for less density materials are less noticeable, it is possible to see them for liver and muscle. Under 0 HU these differences disappeared.

Figure 9 shows the comparison between Catphan 504 and CIRS 062MA phantom on the same scale. It is noticeable that above 0 HU the curves for these phantoms do not follow the same trend. Only the curves belonging to the CIRS phantom match the calibration curve.

Results of head configuration CIRS 062MA phantom scan are listed in Table 4. Figure 10 shows the comparison between results obtained by scanning CIRS 062MA abdomen configuration versus head configuration. The dashed lines

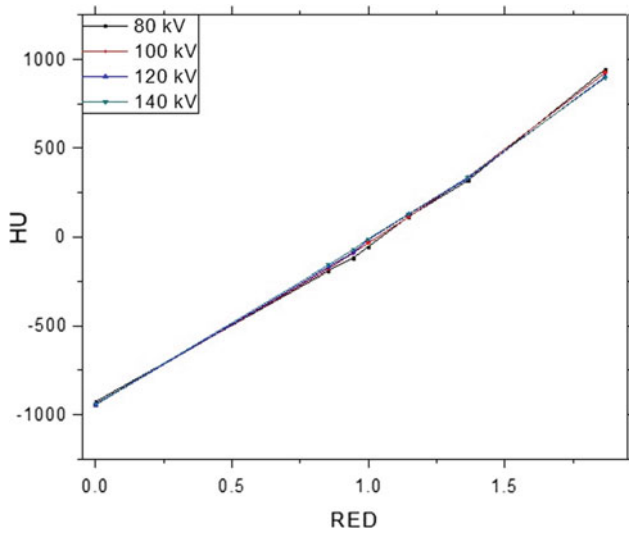


Fig. 7 Catphan 504 phantom scan on four different voltages

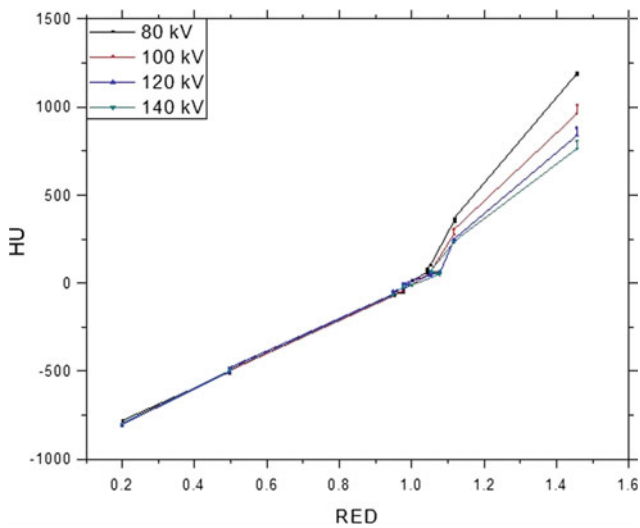


Fig. 8 CIRS 062MA phantom (abdomen configuration) scan

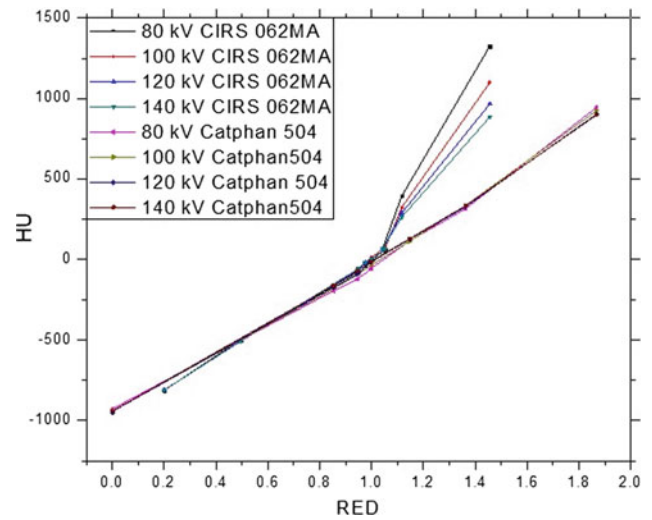


Fig. 9 Catphan 504 and CIRS 062 MA head configuration scan comparison

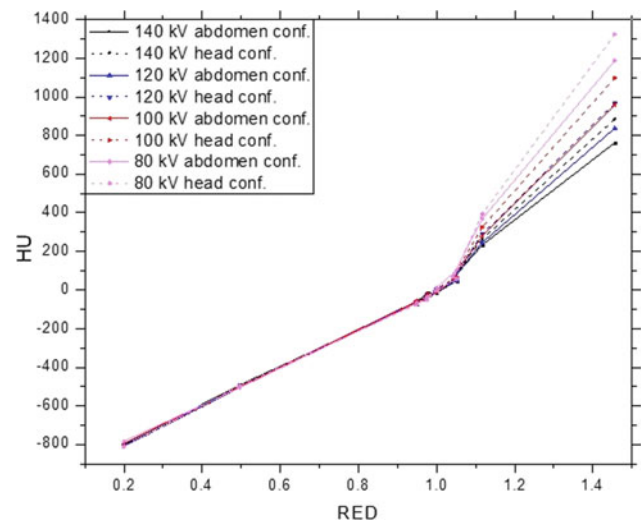
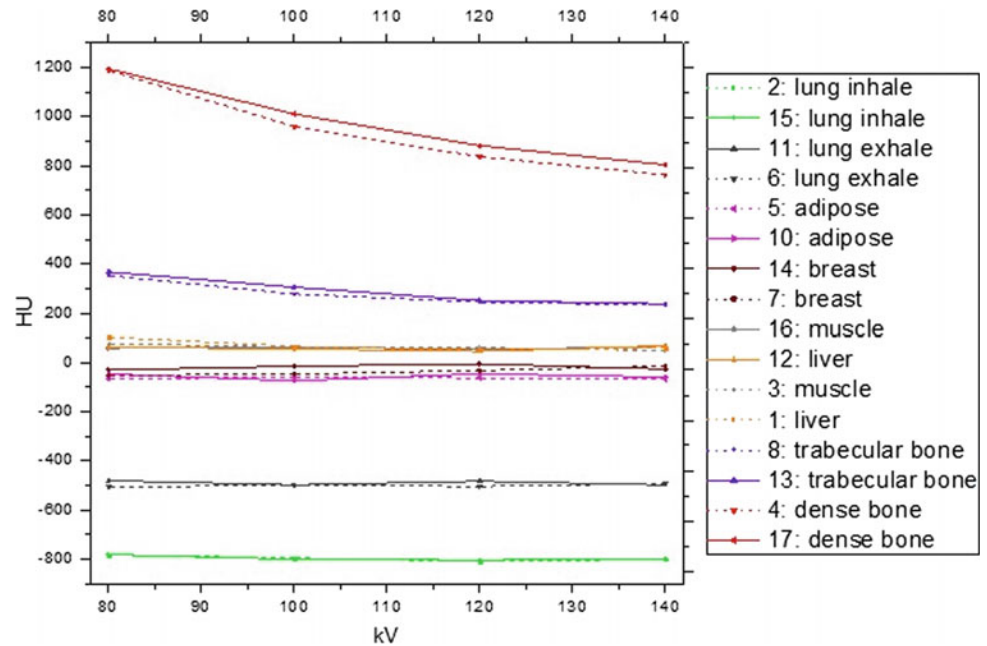


Fig. 10 CIRS 062MA abdomen and head configurations scan comparison

Fig. 11 CIRS 062MA phantom scan—voltage dependence



show the results of the measurement for the insert places in the inner cylinder, while the same materials from the outer shell of the phantom are shown in full lines. It can be seen that HU values for inner cylinder materials follow the same trend as HU values for outer phantom part materials. Differences in HU values for the same materials scanned at different voltages become noticeable for denser materials.

HU values for high density materials are significantly different from the analogous materials at the same positions when phantom is scanned in head configuration in comparison to abdomen configuration (Fig. 11).

Simple calculations show that differences in HU numbers between the same materials, in the same positions under the same conditions, can move up to 135 HU due to different dimensions of the phantom.

Linear attenuation coefficient definition explains the difference in HU between the analogous tissue inserts in inner and outer cylinder of the CIRS 062MA phantom. Since the inner cylinder is scanned alone, it was surrounded by a thick layer of air, unlike the entire phantom which can be considered as inner cylinder surrounded by wrapper, significantly denser than air. It means that in abdomen configuration more attenuator is placed on the beam path. Since linear attenuation coefficient depends on type and thickness of material, it is expected that altered signal reach detector in CT.

Additionally, the CT detectors have some energy dependence, and the scatter contribution further complicate situation. Scatter contribution is dependent on beam width and scanned object size, shape and composition [10].

The internal CIRS 062MA phantom cylinder dimensional corresponds to the human head, while the entire phantom corresponds to human torso. It is proven that the HU number depends on the dimensions of the phantom, and according to that fact, patient scanning protocols need to be adjusted to particular situation.

5 Conclusions

By scanning Catphan 504 phantom and comparing results with the reference values, HU determination methodology is confirmed.

It was shown that HUs are dependent on the CT tube voltage. This is the reason why CC in TPS was established on 120 kV, and in the same time justification of scanning protocol based on same voltage (120 kV) for each patient.

According to results shown in Fig. 9, Catphan 504 phantom can't be used for CC assessment.

Based on CIRS 062MA phantom scan, it was founded that HUs depend on size of phantom in the region of high-density materials (bonelike materials). It means that once established CC is not appropriate for each human body localization. According to these results, HUs of particular tissue are expected to have different value depending on depth in human body.

In order to avoid dose calculation mistakes, it is recommended to establish CC adapted to various localizations.

Conflict of Interest None declared.

References

1. Garcia-Ramirez, J.L., et al.: Performance evaluation of an 85-cm-bore X-ray computed tomography scanner designed for radiation oncology and comparison with current diagnostic CT scanners. *Radiat. Oncol. Biol. Phys.* **52**, 1123–1131 (2002)
2. Khan, F.M., Gibbons, J.P.: *Treatment Planning in Radiation Oncology*. Wolters Kluwer, Philadelphia, USA (2010)
3. Hoffer M.: *CT Teaching Manual*. Georg Thieme Verlag (2000)
4. Fosbinder, R., Orth, D.: *Essentials of Radiologic Science*. Wolters Kluwer, Philadelphia, USA (2010)
5. Bushberg, J.T., Boone, J.M.: *The Essential Physics of Medical Imaging*. Lippincott Williams & Wilkins, Philadelphia, USA (2001)
6. Cann, C.E.: Quantitative CT applications: comparison of current scanners. *Radiology* **162**, 257–261 (1987)
7. McKetty M.H.: The AAPM/RSNA physics tutorial for residents. *Radiographics* **18**, 151–163 (1998)
8. Birnbaum, B.A., et al.: Multi-detector row CT attenuation measurements: assessment of intra- and interscanner variability with an anthropomorphic body CT phantom. *Radiology* **242**, 109–119 (2007)
9. Gulliskrud, K.: How to measure CT image quality: Variations in CT-numbers, uniformity and low contrast resolution for a CT quality assurance phantom. *Physica Medica* **30**, 521–526 (2014)
10. The Phantom Laboratory: *Catphan 504 Manual*. Salem, NY (2013)
11. CIRS Product Guide—CBCT Electron Density & Image Quality Phantom System: Model 062M, 062MA & 062MQA. Norfolk, Virginia (2013)
12. Skaug Sande, E.P., et al.: Interphantom and interscanner variations for HU—establishment of reference values for HU in a commercial QA phantom. *Phys. Med. Biol.* **55**, 5123 (2010)

Dose Optimization of CT Thorax Exam in University Clinical Hospital Mostar

Ivan Lasić, Kristina Galić, Adnan Beganović, Valentina Lasić, Lejla Čiva, and Antonela Krasić-Arapović

Abstract

Aim To determine the impact of decreasing patient dose on image quality or diagnostic information during diagnostic thorax examination using computed tomography/CT/at University Clinical Hospital Mostar/UCH/. **Methods** Images were acquired using a CT General Electric LightSpeed 16 slice scanner. There were 62 adult patients with different input diagnoses involved in this research, which lasted from March 1st 2018 to June 1st 2018. After determination of patient dose, the objective was optimization of protocol parameters for the purpose of lowering the dose received by patients, in a manner that does not jeopardize image

quality or diagnostic information. A thoracic radiologist using a double-stimulation method assessed image quality according to the European Guidelines on image quality criteria for CT 16262/EUR16262 EN/, followed by calculation of dose efficiency factor figure of merit/FOM/. **Results** Changing the protocol parameters enabled a significantly decreased patient dose. Visualization of pulmonary anatomical structures was not significantly changed by decreasing the dose. The mean FOM before optimization was 1.28 mSv^{-1} and 2.46 mSv^{-1} after optimization ($p < 0.001$). **Conclusion** By changing the parameters of the protocol a significant dose reduction was achieved without affecting the diagnostic information.

Keywords

Dose • Optimization • Computerized tomography • CTDI • DLP • CT thorax exam • FOM

I. Lasić (✉)

Medical Physics and Radiation Protection Office, University Clinical Hospital Mostar, Bijeli Brijeg bb, 8800 Mostar, Bosnia and Herzegovina

e-mail: Ivan.lasic.phy@gmail.com

K. Galić

Department for Lung Diseases, University Clinical Hospital Mostar, Bijeli Brijeg bb, 8800 Mostar, Bosnia and Herzegovina

Department for Internal Diseases, University of Mostar School of Medicine, Bijeli Brijeg bb, 8800 Mostar, Bosnia and Herzegovina

A. Beganović

Department of Radiation Protection and Medical Physics, Clinical Centre of Sarajevo University, Bolnička 25, 71000 Sarajevo, Bosnia and Herzegovina

Faculty of Science, University of Sarajevo, Zmaja od Bosne 33-35, 71000 Sarajevo, Bosnia and Herzegovina

V. Lasić

Department for Pediatric Surgery, University Clinical Hospital Mostar, Bijeli Brijeg bb, 8800 Mostar, Bosnia and Herzegovina

L. Čiva

Sarajevo School of Science and Technology, Sarajevo Medical School, Hrasnička cesta 3a, 71210 Ilidža, Bosnia and Herzegovina

A. Krasić-Arapović

Department for Radiology, University Clinical Hospital Mostar, Bijeli Brijeg bb, 8800 Mostar, Bosnia and Herzegovina

1 Introduction

Every day around the world, ionizing radiation is used for the imaging of patients in more than 10 million diagnostic radiology procedures. Unnecessary exposure of patients can arise from medical procedures that are not justified for a specified objective, the application of procedures to individuals that are not justified on the basis of their conditions, and medical exposures that are not appropriately optimized for the situation in which they are used. There are a number of current trends in the medical use of ionizing radiation, which have led to current attempts to address this issue in relation to the radiation protection of patients. A major trend is the rapid increase of new technology for medical exposure and the corresponding speed of the clinical introduction of this technology. In particular, the increased use of CT scanners for radiological imaging procedures, associated with relatively high patient doses, is a clear trend [1].

University Clinical Hospital Mostar performs approximately 3500 thoracic CT examinations for different diagnostic purposes yearly. This anatomical region was chosen as the first imaging region for parameter optimization in University Clinical Hospital Mostar, due to the large number of patients that have exams performed on this area. The structure of the thorax is characterized by large differences in the attenuation of the high native contrast ratio, making it possible to significantly decrease the dose without affecting image quality.

2 Methods

This prospective study lasted from March 1st 2018 to June 1st 2018 and was divided into two phases. In the first phase of this study, 31 patients with a mean age of 62.96 years were imaged using a standard CT protocol for the thorax (Table 1).

In the second phase, 31 patients with a mean age of 57.97 years were imaged using an optimized CT protocol for the thorax (Table 2).

After processing the data from the first phase of the study, a multidisciplinary approach was taken to optimize the CT protocol. The team consisted of a thoracic radiologist, a medical physicist and a radiographer.

The first important step is to provide optimal patient centering. Prior studies have proved the importance of appropriate patient centering in the gantry isocenter for CT scanning [2].

Tube current increase strength increases the number of photons emitted by the X-ray tube. For practical reasons, the magnitude of the mAs is usually used, which is the current strength multiplied by the scan time expressed in seconds [3]. Reducing current power is the simplest way of reducing the current because the radiation dose is proportional to the power of the current. For example, if the current is reduced by 50% this will also reduce the radiation dose by half, but increases in image noise which can affect the diagnostic outcome of the examination must be considered [4].

In the basic protocol, the current was fixed at 400 mA. In this study the ACE technique CT offers has been utilized, which is a technique with a user specified image quality metric to modulate tube current according to body shape and body regions [2]. On the GE CT device, when selecting the AEC technique the noise index parameters and the minimum and maximum mA can be set (Table 2). To decrease motion artifacts, it is prudent to keep faster rotation times for most chest CT examinations. Most modern CT scanners should allow the use of 0.4 to 0.5 s gantry rotation times for chest CT, which reduces scan time and, if all other parameters are kept constant, helps dose reduction as well [2]. Gantry rotation time was reduced for this study from 0.8 to 0.6 s.

Table 1 Protocol parameters of CT thorax exam before optimization

Scan type	Helical
Rotation time	0.8 s
Slice thickness	2.5 mm
Pitch factor	1.375:1
SFOV filter	Large
Tube voltage (kV)	120
Tube current (mA)	400
Noise index	–

Table 2 Optimized protocol parameters of CT thorax exam

Scan type	Helical
Rotation time	0.6 s
Slice thickness	2.5 mm
Pitch factor	0.938:1
SFOV filter	Large
Tube voltage (kV)	120
Tube current (mA)	105–440
Noise index	20

The pitch factor for most chest CT examinations should be kept close to or slightly higher than 1:1 [2]. According to this recommendation the pitch factor was changed from 1.375:1 to 0.938:1 (Table 2).

Parameters for the estimation of image quality were defined according to guidelines EUR16262 EN and were used in the analysis of various anatomical structures of the chest: the thoracic wall, mediastinum, trachea, mousse par-enchyma and principal bronchi.

In this study, a double-stimulation method\DS\ was used. The observer, a thoracic radiologist, was provided in a blinded manner with the original and the optimized image being tested.

This method can have two modes of assessment:

1. The observer evaluates both images and the result is a comparison of these ratings
2. The viewer chooses a higher quality image.

The first evaluation method was used in this research.

For evaluation, the observer used a five-degree scale: 1—very poor visibility, 2—poor visibility, 3—acceptable visibility, 4—good visibility, 5—excellent visibility. Based on the sum of all parameters, the final image quality rating (Ci) was determined. The value of the image quality rating index (the sum of all parameter values divided by the

number of parameters—Fi) was calculated using Formula (1).

For the effective dose calculation, a simple estimate of the effective dose was used [5]. The figure of merit/FOM/value for each patient was calculated by Formula (2).

$$Fi = \frac{\sum_i Ci}{n} \tag{1}$$

$$FOM = \frac{Fi}{dose} \tag{2}$$

The mean FOM value was used as a relative indicator of the image quality difference between the groups of patients scanned before and after optimization of the imaging protocol [6].

3 Results

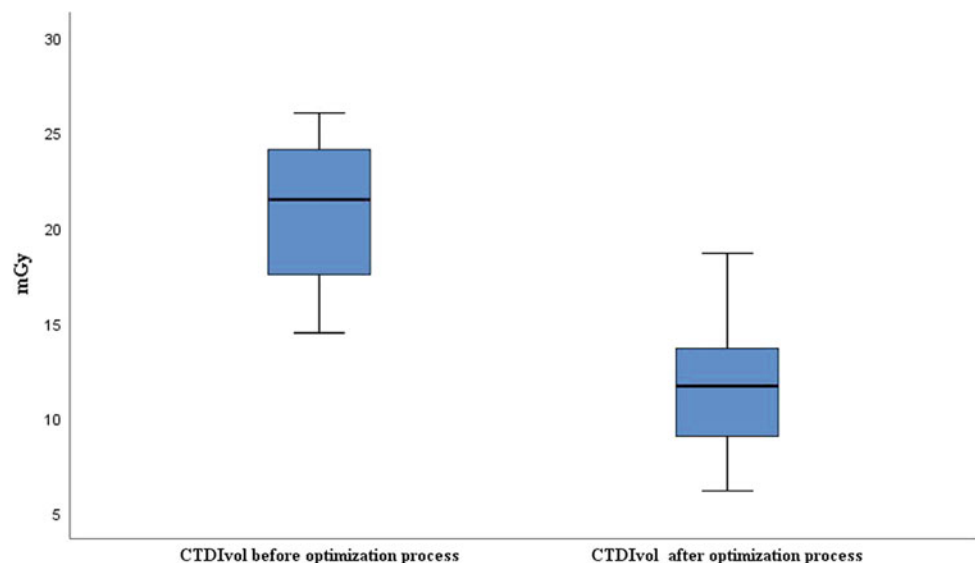
A total of 62 adult patients were involved in this study, consisting of 26 (42%) males and 36 (58%) females. The age of patients ranged from 38 to 80 years, with a median age of 62 years (Table 3). Patient ages were normally distributed ($p = 0.0961$).

A comparison of CT dose index volume/CTDIvol/was made before and after optimization. A T-test showed significant reduction of CTDIvol after protocol optimization

Table 3 Demographic data

		Gender		Total
		M	F	
Age	Median	63	61	62
	Min	38	40	38
	Max	80	79	80

Fig. 1 Comparison of CTDIvol before and after the optimization process



($p < 0.001$). Median CTDIvol before optimization was 21.48 mGy, with a maximum value of 26.05 mGy and a minimum value of 14.48 mGy. Median CTDIvol after optimization was 11.67 mGy, with minimum and maximum values of 6.13 and 18.65 mGy, respectively (Fig. 1).

A T-test confirmed a significant reduction in dose-length product/DLP/after protocol optimization ($p < 0.01$). The median DLP value prior to the imaging was 2111 mGy \cdot cm, with a minimum value of 1361 mGy \cdot cm and a maximum of 2964 mGy \cdot cm. After the optimization of the DLP median value, 1352, 668 and 1952 mGy \cdot cm were measured as the median, minimum and maximum values, respectively (Fig. 2).

The average image quality grade before and after the optimization was compared. A Mann Whitney U test showed no significant improvement ($z = -2.408$, $p = 0.016$), but no significant reduction in image quality after optimization of the CT thorax exam protocol. The image quality rating range before optimization was 3.20 to 4.70, while the median was 3.90. After optimization, the median image quality rating was 4.20, and the image quality rating ranged from 3.20 to 5.00 (Fig. 3).

The median FOM factor before optimization was 1.28 mSv $^{-1}$ (IQR 0.23 mSv $^{-1}$). The median FOM factor after optimization was 2.46 mSv $^{-1}$ (IQR 0.97 mSv $^{-1}$).

Fig. 2 Comparison DLP before and after optimization process

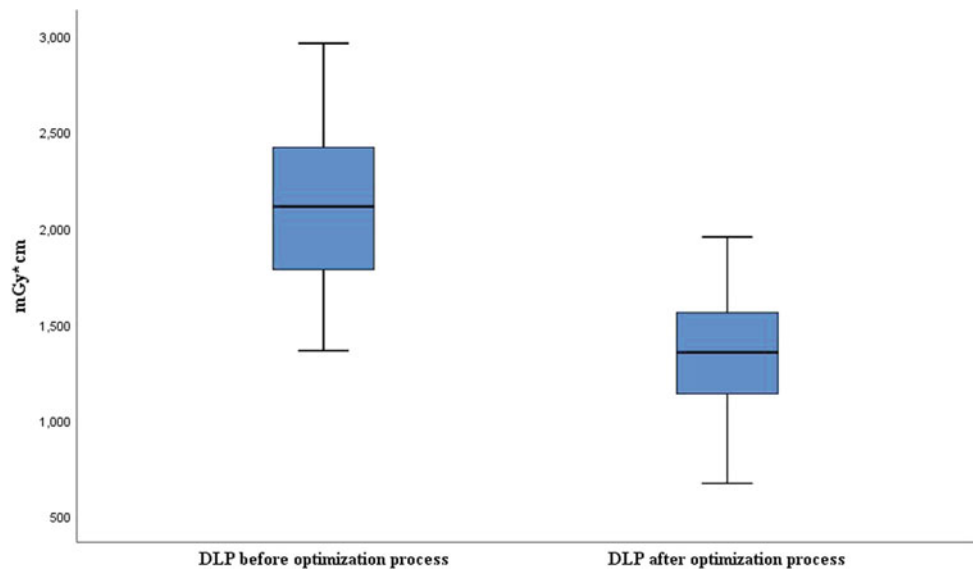


Fig. 3 Comparison of mean image quality grade before and after the optimization process

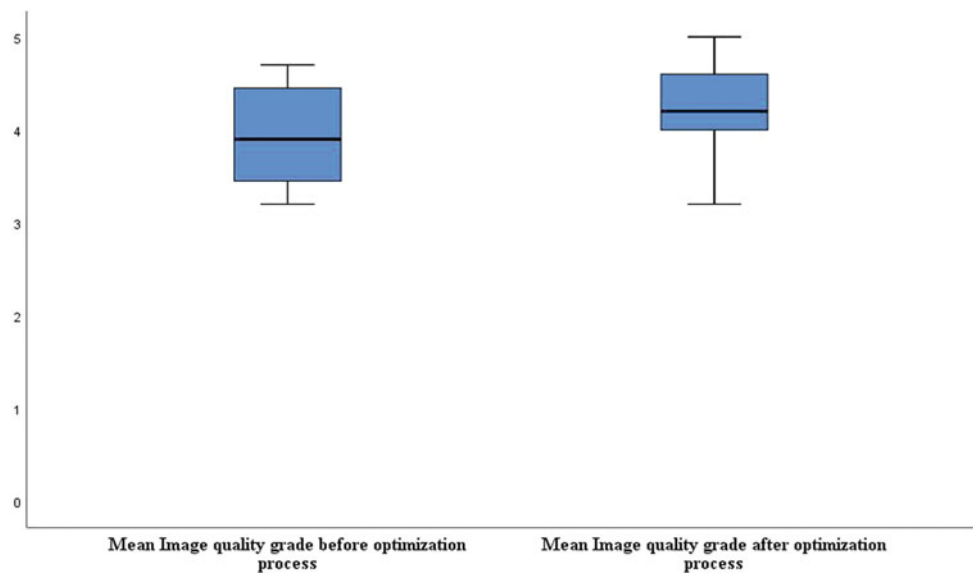
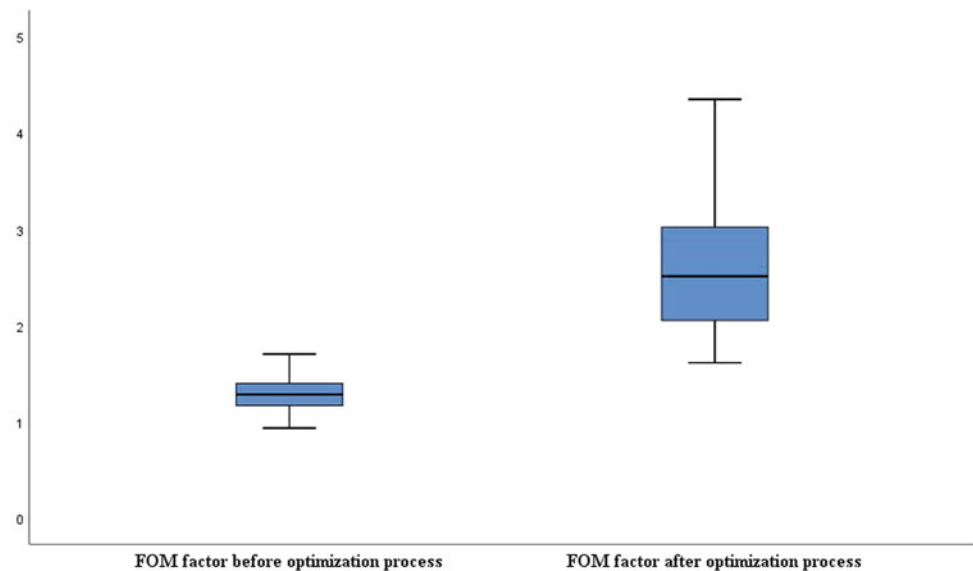


Fig. 4 Comparison of the FOM factor before and after the optimization process



A Mann Whitney U test showed a significant increase in the FOM factor ($z = 5.777$, $p < 0.001$) (Fig. 4).

4 Discussion

By changing the parameters of the protocol a significant dose reduction was reached without affecting the diagnostic information.

The median value of $CTDI_{vol}$ in the images scanned with the optimized protocol was significantly lower than the images acquired with the standard protocol ($p < 0.001$). The same difference was obtained by changing the exposure parameters of Tables 1 and 2. Similar results were obtained from Prasad et al. [7] in a lung cancer study in patients older than 65 years.

However, the tube potential (measured in kilovolts) was not changed in this study. The change in radiation dose is approximately proportional to the square of change in tube potential. In general, the recommendation for chest CT is to perform the exam at 80 kV in patients smaller than 50–60 kg and at 100 kV for patients weighing up to 75–80 kg [2].

The DLP per sequence was also analyzed, and found to be significantly lower in the optimized protocol in comparison to the standard protocol ($p < 0.01$), this is a consequence of the decreased $CTDI_{vol}$.

The significant increase of the FOM factor ($p < 0.001$) is a clear indicator that a reduction of the patient dose while maintaining quality diagnostic information has been achieved.

4.1 Limitations of This Study

- In this study patients with different input diagnoses on CT exam of the thorax were included. For better results patients with same input diagnosis need to be involved.
- Most chest CT scans should be performed as a single pass or phase examination. Either single noncontrast or single postcontrast image series are sufficient for most chest CT examinations. The number of phases was not reduced in our study.
- The tube potential (measured in kilovolts) was not changed in this study.

Conflicts of Interest None.

References

1. Holmberg, O., Malone, J., Rehani, M., et al.: Current issues and actions in radiation protection of patients. *Eur. J. Radiol.* **76**, 15–19 (2010)
2. Singh, S., Kalra, M., et al.: Radiation dose optimization and thoracic computed tomography. *Radio Clin. N. Am.* **52**, 1–15 (2014)
3. Øberg, M.: Patient doses for CT examinations in Denmark. Doctoral thesis. Submitted to the Department of Electrical Engineering at the Technical University of Denmark, University of Copenhagen (2011)
4. Kalra, M., Maher, M.M., Toth, T.L., et al.: Strategies for CT radiation dose optimization. *Radiology* **230**, 619–628 (2004)
5. ICRP. ICRP Publication 60: Recommendations of the international commission on radiological protection. *Int. Comm. Radiol. Prot.* **60**, 1–3 (1991)

6. Simonji, H.D.: Procjena doza i optimizacija protokola pri standardnim pregledima višeslojnom kompjuterizovanom tomograjom; Doktorska disertacija. Univerzitet u Novom Sadu, Medicinski fakultet (2015)
7. Prasad, S., et al.: Standard-dose and 50% reduced dose chest CT: comparing the effect on image quality. *AJR* **179**(2), 461–465 (2002)
8. Holmberg, O., Czarwinski, R., Mettler, F.: The importance and unique aspects of radiation protection in medicine. *Eur. J. Radiol.* **76**, 6–10 (2010)
9. Beganović, A.: Kožne doze kod perfuzije kompjuterizovanom tomograjom; Doktorska disertacija. Univerzitet u Sarajevu, Prirodno—Matematički fakultet (2013)
10. European Guidelines on quality criteria for computed tomography. EUR16262 EN

Radiation Exposure of Patients in Neonatal Intensive Care Unit

Adnan Beganović, Irmina Sefić-Pašić, Maja Gazdić-Šantić, Rahima Jašić, Amra Skopljak-Beganović, Adnan Šehić, and Sandra Vegar-Zubović

Abstract

The chest radiography is the most valuable imaging modality in the assessment of respiratory problems in neonates. However, use of X-rays is associated with exposure to ionising radiation. Scattered and leakage radiation increases over-all dose received by each patient in the ward. In this study we explore medical and public exposure of patients in neonatal intensive care unit (NICU) in the Clinical Centre of Sarajevo University (CCSU). Study included 120 randomly selected patients. The effective dose arising from medical and public exposure was estimated using direct measurements and appropriate software tools. The entrance surface air kerma for a single chest radiography exposure is 86 μGy , which corresponds to 0.60 mSv effective dose. On average, patients are exposed 2.1 times, so the average cumulative effective dose is 0.13 mSv. The estimated effective dose from public exposure was 1.25×10^{-4} mSv, which could be considered negligible. For patients undergoing more examinations, one could consider introducing ultrasound (LUS) as a method of choice.

Keywords

Radiology • Radiography • Radiation protection

1 Introduction

The chest radiography is the most valuable imaging modality in the assessment of respiratory problems in neonates. Although the examination might be non-specific, when combined with clinical findings, it will yield to correct diagnosis [2]. Use of X-rays is associated with exposure to ionising radiation. Ultrasound procedure, which is considered safer, gave promising results in detection of respiratory distress syndrome, which is the leading cause of morbidity in preterm new-born babies (<37 weeks gestation age). However, further research is necessary before lung ultrasound can replace chest radiography as the reference standard imaging component [7].

Medical exposure of patients is not the only concern. Scattered and leakage radiation increases over-all dose received by each patient in the ward. Both have been addressed in different studies. The similar topic has been addressed in other studies [1, 3, 6, 12, 14, 18]. However, it remains an interesting topic. Exposure due to scatter and leakage is a primary concern for calculation of occupational exposure, and it has been a subject of interest in many national and international publications [5, 8, 9]. They focus on effective dose received by workers. Other publications give practical solutions for calculation of structural shielding required in some installations, where the main concern is radiation protection of professionals [13]. However, the same methods can be used when estimating doses to public (i.e. neighbouring patients, non-categorized workers etc.) and comforters (i.e. parents, volunteers etc.).

Dose limit for exposed workers in majority of the world countries is 20 mSv, which in accordance to recommendations of the International Commission for Radiological Protection [10]. Public exposure limit is 1 mSv, which

A. Beganović (✉) · M. Gazdić-Šantić · R. Jašić ·
A. Skopljak-Beganović
Department of Radiation Protection and Medical Physics,
Clinical Centre of Sarajevo University, Bolnička 25,
71000 Sarajevo, Bosnia and Herzegovina
e-mail: adnanbeg@gmail.com

A. Beganović
Faculty of Science, University of Sarajevo, Zmaja
od Bosne 33–35, 71000 Sarajevo, Bosnia and Herzegovina

I. Sefić-Pašić · S. Vegar-Zubović
Clinic of Radiology, Clinical Centre of Sarajevo University,
Bolnička 25, 71000 Sarajevo, Bosnia and Herzegovina

A. Šehić
Faculty of Health Studies, University of Sarajevo,
Bolnička 25, 71000 Sarajevo, Bosnia and Herzegovina

applies to patients exposed to radiation not intended for their own medical benefit. In a case of paediatric neonatal patients, this would be leakage and radiation scattered during other patients X-ray examination.

In this study we explore medical and public exposure of patients in neonatal intensive care unit (NICU) in the Clinical Centre of Sarajevo University (CCSU).

2 Materials and Methods

2.1 Medical Exposure

Study included 120 randomly selected patients. They were evenly distributed amongst males and females (47%) (binomial test, $p = 0.712$). Median (\bar{x}) gestational age of neonates was 31 weeks, with interquartile range (IQR) of 3 weeks. Mean value (\bar{x}) of normally distributed birth body mass was 1.67 kg, with standard deviation (σ) of 0.51 kg. Chest radiography was performed on all patients, at least once, using a single X-ray unit, GE TMX + (General Electric, Boston, MA, USA) and Agfa CR30-X computed radiography (CR) imaging system (Agfa-Gevaert, Mortsel, Belgium). They were operated by different radiographers using the same exposure technique (Table 1).

Radiation output measurements, Y , together with exposure parameters from Table 1, were used to calculate the entrance surface air kerma ($K_{a,e}$ or ESAK) for each patient. The applied backscatter factor (BSF) was 1.1 [15, 16]. $K_{a,e}$ alone could be used as a relevant dose descriptor. However, in order to make a comparison with doses to neonates arising from scattered and leakage radiation possible, we estimated the patient effective dose using Monte Carlo simulations in PCXMC 2.0.1 (STUK, Helsinki, Finland) software package.

2.2 Public Exposure

Calculations of scattered and leakage radiation were based on the Report No. 147 Structural Shielding Design for

Medical X-ray Imaging Facilities published the National Council on Radiation Protection and Measurements [13]. The report provides methodology to calculate radiation attenuation in shielding materials. However, some adjustments had to be made.

Due to the fact that scatter radiation greatly depends on patient size, as well as energy of X-rays, we could not rely on data for adult patients provided in the Report. Rather, we made our own measurements with a cylindrical water phantom similar in size to a neonatal patient (height: 28 cm, diameter 8 cm). Scattered and leakage radiation was measured with an appropriate instrument (RTI Piranha Dose Probe, Mölndal, Sweden), calibrated in terms of ambient dose equivalent at 10 mm phantom depth, denoted as $H^*(10)$. Measured $H^*(10)$ at 1 m distance from the phantom centre at exposure parameters used for imaging was $0.061 \mu\text{Sv}$ per patient. This value was used as the effective dose, E , in further calculations. However, it should be noted that use of $H^*(10)$ as a surrogate for effective dose is conservative [11].

Radiation attenuation in surrounding barriers had to be adjusted to take into consideration building materials different from those presented in the NCRP Report. While reported data could be used for glass windows and doors, values from literature had to be used in case of walls that are built with autoclaved aerated concrete [17]. In-house software was used to automate the calculation process and provide numerical and graphical results.

3 Results and Discussion

The relationship between gestational age and birth body mass is presented in Fig. 1. The correlation between two parameters is significant (Pearson correlation coefficient 0.806, $p < 0.001$). Both birth body mass and gestational age are equally distributed across two genders (independent samples Mann-Whitney U test, $p = 0.161$ and $p = 0.914$, respectively).

All patients have undergone a chest radiography examination. Most of them once (82 or 68.3%), some twice (15 or

Table 1 Exposure parameters used in chest radiography of neonates in the Clinical Centre of Sarajevo University in 2018

Technical parameter	Value
Projection	Anterior-Posterior (AP)
Tube potential (kV)	53
Tube loading (mAs)	3.2
Filtration (mmAl)	3
Focal spot size (mm)	0.8
Radiation output, Y ($\frac{\mu\text{Sv}}{\text{mAs m}^2}$)	52.3
Focus-skin distance (cm)	87.7
CR detector size (cm ²)	18 × 24

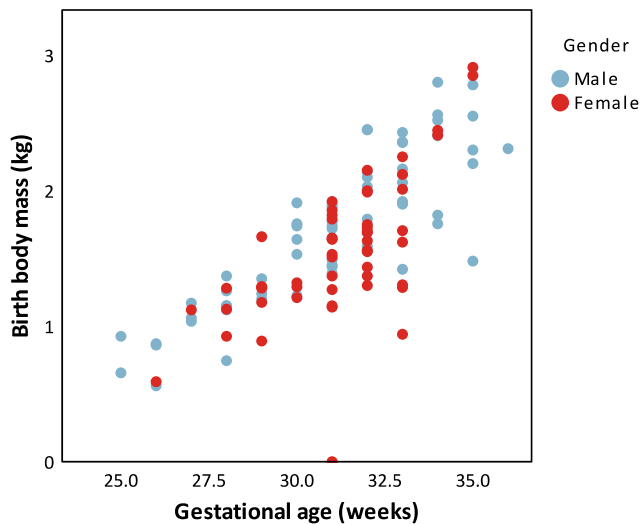


Fig. 1 Correlation between gestational age and birth body mass for male and female neonates. Correlation between two parameters is significant ($p < 0.001$)

12.5%), while other 23 or 19.2% of patients have had a chest X-ray taken 3–16 times. On average, each patient is exposed 2.1 times. In that respect, there are differences in cumulative entrance surface air kerma and effective dose received by neonates due to medical exposure. Figure 2 illustrates difference in average cumulative entrance surface air kerma between neonates in different birth body mass groups. The negative correlation is significant (Spearman's $\rho = -0.244$, $p = 0.007$).

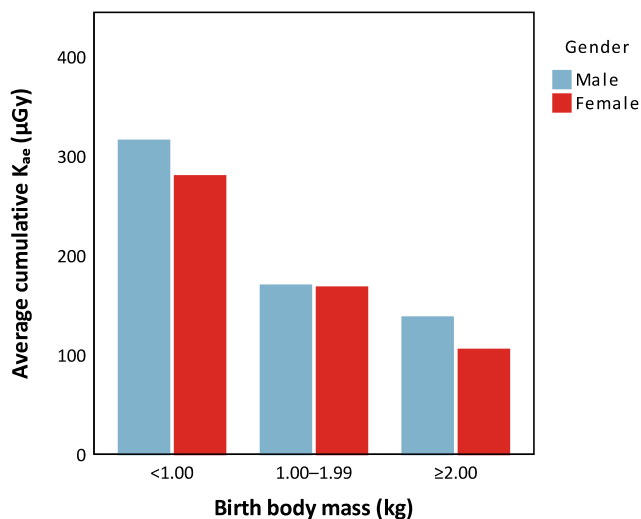


Fig. 2 Average cumulative entrance surface air kerma in different birth body mass groups. Correlation between two parameters is significant (Spearman's $\rho = -0.244$, $p = 0.007$)

The results of patient dosimetry have been summarized in Table 2, which shows mean and median values of cumulative entrance surface air kerma ($K_{a,i}$) and effective dose (E), as well as third quartile (Q_3) and interquartile range (IQR).

Results of the estimated effective dose to neonates due to scattered radiation is presented in Fig. 3. The ward has four rooms, sharing 11 incubators. We can use a viable presumption that, during the stay at the ward, each patient receives the dose arising from scattered radiation of 2 X-ray exposures from other incubators. The estimated effective dose for a patient placed in an incubator positioned in the central part of the second room was 1.25×10^{-4} mSv.

The anthropomorphic data on neonates show the expected result; there is a significant positive correlation between gestational age and birth body mass (Fig. 1). In our study, gender of patients plays no role, as both birth body mass and gestational age are equally distributed between males and females.

All neonates have been exposed to ionizing radiation as part of their regular diagnostic examination. Some needed one or two additional radiographs taken, while almost 20% required more than 3. Neonates with lower gestational age are in greater risk of many health issues, including respiratory distress syndrome [7]. Therefore, they are in need for more X-rays that neonates with higher gestational age. This reflects on their cumulative $K_{a,e}$, as could be seen in Table 2. Average cumulative $K_{a,e}$ has the highest value for neonates with gestational age ≤ 29 weeks (178.8 μGy), and lowest for neonates with gestational age > 32 weeks (154.2 μGy). The median in all three age groups is the same, and this is because median number of X-rays taken is 1—in all three groups. Obviously, values of $K_{a,e}$ reflect on total effective dose. While $K_{a,e}$ and E for a single radiograph are 86 μGy and 60 μSv , respectively, the total average effective dose for all examinations is 0.13 mSv (Table 2).

For patients undergoing more examinations than usual, one could consider changing the algorithm of diagnostic procedures, and introduce lung ultrasound (LUS) as a method of choice. LUS and chest radiography have a high concordance in the differential diagnosis of neonatal respiratory distress [4].

Isodose curves of scattered radiation illustrated in Fig. 3 indicate that the effective dose should be less than 0.001 mSv per patient during the hospitalization. In the worst case scenario, a patient occupying the incubator in the centre of the ward would receive 0.000125 mSv, which is approximately 1,000 times less than dose received due to direct medical exposure. Although the dose could be considered negligible, a graph like the one presented in Fig. 3 could be used when optimizing the positioning of incubators in the room.

Table 2 Values of mean, cumulative entrance surface air kerma ($K_{a,e}$) and estimated effective dose (E) for neonates with different gestational age; mean (\bar{x}), median (\tilde{x}), third quartile (Q_3), and interquartile range (IQR)

		$K_{a,e}$ (μGy)				E (mSv)			
		\bar{x}	\tilde{x}	Q_3	IQR	\bar{x}	\tilde{x}	Q_3	IQR
Gestational age (weeks)	≤ 29	196.7	86.05	215.1	129.1	0.14	0.060	0.15	0.090
	30–32	185.9	86.05	172.1	86.06	0.13	0.060	0.12	0.060
	>32	169.6	86.05	172.1	86.06	0.12	0.060	0.12	0.060
Total		183.8	86.05	172.1	86.06	0.13	0.060	0.12	0.060

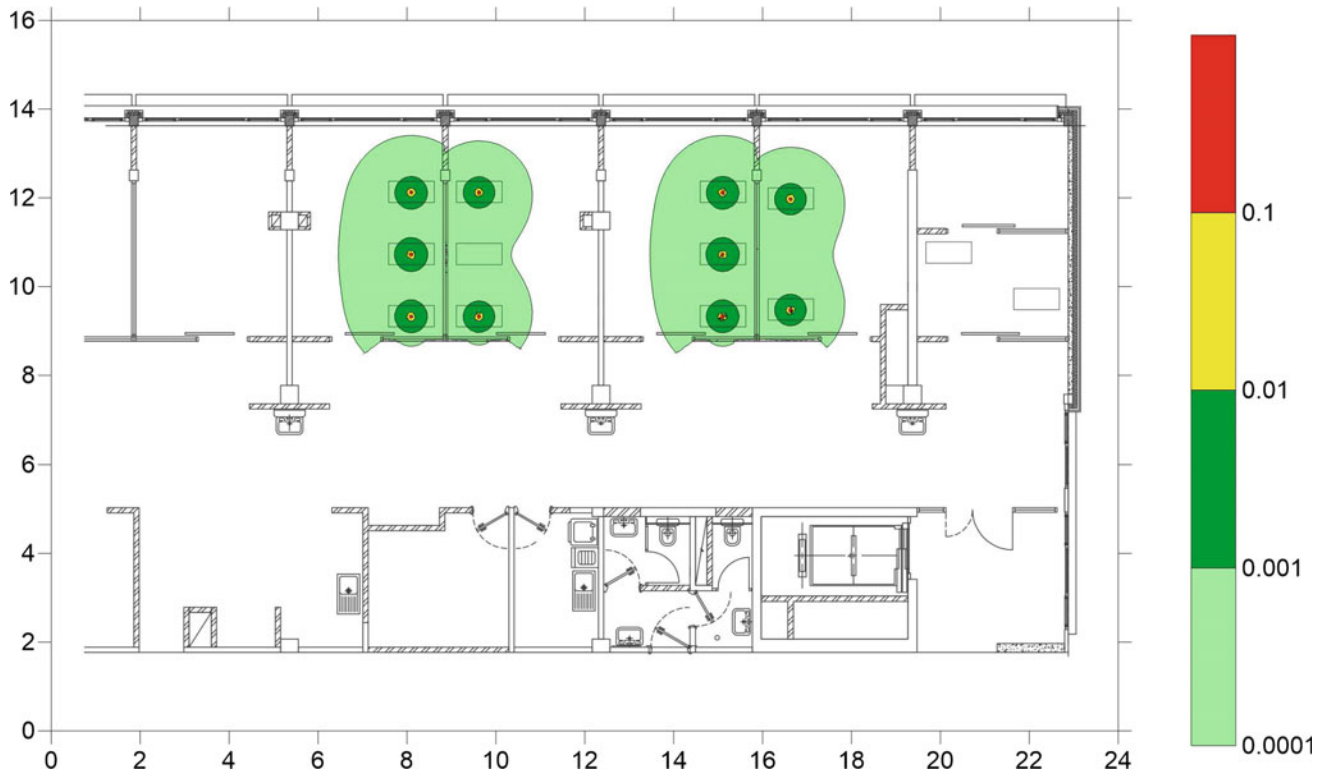


Fig. 3 Isodose curves of simulated scattered radiation, expressed in $H^*(10)$ (mSv), from 10 patients and 2 exposures each in NICU in the CCSU. The average dose in the eleventh incubator is 1.25×10^{-4} mSv

4 Conclusion

The entrance surface air kerma for a single chest radiography exposure is $86 \mu\text{Gy}$, which corresponds to 0.060 mSv effective dose. On average, patients are exposed 2.1 times, so the average cumulative effective dose is 0.13 mSv. From the radiation protection point of view, exposure of neonates to radiation scattered from patients in other incubators is negligible. Nevertheless, layout of incubators in the ward should be optimized to reduce public exposure of neonates. Introduction of LUS in examination algorithm should be considered.

References

1. Aramesh, M., Zanganeh, K.A., Dehdashtian, M., Malekian, A., Fatahiasi, J.: Evaluation of radiation dose received by premature neonates admitted to neonatal intensive care unit. *J. Clin. Med. Res.* **9**(2), 124 (2017)
2. Arthur, R.: The neonatal chest X-ray. *Paediatr. Respir. Rev.* **2**(4), 311–323 (2001)
3. Brindhaban, A., Al-Khalifah, K.: Radiation dose to premature infants in neonatal intensive care units in Kuwait. *Radiat. Prot. Dosimetry* **111**(3), 275–281 (2004)
4. Corsini, I., Parri, N., Gozzini, E., Coviello, C., Leonardi, V., Poggi, C., Giacalone, M., Bianconi, T., Tofani, L., Raimondi, F., Dani, C.: Lung ultrasound for the differential diagnosis of respiratory distress in neonates. *Neonatology* **115**, 77–84 (2018)

5. EC: Technical recommendations for monitoring individuals occupationally exposed to external radiation. European Commission (2009)
6. Edison, P., Chang, P.S., Toh, G.H., Lee, L.N., Sanamandra, S.K., Shah, V.A.: Reducing radiation hazard opportunities in neonatal unit: quality improvement in radiation safety practices. *BMJ Open Qual.* **6**(2), e000128 (2017)
7. Hiles, M., Culpan, A.M., Watts, C., Munyombwe, T., Wolstenhulme, S.: Neonatal respiratory distress syndrome: chest X-ray or lung ultrasound? A systematic review. *Ultrasound* **25**(2), 80–91 (2017)
8. HSE: Occupational exposure to ionising radiation: exposures among classified uk workers as reported to the central index of dose information (CIDI), 2015. Technical Report, Health and Safety Executive (2017)
9. IAEA: Occupational Radiation Protection. International Atomic Energy Agency, Vienna, Austria (2018)
10. ICRP: ICRP Publication 103: Recommendations of the International Commission on Radiological Protection. Technical Report, International Commission on Radiological Protection (2008)
11. ICRU: Determination of dose equivalents resulting from external radiation sources (report 39). Technical Report, International Commission on Radiation Units and Measurements, Bethesda, MD, USA (1985)
12. Longo, M., Genovese, E., Donatiello, S., Cassano, B., Insero, T., Campoleoni, M., Del Vecchio, A., Magistrelli, A., Tomà, P., Cannatà, V.: Quantification of scatter radiation from radiographic procedures in a neonatal intensive care unit. *Pediatr. Radiol.* **48**(5), 715–721 (2018)
13. NCRP: Structural shielding design for medical X-ray imaging facilities. NCRP Report No. 147, National Council on Radiation Protection and Measurements, Bethesda, MD (2005)
14. Olgar, T., Onal, E., Bor, D., Okumus, N., Atalay, Y., Turkyilmaz, C., Ergenekon, E., Koc, E.: Radiation exposure to premature infants in a neonatal intensive care unit in Turkey. *Korean J. Radiol.* **9**(5), 416–419 (2008)
15. Smans, K., Struelens, L., Smet, M., Bosmans, H., Vanhavere, F.: Patient dose in neonatal units. *Radiat. Prot. Dosimetry* **131**(1), 143–147 (2008)
16. Toossi, M.T.B., Malekzadeh, M.: Radiation dose to newborns in neonatal intensive care units. *Iran. J. Radiol.* **9**(3), 145 (2012)
17. Tsalafoutas, I., Yakoumakis, E., Manetou, A., Flioni-Vyza, A.: The diagnostic X-ray protection characteristics of Ytong, an aerated concrete based building material. *Br. J. Radiol.* **71**(849), 944–949 (1998)
18. Yu, C.C.: Radiation safety in the neonatal intensive care unit: too little or too much concern? *Pediatr. Neonatology* **51**(6), 311–319 (2010)

Use of Uptake Values to Estimate the Effective Dose to Patients in Positron Emission Tomography

Adnan Beganović, Rahima Jašić, Maja Gazdić-Šantić,
Amra Skopljak-Beganović, Nermina Bešlić, Šejla Cerić,
Amra Šadija, and Sandra Vegar-Zubović

Abstract

Positron emission tomography (PET) is a diagnostic imaging modality in nuclear medicine. The most common radionuclide in PET is ^{18}F fluoro deoxyglucose (FDG). In this study we used the information on radionuclide uptake from PET images and software to make an estimation of effective dose received by patients during ^{18}F -FDG PET examination. We analysed data from 50 patients who performed positron emission tomography—computed tomography (PET-CT) examination. Uptake values were collected in bladder, bones, heart wall, kidneys, liver, brain and remainder. Using a simplified biokinetic model, residence time was calculated and used as an input parameter in OLINDA/EXM[®] software package. The conversion factor from administered activity to effective

dose was found to be $0.016 \frac{\text{mSv}}{\text{MBq}}$, which is only 15% less than value found in literature. The method described in the paper might be suitable in situations when standard calculation models are not adequate.

Keywords

Medical physics • Nuclear medicine • Dosimetry • Patient dose

1 Introduction

Positron emission tomography (PET) is a nuclear medicine diagnostic imaging modality. It utilizes positron emitting radionuclides to obtain diagnostic information. Radionuclides are radioactive atoms whose nucleus have excess energy, making them unstable, and leading to their decay. In this process alpha or beta particles, or gamma rays are being released from the nucleus. The fact that this emission happens can be used in various ways in nuclear medicine.

Considering that most radionuclides do not have biological properties that would lead them to the targeted organ in the body, they usually have to be combined with tracers, i.e. a molecule that is biologically active and regulates biodistribution. The tracer carries radionuclide to desired location. Radionuclide labelled tracers used in nuclear medicine for diagnostics and therapy are specific chemical compounds called radiopharmaceuticals.

Radionuclides used in PET imaging go through β^+ decay and emit positrons. The emitted positron travels a couple of millimetres inside human body before interacting with an electron. During the interaction positron and electron annihilate, converting their combined mass into energy. The total

A. Beganović (✉) · R. Jašić · M. Gazdić-Šantić ·
A. Skopljak-Beganović
Department of Radiation Protection and Medical Physics,
Clinical Centre of Sarajevo University, Bolnička 25,
71000 Sarajevo, Bosnia and Herzegovina
e-mail: adnanbeg@gmail.com

A. Beganović
Faculty of Science, University of Sarajevo, Zmaja
od Bosne 33–35, 71000 Sarajevo, Bosnia and Herzegovina

N. Bešlić · Š. Cerić · A. Šadija
Clinic of Nuclear Medicine and Endocrinology,
Clinical Centre of Sarajevo University, Bolnička 25,
71000 Sarajevo, Bosnia and Herzegovina

S. Vegar-Zubović
Clinic of Radiology, Clinical Centre of Sarajevo University,
Bolnička 25, 71000 Sarajevo, Bosnia and Herzegovina

energy released equals to 1022 meV, and is emitted in the form of two photons. Photons, each having energy of 511 keV, are emitted in nearly opposite directions.

Photons are detected by scintillation crystal detectors, placed on the ring gantry that surrounds the patient table. Crystals acquire photons coming from a patient and convert them into light. Light is led by light guide to photomultipliers, where it produces electric signal. Signal is analysed and the image is formed [2].

Radiation emitted from an atom of a radionuclide can be used as signal for detecting the position of that atom. In other words, specific radiopharmaceuticals can be used for observing distribution of radioactive material in certain organs in the body. This distribution gives us information on changes in metabolism, i.e. information on functions and processes.

The most common radionuclide in PET is ^{18}F . It is used as a label for deoxyglucose, giving the end product fluoro deoxyglucose (FDG or ^{18}F -FDG). Because of its properties, FDG is commonly used in clinical oncology with glucose-dependent tumours, as well as in non-oncological cases.

One of the main concerns in PET diagnostics is patient exposure to ionising radiation. In nuclear medicine, the most common dose descriptor is the administered activity of radionuclide, A . However, when hybrid modalities are used, or when we need to make comparison to other diagnostic modalities, A is not enough. A suitable quantity that overcomes this issue is the effective dose, defined as the tissue-weighted sum of the equivalent doses in all specified tissues and organs of the human body [4].

Unfortunately, the effective dose cannot be measured, rather it is estimated using the appropriate dose descriptors and simulations in mathematical phantoms.

In this study we used the information on radionuclide uptake from PET images and software to make an estimation of effective dose received by patients during ^{18}F -FDG PET examination.

2 Materials and Methods

We analysed data from 50 patients who performed positron emission tomography—computed tomography (PET-CT) examination on GE Discovery 610 PET-CT scanner (General Electric, Boston, MA, USA) at the Clinical Centre of Sarajevo University (CCSU). All patients included in the study were adults. The average administered activity, A_0 ,

was 350 MBq with standard deviation (σ) of 23 MBq. A standardised scanning procedure was used for all patients. At first, standard registration and attenuation correction CT was performed, followed by 3D acquisition of PET in 8–10 separate scans (beds), that overlap by 5 cm on each side, and last 1.75 min.

Examined patients were evenly distributed amongst males (46%) and females (54%) (binomial test, $p = 0.672$). Median (\tilde{x}) age of patients was 59, with interquartile range (IQR) of 19 years. Mean values (\bar{x}) of normally distributed body mass and height were 77 kg ($\sigma = 16$ kg) and 171 cm ($\sigma = 10$ cm), respectively.

Post-imaging data for patients was acquired on the workstation console, using available tools for uptake measurements. Data included average and standard deviation of ^{18}F -FDG uptake in organs of interest. The selected organs have excess uptake of radionuclide, which is clearly visible in the diagnostic image. The workstation software allows selection of different types of volume region of interest (ROI).

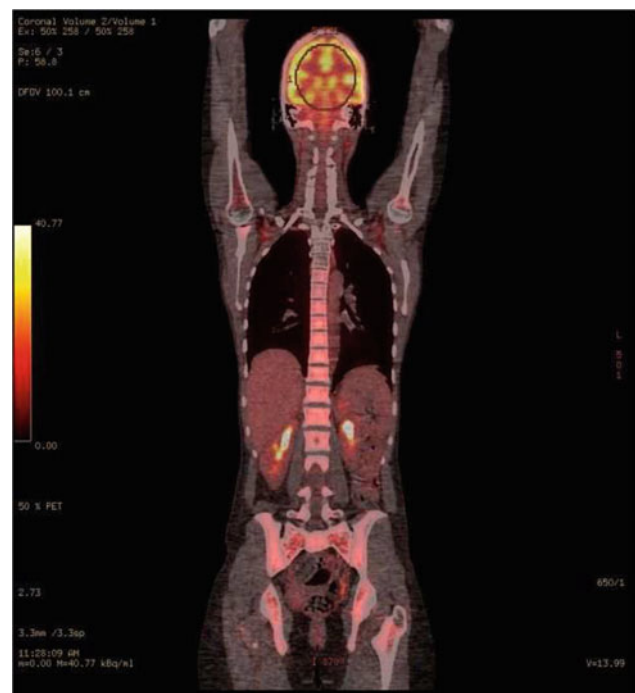


Fig. 1 Collection of brain uptake value from PET image using 160 cm^3 spherical ROI

Uptake values were collected in following organs: bladder, with auto-sized ROI, bones, heart wall, kidneys and remainder with 13.91 cm³ spherical ROI, liver with 100 cm³ and brain with 160 cm³ spherical ROIs (Fig. 1).

By multiplying the average value of uptake (kBq/ml) in a specific organ with the average volume (ml) of that organ for humans (male and female, separately) we calculated the average activity, $A_i(t_s)$, in each organ at the time of scanning t_s , which is approximately 1 h after injection.

The next step was calculating the total number of radioactive decays in an organ (\tilde{A}_i), which depends on biokinetic model used for a specific organ. Since the only available information is $A_i(t_s)$, the model function was approximated with exponential curve of physical decay of ¹⁸F:

$$\tilde{A}_i \approx \int_0^{\infty} A_i(t) e^{-\lambda t} dt, \quad (1)$$

where $\lambda = \frac{\ln 2}{T_{1/2}}$ is the decay constant and $T_{1/2}$ radionuclide half-life. In case of ¹⁸F, $T_{1/2} = 109.8$ min.

Once calculated, \tilde{A}_i is divided by total activity administered to the patient, A_0 . The ratio is called 'residence time', τ [6].

Residence time is used as an input parameter in OLINDA/EXM[®] software which calculates absorbed doses to different organs of the body and makes an estimation of effective dose received by patients [7].

3 Results and Discussion

In the study we collected general data on 50 patients, including sex, age, body mass, height, administered activity, time of administration and imaging. For each patient we analysed the uptake values in 7 specified regions of interest. We recorded mean and standard deviation (SD) of uptake value. The average values are presented in Table 1.

Median effective dose was 5.7 mSv, with interquartile range (IQR) of 2.7 mSv. Figure 2 illustrates differences in effective dose between males and females, and across different age groups. The conversion factor from administered activity to effective dose was found to be $0.016 \frac{\text{mSv}}{\text{MBq}}$.

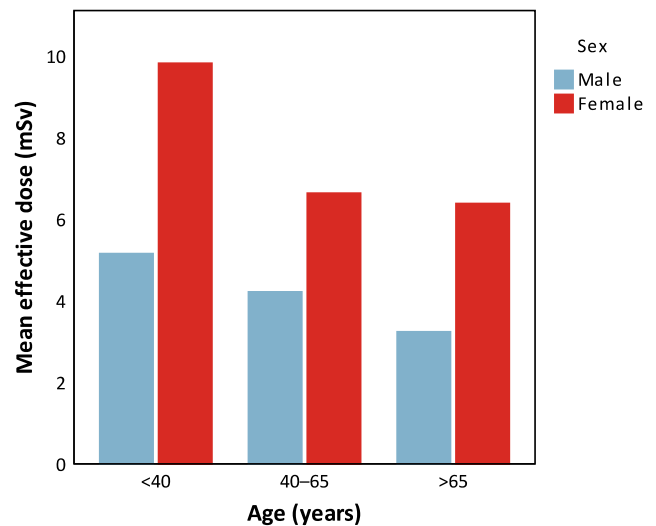


Fig. 2 Mean effective dose (mSv) for different sexes and across different age groups

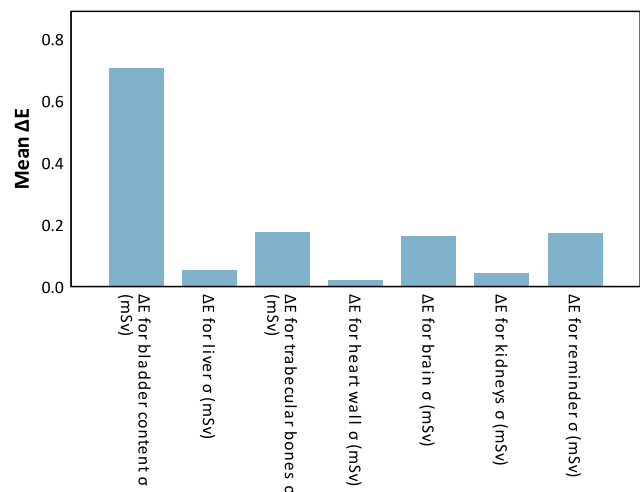


Fig. 3 Differences between effective doses ΔE when calculated with mean uptake value and sum of mean uptake value and standard deviation

The influence of uncertainties that could arise from measuring uptake values from noisy images in specific ROIs were analysed by repeating the calculation procedure with the sum of uptake value and standard deviation. The differences between the two are presented in Fig. 3.

Table 1 Average values of mean and standard deviation (SD) of uptake, volume (V), activity in scanning time $A_i(t_s)$, and residence time (τ) for selected organs

Organ	Uptake (kBq/ml)		V (ml)	$A_i(t_s)$ (MBq)	τ (s)
	Mean	SD			
Bladder content	47	10.1	500	23.51	0.261
Liver	7.7	0.7	1470	11.38	0.1263
Trabecular bones	5.3	1	6875	36.66	0.4073
Heart wall	8.1	2.1	300	2.44	0.0271
Brain	19	7	1350	25.61	0.285
Kidneys	12.5	4.7	270	3.37	0.0375
Remainder	2	0.3	23,000	45.13	0.4996

The uncertainty associated to standard deviation in all ROI uptake measurements is 14%.

Estimation of the effective dose from PET images comes with several approximations and many uncertainties. Some of them need to be explicitly mentioned, as they may greatly affect the final result.

First of all, the exponential approximation of biokinetic model function is not exactly true. At the time of administration activity in the observed organs was 0. It takes some time for FDG to arrive to desired locations. Once the radiopharmaceutical is in the organ, it does not necessarily stay there until decay. The clear example is urinary bladder. Patients void bladder before the examination. This means that some activity is 'lost' and cannot be detected during the scan.

Another uncertainty we considered were possible discrepancies in uptake value measurements. Many factors may influence the displayed uptake value, including noise, interscanner variability, reconstruction parameters, region size etc. [1]. The effect of uptake value variability was examined by repeating the calculations with uptake value increased by its standard deviation in each organ separately. Figure 3 shows that the estimated effective dose would increase by 0.7 mSv if uptake value in the bladder increases by 1 standard deviation of value reading. This dose corresponds to 12% of median value. In case of other organs or tissues the deviation is less than 0.2 mSv, what is 3.5% of calculated median.

Having all of this in mind, one might expect for conversion factor between activity and effective dose to be

significantly different when compared to conversion factor of $0.019 \frac{\text{mSv}}{\text{MBq}}$ found in literature [3, 5]. This is true ($p = 0.001$), but the correct value is underestimated by 15% only.

4 Conclusion

PET images with adequate tools for measuring uptake values can be used for estimation of effective dose received by a group of patients. The method can be suitable in situations when standard models from the literature are not adequate. The conversion factor between administered activity and effective dose is underestimated by 15%.

References

1. Adams, M.C., Turkington, T.G., Wilson, J.M., Wong, T.Z.: A systematic review of the factors affecting accuracy of SUV measurements. *AJR Am. J. Roentgenol.* **195**, 310–320 (2010)
2. Allisy-Roberts, P., Williams, J.: *Farr's Physics for Medical Imaging*, 2 edn. Elsevier (2007)
3. ICRP: ICRP Publication 106: Radiation dose to patients from radiopharmaceuticals. Technical Report, International Commission on Radiological Protection (2007)
4. ICRP: ICRP Publication 103: Recommendations of the International commission on radiological protection. Technical Report, International Commission on Radiological Protection (2008)
5. Mart-Climent, J.M., Prieto, E., Morn, V., Sancho, L., Rodriguez-Fraile, M., Arbizu, J., Garca-Velloso, M.J., Richter, J. A.: Effective dose estimation for oncological and neurological PET/CT procedures. *EJNMMI Res.* **7**, 37 (2017)

-
6. Stabin, M.G.: Mirdose: personal computer software for internal dose assessment in nuclear medicine. *J. Nucl. Med.* **37**(3), 538 (1996)
 7. Stabin, M.G., Sparks, R.B., Crowe, E.: OLINDA/EXM: the second-generation personal computer software for internal dose assessment in nuclear medicine. *J. Nucl. Med.* **46**(6), 1023 (2005)

Evaluation of Computed Tomography X-Ray Beam Dose Profiles

Lejla M. Čiva, Adnan Beganović, Mahira Redžić, Ivan Lasić, Maja Gazdić-Šantić, Amra Skopljak-Beganović, Rahima Jašić, and Sandra Vegar-Zubović

Abstract

Computed tomography (CT) is an imaging procedure that uses X-rays to create detailed pictures, or cross-section scans, of areas inside the body. Benefits of the CT have been proven over the past decades, but they come with a price high radiation doses to patients. Understanding how doses depend on technical parameters is a necessary step towards an optimized imaging procedure. Aim of this study was to assess the air kerma distribution and size of the X-ray beam of a conventional computed tomography scanner.

Keywords

Computed tomography • Dosimetry • Radiation detection

L. M. Čiva (✉)

Sarajevo School of Science and Technology, Sarajevo Medical School, Hrasnička cesta 3a, 71210 Ilidža, Bosnia and Herzegovina
e-mail: lejla.civa@ssst.edu.ba
URL: <https://ssst.edu.ba/professor-single/161/ms-lejla—iva>

A. Beganović · M. Gazdić-Šantić · A. Skopljak-Beganović · R. Jašić

Department of Radiation Protection and Medical Physics, Clinical Centre of Sarajevo University, Bolnička 25, 71000 Sarajevo, Bosnia and Herzegovina

A. Beganović

Faculty of Science, University of Sarajevo, Zmaja od Bosne 33–35, 71000 Sarajevo, Bosnia and Herzegovina

M. Redžić

Institute of Public Health of Federation of Bosnia and Herzegovina, Radiation Protection Centre, Tahtali sokak 17, 71000 Sarajevo, Bosnia and Herzegovina

I. Lasić

Medical Physics and Radiation Protection Office, University Clinical Hospital Mostar, Dr. Petra Rizza bb, 88000 Mostar, Bosnia and Herzegovina

S. Vegar-Zubović

Clinic of Radiology, Clinical Centre of Sarajevo University, Bolnička 25, 71000 Sarajevo, Bosnia and Herzegovina

1 Introduction

The aim of this study was to describe a method of analysis and evaluation of the dosimetric and geometric properties of the X-ray beam in computed tomography. Analysis was performed utilizing two different detector systems—radiochromic films and small sized semiconductors with multichannel electrometer. Calibration of radiochromic films in clinical settings was performed using a semiconductor detector with an appropriate desktop scanner. Films were later used to assess the characteristics of the beam along the x and z -axes. In a different set of measurements a semiconductor detector mounted on a moving jig was used to obtain dose profiles along the z -axis.

2 Materials and Methods

2.1 Dosimetry Systems

Radiochromic film used in the study was XRRV3 Gaf-Chromic[®] film (Ashland Advanced Materials, Bridgewater NJ, USA), which is designed to be used in interventional procedures guided by fluoroscopy. However, it can be calibrated in different X-ray beam qualities, including spectra used in computed tomography [7].

Exposed film strips were scanned by Konica Minolta bizhub 223 (Konica Minolta, Inc. Tokyo, Japan) desktop scanner. Files were saved in a 24-bit TIFF format and analysed with ImageJ software. Data values from the red (R) colour channel were used as dosimetric parameter [2].

Calibration of radiochromic films in clinical settings was performed using Piranha[®] electrometer (RTI, Mölndal, Sweden) equipped with detectors and probes capable of non-invasive measurements of kerma, air-kerma, kerma rate, tube voltage, exposure time etc. The instrument is intended to be used for measuring in low energy range of ionizing radiation in diagnostic radiology. Tube voltage, time

exposure, kerma and air-kerma can be measured by internal detectors, whereas in fluoroscopy and radiography usually the usage of probes is a requirement. Data can be collected in computer programs “Ocean” or “Ocean 2014” [12].

Beam characteristics were measured using Computed Tomography Dose Profiler (CTDP) and Barracuda® multi-channel electrometer (RTI, Mölndal, Sweden) [10]. CTDP is a point dose probe designed to fit into standard phantoms in order to evaluate CT systems. The angular dependence is very low [11]. Accompanied with a detector moving jig, it was capable of assessing the dosimetric and geometric characteristics of the CT X-ray beam. The detector moving device is specially constructed for the purpose of this study. It is run with a direct current (DC) motor, a timing belt and a threaded axle that moves detector at a constant linear speed.

2.2 Methodology

Calibration of radiochromic films in clinical settings was performed using a semiconductor detector, as a reference instrument, and an appropriate desktop scanner capable of saving files in 24-bit TIFF format. Values of R channel were plotted against air kerma values for different tube voltages, and fitted with regression curve:

$$C_R = a + be^{-cK_a},$$

where regression parameters were $a = 126 \pm 2$, $b = 97 \pm 2$ i $c = 2.2 \pm 0.1 \text{ Gy}^{-1}$, with coefficient of determination of $\bar{R}^2 = 0.999$.

Figure 1 shows the measurement locations for both radiochromic and CTDP dosimetry system. The exact positions are denoted as follows:

- the isocentre $(0, 0, 0)$ is denoted as 0;
- measurements made using radiochromic films, when acquiring data for the z -dose profiles assessment, were conducted at positions $(-10, 0, 0)$, $(0, 0, 0)$ and $(+10, 0, 0)$ on x -axis marked as $x_1, 0$ and x_2 . They are placed on the horizontal line which passes through isocenter;
- the red line on the y_1 height indicates the location of the radiochromic film strips in the process of data acquisition for x -axis dose profiles (distance from isocenter was 15.6 cm);
- position $y_2 = 27.1 \text{ cm}$ indicates the location CTDP mounted on the moving jig at $(-10, y_2, 0)$, $(0, y_2, 0)$ and $(+10, y_2, 0)$;

Radiochromic dose measurements along z -axis were performed at tube voltage of 120 kV and tube loading of 3 As, with different filter combinations (no filter, body type and head type filter), and repeated at 5 As for head filter only. Another set of measurements were acquired by

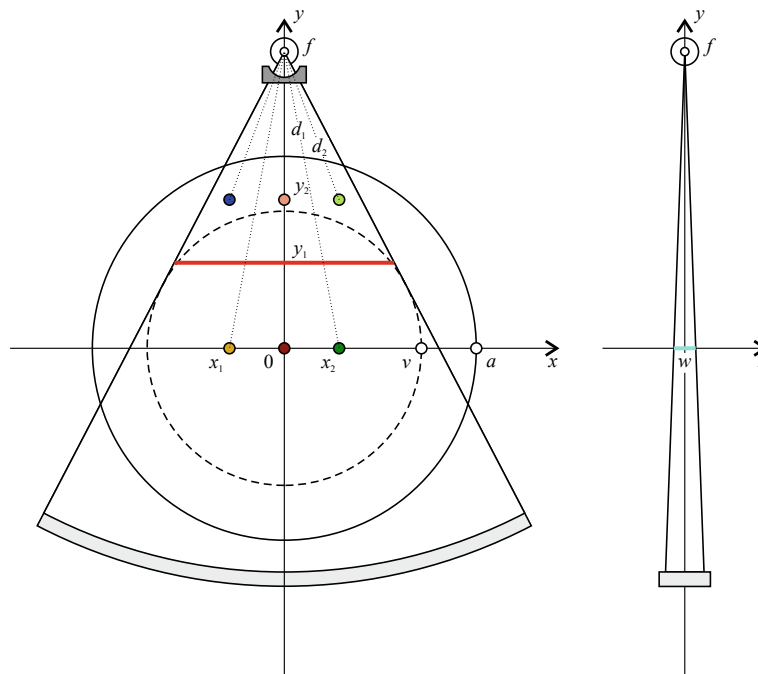


Fig. 1 Measurement locations of radiochromic and CTDP dosimetry system: isocentre $(0, 0, 0)$ is denoted as 0, f indicates the focal point and its distance from the isocenter, d_1 and d_2 were distances of the corresponding dosimetry systems from the isocenter, w stands for the beam width, radiochromic films were placed at $(-10, 0, 0)$, $(0, 0, 0)$

and $(+10, 0, 0)$ on x -axis marked as $x_1, 0$ and x_2 , line on the y_1 height indicates the location of the radiochromic film for assessment of x -axis dose profiles, position $y_2 = 27.1 \text{ cm}$ indicates the location CTDP mounted on the moving jig at $(-10, y_2, 0)$, $(0, y_2, 0)$ and $(+10, y_2, 0)$

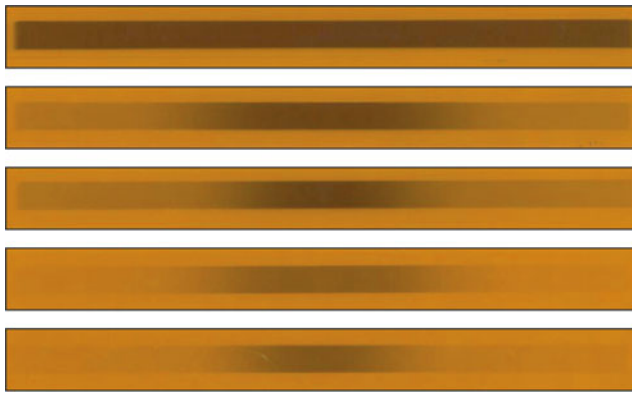


Fig. 2 Film strips of exposed radiochromic film. From top to bottom: first film is exposed without bow-tie filter, second and third with body type filter, and fourth and fifth with head type filter

CTDP-Barracuda detector system with “Ocean” software, using the same radiation quality parameters. Both radiochromic films, and CTDP moving jig were placed positions -10 , 0 and $+10$ along x -axis (Fig. 1).

When scanning the films, the chosen region of interest (ROI) was carefully selected to avoid areas with artefacts

that existed on the edges of the film due to cutting. This reduced the readout uncertainties [6].

Measurements were also performed along the x -axis using radiochromic film strips at 120 kV tube voltage (no filter, filter types body and head), and at 80 kV (filter types body and head). Exposed films are shown on Fig. 2.

3 Results

Dose profile obtained along the x -axis with the radiochromic film strips at 120 kV (no filter) is approximately uniform (Fig. 2). As expected, the central region of dose profiles exposed with the head bow-tie filter are more narrow. Dose profiles tails are more prominent in the case of 120 kV because of higher beam penetration. The FWHM is 32.6 cm, which corresponds to the selected FOV value.

Dose profiles along z -axis for different positions on x -axis obtained with radiochromic film and CTDP are shown in Figs. 3 and 4, respectively. While curve (a) corresponds to measurements with no filter in the beam, profiles (b), (c), and (d) were taken when body and head type bow-tie filters was present.

Fig. 3 Dose profiles along z -axis: **a** no filter, 120 kV, 3 As, **b** body filter, 120 kV, 3 As, **c** head filter, 120 kV, 3 As, **d** head filter, 120 kV, 5 As

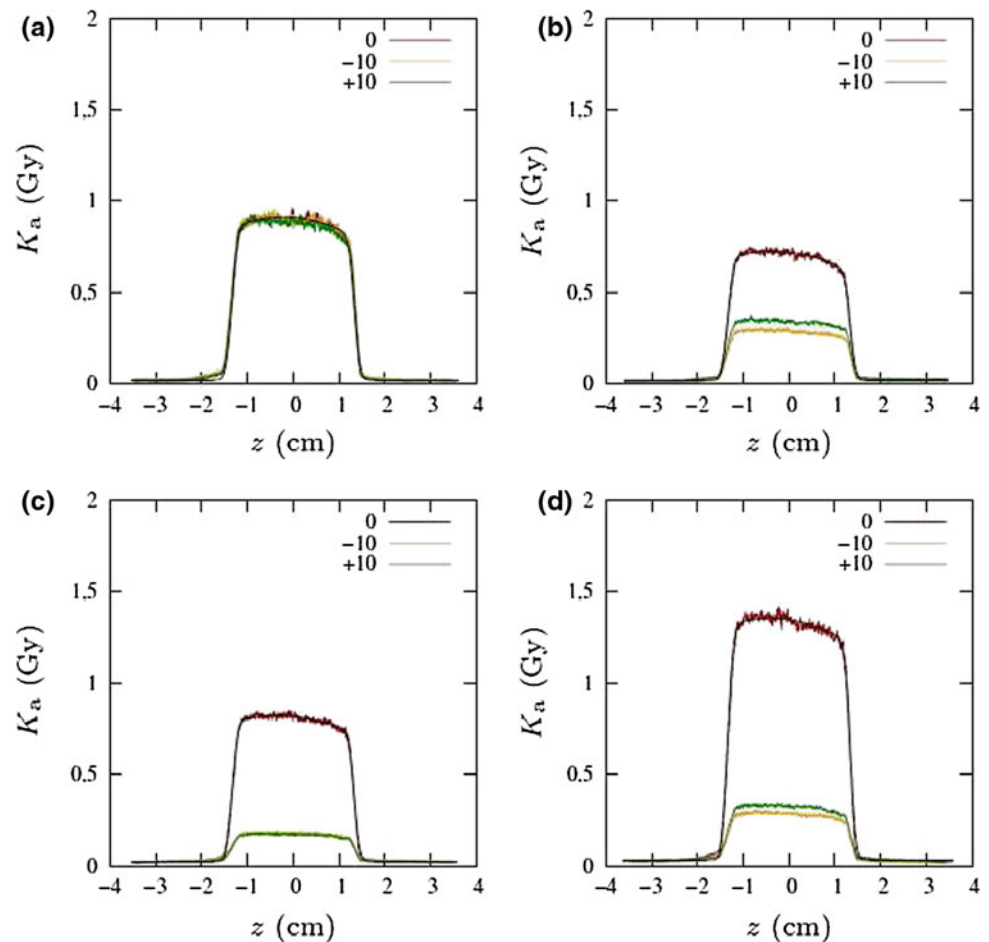
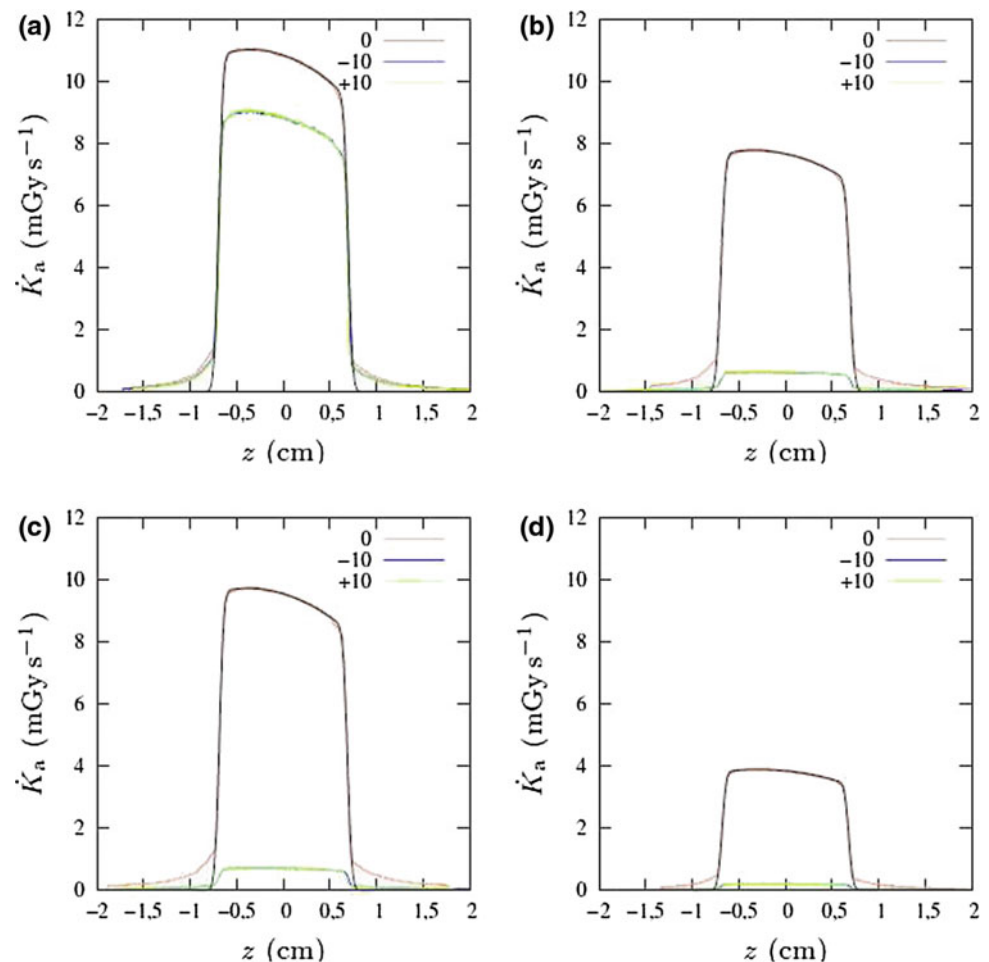


Fig. 4 Dose profiles along z -axis: **a** no filter, 120 kV, 3 As, **b** body filter, 120 kV, 3 As, **c** head filter, 120 kV, 3 As, **d** head filter, 80 kV, 3 As



4 Discussion

Use of bow-tie filters changed the dose distribution on the periphery, closer to edges, where the beam was attenuated. The head type filter is thicker on the edges than body type filter, so the difference in dose distribution is noticeable [5, 8, 13].

Figures 3 and 4 indicate asymmetry of dose profiles. This non-uniform distribution of the X-ray beam intensity is known as heel effect, which may increase by ageing of the anode [1]. It is emphasized in cone beam CTs [9].

Generally, for each dose profile it is possible to identify two zones: central peak due to the direct interaction of the beam with the active layer of the film and lateral tails arising from the scattered radiation. Width of the central zone is associated with collimation of the beam, and the height is proportional to the incident air kerma. It is important to note that the shape of lateral tails would be significantly different in the presence of phantom or patient [4].

When it comes to the CTDP, the plastic cylinder on one side of the CTDP and the aluminium tube on the other can affect the measured signal by increasing the contribution of scattered radiation [3].

5 Conclusion

Although radiochromic films are intended for use in radiotherapy or interventional radiology, they can be used to evaluate CT beam characteristics. CTDP can be used for analysis of air kerma distribution inside the CT beam, which includes analysis of bow-tie filter and heel effect.

Acknowledgements Equipment used in this paper was provided by the International Atomic Energy Agency (IAEA) through national projects of technical cooperation.

Disclosure of Potential Conflicts of Interest All authors confirm that there are no relationships or interests that could have direct or potential influence or impart bias on the work.

References

1. Braun, H., Kachelrieß, M., Kyriakou, Y., Kalender, W.A.: The influence of the heel effect on FDCT imaging with shifted detectors. In: World Congress on Medical Physics and Biomedical Engineering, pp. 439–442. Springer, Munich, Germany, 7–12 Sept 2009

2. Butson, M.J., Peter, K., Cheung, T., Metcalfe, P.: Radiochromic film for medical radiation dosimetry. *Mater. Sci. Eng.: R: Rep.* **41** (3–5), 61–120 (2003)
3. Gronlund, E.: Calibration and clinical measurements in computed tomography—an evaluation of different dosimetric methods. Master's thesis, Dissertação de Mestrado, University of Gothenburg, Gotenburg (2013)
4. Lin, P.J.P., Herrnsdorf, L.: Pseudohelical scan for the dose profile measurements of 160-mm-wide cone-beam mdct. *AJR Am. J. Roentgenol.* **194**, 897–902 (2010)
5. Mail, N., Moseley, D.J., Siewerdsen, J.H., Jaffray, D.A.: The influence of bowtie filtration on cone-beam ct image quality. *Med. Phys.* **36**, 22–32 (2009)
6. Mateus, C.Q.: Radiochromic film dosimetry system. Master's thesis, McGill University (2014)
7. McCabe, B.P., Speidel, M.A., Pike, T.L., Van Lysel, M.S.: Calibration of GafChromic XR-RV3 radiochromic film for skin dose measurement using standardized X-ray spectra and a commercial flatbed scanner. *Med. Phys.* **38**(4), 1919–1930 (2011)
8. McKenney, S.E., Nosratieh, A., Gelskey, D., Yang, K., Huang, S.y., Chen, L., Boone, J.M.: Experimental validation of a method characterizing bow tie filters in ct scanners using a real-time dose probe. *Med. Phys.* **38**(3), 1406–1415 (2015)
9. Mori, S., Endo, M., Nishizawa, K., Ohno, M., Miyazaki, H., Tsujita, K., Saito, Y.: Prototype heel effect compensation filter for cone-beam CT. *Phys. Med. Biol.* **50**(22), N359 (2005)
10. RTI: Barracuda & QABrowser Reference Manual Version 4.3A. Mölndal, Sweden (2012)
11. RTI: CT Dose Profiler Probe for Evaluation of CT Systems—Version 6.4A. Mölndal, Sweden (2015)
12. RTI: Piranha Reference Manual—Version 5.5G. Mölndal, Sweden (2016)
13. Zhang, G., Marshall, N., Jacobs, R., Liu, Q., Bosmans, H.: Bowtie filtration for dedicated cone beam ct of the head and neck: a simulation study. *Br. J. Radiol.* **86**, 20130002 (2013)

Comparison of Specific Fractal and Multifractal Parameters for Certain Regions of Interest from Digital Mammograms

Edis Đedović, Azra Gazibegović–Busuladžić, Mustafa Busuladžić, and Adnan Beganović

Abstract

Fractal analysis of grey-scale digital image is a recognized tool for detection of irregularities in the image and as measure of complexity of the image. Basic idea of this paper is to explore relation of fractal dimensions and some other related parameters in the chosen regions of interest (ROI) of grey-scale digital medical image with corresponding specific tissue characteristics. If difference of the values for calculated parameters is proven to be statistically significant for ROI of mammograms with different specific characteristics, this kind of analysis can be helpful for computer aided diagnostics. Especially, possibility of automatic detection of microcalcifications is considered. Analysis of mammograms in this manner is not a simple task, as there are four different types of parenchym tissue, there are five grades for microcalcifications according to their malignity (BI-RADS), and there are several different types of microcalcifications. Results of fractal and multifractal analysis of 131 ROIs (150×150 pixels) from 60 different mammograms are presented in this paper. Out of total 131, 60 ROIs encloses normal tissue (without dense masses or microcalcifications), and remaining 71 ROIs encloses tissue

with microcalcifications. Out of total 60 mammograms concerning parenchym tissue type, 17 mammograms are for ACR 1 structure, 21 ACR 2, and 22 ACR 3 structure. Fractal parameter that is considered is Hurst coefficient, and it is considered how it changes with size of ROI. Hölder exponent and multifractal spectra for each ROI is calculated, and corresponding histograms are analyzed. Values of suitable parameters from these histograms are tabulated to check their statistical dependence on ACR and BI-RADS grades. Zero hypothesis that there is no difference between normal ROI and ROI with microcalcifications is tested.

Keywords

Mammogram • Microcalcifications • Fractal geometry • Hurst coefficient • Multifractals • Hölder exponent

1 Introduction

Breast and lung cancer are the most common types of cancer in the world. According to an estimation of The International Agency for Research on Cancer (IARC) Global Cancer Observatory (GCO), lung and breast cancer will be contribute with 23.2% (each with 11.6%) in the total number of deaths caused by cancer in the world in 2018 [1, 2]. Based on the same estimation, breast cancer is the most common type of cancer in females (24.2%). 1.67 million of the new breast cancer cases were recorded in 2012. This disease is on the fifth place due to the number of deaths caused by cancer.

Screening film and digital mammography are two basic diagnostic methods in an early detection of breast cancer. The main signs of breast cancer in X-ray mammography, according to the American College of Radiology BI-RADS (Breast Imaging Reporting and Data System) atlas, are: an appearance of the dense masses, microcalcification clusters (MCs), an architectural distortion and bilateral asymmetry

E. Đedović
University Clinical Center Tuzla, prof. dr. Ibri Pašića, 75000
Tuzla, Bosnia and Herzegovina

E. Đedović
Department of Physics, University of Tuzla, Univerzitetska 4,
75000 Tuzla, Bosnia and Herzegovina

A. Gazibegović–Busuladžić
Faculty of Science, University of Sarajevo, Zmaja od Bosne 35,
71000 Sarajevo, Bosnia and Herzegovina
e-mail: gazr@bih.net.ba

M. Busuladžić (✉)
Faculty of Medicine, University of Sarajevo, Čekaluša 90, 71000
Sarajevo, Bosnia and Herzegovina
e-mail: mustafa.busuladzic@mf.unsa.ba

A. Beganović
Clinical Center University of Sarajevo, Bolnička 25, 71000
Sarajevo, Bosnia and Herzegovina

[3]. The interpretation of MCs' presence in an X-ray diagnostic image is a special challenge for radiologists. Due to the very common cases of false positive diagnosis in a digital screening mammography, a computer aided diagnosis (CAD) can be of a great help to the radiologists. CAD systems which analyze clusters of MCs, taking into account their morphological characteristics (size, intensity, shapes), distribution of particular MCs in a cluster as well as a texture of a surrounding tissue of MCs, can be very useful in a precise diagnosis and decreasing the number of the false positive cases of the diagnosis [4]. MCs are very common and are usually benign (noncancerous). On the other side, certain types of breast calcifications may suggest early breast cancer. The presence of the MCs, their differences in shapes and sizes and their number are often related to malignancy. The changes in a surrounding tissue texture could also be a sign of a malignant process [5].

As a human tissue is characterized by a high degree of self-similarity it is possible to analyze it as a fractal object [6]. A fractal characteristics evaluation of the organs or tissue, based on the intensity of a diagnostic image, was introduced by Pentland in 1984 [7].

In this paper an analysis of digital mammogram regions of interest (ROIs) was performed. We were guided by the idea that it is possible to consider a diagnostic image of the tissue like multifractal object, and that the morphological characteristics and the distribution of MCs as well as the changes in the texture of the surrounding tissue are possibly related to a malignancy. There are two purposes of this analysis. The first purpose is to investigate the possibility of computer detection and segmentation of suspicious regions that contains MCs or calcifications. This might be useful especially for dense tissue architecture (ACR 3 and ACR 4) and lower image quality (because of lower dose or non-sophisticated equipment). The second purpose is to try to establish differentiation benign MCs' regions of interest from malignant one, on the basis of their (multi)fractal characteristics.

2 Materials and Methods

For the purpose of analysis 60 digital mammographic images, in MLO and CC projection, were used. It was chosen 131 ROI to inspect, 60 ROIs of a normal structure (nROI) randomly selected one from each mamographic image, and 71 ROIs with the microcalcification (mcROI). The selection of mcROIs on the mammograms was done according to the radiology report. The categorization of mcROIs was done according to the BIRADS classification from the radiology report. The dimensions of ROIs for Hurst coefficient calculation were 250×250 , 200×200 and 150×150 pixels. Only ROIs with the dimension 150×150 were used in all

other parameters' calculations. This is practically square of dimensions $8 \times 8 \text{ mm}^2$.

2.1 Morphological Operations on a DICOM Image

DICOM (Digital Imaging and Communications in Medicine) mammographic images have been changed from 16-bit to the class double. After this transformation, all intensity values of pixels belong to the segment $[0, 1]$ instead to the segment $[0, 65,536]$, which has been the case for a 16-bits image. The main reason for this practical loss of precision are some numerical problems we encountered when tried to obtain binary mask in order to extract problematic regions and determine their boundaries. Another reason is to avoid or decrease numerical errors in results if/when damaged pixels are encountered.

Dilation and erosion are the basic morphological operations on a digital image. A morphological operation means a change of the dimensions of the objects on a digital image for the purpose of theirs segmentation and shape description. A probe of an image is performed using the small objects called structuring elements.

The enlargement of an object on a digital image is performed using dilation in such a way that pixels are added to the inner and outer boundaries of the object. For dilation, it is enough that the central pixel of a structuring element is within the boundaries of an object on the image. Erosion shrinks an object on an image in such a way that pixels on the boundaries of the object are stripped. As a consequence, the small details will be disappeared. For erosion, a structuring object has to be within the boundaries of an object on the image.

In this study, the operations of dilation and erosion were performed using a structuring element of diamond shape, with dimension equal to one and three, respectively.

2.2 Calculation of Hurst Coefficient for a ROI

In the paper published in 1894, Pentland [7] gave the basis of a fractal characteristics evaluation of the organs or tissue, based on the intensity of a diagnostic image. A surface of a diagnostic image may be consider as an intensity variation produced as the end result of the fractional Brownian motion. The intensity $I(r)$ of an image is a fractional Brownian's function with a coefficient H (Hurst coefficient), if a cumulative distribution function, $F(y)$, is defined as:

$$F(y) = Pr \left(\frac{I(r+r) - I(r)}{|r|^H} < y \right)$$

where \mathbf{r} is a vector, $\Delta\mathbf{r}$ is increment of \mathbf{r} , and H is a constant. In the case of a diagnostic image, \mathbf{r} is a vector with space coordinates (x, y) , $I(\mathbf{r})$ is a function of the intensity level at the position of \mathbf{r} , and $\Delta\mathbf{r}$ represents the space distance between the points $I(\mathbf{r})$ and $I(\mathbf{r} + \Delta\mathbf{r})$. The parameter H can be calculated from [25]

$$H = \frac{f(k)}{\log(\Delta r_k)}$$

so that

$$f(k) = \log(id(k)) - \log(id(1))$$

where $id(k)$ is expectation value of intensities differences for all pixels on an image separated by $r_k = k, k = 1, 2, \dots, n$. In the case of this work, the intensities difference calculations were performed taking into account the pairs of pixels separated horizontally, vertically, diagonally and symmetric diagonally by $k = 1, 2, 3, \dots, 15$.

The natural objects are constructed from more than one fractal sets which intersect each other, and each of them has its own scaling characteristics. That is the reason of introducing the term “multifractals”. In the case of multifractals, the self similarity feature was extended from a set to a measure. The measure of a finite subset $S \subset R^n$ denoted by $\mu(S)$, can be imagined as a mass distribution.

2.3 Calculation of Hölder and $f(\alpha)$ Parameters

On a digital image the measure represents the distribution of an intensity level. The finite subsets, S_i , are a neighborhood of a chosen pixel. In this study two the most common used definitions of the measure were used:

$$\text{Maximum} : \mu_i(x, y) = \max_{(x,y) \in S_i} I(x, y)$$

$$\text{Minimum} : \mu_i(x, y) = \min_{(x,y) \in S_i} I(x, y)$$

$I(x, y)$ represents the intensity level of a pixel at the (x, y) location in a domain, and S_i is a subset which contains all pixels in that domain.

A quantitative description of the multifractal structures is possible in the different ways. Usually, the procedure begins from a noninteger exponent, α , calculation. This exponent is known as Hölder’s exponent and it represents a sort of the local fractal dimension. Hölder’s exponent for a cover of the subset S_i is defined as:

$$\alpha_i = \frac{\ln(\mu(S_i))}{\ln(\varepsilon)}$$

When ε goes to zero, Hölder’s exponent of the cover goes to its limit value, α , for a considered point:

$$\alpha = \lim_{\varepsilon \rightarrow 0} \alpha_i,$$

It is a local Hölder’s exponent. When a digital image is a subject of the multifractal analysis, minimal ε value is limited by pixel’s dimension. The most common used measure in the analysis of the digital medical images is minimal measure [8, 9]. In this study, it is also used minimal measure for the purpose of the analysis.

Following the above described procedure, it is possible to associate each pixel with its corresponding α value. In such a way, an α image, a set $\alpha(x, y)$, will be produced and it has the same dimension as an original one. Usually, an α image contains the numbers of pixels with an equal value of α parameter. The next step in the multifractal analysis is to find the distribution of the particular values of α parameter in an α image. As the result a function $f(\alpha)$, called multifractal spectrum (MF), is obtained. The multifractal spectrum is the fractal dimension of a subset of a set $\alpha(x, y)$ represented as:

$$f_\varepsilon(\alpha_i) = \frac{-\ln(N_\varepsilon(\alpha_i))}{\ln(\varepsilon)},$$

where $N_\varepsilon(\alpha_i)$ is a number of boxes S_i which are containing a considered value α_i . Finally, if $\varepsilon \rightarrow 0$ the multifractal spectrum is obtained as:

$$f(\alpha) = -\lim_{\varepsilon \rightarrow 0} \frac{\ln(N_\varepsilon(\alpha_i))}{\ln(\varepsilon)}.$$

In this study, the formalism of calculation of parameters α and $f(\alpha)$ was performed for a chosen ROI on a medical diagnostic image. The boxes with the dimensions $i = 1, 3$ i 5 were formed so that they include the neighborhood pixels of a pixel located at the position (x, y) . A minimum measure was obtained when, from the neighborhood with a corresponding dimension, it was chosen a pixel with a minimum intensity. Then the normalization of that pixel was performed in a way that its intensity value was divided by a minimal intensity value of a pixel in the ROI. The α value was obtained as a slope of a line on the graph where, the values of $\ln(\mu_i(x,y))$ are added on the Y axis and the values of $\ln(i)$ are added on the X axis.

3 Numerical Results

We calculated Hurst parameter for carefully chosen mcROIs and randomly chosen nROIs, and each for two squares with the same center but with different dimensions ($8 \times 8 \text{ mm}^2$ and $13 \times 13 \text{ mm}^2$). These parameters are denoted as $H08$

and $H13$ respectively. Suitable difference between these parameters $(H13-H08)/(1.3-0.8)$ is calculated and denoted with k .

Hölder's exponent is then calculated for every pixel of the ROI of the dimension 150×150 pixels (8×8 mm²). 3D figure of the values of Hölder's exponent on selected ROI can be depicted. Maximum value of the Hölder's exponent for selected ROI is denoted as $Helmax$ (Fig. 1).

After that, multifractal spectrum $f(\alpha)$, is obtained. For each ROI we analyzed obtained $f(\alpha)$ values histogram, and record number of counts for the maximum value of the $f(\alpha)$ as the parameter $falfamax$, and the maximum number of counts for a value on the histogram as the parameter $falfa$. Several other parameters were calculated and recorded, but they did not appear to have statistical significance in the attempt to distinguish different ACR parenchymal tissue density grade or BI-RADs grade of a tumor malignancy (Fig. 2).

3.1 Data Analysis

For a statistical analysis Kruskal–Wallis test was used to determine whether there is significant difference between values of calculated multifractal parameters for ROI-s with normal tissue and tissue with calcifications, and further to check whether there is significant difference between those values for different BI-RADs grades of tumor. That is for two reasons. The first one is the fact that the values of the most parameters belong to the populations which don't follow the normal distribution. The second one is that the asymmetry for the most groups of parameters is significantly different from zero. Kruskal–Wallis is a statistical nonparametric test for comparison of two or more unpaired or unconnected groups. The analysis for this test is based on an analysis of ranks. The null hypothesis, H_0 , of the test is that the samples belong to the populations with the same distribution. For Kruskal–Wallis test, it is not necessary that the

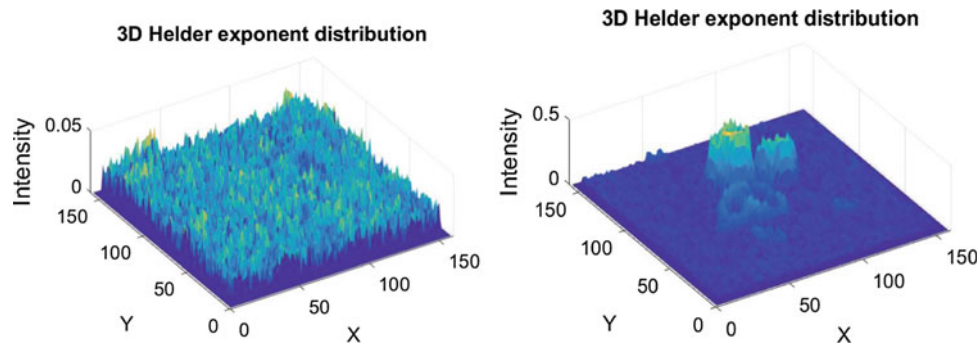


Fig. 1 Left hand panel: Helder exponent distribution presented for a normal ROI. Z coordinate marked as “Intensity” presents Helder exponent value for the corresponding (X, Y) coordinate. Right hand

panel: Helder exponent distribution for a ROI with microcalcifications. Note the scale difference between Helder exponent distribution for nROI and mcROI

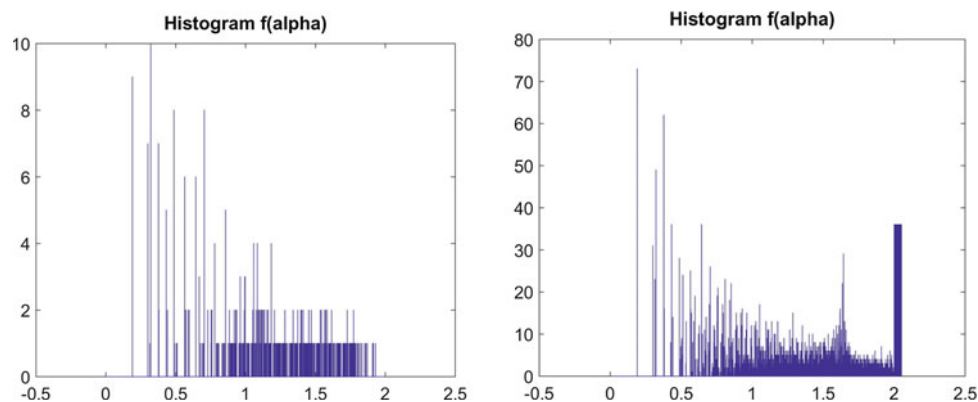


Fig. 2 Left hand panel: Multifractal spectra ($f(\alpha)$) histogram for a normal ROI. Right hand panel: Multifractal spectra ($f(\alpha)$) histogram for a ROI with microcalcifications. Note the scale difference between MF spectra for nROI and mcROI. Number of count for the maximum value

of $f(\alpha)$ was considered as the parameter $falfamax$, and maximum count on the ML spectra (maximum on the y-axis) was considered as the parameter $falfa$

samples be of equal size. Also, the variances of the particular groups of results don't have to be equal.

First, calculated parameters are checked for normal ROIs in order to determine whether some of it can be used to distinguish tissue density grade ACR. From each of the 60 collected mammograms a normal ROI (nROI) was randomly picked. Within the 60 collected mammograms there were 17 with tissue density grade ACR1, 21 with ACR2 and 22 with ACR3. We tested hypothesis that calculated multifractal parameters follow the same distribution for all three ACR types considered. The most significant difference between different types of the tissue is for the *H08* and *H13* parameters with *p*-value for the hypothesis less then 0.01.

Next, we wanted to establish whether there are parameters that are significantly different for normal ROIs (nROI) and ROI of suspicious tissue with calcifications (mcROI). Inspecting of the results of Kruskal-Wallis test and suitable t-test for parameters that satisfies normal distribution leads to conclusion that there are several calculated multifractal parameters that significantly differ for nROIs and mcROIs. The most convincing difference is for parameters *Helmax* and *falfamax*:

<i>Helmax</i>	mean	sd	No
C	0.404807	0.20745199	71
N	0.066460	0.01752552	60

<i>falfamax</i>	mean	sd	No
C	34.647465	22.704843	71
N	7.903167	8.600686	60

Parameter *Helmax* is more confident for the discrimination due to the fact that standard deviation for *falfamax* parameter is relatively large. There are several other multifractal parameters for which mean values for nROI and mcROI differs significantly, but the standard deviations are relatively large. Due to that large standard deviation there is an interval in which values from both distributions can be found with probability larger than 5%.

It is also of high interest to find possible parameter that would indicate BI-RADs grade. Our sample contains 71 mcROI with different BI-RADs grades, from 0 (inconclusive) and 1 (benign) to BI-RADs 5 (high suspicious to malignancy). Moreover, these ROIs are from mammograms corresponding to different types and shapes of calcifications and tumors, and different tissue architecture and density. Detailed analysis and suitable tests showed that difference of the calculated parameters values for mcROIs within ACR group are not significant at all, or less significant comparing to the nROIs. This might be ascribed to the fact that

calcifications within mcROIs effects (multi)fractal parameters values significantly, and that standard deviation for the parameters considered is larger for mcROIs comparing to nROIs.

There are two parameters that, according to Kruskal-Wallis test on our sample, have significantly different distributions for different BI-RADs grades. Those parameters are *falfamaxc* and *falfacmax*. Corresponding mean values, standard deviations and number of samples are given below.

<i>falfamaxc</i>	mean	sd	No
BIRADS0	22.60000	2.12132	2
BIRADS1	21.00000	21.21320	2
BIRADS2	27.81500	13.56256	18
BIRADS3	23.66182	14.45694	11
BIRADS4	30.19071	27.50517	14
BIRADS5	49.54833	22.99057	24

<i>falfacmax</i>	mean	sd	No
BIRADS0	51.50000	9.192388	2
BIRADS1	56.50000	19.091883	2
BIRADS2	62.38889	13.320214	18
BIRADS3	55.63636	20.645933	11
BIRADS4	56.21429	21.365603	14
BIRADS5	76.75000	11.333866	24

Finally, calcifications are grouped according to their size as microcalcifications and calcifications. We learned that parameter *k* has significantly different distribution for mcROIs with calcifications and mcROIs with microcalcifications.

<i>k</i>	mean	var	No
c	-0.10626	0.00539	18
mc	-0.05076	0.00509	53

4 Conclusions

For 131 ROI of approximate size 1 cm × 1 cm from 60 mammograms more then ten fractal and multifractal parameters were calculated and tabulated for further statistical analysis. 71 ROI contained tumor tissue with calcifications, and 60 ROIs that enclosed normal tissue were randomly selected. Some of the calculated parameters were shown with statistical significance to have distributions that are different for different types of tissue. Fractal dimension i.e. Hurst coefficient related to it can be related to density grade of parenchymal tissue, while its' change with ROI size differs significantly for larger calcifications and microcalcifications. Maximum value of Helder exponent that can be

related to sudden gradient of brightness is significantly different for nROIs and mcROIs while characteristic values that can be read from MF spectra has significantly different mean values for tumor tissue with different grade of malignity. Further collaboration with radiologists and larger sample of mammograms with specific type of tumors is needed to obtain smaller standard deviations and even more significant difference of multifractal parameters within different type of tissue.

References

1. IARC: Breast cancer estimated incidence, mortality and prevalence worldwide in 2012
2. IARC: Breast cancer estimated incidence, mortality and prevalence worldwide in 2018
3. Sickles, E.A., D'Orsi, C.J., Bassett, L.W., et al.: ACR BI-RADS® Mammography. In: ACR BI-RADS® Atlas, Breast Imaging Reporting and Data System. American College of Radiology, Reston, VA (2013)
4. Nelson, H.D., O'Meara, E.S., Kerlikowske, K. Balch, S., Miglioretti, D.: Factors associated with rates of false-positive and false-negative results from digital mammography screening: an analysis of registry data. *Ann Intern Med.* **164**(4), 226–235 (2016)
5. Thiele, D.L., Kimme-Smith, C., Johnson, T.D., McCombs, M., Bassett, L.W.: Using tissue texture surrounding calcification clusters to predict benign versus malignant outcomes. *Med. Phys.* **23**(4), 549–555 (1996)
6. Mandelbrot, B.B.: *The Fractal Geometry of Nature*. WH Freeman, Oxford (1983)
7. Pentland, A.: Fractal-based description of natural scenes. *IEEE Trans. Pattern Anal. Mach. Intell.* **6**(6), 661–674 (1984)
8. Lopez, R., Betrouni, N.: Fractal and multifractal analysis: a review. *Med. Image Anal.* **13**, 634–649 (2009)
9. Costa, A.F., Humpire-Mamani G., Traina A.J.M.: An efficient algorithm for fractal analysis of textures. In: *Graphics, Patterns and Images (SIBGRAPI) Conference*, pp. 39–46 (2012)

Diagnosis of Severe Aortic Stenosis Using Implemented Expert System

Lejla Divović Mustafić, Lejla Gurbeta, Alma Badnjevic-Cengic, Almir Badnjević, Behija Berberović Hukeljić, Tamer Bego, and Omer Perva

Abstract

Aortic stenosis [AS] is set on the forth place of all cardiovascular disease in western world. Severe aortic stenosis [SAS] is one of the most common disease that in treatment demand cardiac surgery—replacement of native aortic valve with mechanical or biological prosthesis in our environment. SAS is often a consequence of a relapsed rheumatic heart disease. This paper present the possible modality of diagnosis SAS. Testing was done on 107 samples, 70 samples were SAS, and the rest of 37 were patients who were sent to some another examination, after ultrasound was done and diagnosis of SAS was excluded. In this paper, the application of basic kind of ANN architecture—the feedforward networks with back-propagation training—is explained, since this structure is able to perform nonlinear multiple regressions in a reliable manner, avoid overfitting. Dataset consists of 12 parameters as shown in Table X; sex, age, dizziness/loss of consciousness, dyspnoea, palpitation, systolic murmur of AS, EF, AV morphology, AVVmax, AVPGmean, AVPGmax, Area. Although limited number of data were present in this study, such automated systems can be used

as assistant tool during diagnosis in real-time clinical settings. In the future it is planed to test and use this automated system for classification of aortic stenosis.

Keywords

Expert system • Severe aortic stenosis • Artificial neural network

1 Introduction

History of heart valve surgery started with doctor Harken Dwight who successfully replaced aortic valve in 1960, after he has corrected mitral stenosis for the first time in 1948 [1]. Aortic stenosis (AS) is the most common primary valve disease leading to surgery or catheter intervention in Europe and North America, with a growing prevalence due to the ageing population [2]. By morphology, aortic stenosis can appear because of calcific degeneration or clustering of three leaflets valve or due to bicuspidal aortic valve or often it is recognized as genetic malformation. In our country, second cause of aortic stenosis is the most common. In calcificated aortic valve, calcifications are most prominent in the center or at the basal part of each cups, commissural fusion is absent and orificium in systole looks like a star. In rheumatic aortic stenosis we see commissural fusion, and orificum looks like triangle in systole. By position, aortic stenosis can be valvular, subvalvular or supravalvular. In this paper patients with valvular aortic stenosis were included. Aortic stenosis often colerate with male gender, smoking, high blood pressure, high cholesterol and often diabetes [3].

The most important thing in aortic stenosis is symptomatology. Signs and symptoms can lead us to diagnosis of aortic stenosis; for example: dizziness/loss of consciousness, dyspnoea, palpitation, murmurs. Murmurs of sever aortic stenosis radiates along the aortic outflow tract. It is crescendo-decrescendo, systolic ejection murmur, best heard in the second right intercostal space-right sternal border,

L. D. Mustafić · B. B. Hukeljić · O. Perva
Clinic for Cardiovascular Surgery, Clinical Center University of Sarajevo, Sarajevo, Bosnia and Herzegovina

L. Gurbeta (✉) · A. Badnjević
Department of Genetics and Bioengineering, Faculty of Engineering and IT, International Burch University, Sarajevo, Bosnia and Herzegovina
e-mail: gurbetalejla@gmail.com

L. Gurbeta · A. Badnjević
Verlab Ltd, Sarajevo, Bosnia and Herzegovina

A. Badnjevic-Cengic
Canton Hospital Zenica, Zenica, Bosnia and Herzegovina

T. Bego
Department of Biochemistry and Clinical Analysis, Faculty of Pharmacy, University of Sarajevo, Sarajevo, Bosnia and Herzegovina

with a spread to the right carotid. One more can be seen—angina pain, but differential diagnosis could lead us to patient with coronary artery disease, and because of that we did not take it in consideration. The patient are coming to our Clinic usually with severe symptomatology, clinical manifestation and clear echocardiographic parameters that indicate valve replacement.

Computed tomography [CT] and magnetic resonance [MRI] of heart can tell us more about heart morphology and structural relationships of the heart structures with other organs. In this paper we use ANN do diagnose SAS with preserved EF.

2 Materials and Methods

(a) Dataset

Parameters that lead us to diagnosis of severe aortic stenosis are: (1) Peak transvalvular velocity [AVVmax] 4 m/s; (2) mean transvalvular pressure gradient [AVPGmean] 40 mmHg, (3) max.transvalvular pressure gradient [AVPGmax] 64 mmHg, (4) Aortic valve [AVA] 1 cm² and hypertrophy of left ventricular walls, (5) posterior wall diameter in diastole 11 mm, (6) interventricular septum diastole wall diameter 11 mm, (7) increase of left ventricle internal dimension in diastole [LVIDd] 56 mm, (8) diastolic dysfunction, (9) sex, (10) age, (11) Dizziness/loss of consciousness, (12) Dyspnoea [2]. Walls thickening is also something that is seen in hypertrophic cardiomyopathy caused by long-time hypertension. In this paper, we decided not to present those variables as referent, because of differential diagnose, although we measured them and found significant walls thickening in patient with sever aortic stenosis compared to control group. Same thing is with enlargement of left ventricle measured by LVIDd. It can be seen in ischemic cardiomyopathy after myocardial infarction. In our case dimension of left ventricle in the diastole were larger in group with sever aortic stenosis.

Patients with AVVmax 4 m/s; AVPGmean 40 mmHg, AVA 1 cm², symptoms and preserved ejection fraction (EF) are candidate for heart valve surgery, off course if there is no some contraindications. If patient does not have symptoms, then EF has to be measured. Cut off of EF that can be cause of different approach of dealing with sever aortic stenosis is 50%. When it is not clear, due to all parameters, weather to operate or not, some additional methods can help in definitive decision.

Considering values of AVVmax and AVPGmean in this study, we will talk about “high gradient” aortic stenosis. According to guidelines, high gradient aortic stenosis is

indication for operation, if we remove all other possible causes of high gradient over aortic valve. Aortic valve in sever aortic stenosis can be replaced by standard surgery procedure—median sternotomy, transcatheter aortic valve implantation (TAVI), or Minithoracotomy approach—minimally invasive. In our Clinic, median sternotomy is performed in most of the cases.

The patients from examined group had mechanical valve prosthesis implanted in Clinic for Cardiovascular surgery Clinical Center University of Sarajevo in period from mid-of 2013 to July 2018. All of them had isolated aortic valve stenosis. Control group of 37 patients constitute, those who came in sporadically to our Clinic, because of unspecific cardiac symptoms, at the same period. To all of them echocardiography was done, and the patients, from control group were sent to other cardial exams. Patient with sever aortic stenosis and preserved ejection fraction were set on a list and prepared for operation. Final transesophageal ultrasound was done in operating room, after intubation and before operation started, and then again after replacement of aortic valve, in order to check the gradients and possibly the presence of a paravalvular leak.

All exams were done on all exams were done on General Electric Ultrasound Vivid 7 with transtoracal and transesophagous probe.

The dataset for this study consisted of 107 samples. Out of overall number, 70 samples are for aortic stenosis class and 37 is for healthy class of patients. This dataset is comprised in University Clinical Center Sarajevo as a result of observational and treatment procedures for the patients enrolled in period x to y thus limited number of samples is presented. As indicated in Table 1, 64.8% of the dataset is represented by data from patients with diagnosis of aortic stenosis. The rest of the patients is from control—healthy class presenting no symptoms for aortic stenosis. The average age of male patients is 69.28 years and for female is 62.94 years.

As in any other health study, excluding large epidemiological studies, frequently analysis in healthcare are conducted with smaller series of data, rather than with big ones, thus the smaller dataset presented in this study. This dataset is used for creating an automated model for determining between patients with aortic stenosis diagnosis and healthy patients. Although the dataset is relatively small, appropriate neural network architectures can be used for this purpose.

(b) Feedforward Artificial Neural Network with Back-propagation Training Algorithm

Human body is very complex system considered as itself or together with its relationships with the surrounding

Table 1 Properties of the dataset used for development of artificial neural network

Class	Disease aortic stenosis	Healthy	Total
Male	43	26	72
Average age [years]	63.59	62.38	*Average age 69.28
Female	27	11	38
Average age [years]	64.26	61.63	*Average age 62.94
Total number of patients per class	70	37	107

environment. A dynamical description of such system is very useful for multiple purposes, from predicting diseases, treating diseases, drug behaviour modelling and etc. Artificial neural networks [ANNs] are data driven structures that provide very good modelling of a complex system taking into account all presented linearities and nonlinearities in the system. Nowadays, ANNs are developed and used in many fields, with several different purposes in medical related applications [4–11].

In this paper, the application of basic kind of ANN architecture—the feedforward networks with backpropagation training—is explained, since this structure is able to perform nonlinear multiple regressions in a reliable manner, avoid overfitting, if applied correctly [12]. This type of ANN can be used for modelling most problems while keeping simple architecture and low computational complexity.

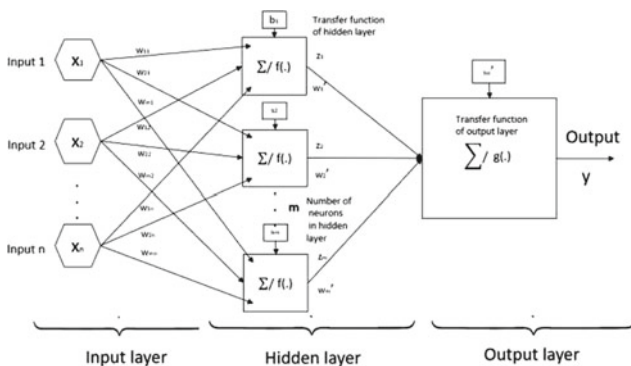


Fig. 1 Feedforward network with backpropagation training algorithm with n inputs, m neurons in hidden layer and 1 output. Transfer function in hidden layer is f. Transfer function in output layer is g. Factors b are biases and w are weights [inner neural network parameters]

The feedforward network with backpropagation training consists of network inputs that are not affected with network output in any way, Fig. 1. The output is result of modifiable connections, represented as summations of signals from hidden and input layer [13]. In hidden layer, the inputs are combined with inner neural network parameter—weights and biases. The resulting combination of such input is then transformed to neuron output by transfer function that can be linear or non-linear. The output of ANN is formed as combination of hidden layer neuron outputs. These connections between hidden and output layer are also weighted.

In these structures, the number of hidden neurons is taken low and a training-validation-test procedure is usually adopted for the optimization of an ANN model. In back-propagation training algorithm the output values are compared with the correct answer to compute the value of some predefined errorfunction. The weights and biases of neural network are corrected in each iteration. Most commonly used error function is mean square error [MSE]. After training is completed, neural network parameters are held constant for subsequent analysis.

(c) **Development of Artificial Neural Network for Classification of Aortic Stenosis Diagnosis**

Due to smaller number of data, and relatively unbalanced dataset [64.81% disease samples and 35.19 healthy samples] a method for ANN training with smaller dataset was applied during development of this system [14–18]. According to this method, the dataset was divided into three subsets: training dataset, validation and test dataset. The distribution of the samples per each class is presented in Table 2. Prior to class distribution, statistical analysis was applied to obtain

Table 2 Training and validation dataset distribution

	Disease aortic stenosis $\sum 0$ [64.81%]	Healthy $\sum 3$ [35.19%]	Percentage of total dataset
Total number of samples 108			
Training	45	24	68 [63%]
Validation	11	6	17 [16%]
Test	14	8	22 [21%]
Total number of patients per class	70	37	

statistical behaviour of samples before distributing them into subclasses.

3 Results

During the development phase, various number of neurons in hidden layer were tested as shown in Fig. 2. The back-propagation algorithm is applied on a training set, then, at each step of iteration, the performance of the obtained input-output map is validated on validation set. At each

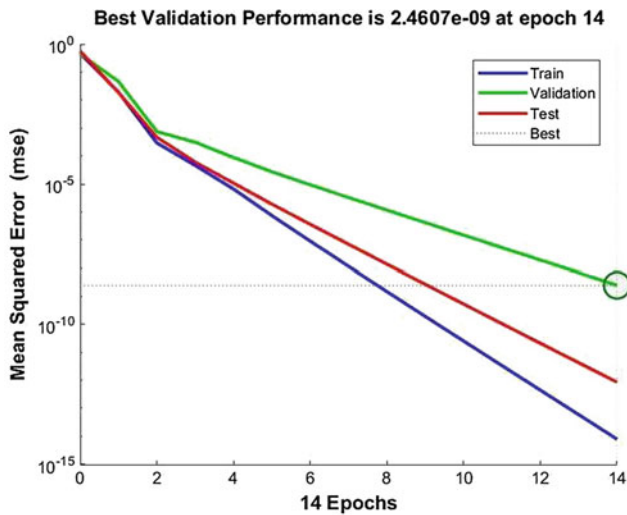


Fig. 2 Graphical overview of neural network performance. Network with 5 neurons in hidden layer

Table 3 Training performance with different number of samples

Number of neurons in hidden layer	Mean square error [MSE]
2 neurons	8.8058e-09
4 neurons	4.5392e-09
5 neurons	4.1415e-10
6 neurons	2.2985e-11
10 neurons	4.8876e-07

Table 4 Testing performance of developed architecture

Total number of samples 108	Test subset disease aortic stenosis	Test subset healthy	Accuracy [%]
ANN Disease aortic stenosis	14	0	100.00
Healthy	0	8	100.00
Total number of patients per class	14	8	100.00

point, network parameters [weights and biases] were adjusted to optimize the performance criteria. The iteration process is stopped when the performance on the validation set begins to decrease. This early stopping procedure is performed to avoid the overfitting due to a too much close reconstruction of the data in the training set (Table 3).

According to neural network performance, architecture with 12 input neurons, 5 neurons in hidden layer and one output neuron was chosen for development of this system for classification of aortic stenosis.

This network has non-linear transfer function in neurons in hidden layer. The output is determined by linear transfer function. Training performance of this architecture is presented in Fig. 2.

Finally, a test set of data, completely unknown to the network, is considered. Just on this test set one can measure the real performance of the ANN model in reconstructing new data and events.

The result presented in Table 4. is expected due to limited number of data which is one limitation of this study. Nevertheless, it proved that such automated systems can be used as assistant tool during diagnosis in real-time clinical settings. This automated system for classification of aortic stenosis will be tested in real-time clinical environment in future in order to validate clinical effectiveness.

4 Conclusion

In the future we expect less patients with SAS caused by rheumatic heart disease. Generation of patients that were affected by rheumatic fever and did not asked for help are extinguishing nowadays. Today patients are more educated and informed about consequences of non treated conditions. In the future we will have patients with not so high gradient and not so small area of aortic valve. Are we going to operate them and replace valve or are we going to wait for gradient to be higher, and area to be smaller. With waiting we are acting as guidelines demand. But with waiting we are risking irreversible changes such as fibrosis to appear on myocardium. The result is great technical performed operation but not always great

feed back from patient. Increasing of some novel biomarkers of cardiovascular stress such as: growth differentiation factor 15 [GDF15], soluble ST2 [sST2], amino-terminal pro-B-type natriuretic peptide [NTproBNP], galectin-3, high-sensitivity cardiac troponin T, myeloperoxidase, high-sensitivity C reactive protein and monocyte chemotactic protein-1, correlates with mortality in patients with SAS undergoing aortic valve replacement [19]. Some of them are available on our market, for some of them we will wait-hope not so long. Further studies are needed to evaluate their utility of these biomarkers and many others in clinical decision-making of right timing for operation. All those new data will forced us to do work on more complicated and more useful Artificial Neural Network. Because of small sample, this ANN can be a good basis for developing a more sophisticated ANN, which could be used in everyday practice in diagnosis and making a decision on treatment not just all kinds of aortic valve, but also all other cardiovascular diseases.

References

- Cohn, L.H., Tchanchaleishvili, V., Rajab, T.K.: Evolution of the concept and practice of mitral valve repair. *Ann. Cardiothorac. Surg.* **4**(4), 315–321 (2015)
- Baumgartner, H., Falk, V., Bax, J.J., De Bonis, M., Hamm, C., Holm, P.J., Iung, B., Lancellotti, P., Lansac, E., Rodriguez, D., Rosenhek, R., Sjögren, J., Mas, P.T., Vahanian, A., Walther, T., Wendler, O., Windecker, S., Zamorano, J.L.: 2017 ESC/EACTS Guidelines for the Management of Valvular Heart Disease. The Task Force for the Management of Valvular Heart Disease of the European Society of Cardiology [ESC] and the European Association for Cardio-Thoracic Surgery [EACTS]
- Brinkley, D.M., Gelfand, E.V.: Valvular Heart Disease: Classic Teaching and Emerging Paradigms. Beth Israel Deaconess Medical Center [Cardiovascular Division] and Harvard Medical School, Boston, Mass
- Catic, A., Gurbeta, L., Kurtovic-Kozaric, A., Mehmedbasic, S., Badnjevic, A.: Application of Neural Networks for classification of Patau, Edwards, Down, Turner and Klinefelter Syndrome based on first trimester maternal serum screening data, ultrasonographic findings and patient demographics. *BMC Med. Genomics* **11**, 19 (2018). <https://doi.org/10.1186/s12920-018-0333-2>
- Badnjevic, A., Gurbeta, L., Cifrek, M., Marjanovic, D.: Classification of asthma using artificial neural network. In: IEEE 39th International Convention on Information and Communication Technology, Electronics and Microelectronics [MIPRO], 30 May to 03 June 2016. Opatija, Croatia
- Aljovic, A., Badnjevic, A., Gurbeta, L.: Artificial Neural networks in the discrimination of Alzheimer's disease using biomarkers data. In: IEEE 5th Mediterranean Conference on Embedded Computing [MECO], 12–16 June 2016, Bar, Montenegro
- Alic, B., Sejdinovic, D., Gurbeta, L., Badnjevic, A.: Classification of stress recognition using artificial neural network. In: IEEE 5th Mediterranean Conference on Embedded Computing [MECO], 12–16 June 2016, Bar, Montenegro
- Halilovic, S., Avdihodžić, H., Gurbeta, L.: Micro cell culture analog apparatus [μ CCA] output prediction using artificial neural network. In: 5th Mediterranean Conference on Embedded Computing [IEEE MECO 2016], Bar, Montenegro (2016)
- Veljovic, E., Spirtovic-Halilovic, S., Muratovic, S., Osmanovic, A., Badnjevic, A., et al.: Artificial neural network and docking study in design and synthesis of xanthenes as antimicrobial agents. In: IFMBE Proceedings. CMBEBIH 2017, vol. 62, pp. 617–626. Springer, Singapore. https://doi.org/10.1007/978-981-10-4166-2_93
- Alic, B., Gurbeta, L., Badnjevic, A.: et al.: Classification of metabolic syndrome patients using implemented expert system. IFMBE Proceedings. CMBEBIH 2017, vol. 62, pp. 601–607, Springer, Singapore. https://doi.org/10.1007/978-981-10-4166-2_91
- Sejdinovic, D., Gurbeta, L., Badnjevic, A., Malenica, M., Dujic, T., Causevic, A., Bego, T., Divovic, L.: Classification of prediabetes and type 2 diabetes using artificial neural network. IFMBE Proceedings. CMBEBIH 2017, vol. 62. Pp. 685–689. Springer, Singapore. https://doi.org/10.1007/978-981-104166-2_103
- Pasini, A.: Artificial neural networks for small dataset analysis. *J Thorac Dis.* **7**(5), 953–960 (2015)
- Guenther, F.H.: Neural networks: biological models and applications. In: International Encyclopedia of the Social and Behavioral Sciences
- Pasini, A., Potestà, S.: Short-range visibility forecast by means of neural-network modelling: a case study. *Il Nuovo Cimento C* **18**, 505–516 (1995)
- Pasini, A., Pelino, V., Potestà, S.: A neural network model for visibility nowcasting from surface observations: results and sensitivity to physical input variables. *J. Geophys. Res.* **106**, 14951–1499 (2001)
- Pasini, A., Lorè, M., Ameli, F.: Neural network modelling for the analysis of forcings/temperatures relationships at different scales in the climate system. *Ecol. Model.* **191**, 58–67 (2006)
- Pasini, A., Langone, R.: Influence of circulation patterns on temperature behavior at the regional scale: a case study investigated via neural network modeling. *J. Clim.* **25**, 2123–2128 (2012)
- Pasini, A., Modugno, G.: Climatic attribution at the regional scale: a case study on the role of circulation patterns and external forcings. *Atmos. Sci. Lett.* **14**, 301–305 (2013)
- Lindman, B.R., Breyley, J.G., Schilling, J.D., Vatterott, A.M., Zajarias, A., Maniar, H.S., Damiano R.J., Moon, Jr M.R.J., Lawton, S., Gage, B.F., Sintek, M.A., Aquino, A., Holley, C.L., Patel, N.M., Lawler, C., Lasala, J.M., Novak, E.: Prognostic utility of novel biomarkers of cardiovascular stress in patients with aortic stenosis undergoing valve replacement. *Heart* **101**(17), 1382–1388 (2015). <https://doi.org/10.1136/heartjnl-2015-307742>. Epub 2015 Jun 2
- Jurilj, R., Božić, I.: *Ehokardiografija*. Medicinska naklada, Hrvatska (2013)
- Katritsis, D.G., Gersh, B.J., Camm, A.J.: *Clinical Cardiology: Current Practice Guidelines*. Oxford University Press (2014)
- Vegas, A.: *Perioperative Two Dimensional Transesophageal Echocardiography: A Practical Handbook*. 2nd edn. Springer
- Armstrong, W.F., Ryan, T., Feigenbaum, H.: *Feigenbaum's Echocardiography*, 7th edn. Wolters Kluwer/Lippincott, Williams and Wilkins Health, Philadelphia
- Yuh, D.D., Vricella, L.A., Yang, S.J., Doty, R.: *Textbook of Cardiothoracic Surgery*, 2nd edn. Johns Hopkins Medicine

Portable X-Ray Devices: Loosing Border Between Controlled and Supervised Areas

Jovica Ž. Praskalo, Biljana V. Petrović, and Adnan Beganović

Abstract

The introduction of portable hand-held X-ray devices opened a new chapter in dental radiology. The strict border between the controlled and supervised areas ceases to exist. The aim of this paper is to measure the dose rate around a portable dental X-ray device, as well as to provide spatial distribution of the ambient dose equivalent of scattered radiation. Results also include measurements of X-ray tube voltage, incidence air kerma, exposure time, half-value layer and total filtration according to the international standard IEC 61223-3-2:2015 Evaluation and routine testing in medical imaging departments for the quality control of dental X-ray devices. Measured values of incidence air kerma indicate the values of the patient doses which are much lower than existing national diagnostic reference values.

Keywords

Portable X-ray device • Occupational exposure

1 Introduction

Regulations on radiation protection in dental diagnostic practice in Bosnia and Herzegovina require that X-ray devices are used in premises that are designed to meet specific requirements [4–6]. The great majority of regulatory requirements are in line with international standards. The X-ray room is usually considered as controlled area, where only the radiographed patient is exposed to ionizing radiation. The operator, staff and other patients are in a supervised area, where no special protective measures and compliance with special procedures are required [5].

The hand-held portable X-ray devices were invented in the 1990s, with intention to be used in military [2]. However, they have been recently marketed for use in civil dental diagnostics, which raised concern among professionals [7]. Although the X-ray unit is equipped with built-in lead shear, the distance between the patient and the operator is close to minimal. During the exposure that usually happens when patients is in the dental chair, the operator and sometimes other personnel, as well as patients who are present but do not undergo radiological examinations, are exposed to scattered radiation. The clear difference between controlled and supervised area ceases to exist. Similarly, persons operating the source of ionizing radiation may be classified into category A or B, but others are usually not classified, and therefore are members of the public [5]. Unclassified staff are not covered by personal dosimetry, which is also true supporters and for patients that do not undergo diagnostic X-ray procedure but who might be in the same room as exposed patient.

The aim of this paper was to evaluate the spatial distribution of the dose rate of scattered radiation emitted by the portable dental X-ray device designed for imaging in dental radiology, as well as to examine its performance (output, entrance surface dose, exposure time, HVL and total filtration) according to the according to the method from international standard ISO 61223-3-2:2015 Evaluation and routine testing in medical imaging departments [3].

J. Ž. Praskalo (✉) · B. V. Petrović
Public Health Institute of Republic of Srpska, Banja Luka Jovana
Dučića 1, 78000 Banja Luka, Bosnia and Herzegovina
e-mail: jovica.praskalo@phi.rs.ba

A. Beganović
Department of Radiation Protection and Medical Physics, Clinical
Centre of Sarajevo University, Bolnička 25, 71000 Sarajevo,
Bosnia and Herzegovina

A. Beganović
Faculty of Science, University of Sarajevo, Zmaja od Bosne
33–35, 71000 Sarajevo, Bosnia and Herzegovina

2 Materials and Methods

2.1 Medical Exposure

In this study we used X-ray unit “Vatech EzRay Air”, a portable X-ray device for intraoral dental imaging. It has been available on the market in Bosnia and Herzegovina since September 2018.

The device has a fixed tube voltage of 65 kV and tube current of 2.5 mA. The exposure time ranges between 0.05 and 0.5 s. The distance between focal spot (source of ionizing radiation) and the patient’s skin is 20 cm. The device’s tubehead is made of carbon nanotubes. Its input voltage is 22.2 V and diameter of protective barrier is 165 mm. Backscatter shield is made of transparent lead-acrylic sheet. Mass of the device is 1.8 kg. Image detector named “RVG EzSensor Classic” is using a CMOS digital picture receiver. The detector is 4.8 mm thick, 29.6 μm pixel size and resolution of 17 lp/mm.

Scattered radiation was measured by Automess Scintillator Probe 6150 AD-b, while RTI Electronics Barracuda was used to assess the parameters of the device (tube voltage, air kerma, total filtration, half-value layer, and exposure time). The patient was simulated by the anthropomorphic head phantom RS 900.

Measurements of ambient dose equivalent of scattered radiation were performed at different positions against X-ray tube. Selected measuring points were roughly at the height of operator’s head, chest, gonads, and knees (180, 150, 100, 50 cm from the floor) and at different distances from X-ray tube. Scattered radiation doses were measured with and without protective apron. All exposures were performed with phantom in the X-ray beam.

3 Results and Discussion

Measured values of dose rate at different distances from the X-ray tube during exposure are presented in Table 1. The first column shows the values obtained when measuring behind the protective apron (equivalent to 0.5 mm Pb), while values from the second column represent what would be the dose rate at operator’s position without the protective apron. Table 2 shows values of dose rate depending on the distance of the X-ray device, in the central air axis, behind the phantom. Results represent maximum dose rate values measured at certain points, using the exposure parameters that are most frequently used in intraoral dental radiology, with exposure time of 180 ms, tube voltage of 65 kV and tube current of 2.5 mA. Quality control parameters are given in a Table 3.

Table 1 Dose rate measured in different points, with and without the protective apron

		Dosimeter readout (μSvh^{-1})	
		With apron	Without apron
Position	Hand	.	74.7
	In front of phantom	.	93.2
	2 m (lateral)	.	4.63
	Head (180 cm)	35.9	35.9
	Chest (150 cm)	10.7	74.7
	Gonads (100 cm)	1.8	17.5
	Knees (50 cm)	16.1	16.1
	Next to the tubus	.	15.8
	Behind apparatus	.	8.71

Table 2 Dependence of dosimeter readout from distance

Distance (m)	Dosimeter readout (μSvh^{-1})
2.5	20.4
4	7.1
6	3.28
8	1.47
10	0.99
15	0.42
25	0.18
2.5 (without phantom)	12.1

Table 3 Results of quality control and in-beam dosimetry

Test	Value	Result
Tube voltage accuracy	2.6% Deviation from set value	Passed
Repeatability of tube voltage	1.5% Coefficient of variability	Passed
Filtration	1.6 mm Al	Passed
Half-value layer	1.6 mm Al	Passed
Repeatability of radiation output	0.7%	Passed
Incidence air kerma at 2.5 mA per unit of exposure time (mGys^{-1})	3.34 ± 0.08	

According to the national regulations, the effective dose (E), for exposed workers, must not exceed 20 mSv in a single year. Limit for the general public, however, is 1 mSv [5].

Taking into account these limits, we can calculate what would be the upper limit of dose rate values in a given situation, taking into account the characteristics of measuring equipment, such as time and energy response.

The factor that has the most influence, besides the dose rate, is the estimated number of patients who will undergo diagnostic procedure. Another relevant quantity is the exposure time, which is limited by the device itself. Finally, the effective dose is approximated by the ambient dose equivalent, which is an operational quantity designed for area monitoring [1].

Thus, the effective dose for an operator on a given device, E , can be estimated according to the following expression:

$$E = \dot{H}^*(10) \times N \times t, \quad (1)$$

where E is the annual effective dose, $\dot{H}^*(10)$ annual ambient dose rate equivalent, N the expected number of exposures in a single one year, and t exposure time.

The use of protective equipment will have a significant impact on the effective dose received by the operator, as can be seen in Table 3. Measured values of incidence air kerma, $K_{a,i}$ indicate that patient doses, expressed in entrance surface dose, $D_{s,e}$, would lower than the 7 mGy per the projection, which is the national diagnostic reference level (DRL) [6]. Although, DRL is not the limit, this is seen as an indicator of acceptability of certain diagnostic procedures from the radiation protection point of view.

4 Conclusion

Persons professionally exposed to ionizing radiation, as well as staff not classified as exposed workers, or patients in the waiting room can be exposed to scattered radiation generated

by the hand-held X-ray device. This exposure greatly depends on the position where persons are located, as well as the distance from the X-ray unit. Justification of exposure of people, other than supporters, in the room is questionable.

References

1. A. Endo on behalf of ICRU Report Committee 26 on Operational Radiation Protection Quantities for External Radiation: Operational quantities and new approach by ICRU. *Annals of the ICRP*, vol. 45, suppl 1, pp. 178–187 (2016)
2. Berkhout, W.E.R., Suomalainen, A., Brillmann, D., Jacobs, R., Horner, K., Stamatakis, H.C.: Justification and good practice in using handheld portable dental X-ray equipment: a position paper prepared by the European Academy of Dentomaxillofacial Radiology (EADMFR). *Dento Maxillo Facial Radiol.* **44**, 20140343 (2015)
3. IEC: 61223-3-2:2015 Evaluation and routine testing in medical imaging departments. International Standard (1999)
4. State Regulatory Agency for Radiation and Nuclear Safety: Regulation on the conditions for the traffic and use of ionizing radiation sources. *Official Gazzette of Bosnia and Herzegovina* (2010)
5. State Regulatory Agency for Radiation and Nuclear Safety: Regulation on radiation protection for occupational and public exposure. *Official Gazzette of Bosnia and Herzegovina* (2011)
6. State Regulatory Agency for Radiation and Nuclear Safety: Regulation on the ionizing radiation protection in medical exposure. *Official Gazzette of Bosnia and Herzegovina* (2011)
7. Ramesh, D.V., Wale, M., Thriveni, R., Byatnal, A.: Hand-held X-ray device: a review. *J. Indian Acad. Oral Med. Radiol.* **30**(2), 153–157 (2018)

Effectiveness of Asymmetry Analysis Technique Based on Statistical Features in Breast Cancer Detection with Modern Thermographic Imaging Systems

Irfan Karagoz

Abstract

This paper discusses the diagnostic performance of the modern medical thermal imaging system with the other imaging modalities for breast cancer detection. In this study, the digital infrared thermal imaging system is used for analyzing the thermal images of the 270 breast patients diagnosed by the conventional imaging techniques. The thermographic images of these patients are analyzed and then classified according to the 6 different BI-RADS categories by means of the asymmetry analysis technique based on the commonly used 11 statistical features. Finally, higher sensitivity, specificity values and higher accuracy rates are obtained for the 270 breast patients.

Keywords

Breast cancer • Cancer diagnosis • Thermography • Asymmetry analysis • Feature extraction • Infrared imaging

1 Introduction

Breast cancer has been known for decades to be the most common type of cancer among women. It has a high incidence rate. Mammography is the widely used diagnostic method for breast cancer detection but it is not as an effective method for women aged 40 and younger with dense breasts because of lower sensitivity [1]. At the same time, it has an ionizing radiation risk and it is a discomfort technique because of the compression of breasts. Digital infrared thermal imaging techniques can be used for early detection of breast cancer as a physiological imaging technique as a complimentary method together with the other techniques.

I. Karagoz (✉)
Electrical and Electronics Engineering Department, Engineering Faculty, Gazi University, 06570 Ankara, Turkey
e-mail: irfankaragoz@gazi.edu.tr

In this perspective, the Food and Drug Administration approved breast thermography as an adjunctive breast cancer diagnostic screening procedure for the detection of breast cancer in 1982.

Digital infrared thermal imaging for detection of breast cancer has undergone for several decades. Numerous medical centers have been used thermography as diagnostic purposes. Clinical thermography is a procedure that detects, records, and produces an image of a patients skin surface temperatures. Digital infrared thermal imaging does not include ionizing radiation and it does not pose harm to the patient. The breast thermography provides information on the normal and abnormal physiologic functioning of the tissues.

Several studies show that thermographic imaging systems can be used as an alternative and adjunct method for determining the breast cancer risk.

Gautherie and Gros studied 58,000 patients having thermographic images during 12 years. They detected initially 1527 patents having healthy breasts but abnormal asymmetric thermograms. After 5 years, they saw that 44% of these patients have malignancies [2].

Spitalier et al. screened 61,000 women's thermographic images during 10 years period. They detected 1416 patients having no clinical and radiographic malignancy suspicion but having abnormal breast thermogram. They saw that 26% of these patients had actuarial breast cancer after 5 years. In this study, the specificity and sensitivity rates were found to be 89% [3].

For comparing purposes, clinical examination, mammography, and thermography were studied in the diagnosis of breast cancer in another study. In this study including 16,778 patients, it was found that clinical examination had an average sensitivity of 75% in detecting all tumors and 50% in cancers less than 2 cm in size, mammography had an average 80% sensitivity and 73% specificity, but thermography was found to have an average sensitivity of 88% and a specificity of 85%. As a result of this study, none of these techniques is sufficiently accurate to be used alone for

evaluating patients with breast cancer. The authors said that a multi modal approach should be used [4].

The aim of this study is to evaluate the performance of a modern medical thermal imaging system and to compare the performance of this system with other modalities.

2 Material and Method

2.1 Equipment

Medical Thermal Imaging System detects changes of temperatures on human body and enables doctors to diagnose specific diseases and disorders in early stages. Medical thermography is a passive imaging system with no harmful side-effects that can diagnose effects that cannot be seen by traditional medical imaging devices. In this study, Misther Medical Thermal Imaging System (MISTHER) is used. MISTHER is a leading-edge medical thermal imaging system with its outstanding features. It has a 8–14 μm spectral band uncooled microbolometer type LWIR thermal sensor with thermal precision of 50 mK, 50 Hz frame rate, 16 bit data resolution, 17 μm pixel size, and 640 × 480 thermal resolution. This system has a vertical software based motion control system with high quality servo motor to adapt patient position, 18 mm f/1, HFOV 42.6, standard optical lens with manual/automatic focus options, and integrated medical approved PC based on Intel i5 processor and 24 Full HD screen and medical approved antibacterial keyboard.

For analyzing the thermal images, this device has 9 different coloring algorithms to show temperature differences on human body. Adjustable and adaptive maximum/minimum values on the coloring scale are used to allow deeper analysis on different temperature levels.

Real-time zoom on the live camera view with sensitive zoom controls is used for statistical calculations. Additionally, pointwise temperature measurements in camera view and zoom views are used for deeper analysis and detection of anomalies.

2.2 Patient Preparation Protocols

The imaging room must be temperature and humidity-controlled and maintained between 18 and 23 °C,

and kept to within 1 °C of change during the examination. The patient must undergo 15 min of waist-up nude acclimation in order to reach a condition in which the body is at thermal equilibrium with the environment.

2.3 Imaging

A special process is applied to detect infrared emissions from the breast surfaces. At least 5 different images are needed for infrared analysis of each breast. The series includes the bilateral frontal breast along with the right and left oblique views (approximately 45 °C to the detector) and lateral left and right breast views.

In the seated position, the patient places their arms on the arm rests away from the body to allow for proper acclimation. When positioning the patient in front of the camera, a rotating chair is required for taking the necessary views.

In this study, 270 breast patients are screened with the MISTHER Medical Thermal Imaging Device. The **BIRADS** “Breast Imaging Reporting And Data Systems” method is used for classifying the patients having mammography, ultrasound, MR images and/or biopsies in 6 different categories. BI-RADS classification is proposed by the American College of Radiology (ACR). The BI-RADS which is a widely accepted risk assessment and quality assurance tool in mammography, ultrasound or MRI is used for true classification of these patients. The related classification is given in Table 1.

The explanation for the 6 different BI-RADS categories is given below [5]:

- BI-RADS I: Negative—symmetrical and suspicious calcifications present but no masses
- BI-RADS II: Benign
- BI-RADS III: Probably Benign
- BI-RADS IV: Suspicious abnormality—there is a mammographic appearance which is suspicious for malignancy and biopsy should be considered for such a lesion. This category can be further divided as:
 - BI-RADS 4A: Low suspicion for malignancy
 - BI-RADS 4B: Moderate suspicion for malignancy
 - BI-RADS 4C: High suspicion for malignancy
 - BI-RADS V: Highly Suggestive of Malignancy
 - BI-RADS VI: Known Biopsy-Proven Malignancy.

Table 1 BI-RADS categories for screened patients

BI-RADS	1	2	3	4	5	6
Number of patients	55	16	63	4A: 16	16	2
				4B: 6		
				4C: 9		

2.4 Method

Human body has a thermal symmetry. Asymmetry analysis is an important technique for detecting abnormalities in the breast thermographs. An automated approach based on asymmetry analysis is developed for breast cancer detection using thermal infrared images [6]. For this purpose different features are extracted from the breast images. Comparison of these features is done to detect any asymmetry and then to classify the image as cancerous or non-cancerous. Asymmetry analysis in breast thermography includes four stages: ROI Selection, Segmentation, Feature Extraction and Classification.

In this study 11 features are used for asymmetry analysis [7]. These features are mean, variance, skewness, kurtosis, mode, median, entropy, energy, correlation, contrast, and homogeneity.

270 patients are analyzed and classified by using these features and compared with the clinical evaluations based on mammography, ultrasound and biopsy results by taking into account these criteria:

- True Positive (TP): Sick people correctly identified as sick
- False Positive (FP): Healthy people incorrectly identified as sick
- True Negative (TN): Healthy people correctly identified as healthy

- False Negative (FN): Sick people incorrectly identified as healthy and the classification results are given in Table 2.

Analysis results are given below:

- Sensitivity (or true positive rate) = $\frac{TP}{TP+FN} = 97.29\%$
- Specificity (or true negative rate) = $\frac{TN}{TN+FP} = 88.88\%$
- Accuracy = $\frac{TP+TN}{TP+FP+FN+TN} = 90.00\%$

Thermography had 26 false positive, 207 true negative, 36 true positive, 1 false negative results. Sensitivity was calculated as 97.29%, specificity as 88.88% and accuracy as 90.00%.

As an example, the analysis results are given below for two different patients having different BI-RADS categories.

11 features for right and left breasts of the patient evaluated as BI-RADS 3 category are extracted and they are given in Table 3.

For this patient, as a result of the asymmetry analysis based on the 11 features it is seen that there is no important difference between features of her two breasts as shown in Fig. 1.

11 features for right and left breasts of the patient evaluated as BI-RADS 5 category are extracted and they are given in Table 4.

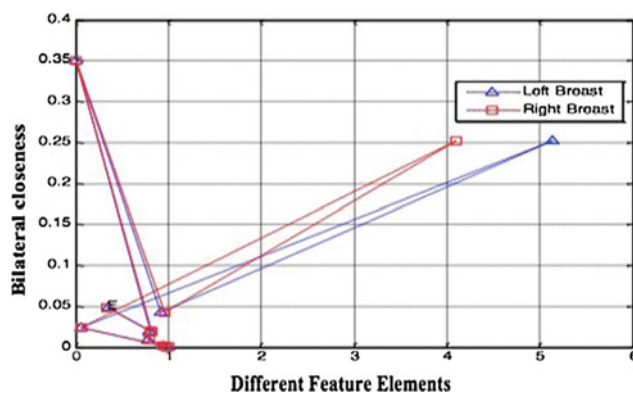
For this patient, as a result of the asymmetry analysis based on the 11 features, it is seen that there is an important difference between features of her two breasts, especially in the skewness and kurtosis values as shown in Fig. 2.

Table 2 Classification results

BI-RADS	1	2	3	4	5	6
Number of patients	55	16	63	4A: 16 4B: 6 4C: 9	16	2
Classification results	FP: 7 TN: 48	FP: 10 TN: 93	FP: 9 TN: 54	4A TP: 10 FN: 1 TN: 5 4B TP: 4 TN: 2 4C TP: 7 TN: 2	TP: 13 TN: 3	TP: 2

Table 3 The statistical feature results related to the right and left breasts of the patient evaluated as BI-RADS 3 category

Patient category: BI-RADS 3	Left breast values	Right breast values
Skewness	0.91585	0.95727
Kurtosis	5.1353	4.1034
Variance	0.003086	0.002285
Mean	0.80442	0.82028
Entropy	0.35065	0.33441
Contrast	0.058656	0.057289
Correlation	0.97222	0.97279
Energy	0.94058	0.94275
Homogeneity	0.99756	0.99838
Mode	0.78243	0.78903
Median	0.79079	0.80571

**Fig. 1** The graphical representation of the asymmetry analysis results based on the 11 features for the two breasts of the patient evaluated as BI-RADS 3 category**Table 4** The statistical feature results related to the right and left breasts of the patient evaluated as BI-RADS 5 category

Patient category: BI-RADS 5	Left breast values	Right breast values
Skewness	3.8631	0.075112
Kurtosis	34.92	13.079
Variance	0.005951	0.003324
Mean	0.83483	0.78126
Entropy	0.7206	0.64196
Contrast	0.080904	0.079831
Correlation	0.98263	0.97832
Energy	0.87415	0.88691
Homogeneity	0.99562	0.99625
Mode	0.79608	0.77255
Median	0.83922	0.77255

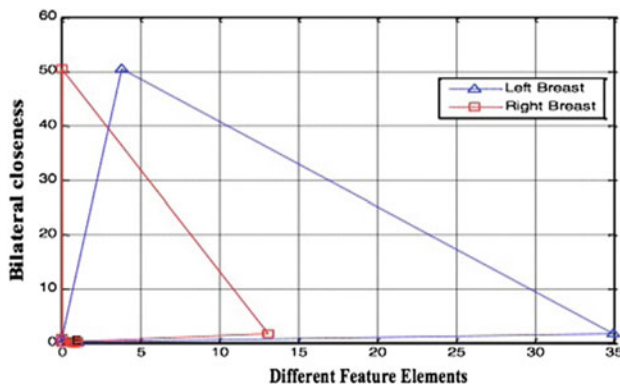


Fig. 2 The graphical representation of the asymmetry analysis results based on the 11 features for the two breasts of the patient evaluated as BI-RADS 5 category

3 Discussion

This study has shown that modern digital thermography has a higher sensitivity, specificity values and higher accuracy rates with respect to other imaging modalities for breast cancer detection. Although it is a harmless functional imaging technique, it has a limited clinical applications at the present time because of problems coming from the past like incorrect assessment that infrared imaging might replace mammography, application by untrained technicians, erroneous reporting by radiologists who had no experience and knowledge in reading infrared images, improper laboratory environmental, and no standardized reading protocol [8].

Abnormal functional infrared breast images taken from these modern systems can be considered as a future risk indicator for breast cancer because these systems have the ability to detect the first signs that a cancer may be forming up to 10 years before any other procedure can detect it [9].

There are many peer-reviewed studies on breast thermography in the index medicus literature. These studies were realized with very large participants by following patients up to 12 years. In these studies, higher sensitivity and specificity values were obtained with respect to the other imaging modalities.

At the present time, it is possible to detect minute variations in the thermal emissions by means of the higher resolution thermal sensors, higher speed computers and the sophisticated computerized analytical processing techniques.

In this study, we obtained higher specificity, sensitivity, and accuracy rates from the breast thermographic images by means of the modern thermographic imaging systems and the asymmetry analyzing technique based on the statistical features.

4 Conclusion

Medical thermal imaging systems give us a functional image provides a reflection of metabolic activity and angiogenesis indicating tumor formation rather than anatomical parameters like microcalcifications [10]. When this system is used as a part of multi modal applications like clinical examination, mammography, ultrasonography, and biopsy, it is possible to detect early stage cancers, truly.

By means the Medical Thermal Imaging System-Misther, we obtained higher sensitivity, specificity, and accuracy rates with respect to the multi modal approaches which can only detect an already developed cancer.

Acknowledgements I would like to thank Prof. Dr. Serap Gultekin, who is radiologist in Gazi University Radiology Department, for her helps in screening process of the breast patients and for accessing the clinical results of these patients obtained from conventional imaging modalities.

References

1. Brekelmans, C.T.M., Westers, P., Faber, J.A.J., Peeters, P.H.M., Collette, H.J.A.: Age specific sensitivity and sojourn time in a breast cancer screening programme (DOM) in The Netherlands: a comparison of different methods. *J. Epidemiol. Commun. Health* **50**, 6871 (1996)
2. Gros, C., Gautherie, M.: Breast thermography and cancer risk prediction. *Cancer* **45**, 51 (1980)
3. Spitalier, H., Giraud, D., et al.: Does infrared thermography truly have a role in present-day breast cancer management? In: *Biomedical Thermology*, pp. 269–278. Alan R. Liss, New York, NY (1982)
4. Nyirjesy, I., Ayme, Y., et al.: Clinical evaluation, mammography, and thermography in the diagnosis of breast carcinoma. *Thermology* **1**, 170 (1986)
5. BI-RADS: The American College of Radiology (ACR) BI-RADS Atlas, 5th edn. BI-RADS Assessment Categories (2013)
6. Ng, E.Y.K., Ung, L.N., Ng, F.C., Sim, L.S.J.: Statistical analysis of healthy and malignant breast thermography. *J. Med. Eng. Technol.* **25**, 253–263 (2001)
7. Diakides, M., Bronzino, J.D., Peterson, D.R.: *Medical Infrared Imaging: Principles and Practices*, pp. 13–8 to 13–12. CRC Press (2013)
8. Bronzino, J.D.: *Medical Devices and Systems*, Chapter 25, *Infrared Imaging of the Breast* (2006)
9. Diakides, M., Bronzino, J.D., Peterson, D.R.: *Medical Infrared Imaging: Principles and Practices*, pp. 10–13. CRC Press, Boca Raton (2013)
10. Gamagami, P., Indirect signs of breast cancer: angiogenesis study. In: *Atlas of Mammography*, pp. 231–26. Blackwell Science, Cambridge, Mass (1996)

Part III

Biosensors and Bioinstrumentation

Microneedle-Based Sensor Systems for Real-Time Continuous Transdermal Monitoring of Analytes in Body Fluids

Edina Vranić, Amina Tucak, Merima Sirbubalo, Ognjenka Rahić, Alisa Elezović, and Jasmina Hadžiabdić

Abstract

Microneedles, tiny micron-sized structures, made of a variety of materials, have been recently developed for a painless and safe transdermal delivery of drugs through the skin. While microneedles minimally disrupt the outermost layer of the skin and create a pathway to deliver the therapeutic agents, they could also act as conduits for biosignal sensing. Microneedle-based sensors made of conductive and electrochemically reactive biomaterials can provide the valuable information on the levels of analytes in the blood. Also, researchers have realized the great potential of microneedles integrated with microelectrodes for extraction of interstitial fluid and capillary blood, for enhanced monitoring of patient health. Furthermore, they could serve as a tool for analysis of complex medical conditions and illnesses. This microneedle sensor technology can provide a sophisticated analytical approach for in situ and simultaneous detection of numerous analytes. The microneedles can also be used to measure metabolites, biomarkers, and drug level in the interstitial fluid and capillary blood, as well as for the use of microneedle array technology as biosensors for continuous monitoring of analytes in body fluids.

Keywords

Microneedles • Biosensors • Diagnostics • Drug monitoring • Lab-on-a-chip

1 Introduction

Biomedical devices play an important role in establishing an early diagnosis of medical conditions or illnesses as they provide the necessary information about the levels of crucial elements in the patient's blood (e.g., glucose, haemoglobin, heparin, hormones, enzymes, pH, proteins, alcohol, narcotics and other addictive drugs, tobacco metabolites, toxins) [1].

Historically, to collect data about the level of analytes, the first step was to withdraw a blood followed by laboratory analysis or by sensors attached to equipment for signal processing and monitoring [2]. Currently, the most common method for monitoring analytes is the point-sample blood drawing where a drop of blood is transferred to a test strip and inserted into a digital meter where the result appears on the screen [3]. Blood extraction for diagnostic purposes by conventional methods has many disadvantages including [4–7]:

- pain caused by venipuncture and lancets,
- needle phobia,
- possible delayed skin healing,
- generation of biohazardous sharp waste,
- the need for trained healthcare professionals for administration,
- increased risk of infection or chance of cross-contamination if the device is used on more than one person.

Many technological approaches have been explored and implemented for continuous monitoring using both invasive and noninvasive devices. As the largest organ of the body (~15% of the total area), human skin performs several functions including temperature regulation, water retention, protection against external factors (pathogens, toxins, visible radiation), and has a function as a barrier for transdermal delivery of drugs through the skin as well as for blood extraction [5, 8–10]. Since hypodermic needles cause pain

E. Vranić · A. Tucak (✉) · M. Sirbubalo · O. Rahić · A. Elezović · J. Hadžiabdić

Department of Pharmaceutical Technology, Faculty of Pharmacy, University of Sarajevo, Zmaja od Bosne 8, 71000 Sarajevo, Bosnia and Herzegovina
e-mail: aminatucak@hotmail.com; amina.tucak@ffsa.unsa.ba

E. Vranić
e-mail: evranic@yahoo.com

during application due to their size and deep penetration, Kaushik et al. have introduced microneedles, micron-sized structures that by-pass the stratum corneum barrier by creating microchannels and overcoming problems associated with traditional needles for delivery of therapeutic agents [5, 11, 12].

Microneedles are solid or hollow tubes with the length of 50–900 μm , different shape, size and density which create pores of micron dimensions and penetrate up to 70–200 μm through the epidermis but do not reach the nerve endings located in the dermis which allows painless delivery [13]. They can be divided into three types: porous, hollow, and hydrogel microneedles. Porous microneedles can create microchannels through the skin before application of drug-loaded patches or can be drug-coated. These large-volume channels can be prefilled with electrolyte by capillary action. Hollow microneedles with a cylindrical channel in the body of the microneedle deliver drugs by diffusion or pressure-given flow through the channel [4, 14]. In the other hand, hydrogel microneedles swell after insertion into the skin and collect interstitial fluid over the time. After that, the swollen patches which function as ionic conductors can be analyzed to get information on the level of analytes or biomarkers in body fluids [7, 12, 15].

Previously, while most of the research focus was on the minimally-invasive painless transdermal delivery of therapeutic agents, microneedles for transdermal biosensing were described in just a few studies [9, 12, 14, 16, 17]. Nowadays, there is a great interest in the application of microneedles as a tool for fluid extraction and monitoring.

2 Transdermal Biosensing with Microneedles

The ability to continuously extract and collect biological fluids, as well as to monitor useful biological markers or exogenous molecules in a minimally invasive manner which is sometimes self-administered by patients, could have the potential to improve diagnosis of diseases and enable a more personalized approach for therapy [7, 9, 17]. Sensing application of microneedles have attracted interest in the real-time detection of relevant biomarkers and providing diagnostic information by enhancing the resolution of biosignal detection [2, 12, 16]. The first microneedle-based extraction systems were focused on the sampling of interstitial fluid or capillary blood [18]. In these systems, microneedle-based monitors provide transfer of biological samples to the electrode, as well as reduction of energy consumption and device dimensions compared to conventional ones [19]. Next, the extract can be analyzed externally, or a sensor can be integrated to perform the analysis in situ [20].

The interstitial fluid located 1 mm below the surface of the skin has a composition that is quite similar to the blood, with the main exception being that it has almost no blood cells and contains approximately 25% of the proteins [9, 21]. It is a valuable medium for monitoring analytes because the concentration of molecules in this fluid is often in correlation with their blood concentration so it could be analyzed in situ [4]. Penetration depths for interstitial fluid collection should be 50–100 μm , where microneedle arrays designed for blood sampling could penetrate through the skin in depth of 1000–1500 μm which allows successful and reproducible penetration without fractures [4, 5, 22].

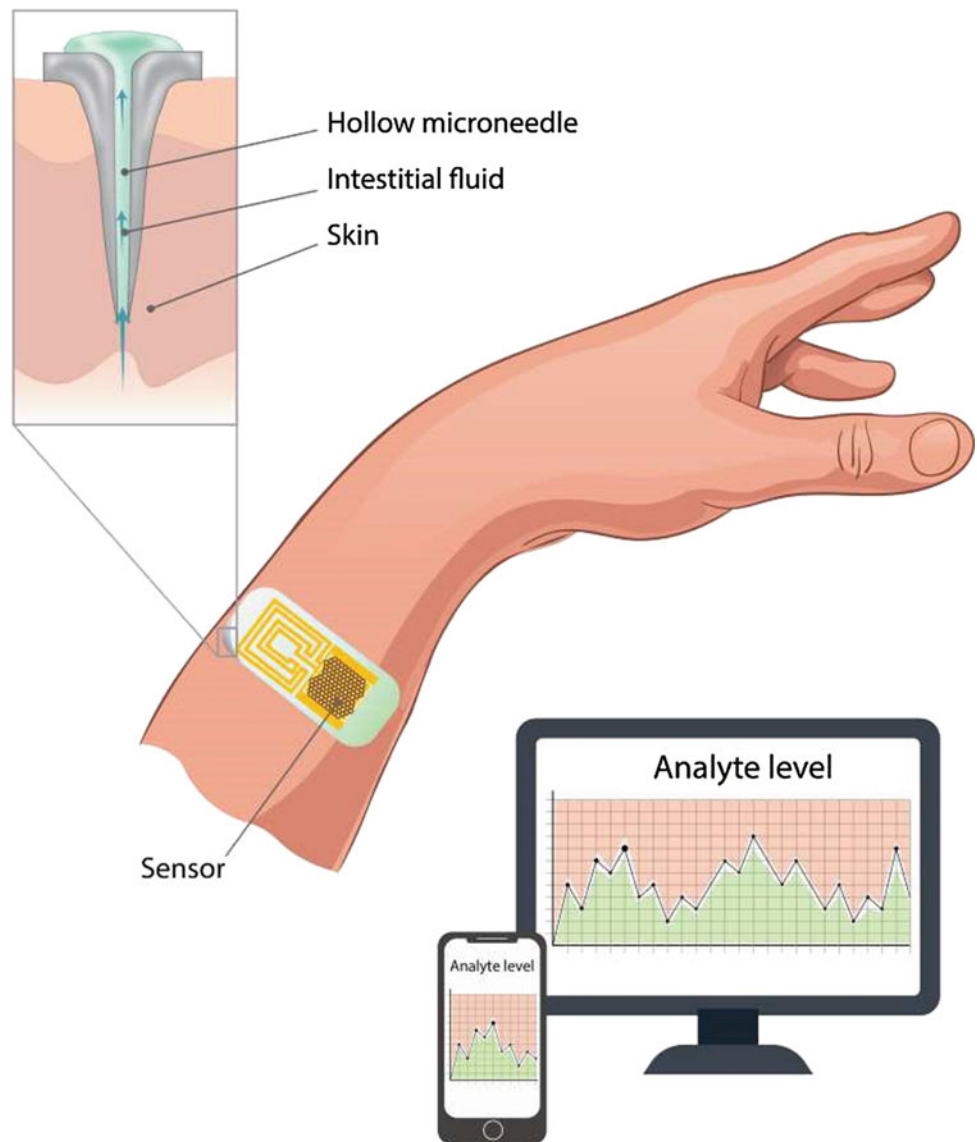
Microsensors, micro-heaters and other sensing devices can be integrated into the microneedle device itself [3]. Sensors are based on various analytical principles including calorimetric, electronic, electrochemical, potentiometric or thermal systems. Since microneedle materials are electrically conductive or electrochemically reactive, it is possible to achieve continuous monitoring of analytes by using PDMS, silicon or glass electrode or via electrochemical activity. In vivo sensors should provide realtime detection of physiological processes by monitoring relevant molecules, biomarkers, neurotransmitters, and pathogenic microorganisms [23], so ideal sensor should have several properties including [19, 24]:

- minimal tissue damage,
- the capability of monitoring numerous biological markers and analytes, and
- compatibility with small sample volumes.

First devices were microneedle sensors based on the extraction of interstitial fluid via enzymatic reactions and real-time monitoring [18, 25]. Microneedle arrays for monitoring of various biomarkers in blood, such as [26, 27] glucose [16, 18, 25, 28–30], hydrogen peroxide [31], ascorbic acid [19], theophylline and caffeine [11], nucleic acids and proteins [32], lactate [33], glucose and lactic acid [34], cholesterol [35], ethanol [36], glutamate [17], have been designed by using fluid extraction.

Also, non-enzymatic glucose biosensors have been developed [37]. Biosensors for multiplex protein detection based on antibody-antigen interactions have been used for recognition of specific target proteins in the interstitial fluid without extracting the fluid itself. Analyte detection is provided by electrochemical, fluorescence or colourimetric techniques [38]. Recent techniques use the more complex mechanism of extraction such as osmotic pressure or vacuum [18]. Moreover, microelectromechanical systems (MEMS) technologies allow the integration of different mechanical elements, as well as sensors, and electronics in a small device which could be suitable for investigation of

Fig. 1 Microneedle-based sensor for real-time continuous transdermal monitoring of analytes from interstitial fluid. It consists of a hollow microneedle array which samples the fluid, and sensors that detect the signal so analyte level could be shown on the display



integrated multi-analyte sensors for biological applications [39]. Recently, microelectrodes integrated with microneedles have attracted even more interest as they could provide simultaneous measurements of analytes from body fluids [39].

Whitson has proposed hollow microneedles for point-of-care transdermal biosensing. A disposable microneedle-based patch device which contains 127 μm long hollow microneedles arranged in a 20×20 array was coupled to a test chamber. The reagent from the chamber reacted with analyte from blood and produced a signal that is then detected by the sensor and displayed on the screen of the device (Fig. 1) [40]. Prausnitz et al. patented a microneedle-based diagnostic device for sensing and collecting the samples. In this system, microneedles have been connected to a substrate, collection chamber and sensor for analyte analysis [1]. Furthermore,

Gonnelli patented a microneedle membrane device with tips covered by an analyte selective membrane for achieving effective analyte monitoring [41].

2.1 Microneedle-Based Systems for Continuous Monitoring of Analyte Concentrations

Since conventional techniques for self-monitoring of glucose level are not able to monitor the fluctuating levels of glucose during the day, microneedles are proposed for real-time glucose measurements [30]. Using hollow glass microneedles that extracted interstitial fluid by vacuum for 2–10 min, Wang et al. have achieved realtime monitoring of glucose levels [18]. Microneedle-based glucose sensors monitor the changes in glucose level continuously over time indirectly from the

interstitial fluid of subcutaneous tissues. For manufacturing, it is necessary to use biocompatible materials (e.g., steel, nickel, carbon nanotubes, silicon), because microneedle patches should be worn for several days [30]. Furthermore, integrated diagnostic systems with microneedles, as well as microactuators, microfluidic control and sensor have been developed for glucose monitoring [42].

Zimmerman et al. have proposed a disposable, hollow-based glucose monitor system integrated with enzyme-based sensors [43], and Hwa et al. have fabricated a continuous glucose monitoring system with a transdermal sensor and immobilized glucose oxidase on the modified Au electrode and microneedles. The H_2O_2 produced from the reaction is electrochemically measured on the surface of the working electrode and is in correlation with glucose concentration [30].

Jina et al. have used 200 hollow microneedles with integrated glucose sensors to extract interstitial fluid and transport glucose via passive diffusion to amperometric sensors. They have shown that the device is as well as accurate and well tolerated by the subjects [28].

Non-enzymatic glucose sensors have been recently described in the literature. They have several advantages including acceptable stability, easy fabrication and reproducibility. Chinnadayala et al. have designed 3×5 Au/pt black/Nf microneedle array systems for the amperometric detection of glucose, where the microneedles were used also as the functional electrodes. They have achieved highly linear glucose detection along with high selectivity, but the stability of the sensor was moderate when continuously operated for more than 5 h [37].

In some monitoring systems, microneedles are incorporated in a closed feedback loop systems where they monitor the level of analyte (e.g., glucose) in the interstitial fluid after which therapeutic agents such as insulin are released depending on the concentration of an analyte [9, 38]. Kim et al. have investigated a similar approach, but with a therapeutic agent. In their work, they have integrated the components that accumulated sweat from the skin for 10–20 min and analyzed the content of glucose, pH, humidity, temperature with a microneedle-based system for the delivery of heat-responding drugs. Sensors on the graphene were interconnected by a gold net, while microneedles contained metformin, a drug used in the treatment of Diabetes mellitus type 2. When a level of glucose increased, the heater in the patch heated the microneedle and the drug was slowly released [44].

Lactate concentrations are increased in several pathological conditions, such as endotoxic shock, pulmonary embolism, cardiac diseases, liver disease, and diabetes. Also, lactate has been recently discovered to be “the major cause of acidification in the microenvironment of cancer cells” that plays a significant role in cancer diagnosis [33]. Alterations

in the tissue environment are noted with many tumours, especially decreased glucose concentration and pH levels, and increased lactate production [19]. Microneedle-based biosensors represent a valuable approach since they measure lactate in the dermal interstitial fluid [33, 45]. Bollella et al. have described 64 polycarbonate microneedle arrays integrated with sensors for lactate monitoring that showed an interference-free lactate detection without compromising the stability, selectivity, sensitivity and response time [33]. Furthermore, Miller et al. have proposed a hollow microneedle array system for simultaneous detection of pH, glucose and lactate which could possibly be used for characterization of complex tumour environments [19].

Determination of lactate level in blood is also necessary for sports medicine. Since polymeric microneedles can lock enzymes and allow diffusion of analyte molecules from interstitial fluid, Dardano et al. have developed wearable electrochemical sensing devices based on three electrodes and polymeric microneedles. They detected glucose and lactate concentrations via redox reaction with glucose oxidase and lactose oxidase enzymes. Sensitivities in both cases were in the order of $nA\ mM^{-1}$ with a limit of detection of 0.5 Mm after five minutes of swelling time [33].

Windmiller et al. have developed a microneedles sensing device for the electrochemical determination and monitoring of the glutamate and glucose. Acrylate-based microneedles facilitated the electropolymeric entrapment of enzymes where glutamate oxidase and glucose oxidase were entrapped within microcavities of the microneedle. This system showed high selectivity, sensitivity, and response time so they could be used as minimally-invasive devices that extract/sample the biological fluid [17].

Caffarel-Salvador et al. have shown that hydrogel microneedles could have potential as a tool for diagnostic purposes since they can detect and quantify analytes and drugs from interstitial fluid in vivo (glucose, caffeine, and theophylline) [12]. Lee et al. have produced gold coated borosilicate glass microneedle arrays for in situ measurement of dissolved oxygen levels and oxidation-reduction potential. They concluded that it would be possible to integrate additional sensors such as pH or phosphate to the microelectrode array and reference electrode [39].

Microneedles can be used for monitoring not only bioanalytes or biomarkers but also intercellular swelling in case of oedema. Nagamine et al. have used a 6×6 porous microneedle array chip (length 100 μm) on the skin of healthy volunteers. The results have shown that these devices are significant for continuous monitoring of hydration state in the body especially in the case of hemodialysis patient where it is necessary to avoid intradialytic hypotension or inappropriate volume removal. Furthermore, this type of microneedle-based electrode system could be a platform for transdermal electrical diagnosis or therapy [14].

3 Conclusion

Microneedle-based sensor systems provide the ability for a transdermal sampling of body fluids in a completely painless manner. This concept of continuous monitoring is a valuable solution for keeping a number of diseases under control. Compared to other continuous monitoring systems, they offer advantages such as minimal invasiveness and reduced biofouling effects because they are changed on a daily basis. Also, they reduce pain and tissue trauma and have minimized the risk of the infections.

Furthermore, the success of minimally-invasive microneedle-based monitor and detection of analytes of clinical interest will open up a broad field of therapeutic opportunity. Also, microneedle sensing systems could incorporate „lab-on-a-chip“ technology that will allow detection of widely used biomarkers not only in hospitals and clinical laboratories.

Moreover, the ability of microneedle-based devices to do both, delivering and sampling of molecules across the skin, opens up the possibility for manufacturing of closed-loop devices, where a microneedle-based delivery component of system delivers a drug based on information given by microneedle-based monitoring component. Due to this potential, these systems will be investigated intensively in the future.

Conflict of Interest The authors have no conflicts of interest to disclose.

References

1. Prausnitz, M.R., Allen, M.G., Gujral, I.J.: Microneedle device for extraction and sensing of bodily fluids. US007344499
2. Cahill, E., O’Cearbhaill, E.: Toward biofunctional microneedles for stimulus-responsive drug delivery. *Bioconjug. Chem.* **26**, 1289–1296 (2015)
3. Sachdeva, V., Banga, A.K.: Microneedles and their applications. *Recent Pat. Drug Deliv. Form.* **5**(2), 95–132 (2011)
4. Donnelly, R., Mooney, K., Caffarel-Salvador, E., Torrisi, B., Eltayib, E., McElnay, J.: Microneedle-mediated minimally invasive patient monitoring. *Ther. Drug Monit.* **36**(1), 10–17 (2013)
5. Li, C., Lee, C., Lee, K., Jung, H.: An optimized hollow microneedle for minimally invasive blood extraction. *Biomed. Microdevices* **15**, 17–25 (2012)
6. McGrew, R., McGrew, M.: *Encyclopedia of Medical History*. McGraw Hill, New York (1985)
7. Romanyuk, A., Zvezdin, V., Samant, P., Grenader, M., Zemlyanova, M., Prausnitz, M.: Collection of analytes from microneedle patches. *Anal. Chem.* **86**(21), 10520–10523 (2014)
8. Williams, A.: *Transdermal and topical drug delivery. From theory to clinical practice*. 1st edn, pp. 3–45. Pharmaceutical Press, London (2003)
9. Cass, A., Sharma, S.: Microneedle enzyme sensor arrays for continuous in vivo monitoring. *Methods Enzymol.* **589**, 413–427 (2017)
10. El-Laboudi, A., Oliver, N., Cass, A., Johnston, D.: Use of microneedle array devices for continuous glucose monitoring: a review. *Diabetes Technol. Ther.* **15**(1), 101–115 (2013)
11. Kaushik, S., Hord, A.H., Denson, D.D., McAllister, D.V., Smitra, S., Allen, M.G., et al.: Lack of pain associated with microfabricated microneedles. *Anesth. Analg.* **92**(2), 502–504 (2001)
12. Caffarel-Salvador, E., Brady, A., Eltayib, E., Meng, T., Alonso-Vicente, A., Gonzalez-Vazquez, P., et al.: Hydrogel-forming microneedle arrays allow detection of drugs and glucose in vivo: potential for use in diagnosis and therapeutic drug monitoring. *PLoS One.* **10**(12), e0145644 (2015)
13. Yadav, D.J., Vaidya, K.A., Kulkarni, P.R., Raut, R.A.: Microneedles: promising technique for transdermal drug delivery. *Int. J. Pharm. Bio. Sci.* **2**(1), 684–708 (2011)
14. Nagamine, K., Kubota, J., Kai, H., Ono, Y., Nishizawa, M.: An array of porous microneedles for transdermal monitoring of intercellular swelling. *Biomed. Microdevices* **19**(3), 68 (2017)
15. Donnelly, R.F., Singh, T.R., Garland, M.J., Migalska, K., Majithiya, R., McCrudden, C.M. et al.: Hydrogel-forming microneedle arrays for enhanced transdermal drug delivery. *Adv. Funct. Mater.* **22**(23), 4879–4890 (2012)
16. Valdés-Ramírez, G., Li, Y., Kim, J., Jia, W., Bandodkar, A., Nuñez-Flores, R., et al.: Microneedle-based self-powered glucose sensor. *Electrochem. Commun.* **47**, 58–62 (2014)
17. Windmiller, J., Zhou, N., Chuang, M., Valdés-Ramírez, G., Santhosh, P., Miller, P., et al.: Microneedle array-based carbon paste amperometric sensors and biosensors. *Analyst* **136**(9), 1846–1851 (2011)
18. Wang, P., Cornwell, M., Prausnitz, M.: Minimally invasive extraction of dermal interstitial fluid for glucose monitoring using microneedles. *Diabetes Technol. Ther.* **7**(1), 131–141 (2005)
19. Miller, P., Gittard, S., Edwards, T., Lopez, D., Xiao, X., Wheeler, D., et al.: Integrated carbon fiber electrodes within hollow polymer microneedles for transdermal electrochemical sensing. *Biomicrofluidics* **5**(1), 13415 (2011)
20. Kolli, C.S.: Microneedles: bench to bedside. *Ther. Deliv.* **6**(9), 1081–1088 (2015)
21. Miller, P.R., Narayan, R.J., Polsky, R.: Microneedle-based sensors for medical diagnosis. *J. Mater. Chem. B* **4**(8), 1379–1383 (2016)
22. Chaudhri, B., Ceyssens, F., De Moor, P., Van Hoof, C., Puers, R.: A high aspect ratio SU-8 fabrication technique for hollow microneedles for transdermal drug delivery and blood extraction. *J. Micromech. Microeng.* **20**(6), 064006 (2010)
23. Justino, C.I., Rocha-Santos, T.A., Duarte, A.C.: Review of analytical figures of merit of sensors and biosensors in clinical applications. *Trends. Analyt. Chem.* **29**(10), 1172–1183 (2010)
24. Vaddiraju, S., Tomazos, I., Burgess, D.J., Jain, F.C., Papadimitrakopoulos, F.: Emerging synergy between nanotechnology and implantable biosensors: A review. *Biosens. Bioelectron.* **25**(7), 1553–1565 (2010)
25. Strambini, L.M., Longo, A., Scarano, S., Prescimone, T., Palchetti, I., Minunni, M., et al.: Selfpowered microneedle-based biosensors for pain-free high-accuracy measurement of glycaemia in interstitial fluid. *Biosens. Bioelectron.* **66**, 162–168 (2015)
26. Mukherjee, E., Collins, S., Isseroff, R., Smith, R.: Microneedle array for transdermal biological fluid extraction and in situ analysis. *Sens. Actuators A Phys.* **114**, 267–275 (2004)
27. Tsuchiya, K., Nakanishi, N., Uetsuji, Y., Nakamachi, E.: Development of blood extraction system for health monitoring system. *Biomed. Microdevices* **7**(4), 347–353 (2005)
28. Jina, A., Tierney, M.J., Tamada, J.A., McGill, S., Desai, S., Chua, B., et al.: Design, development, and evaluation of a novel microneedle array-based continuous glucose monitor. *J. Diabetes Sci. Technol.* **8**(3), 483–487 (2014)

29. Sharma, S., Huang, Z., Rogers, M., Boutelle, M., Cass, A.E.: Evaluation of a minimally invasive glucose biosensor for continuous tissue monitoring. *Anal. Bioanal. Chem.* **408**, 8427–8435 (2016)
30. Hwa, K.-Y., Subramani, B., Chang, P.-W., Chien, M., Huang, J.-T.: Transdermal microneedle array-based sensor for real time continuous glucose monitoring. *Int. J. Electrochem. Sci.* **10**, 2455–2466 (2015)
31. Zhou, J.X., Tang, L.N., Liang, F.X., Wang, H., Li, Y.T., Zhang, G. J.: MoS₂/Pt nanocomposite-functionalized microneedle for real-time monitoring of hydrogen peroxide release from living cells. *Analyst* **142**(22), 4322–4329 (2017)
32. Esfandyarpour, R., Javanmard, M., Koochak, Z., Esfandyarpour, H., Harris, J.S., Davis, R.W.: Label-free electronic probing of nucleic acids and proteins at the nanoscale using the nanoneedle biosensor. *Biomicrofluidics* **7**, 044114 (2013)
33. Bollella, P., Sharma, S., Cass, A.E., Antiochia, R.: Microneedle-based biosensor for minimally-invasive lactate detection. *Biosens. Bioelectron.* **123**, 152–159 (2019)
34. Dardano, P., Calio, A., Di Palma, V., Babilacqua, M.F., Di Matteo, A., De Stefano, L.: Multianalyte biosensor patch based on polymeric microneedles. 2018. In: Andò, B., Baldini, F., Di Natale, C., Marrazza, G., Siciliano P. (eds.) *Sensors. CNS 2016. Lecture Notes in Electrical Engineering*, vol 431, pp. 73–81. Springer, Cham
35. Li, C.G., Joung, H.-A., Noh, H., Song, M.-B., Kim, M.-G., Jung, H.: One-touch-activated blood multidagnostic system using a minimally invasive hollow microneedle integrated with a paper-based sensor. *Lab Chip* **15**(6), 3286–3292 (2015)
36. Campbell, A.S., Kim, J., Wang, J.: Wearable electrochemical alcohol biosensors. *Curr. Opin Electrochem.* **10**, 126–135 (2018)
37. Chinnadayala, S.R., Park, I., Cho, S.: Nonenzymatic determination of glucose at near neutral pH values based on the use of nafion and platinum black coated microneedle electrode array. *Mikrochim. Acta* **185**(5), 250 (2018)
38. Ng, K.W., Moghimi, S.M.: Skin biosensing and bioanalysis: what the future holds. *Prec. Nanomed* **1**(2), 125–127 (2018)
39. Lee, J.-H., Seo, Y., Lim, T.-S., Bishop, P.L., Papautsky, I.: MEMS needle-type sensor array for in situ measurements of dissolved oxygen and redox potential. *Environ. Sci. Technol.* **41**, 7857–7863 (2007)
40. Whitson, R.C.: Hollow microneedle patch. US20020006355
41. Gonnelli, R.R.: Microneedle with membrane. US20090043250
42. Gattiker, G., Kaler, K.I., Mintchev, M.: Electronic Mosquito: designing a semi-invasive Microsystem for blood sampling, analysis and drug delivery applications. *Microsyst. Technol.* **12** (1–2), 44–51 (2005)
43. Zimmermann, S., Fienbork, D., Stoeber, B., Flounders, A., Liepmann, D.: In-device enzyme immobilization: wafer-level fabrication of an integrated glucose sensor. *Sens. Actuators B Chem.* **99**(1), 163–173 (2003)
44. Guy, R.: Diagnostic devices: Managing diabetes through the skin. *Nat. Nanotechnol.* **11**(6), 493–494 (2016)
45. Gupta, V.K., Singh, A.K., Kumawat, L.K.: Thiazole Schiff base turn-on fluorescent chemosensor for Al³⁺ ion. *Sens. Actuators B Chem.* **195**, 98–108 (2014)

Review of Electrochemical Biosensors for Hormone Detection

Selma Cifrić, Jasna Nuhić, Dina Osmanović, and Emina Kišija

Abstract

This review summarizes types of electrochemical biosensors used for hormone analysis and provides overview of their characteristics for medical applications. Comparison between different types of electrochemical biosensors used in: insulin, cortisol, testosterone and thyroid-stimulating (TSH) hormone is represented. Focus is on the linear range and the limit of detection (LOD) of biosensors used for detection of various hormones. According to the before mentioned hormones, similar categories of biosensors deliver correlating results in terms of linear range and LOD.

Keywords

Medical diagnosis • Hormones • Electrochemical biosensors • Linear range • Limit of detection

1 Introduction

There is a wide range of methods that are used for medical diagnosis. Many of them are time-consuming processes and require trained personnel to perform adequate analysis. The

S. Cifrić (✉) · D. Osmanović
Genetics and Bioengineering, Faculty of Engineering and Natural Sciences, International Burch University, Sarajevo, Bosnia and Herzegovina
e-mail: selma.cifric@stu.ibu.edu.ba; selma.cifric@hotmail.com

D. Osmanović
e-mail: dina.osmanovic@stu.ibu.edu.ba

J. Nuhić
Experimental and Health Sciences, Faculty of Health and Life Sciences, Universitat Pompeu Fabra, Barcelona, Spain
e-mail: jasna.nuhic01@estudiant.upf.edu

E. Kišija
Electrical and Electronics Engineering, Faculty of Engineering and Natural Sciences, International Burch University, Sarajevo, Bosnia and Herzegovina
e-mail: emina.kisija@stu.ibu.edu.ba

accuracy of specific biochemical parameter is essential for good healthcare [1]. Biosensor is an analytical device used for detection of presence of chemical substances and is composed of biorecognition element and transducer [2]. Biosensors provide good solutions, since they are usually small in size, response time is fast and it is inexpensive tool. Particularly, electrochemical biosensors show good affinity for the detection of analytes related to medical diagnostics (e.g., cancer markers, allergy markers, heart-attack markers, antibodies, drugs, and hormones) [1].

Electrochemical sensor is the biosensor that transforms chemical information into analytically useful signal. We need to distinguish single use biosensors, that are disposable after one measurement from the biosensors that can be used x number of times, and that can be repeatedly calibrated. Biosensors have some calibration characteristics as sensitivity, selectivity, linear concentration range, response time, regeneration, lifetime, etc. [3].

Hormones are secreted by endocrine cells and transported by the circulatory system to the target tissues. They are found in very low concentrations and detection of these molecules requires high sensitivity. Hormones are synthesized and secreted by endocrine cells that are found in endocrine glands [4]. Compared to other methods for hormone analysis [5], like high-performance liquid chromatography/tandem mass spectrometry (LC-MS/MS), electrochemical sensing is much easier and faster method. The problem with immunoassays for the measurement of steroids is emphasized, as well as the arised role of LC-MS/MS in the measurement of clinically relevant steroids. It has high sensitivity range and it does not require expensive instrumentation or lot of time to be performed [5]. Detection of hormones by electrochemical biosensors is usually done by using enzymes or antibodies as biorecognition elements. The basic principle in electrochemical biosensors is chemical reaction between immobilized molecules and target compounds producing electrons that affect properties of the solution [6].

Some of the challenges for biosensing processes are: biomolecules have a limited life span; sometimes biosensors

require a special pretreatment prior to each use; a number of existing sensors lack long-term stability [3].

Biosensors can be classified based on biorecognition elements they are using for target detection (enzyme, antigen, nucleic acids) [7]. Also, biosensors are frequently categorized according the transduction methods they perform: piezoelectric, electrochemical and optical [8]. Among many types of biosensors, the most useful in medical diagnostics are electrochemical biosensors (amperometric, potentiometric and conductometric/impedimetric biosensors) and optical biosensors [9].

Electrochemical biosensors work on principle that ions or electrons are produced or consumed by chemical reactions among immobilized biomolecule and target analyte [10]. The reaction affects electrical properties of the solution and therefore we have four different types of electrochemical transducers: amperometric when measurable current is generated, potentiometric when measurable potential is generated, conductometric when the conductive properties of a medium are altered and impedimetric when impedance of a medium between electrodes is measurably altered [11, 12].

This review paper represents comparison between different types of electrochemical biosensors used in hormone detection of the following hormones: insulin, cortisol, testosterone and thyroid-stimulating hormone (TSH). Three types of electrochemical biosensors were inspected including amperometric, potentiometric and conductometric biosensors. Comparison was based on linear range and limit of detection.

2 Methods

This paper will focus on review of biorecognition elements and use of different detection methods in amperometric, potentiometric and conductometric biosensors, as shown in Fig. 1.

This review was based on 30 papers found on Google Scholar, for which selection criteria was:

- The paper must be in English,
- Availability of full text,
- Include detection of target hormones (insulin, cortisol, testosterone, TSH),
- Hormone detection by electrochemical biosensor,
- The results must indicate linear range and limit of detection (LOD) of biosensor devices.

In order to provide clearer quantitative relationships among molecular species and some standardization of databases the international Federation of Clinical Chemistry (IFCC) recommended the use of selected or favored, SI units

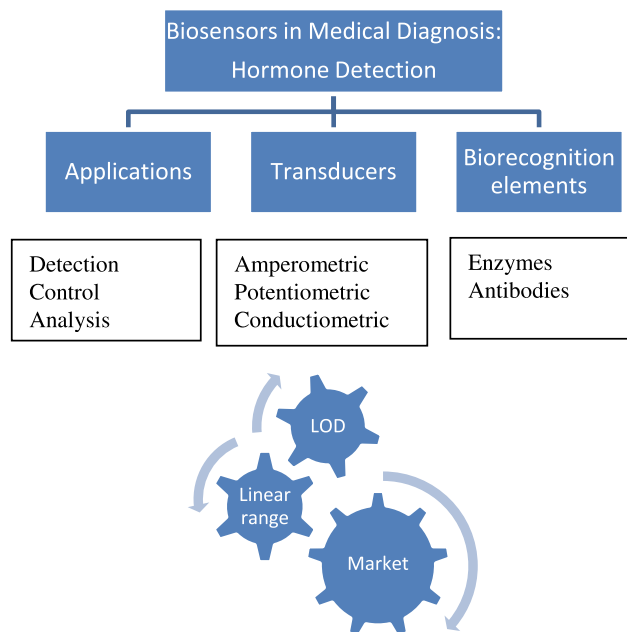


Fig. 1 Diagram that summarizes different methods and conclusion of this review

for clinical laboratory [13]. Concentration measurements differ in units due to the partial application of SI units to laboratory data. In many instances the molecular weight or the homogeneity of the measured analyte is not clear, and gravimetric units rather than molar units are preferred [13].

3 Results

The linear range is that range of input or output values for which an electronic amplifier produces an output signal that is linear function of the input signal. Linearity shows the accuracy of the measured response to a straight line. Linearity can be associated with the resolution and range of analyte concentrations under test [14].

Limit of detection (LOD) is the lowest quantity of a specific substance that can be detected with reasonable certainty. LOD is based on the sensitivity and on instrument's resolution [15].

Eguilaz et al. used amperometric biosensor for the detection of testosterone concentration [16]. In amperometric measurement current is measured when fixed potential is applied between working and reference electrode where conversion of electroactive species occurs in enzyme layer [15]. If a current is measured while the potential difference between the working and reference electrode is controlled, this is referred to as amperometry. On the other hand, voltammetry occurs if current is measured during controlled variations of

the potential [11]. Amperometric biosensor was analyzing human serum spiked with 1 and 10 ng/mL testosterone. It works as an immunobiosensor using screen-printed carbon electrodes and functionalized magnetic beads. On the surface of magnetic beads anti-testosterone is immobilized, while testosterone is labeled with peroxidase, and the immunoreaction is performed [16]. This is then attached to screen-printed carbon electrode with the magnet. The detection limit was 1.7 ng/L, as shown in Table 2 [16].

Testosterone is a steroid hormone that plays an important role for development of male sexual characteristics [16, 18]. This hormone is detected by using antibodies as biorecognition elements. On the surface of the electrode anti-testosterone antibody was immobilized. When antigens are present in the solution the chemical reaction that occurs between antibody and antigen will cause change in the surface charge. This detection was based on the difference in the potential on the surface before and after this immunochemical reaction [18, 19]. Potentiometric biosensors determine the potential difference between working and reference electrode using voltmeter at virtually zero current flow [6].

Chemical reactions of the species in solution, namely oxidation and reduction, are the reason for the potential difference measured between electrodes of the device. Another thing that is determined in potentiometry is the ion activity in an electrochemical reaction. When transducer converts the biorecognition process into a potential signal, the analytical information is obtained [20]. Linear range and LOD of potentiometric biosensors used in hormone detection are summarized in Tables 1 and 2.

Conductivity or resistivity of the solution is changing as a consequence of ions or electrons production during chemical reaction. Conductometric biosensors measure the electrical conductance/resistance of the solution. These measurements are of the relatively low sensitivity [6]. Undesirable effects may occur, e.g. double layer charging, concentration polarization and Faradaic effect, may occur. They are minimized when electric field is generated by using AC voltage [19]. The name conductometric is derived from conductance which represents the inverse of resistance [6]. Changes in electrical properties at the surfaces of electrodes are monitored by impedimetric measurements [21].

Conductometric biosensors are used for insulin and TSH detection. Insulin is also polypeptide hormone that is synthesized by the pancreas. The role of insulin is to regulate blood glucose level [4]. High concentrations of insulin can be very dangerous for human organism, it can lead to diabetes, that is why detection of this hormone is significant [4, 22]. Researcher from the paper [22] explained that impedimetric biosensor can detect low concentrations of insulin from the blood serum. Biosensor can be reused if its surface is emerged into 0.2 M Gly-HCl buffer to disassociate antibody-antigen complex [22].

TSH is a hormone that stimulates secretion of hormones from thyroid gland and it regulates its function [4]. The conductometric biosensor was used for the detection of TSH. These biosensors have integrated electrodes on the surface of sensing site. The presence of TSH is determined by calculating the conductance on the integrated electrodes [23].

Table 1 Linear range of different biosensors used for hormone detection

Linear range of electrochemical biosensors	Type of biosensor used in hormone detection		
	Amperometric biosensors	Potentiometric biosensors	Conductometric/impedimetric biosensors
Hormone			
Cortisol	10 pM–100 nM [24]	1 ng/L–10 µg/L [25]	1 pM–100 nM [26]
Testosterone	0.005–50 µg/L [16]	1 ng/L–10 µg/L [18]	n/a
Thyroid-stimulating hormone (TSH)	1.4–17 mIU/L [27]	n/a	0.02–100 mIU/L [23]
Insulin	10 fM–100 pM [28]	n/a	5 pM–50 nM [22]

Table 2 Limit of detection of different biosensors used for hormone detection

Limit of detection of electrochemical biosensors	Type of biosensor used in hormone detection		
	Amperometric biosensors	Potentiometric biosensors	Conductometric/impedimetric biosensors
Hormone			
Cortisol	10 ng/L [24]	1 ng/L [25]	1 pM [26]
Testosterone	1.7 ng/L [16]	1 ng/L [18]	n/a
Thyroid-stimulating hormone (TSH)	1.4 mIU/L [27]	n/a	0.012 mIU/L [23]
Insulin	10 fM [28]	n/a	1.24 pM [22]

Linear ranges of four chosen hormones measured with different electrochemical biosensors are shown in Table 1, while LODs are shown in Table 2.

For detection of hormone cortisol, it can be seen that conductimetric biosensors show the widest linear range. Also, the lowest LOD is calculated by conductimetric biosensors. Hormone testosterone is measured with amperometric and potentiometric biosensors. Results from Table 1 show that amperometric biosensors have the best linear range. In the Table 2 the LOD of the potentiometric biosensor is the lowest for this hormone.

Detection of TSH is done by conductimetric biosensor and by amperometric biosensor as well. Linear range of TSH is larger, while LOD is lower when measured by conductimetric biosensor. Linear range of amperometric compared to linear range of conductimetric biosensors is also shown on the example of hormone insulin. The best biosensor for detection of insulin is amperometric biosensor based on the linear range from the Table 1. By looking at the Table 2 LOD for the hormone insulin is the lowest in amperometric biosensors.

Figure 2 graphically shows the LOD comparison between two different electrochemical biosensors. This Figure is based on the results obtained from Table 2. In Fig. 1 two hormones are shown: cortisol and testosterone. Based on the data from the figure above, it is easy to conclude that potentiometric biosensors show lower LOD, which makes them better for hormone detection.

Biosensors in medical application make 66% of biosensor market revenue share. Medical biosensors are essential tool for monitoring, treatment and detection of various medical conditions. Electrochemical biosensors dominate in industry making 71% of incomes in 2015, and it is anticipated to outgo USD 21 billion by 2024. End-user based biosensors market valued USD 7 billion in 2015, that contributes

mostly to home healthcare (diabetes) [29]. They are crucial for acquiring data needed for running intelligent systems in healthcare [30–32].

4 Conclusion

This review summarizes modern techniques used for fast and accurate hormone detection for medical purposes. Biosensors represent great analytical tool for clinical diagnosis since they are user-friendly, inexpensive and simple devices.

Based on the performed research it can be concluded that the most widely used electrochemical biosensors are amperometric biosensors. LOD depends on the hormones that are analyzed.

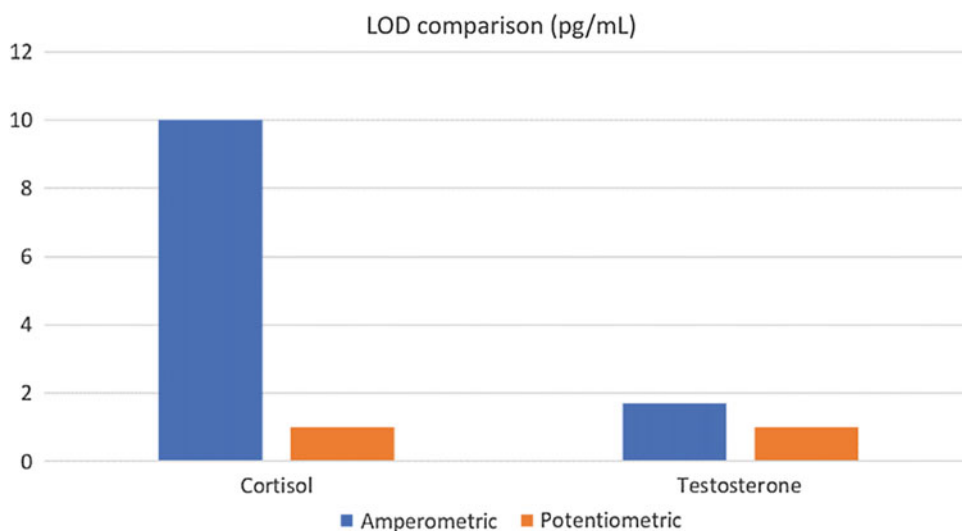
In the case of hormones observed in this paper, great correspondence occurs and for each of them the same category of biosensor gives the best results for both linear range and LOD.

From results presented in Tables 1 and 2 it can be seen that the best biosensor for detection of hormone cortisol, based on linear range and LOD is conductimetric biosensor. Conductimetric biosensors measure the electrical conductance of the solution.

Even though the widest linear range for detection of testosterone is shown by amperometric biosensors, comparison of LOD and linear range leads to conclusion that potentiometric biosensors are better choice. In the case of the TSH detection, conductimetric biosensor shows the best linear range and LOD, that makes it the most suitable type of biosensor for that purpose. Amperometric biosensor shows the best characteristics for insulin detection.

To conclude, after comparison of all three types of biosensors, in general the best properties for hormone detection is shown by conductimetric biosensor.

Fig. 2 Comparison of amperometric and potentiometric measurements on examples of cortisol and testosterone hormones



References

1. Malhotra, B.D., Chaubey, A.: Biosensors for clinical diagnostics industry. *Sens. Actuators B: Chem.* **91**(1–3), 117–127 (2003)
2. Bănică, F.-G.: *Chemical Sensors and Biosensors: Fundamentals and Applications*, p. 576. Wiley, Chichester (2012). ISBN 9781118354230
3. Thévenot, D.R., Toth, K., Durst, R.A., Wilson, G.S.: Electrochemical biosensors: recommended definitions and classification. *Biosens. Bioelectron.* **16**(1–2), 121–131
4. Costanzo, L.S.: *Physiology*, 6th edn., pp. 383–428. Elsevier, Philadelphia (2018)
5. Soldin, S.J., Soldin, O.P.: Steroid hormone analysis by tandem mass spectrometry. *Clin. Chem.* **55**(6), 1061–1066 (2009)
6. Monošík, R., Středanský, M., Šturdík, E.: Biosensors-classification, characterization and new trends. *Acta Chim. Slovaca* **5**(1), 109–120 (2012)
7. Teles, F.R.R., Fonseca, L.P.: Trends in DNA biosensors. *Talanta* **77**(2), 606–623 (2008)
8. Yogeswaran, U., Chen, S.M.: A review on the electrochemical sensors and biosensors composed of nanowires as sensing material. *Sensors* **8**(1), 290–313 (2008)
9. Luong, J.H., Male, K.B., Glennon, J.D.: Biosensor technology: technology push versus market pull. *Biotechnol. Adv.* **26**(5), 492–500 (2008)
10. Thévenot, D.R., Toth, K., Durst, R.A., Wilson, G.S.: *Pure Appl. Chem.* **71**, 2333–2348 (1999)
11. Grieshaber, D., MacKenzie, R., Vörös, J., Reimhult, E.: Electrochemical biosensors-sensor principles and architectures. *Sensors* **8**, 1400–1458 (2008)
12. Justino, C.I., Rocha-Santos, T.A., Duarte, A.C.: Review of analytical figures of merit of sensors and biosensors in clinical applications. *TrAC Trends Anal. Chem.* **29**(10), 1172–1183 (2010)
13. Fraser, G.G., Harris, E.K.: Generation and application of data on biological variation in clinical chemistry. *Crit. Rev. Clin. Lab. Sci.* **27**(5), 409–437 (1989)
14. Bhalla, N., Jolly, P., Formisano, N., Estrela, P.: Introduction to biosensors. *Essays Biochem.* **60**(1), 1–8 (2016)
15. Mohanty, S.P., Kougiyanos, E.: Biosensors: a tutorial review. *Potentials* **25**, 35–40 (2006)
16. IUPAC.: *Compendium of Chemical Terminology*, 2nd ed. (the “Gold Book”). Compiled by McNaught, A.D., Wilkinson, A. Blackwell Scientific Publications, Oxford (1997). XML on-line corrected version: <http://goldbook.iupac.org> (2006) created by M. Nic, J. Jirat, B. Kosata; updates compiled by A. Jenkins. ISBN 0-9678550-9-8. <https://doi.org/10.1351/goldbook>
17. Eguílaz, M., Moreno-Guzmán, M., Campuzano, S., González-Cortés, A., Yáñez-Sedeño, P., Pingarrón, J.M.: An electrochemical immunosensor for testosterone using functionalized magnetic beads and screen-printed carbon electrodes. *Biosens. Bioelectron.* **26**(2), 517–522 (2010)
18. Liang, K.Z., Qi, J.S., Mu, W.J., Chen, Z.G.: Biomolecules/gold nanowires-doped sol-gel film for label-free electrochemical immunoassay of testosterone. *J. Biochem. Biophys. Methods* **70**(6), 1156–1162 (2008)
19. Bahadır, E.B., Sezgintürk, M.K.: Electrochemical biosensors for hormone analyses. *Biosens. Bioelectron.* **68**, 62–71 (2015)
20. Iles, R.K., Kallichum, H.: *J. Bioeng. Biomed. Sci.* **2**, 1–5 (2012)
21. Ndangili, P.M., Jijana, A.M., Baker, P.G.L., Iwuoha, E.I.: *J. Electroanal. Chem.* **653**, 67–74 (2011)
22. Xu, M., Luo, X., Davis, J.J.: The label free picomolar detection of insulin in blood serum. *Biosens. Bioelectron.* **39**(1), 21–25 (2013)
23. Wang, H., Wu, X., Dong, P., Wang, C., Wang, J., Liu, Y., Chen, J.: Electrochemical biosensor based on interdigitated electrodes for determination of thyroid stimulating hormone. *Int. J. Electrochem. Sci.* **9**, 12–21 (2014)
24. Vasudev, A., Kaushik, A., Tomizawa, Y., Norena, N., Bhansali, S.: *Biosens. Bioelectron. B* **182**, 139–146 (2013)
25. Tlili, C., Myung, N.V., Shetty, V., Mulchandani, A.: *Biosens. Bioelectron.* **26**, 4382–4386 (2011)
26. Arya, S.K., Dey, A., Bhansali, S.: Polyaniline protected gold nanoparticles based mediator and label free electrochemical cortisol biosensor. *Biosens. Bioelectron.* **28**(1), 166–173 (2011)
27. Lin, Z.H., Shen, G.L., Miao, Q., Yu, R.Q.: A thyroid-stimulating hormone immuno-electrode. *Anal. Chim. Acta* **325**(1–2), 87–92 (1996)
28. Regonda, S., Tian, R., Gao, J., Greene, S., Ding, J., Hu, W.: Silicon multi-nanochannel FETs to improve device uniformity/stability and femtomolar detection of insulin in serum. *Biosens. Bioelectron.* **45**, 245–251 (2013)
29. *Biosensors Market Size, Analysis—Global Industry Share Report 2024*. (n.d.). Retrieved from <https://www.gminsights.com/industry-analysis/biosensors-market>
30. Alić, B., Gurbeta, L., Badnjević, A.: Machine learning techniques for classification of diabetes and cardiovascular diseases. In: 2017 6th Mediterranean Conference on Embedded Computing (MECO), pp. 1–4. Bar, Montenegro (2017). <https://doi.org/10.1109/meco.2017.7977152>
31. Sejdinovic, D., Gurbeta, L., Badnjevic, A., Malenica, M., Dujic, T., Causevic, A., Bego, T., Divovic, L.: Classification of prediabetes and Type 2 Diabetes using artificial neural network. In: IFMBE Proceedings of CMBEBIH 2017, vol. 62, pp. 685–689. Springer, Singapore. https://doi.org/10.1007/978-981-10-4166-2_103
32. Alic, B., Sejdinovic, D., Gurbeta, L., Badnjevic, A.: Classification of stress recognition using artificial neural network. In: IEEE 5th Mediterranean Conference on Embedded Computing (MECO), 12–16 June 2016. Bar, Montenegro

Development of a Tray-Separated Microbiological Incubator by Means of Electronic Components and Testing Its Performance

Tarik Ibrahimpašić and Dejan Jokić

Abstract

Within the realm of genetics, bioengineering and especially microbiology, it is often necessary to develop and grow a certain type of microbial culture for purposes of investigating certain microbiological phenomena or conducting a research. In order to perform the process of incubation, it is required to maintain a constant temperature for the time frame within the range of 24–48 h, depending on the type of bacteria under investigation. The device which enables us to grow such group of microorganisms is called a microbiological incubator. Two crucial parts in the microbiological incubator are heater and temperature sensor. Usually, such incubators have one chamber, whose temperature is controlled by a microcontroller. This project aims to improve the functionality of regular microbiological incubators by designing one which will have two separately controlled chambers and therefore be more functional than a conventional one. The incubator will be controlled with NodeMCU platform with integrated Wi-Fi module, so it will have IoT prefix, which basically means that one will be able to control it and to obtain certain data from it via the internet.

Keywords

Biofilms • IoT • NodeMCU • Microbiological incubator

1 Introduction

Microbiological incubators are widely used today in modern genetics and bioengineering field. They are mostly used to grow and culture microbiological organisms by maintaining an optimal temperature, as well as some other parameters such as humidity, CO₂ levels and oxygen content [1].

Typical microbiological incubator consists of an adjustable heater, placed into the insulated box [1]. The temperature range of typical incubator is usually up to 60–65 °C, but there are also some incubators whose temperature range reaches 100 °C [2]. The typical incubation temperatures for several different types of microorganisms are listed in Table 1.

Since different microorganisms require different incubation temperature, as it can be concluded from the table above, and since by using the conventional incubator it is possible to adjust only one temperature for the entire machine, it is a time-consuming process if we have many different bacterial cultures to incubate at different temperatures. In this paper we represent the idea of innovative incubator which allows incubation of multiple cultures at different temperatures simultaneously, thus increasing the efficiency in terms of energy, time and scientific precision of obtained results. This project will provide users with two distinct cells, which can be controlled independently, thus, allowing two types of microbial cultures to be developed at the same time.

Furthermore, the price of the conventional microbiological incubator at the market is within the range from \$300 to \$2500 (500 BAM to 4200 BAM) [7]. The price of all parts in this project will not surpass the amount of 200 BAM, which is significantly less.

Moreover, the incubator will have prefix IoT, which basically means that one will be able to control it and obtain the data from it by using the internet. This feature provides us with the ability to have the overview of the current state

T. Ibrahimpašić (✉)

Department of Electrical and Computer Engineering, Technical University of Munich, Munich, Germany
e-mail: tarik.ibrahimpasic@tum.de

D. Jokić

Department of Electrical and Electronics Engineering, Faculty of Engineering and Natural Sciences, International Burch University, Sarajevo, Bosnia and Herzegovina
e-mail: dejan.jokic@ibu.edu.ba

Table 1 Typical incubation temperatures required to incubate different microorganisms

Organism	Incubation	
	Temperature (°C)	References
<i>Agrobacterium tumefaciens</i>	28	[3]
<i>Escherichia coli</i>	25	[4]
<i>Pseudomonas aeruginosa</i>	25–37	[4]
<i>Pseudomonas aeruginosa</i>	25–37	[5]
<i>Pseudomonas fluorescenas</i>	25–30	[4]
<i>Staphylococcus aureus</i>	37	[6]
<i>Streptococcus mutans</i>	37	[4]
<i>Vibrio cholerae</i>	25–30	[4]

of the incubator, without having to be physically present, which is additional advantage of this device.

If we take into consideration all of these three aspects, the final product would be an IoT-based microbiological incubator, with two independently controlled cells, which is at the same time less expensive than the conventional microbiological incubators. The development and the testing phase of this project were carried out as a part of the senior design project [8].

2 Methods

The main controlling algorithm which is conducted by NodeMCU consists of four basic parts, and they include part of code related to observing state of the buttons. Another segment is responsible for obtaining data from temperature sensors, and afterwards the information is written onto LCD display and the relays are turned on or off, depending on the desired and current values of temperature.

There are four buttons in this project, which control the desired value of the temperature in two chambers, two buttons for each chamber. The desired value will be increased/decreased, depending on which button was pressed. The increment/decrement will occur on positive edge of the button being pressed.

The value of current temperature will be obtained using two temperature sensors and a multiplexer. The rate at which the values will be obtained from sensors is one per second. Afterwards, the current and desired temperature values will be displayed on 16 × 2 LCD display.

The relays which control the heaters turn on/off depending on the values of desired and current temperature. The differential gap of 1 °C is used while controlling the relays. This means that relays will not be turned on as long as desired temperature is not at least 1 °C above the current temperature in the chamber. After being turned on, the relays

will be turned off when current temperature readings reach at least 1 °C higher value than that of the desired temperature. That means that our system will have the accuracy tolerance of ±1 °C. Figure 1 represents the Breadboard connecting for the whole system.

The flowchart of the control algorithm presented in the Fig. 2 represents the main loop in NodeMCU code, which makes iteration every 50 ms. It starts with observing if there are any changes on buttons. If the button is pressed, its state will change from 0 to 1, thus triggering the main controlling unit to increase/decrease the value of desired temperature of certain chamber. This only occurs with the positive edge of the button being pressed. So there will not be any effect in case the button is held down for larger amount of time.

After the state of buttons has been checked, algorithm proceeds to obtain data from temperature sensors, which is done each second, since temperature does not change fast over time. Next step is where current temperature values are being compared with desired temperature values. In case the desired values are greater than current temperature values, the relays will be signaled to turn the heaters on. If the situation is opposite, the relays will turn the heaters off.

There is an additional feature used in this project. In order to prevent data loss regarding desired temperatures in case of temporal power outage or even some errors in the behavior of the device itself, data storage to flash file system has been employed. Whenever desired value of temperature of certain chamber has been changed, it is automatically updated in the SPIFFS (Serial Peripheral Interface Flash File System). When the device is booted up, it checks the data from SPIFFS, and sets the desired values of temperature. In this manner, the whole system itself becomes more resilient to eventual electricity shortages and/or possible restarts of the device itself.

As it is mentioned earlier, the NodeMCU has the possibility to connect to the Wi-Fi network, and by doing so, the user is able to send/receive some data to/from the internet. In

Fig. 1 Breadboard connection for the whole system [8]

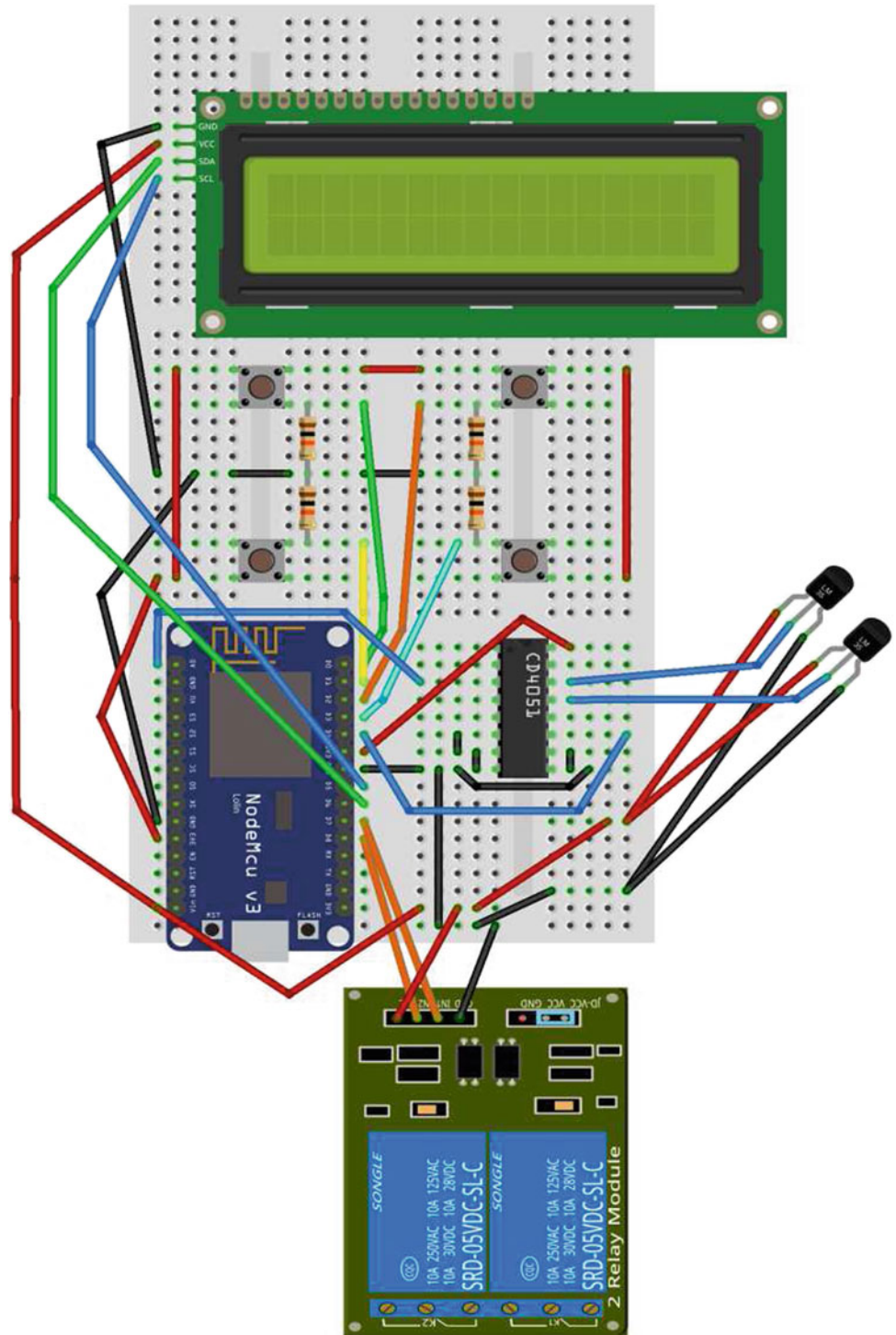
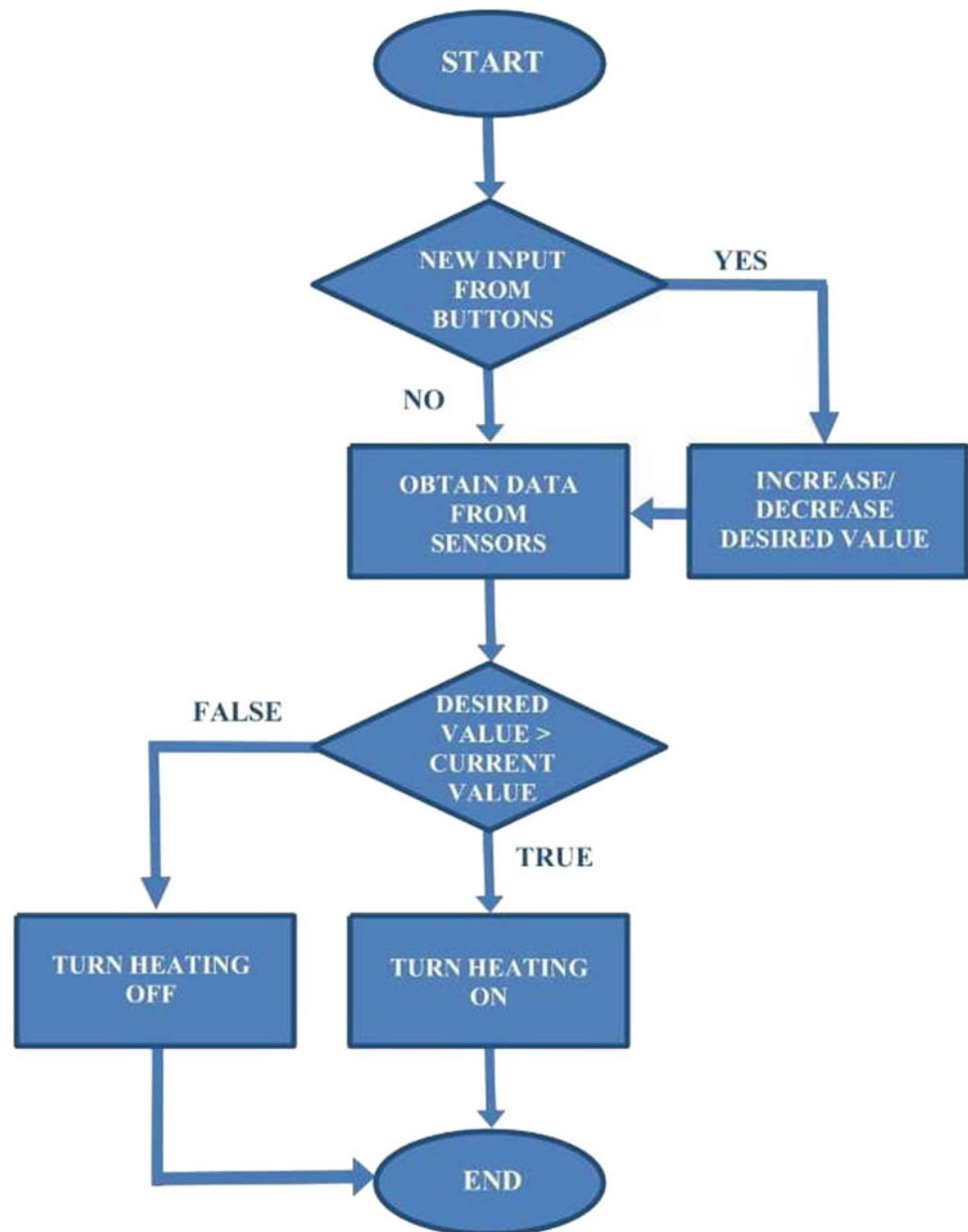


Fig. 2 Flowchart of the control algorithm [8]



this particular project, there is possibility to obtain the data regarding current and desired temperature in both chambers, and moreover, to set new values of desired temperature.

To be able to do so, it was required to create a server on NodeMCU, which will provide us with opportunity to exchange data with network. Since the server was in our experiment connected to the Wi-Fi network of International Burch University where research was conducted, only devices connected to International Burch University Wi-Fi network were able to access the data on NodeMCU.

The NodeMCU sends 4 values on the server, which include current and desired temperature values of two

chambers of the microbiological incubator in this project. It also receives 4 inputs from server, which are buttons used to set the desired temperature values of both chambers.

The webpage is able to fetch the data regarding current and desired temperature values, and it displays them in a neat fashion. It is well illustrated in Fig. 3. Besides that, there are four buttons included as well, which have a similar function like the real physical buttons to control and set the desired value of temperature. To do so, for each chamber beneath the output of current and desired temperature values there are two buttons; one for increasing (red) the value of desired temperature, and another for decreasing (blue).



Fig. 3 Web page of the microbiological incubator [8]

3 Results

After connecting all hardware parts and uploading the control algorithm to the NodeMCU platform, it was required to test how the system actually works. In order to accomplish this, an experiment on chamber one was conducted. Temperature was measured and recorded each second, and afterwards it was plotted using Serial Plotter option in the Arduino IDE.

Initial temperature of the chamber was 38 °C, and desired temperature was set to 40 °C. Differential gap was used in the controlling algorithm of the system, with upper boundary being 1 °C greater than the desired value, and lower boundary 1 °C lower than the desired value.

The heater was turned on at the beginning, and it continued to work until the current value of temperature in chamber reached upper boundary of the differential gap (1 °C greater than the desired temperature). At that point, heater

was turned off, waiting for temperature drop. After the temperature value decreased to the lower boundary of the differential gap (1 °C lower from the desired temperature, heater was turned again on. The graph obtained using Serial Plotter feature of Arduino IDE is presented on the Fig. 4.

While observing the graph obtained using Serial Plotter, several conclusions can be made. Generally speaking, the results were good, the device was performing well. However, there are some aspects which need improvement.

It can be observed that the temperature values were slightly outside the desired temperature range, ranging from 39 to 41 °C. This effect was caused by heater, since it cannot cool immediately down after being turned off. So the heater will still be warm for some time after being turned off, thus contributing to the further increase of temperature in the chamber.

Furthermore, we can observe that the overshoot was higher in case when heater was working longer (in the initial case when temperature needed to go from 38 to 41 °C). After desired value was reached, overshoots were slightly lower, but still present. In order to decrease the overshoots, several things can be done. One of them is to lower upper boundary of differential gap.

This value can be set to be equal to the desired temperature value, so the heater would be earlier turned off, thus decreasing possible overshoot.

Another way to improve the performance of the device would be including the PID controller into the system. When choosing the P, I and D constants, one must choose them in such manner, so that the control algorithm could anticipate

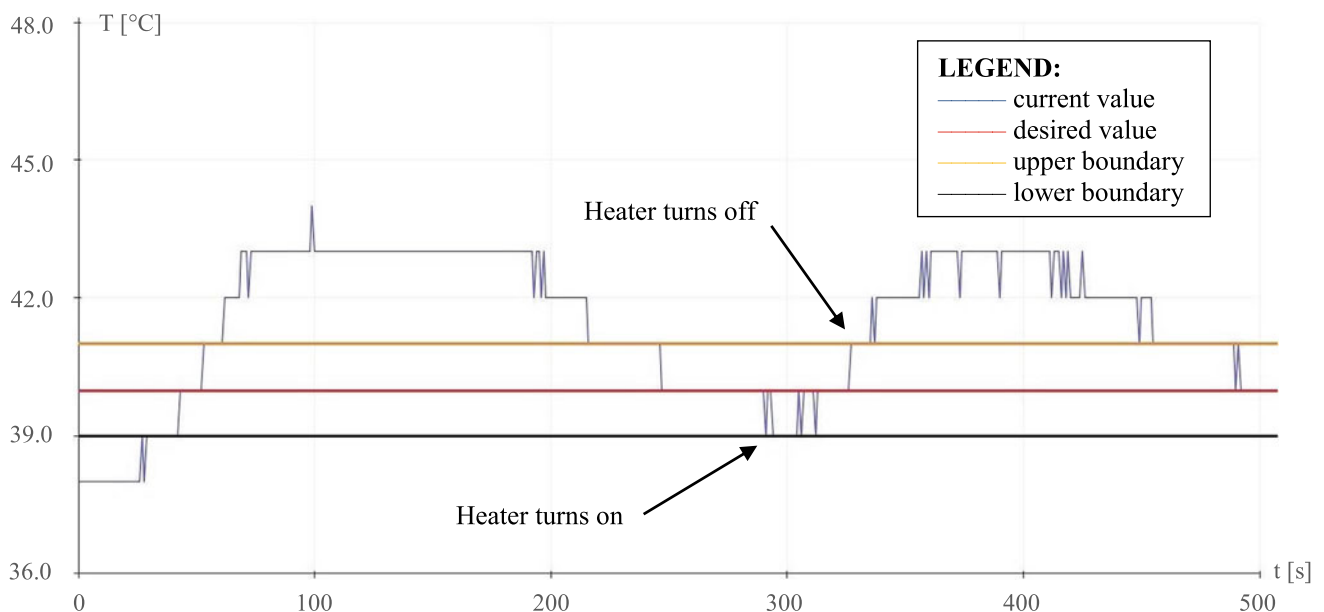


Fig. 4 Temperature versus time diagram of microbiological incubator in range from 0 to 500 s [8]

the future results (property of D component), so it could potentially turn the heater down before the overshoot occurs.

4 Conclusion

In this project we have successfully developed microbiological incubator, which is capable of steadily incubating up to two types of the microbial cultures at the same time independently. Besides being reliable, this project has IoT prefix, which means that users are able to control it via internet. The incubator is connected to the Wi-Fi network of International Burch University, and it can be controlled by using webpage included in this project, so the user does not need to be present at the location of microbiological incubator in order to check or to adjust current temperature of the incubator.

The total price of the project is around 200 BAM, which is significantly less than the conventional microbiological incubators currently present at the market. After prototyping and testing phases are done, and with certain improvements, this project could be easily developed into final product for the market.

References

1. Pratt, L.A., Kolter, R.: Genetic analysis of *Escherichia coli* biofilm formation: roles of flagella, motility, chemotaxis and type I pili. *Mol. Microbiol.* **30**(2), 285–293 (1998)
2. Parsek, M.R., Singh, P.K.: Bacterial biofilms: an emerging link to disease pathogenesis. *Annu. Rev. Microbiol.* **57**(1), 677–701 (2003)
3. Danhorn, T., Hentzer, M., Givskov, M., Parsek, M.R., Fuqua, C.: Phosphorus limitation enhances biofilm formation of the plant pathogen *Agrobacterium tumefaciens* through the PhoR-PhoB regulatory system. *J. Bacteriol.* **186**(14), 4492–4501 (2004)
4. O’Toole, G.A., Pratt, L.A., Watnick, P.I., Newman, D.K., Weaver, V.B., Kolter, R.: Genetic approaches to study of biofilms (1999)
5. Zegans, M.E., Wagner, J.C., Cady, K.C., Murphy, D.M., Hammond, J.H., O’Toole, G.A.: Interaction between bacteriophage DMS3 and host CRISPR region inhibits group behaviors of *Pseudomonas aeruginosa*. *J. Bacteriol.* **191**(1), 210–219 (2009)
6. Stepanović, S., Vuković, D., Ježek, P., Pavlović, M., Švabic-Vlahović, M.: Influence of dynamic conditions on biofilm formation by staphylococci. *Eur. J. Clin. Microbiol. Infect. Dis.* **20**(7), 502–504 (2001)
7. Alibaba.com. (2018). Prices of microbiological incubators. Retrieved from Alibaba’s official website: <https://www.alibaba.com/showroom/pricemicrobiology-incubator.html>
8. Ibrahimpašić, T., Jokić, D.: Development of Microbiological Incubator (Senior Design Project). International Burch University, Sarajevo, Bosnia and Herzegovina (2018)

Honeybee Activity Monitoring in a Biohybrid System for Explosives Detection

Mitar Simić, Ross Gillanders, Aleksej Avramović, Slavica Gajić, Vedran Jovanović, Vladan Stojnić, Vladimir Risojević, James Glackin, Graham Turnbull, Janja Filipi, Nikola Kezić, Mario Muštra, and Zdenka Babić

Abstract

Free-flying honeybees can electrostatically collect particles from air in the flying and foraging areas, which in conjunction with organic-based explosive vapor sensing films, placed at the entrance to the beehive, can be used as a passive explosive sensing mechanism. Moreover, bees can be trained to actively search for a smell of explosive. Using trained honeybees in conjunction with a system for honeybee localization enables generation of a spatial-time honeybee density map, where the most visited places point to suspicious areas. In both methods (passive and active), bees' activity monitoring plays a significant role, providing information about environmental parameters and activities of bees at the entrance and exit of a beehive. In this paper we present the design and realization of an electronic system for bee activity monitoring at the front of a hive while using bees for explosive detection. The system also monitors air temperature and relative humidity. Results obtained to date from activity monitoring are useful in planning testing activities within our active and passive method, as it can determine the optimal period of the day and environmental parameters in which bees are most active.

Keywords

Biosensors • Explosive detection • Honeybees • Organic-based explosive vapor sensing films • UAV

1 Introduction

Detection of legacy landmines is a very important step in humanitarian mine clearance (demining) which is a pressing concern in many countries [1, 2]. It is estimated that today there are still tens of millions of anti-personnel mines in the ground in over 60 countries [3]. According to the United Nations, approximately 2000 people are killed or injured by landmines every month. Over half the landmine casualties are civilians [4].

Current humanitarian mine detection and demining methods mainly include: (1) manual detection with a metal detector, (2) detection by specially trained dogs or rats, and (3) mechanical clearance. Each of these methods has some advantages over others, but in general the main disadvantages of all three are high cost, time-consuming training procedures, and the risks and dangers for involved personnel. Thus, there are ongoing demands for new technologies which may provide effective demining additional method to conventional methods.

Our research within the project “Bees for explosive detection (Bee4Exp)” funded by NATO Science for Peace and Security Programme is directed towards the use of honeybees as biosensors for legacy landmine detection. Honeybees are known to have an excellent sense of smell, which they use to find the food. Training honeybees to smell explosives (e.g. TNT and DNT odors), enables us to actively use them to search for landmines. With a few days' conditioning in a mesh tent, bees associate the scent of TNT and DNT with food (sugar solution). The conditioned honeybee colony is then transferred to the mine field to search for TNT and DNT odors. So, bees can passively collect particles from

M. Simić (✉) · A. Avramović · S. Gajić · V. Jovanović
V. Stojnić · V. Risojević · Z. Babić
Faculty of Electrical Engineering, University of Banja Luka,
Patre 5, 78000 Banja Luka, Bosnia and Herzegovina
e-mail: mitar.simic@etf.unibl.org

R. Gillanders · J. Glackin · G. Turnbull
School of Physics and Astronomy, University of St Andrews,
North Haugh, St. Andrews, KY16 9SS, UK

J. Filipi
Department of Ecology, Agronomy and Aquaculture, University
of Zadar, Trg kneza Višeslava 9, 23000 Zadar, Croatia

N. Kezić
University of Zagreb, 10000 Zagreb, Croatia

M. Muštra
Faculty of Transport and Traffic Sciences, University of Zagreb,
Vukelićeva 4, 10000 Zagreb, Croatia

the air while free-flying in foraging areas, and can be trained to actively search for smell of TNT and DNT—these two options are exploited for the development of methods for the use of bees in explosive detection. In the active method we monitor bees over a minefield and find the most frequently visited places, which then could be marked as suspected mine-contaminated areas. Our approach is based on using an Unmanned Aerial Vehicle (UAV) for capturing high definition georeferenced video in both visible and infrared parts of the spectrum, and applying sophisticated video analysis algorithms [5, 6]. The passive method is based on the fact that during foraging honeybees are collecting particles and odors from surrounding. We are using bees applied to free fly on test minefields in order to collect TNT and DNT particles which they are accumulating in the hive. The main advantages of using bees include the short period required for conditioning, the ability to cover a wide area in large numbers, and using honeybees for explosive detection is safer and cheaper additional method to the conventional methods [5].

However, well-known restriction in the use of bees is low temperature (below 15 °C) [2]. Wind and rain can also interfere with the activity of bees. Investigation of the influence of other environmental parameters is very important for understanding bee behavior in the field. In this paper we present an electronic system for bee activity monitoring which should provide information about environmental parameters with a time and date stamp, along with detected activity of bees at the entrance and at the exit of the beehive. Such information can be very useful in planning testing activities within our active and passive method, as it can determine the optimal period of the day and environmental parameters in which bees are most active.

This paper is organized as follows: in Sect. 2 the passive and active methods of using bees as biosensors for explosive detection are described. In Sect. 3 the electronic system for bee activity monitoring is presented. The main experimental results of testing the hardware-based prototype of the electronic system is presented in Sect. 4. Conclusion remarks and discussion related to our future work are given in Sect. 5.

2 Honeybees for Explosive Detection

2.1 Passive Method

For trace collection of polluting materials like explosives in the environment, a method known as “preconcentration” can be used [7–10]. Preconcentrator materials typically have a certain affinity to a specific, or class of, compounds, allowing them to be sorbed to the preconcentrator surface over time. The sorbed material can then be thermally desorbed to

deliver a much higher concentration of analyte to the sensing probe than can normally be detected in real time.

Organic semiconductor films have been used as optical explosive sensors in recent years owing to their solution processing, reversibility, sensitivity and spectroscopic properties [11–14]. These films emit light in the yellow when photoexcited by blue light, and this strong emission can be quenched by trace amounts of explosives, leading to a characteristic decrease in the peak intensity.

As mentioned above, free-flying, foraging honeybees are known to electrostatically collect explosives and other materials on their body hair. By using preconcentrators to sorb the explosives from the returning bees, the presence of landmines in the area may be reliably detected, leading to faster and safer surveying for landmine-contaminated land.

A fluoropolymer, Aflas (AGC Chemicals), was dissolved in tetrahydrofuran and spot- or blade-coated onto a paper or canvas substrate, respectively, and allowed to dry. For collecting the explosives from the honeybee body hair, the canvas substrates were inserted into 1 cm² tubes made of multiwall polycarbonate sheets, four for insertion in the entrance and four for insertion in the exit. This allowed the separation of returning bees and those leaving the colony. The paper-based substrates were also used to sample the colony air by placing the substrate in the nozzle of an air sampler, placing the nozzle into the hive via a specialized cupola, and sampling for 10 min at 60 L min⁻¹.

The passive method, in contrast to the tent-based training of the active method, allows the honeybees to free-fly during standard foraging activity in a given area and return to the hive. Typically control samples are taken on a known non-contaminated site over 24 h before the colonies are moved to the test site. The cartridges containing the four preconcentrators are placed in the colony for 24 h, prior to collection, sealing in an airtight bottle, and subsequent thermal desorption and optical detection.

To analyse the field samples, the commercial organic semiconductor Super Yellow (Merck) was dissolved in toluene and spin-coated onto clean glass slides. The sensor film was placed in a chamber containing the preconcentrator and a heating element to allow the preconcentrator to desorb the explosives. The heating element was ramped to 100 °C over approximately 90 s, and the sensor film excited by a 405 nm laser from Photonic Solutions. The emission was monitored for 300 s with a fibre-couple spectrometer.

Our test site was at Benkovac, Croatia during September 2018. Benkovac test site, inaugurated in 2000, has 1000 buried mine targets in a Mediterranean climate over 10,000 m². There are 39 blind test lanes each 47 m long, 1 m wide, and various mines are buried at 5–27 cm depth. Distance between the lanes is 3 m. The lanes are divided into 1 × 1 m².

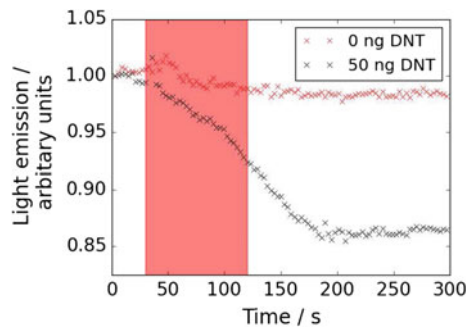


Fig. 1 Decrease in Super Yellow emission from a DNT-exposed Aflas preconcentrator

Initial results from the passive method indicate Aflas is a good preconcentrator material for explosives. The emission from the Super Yellow film shows a decrease of around 15% when 50 ng of DNT is desorbed from a preconcentrator substrate under laboratory conditions compared to the control experiment where around 1% of emission is lost over the same time period due to photo-oxidation of the sensor film, as shown in Fig. 1.

2.2 Active Method

The active method for using honeybees as bio sensors implemented in this project refers to monitoring the activity of honeybees, over a field which is suspected to be contaminated with mines. Trained honeybees are expected to sense the smell of explosives as food, and the active method has a goal to track honeybees on a field and determine the exact spots where they gather. It is important to emphasize that this method is primarily intended for safety and quality control.

The proposed method is carried out in two phases. The first one includes the specially designed preparation of honeybees so they would react on vapors of explosive substances contained in landmines. The goal is to train honeybees to recognize explosives as food. If training is successful, honeybees will associate the scent of explosive with food and will behave similarly in the vicinity of landmines as in the vicinity of food. The second phase includes tracking and tracing of honeybees over the inspected area, in order to pinpoint the exact locations where they gather. Detected locations with the most frequent detections of honeybees are the most suspicious to contain unexploded ordnances. In order to detect honeybees during their flight over an area, features which provide good detection possibility of honeybees must be extracted, either from the visual spectrum or infrared spectrum.

The important preparation step includes setting up the data acquisition parameters correctly. Having in mind that

honeybees can cover a large area during their flight outside a hive, it is impossible to track and trace each individual honeybee. An approach used in our experiments relies on high-resolution video capturing of part of the field where we can expect their major presence. Captured data should provide enough information for automatic motion detection of small objects and estimation of the most frequent places of detection. We used UAV equipped with an ultra-high definition video (UHD) and a thermal camera (TC). To avoid strong winds coming from the UAV's propellers, an UAV should hover at least 8–10 m above the ground. In that case, winds will not distract honeybees, although they can cause additional movement of small objects on the ground (leaves, branches, etc.). For example, UHD camera equipped with 50 mm lens, will cover an area around 7 m in width and 4 m in height and will use more than 8 million pixels to store the data for one frame only. Considering the size of an individual honeybee (about 1 cm) each honeybee covers the part of the frame of size around 20 pixels. Beside usual RGB cameras, a good choice of a sensor is thermal camera, since the temperature of a flying honeybee is usually 35 °C. Currently available TCs are rather low-resolution and expensive but offer a good (thermal) resolution, which can be used to enhance UHD video. Therefore, a combination of visual and thermal features should provide more useful data for automatic filtering of honeybees and easier filtering of other moving objects of no interest (such as grass, plants, sticks, branches, etc.).

After the video is captured, a large amount of data is collected and must be processed to come up with the final results. Since video must be captured from multiple locations and/or from multiple sensors (for example three UAVs with cameras), the exact determining of actual coordinate is very important. So, system navigation is another crucial aspect of the active method. Standard satellite navigation can provide the positioning accuracy of couple of meters, which can be reduced with further postprocessing. If possible, it is recommended to use Real-Time Kinematic GPS (RTK), which provides much greater accuracy than standard GPS and overall accuracy under 2 cm. Basically, the proposed capturing system must contain UAV with accurate GPS, and UHD and TC sensors, but additional sensors can be considered as well.

Considering that honeybees are very small insects (in average 1 cm long) and that their natural color makes them hard to detect when flying above grass covered or bare-terrain, the complete and final solution for their tracking and tracing is still missing. By analysing large amount of captured video, we concluded that most descriptive feature that can separate honeybees from the background is their style of movement. Therefore, our research methodology is mostly based on state-of-the-art algorithms like Gaussian mixture model and Convolutional Neural Networks. Next, we

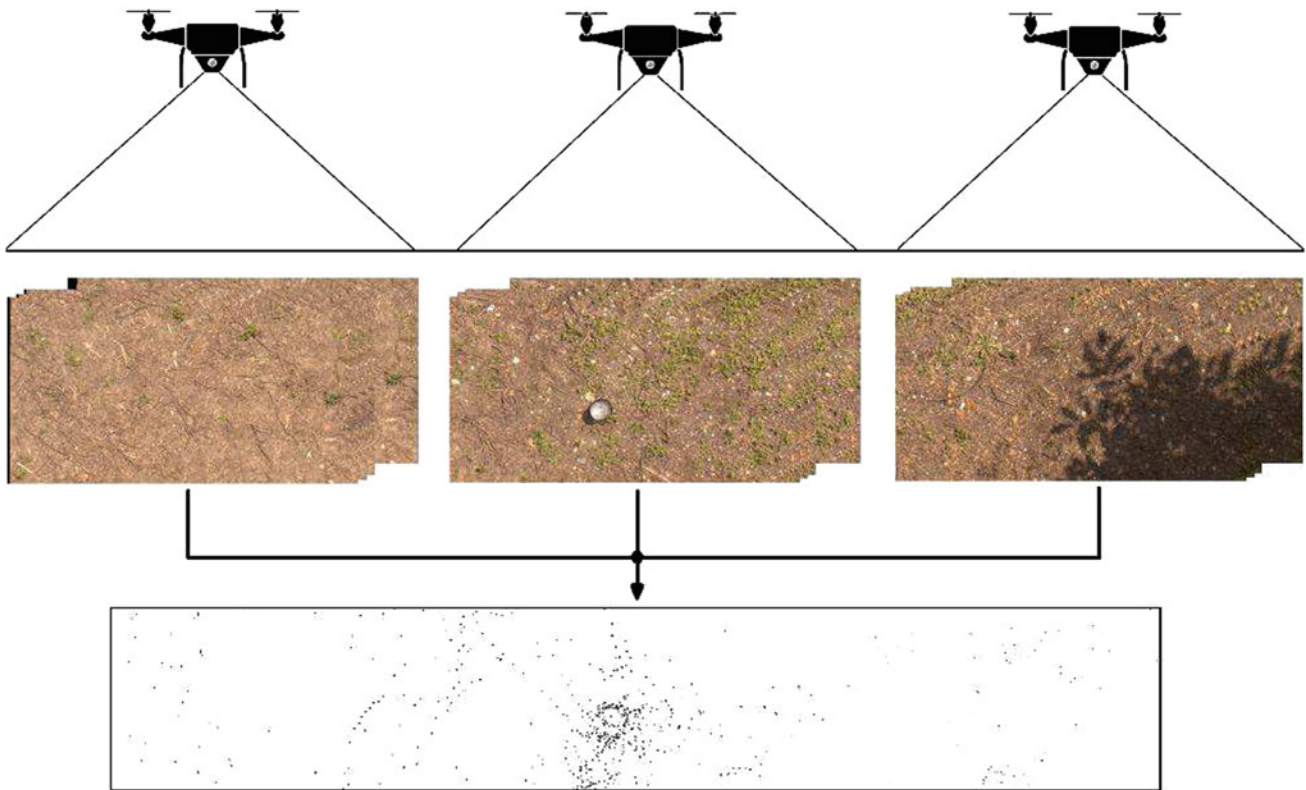


Fig. 2 Schematic representation of the active method

implemented several case-specific methods for preprocessing (image filtering, video stabilization, etc.) and postprocessing (morphological operations, noise removal, etc.). The overall result of several overflights is a spatio-temporal occurrence density map (Fig. 2). This map shows the most frequently visited places, which can indicate the possible locations of legacy landmines and other unexploded ordnances.

3 Electronic System for Bees' Activity Monitoring

The schematic overview of our electronic system for bee activity monitoring is shown in Fig. 3. We use an infrared (IR) LED as a source and a phototransistor in switching mode as a detector. The IR LED emits a light beam and if there is no bee in the input channel the phototransistor will be off, which can be detected by a voltage measurement between the OUT pin and the ground (GND). If the phototransistor is off, the expected value of voltage at the OUT pin

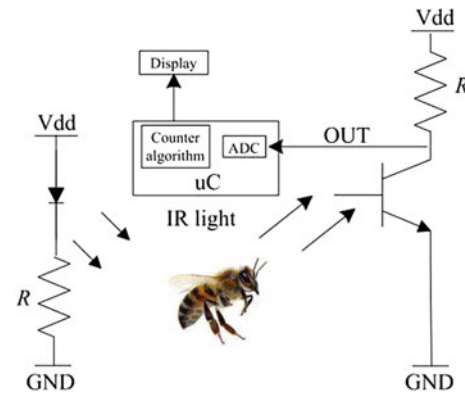


Fig. 3 Schematic overview of proposed system for monitoring of bees' activities

is equal to the V_{dd} . However, if a bee is present in the input channel she will reflect light towards the phototransistor which will go to the on state, and voltage at the OUT pin will drop to the collector-emitter saturation voltage.

A Microcontroller (uC) is used for voltage measurement with an embedded analog-to-digital converter (ADC). Monitoring the daily activities of bees is registered with information regarding time and date collected with a real time clock (RTC), as well as ambient temperature and relative humidity (RHT sensor).

4 Experimental Results

Hardware realization of the electronic system for bee activity monitoring (Fig. 4) is based on an ATmega2560 microcontroller, 6 QTR Pololu pairs of IR LED and phototransistor, DS3231 RTC and a Sensirion SHT11 RHT sensor. Tubes used for placement of the canvas substrates were used for Pololu sensors as well. Additionally, black tape was used to prevent penetration of daylight (includes also infrared wavelengths) which can cause faulty turning on of phototransistors.

The electronic system for bee activity monitoring was tested at the same time as the passive method at the Benkovac test site during September 2018. One small part of obtained results in monitoring of ambient air temperature ($^{\circ}$ C), relative humidity (%RH) and percentage of input voltage

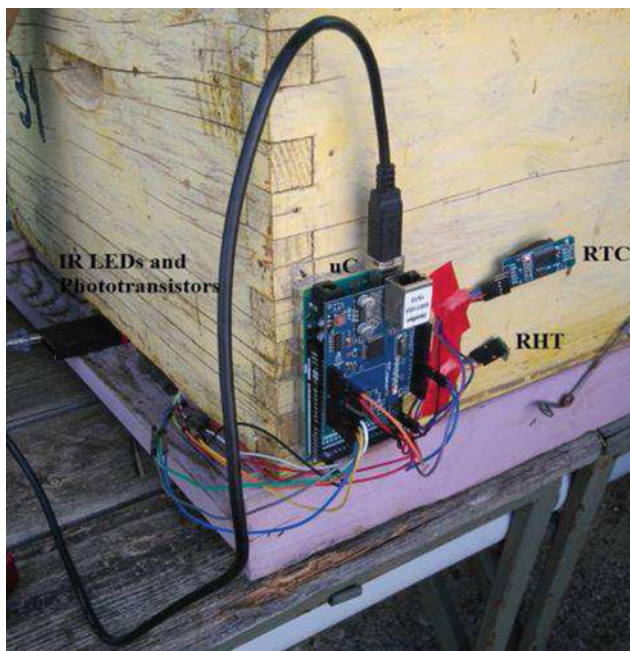


Fig. 4 Hardware realization of the electronic system for bee activity monitoring

compared to the Vdd are shown in Figs. 5 and 6. Results are presented starting from 5 am, with samples obtained every second. As shown in Fig. 5, it can be noticed that around 6:30 am bees started leaving the beehive along with the increase of temperature and decrease in relative humidity.

However, channels at the entrance of the beehive (Fig. 6) registered lower level of activities, which was expected as bees early in the morning start going out to look for food.

However, the inverse behavior was registered at the end of the day- relative humidity was increasing while temperature and bee activities were decreasing.

Monitoring over longer periods of time during changes of environmental parameters can be very useful in planning testing activities and interpreting data within our active and passive methods, as it can determine optimal period of the day or ambient parameters in which bees are most active.

5 Conclusion

In this paper we presented an electronic system for monitoring bees' activity. Our approach is to monitor environmental parameters as well as the detection of bees which are going out from the beehive to look for food. Such an electronic system is very important for our research for explosive detection with bees. Experimental results showed that both our approaches are promising with great potential for high-impact delivery of this research.

Obtained results showed that our active approach can be used for detection, tracking and tracing of honeybees, therefore for monitoring of their activity. Further work will include mathematical modeling of honeybee's occurrence and validation based on expert's opinion.

The promising early results from the passive method of collecting and subsequently detecting explosives in the environment indicate that free-flying honeybees can electrostatically collect enough explosive materials from the environment to be concentrated onto a fluoropolymer substrate and be detected by optical sensors. Efforts are ongoing to increase the sorbing affinity and detection sensitivity of the system.

As the future work, we are directed towards further research regarding electronic systems for bee activity monitoring. We have recognized the need for development of an algorithm for bee counting based on the measured voltage, as well as expansion of environmental parameters which can be monitored, such as direction and wind speed, UV level, or presence of volatile organic compounds.

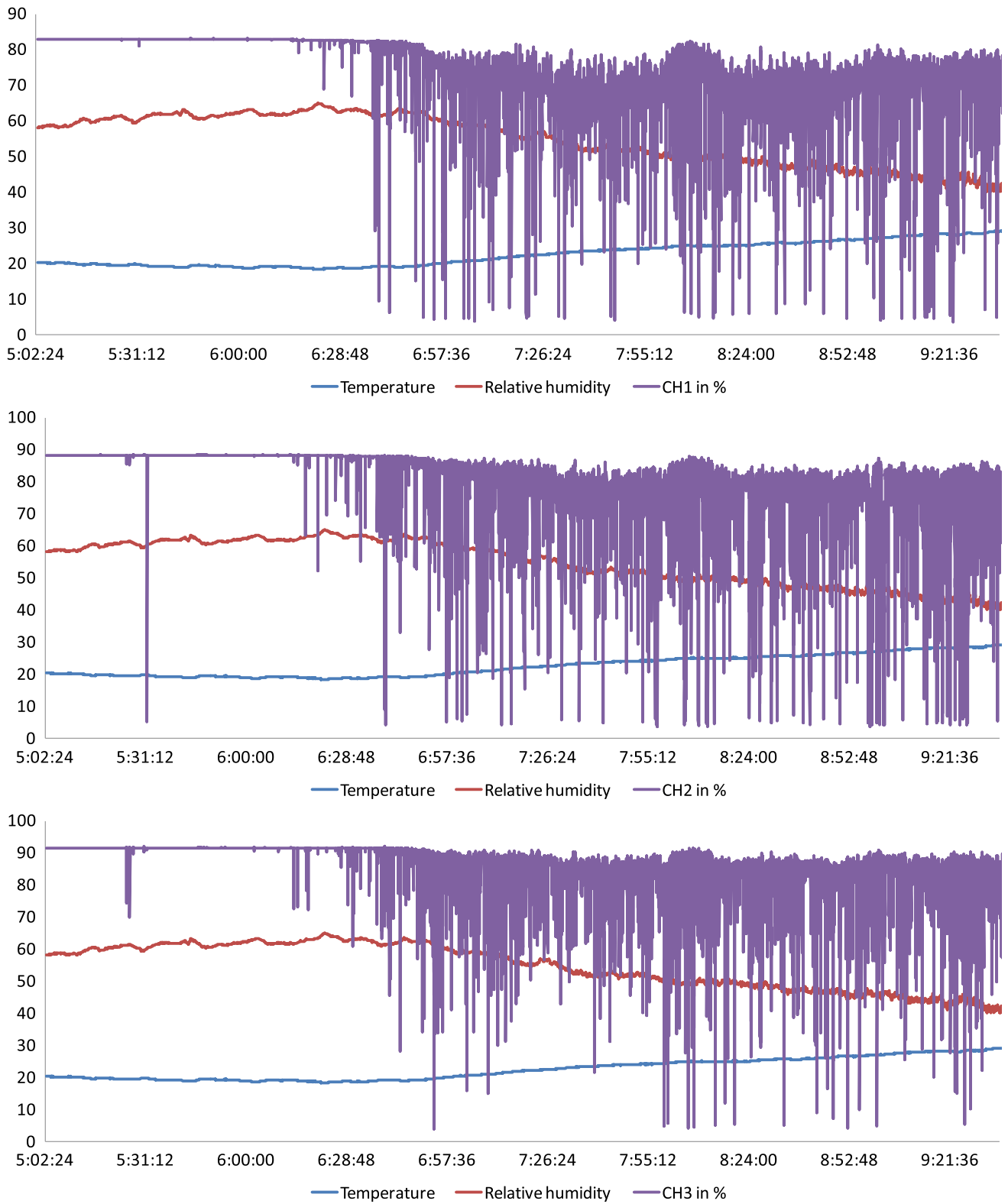


Fig. 5 Obtained results for channels at the exit of the hive

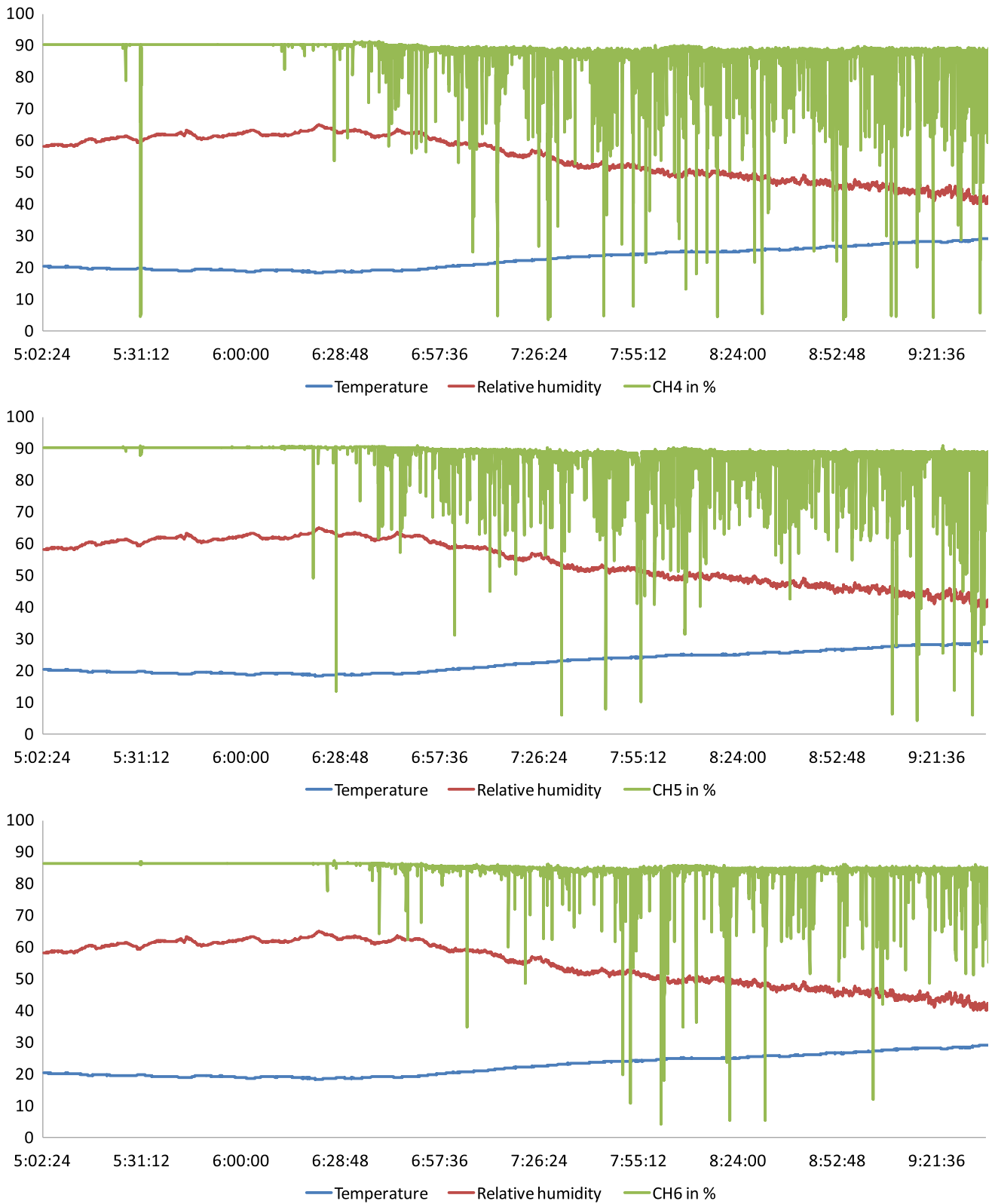


Fig. 6 Obtained results for channels at the entrance to the hive

Acknowledgements This research is partially supported by the “Biological Methods (Bees) for Explosive Detection” international project, supported by NATO Science for Peace and Security (SPS) Programme, project number SPS 985355, and Ministry of Science and Technology Republic of Srpska, Bosnia and Herzegovina, “UAV Video Analysis in Biological Methods for Explosive Detection”, project number 19/6-030/3-2-21-1/17.

Conflicts of Interest The authors declare no conflict of interest.

References

- Babic, Z.: Signal processing challenges in biohybrid system design. In: Proceedings of the IEEE 7th International Conference on Reliability, Infocom Technologies and Optimization (ICRITO'2018) (in press), invited paper, Noida, India, August 2018
- Kezić, N., Babić, Z., Filipi, J., Turnbull, G., Gillanders, R., Glackin, J., Mirjanić, G., Muštra, M., Pavković, N.: Bees for explosive detection. In: Proceedings of 15th International Symposium Mine Action 2018, Slano, Croatia, April 9–12, 2018, pp. 42–44
- http://marshall-legacy.org/about-2/landmine_facts/. Accessed 10 Dec 2018
- <https://research.un.org/en/mines/un-documents>. Accessed 10 Dec 2018
- Avramović, A., Jovanović, V., Pilipović, R., Stojnić, V., Risojević, V., Gajić, S., Simić, M., Ševo, I., Muštra, M., Babić, Z., Filipi, J.: Automatic monitoring of honeybees' activity outside of the hive from UHD video. In: Proceedings of 14th Symposium on Neural Networks and Applications (NEUREL), Belgrade, Serbia, November 20–21, 2018
- Avramović, A., Pilipović, R., Stojnić, V., Jovanović, V., Ševo, I., Simić, M., Risojević, V., Babić, Z.: Honeybees video-tracking for explosive detection. In: Proceedings of 15th International Symposium Mine Action 2018, Slano, Croatia, April 9–12, 2018, pp. 45–48
- Egorov, O.B., O'Hara, M.J., Grate, J.W.: Equilibration-based preconcentrating minicolumn sensors for trace level monitoring of radionuclides and metal ions in water without consumable reagents. *Anal. Chem.* **78**(15), 5480–5490 (2006)
- Cizek, K., Prior, C., Thammakhet, C., Galik, M., Linker, K., Tsui, R., Cagan, A., Wake, J., La Belle, J., Wang, J.: Integrated explosive preconcentrator and electrochemical detection system for 2,4,6-trinitrotoluene (TNT) vapor. *Anal. Chim. Acta* **661**(1), 117121 (2010)
- Camara, M., James, F., Breuil, P., Pijolat, C., Briand, D., de Rooij, N.F.: MEMS-based porous silicon preconcentrators filled with Carbo-pack-B for explosives detection. In: Sberveglieri, G., Ferrari, V., (eds.) 28th European Conference on Solid-State Transducers, 2014, vol. 87, pp. 84–87
- Tiwary, N., Vinchurkar, M., Patel, M., Nathawat, R., Pandey, S., Rao, V.R.: Fabrication, characterization and application of ZnO nanostructure-based micro-preconcentrator for TNT sensing. *J. Microelectromech. Syst.* **25**(5), 968–975 (2016)
- Toal, S.J., Trogler, W.C.: Polymer sensors for nitroaromatic explosives detection. *J. Mater. Chem.* **16**(28), 2871–2883 (2006)
- Thomas, S.W., Joly, G.D., Swager, T.M.: Chemical sensors based on amplifying fluorescent conjugated polymers. *Chem. Rev.* **107**(4), 1339–1386 (2007)
- Gillanders, R.N., Samuel, I.D.W., Turnbull, G.A., Low-Cost, A.: Portable optical explosive-vapour sensor. *Sens. Actuators B-Chem.* **245**, 334–340 (2017)
- Bolse, N., Eckstein, R., Schend, M., Habermehl, A., Eschenbaum, C., Hernandez-Sosa, G., Lemmer, U.: A digitally printed optoelectronic nose for the selective trace detection of nitroaromatic explosive vapours using fluorescence quenching. *Flex. Print. Electron.* **2**(2), 024001 (2017)

HaBEEtat: A Novel Monitoring Platform for More Efficient Honey Production

Semir Sakanovic and Jasmin Kevric

Abstract

Bees immensely contribute to mankind. Over the years, bees have performed a task that is vital to the survival of agriculture and pollination. One third of our global food supply depends on bees' pollination, which simply means that bees keep crops and plants alive. If bees were to go extinct, mankind would not survive because the food we eat depends on bees' pollination. Humans can only last for four years without bees. Monitoring of bees should be a priority. This is one of the reasons why HaBEEtat has done research to create a platform that helps beekeepers keep bees safe. The objective of HaBEEtat is to remove the greatest threat to bees' lives, which is climate change. HaBEEtat has created a platform that is going to help beekeepers to monitor the temperature, humidity and weather, which will help to preserve the lives of millions of bees. The platform will thereby decrease the declination of bees and increase their population, as well as production.

Keywords

HaBEEtat • Bees • Data • Analysis • Platform • Monitor • Climate • Smart Frame

1 Introduction

Keeping bees is both rewarding and an investment opportunity in today's world, with many people worldwide keeping bees for different reasons. At a broader view, bees are significant in the discipline of Agriculture because of the role they play in pollination following an approximation of

80% worldwide [1]. Beekeepers also raise bees for their honey production, pollen and wax, which is mostly harvested for candles, balms, and other body products, royal jelly, and bee venom, having a wide range of usage. Besides human nutrition, honey is also used in the medical field for the creation of medicines. Beekeeping was initially a hobby for most beekeepers, but as years passed, certain beekeepers realised the importance of beekeeping. Beekeepers mostly keep their records in handwritten formats because there was no exact technology to monitor bees. Now, most beekeepers are more than ever determined to ensure the safety of bees. Being a beekeeper is not as easy as it seems since beekeeping requires a lot of time, materials, and equipment maintenance. It also involves different locations due to climate change, provision for the bees' safety and so much more.

Hives are created depending on the size and numbers of bees and honey that it contains. However, larger hives have more effective ways of producing honey considering a number of significant factors such as geographical location, weather, temperature, pests, local flora, and so forth [2]. The end results of examining these factors are for the purpose of increasing the production of honey and ensuring a healthy population of bees globally. There is a significant number of colonies that die every single day due to the lack of effective management [3]. Most of the bees die during the winter seasons [4] therefore, with the use of HaBEEtat's platform results can be different in the yield growth and quality products.

To ensure the achievement of the objective in producing great amounts of honey, quality honey, and healthy products, the HaBEEtat platform comes in the middle to help propagate the idea by taking it to greater heights. The platform is meant to provide the most suitable management conditions of the hives, ensuring accomplishment of one's goals through utilization of technology.

All of the data that the HaBEEtat platform is collecting is sent by custom hardware that contains several sensors for measuring. It contains twenty sensors for measuring the

S. Sakanovic (✉) · J. Kevric
International Burch University, Sarajevo, Bosnia and Herzegovina
e-mail: semir@habeetat.io; symorgh13@gmail.com

J. Kevric
e-mail: jasmin.kevric@ibu.edu.ba



Fig. 1 HaBEEtat Hardware v5.0

weight of each single frame inside of the beehive. It also contains sensors for temperature and humidity that collects data from the inside and outside of the beehive, so that it can assess what the correlation is between what is happening inside and outside of the beehive in terms of temperature and humidity. There were five hardware versions of HaBEEtat, and on Fig. 1, the fifth version of the hardware can be seen [5]. For transferring data, Tele2 IoT sim-card is used. This card can be used anywhere in the world to send data to the network via 2G or 3G. It connects automatically on any available network.

This paper is focusing on the analysis of the HaBEEtat software including the significance of the mobile application, what it entails, as well as what it does. Additionally, the analysis entails interpretation of the database.

2 Literature Review

The main reason to have a good location for your hive is so you can have access to a good drainage system to prevent bees from getting wet, dappled sunlight, minimal wind and a good water source for bees [6]. Hives should be placed in dappled sunlight because direct sunlight access all day causes hotness in the hive during the summer. The position

should be at a location that will easily be accessible for honey harvest time [7]. The hive's temperature is going to be monitored by the "Smart Frame".

Selecting a good location for your hive makes a difference for the production of honey and the honeybees' health. Moving colonies around causes stress for bees, and stressed colonies are likely to have diseases of many kinds [8]. To get your bees well settled, your hive should be facing North East, or South East if you are not in the northern hemisphere [9]. By placing the hive this way, bees can fly out in the morning for foraging [10]. Honeybees start flying around at 14–16 °C. The longer the day a bee has to forage, bring back pollen and nectar, the better that day for the entire hive's health. Bees should be protected from direct sunlight in the afternoons, especially during the summer. The "Smart Frame" will help monitor internal temperature and humidity with its humidity and temperature sensors, placed for optimal colony health. Honeybees have skin foraging radius, so the "Smart Frame" will monitor environment to see if they have enough to eat, over the year with twenty sensors that are located inside of the beehive.

HaBEEtat's mission is to empower a more effective nectar generation and enhance the prosperity of honeybees' populace through continuous observation and information investigation using its "Smart Frame". Our central goal is to offer an innovative arrangement available to a wide array of people and socioeconomics, particularly focusing on more youthful populations who are starting their enthusiasm for beekeeping exercises [11]. We endeavor to elevate a new point of view to conventional beekeeping by foremost presenting a versatile application and completely incorporated web arrangement interoperable with equipment segment as extra to standard apiary with an end goal to expand nectar generation efficiencies. At its center, our vision is to utilize immense measures of continuous information accumulation, offer investigation and forecast to the world's beekeepers, with the end goal of enhancing nectar generation processes and states of honeybees' populace.

To date, beekeepers utilized conventional beekeeping horticultural strategies, for example, putting hives at areas that are anticipated to be appropriate for higher nectar gain by outwardly assessing hives with the end goal to get vital data. Gathered information still relies upon their eye observations and gut expectations as opposed to exact information readings, which by and large never get recorded or put away for future reference or investigation. So, our center is to upgrade customary nectar generation processes and change it towards an IT-empowered information-driven approach and process.

The essential objective is to empower all existing beekeepers, and also pristine beekeepers, screening and tracking beekeeping conditions, thereby estimating all accessible ecological information pertinent to nectar generation, with

the use of online applications. Web, mobile and “Smart Frame”, are made to be to a great degree easy to assemble and easy to use, intended for disconnected socioeconomics. With our methodology beekeepers would have the capacity to get figured, delineate, colony conditions dependent on current, recorded climate and different factors, for example, temperature, dampness, barometrical weight, vegetation, nectar gain, dust, elevation, landscape, and so forth. These monitoring conditions will be implemented in next generation of “Smart Frame”. By social affair and dissecting, all these data stages will have the capacity to give the best reasonable area to hives dependent on memorable information. Moreover, it will alarm beekeepers about conceivable generation inadequacies, for example, abnormalities inside every day and week by week, nectar creation gains and in addition honey’s bee maladies and their potential spread in the region.

All things considered, the information process begins with the correct information accumulation, which is guaranteed by our equipment segment, and is approved by the professional beekeepers. Taking into account that beekeepers still use the customary strategies for beekeeping, it is evident that our advancement will give various advantages to the beekeepers.

3 Methodology and Results

HaBEEtat’s software is made to access and record bees’ activities in enclosed beehives through a digital manner round the clock called “Smart Frame” (shown in Fig. 2) through real-time monitoring and collection of the data analysis. The purpose of this software is to observe the population of bees, behavior, health, productivity and

monitoring of temperature and humidity. The software has been developed to track the weather, temperature, as well as the humidity inside and outside of the beehive. This software is going to help preserve the lives of millions of bees in existence; it will also help the production and preservation of honey being distributed into the market worldwide.

The HaBEEtat mobile application can be found on the Google Play Store and the App Store. After installing it, one will be required to sign up or to create an account using valid personal information that is one’s full name, e-mail address, place of residence (street address) and phone number. By registering using one’s email address and phone number, the user will be able to receive e-mail and text notifications respectively when there’s an issue to be addressed. The notifications will particularly be sent directly from the beehives where the temperatures and humidity level need to be adjusted, when the health of bees is at risk, and when the honey needs to be harvested, which is measured by the increase of beehive weight [12]. The data collected is stored in a database and later on, the user can retrieve it from the Application for further analysis. This helps to maintain and improve the production of honey where the beehives’ conditions are tracked and improved, for example, the analysis of temperatures and humidity [13]. The software can also work as the social meeting hub for all beekeepers in the world, where they will discuss and share ideas about the productivity, viable markets for their products, the best species to keep, the behavior of the bees and much more [14].

When the users sign in into the HaBEEtat Application, it will direct to a section on the left-hand side where they will access the locations tabs for various farm sites (shown in Fig. 3). The locations will be numbered depending on the number of the beehive sites.

Fig. 2 HaBEEtat Hardware module v3.0/Smart Frame



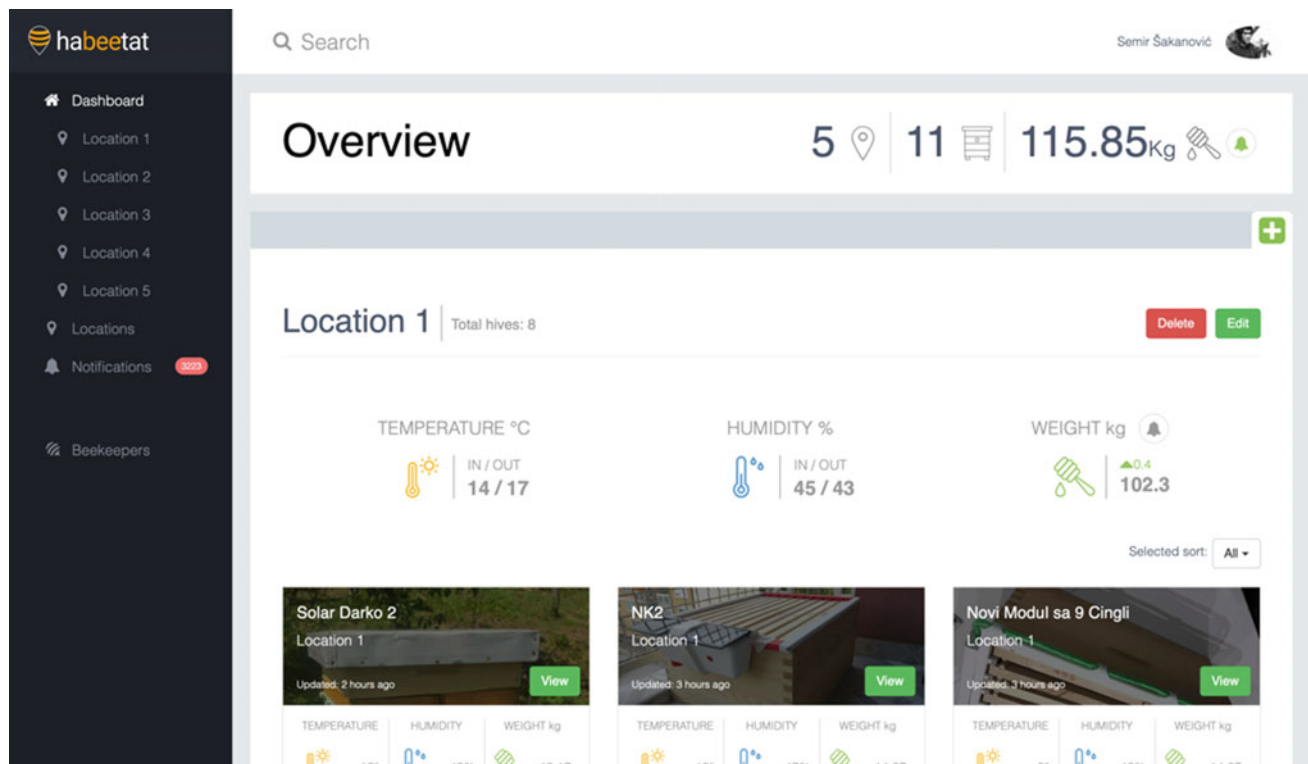


Fig. 3 HaBEEtat dashboard

When one clicks any of the locations, the tab will display the activities of the bees and an analysis of beehives' standards through graphs, charts, and saved photos of the activities carried. The most common features that will appear in the overview are temperature, weight, humidity, and measurement. The Application is designed to be simple and user-friendly. Its connectivity through Wi-Fi and GSM protocols enables real-time monitoring capabilities, in order for modern beekeepers to have access to the optimization of their operations, decreasing costs and reducing colony losses. This software enables an individual to inspect one's beehives and save images of each frame using the mobile app and also get insights into how the colonies are developing through time (shown in Figs. 4 and 5).

The core objective is to offer technological solutions that are accessible to a wide audience and demographic, especially targeting younger generations initiating their interest in beekeeping activities. We strive to promote a new perspective to traditional beekeeping by introducing the first mobile application and fully integrated web solution interoperable with hardware component as an add-on to a standard beehive in order to increase honey production efficiencies. (Fig. 6).

At its core, our vision is to leverage a great amount of real-time data analysis and prediction, presenting it to the

world's beekeepers in order to improve honey production processes and the conditions of the bee population (Figs. 7 and 8).

HaBEEtat's "Smart Frame" has sensors that monitor temperature inside and outside of the hive, as well sensors that monitor the humidity levels. Humidity is an important factor to consider for the comfort of bees when thinking of beekeeping [15]. Humidity sensors work by detecting the changes altered by electric currents and temperature in the air. There are three types of humidity sensors: thermal, resistive and capacitive. All three types of sensors monitor and detect changes made in the atmosphere in order to calculate the humidity of the air.

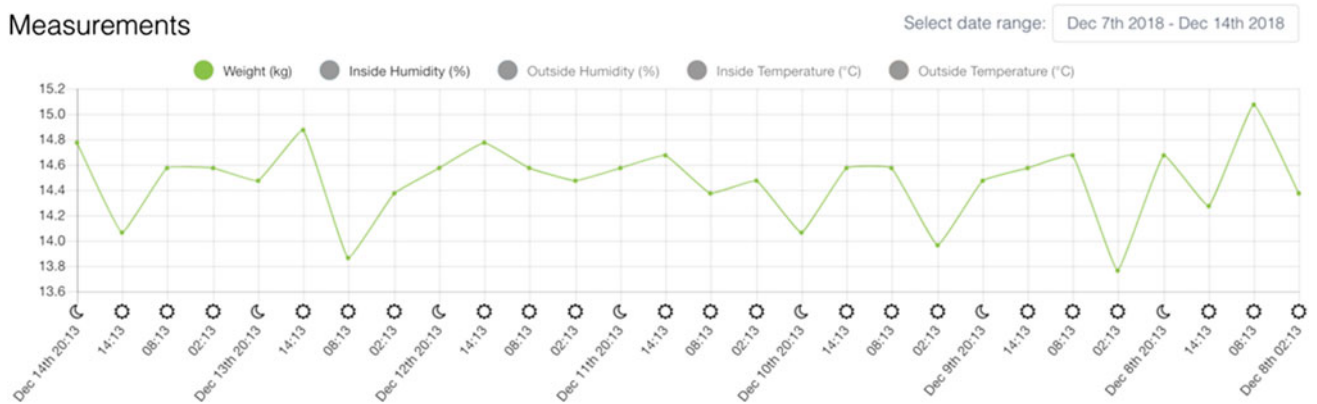
Thermal: There are two types of thermal sensors that conduct electricity based on the humidity of the surrounding air. One of the sensors covers or is in close fitting surrounding dry nitrogen, while the other thermal sensor measures the ambient air.

Resistive: The resistive humidity sensors use ions in salt to measure electrical impedance of atoms. When humidity changes, so does the resistance of the electrodes on both sides of the salt medium.

Capacitive: The capacitive sensors are linear and measure relative humidity from 0 to 100%. It has a complex circuit and regular calibration. The low temperature effect they have



Fig. 4 HaBEEtat platform



Weight by frame on Dec 14th 2018

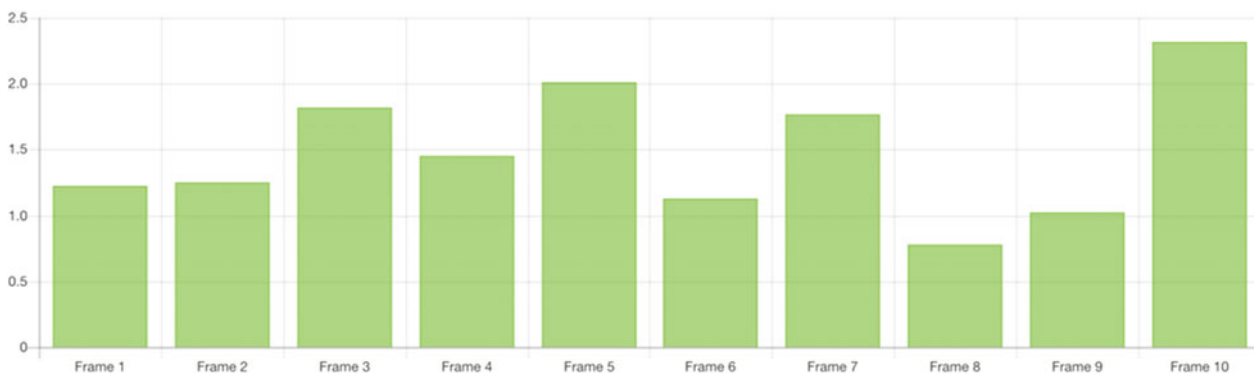


Fig. 5 HaBEEtat measurements

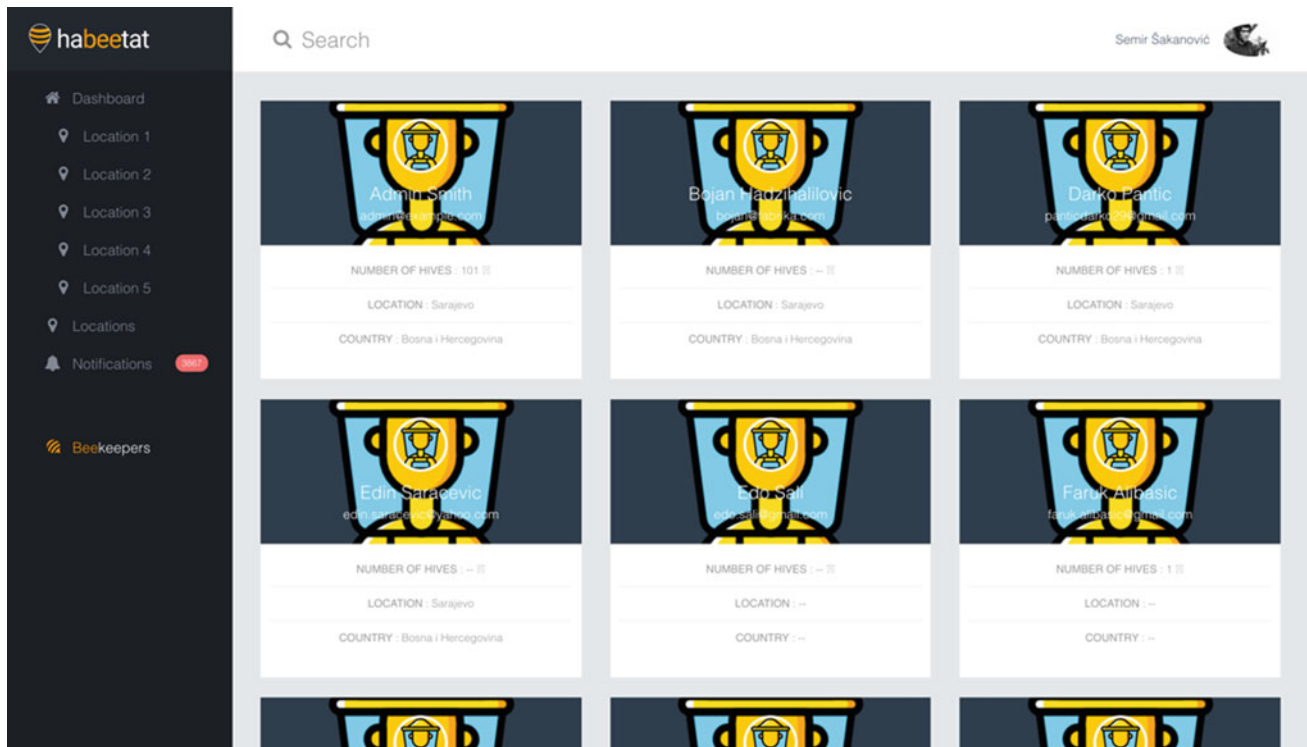


Fig. 6 Beekeepers on HaBEEtat platform

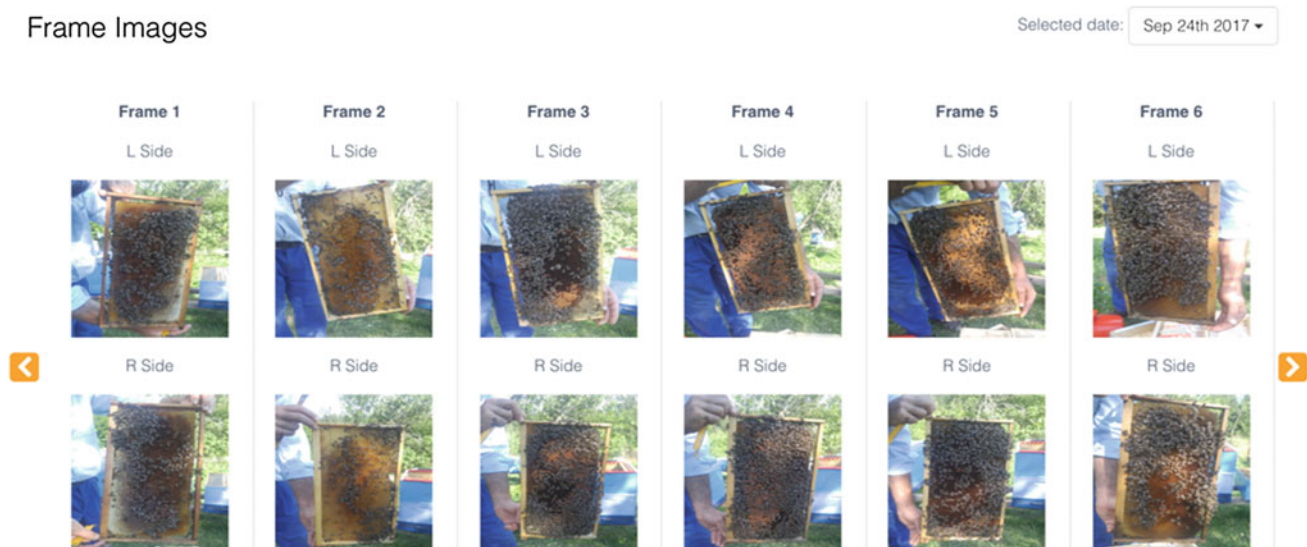


Fig. 7 Pictures of Frames taken with HaBEEtat app

often makes them usable over wider ranges without active temperature compensation. These sensors are used in “Smart Frame” hardware.

HaBEEtat’s platform is to collect more than just temperature, humidity; it also includes geographical locations and vegetation. The software is created to provide solutions that will enable the younger generations’ quantities of safe

and high quality of honey under the increase of resources and cost-efficient ways compared to the traditional methods. The population of bees is directly influencing companies in the field of agriculture since their cost is projected to increase greatly if bees die. The platform will help to promote the importance of beekeeping to the younger generations and more generations to come. The process of

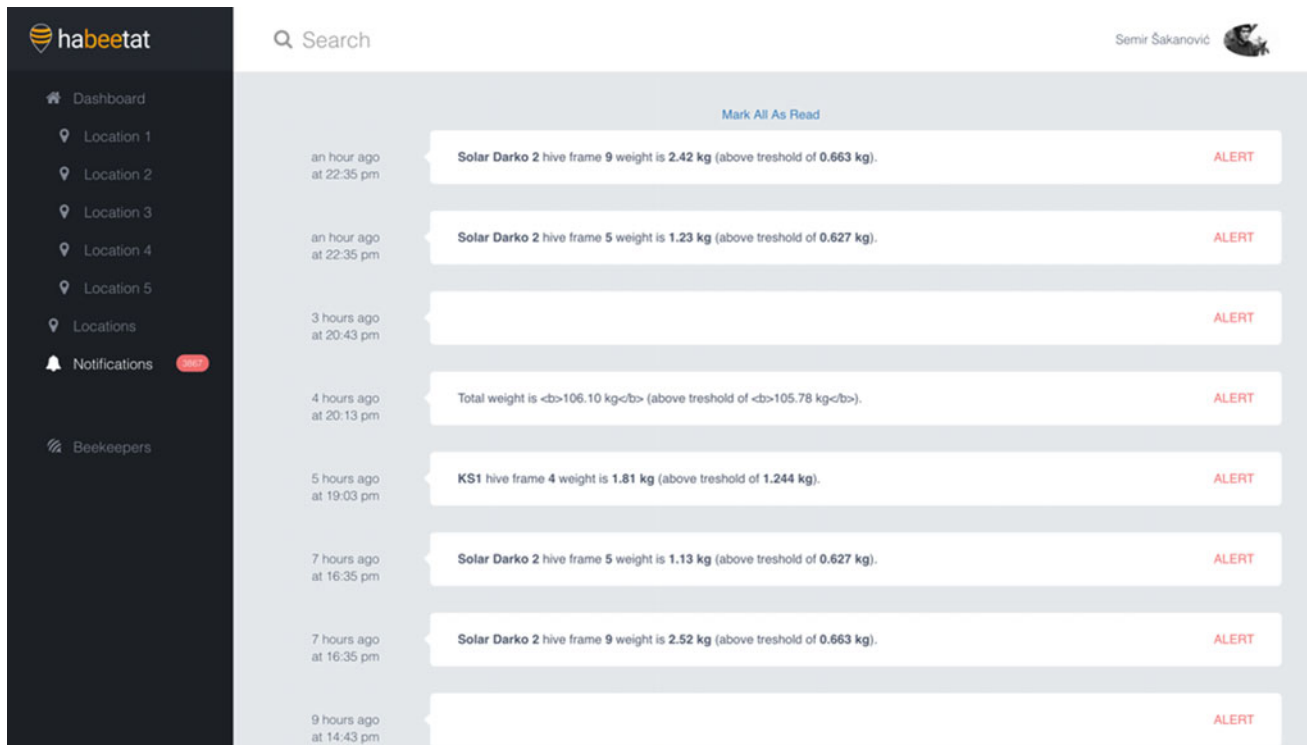


Fig. 8 Alert/Notifications on the HaBEEtat platform

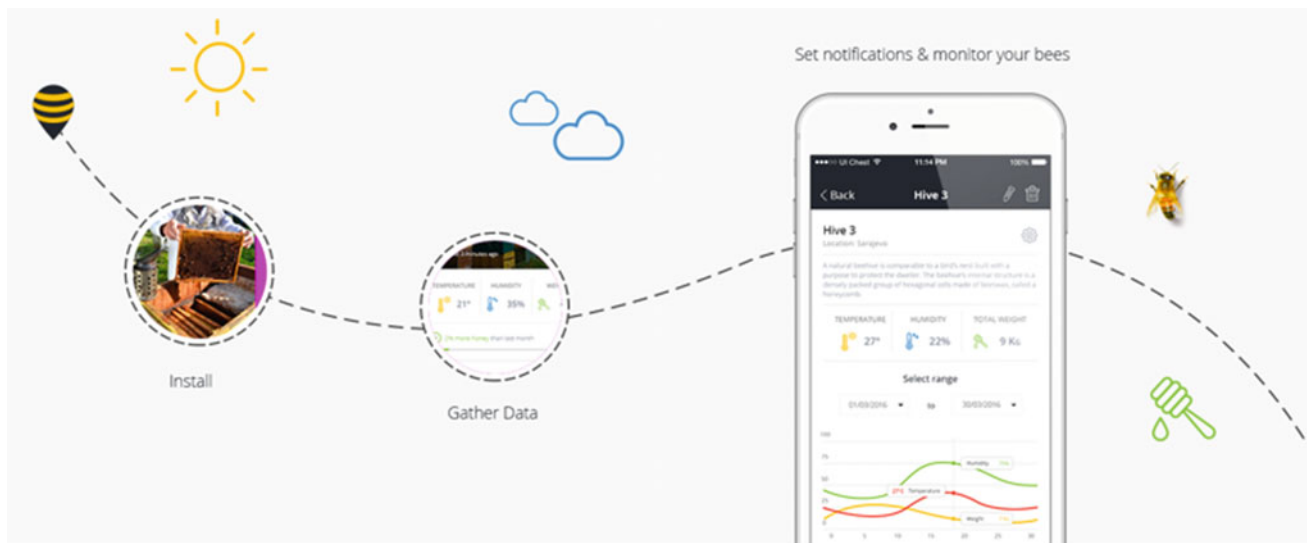


Fig. 9 HaBEEtat application

gathering data will enable the already established ecosystem of beekeeping, and it's been complemented by adding aspects which will then respond to the problems occurring in each hive, with the sole aim of reducing losses and prevent the death of bees. Our solution will provide answers to the EU-wide challenge in multiple ways (Fig. 9).

4 Discussion

In today's world, global beekeepers are still using traditional agricultural methods for honey production, whether they are big scaled businesses or just small individual operations. The

traditional beekeepers have not yet begun to utilize IT technology for their benefits. This software is meant to provide solutions and strengths to the already existing traditional methods of harvesting quality honey. Keeping in mind, the introduction of the Application is meant also to increase the percentage in the production of honey. The way honey production is done and managed is by a data driven calculations and predictions. For example, a key index of honey production is based on the number of hives and kilograms of honey produced at a given time in a given location.

It is evident that beekeepers are in a need of an up-to-date technological approach, not only to increase their production efficiency, but also to do so in the most effective and accurate way [16]. These specific needs were key requirements to our solution design, which would enable them to make decisions based on all available relevant data information such as weather conditions (past and present), geographical location and terrain, daily and weekly honey gain, vegetation and daily activity alerts. With this kind of data-driven approach, we see a huge opportunity within the existing honey production ecosystem, as well as significant opportunity to spread new methodology to the “non-professional segment” such as small-scale production units or individuals perceived as hobby activities in the field of beekeeping [16]. This is due to the fact that our solution enables beekeepers to produce more honey and as a result save more bees.

5 Conclusion

HaBEEtat is a pioneer in terms of smart agricultural innovations when it comes to honey production and integration with IT-designed solutions. The Application will provide up-to-date calculations and data that will directly increase honey production and save the population of bees. We can say with confidence that our tech approach and product design are completely unique. An IT-driven platform interoperable with a smart hardware component designed as a supplement to the standard 10 frame Langstroth hive model has not to be invented yet. At the center, it is a centralized online platform, which is considered to become a core tool for all the world’s beekeeping and honey production countries. Since, this would be the first product of this kind to address honey production; we strongly believe that our solution will bring unique value to the existing beekeepers’ ecosystem. One of the major benefits would be a user-friendly tech solution that all the world’s beekeepers would be able to use in order to increase their honey production, save the bee population, as well as to accurately and remotely monitor their production facilities with the ability to compare and forecast based on accurate data measurements. The idea of

creating this Application will enhance and motivate the younger generations to get involved in the beekeeping business; this is favored by a high percentage of the youth possessing smart-phones where they can install the Application and are able to manage this venture wherever they are—in classrooms, on vacations, offices, training fields and so on. We believe this is one of the standout innovations of the 21st century; the future of beekeeping is bright.

References

1. Garibaldi, L.A., Steffan-Dewenter, I., Winfree, R., Aizen, M.A., Bommarco, R., Cunningham, S.A., Bartomeus, I.: Wild pollinators enhance fruit set of crops regardless of honey bee abundance. *Science* **339**(6127), 1608–1611 (2013)
2. Winfree, R., Williams, N.M., Dushoff, J., Kremen, C.: Native bees provide insurance against ongoing honey bee losses. *Ecol. Lett.* **10** (11), 1105–1113 (2007)
3. Whitehorn, P.R., O’connor, S., Wackers, F.L., Goulson, D.: Neonicotinoid pesticide reduces bumble bee colony growth and queen production. *Science* **1215025** (2012)
4. Genersch, E., Von Der Ohe, W., Kaatz, H., Schroeder, A., Otten, C., Böhler, R., Berg, S., Ritter, W., Mühlen, W., Gisder, S., Meixner, M.: The German bee monitoring project: a long-term study to understand periodically high winter losses of honey bee colonies. *Apidologie* **41**(3), 332–352 (2010)
5. Šakanović, S., Kevrić, J.: HaBEEtat: integrated cloud-based solution for more efficient honey production and improve well-being of Bee’s population. In: Avdaković, S. (ed.) *Advanced Technologies, Systems, and Applications III. IAT 2018. Lecture Notes in Networks and Systems*, vol. 59. Springer, Cham (2019)
6. Kuhnholz, S.: The control of water collection in honey bee colonies. *Behav. Ecol. Sociobiol.* **41**, 407–422 (1997)
7. Mazar, A., Panitz-Cohen, N.: It is a land of honey, December 2010
8. Head, R.J.: A Brief survey of Ancient Near Eastern Beekeeping (2008)
9. Better Beekeeping in top bar Beehive (Gregory, Pam 21 March 2018)
10. Gould, J., Gould, C.: *The Honey Bee* (1988)
11. Gillott, C.: *Entomology* (1995)
12. Bicikliski, O., Trajkova, F., Mihajlov, L.: Evaluation of the current status in organic agricultural production in the Republic of Macedonia and European countries. *J. Agric. Plant Sci.* **16**(1), 27–35 (2018)
13. Seeley, T.D.: *The Wisdom of the Hive: the Social Physiology of Honey Bee Colonies*. Harvard University Press, Cambridge (2009)
14. Adgaba, N., Al-Ghamdi, A., Shenkute, A.G., Ismaiel, S., Al-Kahtani, S., Tadesse, Y., Ansari, M.J., Abebe, W., Abdulaziz, M.Q.A.: Socio-economic analysis of beekeeping and determinants of box hive technology adoption in the Kingdom of Saudi Arabia. *J. Anim. Plant Sci.* **24**(6), 1876–1884 (2014)
15. Jankowsky, H.-D.: *Body temperature and external temperature. In: Temperature and Life* (1973)
16. Bruni, I., Galimberti, A., Caridi, L., Scaccabarozzi, D., De Mattia, F., Casiraghi, M., Labra, M.: A DNA barcoding approach to identify plant species in multi-flower honey. *Food Chem.* **170**, 308–315 (2015)

Design and Implementation of a Monitoring System for Elastomeric Infusion Pumps

Andrea Felici, Michele Sorelli, and Leonardo Bocchi

Abstract

Elastomeric infusion pumps have found widespread application for the long-term administration of drug treatments. Nevertheless, their actual reliability is debated; thus, the development of integrated monitoring systems, able to provide an accurate, continuous assessment of the drug infusion dynamics, is of extreme relevance. The present work briefly introduces a prototype system which estimates the volume of the drug solution, by measuring the relative distances from the wall of the reservoir, during the emptying time.

Keywords

Elastomeric pump • Drug infusion monitoring

1 Introduction

Elastomeric pumps are disposable biomedical devices, widely applied in pain therapy and oncology for the continuous administration of liquid drugs. In these pumps, the solution flow rate into the infusion line is sustained by the elastic properties of the silicon reservoir, i.e. the elastomer, which exerts a steady pressure on its content, in accordance with the Poisson equation. Thus, elastomeric pumps do not require any power and electronics for their functioning and, in specific, do not include any infusion monitoring system. In fact, the constant delivery of drugs is only controlled by passive flow regulators. Therefore, these devices are generally low-cost, lightweight, compact and particularly suitable for the long-term delivery of treatment in domestic scenarios.

A. Felici · M. Sorelli (✉) · L. Bocchi
Department of Information Engineering, University of Florence,
Florence, Italy
e-mail: michele.sorelli@unifi.it

L. Bocchi
e-mail: leonardo.bocchi@unifi.it

However, several issues might interfere with the desired infusion rates (namely: leakage of the solution, precipitation of the solute, needle occlusion, presence of air bubbles). Moreover, in accordance with the Hagen-Poiseuille law [1], the flow rate is dependent on the density and the viscosity of the solution (and, thus, on its temperature) and, furthermore, on the positioning of the device. Therefore, due to these intrinsic and extrinsic factors, the actual administration kinetics might deviate from the nominal ranges. Indeed, the *in vivo* reliability of these devices has been questioned [2].

On this basis, the present work was aimed at developing an infusion monitoring system for elastomeric pumps, able to continuously track the drug release kinetics and detect undesired deviations from the nominal flow rates, through an indirect model-based estimation of the reservoir volume.

2 Materials and Methods

The development of the infusion monitoring system relied on a SKA6020 Aptē elastomeric pump (SURGIKA, Italy). This model, in specific, has a nominal filling volume of 60 ml, and a corresponding flow rate of 2.0 ml/h (for a reference 5% glucose solution, at a nominal infusion temperature $T = 32\text{ }^{\circ}\text{C}$). The elastomer is contained in a rigid heptagonal case which prevents undesired compressions. The designed monitoring system includes: two (or, alternatively, three) VL6180X Lidar sensors (ST Microelectronics, Switzerland), positioned around the case so as to track the relative distance from the wall of the pump reservoir (resolution: 1 mm); an MPU-6050 sensor (InvenSense, US), with a MEMS accelerometer and a MEMS gyroscope; and two TMP102 temperature sensors (Texas Instruments, US), used to record the temperature of the elastomer and the infusion catheter. These sensors are connected to a Raspberry Pi Zero W, powered by means of a 6600 mAh LiPo battery. The circuit diagram of the monitoring system is shown in Fig. 1.

The main idea behind this prototype is to derive an estimate of the reservoir volume from the distance measures

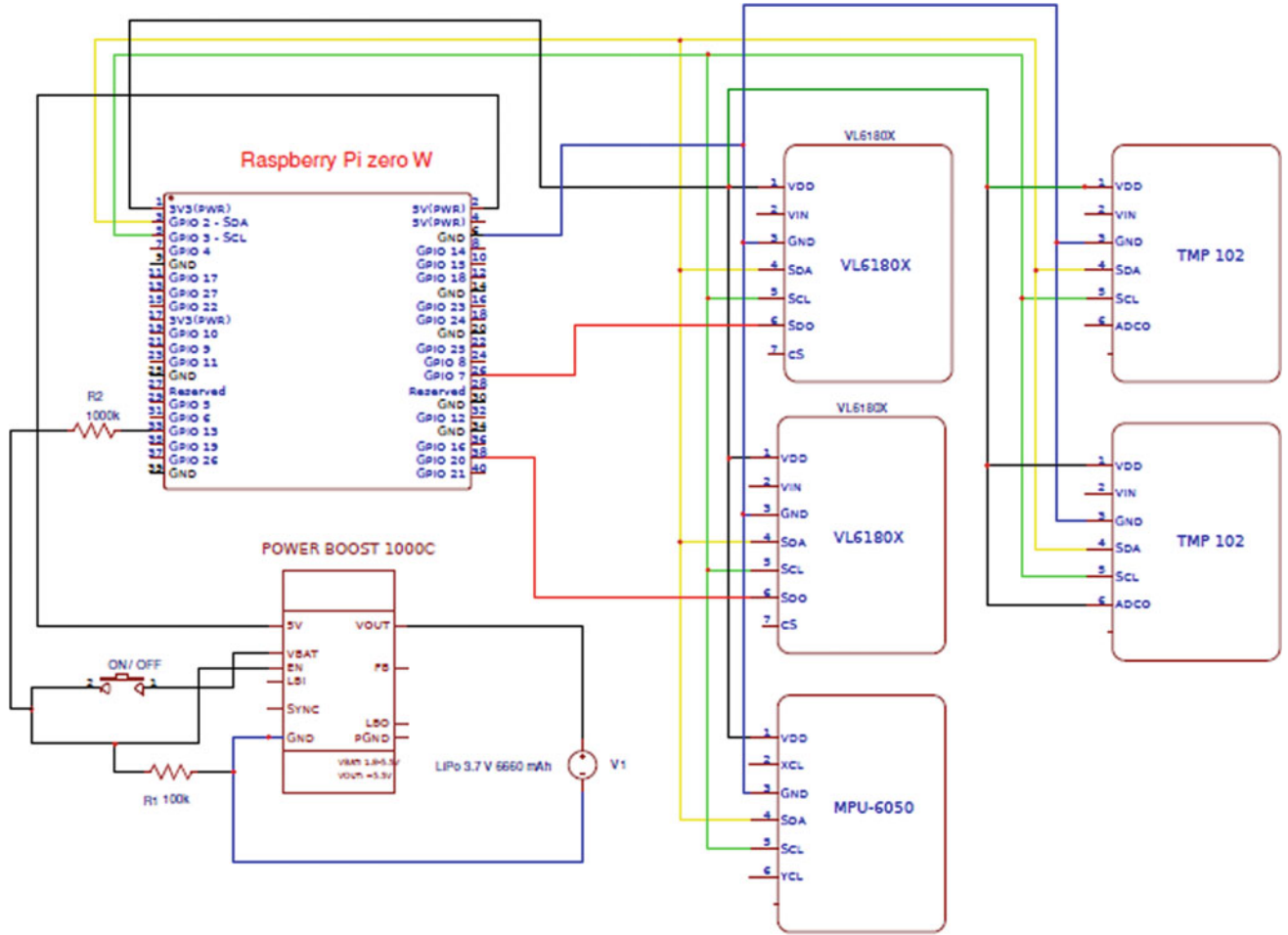


Fig. 1 Circuit diagram of the prototype infusion monitoring system

provided by the Lidar sensors, based on data models tuned over a dataset of reference volumes and corresponding distance vectors. Two different setups were tested, including two or three Lidar sensors, positioned with respect to the rigid case as shown in Fig. 2.

Three different models were considered in order to track the volume of the solution throughout the emptying process. The first, named M_1 , exploits a priori geometric assumptions; in detail, the empty reservoir is approximated as a cylinder, which is hypothesized to expand with an elliptic shape when filled with fluid. By assuming the minor semi-axes to be equal, the volume of the solution can be estimated as follows (Fig. 2a):

$$V_{M_1} = \frac{4}{3} \pi \cdot d_1^2 \cdot d_2. \quad (1)$$

The second model, M_2 , corresponds instead to the bilinear interpolation of the distance measures, x_1 and x_2 , shown in Fig. 2a:

$$V_{M_2} = a + b \cdot x_1 + c \cdot x_2 + d \cdot x_1 \cdot x_2; \quad (2)$$

M_3 , finally, represents an extension of M_2 , as it computes the volume of the reservoir through the interpolation of three distance measures, obtained thanks to the inclusion of an additional Lidar sensor, vertically aligned with 1 (Fig. 2b):

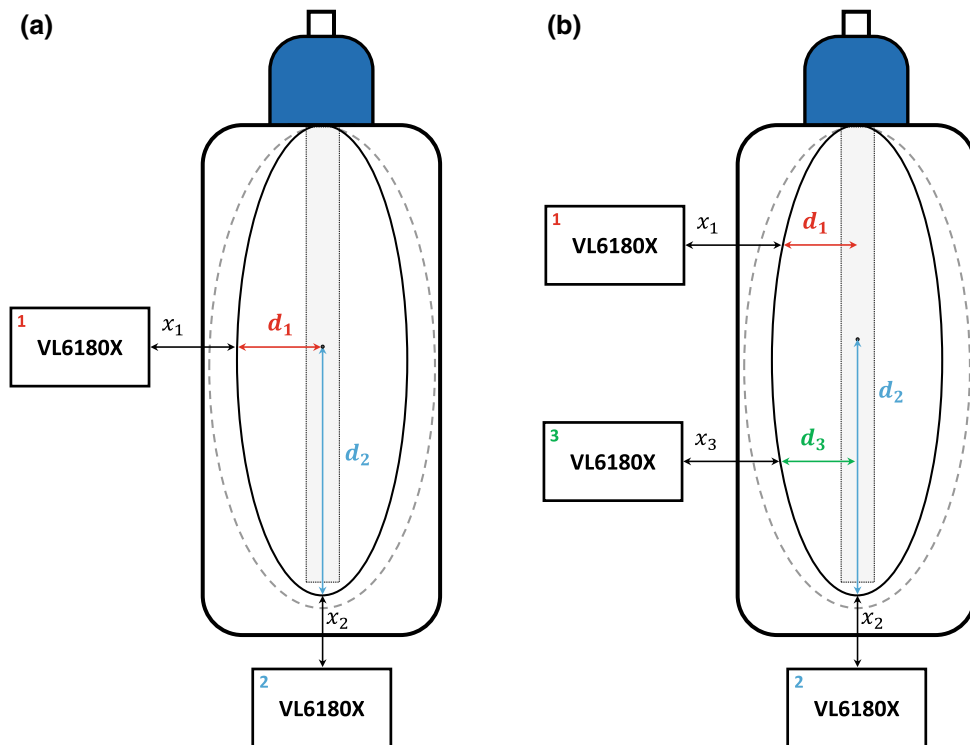
$$V_{M_3} = (1 - \alpha) \cdot f(x_1, x_2) + \alpha \cdot g(x_1, x_2, x_3), \quad (3)$$

where $f(\cdot)$ and $g(\cdot)$ are polynomial functions of the above relative distances.

3 Results

The monitoring system was calibrated against reference volumes (V_{REF}) of saline solution under strictly controlled thermal conditions: during the procedure, the device body was kept at a stable temperature of ± 24 °C (± 1 °C). In detail, the experimental data were obtained from nine filling cycles, carried out on three different elastomeric pumps (3 cycles per pump). During each experiment, 10 ml of 0.9% NaCl solution were injected every 10 min, until the 60-ml

Fig. 2 Schematic representation of the infusion monitoring system: **a** two distance measures from the reservoir wall; **b** second design, with the additional Lidar sensor



reservoir was filled (i.e. after 1 h). The distances from the elastomer walls were measured at a sampling time of 1 min, resulting in an overall dataset of 540 volume measurements and corresponding distance vectors. These experimental data were then used to identify the model parameters by least square optimization of the volumetric prediction error.

The performance of the investigated models is reported below, in Table 1, which summarizes the norm of the residual errors related to the three tested models. In detail, the M_3 model exhibits the highest accuracy, thanks to the availability of a third additional distance measure. On the other hand, the M_1 model, which relies on a priori geometric assumptions on the reservoir’s shape, is associated with the worst performance; this outcome might be ascribed to the introduction of a cubic dependence on the distance measures.

In conclusion, based on this analysis, model M_3 appears to be particularly suitable for tracking the volume of the drug reservoir, during the infusion process, exhibiting an overall percentage error of 0.9%. Nevertheless, model M_2 is

associated to comparable performances, with a percentage volumetric error of 1.2%; however, since the corresponding design relies on fewer LIDAR sensors (i.e. on a simpler and cheaper system) and fewer model parameters (thus offering a higher theoretical stability), this latter model might represent an attractive alternative, worth to be developed (Fig. 3).

Table 1 Modeling error

	$\ V_M - V_{REF}\ \text{ (cm}^3\text{)}$
M_1	1.06
M_2	0.72
M_3	0.54

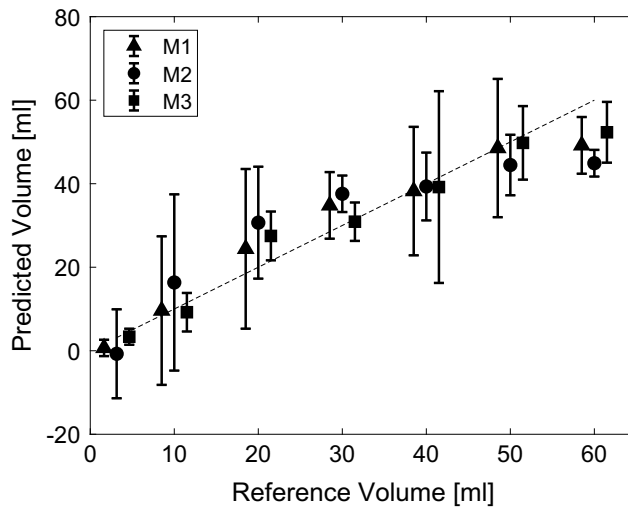


Fig. 3 Correlation plot between reference and predicted reservoir volumes

4 Conclusion

The results presented in this work show that the designed infusion monitoring system is able to track the instantaneous volume of the solution inside an elastomeric pump and, thus, the effective drug infusion profile, through the measurement of reference distances from the reservoir walls.

This represents a first step towards the development of a clinically applicable device, which might significantly improve the reliability of drug infusion therapies, delivered by means of standard elastomeric pumps. Further work must deal with the refinement of the model underlying the volumetric estimation. In this respect, new formulations might consider the mechanical properties of the elastomer and, also, the temperature of the drug solution. Moreover, the

proposed monitoring system should be validated on a wider dataset, and tested on different infusion pumps.

Conflicts of Interest All authors have no conflict of interest to disclose in relation to the current work.

References

1. Munson, B.R.: *Fundamentals of Fluid Mechanics*. Wiley (2010)
2. Remerand, F., Vuitton, A.S., Palud, M., Buchet, S., Pourrat, X., Baud, A., Laffon, M., Fuscuardi, J.: Elastomeric pump reliability in postoperative regional anesthesia: a survey of 430 consecutive devices. *Anesth. Analg.* **107**, 2079–2084 (2008). <https://doi.org/10.1213/ane.0b013e318187c9bb>

Wearable System for Early Diagnosis and Follow Up of Spine Curvature Disorders

E. Valchinov, K. Rotas, A. Antoniou, V. Syrimpeis, and N. Pallikarakis

Abstract

This paper presents an IMU-based wireless wearable system for real-time three-dimensional measurement of spinal deformities in a noninvasive manner. Applications of the proposed system range from diagnosis of spine abnormalities to postural monitoring, on-field as well as in a lab setting. The system is comprised of one wireless and 26 sensor nodes wired along to form a lightweight wearable sensor stripe for superficially attachment above human spine. The nodes size and arrangement is optimized so that each node to approximately track an individual vertebra. All sensors communicate to the main unit through I2C bus in a daisy chain fashion. Spine is modeled as a compound flexible with 26 segments allowing dynamic measurement of three-dimensional spine motion, which is animated and monitored in real-time using dedicated Android application with interactive GUI. The proposed system detects Kyphosis, Lordosis and Scoliosis and calculates the related Cobb angles. It can be integrated in wearable chest harness and is highly suitable for both diagnose spinal deformities in early stages and follow up the progress of the spine.

Keywords

Accelerometer • Gyroscope • Wearable devices • Spinal deformities

1 Introduction

In most cases spinal deformities are mild, but in some patients the deformity continues to get more severe as the children grow up resulting to adolescent and adult spinal

E. Valchinov (✉) · K. Rotas · A. Antoniou · V. Syrimpeis · N. Pallikarakis
Biomedical Technology Unit, Department of Medical Physics,
University of Patras, Patras, Greece
e-mail: emil@upatras.gr

deformities. A severe deformity of the spine, such as scoliosis, can reduce the amount of space within the chest, making it difficult for the lungs to function properly.

There have been solutions that proposed body dynamics monitoring with accelerometers and similar sensors, however, in most cases the small number of sensors results in limited 3D resolution, for example, human back surface and spine [1–3]. Exceptions are the proposed flexible glove using 16 Inertial Measurement Units (IMUs) by customized PCB [4] and a novel smart fabric system, which integrates 63 sensors in wearable sensor grid architecture [5]. However, previous approaches to measure spinal abnormalities are limited [6–9], so the need to detect and measure objectively the degree of spinal deformities and stiffness still exist.

In this paper the tilt/twist method [10], for determining 3D joint angles, has been modified and used as spinal model [6], resulting in the output of flexion-extension and lateral bending for each sensor node. Based on those developments, we propose a system for accurately measuring the real-time position of the spine, thus allowing early diagnosis and follow up of spinal disorders in a portable, noninvasive, and clinically meaningful manner.

2 Materials and Methods

2.1 Hardware Architecture

The proposed hybrid system is using a wired and wireless approach allowing sensor nodes to share the power source, data processing, and wireless link, thus increasing the number of available sensors and resolution. The system is comprised of 26 sensor nodes (14×2.5 mm) with six degrees of freedom (DoF) each, arranged in a lightweight wearable sensor strip allowing easy attachment on the skin above the human spine, and a main unit, as shown in Fig. 1.

The sensor nodes communicate to the main unit through I2C bus in a daisy chain fashion and are designed so each node to be attached on the skin over individual vertebra as

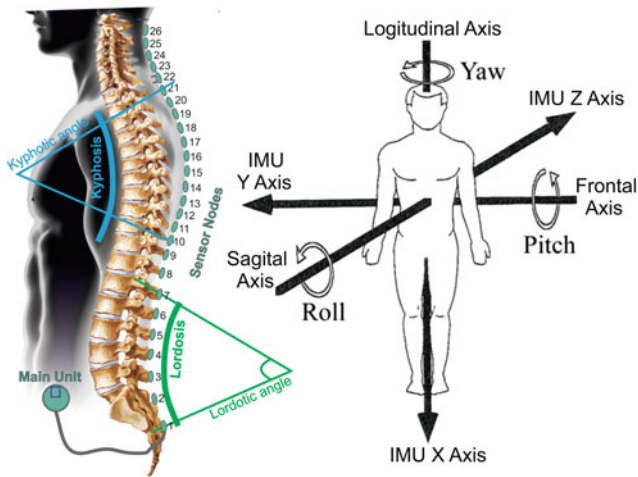


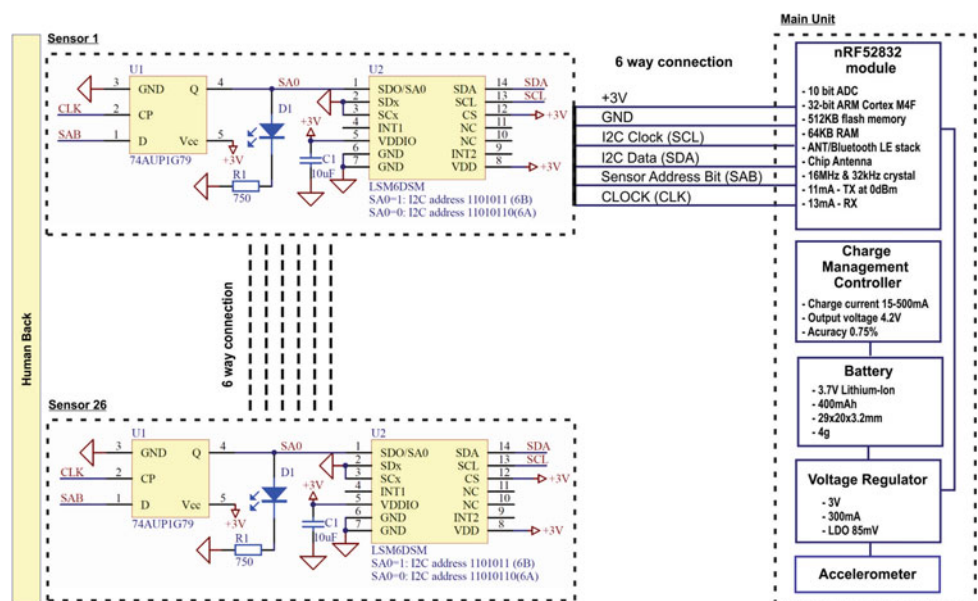
Fig. 1 Human body axes and sensor nodes arrangement and placement

follows: two sensors over fused S1_5 (Sacrum), five over L1–L5 (Lumbar), twelve sensors over T1–T12 (Thoracic) and seven sensors C1–C7 (Cervical).

A simplified schematic diagram of the proposed system is shown in Fig. 2. The main wireless unit contains a microcontroller (MC) and 2.4 GHz radio. The last two are implemented with an MDBT42Q module [11], based on the ultra-low power system-on-chip (SoC) BLE nRF52832 built around a 32-bit ARM Cortex M0 CPU, thus avoiding the use of an extra microcontroller, reducing the part count and keeping the system dimensions small.

Each sensor nodes is comprised of one flip-flop (74AUP1G79) and 6 DoF IMU (LSM6DSM) selected for its ultra-low power, high accuracy, 4 kb FIFO buffer and embedded low-pass digital filters. The specific flip-flop, was

Fig. 2 Simplified schematic of the system



selected for its very low static and dynamic power consumption, small dimensions and Schmitt trigger action at all inputs. Sensor nodes (IMU) axes, their PCB design and a partial photo of the sensor stripe are show in Fig. 3.

The output (Q) of each flip-flop is connected to the I2C less significant bit of the device address (SA0), so when it is Set (SA0 = 1), the I2C address of the IMU of the specific sensor node becomes 1101011 (6B) and respectively when Reset (SA0 = 0), the address becomes 1101010 (6A). All the sensor

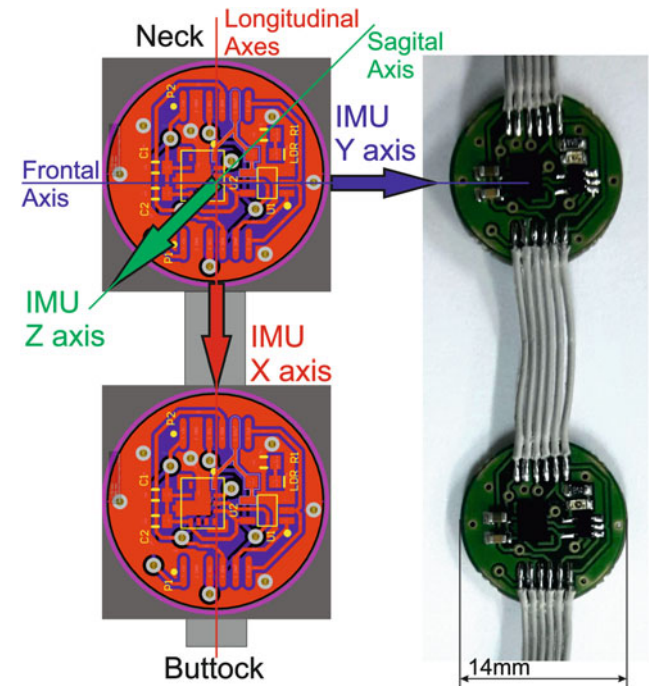


Fig. 3 Sensor nodes PCBs and IMU axes

nodes are connected in a chain with a common clock pulse line (CLK) connected to clock pulse inputs (CP) of all 26 flip-flops. Thus, flip-flops form a 26 bit shift register, where register's input (SA0 of the first sensor node) is connected and controlled by the MC. During initialization, the MC sets the Sensor Address Bit (SAB) line, logic HIGH, and the clock pulse line, logic LOW. Next MC applies the first clock pulse (sets CLK line logic High), thus setting the I2C address of first sensor node to 6B. Subsequently MC reads IMU with address 6B, which in this case corresponds to the first sensor node, since all others IMUs have address 6A.

Next MC sets the SAB line to logic LOW and applies a second clock pulse, hence setting the addresses of the first and second sensor nodes (IMUs) to 6A and 6B respectively. Consequently, reading again from I2C address 6B will result in sampling the second sensor node. In this manner, only one of the IMUs is with valid address (6B) at a time.

2.2 Firmware Design

The system application firmware is executed on the main unit, where its core functionality is the periodic sampling of the gyroscope and accelerometer data from each of the successive sensor nodes, which are then used as input for the calculation of the Pitch and Roll Euler angles per sensor.

The last are calculated using both accelerometer and the gyroscope readings employing complimentary filter, which was preferred than Kalman filter due to reduced computational workload [12]. The Yaw angle is not calculated, since the proposed system does not employ magnetometers. This design approach was preferred based on the simplicity and lower cost. Additionally, the firmware handles the communication with a client device (e.g. a smartphone) via Bluetooth v4.0 (BLE), the power management of IMUs by performing power saving operations, and the monitoring of the power levels and charging status of the battery.

The sensors nodes are sampled in quick succession from bottom to top and in a cyclical manner. The sampling interval between sampling cycles (scanning sessions) is set to 250 ms and the 16 bit signed integer sampled values are provided from the IMU's gyroscope and accelerometer on the x, y, z axis. The last are used to calculate Pitch and Roll Euler angles for each node, which are stored as 32 bit float numbers on the main unit. Each IMU is set to operate in Normal Mode with a sampling frequency (Output Data Rate) of 104 and 26 Hz bandwidth of the embedded digital low pass filter (DPF1). The accelerometer and the gyroscope range were set to ± 2 g and $\pm 245^\circ/\text{s}$ respectively.

The main routine in the code is as follows; during the setup stage, all the IMUs on the spine nodes are initialized and configured, according to the requirements specification. If errors are detected at this step or at any point during the device's main

operation, they are communicated via a led blinking pattern and wireless notifications. If the initial peripheral tests are passed without issues, the firmware launches the Bluetooth interface and sets up a few application timers for scheduling its main tasks. Out of those, one timer is dedicated to control the repetition of the scan sessions, and another handles the transmission of pending data packets containing the Pitch, Roll and accelerometer x-axis values (Accx).

A custom communication protocol has been implemented in order to allow a client device to receive the streaming data from the system. This stream consists of data packets of 18 bytes length each. All packets that belong to the same scan session use the same identifier as a header. Twenty such subsequent packets are used in order to send the Pitch, Roll and Accx for all 26 nodes in the scan session. The specified scan interval of 250 ms (4 Hz) corresponds to a requirement of sending eighty (80) packets per second which translates to a bandwidth requirement of 11.52 kbps, well within the capabilities of the low power Bluetooth interface, with a Bluetooth Connection Interval (CI) of 30 ms, assuming at least three data packets are sent per CI (effective 15 kbps bandwidth). The communication protocol also facilitates the issuing of basic configuration and control commands to the end system.

Finally, the firmware supports auxiliary functionalities such as Over the Air (OTA) updates, which can be initiated from a client device with Bluetooth capabilities, and power management tasks, namely putting IMUs in low power (sleep) mode when they are not used or prolonged inactivity is detected in order to interrupt the system operation, thus saving battery life.

The main services provided by the system are exposed via the Bluetooth interface in the form of Bluetooth services and characteristics. The battery monitoring service implements the basic GATT battery service, while the other characteristics such as data stream notifications, firmware and error information, device operation status, commands management and charging status notifications are grouped in a custom Bluetooth service created for our specific application case.

The code for the firmware was built using Nordic Semiconductor NRF5 v14.2 SDK, with the support of their NRF52 SoftDevice S132 v5.1.0. The SoftDevice is a pre-compiled library that implements the BLE communications stack and in combination with the SDK, it provides a development friendly framework for quick implementation, deployment and testing of custom application firmware on the Nordic's NRF52 Series SoC.

2.3 Application Program Design

The mobile application is written in Java with Android Studio v3.1.3 for Linux, using object oriented methodology.

It contains three main parts. The first part handles the graphical user interface (GUI) and uses Android SDK functions and OpenGL to draw a spine model in 2D and 3D graphics respectively. The second program part deals with the wireless communication, based on the provided BLE libraries and our custom communication protocol. It handles the communication with the system, the transmissions faults and interrupts. The third program part manages the digital signal processing and includes algorithms for calculation of 3D positions of each sensor node, and detection and calculation of the kyphotic, lordotic and scoliosis angles base on the sensors data as received from the main unit. The position of each node, and so the approximate position of the corresponding vertebrae is calculated based on the Pitch and Roll Euler angles.

The first sensor node (over Sacrum) serves as a reference and is assumed to have zero coordinate values. The coordinates of every successive node are calculated as sum of the coordinates of preceding sensor node and the relative displacement (dx , dy , dz) of the specific node with respect to the previous one. The last are calculated using trigonometry based on the Pitch and Roll values of the two nodes and the distance between them or specifically between the centers of the related IMUs. The internode distances depend on nodes placement and may be approximated as distances between the centers of the vertebrae. They have default values based on the length of the internode connection cables and node PCB size but can also be adjusted by the user in case of a dedicated closer sensor placement.

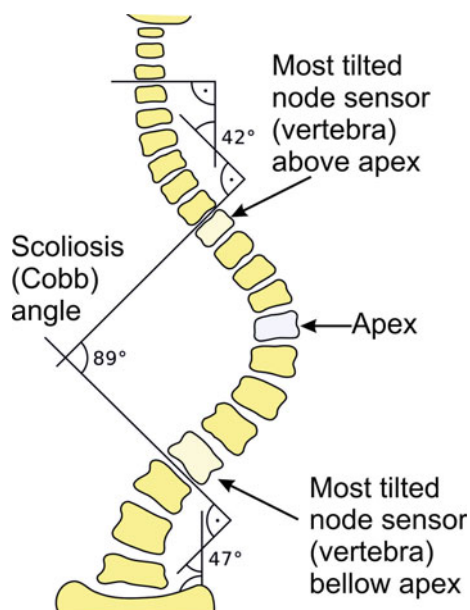


Fig. 4 Method for defining the Cobb angle of a C-shaped Scoliosis to the left

Custom algorithms were developed to detect cases of Lordosis, Kyphosis and Scoliosis (S-shaped and C-shaped) and calculate related Cobb angles. The algorithms exploit the classical methods for the defining the Cobb angles as shown on Fig. 4, assuming that the tilt (Pitch and Roll) of each sensor node, placed over the skin, is approximately equal to the vertebrae tilt, located underneath.

The detection of Lordosis/Kiphosis and the calculation of the related angles are based on the Pitch angle of each sensor node, where Scoliosis, and the related angle are based on Roll values.

3 Results and Discussion

In order to validate the measurements made by the IMUs and the calculation of the Euler angles, the last were compared to angles read from precision digital goniometer, which are considered to be accurate, and hence a good benchmark. The analysis of the data showed that Pitch and Roll Euler angles measured by the goniometer are very similar to ones measured by the proposed system.

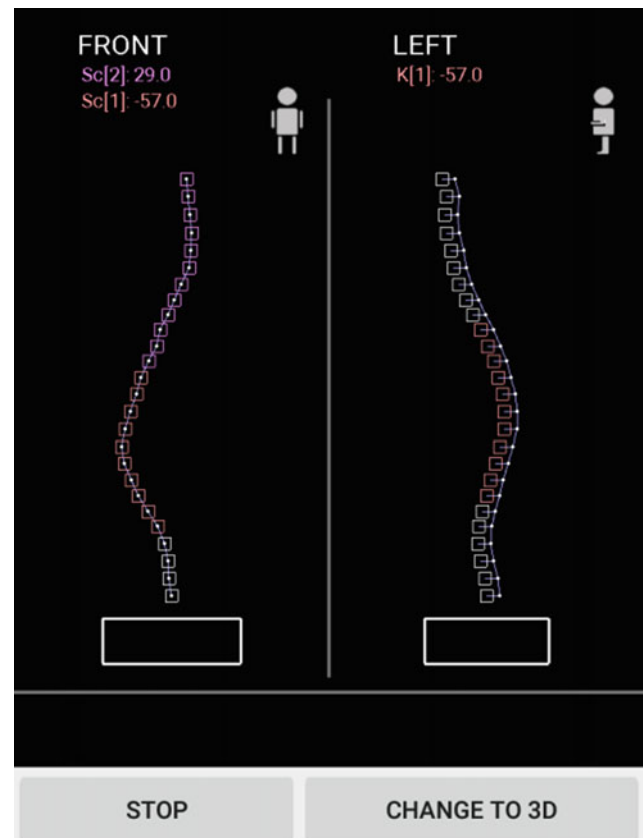


Fig. 5 A screenshot of the Android App while detecting C shaped Scoliosis and Kiphosis

The system was tested on flexible soft disc vertebral column anatomy model [13], where the correct detection, and calculation of the kyphotic, lordotic and scoliosis angles, was verified using X-ray imaging. Figure 5 shows a screenshot of the Android App while detecting two C shaped Scoliosis with angles of 57° and 29°, and Kiphosis of 57°, as simulated on the human spine model.

Preliminary test measurements were performed with the proposed system on 46-year-old male, using double-sided adhesive pads to ensure optimal sensor fixation to the body. Preexisting spine X-ray images of the patient were compared with the test measurements, showing identical results. A further testing protocol is organized based on human subjects with already known spine deformities for the assessment and effectiveness of the system.

The power consumption during scanning and transmitting was 10 mA, measured at +3.43 dBm (2.2 mW) output power and on-air data rate of 15 kbps. The maximum measured data transfer range was 80 m, obtained in a building corridor with the same power output and the embedded ceramic chip antenna [11]. The system is powered by a 3.7 V, 400 mAh (402,030) rechargeable lithium-ion polymer battery providing about 40 h of continuous monitoring, before recharging.

4 Conclusion

In this study, a wearable system for early diagnosis and follow up of spine curvature disorders using multiple IMUs was presented. It was shown that by combining proper sensor and overall system design, spinal model, digital filters and computational algorithms, it is possible to detect different spine deformities and calculate the approximate kyphotic, lordotic and scoliosis angles, thus eventually avoiding excessive X-ray examinations.

Moreover, the preliminary results showed that the proposed system allows detecting, in real time, spinal cord curvatures noninvasively. This feature is of significant importance in clinical medicine since the imaging exams (MRIs, CTs and X-rays) provide instantaneous images of the spine at a specific position, but they cannot provide information regarding the motion and trajectory of the spine.

The combination of a multiple, low profile sensor nodes, flexible internode connections, and a wireless data transfer, resulted in excellent mobile wearable system with acceptable accuracy, making it a potential solution for early detection of spine disorders especially in school screening and primary

orthopedic evaluation of the spine. However, further studies are needed to fully evaluate the proposed system, in terms of accuracy of measured and calculated Cobb angles, along with, the influence of different body types and level of obesity. As future work, we plan to add a magnetometer, in order to achieve a full real time 3D motion tracking of the spine, including rotational deformity, and to evaluate its contribution to the clinical accuracy and diagnostic ability of the system.

References

1. Wang, Q., Markopoulos, P., Yu, B., Chen, W., Timmermans, A.: Interactive wearable systems for upper body rehabilitation: a systematic review. *J. Neuroeng. Rehabil.* **14**(1), 20 (2017)
2. Luinge, H., Veltink, P.: Inclination measurement of human movement using a 3-daccelerometer with autocalibration. *IEEE Trans. Neural Syst. Rehabil. Eng.* **12**(1), 112–121 (2004)
3. Wong, W.Y., Wong, M.S.: Measurement of postural change in trunk movements using three sensor modules. *IEEE Trans. Instrum. Measur.* **58**(8), 2737–2742 (2009)
4. O'Flynn, B., Sanchez, J.T., Tedesco, S., et al.: Novel smart glove technology as a biomechanical monitoring tool. *Sens. Transducers* **193**(10), 23–32 (2015)
5. Hermans, A., Cacurs, R., Nesenbergs, K., et al.: Wearable sensor grid architecture for body posture and surface detection and rehabilitation. In: *ACM Proceedings of the 14th International Conference on Information Processing in Sensor Networks*, Seattle, pp. 414–415 (2015)
6. Goodvin, C., Park, E.J., Huang, K., et al.: Development of a real-time three-dimensional spinal motion measurement system for clinical practice. *Med. Biol. Eng. Comput.* **44**(12), 1061–1075 (2006)
7. Carvalho, P., Queirós, S., et al.: Instrumented vest for postural reeducation. In: *IEEE Proceedings of the 5th International Conference on Serious Games and Applications for Health (SeGAH)*, Perth, WA, Australia (2017)
8. Fathi, A., Kevin, C.: Detection of spine curvature using wireless sensors. *J. King Saud Univ. Sci.* **29**(4), 553–560 (2017)
9. Bartalesi, R., Lorussi, F., et al.: Wearable monitoring of lumbar spine curvature by inertial and e-textile sensory fusion. In: *IEEE Conf Proc IEEE Eng Med Biol Soc Buenos Aires, Argentina*, pp 6373–6376 (2010)
10. Crawford, N., Yamaguchi, G., Dickman, C.: A new technique for determining 3-D joint angles: the tilt/twist method. *Clin. Biomech.* **14**, 153–165 (1999)
11. Raytac Homepage: <https://www.raytac.com>. Accessed 23 Dec 2018
12. Gui, P., Tang, L., Mukhopadhyay, S.C.: MEMS based IMU for tilting measurement: comparison of complementary and Kalman filter based data fusion. In: *IEEE Conference on the Proceedings of IEEE 10th Conference on Industrial Electronics and Applications (ICIEA)*, pp. 2004–2009 (2015)
13. Anatomy Warehouse Homepage: <https://www.anatomywarehouse.com>. Accessed 23 Dec 2018

Part IV

Bio-micro/nano Technologies

Biogenic Nanoparticle Synthesis Using Marine Alga *Schizochytrium* sp.

Tuğçe Mutaf, Gülizar Çalışkan, Cafer Meydan, Suphi Şurişvan Öncel, and Murat Elibol

Abstract

Nanotechnology is one of the most promising science and technology discipline that targets to bring new solutions for many applications in biotechnology, biomedical, energy and cosmetic industry by improving particles and devices scale of nanometers. Various sized and shaped nanoparticles can be synthesized by several methods. Up to now, scientists prefer physical and chemical fabrication of nanoparticles. But, these methods contain use of toxic, expensive and non-environmentalist solvents, reducing and stabilising agents. For a sustainable science, there is a necessity development of more eco-friendly, cost-effective and trustable alternative processes. In this context, using biological sources as reaction agent, have a strong potential. Plants, bacteria, fungi are essential biological sources for transformation of metals to nanoparticles. Many researchers focus on fungi and bacteriological potential in nanofabrication whereas algae are highly intriguing biological systems in nanotechnological approach. Some of cyanobacteria and algae have previously been used to synthesize intracellular or extracellular metal nanoparticles. Most of the research concentrate especially on gold and silver nanoparticle production from algae. In this work; bioreduction of silver, zinc and iron metals have been investigated using culture supernatant of marine algae *Schizochytrium* sp. For characterization of nanoparticles, UV visible spectroscopy, zeta sizer were used. Nanoparticle size was determined by zeta sizer and particles' surface plasmon resonance band detected by UV-Visible Spectroscopy.

Keywords

Biogenic • Nanoparticle • Microalgae • *Schizochytrium* sp.

1 Introduction

Nanotechnology is a scientific discipline which aims to synthesize nanoscale materials in different shapes and sizes ranging in size from 1 to 100 nm [1].

The first point of modern nanotechnology as a scientific approach was passed by Richard Feynman who gave a speech at the American Institute of Technology in 1959 [2]. Feynman, who presented the title of his speech as “There’s plenty of room at the bottom”, drew attention that when it is thought atomic dimensions of matter, there is a lots of thing waiting to be discovered. As a term, nano derived from the word “nanos” which means dwarf in Greek and is a billionth of meter [2].

When they synthesize in nanoscale, nanomaterials which their physical and chemical properties like surface area, electronic, optic and conductivity change according to macro and micro sized particles. Therefore, these nano sized particles have high usage potential in biotechnology, medicine, biomedical, space, cosmetic, food and agriculture industries [3].

Each metal nanoparticle, which are synthesized from different metal salts such as silver, zinc, iron, palladium, gold, titanium, gives more successful results in a different area of use. For instance, silver nanoparticles attract attention in studies on antibiotic resistance and development of new antibiotics due to their high antimicrobial activity against gram positive and gram negative bacteria. Gold nanoparticles have high potential in drug delivery systems whereas use of palladium nanoparticles have been focused on catalyses, electrocatalysis applications, batteries, chemical and optical sensors [1, 4]. In cosmoceutical and pharmaceutical formulations, iron, selenium, zinc and copper nanoparticles can be used [1].

T. Mutaf (✉) · G. Çalışkan · C. Meydan · S. Ş. Öncel · M. Elibol
Bioengineering Department, Ege University, 35040
Bornova-Izmir, Turkey
e-mail: tucemutaf@gmail.com

G. Çalışkan
Izmir University of Economics, 35330 Balçova-Izmir, Turkey

In addition, TiO₂ and ZnO nanoparticles provide UV protection as scattering or absorbing of UV radiation in nanoscale and they provide higher protective effect in nano sized according to bulk material [5].

Production method affects the morphological and physicochemical properties of nanoparticles and also has significant effects on particle stability. Thus, many nanoparticle synthesis methods have been improved.

Chemical and physical nanoparticle production methods are preferred in most of scientific research because of providing low cost at high volumes [2, 4]. Technics such as laser ablation, lithography and high energy irradiation are performed with physical approaches whereas chemical, electrochemical and photochemical reduction methods are used in chemical production [1].

Advanced technological methods are required for synthesis by physical methods, although they appear to be more economical on large scales. On the other side, high-cost organic solvents, reduction agents and stabilizers are needed in conventional chemical production technics. Since many of these chemicals are toxic, their use on especially large scales will bring with environmental problems. Moreover, synthesized nanoparticles, contained toxic chemicals, will have low usage potential in biotechnology [1, 4].

Because of these limitations in physical and chemical methods, scientists have been looking for ways to make nanotechnological work more sustainable in recent years. As a new approach biological nanoparticle synthesis method is very reliable alternative against traditional technics.

Almost every biological organism has the ability to reduce metal ions and synthesize metal nanoparticles thanks to its metabolic activity and biochemical molecules. Plant extract, fungi, yeast, viruses, actinomycetes, bacteria and enzymes are common nanofactories that focused in recent years [1, 6–8].

Recently, microalgae, macroalgae and cyanobacteria groups within the biological organisms have attracted the attention to cost-effective and ecological nanoparticle synthesis and biotechnological using potential of these particles. Since, algae have high biodiversity, growth rate and biomass efficiency, eco-friendly cultivation process and especially their heavy metal accumulation and bioremediation capabilities [9, 10].

Nanoparticles have been obtained extracellularly or intracellularly from prokaryotic and eukaryotic biological sources [10]. If the mechanism of forming metal nanoparticles by reducing the metal salts occurs inside of cell as in vivo, this synthesis is defined intracellular nanoparticle synthesis [11]. Microorganism is cultured in optimum growth conditions till end of exponential phase. Thus maximum amount biomass is produced, after that biomass is centrifuged. Obtained wet biomass or dried biomass can be suspended in metal salt and incubated to synthesis metal nanoparticles [8].

In order to describe extracellular; cell free extract, supernatant removed culture medium, extracellular metabolites or extracted biomolecule from cell must be used for nanoparticle synthesis [11].

Algal nanomaterial synthesis can be carried out in different ways both intracellularly or extracellularly. Firstly, metal salts have been added into the culture medium and microorganism is continued cultivation with metal supported medium. Secondly, cells which cultivated in optimum growth conditions, are harvested by centrifuge. These cell free supernatant can be used for nanoparticle synthesis. Because some algae may secrete extracellular metabolites such as extracellular polysaccharides during growth. On the other hand, after harvesting, biomass is washed with distilled water. Obtained whole cells are re-suspended with metal salt solution. Another method has been reported which bases on using extracted intracellular metabolites or purified biomolecules [11].

There are many researches reported about nanoparticle synthesis potential of algae intracellularly and extracellularly by focusing on gold and silver metals. Jena et al. [9] have been published to product silver nanoparticle as in vivo and in vitro from green alga *Chlorococcum humicola*. Patel et al. [10] have been investigated some cyanobacteria such as *Anabaena* sp. 66-2, *Lyngbya* sp. 15-2, *Synechococcus* sp. 145-6 and some green algae like *Botryococcus* sp., *Chlorella* sp. 2-4 potential to form silver nanoparticles. Also they have been tested C-phycoyanin pigment role in nanoparticle synthesis. Mata et al. [12], Rajasulochana et al. [13] and Senapati et al. [14] also have been studied and reported on gold nanoparticle synthesis with brown alga *Fucus vesiculosus*, marine alga *Kappaphycus alvarezii*, *Tetraselmis kochinensis* respectively.

In this current investigation, we aimed production of silver, zinc and iron nanoparticles extracellularly by utilizing marine microalga *Schizochytrium* sp. culture supernatant. Previous studies have been focused on photoautotrophic microalgae for nanoparticle synthesis but heterotrophic microalgae *Schizochytrium* sp. intracellular and extracellular nanoparticle synthesis ability has not been tested.

2 Material and Methods

2.1 Organism, Culture Conditions and Growth Curve

Marine microalgae *Schizochytrium* sp. was obtained from SAG culture collection. In order to grow microorganism culture from agar slant, heterotrophic culture medium composed of 17.5 gr/lit sea salt, 20 gr/lit D-Glucose (C₆H₁₂O₆) and 15 gr/lit yeast extract is prepared and pH was adjusted 7.0 ± 0.3. After culture medium autoclaved at

121 °C during 15 min, microorganisms were inoculated in fresh sterile culture medium at 10% (v/v) inoculum ratio.

To produce microalgal biomass, liquid cell culture was cultivated in the dark at ambient temperature of 25 °C, agitated at 120 rpm in incubator shaker. First, to obtain growth curve; dry weight and turbidity measurement at 660 nm (OD_{660}) [15], were performed from the zero day of the culture to the beginning of the stationary phase. Time dependent cell growth curve was then drawn according to the analyzed results.

2.2 Synthesis of Ag, Zn and Fe Nanoparticles Using Supernatant

Schizochytrium sp. culture in exponential phase was inoculated fresh sterile medium and cultivated at optimum growth conditions described above. After 7 days, the cells were harvested by centrifuge at 4000 rpm during 5 min. In order to remove residues, obtained supernatant was centrifuged again for 5 min at 4000 rpm.

Metal salt solutions were prepared by three metal salts as $AgNO_3$, $ZnSO_4 \cdot 7H_2O$ and $FeSO_4 \cdot 7H_2O$. For nanoparticle synthesis, the effects of metal salt solutions' molarity and volumetric mixing ratios of metal salt solutions against supernatant on nanoparticle size, were investigated using statistical experimental design.

In the optimization of biogenic nanoparticle production with supernatant, a stock solution of each metal has been prepared different concentrations the minimum and maximum value range selected in the optimization is as follows: metal solution concentration ranges were that 1–10 mM for $AgNO_3$, 0.25–5 mM for $ZnSO_4 \cdot 7H_2O$ and 1–15 mM for $FeSO_4 \cdot 7H_2O$. According to these molarity ranges, 13 experimental run have been identified for each metal salt by Response Surface Methodology, Central Composite Experimental Design (Tables 1, 2 and 3).

After metal salt solutions were prepared according to determined molarity, supernatant was dripped into the metal solutions as 1 drop/second. The working volume was 90 ml of the total volume of supernatant and metal solution. The reaction of nanoparticle synthesis was continued in neutral conditions by incubating for 24 h at room temperature and 200 rpm agitation rate in rotary shaker.

2.3 Characterization of the Nanoparticles

UV-vis spectroscopy

In order to detect particles' surface plasmon resonance band, Lambda 750 UV/VIS/NIR Spectrometer was used to characterize the medium obtained after 24 h in the

optimization of the biological synthesis of the nanoparticles from the supernatant. The range of 250–600 nm was used to scan nanoparticles because of different experimental design sets.

Zeta sizer analysis

Synthesized particles' size has been measured by Malvern Zeta Sizer Analyzer and each particle's size distribution report and average particle size have been obtained.

3 Results and Discussion

3.1 *Schizochytrium* sp. Growth Curve

Schizochytrium sp. has been cultivated until end of the 7th day from inoculation. After the first day, the microorganism continued growing as logarithmic for the following 6. End of the exponential phase was on the 7th day and at that point, the maximum dried cell weight was measured as 14.9 mg/ml (Fig. 1).

3.2 UV-vis Spectroscopy and Zeta Sizer Analyser Characterization of Particles

It is well known that, in case of silver ion reduction to silver nanoparticles, medium color changes to ivory at first and after to dark yellow or brown [9, 16]. Thus, reduction of silver ions to silver nanoparticles could be determined by color change and UV-vis spectroscopy. It has been reported that silver nanoparticles give maximum peak in the range of 410–450 nm due to their surface plasmon resonance [16] (Fig. 2).

In this study, while yellowish colored culture supernatant was added into metal salt solutions, a change of the solution color was observed visually (Fig. 3). The color of $AgNO_3$ solution changed from transparent to ivory at first and after the incubation, ivory color became to even darker. In $ZnSO_4 \cdot 7H_2O$ solution, first transparent color changed to yellow because of natural color of supernatant but it was considered that bioreduction reaction did not occur, because no color change was observed during the incubation. On the other side, color of supernatant-iron metal solution became darker from transparent yellow throughout the incubation.

According to Zeta Sizer Analyzer results, minimum average particle size was measured as 540 nm for silver in run 2 of experimental design, 1010 nm for zinc in run 1 of experimental design and 1703 nm for iron particles in run 11 of experimental design (Tables 1, 2 and 3).

For iron and zinc metal salts, nanometric sized particles have not obtained. Large particle size may be due to

Fig. 1 *Schizochytrium* sp. growth curve dependent dry weight against time

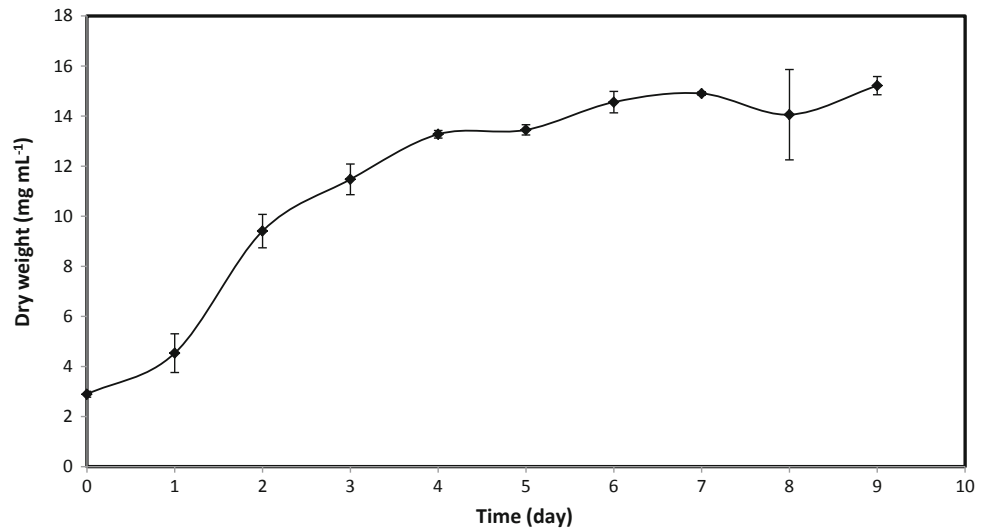
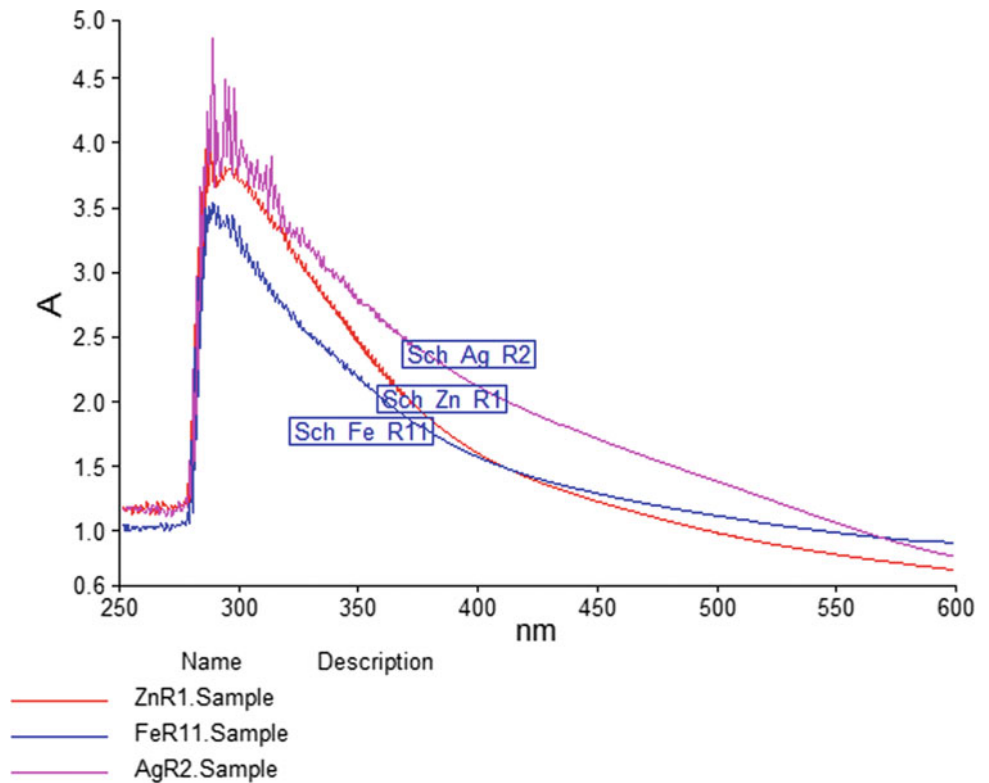


Fig. 2 UV-vis spectra of Ag (run 2), Fe (run 11), Zn (run 1) nanoparticle experiments



agglomeration of iron and zinc nanoparticles during storage at +4 °C. The particles in the solution, could not remain stable and might have collapsed over time. Then again, the absence of discolouration during the incubation, might indicate that no biodegradation reaction and no nanoparticle formation has occurred.

In the experiment of silver metal salt, smaller sized particles than iron and zinc metals, could be obtained. The expected color change during incubation indicates that a biodegradation reaction has occurred. However in the results of UV-vis spectroscopy, a peak expected wavelength band according to literature has not been observed (Fig. 2). This

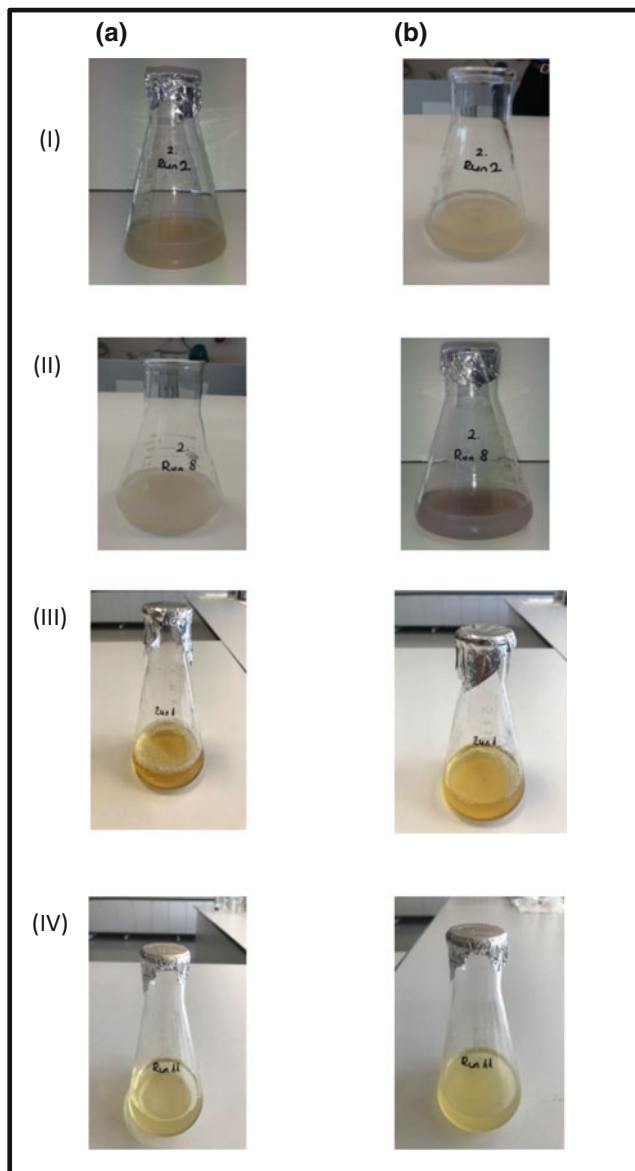


Fig. 3 Initial moment of silver, silver, zinc and iron metal solution and supernatant visuals respectively (Ia, IIa, IIIa, IVa); after 24 h incubation metal solution and supernatant (Ib, IIb, IIIb, IVb)

result might be due to the fact that the particle sizes were greater than 100 nm and the surface plasmon resonance of the particles have changed. Also, according to Patel et al. [10] some extracellular polysaccharides were active for

Table 1 AgNO₃ experimental design and particle size

Run	AgNO ₃ (mM)	AgNO ₃ : supernatant (v/v)	Particle size (nm)
1	10	5.1	843.4
2	2.32	8.56	539.7
3	5.5	5.1	857
4	5.5	5.1	822.8
5	8.68	1.64	1524
6	5.5	5.1	841.1
7	5.5	0.2	1477
8	5.5	1	569.8
9	2.32	1.64	924.4
10	1	5.1	617.2
11	8.68	8.56	619.7
12	5.5	5.1	914.9
13	5.5	5.1	961.9

Table 2 ZnSO₄·7H₂O experimental design and particle size

Run	ZnSO ₄ ·7H ₂ O (mM)	ZnSO ₄ ·7H ₂ O: supernatant (v/v)	Particle size (nm)
1	0.95	1.64	1010
2	2.63	0.2	1475
3	0.95	8.56	1521
4	2.63	5.1	1987
5	2.63	5.1	2600
6	2.63	5.1	1163
7	4.3	8.56	1923
8	2.63	10	2558
9	4.3	1.64	1930
10	2.63	5.1	1198
11	0.25	5.1	1544
12	5	5.1	1432
13	2.63	5.1	1200

formation of nanoparticles in the presence of light not in the dark. Therefore in our experiment, dark incubation conditions might affect to nanoparticle formation reaction activity (Tables 1, 2 and 3).

Table 3 FeSO₄·7H₂O experimental design and particle size

Run	FeSO ₄ ·7H ₂ O (mM)	FeSO ₄ ·7H ₂ O: Supernatant (v/v)	Particle size (nm)
1	8	5.1	3429
2	12.95	8.56	3830
3	8	5.1	3770
4	12.95	1.64	3866
5	8	10	3121
6	8	5.1	3524
7	8	5.1	2949
8	8	0.2	3150
9	15	5.1	3055
10	8	5.1	3788
11	1	5.1	1703
12	3.05	8.56	3136
13	3.05	1.64	1223

4 Conclusion

In this study, the potential of nanoparticle formation from *Schizochytrium* sp. supernatant was investigated. It has been observed that there was no bioreduction reaction in iron and zinc metals. On the other hand, extracellular metabolites in supernatant have the potential to reduce silver ions. Research and experiments have still been in progress to improve and for better understanding the mechanism of nanoparticle synthesis as well as effective parameters in order to achieve desired surface properties of nanoparticle.

Acknowledgements This research was supported by The Scientific and Technological Research Council of Turkey (TUBITAK) with 117M052 Project Number.

Conflict of Interest The authors declare no conflict of interest.

References

- Shah, M., Fawcett, D., Sharma, S., Tripathy, S.K., Jai Poinern, G. E.: Green synthesis of metallic nanoparticles via biological entities. *Materials* **8**, 7278–7308 (2015)
- Narayanan, K.B., Sakthivel, N.: Biological synthesis of metal nanoparticles by microbes. *Adv. Coll. Interface. Sci.* **156**, 1–13 (2010)
- Rai, M., Posten, C.: *Green Biosynthesis of Nanoparticles Mechanisms and Applications*. UK (2013)
- Pantidos, N., Horsfall, L.E.: Biological synthesis of metallic nanoparticles by bacteria, fungi and plants. *J. Nanomed. Nanotechnol.* **5**(5), 1 (2014)
- Wong, Y.W.H., Yuen, C.W.M., Leung, M.Y.S., Ku, S.K.A., Lam, H.L.I.: Selected applications of nanotechnology in textiles. *AUTEX Res. J.* **6**(1), 1–8 (2006)
- Castro, L., Blazquez, M.L., Munoz, J.A., Gonzales, F., Ballester, A.: Biological synthesis of metallic nanoparticles using algae. *IET Nanobiotechnol.* **7**(3), 109–116 (2013)
- LewisOscar, F., Vismaya, S., Arunkumar, M., Thajuddin, N., Dhanasekaran, D., Nithya, C.: Algal nanoparticles: synthesis and biotechnological potentials. In: *Algae—Organisms for Imminent Biotechnology*. <http://dx.doi.org/10.5772/62909>. Last Accessed 13 Jan 2019
- Singh, P., Kim, Y.J., Zhang, D., Yang, D.C.: Biological synthesis of nanoparticles from plants and microorganisms. *Trends Biotechnol.* **34**(7), 588–599 (2016)
- Jena, J., Pradhan, N., Dash, B.P., Sukla, L.B., Panda, P.K.: Biosynthesis and characterization of silver nanoparticles using microalga *Chlorococcum humicola* and its antibacterial activity. *Int. J. Nanomater. Biostructures* **3**(1), 1–8 (2013)
- Patel, V., Berthold, D., Puranik, P., Gantar, M.: Screening of cyanobacteria and microalgae for their ability to synthesize silver nanoparticles with antibacterial activity. *Biotechnol. Rep.* **5**, 112–119 (2015)
- Dahoumane, S.A., Mechouet, M., Alvarez, F.J., Agathos, S.N., Jeffries, C.: Microalgae: an outstanding tool in nanotechnology. *Bionatura* **1**(4), 196–201 (2016)
- Mata, Y.N., Torres, E., Blazquez, M.L., Ballester, A., Gonzales, F., Munoz, J.A.: Gold (III) biosorption and bioreduction with the brown alga *Fucus vesiculosus*. *J. Hazard. Mater.* **166**, 612–618 (2009)
- Rajasulochana, P., Dhamotharan, R., Murugakoothan, P., Murugesan, S., Krishnamoorthy, P.: Biosynthesis and characterization of gold nanoparticles using the alga *Kappaphycus alvarezii*. *Int. J. Nanosci.* **9**(5), 511–516 (2010)
- Senapati, S., Syed, A., Moez, S., Kumar, A., Ahmad, A.: Intracellular synthesis of gold nanoparticles using alga *Tetraselmis kochinensis*. *Mater. Lett.* **79**, 116–118 (2012)
- Jakobsen, A., Aasen, I.M., Strom, A.R.: Endogenously synthesized (–)-proto-quercitol and glycine betaine are principal compatible solutes of *Schizochytrium* sp. strain S8 (ATCC 20889) and three new isolates of phylogenetically related thraustochytrids. *Appl. Environ. Microbiol.* **73**(18), 5848–5856 (2007)
- Soleimani, M., Habibi-Pirkoochi, M.: Biosynthesis of silver nanoparticles using *Chlorella vulgaris* and evaluation of the antibacterial efficacy against *Staphylococcus aureus*. *Avicenna J. Med. Biotech.* **9**(3), 120–125 (2017)

Green Synthesis of Metal Nanoparticles Using Microalga *Galdieria* sp.

Gülizar Çalışkan, Tuğçe Mutaf, Suphi Şurişvan Öncel, and Murat Elibol

Abstract

Green synthesis of nanoparticles has recently been a preferred method since it offers useful approaches such as non-toxic, biocompatible, environmentally friendly, cost-effective, stable product and trustable alternative processes compared to other methods. Various biological sources such as plant, algae, fungus and bacteria are widely used in biological synthesis of nanoparticles. Algae are more adapted organisms compared to the others for having high growth rate and biomass productivity, high heavy metal accumulation capacity, etc. Nanoparticles can be used in various area such as antimicrobial, antifungal, antioxidant agent, admixture of biosensor and drug transport/release, also diagnosis and treatment systems. Since each organism has different biochemical composition and metabolic pathways, their synthesized nanoparticles are going to show various characteristics and application area. In this study, silver, iron (II) and zinc nanoparticles were produced by using microalga *Galdieria* sp. The synthesized nanoparticles were characterized by using UV visible spectroscopy, Fourier transform infrared spectroscopy (FTIR) and zeta sizer. Antimicrobial activity against gram negative and gram-positive bacteria was also examined throughout the study. In conclusion, the potential of this biogenic nanoparticle was discussed.

Keywords

Biogenic • Green synthesis • Nanoparticle • Microalgae • *Galdieria* sp.

1 Introduction

Over the last decade, novel synthesis approaches for nanoparticles increase their popularity and present interesting area such as energy, medicine, pharmaceutical industries, electronics and space industries in nanoscience and technology [1, 2]. Nanotechnology concern with small-sized materials less than 100 nm. These nanoparticles have great advantages such as quantum size effects, high surface to volume ratio etc. [3].

Generally, nanoparticles are produced by using physical, chemical, biological methods. However, some chemical methods, cannot avoid the use of toxic chemicals during the synthesis. Since many metal nanoparticles are widely applied to human contacting areas, there is a growing need to develop environmentally friendly processes of nanoparticles synthesis that do not use toxic chemicals. This becomes more significant when toxic solvents and chemicals are used in abiotic (chemical and physical) processes during the preparation of nanoparticle, limiting their potential use in biomedical and other bio-based applications. Therefore a safe, non-toxic way of synthesizing metallic nanoparticles is needed in order to allow them to be used in a wider range of industries. This could potentially be achieved by using biological methods. Recently applicability of bio-nanoparticles (Bio-NPs) synthesized by different microorganisms with known chemical and physical properties has been proven in a wide range of technological area [4, 5].

Microalgae can also be used in Bio-NP synthesis which is relatively unexplored, but it is more biocompatible an alternative method than the other biological methods [5]. Since biogenic production of nanoparticles can easily be scaled up and they are non-toxic. Bio-NPs can be applied on many areas such as biomedical, cosmetics, catalysis, photo-imaging, diagnostic and therapeutic purposes [6].

Galdieria sulphuraria belongs to the Cyanidiophyceae family, which belongs to the single-cell red algae class. The

G. Çalışkan (✉)
Izmir University of Economics, 35330 Balcova-Izmir, Turkey
e-mail: gulizar.caliskan@ieu.edu.tr

G. Çalışkan · T. Mutaf · S. Ş. Öncel · M. Elibol
Bioengineering Department, Ege University, 35040
Bornova-Izmir, Turkey

ideal temperature and pH range for this microalga, which can grow under extreme acidophilic (pH 0–4) conditions, are 40–56 °C and 1–2, respectively. According to the literature, *Galdieria sulphuraria* can be cultivated in phototrophic, mycotrophic and heterotrophic growth conditions. Compared with other production conditions, it has been reported that heterotrophic growth can be resulted in higher biomass (>100 g/L) and shorter doubling time [7].

In this study, silver, iron (II) and zinc metals were used to synthesis bio-nanoparticles using microalga *Galdieria* sp. Then the nanoparticles were characterized by using UV visible spectroscopy, Fourier transform infrared spectroscopy (FTIR) and zeta sizer. Antimicrobial activity against gram negative and gram-positive bacteria was also examined throughout the study. In conclusion, the potential of this biogenic nanoparticle was discussed.

2 Materials and Methods

2.1 Strain and Growth Conditions

Biosynthesis of silver, iron and zinc nanoparticles were assessed by use of *Galdieria* sp. algae strain. Marine microalgae *Galdieria* sp. was obtained from SAG culture collection. The culture was maintained through usual sub-culturing techniques under laboratory conditions at 42 °C and initial pH to 2. The cultures were grown in the *Galdieria* medium supplemented with 20 g/L glucose.

Heterotrophic batch cultures were grown in 250 mL conical flasks containing 100 mL of liquid medium. The flasks were incubated in an orbital shaking incubator operated at 200 rpm. After cultivation stopped in exponential phase, algal biomass was harvested by centrifugation and the supernatant was used to synthesis of nanoparticles.

2.2 Biosynthesis of Metal Nanoparticles by *Galdieria* sp.

Silver, iron (II) and zinc metal solutions were used to synthesis of nanoparticles. Metals were dissolved in double distilled water separately to prepare stock solutions. From the stock solution, different concentration (1–15 mM) were made and thereafter used.

After separation of the microalgal biomass by centrifugation, the remaining supernatant portion contains many microalgal metabolites such as reducing enzymes etc. At this stage, it was thought that the present supernatant could also be the source of Bio-NP synthesis and it was decided to investigate the potential of NP synthesis.

The amount of supernatant with the concentration of metal salt is important parameter to get different sized nanoparticles. In our study, we aimed to optimize extracellular biogenic nanoparticle production from *Galdieria* sp. To observe the effect of metal ion concentration and supernatant ratio on nanoparticle synthesis, a statistical experimental design was made in which minimum and maximum 2:10–100:10 ratio was used at constant room temperature, incubation time (24 h), mixing speed (200 rpm) and dark condition.

2.3 Characterization of Metal Nanoparticles

The synthesized metal nanoparticles were monitored after 24 h in the optimization of the biological synthesis of the nanoparticles from the supernatant by UV-vis spectroscopy using Lambda 750 UV/VIS/NIR Spectrometer. 600–250 nm range of different trial sets in which the nanometer was scanned. Also, Zeta-Sizer (Malvern Zeta Sizer Analyzer) and FTIR is used to measure dimensions and identify the chemical composition on the surface of the nanoparticle, respectively.

2.4 Antimicrobial Activity Test


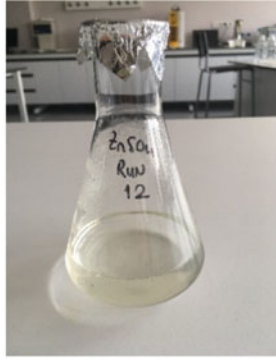
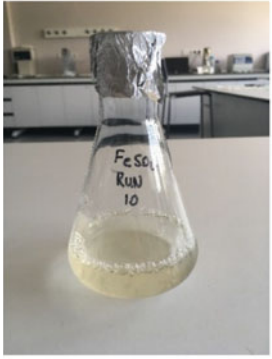
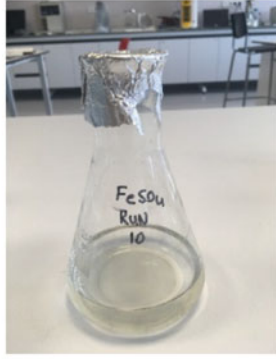
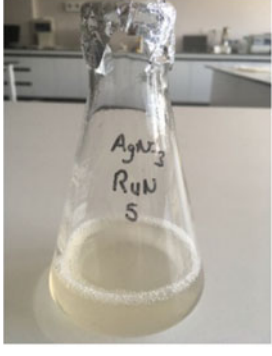

Antimicrobial effect of biogenic nanoparticles synthesized from different microalgae will be investigated with the agar disc-diffusion method specified in the study [8]. This effect will be tested on gram negative (*Escherichia coli*) and gram positive (*Streptococcus aureus*). The antimicrobial effect of the nanoparticles will be compared with the control group by measuring the white plaque diameter formed on the agar surface after incubation under appropriate conditions.

3 Results and Discussion

The biosynthesis approach for silver, iron (II) and zinc nanoparticles synthesis have been proven to be a better method due to their nontoxic, biocompatible, stabile properties. Microalgae systems offer efficient production of reducing components for the green synthesis of nanoparticles.

Visually, the color changes in the culture and media fluid will give an idea about the production and formation of nanoparticles (Fig. 1). Especially in the literature there will be different solution color changes according to particle size [3, 4, 9].

Fig. 1 Visuals of before and after incubation of nanoparticle processes

Run Number	Design Parameters	Before incubation	After incubation
R12	5 mM ZnSO ₄ ·7H ₂ O + 51/10 (ZnSO ₄ ·7H ₂ O/supernatant)		
R10	8 mM FeSO ₄ ·7H ₂ O + 51/10 (FeSO ₄ ·7H ₂ O /supernatant)		
R5	8,68 mM AgNO ₃ + 16,4/10 (AgNO ₃ /supernatant)		

Detailed characterization and description of nanoparticles due to their specific properties, behavior and effects is an important requirement for risk assessment. The properties, behavior and biological effects of nanoparticles can be affected by more than one physicochemical parameter. Characterization should also include measurement of important physicochemical parameters (size, morphology, surface area) [10].

Antibacterial activity of the different NPs synthesized by *Galdieria* sp. against the *E. coli* and *S. aureus* was analyzed by disc diffusion method (Fig. 2). Silver nanoparticles has same antimicrobial activity against the both gram (+) and (–) bacteria.

Surface-plasmon resonances of nanoparticles (SPR) were determined using UV-vis spectrophotometry [11] (Fig. 3). Inspection of UV-vis spectra of samples showed that the

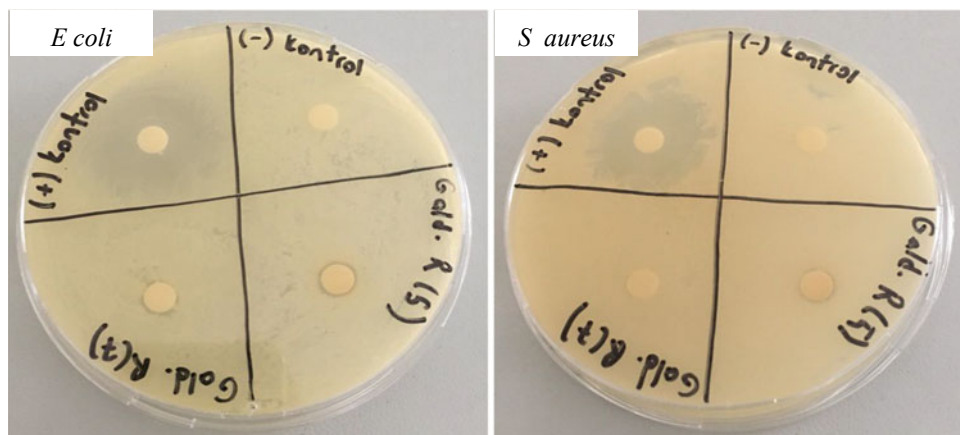


Fig. 2 Antimicrobial activity tests of silver nanoparticles

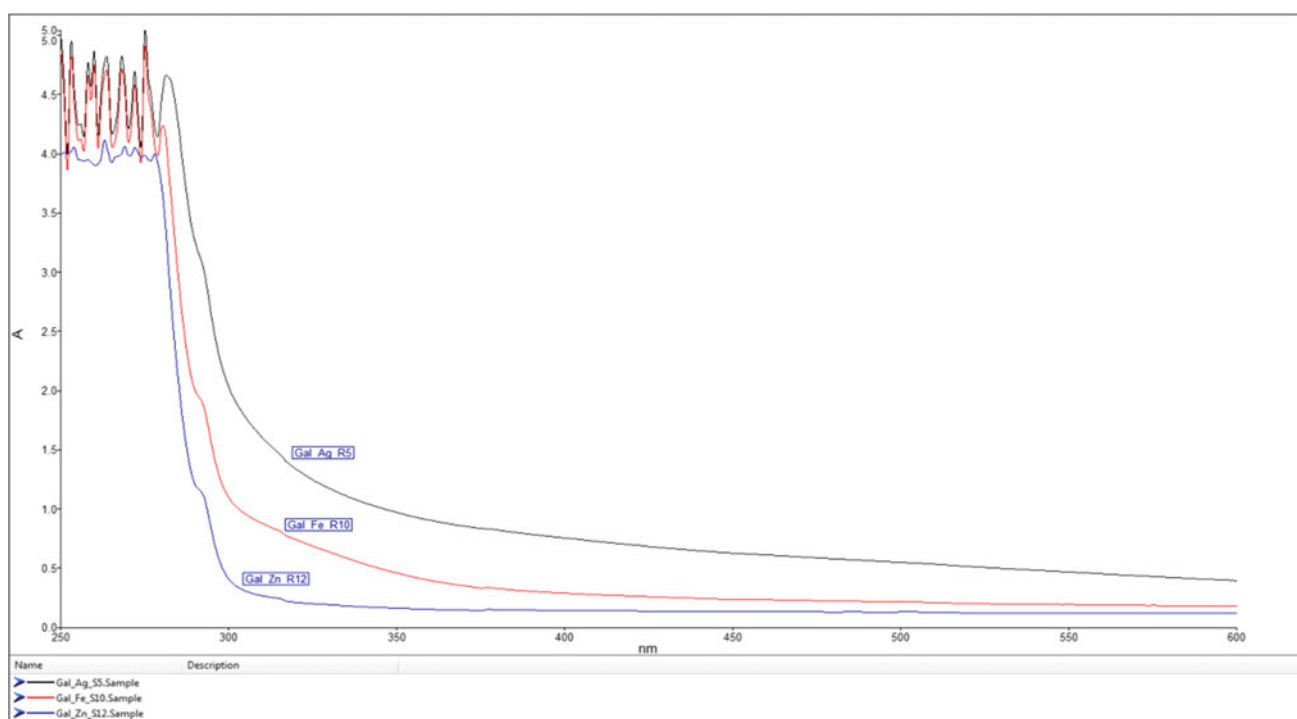


Fig. 3 Absorbance spectra of silver, iron and zinc solutions when incubated with *Galdieria* sp.

different metal nanoparticle suspensions have different results. Silver solution showed a prominent effect on nanoparticle production. The best ratio of metal: supernatant solution was found as 16:10 with using 8.68 mM AgNO_3 solution.

FTIR is used to identify the chemical composition on the surface of the nanoparticle. By this method, molecular bond characterization; functional groups in the form of solid, liquid, gas or solution organic compounds, whether the two compounds are the same, the state of the bonds in the

structure, the binding sites and whether the structure is aromatic or aliphatic can be determined (Fig. 4).

In addition, there are some search reference spectrum description for these metal nanoparticles. All of metal nanoparticles were H007.SP antistat, antistatic agent with 0.9858 similarity.

The dimensions of the nanoparticles are analyzed, and the results are over 100 nm. According to our results, the particles were determined as microparticles because of being greater than 100 nm (Table 1).

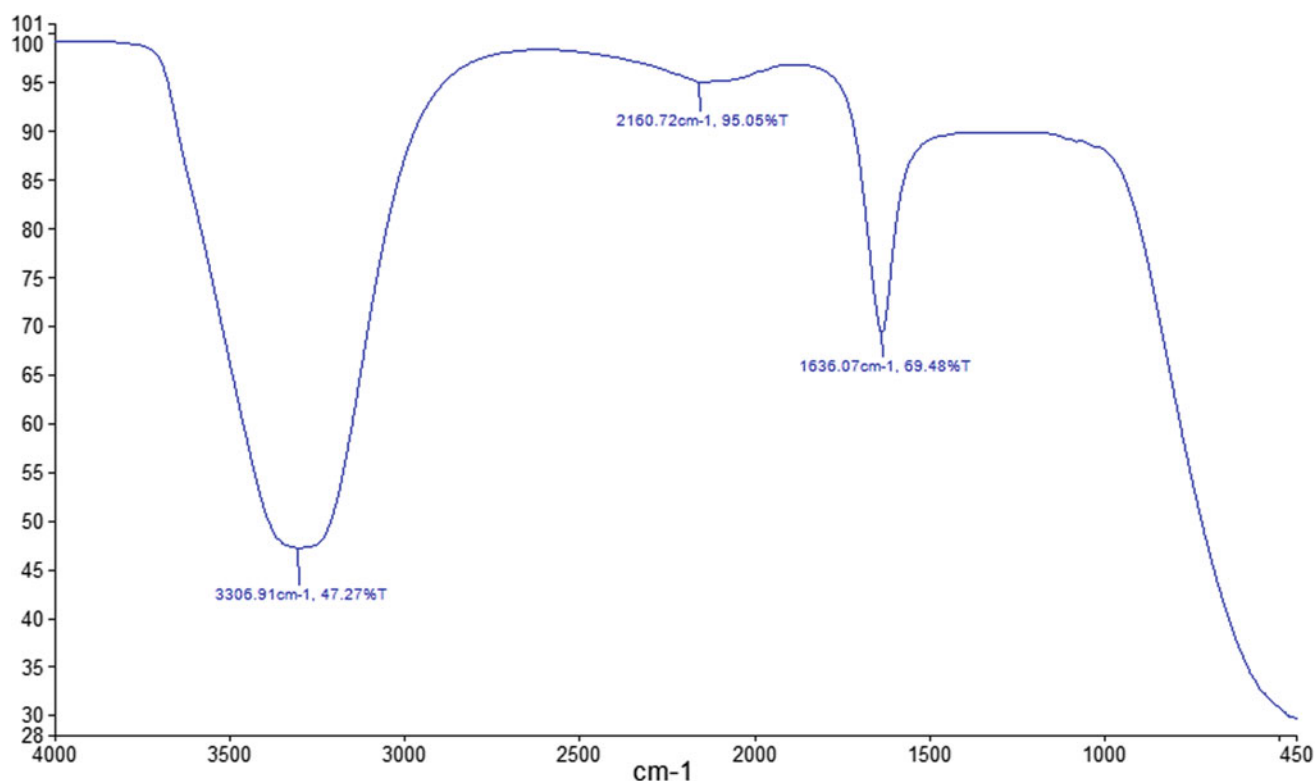


Fig. 4 FTIR spectra of nanoparticles

Table 1 Results of nanoparticle size by zeta-sizer

Supernatant: metal solution ratio	Sample	Diameter of nanoparticles by zeta-sizer, nm
R5	Silver	1134 ± 930
R10	Iron (II)	340 ± 106
R12	Zinc	390 ± 133

The amount of supernatant with the concentration of metal salt, pH, temperature, incubation time, mixing speed are important parameters that directly affect the formation of nanoparticles [5, 9, 12]. In addition, the size and morphology of nanoparticles are affected by pH, temperature, light, metal concentration, metal exposure time, NP-protein nucleation, microorganism cell surface, metabolite content (purity and molecular weight), synthetic peptide (mimicking structural proteins) [13–15].

4 Conclusion

In the present study, it was observed that concentration of all metal ions, and ratio of metal: supernatant solution plays a key role in the production rate of nanoparticles. To convert the generated particles to nanoparticles pH, temperature and incubation time should be examined on the particle size. This is an important optimization process planned to be

carried out and must definitely be improved in the next phase of our study. This work is only a brief part of the project and still in progress.

Acknowledgements This research was supported by The Scientific and Technological Research Council of Turkey (TUBITAK) with 117M052 Project Number.

Conflict of Interest The authors declare no conflict of interest.

References

- Sing, J., Dutta, T., Kim, K.H., Rawat, M., Samddar, P., Kumar, P.: 'Green' synthesis of metals and their oxide nanoparticles: applications for environmental remediation. *J. Nanobiotechnol.* **16**(1), 84 (2018)
- Dahoumane, S.A., Mechouet, M., Alvarez, F., Agathos, S.N., Jeffryes, C.: Microalgae: an outstanding tool in nanotechnology. *Bionature (Review)* **1**(4), 196–201 (2016)
- Rai, M., Maliszewska, I., Ingle, A., Gupta, I., Yadav, A.: Bio-nanoparticles: biosynthesis and sustainable biotechnological implications. In: Om V. Singh (ed.). Wiley, Hoboken, New Jersey (2015)

4. Jena, J., Pradhan, N., Dash, B.P., Sukla, L.B., Panda, P.K.: Biosynthesis and characterization of silver nanoparticles using Microalga *Chlorococcum humicola* and its antibacterial activity. *Int. J. Nanomater. Biostruct.* **3**(1), 1–8 (2013)
5. Parial, D., Pal, R.: Biosynthesis of monodisperse gold nanoparticles by green alga *Rhizoclonium* and associated biochemical changes. *J. Appl. Phycol.* **27**(2015), 975–984p (2015)
6. Patela, V., Berthold, D., Puranik, P., Gantar, M.: Screening of cyanobacteria and microalgae for their ability to synthesize silver nanoparticles with antibacterial activity. *Biotechnol. Rep.* **5**, 112–119 (2015)
7. Graverholt, O.S., Eriksen, N.T.: Heterotrophic high-cell-density fed-batch and continuous-flow cultures of *Galdieria sulphuraria* and production of phycocyanin. *Appl. Microbiol. Biotechnol.* **77**(1), 69–75 (2007)
8. Balouiri, M., Sadiki, M., Ibsouda, S.K.: Methods for in vitro evaluating antimicrobial activity: a review. *J. Pharm. Anal.* **6**, 71–79 (2016)
9. Mahdieh, M., Zolanvari, A., Azimee, A.S., Mahdieh, M.: Green biosynthesis of silver nanoparticles by *Spirulina platensis*. *Scientia Iranica F* **19**(3), 926–929p (2012)
10. Mu, L., Sprando, R.L.: Application of nanotechnology in cosmetics. *Pharm. Res.* **27**, 1746–1749 (2010)
11. Kariuki, V.M., Hoffmeier, J.C., Yazgan, I., Sadik, O.M.: Seedless synthesis and SERS characterization of multi-branched gold nanoflowers using water soluble polymers. *Nanoscale* **9**(24), 8330–8340 (2017)
12. Singh, P., Kim, Y.J., Zhang, D., Yang, D.C.: Biological synthesis of nanoparticles from plants and microorganisms. *Trends Biotechnol.* **34**(7), 588–599 (2016)
13. Wu, W., He, Q., Jiang, C.: Magnetic iron oxide nanoparticles: synthesis and surface functionalization strategies. *Nanoscale Res. Lett.* **3**(11), 397–415 (2010)
14. Li, X., Xu, H., Chen, Z., Chen, G.: Biosynthesis of nanoparticles by microorganisms and their applications (review article). *J. Nanomater.*, **16** (2011). Hindawi Publishing Corporation <https://doi.org/10.1155/2011/270974>
15. Friedman, A.D., Claypool, S.E., Liu, R.: The smart targeting of nanoparticles. *Curr. Pharm. Des.* **19**(35), 6315–6329 (2013)

HIV Infection Mathematical Modeling and Future Trends of Treatment Using Nanotechnology and Nanorobots

Nataša Popović, Milica Naumović, and Sonja Roganović

Abstract

In this paper, a system of ordinary differential equations, which describes the interaction of HIV and T-cells in the immune system of the human body, is used for infection modeling. The goal of this approach is better understanding of HIV immunology for the purpose of improving the existing models and testing different treatment strategies. Possible use of nanotechnology and micro/nanorobots, as future technologies that will make HIV treatment more efficient, are considered as well.

Keywords

HIV • AIDS • Mathematical modeling • Nanotechnology • Nanorobots

1 Introduction

According to the World Health Organization, HIV/AIDS is still a world's global major health issue. At the end of 2017, there were approximately 36.9 million people living with HIV and 1.8 million people became newly infected in 2017 around the world. On a global scale, 940,000 people died from HIV-related causes in the same year [1]. This statistic requires permanent research related to HIV/AIDS mechanism and treatment.

N. Popović (✉)

Faculty of Electrical Engineering, University of East Sarajevo,
East Sarajevo, Bosnia and Herzegovina
e-mail: natasa.popovic@etf.ues.rs.ba

M. Naumović

Faculty of Electronic Engineering, University of Niš, Niš,
Republic of Serbia
e-mail: milica.naumovic@elfak.ni.ac.rs

S. Roganović

Faculty of Medicine, University of Niš, Niš, Republic of Serbia
e-mail: sonja.roganovic@yahoo.com

HIV/AIDS is often written and pronounced together, although they have a different meaning. HIV is an acronym for the Human Immunodeficiency Virus. This virus attacks the body's immune system, which protects us from infectious diseases. HIV positive people are infected with HIV, which means that the virus has penetrated their bloodstream, from which it attacks and slowly destroys the immune system. AIDS is an acronym for the Acquired Immune Deficiency Syndrome and is a disease that develops over time as a result of HIV infection. AIDS is the most advanced stage of HIV infection. A person who is HIV positive does not necessarily have AIDS. With some of today's available drugs, which, unfortunately, cannot completely cure HIV infection, it is possible to prevent the development of AIDS.

The virus is an organism with dimension of several dozens to several hundred micrometers. The protective wrapper of the virus is a thin protein coat, which contains a single chain of DNA (deoxyribonucleic acid) and RNA (ribonucleic acid) [2]. Recall that nucleic acids are carriers of genetic information on the basis of which all processes that enable survival, development and reproduction take place in the living organism. A protein coat allows the virus to be transmitted from one cell to another. The virus cannot produce its own proteins, nor can it grow and reproduce itself. In order to perform reproduction process, viruses must insert their nucleic acids into a host functional cell. Upon entering the host cell, the virus acts as a parasite, and using the material and energy of the host cell, it begins to replicate itself by forming its own DNA. The newly formed viral DNA is then multiplied many times.

CD4-T cells, known as T4 cells, T4 lymphocytes or T-helper cells, are the most important part of our immune system, which with proper coordination successfully fight against infection. After penetrating a healthy person's bloodstream, HIV has a particular tendency towards CD4-T cells, in which it is absorbed and then multiplied. The infected T-cells are being destroyed over time, while new free viruses find other CD4-T cells, where the infection process is repeated. Hence, it is important to regularly do

blood tests and check the number of CD4-T cells in order to get additional information about the harm that the HIV does to the immune system of the human body.

There is a number of antiretroviral drugs (ARV), which cannot directly destroy the virus, but can significantly slow down its replication and sometimes even completely stop it. Various HIV treatment schemes are used, high activity antiretroviral therapy (HAART) for example, but issues of chemotherapy are always related to the size of the dose and length of treatment, drug resistance, as well as its periodicity. Using nanotechnology in HIV/AIDS treatment can overcome these issues and improve drug delivery in patient's body. Furthermore, micro and nanorobots play important role in future HIV/AIDS treatment, especially in targeted therapy.

Many approaches to mathematical modeling of HIV immunology can be found in the literature [3–11]. The role of statistics and its significance in understanding the dynamics of disease in all its phases is known. Some researchers have developed stochastic versions of the HIV infection model [12]. In this paper, a deterministic approach to the problem is presented, since it is possible to describe the infection process in an adequate way using ordinary and/or partial differential equations. Although numerous phenomena can be explained by the various models given in the literature, none of them are able to describe all the issues that are clinically observed, since many disease mechanisms are still unknown. However, if it appears that the model behaves in accordance with clinical data in qualitative and quantitative terms, it can be further applied to test various treatments and treatment strategies [8]. The application of the classical theory of optimal control when determining the strategy of HIV chemotherapy is considered in [13–15]. Nanotechnology in HIV treatment is studied in [16–18], while micro/nanorobots are studied in [19–23]. Current research in biomedicine and nanomedicine include disciplines such as biotechnology, proteomics, molecular biology, mechatronics, control engineering, computer

science, material science, etc. This paper demonstrates multidisciplinary approach in HIV modelling and treatment that can provide better understanding of the infection and innovative treatment techniques, primarily regarding drug delivery.

2 HIV Infection

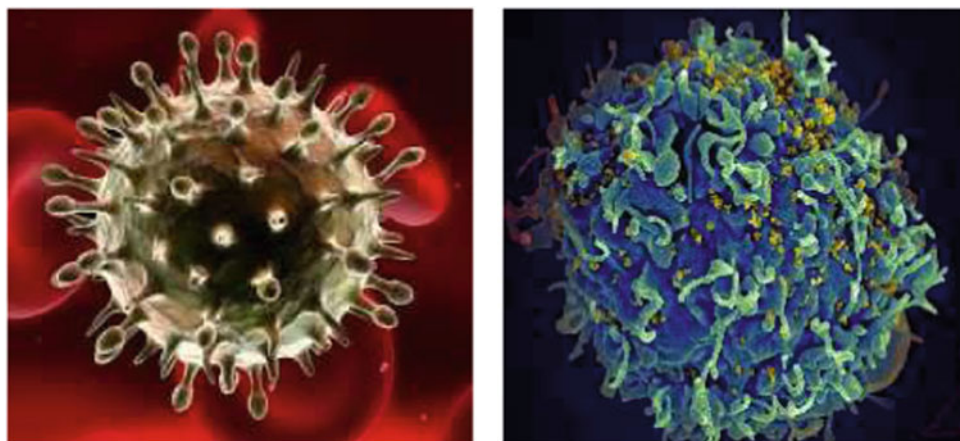
HIV (Fig. 1a) attacks the CD4⁺T cell (CD4 positive T lymphocyte) directly and multiplies therein, leading to its destruction. The CD4⁺T cell is a type of white blood cells with a key role in the defensive mechanism of the organism. In normal conditions their number is about 1000 in 1 mm³ of blood. The letter T indicates its relationship to the thymus gland where the cell matures, since it transits to thymus gland after it is generated in the bone marrow. The CD4 is a protein marker on the surface of the CD4⁺T cell to which the GP120 protein, located on the surface of the virus, has a high affinity. The infected CD4-T cell is shown in Fig. 1b.

By duplicating the DNA of the virus, new virus particles are created from the CD4⁺T cell at different rates. It is possible to distinguish three major stages in the development of the disease. At the beginning, the virus enters the body (acute infection) and after a relatively short transition process, the so-called clinical latency occurs (chronic infection), which corresponds to the stationary state of the disease. The last, AIDS stage, is characterized by almost annihilation of T-cells, which leads to unlimited replication of viruses and safe death.

3 HIV Mathematical Modeling

Schematic representation of the basic HIV model is given in Fig. 2. Thymus generates healthy CD4⁺T cells at a constant rate s , with death rate of μ_T . The cells are infected by the

Fig. 1 HIV and infected CD4-T cell [24]



(a) HIV

(b) Infected CD4-T cell

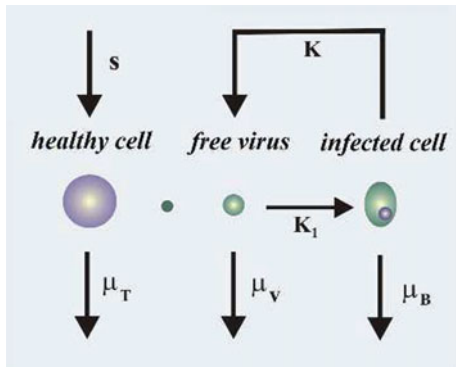


Fig. 2 Illustration of HIV model

virus at a rate that is proportional to the product of their concentration and the amount of free virus particles. The proportionality constant K_1 indicates the effectiveness of the infection process. The infected CD4⁺T cells, whose death rate is μ_B , occur after the infection of healthy CD4⁺T cells. Free virus particles, which are produced from infected CD4⁺T cells at a rate K , have a death rate μ_v .

Let $T = T(t)$ represents the concentration of healthy CD4⁺T cells per mm³ of blood over a period of t days. The process of destroying and proliferating new T-cells can be described by the equation

$$\frac{dT}{dt} = s - \mu_T T + rT \left(1 - \frac{T}{T_{\max}}\right)_+, \quad (1)$$

where r is the rate of proliferation of T-cells, and notation used above corresponds to $F_+ = \max\{F, 0\}$. The last term in Eq. (1) provides the increase of concentration only to the value of T_{\max} . At first, in order to obtain a simpler model, the dynamics of T-cell proliferation will be ignored.

After the virus enters the organism, a certain number of T-cells get infected, so their total concentration can be divided into three different groups. Let $T = T(t)$, $T^* = T^*(t)$ and $T^{**} = T^{**}(t)$ be the concentration of uninfected, latently infected and actively infected CD4⁺T cells at time t . The concentration of free infectious virus particles per mm³ of blood is indicated by $V = V(t)$. The description and numerical values of the parameters used in the modeling process can be found in Table 1 [4].

Equations (2)–(4) describe population dynamics of uninfected, actively infected CD4⁺T cells and free viruses, respectively, in the simplest way:

$$\frac{dT}{dt} = s - \mu_T T - K_1 VT \quad (2)$$

$$\frac{dT^{**}}{dt} = K_1 VT - \mu_B T^{**} \quad (3)$$

$$\frac{dV}{dt} = KT^{**} - \mu_v V. \quad (4)$$

In the previous model, a member corresponding to the proliferation of existing T-cells was not specifically considered, since the effect of proliferation can be included in the constant μ_T . Note that in the case of the healthy T-cells infection some viruses are lost, since viruses are attached to newly infected cells. Hence, the term $K_1 VT$ in Eq. (2) is with a negative sign. In Eq. (4), however, the loss of viruses in the process of T-cell infection is ignored.

In the absence of viruses, the steady state of the T-cell population is

$$T_0 = \frac{T_{\max}}{2} \left[1 - \frac{\mu_T}{r} + \sqrt{\left(1 - \frac{\mu_T}{r}\right)^2 + \frac{4s}{rT_{\max}}} \right], \quad (5)$$

Table 1 HIV model relevant parameters

Parameter	Value	Description
μ_T	0.02	Death rate of uninfected CD4 ⁺ T cells (per day)
μ_T^*	0.02	Death rate of latently infected CD4 ⁺ T cells (per day)
μ_B	0.24	Death rate of actively infected CD4 ⁺ T cells (per day)
μ_v	2.4	Death rate of free virus (per day)
K_1	2.4×10^{-5}	Rate that CD4 ⁺ T cells become latently infected by free virus (mm ³ per day)
K_2	3×10^{-3}	Rate that latently infected CD4 ⁺ T cells become actively infected (mm ³ per day)
r	0.03	Rate of proliferation of CD4 ⁺ T cells (per day)
r^*	0.015	Rate of proliferation of latently infected CD4 ⁺ T cells (per day)
r^{**}	0.015	Rate of proliferation of actively infected CD4 ⁺ T cells (per day)
T_{\max}	1500	Maximum number of CD4 ⁺ T cells (healthy and infected) (per mm ³)
N	1000	Number of free viruses produced during the lifetime of an actively infected cell
s	10.0	Rate of production of new CD4 ⁺ T cells (per day per mm ³)
K	100	Rate of free viruses produced per infected CD4 ⁺ T cell

and, if the effects of proliferation are ignored, it is given with

$$T_0 = \frac{s}{\mu_T}. \quad (6)$$

Initial conditions for Eqs. (2)–(4) are $T(0) = T_0$, $T^{**}(0) = 0$, $V(0) = V_0$ for the infection by free virus, and $T(0) = T_0$, $T^{**}(0) = T_0^{**}$, $V(0) = V_0$ for the infection by both free virus and infected cells.

4 HIV/AIDS Model Analysis

Consider the infection process described by Eqs. (2)–(4) as an autonomous system given with

$$\dot{\mathbf{x}} = \mathbf{f}(\mathbf{x}) \quad (7)$$

where $\mathbf{f}(\mathbf{x})$ is vector function of vector argument $\mathbf{x} = [T \ T^{**} \ V]^T$ which satisfies Lipschitz condition [25]. Recall that function $\mathbf{f}(t, \mathbf{x})$ satisfies a Lipschitz condition on an area (t_0, \mathbf{x}_0) if there is a positive constant L such that

$$\|\mathbf{f}(t, \mathbf{x}) - \mathbf{f}(t, \mathbf{y})\| \leq L\|\mathbf{x} - \mathbf{y}\| \quad (8)$$

for all (t, \mathbf{x}) and (t, \mathbf{y}) near by (t_0, \mathbf{x}_0) .

Equilibrium points \mathbf{x}_e of system described with (7) are determined by

$$\mathbf{f}(\mathbf{x}_e) = \mathbf{0}, \quad (9)$$

from which the following is obtained

$$\mathbf{x}_{e1} = \left[\frac{s}{\mu_T} \quad 0 \quad 0 \right]^T \quad (10)$$

and

$$\mathbf{x}_{e2} = \left[\frac{\mu_B \mu_V}{KK_1} \left| \frac{s}{\mu_B} - \frac{\mu_V \mu_T}{KK_1} \right| \left| \frac{Ks}{\mu_B \mu_V} - \frac{\mu_T}{K_1} \right| \right]^T \quad (11)$$

Expanding each component of $\mathbf{f}(\mathbf{x})$ in the Taylor series in an equilibrium point \mathbf{x}_e and rejecting higher order terms, the so-called variational equation is obtained in a form

$$\delta \dot{\mathbf{x}} = \mathbf{J}(\mathbf{x}_e) \delta \mathbf{x}, \quad (12)$$

where

$$\mathbf{J}(\mathbf{x}_e) = \begin{bmatrix} \frac{\partial f_1}{\partial x_1} & \frac{\partial f_1}{\partial x_2} & \frac{\partial f_1}{\partial x_3} \\ \frac{\partial f_2}{\partial x_1} & \frac{\partial f_2}{\partial x_2} & \frac{\partial f_2}{\partial x_3} \\ \frac{\partial f_3}{\partial x_1} & \frac{\partial f_3}{\partial x_2} & \frac{\partial f_3}{\partial x_3} \end{bmatrix}_{\mathbf{x}=\mathbf{x}_e} \quad (13)$$

represents Jacobian calculated for $\mathbf{x} = \mathbf{x}_e$. In accordance with the indirect Lyapunov method, in the equation of the disturbed equilibrium state given with

$$\delta \dot{\mathbf{x}} = \mathbf{J}(\mathbf{x}_e) \delta \mathbf{x} + \mathbf{h}(\mathbf{x}_e, \delta \mathbf{x}), \quad (14)$$

where

$$\lim_{\|\delta \mathbf{x}\| \rightarrow 0} \frac{\mathbf{h}(\mathbf{x}_e, \delta \mathbf{x})}{\|\delta \mathbf{x}\|} = 0, \quad (15)$$

linear homogenous differential Eq. (12) is equation of linearized system, whose stability can be examined using a characteristic equation

$$\det(\lambda \mathbf{I} - \mathbf{J}(\mathbf{x}_e)) = 0. \quad (16)$$

However, according to the indirect Lyapunov method, stability is only a local property of the examined equilibrium state. The Jacobian, in the case of the HIV infection model (2)–(4), takes the form

$$\mathbf{J}(\mathbf{x}) = \begin{bmatrix} -\mu_T - K_1 V & 0 & -K_1 T \\ K_1 V & -\mu_B & K_1 T \\ 0 & K & -\mu_V \end{bmatrix} \quad (17)$$

Let define parameter R_0 as

$$R_0 = \frac{K_1 s K}{\mu_T \mu_V \mu_B} \quad (18)$$

Using the indirect Lyapunov method, we can evaluate the stability of the nonlinear system (2)–(4) near to points of equilibrium \mathbf{x}_{e1} and \mathbf{x}_{e2} and conclude the following.

1. The roots of the characteristic equation of the linearized system near to point \mathbf{x}_{e1} are:

$$\lambda_{1,2} = -\frac{\mu_B + \mu_V}{2} \pm \sqrt{\left(\frac{\mu_B + \mu_V}{2}\right)^2 - \mu_V \mu_B (1 - R_0)} \quad (19)$$

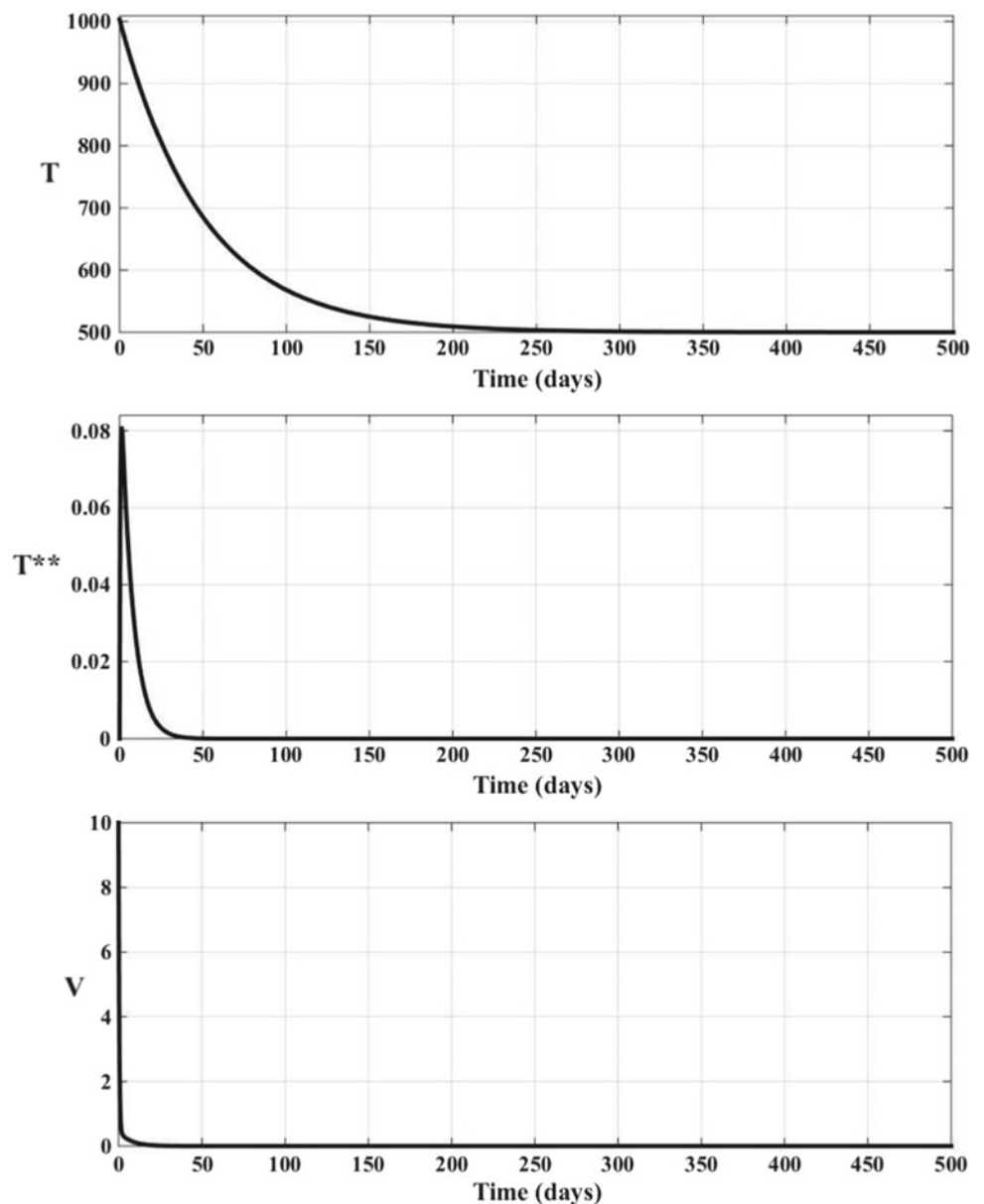
and $\lambda_3 = -\mu_T$.

Therefore, for $R_0 < 1$, the equilibrium state (10), which for the values of the parameters given in Table 1 becomes

$$\mathbf{x}_{e1} = [500 \quad 0 \quad 0]^T, \quad (20)$$

is locally asymptotically stable. So, the virus will not be multiplied. This situation is shown in Fig. 3.

Fig. 3 Simulation results without virus multiplication ($R_0 = 0.208$)



2. If $R_0 > 1$, the equilibrium state (10) is unstable, while the equilibrium state (11) is locally asymptotically stable. Namely, if the characteristic Eq. (16) is written in a polynomial form, then:

$$\begin{aligned} \lambda^3 + a_2\lambda^2 + a_1\lambda + a_0 &= 0, \\ a_2 &= \mu_B + \mu_v + \mu_T R_0, \quad a_1 = (\mu_B + \mu_v)\mu_T R_0, \\ a_0 &= \mu_B \mu_v \mu_T (R_0 - 1), \end{aligned} \tag{21}$$

from where the required and sufficient condition of stability is obtained for $R_0 > 1$. A situation that corresponds to the equilibrium state \mathbf{x}_{e2} , with

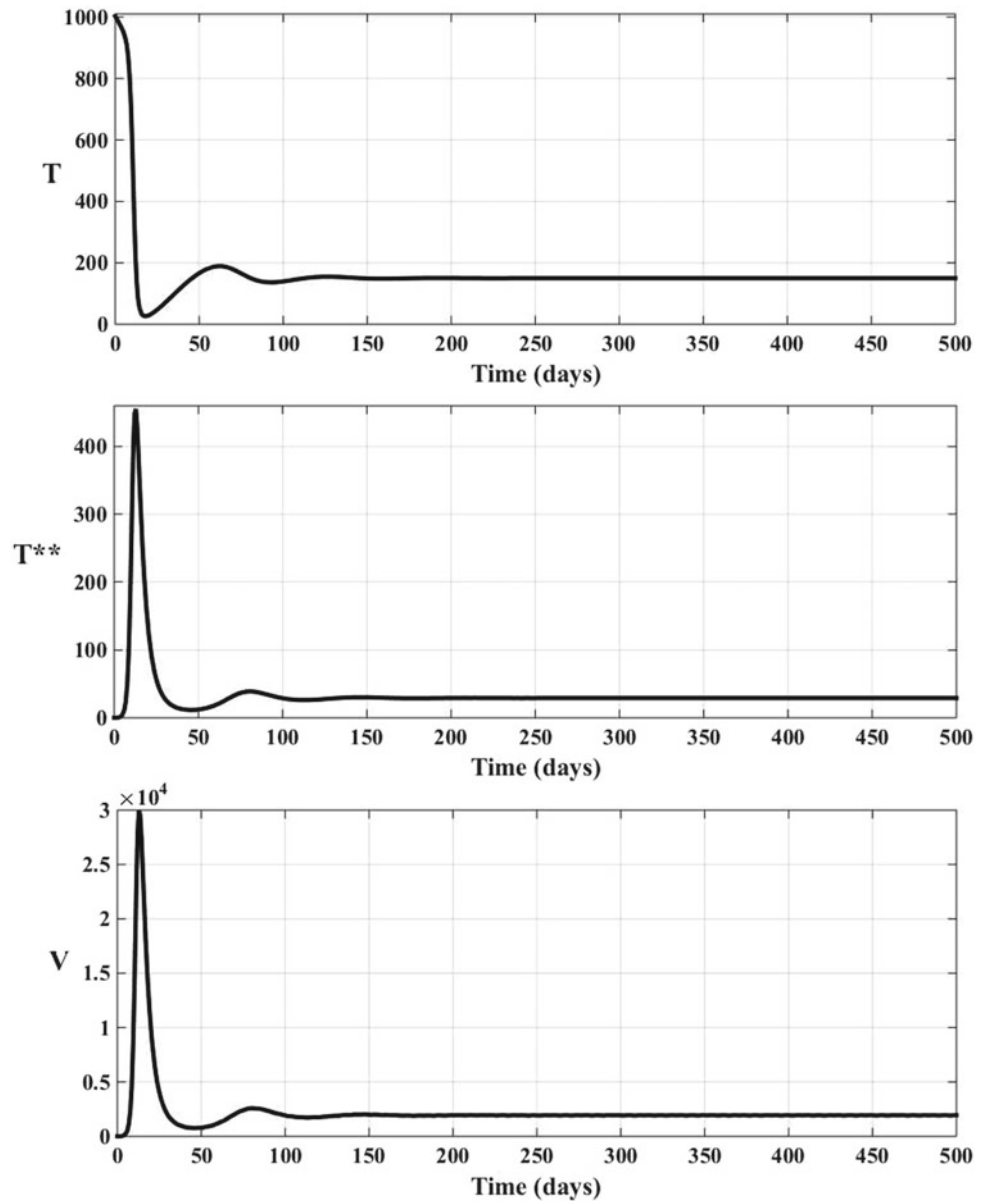
$$\mathbf{x}_{e2} = [240.00 \quad 21.67 \quad 902.78]^T, \tag{22}$$

is shown in Fig. 4.

5 Improving HIV/AIDS Model for Adequate Treatment of Disease

In order to choose the correct treatment procedure, it is necessary to have a model that accurately describes the infection scenario. To improve the model, system Eqs. (2)–(4) will be modified so the process will be described with the following equation system:

Fig. 4 Typical HIV infection
($R_0 = 3.33$)



$$\frac{dT}{dt} = \frac{s}{1+V} - \mu_T T + rT \left(1 - \frac{T+T^*+T^{**}}{T_{\max}}\right) - K_1 VT \quad (23)$$

$$\frac{dT^*}{dt} = K_1 VT - \mu_T T^* - K_2 T^* \quad (24)$$

$$\frac{dT^{**}}{dt} = K_2 T^* - \mu_B T^{**} \quad (25)$$

$$\frac{dV}{dt} = N\mu_B T^{**} - K_1 VT - \mu_V V, \quad (26)$$

with initial conditions $T(0) = T_0$, $T^*(0) = T_0^*$, $T^{**}(0) = T_0^{**}$, $V(0) = V_0$ for infection by both free virus and infected cells.

In (23), the term $s/(1+V)$ represents the rate of generation of new CD4⁺T cells. Comparing with clinical data, the best results are obtained when the generation of T-cells is monotonically decreasing function depending on the virus concentration [15]. The same equation monitors the increase in the concentration of T-cells to the value of T_{\max} . In (23) and (24), the rate at which free viruses infect T-cells is modeled by $K_1 VT$.

Although it depends on many factors, it is assumed that the death rate of latently infected cells is μ_T , e.g. it is the same as death rate of healthy cells. In (24) and (25), latently infected cells become actively infected at the rate K_2 , which then produce new viruses and die at rate μ_B per cell. Before they die, each of them generates N viruses. A term $-\mu_V V$ in Eq. (26) describes a reduction in infection due to virus loss.

In the treatment of HIV infection, antiretroviral drugs (ARV) are used. They can be classified into two main categories:

- reverse transcriptase inhibitors (RTIs).
- protease inhibitors (PIs).

The first reduces the infection of new cells but does not block the production of viruses by already infected cells at the last stage when reverse transcriptase occurs. If pharmacokinetic or metabolic changes are not considered, RTI treatment can be included in the mathematical model by changing the parameter K_1 in (23) and (24). Similarly, the effects of protease inhibitors are included in the model Eq. (26) by changing the parameter N . Therefore, model Eqs. (23) and (24) can be modified to accommodate control actions $0 \leq u_1(t) \leq 1$ and $0 \leq u_2(t) \leq 1$ which correspond to RTI and PI treatment, respectively, in a way

$$\frac{dT}{dt} = \frac{s}{1+V} - \mu_T T + rT \left(1 - \frac{T+T^*+T^{**}}{T_{max}} \right) - (1-u_1(t))K_1VT \tag{27}$$

$$\frac{dT^*}{dt} = (1-u_1(t))K_1VT - \mu_T T^* - K_2T^* \tag{28}$$

$$\frac{dT^{**}}{dt} = K_2T^* - \mu_B T^{**} \tag{29}$$

$$\frac{dV}{dt} = u_2(t)N\mu_B T^{**} - K_1VT - \mu_v V. \tag{30}$$

In doing so, chemotherapy is only applied over a given time interval $[t_0, t_1]$ for two reasons. Namely, HI virus can become resistant during treatment due to different mutations. Also, in the case of a prolonged interval of time, usually a period longer than 500 days, the effects of chemotherapy can be hazardous.

6 Nanotechnology and Micro/Nanorobots in HIV/AIDS Treatment

Antiretroviral drugs have been used for HIV treatment for thirty years now. AIDS treatment is achieved with high activity antiretroviral therapy which is a combination of at least three ARV drugs. When determining the strategy of HIV chemotherapy, drug properties, cost, resistance status and patient characteristics should be taken into consideration. Difficulties that are present in current HIV treatment are: short residence time of ARV drug which requires higher doses of a drug to be consumed for a longer time, resistance to certain drugs due to long time consumption, drug toxicity, interaction of ARV drugs and other drugs, ARV drugs

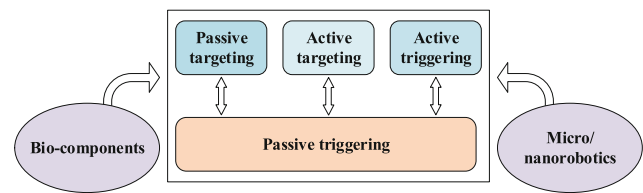


Fig. 5 Targeting therapy with nanotechnologies and nanorobotics

side effects, and so on. Current treatment methods cannot cure HIV/AIDS completely. Hence, there is a great need for seeking innovative approaches that would be able to do so. The most promising approach is to use nanotechnology in prevention (vaccines, microbicides), diagnostics (CD4⁺T count) and treatment (drug delivery) of HIV/AIDS. In HIV/AIDS treatment, targeting therapy is of special interest, since it can be achieved by both using nanotechnology and micro/nanorobots, Fig. 5.

6.1 Nanotechnology in HIV Treatment

Nanotechnology can be defined as a set of activities at the atomic and molecular level that have applications in the real world, with the ability of measuring, manipulating, and assembling matter with features on the scale of 1–100 nm. In HIV treatment, nanotechnology is used to modulate pharmacokinetics of incorporated molecule in a way that it is capable of removing the HIV. Absorption, distribution, metabolism and excretion of anti-HIV drug enclosed in nanosystem are governed by the physical and chemical properties of such a system (surface-exposed molecules, electric charge, size). Nanosystems are comprised of nanocarriers which are entities with a diameter typically between 10 and 1000 nm used for the controlled delivery of pharmaceutical agents that are encapsulated within, or adsorbed or conjugated onto their surface. Main nanotechnology-based systems explored for HIV treatment are: liposomes, nanoparticles, niosomes, polymeric micelles and dendrimers [16–18], Fig. 6.

Liposomes are microscopic spherical vesicles consisting of at least one phospholipid bilayer which usually surrounds an aqueous core. Liposome surface ligands can be used for attaching to unhealthy tissue. After entering the human body, immune system detects liposomes as foreign bodies, what enables the mononuclear phagocytic cells to take them up. The HIV is concentrated in mononuclear phagocytic cells of infected person, which makes liposomes suitable carriers for targeting anti-HIV drugs to the infected cells. Thus, liposomes can improve the efficacy of anti-HIV drugs and reduce their side effects [17].

Nanoparticles are solid colloidal particles with diameter of 10–1000 nm which can be made of polymeric and

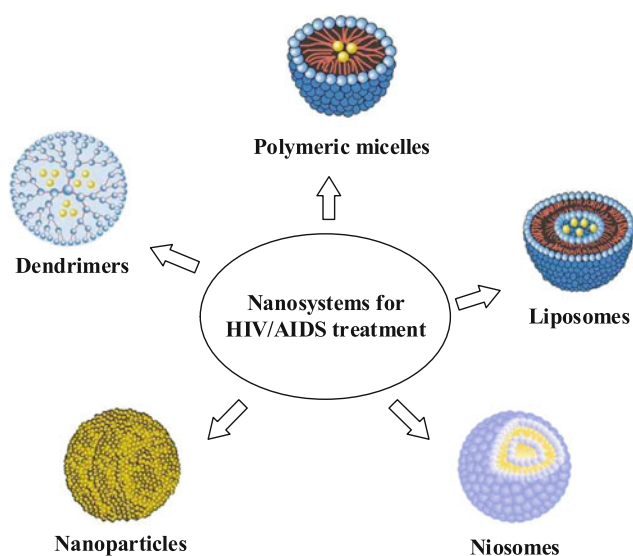


Fig. 6 Nanosystems for HIV/AIDS treatment

non-polymeric material. Depending on the colloidal size and polymeric composition, nanoparticles can target drug to specified locations in the body where HIV resides what makes them suitable for targeted delivery of ARVs. For antiHIV treatment, there are three types of nanoparticles that are mainly employed: polymeric nanoparticles, solid lipid nanoparticles and nanostructured lipid carriers, and inorganic nanoparticles. Nanoparticles can also be used for improvement of formulation and efficacy of drugs with physico-chemical drawbacks such as poor stability and solubility, as well as to achieve sustained drug-release kinetics. There are two types of drug containers: nanospheres in which the drug is dispersed throughout the particle and nanocapsules in which the drug is entrapped in a cavity surrounded by a polymeric membrane. Drug encapsulation into nanoparticles may provide improved efficacy, decreased drug resistance, the reduction in dosage, a decrease in systemic toxicity and side effects, and an improvement in patient compliance [17].

Niosomes are also known as nonionic surfactant-based vesicles. They consist of hydrated synthetic nonionic surfactant monomers. They are structurally similar to liposomes and are capable of entrapping drugs. Anti-HIV drug delivery with niosomes is achieved through intravenous or topical routes. Using niosomes in drug delivery alters bio distribution to provide a greater degree of targeting of the drug to selected tissue, sustained release and altered pharmacokinetics [17].

Polymeric micelles are amphiphilic copolymers that self-assemble in aqueous environment forming spherical colloidal system. They consist of hydrophobic core and hydrophilic surface-corona. Their structure enables them to be used as drug delivery nanocarriers where drug molecules

can be entrapped in the core, corona and in-between core and corona. Hydrophilic blocks from corona can be attached to antibodies or other ligands specific for receptors present in HIV/AIDS. Polymeric micelles have been utilized for improving aqueous solubility, intestinal permeability, and disease site targeting of several drug molecules. Some of the micelles advantages are: solubilization poorly water-soluble drugs, protection toward chemical degradation, controlled release of drugs, etc. [17].

Dendrimers are branched polymeric nanostructures (<100 nm) with controlled threedimensional structure. Several branching units are surrounding the core in a layered architecture which defines the growth, size, and the microenvironment within the dendrimer. Dendrimers are composed of dendrons. The empty space inside the dendrons can be used for the entrapment of drug molecules for solubilization, controlled release, targeting, or protection from surrounding degrading environment. Dendrimers allow mathematically defined control and systematic engineering of their nanostructure, which enables dendrimer-drug conjugates to be more adaptable to targeting strategies than the other nanoparticle categories [16]. This means that dendrimers can be used effectively in targeting elimination of HIV.

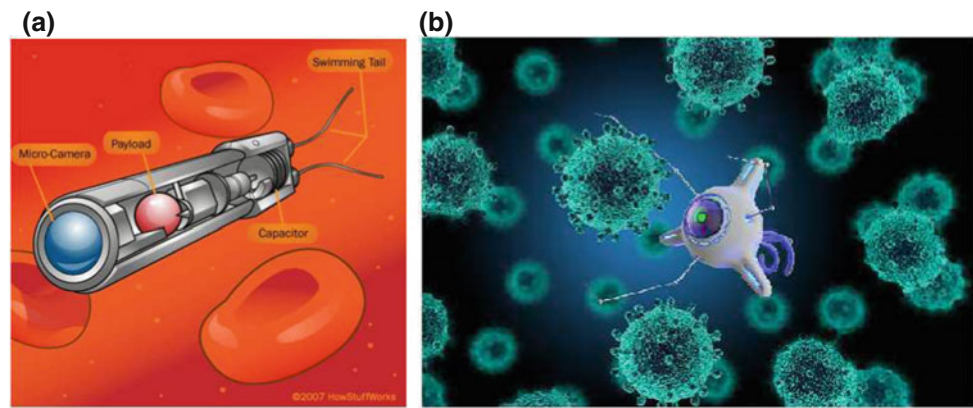
6.2 Micro/Nanorobotics in HIV Treatment

Biomedical micro and nanotechnology finds its place in many areas of medicine, from surgery and dentistry to diagnostics and disease treatment. Operations at the micro/nanoscale can be achieved through miniaturized controllable devices, known as microrobots and nanorobots. Some kinds of microrobots have already been developed and experimentally used on living organisms, but nanorobots are still to be investigated.

Nanorobots would constitute any passive or active structure capable of actuation, sensing, signaling, information processing, intelligence, swarm behavior at the nano scale. Some of desirable abilities of a nanorobot are [21]:

- swarm intelligence—decentralization and distributive intelligence,
- cooperative behavior—emergent and evolutionary behavior,
- self-assembly and replication—assemblage at nano scale and “nanomaintenance”,
- nanoinformation processing and programmability—for programming and controlling nanorobots (autonomous nanorobots),
- nano to macroworld interface architecture—an architecture enabling instant access to the nanorobots and its control and maintenance.

Fig. 7 Nanorobots.
a Pharmacyte [26]. **b** Nanorobot
 in HIV treatment [27]



Depending on an application area, nanorobots can be manufactured from non-biomaterial or biomaterial. Nanorobots based on non-biomaterial have features of traditional robots from the macro world, while nanorobots based on biomaterial behave as molecular machines (bio-nanorobots). Molecular machines use different biological elements as machine components. These components act as motors, gears, mechanical joints, transmission elements, sensors, and could be made of proteins, DNA and inorganic (chemical) substances. If all these different components were assembled together in the proper manner they would form nanodevices with multiple degrees of freedom, able to apply forces and manipulate objects in the nanoscale world [21] (Fig. 7).

Types of nanorobots, proposed to be used in medical applications so far, are: respirocyte (artificial mechanical red blood cells), microbivore (artificial white blood cells also known as nanorobotic phagocytes), clottocyte (artificial mechanical platelet that would complete hemostasis), pharmacytes (for nanorobotic drug delivery), dentifrobots (dental nanorobots) and vasculoids (as an artificial nanomechanical vascular system) [20]. For HIV treatment, nanorobots should perform precise transport and targeted delivery of drug payloads to the infected cells where the drug would be released via nano-injection or by progressive cytopenetration. To obtain such tasks, nanorobots are desired to have appropriate propelling force, controlled navigation, cargo-towing and release, and tissue penetration. Ability of locomotion inside the human body is the most important feature that drug delivery nanorobot must achieve. Since it is intended to move through the fluid environment, nanorobot moving should rely on motion strategies, like swimming, that are appropriate for the low Reynolds number environment. Nanorobot navigation is another issue in drug delivery operation and is related to development of control algorithms for overcoming the Brownian motion and obstacle avoidance strategies that include trajectory planning. There are two ways of nanorobot propulsion: external powering and self-propelling. External powering (wireless powering)

mostly implies the use of magnetic field to reproduce the motion of nanorobot similar to motion of microorganisms with helical or elastic flagella and enables wireless control of a nanorobot in three-dimensional space, ultrasound energy, as well as optical, electrical and thermal energy. Self-propelling uses chemically powered motors that convert locally supplied fuels to force and movement, and is achieved by motors using the surface reaction to generate local gradients of concentration, electrical potential and gas bubbles. These propulsion mechanisms are proposed in drug delivery process in general and thus could be used in HIV treatment after certain modifications.

Interesting issue in drug delivery is intracellular delivery where nanorobots penetrate through cellular membranes and directly deliver various therapeutic compounds into the cells, such as small interfering RNA (siRNA). Similarly, the potential use of DNA nanostructures as drug delivery nanovehicles is studied as well, where, for example, motors loaded with plasmid DNA (pDNA) were steered wirelessly toward the human embryonic kidney cells and released their genetic cargo into the cells upon contact [22].

Nanorobots can be used in HIV treatment not only as drug delivery devices but as devices that would be able to convert the HIV infected cells into healthy ones [23], replacing or repairing damaged DNA.

7 Conclusions

In this paper a mathematical model of interaction of HIV and T-cells in the immune system of the human body is obtained and analyzed. HIV model is later modified to meet the requirements of correct infection treatment using antiretroviral therapy that can slow down the multiplication of viruses and reduce their negative effect on the immune system of the human. Modern research in control engineering aims to develop new models and treatment strategies in order to stop the HIV infection. Besides that, improvements

in biotechnology, molecular biology, mechatronics, material science and so on make possible the application of nanorobots and nanotechnology in HIV treatment. Benefits of nanotechnology-based systems used in HIV treatment are recognized in drug delivery operations and can greatly overcome the limitations of traditional HIV chemotherapy. Although this has already been demonstrated in vitro and in vivo, many issues remain open to investigate in the future research, including nanorobots biocompatibility, toxicity and retention. Furthermore, if multiple nanorobots are needed to perform a task, they must be coordinated and synchronized through intelligent communication. Localization and mapping of nanorobots inside the human body have to be achieved with modern imaging systems and feedback control systems. All this and many more features greatly affects the HIV infection treatment strategies and lead to predictive and personalized medicine paradigm, which is a certain future of health care.

References

- <http://www.who.int/news-room/fact-sheets/detail/hiv-aids>
- Tomin, J., Abramović, M.: *Organska hemija*. Univerzitet u Nišu, Medicinski fakultet, Prosveta, Niš (2004)
- Kirschner, D.: Using mathematics to understand HIV immune dynamics. *AMS Not.* **43**, 191–202 (1996)
- Spagnuolo, A.M., Hanna, D.M., Lindsey, W., Stryker, G.A.: Modeling HIV-1 dynamics and the effects of decreasing activated infected T-cell count by filtration. In: *Proceedings of the 26th Annual International Conference of IEEE-EMBS, San Francisco* (2004)
- Xia, X.: Estimation of HIV/AIDS parameters. *Automatica* **39**, 1983–1988 (2003)
- Craig, I.K., Xia, X., Venter, J.W.: Introducing HIV/AIDS education into the electrical engineering curriculum at the university of pretoria. *IEEE Trans. Educ.* **47**(1), 65–73 (2004)
- Staffoed, M.A., et al.: Modeling plasma virus concentration and CD4⁺T cell kinetics during primary HIV infection, SFI (Santa Fe Institute). Working Paper, No. 99-05-036, pp. 1–38 (1999)
- Craig, I.K., Xia, X.: Can HIV/AIDS be controlled? *IEEE Control Syst. Mag.* **25**(1), 80–83 (2005)
- Landi, A., et al.: Modelling and control of HIV Dynamics. *Comput. Methods Programs Biomed.* **89**, 162–168 (2008)
- Chirove, F., et al.: Analysis of combined langerhans and CD4⁺T cells HIV infection. *Soc. Ind. Appl. Math.* **74**(4), 1174–1193 (2014)
- Naumović, M., Popović, N.: Matematičko modeliranje HIV infekcije (eng. HIV infection mathematical modelling). In: *INFOTEH-JAHORINA*, vol. 4, ref. E-I-7, p. 227–231 (2005)
- Dalal, N., Greenhalgh, D., Mao, X.: A stochastic model for internal HIV dynamics. *J. Math. Anal. Appl.* **341**, 1084–1101 (2008)
- Heris, S.M.K., Khaloozadeh, H.: Multi-objective optimal HIV therapy based on a new model of infection dynamics. In: *Iranian Conference on Intelligent Systems (ICIS)* (2014)
- Fister, K.R., Lenhart, S., McNally, J.S.: Optimizing chemotherapy in an HIV model, electronic. *J. Differ. Equ.* **1998**(32), 1–12 (1998)
- Kirschner, D., Lenhart, S., Serbin, S.: Optimal control of the chemotherapy of HIV. *J. Math. Biol.* **35**, 775–792 (1997)
- Ricotti, L., et al.: Advanced micro-nano-bio systems for future targeted therapies. *Curr. Nanosci.* **11**, 144–160 (2015)
- Kumar, L., et al.: Nanotechnology: a magic bullet for HIV AIDS treatment. *Artif. Cells Nanomed. Biotechnol. Int. J.* **43**(2), 71–86 (2015). <https://doi.org/10.3109/21691401.2014.883400>
- Parboosing, R., et al.: Nanotechnology and the treatment of HIV infection. *Viruses* **4**, 488–520 (2012). <https://doi.org/10.3390/v4040488>
- Upadhyay, V.P., et al.: Nano robots in medicine: a review. *Int. J. Eng. Technol. Manag. Res.* **4**(12: SE), 27–37 (2017). <https://doi.org/10.5281/zenodo.1157965>
- Manjunath, A., Kishore, V.: The promising future in medicine: nanorobots. *Biomed. Sci. Eng.* **2**(2), 42–471 (2014). <https://doi.org/10.12691/bse-2-2-3>
- Ummat, A., Dubey, A., Mavroidis, C.: Bio-nanorobotics—a field inspired by nature. In: *Biomimetics: Biologically Inspired Technologies*, by Yoseph Bar-Cohen. CRC Press, Boca Rotan, pp. 201–226 (2006)
- Li, J., et al.: Micro/nanorobots for biomedicine: delivery, surgery, sensing, and detoxification. *Sci. Robot.* **2**(4), 1–9 (2017)
- Bhuyan, M., Bardoloi, S.: Nanorobots—a panacea to HIV. *Int. Res. J. Eng. Technol. (IRJET)* **3**(11), 1309–1315 (2016)
- <https://www.verywellhealth.com/hiv-microscopy-in-pictures-48651>
- Khalil, H.K.: *Nonlinear systems*. Prentice Hall Inc, New Jersey (1996)
- <https://electronics.howstuffworks.com/nanorobot.htm>
- <https://www.azonano.com/article.aspx?ArticleID=4679>



Nanomedical Devices as a Tool for Consumer Research

Zvezdana Gavrilović and Mirjana Maksimović

Abstract

The recent intensive technology advancements fuel innovation in every area of modern society. Nanotechnology together with biotechnology, and ICT (Information and Communication Technology) represents a technology triad that has the potential to revolutionize every aspect of our lives in the 21st Century. The unique and fundamentally different physical, chemical, electrical, mechanical and biological properties of nanomaterials from the properties of largesize bulk counterparts, enable the fabrication, characterization, and the manipulation of functional and intelligent materials, devices, and systems opening a whole new universe of the applications. In the nanotechnology industry, which is expected to reach USD 132.41 by 2023, it is crucial to adequately market a product, service, or even new technology in order to successfully position it. The environment in which businesses operate is characterized by numerous competitions, products, dynamic and rapid changes, strong technology development and increasingly demanding consumers. Consumers are at the center of marketing activities and therefore it is crucial to get to know the consumers and establish a long-term relationship with them. It can be anticipated that economic expansion will lead to the rise of the nanotechnology sector through the stimulation of consumers and industry to use a wide range of nanotechnology-enabled products. Therefore, this paper deals primarily with the analysis of how nanotechnologies affect marketing and measure consumer

satisfaction that is crucial to the success of the enterprise in this industry. Nanotechnology's influence on sustainability is presented as well.

Keywords

Nanotechnology • Neuroscience • Nanomarketing • Nanomedicine • Sustainability • Consumer research

1 Introduction

Nanotechnology is a kind of technology that enables carrying out of science and engineering on the nanometer scale. Its advance is in the specific properties of nanoscale materials, compared to their bulk counterparts what enables the design and production of completely new materials and devices. Networking nanoscaled devices with existing communication networks and the Internet, have enabled the creation of a new networking paradigm, known as the Internet of Nano Things (IoNT). Although nanotechnology is present in a wide range of industrial and academic applications (Fig. 1), it is estimated that in the close future there will be no aspect of life untouched by nanotechnology and IoNT, opening a whole new world of previously unexplored application domains.

These facts imply the increasing interest in research and investments in the nanotechnology and IoNT that promise to bring significant innovations and enhancements in diverse domains. The nanotechnology market is estimated to exceed USD 132.41 billion by 2023, at an estimated Compound Annual Growth Rate (CAGR) of more than 19.8% during 2018–2023 [1] while the nanosensors market projects the growth from USD 90.6 million in 2017, to USD 4024.4 million by 2023, at a CAGR of 88.19%, during the same period [2]. According to the [3], the IoNT market is expected to grow from USD 6.42 billion in 2017 to USD 22.04 billion by 2023, at a CAGR of 22.81% (Fig. 2). Nanomedical devices market scenario anticipates the grow at a CAGR of

Z. Gavrilović

Faculty of Business Economy, University of East Sarajevo,
Semberskih ratara bb, 76300 Bijeljina, Bosnia and Herzegovina
e-mail: zvezdana.gavrilovic@fpe.ues.rs.ba

M. Maksimović (✉)

Faculty of Electrical Engineering, University of East Sarajevo,
Vuka Karadžića 30, 71123 East Sarajevo, Bosnia and Herzegovina
e-mail: mirjana.maksimovic@ef.ues.rs.ba

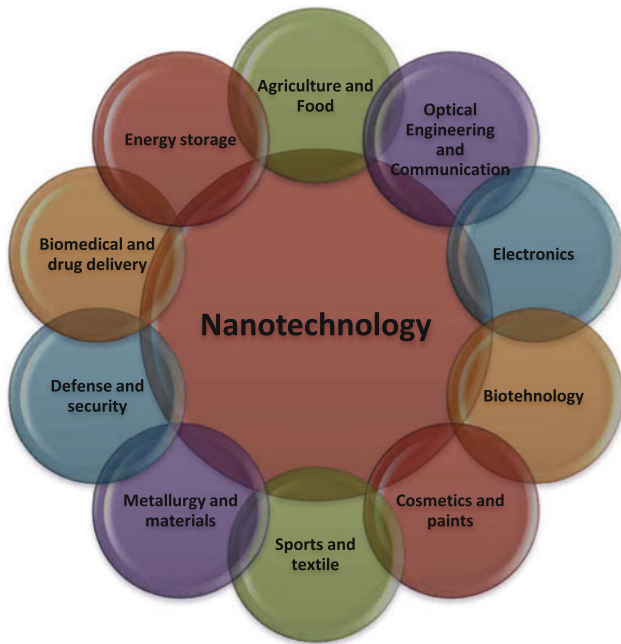


Fig. 1 Nanotechnology application areas

10.29% during forecasted period 2017–2023. Such huge nanotechnology-related markets will undoubtedly lead to their high influence in various fields. However, on that road, there are few challenges, such as huge capital investment in the research and development of nanotechnology and IoNT as well as their influences on human and the environment.

Nanotechnology utilization can solve the world’s numerous current problems. It is expected that in the coming decade nanotechnology will be omnipresent, bringing numerous benefits, mainly in industry, medicine, new computing systems, and sustainability [4]. In order to achieve the full potential nanotechnology has to offer, continued and focused investment in nanotechnology theory,

innovations, and commercialization, are demanded. This should lead to more sustainable nanotechnology applications, adapted to market needs.

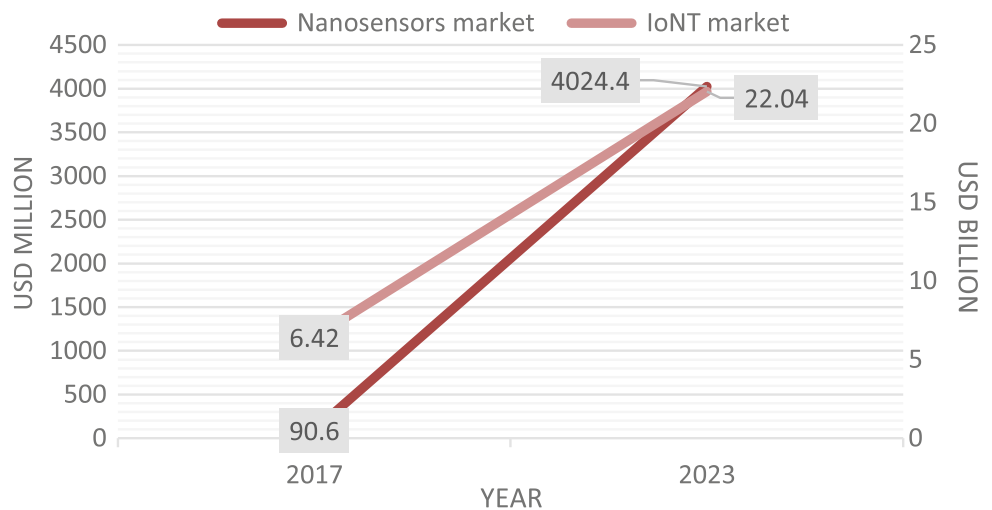
As people play the main role in the creation and acceptance of novel technology and approaches, there is an essential need to present benefits, potentials, applications, challenges, risks, and concerns of nanotechnology and nano-enabled products to potential consumers very clearly. The success of the nanotechnology and any other industry depends mainly on consumer acceptance. Appropriate advertising and marketing undoubtedly influence consumer acceptance. As well as numerous application domains, so marketing also didn’t remain immune to nanotechnology progress. Nanotechnology and Neuromarketing together have enabled the creation of a completely new marketing approach, known as Nanomarketing that enables a better and deeper understanding of consumers’ behavior.

The aim of this paper is to present the nanotechnology role in consumer research through the utilization of nanodevices, mainly used for medical purposes. Understanding consumer behavior helps marketers in improving their products, marketing, and advertising activities, prices, etc. Nanomarketing can also play a key role in the wide acceptance of nanotechnology and contribute to the realization of a sustainable world.

2 The Impact of Nanotechnology on Consumer Research

The medical applications of the nanotechnology knowledge and tools refer to nanomedicine. There is a wide range of nanomedicine applications, including diagnostics, therapeutics, synthesis and delivery of nanomedicines, regenerative medicine, biosensors, biomimetics, and bioinformatics among many others. With the help of nanomedical devices,

Fig. 2 The growth of nanosensors and IoNT markets



medical activities become smarter, minimally invasive, more precise and effective. However, numerous uncertainties and knowledge gaps related to the safety of nanotechnology influence its widespread acceptance.

The success of nanotechnology and any company and their long-term profit growth are directly linked with consumer loyalty. Connecting consumers with the company, and its services and products are of immense importance. Adequate marketing and advertising have been established on collected and analyzed consumer behavior data and market research. Therefore, numerous market actors largely invest in consumer behavior research. Novel technologies significantly contribute to obtaining data, demanded for appropriate marketing activities [5].

Nanotechnology, as one of the six key technologies of the 21st Century, has contributed, together with the Neuromarketing, to the development of a new multidisciplinary field known as Nanomarketing.

Neuromarketing uses neuroscience and its methods for marketing research. Neuroscience, with the help of nanotechnology, enables a better and deeper understanding of consumer behavior. The utilization of nanomedical devices to measure biometrics and brain activities of consumers can help in consumer behavior research, ultimately leading to enhanced marketing activities that will result in increased consumer acceptance and loyalty.

For instance, as a reaction to the products are mostly subconscious, electroencephalography (EEG) recordings give information about consumer emotional response to the commercial or product. The use of novel nano-sized EEG electrodes contributes to the development of new biomedical devices and the enlargement of their application domains.

With the help of Functional Magnetic Resonance Imaging (fMRI), it can be determined which product designs, commercials, price, etc., cause the most brain activity. Some recent studies prove that fMRI predicts consumer behavior better than questionnaires [6]. With the nanoscale magnetic resonance imaging (nano-MRI), the resolution of MRI measurements is scaled to the nanoscale. Nano-MRI includes the following techniques [7]:

- magnetic resonance force microscopy (MRFM),
- optically-detected magnetic resonance (ODMR) using nitrogen-vacancy (NV) centers, and
- many other applications of quantum mechanics and nanotechnologies.

As such nano-MRI improves MRI technology, and it is likely that nano-fMRI methods will be used in consumer research.

As visuals are processed faster than words, tracking eye movement enables quicker data about what consumers are interested in and attracted to. Combination of eye tracking

and EEG gives a more complete picture, what grabs consumers' attention and what happens in the consumer's brain at that moment.

In addition, the certain biometric measure is also helpful. Many psychological phenomena have their counterparts that can be measured with modern equipment. For instance, sweat rate can be measured via electrodermal activity (EDA) or galvanic skin response (GSR) respectively, while electromyogram (EMG) measures muscle potentials (e.g. face muscle activity) [8]. The future of devices which measure these biometric parameters is in nanotechnology solutions like a nano galvanic skin response—nano GSR, etc.

The presented facts show that nanotechnology is powerful in measuring neurophysiological signals. Based on advanced algorithms, the evaluation of customer' emotional states can be performed. The integration of nanotechnology and Neuromarketing, have resulted in Nanomarketing that solve all the limitation of Neuromarketing. The main benefits of Nanomarketing are [9]:

- Real-time measurements of emotional states,
- Utilization of unobtrusive and portable nanomarketing devices,
- Utilization of multifunctional nanomarketing devices to measure both neuronal and bio-physiological signals,
- Combination of laboratory experiments with daily life tests involving nanodevices, and
- Getting a balance between advanced nanomarketing techniques and moral, social, and ethical demands.

The progress in Neuroscience and appearance of Nanomarketing and its more precise and less invasive techniques and tools, help in better understanding the brain and its functioning. Understanding consumers' unconscious reactions and emotions, and their influence on decision-making increase effectiveness in marketing goals [10].

3 Nanomarketing and Sustainability

In order to achieve the full potential nanotechnology has to offer in numerous application domains, including marketing research, continued and focused investment in nanotechnology theory, innovations, and commercialization, are demanded. This should lead to more sustainable nanotechnology applications, adapted to market needs. The complete definition of sustainability includes environmental, economic, and social sustainability.

Nanotechnology, like any other technology, may have a negative influence on human health and the environment. The main disadvantages are related to potential nanotoxicity, increased waste quantities, greenhouse emissions and/or the

consumption of non-renewable raw materials. In order to create a smart and sustainable world, it is necessary to minimize the negative impacts of technological applications to human health and the environment. This can be achieved moving towards green nanotechnology, which aim is to maximize benefits and minimize harm. Green nanotechnology brings significant environmental, societal and economic benefits [11]. One of the key points for selling and wider acceptance of nanotechnology is its promise of more sustainable production of goods, using less non-renewable resources and hazardous substances, alongside decreased energy consumption. Green nanotechnology will lead to reduced costs and increase the likelihood of further investment and sustainable development of this technology field [12]. Nevertheless, intensive commercialization and market growth depend on better understanding of the nanotechnology benefits and risks, and on appropriate standards and regulations. The overall success of green nanotechnology depends on consumer acceptance.

Nanomarketing can contribute to sustainability in different ways, including the adoption of green nanotechnology among others. This can be achieved by better understanding how to increase consumers' attention and interest in green nanotechnology use, sustainable consumption, recycling, reuse, etc. [10]. The Nanomarketing can be applied in the development of more sustainable nanodevices and nanoproducts, more suitable marketing strategies for sustainable nanodevices and nanoproducts, and in increasing consumers' awareness about sustainable consumption.

4 Conclusion

Nanotechnology, as a key technology of the 21st Century, shows its power in improving existing materials and enable the creation of novel materials. Various types of novel nanomaterials and their unprecedented properties tailored specifically for use-case scenario, add the novel capabilities to the nanodevices. Nano-enabled devices are tiny, cheap, highly sensitive and efficient, with a wide spectrum of potential applications, among marketing didn't remain immune. Nanotechnology's role in marketing consists in the utilization of nanomedical devices for measuring brain activities, such as nanofMRI, nano EEG electrodes, nano GSR, etc. Based on measured neurophysiological signals, and applying sophisticated algorithms, the customer' emotional states can be evaluated. In this way, nanotechnology and neuroscience have created Nanomarketing, a multidisciplinary approach that enables insights into consumer behavior, what further helps marketers to perform adequate actions that will increase consumer acceptance and loyalty

and hence their profit. Nanomarketing can play a key role in the realization of a sustainable world through a deeper and better understanding of consumers' behavior related to sustainable activities, including green nanotechnology utilization. Even there are some moral, ethical, and social issues, Nanomarketing will undoubtedly revolutionize the understanding of consumer behavior. This will result in the development of consumer-tailored and sustainable products and services that will enhance consumers' lifestyles.

Conflict of Interest The authors declare that there is no conflict of interest regarding the publication of this paper.

References

1. IndustryARC: Nanotechnology market: by type (nano composites, nano devices, nano tools, nano materials and others), by applications (medicine & healthcare, environment, ICT, energy, nano EHS and others), by end-user industries (biotechnology, cosmetics, textile, electronics & semi-conductor, automobile and others)—Forecast (2018–2023) (2018)
2. Mordor Intelligence: Nanosensors market—segmented by type (physical nanosensor, chemical nanosensor, biological nanosensor), industry (healthcare, consumer electronics, automotive and industrial, aerospace and defense, power generation), and region—growth, trends, and forecast (2018–2023) (2018)
3. Research and Markets: Global internet of nano things (IoNT) market 2018–2023: nano sensors, nano processors, nano memory cards, nano power systems, nano antennas, nano transceivers (2018)
4. Omanović-Miklićanin, E., Maksimović, M., Vujović, V.: The future of healthcare: nanomedicine and internet of nano things. In: 1st Conference on Medical and Biological Engineering in Bosnia and Herzegovina. *Folia Med. Fac. Med. Univ. Saraeviensis.* **50**(1), 23–28 (2015)
5. Maričić, B.: Ponašanje potrošača, Ekonomski fakultet, Beograd, pp. 3–8 (2011)
6. The Neuromarketing labs: Technology [online]. <https://www.neuromarketinglabs.com/science/technology/> (n.d.)
7. Rosa, L., Blackledge, J., Boretti, A.: Nano-magnetic resonance imaging (NanoMRI) gives personalized medicine a new perspective. *Biomedicine* **5**(1), 7 (2017). <https://doi.org/10.3390/biomedicine5010007>
8. Müller, S.: Using Biometric Sensors to Increase Developers' Productivity. Faculty of Economics, University of Zurich, Zurich (2016)
9. Miletić, A., Guido, G., Prete, M.I.: Nanomarketing: a new frontier for neuromarketing. *Psychol. Mark.* **33**(8), 664–674 (2016)
10. Oliviera, J.H.C.: Neuromarketing and sustainability: challenges and opportunities for Latin America, *Latin American. J. Manag. Sustain. Dev.* **1**(1), 35–42 (2014)
11. Maksimović, M., Omanović-Miklićanin, E.: Towards green nanotechnology: maximizing benefits and minimizing harm. *CMBE-BIH* **2017**, 164–170 (2017). https://doi.org/10.1007/978-981-10-4166-2_26
12. Iavicoli, I., Leso, V., Ricciardi, W., Hodson, L.L., Hoover, M.D.: Opportunities and challenges of nanotechnology in the green economy. *Environ. Health* **2014**, 1378 (2014)

Near IR Exciton Theory of Ultrathin Crystalline Film Optics and Possibilities for Drug Delivery

S. M. Vučenović, J. P. Šetrajčić, and A. J. Šetrajčić-Tomić

Abstract

In this paper we have applied theory of exciton on the ultrathin molecular dielectric films—layered nanostructures with the thickness up to 20 atomic layers. We have calculated optical properties: the absorption, reflection and transparency indices as the function of frequencies of external electromagnetic field in near IR region. We showed that one of the significant properties of the ultrathin film is their interaction with substrate or environment, which could be represented through perturbation parameters. For symmetrically perturbed films, all optical properties depend on the position of the crystal plane with regard on boundary planes of the film. We have analyzed optical properties for the whole film structure based on the consideration for multiple reflection, absorption and transparency. The theory has been applied for the four-layered dielectric nanofilms with various different boundary conditions on film surfaces. As a result, we obtain some discrete resonant absorption lines, where their number, position and distribution strongly depend on the boundary parameter values, i.e. on the type and the technological process of their preparation/fabrication. While bulk made from the same material totally absorb the near IR region, in ultrathin films will appear only selective and discrete absorption (also with reflection and transparency too). These results could be used in optical engineering of nanostructures and technology of designing of new electronic, photonic and

photovoltaic devices. In addition, particularly designed nanoparticles are used in nanomedicine, whose behavior strongly depends on external electromagnetic field, in purpose of drug carry or delivery.

Keywords

Ultrathin crystalline films • Optical properties • Photonic engineering

1 Introduction

In the last decades an increasing interest in science is for nanotechnology and low—dimensional systems. This is primarily due to the possible practical application of these structures in electronics, optoelectronics, high-temperature superconductivity, biology and medicine [1, 2].

Nano-medicine is term referred as nanotechnology used in medicine, i.e. the repair, monitoring and control of human biological systems at the molecular level using nanostructures and nanotechnologies. This multidisciplinary science carries the possibility of observing and diagnosing, treating, constructing and controlling human biological systems at the cellular level, using nanoparticles and other nano-dimension materials, or low-dimensional systems [3–5].

Nano-medicine is based on idea that low-dimensional systems (such are nanoparticles) could easily penetrate into the human cells and treat the disease on their source, i.e. in the cell [6–8].

Except the fact that nanoparticles are actually very small (or small enough) that could easily penetrate into the cell, low-dimensional systems have one more important characteristic—they are highly reactive. This is consequence of their huge surface to volume ratio. However, for complete understanding of remarkable and very different characteristics of nano-dimensional systems, we need to understand the behavior of elementary charges and their transfer through nanostructures, especially on their boundaries. Thereby we

S. M. Vučenović

Faculty of Natural Sciences and Mathematics, University of Banja Luka, Republic of Srpska, Bosnia and Herzegovina
e-mail: sinisa.vucenovic@pmf.unibl.org

J. P. Šetrajčić

Faculty of Sport, University “Union – Nikola Tesla”, Novi Beograd, Vojvodina, Serbia
e-mail: jovan.setrajcic@gmail.com

A. J. Šetrajčić-Tomić (✉)

Faculty of Medicine, University of Novi Sad, Vojvodina, Serbia
e-mail: setrajcic.a@gmail.com

assume boundary-processes as interaction between boundary layer of nanostructure and their environment (which could be—and usually it is electrolytic or charged). This interaction is responsible for the active diffusion processes and one way to trigger it could be using the light or electromagnetic field.

Low-dimensional systems include various nanostructures such are nanoparticles, ultrathin films, quantum wires and quantum dots...), but we would limit our theoretical research on ultrathin films. This assumption is justified while film structures are somewhat uncomplicated for theoretical modeling, and in the same time they simultaneously retains maximum surface to volume ratio.

Ultrathin films could be excellent candidates in nano-medicine as drug carriers (for example, drug molecules being absorbed and linked on boundary surface on the ultrathin film). In addition, nanoparticles could be used as drug carriers as well, within drug molecules encapsulated, where we assume that ultrathin film are curved (and closed) surfaces! Is that sense our further research is justifying limited on ultrathin film modeling. The exact moment of drug release (or triggering) is defined with the external light, where under specific conditions (when required) capsulated structure (i.e. curved layers of ultrathin film) disintegrate. This could be achieved according the fact and prediction that nanoparticles (and ultrathin films) have different physical properties, compared with bulk. One of the proposed mechanism of triggering is model of excitons, quasiparticles composed of electron-hole pairs, bounded with Coulomb's interaction. Excitons, which are being created from external electromagnetic field, could absorb and transfer energy trough the crystal but not the charge. Hypothesis, that some discrete energy could trigger process of controlled release of drug, open new possibilities for nanoparticle drug engineering. It has been reported that process of triggering for anticancer drug delivery could be achieved by the near IR region of electromagnetic field [9, 10], and this region of light is precisely that where optical properties of ultrathin molecular films dramatically change their behavior, due to the exciton creation processes.

2 Optical Properties of Ultrathin Films

If we want to calculate optical characteristics of ultrathin film, we need to determine dynamic dielectric permittivity. One of the approach is using method of the Green's function [11], where:

$$\varepsilon_{n_z}^{-1}(\omega) = 1 - 2\pi i F [G_{n_z}(\omega) + G_{n_z}(-\omega)], \quad (1)$$

here F is structural factor, and $G_{n_z}(\omega)$ are Green's function $G_{n_z}(\omega) \equiv G_{n_z, m_z}(\omega)$, where Green' function are defined by Bose-operators $G_{\vec{n}\vec{m}}(t) = \langle\langle B_{\vec{n}}(t) | B_{\vec{m}}^+(0) \rangle\rangle$ defined by position vector in crystals \vec{n}, \vec{m} .

In ultrathin film model, crystalline parallel surfaces along XY planes are infinite, while in Z direction has finite thickness $L = Na$, where N is maximum number of the film planes (Fig. 1).

Ultrathin films could be made by various method of deposition (chemical vapor deposition CVD or physical vapor deposition PVD) or with doping methods. No matter what method is used—boundary layers are somewhat different from the internal planes, while boundary planes interact with substrate (on the lower layer) and environment (on the upper layer of ultrathin film). When excitons appear in dielectrics, as consequence of incoming external light, they are usually localized on site (Frenkel's excitons), and they could exchange energy with closest neighbor. However, because of existence of boundary surfaces, energies of excitons on sites (nodes) and transfers of energies of excitons between boundary ($n_z = 0; n_z = N$) and their neighbor surfaces ($n_z = 1; n_z = N - 1$) are being perturbed, which could be presented on following way [12–14]:

$$\begin{aligned} \Delta_{\vec{n}} &\equiv \Delta(1 + d_0\delta_{n_z,0} + d_N\delta_{n_z,N}); \\ X_{\vec{n},\vec{n}+\vec{\lambda}} &\equiv X(1 + x_0\delta_{n_z,0} + x_N\delta_{n_z,N-1}); \\ X_{\vec{n},\vec{n}+\vec{\lambda}} &\equiv X(1 + x_0\delta_{n_z,1} + x_N\delta_{n_z,N}), \end{aligned} \quad (2)$$

where d is perturbation parameter for the energy on site, and x is perturbation parameter for the transfer energy in boundary (upper and lower) layers.

As we can see from Eq. 1, for obtaining optical properties, we must first calculate exact Green's function. To do so, we assume that exciton Hamiltonian is in harmonic approximation [15], and that Green's function satisfy equation of motion for the Green's function [11]. Taking into account boundary conditions (2) and after fully time and partially spatial Fourier transformations we obtain system of $N + 1$ nonhomogenous algebraic—difference equations for unknown Green's functions $G_{n_z}(\omega)$.

2.1 Optical Properties Calculated by Layers

From the Maxwell theory dielectric permittivity is complex value: $\varepsilon(\omega) = \varepsilon'(\omega) + i\varepsilon''(\omega)$. Maxwell showed that permittivity is equal to the square of refraction index, and that its real and imaginary parts is related with optical properties of medium: $\varepsilon = |n + i\kappa|^2$, from where we obtain relations: $\varepsilon' = n^2 - \kappa^2$ and $\varepsilon'' = 2n\kappa$, and from there we obtain:

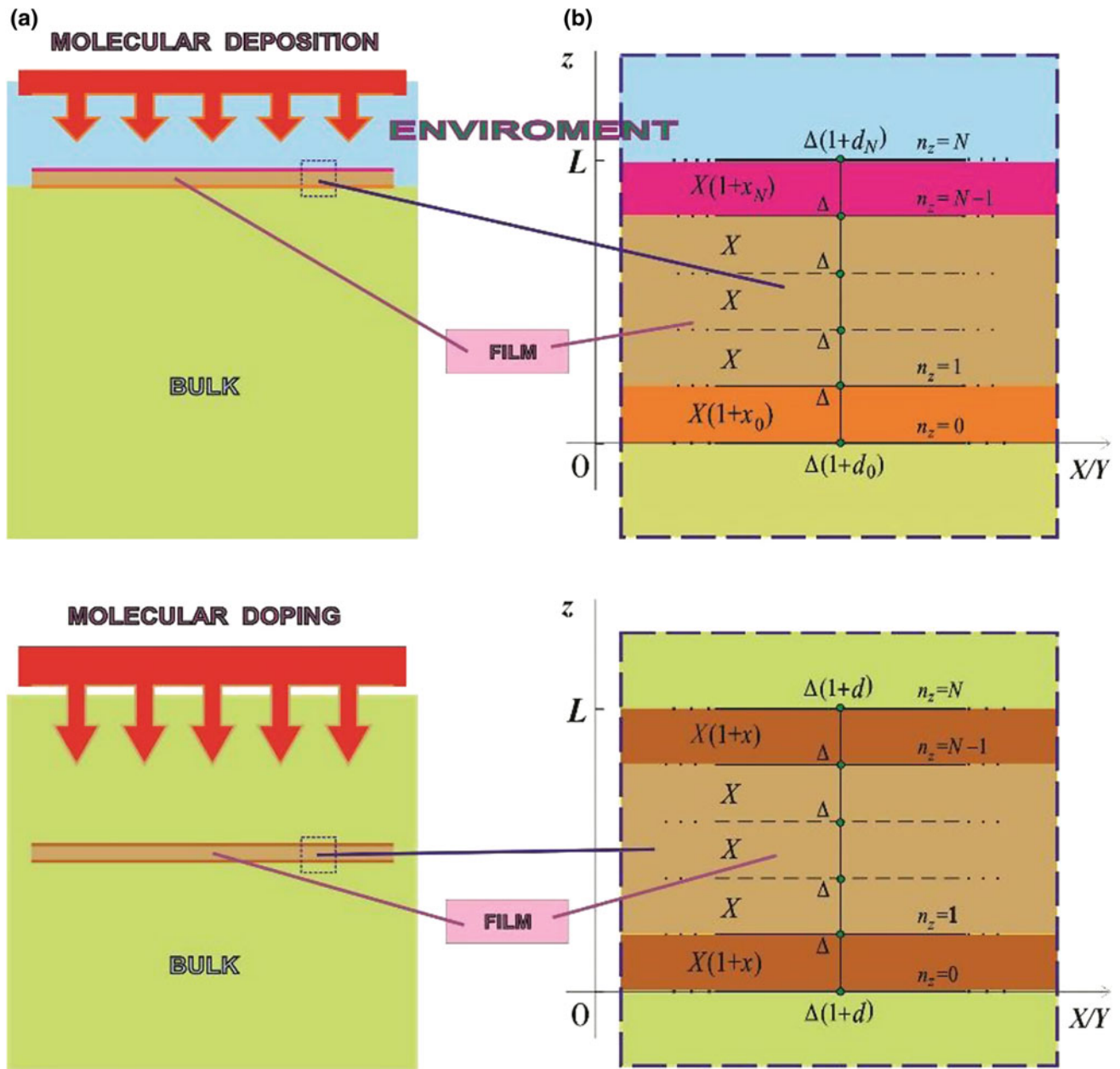


Fig. 1 Model of ultrathin film

$$\kappa_{n_z}(\omega) = \sqrt{\frac{\varepsilon'_{n_z}(\omega)}{2} \left\{ \sqrt{1 + \left[\frac{\varepsilon''_{n_z}(\omega)}{\varepsilon'_{n_z}(\omega)} \right]^2} - 1 \right\}}, \quad (3)$$

$$n_{n_z}(\omega) = \sqrt{\frac{\varepsilon'_{n_z}(\omega)}{2} \left\{ \sqrt{1 + \left[\frac{\varepsilon''_{n_z}(\omega)}{\varepsilon'_{n_z}(\omega)} \right]^2} + 1 \right\}}. \quad (4)$$

Knowing above expressions, we could calculate reflection and transparency indices [16]:

$$r_{n_z}(\omega) = \frac{[n_{n_z}(\omega) - 1]^2 + \kappa_{n_z}^2(\omega)}{[n_{n_z}(\omega) + 1]^2 + \kappa_{n_z}^2(\omega)}, \quad (5)$$

$$t_{n_z}(\omega) = 1 - n_{n_z}(\omega) - \kappa_{n_z}(\omega). \quad (6)$$

All equations depend strongly on layer position and perturbations on boundaries. One example of calculated optical indices is shown on Fig. 2, when we observe asymmetrical perturbed ultrathin film (with different perturbation parameters above and on the top of the film). One can see that all optical indices manifest discrete lines within one

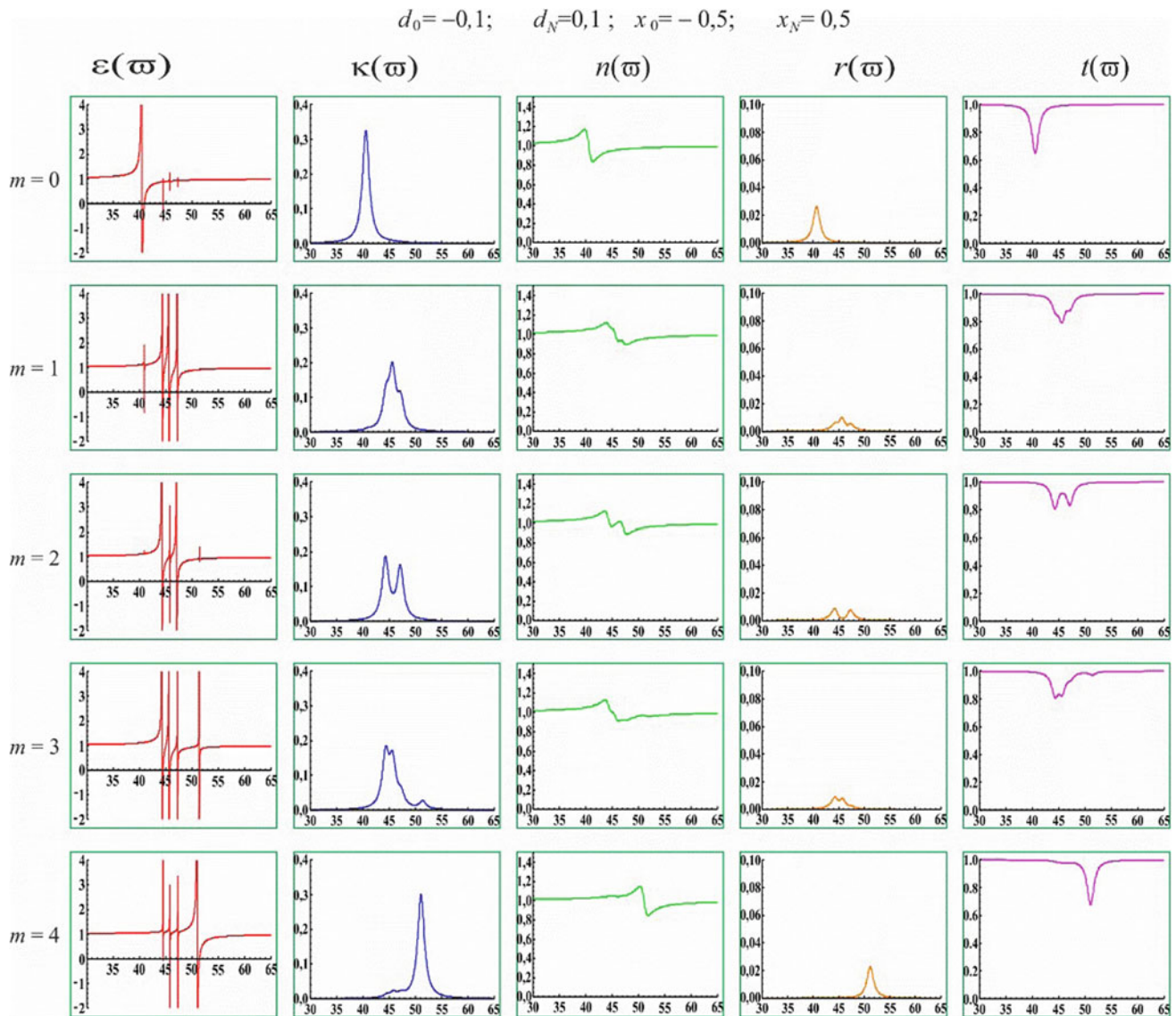


Fig. 2 Permittivity and optical indices of asymmetrically perturbed film

layer of the film. Number of lines corresponds to the number of atomic planes in ultrathin films, but intensity of lines and their distribution depends on perturbation parameters on boundary layers. If we compare this behavior with optical properties of the bulk we can see that absorption zone in bulk is complete continual and for molecular crystal that zone laying in the IR range [11]. In numerous calculations we conclude that perturbation parameters (i.e. conditions on boundary planes of the film) strongly determine optical properties, such as number of discrete lines in optical spectra. As we see in Fig. 2, on the first plane ($m = 0$) dominate one resonant peak, but for the complete optical characteristics we need to calculate contribution of the whole film, i.e. of the all other planes in ultrathin film. In bulk structure reflection occur outside the absorption zone, while

in ultrathin films reflection is present partially on every crystalline plane. This is the reason of non-transparency in bulk, while ultrathin film becomes transparent except $N + 1$ discrete frequencies. Those frequencies are absorbed and/or reflected on ultrathin planes.

2.2 Optical Properties for the Whole Ultrathin Film

To calculate optical properties for the whole film we need define values which represent overall optical properties of the film. If we observe film made from only two planes (each plane have their own refraction index) and calculate overall refraction index for that film, we obtain $\frac{2}{n} = \frac{1}{n_1} + \frac{1}{n_2}$. We

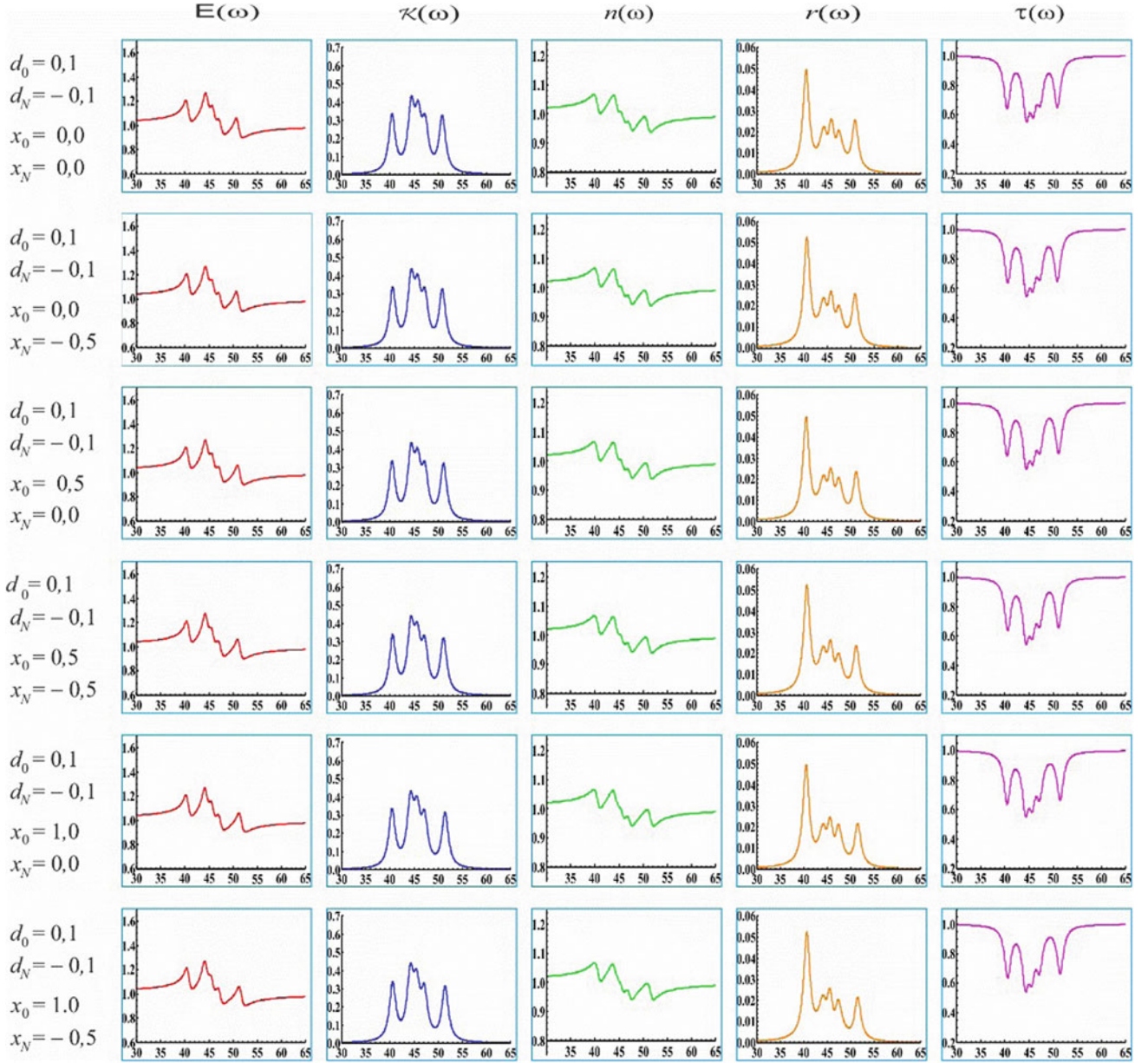


Fig. 3 Optical properties for the whole ultrathin film for the various perturbations

could expand this relation on 3-planes film as two planes + 1, and generalizing that we obtain overall refraction index for the $N + 1$ planes ultrathin film:

$$\frac{N}{n_f(\omega)} = \sum_{N_z=0}^N \frac{N}{n_{N_z}(\omega)} \Rightarrow n_f(\omega) = N \left(\sum_{N_z=0}^N n_{N_z}^{-1}(\omega) \right)^{-1}. \quad (7)$$

If we observe incoming polychromatic light beam (in the near IR region) with their intensity equal to unity, it could be shown that it is possible to neglect all inner plane multiple reflection, refraction and absorption processes [17]. Passing

near IR light through the each plane of the whole film, overall transparency become:

$$\tau_f(\omega) = \tau_0 \prod_{n_z=0}^N (1 - \kappa_{n_z}), \quad (8)$$

while the whole ultrathin film absorb:

$$\kappa_f(\omega) = \kappa_0(\omega) + \sum_{n_z=1}^N \kappa_{n_z} \tau_{n_z-1}, \quad (9)$$

where $\tau_{n_z}(1 - \kappa_{n_z})\tau_{n_z-1}$, $n_z = 1, 2, 3, \dots, N$. According to the energy conservation law must be $\tau_f + \kappa_f + r_f = 1$. Also, overall permittivity is calculated with $\varepsilon_f(\omega) \equiv |\varepsilon_f(\omega)| = n_f^2(\omega) + \kappa_f^2(\omega)$. Results of calculation of optical properties for the whole film are shown on Fig. 3.

From the graphics on Fig. 3 one can see that, taking into account $r \ll \kappa \wedge \tau$, width of transparency zones are much bigger than absorption zone. This is the most important difference of optical properties of the film, when compared with optical characteristics of the bulk structures, which are completely opaque. Therefore, instead bulk sample—total absorber, samples with the same chemical and crystalline structure, made as ultra-thin films (quasi 2D structure), exist as transparent in the greater part and as selective absorbers of some (one or more) almost discrete frequencies from the same near IR and complete IR region.

3 Conclusion

In this paper we have showed that excitons are responsible for specific optical properties in ultrathin films, when compared with bulk samples. Nano-films become almost discrete absorbers, with resonant frequencies strongly dependant on boundary conditions between ultrathin film and his environment. Properties of discrete absorption could make ultrathin films a good candidates for specific sort of filters of external radiation, with near IR absorption zone for molecular nanostructures. In that way, ultrathin films or nanoparticles (that could be considered as lamellar nanostructures with mutually curved planes) could carry some attached molecules, such as medicine drugs, that could be controlled and released with external discrete IR light. Interaction of molecular ultrathin film and medicine drug molecules is represented trough the perturbation parameters. Our model, knowing these perturbations, could predict what resonant absorption frequencies are needed for medicine drug manipulation.

Acknowledgements This work was partially supported by the Ministry of Education, Science and Technological Development of the Republic of Serbia (Grants: ON-171039 and TR-34019) and by the Provincial Secretariat for High Education, Science and Technological Development of Vojvodina (Grant: 142-451-2469/2017-01/02) as well as by the Government of Republic of Srpska, Ministry for Scientific and Technological Development, Higher Education and Information Society.

References

1. Guozhong, C.: Nanostructures and Nanomaterials Synthesis, Properties and Applications. World Scientific, Singapore (2004)
2. Štrajčić-Tomić, A.J., Popović, J.K., Vojnović, M., Džambas, L. D., Štrajčić, J.P.: Review of core-multishell nanostructured models for nano-biomedical and nanobiopharmaceutical application. *Bio-Med. Mater. Eng.* **29**, 451–471 (2018). <https://doi.org/10.3233/bme-181002>
3. Morrow, K.J., Bawa, R., Wei, C.: Recent advances in basic and clinical nanomedicine. *Med. Clin. N. Am.* **91**, 805–843 (2007)
4. Delerue, C., Lannoo, M.: Nanostructures—Theory and Modelling. Springer, Berlin (2009). ISBN 978-3-662-08903-3
5. Schaefer, H.E.: Nanoscience—The Science of the Small in Physics, Engineering, Chemistry, Biology and Medicine. Springer, Berlin (2010). ISBN 978-3-642-10559-3
6. Gupta, R.B., Kompella, U.B.: Nanoparticle Technology for Drug Delivery. Taylor & Francis, New York, USA (2006)
7. Balandin, A.A., Nika, D.L.: Phononics in low-dimensional materials. *Mater. Today* **15**(6), 266–275 (2012)
8. Vučenović, S.M., Rodić, D., Štrajčić, J.P.: Preferences for Nano-Delivery Optical Multilayer Core-Shell Model. LAP Lambert Academic Publishing, Saarbrücken, Germany. p. 101, ISBN:978-613-4-94013-9 (2018)
9. Liu, J., Bu, W., Pan, L., Shi, J.: NIR-triggering anticancer drug delivery by upconverting nanoparticles with integrated azobenzen-modified mesoporous silica. *Angew. Chem.* **125**(16), 4471–4475 (2013). <https://doi.org/10.1002/ange.201300183>
10. Štrajčić-Tomić, A.J., Rodić, D., Štrajčić, I.J., Sajfert, V.D., Štrajčić, J.P.: Basics of optical engineering—analysis of environmental and quantum size effects on the optical characteristics of molecular crystalline nanofilms. *Photonic Nanostruct.* **31**, 115–128 (2018). <https://doi.org/10.1016/j.photonics.2018.05.011>
11. Dzialoshinski, I.E., Pitaevski, L.P.: Van der waals forces in an inhomogeneous dielectric. *Zh.eksp. teor. Fiz.* **36**, 1977, (1959)
12. Štrajčić, J.P.: Exact microtheoretical approach to calculation of optical properties of ultralow dimensional crystals. [arXiv.org/1004.2387v1](https://arxiv.org/abs/1004.2387v1) [cond-mat-sci] (Apr 2010)
13. Pelemiš, S.S., Štrajčić, J.P., Markoski, B., Delić, N.V., Vučenović, S.M.: Selective absorption in two layered optic films. *J. Comput. Theor. Nanosci.* **6**(7), 1474–1477 (2009)
14. Štrajčić, J.P., Jaćimovski, S.K., Sajfert, V.D., Štrajčić, I.J.: Specific quantum mechanical solution of difference equation of hyperbolic type. *Commun. Nonlinear Sci. Numer. Simulat.* **19**(5), 1313–1328 (2014)
15. Agranovich, V.M., Ginzburg, V.L.: Crystaloptics with Space Dispersion and Theory of Excitons, Moskwa. Nauka, USSR (1979)
16. Mahan, G.: Many Particle Physics. Plenum Press, New York, USA (1990)
17. Štrajčić, I.J., Rodić, D., Štrajčić, J.P.: Optical properties of layers of symmetric molecular nanofilms. *J. Opt.* **44**(1), 1–6 (2015)

Phonon Engineering in Nanostructures for Targeted Drug Delivery

Dušan I. Ilić, Silvija Lučić, Saša Vujnović, Li Sen, Ranko Škrbić, and Miloš A. Lučić

Abstract

In this paper, the possibilities of efficient targeted delivery of drugs by using nano-devices are pointed out, with special emphasis on the physical properties of used materials. Particular attention was paid to the analysis of the phonon subsystem in the above-mentioned structures since it is expected that it can play a significant role in the transport and release of drugs, as well as in the biodegradation of the carrier nanomaterials. Nano-devices used as carriers also need to have properties that make them suitable for biomarkers so that they can be transferred to precisely defined sites in the body. This reduces the side effects of drugs and increases the efficiency of their use.

Keywords

Targeted drug delivery • Nanostructures • Phonon subsystem

1 Introduction

Nanotechnology is a multidisciplinary field based on the study of processes that take place on the nanometer scale, as well as on the design, synthesis and application of materials

D. I. Ilić (✉)

Faculty of Technical Sciences, University of Novi Sad,
Novi Sad, Serbia
e-mail: dusilic69@uns.ac.rs

S. Lučić · M. A. Lučić

Faculty of Medicine, University of Novi Sad, Novi Sad, Serbia

S. Vujnović · R. Škrbić · M. A. Lučić

Faculty of Medicine, University of Banja Luka, Banja Luka,
Republic of Srpska, Bosnia and Herzegovina

L. Sen

Medical Imaging Department, Cancer Hospital of China Medical
University, Liaoning Cancer Hospital, Shenyang, Liaoning
Province, People's Republic of China

with nanometer dimensions [1–3]. It is, therefore, a technology that manipulates with individual atoms, small molecules, or with a single macromolecule. The development of nanotechnology began intensively when it was discovered that the reduction of dimensions in order to confine the motion of the carriers results in completely altered physical properties of the observed nanostructure compared to the corresponding bulk sample.

The essential connection between biology and medicine with nanotechnology arises from the fact that bacteria, cells and active components of biological living organisms have nanometer-size dimensions. Our current understanding of the processes taking place in biological organisms at the nanometer level treats molecular biology as a “living proof of nanotechnology”. Understanding the role of nano-physics in biological structures in nature can indicate the design of artificially made sensors, motors and other devices for applications in biomedicine [4–6]. It is also important to note that biological labelling is far more efficiently carried out with the help of nanostructures (mostly CdSe quantum dots) than with conventional organic fluorescence molecules or radioactive sources [7]. The reason lies in the fact that quantum dots have a very narrow emission spectrum (~30 nm) and that due to the quantum confinement, color (wavelength) which the quantum dot emits depends on its size. But the very same example indicates the potential dangers of the applications of nanostructures since the CdSe quantum dots are lethal for living cells because they release extremely deadly Cd-ions.

Artificial nanostructures (nanoparticles and nano-devices), which are of the same size as the biological entities, can be put in the controlled interaction with biomolecules both on the surface and inside the cell. In this context, the application of nanotechnology in medicine has led to the foundation of an extremely promising field—nanomedicine, which consists of three interrelated areas: nanodiagnostics, regenerative medicine and targeted delivery of drugs. Nanodiagnostics aims at identifying the disease at the earliest stage, ideally at the level of a single cell, while

regenerative medicine focuses on the mechanisms of self-recovery of the body in preventing and treating chronic diseases and helping to the victims of injuries. The purpose of targeted delivery of drugs is the development of alternative techniques for more efficient transport of the medications to the site of the disease, improved patient response, reduction in the cost of health care, but primarily the identification of new ways of delivering those classes of medicines that can not be effectively delivered by conventional means.

Studies have shown [8] that the effectiveness of the administration of a drug largely depends on the way in which it is administered, which particularly refers to the therapeutic effects in malignancies. One of the most promising potentials for use of the nano-devices, such as fullerenes, nanotubes, nanoparticles, smart polymers etc. [9], is that they can be filled with drugs, lead to an appropriate site in the body, forced by some external stimulus (electric or magnetic field etc.) to disintegrate and release the drug and then to be safely removed from the body. To make this possible, it is necessary to understand the basic physical properties of nanostructures, such as their mechanical, thermodynamic and optical characteristics. Research shows that the realization of this goal is practically impossible without examining the nano-devices phonon subsystem, being the most important and always present quasi-particle collective in condensed matter.

2 Phonon Subsystem in Nanostructures

Phonons are collective mechanical oscillations of atoms (molecules) and constitute the most important system of excitations in a condensed matter because they are present in all systems and their influence, more or less, changes the behaviour of all other objects or excitations in the structure. This influence reflects primarily in that they determine the thermodynamics of the system, but also its optical and conductive properties could not be exactly explained without phonons. The main fact related to phonon properties in nanostructures is the absence of the so-called acoustical phonons, i.e. phonons whose energy tends to zero when phonon momentum tends to zero. This means that an activation energy not equal to zero is necessary for exciting phonons in these structures. Such surprising characteristics require revision of all results obtained regarding bulk theories of phonons. Therefore, the contribution of phonon subsystems to physical analysis is the first step in a research of nanostructure properties. By selecting the suitable materials for nanostructure and by tailoring of the desired properties of its phonon energy spectra, it is possible to achieve that they act as drug carriers with desirable physical properties, which include biocompatibility, physical and

chemical stability in the transport of the drug to the targeted place in the body and biodegradability without toxic effects. It turned out that nanostructures in the form of ultrathin films (graphene and its derivatives such as graphene oxide—GO, reduced graphene oxide—RGO and GO-nanocomposites) [10] and quantum dots have the greatest perspective in this respect.

2.1 Phonon Properties of Ultrathin Films

Ultrathin crystalline films are crystalline structures with disturbed translational symmetry along a direction perpendicular to the plane of the film (z direction in the model on Fig. 1), in which states on boundaries are different from those inside the structure [11, 12].

Carrier movement in ultrathin film is confined along z direction, while unbounded along x and y directions. That means that film structure under consideration have two boundary surfaces parallel to the XY planes (for $z = 0$ and $z = N_z a$, N_z is the number of atoms along z direction and a is the lattice constant). Along z -axis there are $N_z + 1$ atoms. Despite the fact that there are no atoms belonging to the film above the upper and below the lower boundary surface of the film, we assume that interaction between boundary layers and atoms of external environment nevertheless exists through changed Hooke's forces. Elastic constants which describe these interactions are modified with appropriate coefficients ε and γ (boundary parameters), as shown in Fig. 1.

Dispersion law of phonons in ultrathin films is obtained in form¹:

$$\varepsilon_{\vec{k}} = 2\sqrt{\sin^2 \frac{ak_x}{2} + \sin^2 \frac{ak_y}{2} + \sin^2 \frac{ak_z(v)}{2}}, \quad (1)$$

(v is the atom counter along z direction, $v = 1, 2, \dots, N_z + 1$) which is almost exactly the same as the one for bulk structures [11, 12], with exception that quasimomentum of phonons in ultrathin films can take only discrete values in z direction (k_z), and is continual in x and y directions (k_x, k_y). The major consequence of this fact is that the phonons in ultrathin films possess lower and upper energy gaps (Δ_{\min} and Δ_{\max}), as depicted in Fig. 2. It means that the zone of allowed phonon energies in ultrathin films is narrower than that in macroscopic samples for the value of the sum of these gaps. This fact makes the basis of the idea of phonon engineering [13, 14].

Confinement of phonons due to the size-reduction in ultrathin films results in dimensional quantization of phonon

¹For a detailed mathematical derivation, we refer the reader to the Refs. [11] and [12].

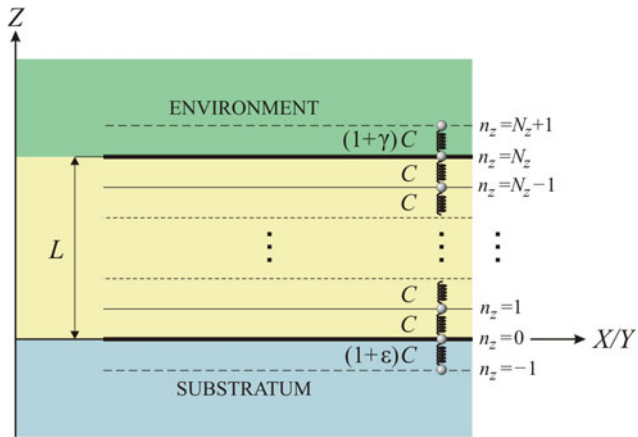


Fig. 1 Model structure of the ultrathin crystalline film that is confined along z direction, while unbounded along x and y directions. Elastic constants which refer to interactions between boundary layers and atoms of the external environments are modified with appropriate coefficients ϵ and γ (boundary parameters)

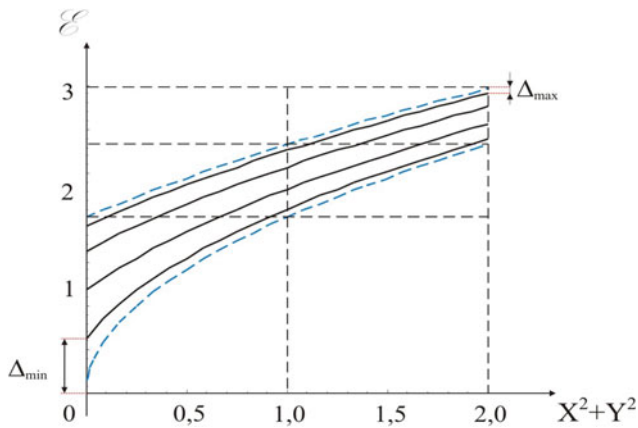


Fig. 2 The phonon dispersion law for the four-layered ultrathin film structure. It can be seen that the energy spectra is discrete and possess lower (Δ_{\min}) and upper (Δ_{\max}) energy gap

branches and substantial modification of their energy spectrum, group velocity, and polarization [15]. The concept of phonon engineering is based on these changes, in order to improve physical properties of the material under study and make it suitable for drug carrier. In homogeneous layers, phonon engineering can be achieved either by changes in the size of the structure or by changes in the exterior surfaces (parameters ϵ and γ).

For the lesser values of the boundary parameters, the localized phonon states do not appear, but all the states are evenly distributed within the phonon bulk zone across all layers of the film. With an increase of the values of parameters, one ($1 \leq \epsilon, \gamma < 1, 5$) or two ($1, 5 \leq \epsilon, \gamma \leq 2, 5$) localized states may occur. Studies have shown [12] that

these are the surface phonon states, with the greatest distribution probability at the very boundary surfaces of the film (one or both). These localized states are of the greatest physical importance because their presence surely changes the behaviour of the phonon subsystem in the ultrathin film. It is not difficult to conclude that due to the presence of these localized phonon states, the interactions of all (quasi)particles present in this structure will have to be redefined.

2.2 Phonon Properties of Quantum Dots

Quantum dots (QDs or artificial atoms) [16] are confined crystalline structures in which translational symmetry is disturbed along all three crystallographic directions (x , y and z , Fig. 3).

Quantum dots have six boundary surfaces: two of them are parallel to the XY planes (for $z = 0$ and $z = N_z a$), two to XZ planes (for $y = 0$ and $y = N_y a$), and two to YZ planes (for $x = 0$ and $x = N_x a$) thus, these structures are confined along x , y and z directions. Along x -axis there are $N_x + 1$ atoms, along y $N_y + 1$ atoms, and along z -axis $N_z + 1$ atoms. It is taken into account that an interaction between atoms in boundary layers of the quantum dot and its surroundings exists, no matter that along x , y and z directions outside boundary surfaces there are no atoms belonging to the quantum dot; however, boundary atoms are coupled through changed elastic constants with the atoms of the external environment, wherefore those elastic constants which describe an interaction between atoms of boundary surfaces and external areas are modified with appropriate coefficients.

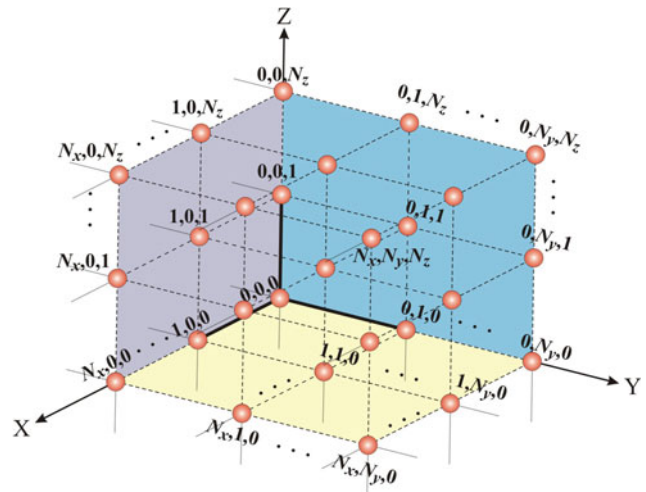


Fig. 3 Quantum dot model; translational symmetry is disturbed along all three crystallographic directions x , y and z

A simpler but more pragmatic and realistic approach implies that the quantum dot atoms are surrounded by atoms or molecules belonging to only two different environments, which leads to the situation similar to that in an ultrathin film.

Theoretical analysis [16] shows that the phonon dispersion law in the described quantum dot model-structure is obtained in the form:

$$\varepsilon_{\vec{k}} = 2\sqrt{\sin^2 \frac{ak_x(\chi)}{2} + \sin^2 \frac{ak_y(\mu)}{2} + \sin^2 \frac{ak_z(v)}{2}} \quad (2)$$

(χ , μ and v are atom counters along x , y , and z directions, $\chi = 1, 2, \dots, N_x + 1$, $\mu = 1, 2, \dots, N_y + 1$, $v = 1, 2, \dots, N_z + 1$, respectively) similar to that of the bulk structures [11, 12] and ultrathin films, Eq. (1). Main difference is, however, that phonon quasimomentum in quantum dots takes discrete values in all three directions. It can also be seen that minimum phonon energy in quantum dots differs from zero, and is given by:

$$\begin{aligned} \Delta_{\min} &= \varepsilon_{\vec{k}_{\min}} = \varepsilon_{k_x^{\min}, k_y^{\min}, k_z^{\min}} \\ &= 2\sqrt{\sin^2 \frac{ak_x^{\min}(\chi)}{2} + \sin^2 \frac{ak_y^{\min}(\mu)}{2} + \sin^2 \frac{ak_z^{\min}(v)}{2}} \end{aligned} \quad (3)$$

$$\begin{aligned} k_x^{\min}(\chi) &= k_x(1) = \frac{\pi}{a} \frac{1}{N_x + 2}; \\ k_y^{\min}(\mu) &= k_y(1) = \frac{\pi}{a} \frac{1}{N_y + 2}; \\ k_z^{\min}(v) &= k_z(1) = \frac{\pi}{a} \frac{1}{N_z + 2} \end{aligned}$$

while the corresponding minimum phonon frequency is:

$$\omega_{\min} = 2 \frac{v}{a} \sqrt{\sin^2 \frac{\pi}{2(N_x + 2)} + \sin^2 \frac{\pi}{2(N_y + 2)} + \sin^2 \frac{\pi}{2(N_z + 2)}} \neq 0. \quad (4)$$

As is the case in ultrathin films, there is an energy gap in phonon spectra of quantum dot due to the influence of the quantum size effect. It can, therefore, be concluded that in quantum dots, as in other nanostructures, spatial restriction of acoustic and optical phonons unavoidably changes their properties in comparison with bulk materials. Phonon confinement in low dimensional structures leads to the emergence of the quantized energy subbands with corresponding alteration of the phonon density of states. The changes in the phonon dispersion law lead to modification in the electron-phonon scattering rates, optical properties of the nanostructured materials, and phonon scattering on defects, boundaries and other phonons.

As regarding potential use of quantum dots in targeted drug delivery, it has been reported [17] that integration of biomaterials and semiconductor nanocrystal quantum dot (the drug-loaded chitosan-encapsulated ZnO:Mn²⁺ QDs) already gave very promising results in delivering tumor-targeted drugs. Moreover, due to the abilities to emits light, to glow or to fluorescence brightly when excited by a light source such as a laser, quantum dots are emerging as a new class of fluorescent probes for biomolecular and cellular imaging, which makes them suitable for imaging, blood cancer assay, cancer detection and treatment [18].

3 Conclusion

Nanotechnology has recently begun to change the methods of medical diagnostics and drug delivery. The development of various laboratory tools and nanoparticle-based methods, as well as the nanoentities for clinical diagnostics and therapy, are among the main goals of current research. In order to release the full potential of nanotechnology, nanoentities must be multifunctional and capable of performing a large number of tasks without any side effects as efficiently as possible. To achieve this goal it is necessary to carry out further basic and applied research aimed at understanding the physical and chemical properties of nanoparticles, as well as their interactions with cells and tissues during various physiological and pathological processes.

In this paper, the possibilities of efficient targeted delivery of drugs by using nanodevices are discussed, with particular attention to the analysis of their phonon subsystem, since it is expected that it can play an important role in the transport and release of drugs, as well as in the biodegradation of the carrier nanomaterials. The phonon subsystem has been pointed out because it is always present in solids, regardless of their conducting properties, and because it is easy to manipulate with. Dimensional confinement of phonons in nanostructures (ultrathin films, quantum dots, etc.) highly influences their physical properties, which creates the foundation for the idea of phonon engineering (nano-phononics). By knowing the phonon dispersion law for the nanostructure used as a drug carrier and its activation energy (i.e. energy of the lower gap), it is possible to manipulate with it in a purpose of the targeted drug delivery and controlled drug release. Moreover, once that the medicine is brought to the desired place in the organism, it is possible to use an external stimulus (for example, electric or magnetic field) to make oscillations of the atoms/molecules so intense that the carrier decompose.

It is understood that these theoretical ideas have yet to find their practical confirmation, for which a lot of research effort is needed.

Acknowledgements This paper was in part supported by the Vojvodina Provincial Secretariat for Higher Education and Scientific-Research Development (Grant: 142-451-2433/2018-03) as well as the Serbian Ministry of Education, Science and Technological Development (Grant: ON-171039).

References

- Poole Jr., C.P., Owens, F.J.: Introduction to Nanotechnology. Wiley, New Jersey (2003)
- Wolf, E.L.: Nanophysics and Nanotechnology. Wiley-VCH, Weinheim (2006)
- Kelsall, R.W., Hamley, I.W., Geoghegan, M. (eds.): Nanoscale Science and Technology. Wiley, Chichester (2005)
- Morrow Jr., K.J., Bawa, R., Wei, C.: Recent advances in basic and clinical nanomedicine. *Med. Clin. N. Am.* **91**(805), 843 (2007). <https://doi.org/10.1016/j.mcna.2007.05.009>
- Cao, Y.C.: Nanomaterials for biomedical applications. *Nanomedicine* **3**(4), 467–469 (2008). <https://doi.org/10.2217/17435889.3.4.467>
- Salata, O.V.: Applications of nanoparticles in biology and medicine. *J Nanobiotechnol.* **2**(1), 3 (2004). <https://doi.org/10.1186/1477-3155-2-3>
- Rogach, A.L. (ed.): Semiconductor Nanocrystal Quantum Dots. Springer, Wien (2008)
- Bae, Y.H., Park, K.: Targeted drug delivery to tumors: myths, reality and possibility. *J Control Release* **153**(3), 198–205 (2011). <https://doi.org/10.1016/j.jconrel.2011.06.001>
- Mooranian, A., Zamani, N., Mikov, M., Goločorbin-Kon, S., Stojanovic, G., Arfuso, F., Al-Salami, H.: Novel nano-encapsulation of probutcol in microgels: scanning electron micrograph characterizations, buoyancy profiling, and antioxidant assay analyses. *Artif. Cells Nanomed. Biotechnol.* **27**(1), 7 (2018). <https://doi.org/10.1080/21691401.2018.1511571>
- Yang, K., Feng, L., Shi, X., Liu, Z.: Nano-graphene in biomedicine: theranostic applications. *Chem. Soc. Rev.* **42**(530), 547 (2013). <https://doi.org/10.1039/C2CS35342C>
- Šetrajić, J.P., Mirjanić, D.L., Vučenović, S.M., Ilić, D.I., Markoski, B., Jaćimovski, S.K., Sajfert, V.D., Zorić, V.M.: Phonon contribution in thermodynamics of nano-crystalline films and wires. *Acta Physica Polonica A.* **115**(4), 778–782 (2009). <https://doi.org/10.12693/APhysPolA.115.778>
- Šetrajić, J.P., Ilić, D.I., Jaćimovski, S.K.: The influence of the surface parameter changes onto the phonon states in ultrathin crystalline films. *Physica A* **496**(434), 445 (2018). <https://doi.org/10.1016/j.physa.2017.12.138>
- Balandin, A.A., Nika, D.L.: Phononics in low-dimensional materials. *Mater. Today* **15**(6), 266–275 (2012). [https://doi.org/10.1016/s1369-7021\(12\)70117-7](https://doi.org/10.1016/s1369-7021(12)70117-7)
- Fomin, V.M., Balandin, A.A.: Phonon spectrum engineering in rolled-up micro- and nano-architectures. *Appl. Sci.* **5**(4), 728–746 (2015). <https://doi.org/10.3390/app5040728>
- Šetrajić, J.P., Jaćimovski, S.K., Sajfert, V.D.: Diffusion of phonons through (along and across) the ultrathin crystalline films. *Physica A* **486**(839), 848 (2017). <https://doi.org/10.1016/j.physa.2017.06.003>
- Ilić, D.I., Šetrajić, J.P., Šetrajić, I.I.: Phonon contribution in thermodynamic properties of single quantum dot. *Acta Physica Polonica A*, accepted for publication (2018)
- Misra, R.D.K.: Quantum dots for tumor-targeted drug delivery and cell imaging. *Nanomedicine* **3**(3), 271–274 (2008)
- Dey, N.S., Rao, M.E.B.: Quantum dot: novel carrier for drug delivery. *Int. J. Res. Pharm. Biomed. Sci.* **2**(2), 448–458

Zeolite Microneedles: Recent Advancements and Implications in the Delivery of Collagen

Amar Ramović, Zerina Zorlak, Đenana Husić, and Samir Ramić

Abstract

Zeolites are one of the most interesting areas of nanotechnology. They have wide application because of their properties, so they are also used for microneedles for delivery of various drugs. Until now, they have been used for the delivery of insulin, diclofenac and ketoprofen and our work will reveal collagen delivery capabilities and thus the application of zeolite microgels in the application of anti-age preparations based on the comparison of insulin molecule characteristics and collagen molecules. Since it is a preparation that is increasingly used in cosmetology and dermatology, we also find out how the best microneedles made of zeolite are applied for delivery of collagen and explain the application of dermaroller and dermapen with this microneedles.

Keywords

Zeolites • Microneedles • Collagen • Dermaroller • Dermapen • Skin

The primary function of the microneedles is to make translucent pores in the *stratum corneum* and to allow high-molecular-weight molecules to pass through it. When the formation of a pore in the *stratum corneum* occurs, the drug is administered via microneedles, which extends to the basic subcutaneous tissues, and is absorbed and distributed systemically. Accordingly, it was noticed that by using microneedles it was possible to provide better delivery of proteins, peptides and vaccines. But the use of these drugs through microneedles is only possible after a detailed study of their production and physical properties is completed, which is the actual stage of their development [1].

Four methods of their application have been identified [1]:

1. “poke and patch”;
2. “poke and released”;
3. “coat and poke” and
4. “poke and flow”.

The first three methods use solid microneedles, while the fourth uses hollow microneedles. The “poke and patch” method consists of two steps: the first step is to microneedles a transient line in the *stratum corneum*, and then in the second step the delivery of carried drugs, while the delivery speed depends on the size of the pores, as well as the concentration of the drug. The advantage of this method is simplicity of administration while the disadvantages are much more like [1]:

- a small amount of the drug is applied,
- a more severe control of the dose of the drug, and
- that the pores remain open for up to three days, which are exposed to occlusive conditions and there is a possibility of developing the infection.

The other method is “coat and poke”, it is based on the surface of the microneedles coated with the drug, in such a way enabling the delivery of the drug dip coating, roll

1 Introduction

The concept of microneedles has been developed over the past few decades as a minimally invasive drug for the treatment of skin through the skin. The first models of miniature needles date back to the 1970s, the patent filed by Alza Corporation in 1971. This patent contained a device for the delivery of drugs with small microneedles that are sufficiently strong to penetrate only the *stratum corneum* and can be solid or hollow. A special advantage of the microneedles is that they can be designed for minimal invasiveness and specifically programmed drug delivery [1].

A. Ramović · Z. Zorlak (✉) · Đ. Husić · S. Ramić
Faculty of Pharmacy, University of Sarajevo, Zmaja od Bosne 8,
71000 Sarajevo, Bosnia and Herzegovina
e-mail: zerina_zorlak@hotmail.com

coating, or spray coating manner. The advantage of this application is that it allows the application of the drug locally and distributes in the systemic circulation, while the disadvantage is that the delivery of the drug to the thickness of the coating is limited, then the microneedle's sharpness can be reduced, and the adhesion of the drug to the microneedle is reduced. The third method is "poke and released", based on the use of dissolve microneedles. Dissolve microneedles are a newer strategy that has been developed to better deliver drugs. This type of microneedle is made of a biodegradable polymer and contains a drug in the polymer capsule. After the application of these microneedles, the micro-powder is inserted under the skin and further distributed in the body [1].

The advantage of this method is that it is possible to precisely administrate the drug as well as small losses during encapsulation. While the disadvantages are that microneedles cannot be very sharp, reducing penetration, as well as a small dose of the drug [2].

The last method is the "poke and flow" and is based on the delivery of the drug through injections. It is based on the application of hollow microneedles with a reservoir that is applied to the skin and through which the liquid formulation of the active substances flows. The advantage of using these microneedles is the dosage control, the drug flow rate control, while the defect can represent an incorrect control of the pressure and penetration of the microneedles, otherwise, they may be blocked or leakage occurs [1].

Zeolites are class of crystalline oxides having the uniform and molecular ports (3–12 Å in diameter). Natural zeolites were discovered in 1756. Commercial development did not begin until the 1950s. In 1950s synthetic zeolites with high purity and controlled chemical composition became available. Since then large commercial applications of zeolites are limited to catalysis, adsorption and ion exchange, all used in the form of zeolite powders. Although researchers have been exploring thin zeolite films for the past 15 years, most of these studies are motivated by the potential applications of these materials as a membrane of separation and membrane reactors. In the last decades, they have recognized thin zeolite films that can have new, diverse and economically significant applications that others have not previously considered [3].

Zeolites have been shown to be biocompatible molecules and find their place in the production of microneedles. Such microneedles are used for transdermal delivery of drugs. The first microneedles made from zeolites were used for insulin delivery and against rodent influence [4].

2 Zeolites Films and Membranes

Zeolites can be grown in many different ways. They can be grown as individual crystals, or as crystals that are grown together in layers on different kind of surfaces, such as metal surfaces, metal wires, ceramic, polymeric plates, organic and inorganic fibres and even on surfaces with special properties such as electronic circuits [3].

They are nanostructural on the inside, and because of that zeolites are capable of very specific reactions with individual molecules, and many times it is possible to implement molecular function recognition. It is also possible to discover their other well-known properties, such as their catalytic adsorption and diffusion/permeation characteristics. Zeolites have new apply opportunities such as applicability on microscope and microneedles [4].

They can be organic (glass, ceramic, metal) or inorganic (plastic, cellulose, etc.). That allows us transfer of some their properties such as absorption, catalysis, molecular recognition and diffusion to two—dimensional structure, with the potential of applications, and areas from reactive engineering to molecular separation and chemical analysis [5].

Based on many experiences and researches lately, we can grow zeolite fills on almost any kind of surface. That gives us unbelievable control of their morphology, orientation, and level of crystal intergrown. Unfortunately, the only industrial zeolite application is one decade old. Today, very popular are numerous little applications that seem to be very promising. Some of them are in micromembranes, in microreactors, etc. [5].

3 Zeolite-Based Microneedles

Microneedles were produced using microporous zeolites and tested for transdermal delivery. Interpolated zeolites provide excellent mechanical strength and can penetrate the porcine skin (i.e. *S. Scrofa domesticus*) without damaging it. The controlled dose of the drug was reached through the permeable zeolite wall. Just the grid already mentioned is responsible for micrograph collagen diffusion into the subcutaneous tissue [4]. A pure silica zeolite having a similar chemical composition as a glass, but porous is grown on a needle-like template to create a set of free hollow microtome zeolites. Lumen and length of needles are designed for effective delivery of the drug while maintaining good mechanical strength for insertion into the skin layer [5].

The zeolite growth conditions are adapted to obtain a different and intracellular pore size for controlled delivery of the drug and the strength that has a high safety margin compared to the metal micronic apertures [5].

4 Reasons for the Use of Zeolite in the Production of Microneedles

Zeolites are crystal aluminosilicates of open 3D structures constructed of SiO_4 and AlO_4 tetrahedra which are interconnected by the division of all oxygen atoms to form proper intra-crystalline cavities and molecular dimension channels. It is also often referred to as a molecular sieve. A significant feature of the zeolite is that their frames are composed of 4 coordinated atoms forming the tetrahedron. These tetrahedrons are interconnected to the corners and make up the wealth of beautiful structures. The frame structure may include associated cages, cavities or channels that are large enough to allow small molecules to enter. The system of large gaps explains the consistent low specific density of these compounds. For zeolites used for different applications, the gaps are interconnected and form wide channels of varying magnitude, depending on the joint. These channels allow the slight movement of the remaining ions and molecules in the structure and from them. Aluminosilicate frame is negatively charged and attracts positive cations living in cages to compensate for the negative charge of the frame. Unlike most other silicosis, zeolites have larger cages in their structures [6–8].

Many of them appear naturally as minerals and are extensively mined in many parts of the world by finding applications in industry, medicine, and pharmacy [8]. However, most zeolites are synthetically designed for commercial use. There are currently 191 unique zeolite frames and 40 natural zeolites [9, 10].

According to a first aspect of the present invention, there is provided with a method for preparing microns surfaces of a zeolite comprising the step of preparing a polymeric needle template by a photolithographic process, wherein the layer of photosensitive polymer material is coated on the substrate, silica, glass, quartz, metal, etc. The production of zeolite microns plates includes precise control of the pre-condition photolithography conditions [11].

To achieve polymeric micronized surfaces with different degrees of dimming, the exposure time and the time of development in the microfiltration process are different. According to another aspect of the present invention, there is provided with a method for making hollow micron zeolites comprising the step of removing templates of polymeric needles from a shell of a molecular sieve by an air calcination method or an ozonation method. According to a third aspect of the present invention, there is provided with a

method for obtaining either a closed or open microneedle peak [12, 13].

Microneedles with the closed or open tip can be prepared by changing the sowing method and the growth conditions of zeolites. According to a fourth aspect of the present invention, potential applications of micronucleosides include drug delivery, body fluid extraction, and cosmetic purposes [4, 13].

Zeolite microneedles are used for the delivery drugs in the body, extraction of body fluids and cosmetic application. Advantages of microneedles are [14]:

- painless application,
- good mechanical strength,
- biocompatibility,
- reliable and precise delivery.

5 Collagen and Insulin Characters

The name “collagen” is used as a generic term for proteins forming a characteristic triple helix of three polypeptide chains and all members of the collagen family form these supramolecular structures in the extracellular matrix. So far, 26 genetically distinct collagen types have been described. Based on their structure and supramolecular organization, they can be grouped into fibril-forming collagens, fibril-associated collagens (FACIT), network-forming collagens, anchoring fibrils, transmembrane collagens, basement membrane collagens and others with unique functions. The classical fibril-forming collagens include collagen types I, II, III, V, and XI. These collagens are characterized by their ability to assemble into highly orientated supramolecular aggregates with a characteristic suprastructure, the typical quarter-staggered fibril-array with diameters between 25 and 400 nm. In the electron microscope, the fibrils are defined by a characteristic banding pattern with a periodicity of about 70 nm (called the D-period) based on a staggered arrangement of individual collagen monomers [15].

The insulin molecule contains 51 amino acids; it is made up of two peptide chains linked by disulfide bonds. Although it is active as a monomer, during its biosynthesis and storage it assembles to dimers and, in the presence of zinc, to hexamers. X-ray analysis has revealed the 3-dimensional structure of the insulin molecule in its hexameric, dimeric and monomeric states. Two main conformations of insulin which differ in the extent of the helix in the B chain (B9–B20 and B1–B20, respectively) have been identified [16]. The molecular weight of insulin is 5807.629 g/mol and radius of the monomer is 5 nm, but insulin comes in hexamerform [17].

6 Microneedle-Assisted Delivery of Collagen

The human body consists essentially of carbohydrates, proteins, fats, minerals, vitamins and other numerous components, of which proteins make up 20% by weight, of which 25–35% of the total protein in the body forms collagen, of which the most common is collagen type I or C1, which makes up to 90%. Type I collagen enters the body of a large number of tissues in the body including bones, teeth, skin, and tendons. A lack of collagen in the body can lead to a number of deficiencies such as wrinkles, reduced wound healing ability and severe diseases such as congenital defect, infection, skin damage, autoimmune disease, and ageing. Ageing is one of the main causes of reduced collagen content on the skin's human skin. It is thought to be the consequence of the formation of the ethere eradicant also, which lead to the enzymatic destruction of skin layers and inhibition of collagen fibre synthesis. Therefore, the application of collagen by means of the rare preparations began. Different approaches to the application of collagen type I have been introduced in the treatment of cosmetic stains and the improvement of wound healing [18]. The common use of collagen is based on injection or curvature. Although these methods of application are very effective, they still have their drawbacks, the use of injections can lead to accidental injuries that can then act destructively on the face, therefore the commercial application of collagen in the areas around the lips and around the mouth is not recommended [10, 19].

The method of administration may cause a large amount of collagen beneath the surface of the skin to be applied, which does not provide adequate distribution in the skin. On the other hand, turns have proved to be very effective in treating wound healing accelerated, but because they are superimposed, restricts their use and effectiveness [20]. Therefore, micro-systems for the delivery of collagen are developed. As mentioned above, metal rollers (Dermaroller) rollers induce a collagen deposit in the skin. Regarding the microneedles, there are not many studies that show us that collagen is safe through these micro-systems, so far microneedles have been tested for soluble transdermal collagen-type polymer delivery of collagen type I [21]. That method of administration is much more effective because it eliminates the danger of a blade that is present when using injections. This would facilitate the use of collagen type I, and allow the use of type I collagen at home. In addition, microneedles eliminate globular distribution, which contributes to the natural appearance of the skin, compared to the bulbous appearance after administration of injections [18, 22].

7 Commercially Available Microneedle Devices

For a long time, the skin has been considered an appropriate administration site for the delivery of medications. The reason for that is its accessibility and ability for feasible controlled delivery, as well as to the avoidance of the first-pass metabolism in the liver and enzymatic degradation in the gastrointestinal tract. Nevertheless, the formidable barrier properties of the outermost layer of the skin, the *stratum corneum*, cause significant limitations in the achievement of successful delivery. The important innovation in disrupting this layer is the use of microneedles (MN). MNs are minimally invasive devices that painlessly bypass the *stratum corneum* which allows enhanced delivery across the skin by increasing its permeability. These micro-projections, which create temporary channels to the dermal microcirculation, range from 25 to 200 μm in height. They have different geometries and shapes and they are typically assembled on one side of supporting base plate. Lifestyle, environment (chronic sun exposure and UV radiation), genetics, hormones and nutrition influence skin health. Ageing of the skin is caused by many factors such as the cumulative effect of chronic exposure to the elements, primarily UV radiation, as well as degradation of elastin fibres and marked collagen reduction causing wrinkle development. MNs and subsequently MN devices are examples of such innovative therapies. The Food and Drug Administration (FDA) has approved following commercially available MN devices: Dermaroller[®] and Dermapen[®]. They were developed based on Fernandespercutaneous collagen induction (PCI) innovation. PCI is achieved via multiple needle application. Roller devices with projecting needles have been designed to achieve this aim. Dermaroller[®] described as a hand-held device equipped with medical grade solid steel MNs, projecting from cylindrical roller has been approved by FDA. The rolling mechanism is applied directly over the skin, vertically, horizontally and diagonally. On the roller, there are 24 circular areas of eight needles and the heights of the needles are specific to the nature of the treatment being employed [23, 24].

Dermapen[®] is an advanced MN device which was designed to overcome the issues of varying pressure application by physicians-users and to achieve the subsequent MN depth penetration. It is described by manufacturers as a spring-loaded, fractional MN device, with an adjustment ring allowing for alteration of the heights of the MN, which carries out the function of 'fractional mechanical resurfacing'. It utilizes an electrically powered pen to deliver a vibrating stamp like

motion to the skin, creating a series of microchannels in it. The manufacturers are investigating treatment in acne scarring, burn scars and photo ageing. However, no research studies focusing on this MN device have yet been published. Because of the substantial interest in these MN devices, currently, there are more commercial products based on the same principles under development [23, 25].

8 Conclusion

On the basis of all the properties mentioned, both the zeolite and the microneedles it is evident that the zeolites can be used as a micrograph material for microneedles. These microneedles find their application in cosmetology and dermatology for collagen delivery. Based on the insulin characteristics which as macromolecules can pass through pores and membranes of zeolites of which microgels are, theoretically, there is not the reason why collagen cannot. The easiest way to apply would be dermaroller or dermapen because of the apparent results and the application is not painful. Collagen is not a drug, but it's not just a cosmetic product. That's why it not only beautifies it, it already acts on the tissues (characteristic of medicines), and he is rightly included in the cosmeceutical group. This term is proposed by American dermatology professor Alberto Kligman to emphasize the fact that these drugs link the activity of cosmetics and medicines. Combining zeolites microneedles as material for dermaroller and dermapen we can delivery collagen transdermal very easily without pain and it is very effective.

Conflict of Interest Authors have no conflicts of interest to disclose.

References

1. Iliescu, S.F., Ionescu, D., Petrescu, M., Iliescu, C.: A review on transdermal drug delivery using microneedles: current research and perspective. *Ann. Acad. Rom. Sci. Series Sci. Technol. Inf.* **7**(1), 734 (2014)
2. Tucak, A.: Mikroiglama posredovana dostava lijekova kroz kožu – Formulacijski aspekti. Unpublished Master Thesis, University of Sarajevo, Sarajevo (2017)
3. Jha, B., Singh, D.: Basics of zeolites. In: *Advanced Structured Materials*, pp. 5–31 (2016)
4. Wong, L., Sun, W., Chan, N., Lai, W., Leung, W., Tsang, J., et al.: Zeolite microneedles for transdermal drug delivery. In: *Zeolites to Porous MOF Materials—The 40th Anniversary of International Zeolite Conference, Proceedings of the 15th International Zeolite Conference*, pp. 525–530 (2007)
5. Pina, M.P., Mallada, R., Arruebo, M., Urbiztondo, M., Navascués, N., de la Iglesia, O., Santamaria, J.: Zeolite films and membranes. Emerging applications nanoscience. Institute of Aragon, University of Zaragoza, 50009 Zaragoza, Spain
6. Defect-free zeolite membrane. *Membr. Technol.* **1998**(104), 13 (1998)
7. Hovhannisyanyan, V., Dong, C., Lai, F., Chang, N., Chen, S.: Natural zeolite for adsorbing and release of functional materials. *J. Biomed. Opt.* **23**(09), 1 (2018)
8. Andronikashvili, T., Pagava, K., Kurashvili, T., Eprikashvili, L.: Possibility of application of natural zeolites for medicinal purposes. *Bull. Georgian Nat. Acad. Sci.* **3**(2), 158–167 (2009)
9. Jacobs, P., Martens, J.: *Synthesis of High-Silica Aluminosilicate Zeolites*, 1st edn. Elsevier, Amsterdam (1987)
10. Cerrí, G., Farina, M., Brundu, A., Daković, A., Giunchedi, P., Gavini, E., et al.: Natural zeolites for pharmaceutical formulations: preparation and evaluation of a clinoptilolite-based material. *Microporous Mesoporous Mater.* **223**, 58–67 (2016)
11. Poon, T.: Zeolite microneedles: fabrication, mechanics and transdermal drug delivery. M. Phil Thesis, Hong Kong University of Science and Technology (2013)
12. Wong, L.: Molecular delivery system based on the nanoporous zeolite microstructures. M. Phil Thesis, Hong Kong University of Science and Technology (2006)
13. Bacakova, L., Vandrovцова, M., Kopova, I., Jirka, I.: Applications of zeolites in biotechnology and medicine—a review. *Biomater. Sci.* **6**(5), 974–989 (2018)
14. Sim, V., Poon, H.Y., Wong, W., Chau, L.Y.K., Han, W., Kwan, S. M., et al.: Zeolite microneedle: design for drug delivery. In: *Proceedings of the AIChE Annual Meeting* (2013)
15. Gelse, K.: Collagens—structure, function, and biosynthesis. *Adv. Drug Deliv. Rev.* **55**(12), 1531–1546 (2003)
16. Derewenda, U., Derewenda, Z., Dodson, G., Hubbard, R., Korber, F.: Molecular structure of insulin: the insulin monomer and its assembly. *Br. Med. Bull.* **45**(1), 4–18 (1989)
17. Shorten, P., McMahon, C., Soboleva, T.: Insulin transport within skeletal muscle transverse tubule networks. *Biophys. J.* **93**(9), 3001–3007 (2007)
18. Sun, W., Inayathullah, M., Manoukian, M., Malkovskiy, A., Manickam, S., Marinkovich, M., et al.: Transdermal delivery of functional collagen via Polyvinylpyrrolidone Microneedles. *Ann. Biomed. Eng.* **43**(12), 2978–2990 (2015)
19. Barbosa, G., Debone, H., Severino, P., Souto, E., da Silva, C.: Design and characterization of chitosan/zeolite composite films—effect of zeolite type and zeolite dose on the film properties. *Mater. Sci. Eng. C.* **60**, 246–254 (2016)
20. Tsioris, K., Raja, W., Pritchard, E., Panilaitis, B., Kaplan, D., Omenetto, F.: Fabrication of silk microneedles for controlled-release drug delivery. *Adv. Funct. Mater.* **22**(2), 330–335 (2011)
21. Faraji, D., Jahandideh, A., Asghari, A., Akbarzadeh, A., Hesarak, S.: Effect of zeolite and zeolite/collagen nanocomposite scaffolds on healing of segmental femur bone defect in rabbits. *Iran. J. Vet. Surg.* **12**(2), 63–69 (2017)
22. Kochhar, J., Anbalagan, P., Shelar, S., Neo, J., Iliescu, C., Kang, L.: Direct microneedle array fabrication off a photomask to deliver collagen through skin. *Pharm. Res.* **31**(7), 1724–1734 (2014)
23. McCrudden, M., McAlister, E., Courtenay, A., González-Vázquez, P., RajSingh, T., Donnelly, R.: Microneedle applications in improving skin appearance. *Exp. Dermatol.* **24**(8), 561–566 (2015)
24. Park, K., Kwon, H., Lee, C., Kim, D., Yoon, J., Kim, M., et al.: Efficacy and safety of a new microneedle patch for skin brightening: a Randomized, split-face, single-blind study. *J. Cosmet. Dermatol.* **16**(3), 382–387 (2017)
25. Jung, H.: Microneedle: the future of pharmaceutical and cosmeceutical delivery systems. *J. Pharm. Drug Deliv. Res.* **06**(03), 1 (2017)

Application of Raman Spectroscopy in Food Forensics: A Review

Anera Kazlagić and Enisa Omanović-Miklićanin

Abstract

The need for accurate and reliable methods for food analysis on molecular level has been steadily increased during past decades. This trend is connected with the recent food scandals caused by food adulteration. Raman spectroscopy has very important role in identification of food fraud and food adulteration. Through this specific technique, the food quality control and authentication of food products can be easily performed. Adulteration, contamination and origin of food can be investigated through new field of food science—food forensics. Raman spectroscopy is one of the most valuable spectroscopic techniques used in different research fields. It has gained popularity due to its advantages over other analytical techniques. It is used in chemistry to study vibration, rotational, and other low-frequency modes of the system. This technique allows obtaining a chemical information from samples in nondestructive manner. It is useful for both solid and liquid samples. The main advantage of the Raman spectroscopy is that samples doesn't require preparation. Another advantage is that water does not interfere in analysis. Raman spectra is captured within few seconds from sample, and after that analysed. In this review, relationship of food forensics with Raman spectroscopy is briefly explained. Raman spectroscopic techniques such as Fourier transform Raman spectroscopy, Surface-enhanced Raman spectroscopy and Visible—micro Raman spectroscopy are briefly introduced.

Keywords

Food forensics • Raman spectroscopy • SERS

1 Introduction

Food forensics is defined as a scientific discipline which studies a food origin, adulteration and contamination. Food forensics investigates the possibility of using powerful scientific methods for the authentication and traceability of foodstuffs, in a way similar to popular TV series such as CSI in which scientific methods are used to solve forensic problems [1].

Food and agricultural products are essential to life. With the increasing demand for a high quality and healthy life, safety control gains the attention of researches and wider audience. Developments in spectrophotometry, chromatography, and spectrometry often had immediate applications to food analysis, due to development of chemical analysis: which started from “wet chemistry” laboratory methods, to the modern analytical instrumental techniques such as spectroscopy [2].

Through specific methods such as vibrational spectroscopy, the food quality control can be performed. Vibrational spectroscopy is based upon periodic changes of dipole moments (infrared spectroscopy—IR) or polarizabilities (Raman scattering) caused by molecular vibrations of molecules or groups of atoms and the combined discrete energy transitions and changes of frequencies during absorption (IR) or scattering (Raman) of electromagnetic waves [3].

Authentication of food products is of primary importance for both consumers and industry. Food adulteration represents the act of intentionally debasing the quality of food offered for sale either by the admixture or substitution of inferior substances or by the removal of some valuable ingredient [4]. From the regulative point of view, quality standards were established through the requirement of quality labels that specify the chemical composition of each product. From the economic point of view, product authentication is essential to avoid unfair competition that can eventually create a destabilized market and disrupt the regional or national economy [5].

A. Kazlagić (✉) · E. Omanović-Miklićanin
Faculty of Agriculture and Food Sciences, University of Sarajevo,
Zmaja od Bosne 8, 71000 Sarajevo, Bosnia and Herzegovina
e-mail: a.kazlagic@ppf.unsa.ba

E. Omanović-Miklićanin
e-mail: e.omanovic-miklicanin@ppf.unsa.ba

Adulteration (food authenticity) is nowadays a major concern for the food industry. Adulterants are often difficult to detect because they are usually similar to the authentic product. The most notable example of food adulteration is production of oil, specially olive oil, where cheaper oil of similar chemical structure is added to reduce manufacturing costs [6, 7]. Another example of food adulteration are fruit juices, where some components are added, such as colorants and other compounds which have a nice and desirable taste, but have no nutritive value. A number of reviews have appeared focusing on food adulteration connected to fruit juices or soft drink production [8–11].

There are numerous examples of honey adulteration known as “Honey Laundering Conspiracy”. The application of various Raman spectroscopy techniques for the detection of honey adulteration has been proposed and investigated, including Dispersive Raman Spectroscopy [12], FT-Raman Spectroscopy [13–15] or FT-micro Raman spectroscopy [16–18].

The primary concern of food producers and scientists working in the food-processing industry and in academic laboratories is evaluation of food quality, food safety, food stability, nutrition and sensory properties of food products. Food safety can be quantitatively assessed by many methods, which often require from several hours to days of analysis, mostly with pretreatment steps.

In the evaluation of food quality process, the key role is given to spectroscopic methods, due to their rapidity and nondestructive sample preparation. Among them, vibrational spectroscopy is highlighted, because of its fast, reliable, and simple perform [2, 3].

2 Raman Spectroscopy in General

Structural and chemical information about molecules based on a vibrational transition can be unfold using vibrational spectroscopy, infrared absorption and Raman scattering. In infrared spectroscopy, the sample is exposed to radiation with infrared light. Different chemical bonds absorb at different wavelengths, depending on the atoms connected, the surrounding molecules, and the type of vibration the absorbance gives rise to. Raman spectroscopy is based on irradiation of a sample with a monochromatic visible or near infrared light which comes from a laser. As a result, vibrational energy levels in the molecule go to a short-lived, high-energy collision state. Most of the molecules go back to the original low energy state, phenomenon called Rayleigh scattering, with emission of a photon of the same wavelength as the exciting light.

A very small percentage of the excited molecules relax back to ground state, hence the emitted photons have a lower frequency, which is known as a Stokes Raman scattering.

Raman shift represents the difference between the frequency of the laser and frequency of the scattered photon. The Raman shift corresponds to the frequency of the fundamental infrared absorbance band of the bond. Because of the small percentage of molecules which use this relaxing pathway, Raman scattering is always of very low intensity and its investigation requires high-quality instrumentation. Even though both methods probe molecular vibrations, they do not provide exactly the same information. Whereas infrared spectroscopy detects vibrations due to electrical dipole moment changes, Raman spectroscopy is based on the detection of vibrations due to changes in polarizability. This implies that bonds that connect two identical or nearly identical parts of a molecule (e.g., the C=C bond) tend to be more active than a weakly polarizable bond (e.g., the OH bond). For this reason, water is practically invisible in Raman spectroscopy, but it dominates the infrared spectra [19]. This is a main advantage of Raman spectroscopy analysis of water-based foods.

2.1 Theoretical Basis of Raman Spectroscopy

After irradiating a sample using a laser beam, a tiny portion of photons with a known frequency and polarization are scattered from the sample. In this process, the incident photon and the molecule collide in inelastic way. As a result, the vibrational or rotational energy of the molecule changes, and the scattered radiation is shifted to a different wavelength. Raman shift presents the frequency difference between scattered radiation and incident radiation. If the molecule gains energy, scattered photons are shifted to longer wavelengths, giving rise to Stokes lines in the Raman spectra.

Otherwise, they are shifted to shorter wavelengths, giving rise to anti-Stokes lines in the Raman spectra. Figure 1 shows an energy level diagram for Raman scattering. The frequency shifts of scattered light can be analyzed and presented as spectra. Spectral bands represent vibrational characteristics for chemical bonds and functional groups that constitute the components in the examined samples. The spectra represents a fingerprint of a specific substance, which gives the basis for structural and qualitative analysis. Raman spectroscopy can also be used to perform quantitative determination, because the intensity of an analyte band is proportional to concentration of the analyte [20].

3 Fourier Transform Raman Spectroscopy

In Ozaki et al., the 1064-nm excited Fourier transform (FT) Raman spectra have been measured in situ for various foods in order to investigate the potential of near-infrared

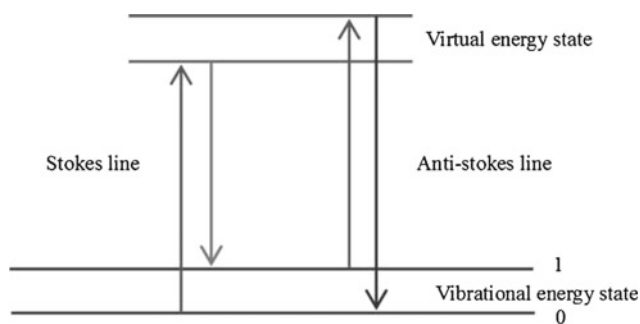


Fig. 1 Energy level diagram for Raman scattering [20]

(NIR) FT-Raman spectroscopy in food analysis. Obtained results showed that NIR FT Raman spectroscopy presents a very powerful technique for detecting selectively the trace components in foodstuffs, estimating the degree of unsaturation of fatty acids included in foods, and investigating the structure of food components, included with monitoring the changes in the quality of foods [21].

FT-Raman spectroscopy can be a good alternative to time-consuming and complex methods. In FT-Raman spectroscopy, no solvents or consumables are needed for such simple analyses, and so the cost analysis can be significantly reduced. This method further demonstrates the efficiency of transmittance spectroscopy methods for the quantitative analysis of complex mixtures. Comparing FT-Raman spectroscopy with standard HPLC, the capacity of a setup based on the proposed method may be many times higher [13].

3.1 NIR FT-Raman Spectroscopy

NIR FT-Raman spectroscopy has the several advantages in food analysis over other analytical methods: First of all, it is a nondestructive method and does not require any pretreatment.

Raman spectra of various kinds of foods can be measured in situ. Another advantage is that, not only qualitative and quantitative analysis of food components but also their structural analysis can be carried out. Third advantage is that the use of FT-Raman micro spectroscopy allows micro-analysis of food components. Selective analysis of trace components in food and drink is possible using the resonance or pre-resonance Raman effect. And the last advantage is that the fiber techniques can be used for remote measurements and on-line analysis of food products. Recently, the Southampton and Norwich group in the U.K. reported NIR FT-Raman spectra of various foodstuffs [21]. Ozaki et al. discussed the potential of NIR FT-Raman spectroscopy in food analysis from its various aspects, which includes estimation of the degree of unsaturation, and selective

detection of trace components, investigation of structural changes upon denaturation, and monitoring changes of quality of foods [21].

4 Surface-Enhanced Raman Spectroscopy

In the last few years, plasmonics based sensor device, such as surface enhanced Raman spectroscopy (SERS), has attracted lots of attention to the analytical chemists. When an electromagnetic wave interacts with a molecule in the vicinity of nano-metal surface, an enhanced electric field is observed, due to the collective oscillation of conduction electrons. The Raman scattering observation with this enhanced electric field close to metal surface leads to an enhanced Raman scattering, which is known as Surface-enhanced Raman Scattering [22].

The use of metallic nanosubstrates can improve the sensitivity and capacity of conventional Raman spectroscopy, which is the main reason why we designate this technique—Surface-enhanced Raman spectroscopy (SERS) as a promising technique for the chemical analysis of food. Various SERS substrates have been fabricated and applied in different applications.

The key role in SERS application is a well-performing SERS substrate, which is important for real-life application, such as food analysis. One of the most important parameters for chemical analysis is sensitivity and reproducibility. The uniform and reproducible substrate is the key to provide consistent signals for quantitative analysis. In screening and trace analysis the maximized enhancement is the precondition for a sensitive determination [23]. Yunfei Xie and colleagues designed a novel SERS substrate which could be used to characterize prohibited colorants, showed in Fig. 2.

They developed a G/Ag SERS model, which exhibited potential application for detecting prohibited colorants, and showed an excellent enrichment effect between colorant molecules and graphene, as well as excellent Raman enhancement effect due to the presence of silver nanoparticles. All the obtained SERS spectra suggest that the method can be used as an effective method in detecting qualitatively and quantitatively prohibited additive colorants in food [24].

5 Visible Micro-Raman Spectroscopy

Delfino et al. had applied micro-Raman spectroscopy with excitation in the visible micro-Raman spectra to food industry liquid products. Different sport drink composition, with particular attention to glucose content, has been successfully characterized with this approach. They determined glucose content because it has a key role in food and

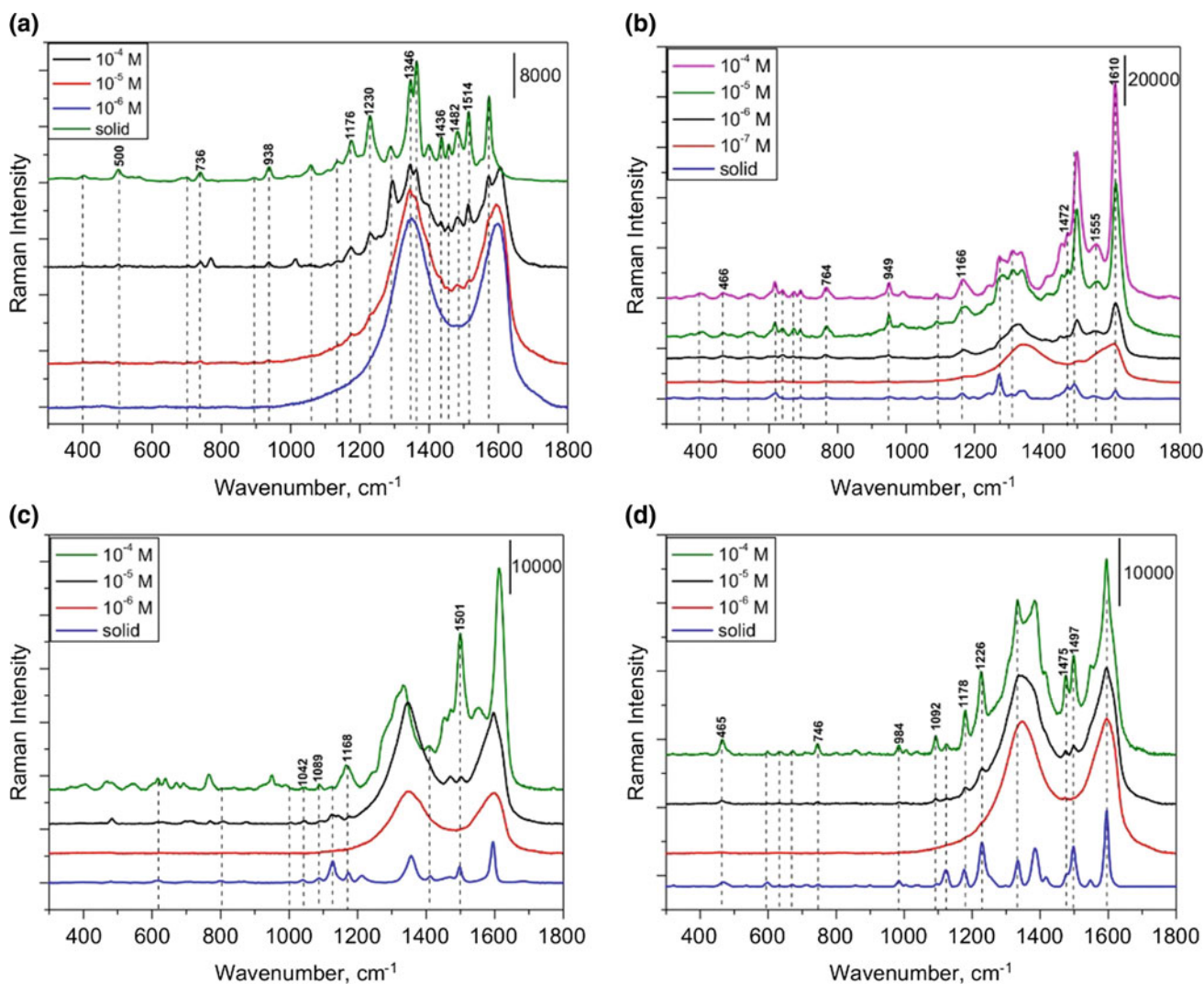


Fig. 2 SERS spectra of amaranth (a); erythrosine (b); lemon yellow (c); sunset yellow (d) at concentrations (a)–(d) 1×10^4 , 1×10^5 , 1×10^6 , and 1×10^7 M, respectively. The entire characteristic Raman peak in the prohibited colorant solid is been marked by dashed line,

according to the different concentrations of colorant. The peaks are also labeled by wavenumbers, which show an evident corresponding relationship [24]

beverage industry. Raman spectroscopy allows glucose quantification in various matrices [25]. Experimental set-up for micro-Raman spectroscopy is shown in Fig. 3.

Determination of glucose content in commercial untreated samples has been quantitatively obtained with their Raman spectra by means of the interval Partial Least Square (iPLS) procedure. This procedure is multivariate statistical analysis approach. It has been shown to be very powerful in the analysis of Raman spectra [25, 26]. The iPLS model has been built using Raman spectra obtained from glucose aqueous solutions of known composition as calibration data. It has been compared to the spectra of sport drink samples, giving glucose concentrations in good agreement with the

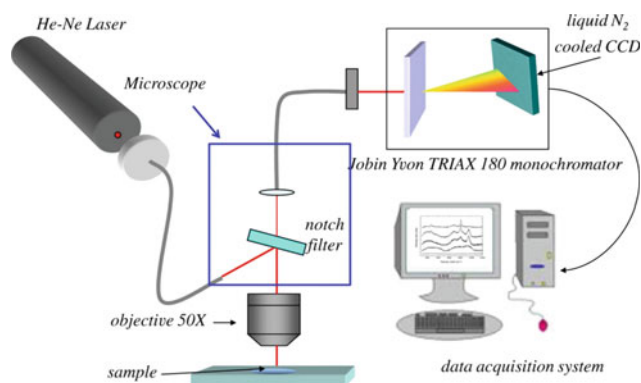


Fig. 3 Experimental set-up for micro-Raman spectroscopy [25]

values obtained by a biochemical assay. The results have demonstrated that visible micro-Raman spectroscopy is a feasible method for glucose quantification in industrial products, such as beverages and fruit juices, without using specific substrates and/or sample preparation procedures. From now on, this approach represents a significant step towards the development of a simple, cost-effective Raman based method for glucose quantification in products of food and beverage industry, alternative to expensive, time-, sample- and chemicals-consuming biochemical assays currently used in production and quality control processes [27].

6 Multivariate Mathematical Methods

In order to be defined as authentic, a foodstuff needs to be characterized by all the possible variations, which implies determination of several variables, for example trace elements or molecular ionic fragments. For authenticating or tracing a product, determining a large number of variables is very important. Obtained variables are used for identification of groups of samples as authentic and non-authentic samples, which implies the need of managing large sets of data.

This can be carried out with pattern recognition (or classification) multivariate mathematical methods, using well-known techniques such as principal components analysis (PCA), cluster analysis (CA), discriminant analysis (DA), or soft independent modeling of class analogy (SIMCA) [28, 29].

In particular, PCA, CLA, and CA proved to be very useful for grouping and detecting honey of various origins [18, 30–34].

In addition, Mircea Orian and colleagues in their paper discussed about Linear discriminant analysis (LDA), which can also be very useful for characterization of Raman Spectra, in this case for honey Raman Spectra [35].

7 Application of Raman Spectroscopy

Raman spectroscopy has a great potential in food applications, which involves monitoring and quality control in food processing and food safety in agricultural plant production. The main advantages of Raman spectroscopy over other analytical methods applied in food forensics are short analysis time and ability to probe water-rich samples. Disadvantages of Raman spectroscopy in food analysis mostly are poor signal intensity and very strong fluorescence signal which can, sometimes, overlap with Raman signal [36].

The types of Raman spectroscopy applications in food industry may be classified as follows:

- (a) **Raman spectroscopy in monitoring of food processes**, such as fermentation, during different food production processes, where the main disadvantage is resulting fluorescence signal. This difficulty can be overcome by using a laser light source in the relatively far ultraviolet or infrared range where fluorescence would not overlap with Raman signals [3].
- (b) **Raman spectroscopy in food contamination** A number of reviews have appeared focusing on Raman spectroscopy applied in food safety by evaluation of food contamination. For example, determination of pesticides and fungicides in food, fungal pathogens, examined by Raman spectroscopy. Another example is determination of bacteria in food, which can be also successfully examined by conventional Raman spectroscopy [3].

Raman spectroscopy is greatly suited for food forensics, largely due to the specificity of the method and the diversity of the analytes which can be probed; ranging from the macro-food, lipids, proteins and carbohydrates, to the minor components, such as preservatives, dyes and pigments [3]. Adulteration (food authenticity) presents a major concern for the food industry, and the key role is played by adulterants. They are often difficult to detect since adulterant components are usually similar to the authentic product. The most notable example of food adulteration is in the production of oil, for example extra-virgin oils, where cheaper oil of similar chemical structure is added in order to reduce manufacturing costs. Raman spectroscopy has been exceptionally useful in the identification and authentication of olive oils adulterated with hazelnut oil, while chromatographic methods were unable to detect adulterations at relatively low concentrations (5–20%) [3]. Use of Raman spectroscopy in the area of the fruit juices production, such as apple, pomegranate and bayberry juices, has also been reported. Raman spectroscopy has also been successful in confirming the botanical and geographical origins of honey, and in characterization of food additives [15, 37].

Another key area of food forensics belongs to microbial food spoilage and contamination. Compared to IR spectroscopy, there is not too much published literature on the use of Raman spectroscopy to monitor food spoilage [3].

8 Conclusion

Spectroscopic and nanospectroscopic methods are very important in the evaluation of food quality and safety. The methods of vibrational spectroscopy: infrared (IR) Raman are the most important spectroscopic methods while

Surface-enhanced Raman spectroscopy (SERS) is the most important nanospectroscopic method applied in food science and agriculture.

It is hoped that this SERS platform opens vast possibilities for the rapid and portable ultra-trace detection in real-world. Novel and reproducible substrates with high enhancement parameters were designed, in order to be useful in various applications in food forensics. Extension of laser excitation into the ultraviolet range is a promising approach for further investigations. By integrating chemometrics methods and spectral data analysis, as well as with the development of micro-Raman spectrometers and nanosubstrates, SERS could be used as a rapid technique for both qualitative and quantitative analyses in foodstuffs.

Therefore, a new approach for the application of Raman spectroscopy to agricultural and food sciences has become available. However, more research is needed to determine the best conditions for obtaining the information and providing adequate data in complex food matrices.

References

- Omanović-Miklićanin E.: Food forensics. In: Marjanović, D., Primorac, D., Dogan, S. (eds.) *Forensic Genetics, Theory and Applications*. International Burch University (2018)
- McGorin, R.J.: One hundred years of progress in food analysis. *J. Agric. Food Chem.* **57**, 8076 (2009)
- Omanović-Miklićanin E.: Application of nanospectroscopy in food science and agriculture. In: MacMillan, N., Sheremet, E., Fleischer, M., De Gryte (eds.) *Optical Nanospectroscopy, Part III "Optical Nanospectroscopy: Applications"*
- Jha, S.N.: Rapid detection of food adulterants and contaminants (Chap. 1). In: *Food Safety and Quality, Theory and Practice*, pp. 1–24 (2016)
- Cordella, C., Faucon, J.P., Cabrol-Bass, D., Sbirrazzuoli, N.: Application of DSC as a tool for honey floral species characterization and adulteration detection. *J. Therm. Anal. Calorim.* **71**, 279–290 (2003)
- Brewster, V.L., Goodacre, R.: Vibrational spectroscopy for "food forensics". In: *Infrared and Raman Spectroscopy in Forensic Science*, pp. 583–592 (2012)
- Yang, H., Irudayaraj, J., Paradkar, M.M.: Discriminant analysis of edible oils and fats by FTIR, FT-NIR and FT-Raman spectroscopy. *Food Chem.* **93**, 25–32 (2005)
- Zhu, Y., Zhang, L., Yang, L.: Designing of the functional paper-based surface enhanced Raman spectroscopy substrates for colorants detection. *Mater. Res. Bull.* **63**, 199–204 (2015)
- Baeten, V., Meurens, M.: Detection of virgin olive oil adulteration by Fourier Transform Raman spectroscopy. *J. Agric. Food Chem.* **44**, 2225–2230 (1996)
- Mathlouthi, M., Luu, D.V.: Laser-Raman spectra of D-glucose and sucrose in aqueous solution. *Carbohydr. Res.* **81**, 203–212 (1980)
- Baranska, M., Schutze, W., Schulz, H.: Determination of lycopene and β -carotene content in tomato fruits and related products: comparison of FT-Raman, ATRIR, and NIR spectroscopy. *Anal. Chem.* **78**, 8456–8461 (2006)
- Radovic, R., Radovic, B., Anklam, E.: Progress toward the rapid nondestructive assessment of the floral origin of European honey using dispersive Raman spectroscopy. *Appl. Spectrosc.* **56**, 521–527 (2002)
- Batsoulis, A.N., Siatis, N.G., Kimbaris, A.C., Alissandrakis, K.E., Pappas, C.S., Tarantilis, P.A., Harizanis, P.C., Polissiou, M.G.: FT-Raman spectroscopic simultaneous determination of fructose and glucose in honey. *J. Agric. Food Chem.* **53**, 207–210 (2005)
- de Olivera, L.F., Colombara, R., Edwards, H.G.M.: Fourier Transform Raman spectroscopy of honey. *Appl. Spectrosc.* **56**, 306–311 (2002)
- Shuifang, L., Shan, Y., Xiangrong, Z., Zhang, X., Ling, G.: Detection of honey adulteration by high fructose corn syrup and maltose syrup using Raman spectroscopy. *J. Food Compos. Anal.* **28**, 69–74 (2012)
- Özbalci, B., Boyaci, I.H., Topcu, A., Kadilar, C., Tamer, U.: Rapid analysis of sugars in honey by processing Raman spectra using chemometric methods and artificial neural networks. *Food Chem.* **136**, 1444–1452 (2013)
- Kneipp, K., Kneipp, H., Itzkan, I., Dasari, R.R., Feld, S.M.: Ultrasensitive chemical analysis by Raman spectroscopy. *Chem. Rev.* **99**, 2957–2976 (1999)
- Corvucci, F., Nobili, L., Dora Melucci, D., Grillenzoni, F.V.: The discrimination of honey origin using melissopalynology and Raman spectroscopy techniques coupled with multivariate analysis. *Food Chem.* **169**, 297–304 (2015)
- Thygesen, L.G., Lokke, M.M., Micklander, E., Engelsen, S.B.: Vibrational microspectroscopy of food. Raman vs. FT-IR. *Trends Food Sci. Technol.* **14**, 50–57 (2003)
- Yang, D., Ying, Y.: Applications of Raman spectroscopy in agricultural products and food analysis: a review. *Appl. Spectrosc. Rev.* **46**, 539–560 (2011)
- Ozaki, Y., Cho, R., Ikegaya, K., Muraishi, S., Kawauchi, K.: Potential of nearinfrared Fourier Transform Raman spectroscopy in food analysis. *Appl. Spectrosc.* **46**, 1503–1507 (1992)
- Das, G., Patra, N., Gopalakrishnan, A., Zaccaria, R.P., Toma, A., Thorat, S., Di Fabrizio, E., Diaspro, A., Salerno, M.: Surface enhanced Raman scattering substrate based on gold-coated anodic porous alumina template. *Microelectron. Eng.* **97**, 383–386 (2012)
- Zheng, J., He, L.: Surface-enhanced Raman spectroscopy for the chemical analysis of food. *Compr. Rev. Food Sci. Food Saf.* **13**, 317–328 (2014)
- Xie, Y., Li, Y., Niu, Y., Wang, H., Qian, H., Yao, W.: A novel surface-enhanced Raman scattering sensor to detect prohibited colorants in food by graphene/silver nanocomposite. *Talanta* **100**, 32–37 (2012)
- Delfino, I., Camerlingo, C., Portaccio, M., Della Ventura, B., Mita, L., Mita, D.G., Lepore, M.: Visible micro-Raman spectroscopy for determining glucose content in beverage industry. *Food Chem.* **127**, 735–742 (2011)
- Hanlon, E.B., Manoharan, R., Koo, T., Shafer, K.E., Motz, J.T., Fitzmaurice, M., Kramer, J.R., Itzkan, I., Dasari, R.R., Feld, M.S.: Prospects for in vivo Raman spectroscopy. *Phys. Med. Biol.* **45** (2000)
- Delfino, I., Camerlingo, C., Zenone, F., Perna, G., Capozzi, V., Cirillo, N., Lepore, M.: Oral pathology follow-up by means of micro-Raman spectroscopy on tissue and blood serum samples: an application of wavelet and multivariate data analysis. In: *Proceedings of SPIE*, 71652 (2009)
- Chen, Y.Q., Ni, Y.N.: Application of chemical pattern recognition techniques in food quality control. *Chem. Res. Appl.* **21**, 1–7 (2009)
- Lingxia, S., Jinping, C., Gaiming, Z., Miaoyun, L.: Research progress in application of chemometrics in food analysis. *Sci. Technol. Food Ind.* **33**, 444–448 (2012)
- Arvanitoyannis, I.S., Chalhouh, C., Gotsiou, P., Lydakis-Simantiris, N., Kefalas, P.: Novel quality control methods

- in conjunction with chemometrics (multivariate analysis) for detecting honey authenticity. *Crit. Rev. Food Sci. Nutr.* **45**, 193–203 (2005)
31. Ballabio, D., Robotti, E., Grisoni, F., Quasso, F., Bobba, M., Vercelli, S., Gosetti, F., Calabrese, G., Sangiorgi, E., Orlandi, M., Marengo, E.: Chemical profiling and multivariate data fusion methods for the identification of the botanical origin of honey. *Food Chem.* **21**, 1–7 (2018)
 32. Zhilin, G., Yang, Y., Jing, L., Xin, W., Minghui, Z., Yundong, J., Yuanying, N.: Using sensor and spectral analysis to classify botanical origin and determine adulteration of raw honey. *J. Food Eng.* **178**, 151–158 (2016)
 33. Orian, M., Ropciuc, S.: Botanical authentication of honeys based on Raman spectra. *Food Measur.* **12**, 545–554 (2017)
 34. Xiangrong, Z., Shuifang, L., Yang, S., Zhouyong, Z., Gaoyang, L., Donglin, S., Feng, L.: Detection of adulterants such as sweeteners materials in honey using nearinfrared spectroscopy and chemometrics. *J. Food Eng.* **101**, 92–97 (2010)
 35. Oroian, M., Ropciuc, S., Paduret, S.: Honey adulteration detection using Raman spectroscopy. *Food Anal. Methods* **11**, 959–968 (2017)
 36. Huaizhou, J., Qipeng, L., Xingdan, C., Haiquan, D., Hongzhi, G., Shangzhong, J.: The use of Raman spectroscopy in food processes: a review. *Appl. Spectrosc. Rev.* **51**, 12–22 (2015)
 37. Peica, N., Pavel, I., Pinzaru, S.C., Rastogi, V.K., Kiefer, W.: Vibrational characterization of E102 food additive by Raman and surface-enhanced Raman spectroscopy and theoretical studies. *J. Raman Spectrosc.* **36**, 657–666 (2005)

Part V

**Biomaterials, Biomechanics, Robotics and
Minimally Invasive Surgery**

Evaluation of Several Microalgal Extracts as Bioactive Metabolites as Potential Pharmaceutical Compounds

Ceren Gürlek, Çağla Yarkent, Ayşe Köse, İzel Oral, Suphi Ş. Öncel, and Murat Elibol

Abstract

The nature derived therapeutics is getting intense attention rather than chemical synthesis and synthetic ones. Today the expansion of natural bioactive molecule market is started to be dominated and generic drug and therapeutic understanding looks like to leave its place to a new horizon. Thus, natural originated therapeutics under controlled production conditions are of importance. Besides the public attention on natural molecules are also gain advance and the demand on this bioactive molecules is also increasing dramatically. The bioactive molecules from microalgae show antioxidant, antibacterial, antiviral, anticancer, skin regenerative, sunscreen, antihypertensive, neuroprotective and immunostimulatory effects which are favorable for pharmaceutical, nutraceutical and cosmetics industry. Also a new concept known as functional nutrition also broaden the acceptability and utilization of microalgae derived bioactive metabolites in new dietary formulations. The expansion of microalgal biotechnology and the number of research gained from the role of biologically active microalgal metabolites display the emergence of the microalgae farming for new pharmaceutical formulations. In this study, we prepared solvent and water extracts of *G. sulphuraria*, *N. texensis*, *S. bacillaris*, *E. carotinosus*, *C. minutissima*, *S. limacinum*, *C. cohnii*, and *C. vulgaris*. Antioxidant activity using DPPH radical scavenging activity and total phenolic compounds were measured from the methanolic extracts and water extracts. With the bioactive extracts cytotoxicity test were performed on Hep-G2 and B16-F10 cell lines. The results display potential onset of novel therapeutic compounds derived from microalgae.

Keywords

Microalgae • Cyanobacteria • Bioactivity • Pharmaceutical • Extraction

1 Introduction

The natural sources are becoming a sustainable and reliable resource in order to develop new pharmaceuticals with its high potential of patentability criteria and formulation [1]. Microalgae as being one of the promising source in single cell protein market is also a promising volunteer with its biologically active molecules [2]. Microalgae are the simple microscopic autotrophic photosynthetic organisms, ranging from unicellular to multi-cellular forms in aquatic environments. In contrast to microalgae do not have real embryos, roots, stems and leaves. They have the competence to use utilize water, sun-light and CO₂ to synthesize biomass through photosynthesis.

For a long time ago humans started to consume microalgae for dietary purposes as well as a source for traditional medicine and cosmetics [3]. The benefits and health promising characteristics of microalgae derive from the essential fatty acids, proteins, peptides, free amino acids, minerals, polysaccharides, carotenoids, phenolic compounds and other microalgae specific molecules [4–6]. However the biologically active molecules of microalgae opened a new era in bioactive metabolites for pharmaceutical and cosmetic purposes [7].

Microalgal compounds show antioxidant, antibacterial, antiviral, anticancer, skin regenerative, sunscreen, antihypertensive, skin whitening, immunomodulatory, neuroprotective and immunostimulatory effects which are favorable for pharmaceutical, nutraceutical and cosmetics industry [4, 5, 8]. Also a new concept known as functional nutrition also broaden the acceptability and utilization of microalgae derived bioactive metabolites in new dietary formulations [9]. The expansion of microalgal biotechnology and the

C. Gürlek · Ç. Yarkent · A. Köse (✉) · İ. Oral · S. Ş. Öncel · M. Elibol
Department of Bioengineering, Ege University,
35100 İzmir, Turkey
e-mail: ayse.kose@ege.edu.tr

number of research gained from the role of biologically active microalgal metabolites display the emergence of the microalgae farming for new therapeutic, nutritional and cosmetic formulations [10]. Considering the food sector along with agriculture and livestock sectors globally, adaptation of valuable sources from microalgae can give birth to a new biotechnological investment area and/or make it possible to improve existing technologies.

Synthetic compounds are started to be replaced with natural bioactive substances due to the low stability, cytotoxicity and carcinogenicity. Butylate hydroxytoluene (BHT), the most generally utilized antioxidant compound is also show carcinogenic effects. Therefore, natural antioxidants are emerging [11]. Phototrophic microalgae are highly exposed to oxidative and radical stresses, thus effective antioxidative complexes accumulate to protect their cells from free radicals [12].

Phenolic compounds are important in the classification of antioxidants in plants. However, the importance of phenolic compounds for antioxidants in microalgae is not clear. The content of phenolic substances in microalgae has been shown to play a role in antioxidant response when exposed to stress under UV light. However, there is no consensus on the importance of phenolic compounds in microalgae for antioxidants.

The aim of this study is to investigate DPPH radical scavenging antioxidant activity and total phenolic compounds of several biotechnologically important and/or emerging microalgal species. Conventional extraction techniques are used to obtain crude extracts.

2 Materials and Methods

2.1 Cultivation of Microalgae

Several microalgae species are cultivated in different media (see Table 1). *Galderia sulphuraria* were cultivated in CM (Cyanidium Medium), *Neochloris texensis* were cultivated in PM (Proteose Medium), and *Stichococcus bacillaris* were cultivated in TAP + Soil Extract, *Ettlia carotinos*, *Chlorella minutissima*, and *Chlorella vulgaris* were cultivated in BG-11 medium. *Cryptocodinium cohnii* and *Schizochytrium limacinum* were cultivated heterotrophically in ATCC 30772 medium and HM (Heterotrophic Medium) respectively. Cultures were cultivated respectively in 50, 100, and 250 mL flasks at 23 °C at 100 rpm agitation. *Galderia sulphuraria* were cultivated at 30 °C. Then, cultures that reached stationary phase were harvested at 3500 rpm (Nuve, Turkey) for 10 min and freeze-dried and kept at -20 °C for further experiments.

2.2 Extraction of Crude Extract

Methanol extraction

20 mL methanol was added on 0.5 g dry biomass and sonicated by using Bandelin Sonopuls HD2070 sonicator (9 cycle, %50 power) for 20 min. Samples were centrifuged at 3500 rpm for 5 min. Pellets were re-extracted with 20 mL methanol 3 times and supernatant was collected. The samples were filtered through 0.45 µm syringe type filters and evaporated at 40 °C (Stuart RE300DB, UK). The crude extracts were kept at -20 °C for further analysis.

Hot water extraction

1 g dry weight of certain species (*Cryptocodinium cohnii*, *Stichococcus bacillaris*, *Neochloris texensis*) were collected and 100 mL distilled water added on and boiled for 30 min. After cooling down extracts were centrifuged at 3500 rpm for 10 min, supernatants were freeze-dried. The crude extracts were kept at -20 °C for further analysis.

Radical scavenging activity

The extracts were dissolved in methanol with a final concentration of 250 µg/mL and 0.5 mL of 1 mM methanolic solution of DPPH. (2,2-diphenyl-1-picrylhydrazyl hydrate radical from Sigma) were added on. Mixture were stirred for 15 s and incubated at room temperature for 30 min. The change in the colour was measured with Optizen Pop UV/VIS Spectrophotometer (Korea) at 517 nm and methanol was used as a blank. The radical scavenging activity was determined with using the Eq. 1.

$$\text{Radical scavenging activity} (\%) = \left(1 - \frac{A_{\text{sample}}}{A_{\text{DPPH}}}\right) \times 100 \quad (1)$$

A_{sample} : Absorbance of the methanolic solution of extract in DPPH. A_{DPPH} : Absorbance of methanolic solution of DPPH [13].

Total phenol assay

The total phenolic content of the extract was determined by Folin-Ciocalteu method. The extracts were dissolved in methanol with a final concentration of 7 mg/mL. 100 µL of this solution were transferred into a flask which contains 10 mL of distilled water. 500 µL Folin-Ciocalteu reagent (Sigma) was added then stirred and let it stand for 5 min and 1.5 mL of 20% (w/v) Na₂CO₃ were added and incubated at

Table 1 Culture conditions and media of several microalgae species

Cells	Medium	Culture conditions
<i>Galderia sulphuraria</i> SAG 108-78	CM	30 °C, 100 rpm, $70 \pm 5 \mu\text{E m}^{-2} \text{s}^{-1}$
<i>Neochloris texensis</i> EGEMACC-68	PM	23 °C, 100 rpm, $70 \pm 5 \mu\text{E m}^{-2} \text{s}^{-1}$
<i>Stichococcus bacillaris</i> SAG 379-2	TAP + soil extract	23 °C, 100 rpm, $70 \pm 5 \mu\text{E m}^{-2} \text{s}^{-1}$
<i>Ettlia carotinoso</i> SAG 2134	BG-11	23 °C, 100 rpm, $70 \pm 5 \mu\text{E m}^{-2} \text{s}^{-1}$
<i>Chlorella minutissima</i> UTEX 2341	BG-11	23 °C, 100 rpm, $70 \pm 5 \mu\text{E m}^{-2} \text{s}^{-1}$
<i>Schizochytrium limacinum</i> PA-968	HM	23 °C, 100 rpm
<i>Cryptocodinium cohnii</i> CCMP 316	ATCC 30772	23 °C, 100 rpm
<i>Chlorella vulgaris</i> SAG 211-11b	BG-11	23 °C, 100 rpm, $70 \pm 5 \mu\text{E m}^{-2} \text{s}^{-1}$

room temperature for 1 h. Absorbance was measured using Optizen Pop UV/VIS Spectrophotometer (Korea) at 760 nm and the concentration of phenolics in the solutions were calculated with calibration curve of gallic acid. 25, 50, 100, 250 ppm of gallic acid solutions were used for calibration curve. The solution which contains distilled water, Folin-Ciocalteu reagent and 20% (w/v) Na_2CO_3 (without the extracts) was used as blank for both samples and gallic acid.

3 Results and Discussion

3.1 Antioxidant Efficiency/Potential of Extracts

Antioxidant activity is one of the most studied characteristics of the compounds due to the importance of prevention of radical mediated mutagenesis and preservatives for food, pharmaceuticals, and cosmetics industries [14]. Microalgae due to their photosynthetic features have internal protection mechanism against free radical mediated oxidative stress and accumulate photosynthetic primary and secondary pigments to reduce increased oxidative stress responses to balance cellular metabolism [15]. Microalgae are attractive sources due to the diversity of the species and compounds derived from them [16]. In this study, we evaluate the DPPH radical scavenging activity to measure antioxidant capacity of methanolic extracts obtained from *G. sulphuraria*, *N. texensis*, *S. bacillaris*, *E. carotinoso*, *C. minutissima*, *S. limacinum*, *C. cohnii*, and *C. vulgaris*. Hot water extracts from *N. texensis*, *S. bacillaris*, and *C. cohnii* were also investigated. BHT was used as a reference antioxidant compound. The results showed that methanolic extract from almost all microalgal samples had great antioxidant capacity (see Table 2). Radical scavenging activity (RSA) of BHT was determined as $\% 98 \pm 0.01$. *G. sulphuraria* showed the highest RSA among all species. But the capacity of the other species was also significant. *G. sulphuraria* were cultivated at higher temperature than other species. This is a result of rapid adaptation of strain itself to survive in extreme conditions. *E. carotinoso* and *N. texensis* species are known as

synthesizing carotenoid-like astaxanthin, lutein, zeaxanthin and the results are in good accordance with previous studies expressing the antioxidant capacity of these species. *Chlorella* being one of the most conventional microalgal species showed also high RSA as expected [17].

In this study for the first time, RSA of crude extract from *S. bacillaris* was determined. The result showed that in the search of candidate species for novel compounds *S. bacillaris* can be one of the alternatives when the rapid growth of the strain is considered ($t_d = 14 \pm 2$ h, data obtained from previous studies).

S. limacinum and *C. cohnii* species are known to be producers for omega-3 fatty acids however other bioactive compounds from those are not determined well [18]. This study showed that crude extracts were promising candidates. Because of heterotrophic production extracts were colourless which may increase the acceptability. Also, heterotrophic cultures have more rapid growth rate and scaling up is easier in comparison to photoautotrophic cultures due to their applicability to conventional production systems [19].

Hot water extracts also showed high RSA. Water is non-toxic and cheaper solvent than methanol. Hence water extraction process can be suitable for mass production for biopharmaceutical [20].

3.2 Total Phenol Content of Extracts

Phenolic compounds, mainly classified as phenolic acid, tannins, and polyphenols, are major contributors for the investigation antioxidant capacity [21]. Phenolic compounds may show certain bioactivity on cell culture assays. In this study we investigated the total phenol content of the extracts as a parameter for antioxidant activity.

The total phenol content of methanolic extracts, which was determined by FolinCiocalteu method, varied from 41 to 312 mg GAE/g extract (see Table 3). Extracts that contained high phenol content had showed a blueish colour as the standard gallic acid had. *G. sulphuraria* had much higher total phenol content when compared to other species which

Table 2 Radical scavenging activities of methanolic extracts of several microalgae

Microalgae species	%RSA
Methanolic extracts	
<i>Galderia sulphuraria</i> SAG 108-78	95 ± 0.7
<i>Ettlia carotinoso</i> SAG 213-4	92 ± 0.5
<i>Neochloris texensis</i> EGEMACC-68	91 ± 0.03
<i>Chlorella minutissima</i> UTEX 2341	90 ± 0.2
<i>Chlorella vulgaris</i> SAG 211-11b	90 ± 0.03
<i>Stichococcus bacillaris</i> SAG 379-2	89 ± 0.1
<i>Schizochytrium limacinum</i> PA-968	90 ± 0.1
<i>Cryptocodinium cohnii</i> CCMP 316	89 ± 0.2
Hot water extracts	
<i>Neochloris texensis</i> EGEMACC-68	89 ± 2
<i>Stichococcus bacillaris</i> SAG 379-2	89 ± 0.1
<i>Cryptocodinium cohnii</i> CCMP 316	90 ± 0.02

Table 3 Total phenol content of methanolic extracts of microalgal species

Microalgae species	mg GAE/g extract
Methanolic extracts	
<i>Galderia sulphuraria</i> SAG 108-78	312 ± 20
<i>Chlorella minutissima</i> UTEX 2341	175 ± 12
<i>Neochloris texensis</i> EGEMACC-68	174 ± 4
<i>Schizochytrium limacinum</i> PA-968	129 ± 4
<i>Ettlia carotinoso</i> SAG 213-4	107 ± 5
<i>Chlorella vulgaris</i> SAG 211-11b	78 ± 19
<i>Stichococcus bacillaris</i> SAG 379-2	53 ± 12
<i>Cryptocodinium cohnii</i> CCMP 316	42 ± 3
Hot water extracts	
<i>Neochloris texensis</i> EGEMACC-68	-2 ± 0
<i>Stichococcus bacillaris</i> SAG 379-2	41 ± 3
<i>Cryptocodinium cohnii</i> CCMP 316	117 ± 5

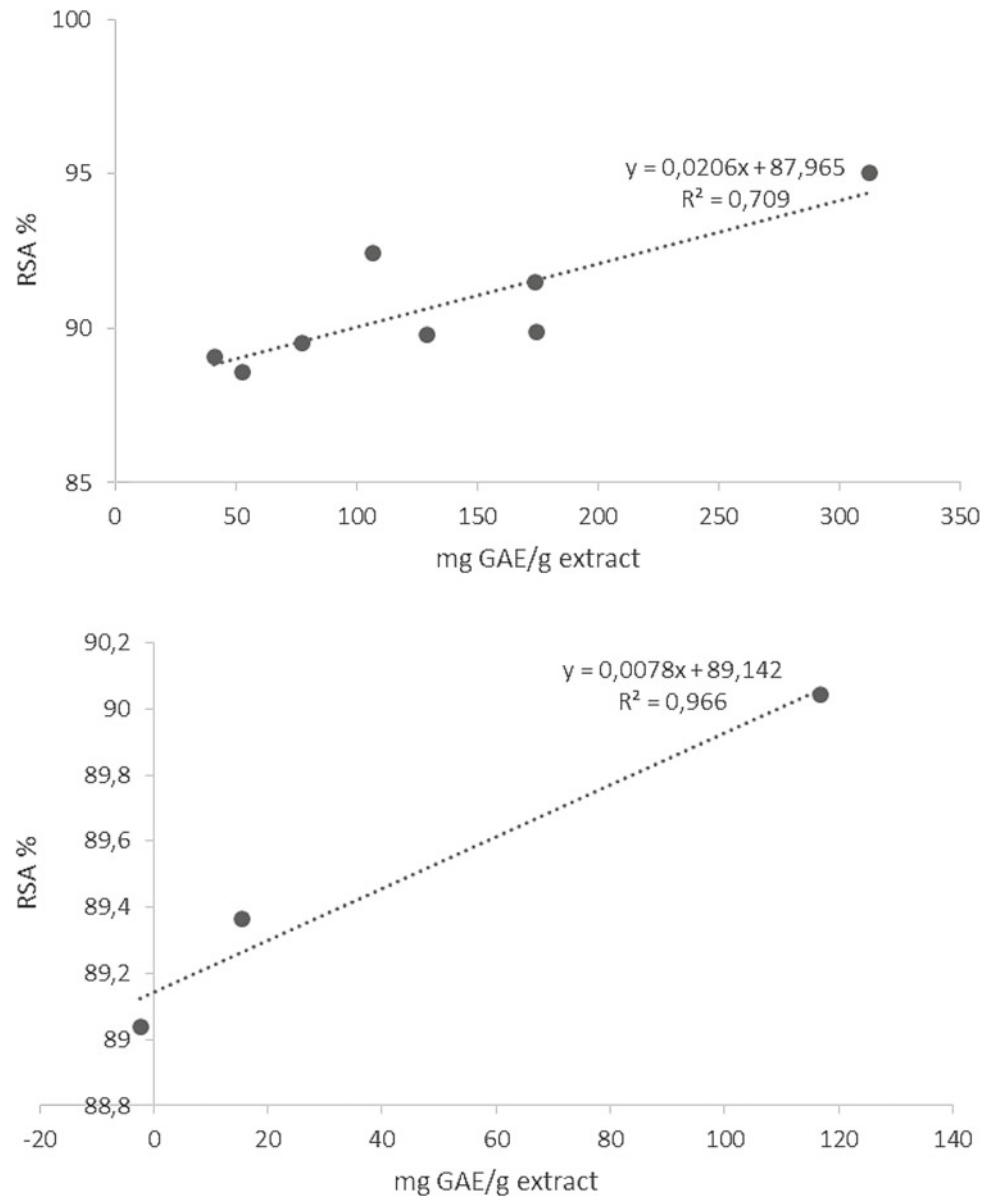
also showed the highest RSA. *C. minutissima*, *N. texensis* followed *G. sulphuraria* with high total phenol contents of 174 and 173 mg GAE/g extract respectively. *S. limacinum*, *E. carotinoso*, *C. vulgaris*, *S. bacillaris*, and *C. cohnii* had total phenol contents of 129, 106, 77, 52, and 41 mg GAE/g extract respectively.

Correlation between antioxidant activity and total phenol content of extracts was determined. The correlation for methanolic extracts ($R^2 = 0.709$) and hot water extracts ($R^2 = 0.966$) were significant (Fig. 1). This result showed that total phenol content made a contribution on antioxidant capacity of selected microalgae species.

4 Conclusion

Microalgae possess great contribution to the development of novel compounds. In this study we investigate the total phenolic and DPPH radical scavenging activities of several microalgal extracts. *G. sulphuraria* were found to have strong RSA and total phenolic content among all the samples. The strong correlation coefficient between antioxidant activity and phenolic content contributed that the antioxidant activity can be rooted from the phenolic compounds. The cell line experiments on HepG2 and B16F10 melanoma cells

Fig. 1 The correlation of antioxidant activity and total phenol content for methanolic extracts (above); for hot water extracts (below)



are ongoing to investigate in vitro proliferative and cytotoxic effect of the extracts. The overall results indicated that even crude extracts of microalgae can be utilized as novel formulations for food, pharmaceuticals and cosmetics industry.

Acknowledgements This study is a joint project with Ege University (Turkey), Liege University (Belgium), and Daegu Haany University (South Korea) named, KONNECT (Exploring the potential bioactive molecules from microalgae and understanding of their gene regulations-ALGACTIVE). The authors would like to thank The Scientific and Technological Council of Turkey (TÜBİTAK) for funding the project KONNECT 216M390. The authors declare that there is no conflict of interest.

References

1. Köse, A., Oncel, S.S.: Microalgal biotechnology ethics and intellectual property rights. *Dokuz Eylül Üniversitesi Mühendislik Fakültesi Fen Ve Mühendislik Dergisi* **18**(52), 116–127 (2016)
2. Becker, E.W.: Micro-algae as a source of protein. *Biotechnol. Adv.* **25**, 207 (2007)
3. Oncel, S., Kose, A., Vardar, F., Torzillo, G.: From ancient tribes to modern societies, microalgae evolution from a simple food to an alternative fuel source. In: Kim, S.K. (ed.) *Handbook of Marine Microalgae*. Biotechnology Advances, pp. 127–144. Academic Press (2015)
4. Cha, K.H., Koo, S.Y., Lee, D.U.: Antiproliferative effects of carotenoids extracted from *Chlorella ellipsoidea* and *Chlorella*

- vulgaris* on human colon cancer cells. *J. Agric. Food Chem.* **56**, 10521–10526 (2008)
5. Samarakoon, K.W., Ko, J.Y., Shah, M.R., Lee, J.H., Kang, M.C., Nam, K.O., Lee, J.B., Jeon, Y.J.: In vitro studies of anti-inflammatory and anticancer activities of organic solvent extracts from cultured marine microalgae. *Algae* **28**(1), 111–119 (2013)
 6. NGo, D.-H., Vo, T.-S., Ngo, D.-N., Wijesekara, I., Kim, S.-K.: Biological activities and potential health benefits of bioactive peptides derived from marine organisms. *Int. J. Biol. Macromol.* **51**, 378–383 (2012)
 7. Michalak, I., Chojnacka, K.: Algae as production systems of bioactive compounds. *Eng. Life Sci.* **15**(2), 160–176 (2015)
 8. de Moraes, M.G., da Silva Vaz, B., de Moraes, E.G., Costa, J.A.V.: Biologically active metabolites synthesized by microalgae corporation. *BioMed Research International Volume Article ID 835761* (2015)
 9. Wells, M.L., Potin, P., Craigie, J.S., Raven, J.A., Merchant, S.S., Helliwell, K.E., Smith, A.G., Camire, M.E., Brawley, S.H.: Algae as nutritional and functional food sources: revisiting our understanding. *J. Appl. Phycol.* **29**(2), 949–982 (2017)
 10. Wang, H.D., Chen, C.C., Huynh, P., Chang, J.S.: Exploring the potential of using algae in cosmetics. *Bioresour. Technol.* **184**, 355–362 (2015)
 11. Chemat, F., Vian, M.A., Cravotto, G.: Green extraction of natural products: concept and principles. *Int. J. Mol. Sci.* **13**(7), 8615–8627 (2012)
 12. Pulz, O., Gross, W.: Valuable products from biotechnology of microalgae. *Appl. Microbiol. Biotechnol.* **65**, 635–648 (2004)
 13. Akay, S., Alpak, I., Yesil-Celiktas, O.: Effects of process parameters on supercritical CO₂ extraction of total phenols from strawberry (*Arbutus unedo L.*) fruits: an optimization study. *J. Sep. Sci.* **34**(15), 192531 (2011)
 14. Balboa, E.M., Conde, E., Moure, A., Falque, E., Dominguez, H.: In vitro antioxidant properties of crude extracts and compounds from brown algae. *Food Chem.* **138**(2–3), 1764–1785 (2013)
 15. Goiris, K., Muylaert, K., Fraeye, I., Foubert, I., De Brabanter, J., De Coman, L.: Antioxidant potential of microalgae in relation to their phenolic and carotenoid content. *J. Appl. Phycol.* **24**(6), 1477–1486 (2012)
 16. Singh, S., Kate, B.N., Banerjee, U.C.: Bioactive compounds from cyanobacteria and microalgae: an overview. *Crit. Rev. Biotechnol.* **25**(3), 73–95 (2008)
 17. Li, H.B., Cheng, K.W., Wong, C.C., Fan, K.W., Chen, F., Jiang, Y.: Evaluation of antioxidant capacity and total phenolic content of different fractions of selected microalgae. *Food Chem.* **100**(3), 771–776 (2007)
 18. Yu, J.H., Wang, Y., Sun, J., Bian, F., Chen, Y., Zhang, Y., Bi, Y. P., Wu, Y.J.: Antioxidant activity of alcohol aqueous extracts of *Cryptocodinium cohnii* and *Schizochytrium* sp. *J. Zhejiang Univ. Sci. B (Biomed. & Biotechnol.)* **18**(9), 797–806 (2017)
 19. Pleissner, D., Lim, W.C., Sun, Z., Lin, C.S.K.: Food waste as nutrient source in heterotrophic microalgae cultivation. *Bioresour. Technol.* **137**, 139146 (2013)
 20. Shanab, S.M.M., Mostafa, S.S.M., Shalaby, E.A., Mahmoud, G.I.: Aqueous extracts of microalgae exhibit antioxidant and anticancer activities. *Asian Pac. J. Trop. Biomed.* **2**(8), 608–615 (2012)
 21. Marxen, K., Vanselow, K.H., Lippemeier, S., Hintze, R., Ruser, A., Hansen, U.P.: Determination of DPPH radical oxidation caused by methanolic extracts of some microalgal species by linear regression analysis of spectrophotometric measurements. *Sensors* **7**, 2080–2095 (2007)

A Novel Approach in Determination of Biofilm Forming Capacity of Bacteria Using Random Forest Classifier

Monia Avdić, Zerina Mašetić, Ahmed El Sayed, Lejla Odošajić, and Mirsada Hukić

Abstract

Biofilms are microbial mono-specie or multi-specie (consortium) communities that play a significant role in the clinical, industrial and natural settings. Biofilm formation can be determined by using qualitative and quantitative tests, where the latter are considered more reliable. The prominently accepted result interpretation procedure for quantitative tests includes the calculation of optical density cut off value (ODc) followed by the determination of biofilm forming categories using formulas. This procedure is time consuming and many laboratories resort to the use of less reliable tests to conduct biofilm formation analysis. This is where Machine Learning (ML) could play a significant role. In this study Random Forest Classifier has been applied to a dataset of 960 bacterial isolates, where biofilm formation was tested using the spectrophotometric assay and biofilm categorization was carried out using formulas based on ODc calculations. The proposed model, based on the Random

Forest Classifier, achieved the classification accuracy of 96.35% and the classification error is a bare 3.65%. Absolute and relative errors of the prediction model are 0.208 ± 0.167 and $20.82\% \pm 16.72\%$, respectively. Finally, the correlation coefficient between the predicted and actual value is 0.980. This paper illustrates how ML could be used to determine the biofilm forming categories and as such aid in the development of a unique standardized procedure for the evaluation of results obtained by quantitative tests of biofilm formation.

Keywords

Biofilm • Cut-off value • Machine learning • Random forest • Spectrophotometer

M. Avdić

Department of Genetics and Bioengineering, International Burch University, Sarajevo, Bosnia and Herzegovina

Z. Mašetić

Department of Information Technologies, International Burch University, Sarajevo, Bosnia and Herzegovina

A. El Sayed

Department of Civil Engineering, International Burch University, Sarajevo, Bosnia and Herzegovina

L. Odošajić (✉)

Department of Architecture, International Burch University, Sarajevo, Bosnia and Herzegovina
e-mail: lejla.odobasic@ibu.edu.ba

M. Hukić

Institute for Biomedical Diagnostics and Research NALAZ, Sarajevo, Bosnia and Herzegovina

M. Hukić

Academy of Sciences and Arts of Bosnia and Herzegovina, Sarajevo, Bosnia and Herzegovina

1 Introduction

Bacteria are ubiquitous, they inhabit all niches on earth where their growth requirements are met [1]. Over 99% of these bacteria have the ability to form biofilms which in fact represents their natural state of being [2], making them the most successful colonizers among all microorganisms [3]. Since biofilms hold a significant role in the clinical, industrial and natural settings, their importance has been recognized and as a result the interest in their study has increased dramatically in the recent decades [4].

Various biofilm research methodologies have been developed [4–6] and in the realm of phenotypic determination of biofilm forming capacity of microbes following tests are most commonly used: tube test, TCP (Tissue Culture Plate) method, spectrophotometric assays and congo red agar test [7, 8]. Quantitative tests in general are considered to be more reliable. The results—which are obtained in the form of absorbance values—are read at specific wavelengths which correspond to “raw data” generated in the test system [4, 9].

However, in order to get more descriptive results, further analysis of the obtained “raw data” is mandatory. This can be achieved by using different approaches such as: categorization according to predefined values, use of standardized formulas and the use of positive control as the starting point or by considering a strain positive if its OD (Optical Density) is double the value of the negative control [10].

Currently the most referent approach does not include the use of positive standards while the cut off is calculated as three standard deviations above the mean OD of the negative control which as such is an endpoint titre. The endpoint titre is defined as “the reciprocal of the highest analyte dilution that gives a reading above the cut off” [11]. The cut off value is further used in standardized formulas to determine the biofilm categories (such as non-adherent, weak, moderate and strong). However, there have been no standard procedures established to determine the cutoff and predefined values from earlier assays are often used as referees due to the fact that other approaches are labor intensive, costly and impractical for most diagnostic procedures [9]. The downfall of the use of predefined values does not provide statistically meaningful information and can generate false negative or false positive results.

In order to address the above-mentioned issue, as discussed by Stepanović et al., a need for further optimization and guideline establishment in the field of biofilm studies, especially in the realm of result interpretation, is of crucial importance [10]. The potential for such development could rest within the field of artificial intelligence and the application of machine learning (ML) algorithms, as it could potentially solve the above-mentioned issues and lead to the faster and better result interpretation.

Following practice adopted in other fields [12–16], it can be seen that machine learning (ML) has application in many fields including microbiology [17–22]. The most common usage of ML is that of entering datasets with varying parameters and outcomes in order to allow ML to create relations between them through the use of algorithms [23, 24].

This study focuses on the interpretation of results in the biofilm formation through the application of ML technique, called *Random Forest Classifier*, on a dataset obtained by studying biofilms using spectrophotometric assay.

Random forest is the method being successfully applied in many biomedical studies [23–26]. Moreover, random forest method is ensemble method that combines multiple trees. Ensemble methods have advantages over single-classifier approach as they engage multiple methods that work together and complement each other. Therefore, Random Forest classifier is a proposed method for determination of biofilm forming capacity of bacteria.

2 Materials and Methods

A total of 960 bacterial isolates from urine specimen were tested. The criteria for inclusion into the study was that the sample had only one causative agent of UTI and that only one of three successive urine samples from the same patient was taken into consideration. Species identification was carried out using standardized biochemical testing. The isolated species included: *Escherichia coli* (504), *Enterococcus faecalis* (168), *Staphylococcus aureus* (88), *Pseudomonas aeruginosa* (40) and various *Enterobacteriaceae* (160).

Biofilm formation of all the bacterial isolates was tested using the spectrophotometric assay. The spectrophotometric assay consists of incubated tested bacterial strain in 5 ml of desired medium (pure culture) in plastic test tubes, subsequent disposal of the liquid culture and staining of tubes with crystal violet. Ethanol (96%) was added as a solvent to the crystal violet stained tubes and incubated for 10 min. Volume of 1 ml dissolved solution was transferred to a plastic cuvette and the absorbance was measured on a spectrophotometer. The maximum absorbance of the crystal violet solution was determined by measuring the absorbance spectra for this dye (wavelength 595 nm). Consequently, all further measurements were carried out at this wavelength. Inoculated tubes were used as a negative control [6]. All testing was carried out in triplicate and average values were used for further processing.

From the obtained measurements the following parameters were determined: STDEV, Average and cut-off OD.

The cut-off OD for the spectrophotometric determination of biofilm formation was calculated as three standard deviations above the mean OD of the negative control. Classification of bacterial adherence was calculated as per given formulas for all tested conditions and bacterial adherence was determined as one of four possible categories: non-adherent, weak, moderate and strong biofilm formation as shown in Table 1 [10].

This dataset was used for prediction model development. As input data the following parameters were used: value of negative control in quadruplet, STDEV of the negative control, average of the negative control and measured average of the OD for each well. Output data were as following: non-adherent, weak, moderate and strong biofilm formation.

2.1 Random Forest

Random Forest is a meta estimator that combines a number of tree predictors, in a way that each tree depends on a value of random vector that is distributed among all these trees in

Table 1 Cut off OD values (at 595 nm) and classification of bacterial adherence by spectrophotometric assay

Formula	Biofilm formation
$OD \leq OD_c$	Not adherent
$OD_c < OD \leq 2 \times OD_c$	Weak
$2 \times OD_c < OD \leq 4 \times OD_c$	Moderate
$4 \times OD_c < OD$	Strong

the forest, in the same distribution. For the i th tree, the random vector θ_i is generated, independent from previously generated vectors, but with the same distribution. The tree is grown using the training set and generated vector θ_i , resulting in the collection of tree-structured classifiers. When the tree ensemble is created, trees vote for the most popular class [27]. In *Random Forest*, margin function defines the extent to which the average number of votes at random vectors for the right class exceeds the average number of votes for any other input, and is defined by [27]:

$$mg(X, Y) = \text{avg}_i I(h_i(X) = Y) - \max_{j \neq Y} \text{avg}_i I(h_i(X) = j) \quad (1)$$

where I is indicator function, and X and Y indicate the probability over X, Y space. The larger margin is, the more confidence in the classification exists. Additionally, generalization error is defined by the formula [27]:

$$PE^* = P_{x,y}(mg(X, Y) < 0) \quad (2)$$

In this study, a forest consists of 12 trees, where gini_index is used as a splitting criterion. Increasing the number of trees, the classification accuracy remains the same, whereas decreasing the number of trees led to the decrease in classification accuracy. Therefore, 12 was selected as an optimal number of trees, when the classification accuracy is considered as a fitting function. Moreover, pruning with the confidence level of 0.25 for error calculation was used. Finally, the confidence vote strategy, which selects the class with the highest accumulated confidence was selected as the preferable voting strategy.

3 Results

Spectrophotometric Determination of biofilm forming capacity of the isolated bacterial strains

Since the biofilm category determination according to the recommended procedure, using OD_c and formulas, is same regardless of the bacterial species in question biofilm category was determined as shown in Table 2 and as such further used for the creation of the used dataset. Results of the spectrophotometric analysis of the biofilm forming potential of the tested bacterial isolates indicate that the highest

percentages of isolates were non-adherent, while the lowest percentage of strong biofilm formers was determined.

3.1 Performance Evaluation

The whole dataset, which consists of 960 instances is divided into training and testing subsets, in ratio of 80–20% respectively. While dividing the dataset into training subsets, stratified sampling is applied, ensuring that the class distribution in both subsets is the same as in the whole dataset. The model was trained with 768 instances, while the testing was done with 192 instances. The performance of the model was evaluated through several performance metrics: classification accuracy and error, recall and precision, absolute and relative errors, and correlation (Table 3).

Accuracy of the model is the performance metric that presents the number of correctly classified instances within the input set, or percentage of correctly classified instances. Moreover, accuracy can also be represented in terms of true positive (TP), true negative (TN), false positive (FP) and false negative (FN) outcomes.

$$Accuracy = \frac{TP + TN}{TP + TN + FP + FN} \quad (3)$$

Additional performance metric used for results presentation is classification error, which represents the relative number of misclassified examples, or percentage of incorrect predictions. Recall and precision represents the proportion of actual positive examples identified correctly and proportion of positive examples identified correctly, respectively. They are represented by following formulas:

$$Recall = \frac{TP}{TP + FN} \quad (4)$$

$$Precision = \frac{TP}{TP + FP} \quad (5)$$

Absolute error represents the average absolute deviation of the predicted value from the actual value, while relative error represents the average of absolute deviation of the predicted value from the actual value, divided by the actual value. Finally, the correlation calculates the coefficient between the predicted and the actual value.

Table 2 Biofilm categories of the 960 tested bacterial isolates, total number and percentage

Biofilm category	Total number of bacterial isolates	Percentage (%)
Non-adherent (NA)	409	42.6
Weak (W)	311	32.39
Moderate (M)	160	16.67
Strong (S)	80	8.33
Total	960	100

Table 3 Biofilm categories of the 960 tested bacterial isolates divided into training and testing subsets (80:20)

Biofilm category	Training subset	Testing subset	Total
Non-adherent (NA)	327	82	409
Weak (W)	249	62	311
Moderate (M)	128	32	160
Strong (S)	64	16	80
Total	768	192	960

3.2 Experimental Results

The proposed model, based on the *Random Forest Classifier*, achieved the classification accuracy of 96.35%. The results are shown in forms of confusion matrices (Table 4).

It is important to note, that the total classification error is a bare 3.65%. From the Table 2, it can be seen that only 7 instances in the whole testing subset were misclassified, whereas 185 instances were correctly classified. This also leads to a high true positive rate per each class (Fig. 1).

Hence, the recall value for the, NA class is 96.34, for W class is 98.39 for M class 90.62 and for S class 100. These results are shown in the Table 5.

The precision values are also given for a specific class and shown in the Table 6.

Absolute and relative errors of the prediction model are 0.208 ± 0.167 and $20.82\% \pm 16.72\%$, respectively. Finally, the correlation coefficient between the predicted and actual value is 0.980.

Table 4 Confusion matrix of classification process, representing the number of correctly classified instances per each classification class

	True NA (non-adherent)	True W (weak)	True M (moderate)	True S (strong)
Predicted NA (non-adherent)	79	0	0	0
Predicted W (weak)	3	61	3	0
Predicted M (moderate)	0	1	29	0
Predicted S (strong)	0	0	0	16

4 Discussion

Biofilms are microbial mono-specie or multi-specie (consortium) communities that are the most successful colonizers among microorganisms, because they are ubiquitous in nature and responsible for many diseases [3]. Despite this fact, routine testing of biofilm forming capacity of bacteria is not common practice and can partially be attributed to the fact that the interpretation of the obtained results from quantitative tests need further processing [10] in order for the results to be meaningful to the specialist in the field. The use of standardized formulas is time ineffective while the use of predefined values for comparison purposes is statistically insignificant. As such, new approach needs to be developed in order to facilitate the interpretation of the “raw data” obtained by quantitative biofilm testing.

Considering that biofilms represent a new frontier in microbiology, the introduction of ML techniques to the

Fig. 1 Scatter plot of the classified instances

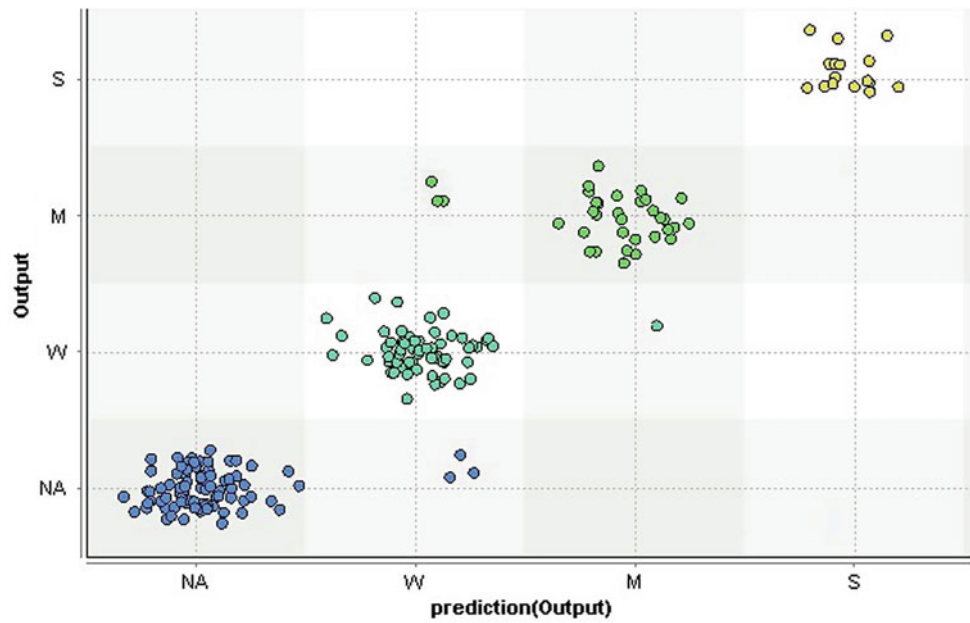


Table 5 Recall values representing the percentage of correctly classified instances per classes

Actual class	NA (non-adherent)	W (weak)	M (moderate)	S (strong)
Class recall	96.34	98.39	90.62	100

Table 6 Precision values representing the percentage of relevant instances per classes

Predicted class	Class precision
Predicted NA (non-adherent)	100
Predicted W (weak)	91.04
Predicted M (moderate)	96.67
Predicted S (strong)	100

interpretation of the data testing is of great value in the further study of this subject. This process would aid in the determination of the biofilm forming categories (output) based on the results of the OD of the negative control (in quadruplet), its STDEV, average and average OD of the tested sample (inputs). Furthermore, this method would allow the establishment of a standard in the interpretation of quantitative biofilm tests by enabling a very accurate testing of bacteria in their natural state which is the biofilm.

In this study we employed a ML technique on the obtained dataset of 960 bacterial isolates from clinical specimen. Biofilm forming capacity of the isolates was determined spectrophotometrically at the wavelength of 595 nm where the negative control was used for the determination of the cut-off OD value (three STDEV above the mean OD of the negative control) and this value was further used for the biofilm categorization according to formulas. As input data the following parameters were used: value of negative control in quadruplet, STDEV of the negative

control, average of the negative control and measured average of the OD for each well. Output data were as following: non-adherent, weak, moderate and strong biofilm formation.

Up to now ML techniques were applied for biofilm quantification by analysis of images obtained by different types of microscopy i.e. automatic machine learning processes were used to evaluate the efficiency of biofilm removal from surfaces using Scanning Electron Microscopy images [20]. Other studies were directed towards quantification of dental biofilms using data obtained by Quantitative light-induced fluorescence (QLF) images of teeth [16]. While machine learning based prediction, models were used in the prognosis of biofilm inhibiting peptides [22]. However, no data can be found on the application of ML techniques in the interpretation of results for biofilm categorization using cut-off OD.

The proposed model, based on the *Random Forest Classifier*, achieved the classification accuracy of 96.35%

and the classification error is a bare 3.65%. Absolute and relative errors of the prediction model are 0.208 ± 0.167 and $20.82\% \pm 16.72\%$, respectively. Finally, the correlation coefficient between the predicted and actual value is 0.980.

Different values of Random Forest parameters were evaluated, with following values of number of trees: 5, 10, 12, 15, 20, 25, 50 and 100. However, the classification accuracy decreased with number of trees less than 12 and remains the same with the number of trees bigger than or equal to 12. However, the computational time was significantly reduced when higher number of trees were employed. Therefore, the optimal number of trees was selected to be 12. It is obvious that the performance of the classifier highly depends on the input features. Additionally, high classification performance of Random Forest classifier gives the understanding of the input data that represent the biofilm.

Considering the high classification accuracy of the employed classification in our research using random forest it is evident that it could potentially be used for the determination of biofilm forming capacity in interpretation of results using quantitative phenotypic tests. In our future work we aim to compare different ML techniques for biofilm categorization.

Considering that 99% of bacteria have the ability to form biofilms and biofilms represent their natural state standardization of methods for interpretation of results of quantitative tests is highly recommended.

5 Conclusion

The inquiry into biofilms is still an uncharted territory in the field of microbiology and as such the introduction of ML techniques to the interpretation of the data testing is of great value in the further study of the subject. This paper illustrates how ML could be used to determine the biofilm forming categories (output) based on the results of the OD of the negative control (in quadruplet), its STDEV, average and average OD of the tested sample (inputs).

This method would allow for development of standardization of biofilm testing in microbiology laboratories and thus would also enable a very highly accurate testing of bacteria in their natural state which is the biofilm.

References

- Fenche, T., Finlay, B.J.: The ubiquity of small species: patterns of local and global diversity. *BioScience* **54**(8), 777–784 (2004). [https://doi.org/10.1641/0006-3568\(2004\)054%5b0777:TUOSSP%5d2.0.CO;2](https://doi.org/10.1641/0006-3568(2004)054%5b0777:TUOSSP%5d2.0.CO;2)
- Vu, B., Chen, M., Crawford, R.J., Ivanova, E.P.: Bacterial extracellular polysaccharides involved in biofilm formation. *Molecules* **14**(7), 2535–2554 (2009). <http://www.mdpi.com/1420-3049/14/7/2535>
- Estela, C.R.L., Alejandro, P.R.: Biofilms: a survival and resistance mechanism of microorganisms. In: *Antibiotic Resistant Bacteria—A Continuous Challenge in the New Millennium*. InTech (2012). https://scholar.google.com/scholar?hl=en&as_sdt=0%2C5&q=Biofilms%3A+a+survival+and+resistance+mechanism+of+microorganisms&btnG=
- Merritt, J.H., Kadouri, D.E., O’Toole, G.A.: Growing and analyzing static biofilms. *Curr. Protoc. Microbiol.* **22**(1), 1B-1 (2011). <https://currentprotocols.onlinelibrary.wiley.com/doi/abs/10.1002/9780471729259.mc01b01s22>
- Oliveira, A., de Lourdes R.S.M.: Comparison of methods for the detection of biofilm production in coagulase-negative staphylococci. *BMC Res Notes* **3**(1), 260 (2010). <https://bmcresnotes.biomedcentral.com/articles/10.1186/1756-0500-3-260>
- Ibrišimović, M.A., Ibrišimović, M., Mehmedinović, N.I., Hukić, M.: A novel spectrophotometric assay for the determination of biofilm forming capacity of causative agents of urinary tract infection. *Int. J. Eng. Technol. (IJERT)* **6**(4) (2017) https://www.researchgate.net/profile/Mirsada_Hukic/publication/316674530_A_Novel_Spectrophotometric_Assay_for_the_Determination_of_Biofilm_Forming_Capacity_of_Causative_Agents_of_Urinary_Tract_Infections/links/590b8b02af6d5421ed580/A-Novel-Spectrophotometric-Assay-for-the-Determination-of-Biofilm-Forming-Capacity-of-Causative-Agents-of-Urinary-Tract-Infections.pdf
- Hassan, A., Usman, J., Kaleem, F., Omair, M., Khalid, A., Iqbal, M.: Evaluation of different detection methods of biofilm formation in the clinical isolates. *Braz. J. Infect. Dis.* **15**(4), 305–311 (2011). http://www.scielo.br/scielo.php?pid=S1413-86702011000400002&script=sci_arttext
- Mathur, T., Singhal, S., Khan, S., Upadhyay, D.J., Fatma T., Rattan, A.: Detection of biofilm formation among the clinical isolates of Staphylococci: an evaluation of three different screening methods. *Indian J. Med. Microbiol.* **24**(1), 25 (2006). <http://www.ijmm.org/article.asp?issn=0255-0857;year=2006;volume=24;issue=1;spage=25;epage=29;aulast=Mathur>
- Wright, P.F., Nilsson, E., Van Rooij, E.M.A., Leleta, M., Jeggo, M.H.: Standardization and validation of enzyme-linked immunosorbent assay techniques for the detection of antibody in infectious disease diagnosis. *Rev. Sci. Tech. Office Int. Epizooties* **12**, 435–435 (1993). <https://pdfs.semanticscholar.org/8102/b6853a0816a21134647bce821351ec88bf61.pdf>
- Štepanović, S., Vuković, D., Hla, V., Bonaventura, G.D., Djukić, S., Čirković, I., Ruzicka, F.: Quantification of biofilm in microtiter plates: overview of testing conditions and practical recommendations for assessment of biofilm production by staphylococci. *Apmis* **115**(8), 891–899 (2007). https://onlinelibrary.wiley.com/doi/abs/10.1111/j.1600-0463.2007.apm_630.x
- Frey, A., Di Canzio, J., Zurakowski, D.: A statistically defined endpoint titer determination method for immunoassays. *J. Immunol. Methods* **221**(1–2), 35–41 (1998). <https://www.sciencedirect.com/science/article/pii/S0022175998001707>
- Badnjevic-Cengic, A., Kovacevic, P., Dragic, S., Momcicevic, D., Badnjevic, A., Gurbeta, L., Hasanefendic, B.: Serum nitric oxide levels in patients with acute myocardial infarction with ST elevation (STEMI). *Respiron J.* **5**(1–2) (2015)
- Hodzic, J., Gurbeta, L., Omanovic-Miklicanin, E., Badnjevic, A.: Overview of next-generation sequencing platforms used in published draft plant genomes in light of genotypization of immortelle plant (*Helichrysum Arenarium*). *Med. Arch.* **71**(4), 288–292 (2017). <https://doi.org/10.5455/medarh.2017.71.288-292>
- Catic, A., Gurbeta, L., Kurtovic-Kozaric, A., Mehmedbasic, S., Badnjevic, A.: Application of Neural Networks for classification of

- Patau, Edwards, Down, Turner and Klinefelter Syndrome based on first trimester maternal serum screening data, ultrasonographic findings and patient demographics. *BMC Med. Genomics* **11**, 19 (2018). <https://doi.org/10.1186/s12920-018-0333-2>
15. Gurbeta, L., Badnjevic, A., Maksimovic, M., Omanovic-Miklicanin, E., Sejdic, E.: A telehealth system for automated diagnosis of asthma and chronic obstructive pulmonary disease. *J. Am. Med. Inform. Assoc.* **25**(9), 1213–1217 (2018). <https://doi.org/10.1093/jamia/ocy055>
 16. Badnjevic, A., Gurbeta, L., Custovic, L.: An expert diagnostic system to automatically identify asthma and chronic obstructive pulmonary disease in clinical settings. *Nat. Sci. Rep.* **8**, 11645 (2018). <https://doi.org/10.1038/s41598-018-30116-2>
 17. Elli, D.I., Broadhurst, D., Kell, D.B., Rowland, J.J., Goodacre, R.: Rapid and quantitative detection of the microbial spoilage of meat by Fourier transform infrared spectroscopy and machine learning. *Appl. Environ. Microbiol.* **68**(6), 2822–2828 (2002). <http://aem.asm.org/content/68/6/2822.short>
 18. Burstein, D., Zusman, T., Degtyar, E., Viner, R., Segal, G., Pupko, T.: Genome-scale identification of *Legionella pneumophila* effectors using a machine learning approach. *PLoS Pathog.* **5**(7), e1000508 (2009). <http://journals.plos.org/plospathogens/article?id=10.1371/journal.ppat.1000508>
 19. De Bruyne, K., Slabbinck, B., Waegeman, W., Vauterin, P., De Baets, B., Vandamme, P.: Bacterial species identification from MALDI-TOF mass spectra through data analysis and machine learning. *Syst. Appl. Microbiol.* **34**(1), 20–29 (2011). <https://www.sciencedirect.com/science/article/pii/S0723202010001669>
 20. Vyas, N., Sammons, R.L., Addison, O., Dehghani, H., Walmsley, A.D.: A quantitative method to measure biofilm removal efficiency from complex biomaterial surfaces using SEM and image analysis. *Sci. Rep.* **6**, 32694 (2016)
 21. Mansoor, A., Patsekina, V., Scherl, D., Robinson, J.P., Rajwa, B.: A statistical modeling approach to computer-aided quantification of dental biofilm. *IEEE J. Biomed. Health Inform.* **19**(1), 358–366 (2015)
 22. Gupta, S., Sharma, A.K., Jaiswal, S.K., Sharma, V.K.: Prediction of biofilm inhibiting peptides: an in silico approach. *Front. Microbiol.* **7**, 949 (2016)
 23. Bayjanov, J.R., Starrenburg, M.J., van der Sijde, M.R., Siezen, R. J., van Hijum, S.A.: Genotype-phenotype matching analysis of 38 *Lactococcus lactis* strains using random forest methods. *BMC Microbiol.* **13**(1), 68 (2013)
 24. Xu, S., Huang, X., Xu, H., Zhang, C.: Improved prediction of coreceptor usage and phenotype of HIV-1 based on combined features of V3 loop sequence using random forest. *J. Microbiol.* **45** (5), 441–446 (2007)
 25. Nannapaneni, P., Hertwig, F., Depke, M., Hecker, M., Mäder, U., Völker, U., Steil, L., van Hijum, S.A.: Defining the structure of the general stress regulon of *Bacillus subtilis* using targeted microarray analysis and random forest classification. *Microbiology* **158**(3), 696–707 (2012)
 26. Polishchuk, P.G., Muratov, E.N., Artemenko, A.G., Kolumbin, O. G., Muratov, N.N., Kuz'min, V.E.: Application of random forest approach to QSAR prediction of aquatic toxicity. *J. Chem. Inf. Model.* **49**(11), 2481–2488 (2009)
 27. Breiman, L.: Random forests. *Mach. Learn.* **45**, 5–32 (2001)
 28. Gui, C., Chan, V.: Machine learning in medicine. *Univ. Western Ontario Med. J.* **86**(2), 76–78 (2017). <https://www.ncbi.nlm.nih.gov/pmc/articles/PMC5831252/>
 29. Cleophas, T.J., Zwinderman, A.H., Cleophas-Allers, H.I.: *Machine Learning in Medicine*, pp. 1–271. Springer, New York (2013). <https://link.springer.com/book/10.1007%2F978-94-007-6886-4>

Analysis of Vertical Ground Reaction Force and Center of Pressure During Stair Climbing

Vesna Raspudić

Abstract

In this study, the vertical component of the ground reaction force (GRF), the maximum pressure value and the center of pressure (COP) motion in the longitudinal direction during stair climbing with and without a handrail have been determined. The measurement was carried out using the zebris FDM-S measuring system. For both climbing modes (NH—no handrail, H—handrail) the maximum and minimum values of the vertical component of the GRF were achieved in approximately equal percentages of the stance period (SP), with the greatest influence of the handrail use at the first maximum value. The COP position provides important information about a person's postural control during locomotion. It has been found that in the case of climbing with a handrail, the COP position is moved more anteriorly, indicating a greater inclination of the entire body forward. The analysis of the maximum pressure values showed two pronounced maximums with one minimum between them. The impact of the handrail use on reducing the pressure is most evident in the area around both maximum values.

Keywords

Stair climbing • Ground reaction force • Center of pressure

1 Introduction

Stair locomotion is an activity that requires large amount of metabolic energy due to much higher loads placed on the lower limbs than by level walking, with larger muscle efforts

V. Raspudić (✉)
Faculty of Mechanical Engineering, Computing and Electrical Engineering, University of Mostar, Matice hrvatske bb, 88000 Mostar, Bosnia and Herzegovina
e-mail: vesna.raspudic@fsre.sum.ba

and ranges of motion in the ankle and knee joints. Numerous studies have investigated movement patterns during stair ascent and descent. They describe the sagittal kinematics of lower limb segments and the corresponding joint powers, muscle activities and EMG data for healthy persons [1–4], as well as for persons with reduced motor functions, for example in elderly subjects, subjects affected by lower limb diseases and those with joint or limb replacements [5, 6].

Recently there has also been an increased interest in stair climbing biomechanics due to the development of powered prosthesis, which aim to restore natural locomotion by performing appropriate net works at the ankle and knee joints [7, 8]. Such prosthesis would require power generation capabilities comparable to an actual limb and a control framework for generating required joint torques while ensuring stable and coordinated interaction with the user and the environment [9]. Applying the inverse dynamics method, the determination of necessary joint torques and powers requires knowledge of the ground reaction force (GRF) and center of pressure (COP). The GRF is an equalling and opposing force due to body mass passing through the foot to the ground surface, which can be resolved into vertical (counteracting body weight) and horizontal (leading to forward movement) components. The COP is defined as the origin of the GRF vector or the centroid of external forces acting on the plantar surface of the foot. By tracking the path of the instantaneous COP during the stance period (SP), the balance and pattern of movement progression can be determined [10]. There are several variations of stair climbing patterns, one of which is the use of a handrail. It is often used by older adults and disabled individuals in order to decrease loads through the lower limb, stabilize their movement and prevent fall [11–13].

The objective of this investigation was to examine the vertical component of the GRF and COP position in anterior-posterior direction during stair ascent in healthy adult populations while climbing with a handrail (H climbing) and without a handrail (NH climbing).

2 Methods

The zebris FDM-S measuring system, product of zebris Medical GmbH [14], was used to record data during stair climbing. The system enables static and dynamic analysis of load distribution under feet during quiet standing and walking. It consists of a force measuring plate that can be used with a commercially available personal computer. The force plate contains a number of individually calibrated capacitive force sensors. The total number of sensors for the FDM-S platform is 2560, and they are arranged in a 64×40 dimension matrix, with a single cell size of 8.5×8.4 mm. The recording frequency is 100 Hz. The measuring plate has a video synchronization output as a standard feature and is designed for connecting the video module. Also, an infrared transmission module is available for synchronizing the EMG radio adapter. The processing of the measurement data is done using zebris FDM Software, which consists of a database, a “Viewer” and a report generator. All the stored force measurement data can be replayed with the video or EMG signals in slow motion and completely synchronized. Also, recorded data can be exported to other programs for subsequent processing (ASCII and APD Export).

The measurements were performed on a custom-build standard dimension staircase consisting of three steps with the slope of 30° (rise height: 17 cm; tread: 29 cm; width: 80 cm). The staircase had a handrail (height: 90 cm) that could be mounted on the left and on the right side. During the measurement, the handrail was mounted on the left side of the participant. The frame of the staircase was constructed using firm steel profiles and it was placed on the flat sturdy floor, which ensured a mechanically stiff structure that enabled forces to be correctly recorded. The force plate was embedded in the second step of the staircase, and it was connected to a video camera and a PC.

Ten healthy male participants with no current pain or history of lower extremity injury volunteered in this study. Participants were on average 27 ± 7 years old with a mean body mass and height of 81 ± 11 kg and 1.82 ± 0.05 m, respectively. During the measurements they were barefoot and dressed in appropriate sports equipment. Five reflective markers of 1 cm in diameter have been attached to palpable landmarks of their lower right side extremities, in order to monitor the orientation of thigh, shank and foot segments. Special attention was given to naturalness in walking, so that a number of preliminary tests has been repeated for each participant. They were explained the way to climb the stairs, i.e. to walk at speed they consider as their normal climbing speed and thereby not to look at the floor, in order to avoid being distracted by the force plate.

For each participant, the load distribution under the feet during a quiet stand on the force plate was performed first, in order to determine the possible disturbances of the locomotor system during static weight transfer to the ground. Figure 1 shows an example of static analysis results.

The average load distribution underneath the feet is expressed in N/cm^2 . On each foot there is a line connecting the end point markings representing the center of pressure (CP) on the front foot and the back foot. The transverse line connects the resultant CPs for both feet, while the central mark on that line represents the CP for the entire body. The ellipse around this CP marks the area which includes 95% of all CP positions during the testing and its characteristics, like confidence ellipse width, height, angle of the longitudinal axis relative to the x axis of the force plate and the ellipse area. The histograms in Fig. 2 show an example of an average percentage distribution of pressure at the front and back of the left and right foot, as well as the total percentage of pressure distribution between the feet. For all participants, normal load distribution was established for standing upright.

Finally, each participant climbed 20 times. The first ten times referred to NH climbing, and the next ten times to H climbing with the handrail on the left side. Only successfully saved files have been used for further analysis, where it was possible to reconstruct the cycle of climbing and where the full contact between foot and the force plate had been achieved.

Figure 3 shows an example of 2D and 3D plantograms with foot load values during the measurement and with the representation of the COP path.

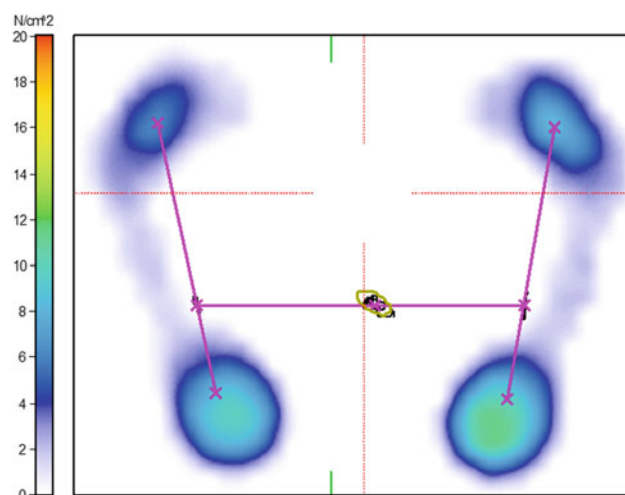


Fig. 1 Average force distribution

Fig. 2 An example of average percentages of pressure distribution

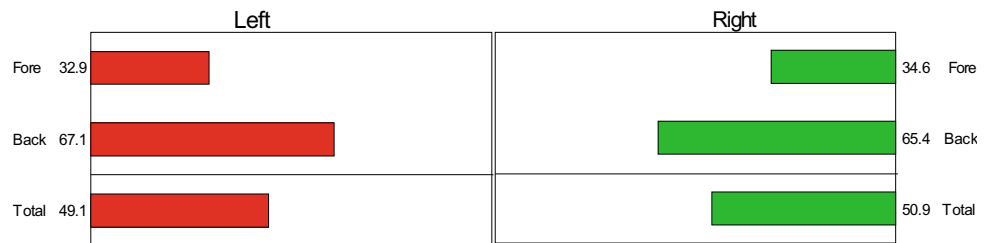
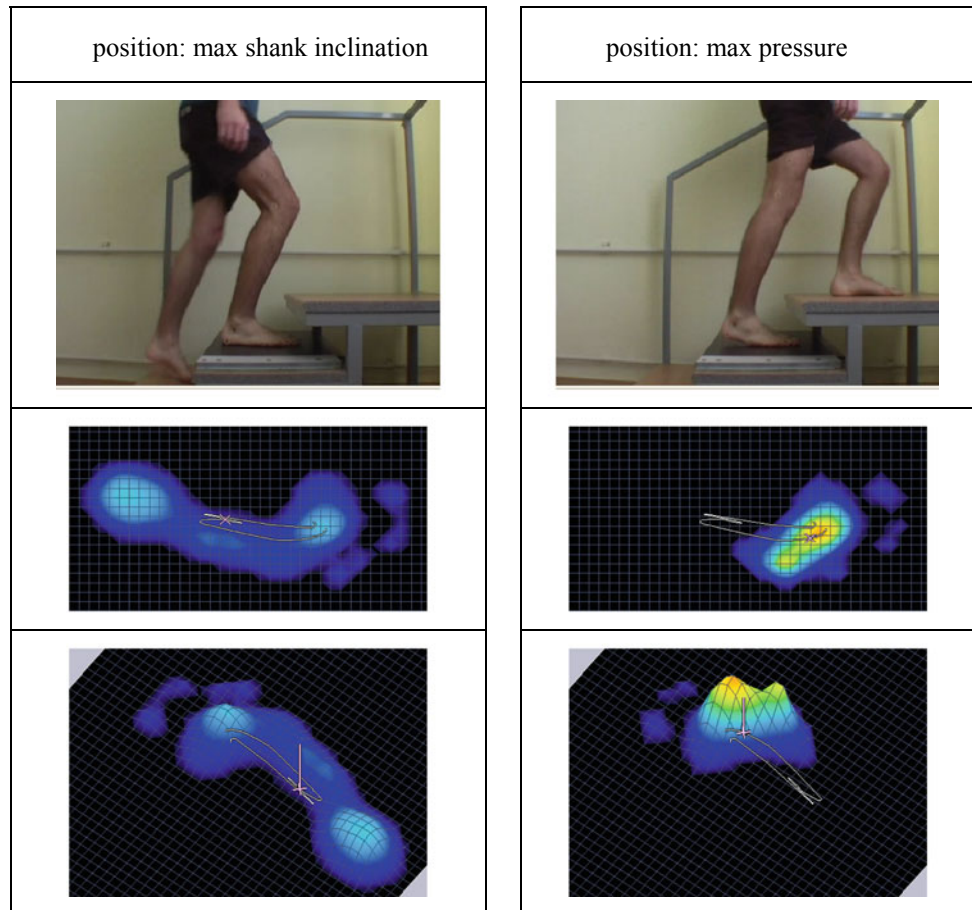


Fig. 3 2D and 3D plantograms



3 Results

The parameters that were analyzed when processing the data determined by the zebris FDM-S measuring system included the value of the vertical component of the GRF, the maximum pressure value and the COP position in the longitudinal direction. Thereby, the ability of zebris measuring system to export all recorded data into ASCII files was exploited. A program code in C programming language was written that processed these files and generated new files containing only the requested quantities in a form suitable for further processing.

In order to compare data for different participants, their normalization was performed. The values of the vertical component of the GRF were divided by the individual weight of the participant. The COP position values were normalized by being divided by the foot length of the participant, so that the analyzed value represents the distance of the COP from the posterior end of the foot. The time axis was normalized to display the values depending on the percentage of the stance period (SP), during which the foot was in contact with the force plate.

Figure 4a shows the general patterns of the vertical component of the GRF. When climbing up the stairs, similar

to walking on a flat surface, the vertical component of the GRF has a characteristic “M” appearance with two smooth peaks. During the period when the vertical component of the GRF is greater than the body weight (Norm. $F_v > 1$), the center of mass (COM) has an acceleration in the direction of the positive y axis (vertically upwards), and during the period in which its value is less than the body weight (Norm. $F_v < 1$), the center of mass is accelerated in the direction of the negative y axis (vertically downwards).

During NH climbing, the first maximum of the GRF, in the amount of $F_{v,max1} = 1.082G$, is achieved at 30% SP, where the acceleration of the body COM is 0.8 m/s^2 . The second maximum is achieved at 80% SP, and its value is $F_{v,max2} = 1.098G$, with the body COM acceleration of 0.96 m/s^2 . The minimum value of the vertical component of the GRF occurs at half of the SP (50% SP), and its value is $F_{v,min} = 0.847G$. The acceleration of the body COM at that point achieves a value of 1.5 m/s^2 .

As part of previous study which analysed stair climbing kinematics [15], it has been found that the maximum inclination of shank (P1 position) occurs at 20% SP, and that the leftmost position in the loop of knee trajectory (P2 position) occurs at 60% SP. These percentages of the SP have also been used as reference points in the present study. It has been found that at the characteristic P1 position (20% SP) the value of the vertical component of the GRF is $F_{v,P1} = 0.828G$, and in P2 (60% SP) its value is $F_{v,P2} = 0.929G$.

By analyzing the general sample of the vertical component of the GRF curve when H climbing, it has been found that it follows the shape of the curve when NH climbing, with the maximum and minimum values being achieved in approximately equal percentages of the SP. The force values are thereby smaller because part of the load is transferred to the handrail. In this case, the values of the first and second maximum are $F_{v,max1} = 0.992G$ and $F_{v,max2} = 1.053G$, and the value of the minimum is $F_{v,min} = 0.787G$. In the characteristic P1 and P2 positions the values are: $F_{v,P1} = 0.764G$ and $F_{v,P2} = 0.838G$.

Table 1 lists the normalized values of the first and second maximum (max1 and max2), and the minimum between them (min), as well as the values in the characteristic P1 and P2 positions.

The curves representing the change of maximum pressure between foot and ground for both climbing ways, without and with handrail (Fig. 4b), show two pronounced maximums, with a single minimum between them. The first maximum load occurs on the heel, and the second maximum on the front of the foot. In order to achieve normal dynamics, it is recommended that when walking on level ground maximum load should not exceed the value of 40 N/cm^2 below the heel and 55 N/cm^2 under the front part of the foot [16]. In the analyzed measurements of stair ascent, these values were also satisfied. Thereby, there is a considerably higher percentage of frontal foot load than the heel load compared to the walking on a flat surface, where this difference in load

Fig. 4 Comparison of general samples for norm. F_v and max. pressure for NH and H climbing

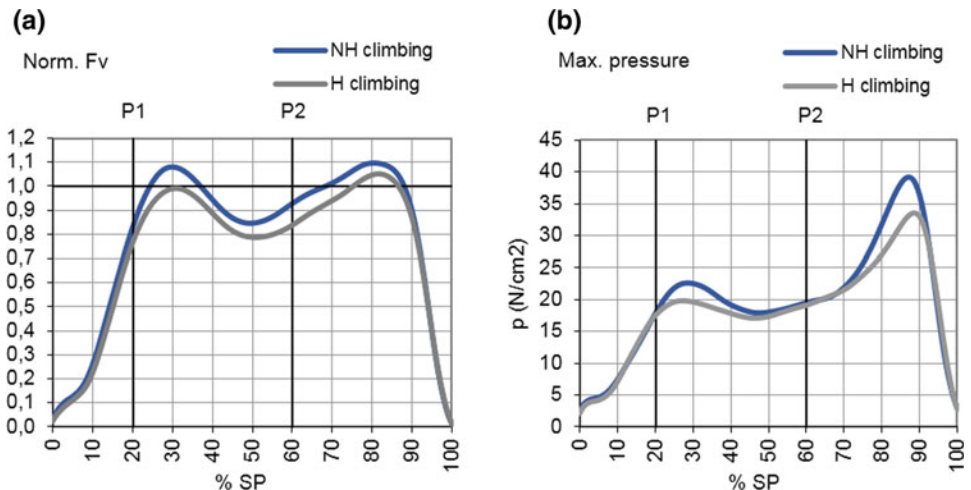


Table 1 Normalized vertical component of GRF

	Position	P1	max1	min	P2	max2
NH climbing	% SP	20%	30%	50%	60%	80%
	Norm. F_v	0.828	1.082	0.847	0.929	1.098
H climbing	% SP	20%	31%	50%	60%	82%
	Norm. F_v	0.764	0.992	0.787	0.838	1.053

Table 2 Max pressure (N/cm²)

	Position	P1	max1	min	P2	max2
NH climbing	% SP	20%	29%	48%	60%	87%
	max p	17.80	22.62	17.91	19.54	39.20
H climbing	% SP	20%	27%	46%	60%	89%
	max p	17.47	19.82	17.09	19.11	33.46

reaches 37.5%. When NH climbing, the value of the second maximum pressure increased by 73.25% compared to the first maximum, while in the case of H climbing the second maximum increased by 68.80%. Table 2 gives values of maximum pressures in characteristic moments.

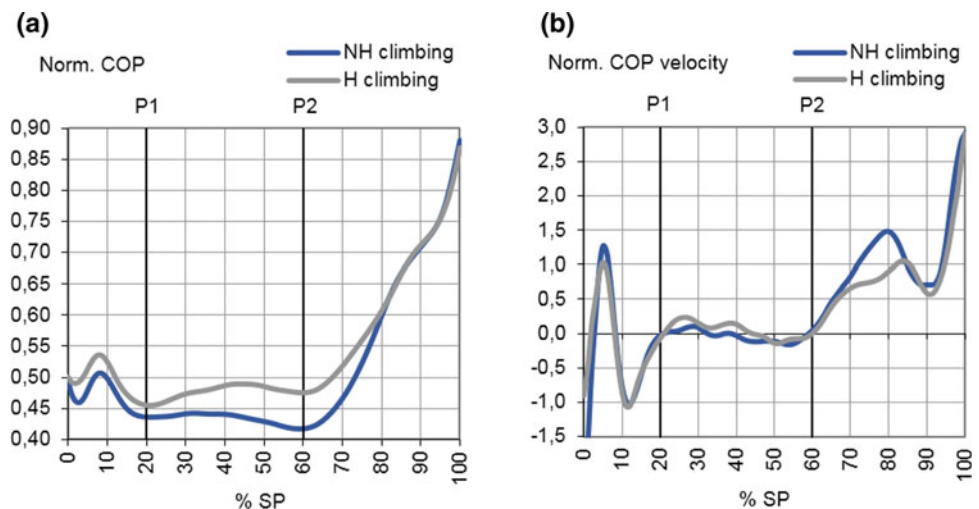
Comparing the maximum values of pressure when NH and H climbing (Fig. 4b), it can be noticed that for both climbing modes the maximum loads match up to the P1 position (max. slope of the lower leg), and in the final stage of the foot contact with the ground, when the load is fully transferred to the front of the foot. Also, the same load value is present in P2 position.

The analysis of body weight transfer to the foot, performed on 2D and 3D plantograms, showed that the COP was at half the length of the foot (Norm. COP = 0.5, Fig. 5) at the initial contact of the foot with the platform. For both climbing modes (NH and H climbing), the COP moves in the posterior direction during the first 3% of SP, followed by a change in the anterior direction during the next 5% SP (up to 8% SP). After 8% of the SP, the displacement is repeated in the posterior direction, until the maximum inclination of the lower leg is reached, i.e. until reaching the characteristic P1 position. At that point, the normalized positions of the COP are Norm. CP = 0.44 and Norm. CP = 0.46 for NH and H climbing, respectively.

With the change of the knee movement direction in the characteristic P1 and P2 positions, the direction of the COP also changes. In the period between these positions, the COP changes very little, in an amount corresponding to the value of 0.03 of the normalized foot length. From Fig. 5a it is noticed that in this period there is another mild change of direction of motion for both modes of climbing, first in the anterior and then in the posterior direction. The COP moves in the anterior direction up to 32% SP in the case of NH climbing, i.e. up to 44% SP in the case of H climbing, and then reverses in the posterior direction until the P2 position is reached. At the P2 position, the values of normalized COP are Norm. CP = 0.42 and Norm. CP = 0.48 for NH and H climbing, respectively.

Once the P2 position has been reached, the direction of the COP movement is exclusively anterior. From Fig. 5b, it can be seen that after the P2 position is reached, the first peak velocity of the COP is achieved by the percentages of the SP corresponding to the maximum values of the vertical components of the GRF (80 and 82% SP for NH and H climbing, respectively). The velocity of the COP is then reduced by up to 90% of the SP when full knee extension is achieved and the load transfer is completely transferred to the front of the foot at which maximum loads are present at that moment. During the last 10% of the SP, there is a raise

Fig. 5 Comparison of general samples for norm. COP and norm. COP velocity for NH and H climbing



of the foot toes from the surface, during which the fastest positioning of the COP is taking place.

4 Conclusion

Analysis of the vertical component of the GRF, the maximum pressure value and the position of the COP in the longitudinal direction during stair climbing can significantly contribute to the understanding of the mechanics of stair locomotion, as well as to development of appropriate control systems for powered prosthetic devices in order to achieve the desired movement pattern. In this study, the measurement of these parameters was carried out using the zebris FDM-S measuring system. In order to determine the influence of a handrail use on reducing leg loading, the climbing with and without a handrail has also been analysed. The results obtained when NH climbing are consistent with previous findings reported in [3, 4, 10]. It has been determined that for both climbing modes the maximum and minimum values of the vertical component of the ground reaction force were achieved in approximately equal percentages of the stance period. The highest value of the GRF is achieved at the second maximum (80% SP), which is higher than the first maximum by 1.5% when NH climbing and by 6% when H climbing. The analysis of the results showed that the greatest influence of the handrail on the reduction of the vertical component of the GRF is achieved at the first maximum, when the amount of force in the case of NH climbing is higher by 9% than by H climbing.

The COP position provides important information about the balance and pattern of movement progression. Its accurate estimation is especially important in the calculation of joint torques of the lower segments. Also, knowledge of centre of pressure velocity helps in understanding of strategies for improving stability during stair negotiation [11, 12]. This study adds to the literature by providing normalized COP position and normalized COP velocity in healthy adults for NH and H climbing. It has also been showed that in the case of H climbing the COP position is moved more anteriorly up to 80% SP, indicating a greater inclination of the entire body forward.

The analysis of the maximum pressure change showed two pronounced maximums with one minimum between them. The impact of the handrail on reducing the load is most evident in the area around both maximum values. The maximum load is at the front of the foot, approximately ten percent of the SP before lifting the toes from the surface.

In further work, these data will be helpful for the development of appropriate control systems for powered prosthesis design in order to achieve the desired movement pattern.

Conflict of Interest None declared.

References

1. Andriacchi, T.P., Andersson, G.B., Fermier, R.W., Stern, D., Galante, J.O.: A study of lower-limb mechanics during stair-climbing. *J. Bone Joint Surg.* **62A**, 749–759 (1980)
2. McFadyen, B.J., Winter, D.A.: An integrated biomechanical analysis of normal stair ascent and descent. *J. Biomech.* **21**, 733–744 (1988)
3. Zachazewski, J., Riley, P.O., Krebs, D.E.: Biomechanical analysis of body mass transfer during stair ascent and descent of healthy subjects. *J. Rehabil. Res. Dev.* **30**(4), 412–422 (1993)
4. Riener, R., Rabuffetti, M., Frigo, C.: Stair ascent and descent at different inclinations. *Gait Posture* **15**, 32–44 (2002)
5. Bae, T.S., Choi, K., Mun, M.: Level walking and stair climbing gait in above-knee amputees. *J. Med. Eng. Technol.* **33**(2), 130–135 (2009)
6. Fenner, V., Behrend, H., Kuster, M.S.: Whole body gait function during stair ascending and level walking in patients following total knee arthroplasty. *Int. J. Phys. Med. Rehabil.* **2**(5) (2014)
7. Hoover, C.D., Fulk, G.D., Fite, K.B.: Stair ascent with a powered transfemoral prosthesis under direct myoelectric control. *IEEE/ASME Trans. Mechatron.* **18**(3), 1191–1200 (2013)
8. Lawson, B.E., et al.: Control of stair ascent and descent with a powered transfemoral prosthesis. *IEEE Trans. Neural Syst. Rehabil. Eng.* **21**(3), 466–473 (2013)
9. Sup, F., Bohara, A., Goldfarb, M.: Design and control of a powered transfemoral prosthesis. *Int. J. Rob. Res.* **27**(2), 263–273 (2008)
10. Perry, J.: *Gait Analysis Normal and Pathological Function*. SLACK Inc (1992)
11. Reid, S.M., Novak, A.C., Brouwer, B., Costigan, P.A.: Relationship between stair ambulation with and without a handrail and center of pressure velocities during stair ascent and descent. *Gait Posture* **34**, 529–532 (2011)
12. Reeves, N.D., Spanjaard, M., Mohagheghi, A.A., Baltzopoulos, V., Maganaris, C.N.: Influence of light handrail use on the biomechanics of stair negotiation in old age. *Gait Posture* **28**, 327–336 (2008)
13. Maki, B.E., et al.: Reducing fall risk by improving balance control: development, evaluation and knowledge-translation of new approaches. *J. Saf. Res.* **42**, 473–485 (2011)
14. <https://www.zebris.de/>
15. Raspudić, V.: 3D reconstruction of motion paths during stair climbing. In: *Proceedings of the 15th International Research/Expert Conference “Trends in the Development of Machinery and Associated Technology”, TMT 2011, Prague*, pp. 597–600 (2011)
16. WinFDMS 0.1.x for Windows, User Manual, Zebris Medical GmbH (2007)

Reference Tracking of the Robotic Above-Knee Prosthetic Leg with Actuated Knee and Ankle Joints Using Robust Control

Zlata Jelačić and Remzo Dedić

Abstract

The locomotion of people with amputation is slower, less stable and requires more metabolic energy than the locomotion of physically fit individuals. Individuals with amputation of the lower extremities fall more often than able individuals and often have difficulty moving on uneven terrain and stairs. These challenges can mostly be attributed to the use of passive mechanical prosthetic legs that do not react actively to perturbations. Latest submitted solutions for active prosthetic devices of the lower extremities can significantly improve mobility and quality of life for millions of people with lower limb amputation, but challenges in control mechanisms of such devices are currently limiting their clinical viability. In this paper we present a prototype of an above-knee prosthetic leg with active knee and ankle joints while using the proposed robust control law.

Keywords

Robust adaptive control • Active prosthetic leg • Actuated joints • Reference tracking

1 Introduction

Dynamic equations of robotic manipulators present a complex, nonlinear and multivariable system. One of the first methods of controlling such systems was inverse dynamics which is also known as a special case of the method of feedback linearization. However, plant variability and uncertainty are obstacles to exact dynamic inversion.

Z. Jelačić (✉)

Faculty of Mechanical Engineering, University of Sarajevo,
Sarajevo, Bosnia and Herzegovina
e-mail: jelacic@mef.unsa.ba

R. Dedić

Faculty of Mechanical, Computer and Electrical Engineering,
University of Mostar, Mostar, Bosnia and Herzegovina

Therefore, inverse dynamic control has limited practical validation.

Variable impedance control is one of the most popular prosthetic controls because of the independence of the system model. However, impedance control is missing optimality and robustness due to several shortcomings: time consuming estimation of impedance parameters (unique for each amputee), difficulties in detection of subphases in one step, lack of the feedback and passivity [1]. There have been several attempts to solve the limitations of ordinary impedance control. However, the above controls are independent of the system model and are missing mathematical proof of stability and robustness in the presence of system uncertainty, unmodelled dynamics and disorders.

In order to overcome these difficulties, motion control techniques based on the passivity property of Euler-Lagrange equations have been considered. Especially for the robust and adaptive control problems, the passivity-based approach shows great advantage over inverse dynamic method. Therefore, robust passivity-based control (RPBC) gained attention as a powerful nonlinear control law that can guarantee stability and tracking of arbitrary trajectories efficiently, despite uncertainties in plant model parameters.

2 Robust Passivity Based Control

2.1 Problem Description

Most robotic systems have parametric uncertainty problems, the active prosthetic above-knee prosthesis is not an exception. Robust controller is considered due to its robust characteristic which is good at maintaining the performance in terms of stability, tracking errors, or other specifications despite parametric uncertainty, external disturbances or unmodelled dynamics present in the system.

The simulated active prosthetic leg is based on the so-called SmartLeg, developed at the University of Mostar, Bosnia and Herzegovina (Fig. 1). The latest prototype of the

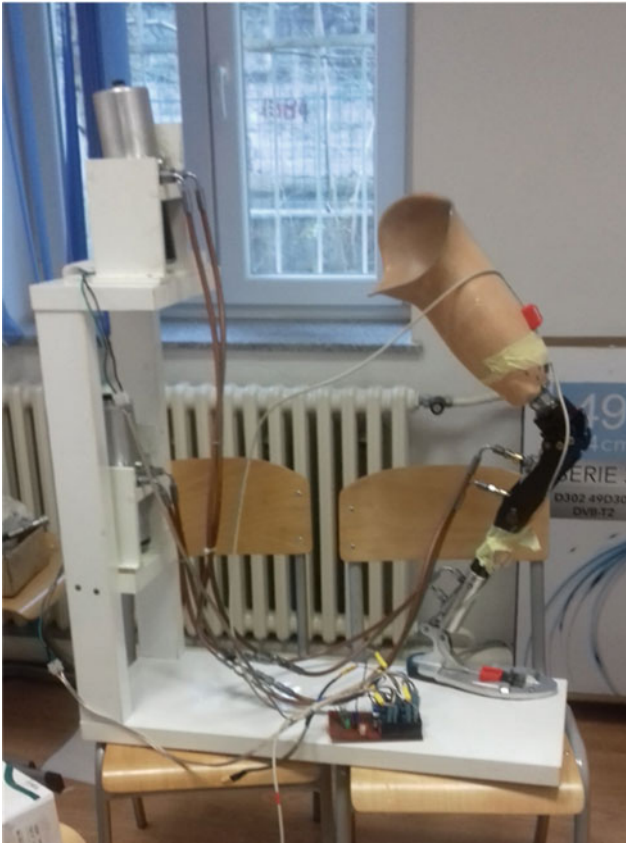


Fig. 1 SmartLeg, actuated above-knee prosthetic leg

SmartLeg has a separate hydraulic actuation for both the knee and the ankle joints [2]. Experiments on the previous prototypes showed that this is necessary in order to simulate the leg movement in; a natural way. For the sake of comparison, in a biological leg different groups of muscles actuate flexion and extension in the knee and ankle joints, respectively.

In this section, a robust passivity based controller is applied to the three link prosthetic leg robot system with actuated joints and is used for trajectory tracking of these joints.

Controllers use only the coordinates of the body and the reference trajectories of a healthy leg, without any dynamic information of the healthy body, in order to generate the prosthetic angular momentum of the knee. This makes it possible for the combined human-prosthesis system to mimic the movements of a person without amputation. The proposed passivity-based robust controller is not only robust in relation to parametric uncertainties and unmodelled dynamics of the prosthesis, but also to different subjects with amputations.

2.2 RPBC for Active Above-Knee Prosthesis

For the purposes of simulation, the system of the active above-knee prosthesis can be considered as a robotic manipulator consisting of three links with two one-axis joints. The coordinate system is set according to the standard Denavit-Hartenberg convention. The coordinate q_1 represents the angle in the hip in relation to the vertical axis. Coordinates q_2 and q_3 represent the angles in the knee and ankle joint, respectively (Fig. 2). In Fig. 2, the prosthetic part is shown in full black line, the remaining part of the human leg, including the hip and the point mass representing the rest of the healthy body is shown in grey, interrupted line. This model has been used in the simulations.

Above-knee controller of the prosthetic leg receives input information for the knee and ankle joints $S_{in} = \{q_k^d, q_a^d\}$ from the healthy human leg. Using linear transformation, set of input values for the hip joint $S_h = \{q_h, q_h^d\}$ is generated from S_{in} , where q_h^d is the desired path for q_h , the generalised coordinate representing the angle in the hip. Controllers use S_{in} to generate prosthetic knee moment during the swing

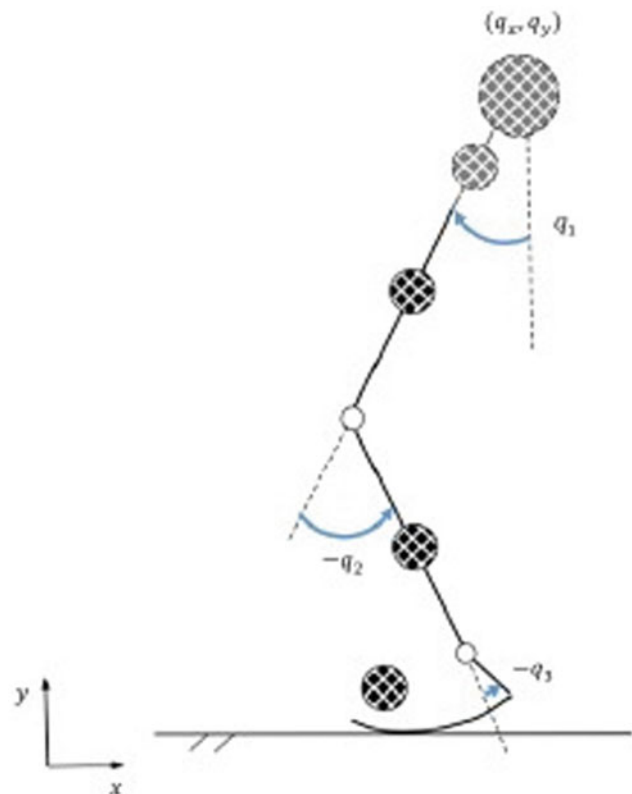


Fig. 2 Model of active above-knee prosthesis

phase and a period of stance, enabling the combined prosthetic system to mimic human movement, i.e. $q_a \rightarrow q_a^d \Rightarrow q_k \rightarrow q_k^d \Rightarrow y_h \rightarrow y_h^d$ with limited tracking trajectory errors.

The flexible foot is attached to the ankle at an angle over the pylon. During the experiments, the foot will be placed on the Zebris plate [3] to measure the vertical force of the reaction of the ground. This data is implemented in the control algorithm as an external non-conservative force because it can play an important role in the feedback part of the control algorithm.

In this case, the system can be considered as an active three-link planar robot, because the movement is only observed in the sagittal plane. A robotic dynamic model in joint coordinates can be written as:

$$D(q)\ddot{q} + C(q, \dot{q})\dot{q} + J_e^T F_e + g(q) = F_a \quad (1)$$

where $q = [q_1 \ q_2 \ q_3]^T$ is the vector of joint angles, $D(q)$ is matrix of inertia, $C(q, \dot{q})$ is the vector of Centripetal and Coriolis torques, J_e is the kinematic Jacobian of the point where external Fig. 2: Model of active above-knee prosthesis force acts, $g(q)$ is the gravitational vector and F_a is the vector of combined actuator inputs, where the effects of inertia and friction are incorporated [4].

As the position vector of the point where the maximum value of the reaction force of the ground is known, its global location can be calculated using the transformation matrix:

$$Z_{LC} = q_1 - l_{cy}\cos(q_2 + q_3) + (c_3 + l_{cx})\sin(q_2 + q_3) + l_2\sin(q_2) \quad (2)$$

where l_i represents the length of the i th link of the mechanism; l_{ci} represents the distance from the centre of the mass of the i th link to the previous joint.

Jacobian at the location of the maximum ground reaction force is given by:

$$\begin{aligned} J_e(1, 1) &= 0 \\ J_e(1, 2) &= -(c_3 + l_{cx})\sin(q_2 + q_3) + l_{cy}\sin(q_2 + q_3) - l_2\sin(q_2) \\ J_e(1, 3) &= -(c_3 + l_{cx})\sin(q_2 + q_3) + l_{cy}\sin(q_2 + q_3) \\ J_e(2, 1) &= J_e(2, 2) = J_e(2, 3) = 0 \\ J_e(3, 1) &= 1 \\ J_e(3, 2) &= (c_3 + l_{cx})\cos(q_2 + q_3) + l_{cy}\sin(q_2 + q_3) - l_2\cos(q_2) \\ J_e(3, 3) &= (c_3 + l_{cx})\cos(q_2 + q_3) + l_{cy}\sin(q_2 + q_3) \end{aligned} \quad (3)$$

Horizontal component of the foot velocity V_f can be obtained from the Jacobian above, so the horizontal friction force F_{GH} can be calculated as:

$$F_{GH} = -\mu F_{GV} \text{sign}(V_f) \quad (4)$$

where F_{GV} is the vertical component of the measured ground reaction force, μ is empirically calculated friction coefficient and equals 0.15. Hence,

$$F_e = [F_{GH} \quad 0 \quad -F_{GV}]^T \quad (5)$$

where m_1 is the mass of the upper part of the prosthetic leg and the corresponding components; m_2 is the total mass of the lower part of the prosthetic leg and the associated components; m_3 is the mass of the foot of the prosthetic leg; m_0 is the equivalent inertial mass for rotational components belonging to the link 1 of the mechanism; l_2 is the nominal length of the upper part of the prosthetic leg; l_3 is the overall length of the lower part of the prosthetic leg, from the knee joint to the heel; c_2 is the distance from the centre of mass of link 2 to the origin of the coordinate system; c_3 is the distance from the knee to the centre of mass of link 3 including foot; I_{2Z} is the total inertia of link 2; I_{3Z} is the total inertia of link 3 including foot; J_m is the inertia of the rotary engine; f is the linear ratio of damping in link 1; b_1 is the damping of the rotating actuator and b_2 is damping on the knee joint.

In order to run the three link prosthetic leg robot with the robust passivity based controller, the parameters of this manipulator are chosen as shown in Table 1. In addition, the uncertainty level is determined as 0.1 in this simulation, which means the value of parameters is selected arbitrarily in the range of 10 percent fluctuation from the nominal value, the dead zone of the controller is chosen as 1. The knee and ankle joints of the robot are driven by servo DC motors with amplifier gains $k_1 = 375 \text{ Nm/V}$ and $k_2 = 15 \text{ Nm/V}$. The hip joint, as a part of a remaining part of the body, for the sake of simulation is assumed to be ideally driven by torque directly.

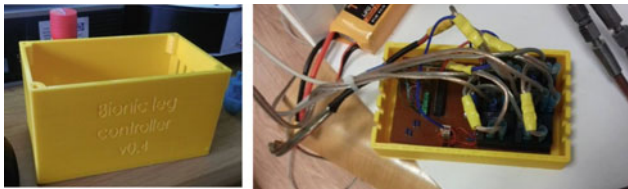
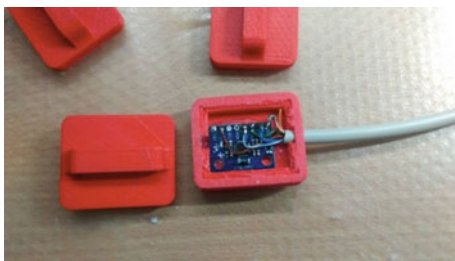
2.3 Control Unit

Control unit uses the developed control algorithm to control the joints of the above-knee prosthetic leg separately in order to follow the desired angle trajectories (Fig. 3). Control sensors form an integral part of the control unit and allow the reference tracking of the prosthesis (Fig. 4).

For the measurement we used the sensors of our control unit, based on accelerometer and gyroscope. A set of three sensors is placed on the prosthetic leg prototype and is able to directly measure the angle of foot (metatarsal joint) and the angle in ankle and knee joints. The angle in the hip joint, here also referred to as thigh angle, is measured as the angle

Table 1 Simulation parameters for the three-link prosthetic leg

Parameters	Values	Units
m_1	315.5	kg
m_2	43.28	kg
m_3	8.75	kg
m_0	2.33	kg
l_2	0.425	m
l_3	0.527	m
c_2	-0.339	m
c_3	0.32	m
I_{2Z}	0.435	kgm ²
I_{3Z}	0.062	kgm ²
J_m	0.000182	kgm ²
b_1	9.75	Nms
b_2	1	Nms
f	83.33	Ns/m

**Fig. 3** Control unit of the prosthetic leg**Fig. 4** Control/measurement sensors

between the vertical axis and the position of the sensor mounted on the socket of the prosthetic leg.

3 Results and Discussion

In this section, simulation and measurement results are presented. Simulations show the implementation of the passivity based robust controller for the system of the active above-knee prosthesis with actuated knee and ankle joints. This controller is ideal for monitoring the change in the angles of the prosthetic leg with reference signals for a

particular stage of movement. The trajectory references for the hip, knee and ankle joints are normalized values of the corresponding angle trajectories of a healthy subject, as given in Fig. 5. The controller is adjusted to give a better performance by tuning the controller gains L and K through trial and error.

The level of uncertainty is set to 0.1, which means that 10% parametric uncertainty is present in the system. The angle of the hip joint is marked with q_1 and the angles in the knee and ankle joints with q_2 and q_3 , respectively. Other simulation parameters are given in Table 1. It should be noted that the hydraulic aggregates of both activated joints of the prosthetic leg are driven by DC engines. In practice, the hydraulic power system is rather controlled through the voltage of the DC engines than via hydraulic valves. This control method proved to be effective in practice. However, in simulations the problem of control signal vibration is obvious. Although jumps in voltage signals are not too troublesome themselves, they can cause a problem in case of the hydraulic controller drive [5]. The system is simulated for 20 s of which 5 s are shown in Figs. 6 and 7. Diagrams show the tracking of the preset angular values in the knee and thigh joints. Measured output values are shown in red while desired reference input values are given in blue.

If the management of the active hydraulic prosthesis is switched to the regulation of the flow through (servo) valves, then this mode of operation gives certain deviations. The deviations are the clearest in the knee angle where the greatest discrepancies can be seen (Fig. 8).

In Fig. 8 we see that the given values cannot be reached within the given time interval, which is set to 5 s in accordance with the experimental results. The reason is that large

Fig. 5 Reference signals of a healthy subject

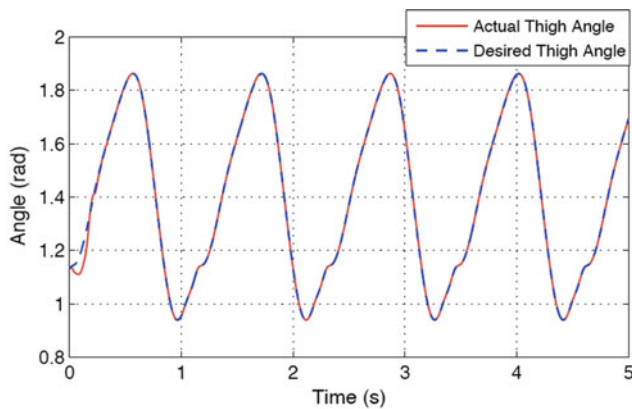
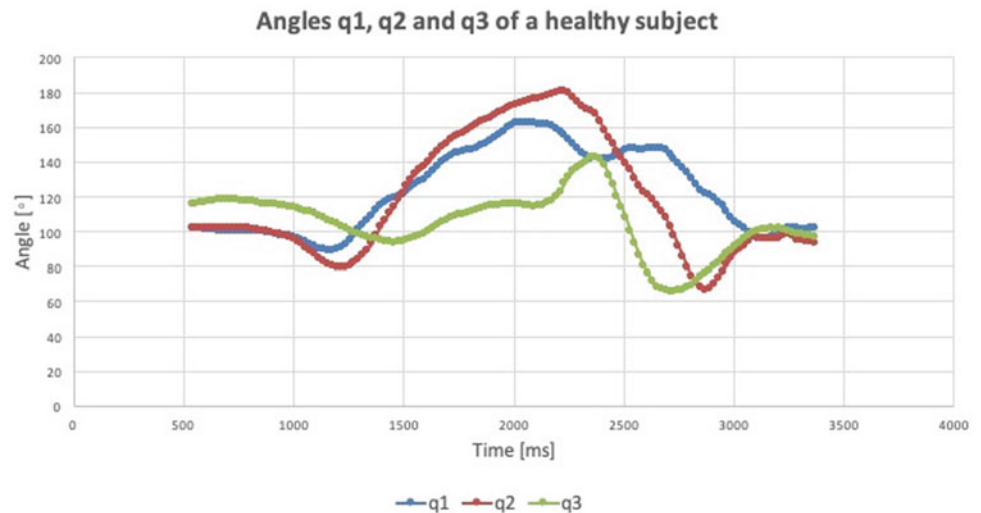


Fig. 6 Comparison of thigh angle tracking between actual and desired value

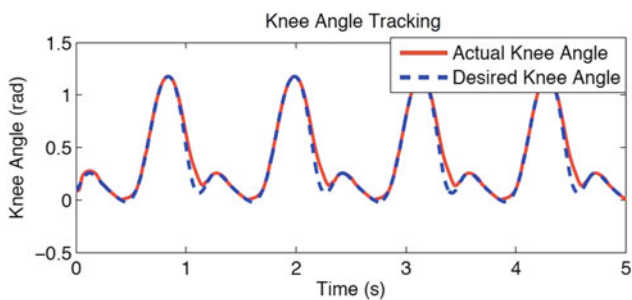


Fig. 7 Comparison of knee angle tracking between actual and desired value

jumps at the controller input signals u_1 and u_2 negatively affect hydraulic system and can lead to wear and damage over time (Figs. 9 and 10).

By installing a low-pass filter this effect is significantly reduced and the results come in the range of what we saw in the regulation of the voltage of the DC motors of hydraulic aggregates (Figs. 11, 12 and 13).

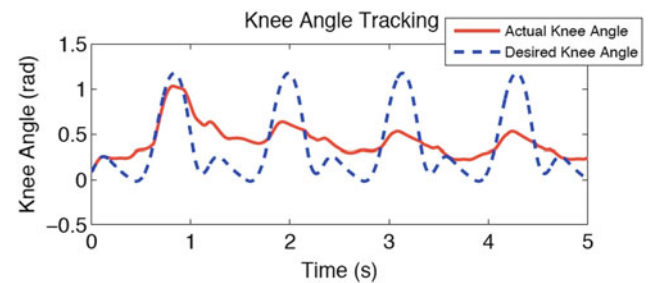


Fig. 8 Knee angle tracking for hydraulic valve control

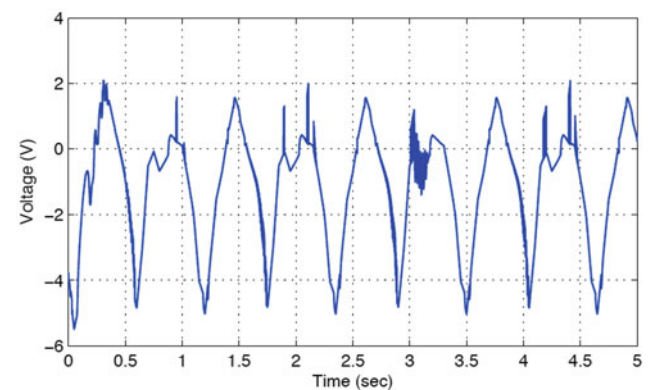


Fig. 9 Control signal u_1

The results of the simulations show that the passivity-based robust regulator is able to trace the trajectory of the joints close to the desired values, although another 10% of the parametric uncertainty is present within the model. Parametric uncertainty, which is an inevitable element in the robot management system, is successfully solved by the implementation of the robust passivity-based control.

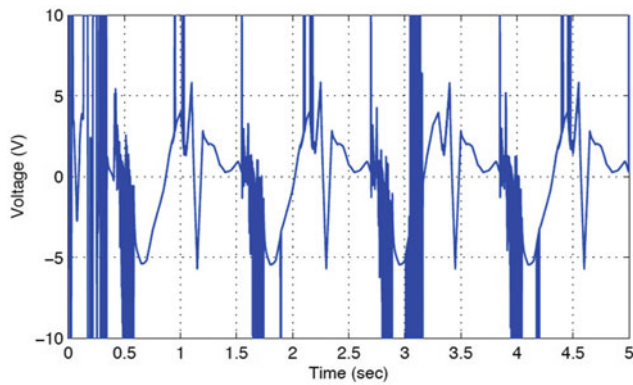


Fig. 10 Control signal u_2

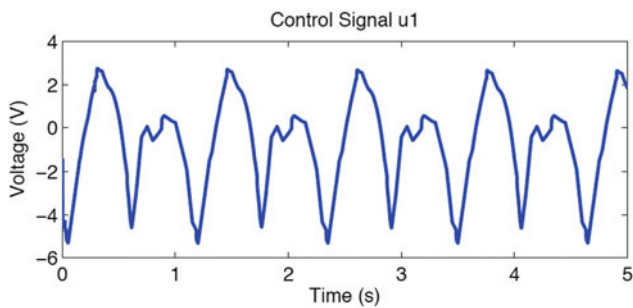


Fig. 11 Control signal u_1 after low-pass filter

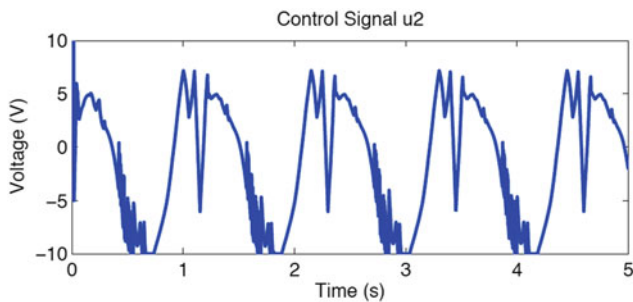


Fig. 12 Control signal u_2 after low-pass filter

4 Conclusion

Most robotic systems have parametric uncertainties, robotic prosthetic devices are no exception. In order to overcome this problem, a robust controller based on passivity has been

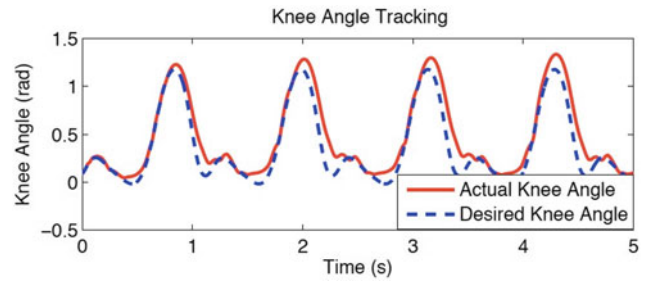


Fig. 13 Knee angle tracking after implementation of low-pass filter

implemented. Its benefits include that it is good in maintaining performance in terms of stability, error tracking and/or other specification in spite of parametric uncertainty, external disturbances or unmodelled dynamics within the system. In this paper, the robust controller is applied to a robotic system consisting of three links and showed good results regarding tracking of angle trajectories.

Conflict of Interest The authors declare that there is no conflict of interest.

References

1. Jelačić, Z. Impedance control in the rehabilitation robotics. In: *Advanced Technologies, Systems and Applications II*. Springer International Publishing AG (2018). ISBN 978-3-319-71320-5
2. Rupar, M., Jelačić, Z., Dedić, R., Vučina, A.: Power and control system of knee and ankle powered above knee prosthesis. In: *4th International Conference "New Technologies NT-2018" Academy of Sciences and Arts of Bosnia and Herzegovina, Sarajevo, B&H, 28–30th June 2018*
3. Zebris Medical products. <https://www.zebris.de/en/medical/products-solutions/>
4. Jelačić, Z., Dedić, R., Isić, S., Husnić, Ž.: Matlab simulation of robust control for active above knee prosthetic device. In: *Advanced Technologies, Systems and Applications III*. Springer International Publishing AG (2019), ISBN -3-030-02577-9
5. Jelačić, Z.: Scattering problem in the rehabilitation robotics control design, Mathematical Institute SANU, Mini-symposium "Stochastic oscillations and fatigue: theory and application", Belgrade, 04.07.2017

Comparison of CFD-Computation Fluid Dynamics Analysis of Shorter Designed Stent Graft in Abdominal Aorta

Aida Botonjić Karahusić, Tino Kostić, and Nedim Begić

Abstract

This paper is sequel of the previous research about determining blood flow through new designed stent graft in abdominal aorta. The goal of this research is to show that a very short stent graft can significantly reduce pressure in the abdominal aorta, which can lead to savings in operating time, material and lower the quantity of artificial materials in the body of the patient. Methods of Computation Fluid Dynamics (or shorter CFD) were used to determine characteristics of blood flow in the abdominal aorta. CFD is a powerful tool, used for solving fluid flow problems in a variety of engineering disciplines such as hydraulic engineering, mechanical engineering, meteorology, environmental engineering, biomedical engineering and many more. During a CFD simulation, the fluid flow domain is divided in smaller sub regions. Afterwards, the governing equations of fluid flow are solved for each particle in an iterative process, which is conducted till the accomplishment of the desired residual error. After completing research regarding shortening of the existing length of stent and work based on 2d check ups and simulations we decided to do 3d models to try to confirm objectivity of the results. Comparing 2d and 3d results the clearer interpretation of results and design was shown. This confirmed the thesis that smaller stent dimensions can also present adequate treatment for this clinical state.

Keywords

Computation Fluid Dynamics • Abdominal aorta • Aneurysms • Stent graft • Design • 2d and 3d model • Atherosclerosis

1 Introduction

This paper is sequel of the previous research about determining blood flow through new designed stent graft in abdominal aorta. The goal of this research is to show that a very short stent graft can significantly reduce pressure in the abdominal aorta, which can lead to savings in operating time, material and lower the quantity of artificial materials in the body of the patient.

Methods of Computation Fluid Dynamics (CFD) were used to determine characteristics of blood flow in the abdominal aorta. CFD is a powerful tool, used for solving fluid flow problems in a variety of engineering disciplines such as hydraulic engineering, mechanical engineering, meteorology, environmental engineering, biomedical engineering and many more [1, 2]. During a CFD simulation, the fluid flow domain is divided in smaller sub regions. Afterwards, the governing equations of fluid flow are solved for each particle in an iterative process, which is conducted till the accomplishment of the desired residual error.

The circulatory system consists of blood and lymphatic vascular system. Function of circulation is transportation of nutritive materials to the tissues and “waste material” in the opposite direction. Other functions of circulation include transport of hormones from one part of the body to another and regulation of the homeostasis in the whole body. Heart is the organ that “pumps” blood, while the arteries transport blood under high pressure and with great velocities to the tissues. That is the reason why arteries have relatively strong walls. The vascular wall is made of 3 basic structure parts: endothelium, muscular tissue and connective tissue. Endothelium is a non-thrombogenic surface which has a

A. Botonjić Karahusić (✉)
Faculty of Architecture, University of Sarajevo, Sarajevo, Bosnia and Herzegovina
e-mail: aidabotonjic274@gmail.com; aidab@af.unsa.ba

T. Kostić
Department for Hydraulic Engineering and Water Resources Management, University of Kassel, Kassel, Germany

N. Begić
Pediatric Clinic, Clinical Center University of Sarajevo, Sarajevo, Bosnia and Herzegovina

function to prevent blood coagulation. When the endothelium cells are damaged subendothelial connective tissue induces platelet collecting.

Aortic aneurysmal disease is recognized as a degenerative process which involves all layers of the wall of blood vessels. The pathophysiology can be described through four processes: infiltration of the wall of blood vessel by lymphocytes and macrophages; destruction of elastin and collagen in the media and adventitia by enzymes proteases, including matrix metalloproteinase; loss of smooth muscle cells; and neovascularization [3, 4].

For very small aneurysms, with size around 3.0–3.9 cm, the risk of rupture is negligible. Therefore, these aneurysms do not require surgical intervention and should be kept under regular ultrasound surveillance. For aneurysms between 4 and 5.5 cm in diameter, rapid growth (>1 cm/year) and the development of certain symptoms due to aneurysm growth demands intervention. Aneurysm repair should be considered at a maximum aneurysm diameter of 5.2 cm in females and 5.5 cm in males. This is because females appear more likely to suffer abdominal aortic aneurysm rupture with smaller aneurysm diameters than males [5].

Open surgery can treat these aneurysms; this involves surgical techniques that involve opening the abdomen and placing an artificial graft over the widening [6, 7]. A newer, alternative method involves an artificial stent graft, delivered through an arterial blood vessel in the groin, fixed over the widening. This technique is called endovascular repair [6, 7].

There are many different types of stent grafts available, usually spreading through the entire body of the aneurysm. The objective of this research is to show that a much smaller stent graft can drastically lower the pressure in the aneurysm of the abdominal aorta.

1.1 Numerical Models

The numerical models used for this research were conducted with the software ANSYS CFX. The goal of this research was to show the difference in pressure distribution between the model of the abdominal aorta with aneurysm and the model with the introduced short stent graft. Therefore, an arbitrary aneurysm was modeled and attached to the model of the abdominal aorta. The length of the short stent is also arbitrary, however, it must be taken in account that variations in the stents length would lead to slightly different results of the research. Figure 1 shows the schematic view of the numerical models, while Fig. 2 show the geometry and the computational mesh of the model.

The numerical simulations were conducted with the solver CFX which solves the Navier-Stokes equations for incompressible, steady state fluid flow. The SSG Reynolds Stress turbulence model was used in this research. In the

inlet area of the models (aorta with the 2.5 cm diameter) an constant inlet velocity of 0.33 m/s was prescribed, while the two outlet areas (two aortas with 1.6 cm diameter) have a constant prescribed pressure of 16.0 kPa. The density of blood was assumed to be 1060 kg/m³, while the blood kinematic viscosity value of 2.3 mm²/s was chosen for the simulations. The numerical parameters used for the simulations in this research were chosen from the literature stated in the list of literature.

2 Results

Figures 3, 4 and 5 show respectively pressure distribution, velocity distribution and velocity vectors for the model of the healthy abdominal aorta in a horizontal plane through the center of the model.

In Figs. 4 and 5 is visible that the highest pressure and lowest velocities are at the bifurcation point of the abdominal aorta. The next three figures show pressure distribution, velocity distribution and velocity vectors for the model of the abdominal aorta with aneurysm in a horizontal plane through the center of the model.

In Figs. 4 and 5 is visible that the highest pressure and lowest velocities are at the bifurcation point of the abdominal aorta. The next three figures show pressure distribution, velocity distribution and velocity vectors for the model of the abdominal aorta with aneurysm in a horizontal plane through the center of the model.

Figure 6 shows that the pressure value in the aneurysm region is much higher than for the healthy abdominal aorta (Fig. 3). Figures 7 and 8 show how the velocities in the region of the aneurysm decrease in comparison with the healthy abdominal aorta (Figs. 4 and 5) due to widening of the geometry. The next three figures show respectively pressure distribution, velocity distribution and velocity vectors for the model of the abdominal aorta with aneurysm and with the installed shortened stent graft.

Figure 9 shows the pressure drop with the installed shortened stent graft, when it is compared to the model without stent graft (Fig. 6). In Fig. 10, it is visible that the velocity distribution of the model with the stent graft is more similar to the model of the healthy abdominal aorta than it is to the model of the abdominal aorta with aneurysm. It is also visible that the stent graft directs the blood flow towards the center of the aneurysm, which makes the velocities outside the center jet close to zero (Figs. 10 and 11).

It is of great interest to compare the pressure values on the walls on the abdominal aorta for the different models. In order to do so, only the pressure on the walls of the aneurysm for both models was measured. The pressure on the walls of the healthy part of the aorta was ignored. It was calculated that the average pressure on the walls of the

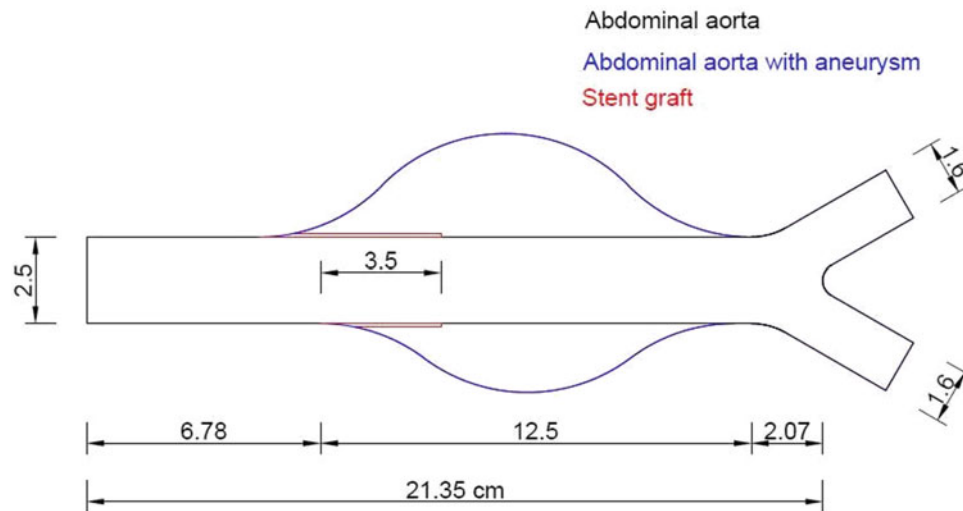
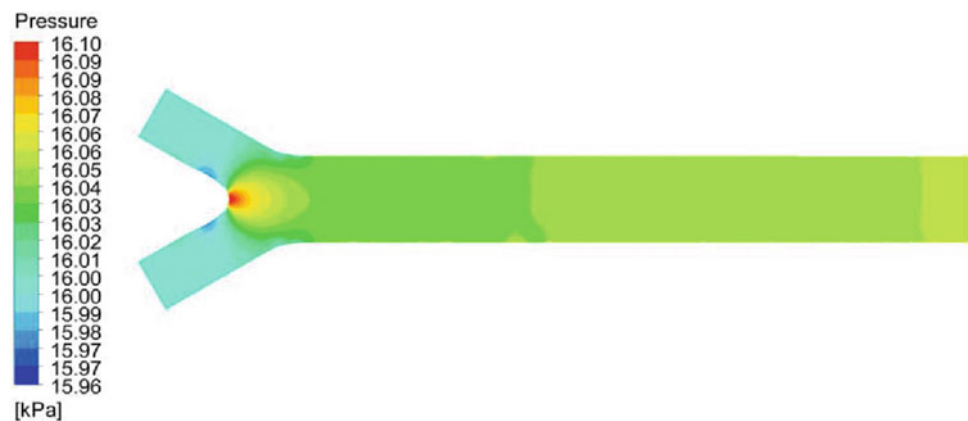


Fig. 1 Schematic view of the simulation models of abdominal aorta



Fig. 2 Geometry (left) and computational mesh (right) of the numerical model of abdominal aorta

Fig. 3 Pressure distribution for the model of the healthy abdominal aorta



model with the abdominal aorta with aneurysm is 16,083.2 Pa. The average pressure on the model with the introduced stent graft is equal to 16,066.4 Pa. For comparison, the pressure in the healthy aorta equals 16,064.9 Pa. With the appearance of the aneurysm, the average pressure on the wall of the aorta rises for 18.3 Pa, while introduction

of the short stent reduces the pressure on the walls of the aorta for 16.8 Pa, which is 91.8% of the additional pressure produced by the appearance of the aneurysm.

Figures 12 and 13 shows velocity streamlines for the two 3D models. It is visible in the Fig. 13, that the streamlines for the model with the short stent graft are concentrated only

Fig. 4 Velocity distribution for the model of the healthy abdominal aorta

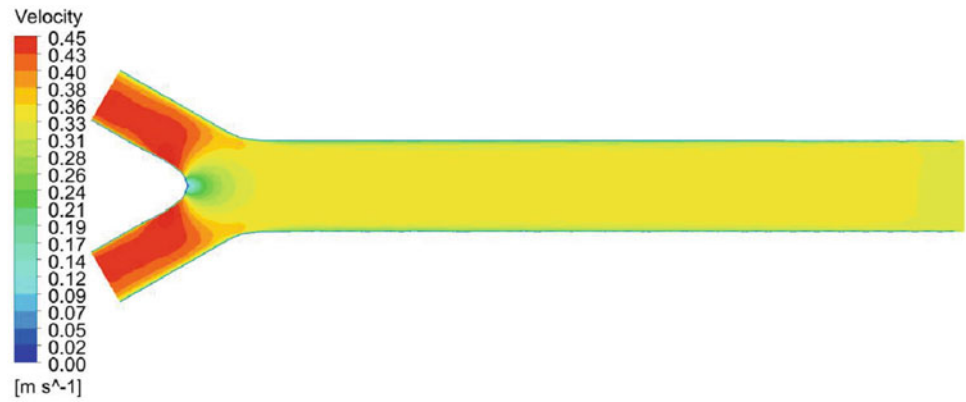
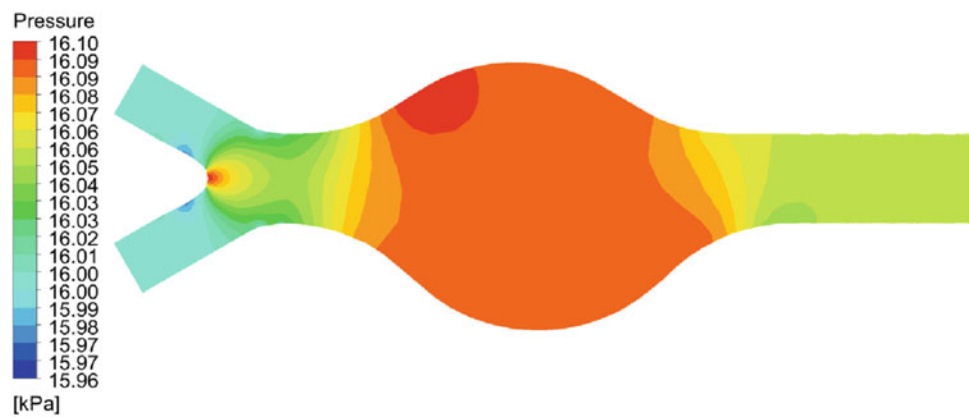


Fig. 5 Velocity vector distribution for the model of the healthy abdominal aorta



Fig. 6 Pressure distribution for the model of the abdominal aorta with aneurysm



in the middle area of the model. This indicates that the vast majority of the blood flow process is occurring in the central region of the aneurysm, which is a very similar hydraulic situation as it is for the healthy abdominal aorta without

aneurysm. The streamlines of the 3D model without the stent graft are distributed all over the aneurysm, also indicating that the blood flow is directed towards the wall of the aneurysm.

Fig. 7 Velocity distribution for the model of the abdominal aorta with aneurysm

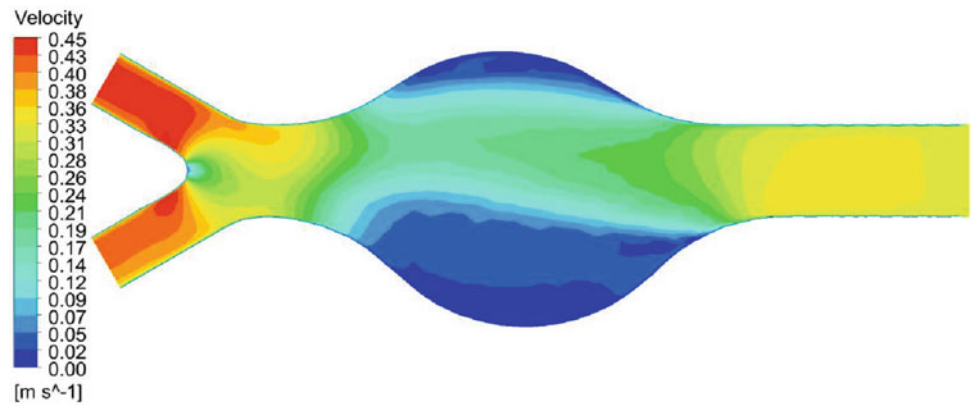


Fig. 8 Velocity vector distribution for the model of the abdominal aorta with Aneurysm

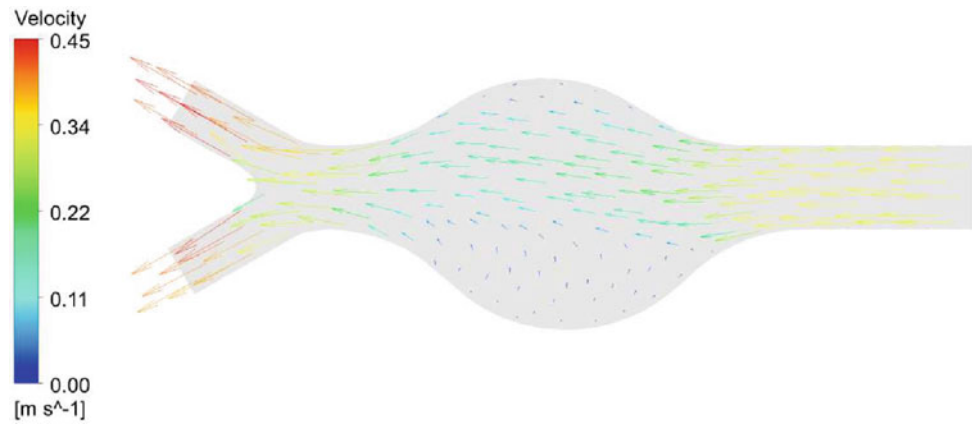


Fig. 9 Pressure distribution for the model of the abdominal aorta with aneurysm with the stent graft

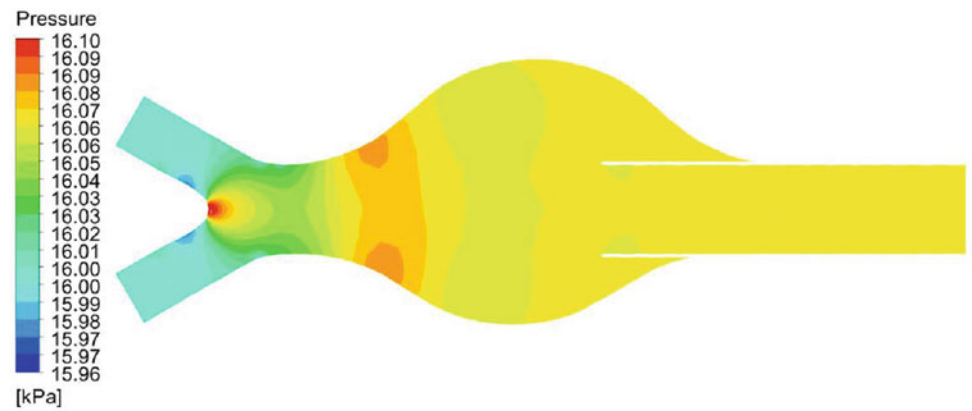


Fig. 10 Velocity distribution for the model of the abdominal aorta with aneurysm with the stent graft

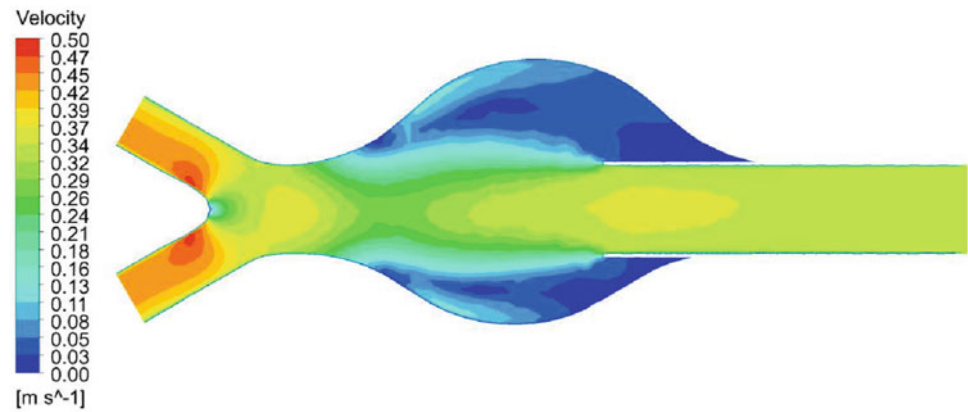


Fig. 11 Velocity vector distribution for the model of the abdominal aorta with aneurysm with the stent graft

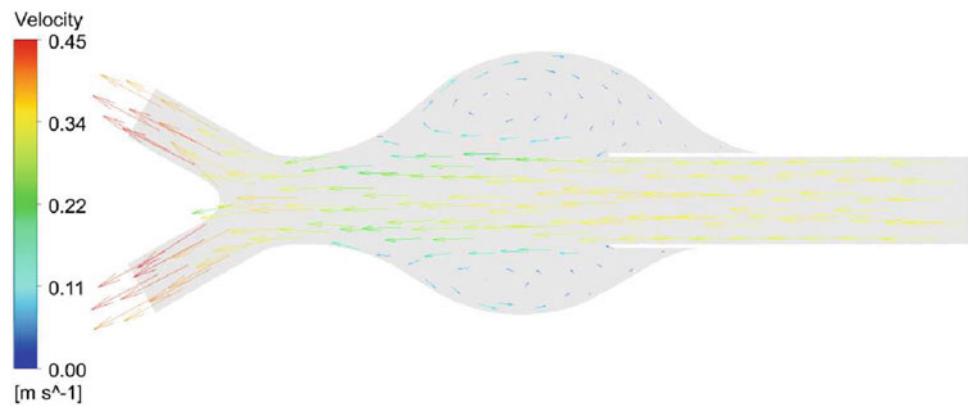
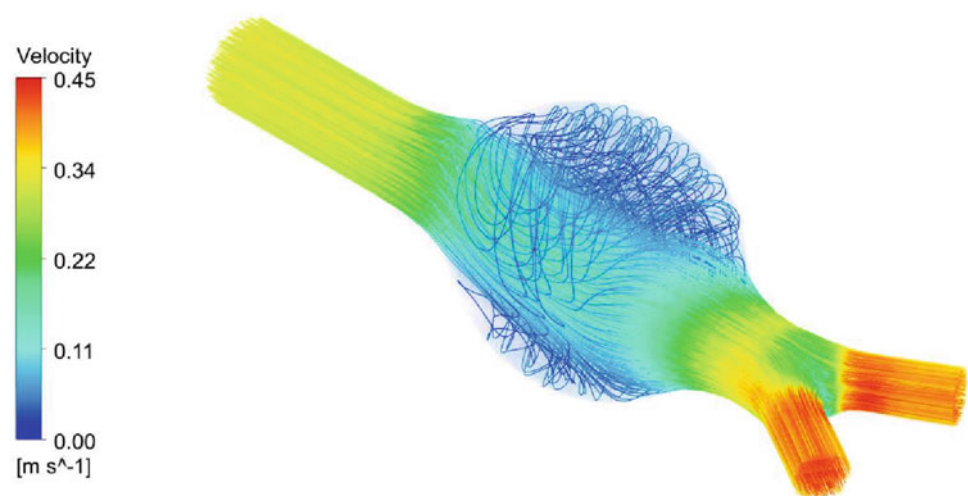


Fig. 12 Representation of the velocity streamlines for the model of the abdominal aorta with aneurysm



3 Conclusion

Although the exact cause of abdominal aortic aneurysms is unknown, a number of factors play a role in its appearance, including: tobacco use, atherosclerosis, high blood pressure, infection in the aorta, trauma and heredity. Atherosclerosis, as an inevitable process, cannot be stopped, but treatment and

follow up of this state, especially in the presence of aortic aneurysm, is extremely important.

Treatment and monitoring of abdominal aortic aneurysm can decrease the risk of complications connected with aneurysm of the aorta. When there are indications, open surgery or endovascular intervention are necessary.

In relevant medical literature, so far it is not stated that any specific stent graft performs better than another. More

Fig. 13 Representation of the velocity streamlines for the model of the abdominal aorta with aneurysm and short stent graft



research is required to help decide which specific type of stent graft is to use.

After completing research regarding shortening of the existing length of stent and work based on 2D check ups and simulations we decided to do 3D models to try to confirm objectivity of the results. Comparing 2D and 3D results the clearer interpretation of results and design was shown. This confirmed the thesis that smaller stent dimensions can also present adequate treatment for this clinical state.

Conflict of Interest Declaration None.

References

1. Morris, P.D., Narracott, A., von Tengg-Kobligk, H., et al.: Computational fluid dynamics modelling in cardiovascular medicine. *Heart* **102**(1), 18–28 (2015)
2. Cheng, Z., Juli, C., Wood, N.B., et al.: Predicting flow in aortic dissection: comparison of computational model with PC-MRI velocity measurements. *Med. Eng. Phys.* **36**, 1176–1184 (2014)
3. Mathur, A., Mohan, V., Ameta, D., Gaurav, B., Haranahalli, P.: Aortic aneurysm. *J. Transl. Int. Med.* **4**(1), 35–44 (2016)
4. Ailawadi, G., Eliason, J.L., Upchurch Jr., G.R.: Current concepts in the pathogenesis of abdominal aortic aneurysm. *J. Vasc. Surg.* **38**, 584–588 (2003)
5. Van, H.C., Renard, M., Loeys, B.: The Loeys-Dietz syndrome: an update for the clinician. *Curr. Opin. Cardiol.* **25**, 546–551 (2010)
6. Lederle, F.A., Johnson, G.R., Wilson, S.E., Chute, E.P., Hye, R.J., Makaroun, M.S., et al.: The aneurysm detection and management study screening program: validation cohort and final results. *Arch. Intern. Med.* **160**, 1425–1430 (2000)
7. Handa, N., Onohara, T., Akaiwa, K., et al.: Early outcomes of endovascular aneurysm repair for abdominal aortic aneurysm: first preliminary report of national hospital organization network study in Japan. *Ann. Vasc. Dis.* **4**(3), 218–222 (2011)

Part VI

**Cardiovascular, Respiratory and Endocrine
Systems Engineering**

A Novel Enzymatic Microreactor: Towards Transforming the Pharmaceutical Industry

Medina Hamidović, Ferenc Ender, and Andreas Springer

Abstract

Offering many fundamental and practical advantages of relevance for today's chemical and biological industry, microreactors are rapidly replacing round-bottomed flasks in modern biochemical labs. Compared to the batch processing, microreactors can offer precise control of reaction variables, high-throughput scanning of reaction conditions, increased safety parameters and they require small quantities of reagents. These miniaturized devices are widely used to facilitate routine work in biochemical analysis and also have applications in biocatalysis where they are termed as enzymatic microreactors. In this work, enzymatic microreactors are used to ease characterization of CaLB enzyme activity as a function of a substrate concentration. The work demonstrates potential of Lab-on-a-Chip devices with enzymatic microreactors as an evolving platforms for performing reliable on-chip biocatalytic measurements and a possible foundation for future flow-chemistry based industrialization.

Keywords

Enzymatic microreactors • Lab-on-a-Chip • Biochemical analysis • Immobilization • Nanofiber

1 Introduction

At present, many synthetic organic chemicals are still produced using well known batch processing that employs techniques and apparatus that have been in place for decades [1, 2]. To manufacture a new chemical, or to synthesize new molecules for drugs, biocides, herbicides or pesticides, it is necessary to determine the optimal working conditions for a chemical process. This requires a number of time-consuming tests to be conducted on the samples of smaller (picoliter to milliliter) volumes. The trial period is usually a complex and demanding step which takes place over the period of weeks or even months. Here, the process pathways and reaction conditions must be optimized [1].

Once the working conditions are found and the chemical process is repeatedly successful, the process needs to be scaled-up in order to achieve mass production and meet the demands for larger quantities. Here, the whole chemical process needs to be revised again and readjusted for larger batch sizes—a procedure that requires years of additional research and leads to substantial financial costs [3, 4] (c.f. Fig. 1).

The traditional approach has started to change with the advancement of the microreaction technology that has the potential to bypass the major difficulties of scaling-up in the conventional batch processing [2]. Instead of readjusting the chemical process every time the batch size becomes larger in volume, the microreaction technology achieves large scale production through the replication of the basic unit process [3, 4] (c.f. Fig. 1). Therefore, once the optimised conditions are achieved for a basic process, it is possible to achieve the mass production simply by employing multiple basic processing units in parallel and directly transferring the optimised operating conditions to each of the units [2].

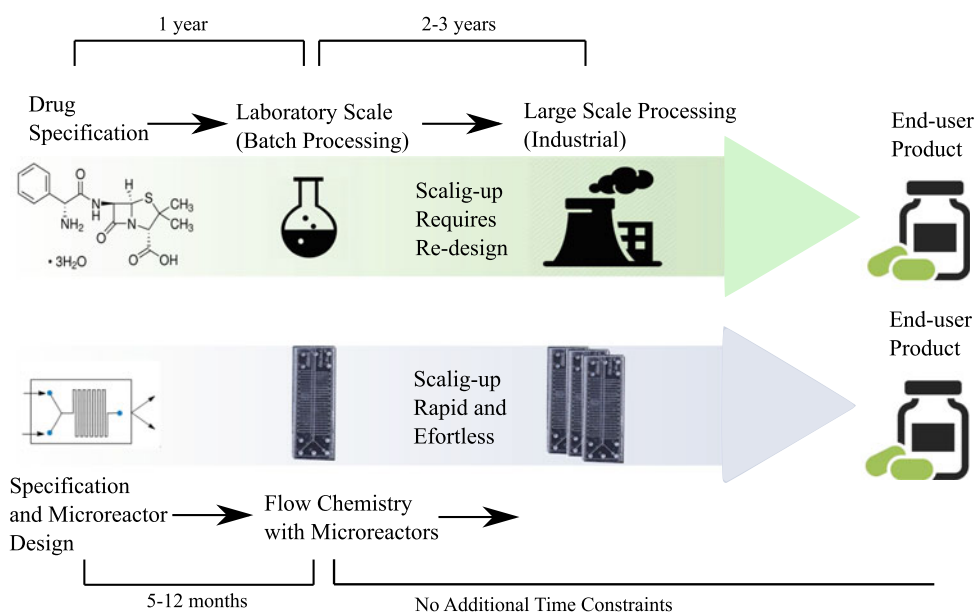
Basic processing units in which the chemical reaction takes place, are commonly known as microreactors. In its simplest form, a microreactor is a device that contains microstructured features (reservoirs) that are typically of

M. Hamidović (✉) · A. Springer
Johannes Kepler University Linz, Linz, Austria
e-mail: medina.hamidovic@jku.at

A. Springer
e-mail: andreas.springer@jku.at

F. Ender
Budapest University of Technology and Economics,
Budapest, Hungary
e-mail: ender@eet.bme.hu

Fig. 1 Difference in conventional batch processing and novel flow chemistry utilizing microreactors. Figure indicates typical procedures and corresponding timeline for both approaches



submillimetre dimensions, in which chemical reactions are performed in a continuous manner [5, 6]. The reservoirs are interconnected through a network of microchannels that enable delivering of the chemical reagents, products and/or waste to the reservoirs, thus forming a complete microfluidic device that is termed as a LoC (Lab-on-a-Chip) [7].

In sharp contrast to the space-resolved batch processing, the chemical reaction inside the microreactor is a time-resolved process. Here, reagent streams are continuously supplied into the microreactor through the pumps, where they are mixed and allowed to react for a specified time in a highly controllable environment [7]. The product of the reaction instantly leaves the reactor as the continuous stream flows through the network of microfluidic channels towards the output of a microfluidic device. This implies that simply by controlling a reagent flow rates and operation times, the scale of the chemical process can be defined. As a result, by the parallel operation of multiple chip devices for a longer time, microreactors with an inner volume of less than a millilitre can produce industry demanding (multi gram—kilogram) quantities of a product material [8].

Today, academic labs are publishing continuous synthetic routes for drugs such as Ibuprofen [4] and major pharmaceutical cooperations have started the production of drugs and drug intermediates using microreactor platforms [1]. Combining LoC devices with the microreactor technology enables performing multiple functions on a single, integrated device, resulting in an overall reduction in the time taken to discover new lead compounds and transfer them to mass production [2].

Although the microreactors find many applications in biochemical research and biotechnology, biocatalytic applications of microreactors are of a particular importance.

A special class of microreactors, known as enzymatic microreactors, has been developed in order to facilitate routine work in biochemical analysis and biocatalysis [9]. Although in its infancy, the field of enzymatic microreactors is growing rapidly with potential applications in biotechnology, medicine, biochemistry and most importantly, pharmacy [9]. With this in mind, this work introduces a novel LoC device with enzymatic packed-bed microreactors as a promising platform for performing reliable on-chip biocatalytic measurements and a possible foundation for the future flow-chemistry advancements.

2 Enzymes Inside the Microreactors

Enzymes are micromolecular biocatalysts that serve for accelerating chemical reactions [3]. These catalysts are not only important for optimal functioning of all living beings but are also widely used in diverse sectors of bioprocess technology due to their green chemistry [6]. For this reason, various research studies on enzymatic reactions and enzymatic microreactors have been proposed over the last years [9].

Inside the microreactor, enzymes can be free to move (free enzyme system) or they can be attached to a solid surface (immobilized enzyme system), which is furthermore anchored in the internal volume of the reactors (packed-bed reactors) [5]. Today, immobilized enzymes are preferred over their free counterparts since the immobilization enables enzyme recycling after usage, thus making the process more economical and environmentally friendly. Moreover, immobilization enables long-term stability and temperature resistance of the enzymes [10].

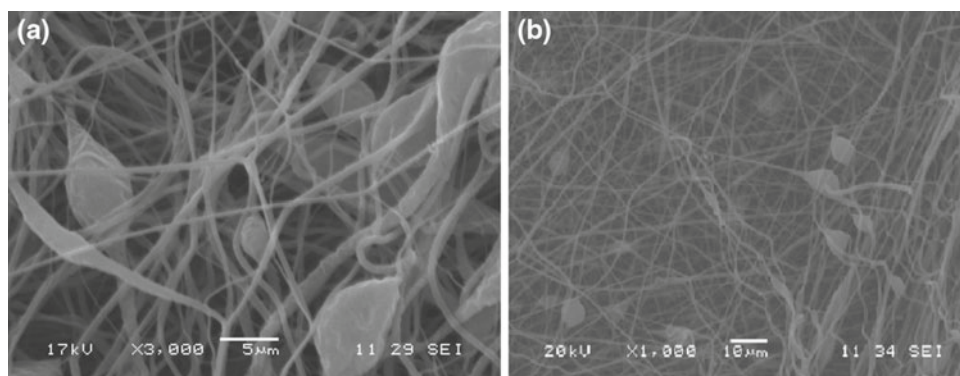


Fig. 2 SEM analysis of Lipase CaLB enzyme entrapped within the: **a** PVA (Polyvinyl alcohol) and **b** PLA (Polylactic acid) nanofiber. Diameters are ranging from 200 to 700 nm. Results are obtained for input flow rate $Q = 3 \mu\text{L}/\text{min}$, distance $d = 10 \text{ cm}$ and applied voltage of $V = 10 \text{ kV}$

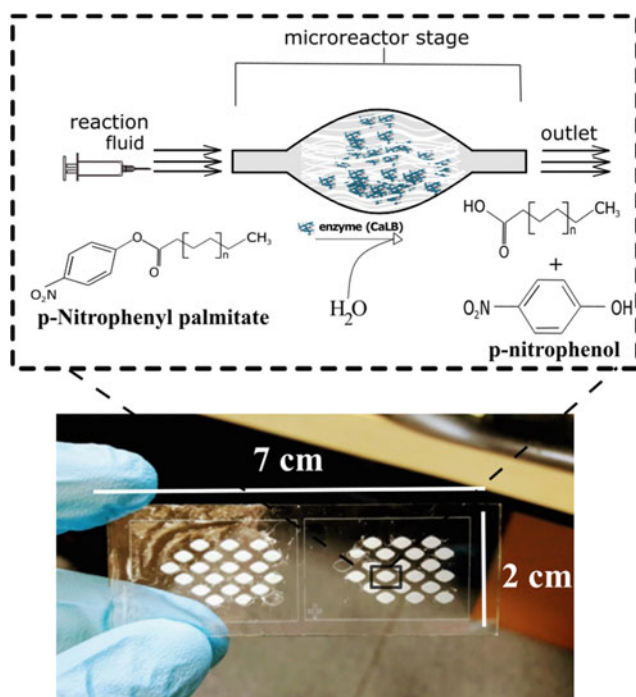


Fig. 3 Top: Schematic view of a packed-bed reactor: the enzyme-substrate reaction between the immobilized enzyme CaLB and the reaction fluid p-Nitrophenyl palmitate takes place inside the microreactor stage, where the polymer nanofiber acts as the support of the enzymes is anchored. Bottom: Novel LoC device that hosts multiple packed-bed microreactors

Immobilization of enzymes is a confinement of an enzyme to some sort of support such as beads, gels, nanopores, magnetic nanoparticles, and recently, polymer nanofibers [5, 10]. Immobilization allows for enzymes to be held in place throughout the biochemical reaction, following which they are easily separated from the products and may be re-used for another set of biochemical reactions, therefore enabling enzyme recycling.

Although various techniques were demonstrated successful for enzyme immobilization over the last decade,

entrapment of enzymes within the electrospun nanofibers, as shown in Fig. 2, has truly revolutionized the world of enzyme immobilization [10]. This is due to the wide applicability of the entrapping methods in the fields of chemistry, biomedicine biosensors and biofuels [6, 10]. Moreover, a broad spectrum of structural materials available to construct the nanofibers makes the method suitable for various microfluidic applications. Figure 3 shows SEM (Scanning Electron Microscopy) results of CaLB enzyme entrapped within the PVA (Polyvinyl alcohol) and PLA (Polylactic acid) nanofibers of different diameters.

In the following section, we exploit the advantages of the enzyme immobilization within the nanofibers to introduce a novel enzymatic microreactor that is able to perform high-throughput, on-chip biocatalytic measurements.

3 Novel Enzymatic Microreactor

In this section we present a novel LoC device for performing fast, efficient and reliable on-chip biocatalysis. In the proposed, novel microreactors are designed as a network of cylindrical chambers (hollows) in the chip body and the chambers are filled by enzymes encapsulated within polymer nanofibers, as shown in Fig. 3. When a microreactor holds supporting materials, such as nanofibers, and biocatalyst is immobilized onto their surfaces, it is defined as a special class known as the packed-bed reactor [11].

As shown in Fig. 3, in the basic working principle, the reaction fluid enters the packed bed reactor, the reaction with biocatalyst develops in the microreactor stage, and outlet fluid (the product) is collected at the end of the microreactor. In this case, Lipase enzyme (CaLB) catalyses the transformation of the substrate p-Nitrophenyl palmitate (pNPP) to the product p-nitrophenol (pNP).

Candida antarctica lipase B (CaLB) is a member of the lipase family, and as the name suggests, it originates from the yeast *Candida antarctica* [12]. CaLB is source of

industrially important lipases and an ideal and robust enzyme catalyzing a diversity of reactions with applications ranging from synthesis of biodiesel, bioplastics, as well as kinetic resolution of chiral compounds in pharmaceutical applications [12].

Noticing the importance of the CaLB enzyme, we introduce a platform for performing high-throughput biocatalytic measurements that will enable more insight into the enzymatic activity, productivity, stability and efficiency of the CaLB enzyme. Novelty of the microreactor design is in its uniqueness in the way it maximizes the reactor area by connecting multiple microreactors onto a single platform (c.f. Fig. 3), which further provides the opportunity to perform multiple biocatalytic measurements using a single device. Moreover, utilizing nanofibers to immobilize the enzymes inside the microreactors, it is possible to achieve precise control over the concentration of the enzyme inside the chambers which leads to high reproducibility of analytical steps and measurements.

4 Materials and Methods

4.1 Tools and Materials

PLA (D-isomer 10%, PURASORB PL 24) was obtained from PURAC (Gorinchem, Netherlands). Solvents (chloroform and ethanol) were obtained from Molar Chemicals (Budapest, Hungary). N,N-Dimethylformamide (DMF) was obtained from Merck (Budapest, Hungary). PLA solution is 10% m/m (9% polymer and 91% solvent). CaLB as lyophilized enzyme powder (recombinant *C. antarctica* lipase B) was obtained from c-LEcta (Leipzig, Germany). For an enzyme entrapment within the nanofibers, the PLA solution (PLA solved in chloroform) with CaLB as lyophilized enzyme powder was prepared where 1 g of PLA solution contains 10 mg of CaLB enzyme powder. Since PLA polymer solution is 10% polymer and 90% solvent, the final polymer emulsion contains 10% enzyme. Silicon Elastomer kit for fabricating PDMS chip was obtained from Sigma-Aldrich (Saint Louis MO, USA). For the purpose of plasma treatment, Femto plasma cleaner (Diener electronics, Germany) was used. To follow the enzyme kinetics, gas chromatography (GC) on an Agilent 4890 equipment using Hydrodex b-6TBDM column (Machery-Nagel, 25 m 25 mm 0.25 m, heptakis-(2,3-di-Omethyl-6-O-t-butylidimethylsilyl)- β -cyclodextrin) was used. Microfluidic setup to dispense reagents and control flows was provided by spFlow Chip system (Spinsplit LLC, Budapest, Hungary).

4.2 Preparation of Nanofibers

The formation of PLA nanofibers was done by eSpin Tube Base electrospinning system (Spinsplit LLC, Budapest, Hungary) shown in Fig. 4. The electrospinning parameters (voltage, input flow rate and distance needle-collector plate) were adjusted using the controlled system and the parameters used are: voltage of 10–15 kV, distance needle-collector of 10–12 cm and the input flow rate of 3–4 $\mu\text{L}/\text{min}$. The electrospun mass is measured to be 3600 mg (3000 mg of PLA solution and 60 mg enzyme). Considering that PLA solution is 10% w/w solution, this implies that total chip holds 300 mg of PLA polymer. Therefore, at the end of electrospinning process the chip hosts 300 mg of PLA and 60 mg of CaLB enzyme, which means that enzyme/polymer ration on the chip is $60/300 = 20\%$. In average, it was measured that every electrospun chip carries 2–3 mg of CaLB enzyme.

4.3 Patterning the Nanofiber Filled Chambers

To engrave the microreactor layout, the electrospun nanofibers were patterned using the Nd:YAG (AVIA Coherent, USA) laser. The PLA nanofiber layer was mounted onto the

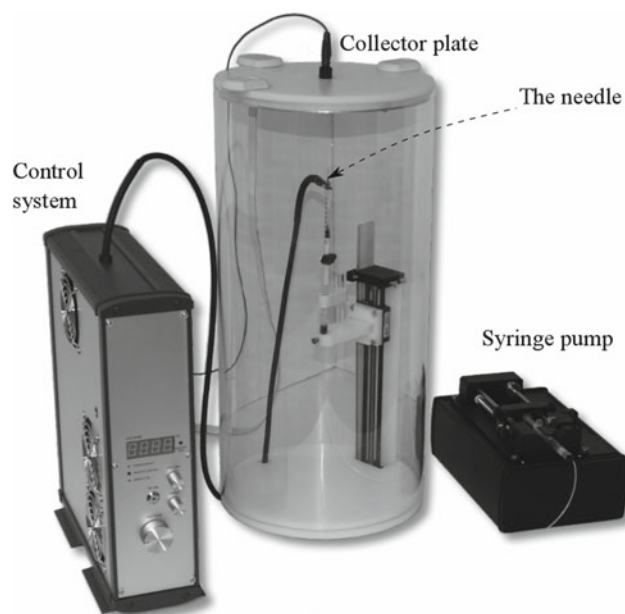


Fig. 4 Experimental set-up for nanofiber fabrication. Left to right: automated system for adjusting electrospinning parameters, Plexiglas protective chamber system for carrying out the electrospinning process and controlled syringe pump

50 × 50 mm working area of the laser and patterned using the output power of 3 W, pulse width of 10 μs and the mark speed of 80 mm/s.

4.4 Following the Transformation of pNPP to pNP

The assay was performed by measuring the increase in the absorbance expected at around 350–400 nm produced by the release of p-nitrophenol in the hydrolysis of 0.4 mM pNPP (MW = 377:52 g/mol) in a PBS buffer (m = 0.1 M, pH = 7.5) at the temperature of 30 °C. To make a final reaction fluid, 7.8 mg of pNPP was solved in 20 ml PBS buffer. This stock solution was mixed for 27 h to be diluted completely for the on-chip reaction. Reaction fluid enters the chip over the inlets with input flow rate in the range of 1–5 μL/min. The substrate-enzyme reaction is carried in situ, and the product is collected at the output.

5 Experimental Results

This section presents results for the on-chip biocatalytic measurements carried out using the prototype of the novel enzymatic microreactor. The complete experimental set-up is shown in Fig. 5a, while Fig. 5b shows close view of the microfluidic chip during the testing.

For following the enzyme kinetics, we provide the substrate (pNPP) through the inlets of the microfluidic chip. Travelling throughout the the chip, the substrate interacts with the lipse enzymes and results of the reaction is a creation of a novel chemical component, a product, known as a p-nitrophenol (c.f. Fig. 5).

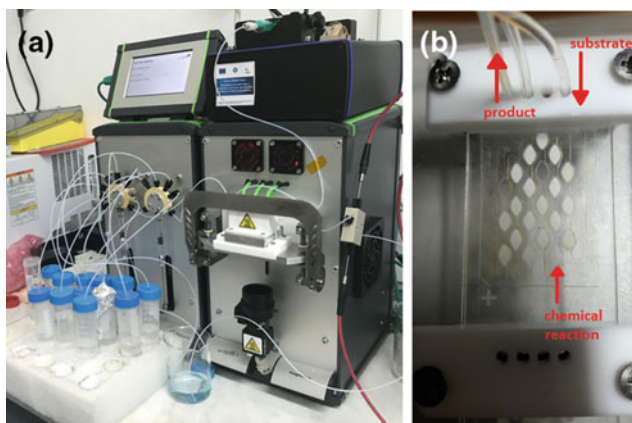


Fig. 5 Experimental set-up for carrying biocatalytic measurements using novel microreactor design: **a** complete set-up and **b** close view of the microfluidic chip

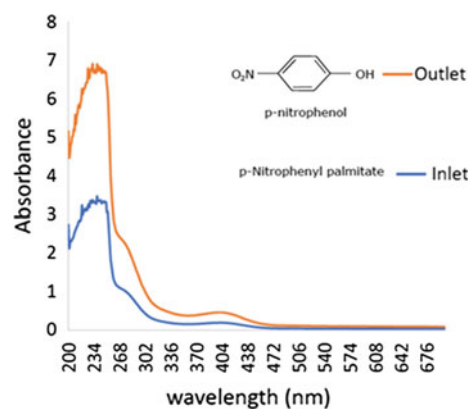


Fig. 6 UV absorbance spectra of substrate (p-Nitrophenyl palmitate) and product (p-nitrophenol) as a result of a successful enzymatic activity of a CalB enzyme

To measure if the enzymatic reactions was carried out successfully, measurements using the UV-Vis technique were carried out. This enables following the change in concentration decrement of the substrate, or the concentration increment of the product as a consequence of the biocatalytic reaction inside the microreactor. The result of the measurements is shown in Fig. 6. Since two different absorbance spectra are detected, it is verified that the biocatalytic process of manufacturing a new chemical component was carried out successfully on the chip.

6 Conclusion

This work demonstrated means of improving the way conventional drug discovery and manufacture are carried out. The prototype of a novel LoC device with enzymatic microreactors was designed, fabricated and experimentally validated. The obtained results have shown that the device can be used to successfully conduct on-chip chemical production which provides a foundation for future flow-chemistry based industrialization. Moreover, compared to the conventional batch processing, the device was shown to be significantly more time and resource efficient by reducing the time needed to discover and produce new chemical components from 3–4 years to only 5–12 months—a crucial accomplishment in exploiting full potential of modern pharmaceutical industry.

References

1. Calabrese, G.S., Pissavini, S.: From batch to continuous flow processing in chemicals manufacturing. *AIChE J.* (2011). <https://doi.org/10.1002/aic.12598>
2. Watts, P., Wiles, C.: Recent advances in synthetic micro reaction technology. *Chem. Commun.* (2007). <https://doi.org/10.1039/B609428G>

3. Bisswanger, H.: *Enzyme Kinetics*. Wiley-Blackwell (2005). <https://doi.org/10.1002/3527601759.ch2>
4. Bogdan, A., Poe, S., Kubis, D., Broadwater, S., McQuade, D.: The continuous-flow of ibuprofen. *Angew. Chem. Int. Ed.* (2009). <https://doi.org/10.1002/anie.200903055>
5. Balogh-Weiser, D., Nmeth, C., Ender, F., Gyarmati, B., Szilgyi, A., Poppe, L.: Electrosun nanofibers for entrapment of biomolecules. *IntechOpen* (2018). <https://doi.org/10.5772/intechopen.76068>
6. Bartsch, S., Bornscheuer, U.: A single residue influences the reaction mechanism of ammonia lyases and mutases. *Angew. Chem. Int. Ed.* (2009). <https://doi.org/10.1002/anie.200900337>
7. Fletcher, P.D.I., Haswell, S.J., Pombo Villar, E., Warrington, B., Watts, P., Wong, S.Y., Zhang, X.: *Micro reactors: principles and applications in organic synthesis* (2002). [https://doi.org/10.1016/S0040-4020\(02\)00432-5](https://doi.org/10.1016/S0040-4020(02)00432-5)
8. Weiler, A., Junkers, M.: Using microreactors in chemical synthesis: Batch process versus continuous. *Flow. Sigma Aldrich ChemFiles*
9. Urban, P.L., Goodall, D.M., Bruce, N.C.: Enzymatic microreactors in chemical analysis and kinetic studies. *Biotechnol. Adv.* <https://doi.org/10.1016/j.biotechadv.2005.06.001>
10. Datta, S., Christena, L.R., Rajaram, Y.R.S.: Enzyme immobilization: an overview on techniques and support materials (2013). <https://doi.org/10.1007/s13205-012-0071-7>
11. Strnia, F., Baji, M., Panjan, P., Plazl, I., Sesay, A.M., Žnidar Plazl, P.: Characterization of an enzymatic packed-bed microreactor: Experiments and modeling. *Chem. Eng. J.* (2018). <https://doi.org/10.1016/j.cej.2018.05.028>
12. Sharma, N.: Calb lipase. Fermenta Biotech Limited (2011). <https://www.fermentabiotech.com/calb-lipase.php>

Modeling of Voltage Imaging for the Study of Action Potential Propagation

Pietro Tarchi, Francesca Bologna, Costanza Scortecci, Eleonora Tiribilli, Diletta Pennati, Leonardo Sacconi, Michele Sorelli, and Leonardo Bocchi

Abstract

Voltage imaging allows to visualize the propagation of the action potential while it propagates in cardiac tissue. In our experiment we acquire a stack of voltage images, using a fluorescence microscope. In this work we focus on the development of a model of the signal and on the estimation of its parameters. We assumed the signal can be represented as the sum of two exponential functions, starting from the instant of activation of the cell. Results indicate the model is able to adequately describe the shape of the waveform, despite the high noise level in the original images.

Keywords

Voltage imaging • Modeling • Action potential

1 Introduction

Life-threatening arrhythmias, including atrial and ventricular fibrillation, represent a social and economic burden in the general population. The electro-anatomical substrate of these arrhythmias is characterized by conduction heterogeneities that facilitate micro and macro re-entrant circuits [1]. Although multifaceted, a common trait of these abnormalities is the alteration of action potential propagation across the heart. Optical mapping is a very useful approach for investigating the electrical activity at the whole heart level. This consists in the combination of an ultra-fast wide-field microscope and of a fluorescent sensor revealing variations in the membrane potential (voltages sensitive dye VSD). Using this approach, the electrical potential can be mapped

P. Tarchi · F. Bologna · C. Scortecci · E. Tiribilli · D. Pennati · M. Sorelli · L. Bocchi (✉)
University of Florence, Florence, Italy
e-mail: leonardo.bocchi@unifi.it

L. Sacconi · L. Bocchi
LENS, Sesto Fiorentino, Italy

by visualizing the fluorescence variations in the video frames. The video sequences are generally used to produce the activation map of the action potential (by measuring the temporal shift across different position of the images) thus visualizing the propagation wave-front of the electrical activity. However, additional information can be potentially achieved by a more detailed analysis of the action potential profile across different positions and phases of the conduction. Here we developed a model-based approximation of the electrical activity, representing the activation waveform as the output of a 2nd-order linear model. Model parameters are identified by using a least squares fitting procedure, thus obtaining an optimal estimate of the activation time and of the shape of the action potential.

2 Materials and Methods

A wide-field mesoscope [2] operating at 1.6 kHz was used to map the action potential propagation in Langendorff horizontally perfused mouse hearts, stained with a red-shifted VSD (di-4-ANBDQPQ) [3]. The whole mouse heart was illuminated in wide-field configuration using a $\times 2$ objective and a light emitting diode (LED) operating at a central wavelength of 625 nm. A dichroic beam splitter followed by a band-pass filter at was used for collecting the VSD-emitted fluorescence. A $\times 20$ objective was used to focus the fluorescence in a central portion (128×128 pixels) of the sensor of a sCMOS camera operating at a frame rate of 1.6 kHz (630 μ s actual exposure time). A typical frame is shown in Fig. 1. For each sample, a sequence of about 5000 frames was acquired, corresponding to a capture time of 3 s.

During the activation of each cardiac cell, the fluorescence signal decreases, producing a corresponding decrease in gray level of the image. The effect can be visualized by computing the average gray level of each frame and plotting its time profile, as shown in Fig. 2. The plot clearly shows

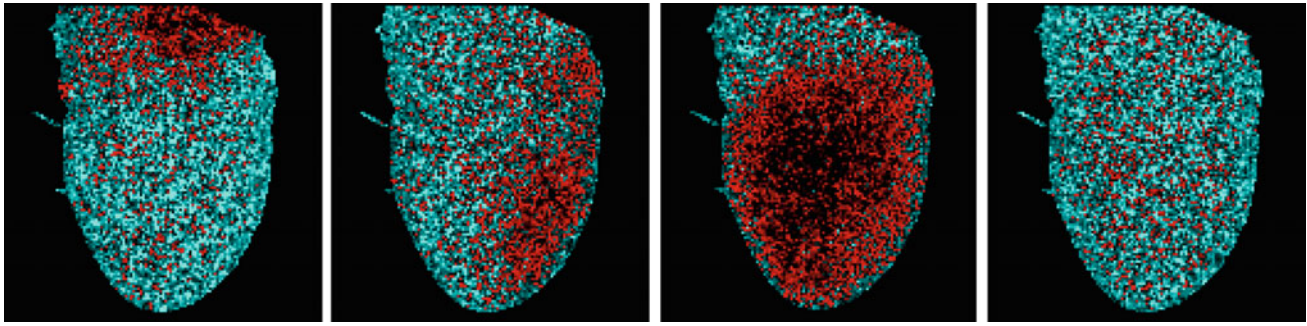


Fig. 1 Sample voltage images of a heart: four frames showing the propagation of the potential in a normal contraction

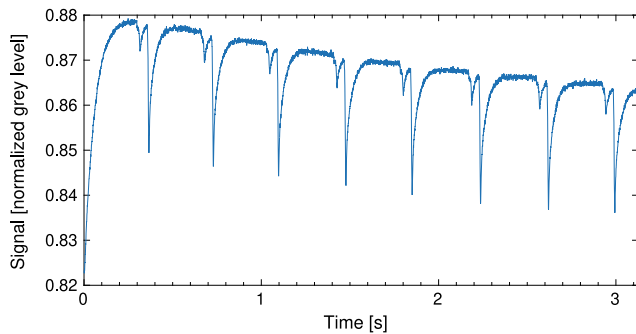


Fig. 2 Sample signal corresponding to the heart in physiological conditions

the typical shape of the signal, highlighting the fast depolarization followed by the re-polarization of the tissue.

Our method extracts a signal describing a single contraction period from each region of the image; this signal is approximated with a bi-exponential function, whose parameters are estimated using a Least Squares (LS) method, starting from a rough estimation of the parameter values. The spatial map of the parameters is then used to assess the propagation of the action potential and the characteristics of the activation process. In the following paragraphs, each step is described in detail.

2.1 Preprocessing

The image stack presents an high level of noise, caused by the low photon count associated with the fluorescence process. Thus, spatial averaging is a valid approach for increasing the signal-to-noise ratio, at expense of the spatial resolution of the signal. We experimented three different levels of averaging, namely using a square region of 4×4 and 2×2 pixel as well as the original resolution (1×1 pixel, no averaging). The average gray level of each region constitutes a temporal signal, named $s_{ij}(t)$, where t corresponds to the frame, and (i, j) identifies the region in the image.

The first preprocessing step builds a binary mask identifying the pixels corresponding to the earth tissue against the background. A binary threshold, applied to the average value of $s_{ij}(t)$, is sufficient to correctly discriminate the background from the heart tissue.

The following step aims at identifying the contraction period T . An average signal is obtained by averaging $s_{ij}(t)$ over the points of the image belonging to the tissue mask. In normal heart and in mild arrhythmia (as well as in cases of external stimulation of the tissue) the action potential propagates very fast in comparison to the contraction period, thus a well-defined waveform is visible in the average signal (see Fig. 2). The two distinct peaks correspond to the depolarization of atria and ventricles, respectively. Also, a slow variation of the baseline is present. Only in most severe cases of arrhythmia there is no identifiable contraction pattern in the tissue, and this is reflected in a lack of periodicity of the average signal. The first maximum (beside the one in the origin) of the auto-correlation function identifies the signal period. In case of lack of evident periodicity, there is no evident maximum beside the one in the origin, and a fixed period is used.

The algorithm focuses on a single contraction period for obtaining a fast processing; moreover, in arrhythmic situations, each heart beat can present a different activation pattern, requiring the process to be performed independently on each contraction.

The period used for the analysis is manually defined by the operator, by an approximate selection of the local minimum on the average signal. The algorithm locates the time instant t_a corresponding to the closest minimum of the signal, and extracts a full period ranging from $t_a - T/2$ to $t_a + T/2$, in order to have the action potential close to the center of the examined interval. This selection ensures that all signal refers to the same contraction, even for large delays between the start and the end of the contraction. The resulting signal is shown in Fig. 3.

Afterward, a smoothing step, using a moving average spanning 5 frames, improves the robustness of the fitting process by reducing the noise level without introducing

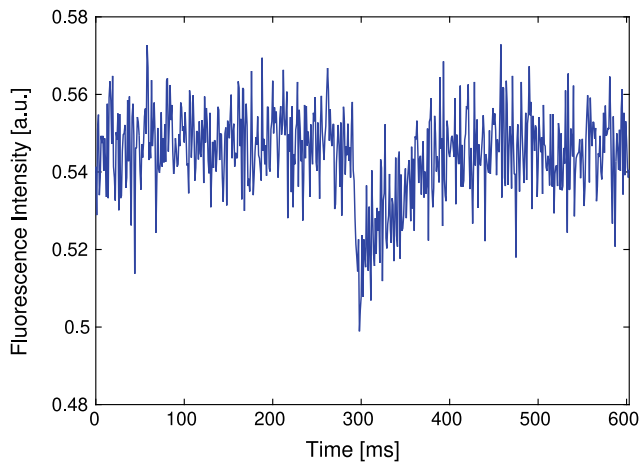


Fig. 3 Sample signal corresponding to a single contraction periods, obtained in a 4×4 pixel window located in the ventricular region

significant deformations of the signal. Also, a de-trending step cancels the slow decay of the fluorescence signal.

2.2 Signal Model

The exact shape of the action potential, as described by the classical cell membrane model, is fairly complex, being generated by non linear processes. However, the imaging process averages several neighboring cells in each image pixel, smoothing out the exact signal shape. Thus, we adopted a simplified function able to give an approximate shape of the curve; the most basic model is represented by the output of a linear 2-nd order model, defined as:

$$f(t) = \begin{cases} k - A \left(e^{-\frac{t-t_0}{\tau_d}} - e^{-\frac{t-t_0}{\tau_r}} \right) & \text{if } t > t_0 \\ k & \text{otherwise} \end{cases} \quad (1)$$

where the parameters of the model are: k , representing the potential at equilibrium; t_0 , representing the activation instant; A , related to the amplitude of the depolarization; τ_d , the time constant of the depolarization phase; and τ_r , the time constant of the re-polarization phase.

2.3 Parameter Estimation

A simple but effective procedure, shown in Fig. 4, allows to estimate suitable values ($\hat{k}, \hat{t}_0, \hat{A}, \hat{\tau}_d, \hat{\tau}_r$) of the model parameters from the signal $s(t)$ in order to obtain a good convergence of the LS algorithm.

The procedure starts by estimating the value of t_m , the time instant where the maximum depolarization is present (i.e. s_m , the minimum level of the signal), and the maximum value $\hat{k} = s_M$, that is used as an approximation of k ,

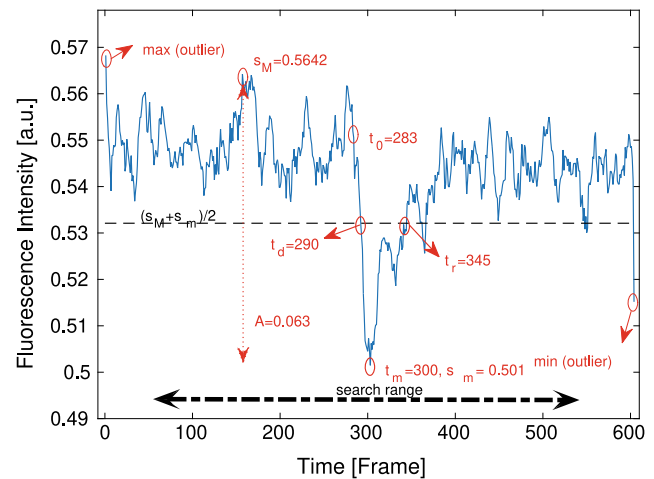


Fig. 4 Parameter estimation procedure

corresponding to the constant potential at the beginning and at the end of the activation cycle. The difference $\hat{A} = s_M - s_m$ is used as an estimate of the amplitude A . The halving times t_d and t_r represents the time instants where $s(t) = s_m + (s_M - s_m)/2$, respectively during de-polarization and re-polarization. The halving times allow to estimate the two time constants: $\hat{\tau}_d = \ln(2) * (t_m - t_r)$ and $\hat{\tau}_r = \ln(2)(t_r - t_m)$. Last, the start of the depolarization \hat{t}_0 is estimated as the point where $s(t) = s_M - 0.2(s_M - s_m)$. As shown in the figure, several points in the signal may met the above requirements (in the example, several candidates exists for t_r); in such cases, the point closest to t_m is selected.

2.4 Fitting and Optimization

The result of the estimation procedure produces a rough estimate of the input signal, that is suitable for further optimization. An example model, corresponding to the parameter values estimated as described in the previous section, is shown in Fig. 5. However, the curve does not represent an optimal description of the signal; thus a LS optimization tunes the parameter to their optimal values ($\tilde{k}, \tilde{t}_0, \tilde{A}, \tilde{\tau}_d, \tilde{\tau}_r$). The variability ranges imposed on the parameters are defined as follows: the range of the parameter t_0 equals to half of the signal period, while the variability range of the other parameters spans from half to double of the estimated value. Sensible variations in computational time are related to the stopping criterion; in particular, a large effect is associated with the parameter accuracy threshold. A preliminary optimization step aims at analyzing the relation between the fitting error, the computational time, and the difference between the estimated and the fitted values, in order to determine the optimal tolerance value. The estimation and fitting steps were performed on each ROI of

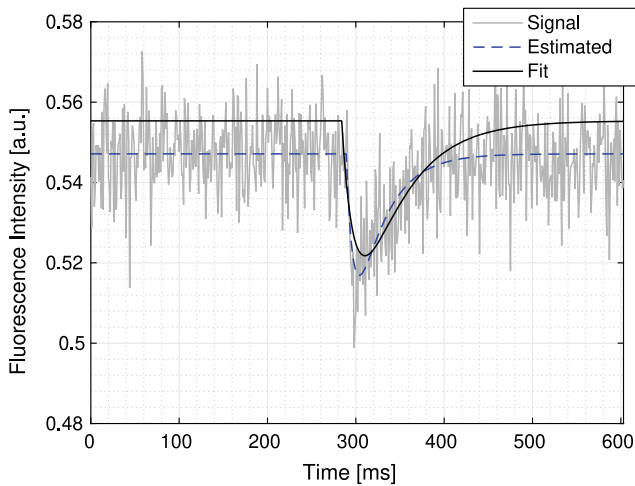


Fig. 5 Sample signal, model resulting from parameter estimation and after least squares fitting

the image, averaging the respective results. Given the large percentage of the fitting error associated to high frequency noise, we analyzed the error between the model and a smoothed replica of the signal. This procedure considers the difference $\Delta t_0 = |\hat{t}_0 - \tilde{t}_0$, i.e. between the value of t_0 before and after the fitting procedure, as this value represents a location-independent estimate of the quality of the fit. Indeed, as the value of \tilde{t}_0 depends on the ROI selection, it is not significant to plot an average value of \tilde{t}_0 . The utilization of the estimated \hat{t}_0 , which depends on the ROI selection but not on the tolerance value, as a reference point allows to transform the values of \tilde{t}_0 into an homogeneous scale.

3 Results

The results of the preliminary optimization step are shown in Fig. 6. The figure refers to ROIs of size 4×4 pixel, however the results were very similar for all considered region sizes. The plot shows that the tolerance value is roughly inversely proportional to the computational time; indeed, the number of iterations required to achieve the desired precision in the parameter estimate increases almost linearly with the tolerance. The sum of the residuals, i.e. the fitting error, increases non linearly with tolerance; in particular, tolerance values up to 10^{-5} are associated with very small differences in the fitting error. Increasing the tolerance above this critical value, we observed a dramatic increase in the fitting error, which suggests that the procedure is no longer able to accurately model the signal. This is also supported by the Δt_0 plot. Thus, the plot confirms that increasing the tolerance up to values equal to 10^{-5} does not significantly alter the

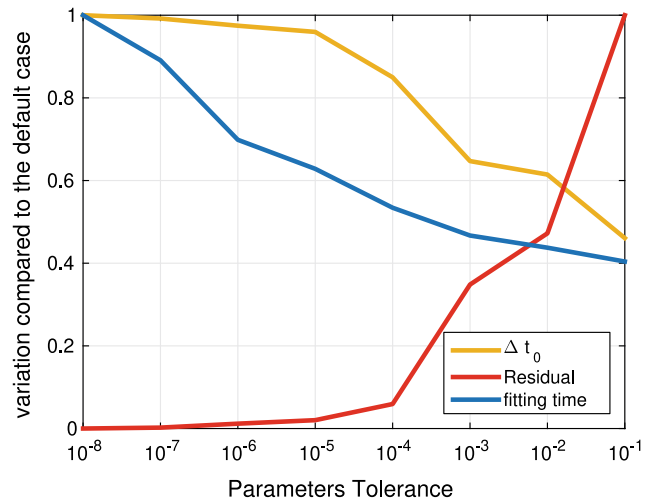


Fig. 6 Results of the optimization step: plot of the residuals (fitting error), processing time, and parameter variation with respect to parameter tolerance (10^{-8})

value of t_0 ; again, larger values are associated to a considerable variation in the outcome of the fitting procedure. Therefore, a tolerance value equal to 10^{-5} was selected.

The model was tested in four different situations; namely, normal heart beat, arrhythmia and two different typologies of external stimulation. In all cases, we applied the procedure using three different ROI sizes, i.e. 4×4 , 2×2 , and 1×1 pixel. In this work, we focused on the analysis of the parameter t_0 , as it relates to the activation of the contraction. However, the model also provides estimates of the amplitude and the two time constants of the model, not discussed here for sake of brevity.

Figure 7 shows the spatial distribution of t_0 in the normal case, using different ROI sizes; the procedure provides a high quality estimates at large ROI sizes, with an increased presence of noise at higher resolution. The image clearly distinguishes between the activation of the atrial and ventricular regions, as expected. Moreover, it is also able to detect the propagation of the action potential inside the ventricular tissue, as shown in the right column, where the time interval between 270 and 300 frames is expanded. It is worth noting that the procedure is successfully oversampling the data, being able to show differences in the activation time below the acquisition rate (each level in the images is shown in the right column corresponds approximately to 0.1 frames in the original sequence). Also, at maximum resolution, we may observe a few points, appearing as salt-and-pepper noise in the image, where the fitting procedure fails to properly optimize the model parameters. A detailed analysis shows that in such cases the fitting procedure is captured by local minima; improved signal-to-noise ratio, parameter

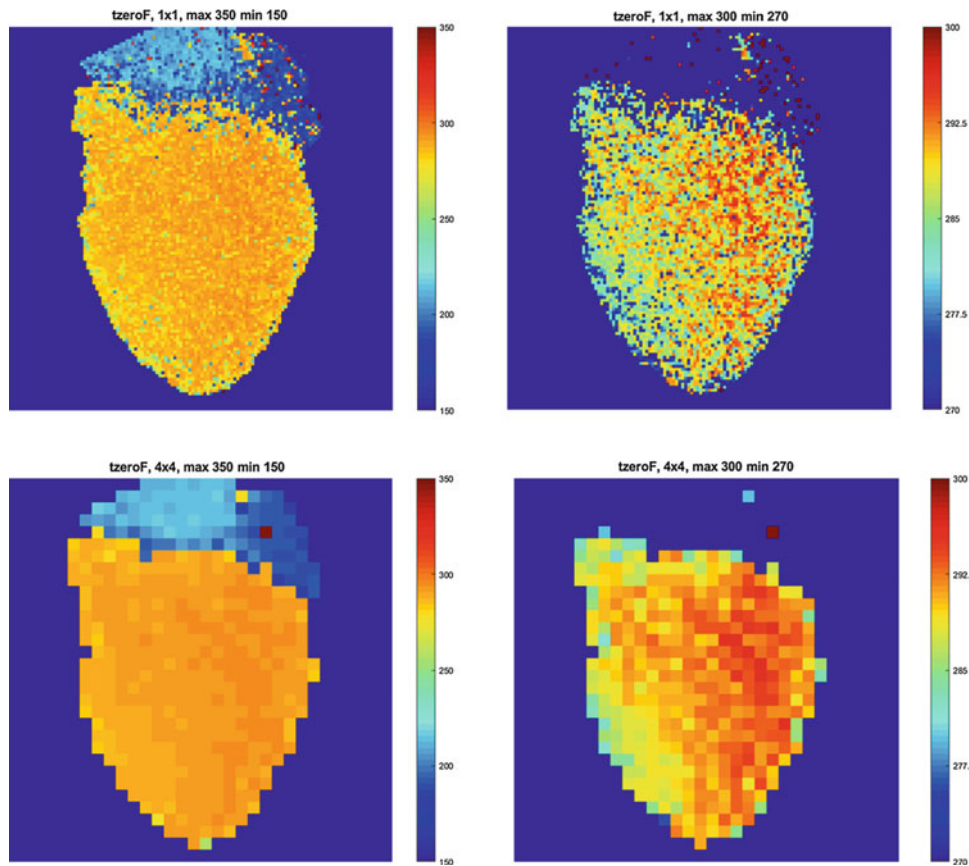


Fig. 7 Sample maps of the distribution of t_0 ; upper row: 1×1 ROI, lower row: 4×4 ROI; left: full time scale (frames from 150 to 350), right: during ventricular activation (frames 270–300)

estimation, or parameter boundaries may provide a sensible improvement.

For comparison, we analyzed also some abnormal situations, shown in Fig. 8. The corresponding images indicate that the model is able to correctly fit the signal shape, highlighting the propagation of the action potential. However, a large difference with respect to the physiological condition is evident; in particular, no distinct ventricular activation is visible.

4 Discussion

The proposed model allows to characterize the local activation pattern of the heart; the propagation of the action potential has already proved to be of great relevance in the characterization of heart failure [4], and its duration is correlated to different anomalies in contraction [5, 6]; also, the assessment of action potential parameters is essential for

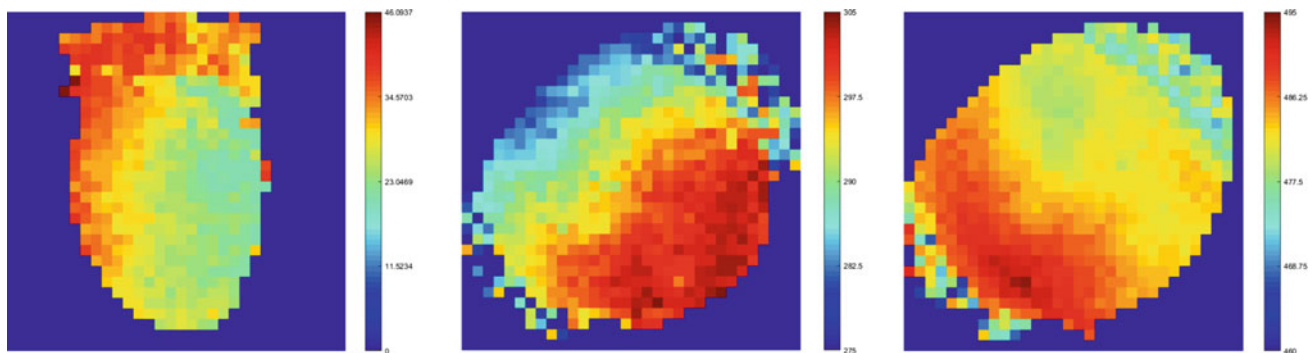


Fig. 8 Sample maps of the distribution of t_0 ; from left to right: arrhythmia, apical stimulation, sinusal stimulation

driving optogenetic procedures aimed at controlling the heart activity [7]. The proposed technique can provide an unified method for the simultaneous estimation of all the parameter describing the action potential, overcoming the difficulties related to the poor signal-to-noise ratio of the fluorescence images, and the possible incongruities resulting from the application of different techniques for the estimation of the relevant parameters.

Conflict of Interest The authors declare no conflict of interest.

References

1. Davidenko, J.M., Pertsov, A.V., Salomonsz, R., Baxter, W., Jalife, J.: Stationary and drifting spiral waves of excitation in isolated cardiac muscle. *Nature* **355**(6358), 349–351 (1992)
2. Scardigli, M., Mllenbroich, C., Margoni, E., Cannazzaro, S., Crocini, C., Ferrantini, C., Coppini, R., Yan, P., Loew, L.M., Campione, M., Bocchi, L., Giulietti, D., Cerbai, E., Poggesi, C., Bub, G., Pavone, F.S., Sacconi, L.: Real-time optical manipulation of cardiac conduction in intact hearts. *J. Physiol.* **596**(17), 3841–3858 (2018)
3. Matiukas, A., Mitrea, B.G., Qin, M., Pertsov, A.M., Shvedko, A.G., Warren, M.D., Zaitsev, A.V., Wuskell, J.P., Wei, M., Watras, J., Loew, L.M.: Near-infrared voltage-sensitive fluorescent dyes optimized for optical mapping in blood-perfused myocardium. *Heart Rhythm* **4**(11), 1441–1451 (2007)
4. Sacconi, L., Ferrantini, C., Lotti, J., Coppini, R., Yan, P., Loew, L.M., Tesi, C., Cerbai, E., Poggesi, C., Pavone, F.S.: Action potential propagation in transverse-axial tubular system is impaired in heart failure. *Proc. Natl. Acad. Sci. U.S.A.* **109**(15), 5815–5819 (2012)
5. Frame, L.H., Simson, M.B.: Oscillations of conduction, action potential duration, and refractoriness. A mechanism for spontaneous termination of reentrant tachycardias. *Circulation* **78**(5), 1277–1287 (1988)
6. Park, S.A., Lee, S.R., Tung, L., Yue, D.T.: Optical mapping of optogenetically shaped cardiac action potentials. *Sci. Rep.* **4** (2014)
7. Kulkarni, K., Tolkacheva, E.G.: Real-time feedback based control of cardiac restitution using optical mapping. In: Proceedings of the Annual International Conference of the IEEE Engineering in Medicine and Biology Society, EMBS, volume 2015-November, pp. 5920–5923 (2015)

Atherosclerotic Plaque Formation in the Coronary Arteries

Igor Saveljic[✉], Dalibor Nikolic[✉], Zarko Milosevic, and Nenad Filipovic[✉]

Abstract

Atherosclerosis is a disease of arterial blood vessels characterized by the accumulation of lipids in the arterial wall, starting with endothelial dysfunction, which favors lipid and cell elements crossing inside blood vessel wall. In this study, using DICOM images, a numerical model of atherosclerosis progression was developed. Fluid domain (blood) was modeled using Navier-Stokes equations in conjunction with continuity equation, while the solid domain (arterial wall) was modeled using Darcy's law. For the purpose of modeling lowdensity lipoprotein (LDL) and oxygen transport, convection-diffusion equations were used. Kedem-Katchalsky equations were used for coupling fluid and solid dynamics. Determination of plaque location and plaque volume with computer simulation for a specific patient shows a potential benefit for prediction of disease progression. The results for plaque concentration for the right and left coronary arteries are presented.

Keywords

Plaque concentration • Coronary artery • Wall shear stress

1 Introduction

Atherosclerosis is a disorder in the function of the membrane (endothelium) of the first layer of the blood vessel that leads to accumulation of lipids in the intima layer of the blood vessel. Atherosclerosis starts with endothelial dysfunction and after that comes to accumulations of lipid, cholesterol,

calcium and cell elements inside blood vessel wall (Fig. 1). There are many factors that influence the development of this disease. Some of them are high blood pressure, use of cigars, physical inactivity, obesity, age etc.

In this work, finite element method was used to determine wall shear stress (WSS) and plaque concentration in the human coronary arteries. For many years, the influence of the WSS on the occurrence of plaque and its further progression has been studied [1–3]. It was concluded that a low value of shear stress leads to dysfunction of the first layer of the vessel wall. Finite element method, used in this work, is for many years the dominant numerical methods for solving fields of physical quantities. Two time periods were analyzed: baseline (0 months) and follow-up (after 8 months).

Our approach for simulation of the plaque formation starts with mass transport of LDL through the wall and the simplified inflammatory process which is coupled with the Navier-Stokes equations, the Darcy equation for model blood filtration and Kedem-Katchalsky equations [5, 6] for the solute and flux exchanges between the lumen and the intima. Then we used three additional reaction-diffusion equations for the inflammatory process and lesion growth model in the intima. The specific patient left and right coronary arteries plaque concentration for baseline and follow up is presented.

2 Materials and Methods

2.1 Computer Model

The fundamental equations for the low density lipoprotein transport through the lumen and solid domain and for plaque development are given within this section. Navier–Stokes equation (Eq. 1), and continuity equation (Eq. 2) of incompressible fluid was used for 3D blood flow:

I. Saveljic (✉) · D. Nikolic · Z. Milosevic · N. Filipovic
Faculty of Engineering, University of Kragujevac, 34000
Kragujevac, Serbia
e-mail: isaveljic@kg.ac.rs

Bioengineering Research and Development Center, 34000
Kragujevac, Serbia

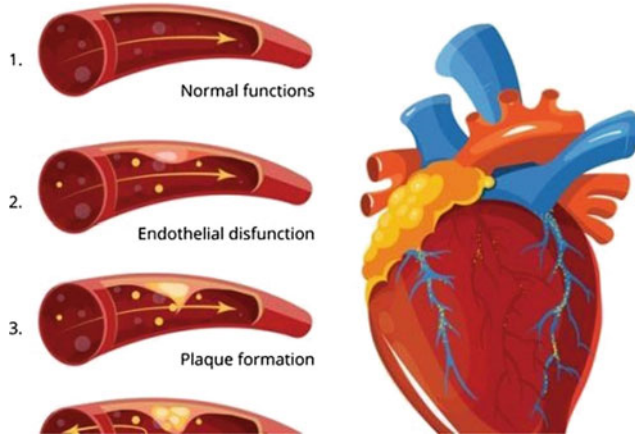


Fig. 1 Progressing of atherosclerosis [4]

$$-\mu\nabla^2 u_l + \rho(u_l \cdot \nabla)u_l + \nabla p_l = 0 \quad (1)$$

$$\nabla u_l = 0 \quad (2)$$

where u_l is blood velocity, p_l is pressure, μ is blood dynamic viscosity and ρ is density [7, 8]. Darcy's Law for Newtonian fluids was used to model mass transfer across the wall of the blood vessel:

$$u_w - \nabla \left(\frac{k}{\mu_p} p_w \right) = 0 \quad (3)$$

$$\nabla u_w = 0 \quad (4)$$

where u_w is transmural velocity, k is the Darcian permeability coefficient of the arterial wall, p_w pressure in the vessel wall and μ_p is viscosity of blood plasma. Mass transfer in the lumen domain was modeled using convective diffusion equations (Eq. 5):

$$\nabla \cdot (-D_l \nabla c_l + c_l u_l) = 0 \quad (5)$$

where D_l is diffusion coefficient of the lumen while the c_l represents blood concentration. Convective diffusion reactive equations (Eq. 6) were used for modeling mass transfer in the wall which was related to transmural flow:

$$\nabla \cdot (-D_w \nabla c_w + K c_w u_w) = r_w c_w \quad (6)$$

where D_w is diffusive coefficient of solution in the wall, c_w is solute concentration, K is solute lag coefficient and r_w is consumption rate constant.

Low density lipoprotein transport in the lumen of the vessel was coupled with Kedem-Katchalsky equations (Eqs. 7 and 8):

$$J_v = L_p (\Delta p - \delta_d \Delta \pi) \quad (7)$$

$$J_s = P \Delta c + (1 - \delta_f) J_v \bar{c} \quad (8)$$

where L_p is the hydraulic conductivity of the endothelium, Δp is the pressure drop across the endothelium, $\Delta \pi$ is the oncotic pressure difference across the endothelium, Δc is the solute concentration difference across the endothelium, δ_d is the osmotic reflection coefficient, δ_f is the solvent reflection coefficient, P is the solute endothelial permeability, and \bar{c} is the mean endothelial concentration [7, 8].

Three additional partial differential equations were used for solving the inflammatory process [8, 9]:

$$\partial_t O_x = d_2 \Delta O_x - k_1 O_x \cdot M$$

$$\partial_t M + \text{div}(v_w M) = d_1 \Delta M - k_1 O_x \cdot M + S/(1 - S) \quad (9)$$

$$\partial_t S = d_3 \Delta S - \lambda S + k_1 O_x \cdot M + \gamma(O_x - O_x^{thr})$$

where O_x represent oxidized lipoprotein transport or c_w —the solute concentration in the wall, M is concentration in the intima of macrophages, S is concentration in the intima of cytokines, d_1 , d_2 , d_3 are the corresponding diffusion coefficients, λ and γ are degradation and lipoprotein transport oxidized detection coefficients, and v_w is the inflammatory velocity of plaque growth.

2.2 Boundary Conditions

Computer finite element model used here for performing simulations were generated using medical images (CT). There are 512 and 492 DICOM images for these models. The process of obtaining a three-dimensional model using an automatic segmentation algorithm was performed using the Materialize Mimics 10.01 software. Blood flow through the coronary artery was simulated using PAK solver [8]. Blood was considered as a Newtonian fluid with a dynamic viscosity of $\mu = 0.00365$ Pas and incompressible with a density of $\rho = 1050$ kg/m³. Pulsatile coronary inlet velocity waveform was used (Fig. 2). A three-dimensional mesh consists of 204,242 nodes and 167,632 elements, for the first geometry—right coronary segment; baseline, 198,256 nodes and 158,888 elements, for the second geometry—right coronary segment; follow up, 206,436 nodes and 169,486 elements for the third geometry—left coronary segment; baseline, and 206,192 nodes and 168,994 elements for the fourth geometry—left coronary segment; follow up.

3 Results

3D simulation of blood flow through lumen and plaque progression in vessel wall was simulated. The bio molecular parameters such as LDL, HDL and triglycerides are used for

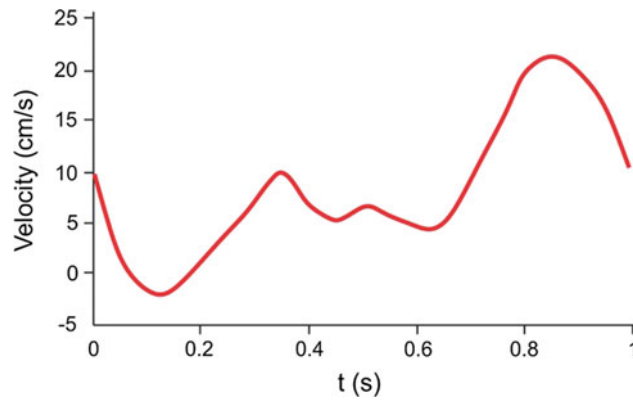


Fig. 2 Pulsatile coronary inlet velocity waveform [8]

Table 1 The bio molecular parameters and adhesion molecules for the patient #01 and patient #02

Time period	LDL	HDL	Triglycerides	ICAM1	VCAM1	E-Selectin
Baseline (left seg.)	186.1	61	148	168.3	334.9	28
Follow up (left seg.)	133.7	77	109	186.5	399.1	24.8
Baseline (right seg.)	199.9	58	133	194.1	448.7	46.8
Follow up (right seg.)	101.8	73	92	206.9	569.2	52.2

the computer simulation, as well as adhesion molecules ICAM1, VCAM1 and E-Selectin (Table 1).

Plaque progression for specific patient at left coronary artery was detected using CTA image analysis at baseline and after 8 months. We firstly examined baseline and follow up shear stress distribution for patient #01—left coronary artery (Fig. 3). Boundary conditions for the blood inflow were the same for both baseline and follow up studies

because we consider there was not significant change. At 35 mm from the artery entrance, a low value of WSS can be observed, which in Fig. 3b results in the occurrence of plaque deposits. After 8 months, there is a reduction in the segment diameter due to the accumulation of plaque concentration in the observed place (Fig. 3c).

A similar situation with the patient #02 was observed on the right coronary artery in the middle of the artery. Location

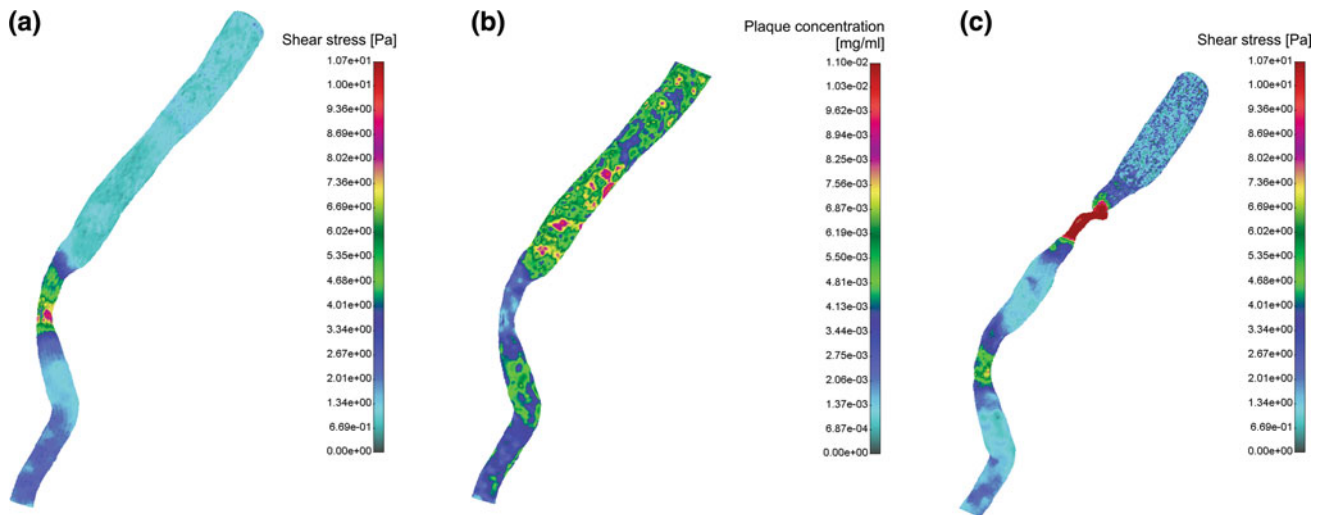


Fig. 3 Patient #01—left coronary artery; baseline shear stress distribution (a); baseline plaque concentration (b); follow-up shear stress distribution (c)

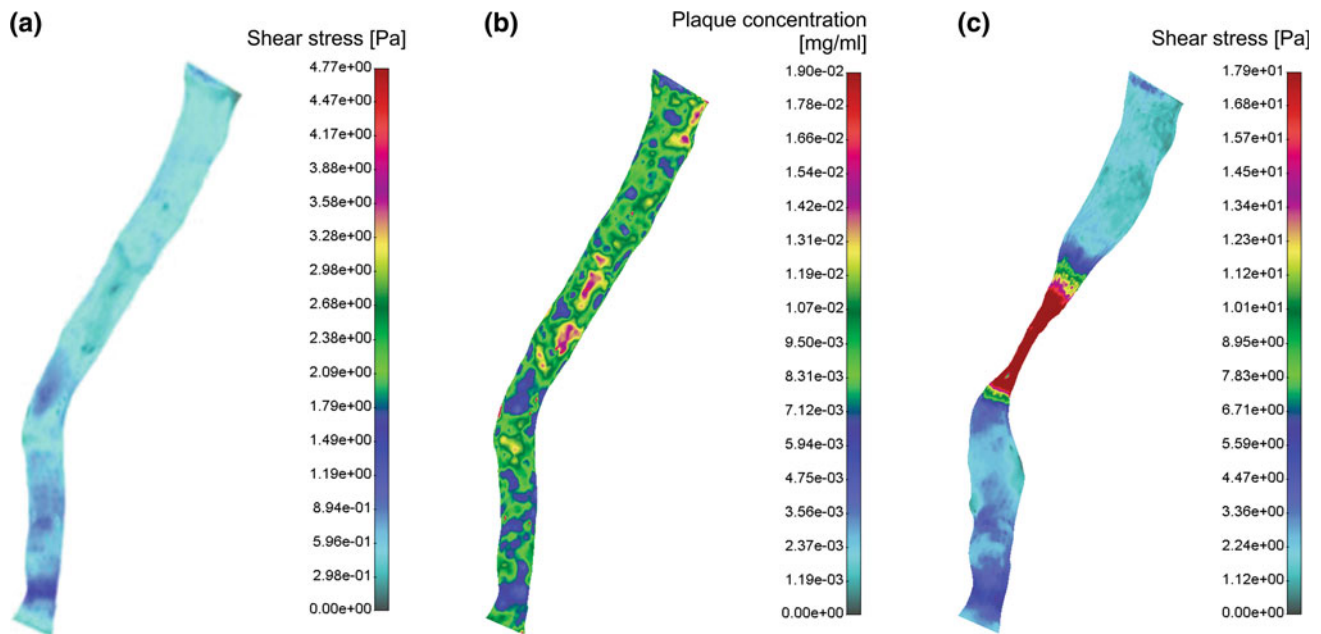


Fig. 4 Patient #02—right coronary artery; baseline shear stress distribution (a); baseline plaque concentration (b); follow-up shear stress distribution (c)

of the lowest WSS in the middle of the vessel corresponded to the site of plaque growth after 8 months (Fig. 4).

4 Discussion and Conclusion

Cardiovascular disease is responsible for an increasing number of mortality in all developed countries. Great attention is focused on studying this disease in order to reduce the mortality rate. The three-dimensional model for plaque formation and development in coronary arteries was presented. The model contains partial differential equations with space and times variables and it describes the bio-molecular process that takes place in the intima during the initiation and the progression of the plaque. The Navier-Stokes equations described the blood motion in the lumen, the Darcy law was used for model blood filtration, Kedem-Katchalsky equations for the solute and flux exchanges between the lumen and the intima. Additional reaction-diffusion equations are used for simulation of the inflammatory process and lesion growth model. Computer simulations data for the specific patient for the left and right coronary arteries for plaque position are presented. The results of the performed analyzes have shown that sites with

lower shear stress values were correlated with the sites of plaque accumulation measurements. It could be used for future diagnostic system for prediction of plaque development.

Acknowledgements This study was funded by the grants from the Serbian Ministry of Education, Science and Technological Development III41007, ON174028 and European Union's Horizon 2020 research and innovation programme under grant agreement No. 689068.

References

1. Filipovic, N., Rosic, M., Tanaskovic, I., Milosevic, Z., Nikolic, D., Zdravkovic, N., Peulic, A., Kojic, M., Fotiadis, D., Parodi, O.: ARTreat project: three-dimensional numerical simulation of plaque formation and development in the arteries. *Inf. Technol. Biomed.* **16**, 272–278 (2011)
2. Caro, C.G., Fitz-Gerald, J.M., Schroter, R.C.: Atheroma and arterial wall shear observation, correlation and proposal of a shear-dependent mass transfer mechanism for atherogenesis. *Proc. R. Soc. Lond.* **177**, 109–159 (1971)
3. Giannogolou, G.D., Soulis, J.V., Farmakis, T.M., Farmakis, D.M., Louridas, G.E.: Haemodynamic factors and the important role of local low static pressure in coronary wall thickening. *Int. J. Cardiol.* **86**, 27–40 (2002)

4. <https://www.belmarrahealth.com/a.therosclerosis-prevention-natural-home-remedies-dietexercise/>. 20 Dec 2018
5. Kedem, O., Katchalsky, A.: Thermodynamic analysis of the permeability of biological membranes to non-electrolytes. *Biochim. Biophys* **27**, 229–246 (1958)
6. Kedem, O., Katchalsky, A.: A physical interpretation of the phenomenological coefficients of membrane permeability. *J. Gen. Physiol.* **45**, 143–179 (1961)
7. Filipovic, N., Kojic, M., Ivanovic, M., Stojanovic, B., Otasevic, L., Rankovic, V.: MedCFD, Specialized CFD Software for Simulation of Blood Flow through Arteries. University of Kragujevac, Kragujevac, Serbia (2006)
8. Kojic, M., Filipovic, N., Stojanovic, B., Kojic, N.: *Computer Modeling in Bioengineering: Theoretical Background, Examples and Software*. Wiley, Chichester, UK (2008)
9. Johnston, B.M., Johnston, P.R., Corney, S., Kilpatrick, D.: Non-Newtonian blood flow in human right coronary arteries: transient simulations. *J. Biomech.* **39**, 1116–1128 (2005)

Coronary Angiography Evaluation of Atherosclerosis in Diabetic Patients

Aida Hasanović, Aida Šapčanin, and Jakub Hasanović

Abstract

Background Atherosclerosis is chronic disease, the prevalence of which has increased steadily as the population ages. We assessed prevalence, quality, and extent of coronary atherosclerosis using coronary angiography in a group of diabetic patients compared to nondiabetic patients. **Methodology** One hundred patients with suspected coronary artery disease underwent coronary angiography of the right coronary artery (RCA) and the left coronary artery (LCA) and were tested for the differences between diabetic (50) and non-diabetic (50) patients in ischemia detection by this method. All patients underwent coronary angiography in Heart Centre of the Clinical Center University of Sarajevo in period from January 2012 to January 2015. Coronary angiography was performed in the right and left anterior oblique position. **Results** Significant differences in sedentary lifestyle, and hypertension were seen among the diabetic and the non-diabetic group. Development of critical and diffuse coronary artery lesions was significantly higher among diabetics than non-diabetics. Changes in the proximal segment of the left anterior descending artery were the most common finding in diabetic patients. Stenotic atherosclerotic lesions of the large coronary arteries were significantly more common in the left than in the right coronary artery, but the difference between the diabetic and the non-diabetic group did not reach statistical significance. The most frequently atherosclerotic lesion of the RCA was seen in the middle segment,

rarely in the proximal and distal part. **Conclusion** Diabetic patients were found to have a significantly higher prevalence of stenotic atherosclerotic lesions of the coronary arteries. Diabetes significantly affects the anatomy of coronary arteries, and is associated with age, sedentary lifestyle, and hypertension. These findings may prove clinically useful in the follow-up of diabetic patients, the choice of diagnostic procedures as well as in active treatment either by atherectomy or by percutaneous angioplasty and stenting.

Keywords

Coronary artery disease • Atherosclerosis • Diabetes • Angiography

1 Introduction

Atherosclerosis in patients with diabetes manifests in a more accelerated and progressive manner. Overall, a twofold risk for developing coronary artery disease (CAD) has been observed in this patient population. Patients with diabetes may have a similar risk for new onset myocardial infarction as patients without diabetes with prior myocardial infarction [1].

The implications of a diagnosis of diabetes mellitus (DM) are as severe as a diagnosis of coronary artery disease (CAD). Cardiovascular mortality in all age groups and for both sexes rises equivalently with DM or a history of myocardial infarction (MI) and the two are profoundly synergistic. In addition, DM (especially type 2 DM), is associated with clustered risk factors for cardiovascular disease (CVD) [2–4].

Patients with diabetes are at high risk for coronary artery disease (CAD) Their risk of myocardial infarction (MI) was initially reported to be equal to that of patients without diabetes with a history of MI. However, subsequent studies have suggested that the impact of diabetes on the risk of

A. Hasanović (✉)

Department of Anatomy, Faculty of Medicine, University of Sarajevo, Sarajevo, Bosnia and Herzegovina
e-mail: h.hasanovica@gmail.com

A. Šapčanin

Department of Natural Sciences, Faculty of Pharmacy, University of Sarajevo, Sarajevo, Bosnia and Herzegovina

J. Hasanović

Faculty of Mechanical Engineering, University of Sarajevo, Sarajevo, Bosnia and Herzegovina

future CAD is overestimated, although diabetes remains associated with an increased risk of MI. Adequate risk assessment of patients with diabetes is of great clinical and economic importance [5].

Atherosclerosis is a diffuse disease with segmental lesions frequently involving particular vessels or their segments. In diabetic patients, these lesions are more extensively, diffusely and unevenly distributed than in non-diabetics. Diabetes mellitus (DM) as a risk factor for atherosclerosis further increases the effect of other risk factors, contributes to the more pronounced macroangiopathic changes, and increases the incidence of arterial wall calcification [6–11].

The purpose of the present study was to compare the extent and localization of stenosing lesions of the coronary arteries between diabetic and non-diabetic patients with a history of coronary artery disease and to elucidate which risk factors influence the progression of coronary artery sclerosis in patients with diabetes.

2 Materials and Methods

2.1 Subjects

In the study of 100 patients with suspected coronary artery disease (CAD) we performed coronary angiography and tested the differences between diabetic (50) and non-diabetic (50) patients in ischemia detection by this method. Coronary angiography was performed in the Heart Center, Clinical Centre University of Sarajevo (CCUS) in period from January 2012 to January 2015.

All the patients underwent angiographic and laboratory analyses including total cholesterol and triglyceride. In addition, patients were assessed for the prevalence of coronary risk factors, i.e., hypertension, hyperlipidemia, smoking habits, and family history, and for the presence of diabetes complications, i.e., nephropathy, a history of myocardial and cerebral infarction, and the presence of arteriosclerotic obliteration. BMI was calculated as the weight in kilograms divided by the square of height in meters.

2.2 Methods

Coronary angiography was performed by the percutaneous transfemoral approach using the Judkins technique. Selective coronary angiography was performed in multiple projections. The aim of the coronary angiography was to establish the coronary anatomy and the degree of the obstruction of coronary artery. The information obtained in this manner includes identifying localisation, the presence and severity of coronary luminal obstruction, as well as an estimate of the blood flow quality.

The analysis included each major coronary artery: the right coronary artery (RCA); the left anterior descending artery (LAD); and the left circumflex artery (CX). We defined significant coronary stenosis (stenosis >70%).

2.3 Statistical Analysis

The statistical analysis of the results was performed using Kolmogorow-Smirnow test and the differences in the angiographic changes of all coronary arteries obtained in diabetic and nondiabetic patients were considered significant on the level $p < 0.05$.

3 Results

Out of 100 patients with suspected coronary artery disease treated in the Heart Center of the University Clinical centre in Sarajevo the diabetic patients (50) had a higher prevalence of hypertension, higher BMI and triglyceride and cholesterol levels than non diabetic patients (Tables 1 and 2).

Diabetic patients were found to have a significantly higher prevalence of stenotic atherosclerotic lesions of the coronary arteries.

Stenotic lesions of the large coronary arteries were significantly more common in the left than in the right coronary artery but the difference between the diabetic and the non-diabetic group did not reach statistical significance

Table 1 Demographic data and risk factors in diabetic and non diabetic patients

Patients	Gender		Age (mean years)		Hypertension		Hyperlipidemia		Cigarette smoking	
	M	F	M	F	n	%	n	%	n	%
Non-diabetic (n = 50)	30	20	60		30	60	25	50	20	40
Diabetic (n = 50)	34	16	60		38	76	35	70	30	60
	$p = 0.407$				$p = 0.0475$		$p = 0.0412$		$p = 0.0455$	

Table 2 Type of vessel with coronary stenosis in diabetic and non-diabetic group

Coronary artery	Diabetic patients (n = 50)			Non diabetic patients (n = 50)		
	N	%	N of lesions	N	%	N of lesions
RCA	15	30	27	16	32	18
CX	5	10	18	9	18	9
LAD	30	60	50	25	50	32
Total			95			59

$p = 0.0245$

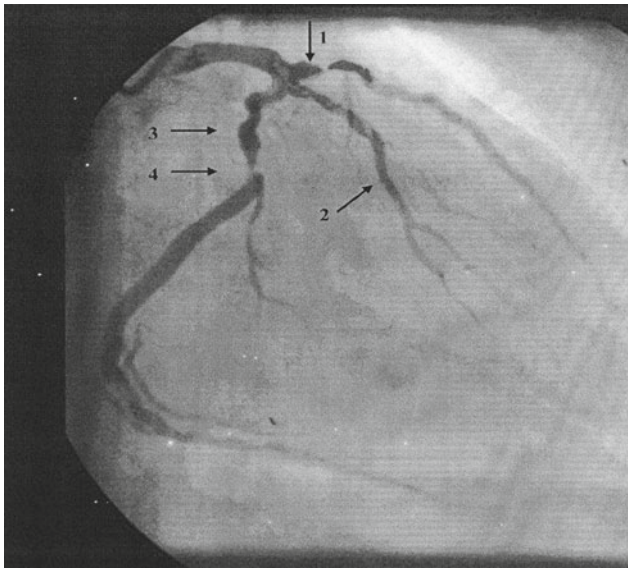


Fig. 1 Coronary angiogram of the left coronary artery showing (1) stenosis of the left anterior descending artery (99%), (2) ramus intermedius, (3) circumflex branch, (4) subocclusion of the CX (99%)

Coronary angiograms of diabetic group showed the morphological changes caused by significant stenosis of coronary arteries (>70%). Changes in the proximal segment of the left anterior descending artery (LAD) were the most common finding in diabetic patients. As well as stenosis of the CX branch was found in diabetic and non-diabetic group (Fig. 1).

The most frequently atherosclerotic lesion of the RCA was seen in the middle segment, rarely in the proximal and distal part.

4 Discussion

Diabetes mellitus is frequently associated to more severe coronary artery disease, with involvement of a larger number of vessels and more lesions. This metabolic disorder facilitates the development of coronary atherosclerosis, the frequency and severity of which usually increases with the severity of diabetes mellitus. Due to this relation, coronary

accidents are the main cause of death in diabetic patients and more serious clinical manifestations of ischemic heart disease, like acute coronary syndrome and acute myocardial infarction, are up to three times more frequent in diabetics than in non-diabetics. In addition, the diabetic patient usually has a more depressed ventricular function [3, 4].

The prevalence, localization and morphological features of atherosclerotic plaques have been thoroughly investigated in coronary angiograms of diabetic patients involved [1, 2, 5, 6, 8].

Results of the present study showed that diabetic patients had a significantly higher prevalence of stenotic atherosclerotic lesions of the coronary arteries ($p = 0.0245$). Our results are similar to results of other studies [1, 3, 6]. Atherosclerotic lesions of the large coronary arteries were significantly more common in the left than in the right coronary artery, but the difference between the diabetic and the non-diabetic group did not reach statistical significance. Changes in the proximal segment of the left anterior descending artery (LAD) were the most common finding in diabetic patients. The present study also revealed that stenoses affected proximal segments of the left anterior descending artery more frequently in diabetic patients. The most frequently atherosclerotic lesion of the RCA was seen in the middle segment, rarely in the proximal and distal part.

The diabetic patients had a higher prevalence of hypertension, higher BMI and triglyceride and cholesterol levels. Jakljević et al. [9] in the study of 286 patients with suspected coronary artery disease and recent exercise single photon emission computed tomography (SPECT) test, performed coronary angiography with coronary fractional flow reserve (FFR) measurement, tested the differences between diabetic (103) and non-diabetic (183) patients in ischemia detection by this two methods and found that the diabetic patients had a higher prevalence of hypertension, higher BMI and cholesterol levels, as well as longer duration of hospitalization than non-diabetic patients.

Wendler et al. [10] found that patients with diabetes mellitus who underwent surgical revascularization had a significantly higher prevalence of three-vessel disease, and a mean ejection fraction 5 points lower than that of non-diabetic patients. In our population, similar differences

were appreciated. The diabetics had a significantly greater number of significant coronary stenoses, and a significantly lower ejection fraction, 0.49 versus 0.54, than nondiabetics.

Schofer et al. [11] also found that the mean caliber of the coronary arteries of insulin dependent patients was smaller than in non-diabetics. In addition, the distal beds of these patients often show diffuse disease and have more extensive zones of calcification. These circumstances, although difficult to quantify and record, can make conventional surgery difficult or impossible, and compromise the intermediate and long-term patency of coronary grafts. These unfavorable anatomic abnormalities are more important in older patients, when diabetes is prolonged and other vascular complications are associated.

These findings may prove clinically useful in the follow-up of diabetic patients, the choice of diagnostic procedures as well as in active treatment either by atherectomy or by percutaneous angioplasty and stenting.

5 Conclusions

- The diabetic patients had a higher prevalence of hypertension, higher BMI and triglyceride and cholesterol levels.
- Diabetes significantly affects the anatomy of coronary arteries, and is associated with age, sedentary lifestyle, and hypertension. These findings may prove clinically useful in the follow-up of diabetic patients, the choice of diagnostic procedures as well as in active treatment either by atherectomy or by percutaneous angioplasty and stenting.

Conflict of Interest None declared.

REFERENCES

1. Celeng, C., Maurovich-Horvat, P., Ghoshhajra, B.B., Merkely, B., Leiner, T., Takx, R.A.P.: Prognostic value of coronary computed tomography angiography in patients with diabetes: a meta-analysis. *Diabetes Care* **39**, 1274–1280 (2016)
2. Aronson, D., Edelman, E.R.: Coronary artery disease and diabetes mellitus. *Cardiol. Clin.* **32**(3), 439–455 (2014)
3. Albarzani, M.A.: Angiographic profile in diabetic and non-diabetic patients with coronary artery disease in the cardiac specialty hospital—Cardiac Center, Erbil. *Iraq. Zanco J. Med. Sci.* **21**(2), 1701–1707 (2017)
4. Toth, P.P.: Subclinical atherosclerosis: what it is, what it means and what we can do about it. *Int. J. Clin. Pract.* **62**(8), 1246–1254 (2008)
5. Olesen, K.K.W., Madsen, M., Egholm, G., Thim, T., Jensen, L.O., Raungaard, B., Bøtker, H.E., Sørensen, H.T., Maeng, M.: Patients with diabetes without significant angiographic coronary artery disease have the same risk of myocardial infarction as patients without diabetes in a real-world population receiving appropriate p̄rophylactic treatment. *Diabetes Care* **40**, 1103–1110 (2017)
6. Hasanović, A., Omerbašić, E., Sarač-Hadžihalilović, A.: Morphological characteristics of atherosclerotic lesions of coronary arteries in diabetic patients. *Med. J.* **20**(3), 147–150 (2014)
7. Minana, G., Nunez, J., Sanchis, J.: Coronary angiography, too far to be a gold standard technique for identifying a vulnerable plaque. *J. Clin. Exp. Cardiol.* **2**, 4 (2011)
8. Al-Shudifat, A.E., Johannessen, A., Azab, M., Al-Shdaifat, A., AbuMweis, S.S., Agraib, L.M., Tayyem, R.F.: Risk factors for coronary artery disease in patients undergoing elective coronary angiography in Jordan. *BMC Cardiovasc. Disord.* **17**, 183 (2017)
9. Jakljević, T., Ružić, A., Baždarić, K., Zaputović, L., Mavrić, Ž., Champagne, S., Teiger, E.: Detection of myocardial ischemia in diabetic patients: The limitations of myocardial perfusion imaging. *Coll. Antropol.* **36**(3), 821–826 (2012)
10. Wendler, O., Hennen, B., Markwirth, T., Nikoloudakis, N., Graeter, T., Schafers, H.J.: Complete arterial revascularization in the diabetic patient—early postoperative results. *Thorac. Cardiovasc. Surg.* **49**, 5–9 (2001)
11. Schofer, J., Schluter, M., Rau, T.: Influence of treatment modality on angiographic outcome after coronary stenting in diabetic patients: a controlled study. *J. Am. Coll. Cardiol.* **35**, 1554–1559 (2000)



Optimizing Insulin Pump Therapy: Advanced Bolus Options

Bojana Radošević Carić, Blaženko Vuković, and Katarina Lalić

Abstract

Introduction The advanced bolus options improve glycemic control of patients with type 1 diabetes (T1D) on insulin pump (IP) therapy. This is extremely important for the patients who do not use CGM (continuous glucose monitoring) regularly. **Objective** To compare the difference in the parameters of glycemic control (HbA1c, postprandial increase of blood glucose and number of hypoglycemic episodes per week) between the group of patients who use bolus calculator for <50% of the total daily boluses and the group the patients who use bolus calculator for $\geq 50\%$ of total daily boluses. **Patients and methods** The study included 41 patients aged over 18 years with T1D on IP therapy in Republika of Srpska. All patients used IP for at least one year prior to participation in the study. Before the IP therapy was initiated, all the patients were trained for carbohydrate counting in course of flexible insulin therapy training (FIT). Professional software, CareLink Pro[®] Software (Medtronic Inc., Northridge, CA, USA) was used to download data from insulin pumps to a personal

computer. The default frequency of bolus calculator use was $\geq 50\%$ of total daily boluses. **Results** No statistically significant difference was found in HbA1c (6.61 ± 1.10 vs. 6.77 ± 0.97 , $p = 0.624$) or the number of hypoglycemic episodes (2.00 (1.00, 4.00) (1.0–6.0) versus 3.00 (2.00, 3.50) (1.0–5.0), $p = 0.322$) between the group of patients who have used bolus calculator for <50% of the total daily boluses and the group of patients who used bolus calculator for $\geq 50\%$ of total daily boluses. Patients who have used bolus calculator had significantly lower postprandial increase in blood glucose after breakfast. **Conclusion** Among the patients with T1D on IP therapy, who do not regularly use CGM the use of the bolus calculator and use of different types of boluses, can improve glycemic control on IP therapy.

Keywords

Insulin pump • Bolus calculator • T1D • Glycemic control

B. R. Carić (✉) · B. Vuković
Department of Endocrinology and Metabolic Diseases, University
Clinical Center of the Republic of Srpska, Clinic for Internal
Diseases, 12 beba bb 78000 Banja Luka, Republic of Srpska,
Bosnia and Herzegovina
e-mail: bojanaradosevic@gmail.com; bojana.caric@med.unibl.com

B. R. Carić · B. Vuković
Faculty of Medicine, University of Banja Luka, Banja Luka,
Republic of Srpska, Bosnia and Herzegovina

K. Lalić
School of Medicine, University of Belgrade, Belgrade, Serbia

K. Lalić
Department of Endocrinology, Diabetes and Metabolic Diseases,
Clinical Center of Serbia, Belgrade, Serbia

K. Lalić
Department of Oral Surgery, Faculty of Medicine, Study Program
Dentistry, University of Banja Luka, Banja Luka, Republic of
Srpska, Bosnia and Herzegovina

1 Introduction

Insulin pump therapy (IP) represents one of the two ways of applying intensive insulin therapy in type 1 diabetes (T1D), allowing precise dosing of basal and bolus insulin doses [1].

Technological improvement of IP and use of rapid acting insulin analogues with faster onset of action had provided the development a system that integrates IP and the system for continuous glucose monitoring (CGM), so-called sensor-augmented IP. This system has proved superiority in lowering HbA1c when compared to conventional intensive insulin therapy [2, 3]. By creating a control algorithm that automatically adjusts insulin delivery according to the measured blood glucose or assumed glucose values (i.e. insulin and glucagon in dual-hormone model of artificial pancreas) the artificial pancreas function is set [4, 5]. In the last decade, the effectiveness of different models of artificial

pancreas was demonstrated in order to achieve optimal glycemic control, with a lower incidence of hypoglycemia [6–8]. On September 28, 2016 the first hybrid closed loop system was approved by FDA for the treatment of T1D. Although this automatic system adjusts basal insulin delivery without input from the user, the user must still manually enter carbohydrate amount into IP [9].

Automatic bolus calculators are integrated into commercial insulin pumps, and based on preprogrammed settings of specific algorithms they suggest bolus dose, and thereby increase the accuracy of calculations in relation to manual calculation. These settings should be individually adjusted for each person, and refer to the same parameters required for manually calculating bolus doses: insulin/carbohydrate ratio, corrective factor, active insulin time, target values of blood glucose and actual value of glycaemia [10, 11].

“Smart” IPs have integrated bolus calculators which in the process of calculating the bolus dose calculate also the active insulin of the preceding dose. On that way bolus calculator use can accurately determine the bolus dose or the dose of insulin needed to correct high blood glucose. Furthermore, most commercial pumps with integrated bolus options provide three different types of bolus: (1) normal bolus—the pump delivers the entire bolus at once; (2) square bolus—the pump delivers equally required dosage of insulin during a period of time, and (3) combined bolus—the pump has options of two abovementioned pumps [12]. The previous studies who studied the impact of advanced IP functions on glycemic control, had showed that the use of bolus calculator had no impact on the value of glycosylated hemoglobin HbA1c, but it could contribute to the glycemic excursion and postprandial glycemic decrease, and thus contribute to the improvement of glycemic control [13].

2 Aim

To compare the parameters of glycemic control between the group of patients who use bolus calculator for <50% of the total daily boluses and the group of patients who used bolus calculator for $\geq 50\%$ of total daily boluses based on the difference between the HbA1c, postprandial increase of glucose and the number of hypoglycemic episodes per week.

To compare the difference in the use of bolus option between the group of patients who use bolus calculator for <50% of the total daily boluses and the group of patients who used bolus calculator for $\geq 50\%$ of total daily boluses.

3 Participants and Methods

This study included 41 patients aged over 18 years with T1D on IP therapy in Republika of Srpska. The models used for the purpose of this study were IP MiniMed[®] Paradigm 722 (Medtronic Inc., Northridge, CA, USA) and MiniMed[®] Paradigm 754 (Medtronic Inc., Northridge, CA, USA) which had an integrated bolus calculator (Bolus Wizard) as an advanced insulin pump option. Most patients used MiniMed[®] Paradigm 754 ($n = 25$), while other patients preferred MiniMed[®] Paradigm 722 ($n = 16$). All patients used insulin pump for at least one year prior to participation in the study along with the therapy with short-acting insulin analogues. Implantation of insulin pumps was performed during the period from 2008 to the 2012 at the Department of Endocrinology, Diabetes and Metabolic Diseases at Clinical Center of Banja Luka. Before initiation of IP therapy the patients were trained for carbohydrate counting in course of flexible insulin therapy training (FIT).

Medtronic “CareLink[®] Pro” (Medtronic Inc., Northridge, CA, USA) is a software for professional management and monitoring of diabetes treatment for use on a personal computer. This software has been approved by the FDA for market use in September 2010. In our study, the data from the insulin pumps were downloaded on a personal computer by Medtronic “CareLink[®] Pro 4.0c” (Medtronic Inc., Northridge, CA, USA) software. The amount of data within each pump varied depending on the degree of use of all insulin pump’s technical possibilities and ranged from 63 to 266 days. For the purpose of our study, a period of nine weeks (63 days) was analyzed for each patient. The data were downloaded with a USB CareLink[®] (Medtronic Inc., Northridge, CA, USA) upon arrival of patients for a regular check-up, at the Department of Endocrinology of the Clinic for internal diseases of UKC Republika Srpska in Banja Luka. Body weight, demographic data and variables related to diabetes (the data of chronically complications presence, the data on the duration of diabetes, duration of pump therapy, the average number of hypoglycemia per week, the value of HbA1c and glucose profiles were gathered from patients. During the study, none of the patients used the CGM. The default frequency of bolus calculator use was $\geq 50\%$ of the total daily boluses [15, 16]. Obtained value of HbA1c referred to the period of the observed 9 weeks within which the profile of preprandial and postprandial glycaemia was made. All patients on insulin pump therapy measure HbA1c at the Institute of Laboratory Diagnostic at the

University Clinical Centre of Republic of Srpska using the Cobas c 501, Roche Diagnostics (Basel, Switzerland) apparatus, which is certified as having documented traceability to the Diabetes Control and Complications Trial reference method by the National Glycohemoglobin Standardization Program (NGSP). Glycemic profiles were measured using the Accu-Chek[®] Performa glucometers, Roche Diagnostics (Basel, Switzerland), which has the possibility of wireless transmission of stored values to a computer via Accu-Chek Smart Pix devices (Basel, Switzerland). Informed written consent was obtained from all participants before enrollment in the study, providing patients' personal data protection in the case of the publication of results.

For statistical analysis IBM SPSS Statistics 21.0 software was used. In order to compare the differences in the frequency of observed characteristics between the groups of respondents, the Pearson's χ^2 contingency test was used. Distribution normalcy of the observed characteristics was tested with Kolmogorov-Smirnov normalcy test. In order to compare the average values of characteristics between the groups of respondents, the Student t test for independent samples was used (observed characteristics that have a normal distribution) and non-parametric Mann-Whitney U test for independent samples (observed characteristics that do not have a normal distribution). When using Student's t test for independent samples, F test was used in order to grasp the significance of differences in the variances of observed characteristics. As statistically significant all the values in which $p < 0.05$ were taken/used.

4 Results

A total of 41 adult patients with T1D on insulin pump therapy were included in the study and divided into two groups by bolus calculator use. The first group consisted of 17 patients (41.46%) used bolus calculator <50% of all daily boluses, and the other group consisted of 24 patients (58.54%) in which $\geq 50\%$ of all given daily bolus were given by bolus calculator. Patients older than 30 years were majority in both groups (76.47% in the first group and 58.33% in the second group). The observed difference between the groups was not statistically significant.

Mean HbA1c was not significantly different between the two groups, although bolus calculator users had slightly lower HbA1c (Table 1).

Patients who have used bolus calculator for $\geq 50\%$ of all given daily bolus, had a lower postprandial rise in blood glucose. Bolus calculator users had significant lower postprandial rise after breakfast ($p = 0.085$). The difference between postprandial rise for lunch and dinner was not statistically significant (Fig. 1).

The study patients on IP had an average of three hypoglycemic episodes per week. There was no statistically significant difference between the two groups, although bolus calculator users had slightly more frequent hypoglycemic episodes than bolus calculator non-users (Table 1).

Bolus calculator users had a lower average number of total boluses during the day and statistically significantly higher average number of boluses given with food as compared to bolus calculator non-users. A higher number of corrective boluses was observed in the group of bolus calculator users but with no statistically significant differences between the groups. There was a statistically significant difference between the average number of bolus given by bolus calculator between two groups. The patients who used bolus calculator for <50% of total boluses, were using bolus calculator to some extent.

According to the use of different types of bolus that bolus option offer, both groups of patients most commonly used "normal" boluses, but bolus calculator users had a slightly higher percentage of using "dual" and "square" boluses than bolus calculator non-users. This difference was not statistically significant (Table 1).

5 Discussion

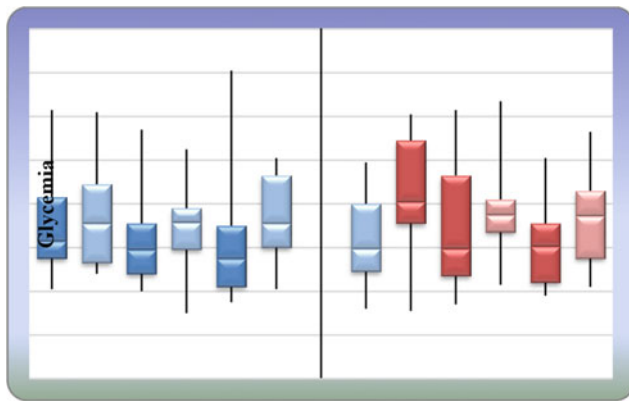
Bolus calculator is used in 86% among all patients with T1D on IP therapy in Republic of Srpska. This result is significantly higher compared to results in other studies in which the use of bolus calculator varied from 16 to 58% [16–18]. The reasons for high percentage of patients who use the bolus calculator in Republic of Srpska could be the result of five days FIT education program, which is obligatory for all patients before IP therapy is initiated. In course of FIT program, all the patients were trained for carbohydrate. Observation of a large number of patients who use bolus calculator and who were at FIT program, was also available [19].

The results from this study regarding the use of bolus calculator correspond to the results from other studies. Klup and colleagues has showed the effect the use of bolus calculator on postprandial blood glucose level but not on HbA1c level [20]. In 12 months controlled randomized study the use of bolus calculator did not show HbA1C decreasing but there is effect on postprandial blood glucose level decreasing [21]. In contrast to the abovementioned, there are studies which confirm the effect of the use of bolus calculator on HbA1C decreasing [22].

The effects of the use of bolus calculator on postprandial glucose decreasing level have been confirmed in numerous studies [21, 23, 24]. In our study significant postprandial glucose decreasing level after breakfast is observed, which is

Table 1 The parameters of glycemic control and “bolus option” parameters for bolus calculator users (BC+) and bolus calculator non-users (BC–)

	BC–	BC+	<i>p</i>
HbA1c (%)	6.61 ± 1.10	6.77 ± 0.97	<i>p</i> = 0.624
The average number of hypoglycemic episodes/week	2.00 (1.00, 4.00) (1.0–6.0)	3.00 (2.00, 3.50) (1.0–5.0)	<i>p</i> = 0.322
The average number of total boluses/day	7.35 (4.90, 7.79) (2.5–16.0)	5.34 (3.98, 6.10) (2.0–9.4)	<i>p</i> = 0.083
The average number of manual boluses/day	5.46 (3.70, 6.63) (2.5–14.3)	0.11 (0.00, 1.00) (0.0–3.8)	<i>p</i> < 0.001
The average number of boluses with food/day	0.11 (0.00, 1.67) (0.0–3.2)	3.48 (2.42, 4.46) (0.0–8.2)	<i>p</i> < 0.001
The average number of corrective boluses/day	1.07 ± 1.06	1.90 ± 1.38	<i>p</i> = 0.045
The average number of boluses given by BC	1.14 ± 1.12	4.68 ± 1.56	<i>p</i> < 0.001
“Normal” boluses (%)	100.00 (97.60, 100.00)(64.8–100.0)	100.00 (87.16, 100.00) (51.3–100.0)	<i>p</i> = 0.615
“Dual wave” boluses (%)	0.00 (0.00, 1.08) (0.0–35.2)	0.00 (0.00, 12.84) (0.0–48.7)	<i>p</i> = 0.555
“Square wave boluses (%)	0.00 (0.00, 0.00) (0.0–4.5)	0.00 (0.00, 0.00) (0.0–11.0)	<i>p</i> = 0.944



B- preprandial breakfast glycemia
 B+ postprandial breakfast glycemia
 L- preprandial lunch glycemia
 L+ postprandial lunch glycemia
 D- preprandial dinner glycemia
 D+ postprandial dinner glycemia

Fig. 1 Box-plot diagram for preprandial and postprandial for two groups of patients

very important result concerning the highest glucose levels are usually after breakfast. One of possibility of improving metabolic control among patients with DT1 could be prevention of postprandial glucose peaks after breakfast [25].

When it comes to the total number of given bolus, patients who use bolus calculator give more bolus during meal, which should provide the more consumption of the food. However, the patients who used bolus calculator used corrective boluses more frequently. This data is inconsistent with the statement about lesser postprandial increases with bolus calculator use [15, 24].

Walsh and colleagues have emphasized that imprecise insulin/carbohydrate ratio, corrective factor and active

insulin time could diminish success of IP therapy, and also the use of “magical numbers” for preprogrammed settings by general practitioners. Due to abovementioned patients who follow instructions of bolus calculator have to give more corrective bolus [10]. This point of view can explain a number of corrective bolus among bolus calculator users in our study.

Furthermore, lack of education of patients and professionals in order to apply and to learn upgraded options of bolus calculator but also, lack of interests to accept new knowledge and to constantly adjust preprogrammed settings [26] can explain low use of different bolus types in our study. In comparison to the normal boluses, the use of combined and square boluses showed a greater effect on the reduction of postprandial excursions for meals composed of fats and those that are composed slowly absorbed ingredients [27–30]. Well educated patients more often use a combined bolus, which can decrease the value of HbA1c [27]. The results of our study, with patients who mostly use normal type of bolus and who do not use combined or squared boluses, do not confirm good education.

One of the reasons for not using the bolus calculator is avoiding selfcontrol of blood glucose due to lack of test stripes which patients treated with insulin pump get by the Health Insurance Fund of the Republic of Srpska. Number of test stripes (100 units/month) is insufficient for the required number of glucose measurements for bolus calculator use. Furthermore, there is no bolus calculator on the market that account the impact of proteins and fats to glycoregulation [30, 31] what could be a point for improved effectiveness of bolus calculator and for the increase of number of patients who have enough confidence in the bolus calculator.

The use of CareLink[®] Pro (Medtronic, Inc., Northridge, CA, USA) could practically facilitate therapeutic decision for diabetologists. This software can determine precisely

how to use an insulin pump and to improve the compliance of patients. It is possible to define the main points in self-control and therapy and to modify certain parameters (basal rates, insulin/carbohydrate ratio, corrective factor). Furthermore, it could be given precise instructions for nutrition adjustment and physical activity. Using professional software, less time would be spent on data interpretation and more time on conversation with patients about the everyday IP treatment challenges, which could contribute to improving glycemic control. This is very important issue for patients in Republic of Srpska. Majority of them, due to economic situation, do not use CGM regularly, although superior glycemic control has been show at patient with either complementary use of IP and CGM, or hybrid closed-loop system [32, 33].

6 Conclusion

Regular re-education about advanced IP functions for both patients and diabetologists are needed in order to maximize use the all advantages of IP therapy for improving the glycoregulation in T1DM. The professional team for IP management should be formed in the endocrinology Department. The use of CareLink[®] Pro (Medtronic, Inc., Northridge, CA, USA) could practically facilitate therapeutic decision for diabetologists by giving precise instructions for insulin adjustment, nutrition and physical activity in order to improve the glycemic control.

References

- Pickup, J.C.: Insulin-pump therapy for type 1 diabetes mellitus. *N. Engl. J. Med.* **366**(17), 1616–1624 (2012)
- Battelino, T., Conget, I., Olsen, B., et al.: The use and efficacy of continuous glucose monitoring in type 1 diabetes treated with insulin pump therapy: a randomised controlled trial. *Diabetologia* **55**(12), 3155–3162 (2012)
- Hermanides, J., Nørgaard, K., Bruttomesso, D., et al.: Sensor augmented pump therapy lowers HbA1c in suboptimally controlled type 1 diabetes; a randomized controlled trial. *Diabet. Med.* **28**(10), 1158–1167 (2011)
- Shalitin, S., Phillip, M.: Closing the loop: combining insulin pumps and glucose sensors in children with type 1 diabetes mellitus. *Pediatr. Diabetes* **7**(Suppl. 4), 45–49 (2006)
- Phillip, M., Battelino, T., Atlas, E., Kordonouri, O., Bratina, N., Miller, S., et al.: Nocturnal glucose control with an artificial pancreas at a diabetes camp. *N. Engl. J. Med.* **368**, 824–833 (2013)
- Kovatchev, B.P., Renard, E., Cobelli, C., Zisser, H.C., Keith-Hynes, P., Anderson, S.M., et al.: Safety of outpatient closed-loop control: first randomized crossover trials of a wearable artificial pancreas. *Diabetes Care* **37**, 1789–1796 (2014)
- Thabit, H., Lubina-Solomon, A., Stadler, M., Leelarathna, L., Walkinshaw, E., Pernet, A., et al.: Home use of closed-loop insulin delivery for overnight glucose control in adults with type 1 diabetes: a 4-week, multicentre, randomised crossover study. *Lancet Diabetes Endocrinol.* **2**, 701–709 (2014)
- Sherr, J.L., Palau Collazo, M., Cengiz, E., Michaud, C., Carria, L., Steffen, A.T., et al.: Safety of nighttime 2-hour suspension of basal insulin in pump-treated Type 1 diabetes even in the absence of low glucose. *Diabetes Care* **37**, 773–779 (2014)
- Aleppo, G., Webb, K.M.: Integrated insulin pump and continuous glucose monitoring technology in diabetes care today: A perspective of real-life experience with the MiniMed[™] 670G hybrid closed-loop system. *Endocr. Pract.* **24**(7), 684–692 (2018)
- Walsh, J., Roberts, R., Bailey, T.: Guidelines for insulin dosing in continuous subcutaneous insulin infusion using new formulas from a retrospective study of individuals with optimal glucose levels. *J. Diabetes Sci. Technol.* **4**(5), 1174–1181 (2010)
- Walsh, J., Roberts, R., Heinemann, L.: Confusion regarding duration of insulin action: a potential source for major insulin dose errors by bolus calculators. *J. Diabetes Sci. Technol.* **8**(1), 170–178 (2014)
- Zisser, H., Robinson, L., Bevier, W., et al.: Bolus calculator: a review of four “smart” insulin pumps. *Diabetes Technol. Ther.* **10**(6), 441–444 (2008)
- Schmidt, S., Nørgaard, K.: Bolus calculators. *J. Diabetes Sci. Technol.* **8**(5), 1035–1041 (2014)
- DAFNE Study Group: Training in flexible, intensive insulin management to enable dietary freedom in people with type 1 diabetes: Dose Adjustment for Normal Eating (DAFNE) randomised controlled trial. *BMJ* **325**(7367), 746 (2002)
- Cukierman-Yaffe, T., Konvalina, N., Cohen, O.: Key elements for successful intensive insulin pump therapy in individuals with type 1 diabetes. *Diabetes Res. Clin. Pract.* **92**(1), 69–73 (2011)
- Boizel, R., Pinget, M., Lachgar, K., et al.: Clinical evaluation of the use of a multifunctional remotely controlled insulin pump: multicenter observational study. *J. Diabetes Sci. Technol.* **8**(6), 1145–1150 (2014)
- Kerr, D., Hoogma, R.P., Buhr, A., Petersen, B., Storms, F.E., for the study investigators: Multicenter user evaluation of ACCU-CHEK[®] Combo, an integrated system for continuous subcutaneous insulin infusion. *J. Diabetes Sci. Technol.* **4**(6), 1400–1407 (2010)
- Joubert, M., Morera, J., Vincete, A., Rod, A., Parienti, J.J., Reznik, Y.: Cross-sectional survey and retrospective analysis of a large cohort of adults with type 1 diabetes with long-term continuous subcutaneous insulin infusion treatment. *J. Diabetes Sci. Technol.* **8**(5), 1005–1010 (2014)
- Riveline, J.P., Jollois, F.X., Messaoudi, N., et al.: Insulin-pump use in everyday practice: data from an exhaustive regional registry in France. *Diabetes Metab.* **34**(2), 132–139 (2008)
- Klupa, T., Benbenek-Klupa, T., Malecki, M., et al.: Clinical usefulness of a bolus calculator in maintaining normoglycaemia in active professional patients with type 1 diabetes treated with continuous subcutaneous insulin infusion. *J. Int. Med. Res.* **36**(5), 1112–1116 (2008)
- Enander, R., Gundevall, C., Strömberg, A., Chaplin, J., Hanas, R.: Carbohydrate counting with a bolus calculator improves postprandial blood glucose levels in children and adolescents with type 1 diabetes using insulin pumps. *Pediatr. Diabetes* **13**(7), 545–551 (2012)
- Shashaj, B., Busetto, E., Sulli, N.: Benefits of a bolus calculator in pre and postprandial glycaemic control and meal flexibility of

- paediatric patients using continuous subcutaneous insulin infusion (CSII). *Diabet. Med.* **25**(9), 1036–1042 (2008)
23. Alemzadeh, R., Palma-Sisto, P., Parton, E.A., Holzum, M.K.: Continuous subcutaneous insulin infusion and multiple dose of insulin regimen display similar patterns of blood glucose excursions in pediatric type 1 diabetes. *Diabetes Technol. Ther.* **7**(4), 587–596 (2005)
 24. Gross, T.M., Kayne, D., King, A., Rother, C., Juth, S.: A bolus calculator is an effective means of controlling postprandial glycemia in patients on insulin pump therapy. *Diabetes Technol. Ther.* **5**(3), 365–369 (2003)
 25. Taki, K., Nishimura, R., Morimoto, A., Tsujino, D., Miyashita, Y., Tajima, N.: Analysis of 24-hour glycemic excursions in patients with type 1 diabetes by using continuous glucose monitoring. *Diabetes Technol. Ther.* **12**(7), 523–528 (2010)
 26. Lawton, J., Kirkham, J., Rankin, D., Barnard, K., Cooper, C.L., Taylor, C., Heller, S., Elliott, J., REPOSE Group: Perceptions and experiences of using automated bolus advisors amongst people with type 1 diabetes: a longitudinal qualitative investigation. *Diabetes Res. Clin. Pract.* **106**(3), 443–450 (2014)
 27. Klupa, T., Skupien, J., Cyganek, K., Kutra, B., Sieradzki, J., Malecki, M.T.: The dualwave bolus feature in type 1 diabetes adult users of insulin pumps. *Acta Diabetol.* **48**(1), 11–14 (2011)
 28. Chase, H.P., Saib, S.Z., MacKenzie, T., Hansen, M.M., Garg, S. K.: Postprandial glucose excursions following four methods of bolus insulin administration in subjects with type 1 diabetes. *Diabet. Med.* **19**(4), 317–321 (2002)
 29. Jones, S.M., Quarry, J.L., Caldwell-McMillan, M., Mauger, D.T., Gabbay, R.A.: Optimal insulin pump dosing and postprandial glycemia following a pizza meal using the continuous glucose monitoring system. *Diabetes Technol. Ther.* **7**(2), 233–240 (2005)
 30. Pankowska, E., Błazik, M., Groele, L.: Does the fat-protein meal increase postprandial glucose level in type 1 diabetes patients on insulin pump: the conclusion of a randomized study. *Diabetes Technol. Ther.* **14**(1), 16–22 (2012)
 31. Schwartz, F.L., Guo, A., Marling, C.R., Shubrook, J.H.: Analysis of use of an automated bolus calculator reduces fear of hypoglycemia and improves confidence in dosage accuracy in type 1 diabetes mellitus patients treated with multiple daily insulin injections. *J. Diabetes Sci. Technol.* **6**(1), 150–152 (2012)
 32. Tauschmann, M., Thabit, H., Bally, L., et al.: Closed-loop insulin delivery in suboptimally controlled type 1 diabetes: a multicentre, 12-week randomised trial. *Lancet* **392**(10155), 1321–1329 (2018)
 33. Bally, L., Thabit, H., Hovorka, R.: Glucose-responsive insulin delivery for type 1 diabetes: The artificial pancreas story. *Int. J. Pharm.* **544**(2), 309–318 (2018)

Parametric Optimization of Stent Design Based on Numerical Methods

Dalibor Nikolić , Igor Saveljić , and Nenad Filipović 

Abstract

Today, endovascular prosthesis—stents are used as a solution for treating many health disorders and diseases. Their major application is found in treating cardiovascular diseases. One of the problems in stent implantation is a process called in stent restenosis (ISR). In the pre-stent era, the occurrence of restenosis ranged between 32 and 55% of all angioplasties, and in bare-metal stent (BMS) era this range dropped to 17–41%. Many factors have influence on this phenomenon. Some studies show that in stent restenosis, strut shape and thickness have significant impact, especially if the stent is implanted in the small arteries. For better stent geometry modeling, in this paper authors suggested novel approach—parametric optimization on the existing stent design. For evaluation of the parametric optimization and mechanical performance of nitinol stents as well as comparison of differences between old design (non-optimized) and new optimized design the finite element method was used. Simulation was performed assuming that the stent devices used for this research were made by laser cutting, from tube form, by application of expanding and crushing force. The behavior of two different stent models was analyzed: old Palmaz-Schatz design and novel optimized design. Novel design based on the results from parametric optimization preceded on the Palmaz-Schatz design. Performed simulation on stent models showed that the new modern design has better clinical behavior due to lower contacting surface, higher radial resistive strength and much better superplastic behavior. Optimization process was based on two optimization rules:

minimization of the model volume and provide the best possible strain field in the model. Comparison of result from FE analyses from old an optimized design show that based on this approach it is possible to engineers in the future create a new and much better stents very easy.

Keywords

Stent • Parametric optimization • Stent design • FEA • Finite element analysis • Endovascular prosthesis

1 Introduction

Arterial disease is a major cause of morbidity and mortality in developed countries [1]. There are several ways to treat blood vessels narrowing and which will be applied depends on the severity of the disease:

- Pharmacological Therapy—The administration of appropriate drugs can increase the flow of blood through the arteries.
- Bypass surgery—Surgical intervention in general anesthesia, which is based on the creation of bridging by which the narrowing and clogging of blood vessels is avoided.
- Percutaneous transluminal coronary angioplasty (PTCA)—The coronary artery is expanding at the place of narrowing to restore normal blood flow. About 500,000 of these procedures are being performed in Europe today.

Modern methods for treating this disease include the insertion of cardio-vascular endoprosthesis—the so-called stents inside diseased blood vessels. The basic tool necessary for performing this procedure is “stent”.

The complications associated with endovascular stents treatment have become manifest and include restenosis [2], stent migration, proximal neck dilation [3], and endoleak [4].

D. Nikolić (✉) · I. Saveljić · N. Filipović
Bioengineering Research and Development Center,
34000 Kragujevac, Serbia
e-mail: markovac85@kg.ac.rs

I. Saveljić · N. Filipović
Faculty of Engineering, University of Kragujevac,
34000 Kragujevac, Serbia

These complications can be overcome with the good selection and adjustment physical and mechanical properties of the endovascular stents. Several studies shown that the shape and thickness of the stent strut have a significant effect on these complications, especially on restenosis [6–8]. Our purpose in this study was to examine the new atomically approach for geometry optimization. Aim of optimization is to stent preserve same radial force, stress and strain with significant strut thickness reduction. Our hypotheses were that it is possible with new approach of optimizing from old stent model (model from the market place) to get a newest design with same mechanical characteristic but with significant smaller strut thickness and potentially with less complications.

2 Materials and Methods

2.1 Stents

The word stent (“esténs”, as the originally pronounced word [9] derives from the dental names of Charles Thomas Stent; (1807–1885). Stent became widely known for his improvements and modifications of gutta-percha, a material that filled the treated root of the tooth that he patented. Later in the literature, the origin of the word stent was explained in more detail, but this term remained to be used among surgeons as a general term for almost any “non-biological” material used as a support for biological tissues [10]. Although very commonly used, in cardiology, the term stent appears for the first time in 1966 after implantation of endoprosthesis into aortic homograft [11] (Fig. 1).

2.2 Parametric Optimization

In a complex process of product development and production environments, designers and engineers have to use a wide range of software tools to design and simulate their products. In the complex optimization process, several thousand simulations need to be performed over some work. This process requires a lot of manual work and time. The parametric analysis itself is performed in a closed loop that needs to be done many times (Fig. 2).

The geometry of the initial model was created based on the geometry parameters from real Palmaz-Schatz stent model on the market (Fig. 3) CAD model was created in software package SolidWorks 2016.

Because of the complex optimization process, i.e. due to the large number of necessary simulations to optimize the model, the model itself was created in such a way that the change of a very small number of parameters can change the entire geometry.

The Isight software [12] package was used for modeling and executive optimization process. Isight uses algorithms and techniques to run various external applications, performs the processes based on the required parameters, and then passes the results to the next application without interfering users.

The input data (in this case, 6 geometry parameters presented in Table 1) are forwarded to the 3D model creation software (CAD¹ SolidWorks). Then, the geometry obtained is directly forwarded to the simulation tool on the 3D model (CAE² Abaqus) The result obtained from the simulation (on this case, the maximum strain) passes the optimization algorithm on the basis of which the optimization algorithm creates new input parameters. This process is repeated when the conditions of convergence are not fulfilled or the closest possible solution is not found. Material property for optimized stent model was NITINOL (Website Nitinol Devices and Components, 2018). This material is better to be optimized by strain then stress, so in this optimization process for the target value maximum strain was used.

The technique that was used for optimization is Pointer. This technique is used for automatic optimization and it contains a set of several standard optimization algorithms.

- Genetic algorithm [13].
- Nelder and Mead downhill simplex [14].
- NLPQL—Non-Linear Programming by Quadratic Lagrangian [15].
- Linear Solver.

This hybrid combination of algorithms enables this technique to have a high robustness in operation and puts it first in the selection of optimization methods. Different approaches in the implemented optimization algorithms make it possible for Pointer to be applied to any problem that greatly facilitates work. At the start point, the “Pointer” optimization technique can control only one or all four implemented algorithms, and as optimization progresses the technique determines which algorithm is most successful and continues to optimize using this method based on internal control parameters (step size, number of repeats, number of repeat startups, etc.). This control procedure is hidden from the user.

Based on the range of input parameters and the step of changing geometric parameters, the $\Delta = 0.005$ algorithm provides 4750 possible combinations (required simulations). The Input Control function contains some of the geometric constraints to prevent the creation of bad geometric models, for example:

—‘Optimization.D0’ >= ‘Optimization.D1’

¹Computer aided design.

²Computer aided engineering.

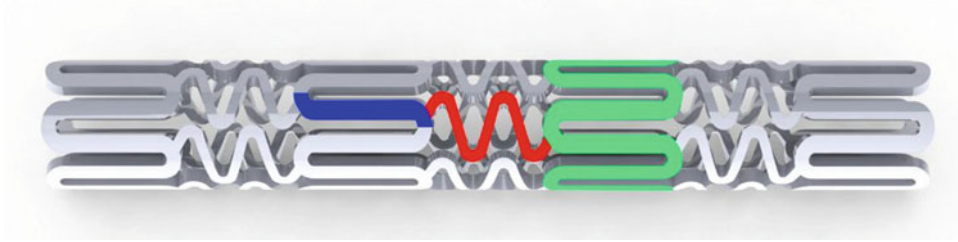


Fig. 1 Basic parts of stent: struts (blue), several struts crate a ring (green) and bridges (red)

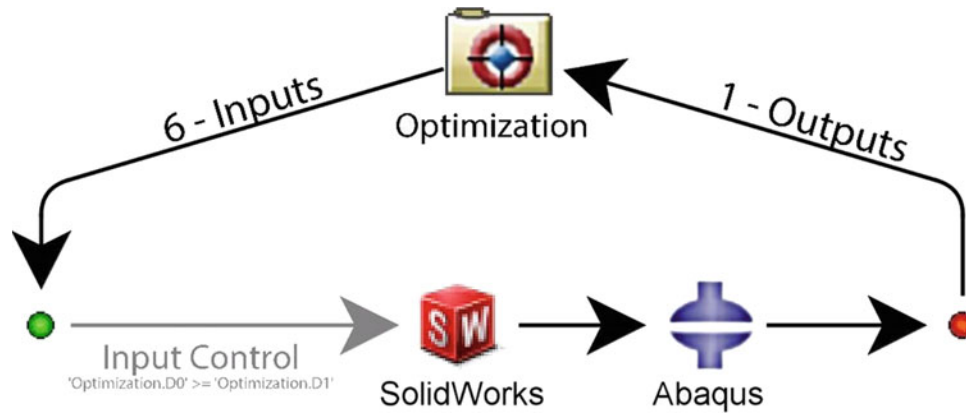


Fig. 2 Graphical representation of the closed parameter optimization circuit

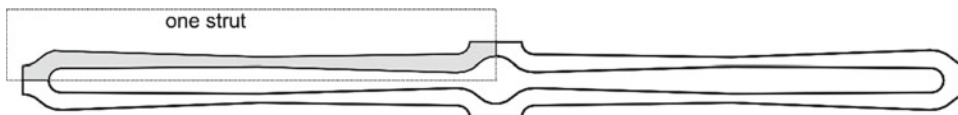


Fig. 3 Parametrically complex stent model obtained based geometry parameter from real stent on the market

Table 1 A list of parameters that define geometry is shown Fig. 4

k	L	D ₀	D ₁	R ₀	R ₁
Width of the contact part	Length of the strut.	Thickness of the strut at the end	Thickness of the strut in the middle	Central radius of indentation	External radius

By design requirements, it is possible to conclude that the thickness of the strut in the middle must be equal to or less than the thickness of the strut at the ends (Fig. 4). On this way the problem is reduced to 3600 possible geometric models.

3 Results and Conclusion

Manual analysis of such a large number of models would require time. By introducing the optimization algorithms, the problem is solved in 117 steps, and the result is shown in

Fig. 5. A number of approximate solutions were obtained (marked in gray), while the most optimal solution is indicated in green.

Using novel optimization approach system generate a several possibility of new stent designs based on some existing design. On this easy way old design is very much improved. New design has the same distribution of strain but significantly less strut cross section. This is huge advantage because this stent will produce less in-stent restenosis in patient and decies number of complications.

The aim of this paper is to present new methods for fast and easy optimization process in designing stents. These

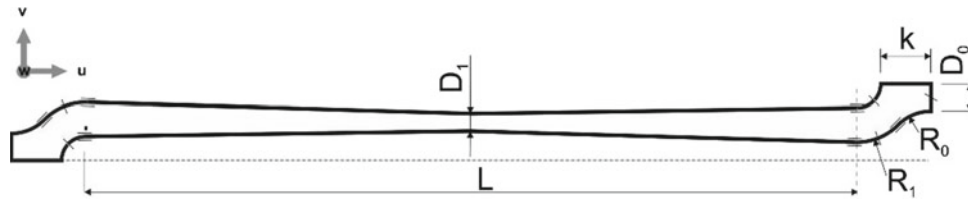


Fig. 4 Unique segment of the stent model shown in Fig. 3 with geometric parameters that define the entire model

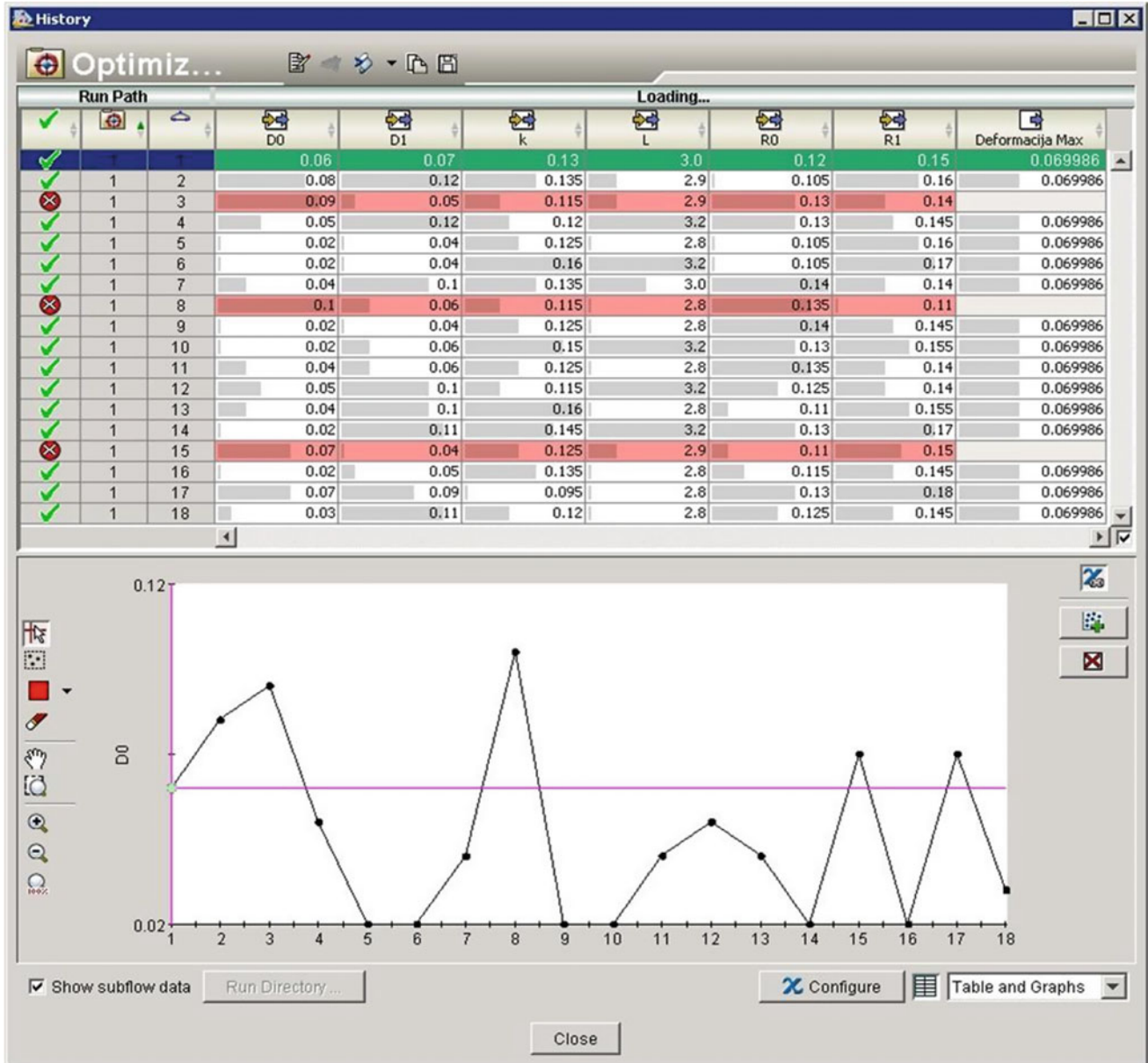


Fig. 5 Parameter optimization solutions

methods can greatly facilitate the process of stent design in the future and prevent possible “expensive” mistakes that are detected at a later stage of prototype testing.

Acknowledgements This study was funded by the grants from the Serbian Ministry of Education, Science and Technological Development III41007, ON174028 and European Union’s Horizon 2020 research and innovation programme under grant agreement No. 689068 and No. 777119.

References

1. Pasternak, R.C., Criqui, M.H., Benjamin, E.J., Fowkes, F.G., Isselbacher, E.M., McCullough, P.A., Wolf, P.A., Zheng, Z.J., American Heart A.: Atherosclerotic vascular disease conference: writing group I: epidemiology. *Circulation* **109**(21), 2605–2612 (2004)
2. Girdt, M., Kaul, H., Maute, C., Kramann, B., Kohler, H., Uder, M.: Enhanced flow velocity after stenting of renal arteries is associated with decreased renal function. *Nephron Clin. Pract.* **105**(2), 84–89 (2007)
3. Roguin, A.: Stent: the man and word behind the coronary metal prosthesis. *Circ. Cardiovasc. Interv.* **4**(2), 206–209 (2011)
4. Bush, R.L., Johnson, M.L., Collins, T.C., Henderson, W.G., Khuri, S.F., Yu, H.J., Lin, P.H., Lumsden, A.B., Ashton, C.M.: Open versus endovascular abdominal aortic aneurysm repair in VA hospitals. *J. Am. Coll. Surg.* **202**(4), 577–587 (2006)
5. Rodway, A.D., Powell, J.T., Brown, L.C., Greenhalgh, R.M.: Do abdominal aortic aneurysm necks increase in size faster after endovascular than open repair? *Eur. J. Vasc. Endovasc. Surg.* **35**(6), 685–693 (2008)
6. Kastrati, A., Mehilli, J., Dirschinger, J., Dotzer, F., Schuhlen, H., Neumann, F.J., Fleckenstein, M., Pfaffert, C., Seyfarth, M., Schomig, A.: Intracoronary stenting and angiographic results: strut thickness effect on restenosis outcome (ISAR-STEREO-2) trial. *Circulation* **103**, 2816–2821 (2001)
7. Pache, J., Kastrati, A., Mehilli, J., Schuhlen, H., Dotzer, F., Hausleiter, J., Fleckenstein, M., Neumann, F.J., Sattelberger, U., Schmitt, C., Muller, M., Dirschinger, J., Schomig, A.: Intracoronary stenting and angiographic results: strut thickness effect on restenosis outcome (ISARSTEREO-2) trial. *J. Am. Coll. Cardiol.* **41**, 1283–1288 (2003)
8. Briguori, C., Sarais, C., Pagnotta, P., Liistro, F., Montorfano, M., Chieffo, A., Sgura, F., Corvaja, N., Albiero, R., Stankovic, G., Toutoutzas, C., Bonizzoni, E., Di Mario, C., Colombo, A.: Instant restenosis in small coronary arteries: impact of strut thickness. *J. Am. Coll. Cardiol.* **40**, 403–409 (2002)
9. Ring, M.E.: How a dentist’s name became a synonym for a life-saving device: the story of Dr. Charles Stent. *J. Hist. Dent.* **49**, 77–80 (2001)
10. Gillies, H.D.: *Plastic Surgery of the Face*, p. 10. Oxford University Press, London (1920)
11. Weldon, C.S., Ameli, M.M., Morovati, S.S., Shaker, I.J.: A prosthetic stented aortic homograft for mitral valve replacement. *J. Surg. Res.* **6**, 548–552 (1966)
12. *Isight & the simulia execution engine*, Isight Documentation, Dassault Systèmes, Providence, RI, USA, (2016)
13. Holland, J.H.: *Adaptation in Natural and Artificial Systems*. University of Michigan Press, Ann Arbor (1975)
14. Nelder, J.A., Mead, R.: A simplex method for function minimization. *Comput. J.* **7**(4), 308–313 (1965)
15. Falk, E.J.: Lagrange multipliers and nonlinear programming. *J. Math. Anal. Appl.* **19**(1), 141–159 (1967)

Numerical Analysis of Plaque Progression in 3D Patient Specific Model of Carotid Artery

Smiljana Djorovic, Igor Saveljic, and Nenad Filipovic

Abstract

The main purpose of this study was to computationally examine the hemodynamic parameters of plaque progression within carotid artery, such as wall shear stress and plaque concentration. The 3D finite element mesh was created for a patient-specific anatomical geometry which was reconstructed on the basis of computed tomography (CT) scan images. The 3D blood flow was governed by the Navier–Stokes equations and continuity equation. Mass transfer within the blood lumen and through the arterial wall was coupled with the blood flow and modelled by the convection–diffusion equation. Kedem–Katchalsky equations described low-density lipoprotein (LDL) transport in lumen of the vessel. Two time periods were considered (baseline and follow-up). The results of the analyzes have shown that zones with lower shear stress values were correlated with the zones of plaque accumulation and progression. This was confirmed at the follow-up, where simulation results had shown that carotid lumen was reduced due to plaque progression. This type of numerical simulations has become significant support to medicine, due to capability to determine the zone of plaque appearance and predict its further progression.

Keywords

Finite element method • Carotid artery • Computational modelling • Plaque progression

S. Djorovic (✉) · I. Saveljic · N. Filipovic
Faculty of Engineering, University of Kragujevac,
34000 Kragujevac, Serbia
e-mail: smiljana@kg.ac.rs

I. Saveljic
e-mail: isaveljic@kg.ac.rs

N. Filipovic
e-mail: fica@kg.ac.rs

S. Djorovic · I. Saveljic · N. Filipovic
Research and Development Center for Bioengineering
(BioIRC), 34000 Kragujevac, Serbia

1 Introduction

Building up of plaque and its progression within arteries, due to deposits of fat, cholesterol, calcium, and other substances in the blood, leads to atherosclerosis. Atherosclerosis is a systemic inflammatory disease which involves large- and medium-sized arteries and commonly affects the carotid artery at its bifurcation. Also, it can affect any artery in the body, including arteries in the heart, brain, arms, legs, pelvis, and kidneys [1]. Carotid artery disease occurs if plaque builds up in the arteries on each side of the neck, which supply oxygen-rich blood to the brain. If blood flow to the brain is reduced or blocked, it may cause an ischemic stroke which is serious complication and attack on human organism. Ischemic stroke can develop as a result of embolism of atherosclerotic debris or thrombotic material from the plaque into the distal cerebral vasculature.

Computational modelling of atherosclerosis [2] has been performed last years, while the mechanisms of atherosclerosis have been used to provide insights for the understanding of the processes which lead to the plaque initiation and progression, as well as to predict plaque regions and mechanisms which are prone to disease progression [3, 4]. It is found that wall shear stress distribution and low-density lipoprotein (LDL) transport are associated with plaque progression [5]. It is unique among other atherosclerosis-induced cardiovascular diseases that the building up of the plaque takes place at a very specific location, (e.g. at the carotid bifurcation), which makes possible the studying of its phenotypic appearance and biology for diagnostic and prognostic purposes.

Based on previous achievements, the main aim of this study was to computationally simulate plaque progression within carotid artery, considering patient specific geometry and biomolecular parameters. Computerized Tomography (CT) scan images were used for patient specific geometry reconstruction. The hemodynamic parameters such as mass flow and wall shear stress were determined in two time

periods (1. baseline and 2. follow-up) using computational fluid dynamics approach.

The rest of the paper is organized as follows. The creation of a 3D patient-specific model is presented in the part 2. The CT scans of patient were used for geometrical reconstruction, that required usage of several software packages. The general concept for finite element analysis of the blood flow and mass transport, the material properties and boundary conditions that were applied are given in the part 2 also. The 3D blood flow is governed by the Navier–Stokes equations, together with the continuity equation. Mass transfer within the blood lumen and through the arterial wall is coupled with the blood flow and is modelled by the convection–diffusion equation. Kedem–Katchalsky equations described the LDL transport in lumen of the carotid artery. It should be noted that the PAK solver was employed for performing the computational simulation. The part 3 covers discussion of results given for baseline and follow-up of the patient, such as plaque concentration and wall shear stress distribution. In the part 4 main conclusions are given with plans for further improvements of presented work.

2 Materials and Methods

Creation of the 3D patient specific carotid artery model, as well as the computational simulation of mass transfer coupled with the blood flow and based on Finite Element Method (FEM) are described in this section.

2.1 Geometrical Model

In order to perform the computational analysis of plaque progression within the carotid artery, the patient-specific 3D model was created. Geometry of the lumen domain was

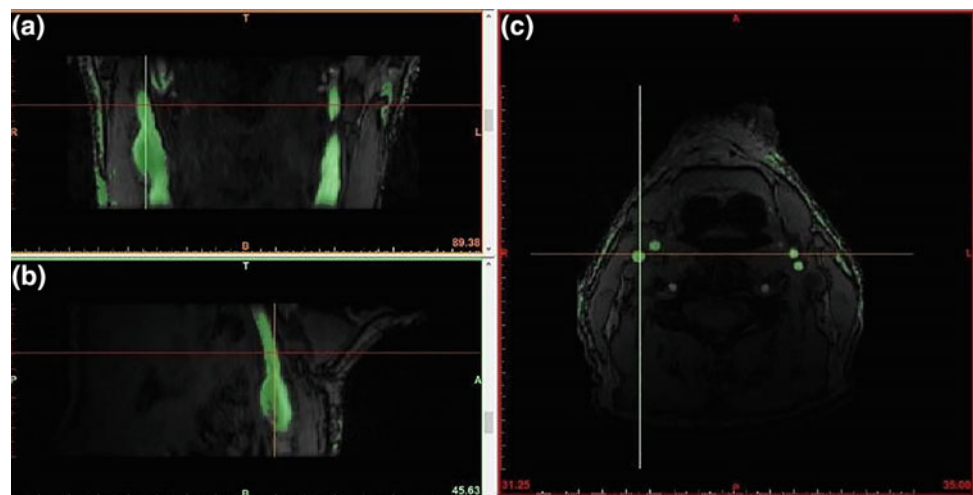
reconstructed using the CT scan images. The set of DICOM images, with resolution of 512×512 mm were imported in segmentation software Mimics [6], able to calculate 3D model from 2D images. In order to reconstruct the region of interest, each image was segmented using the manipulation in three different planes (Fig. 1), which enabled creation of more accurate 3D model of the patient's anatomy.

The stereolithography (STL) representation set the boundary surface for the lumen. After obtaining an initial 3D model, optimization of the surface mesh was performed in Geomagic [7] software, in order to create mesh suitable for computational simulation. After reconstruction of carotid artery, the surface model was exported in STL format from Geomagic to Femap software [8]. With aim to obtain the 3D model consisted of eight-node brick elements, Femap was used in combination with our *inhouse* software for the conversion of tetrahedral elements to eight-node brick elements. The dataset was imported into the PAK solver for further simulation of blood flow and mass transport through the carotid artery [9].

2.2 Numerical Simulation

Modeling of LDL mass transfer through the blood lumen and arterial wall, in order to simulate plaque progression for this specific patient, was governed by different sets of equations. First, the blood motion in the lumen domain was described with Navier–Stokes equations and continuity equation. The fluid filtration (mass transfer across the wall of the blood vessel) was modelled with the Darcy's law. Mass transfer in the lumen domain was modeled using convective diffusion equations, while convective diffusion reactive equations were used for modeling mass transfer in the wall. The LDL transports in the lumen of the carotid artery and through its tissue were coupled by Kedem–Katchalsky

Fig. 1 Coronal (a), sagittal (b) and transversal (c) cross-section of modeled carotid artery



equations. The biomolecular parameters and adhesion molecules were used for computer simulation. The detailed explanation of mentioned methods can be found in Ref. [3]. Also, a 3D mesh-moving Arbitrary LagrangianEulerian (ALE) formulation was applied to follow the wall displacements and change of the carotid wall geometry during plaque growth [10].

With aim to perform analysis which reflects the realistic human blood flow, we used the average blood properties: a dynamic viscosity of 3.5×10^{-3} Pa s and a density of 1.05×10^{-3} g/mm³. Also, appropriate boundary conditions were employed, such as: prescribed blood velocity at the inlet of the arterial segment and physiological resistance pressure at the arterial outlets. Wall velocities at the common blood-blood vessel surface are taken as the boundary condition for the fluid.

After employed different sets of equations for mass transfer modeling, applied boundary conditions and material characteristics, the PAK software was used for the computational simulation, which calculated the plaque concentration and wall shear stress distribution within the patient specific carotid artery, considering the baseline and follow-up time steps.

3 Results and Discussion

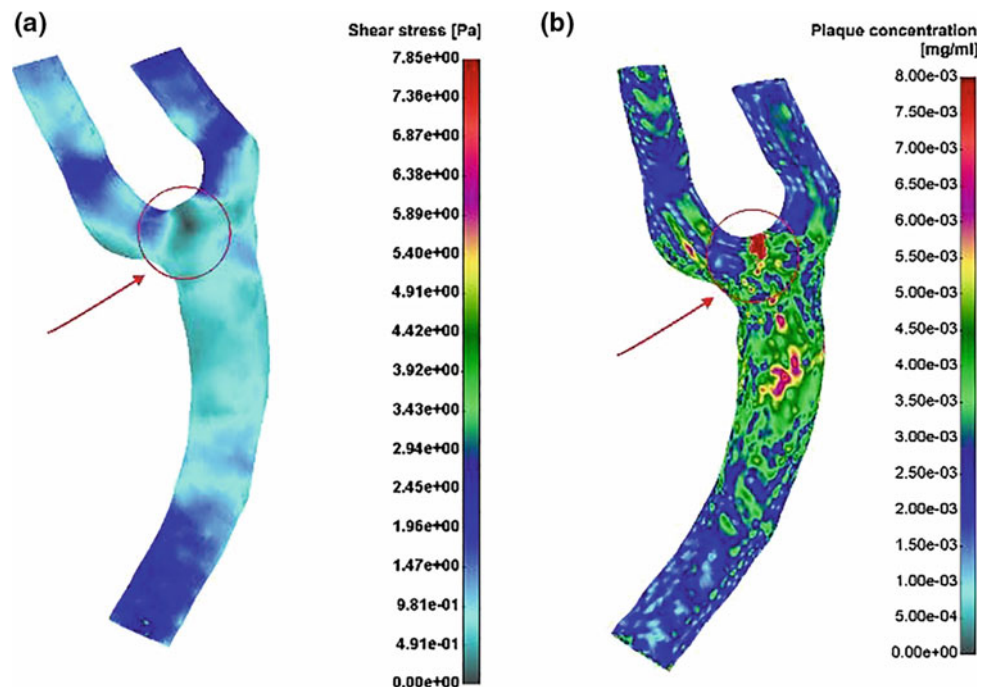
The 3D finite element model of the carotid artery was created using the patient specific CT scan images in combination with several different software packages. The 3D blood flow with the LDL transport through lumen and through the

artery wall, coupled with plaque progression in vessel wall were simulated. Also, appropriate boundary conditions were prescribed. The hemodynamic parameters such as mass flow and wall shear stress were determined in two time periods (1. baseline and 2. follow-up) based on computational fluid dynamics approach. The biomolecular parameters and adhesion molecules were prescribed for computer simulation (baseline and follow-up). This analysis was built on previous experiences in performing simulations of plaque progression within carotid artery. The obtained and analyzed results correspond to the previous works [3, 11].

The baseline results of a numerical analysis are shown in Fig. 2. Figure 2a depicts the result of the shear stress distribution along the carotid artery. The red circle indicates the zone of a low shear stress value; mean value 0.35–0.47 Pa, measured in cross sections at distances 0.5 mm. At the same site, plaque concentration is determined (Fig. 2b) and the highest measured value is 8.0×10^{-3} mg/mL. The marked area represents the greatest risk of plaque position and progression, which is confirmed after follow-up.

Further development of atherosclerosis leads to increasement of plaque volume and decrease of lumen diameter, which is followed by reduced blood flow through stenotic zone. Thus, after the follow-up, a decreased diameter of the carotid artery can be seen (Fig. 3). The maximum value of the shear stress for the obtained geometry is 7.85 Pa. The carotid diameter is approximately 45% reduced comparing with baseline. The estimation of diameter reduction is significant for further steps in medical treatment and prognosis.

Fig. 2 Baseline: **a** Shear stress distribution; **b** Plaque concentration



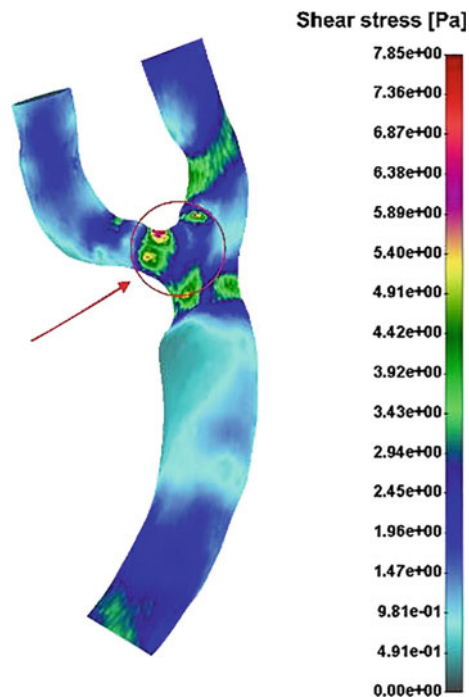


Fig. 3 Follow-up: shear stress distribution

Using presented numerical approach, the zone of plaque appearance can be determined, as well as its further propagation. Therefore, this type of simulations has an increasing importance in medicine with aim to facilitate patient's monitoring and contribute to prognosis and decision making. Also, determination of plaque location and composition, coupled with computer simulation of progression in time for a specific patient, has a potential benefit for prediction of disease progression.

4 Conclusion

Great attention is paid to the prevention of cardiovascular diseases. In this study the three-dimensional simulation, based on computational fluid dynamics, was performed in order to investigate the hemodynamic parameters such as wall shear stress distribution and plaque concentration in the carotid artery, using patient-specific data from computed tomography. Two time periods were observed (baseline and followup). The results of the analyzes have shown that sites with lower shear stress values were correlated with the sites of plaque accumulation and progression. By knowing biomolecular parameters (LDL, HDL, triglycerides) and

adhesion molecules it is possible to predict the sites of plaque occurrence as well as concentration in certain places of the artery using computer simulation. Thus, this type of numerical simulations has an increasing importance as support to medicine because in this way the zone of plaque appearance can be determined, as well as its further propagation which may facilitate the daily practice in patient monitoring.

As presented study has shown potential benefit for the prediction of disease progression, a larger number of more realistic patient specific models will be investigated in the next ones, with aim to constantly improve the computational determination of plaque location and its progression in time, as well as contribute to the medical daily practice.

Acknowledgements This paper is supported by TAXINOMISIS project that has received funding from the European Union's Horizon 2020 research and innovation programme under grant agreement No. 755320, and by projects III41007 and OI174028 of Ministry of Education, Science and Technological Development of Serbia. This article reflects only the author's view. The Commission is not responsible for any use that may be made of the information it contains.
Declaration The authors declare no conflict of interest.

References

1. What Are the Signs and Symptoms of Atherosclerosis? NHLBI, NIH. www.nhlbi.nih.gov
2. Parton, A., et al.: Computational modelling of atherosclerosis. *Brief. Bioinform.* **17**(4), 562–575 (2016)
3. Filipovic, N., Teng, Z., Radovic, M., et al.: Computer simulation of three dimensional plaque formation and progression in the carotid artery. *Med. Biol. Eng. Comput.* **51**, 607–616 (2013)
4. Bourantas, C.V., et al.: Noninvasive prediction of atherosclerotic progression: the PROSPECT-MSCT Study **9**(8), 1009–1011 (2016)
5. Sakellarios, A., et al.: Prediction of atherosclerotic disease progression using LDL transport modelling: a serial computed tomographic coronary angiographic study. *Eur. Hear. J.-Cardiovasc. Imaging* **18**(1), 11–18 (2017)
6. Mimics 10.01, Materialise, Leuven, Belgium
7. Geomagic Studio 2013, Raindrop Geomagic
8. Femap v.11, Siemens PLM Software, USA
9. Kojic, M., Filipovic, N., Stojanovic, B., Kojic, N.: *Computer Modeling in Bioengineering: Theoretical Background, Examples and Software.* Wiley, Chichester, UK (2008)
10. Filipovic, N., Mijailovic, S., Tsuda, A., Kojic, M.: An implicit algorithm within the arbitrary Lagrangian-Eulerian formulation for solving incompressible fluid flow with large boundary motions. *Comp. Methods Appl. Mech. Eng.* **195**, 6347–6361 (2006)
11. Filipovic, Nenad, Saveljic, Igor, Nikolic, Dalibor, Milosevic, Zarko, Kovacevic, Pavle, Velicki, Lazar: Numerical simulation of blood flow and plaque progression in carotid-carotid bypass patient specific case. *Comput. Aided Surg.* **20**(1), 1–6 (2015)

Forth Heart Sound Detection Using Backward Time-Growing Neural Network

Arash Gharehbaghi, Amir A. Sepehri, and Ankica Babic

Abstract

This paper presents a novel method for processing heart sound signal for screening forth heart sound (S4). The proposed method is based on time growing neural network with a new scheme, which we call the Backward Time-Growing Neural Network (BTGNN). The BTGNN is trained for detecting S4 in recordings of heart sound signal. In total, 83 children patients, referred to a children University hospital, participated in the study. The collected signals are composed of the subjects with and without S4 for training and testing the method. Performance of the method is evaluated using the Leave-One-Out and the repeated random sub sampling methods. The accuracy/sensitivity of the method is estimated to be 88.3%/82.4% and the structural risk is calculated to be 18.3% using repeated random sub sampling and the A-Test methods, respectively.

Keywords

Intelligent phonocardiography • Time-growing neural network • Backward time-growing neural network • A-Test method

1 Introduction

Intelligent phonocardiography has been recently sounded as a frugal and non-invasive approach for screening heart disease with a high potential to improve screening accuracy concomitant with low healthcare costs [1, 2]. Application of this inexpensive and easy-to-use approach ranges from symptom detection [3], screening a specific heart disease [4–8], discrimination between different diseases [9] and severity assessment of a specific heart disease [10]. Time-Growing Neural Network (TGNN) has been increasingly proposed for heart sound signal analysis, resulted from its interesting characteristics in learning temporal contents of the signal [11]. In most of the related studies, the sophisticated learning methods were employed to analyze systolic part of the heart sound signal, and diastolic part of the signal which conveys important information of relaxation phase of heart, has been less considered. Even though a number of the studies addressed such the processing [12], less attention was paid to the development of an efficient method with the capability of detecting forth heart sound in children. Forth heart sound (S4), is a pathological diastolic sound, heard in important pathologies like severe obstructive diseases, i.e. aortic stenosis, or cardiomyopathy. Fatal conditions like left or right heart failure can create S4. It is therefore, of vital importance to detect S4 to prevent irreversible conditions in patients with severe diseases. Our recent efforts showed that use of temporal frames with growing length improves learning performance comparing with the fixed length ones, especially when the mapping function is performed by TGNN [11, 13]. This paper presents a backward TGNN, tailored to detect the presence of S4 in heart sound signal. The method is practically experimented using real data collected from the children referrals to a University hospital. Results of this study can be integrated in a web-based platform to provide an efficient distributed system for screening children with heart diseases, as was already shown in other applications [14].

A. Gharehbaghi (✉)
Department of Innovation, Design and Technology, Mälardalen University, Västerås, Sweden
e-mail: arash.ghareh.baghi@mdh.se

A. A. Sepehri
CAPIS Biomedical Research and Development Centre, Mon, Belgium

A. Babic
Department of Biomedical Engineering, Linköping University, Linköping, Sweden

A. Babic
Department of Information Science and Media Studies, University of Bergen, Bergen, Norway

2 Materials

2.1 The Tools

We employed an electronic stethoscope of WelchAllyn Meditron Analyzer in conjunction with a portable computer for collecting synchronous heart sound and ECG signals, with 44,100 Hz of sampling frequency and 16 bit resolution. The ECG signals do not contribute in the classification process, and were used only for the segmentation purpose. All the processing algorithms were developed under MATLAB platform.

2.2 The Patient Population

Pediatric referrals to the Children Medical Centre, Tehran University of Medical Sciences, participated in the study. The study was conducted according to the Good Clinical Practice, and complied with codes of World Medical Association and Declaration of Helsinki. All the participant gave their informed consent for the participation. The referrals were all auscultated by the pediatricians and pediatric cardiologists, and underwent echocardiography together with the 12-lead ECG, chest X-ray and complementary tests according to the guidelines of the University hospital.

The patient population is listed in Table 1.

3 Methods

3.1 The Heart Sound Processing

The heart sound signals are firstly preprocessed using conventional methods like low-pass filtering amplitude

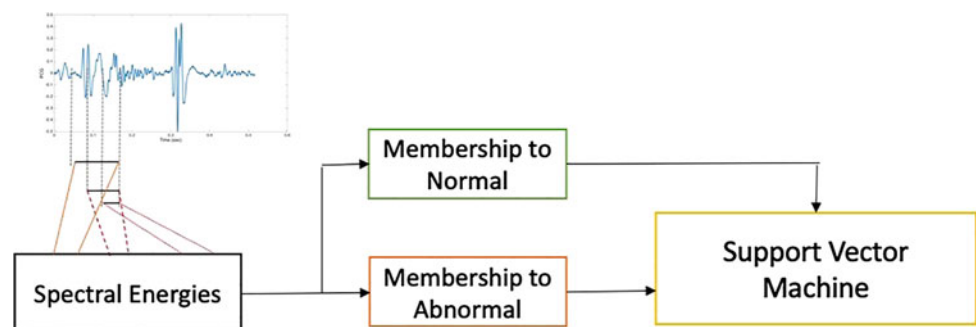
normalization, and segmentation, as has been addressed in many studies on heart sound processing [15–19]. In the segmentation process, either the S4 or ejection click, are encapsulated in the same segment as does for the first heart sound (S1), but the former appears before and the later after the first heart sound, respectively. The learning should therefore, detect S4 as the sound appears right before the S1 and discriminate it from the ejection click that might appear in the segment, but after the S1. Figure 1 illustrates the processing algorithm.

A backward TGNN (BTGNN) is employed to screen S4 from the heart sound signal. The BTGNN characterizes the signals based on the frequency contents of a set of the temporal windows, all having an identical endpoint, but different beginning point. The beginning point grows in time reversely until to cover the whole segment. This architecture is elaborated with a level of deep learning to extract details of the signal by selecting discriminative feature vectors. The deep phase of the learning process comprised of a pursuit for finding the frequency bands for each temporal window that provides a classification with optimal discrimination power. We employed the Fisher discriminant analysis for finding the frequency bands which provide optimal discrimination power for each temporal windows. The next step of the learning process is to calculate the spectral energy of the frequency bands with optimal discrimination power, for each temporal window. The spectral energies constitute input nodes of a three layer perceptron neural network, trained using back-propagation error method. The neural network has 10 neurons and 1 neuron at the hidden and output layer, respectively. The neural network is fed by the spectral energies calculated over the growing time frames, and trained using back propagation error method. The main motivation of using neural network is its ability in quick learning, and hence providing a nonlinear mapping to

Table 1 The characteristics of the participating patients

	Forth heart sound	Ejection click	Diastolic murmur	No murmur
Number of patients	18	20	15	30
The age range	4–10	3–8	4–10	4–15

Fig. 1 An illustration of the processing method for screening S4



another domain in which classification of the signals with S4 is much facilitated. The output layer is averaged over all the cycles of a heart sound recording. Then, membership function of the S4 class is obtained against another class without S4, using Gaussian distribution. The membership values for the two classes are regarded as the discriminative values, employed by a support vector machine for the binary classification. We used a regular support vector machine with linear kernel function for the classification, in order to avoid unnecessary learning complexity. This technique is favored to the study because of its robustness and capability in excluding outlier data.

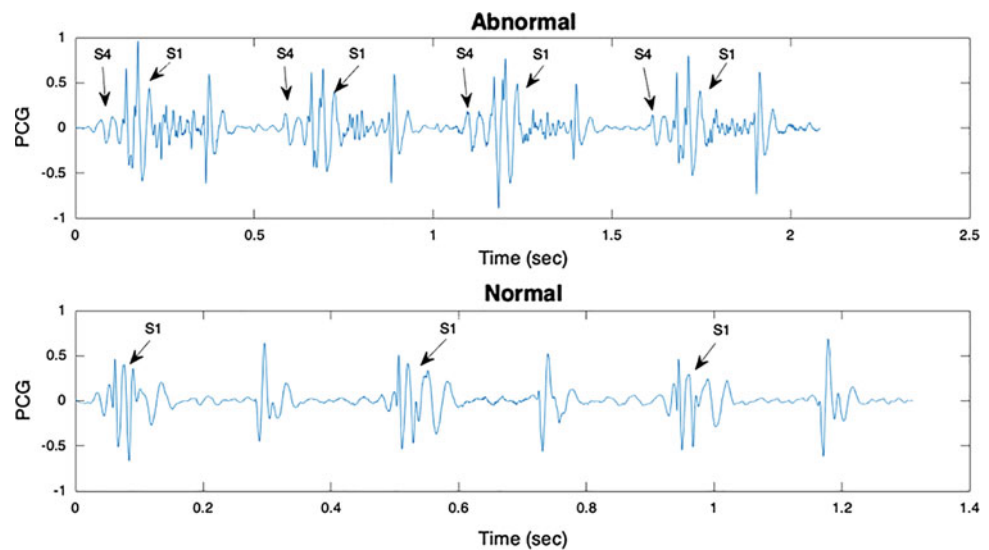
3.2 Statistical Evaluation

We employed Leave-One-Out method as well as repeated random sub sampling to investigate accuracy of the method in screening S4, using accuracy I_{ac} , sensitivity I_{sn} , and specificity I_{sp} as the performance measures:

$$I_{ac} = \frac{\text{Total number of the correctly classified subjects}}{\text{Total number of the subjects}}$$

$$I_{sn} = \frac{\text{Total number of the correctly classified subjects with S4}}{\text{Total number of the subjects with S4}}$$

Fig. 2 Three cycles of a heart sound signal from a patient with S4 (top), and a healthy one (bottom)



$$I_{sp} = \frac{\text{Total number of the correctly classified subjects without S4}}{\text{Total number of the subjects without S4}}$$

In order to evaluate structural risk of the classifier, we employed A-Test method. The A-Test method is based on using the k-fold method several times with different k values, and average of the classification error is considered as a measure of the structural risk. Details of the A-Test method are found in [11, 20].

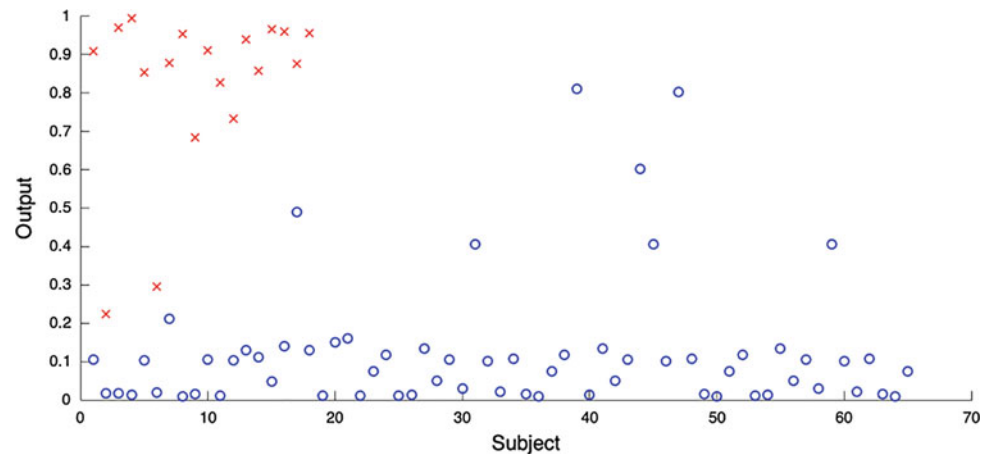
4 Results

The processing method described in the previous sequels was applied to the heart sound signal recordings from our database. Figure 2 demonstrates three cycles of a recording with and without S4.

It is clearly seen that S4 is a sharp sound appears soon before S1. The BTGNN, with the number of the temporal windows of 8, is applied to the signals. Results of the Leave-One-Out validation is depicted in Fig. 3.

As can be seen, all the subjects, but 2, are correctly classified. The mean accuracy, sensitivity and specificity of the method is estimated to be 88.3, 82.4 and 93.7%, respectively when a repeated random sub sampling of 60% training data, and 100 iterations, was used for validation. The structural risk was calculated based on the A-Test

Fig. 3 Output of the method for the children without (blue O) and with (red X) S4



method with the k value spanning from 2 to 10, and an average classification error of 18.3% was obtained.

5 Discussion

This study suggested the use of Backward Time-Growing Neural Network (BTGNN) for screening S4 on heart sound signals. It was previously shown in the related studies that time growing windows can provide superior performance comparing to the temporal windows with fixed-length, especially for the short length signals in which trade-off between time and frequency resolution is problematic [11, 21]. This study innovatively introduces BTGNN for learning heart sound characteristics. The main motivation of using BTGNN instead of Forward Time-Growing Neural Network (FTGNN) lays in the fact that S4 appears before S1. It is known that a TGNN assigns more learning weight to the first temporal window, and hence learns contents of this windows better than the rest [11]. In this study, the training process of the BTGNN is indeed towards accurate learning of S1 and detection of abrupt changes with respect to S1. This is in accordance with our previous studies in which detection of ejection click was objective. In that study a FTGNN was employed as ejection clicks are heard soon after S1. The two TGNN-Based classifiers can be well integrated together to serve as effective machine learning methods for processing S1. It is important to note that screening S4 plays an important role in timely screening of the complicated heart diseases, such as cardiomyopathy, heart failure and diastolic dysfunction, by nurses or practitioners at the primary healthcare centers. Studies show that the screening accuracy is still low in these centers and using artificial intelligence-based algorithms can provide efficient tools for automatic decision making. Such the automated algorithms have shown promising results with the

applicative importance to be employed by the practitioners in different clinical setting as an emerging healthcare technology [22].

6 Conclusions

The paper presented a method for processing heart sound signals for screening one important heart abnormality in children, the forth heart sound. Statistical analysis showed that the method is efficient enough to screen the appearance of forth heart sound. The presented algorithm has the potential to be implemented in the mobile or web-technology to be employed as a decision support system in primary healthcare centres.

Acknowledgements The authors would like to thank Prof. A. Kocharian for his valuable cooperation in data collection. This study was supported by the CAPIS Inc., Mons, Belgium, and also by the KKS financed research profile in embedded sensor systems for health at Mälardalen University, Västerås, Sweden.

Conflict of Interest The authors declare that they have no conflict of interest.

References

1. Gharehbaghi, A., et al.: Assessment of aortic valve stenosis severity using intelligent phonocardiography. *Int. J. Cardiol.* **198**, 58–60 (2015)
2. Sepehri, A.A., et al.: An intelligent phonocardiography for automated screening of pediatric heart diseases. *J. Med. Syst.* **40** (1), 16 (2015)
3. Gharehbaghi, A., et al.: A Hybrid Machine Learning Method for Detecting Cardiac Ejection Murmurs. In *EMBECE & NBC 2017*. 2018. Springer, Singapore
4. Gharehbaghi, A., et al.: Intelligent phonocardiography for screening ventricular septal defect using time growing neural network.

- In: *Informatics Empowers Healthcare Transformation*, pp. 108–111. IOS Press (2017)
5. Gharehbaghi, A., et al.: A novel model for screening aortic stenosis using phonocardiogram. In: *IFMBE Proceedings of 16th Nordic-Baltic Conference on Biomedical Engineering*. Springer, Berlin (2014)
 6. Gharehbaghi, A., et al.: A novel method for screening children with isolated bicuspid aortic valve. *Cardiovasc. Eng. Technol.* **6** (4), 546–556 (2015)
 7. Ramović, A., et al.: Wavelet and Teager Energy Operator (TEO) for heart sound processing and identification. In: *CMBE-BIH 2017*. Springer, Singapore (2017)
 8. Emmanuel, B.S.: A review of signal processing techniques for heart sound analysis in clinical diagnosis AU—Emmanuel, Babatunde S. *J. Med. Eng. Technol.* **36**(6), 303–307 (2012)
 9. Gharehbaghi, A., et al.: An intelligent method for discrimination between aortic and pulmonary stenosis using phonocardiogram. In: Jaffray D.A. (ed.) *World Congress on Medical Physics and Biomedical Engineering*, June 7–12, 2015, Toronto, Canada, pp. 1010–1013. Springer International Publishing, Cham (2015)
 10. Gharehbaghi, A., et al.: A hybrid model for diagnosing severe aortic stenosis in asymptomatic patients using phonocardiogram. In: Jaffray D.A. (ed.) *World Congress on Medical Physics and Biomedical Engineering*, June 7–12, 2015, Toronto, Canada, pp. 1006–1009. Springer International Publishing, Cham (2015)
 11. Gharehbaghi, A., Lindén, M.: A deep machine learning method for classifying cyclic time series of biological signals using time-growing neural network. *IEEE Trans. Neural Netw. Learn. Syst.* **99**, 1–14 (2018)
 12. Tseng, Y.-L., Ko, P.-Y., Jaw, F.-S.: Detection of the third and fourth heart sounds using Hilbert-Huang transform. *Biomed. Eng. Online* **11**, 8–8 (2012)
 13. Gharehbaghi, A., et al.: A novel method for discrimination between innocent and pathological heart murmurs. *Med. Eng. Phys.* **37**(7), 674–682 (2015)
 14. Gharehbaghi, A., Lindén, M.: An internet-based tool for pediatric cardiac disease diagnosis using intelligent phonocardiography. In: Mandler B., et al. (eds.) *Internet of Things. IoT Infrastructures: Second International Summit, IoT 360° 2015*, Rome, Italy, October 27–29, 2015. Revised Selected Papers, Part I, pp. 443–447. Springer International Publishing, Cham (2016)
 15. Voss, A., Mix, A., Hübner, T.: Diagnosing aortic valve stenosis by parameter extraction of heart sound signals. *Ann. Biomed. Eng.* **33** (9), 1167–1174 (2005)
 16. Bhatikar, S.R., DeGroff, C., Mahajan, R.L.: A classifier based on the artificial neural network approach for cardiologic auscultation in pediatrics. *Artif. Intell. Med.* **33**(3), 251–260 (2005)
 17. Akay, M., et al.: Detection of coronary occlusions using autoregressive modeling of diastolic heart sounds. *IEEE Trans. Biomed. Eng.* **37**(4), 366–373 (1990)
 18. Akay, M., et al.: Dynamics of diastolic sounds caused by partially occluded coronary arteries. *IEEE Trans. Biomed. Eng.* **56**(2), 513–517 (2009)
 19. Oskiper, T., Watrous, R.: Detection of the first heart sound using a time-delay neural network. *Comput. Cardiol.* (2002)
 20. Gharehbaghi, A., Babic, A.: Structural risk evaluation of a deep neural network and a Markov model in extracting medical information from phonocardiography. *Stud. Health Technol. Inform.* **251**, 157–160 (2018)
 21. Gharehbaghi, A., et al.: Detection of systolic ejection click using time growing neural network. *Med. Eng. Phys.* **36**(4), 477–483 (2014)
 22. Thompson, W.R., et al.: Artificial intelligence-assisted auscultation of heart murmurs: validation by virtual clinical trial. *Pediatr. Cardiol.* (2018)

Part VII

Bioinformatics and Computational Biology

Using Data Science for Medical Decision Making Case: Role of Gut Microbiome in Multiple Sclerosis

Jasminka Hasic Telalovic and Azra Music Kilic

Abstract

The study of microbiome and its relationship with the host organism has recorded rapid increase in popularity over the past decade. The advances in the sequencing techniques used for extraction of microbiome data have stimulated the development of sophisticated bioinformatics tools used to analyze large amounts of data. The gut microbiome, as a network of microorganisms that is the focus of this study, has been implicated in several disorders such as colorectal cancer, obesity, irritable bowel syndrome, diabetes, and metabolic syndrome, and more recently in the study of Parkinsons and Alzheimers diseases as well. This study aims to examine the relationship between multiple sclerosis, autoimmune central nervous system disease, and gut microbial community composition, using the samples obtained 16s rRNA sequencing technique. Healthy control and multiple sclerosis groups of sequences were analyzed. Using the extracted set of statistically significant bacteria, a Random Forest classifier has been developed. The most significant microbiome alterations in multiple sclerosis patients imply increase in *Akkermansia* and *Methanobrevibacter*, and decrease in *Butyrivcimonas* bacteria at the genus. The highest accuracy scores obtained by the developed classifier are 84.61% using the genus level bacteria. The presented methods and results define a paradigm that can be used to help guide medical decision making.

Keywords

Bioinformatics • Data science • Machine learning • Microbiome • Multiple sclerosis

J. H. Telalovic (✉)

University SSST, Sarajevo, Bosnia and Herzegovina

e-mail: jasminka.hasic@ssst.edu.ba

URL: www.ssst.edu.ba

A. M. Kilic

OlaWell Inc., Lewes, UK

e-mail: amusic@olawell.com

URL: www.olawell.com

1 Introduction

Science is progressively developing into multidisciplinary field, and the potential area of scientific contribution is placed in the crossroad of multiple fields. The moderately new fields of genomics and bioinformatics have developed to be the basic segments of biological research. They incorporate both, mathematical and computational techniques in order to examine the biological information [28]. One of the fields that exhibits rapid increase of development is the study of microbiome and its relationship with the host organism. This is made possible by the development of bioinformatics tools used for the purpose of discovering and analyzing respective sequences.

1.1 The Human Gut Microbiome

Microbiota represents a network of microorganisms. It is a natural network of harmonious and pathogenic microorganisms that share the body space with us, humans. The human microbiota includes the microorganisms that live on and inside the humans. The number of microorganisms is estimated to be ten times larger than the number of somatic cells in humans. Aside from the gut microbiota, the skin, nasal, oral and vaginal microbiota have been researched widely as well [14]. The principle mass of microorganisms related to human bodies is present in the intestinal tract. According to [36], the weight of the microbes living in a human digestive tract is around 1.5 kg, hence composing half of the fecal matter. The majority of bacteria in the human microbiota are considered to be non-pathogenic, but rather present in a beneficial or commensal association with the human host [2]. The gut microbiota is principally made out of bacteria belonging to two significant phyla: *Bacteroidetes* and *Firmicutes*. Regarding the count of species level bacteria, the number of those present in human gut is variable. According to [26], a study of 124 individuals

presented over 1000 species all together, where each person contained around 160 different species. Out of the 160 different species, 18 species were present in all subjects, while 75 species were present in most of the subjects. Therefore, the abundance of the species in samples is highly variable.

The composition of the gut microbiota can be examined from the fecal samples collected in a manner that is not invasive, while the examination of other parts of gastrointestinal system is limited due to the invasive methods of collecting samples. However, the collected fecal samples represent sufficiently large composition in the colon where majority of metabolic activity occurs [37]. The stability of the gut microbiota in the long run has not been examined as much as the variation of composition between individuals. Several studies have reported that one person's microbiota is more comparative between samples taken at different times than the microbiota of different individuals [14, 27, 31]. According to [11], the gut microbiota is steady over the long run and around 70% strains remained the same in the period of the year with few changes occurring after four years.

1.2 Sequencing Techniques: 16s rRNA Gene Sequencing

Since the mid-1980s, the 16s rRNA gene has been the main target for analysis of the human gut and the microorganisms that reside there [17]. The 16s rRNA gene contains conserved and variable regions among the different species which makes it useful for universal primer construction and taxonomic identification. The 16s rRNA is about 1500 base pairs long and its conserved regions enable amplification and marking of only 16s rRNA genes in microbial sample using PCR [23].

2 Background

Recent studies have shown that adult microbiome can be influenced by outside factors. For example drugs, such as antibiotics, easily affect the microbiome composition [29]. Other altering factors include illness, drug addiction, smoking, climate and lifestyle [3]. The gut microbiota has symbiotic relationship with its host, but when commensal bacteria are replaced or outnumbered by pathogenic species, dysbiosis can occur. An imbalance in gut microbiota is associated with various diseases such as colorectal cancer, irritable bowel syndrome and inflammatory bowel disease, obesity, malnutrition, diabetes, metabolic syndrome and rheumatoid arthritis [4, 12, 19, 21, 35]. In the field of neurology, the research is nowadays focused on the role of gut

microbiota in diseases such as Parkinsons disease and Alzheimers disease [24, 33]. Recent studies have explored the relationship between microbes and the development of multiple sclerosis. Multiple sclerosis (MS) is an autoimmune central nervous system disease in a human model. The etiology and pathogenesis of MS remain unknown until the current time but show signs of dysbiosis [9]. The findings in the field of microbiome-MS relationship could help find new ways of treating or preventing the MS relapse.

The aim of this paper is to develop a computational model that will distinguish healthy samples from the ones with a condition. In particular, we use data science to discover characteristics that distinguish microbiome of individuals with multiple sclerosis diagnosis versus the healthy ones. We also test how the discovered characteristics and developed model can be used to classify new microbiome data as healthy or with MS condition without any additional knowledge and with high accuracy. This technique could be applied to the conditions other than MS by building a model in a similar manner. This would involve identification of significant bacteria and development of a classification model.

3 Dataset and Methodology

3.1 Dataset

The data sequences used in this study are obtained using the 16s rRNA sequencing method from the samples obtained from subjects with multiple sclerosis and without multiple sclerosis disease. The samples were collected by [15]. The initial number of subjects used for the analysis was 60 from the multiple sclerosis group, and 43 from the control group. The subjects had comparable demographic characteristics. In the MS group, there was moderately increased number of males. All multiple sclerosis subjects had relapsing-remitting disease rather than active relapse at the time of study. The demographics of the study population is shown in Table 1.

Even though the dataset description contains information about the overall number of female and males samples, the individual samples were not labeled by gender. In the data cleaning phase, we decided to remove MS samples that were already under treatment—thus we kept only samples from individuals who were not treated for MS. In order to gain the most insight into the remaining samples, we calculated the number of healthy samples needed to maximize the statistical power of the t-test.

After data cleaning phase for this study, 28 MS samples were used and 35 healthy ones.

Table 1 Dataset description

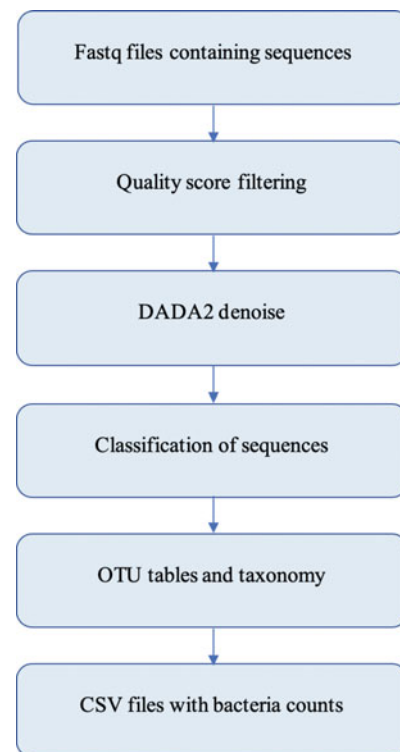
Attribute	Healthy, N = 43	Multiple sclerosis, N = 60
Age	42.2 ± 9.61	49.7 ± 8.50
Male	6 (14%)	19 (32%)
Female	37 (86%)	41 (68%)
Body mass index	26.4 ± 6.3	27.2 ± 4.7
Caucasian	43	58
Disease duration	NA	12.8 ± 8.3
Untreated	NA	28

3.2 Taxonomy Analysis

The sequences were analyzed using QIIME2 tools [7]. The QIIME2 analysis pipeline takes as input sequenced files (for example in *fastq* format) and mapping file that contains metadata that describes samples. The metadata file contains user-generated information that describes each sample and it is of high importance for the rest of the analysis. In this study, metadata file carries information on sample unique identifiers, the barcode used for sample, the primer sequence used, and the column that represents presence of MS in each of the samples. Since the data obtained from the study of [15] is already demultiplexed, the barcodes and primers are not necessary. The next step is quality-filtering of the reads. Quality-filtering in QIIME2 is done through the DADA2 algorithm processing, yet the decision on the trimming or truncating length is made manually. By plotting the quality scores of reads imported in the pipeline, the user selects the length at which the reads decrease in their quality and use those variables as parameters for the DADA2 plugin.

The third step in the pipeline is DADA2 algorithm denoise phase. This method denoises single-end sequences, dereplicates them and performs quality filtering. The reads are truncated based on the parameters obtained in the second step. The result of DADA2 is the feature table that contains frequency of specific reads and the source sequences [5]. The DADA2 produces Amplicon Sequence Variants (ASV), that are for the further analysis considered as OTUs (operational taxonomic units). The process produces fewer sequences which are of high quality, and that is the advantage of ASVs over the cluster-based OTUs (that are used in the previous generation bioinformatics tools). Therefore, since the ASVs are of the similar purpose as the OTUs, the reference picking will not be used in the pipeline for the taxa assignment. After the denoising step, the results are summarized and passed to the classification step. All of the ASVs produced in the previous steps are classified into respective classes produced by classifier database *GreenGenes* at 99% identity (version 13_5). The same classifier

version has been used also for the closed reference clustering. The obtained OTUs are metadata tabulated and taxa is assigned to them in the fifth step. This step associates OTUs to the named organisms which is useful for understanding functional roles for community members. Each identified OTU that has been previously cultured, starting from the phylum level to species level, has its respective name in the database. By using those names, rather than OTU identifiers, it is easier to manipulate the data, as the phylogeny of the particular bacteria is recognized. The table containing the count of each specific bacteria in the sample is the result of this step. This data was normalized by gene number function, and it is used for further statistical analysis (Fig. 1).

**Fig. 1** QIIME2 analysis methodological framework

3.3 Random Forest Classification

The Random Forest Classification algorithm has been implemented in order to train the classifier and develop the classification model. The random forests is supervised learning algorithm based on the decision trees on randomly selected data samples [22]. Moreover, it produces prediction for each of the trees, selects the best solution via means of voting, and provides satisfactory indicator of the feature importance to revise the model. The individual decision trees within the forest are generated using attribute selection indicator such as *gain ratio*, *information gain* and *Gini index* for each attribute. In the first step, the data values and target values are separated. The data sets are used as parameters for the *train_test_split* method that splits the data into training and testing groups. The ratio between the train and test data is 80:20, meaning the 80% of data is grouped for training, and 20% is assigned to be used for testing the model. The number of decision trees generated is 100. With increasing the number of trees in the classifier, the accuracy is also getting increased at the cost of computational time. The testing data was used to predict the target data and measure the accuracy of the model by comparing predicted target data and testing target data. The same process has been repeated for all six taxonomical levels. In order to verify the classification model, the feature importance scores have been calculated for all the variables in the study. Afterwards, the features showing highest importance for the model have

been extracted and used as a new data for re-training the classifier. The accuracy is compared to the previous iteration to confirm that the data selected initially forms a strong basis for the model development.

4 Results

Using QIIME2 pipeline [7], samples were analyzed and abundances of bacteria at different taxonomic levels were established. Figures 2 and 3 show samples' distributions for both examined groups on the phylum taxonomic level. Table 2 summarizes the number of identified bacteria at taxonomic levels for both studied groups.

In order to narrow down the choice of features for the classifier, the independent *t-test* was used to establish whether the difference in each bacteria between the two groups is statistically significant. The bacteria that are statistically significant at $p < 0.05$ are extracted together with their values for six taxonomic levels. Figure 4 shows the mean values of phylum level bacteria established as statistically significant.

By combining the *t-test* results and the previously calculated mean values, the final list of bacteria to be used for model training and testing has been created. The final list of bacteria at each taxonomical level to be used in the further processing is presented in Table 3.

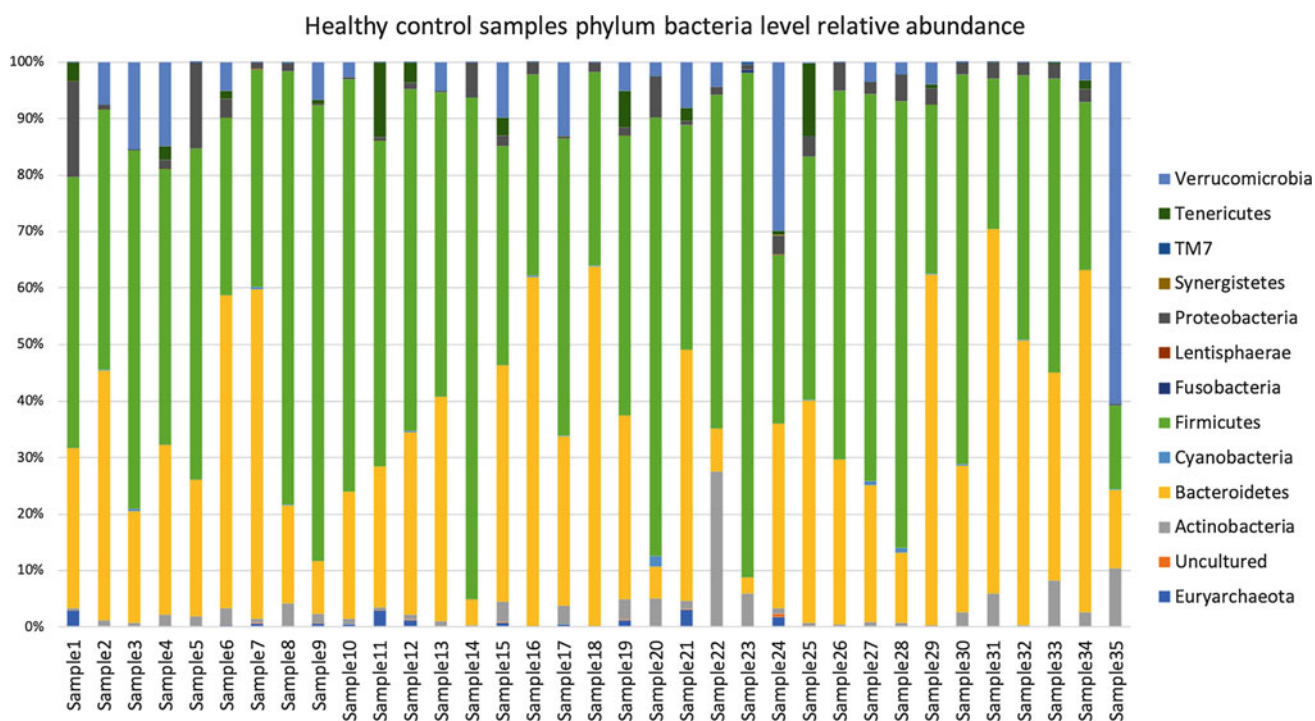


Fig. 2 Plot shows 35 healthy individuals' samples on the x-axis and relative abundance of phylum level bacteria (in %) on the y-axis

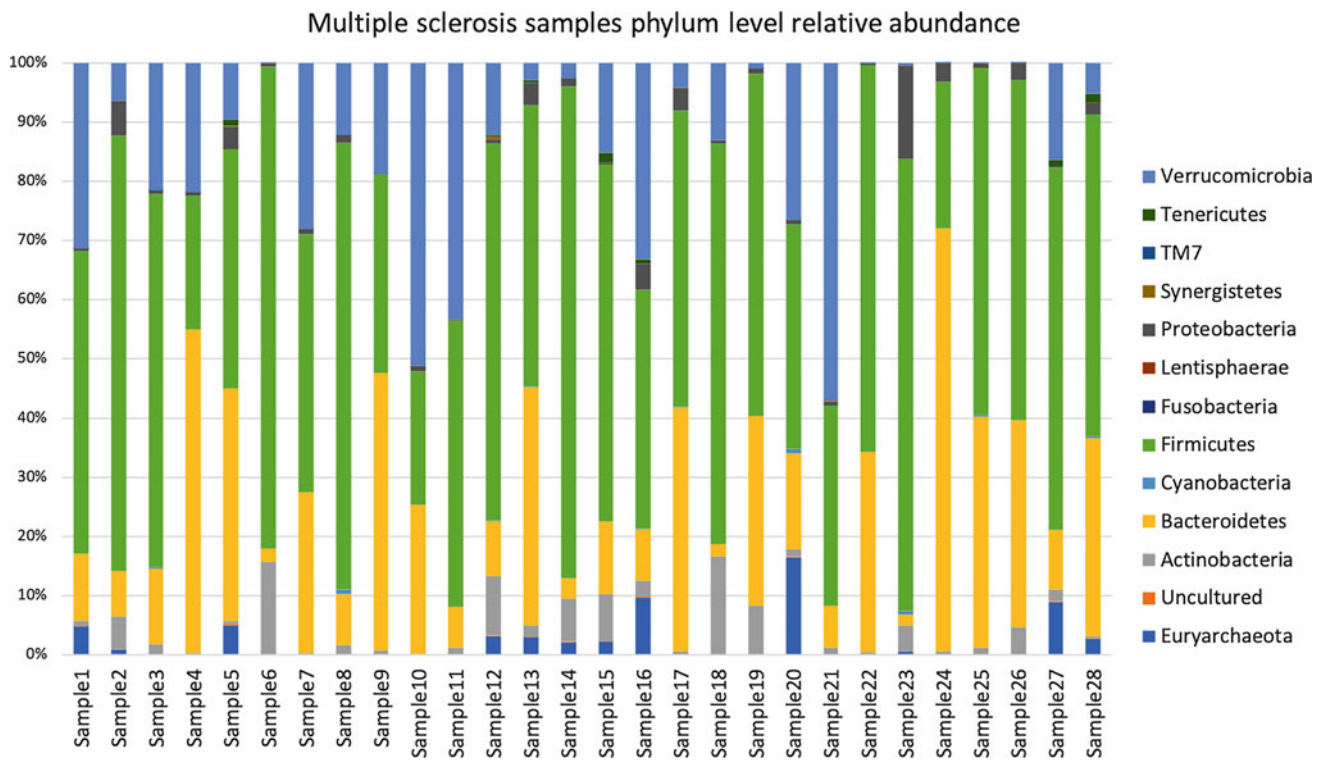


Fig. 3 Plot shows 28 MS samples on the x-axis and the relative abundance of phylum level bacteria (in %) on the y-axis

Table 2 Identified bacteria count per taxonomical level

Level	Healthy control	Multiple sclerosis
Phylum	13	13
Class	29	26
Order	47	39
Family	88	79
Genus	192	174
Species	257	234

Fig. 4 The average relative abundance of the phylum level bacteria (in %) in healthy control and MS phylum groups

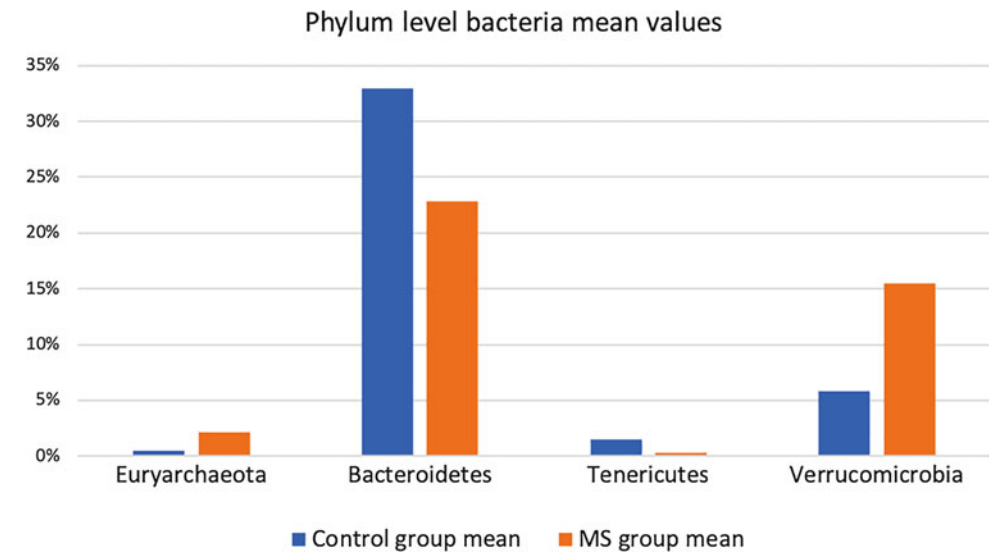


Table 3 Bacteria with high feature importance score

Level	Bacteria and <i>p</i> -value
Phylum	Euryarchaeota (0.0158), Bacteroidetes (0.0456), Verrucomicrobia (0.0059), Tenericutes (0.0492)
Class	Verrucomicrobiae (0.0059), Bacteroidia (0.0458), Methanobacteria (0.016), Mollicutes (0.0491)
Order	Verrucomicrobiales (0.0059), Bacteroidales (0.0458), Methanobacteriales (0.016), RF39 (0.0482), bacteria from class Clostridia (0.0181)
Family	Verrucomicrobiaceae (0.0059), bacteria from order RF39 (0.0482), Barnesiellaceae (0.0133), Methanobacteriaceae (0.016), bacteria from class Clostridia (0.0181), Paraprevotellaceae (0.034)
Genus	Akkermansia (0.0059), bacteria from family Ruminococcaceae (0.0437), Butyricimonas (0.0359), bacteria from family Barnesiellaceae (0.0133), Methanobrevibacter (0.0159)
Species	Akkermansia muciniphila (0.0059), bacteria from family Ruminococcaceae (0.0437), bacteria from genus Butyricimonas (0.0359), bacteria from family Barnesiellaceae (0.0133), bacteria from genus cc_115 (0.0496)

Table 4 Bacteria number for the model development

Level	Accuracy score (%)
Phylum	69.23
Class	76.92
Order	76.92
Family	84.54
Genus	84.61
Species	61.53

The list of bacteria produced in the final step of statistical analysis phase has been used as the input for the Random Forest classifier model. The classifier has been modelled using bacteria at six taxonomical levels as previously mentioned. The data was split into training set (80% of the dataset) and testing set (20% of the data set). The accuracy scores obtained at the taxonomical levels are listed in Table 4.

5 Conclusions and Future Work

We have developed a computational model that distinguishes microbiome samples of individuals diagnosed with MS from the healthy ones. This involved the discovery of the significant bacteria which were the bases of the computation classification model. A number of studies that have been done confirm similar findings as ours on significant bacteria for MS [6, 8, 15, 30, 32, 34]. The research question examined aimed to determine whether the difference in taxonomic classification of bacteria is significant enough so that a machine learning classifier can be built to distinguish multiple sclerosis samples from the healthy ones. Such

classifier is constructed and it exhibited good level of accuracy. The possibility of having over 80% accuracy with distinguishing MS patients from the healthy ones by performing a non-invasive test is of significant value for medical decision making. Even though this is a valuable contribution, it is important to keep in mind its limitations and also outline possible contributions that can be made to strengthen those results in the future.

This study had sample size of 63 individuals, which is a relatively small number for data science. Bigger number of samples needs to be considered to make results applicable to the whole population.

Human gut has different sections with different environments and microbial communities. Since the only non-invasive method available for collecting samples is the collection via stool, it can be difficult to determine which bacteria came from where and how each part of gastrointestinal system contributes to the site differences. In addition, individuals may have different genetic backgrounds, age, ethnicity, sex, life in different environments, and have different diet habits. All mentioned factors may influence the variation in the gut microbiota of human population [4]. For future work datasets enhanced with such information are to be studied.

Further improvements can be made by upgrading the sequencing technique used to obtain the samples. In the future, research should cover the analysis of metagenomics data. Even though the 16s is suited for analyzing large number of samples due to its computational cost benefits, it offers limited taxonomical and functional resolution, and therefore the results should be treated as probabilistic. The metagenomics sequences are more expensive to obtain, but they enable more specific taxonomic and functional classification of sequences, therefore the results can be considered

to be more reliable [16]. The reliable study results can form a strong basis for developing models that can explain the structure and function of the microbial community, and potentially provide deeper insight into the relationship between microbiome and disease states.

Furthermore, the classifier can be remodelled in order to take the bacterial and functional relationships into account. The bacteria at six different taxonomical level have phylogenetic relationship which is a structure that can potentially be source of addition information and results in a more accurate model. We anticipate that such improvements would improve classification accuracy.

The methodology presented in this paper can be applied to build a model to identify samples with conditions other than MS (i.e. Parkinsons and Alzheimers disease).

References

- Amar, J., Lange, C., Payros, G., Garret, C., Chabo, C., Lantieri, O., Courtney, M., Marre, M., Charles, M.A., Balkau, B., et al: Blood microbiota dysbiosis is associated with the onset of cardiovascular events in a large general population: the D.E.S.I.R. study. *PLoS One* **8** (2013)
- Backhed, F., Ley, R.E., Sonnenburg, J.L., Peterson, D.A., Gordon, J.I.: Host-bacterial mutualism in the human intestine. *Science* **307**, 1915–1920 (2005)
- Biedermann, L., Rogler, G.: The intestinal microbiota: its role in health and disease. *Eur. J. Paediatr.* **174**(2), 151–167 (2015)
- Budhram, A., Kremenchutzky, M., Silverman, M.: Breaking down the gut microbiome composition in multiple sclerosis. *Mult. Scler. J.* **23**(5), 628–636 (2017)
- Callahan, B.J., McMurdie, P.J., Rosen, M.J., Han, A.W., Johnson, A.J.A., Holmes, S.P.: DADA2: High-resolution sample inference from Illumina amplicon data. *Nat. Methods* **13**, 581–583 (2016)
- Cantarel, B.L., Waubant, E., Chehoud, C., et al.: Gut microbiota in multiple sclerosis. *J. Investig. Med.* **63**(5), 729–734 (2015)
- Caporaso, J.G., Kuczynski, J., Stombaugh, J., Bittinger, K., Bushman, F.D., Costello, E.K., et al.: QIIME allows analysis of high-throughput community sequencing data. *Nat. Methods* **7**(5), 335–336 (2010)
- Chen, J., Chia, N., Kalari, K.R., et al.: Multiple sclerosis patients have a distinct gut microbiota compared to healthy controls. *Sci. Rep.* **6**(1), article 28484 (2014)
- Chu, F., Shi, M., Lang, Y., Shen, D., Jin, T., Zhu, J., Cui, L.: Gut microbiota in multiple sclerosis and experimental autoimmune encephalomyelitis: current applications and future perspectives. *Hindawi: Mediat. Inflamm.* **2018**, 1–17 (2018)
- Eckburg, P.B., Bik, E.M., Bernstein, C.N., Purdom, E., Dethlefsen, L., Sargent, M., Gill, S.R., Nelson, K.E., Relman, D.A.: Diversity of the human intestinal microbial flora. *Science* **308**, 1635–1638 (2005)
- Faith, J.J., Guruge, J.L., Charbonneau, M., Subramanian, S., Seedorf, H., Goodman, A.L., Clemente, J.C., Knight, R., Heath, A. C., Leibel, R.L., et al.: The long-term stability of the human gut microbiota. *Science* **341**, article 1237439 (2013)
- Fraune, S., Bosch, T.C.: Why bacteria matter in animal development and evolution. *BioEssays* **32**(7), 571–580 (2010)
- Goddard, A.F., Staudinger, B.J., Dowd, S.E., Joshi-Datar, A., Wolcott, R.D., Aitken, M.L., Fligner, C.L., Singh, P.K.: Direct sampling of cystic fibrosis lungs indicates that DNA-based analyses of upper-airway specimens can misrepresent lung microbiota. *Proc. Natl. Acad. Sci. U. S. A.* **109**, 13769–13774 (2012)
- Huttenhower, C., Gevers, D., Knight, R., Abubucker, S., Badger, J.H., Chinwalla, A.T., Creasy, H.H., Earl, A.M., FitzGerald, M.G., Fulton, R.S., et al.: Structure, function and diversity of the healthy human microbiome. *Nature* **486**, 207–214 (2012)
- Jangi, S., Gandhi, R., Cox, L.M., Li, N., et al.: Alterations of the human gut microbiome in multiple sclerosis. *Nat. Commun.* **7** (2016). <https://doi.org/10.1038/ncomms12015>
- Jovel, J., Patterson, J., Wang, W., Hotte, N., O’Keefe, S., et al.: Characterization of the gut microbiome using 16s or shotgun metagenomics. *Front. Microbiol.* **7**, article 459 (2016)
- Karlsson, F.H.: Systems Biology of the Gut Microbiome in Metabolic Diseases. Doctoral dissertation. Chalmers University of Technology, Sweden (2014)
- Karlsson, F.H., Fak, F., Nookaew, I., Tremaroli, V., Fagerberg, B., Petranovic, D., Backhed, F., Nielsen, J.: Symptomatic atherosclerosis is associated with an altered gut metagenome. *Nat. Commun.* **3**, 1245 (2012)
- Kau, A.L., Ahern, P.P., Griffin, N.W., Goodman, A.L., Gordon, J. I.: Human nutrition, the gut microbiome and the immune system. *Nature* **474**(7351), 327–336 (2011)
- Koren, O., Knights, D., Gonzalez, A., Waldron, L., Segata, N., Knight, R., Huttenhower, C., Ley, R.E.: A guide to enterotypes across the human body: meta-analysis of microbial community structures in human microbiome datasets. *PLoS Comput. Biol.* **9** (2013)
- Ley, C.E., Turnbaugh, P.J., Klein, S., Gordon, J.I.: Microbial ecology: human gut microbes associated with obesity. *Nature* **444** (7122), 1022–1023 (2006)
- Loupe, G.: Understanding Random Forests: from theory to practice, Ph.D. Thesis at University of Liège (2014)
- Morgan, X.C., Huttenhower, C.: Human microbiome analysis (Chap. 12). *PLoS Comput. Biol.* **8** (2012)
- Parashar, A., Udayabanu, M.: Gut microbiota: implications in Parkinsons disease. *Park. Relat. Disord.* **38**, 17 (2017)
- Plummer, E., Twin, J., Bulach, D.M., Garland, S.M., Tabrizi, S.N.: A comparison of three bioinformatics pipelines for the analysis of preterm gut microbiota using 16s rRNA gene sequencing data. *J. Proteomics Bioinform.* **8**(12), 283–291 (2015)
- Qin, J., Li, R., Raes, J., Arumugam, M., Burgdorf, K.S., Manichanh, C., Nielsen, T., Pons, N., Levenez, F., Yamada, T., et al.: A human gut microbial gene catalogue established by metagenomic sequencing. *Nature* **464**, 59–65 (2010)
- Rajilic-Stojanovic, M., Heilig, H.G., Molenaar, D., Kajander, K., Surakka, A., Smidt, H., de Vos, W.M.: Development and application of the human intestinal tract chip, a phylogenetic microarray: analysis of universally conserved phylotypes in the abundant microbiota of young and elderly adults. *Environ. Microbiol.* **11**, 1736–1751 (2009)
- Rosenwald, A.G., Arora, G.S., Madupu, R., Roecklein-Canfield, J., Russell, J.S.: The human microbiome project: an opportunity to engage undergraduates in research. *Proc. Comput. Sci.* **9**, 540–549 (2012). International Conference on Computational Sciences
- Scott, A., Sands, S.T., Yankee, T.M., Parker, B.L., Ericsson, A.C., LeVine, S.M.: The effect of omeprazole on the development of experimental autoimmune encephalomyelitis in C57BL/6J and SJL/J mice. *BMC Res. Notes* **7**(1), 605 (2014)
- Tremlett, H., Fadrosch, D.W., Faruqi, A.A., et al.: Gut microbiota in early paediatric multiple sclerosis: a case-control study. *Eur. J. Neurol.* **23**(8), 1308–1321 (2016)

31. Turnbaugh, P.J., Hamady, M., Yatsunenko, T., Cantarel, B.L., Duncan, A., Ley, R.E., Sogin, M.L., Jones, W.J., Roe, B.A., Affourtit, J.P., et al.: A core gut microbiome in obese and lean twins. *Nature* **457**, 480–484 (2009)
32. Weiner, H.L.: The gut microbiome may aid the treatment and prevention of MS. *Neurol. Rev.* **23**(8), 27–30 (2015)
33. Westfall, S., Lomis, N., Kahouli, I., Dia, S.Y., Singh, S.P., Prakash, S.: Microbiome, probiotics and neurodegenerative diseases: deciphering the gut brain axis. *Cell. Mol. Life Sci.* **74**(20), 3769–3787 (2017)
34. Wilson, B.A., Miyake, S., Kim, S., et al.: Dysbiosis in the gut microbiota of patients with multiple sclerosis, with a striking depletion of species belonging to clostridia Xiva and IV clusters. *PLoS One* **10**(9), article e0137429 (2015)
35. Zhang, X., Zhang, D.Y., Jia, H.J., et al.: The oral and gut microbiomes are perturbed in rheumatoid arthritis and partly normalized after treatment. *Nat. Med.* **21**(8), 895–905 (2015)
36. Zhao, L.: The gut microbiota and obesity: from correlation to causality. *Nat. Rev. Microbiol.* **11**, 639–647 (2013)
37. Zoetendal, E.G., Raes, J., van den Bogert, B., Arumugam, M., Booiijink, C.C., Troost, F.J., Bork, P., Wels, M., de Vos, W.M., Kleerebezem, M.: The human small intestinal microbiota is driven by rapid uptake and conversion of simple carbohydrates. *ISME J.* **6**, 1415–1426 (2012)

Discovery of Membrane Permeability, Pharmacokinetics Properties and Mechanism of Action for Analogs of Ethylenediamine-*N,N'*-di-2-(3-Cyclohexyl)Propionic Acid and 1,3-Propanediamine-*N,N'*-di-2-(3-Cyclohexyl)Propionic Acid with Antiproliferative Activity Using In Vitro and In Silico Methods

Biljana Tubić, Bojan Marković, and Tibor Sabo

Abstract

In previously in vitro studies on different cell lines and in vivo on melanoma and 4T1 murine breast cancer and metastasis it was shown antiproliferative activity for ester derivatives of (*S,S*)-ethylenediamine-*N,N'*-di-2-(3-cyclohexyl)propanoic acid, and (*S,S*)-1,3-propanediamine-*N,N'*-di-2-(3-cyclohexyl)propanoic acid. The aim of this study was to predict membrane permeability by parallel artificial membrane permeability assay (PAMPA), molecular mechanism of action, metabolites and absorption, distribution, metabolism, toxicity—ADMET properties for observed substances using in vitro and in silico methods. Obtained results of PAMPA show the best membrane permeability of ethyl esters analogs (DE-EDCP and DE-PDCP) and refer to the hypothesis that the retention in cell membrane is important for cytotoxic activity of investigated substances. Prediction of main metabolic pathways was performed by the Metabolizer software and it was obtained that the major metabolic reactions were the hydrolyses of ester and subsequently intramolecular cyclization. Toxicity of

investigated substances and their potential metabolites are lower than toxicity of observed official cytotoxic drugs. Based on the results obtained by the Molecular docking, it can be assumed that the antiproliferative effects of the investigated substances were realized through the multiple mechanisms by potential metabolites: acids, lactam carboxylate and lactam alkyl esters, while the esters are probably a prodrug substance with favorable properties to provide sufficient bioavailability at the target of action. Based on obtained results it can be proposed there to be investigated the existence of the metabolites: lactam carboxylate and lactam alkyl esters in biological materials.

Keywords

Membrane permeability—PAMPA • Ethylenediamine derivatives with cytotoxic activity • ADMET properties • Molecular docking

B. Tubić (✉)

Department of Pharmacy, Faculty of Medicine, University of Banjaluka, Save Mrkalja 14, 78000 Banjaluka, Bosnia and Herzegovina

e-mail: b.tubic@almbih.gov.ba

B. Tubić

Agency for Medicines and Medical Devices of Bosnia and Herzegovina, Veljka Mla enovića bb, 78000 Banjaluka, Bosnia and Herzegovina

B. Marković

Faculty of Pharmacy, University of Belgrade, Vojvode Stepe 450, 11000 Belgrade, Serbia

T. Sabo

Faculty of Chemistry, University of Belgrade, Studentski trg 12-16, 11000 Belgrade, Serbia

1 Introduction

Cancer is a public health problem all over the world. Chemotherapy is one of the commonly used strategies in clinical protocols for treatment of cancer diseases with different localization. However, this therapy is usually associated with adverse side effects and specifically resistance. The discovery of new compounds for treatment of cancer diseases has become one of the most important goals in medicinal chemistry because of finding new compounds may provide a better cancer treatment.

Recent studies have been found that ethylenediamine-type ligands can induce anticancer activity in various types of cancer cell lines [1].

In the present study we observed a set of 14 compounds representing ester derivatives of (*S,S*)-ethylenediamine-*N,N'*-di-2-(3-cyclohexyl)propanoic acid, and (*S,S*)-1,3-propanediamine-*N,N'*-di-2-(3-cyclohexyl)propanoic acid (Table 1). For novel ester derivatives of (*S,S*)-ethylenediamine-*N,N'*-di-2-(3-cyclohexyl)propanoic acid it was demonstrated toxic

activity to different cell lines. Methyl, ethyl, and n-propyl esters were toxic to HL-60, REH, MOLT-4, KG-1, JVM-2, and K-562 leukemic cell lines, while the nonesterified compound and n-butyl ester were devoid of cytotoxic action. The ethyl ester exhibited the highest cytotoxic activity on leukemic cell line HL-60 (IC₅₀ in the range of 11–45 μM)

Table 1 Derivatives of ethylenediamine and 1,3-propanediamine

Compound	Empirical formula	Abbreviation	MW (g/mol) ^a	R	n	m/z
(<i>S,S</i>)-ethylenediamine- <i>N,N'</i> -di-2-(3-cyclohexyl) propanoic acid dihydrochloride	C ₂₀ H ₃₈ O ₄ N ₂ Cl ₂	EDCP	441.43	H	2	369 → 152 ^b 369 → 198 ^b
(<i>S,S</i>)- <i>O,O</i> -dimethyl - ethylenediamine- <i>N,N'</i> - di-2-(3-cyclohexyl)propanoic acid dihydrochloride	C ₂₂ H ₄₂ O ₄ N ₂ Cl ₂	DM-EDCP	469.48	CH ₃	2	397 → 212 ^b
(<i>S,S</i>)- <i>O,O</i> -diethyl-ethylenediamine- <i>N,N'</i> di-2-(3-cyclohexyl)propanoic acid dihydrochloride	C ₂₄ H ₄₆ O ₄ N ₂ Cl ₂	DE-EDCP		PATENT		
(<i>S,S</i>)- <i>O,O</i> -dipropyl-ethylenediamine- <i>N,N'</i> -di-2-(3-cyclohexyl)propanoic acid dihydrochloride	C ₂₆ H ₅₀ O ₄ N ₂ Cl ₂	DP-EDCP	525.59	C ₃ H ₇	2	453 → 240 ^b
(<i>S,S</i>)- <i>O,O</i> -dibutyl-ethylenediamine- <i>N,N'</i> -di-2-(3-cyclohexyl)propanoic acid dihydrochloride	C ₂₈ H ₅₄ O ₄ N ₂ Cl ₂	DB-EDCP	553.64	C ₄ H ₉	2	481 → 254 ^b
(<i>S,S</i>)-1,3-propanediamine- <i>N,N'</i> -di-2-(3-cyclohexyl) propanoic acid dihydrochloride	C ₂₁ H ₄₀ O ₄ N ₂ Cl ₂	PDCP	455.46	H	3	383 ^a
(<i>S,S</i>)- <i>O,O</i> -dimethyl-1,3-propanediamine- <i>N,N'</i> -di-2-(3-cyclohexyl)propanoate dihydrochloride	C ₂₃ H ₄₄ O ₄ N ₂ Cl ₂	DM-PDCP	483.51	CH ₃	3	411 ^c
(<i>S,S</i>)- <i>O,O</i> -diethyl-1,3-propanediamine- <i>N,N'</i> -di-2-(3-cyclohexyl)propanoate dihydrochloride	C ₂₅ H ₄₈ O ₄ N ₂ Cl ₂	DE-PDCP	511.56	C ₂ H ₅	3	438 ^c
(<i>S,S</i>)- <i>O,O</i> -dipropyl-1,3-propanediamine- <i>N,N'</i> -di-2-(3-cyclohexyl)propanoate dihydrochloride	C ₂₇ H ₅₂ O ₄ N ₂ Cl ₂	DP-PDCP	539.62	C ₃ H ₇	3	467 ^c
(<i>S,S</i>)- <i>O,O'</i> -dibutyl-1,3-propanediamine- <i>N,N'</i> -di-2-(3-cyclohexyl)propanoate dihydrochloride	C ₂₉ H ₅₆ O ₄ N ₂ Cl ₂	DB-PDCP	567.67	C ₄ H ₉	3	495 ^c
(<i>S,S</i>)- <i>O,O</i> -diisobutyl-1,3-propanediamine- <i>N,N'</i> -di-2-(3-cyclohexyl)propanoate dihydrochloride	C ₂₉ H ₅₆ O ₄ N ₂ Cl ₂	DIB-PDCP	567.67	C ₄ H ₉	3	523 ^c
(<i>S,S</i>)- <i>O,O</i> -di- <i>n</i> -pentyl-1,3-propanediamine- <i>N,N'</i> -di-2-(3-cyclohexyl)propanoate dihydrochloride	C ₃₁ H ₆₀ O ₄ N ₂ Cl ₂	DPE-PDCP	595.72	C ₅ H ₁₁	3	495 ^c
(<i>S,S</i>)- <i>O,O</i> -diisopentyl-1,3-propanediamine- <i>N,N'</i> -di-2-(3-cyclohexyl)propanoate dihydrochloride	C ₃₁ H ₆₀ O ₄ N ₂ Cl ₂	DIPE-PDCP	595.72	C ₅ H ₁₁	3	523 ^c

^aMW molecule weight

^bSRM selected reaction monitoring

^cSIM single ion monitoring

[2], in vitro and in vivo on melanoma [3] and in vivo on 4T1 murine breast cancer and metastasis [4]. Derivatives of 1,3-propanediamine-*N,N'*-2-(3-cyclohexyl)propanoic acid are toxic to glioma cell lines. In vitro antitumor potential were investigated for methyl, ethyl, *n*-propyl, and *n*-butyl esters of (*S,S*)-1,3-propanediamine-*N,N'*-di-2-(3-cyclohexyl)propanoic acid on several tumor cell lines: human (U251), and rat (C6) glioma, HL-60, SHSY-5Y, L929. The *n*-butyl ester (DB-PDCP) was showed the highest cytotoxic activity to glioma cells, with 24-h IC₅₀ values lower than those for cisplatin [5].

Lipophilicity of observed novel substances with cytotoxic activity was studied in previously investigation [6] but membrane permeability has not been founded. The method for in vitro prediction of passive membrane permeability that can be often used is the parallel artificial membrane permeability assay (PAMPA). This method is extensively used for the evaluation of early drug candidates. PAMPA was first introduced by Kansy et al. [7]. It is high throughput, low cost and amenable to automation. This method has been shown useful in assessing transmembrane, non-energy dependent, and diffusion of drugs in such a way that a reasonable predictability with in vivo (passive) absorption is possible.

In silico methods are very useful during investigation of novel pharmaceutical substances and development of new drug. These methods can be used for prediction pharmacokinetics proprieties, main metabolic pathways and mechanism of action. According 3R principles: reduction, replacement, refinement [8] and ICH guideline S9 on non-clinical evaluation for anticancer pharmaceuticals [9] in silico methods are proposed for selected investigation data during preclinical phase of development.

The aim of this work was discovery membrane permeability of observed substances using in vitro method. The obtained results were combined with in silico results: ADMET (absorption, distribution, metabolism, extraction and toxicity) data, prediction of the main metabolic pathways and main metabolites, and prediction of potential mechanism of action by docking methods to select and support data for future phase I of clinical study.

2 Materials and Methods

2.1 In Vitro Method—PAMPA Test

Chemicals

Investigated compounds (Table 1) were provided by the Faculty of Chemistry, University of Belgrade, Serbia. Methanol and trifluoroacetic acid (HPLC grade), ammonium acetate (CH₃COONH₄) obtained from Fluka (Sigma-Aldrich Co.) and deionized water (Gen Pure Ultrapure, Germany)

were used. Phosphoric acid (H₃PO₄), monosodium phosphate (NaH₂PO₄), and disodium phosphate (Na₂HPO₄) of analytical grade of purity were Merck (Darmstadt, Germany) products and dimethyl sulfoxide (DMSO) was produced by Sigma-Aldrich Co.) Dimethyl sulfoxide—DMSO (≥ 99.9%) was purchased from Sigma-Aldrich Co., USA.

Equipment

Analyses were performed on a UHPLC-MS system consisting of Thermo ACCELA (Thermo Scientific, Waltham, Mass., USA) UHPLC system coupled to a triple quad Mass Spectrometer Thermo TSQ Quantum Access Max (Thermo Scientific, Waltham, Mass., USA) with a heated electrospray ionization (HESI) interface. A 10 µL samples were injected into a reverse-phase Thermo Scientific Hypersil GOLD aQ column (1.9 µm, 100 mm × 2.1 mm) with guard cartridge (SecurityGuard™ ULTRA cartridges for C18 UHPLC, with 2.1 mm internal diameters (ID) Phenomenex (Værløse, Denmark). Solids were weighted by 5-digit Mettler analytical balance (Mettler-Toledo International Inc, USA). pH-Meter by pH/Ion meter MeterLab PHM240, Radiometer analytical (France) was used. Artificial membrane permeability assay (PAMPA) was carried out in hydrophobic PVDF 96-well filter plates (MultiScreen™ HTS Millipore, France).

Artificial membrane permeability assay (PAMPA)

Phosphate buffer (pH = 7.4) was prepared by dissolving NaH₂PO₄ (10.9 g) and NaH₂PO₄ (3.2 g) in water (900 ml) and adjusted with 0.1 M NaOH till pH = 7.4, and then with water till 1000 ml. The pH values of aqueous phase for shake flask method were measured with a pH-Meter with an accuracy of ±0.002. The 1% DMSO solution were prepared dissolving DMSO in phosphate buffer (v/v). Investigated substances were weighed from solid to an appropriate amount.

Donor solutions for each investigated compound were prepared dissolving 1 mg of investigated substance in 1 ml DMSO. Appropriate 50 µl of obtained solution was dissolving with phosphate buffer (pH = 7.4) in 5 ml volumetric flask to obtain final concentration 20 µM.

Acceptor solutions were 1% DMSO in phosphate buffer 7.4 (v/v).

Membrane permeability by PAMPA test was evaluated using dissolving of porcine polar brain lipid in dodecane [1% porcine polar brain lipid in dodecane (w/v)]. Each well of the donor plate was coated with membrane 5 µl solution: 1% porcine polar brain lipid in dodecane (w/v) for 60 min to completely evaporate the solvent.

Next, in each well of acceptor plate was transferred with automatic pipette 400 µl of acceptor solution and covered by

donor plate, creating a PAMPA sandwich. In each well of the donor plate was transferred by automatic pipette 300 μ l of donor solution. The filtration area was 0.28 cm². The system was incubated for 16 h (57,600 s) at room temperature. After the incubation, concentration of each investigated substance in starting solutions— $C_D(0)$, in donor solution after incubation— $C_D(t)$, and in acceptor solution after incubation— $C_A(t)$ was measured in triplicate at iso-pH conditions by UHPLC/MS method.

Chromatographic conditions and Mass spectrometric (MS) analysis

Quantitative analysis of each investigated compound in starting solutions, in solutions in donor compartments, and in solutions in acceptor compartments were done by UHPLC/MS-MS method [10]. Mobile phase A composed of ammonium acetate (5 mM)—trifluoroacetic acid (99.9:0.1, v/v) and mobile phase B composed of methanol—trifluoroacetic acid (99.9:0.1, v/v).

MS analysis was performed as selected reaction monitoring (SRM) for derivatives of 1,2-ethanediamine-*N,N'*-di-2-(3-cyclohexyl)propanoic acid and single ion monitoring (SIM) for derivatives of 1,3-propanediamine-*N,N'*-di-2-(3-cyclohexyl)propanoic acid in a positive mode. The monitored ions (*m/z*) are shown in Table 1. The spray voltage was 4000 V, temperature in the capillary was adjusted to 300 °C and vaporizer temperature set to 300 °C. Sheath gas pressure was set to 50 units, while the auxiliary valve flow rate to 10 units. MS resolution values were defined to correspond to a mass resolution of 0.7 Da. All data were acquired and processed by Xcalibur software (Thermo Fisher, San Jose, CA, USA).

Calculations of PAMPA parameters

Membrane permeability parameters percent of transport ($\%T$), retention factor (R) and apparent permeability coefficient (P_{app}) were calculated, according to following equations [11]:

$$\%T = 100 \cdot (A_R \cdot V_R) / (A_{D0} \cdot V_D) \quad (1)$$

where A_{D0} and A_R are the peak areas of the initial donor solution and the post-incubation receiving solution (from the acceptor wells), V_R and V_D are the volumes of the receiving and donor solutions.

The $\%T$ is related to P_{app} based on the following equation [11]:

$$P_{app} = (V_D \cdot V_R) / ((V_D + V_R) \cdot S \cdot t) \cdot \ln[(100 \cdot V_D) / (100 \cdot V_D - \%T(V_D + V_R))] \quad (2)$$

where S is the surface area of the artificial membrane and t is the incubation time [12, 13].

$$R = [1 - (C_D(t)/C_D(0))] - [V_A \cdot C_A(t)/V_D \cdot C_D(0)] \quad (3)$$

where V_A is the volume in the acceptor wells (ml); V_D is the volume in the donor wells (ml); $C_D(0)$ is the concentration of investigated substance in starting solutions; $C_D(t)$ is the concentration of investigated substance in donor solution after incubation; and $C_A(t)$ is the concentration of investigated substance in acceptor solution after incubation. Please note that the first paragraph of a section or subsection is not indented. The first paragraphs that follows a table, figure, equation etc. does not have an indent, either.

2.2 In Silico Methods

Metabolizer

The main metabolic pathways and potential metabolites of observed substances were performed by Metabolizer ChemAxon, 2014 [14].

ADMET

ADMET properties (absorption, distribution, metabolism, extraction and toxicity) of observed substances were calculated using ADMET Predictor v.6.5 software [15].

AutoDock Vina

The crystal structure of:

- protein kinases: P38 (PDB ID: 3HEC, 3BV2), Human raf kinase inhibitor protein (rkp) (PDB ID: 2QYQ), B-Raf Kinase V600E oncogenic mutant (PDB ID: 3OG7), Crystal Structure of human AlaRS catalytic domain with R329H mutation (PDB ID: 4XEO), Human Abl kinase domain (PDB ID: 2HYE, 3CS9, 3MS9), Structural basis for the auto-inhibition of c-Abl tyrosine kinase (PDB ID: 1OPK), Braf V600E kinase domain (PDB ID: 4R5Y) and Crystal Structure of Human AKT1 (PDB ID: 3O96);
- matrix-metalloproteases: Crystal Structure of Human ADAMTS-1 (PDB ID: 2JIH), Crystal structure of the catalytic domain of human MMP12 (PDB ID: 1RMZ), MMP9 active site (PDB ID: 1GKD, 1GKC, 5CUH), and
- Apoptosis Inducing Factor (AIF): (PDB ID: 1M6I, 4BV6).

Targets in complex with a ligand were downloaded from Protein Data Bank (PDB) [16] and after that observed complexes were used for AutoDock Vina docking protocol [17]. Target and ligand were prepared using AutoDock Tools 1.5.6 (ADT) [18] so that polar hydrogens and charges

were added, water molecules were removed from the enzyme and all possible torsions were added to the ligand. Docking grid was generated using the co-crystallized ligand at the center of the grid box, with spacing between grid points set to 1 Å. Obtained coordinates were saved in a configuration file and used for docking of the tested compounds. Nine binding modes were generated for each compound and the best pose was determined as the conformation with the highest binding affinity. To validate our docking procedure, we docked the co-crystallized ligand into the enzyme active site and calculated root mean square deviation (RMSD) value between the best ranked pose and the binding position determined by X-ray diffraction. For the calculation of RMSD and visualization of the docking results, we used the Discovery Studio Visualizer v4.1 [19].

3 Results and Discussion

3.1 In Vitro Results—PAMPA Test

In the present study, fourteen compounds (Table 1) expressing in vitro and in vivo antiproliferative activities were experimentally investigated regarding their membrane permeability. The values of percent of transport (%*T*), retention factor (*R*) and apparent permeability coefficient (P_{app}) were calculated and presented in Table 2. Additionally, negative logarithm of P_{app} ($-\log P_{app}$) was also calculated for all investigated compounds.

Regarding on the relationship between retention factor (*R*) and permeation parameter $C_A(t)/C_D(0)$ all substances can be classified into 4 groups—substances which have negligible membrane retention and low permeation (class I),

substances which have low or negligible membrane retention and high permeation (class II), substances which have high membrane retention and low permeation (class III) and substances which have high membrane retention and high permeation (class IV).

The relationship between retention factor (*R*) and permeation parameter ($C_A(t)/C_D(0)$) of investigated substances in PAMPA test is reported in Fig. 1. Most of investigated substances belong to class III (compounds which have high membrane retention and low permeation) except investigated substances EDCP, and PDCP which belong to class I (compounds which have negligible membrane retention and low permeation) and substance DIB-PDCP which belongs to class IV (high membrane retention and high permeation).

Based on reported results it can be assumed that all observed substances show high percent of membrane retention (*R*) and low values of apparent permeability coefficient (P_{app}) except DM-EDCP and DIB-PDCP.

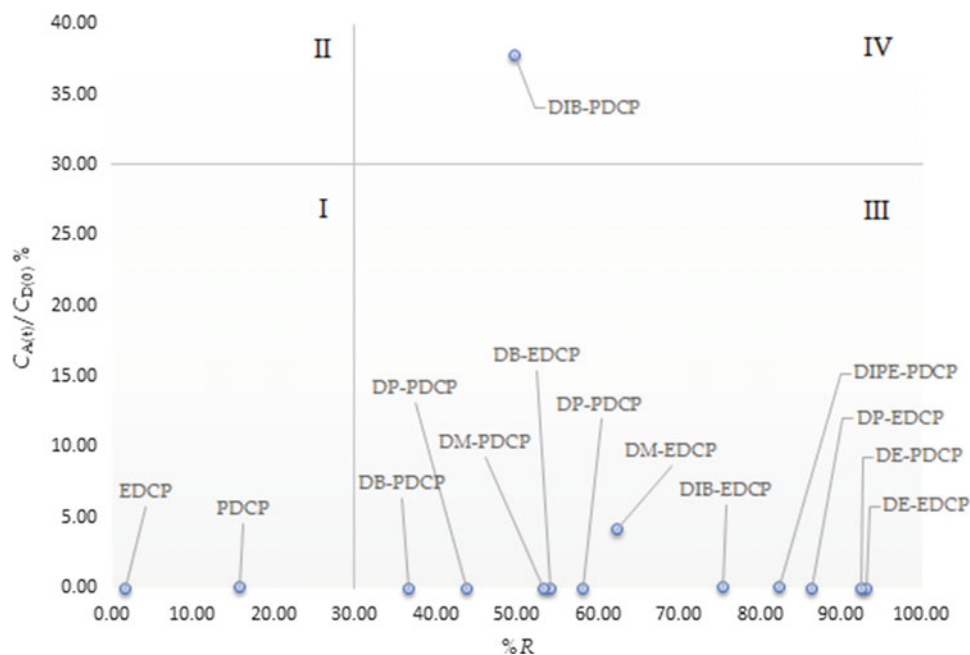
The highest values of retention factor (*R*) were obtained for diethyl ester of (*S,S*)ethylenediamine-*N,N'*-di-2-(3-cyclohexyl)propanoic acid (DE-EDCP). Likewise, this data acquired by the PAMPA test, are correlated with the results gained in the previous in vitro activity studies on various leukemic cell lines [2, 5], in vivo studies on melanoma and on 4T1 murine breast cancer and metastasis [3, 4]. For investigated acids, EDCP and PDCP, it was obtained the lowest values of membrane retention. They are the most hydrophilic and pass through the cell membrane, without retention. At the same time, EDCP and PDCP have the lowest values of antineoplastic activity [2, 5].

In previously study of lipophilicity of observed substances it can be seen that the length of alkyl chain on ester groups has influence on the lipophilicity/hydrophobicity [6].

Table 2 Calculated PAMPA parameters of tested compounds

Compound	P_{app}	$-\log P_{app}$	$CA(t)/CD(0)$	% <i>R</i>
EDCP	0.77×10^{-6}	6.11	0.01	1.59
DM-EDCP	790.00×10^{-6}	3.10	4.19	63.66
DE-EDCP	PATENT			
DP-EDCP	0	0	<0.01	86.48
DB-EDCP	0.38×10^{-6}	6.42	0.01	54.21
DIB-EDCP	3.10×10^{-6}	5.51	0.017	75.49
PDCP	10.00×10^{-6}	5.00	0.06	15.74
DM-PDCP	0	0	<0.001	53.38
DE-PDCP	0	0	<0.01	92.45
DP-PDCP	0	0	<0.01	58.25
DB-PDCP	0	0	<0.01	36.74
DIB-PDCP	$12,000.00 \times 10^{-6}$	1.92	37.75	62.25
DPE-PDCP	0	0	<0.01	43.91
DIPE-PDCP	15.00×10^{-6}	4.82	0.08	82.33

Fig. 1 The relationship between retention factor, R and permeation parameter, $C_{A(t)}/C_{D(0)}$ of examined compounds in PAMPA test



But, obtained results of membrane permeability which were presented in this paper are showed that lipophilicity of observed investigation substances is not correlated with membrane permeability completely. Also, the length of alkyl chain on esters groups have limited influence on the membrane retention (value of retention factor, R) of observed investigated compounds. Esterification of carboxyl groups causes increase of values of permeability parameters, but limited. For diethyl esters (DE-EDCP) it has been shown significantly increase of membrane retention than acid (EDCP and PDCP). However, with further length of alkyl chain on esters groups, there was no influence on increase values of retention factor, R and apparent permeability coefficient, P_{app} .

3.2 In Silico Results

In silico biopharmaceutical characterization of investigated substances, prediction of their metabolites and ADMET properties were performed by several software.

Metabolizer

Prediction of main metabolic pathways, reactions and metabolites was performed by the Metabolizer software and it was obtained that the major metabolic reactions were the hydrolyses of ester and subsequently intramolecular cyclization (lactate formation) (see Figs. 2, 3, 4 and 5).

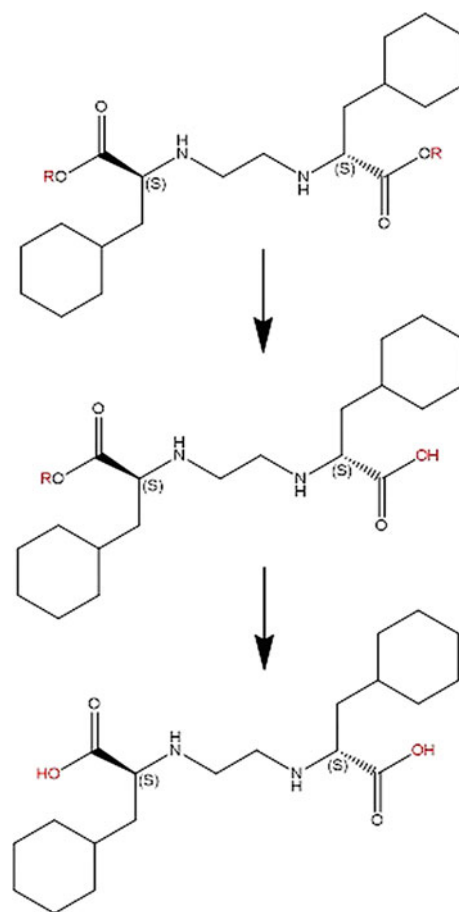


Fig. 2 Main metabolic pathway for ethylenediamine derivatives

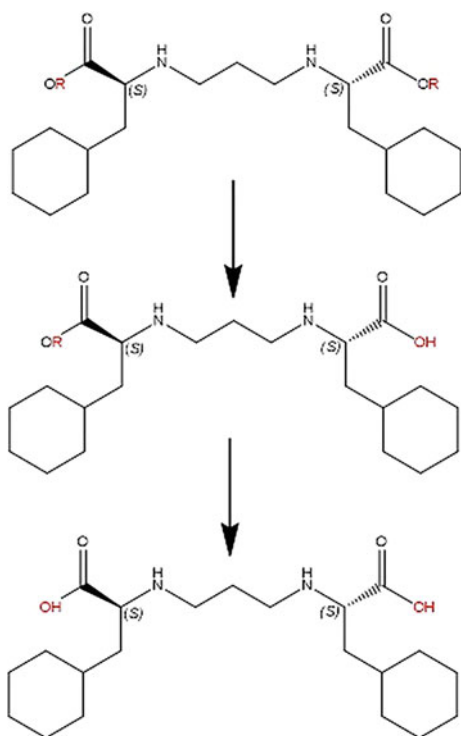


Fig. 3 Main metabolic pathway for derivatives of 1,3-propanediamine

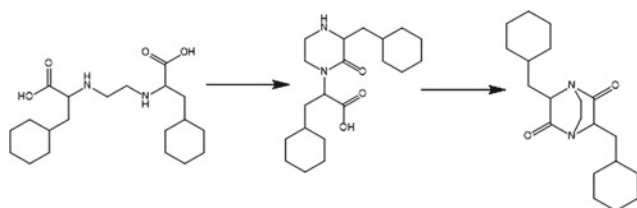


Fig. 4 Main metabolic pathway of EDCP (Lactam carboxylate)

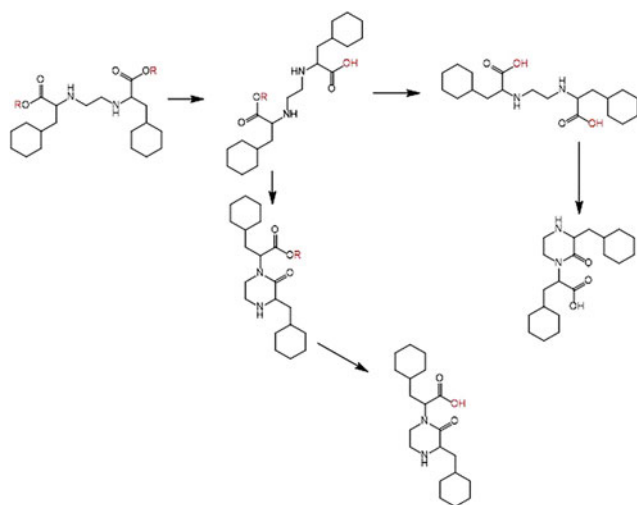


Fig. 5 Main metabolic pathway—intramolecular cyclization (lactate formation)

ADMET predictions and properties

In silico prediction of absorption, distribution, metabolism, elimination and toxicity for all the investigated substances, potential metabolites, and official drugs was performed by using the software ADMET predictor (Tables 3, 4, 5 and 6). Observed data were compared and used for final selection of the most promising drug candidates. Toxicity of investigated substances and their potential metabolites are lower than toxicity of observed official cytotoxic drugs. These data indicated that the investigated substances should have better risk-benefit ratio than observed official drugs, which is a good point respecting the main principle during assessment of a new drugs: risk-based approach.

These data are accordance with results which had demonstrated in previous studies: ability of DE-EDCP to inhibit melanoma progression in vivo without apparent toxicity to bone marrow function, as it observed no change in blood cells. Also, DE-EDCP did not show any effect on renal function, but increase in blood AST levels suggestive, but statistically insignificant of hepatocyte necrosis [3]. DE-EDCP administration exhibits respectable antiproliferative activity with fewer side-effects in comparison with official chemotherapeutics [4].

AutoDock Vina and Molecular docking study

In Table 7 it is obtained the best interaction between investigated substance and (binding affinity < -8 kcal/mol and RMSD < 2 Å). Based on these results, it can be assumed that the anti-proliferative effects of the investigated substances were realized through the multiple mechanisms. Although it can be assumed that the cytotoxic activity was realized by the acids and potential metabolites of ethylene-diamine derivatives: lactam carboxylate (see Fig. 6) and lactam alkyl esters, while the esters are probably a pro-drug substance with favourable properties to provide sufficient bioavailability at the target of action.

In previously study it was shown that DB-PDCP induced ROS production in glioma cells, leading accumulation of cells in the G_0/G_1 phase of the cell cycle, followed by caspase activation and DNA fragmentation [5]. Also, in the first report it was presented that DE-EDCP induced AIF-mediated and therefore caspase-independent human HL60 cell death [2] but after report was suggested that ability of DE-EDCP to induce apoptosis is not species-specific or cell-type specific, but already its mechanism might depend on the tumor cell type [3]. It was shown that DE-EDCP induced expression of Apaf1 [3]. These facts are accordance with obtained affinity of investigated substances on AIF in Molecular docking study and with high percent of membrane retention obtained in PAMPA study.

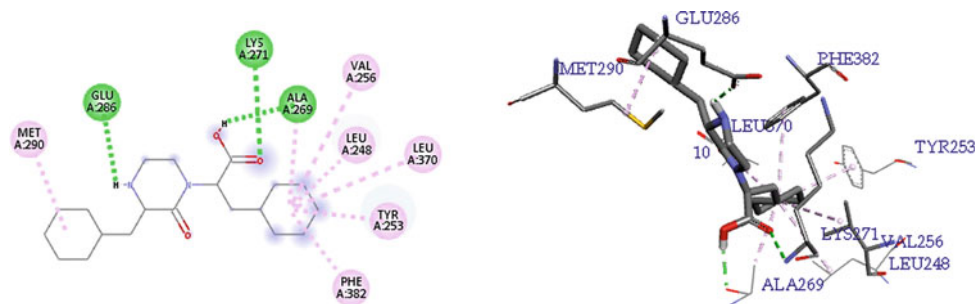


Fig. 6 Compound Lactam carboxylate docked into active site of Human Abl kinase domain (PDB ID: 2HYY). Hydrophobic alkyl and π -alkyl interactions are depicted in rose, hydrogen bond in green—2D display (left); and Compound Lactam carboxylate docked into active

site of Human Abl kinase domain (PDB ID: 2HYY). Hydrophobic alkyl and π -alkyl interactions are depicted in rose, hydrogen bond in green—3D display (right)

Table 3 Physio Chemical and biopharmaceutical values performed by using the software ADMET predictor

Compound	S+BB B_Filter	S+LogB BB	S+PrUnbnd	S+Vd	S+RBP	S + Pg p
EDCP	Low	-1.2	31.04	0.29	0.70	No
DM-EDCP	High	0.49	45.36	0.98	0.76	No
DE-EDCP	PATENT					
DP-EDCP	Low	0.46	40.83	0.84	0.76	No
DB-EDCP	Low	0.55	38.86	0.79	0.72	No
DIB-EDCP	High	0.80	36.78	1.57	0.67	Yes
PDCP	Low	-1.03	47.46	0.64	0.84	No
DM-PDCP	Low	0.46	45.49	0.8	0.74	No
DE-PDCP	Low	0.39	45.05	0.76	0.77	No
DP-PDCP	Low	0.41	41.38	0.76	0.74	No
DB-PDCP	Low	0.51	39.51	1.01	0.71	No
DIB-PDCP	High	0.75	42.31	1.41	0.65	Yes
DPE-PDCP	High	0.81	37.56	1.31	0.67	Yes
DIPE-PDCP	High	0.88	42.01	1.53	0.65	Yes
Lactam carboxylate ^a	High	-0.81	49.22	0.75	0.90	No
Lactam methylester ^b	High	0.58	48.6	0.94	0.79	No
Lactam ethylester ^c	High	0.56	48.31	1.0	0.84	No
Lactam propylester ^d	High	0.57	45.93	1.09	0.82	No
Lactam butylester ^e	High	0.61	44.53	1.06	0.79	No
Cisplatin	High	0.52	100.00	0.81	1.99	No
Carboplatin	High	0.31	100.00	0.89	1.52	No
Oxaliplatin	High	0.60	100.00	0.93	1.64	Yes
Satraplatin	High	0.89	67.47	1.66	1.07	Yes

^aPotential metabolit of EDCP; ^bPotential metabolit of DM-EDCP; ^cPotential metabolit of DE-EDCP

^dPotential metabolit of DP-EDCP; ^ePotential metabolit of DB-EDCP

S+BBB_Filter = likelihood of the Blood-Brain Barrier Penetration

S+logBBB = logarithm of the Blood-Brain partition coefficient

S+PrUnbnd = percent UNBOUND to blood plasma proteins

S+Vd = Volume of distribution (L/kg) in human at steady state

S+RBP = blood to plasma concentration ratio

S+Pg = likelihood of the P-glycoprotein efflux

Table 4 Metabolism values performed by using the software ADMET predictor

Compound	CYP_1A2_		CYP_2 A6_Su bstr	CYP_2D6_		CYP_3A4_		CYP_	
	MET_Inh	Substr		MET_Inh	Substr	MET_Inh	Substr	Risk	Code
EDCP	No (98%)	No (95%)	No	No	No (88%)	No (77%)	No (87%)	0	–
DM-EDCP	No (64%)	No (96%)	No	Yes	No (74%)	Yes (57%)	No (53%)	0	–
DE-EDCP					PATENT				
DP-EDCP	No (84%)	No (97%)	No	Yes	No (86%)	Yes (57%)	Yes (92%)	1	3A
DB-EDCP	No (88%)	No (97%)	No	Yes	No (88%)	Yes (58%)	Yes (92%)	1	3A
DIB-EDCP	No (90%)	No (98%)	No	Yes	No (88%)	Yes (60%)	Yes (91%)	3	3A, CL
PDCP	No (98%)	No (97%)	No	No	No (79%)	No (77%)	No (66%)	0	–
DM-PDCP	No (64%)	No (96%)	No	Yes	No (72%)	Yes (56%)	No (52%)	0	–
DE-PDCP	No (84%)	No (97%)	No	Yes	No (82%)	Yes (56%)	Yes (76%)	1	3A
DP-PDCP	No (84%)	No (99%)	No	Yes	No (86%)	Yes (57%)	Yes (90%)	1	3A
DB-PDCP	No (88%)	No (97%)	No	Yes	No (86%)	Yes (58%)	Yes (90%)	1	3A
DIB-PDCP	No (90%)	No (96%)	No	Yes	No (86%)	Yes (56%)	Yes (89%)	3	3A, CL
DPE-PDCP	No (88%)	No (97%)	No	Yes	No (88%)	Yes (57%)	Yes (88%)	3	3A, CL
DIPE-PDCP	No (92%)	No (96%)	No	Yes	No (86%)	Yes (58%)	Yes (92%)	3	3A, CL
Lactam carboxylate ^a	No (98%)	No (96%)	No	No	No (71%)	No (83%)	Yes (60%)	1	3A
Lactam methylester ^b	No (80%)	No (97%)	No	Yes	Yes (65%)	No (65%)	Yes (69%)	1	3A
Lactam ethylester ^c	No (98%)	No (97%)	No	Yes	Yes (67%)	No (65%)	Yes (90%)	1	3A
Lactam propylester ^d	No (98%)	No (99%)	No	Yes	No (71%)	No (63%)	Yes (95%)	1	3A
Lactam bulylester ^e	No (98%)	No (99%)	No	Yes	No (71%)	Yes (61%)	Yes (94%)	1	3A
Cisplatin	No	Yes (81%)	No	No	No (95%)	No (92%)	Yes	0	–
Carboplatin	No (98%)	Yes (81%)	No	No	No (88%)	No (92%)	Yes (98%)	1	1A
Oxaliplatin	No (98%)	Yes (61%)	Yes	No	No (84%)	No (92%)	Yes (99%)	0	–
Satraplatin	No (98%)	Yes (71%)	No	No	No	Yes (57%)	Yes (99%)	1	1A

^aPotential metabolite of EDCP; ^bPotential metabolite of DM-EDCP; ^cPotential metabolite of DE-EDCP; ^dPotential metabolite of DP-EDCP; ^ePotential metabolite of DB-EDCP

MET_1A2_Inh = Qualitative estimation of general inhibitory properties (Yes/No) against CYP1A2. Numbers in parentheses indicate confidence in prediction

CYP_1A2_Substr = Qualitative assessment of a molecule being the human CYP 1A2 substrate (Yes/No). Numbers in parentheses indicate confidence in prediction

CYP_2A6_Substr = Qualitative assessment of a molecule being the human CYP 2A6 substrate (Yes/No)

MET_2D6_Inh = Qualitative estimation of general inhibitory properties (Yes/No) against CYP2D6

CYP_2D6_Substr = Qualitative assessment of a molecule being the human CYP 2D6 substrate (Yes/No)

MET_3A4_Inh = Qualitative estimation of general inhibitory properties (Yes/No) against CYP3A4. Numbers in parentheses indicate confidence in prediction

CYP_3A4_Substr = Qualitative assessment of a molecule being the human CYP 3A4 substrate (Yes/No)

CYP_Risk = risk connected with P450 oxidation: indicates the number of potential problems a compound might have due to metabolism by or inhibition of 5 major cytochrome P450

CYP_Code-CYP_Risk rule code: 1A-high; 1A2 clearance; 3A-high; 3A4-clearance

Table 5 Toxicity values performed by using the software ADMET predictor

Compound	TOX_hERG_Filter	TOX_hERG	TOX_Risk	TOX_Code
EDCP	Nontoxic (97%)	3.94	1	Hp
DM-EDCP	Toxic (76%)	5.41	1	Hp
DE-EDCP	PATENT			
DP-EDCP	Toxic (83%)	5.72	1	Hp
DB-EDCP	Toxic (93%)	6.02	2	hE, Hp
DIB-EDCP	Toxic (94%)	6.03	2	hE, Hp
PDCP	Nontoxic (82%)	4.11	1	Hp
DM-PDCP	Toxic (80%)	5.51	1	Hp
DE-PDCP	Toxic (85%)	5.73	0	
DP-PDCP	Toxic (88%)	5.82	1	Hp
DB-PDCP	Toxic (96%)	6.12	2	hE, Hp
DIB-PDCP	Toxic (97%)	5.89	1	hE, Hp
DPE-PDCP	Toxic (94%)	6.02	2	hE, Hp
DIPE-PDCP	Toxic (96%)	6.12	2	hE, Hp
Lactam carboxylate ^a	Nontoxic (82%)	3.42	1	Hp
Lactam methylester ^b	Nontoxic (67%)	5.0	1	Hp
Lactam ethylester ^c	Nontoxic (67%)	5.16	1	Hp
Lactam propylester ^d	Nontoxic (67%)	5.22	1	Hp
Lactam butylester ^e	Toxic (71%)	5.38	1	Hp
Cisplatin	Nontoxic (98%)	4.03	3	ra, Hp, Mu
Carboplatin	Nontoxic (97%)	2.61	3	ra, Xr, Mu
Oxaliplatin	Nontoxic (97%)	2.87	3	ra, Hp, Mu
Satraplatin	Toxic (96%)	4.36	2	ra, Mu

^aPotential metabolit of EDCP; ^bPotential metabolit of DM-EDCP; ^cPotential metabolit of DE-EDCP; ^dPotential metabolit of DP-EDCP; ^ePotential metabolit of DB-EDCP

Tox_hERG_Filter = Qualitative estimation of the affinity to the hERG potassium channel in human. Numbers in parentheses indicate confidence in prediction

Tox_hERG = Affinity to the hERG potassium channel in human expressed as pIC₅₀ in mol/L

Tox_Risk-Risk connected with predicted toxicity: indicates the number of protentional toxicity problems a compound might have
Tox_Code-Tox_Risk rule code: hE-hERG inhibition; ra-acute rat toxicity; Hp-hepatotoxicity; SG-SGOT and SGPT elevation

Table 6 Full ADMET values performed by using the software ADMET predictor

Compound	ADMET_Risk	ADMET_Code
EDCP	1	Hp
DM-EDCP	1	Hp
DE-EDCP	PATENT	
DP-EDCP	2	3A, Hp
DB-EDCP	3	3A, hE, Hp
DIB-EDCP	3	3A, hE, Hp
PDCP	1	Hp
DM-PDCP	1	Hp
DE-PDCP	1	3A
DP-PDCP	2	3A, Hp
DB-PDCP	3	3A, hE, Hp

(continued)

Table 6 (continued)

Compound	ADMET_Risk	ADMET_Code
DIB-PDCP	3	3A, hE, Hp
DPE-PDCP	3	3A, hE, Hp
DIPE-PDCP	3	3A, hE, Hp
Lactam carboxylate ^a	2	3A, Hp
Lactam methylester ^b	2	3A, Hp
Lactam ethylester ^c	2	3A, Hp
Lactam propylester ^d	2	3A, Hp
Lactam butylester ^e	2	3A, Hp
Cisplatin	3	ra, Hp, Mu
Carboplatin	4	1A, ra, Xr, Mu
Oxaliplatin	3	ra, Hp, Mu
Satraplatin	3	1A, ra, Mu

^aPotential metabolit of EDCP; ^bPotential metabolit of DM-EDCP; ^cPotential metabolit of DE-EDCP

^d = potential metabolit of DP-EDCP; ^e = potential metabolit of DB-EDCP

ADMET_Code-Full ADMET Risk rules codes

1A-high 1A2 clearance

3A-high 3A4 clearance

ra-acute rat toxicity

Hp-hepatotoxicity

SG-SGOT and SGPT elevation

Table 7 Results of molecular docking study

PDB	Ligand	BA (kcal/mol)	RMSD
2HYY	Imatinib	-12.6	1.1
	PDCP	-8.7	
	EDCP	-8.5	
	DM-PDCP	-8.4	
	Lactam carboxylate	-10.3	
1OPK	Ligand	-11.1	0.9
	PDCP	-8.1	
	EDCP	-8.1	
	Lactam carboxylate	-9.0	
3CS9	Nilotinib	-14.6	0.2
	PDCP	-9.2	
	DIB-PDCP	-8.9	
	Lactam carboxylate	-9.1	
3MS9	Imatinib	-14.0	0.3
	PDCP	-8.7	
	DM-PDCP	-8.7	
	Lactam carboxylate	-10.2	
4R5Y	Ligand	-14.1	0.4
	DIPE-PDCP	-8.2	
3O96	Ligand	-14.3	0.4
	DIB-EDCP	-8.7	
	Lactam isobutylester	-9.9	

(continued)

Table 7 (continued)

PDB	Ligand	BA (kcal/mol)	RMSD
3HEC	Imatinib	-12.2	1.9
	PDCP	-8.2	
	DE-EDCP	PATENT	
	DIB-PDCP	-8.1	
3BV2	Ligand	-14.8	0.5
	DM-PDCP	-8.3	
	DIB-PDCP	-8.3	
2QYQ	Ligand	-7.0	1.9
	EDCP	-7.1	
	PDCP/DP-PDCP	-7.0	
	Lactam methylester	-7.7	
	Lactam carboxylate	-7.6	
3OG7	Ligand	-11.5	0.4
	DIB-PDCP	-8.7	
	DIPE-PDCP	-8.6	
4XEO	Idelalisib	-10.8	1.2
	DIB-EDCP	-8.6	
	EDCP	-8.7	
	Lactam isobutylester	-9.9	
2JIH	Marimastat	-7.6	1.9
	EDCP	-8.7	
	PDCP	-8.6	
1RMZ	Ligand	-5.2	1.2
	EDCP	-8.7	
	PDCP	-8.5	
	Lactam carboxylate	-9.8	
1GKD	Ligand	-6.8	1.1
	EDCP	-8.5	
1GKC	Ligand	-7.0	1.6
	PDCP	-8.8	
	EDCP	-8.4	
5CUH	Ligand	-9.9	1.2
	PDCP	-9.2	
	EDCP	-8.7	
1M6I	Ligand	-14.6	0.6
	DIB-EDCP	-8.7	
	Lactam isobutylester	-9.2	
4BV6	Ligand	-14.5	0.8
	PDCP	-8.4	
	DIPE-PDCP	-8.5	
	Lactam isobutylester	-9.8	

BA binding affinity

RMSD root mean square deviation

Behind of obtained results, in presented Molecular study it was shown good affinity for protein kinases which are important molecules within signal pathway of cell proliferation.

4 Conclusion

Based on the results of this work, it can be proposed there to be investigated the existence of the metabolites: lactam carboxylate and lactam alkyl esters in biological materials. It can be assumed that lactam carboxylate and lactam alkyl esters are biologically active forms.

These results refer to the hypothesis that the retention in cell membrane is particularly important for cytotoxic activity of investigated substances. Also, the mechanism(s) of their cytotoxic activity may be at the level of cell membrane, mitochondrial membrane, or at the level of transmembrane receptors.

References

- Musiliyu, M., Veera, B., Lekan, L.: Cytotoxic activity of N, N'-Bis (2-hydroxybenzyl) ethylenediamine derivatives in human cancer cell lines. *Anticancer Res.* **34**, 16011608 (2014)
- Misirlic, Dencic S., Poljarevic, J., Vilimanovich, U., Bogdanovic, A., Isakovic, A.J., Kravic, Stevovic T., Dulovic, M., Zogovic, N., Isakovic, A.M., Grguric-Sipka, S., Bumbasirevic, V., Sabo, T., Trajkovic, V., Markovic, I.: Cyclohexyl analogues of ethylenediamine dipropanoic acid induce caspase-independent mitochondrial apoptosis in human leukemic cells. *Chem. Res. Toxicol.* **25**, 931–939 (2012)
- Isakovic, A., Petricevic, A., Ristic, S., Popadic, D., Kravic-Stevovic, T., Zogovic, N., Poljarevice, J., Zivanovic Radnic, T., Sabo, T., Isakovic, A., Markovic, I., Trajkovic, V., Misirlic-Dencic, S.: In vitro and in vivo antimelanoma effect of ethyl ester cyclohexyl analog of ethylenediamine dipropanoic acid. *Melanoma Res.* **28**(1), 8–20 (2018)
- Jurisevic, M., Arsenijevic, A., Pantic, J., Gajovic, N., Milovanovic, J., Milovanovic, M., Poljarevic, J., Sabo, T., Vojvodic, D., Radosavljevic, GD., Arsenijevic, N.: The organic ester O,O'-diethyl-(S,S)-ethylenediamine-N,N'-di-2-(3-cyclohexyl)propanoate dihydrochloride attenuates murine breast cancer growth and metastasis. *Oncotarget.* **15**:9(46), 28195–28212 (2018)
- Savić, A., Misirlić-Denčić, S., Dulović, M., Mihajlović-Lalić, L.E., Jovanović, M., Grgurić-Sipka, S., Marković, I., Sabo, T.J.: Synthesis, characterization and ROS-mediated cytotoxic action of novel (S,S)-1, 3-propanediamine-N,N'-di-2-(3-cyclohexyl) propanoic acid and corresponding esters. *Bioorg. Chem.* **54**, 73–80 (2014)
- Tubić, B., Marković, B., Vladimirov, S., Savić, A., Poljarević, J., Sabo, T.: A new model to determine lipophilicity of 1,2-ethanediamine-N, N'-di-2-(3-cyclohexyl)propanoic acid and 1,3-propanediamine-N, N'-di-2-(3-cyclohexyl)propanoic acid derivatives with antiproliferative activity by combining shake flask procedure and UHPLC-MS method. *Pharmazie* **72**, 317–323 (2017)
- Kansy, M., Senner, F., Gubernator, K.: Physicochemical high throughput screening: parallel artificial membrane permeation assay in the description of passive absorption processes. *J. Med. Chem.* **41**, 1007–1010 (1998)
- Russell, W.M.S., Burch, R.L., Hume, C.W.: *The principles of humane experimental technique.* Johns Hopkins University, Methuen & Co.: London (1959)
- ICH: Homepage <http://www.ich.org/products/guidelines/safety/safety-single/article/nonclinical-evaluation-for-anticancer-pharmaceuticals.html>. Last accessed 16 Nov 2018
- Tubić, B., Marković, B., Vladimirov, S., Ristić, S., Ivković, B., Savić, M., Poljarević, J., Sabo, T.: Highly sensitive UHPLC-MS/MS method for quantification of ethylenediamineN, N'-di-2-(3-cyclohexyl) propanoic acid derivatives in mouse serum. *Acta Chromatographica* **2**(29), 235–252 (2017)
- Zhu, C., Jiang, L., Chen, T.M., Hwang, K.K.: A comparative study of artificial membrane permeability assay for high throughput profiling of drug absorption potential. *Eur. J. Med. Chem.* **37**, 399–407 (2002)
- Markovic, B.D., Vladimirov, S.M., Cudina, O.A., Odovic, J.V., Karljikovic-Rajic, K.D.: A PAMPA assay as fast predictive model of passive human skin permeability of new synthesized corticosteroid C-21 esters. *Molecules* **17**, 480–491 (2012)
- Liu, H., Sabus, C., Carter, G.T., Du, C., Avdeef, A., Tischler, M.: In vitro permeability of poorly aqueous soluble compounds using different solubilizers in the PAMPA assay with liquid chromatography/mass spectrometry detection. *Pharm. Res.* **20**, 18201826 (2003)
- Metabolizer ChemAxon, 2014, <http://www.chemaxon.com> last accessed 2017/11/26
- ADMET Predictor v.6.5: Simulations Plus, Inc. 42505 10th Street West, Lancaster, California 93534-7059 USA, 2013, <http://www.simulations-plus.com/>. Last accessed 26 Nov 2017
- Bernstein, F.C., Koetzle, T.F., Williams, G.J., Meyer Jr., E.F., Brice, M.D., Rodgers, J.R., Kennard, O., Shimanouchi, T., Tasumi, M.: The Protein Data Bank: a computer-based archival file for macromolecular structures. *J. Mol. Biol.* **112**, 535–542 (1977)
- Trott, O., Olson, A.J.: AutoDock Vina: Improving the speed and accuracy of docking with a new scoring function, efficient optimization, and multithreading. *J. Comput. Chem.* **31**, 455–461 (2010)
- Morris, G.M., Huey, R., Lindstrom, W., Sanner, M.F., Belew, R. K., Goodsell, D.S., Olson, A.J.: AutoDock4 and AutoDockTools4: Automated docking with selective receptor flexibility. *J. Comput. Chem.* **30**, 2785–2791 (2009)
- Discovery Studio Visualizer 4.1.0.14169. Accelrys Inc., San Diego, USA, 2014; software available at <http://accelrys.com>. Last accessed 2017/11/26

Analysis of miRNA Targets in Correlation to Neurodevelopment and Diagnosis of Autism Spectrum Disorder (ASD)

Emir Šehović, Lemana Spahić, Ajla Kulaglič, Lejla Smajlović-Skenderagić, and Aida Hajdarpašić-Saračević

Abstract

Autism Spectrum Disorder (ASD) is a broad spectrum of disorders which manifests itself through number of different phenotypes including those affecting communication and behavior. Our aim was to investigate small non coding RNA molecules, miRNAs, and their effect on target genes involved in neurodevelopment and ASD. In addition, we performed our study by investigating selected miRNAs as potential biomarkers for diagnosing children with ASD. MiRNAs selected for this study are found in saliva samples; therefore, sampling is non-invasive and very attractive diagnostic tool for ASD. Children diagnosed at an early stage of life would have the most benefit from an early intervention. We have identified 7 target genes of miRNAs suspected to be involved in ASD through an in silico analysis. We have found negative regulatory interactions between differentially expressed miRNAs and putative targets in ASD. The seven genes found through this study are all connected to neurodevelopmental functions and processes. Malfunction of some or all of these genes is found in connection to ASD and/or other neurodevelopmental disorders. The following 7 genes were found as best candidate genes of miRNAs studied: MAPK10, KCNMA1, DST, ZBTB20, GAS7, NTRK2 and SCN2A.

Keywords

Neurodevelopment • miRNA • Gene • Autism spectrum disorder (ASD)

1 Introduction

Autism spectrum disorder (ASD) is a broad spectrum of disorders ranging from mild to severe forms. It presents a combination of multiple neurodevelopmental deficiencies including lack of communication and socialization combined with restrictive and repetitive actions [1]. Current medicine does not use any laboratory tests, in form of biomarkers to diagnose ASD, they use psychological and physician's evaluations to diagnose children with ASD [2]. The fact that every diagnosis is based on observation only, makes ASD remarkably interesting in the field of biomarker studies. One group of such biomarkers can be found in human saliva and are defined as brain related miR-NAs. The advantage that makes miRNAs so attractive for diagnosis is the fact that miRNA biomarkers screening can be performed immediately after birth, non-invasively and therapy and intervention for a potential disorder can be immediately established.

Epigenetic regulation of gene expression is a prominent mechanism that governs a lot of processes in the human body [3]. One of those processes is neurodevelopment which is partially controlled by a specialized group of RNAs termed micro RNAs [4, 5]. miRNAs are regulators of multiple processes in cells some of which are apoptosis, cellular differentiation and metabolism [6]. In addition, they interfere with gene expression by selectively targeting mRNAs 3' untranslated region (UTR), thereby blocking its translation into protein. Many stages of neurodevelopment are controlled by miRNAs fine-tuning and some of them are: cell fate determination, neurogenesis, gliogenesis, neuronal cell-type determination, migration, neuronal polarization and synapse development [7]. Ideal miRNAs for ASD diagnostic

Emir Šehović and Lemana Spahić—The authors have contributed equally to the paper.

E. Šehović · L. Spahić · L. Smajlović-Skenderagić (✉)
International Burch University Sarajevo, Francuske revolucije bb,
71210 Ilidža, Sarajevo, Bosnia and Herzegovina
e-mail: l.smajlovic.skenderagic@ibu.edu.ba

E. Šehović
e-mail: emir.sehovic@stu.ibu.edu.ba

L. Spahić
e-mail: lemana.spahic@stu.ibu.edu.ba

A. Kulaglič · A. Hajdarpašić-Saračević
Sarajevo School of Science and Technology, Hrasnička cesta 3a,
71210 Ilidža, Sarajevo, Bosnia and Herzegovina
e-mail: aida.saracevic@ssst.edu.ba

panel would be: expressed in the brain, functionally related to neurodevelopment, easily measured from the peripheral samples and they should have different expression patterns in ASD individuals when compared to typical individuals. All of these are the features of miRNAs that will be analyzed in this paper [7]. This specific panel of RNAs was proposed by Hicks et al. in 2016 [8]. Their research about miRNA expression in saliva has shown that 14 miRNAs (miR-75p, miR-23a-3p, miR-27a-3p, miR-28-5p, miR-30e-5p, miR-32-5p, miR-127-3p, miR-140-3p, miR-191-5p, miR-218-5p, miR-355-3p, miR-628-5p, miR-2467-5p, miR-3529-3p) previously shown to be related to brain development, were differentially expressed in ASD compared to typically developing children and most of them showing significant correlation to Vineland neurodevelopmental scores [8]. Therefore, salivary miRNA profiles could be used to identify children with ASD but also to correlate with adaptive behavior and implicate ASD candidate genes involved in neurodevelopment [8].

miR-7-5p is involved in gene silencing and negative regulation of sprouting angiogenesis and is the first of 14 miRNAs investigated. It enables mRNA binding involved in posttranscriptional gene silencing and is part of extracellular space [9, 10]. The second miRNA investigated is miR-23a-3p involved in gene silencing, cellular response to vascular endothelial growth factor stimulus, negative regulation of vascular permeability, cell growth involved in cardiac muscle cell development and positive regulation of ERK1 and ERK2 cascade [11, 12]. Next is miR-27a-3p involved in negative regulation of low-density lipoprotein particle clearance, gene silencing, miRNA mediated inhibition of translation, cellular response to vascular endothelial growth factor stimulus, NIK/NF-kappaB signaling and positive regulation of transcription [13, 14]. miR-28-5p is involved in miRNA mediated translation inhibition [15, 16]. It enables mRNA binding involved in posttranscriptional gene silencing and is a part of extracellular space [15, 16]. miR-30e-5p is involved in gene silencing, negative regulation of cardiac muscle cell apoptosis, negative regulation of heart contraction, downregulation of vascular endothelial cell proliferation, negative regulation of endothelial apoptosis and various other processes involved in cardiac muscle control. It enables posttranscriptional silencing and is part of extracellular space [17–19]. miR-32-5p promotes cell proliferation, migration and suppresses apoptosis in breast cancer while inhibiting proliferation and invasion in gastric cancer cell lines [20, 21]. miR-127-3p is cloned from neuroblastoma and known to be a gene expression regulator in this cancer [22]. miR-140-3p enables RNA polymerase II complex binding [23]. miR-191-5p is involved in gene silencing [24, 25]. miR-218-5p is involved in negative regulation of cell migration, proliferation, MAPK activity and

collagen biosynthesis, gene silencing and translation inhibition [26–28]. miR-355-3p is involved in copurification with polyribosomes in mammalian neurons and small RNAs in human cervical cancer [29, 30]. miR-628-5p is involved in direct conversion of fibroblasts to neurons, osteoblast differentiation, colorectal cancer miRNAome and various other processes [31–34]. miR-3529-3p is identified in primary giant congenital nerves in cell line and various other cell lines [35].

This panel of miRNAs, described above, has various effects on different cellular processes and subsequently potential impact on development and health. What proteins these miRNAs regulate, their mode of action and how they impact cellular processes will be discussed next. The focus will be on genes found to be involved in neurodevelopment and highest impact on ASD development.

AUTS2 (Activator of transcription and developmental regulator) gene was found to be correlated to neurodevelopment. It influences neurological disorders, such as ASD, and other developmental disabilities [36]. Mutations occurring in this AUTS2 gene can influence a variety of non-neurological disorders. It is mostly expressed in salivary gland and has molecular functions in chromatin and protein binding [37]. Main processes it is involved in are actin cytoskeleton reorganization, axon extension, dendrite extension, neuron migration, histone methylation, Rac protein signal transduction, histone acetylation, RNA polymerase II transcription regulation [38–40].

MTHFR (methylenetetrahydrofolate reductase) gene encodes a protein that plays a key role as a catalyst in homocysteine remethylation into methionine [41]. Mutations in this gene influence the vascular system, neural tube, colon cancer, leukemia, and consequently the deficiency in methylenetetrahydrofolate reductase [41]. It is mostly expressed in lung and thyroid gland [42]. Main processes it is involved in, other than MTHFR reduction are FAD, NAD, modified amino acid and protein containing complex binding [43]. It is involved in a wide spectrum of metabolic processes, and responses to vitamins. MTHFR is found also to be a component of cytosol and synapses [44].

APOE (Apolipoprotein E) is a gene that encodes a major apolipoprotein constituent of the chylomicron [45]. The protein itself is essential for trygliceride rich lipoproteins, as it binds to specific liver and peripheral cell receptors. In addition to APOE there are C1 and C APO genes, and mutations in these genes lead to increased plasma cholesterol and tryglicerides [46]. As an important factor in lipid metabolism and protein dimerization, APOE plays a great role in maintenance of homeostasis. It is involved in the majority of the most prominent signaling pathways, such as GPCR signaling, cGMP mediated signaling [47, 48]. APOE is found to be involved in late-onset Alzheimer's disease [49].

2 Materials and Methods

Potential target genes for each of the 14 miRNAs of interest were predicted using the mirWALK database [50]. Number of different target sites within mRNAs from each gene targeted by one or more of the 14 miRNAs were counted. In other words, it is the number of different target sites that one mRNA from a certain gene for each miRNA contains. Furthermore, the common genes targeted by 14 miRNAs were also counted. Genes of interest were sorted by the number of unique target sites for each miRNA as well as the number of unique miRNAs it is targeted by (within 14 miRNAs of interest). For the purpose of determining function and interaction of targeted genes between each other as well as with other relevant genes, genemania [51] database was used. The main interactions analyzed were Co-expression, Genetic interactions and Shared Protein Domains. Genes are linked if their expression levels are similar across conditions in a gene expression study, for example if they are functionally associated, if the effects of perturbing one gene were found to be modified by perturbations of a second gene, or if they share the same protein domains.

Genes which are involved in neurodevelopmental functions or pathways were selected for an in-depth analysis. Target genes were analyzed for each individual miRNA. Genes which had an average of 7 or more predicted target sites and were targeted by at least 13 miRNAs were selected for further analysis.

3 Results

Genes which are targeted by all 14 miRNAs and have more than 7 predicted target sites are: MAPK10, KCNMA1 and DST. The full predicted target site number for each respective miRNA for the three selected genes can be seen in Table 1.

Second group of selected genes which are targeted by 13 miRNAs and have more than 7 predicted target sites are: ZBTB20, GAS7, NTRK2 and SCN2A. The full predicted target site number for each respective miRNA for the four selected genes can be seen in Table 2.

Out of seven genes presented in Tables 1 and 2, the gene with the largest number of average predicted target sites is MAPK10 gene (41,42) followed by KCNMA1 (21,42). Furthermore, miRNA with the largest average number of predicted target sites per gene found in Table 1 is miR-28-5p. In addition, miR-28-5p has the largest average number of predicted target sites per gene found, Table 2. MAPK10, KCNMA1 and ZBTB20 are found within the first 20 genes based on the number of target sites in 11, 11 and 5 miRNAs respectively.

Table 1 Numbers of predicted target sites for genes targeted by all 14 miRNAs

	MAPK10	KCNMA1	DST	Average
miR-7-5p	34	21	1	18.67
miR-23a-3p	14	44	11	23
miR-27a-3p	41	19	6	22
miR-28-5p	97	39	8	48
miR-30e-5p	37	21	3	20.33
miR-32-5p	31	11	10	17.33
miR-127-3p	68	45	7	40
miR-140-3p	57	24	7	29.33
miR-191-5p	35	1	1	12.33
miR-218-5p	35	16	7	19.33
miR-335-3p	5	16	13	11.33
miR-628-5p	26	1	5	10.67
miR-2467-5p	86	28	16	43.33
miR-3529-3p	14	14	5	11

Table 2 Number of predicted target sites for genes targeted with 13 miRNAs

	ZBTB20	GAS7	NTRK2	SCN2A	Average
miR-7-5p	7	6	14	10	9.25
miR-23a-3p	22	18	7	5	13
miR-27a-3p	12	11	5	4	8
miR-28-5p	21	13	11	12	14.25
miR-30e-5p	0	6	0	3	2.25
miR-32-5p	4	0	2	9	3.75
miR-127-3p	14	3	13	7	9.25
miR-140-3p	17	11	12	11	12.75
miR-191-5p	9	16	4	4	8.25
miR-218-5p	9	18	4	0	7.75
miR-335-3p	26	12	9	8	13.75
miR-628-5p	16	6	4	7	8.25
miR-2467-5p	9	6	9	13	9.25
miR-3529-3p	13	6	6	7	8

The interaction of the 7 analyzed genes is visualized in Fig. 1. Three main interactions displayed within the figure are: co-expression, shared protein domains and genetic interactions. According to our results there is an overall 94.16% co-expression between the analyzed genes. The overall genetic interaction magnitude is at 1.05% while there are 4.79% shared protein domains. The following genes KCNMA1 and SCN2A have the same protein domain. Out of the seven analyzed genes MAPK10 coexpresses with SCN2A, DST and NTRK2. KCNMA1 does not co-express

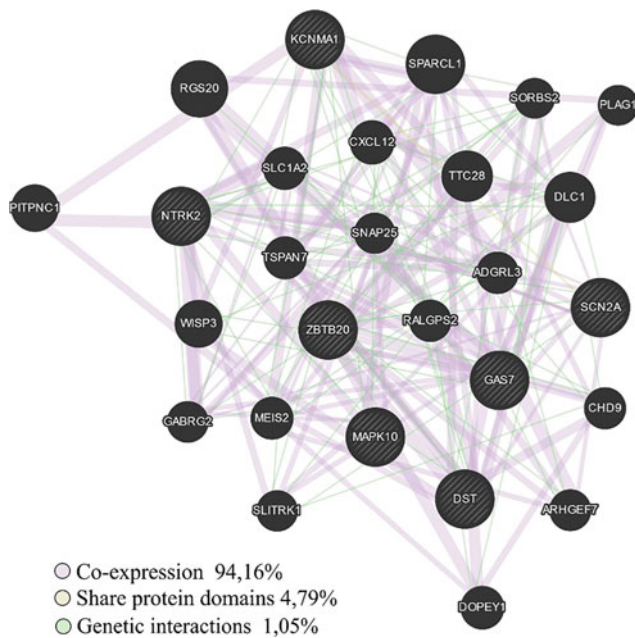


Fig. 1 Interactions among 7 analyzed genes

with any of the other six analyzed genes while *DST* co-expresses with *ZBTB20* and *SCN2A*. *ZBTB20* co-expresses with *DST* and *GAS7* while *NTRK2* co-expresses with *SCN2A* and *MAPK10*.

MAPK10, *KCNMA1* and *DST* have been shown to have genetic interactions. *NTRK2* also has genetic interaction with *MAPK10* and *KCNMA1* but not with *DST*. *ZBTB20* has genetic interactions with *DST* and *SCN2A*.

4 Discussion

In this study, expression profiles of miRNAs and their target mRNAs in correlation to developmental disorders, more specifically autism spectrum disorders (ASD) were evaluated. The study was based on a panel of miRNAs previously described and published [52] in correlation to miRNA detection as biomarkers of ASD in children. Moreover, altered expression of both miRNAs and mRNAs in correlation to brain development and function was found [53].

Target genes of dysregulated miRNAs through in silico analysis and negative regulatory interactions between differentially expressed miRNAs and their putative targets in ASD were identified. The seven genes found through this study are all connected to neurodevelopmental functions and processes. Malfunction of some or all genes is connected to ASD or other neurodevelopmental disorder.

MAPK10 is a gene that encodes proteins from MAP kinase family that are important actors in multiple signaling pathways and therefore influence a lot of cellular processes

ranging from proliferation, to transcription regulation and development. *MAPK10* is activated by threonine and tyrosine phosphorylation [54]. This kinase is specific for neurons in the nervous system and its deletion is connected to neuronal apoptosis [55]. *ZBTB20* (Zinc finger and BTB domain containing 20) belongs to a family of transcription factors with N terminal BTB/POZ domain and DNA-binding zinc finger domain on C terminus [56]. This gene is a transcriptional repressor and functions in neurogenesis, glucose homeostasis and postnatal growth [57–59]. Mutations that happen in *ZBTB20* lead to Primrose syndrome [60]. Main processes in which *ZBTB20* is involved in are cellular response to glucose stimulus, lipid homeostasis, and regulation of interleukin and TNF production [61]. *GAS7* (Growth arrest-specific 7) is a gene expressed mostly in brain cells that are fully differentiated and in mature cerebellar Purkinje fiber neurons [62]. It is found that *GAS7* is an important factor for neurodevelopment and affects brain function and neuropsychiatric disorders [63]. *NTRK2* is a membrane bound receptor which acts as a part of MAPK signaling pathway [64]. Main process regulated by this gene is cellular differentiation, ATP binding, brain-derived neurotrophic binding. *NTRK2* expression levels are found to be decreased in males with ASD [65]. *SCN2A* (sodium voltage-gated channel alpha subunit 2) is a member of a glycoprotein complex within voltage-gated sodium channels that function mainly in action potential propagation across muscles and neurons [66]. Some variants of the gene are associated with ASD development and seizure disorders [67]. *DST* (dystonin) gene is a member of adhesion junction plaque protein family mostly expressed in neurons and muscles. The main functions are actin binding, calcium ion binding and cytoskeletal filaments binding [68, 69]. A breakage in chromosome 7 can cause an interruption in dystonin and therefore a different protein product that can cause autism and mental retardation [70]. In addition, previous studies have shown that the dysregulation of calcium channels play a significant role in the ASD. One such gene found directly correlated came from a study performed in 2004 on *CACNA1C* gene which was found to be associated with Timothy syndrome (a syndromic autism) [71]. In vivo, deletion of the *KCNMA1* gene profoundly alters cerebellar function in mice which show an abnormal conditioned eye blink response, abnormal locomotion and pronounced lack of coordination [72].

All seven genes found as gene targets of 14 miRNAs panel are heavily involved in a number of cellular processes and neurodevelopment. All the evidence points to the fact that miRNAs isolated from the saliva, which target genes involved in neurodevelopment could be potential markers of ASD. Collecting saliva sample is a non-invasive method which would greatly decrease stress for children with ASD

during collection process. Therefore, children can be diagnosed at a very early age thus making it possible for diagnosed children to benefit from an early intervention.

5 Conclusion

An *in silico* analysis of the evidence which supports the hypothesis that previously proposed panel of 14 miRNAs may be used for ASD diagnosis was performed. An overwhelming body of evidence that these 14 miRNAs do indeed regulate various genes involved in developmental processes was found. Therefore, their detection in the saliva could potentially lead to development of biomarkers of developmental disorders such as ASD. This hypothesis has to be further tested on a large cohort of individuals with ASD and other developmental disorders (DD) in order to further confirm its usefulness in distinguishing between DD and ASD. The next study will include a comparative analysis of children with ASD, DD and typically developing children in order to determine if this method can indeed be used for diagnostic purposes. New discoveries in this field will certainly help clinicians improve current diagnosis and time table between diagnosing children and providing intervention.

References

- Vasu, M.M., Anitha, A., Thanseem, I., Suzuki, K., Yamada, K., Takahashi, T., Wakuda, T., Iwata, K., Tsujii, M., Sugiyama, T., Mori, N.: Serum microRNA profiles in children with autism. *Mol. Autism* **5**(1), 40 (2014)
- Galiana-Simal, A., Muñoz-Martinez, V., Calero-Bueno, P., Vela-Romero, M., Beato-Fernandez, L.: Towards a future molecular diagnosis of autism: recent advances in biomarkers research from saliva samples. *Int. J. Dev. Neurosci.* **67**, 1–5 (2018)
- Gaudet, P., Livstone, M.S., Lewis, S.E., Thomas, P.D.: Phylogenetic-based propagation of functional annotations within the Gene Ontology consortium. *Brief. Bioinform.* **12**(5), 449–462 (2011)
- Kim, J., Krichevsky, A., Grad, Y., Hayes, G.D., Kosik, K.S., Church, G.M., Ruvkun, G.: Identification of many microRNAs that copurify with polyribosomes in mammalian neurons. *Proc. Natl. Acad. Sci.* **101**(1), 360–365 (2004)
- Cummins, J.M., He, Y., Leary, R.J., Pagliarini, R., Diaz, L.A., Sjoblom, T., Barad, O., Bentwich, Z., Szafranska, A.E., Labourier, E., Raymond, C.K.: The colorectal microRNAome. *Proc. Nat. Acad. Sci.* **103**(10), 3687–3692 (2006)
- Xue, Y., Ouyang, K., Huang, J., Zhou, Y., Ouyang, H., Li, H., Wang, G., Wu, Q., Wei, C., Bi, Y., Jiang, L.: Direct conversion of fibroblasts to neurons by reprogramming PTB-regulated microRNA circuits. *Cell* **152**(1), 82–96 (2013)
- Chen, H., Ji, X., She, F., Gao, Y., Tang, P.: miR-628-3p regulates osteoblast differentiation by targeting RUNX2: possible role in atrophic non-union. *Int. J. Mol. Med.* **39**(2), 279–286 (2017)
- Hicks, S.D., Ignacio, C., Gentile, K., Middleton, F.A.: Salivary miRNA profiles identify children with autism spectrum disorder, correlate with adaptive behavior, and implicate ASD candidate genes involved in neurodevelopment. *BMC Pediatr.* **16**(1), 52 (2016)
- Stark, M.S., Tyagi, S., Nancarrow, D.J., Boyle, G.M., Cook, A.L., Whiteman, D.C., Parsons, P.G., Schmidt, C., Sturm, R.A., Hayward, N.K.: Characterization of the melanoma miRNAome by deep sequencing. *PloS one* **5**(3), e9685 (2010)
- Dweep, H., et al.: miRWalk—database: prediction of possible miRNA binding sites by “walking” the genes of 3 genomes. *J. Biomed. Inform.* **44**, 839–847 (2011)
- Sagane, K., Sugimoto, H., Akaike, A.: Biological characterization of ADAM22 variants reveals the importance of a disintegrin domain sequence in cell surface expression. *J. Recept. Sig. Transduct.* **30**(2), 72–77 (2010)
- Grotto, S., Drouin-Garraud, V., Öunap, K., Puusepp-Benazzouz, H., Schuurs-Hoeijmakers, J., Le Meur, N., et al.: Clinical assessment of five patients with BRWD3 mutation at Xq21. 1 gives further evidence for mild to moderate intellectual disability and macrocephaly. *Eur. J. Med. Genet.* **57**(5), 200–206 (2014)
- Manganelli, F., Parisi, S., Nolano, M., Tao, F., Paladino, S., Pisciotta, C., et al.: Novel mutations in dystonin provide clues to the pathomechanisms of HSAN-VI. *Neurology* **88**(22), 2132–2140 (2017)
- Makrythanasis, P., Guipponi, M., Santoni, F.A., Zaki, M., Issa, M.Y., Ansar, M., et al.: Exome sequencing discloses KALRN homozygous variant as likely cause of intellectual disability and short stature in a consanguineous pedigree. *Hum. Genomics* **10**(1), 26 (2016)
- Kshatri, A.S., Gonzalez-Hernandez, A.J., Giraldez, T.: Functional validation of Ca²⁺-binding residues from the crystal structure of the BK ion channel. *Biochim. Biophys. Acta (BBA)-Biomembr.* **1860**(4), 943–952 (2018)
- Yoshida, S., Harada, H., Nagai, H., Fukino, K., Teramoto, A., Emi, M.: Head-to-head juxtaposition of Fas-associated phosphatase-1 (FAP-1) and c-Jun NH2-terminal kinase 3 (JNK3) genes: genomic structure and seven polymorphisms of the FAP-1 gene. *J. Hum. Genet.* **47**(11), 614 (2002)
- McGregor, L.M., Baylin, S.B., Griffin, C.A., Hawkins, A.L., Nelkin, B.D.: Molecular cloning of the cDNA for human TrkC (NTRK3), chromosomal assignment, and evidence for a splice variant. *Genomics* **22**(2), 267–272 (1994)
- Buyse, I.M., Shao, G., Huang, S.: The retinoblastoma protein binds to RIZ, a zincfinger protein that shares an epitope with the adenovirus E1A protein. *Proc. Natl. Acad. Sci.* **92**(10), 4467–4471 (1995)
- Wolfson, R.L., Chantranupong, L., Wyant, G.A., Gu, X., Orozco, J.M., Shen, K., Condon, K.J., Petri, S., Kedir, J., Scaria, S.M., Abu-Remaileh, M.: KICSTOR recruits GATOR1 to the lysosome and is necessary for nutrients to regulate mTORC1. *Nature* **543**(7645), 438 (2017)
- Jones, M.H., Furlong, R.A., Burkin, H., Jennifer Chalmers, I., Brown, G.M., Khwaja, O., Affara, N.A.: The *Drosophila* developmental gene fat facets has a human homologue in Xp11. 4 which escapes X-inactivation and has related sequences on Yq11. 2. *Hum. Mol. Genet.* **5**(11), 1695–1701 (1996)
- Velayos-Baeza, A., Vettori, A., Copley, R.R., Dobson-Stone, C., Monaco, A.P.: Analysis of the human VPS13 gene family. *Genomics* **84**(3), 536–549 (2004)
- Hamann, J., Aust, G., Araç, D., Engel, F.B., Formstone, C., Fredriksson, R., et al.: International union of basic and clinical pharmacology. XCIV. Adhesion G protein-coupled receptors. *Pharmacol. Rev.* **67**(2), 338–367 (2015)
- Mondal, K., Ramachandran, D., Patel, V.C., Hagen, K.R., Bose, P., Cutler, D.J., Zwick, M.E.: Excess variants in AFF2 detected by massively parallel sequencing of males with autism spectrum disorder. *Hum. Mol. Genet.* **21**(19), 4356–4364 (2012)

24. Stessman, H.A., Xiong, B., Coe, B.P., Wang, T., Hoekzema, K., Fenckova, M., et al.: Targeted sequencing identifies 91 neurodevelopmental-disorder risk genes with autism and developmental-disability biases. *Nat. Genet.* **49**(4), 515 (2017)
25. Catterall, W.A., Perez-Reyes, E., Snutch, T.P., Striessnig, J.: International union of pharmacology. XLVIII. Nomenclature and structure-function relationships of voltage-gated calcium channels. *Pharmacol. Rev.* **57**(4), 411–425 (2005)
26. Anai, M., Shojima, N., Katagiri, H., Ogihara, T., Sakoda, H., Onishi, Y., et al.: A novel protein kinase B (PKB)/AKT-binding protein enhances PKB kinase activity and regulates DNA synthesis. *J. Biol. Chem.* **280**(18), 18525–18535 (2005)
27. Côté, J.F., Vuori, K.: Identification of an evolutionarily conserved superfamily of DOCK180-related proteins with guanine nucleotide exchange activity. *J. Cell Sci.* **115**(24), 4901–4913 (2002)
28. Sardi, S.P., Murtie, J., Koirala, S., Patten, B.A., Corfas, G.: Presenilin-dependent ErbB4 nuclear signaling regulates the timing of astrogenesis in the developing brain. *Cell* **127**(1), 185–197 (2006)
29. Mitsui, K., Nakajima, D., Ohara, O., Nakayama, M.: Mammalian fat3: a large protein that contains multiple cadherin and EGF-like motifs. *Biochem. Biophys. Res. Commun.* **290**(4), 1260–1266 (2002)
30. Ju, Y.T., Chang, A.C., She, B.R., Tsauro, M.L., Hwang, H.M., Chao, C.C.K., et al.: gas7: A gene expressed preferentially in growth-arrested fibroblasts and terminally differentiated Purkinje neurons affects neurite formation. *Proc. Natl. Acad. Sci.* **95**(19), 11423–11428 (1998)
31. Mori, F., Tanji, K., Miki, Y., Toyoshima, Y., Yoshida, M., Kakita, A., et al.: G protein-coupled receptor 26 immunoreactivity in intranuclear inclusions associated with polyglutamine and intranuclear inclusion body diseases. *Neuropathology* **36**(1), 50–55 (2016)
32. Puffenberger, E.G., Jinks, R.N., Wang, H., Xin, B., Fiorentini, C., Sherman, E.A., Degrazio, D., Shaw, C., Sougnéz, C., Cibulskis, K., Gabriel, S.: A homozygous missense mutation in *HERC2* associated with global developmental delay and autism spectrum disorder. *Hum. Mutat.* **33**(12), 1639–1646 (2012)
33. Miceli, F., Striano, P., Soldovieri, M.V., Fontana, A., Nardello, R., Robbiano, A., Bellini, G., Elia, M., Zara, F., Tagliatalata, M., Mangano, S.: A novel *KCNQ3* mutation in familial epilepsy with focal seizures and intellectual disability. *Epilepsia* **56**(2), e15–e20 (2015)
34. Lin, Z., Liu, J., Ding, H., Xu, F., Liu, H.: Structural basis of *SALM5*-induced *PTPδ* dimerization for synaptic differentiation. *Nat. Commun.* **9**(1), 268 (2018)
35. Mondin, M., Tessier, B., Thoumine, O.: Assembly of synapses: biomimetic assays to control neurexin/neuregulin interactions at the neuronal surface. *Curr. Protoc. Neurosci.* **64**(1), 2–19 (2013)
36. Oksenberg, N., Stevison, L., Wall, J.D., Ahituv, N.: Function and regulation of *AUTS2*, a gene implicated in autism and human evolution. *PLoS Genet.* **9**(1), e1003221 (2013)
37. Oksenberg, N., Ahituv, N.: The role of *AUTS2* in neurodevelopment and human evolution. *Trends Genet.* **29**(10), 600–608 (2013)
38. Engmann, O., Labonté, B., Mitchell, A., Bashtrykov, P., Calipari, E.S., Rosenbluh, C., Loh, Y.H., Walker, D.M., Burek, D., Hamilton, P.J., Issler, O.: Cocaine-induced chromatin modifications associate with increased expression and three-dimensional looping of *Auts2*. *Biol. Psychiatry* **82**(11), 794–805 (2017)
39. Beunders, G., Voorhoeve, E., Golzio, C., Pardo, L.M., Rosenfeld, J.A., Talkowski, M.E., Simonis, I., Lionel, A.C., Vergult, S., Pyatt, R.E., Van De Kamp, J.: Exonic deletions in *AUTS2* cause a syndromic form of intellectual disability and suggest a critical role for the C terminus. *Am. J. Hum. Genet.* **92**(2), 210–220 (2013)
40. Weisner, P.A.: The role of *AUTS2* in neurodevelopment and neurological disease. Doctoral dissertation, University of Illinois at Urbana-Champaign (2015)
41. Lima, C.S., Ortega, M.M., Ozelo, M.C., Araujo, R.C., De Souza, C.A., Lorand-Metze, I., Annichino-Bizzacchi, J.M., Costa, F.F.: Polymorphisms of methylenetetrahydrofolate reductase (*MTHFR*), methionine synthase (*MTR*), methionine synthase reductase (*MTRR*), and thymidylate synthase (*TYMS*) in multiple myeloma risk. *Leuk. Res.* **32**(3), 401–405 (2008)
42. Weisberg, I., Tran, P., Christensen, B., Sibani, S., Rozen, R.: A second genetic polymorphism in methylenetetrahydrofolate reductase (*MTHFR*) associated with decreased enzyme activity. *Mol. Genet. Metab.* **64**(3), 169–172 (1998)
43. TRIMMER, E.E.: Studies of the flavin enzyme Methylenetetrahydrofolate Reductase (*MTHFR*)
44. Blumkin, E., Levav-Rabkin, T., Melamed, O., Galron, D., Golan, H.M.: Genderspecific effect of *Mthfr* genotype and neonatal vigabatrin interaction on synaptic proteins in mouse cortex. *Neuropsychopharmacology* **36**(8), 1714 (2011)
45. Mortimer, B.C., Beveridge, D.J., Martins, I.J., Redgrave, T.G.: Intracellular localization and metabolism of chylomicron remnants in the livers of low density lipoprotein receptor-deficient mice and ApoE-deficient mice evidence for slow metabolism via an alternative apoE-dependent pathway. *J. Biol. Chem.* **270**(48), 28767–28776 (1995)
46. Zhou, Y., Mägi, R., Milani, L., Lauschke, V.M.: Global genetic diversity of human apolipoproteins and effects on cardiovascular disease risk. *J. Lipid Res.* **59**(10), 1987–2000 (2018)
47. Leduc, V., Jasmin-Bélanger, S., Poirier, J.: APOE and cholesterol homeostasis in Alzheimer's disease. *Trends Mol. Med.* **16**(10), 469–477 (2010)
48. Beisiegel, U., Weber, W., Ihrke, G., Herz, J., Stanley, K.K.: The LDL-receptor-related protein, LRP, is an apolipoprotein E-binding protein. *Nature* **341**(6238), 162 (1989)
49. Qian, W., Fischer, C.E., Schweizer, T.A., Munoz, D.G.: Association between psychosis phenotype and APOE genotype on the clinical profiles of Alzheimer's disease. *Curr. Alzheimer Res.* **15**(2), 187–194 (2018)
50. Dweep, H., et al.: miRWalk2.0: a comprehensive atlas of microRNA-target interactions. *Nat. Methods* **12**(8), 697–697 (2015)
51. Warde-Farley, D., Donaldson, S.L., Comes, O., Zuberi, K., Badrawi, R., Chao, P., Franz, M., Grouios, C., Kazi, F., Lopes, C.T., Maitland, A., Mostafavi, S., Montojo, J., Shao, Q., Wright, G., Bader, G.D., Morris, Q.: The GeneMANIA prediction server: biological network integration for gene prioritization and predicting gene function. *Nucleic Acids Res.* **38**(Suppl), W214–W220 (2010). *PubMed Abstract*
52. Seger, R., Krebs, E.G.: The MAPK signaling cascade. *FASEB J.* **9**(9), 726–735 (1995)
53. Filosa, J.A., Bonev, A.D., Straub, S.V., Meredith, A.L., Wilkerson, M.K., Aldrich, R.W., Nelson, M.T.: Local potassium signaling couples neuronal activity to vasodilation in the brain. *Nat. Neurosci.* **9**(11), 1397 (2006)
54. Tanaka, Y., Meera, P., Song, M., Knaus, H.G., Toro, L.: Molecular constituents of maxi KCa channels in human coronary smooth muscle: predominant $\alpha + \beta$ subunit complexes. *J. Physiol.* **502**(3), 545–557 (1997)
55. Chevrier, S., Emslie, D., Shi, W., Kratina, T., Wellard, C., Karnowski, A., Erikci, E., Smyth, G.K., Chowdhury, K., Tarlinton, D., Corcoran, L.M.: The BTB-ZF transcription factor *Zbtb20* is driven by *Irf4* to promote plasma cell differentiation and longevity. *J. Exp. Med.* **211**(5), 827–840 (2014)
56. Rasmussen, M.B., Nielsen, J.V., Lourenço, C.M., Melo, J.B., Halgren, C., Geraldi, C.V., Marques, W., Rodrigues, G.R., Thomassen, M., Bak, M., Hansen, C.: Neurodevelopmental disorders associated with dosage imbalance of *ZBTB20* correlate with the morbidity spectrum of *ZBTB20* candidate target genes. *J. Med. Genet.* **51**(9), 605–613 (2014)

57. Xie, Z., Zhang, H., Tsai, W., Zhang, Y., Du, Y., Zhong, J., Szpirer, C., Zhu, M., Cao, X., Barton, M.C., Grusby, M.J.: Zinc finger protein ZBTB20 is a key repressor of alpha-fetoprotein gene transcription in liver. *Proc. Nat. Acad. Sci.* **105**(31), 10859–10864 (2008)
58. Sutherland, A.P., Zhang, H., Zhang, Y., Michaud, M., Xie, Z., Patti, M.E., Grusby, M.J., Zhang, W.J.: Zinc finger protein Zbtb20 is essential for postnatal survival and glucose homeostasis. *Mol. Cell. Biol.* **29**(10), 2804–2815 (2009)
59. Mattioli, F., Piton, A., Gérard, B., Superti-Furga, A., Mandel, J.L., Unger, S.: Novel de novo mutations in ZBTB20 in Primrose syndrome with congenital hypothyroidism. *Am. J. Med. Genet. Part A* **170**(6), 1626–1629 (2016)
60. Liu, X., Zhang, P., Bao, Y., Han, Y., Wang, Y., Zhang, Q., Zhan, Z., Meng, J., Li, Y., Li, N., Zhang, W.J.: Zinc finger protein ZBTB20 promotes toll-like receptor-triggered innate immune responses by repressing I κ B α gene transcription. *Proc. Nat. Acad. Sci.* **110**(27), 11097–11102 (2013)
61. Kohannim, O., Hibar, D.P., Stein, J.L., Jahanshad, N., Hua, X., Rajagopalan, P., Toga, A., Jack Jr., C.R., Weiner, M.W., De Zubicaray, G.I., McMahon, K.L.: Discovery and replication of gene influences on brain structure using LASSO regression. *Front. Neurosci.* **6**, 115 (2012)
62. Ju, Y.T., Chang, A.C., She, B.R., Tsauro, M.L., Hwang, H.M., Chao, C.C.K., Cohen, S.N., LinChao, S.: gas7: A gene expressed preferentially in growth-arrested fibroblasts and terminally differentiated Purkinje neurons affects neurite formation. *Proc. Nat. Acad. Sci.* **95**(19), 11423–11428 (1998)
63. Chandley, M.J., Crawford, J.D., Szebeni, A., Szebeni, K., Ordway, G.A.: Erratum to: NTRK2 expression levels are reduced in laser captured pyramidal neurons from the anterior cingulate cortex in males with autism spectrum disorder. *Mol. Autism* **6**(1), 38 (2015)
64. Li, Z., Zhang, Y., Wang, Z., Chen, J., Fan, J., Guan, Y., Zhang, C., Yuan, C., Hong, W., Wang, Y., Wu, Z.: The role of BDNF, NTRK2 gene and their interaction in development of treatment-resistant depression: data from multicenter, prospective, longitudinal clinic practice. *J. Psychiatr. Res.* **47**(1), 8–14 (2013)
65. Weiss, L.A., Escayg, A., Kearney, J.A., Trudeau, M., MacDonald, B.T., Mori, M., Reichert, J., Buxbaum, J.D., Meisler, M.H.: Sodium channels SCN1A, SCN2A and SCN3A in familial autism. *Mol. Psychiatry* **8**(2), 186 (2003)
66. Nickel, K., van Elst, L.T., Domschke, K., Gläser, B., Stock, F., Endres, D., Maier, S., Riedel, A.: Heterozygous deletion of SCN2A and SCN3A in a patient with autism spectrum disorder and Tourette syndrome: a case report. *BMC Psychiatry* **18**(1), 248 (2018)
67. Dalpé, G., Leclerc, N., Vallée, A., Messer, A., Mathieu, M., De Repentigny, Y., Kothary, R.: Dystonin is essential for maintaining neuronal cytoskeleton organization. *Mol. Cell. Neurosci.* **10**(5), 243–257 (1998)
68. Ryan, S.D., Ferrier, A., Sato, T., O'Meara, R.W., De Repentigny, Y., Jiang, S.X., Hou, S.T., Kothary, R.: Neuronal dystonin isoform 2 is a mediator of endoplasmic reticulum structure and function. *Mol. Biol. Cell* **23**(4), 553–566 (2012)
69. Vincent, J.B., Choufani, S., Horike, S.I., Stachowiak, B., Li, M., Dill, F.J., Marshall, C., Hrynczak, M., Pewsey, E., Ukadike, K.C., Friedman, J.M.: A translocation t(6;7)(p11-p12;q22) associated with autism and mental retardation: localization and identification of candidate genes at the breakpoints. *Psychiatr. Genet.* **18**(3), 101–109 (2008)
70. Paşca, S.P., Portmann, T., Voineagu, I., Yazawa, M., Shcheglovitov, A., Paşca, A.M., Cord, B., Palmer, T.D., Chikahisa, S., Nishino, S., Bernstein, J.A.: Using iPSC-derived neurons to uncover cellular phenotypes associated with Timothy syndrome. *Nat. Med.* **17**(12), 1657 (2011)
71. Laumonier, F., Roger, S., Guérin, P., Molinari, F., M'Rad, R., Cahard, D., Belhadj, A., Halayem, M., Persico, A.M., Elia, M., Romano, V.: Association of a functional deficit of the BK Ca channel, a synaptic regulator of neuronal excitability, with autism and mental retardation. *Am. J. Psychiatry* **163**(9), 1622–1629 (2006)



Discrete Modelling of Liver Cell Aggregation Using Partial Differential Equations

Tijana Sustersic, Milica Nikolic, Nihal Engin Vrana, and Nenad Filipovic

Abstract

Since the main purpose of generation of organ-on-chips is to reduce and, at some point, replace experiments on the animals, several different organs were point of interest in developing on-chip technology. The paper will therefore focus on creating mathematical model of liver cell aggregation, generating a basis for creation of artificial organs in that way. Some studies have shown that in the case of hepatocytes (liver cells), improved cell viability and functionality is connected to the formation of spheroidal multicellular aggregates in comparison to the traditional monolayer culture techniques. We present one-dimensional mathematical model of liver cell aggregation, meaning how the liver cell clusters are formed on an extracellular matrix (ECM) layer. Model is based on partial differential equations in the function of space and time, which are solved numerically using finite difference method. Results show that velocity of the cells at the beginning is slow, only to increase later on during the formation of the aggregates. Material properties and initial cell seeding have great effects on the formation of the aggregates. With this model, we aim to achieve a prediction of number of cell clusters, velocity during and before/after clustering etc., which is important in experiments to examine how different parameters, such as initial cell seeding or material characteristics affect cell aggregation and viability of liver cells.

Keywords

Liver cell aggregation • Organ-on-chip • Mathematical model

1 Introduction

In vitro tissue engineering has become now a major field to investigate in order to provide solutions for organ transplantation, since there is a shortage of available tissue. Experiments alone cannot provide a full insight into biophysical and biochemical processes that affect tissue growth and behavior of the tissue cells [1]. Therefore, mathematical modelling can provide additional information in different underlying processes, which influence final tissue formation for implantation.

Since the main purpose of generation of organ-on-chips is to reduce and, at some point, replace experiments on the animals, several different organs were point of interest in developing on-chip technology. Liver is of special interest, mainly because of importance of this organ in human organism. Although widely researched, mainly because the liver is estimated to have around 500 different functions, currently there is no artificial organ or medical device that is capable of replacing the liver [2]. Some systems have been designed with a purpose to remove blood toxins that are accumulated during liver failure (e.g. haemodialysis, haemoltration and plasma exchange). However, all these systems have proved disappointing results when it comes to patient survival [3]. As a result, organ transplantation is the only treatment that is currently available for serious, end-stage liver disease.

In vivo and under normal physiological conditions, liver tissue consists of around 80% of hepatocytes [4]. Most of the liver's important functions are performed by these cells, which causes them to be a focus of research [5]. Different techniques have been examined to reduce dedifferentiation of hepatocytes, which causes them to lose their ability to

T. Sustersic (✉) · M. Nikolic · N. Filipovic
Faculty of Engineering, University of Kragujevac,
Kragujevac, Serbia
e-mail: tijanas@kg.ac.rs

Steinbeis Advanced Risk Technologies Institute doo Kragujevac,
Kragujevac, Serbia

T. Sustersic · N. Filipovic
Bioengineering Research and Development Center, Kragujevac,
Serbia

N. E. Vrana
PROTIP SAS, 8 Place de l hopital, Strasbourg, France

function normally and die [6, 7]. This process happens usually after a few days. Therefore, some co-culturing with other cell types (i.e. stellate cells), the use of growth factors or combination with polymer scaffolds have been proposed [7]. The result of these techniques is sometimes formation of multicellular spheroids, which have shown to improve viability by mimicking liver tissue in vivo to some extent [8]. Normal procedure for culturing hepatocytes as spheroids involves seeding cells in culture wells with extracellular matrix (ECM), while nutrients are provided to the cells by culture medium [9]. When the substrate is adequate, cells aggregate within a period of approximately one day [10, 11]. After forming clusters, these aggregates detach from the surface of the ECM and form spheroids with diameter 100–150 μm [12], whilst the cell diameter is of range 10–30 μm [11, 13].

Looking from a biological context, it is necessary to take into account interactions between several different types of materials e.g. cells and extracellular water [14, 15], ECM [16] and other cell populations such as macrophages [17]. These different materials are often considered as different phases, creating multiphase models. Two or multi-phase approaches enable coupling motion of the cells with the culture medium in which they are grown. To the knowledge of the authors, studies with the topic of multiphase models are rare. In most studies, values of the relevant parameters are estimated by fitting to experimental data. With the exception of several studies such as by Glicklis et al. [18], Breward et al. [14] and Green et al. [9], there are no literature on multiphase models, especially regarding liver. The last mentioned study is the only available research that has been examining multiphase model of a liver from the mathematical side and investigated aggregation process. An idealized one-dimensional slab geometry is assumed and chemical signals are neglected by prescribing the forces generated by the cells as a function of cell density.

The importance of these models remains, as diseases of the liver, including hepatitis and cirrhosis are the cause of many deaths in the USA [19]. Mentioned passive systems to remove blood toxins have failed to increase patient survival, so attention has transferred to cell-based liver assistance devices [3]. This has led to interest in understanding the interactions amongst the various cell populations in the liver, and amongst the cells, growth factors and ECM. Therefore, this paper focuses on discrete modelling of one dimensional liver cell aggregation using partial differential equations with the novel approach with possible adaptation of the model to the Finite Element Method (FEM). Such way of solving the problem of cell aggregation would allow extending the modelling approach to two dimensional model and phenomena that are more complex.

2 Materials and Methods

Our model consists of in vitro population of cells (hepatocytes) set in culture medium, so we can say it is a two phase mixture, where two phases (cells and culture) add up to 1 (meaning there are no voids). One-dimensional model is assumed, and the base of the model represents the ECM. Basis for the model are three mass and momentum balance equations for the cells, culture medium and ECM. We also insert constitutive laws for the mechanical properties of each of the three species. Literature suggests that the timescale for aggregation of cells is around 1 day, meaning cell proliferation is not the main cause of cluster formation, and we can neglect hepatocyte proliferation and death, as well as production and degradation of ECM [9], obtaining the following equations for mass balance for n , ω and ρ .

$$\frac{\partial n}{\partial t} + \frac{\partial}{\partial x}(nv_n) = 0 \quad (1)$$

$$\frac{\partial \omega}{\partial t} + \frac{\partial}{\partial x}(n\omega v_\omega) = 0 \quad (2)$$

$$\frac{\partial \rho}{\partial t} + \frac{\partial}{\partial x}\left(\rho \frac{\partial s}{\partial t}\right) = 0 \quad (3)$$

where n is the volume fraction of cells, ω is the volume fraction of culture medium, ρ is the density of ECM and s is the displacement of ECM. Corresponding velocities of the cells and culture medium are v_n and v_ω respectively.

In the momentum balance equations σ_n , σ_ω and σ_ρ are the Cauchy stresses in the cells, culture medium and ECM respectively. The momentum balance in each phase, after neglecting inertial effects, is given by:

$$\frac{\partial}{\partial x}(n\sigma_n) + F_n = 0 \quad (4)$$

$$\frac{\partial}{\partial x}(\omega\sigma_\omega) + F_\omega = 0 \quad (5)$$

$$\frac{\partial \sigma_\rho}{\partial x} + F_\rho = 0 \quad (6)$$

and F_n , F_ω and F_ρ represent the net sources of momentum in each phase.

Suitable boundary and initial conditions are prescribed, and the initial distribution of cells is given by:

$$n(x, 0) = n_0(x) \quad (7)$$

We can assume that ECM layer is initially undeformed and spatially uniform with constant density ρ_0 leading to

$$\rho(x, 0) = \rho_0, \quad s(x, 0) = 0 \quad (8)$$

Without losing any accuracy, we can also assume that the system is symmetric about $x = 0$ and can focus on only $0 \leq x \leq L$, which means:

$$s(0, t) = v_n(0, t) = v_w(0, t) = 0 \tag{9}$$

Another boundary condition is that the ECM is taken to be pinned at the edge of the culture well, meaning the displacement is zero at $x = L$

$$s(L, t) = 0 \tag{10}$$

Out of the culture well we can make an assumption that there is no flux of cells or water:

$$v_n(L, t) = v_w(L, t) = 0 \tag{11}$$

Further, the model developed can be reduced to coupled PDEs for unknown physical quantities of interest n, ρ, v_n, s . After nondimensionalization we obtain:

$$\frac{\partial n}{\partial t} + \frac{\partial}{\partial x}(nv_n) = 0 \tag{12}$$

$$\frac{\partial \rho}{\partial t} + \frac{1}{\hat{\mu}} \frac{\partial}{\partial x} \left(\rho \frac{\partial s}{\partial t} \right) = 0 \tag{13}$$

$$\begin{aligned} \frac{\hat{k}_1 n}{(1-n)} v_n + \hat{k}_2 n \rho \left(v_n - \frac{1}{\hat{\mu}} \frac{\partial s}{\partial t} \right) \\ + \frac{\partial}{\partial x} \left(\frac{n(n-n^*)}{(1-n)^2} \right) - \frac{\partial}{\partial x} \left(n \frac{\partial v_n}{\partial x} \right) = 0 \end{aligned} \tag{14}$$

$$-\hat{k}_2 n \rho \left(v_n - \frac{1}{\hat{\mu}} \frac{\partial s}{\partial t} \right) = \frac{\partial^2}{\partial x^2} \left(\frac{\partial s}{\partial t} + \tau s \right) = 0 \tag{15}$$

where material properties parameters \hat{k}_1 and \hat{k}_2 are the ratios of cell-culture medium and cell-ECM drag to viscous forces; $\hat{\mu}$ is the ratio of the ECM and cell viscosities; and τ is the ratio of the aggregation timescale to the ECM relaxation time.

Simulations were performed using Matlab, and applying finite difference method by discretizing Eqs. (12)–(15). Using discussed initial conditions for n, ρ and s Eqs. (14) and (15) are solved simple matrix inversion to obtain v_n and $\frac{\partial s}{\partial t}$. Determined values were then used to update n and ρ at the next timestep, using Eqs. (13) and (14). After this, s was updated using the values of found in the initial step, solving the differential equation first-order accurate in time. Updated solutions for n, ρ and s were then used to calculate v_n and $\frac{\partial s}{\partial t}$ at the next time step, and the process described is then repeated up to the last time point.

3 Results and Discussion

Based on [9], we fix $n^* = 0.8$ and $\hat{k}_1 = \hat{k}_2 = \hat{\mu} = \tau = 1$, and this assumption is also consistent with the ranges obtained from experiments [9]. In our model, we assume that the initial cell seeding is in the form $n(x, 0) = 0.5 + 0.01 \cos 0.6\pi x$. In the following results, number of peaks in the figures represents the number of aggregates. Due to the numerical instability of the solution, we found it convenient to include a small diffusion coefficient $D = 3 \times 10^{-4}$ in Eq. (12) to reduce the unstable parts in later periods.

We observe that the cell movement is slow in the beginning, $0 \leq t \leq 2$ (Fig. 1), only to become faster in the period $2 \leq t \leq 4$, which corresponds to the faster aggregation process. After $t \geq 5$ (Fig. 2), velocity v_n becomes 0 within the aggregates, while elsewhere $v_n \neq 0$. It should be also said that obtained results show good matching with the reference manuscript [9].

In Fig. 3, volume fraction of the cell $n(x, t)$ for the period of $0 \leq t \leq 2$ is given, and in Fig. 4 for the time point $t = 5$.

When comparing the explained results with the result for density, it was concluded that density is increasing in the first period $0 \leq t \leq 2$, meaning the aggregates are growing and density is increasing. At later times, when velocity of the cells becomes zero, density also reduces and becomes spatially uniform.

It should be also interesting to see how different parameters influence the number of aggregates formed and their speed of aggregation. It was shown that increasing material

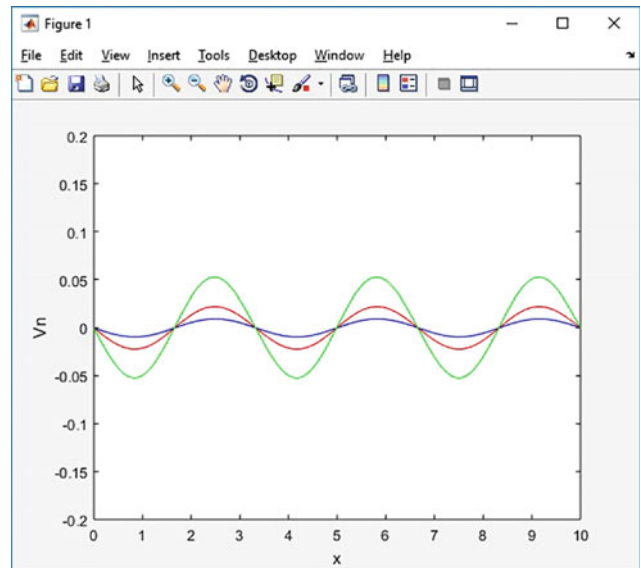


Fig. 1 $v_n(x, t)$ for $t = 0$ (blue), $t = 1$ (red), $t = 2$ (green)

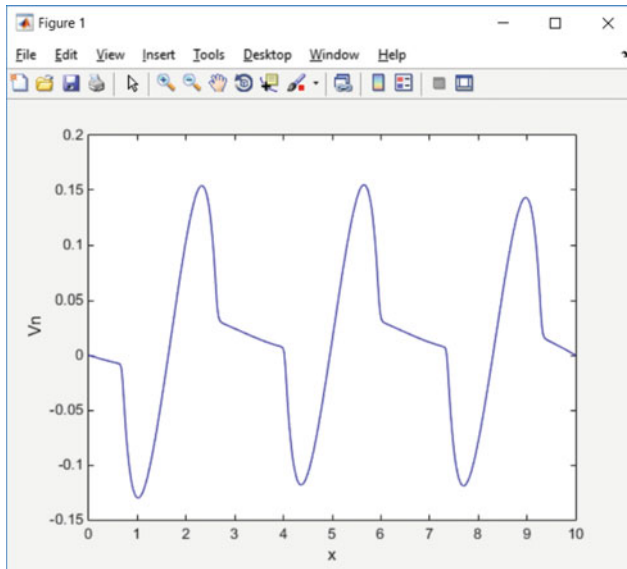


Fig. 2 $v_n(x, t)$ for $t = 5$

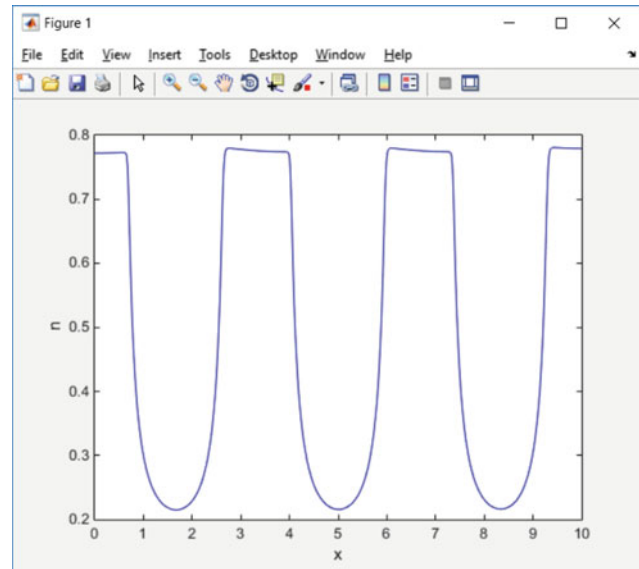


Fig. 4 $n(x, t)$ for $t = 5$

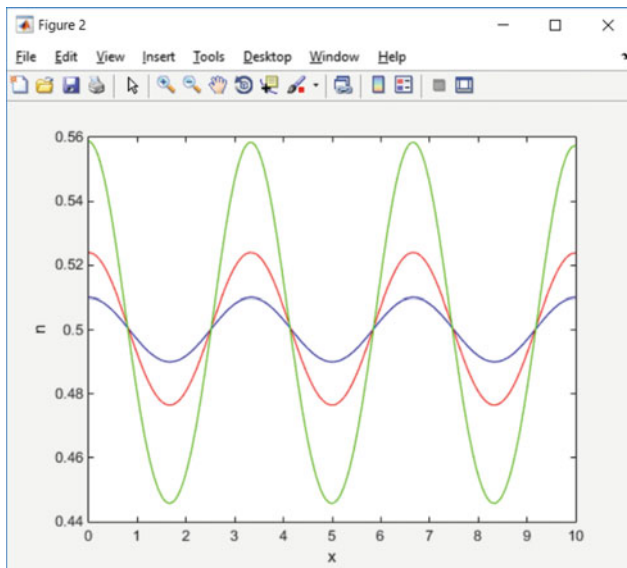


Fig. 3 $n(x, t)$ for $t = 0$ (blue), $t = 1$ (red), $t = 2$ (green)

properties \hat{k}_1, \hat{k}_2 results in formation of greater number of aggregates (when $\hat{k}_1 = 5$, number of aggregates formed was 7, when $\hat{k}_1 = 10$, number of aggregates formed was 9). Similar behavior was present with the increase in \hat{k}_2 . Changes in parameters $\hat{\mu}, \tau$, did not have that much influence on the formation of the aggregates. Initial cell seeding was also investigated, since it was prescribed in the form of cosine function. If we assume that initial cell density is in the form of $n(x, 0) = a + b \cos 0.6\pi x$, changes in a result in the size of the aggregates formed, but also number of aggregates. This happens only to a certain limit

$n(x, 0) > n_c = 2/3$. We can see from these early experiments that the influence of initial cell seeding is complex, and a more and systematic approach in testing the initial cell seeding will be conducted in future. These results correspond to the results obtained by Thomas et al., who showed that strength of cell-ECM adhesion and the material properties affect significantly cell mobility [9, 20]. Additionally, for large numbers of cell-ECM adhesion, cell movement almost completely disappeared, as was obtained in experiments by Riccalton-Banks [21] for cells seeded on tissue culture plastic. As reported in [9], they predict that reduction of the strength of cell-substrate adhesion could affect the promotion of the formation of large aggregates. However, some small degree of cell-substrate adhesion may be necessary for cell movement, meaning that the elimination adhesion would result in undesirable effects.

However, even with the diffusion coefficient, after $t = 6$ (Fig. 5), periodic unstable components appeared in solution for the volume fraction n , which then influenced the solution for v_n and those instabilities accumulate with time (example given for $t = 7$ in Fig. 6). This will be solved in future updates of the model, by using other methods for solving PDE, such as Crank-Nicholson or up-wind scheme etc.

With this model, we aim to achieve a prediction of number of cell clusters, velocity during and before/after clustering etc., which is important for experimentations to examine how different parameters such as initial cell seeding or material characteristics affect cell aggregation and viability of liver cells.

Limitations of this study include adoption of a one-dimensional geometry and disregarding the influence of the chemical factors, which definitely has the effect on cell

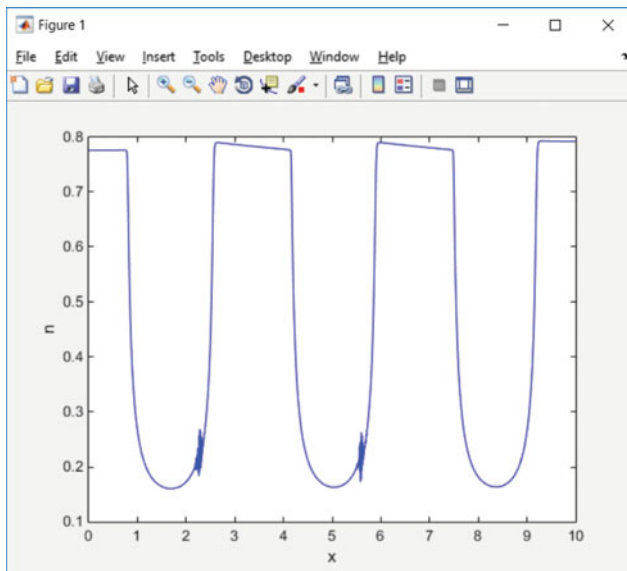


Fig. 5 $n(x, t)$, for $t = 6$

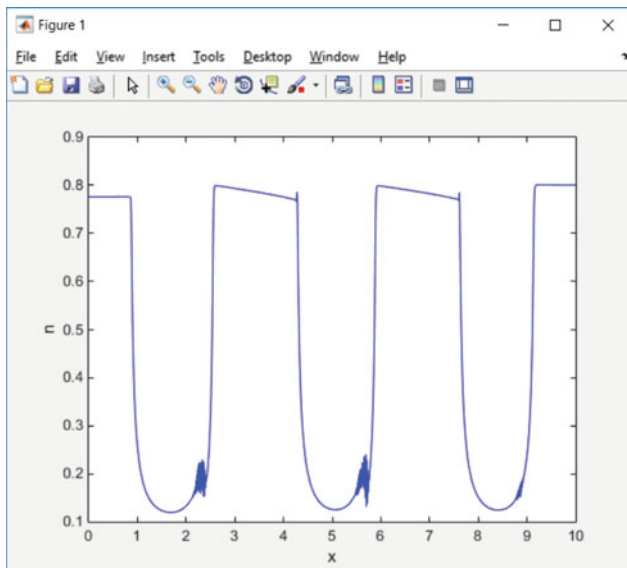


Fig. 6 $n(x, t)$ for $t = 7$

aggregation. However, this is just a starting point in this novel approach of mathematical modelling of liver cell aggregation and not all factors could have been taken into account. Further updates and improvements of the model would include validation of the model against experimental results and inclusion of the additional effects. In future research, we can also implement equations in open source PAK finite element solver developed at the University of Kragujevac, as this would be beneficial in cases of irregular geometry. In other cases, a script in Matlab or another programming language could be written as a standalone application.

4 Conclusion

In this paper we have presented one dimensional model of liver cell aggregation using partial differential equations. Starting from mass and momentum balance equations for the cell and culture phase, neglecting inertia terms, we non-dimensionalize four PDE equations for solving n, ρ, v_n, s . Our simulations show the velocity and volume fraction during the cell aggregation for shorter times $0 \leq t \leq 5$ and longer periods $t \geq 5$. The results show also that material parameters, as well as initial cell seeding influence cell aggregation. This model represents a good start in creation of more complex two dimensional models which could be solved using FEM analysis. Future research will implement finite element method in solving the appropriate equations and more phenomena in the cell aggregation will be included in the model, as well as the numerical instabilities will be solved.

Acknowledgements This study was funded by the European Project H2020 PANBioRA [grant number 760921] and grants from the Serbian Ministry of Education, Science, and Technological Development [grant number III41007 and grant number OI174028]. This article reflects only the author's view. The Commission is not responsible for any use that may be made of the information it contains.

Conflict of Interest Authors declare no conflicts of interest.

References

1. O'Dea, R.D., Byrne, H.M., Waters, S.L.: Continuum modelling of in vitro tissue engineering: a review. In: Computational Modeling in Tissue Engineering, pp. 229–266. Springer, Berlin, Heidelberg (2012)
2. Green, J.E.E.: Mathematical modelling of cell aggregation in liver tissue engineering. Doctoral dissertation, University of Nottingham (2006)
3. Jauregui H.O.: Liver. In: Principles of Tissue Engineering, 2nd edn, pp. 541–551. Academic Press (2000)
4. Mitaka, T.: The current status of primary hepatocyte culture. Int. J. Exp. Pathol. **79**(6), 393–409 (1998)
5. Selden, C., Khalil, M., Hodgson, H.J.F.: What keeps hepatocytes on the straight and narrow? Maintaining differentiated function in the liver. Gut **44**(4), 443–446 (1999)
6. Riccalton-Banks, L., Liew, C., Bhandari, R., Fry, J., Shakesheff, K.: Long-term culture of functional liver tissue: three-dimensional coculture of primary hepatocytes and stellate cells. Tissue Eng. **9**(3), 401–410 (2003)
7. Bhandari, R.N., Riccalton, L.A., Lewis, A.L., Fry, J.R., Hammond, A.H., Tendler, S.J., Shakesheff, K.M.: Liver tissue engineering: a role for co-culture systems in modifying hepatocyte function and viability. Tissue Eng. **7**(3), 345–357 (2001)
8. Abu-Absi, S.F., Friend, J.R., Hansen, L.K., Hu, W.S.: Structural polarity and functional bile canaliculi in rat hepatocyte spheroids. Exp. Cell Res. **274**(1), 56–67 (2002)
9. Green, J.E.F., Waters, S.L., Shakesheff, K.M., Byrne, H.M.: A mathematical model of liver cell aggregation in vitro. Bull. Math. Biol. **71**(4), 906–930 (2009)

10. Riccalton-Banks, L.A.: Maintenance of primary rat hepatocytes in vitro using co culture techniques. Doctoral dissertation, University of Nottingham (2002)
11. Glicklis, R., Shapiro, L., Agbaria, R., Merchuk, J.C., Cohen, S.: Hepatocyte behavior within three-dimensional porous alginate scaffolds. *Biotechnol. Bioeng.* **67**(3), 344–353 (2000)
12. Thomas, R.J., Bhandari, R., Barrett, A.J., et al.: The effect of three-dimensional co-culture of hepatocytes and hepatic stellate cells on key hepatocyte functions in vitro. *Cells Tissues Organs* **181**(2), 67–79 (2005)
13. Higuchi, A., Tsukamoto, Y.: Cell separation of hepatocytes and fibroblasts through surface-modified polyurethane membranes. *J. Biomed. Mater. Res. Part A Official J. Soc. Biomater. Jpn. Soc. Biomater. Aust. Soc. Biomater. Korean Soc. Biomater.* **71**(3), 470–479 (2004)
14. Breward, C.J.W., Byrne, H.M., Lewis, C.E.: The role of cell-cell interactions in a two-phase model for avascular tumour growth. *J. Math. Biol.* **45**(2), 125–152 (2002)
15. Byrne, H.M., King, J.R., McElwain, D.S., Preziosi, L.: A two-phase model of solid tumour growth. *Appl. Math. Lett.* **16**(4), 567–574 (2003)
16. Lubkin, S.R., Jackson, T.: Multiphase mechanics of capsule formation in tumors. *J. Biomech. Eng.* **124**(2), 237243 (2002)
17. Owen, M.R., Byrne, H.M., Lewis, C.E.: Mathematical modelling of the use of macrophages as vehicles for drug delivery to hypoxic tumour sites. *J. Theor. Biol.* **226**(4), 377–391 (2004)
18. Glicklis, R., Merchuk, J.C., Cohen, S.: Modeling mass transfer in hepatocyte spheroids via cell viability, spheroid size, and hepatocellular functions. *Biotechnol. Bioeng.* **86**(6), 672–680 (2004)
19. Compressed Mortality File, CDC WONDER On-line Database, [Online]. Available <http://wonder.cdc.gov>. Accessed 25 Nov 2018
20. Thomas, T.W., DiMilla, P.A.: Spreading and motility of human glioblastoma cells on sheets of silicone rubber depend on substratum compliance. *Comput. Med. Biol. Eng.* **38**, 360–370 (2000)
21. Riccalton-Banks, L., Liew, C., Bhandari, R., Fry, J., Shakesheff, K.: Longterm culture of functional liver tissue: three-dimensional coculture of primary hepatocytes and stellate cells. *Tissue Eng.* **9**(3), 401–409 (2003)

Part VIII

**Clinical Engineering and Health Technology
Assessment**

Smart Ageing: Are We Succeeding?

Jasmina Baraković Husić , Sabina Baraković,
and Enida Cero Dinarević

Abstract

The ultimate goal of smart things and systems should be to improve Quality of Life (QoL), specially of elderly given that population is increasing rapidly. A number of smart ageing solutions are developed without QoL of elderly being noticeably improved. This paper seeks to answer the question are the existing smart ageing solutions succeeding in direct improvement of QoL of elderly. After conducting a survey study for this purpose, the results showed that existing solutions are not succeeding in improving QoL of elderly. In addition to this conclusion, the contribution of this paper reflects in proposed set of QoL indicators for elderly and recommendations for future research activities in this area.

Keywords

Smart ageing • Quality of life • Elderly

1 Introduction

In the following years all life spheres will be flooded with smart things and systems. These systems will completely change everyday activities by creating opportunities for development and innovation, which in turn will bring in countless benefits [1]. Smart systems will connect homes, cars, governments, health, etc. This concept will also change the way people interact with the society and things around them and try to simplify our lives. Generally, the ultimate

goal of smart concept should be to improve our Quality of Life (QoL).

QoL definition and meaning varies for people of different gender and age groups, cultural, economy, education background, context, etc. Simplified version is that QoL is an overall enjoyment of life [2]. However, some authors use a term satisfaction to define QoL [3–5], some a term well-being [6], while others use a word perception in the defining it [7]. The example of the first type is: “*QoL is the degree of need and satisfaction within the physical, psychological, social, activity, material, and structural area*” [3]. Second type defines QoL as “*a state of well-being which is a composite of two components: (1) the ability to perform everyday activities which reflect physical psychological and social well-being, and (2) patient satisfaction with levels of functioning and the control of disease and/or treatment related symptoms*” [6]. The third is used by World Health Organization (WHO) and World Health Organization Quality of Life (WHOQOL) Group. They define QoL as “*apperception of ones position in life in the context of the culture and value systems in which they live and in relation to their goals, expectations, standards and concerns*” [7]. To sum, QoL is a multidimensional concept which emphasizes the self-perceptions of an individual’s current state of mind affected in a complex way by the person’s physical health, psychological state, personal beliefs, social relationships, and their relationship to salient features of their environment [7, 8].

Simplification and facilitation of everyday activities and improvement of QoL is specially important for the elderly since their number is significantly increasing according to available statistics. The number of people aged 60 years or older will rise from 900 million to 2 billion by 2050, and the population ageing is happening more quickly than in the past [9]. Also, the World Population Aging Report shows that older population growth rate is more rapid in developing countries than developed countries [10].

Doing a simple math leads to the conclusion that smart things and systems should be devoted to a large extent to

J. Baraković Husić (✉)
University of Sarajevo, 71000 Sarajevo, Bosnia and Herzegovina
e-mail: jasmina.barakovic@etf.unsa.ba

S. Baraković
Little Mama Labs, 71000 Sarajevo, Bosnia and Herzegovina

E. Cero Dinarević
American University in Bosnia and Herzegovina, 71000 Sarajevo,
Bosnia and Herzegovina

improvement of QoL of elderly given that they will count over 22% of entire world population. This concept is named smart ageing. According to [11], smart ageing is a wide concept defined as technology and innovation usage in both the public and private sectors to produce products, services, solutions, and systems to improve QoL of people ages 50 and over. Healthy ageing is another term used to describe the concept of enabling older people to enjoy a good QoL [12]. Term mentioned in WHO is active ageing and is defined as the process of optimizing opportunities for health, participation, and security in order to enhance QoL as people age [13].

Today we are witnessing multiple smart ageing solutions being developed and produced, with many more in the announcement, but the QoL of elderly is not noticeably improved yet [9]. Motivated by this, we seek to give an answer to the following question: are the existing smart ageing solutions succeeding in direct improvement of QoL of elderly?

In order to find the answer, we have mapped QoL dimensions to smart ageing determinants, resulting in a set of QoL indicators for elderly population which need to be satisfied for QoL improvement. Based on that, we have performed a survey of various existing approaches, systems, and applications of smart ageing. The contribution of this paper is twofold: (1) the mapping between QoL dimensions and smart ageing determinants resulting in a set of QoL indicators for elderly, and (2) determination of success of the existing smart ageing solutions in improving QoL of elderly. Also, in order to contribute to QoL of elderly, we have provided the recommendations for future research activities in this field.

The paper is organized as follows: Sect. 2 depicts the smart ageing ecosystem through its definition, determinants, and relation to QoL dimensions. Section 3 surveys and discusses the existing approaches. Finally, Sect. 4 concludes this paper.

2 Smart Ageing Ecosystem

Smart ageing ecosystem includes key determinants of healthy ageing as described in [14], and covers economic, social and environment dimensions in objective and subjective conditions, and all aspects of people's QoL (see Fig. 1). On the other hand, QoL has eight dimensions [15]: material living conditions, health, education, productive and valued

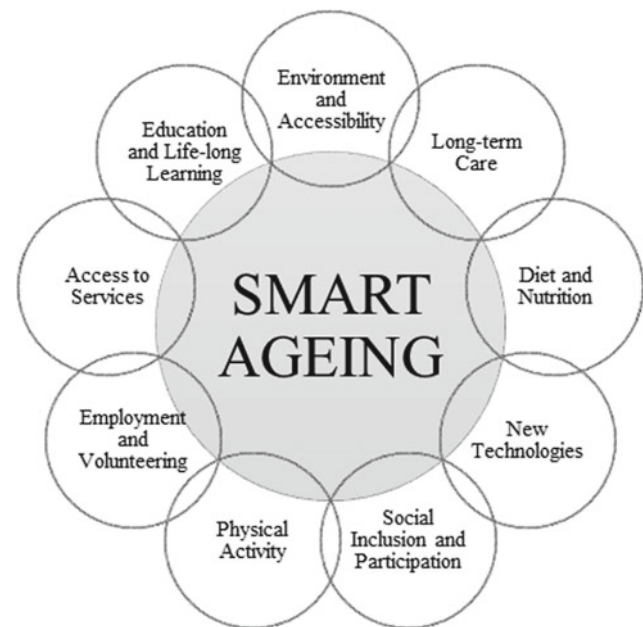


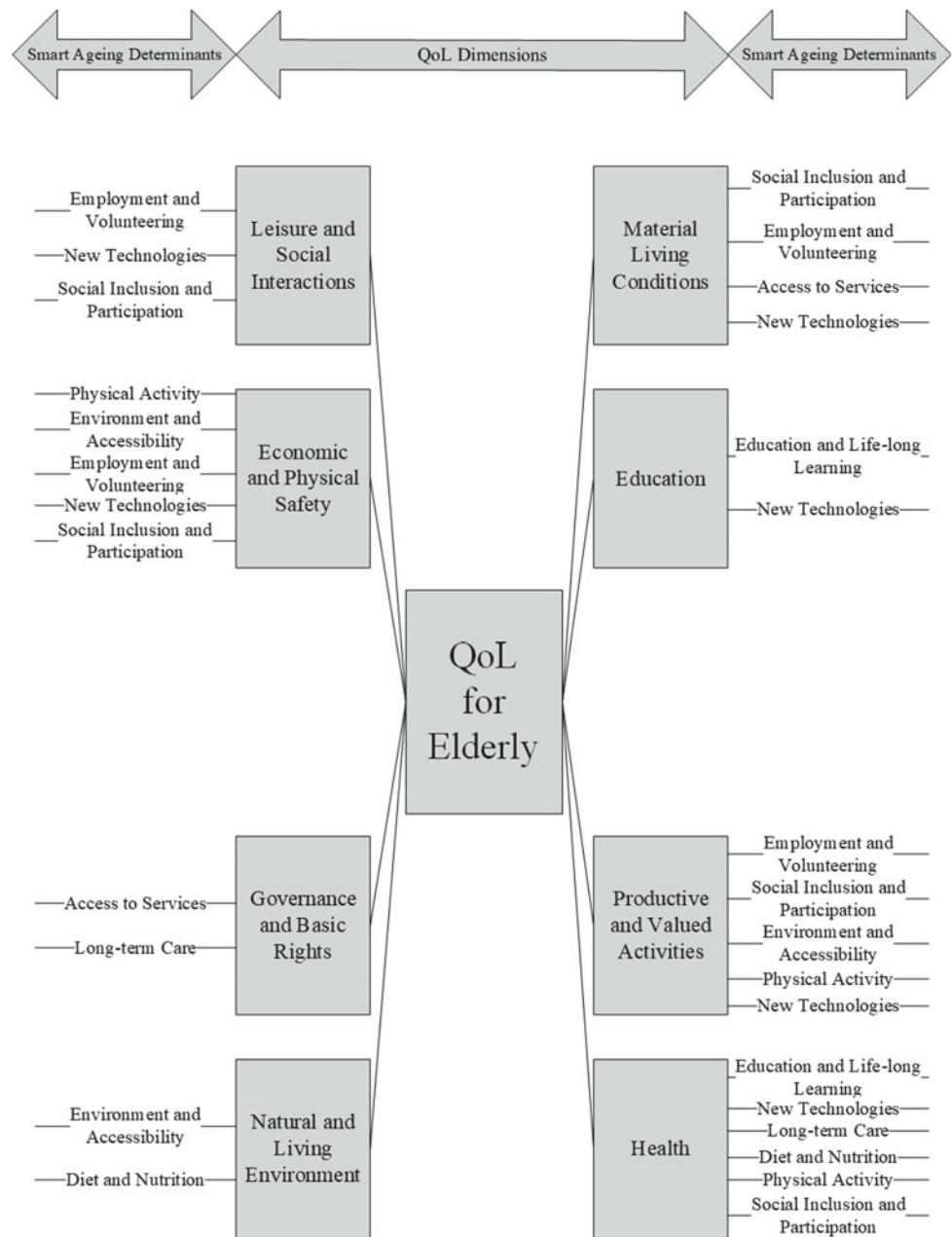
Fig. 1 Smart ageing determinants

activities, governance and basic rights, leisure and social interactions, natural and living environment, and economic and physical safety.

Each smart ageing determinant should be contained at least in one QoL dimension (see Fig. 2). For example, New Technologies (determinant) contributes to Leisure and Social Interactions (dimension) of elderly given that it provides new ways of entertainment and communication options. However, it contributes negatively to Personal insecurity given that usually people over 50 are insecure when using new devices, applications, etc., resulting in the withdrawal and abstinence from new technology products. Further on, usage of New Technologies allows elderly to increase their incomes by doing various paid jobs which consequently affects Material Living Conditions. New Technologies also have an impact on Education, by allowing elderly to expand the scope where they can gain knowledge and stay competitive, Productive and Valued Activities, since they can perform tasks that are contemporary and useful to them and the community, and Health, by at least having better monitoring of their various conditions independently.

This mapping provides a connection between smart ageing determinants and QoL dimensions, and results in QoL indicators for elderly. Knowing which features of smart ageing products and services affect which QoL dimension of

Fig. 2 Mapping between QoL dimensions and smart ageing determinants



elderly allows better targeting and effectively achieving the ultimate goal—better QoL of elderly. Research and industry communities should consider them when developing their products and services.

3 Survey Analysis and Discussion

The survey methodology contains three steps: (1) collection; (2) categorization, and (3) meta-analysis. Collection phase included literature search carried out using the combination of the following keywords: QoL, dimensions, smart, ageing, elderly, home, monitoring, etc. The categorization was done

by several criteria. Firstly, solutions were grouped based on the smart context they included in order to analyze what are the areas that these solutions cover. In this regard, several groups have been created based on the existing solutions: Smart Home, Smart Health Monitoring, Smart Fall Detection, Smart Applications, and Service Robot. Then, they were grouped according to: smart ageing determinants in order to analyze which are covered, Service users in order to determine are the solutions developed for elderly or people around them, and finally, whether the solutions have been verified by the elderly to know do they improve their QoL. Table 1 contains the summary of analyzed smart ageing solutions as described earlier. The meta-analysis of the

Table 1 Summary of analyzed existing smart ageing solutions

Solution	Smart context	Smart ageing determinants	Service users	Service verified by elderly
[16]	Smart Home	AS, LTC	Care providers	Not verified
[17]		AS, LTC, PA	Family Care providers Doctors Emergency Services Elderly	
[18]		EA		
[19]		AS, LTC, PA	Family Care providers Doctors Emergency Services	
[20]		AS, EA, LTC, PA	Family Care providers Doctors	
[21]		AS, PA	Family Care providers Doctors	
[22]		LTC	Elderly, handicapped, decrepit, crippled and disabled people	
[23]		EA	Elderly	
[24]		LTC	Elderly and disabled persons	
[25]		LTC, PA	Elderly	Verified
[26]		EA, LTC	Elderly	Not verified
[27]		AS, LTC	Elderly Care providers	
[28]		AS, LTC	Trained service agent Emergency Services	
[29]		AS, LTC, SIP	Care providers	
[30]		AS, LTC, SIP	Elderly	
[31]		LTC, DN	Elderly	
[32]	Smart Health Monitoring	AS, LTC, PA	Care providers	Verified
[33]		NT, PA	Elderly	
[34]		LTC	Elderly	

(continued)

Table 1 (continued)

Solution	Smart context	Smart ageing determinants	Service users	Service verified by elderly
[35]		AS, LTC	Family Care providers	Not verified
[36]		AS, LTC	Family Care providers Doctors Emergency Services	
[37]		AS, PA	Care providers	
[38]		LTC	Family Emergency Services	
[39]		AS, LTC, PA	Family Care providers Doctors	
[40]		AS, LTC	Doctors	
[41]	Smart Health Monitoring + Smart Fall Detection	LTC	Elderly	
[42]	Smart Fall Detection	PA, LTC	Care providers	
[43]		AS, LTC, PA	Doctors	
[44]		LTC, PA	Elderly	
[45]		LTC	Family Care providers Doctors Emergency Services	
[46]		AS, LTC	Family Care providers	
[47]		AS, LTC	Family Care providers Doctors Emergency Services	
[48]		PA, LTC	Care providers	
[49]	Smart Applications	AS, LTC, PA	Elderly	
[50]	Service Robot	LTC, NT	Elderly and disabled people	

AS access to services; DN diet and nutrition; EA environment and accessibility, LTC long-term care; NT new technologies; PA physical activity; SIP social inclusion and participation

selected solutions addressed them according to aforementioned criteria and provided input data for discussion and conclusion.

We have analyzed 35 existing smart ageing solutions: 44.4% dealing with Smart Home, 27.8% with Smart Health Monitoring, 22.2% with Smart Fall Detection, and 2.8% with Smart Application and with Service Robot. Regardless of context, the addressed solutions are associated to smart ageing determinants with the following percentages: Long-term Care 85.7%, Access to Services 54.3%, Physical Activity 40%, Environment and Accessibility 11.4%, New Technologies and Social inclusion and Participation each 5.7%, Diet and Nutrition 2.8%, and Employment and Volunteering and Education and Life Long Learning 0%. In both cases, percentages for context and determinants show overlapping which implies that some studies addressed several contexts or determinants with their solutions. The obtained results show that the existing solutions cover narrow and limited smart ageing contexts and focus on health and accessibility related determinants while missing to address other listed and important components that, as we already discussed earlier in the paper, contribute to QoL of elderly.

Further on, only 30% of addressed solutions consider elderly as end service users, while the remaining ones are developed or produced for people around elderly such as family, doctors, care providers, etc. This means that the proposed solutions may help and simplify activities for people that take care of elderly. Older people may benefit from that indirect help, but not necessarily. In fact, in most cases they have not been asked does the solution help given that only 8.3% of analyzed approaches are verified by elderly, leaving the rest unverified by the ones for whom they are allegedly developed.

4 Conclusion

The aim of this paper was to answer the question are the existing smart ageing solutions succeeding in direct improvement of QoL of elderly. The results of the conducted survey give a clear answer to it—they are not. We cannot conclude that the existing smart ageing solutions necessarily directly contribute to QoL of elderly due to several reasons. Firstly, the existing approaches have not addressed various dimensions of QoL of elderly, nor have they included different smart ageing determinants, meaning that they are not multidimensional and comprehensive, i.e., not in line with QoL nature. Furthermore, the majority of solutions have not been developed/produced for direct usage by elderly at all, but for people around them. Last and most important, most solutions were never properly verified by the elderly so one cannot say that they have been beneficial to them.

This conclusion opens a wide area of research issues to be addressed and corrections to be applied in the future. However, in order to succeed in true improving QoL of elderly, research and industry communities are recommended to develop smart ageing solutions that cover all elderly QoL dimensions and utilize smart ageing features to do so. Important suggestion is to ask the elderly what would help them and increase their QoL in certain context, produce solutions directly for that population, and afterwards verify their products and services with them.

Conflicts of Interest The authors declare no conflict of interest.

References

1. Cero, E., et al.: IoT's tiny steps towards 5G: Telco's perspective. *Symmetry* **9**(10), 213 (2017)
2. Post, M.: Definitions of quality of life: what has happened and how to move on. *Top. Spinal Cord Inj. Rehabil.* **20**(3), 167–180 (2014)
3. Hörnquist, J.O.: The concept of quality of life. *Scand. J. Soc. Med.* **10**(2), 57–61 (1982)
4. Van Knippenberg, F.C., et al.: Measuring the quality of life of cancer patients: psychometric properties of instruments. *J. Clin. Epidemiol.* **41**(11), 1043–1053 (1988)
5. Emerson, E.: Evaluating the impact of deinstitutionalization on the lives of mentally retarded people. *Am. J. Ment. Retard.* **90**(3), 277–288 (1985)
6. Gotay, C.C., et al.: Assessing quality of life in head and neck cancer. *Qual. Life Res.* **1**(1), 5–17 (1992)
7. WHOQOL Group: Development of the World Health Organization WHOQOL-BREF quality of life assessment. *Psychol. Med.* **28**(3), 551–558 (1998)
8. Theofilou, P.: Quality of life: definition and measurement. *Eur. J. Psychol.* **9**(1) (2013)
9. WHO: <http://www.who.int/features/factfiles/ageing/en/>. Last accessed 10 Sept 2018
10. Sin, A.K.: A wearable device for the elderly: a case study in Malaysia. In: ICIMU, Malaysia (2014)
11. Department of the Taoiseach: https://www.taoiseach.gov.ie/eng/Publications/Publications_2016/Programme_of_Actions_for_Smart_Ageing.pdf. Last accessed 10 Sept 2018
12. EuroHealthNet: <http://www.healthyageing.eu/sites/www.healthyageing.eu/files/featured/Healthy%20and%20Active%20Ageing.pdf>. Last accessed 10 Sept 2018
13. Yang, Q., et al.: Active aging in the workplace and the role of intelligent technologies. In: WI-IAT, Singapore (2015)
14. EuroHealthNet: <http://www.healthyageing.eu/steps-healthy-ageing>. Last accessed 10 Sept 2018
15. Eurostat: <https://ec.europa.eu/eurostat/documents/8131721/8131772/TF3-Final-report-Quality-of-Life.pdf>. Last accessed 10 Sept 2018
16. Agoulmine, N., et al.: U-health smart home. *IEEE Nanotechnol. Mag.* **5**(3), 6–11 (2011)
17. Arcelus, A., et al.: Integration of smart home technologies in a health monitoring system for the elderly. In: AINAW'07, Canada (2007)
18. Bien, Z.Z., et al.: LARES: an intelligent sweet home for assisting the elderly and the handicapped. KAIST (2002)
19. Demir, E., et al.: Smart home assistant for ambient assisted living of elderly people with dementia. *Procedia Comput. Sci.* **113**, 609–614 (2017)

20. Do, H., et al.: RiSH: A robot-integrated smart home for elderly care. *Rob. Auton. Syst.* **101**, 74–92 (2017)
21. Franco, C., et al.: Behavioral telemonitoring of the elderly at home: detection of nycthemeral rhythms drifts from location data. In: WAINA'10, Australia (2010)
22. Ghazal, B., et al.: Smart home automation system for elderly, and handicapped people using XBee. *Int. J. Smart Home* **9**(4), 203–210 (2016)
23. He, J.: The design of smart home for the elderly based on ZigBee. In: ICCAE'16 (2016)
24. Kadalla, A.S., et al.: Android based smart home system. In: ICADI'16, Nigeria (2016)
25. Mocanu, I., et al.: Mobile@Old: a smart home plat-form for enhancing the elderly mobility. *Adv. Electr. Comput. Eng.* **17**(4), 19–27 (2017)
26. Nisar, K., et al.: Smart home for elderly living using Wireless Sensor Networks and an Android application. In: AICT'16, Azerbaijan (2016)
27. Ransing, R.S., et al.: Smart home for elderly care, based on wireless sensor network. In: ICNTE'15, India (2015)
28. GreatCall: <https://www.greatcall.com/>. Last accessed 10 Sept 2018
29. MobileHelp: <https://www.theseniorlist.com/2017/02/mobilehelp-updated-review/>. Last accessed 10 Sept 2018
30. OASIS: <http://www.oasis-project.eu/>. Last accessed 10 Sept 2018
31. Gullà, F., et al.: An adaptive smart system to foster disabled and elderly people in kitchen-related task. In: PETRA'16, Greece (2016)
32. Charlon, Y., et al.: Activity monitoring system for elderly in a context of smart home. *IRBM* **34**(1), 60–63 (2013)
33. Demiris, G., et al.: Senior residents' perceived need of and preferences for "smart home" sensor technologies. *Int. J. Technol. Assess. health care* **24**(1), 120–124 (2008)
34. Di Lecce, V., et al.: Smart postural monitor for elderly people. In: IMEKO TC4, Spain (2017)
35. Lee, J.V., et al.: Smart elderly home monitoring system with an android phone. *Int. J. Smart Home* **7**(3), 17–32 (2013)
36. Lv, Z.: iCare: A mobile health monitoring system for the elderly. In: GreenCom&CPSCoM, China, (2010)
37. Gaddam, A., et al.: Smart home using optimized number of wireless sensors for elderly care. In: AEMC'09, India (2009)
38. Park, S.J., et al.: Development of a real-time stroke detection system for elderly drivers using quad-chamber air cushion and IoT devices. In: WCX'18, USA (2018)
39. Guan, K., et al.: A remote health monitoring system for the elderly based on smart home gateway. *J. Healthc. Eng.* (2017)
40. Ahmed, A.B., et al.: Towards smart health monitoring system for elderly people. In: iCAST'13, South Korea (2013)
41. Diraco, G., et al.: A radar-based smart sensor for unobtrusive elderly monitoring in ambient assisted living applications. *Biosensors* **7**(4), 55 (2017)
42. De Miguel, K., et al.: Home camera-based fall detection system for the elderly. *Sensors* **17**(12), 2864 (2017)
43. Hansen, T.R., et al.: Using smart sensors and a camera phone to detect and verify the fall of elderly persons. In: EMBEC'05, Czech Republic (2005)
44. Muheidat, F., et al.: Context-aware, accurate, and real time fall detection system for elderly people. In: ICSC'18, USA (2018)
45. Noury, N.: A smart sensor for the remote follow up of activity and fall detection of the elderly. In: EEE-EMBS MMB'02, USA (2002)
46. Babu, B.R.P., et al.: Smart mobile application for the safety of women and elderly population. *IJIRD* **3**(5), 575–580 (2014)
47. Wang, J., et al.: An enhanced fall detection system for elderly person monitoring using consumer home networks. *IEEE Trans. Consum. Electr.* **60**(1), 23–29 (2014)
48. Alwan, M., et al.: A smart and passive floor-vibration based fall detector for elderly. In: ICICT'06, Syria (2006)
49. Helal, S., et al.: Smart phone based cognitive assistant. In: UbiHealth'03, Springer, USA (2003)
50. Park, K.H., et al.: A steward robot for human-friendly human-machine interaction in a smart house environment. *IEEE Trans. Autom. Sci. Eng.* **5**(1), 21–25 (2008)

A New Digital Mental Health System Infrastructure for Diagnosis of Psychiatric Disorders and Patient Follow-Up by Text Analysis in Turkish

Zeynep Orhan, Mine Mercan, and Merve Kevser Gökçöl

Abstract

This research focuses on detecting psychiatric disorders in adults by applying a Turkish text analysis system. The study examined pre-diagnosed depression, mania and healthy adults. The distinct words and their categories of the subjects' text data along with their existence, frequency or weighted values were used as the features of the ML techniques Naïve Bayes, Bayesian Logistic Regression and Support Vector Classifier. The promising results of the study, some of which were above 80%, show that language usage can be a good indicator of psychological states of the subjects. The goal of the study is to obtain the semantic ontology and dictionaries specific to various disorders and to develop a new digital mental health system infrastructure as a mobile software that will facilitate the diagnosis of psychiatric disorders and patient follow-up by using computerized content analysis of the big and dynamic communication texts. It will provide means to produce short- and long-term strategies in the health sector by fulfilling the needs in the fastest, the most proper and the most efficient manner.

Keywords

Sentiment analysis • Natural language processing • Machine learning • Mental disorder diagnosis • Follow-up

1 Introduction

Mental disorders are one of the most challenging problems of modern world. Wide spread effects of this phenomenon are influencing deeply the whole society. Nowadays, most people suffer from mental disorders [23]. Mental health and disorders cover many parameters related to the individuals and the society. Mental disorders have high risks and impacts. Early detection of these disorders that are generally under-diagnosed and under-treated [11] could be helpful to get better and quick results. Failure to intervene early and effectively impacts the whole society adversely and results in profound long-term costs.

Unfortunately, health systems have been far below the expectations to fulfill the requirements of mental disorders, which led to a huge gap between the need for treatment and its provision. In low/middle- and high-income countries, the percentage of people with mental disorders who receive no treatment for their disorder is between 76–85% and 35–50%, respectively. Furthermore, the poor quality of care for many of those who do receive treatment is far worse than this situation. The statistics indicate and support these facts asserting that an estimated 20% of people who commit suicide have been in contact with their general practitioners or psychiatric services within one week prior to their deaths, and 40% in the preceding month [23]. The key solution to the mental health problems can be found in technological developments. Today people have an easy access to data through technology and this may lead to many changes. The available data on the internet is generally in the form of text that can be obtained from any platform where people freely share their opinions. The digital and free form data reflect a variety of differences related to culture, location, ethnicity, feelings and are more reliable.

Computer applications can also be used to identify the psychological state of a person by text or speech data analytics, since written or spoken sentences are believed to hide hints and traces about the current and even past states of

Z. Orhan (✉) · M. Mercan
Istanbul, Turkey
e-mail: zorhan@gmail.com

M. Mercan
e-mail: mine.mercan@gmail.com

M. K. Gökçöl
Richmond Park International Secondary School, Sarajevo,
Bosnia and Herzegovina
e-mail: mervekevser@gmail.com

people. The use of language provides important evidence about the human mind, including emotional ups and downs and altering moods caused by psychiatric disorders [18]. Recent studies showed that emotions can affect one's speech [6]. Emotions are complex psychophysical processes that evoke positive or negative psychological responses (or both) and physical expressions, often involuntary. Although it is especially hard to detect feelings in text compared to face-to-face talk, where one can detect facial expressions of a person, it is not impossible at all. The standard approach to diagnose mental disorders is done through a series of clinically administered diagnostic interviews and tests [22]. However, assessment of patients using these tests is expensive and time-consuming. Furthermore, the stigma associated with mental illnesses motivates inaccurate self-reporting by affected individuals and their family members thus, making the tests unreliable [18]. A promising approach and research area related to this fact is the Sentiment Analysis (SA). The diagnosis of psychiatric disorders and patient's follow-up can be aided by computer applications utilizing SA techniques.

The rest of the paper is organized as follows: Sect. 2 presents related research in the field. Section 3 explains the datasets and the methods utilized along with the experimental results. Finally, Sect. 4 makes conclusions, provides a description of the impact of this work, and makes suggestions for future research.

2 Related Work

SA, also called opinion mining, is the field of study that analyzes people's opinions, sentiments, evaluations, appraisals, attitudes, and emotions towards entities such as products, services, organizations, individuals, issues, events, topics, and their attributes [12].

A study [1] on affect intensity analysis of dark web forums introduced a system for analyzing extremist groups' forum postings by using the terms that represent feelings like happiness, anger, sadness, horror, and the like as attributes and linear regression analysis. Social events were examined for analyzing trends of people's sentiments along with timeline [8]. The features were derived from emotion lexicons for automatically categorizing sentences in a text into Ekman's six basic emotion categories, namely happiness, sadness, anger, disgust, surprise, fear and no-emotion, by the study of [3].

Unfortunately, the applications of SA have been generally conducted for languages like English. Turkish SA studies are very limited to the extent of our knowledge. Turkish texts in a labeled dataset of movie reviews varying

in the scale of 0–5 were classified as positive, negative or neutral [7]. A more recent study analyzed Turkish news and the effects of different ML algorithms by using annotated data [10]. The customers' product reviews were examined to determine the polarity of them by considering the language features and very high accuracy results were obtained in another study for Turkish [16].

The application area of SA has been extended to the studies in mental health. Scientists have discussed the relation between language and psychology for many years. McClelland analyzed written stories of people who had food deprivation for 1, 4 or 6 hours [4]. Gottschalk and Gleser [9] also contributed to the idea significantly by providing a content analysis method which is capable of measuring the magnitude of any mental or emotional state or trait that can be clearly defined and categorized. It uses not simply words in isolation to classify content, but rather identifies relationships and attitudes reported by the subject. Tucker and Rosenberg [21] used computer analysis to differentiate the free speech and transcripts of dream material of 10 schizophrenic patients. They concluded that in general, the language content of the schizophrenic patient mirrored an almost agitated attempt to locate oneself in time and space and to defend against internal discomfort and confusion. In another study, the free speech samples and Thematic Apperception Test (TAT) responses of 95 volunteers were compared by using the General Inquirer content analysis computer program and the Harvard III Psychosociological Dictionary [20]. TAT data were found to be superior to free speech in predicting individual differences [19]. Psychological text analysis rapidly developed following these initial studies. Linguistic Inquiry and Word Count (LIWC) has been used as a utility for many interdisciplinary studies on psychology and computational linguistics [17]. LIWC, which uses a dictionary that consists of word categories and includes almost 4500 words and word stems, is a text analysis program for studying the emotional, cognitive, and structural components presented in verbal and written speech of people. The possibility of measuring personality using lexical analysis of natural speech that was obtained by recording free speeches of 35 men and 33 women for 3 min has been proved by some researchers [5].

To date, there have been very few studies in Turkish SA for mental health, and the first published research was completed in 1993 [13]. They analyzed texts of 5-min speech samples of 50 schizophrenics, 50 manic and 50 depressed people by using computerized content analysis. Turkish version of the Harvard-III Psychological Dictionary is designed for using across a variety of contexts and categorized the words as positive or negative. It was used to find categories of words [14] and the General Inquirer (GI) [20]

program was used to analyze the texts yielding 72.5% accuracy classification result. The relation between Turkish language usage in texts and psychological states of the people has been the focus on another study. In this study, depressive, nondepressive, anxious and non-anxious people have written some texts and these texts were classified by using Weka ML algorithms [2].

3 Experimental Setup

In this section, the experimental setup of the system is explained by providing the details of the data collection and processing, feature selection strategies, classification methods and the results.

3.1 Datasets

The data were grouped under three categories: Depression (DPR), Mania (MN) and Healthy Controls (HC) and the analysis were conducted on two groups: Group 1 has DPR and HC, Group 2 has MN and HC. The data which were obtained from 90 adults that reside a psychiatry clinic in Turkey. The data were equally divided as 30 people constituted of 13 males and 17 females, among the categories, namely DPR, MN and HC. 10 min free verbal samples of subjects were collected along with their demographic information.

In the training and test phases 21 and 9 instances of data for each category were used, respectively.

3.2 Data Preprocessing

Harvard-III Psychological Dictionary was translated into Turkish for finding the categories of the words by volunteers. Turkish morphological analyzer [15], disambiguation tool [25] and Weka [24] ML library programs were used in this study. During the pre-processing of the data, the words were converted into root-affix combinations with part-of-speech such as Noun, Adj (adjective), Adv (adverb), Verb, Pnon (pronoun) and the like by the morphological analyzer. After the disambiguation process, the most proper result was chosen by the disambiguation tool. Table 1 shows the preprocessing of a document.

3.3 Features

The roots of the words from all the subjects' texts were analyzed and features were extracted out of them. NLP methods were used to extract useful features for ML training phase using morphological analysis, disambiguator tools and Harvard-III psychological dictionary. Various methods were employed for feature selection such as existence, frequency and category. Each method has existence/binary and frequency types as well. Table 2 depicts example input data for classification methods where the values of features represent the word or category existence or frequency.

In the abbreviations of these methods W is Word, C is Category, B is Binary, and F is Frequency. *Word Existence Feature (WOB)* method uses the binary information of the existence or non-existence of each word and *Word*

Table 1 An example of data, input/output of morphological analyzer and the disambiguator

Raw data/ the input of morphological analyzer	The output of morphological analyzer/ The input of the disambiguator	The output of disambiguator
<DOC> <TITLE> <S> Ben zarar görüyorum . </S>	<DOC> <DOC> <TITLE> <TITLE> <S> <S> ben ben +Noun+A3sg+Pnon+Nom ben ben +Pron+Pers+A1sg+Pnon+Nom zarar zarar +Noun+A3sg+Pnon+Nom görüyorum gör+Verb+Pos+Prog1+A1sg .. +Punc </S> </S> </DOC> </DOC>	<DOC> <DOC> <TITLE> <TITLE> <S> <S> ben ben+Pron+Pers+A1sg+Pnon+Nom zarar zarar+Noun+A3sg+Pnon+Nom görüyorum gör+Verb+Pos+Prog1+A1sg ..+Punc </S> </S> </DOC> </DOC>

Table 2 Example input data for classification methods where the values of features represent the word/category existence/frequency

	Word									Category								
	Id	Gender	W ₁	W ₂	W ₃	W ₄	...	W _n	Class	Id	Gender	C ₁	C ₂	C ₃	C ₄	...	C _n	Class
Binary (word or category existence)	125	M	0	1	1	0	...	1	N	125	M	0	1	0	0	...	1	N
	41	F	1	0	0	1	...	0	P	41	F	1	0	0	1	...	1	P
	134	M	0	1	1	0	...	1	P	134	M	1	0	0	1	...	0	P
Frequency (word or category frequency)	No.	Gender	W ₁	W ₂	W ₃	W ₄	...	W _n	Class	No.	Gender	C ₁	C ₂	C ₃	C ₄	...	C _n	Class
	125	M	0	20	45	0	...	22	N	125	M	0	45	0	0	...	73	N
	41	F	15	0	0	105	...	0	P	41	F	34	0	12	0	...	67	P
	134	M	0	100	35	0	...	43	P	134	M	90	0	0	23	...	0	P

Frequency Feature (WOF) uses the frequency of each word for each subject. Similarly, *Category Existence Feature (COB)* and *Category Frequency Feature (COF)* use the information about existences or frequencies of the categories instead of the words where the categories were obtained from The Turkish version of Harvard-III Psychological Dictionary.

Another approach for feature selection was determining disorder specific lists of words and categories. Weighted and non-weighted values of the features were used for these partial lists. *Weighted Frequency of Disorder Specific Word Feature (WLF)* words were identified, counted, normalized and listed for each class of instances with the frequency values. These words were classified and listed as HC, DPR and MN words considering their frequencies in each class. The words that were in the intersection of more than one class and whose frequencies were close to each other were eliminated from all lists, since these words would not be effective in the classification process and were marked as irrelevant features. The frequency of a word for a specific subject was calculated and normalized by dividing this frequency by the text size (TS) of the subject and multiplied by a common factor for simplicity. Then for all words these values were summed up for all distinct words and they were divided by the number of subjects in that class and multiplied by a factor for getting rid of floating-point numbers. This process produced the lists of words from each class. Then the texts were examined to find out the number of words/categories used from each list. *Frequency of Disorder Specific Word Feature (WL)* is very similar to *WLF*, except that the values for each subject were obtained by summing up the frequency of words used by the subject without multiplying it by the corresponding frequency that appear in each class list. *Weighted Frequency of Disorder Specific Category Feature (CLF)* and *Frequency of Disorder Specific Category Feature (CL)* were very similar to *WLF* and *WL* by using the categories instead of the words.

Positive Negative Words Binary (PNWB) and *Positive Negative Categories Binary (PNCB)* methods used a hybrid

method of the above ones. Firstly, the word/category lists were extracted like *WL/CL*, then each word/category existence information in these lists was used as a feature. *Positive Negative Words Frequency (PNWF)* and *Positive Negative Categories Frequency (PNCF)* methods were applied in the same manner by using the frequencies instead of existence values.

In the last 8 methods, various threshold values of 0, 5, 25 and 50% were used in the determination and elimination of the irrelevant features. The features that were in the intersection of both classes were compared and whenever the differences between them were less than the threshold, they were either erased from both lists completely named as Erase-Both (EB), or their values in the lists were decreased and updated relatively named as Erase-Weighted (EW). The short summary of the methods and their abbreviations are provided in Table 3.

3.4 Classification

Classification was achieved by using ML methods provided by a data mining tool named Weka [24]. In this study, NB, Bayesian Logistic Regression (BLR) and Support Vector Classifier (SVC-SMO in Weka) were used for the classification of subjects.

The summary of the results for DPR versus HC and MN versus HC are depicted in Table 4 and the graphics of Fig. 1. Overall depression results are better than mania. Furthermore, the features based on the words and binary values give the best results in many cases. The most promising results from both performance and accuracy perspectives were obtained by PNWB, PNWF, PNCB and PNCF feature selection methods, since they eliminated the irrelevant features. When erase-both and erase-weighted methods were used, significant improvements could not have been observed, but the best results among the threshold-based elimination methods were achieved for 50% threshold value. This may be due to the lack of huge amount of data, the

Table 3 Methods for feature selection and their explanations

Method	Explanation
CL	Frequency of Disorder Specific Category Feature
CL_EB	Frequency of Disorder Specific Category Feature Erase-Both
CL_EW	Frequency of Disorder Specific Category Feature Erase-Weighted
CLF	Weighted Frequency of Disorder Specific Category Feature
CLF_EB	Weighted Frequency of Disorder Specific Category Feature Erase-Both
CLF_EW	Weighted Frequency of Disorder Specific Category Feature Erase-Weighted
COB	Category Existence Feature
COF	Category Frequency Feature
PNCB	Positive Negative Categories Binary
PNCB_EB	Positive Negative Categories Binary Erase-Both
PNCB_EW	Positive Negative Categories Binary Erase-Weighted
PNCF	Positive Negative Categories Frequency
PNCF_EB	Positive Negative Categories Frequency Erase-Both
PNCF_EW	Positive Negative Categories Frequency Erase-Weighted
PNWB	Positive Negative Words Binary
PNWB_EB	Positive Negative Words Binary Erase-Both
PNWB_EW	Positive Negative Words Binary Erase-Weighted
PNWF	Positive Negative Words Frequency
PNWF_EB	Positive Negative Words Frequency Erase-Both
PNWF_EW	Positive Negative Words Frequency Erase-Weighted
WL	Frequency of Disorder Specific Word Feature
WL_EB	Frequency of Disorder Specific Word Feature Erase-Both
WL_EW	Frequency of Disorder Specific Word Feature Erase-Weighted
WLF	Weighted Frequency of Disorder Specific Word Feature
WLF_EB	Weighted Frequency of Disorder Specific Word Feature Erase-Both
WLF_EW	Weighted Frequency of Disorder Specific Word Feature Erase-Weighted
WOB	Word Existence Feature
WOF	Word Frequency Feature

demographic varieties and language usages of the subjects differing greatly. It is believed that the data effected the results deeply and increasing the size and diversity in data will improve the results positively.

4 Conclusion

There are very few studies which used NLP methods in Turkish text analysis, but they are not enough to provide variety and accuracy in the field. This research contributes to detecting psychiatric disorders of adults by applying a Turkish text analysis system. Since the new generation is expressing themselves mostly in electronic environment, the study gains an important impact in detecting psychiatric disorders in people.

The study examined adults with depression, mania and healthy adults, which were pre-diagnosed by psychiatrics.

The distinct words and their categories of the subjects' text data along with some other feature selection criteria were used as the features of the ML techniques NB, BLR and SMO of Weka library. The promising results of the study show that language usage can be a good indicator of psychological state of the subjects.

In the future, it is planned to obtain the semantic ontology and dictionaries that can be used in these types of researches and specific to various disorders. Additionally, it can lead to practical and economical tools that can be used for early diagnosis for people with psychological disorders.

The goal of the current study is to develop a new digital mental health system infrastructure. It is planned to be a mobile software that will facilitate the diagnosis of psychiatric disorders and patient follow-up by using content analysis of the dynamic communication texts that are obtained from the mobile environment. We will implement software as a product that will assist the diagnosis of disorders,

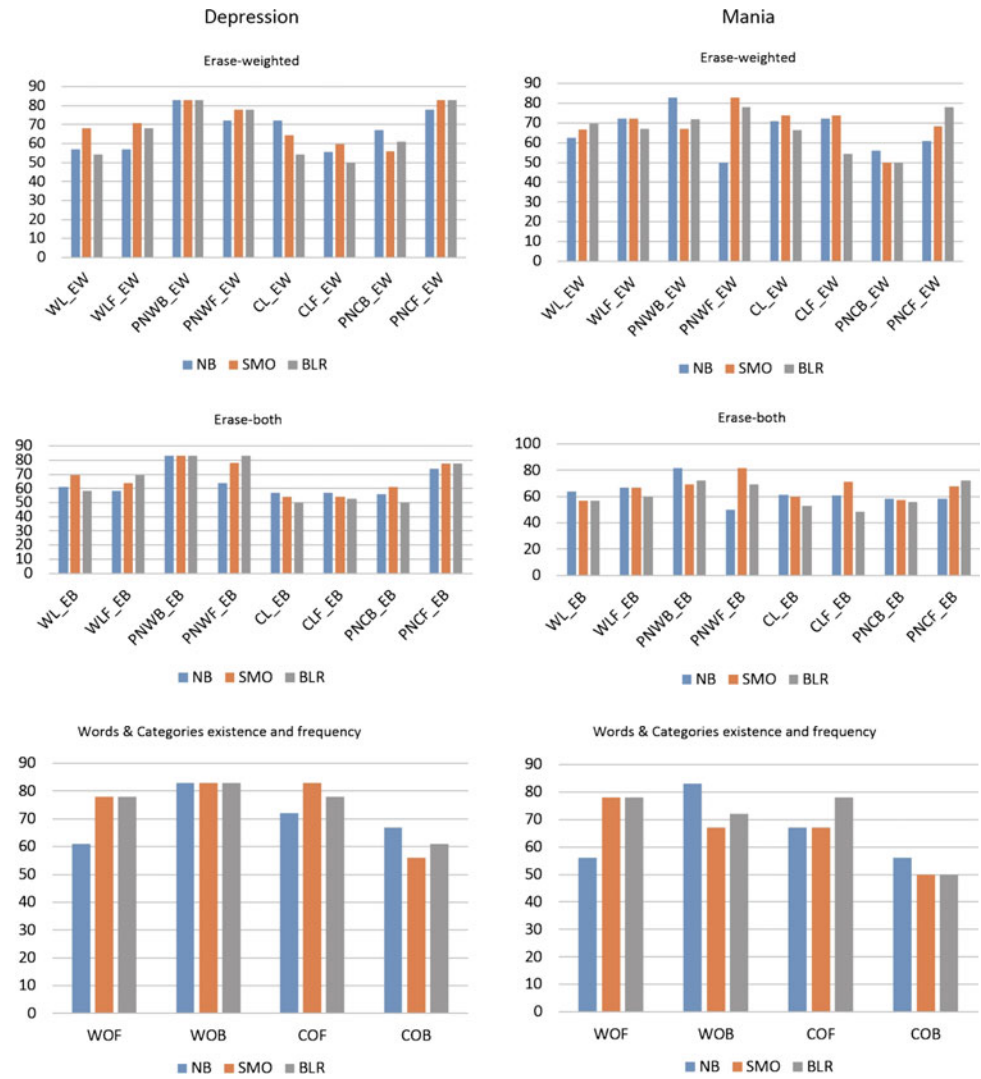
Table 4 Accuracy results of DPR versus HC and MN versus HC for NB, SMO, BLR and various feature selection methods by using thresholds 0, 5, 25, and 50. The results are rounded percentage values

	Depression						Mania					
	Tresh = 0			Tresh = 5			Tresh = 0			Tresh = 5		
	NB	SMO	BLR	NB	SMO	BLR	NB	SMO	BLR	NB	SMO	BLR
CL_EB	61	56	50	56	44	50	67	67	50	67	44	50
CL_EW	67	56	50	67	56	50	67	67	50	67	67	50
CLF_EB	39	39	50	50	56	50	72	78	50	72	72	50
CLF_EW	39	39	50	39	44	50	72	78	50	72	72	50
PNCB_EB	67	56	61	67	61	67	56	56	50	56	56	56
PNCB_EW	67	56	61	67	56	61	56	50	50	56	50	50
PNCF_EB	78	83	78	78	78	78	61	67	83	61	72	78
PNCF_EW	78	83	83	78	83	83	61	67	78	61	67	78
PNWB_EB	83	83	83	83	83	83	83	72	72	83	72	72
PNWB_EW	83	83	83	83	83	83	83	67	72	83	67	72
PNWF_EB	61	78	78	67	78	83	50	83	78	50	83	78
PNWF_EW	72	78	78	72	78	78	50	83	78	50	83	78
WL_EB	56	67	50	67	72	72	50	44	50	67	44	50
WL_EW	61	83	50	50	61	50	61	50	50	67	56	61
WLF_EB	44	61	50	39	78	72	78	72	56	61	67	56
WLF_EW	39	72	50	39	61	72	78	72	56	61	67	56
	Tresh = 25			Tresh = 50			Thresh = 25			Thresh = 50		
	NB	SMO	BLR	NB	SMO	BLR	NB	SMO	BLR	NB	SMO	BLR
CL_EB	61	56	44	50	61	56	61	61	56	50	67	56
CL_EW	72	67	39	83	78	78	78	83	83	72	78	83
CLF_EB	67	61	50	72	61	61	50	67	50	50	67	44
CLF_EW	72	78	50	72	78	50	67	67	50	78	78	67
PNCB_EB	61	61	67	56	61	50	61	56	56	61	61	61
PNCB_EW	67	56	61	67	56	61	56	50	50	56	50	50
PNCF_EB	78	83	83	61	67	72	61	72	72	50	61	56
PNCF_EW	78	83	83	78	83	83	61	72	78	61	67	78
PNWB_EB	83	83	83	83	83	83	83	67	72	78	67	72
PNWB_EW	83	83	83	83	83	83	83	67	72	83	67	72
PNWF_EB	67	78	89	61	78	83	50	83	61	50	78	61
PNWF_EW	72	78	78	72	78	78	50	83	78	50	83	78
WL_EB	61	72	50	61	67	61	61	72	61	78	67	67
WL_EW	56	56	56	61	72	61	50	83	78	72	78	89
WLF_EB	67	61	78	83	56	78	72	72	67	56	56	61
WLF_EW	72	67	72	78	83	78	72	72	78	78	78	78

especially the most frequent ones like depression and mania, and patient's follow up. In the diagnosis phase, it will be used before the medical examination along with the other tests or analyzing the expressions of the patients separately. The results will be used by psychiatrists. The analysis results of the daily communications of patients will be periodically

reported to the psychiatrists. Additionally, we will keep the inferences about the patients and disorders for determination of short- and long-term health policies by the relevant authorities. Furthermore, informed consent of the patients will be requested for collecting and analyzing the information in order to protect patients' privacy. The follow-up of

Fig. 1 Average accuracy percentages of depression and mania results when erase-both, erase-weighted and word & category existence were applied



patients who are off-centered or have time limitations can be performed economically and easily in this way. We expect that the software that will be obtained will fill an important gap in the field.

References

1. Abbasi, A., Chen, H., Salem, A.: Sentiment Analysis in multiple languages: feature selection for opinion classification in web forums. The University of Arizona, ACM 1073-0516/01/0300-0034 (2007)
2. Albayrak, N.B.: Opinion and sentiment analysis using natural language processing techniques. Master thesis, Fatih University (2011)
3. Aman, S., Szpakowicz, S.: Using Roget’s thesaurus for fine-grained emotion recognition. In: Proceedings of the third international joint conference on natural language processing IJCNLP 2008, pp. 296–302 (2008)
4. Atkinson, J.W., McClelland, D.C.: The effect of different intensities of the hunger drive on thematic apperception. *J. Exp. Psychol.* **38**, 643–658 (1948)
5. Cohen, A.S., Minor, K.S., Baillie, L.E., Dahir, A.M.: Clarifying the linguistic signature: measuring personality from natural speech. *J. Pers. Assess.* **90**(6), 559–563 (2008)
6. Colace, F., Casaburi, L., Santo, M.D., Greco, L.: Sentiment detection in social networks and in collaborative learning environments. *Comput. Hum. Behav.* **51**, 1061–1067 (2014)
7. Eroglu, U.: Sentiment analysis in Turkish. Master’s thesis, Middle East Technical University, Ankara Turkey (2010)
8. Fukuhara, T., Nakagawa, H., Nishida, T.: Understanding sentiment of people from news articles: temporal sentiment analysis of social

- events. In: Proceedings of the international conference on weblogs and social media, Colorado (2007)
9. Gottschalk, L.A., Gleser, G.C.: *The Measurement of Psychological States Through the Content Analysis of Verbal Behavior*. University of California Press, Berkeley (1969)
 10. Kaya, M., Fidan, G., Toroslu, I.H.: Sentiment analysis of Turkish political news. In: Proceedings of the 2012 IEEE/WIC/ACM international joint conferences on web intelligence and intelligent agent technology, vol. 01, pp. 174–180. IEEE Computer Society (2012)
 11. Kessler, R.C., Zhao, S., Katz, S.J., Kouzis, A.C., Frank, R.G., Edlund, M., Leaf, P.: Past-year use of outpatient services for psychiatric problems in the National Comorbidity Survey. *Am. J. Psychiatry* **156**, 115–123 (1999)
 12. Liu, B.: *Sentiment Analysis and Opinion Mining*. Morgan & Claypool Publishers (2012)
 13. Mete, L., Schunur, P.P., Rosenberg, S.D., Oxman, T.E., Doğaner, I., Sorias, S.: Language content and schizophrenia in acute phase Turkish patients. *Soc. Psychiatry Psychiatr. Epidemiol.* **28**, 275–280 (1993)
 14. Montague Jr., J.C.: *The Effect of Institutionalization on the Social Behavior and Language of Mentally retarded Children*, pp. 93–109. University of Florida (1971)
 15. Oflazer, K.: Two-level description of Turkish morphology. In: Proceedings of the sixth conference of the european chapter of the association for computational linguistics, April 1993. A full version appears in *Literary and Linguistic Computing*, vol. 9, no. 2 (1994)
 16. Orhan, Z., Domnori, E., Giriş, S.F., Ceyhan, M.: Customer satisfaction measurement tool by analysing Turkish product reviews. In: *TURKLANG'2014*, vol. 1, no. 1, pp. 15–23 (2014)
 17. Pennebaker, J.W., Chung, C.K., Ireland, M., Gonzales, A., Booth, R.J.: *The Development and Psychometric Properties of LIWC*, <http://liwc.net> (2007)
 18. Saleem, S., Prasad, R., Vitaladevuni, S.N.P., Pacula, M., Crystal, M., Marx, B., Sloan, D., Vasterling, J., Speroff, T.: Automatic detection of psychological distress indicators and severity assessment from online forum posts. In: *COLING*, pp. 2375–2388 (2012)
 19. Schnurr, P.P., Rosenberg, S.D., Oxman, T.E.: Comparison of TAT and free speech techniques for eliciting source material in computerized content analysis. *J. Pers. Assess.* **58**, 311–325 (1992)
 20. Stone, P.J., Dunphy, D.C., Smith, M.S., Ogilvie, D.M.: *The General Inquirer: A Computer Approach to Content Analysis*. MIT Press, Cambridge, MA (1966)
 21. Tucker, G.J., Rosenberg, S.D.: Computer content analysis of schizophrenic speech: a preliminary report. *Am. J. Psychiatry* **132** (6), 611–616 (1975)
 22. Weathers, F.W., Keane, T.M., Davidson, J.R.T.: Clinician-administered PTSD scale: a review of the first ten years of research. *Depress. Anxiety* **13**(3), 132–156 (2001)
 23. WHO: *Mental Disorders*, <http://www.who.int/mediacentre/factsheets/fs396/en/>, Oct 2014
 24. Witten, I.H., Frank, E.: *Data Mining: Practical Machine Learning Tools and Techniques*, 2nd edn. Morgan Kaufmann, San Francisco (2005)
 25. Yuret, D., Ture, F.: Learning morphological disambiguation rules for Turkish. In: Proceedings of the main conference on human language technology conference of the North American chapter of the association of computational linguistics. Association for Computational Linguistics (2006)

Only All Together We Can Make It Better on Any Strategic Matter

M. Medvedec and M. Poluta

Abstract

Recent requests for international assistance regarding clinical engineering (CE) registration/certification and related legislation resulted in a survey for the International Federation for Medical and Biological Engineering (IFMBE) leadership. The survey comprising two questions ('What is CE?' and 'How can we advance CE globally?') with five sub-questions each, was e-mailed to 63 members and collaborators of the Clinical Engineering Division of the IFMBE (CED/IFMBE) and to 16 members and collaborators of the Health Technology Assessment Division of the IFMBE (HTAD/IFMBE). The survey response rate was 34%. All respondents were of the view that CE is not synonymous with either biomedical engineering (BME) or health technology management (HTM). Significant affirmative responses included: 'CE is a subset of BME' (89% of respondents); 'CE encompasses HTM' (73%); 'CE practitioners are health professionals' (93%) and 'CE is not only for engineers' (74%). Other responses were as follows: 'Do/can we legislate?' (41% of respondents), 'Do we register?' (74%), 'Do we certify?' (83%) and 'Do we support accredited CE undergraduate programs?' (89%). Survey results should assist both CED/IFMBE leadership and other global stakeholders in defining concrete practical steps to advance formal recognition of CE practitioners.

Keywords

Clinical engineering • Biomedical engineering • Health technology management • Profession regulation • Survey

M. Medvedec (✉)
Department of Nuclear Medicine and Radiation Protection,
University Hospital Centre Zagreb, Zagreb, Croatia
e-mail: mario.medvedec@kbc-zagreb.hr

M. Poluta
Department of Health, Western Cape Government, Cape Town,
South Africa

1 Introduction

The term 'Clinical Engineering' (CE) has been understood and defined in different ways [1–9]. The Clinical Engineering Division of the International Federation for Medical and Biological Engineering (CED/IFMBE) has received requests from some national CE professional associations for assistance and guidance in establishing CE certification/registration programmes and appropriate legislation related to the professional activities and responsibilities of clinical engineers. This initiated lively and productive discussions that surfaced some long-standing issues pertaining to the CE profession. A short list of open questions was drafted to facilitate further discussion of these issues, followed by a decision to conduct a survey targeting CED/IFMBE and Health Technology Assessment Division (HTAD/IFMBE) board members and collaborators.

2 Materials and Methods

The survey consisted of two fundamental general questions:

- Q_A: What is Clinical Engineering (CE)?, and
Q_B: How can we (IFMBE with its partners) advance CE globally?

Each question had five sub-questions (Q_{A1}–Q_{A5} and Q_{B1}–Q_{B5}). Eight of these required a Yes/No answer as a minimum, although more descriptive answers were indeed appreciated.

The sub-questions for Q_A were as follows:

- Q_{A1}: Is CE equal to Biomedical Engineering (BME)?
Q_{A2}: Is CE equal to Health Technology Management (HTM)?
Q_{A3}: Are CE practitioners health professionals?
Q_{A4}: If neither Q_{A1} nor Q_{A2} nor Q_{A3}, then what?
Q_{A5}: Is CE for engineers only?

The sub-questions for Q_B were as follows:

- Q_{B1} : Do/can we legislate?
 Q_{B2} : Do we register?
 Q_{B3} : Do we certify?
 Q_{B4} : What strategy should IFMBE adopt?
 Q_{B5} : Do we support accredited CE undergraduate programs?

The survey was conducted from October 2016 to May 2018. It was emailed to 79 colleagues in total—63 members and collaborators of the CED/IFMBE, and additionally to 16 members and collaborators of the Health Technology Assessment Division of the IFMBE (HTAD/IFMBE). Clarification materials and one to four reminder-emails were additionally sent before finally closing the survey.

3 Results

E-mail addresses of all recipients were updated and approved, so there were no undeliverable e-mails. Overall response rate to the survey was 34% (27/79). Some respondents did not answer all questions, while some responses were ambiguous.

All respondents agreed that CE is not synonymous with either biomedical engineering (BME) or health technology management (HTM): 27/27 and 26/26 respondents, respectively. 89% (24/27) were of the view that CE is a subset of BME, while only 8% (2/26) saw HTM as encompassing CE. 93% (25/27) felt that CE practitioners are health professionals and 74% (20/27) that CE is not for engineers exclusively.

For the two sub-question (Q_{A2} and Q_{B1}) with the lowest agreement amongst responses (73 and 41%, respectively), all descriptive answers provided by the survey respondents are quoted below:

Q_{A2} : Is CE = HTM?:

- “CE is also an expertise in medical technologies, not just management”;
- “CE is also a subset of HTM because ‘health technology includes drugs, procedures, health IT, organizational structures and systems, etc.’ [per World Health Organization (WHO) definition]”;
- “HTM is one of the various activities carried out by CEs. They would be involved in many other activities such as training of users, quality assurance of medical equipment, etc.”;
- “No, although there are significant overlaps. This is the position that AAMI has taken, but in my view is neither universally applicable nor correct (e.g. in *my country*’s public sector, some of the best HT Managers are

ex-nurses or radiographers, not engineering practitioners).”

- “CE is an (applied) domain of engineering practice, whereas HTM is a multi-disciplinary endeavor, although often driven/led (at the very least, supported) by—engineering practitioners”;
- “CE has a wider scope of competencies”;
- “HTM is part of clinical engineer’s responsibilities. My definition of HTM addresses managing health technology after it enters the healthcare system—patient safety, compliance with regulations, educating users, and maintenance. In addition, the CE has an important role in planning, assessment, replacement, budgeting and acquisition of HT.”;
- “Yes and no. They are overlapping, particularly in a hospital setting; but CE is more “engineering” oriented while HTM focuses on management.”;
- “Yes, but not exclusively. HTM is one key element of the role of clinical engineers but it is not all of it.”
- “HTM is one of the potential activities of a clinical engineer. *In my country* most people considered to be clinical engineers are involved in HTM. In reality, ‘clinical engineer’ is not a term that is used widely amongst the healthcare fraternity and is always explained as ‘a biomedical engineer working within the hospital/healthcare setting’.”;
- “Health technology management is the main purpose of clinical engineering practice, but other professionals can be responsible for HTM too”;
- “The activities of a clinical engineer or a biomedical engineer can include health technology management, but are not synonymous, there is no health technology management profession”.

Q_{B1} : Do/can we legislate?:

- “Yes, in a similar way as medical physicists (IAEA—International Atomic Energy Agency, EUROATOM—European Atomic Energy Community) and others do/can do”;
- “This will be nice but difficult as it depends on the jurisdictions. However, we can convince the hospital communities (e.g. hospital accreditation bodies) that CE is a required component in the hospital system.”;
- “No, but we can help national initiatives that advocate for legislation.”;
- “No volunteer organization can legislate, only governments. However, we can and should advocate for legislation that regulates the profession so as to protect the public.”;
- “Similarly to medical physicists. *In my country* it is the state exam.”;

- “No, but work for legislation”;
- “We can try. This could be a good idea, but the question comes up ‘if we do successfully legislate, where will the people come from to fill the jobs?’. I don’t think there are enough available now to fill the need.”;
- “IFMBE can carry out advocacy in support of having well trained clinical engineers. Only governments can legislate. Would suggest the drafting of a white paper to document various options/approaches.”;
- “No. Not as a rule anyway, although there may be exceptions in some special cases/countries where the environment is amenable to such an option. In my view, legislation is not an option internationally, even though it is the case for medical physicists. As has been mentioned, there is no direct link between what CE practitioners do and patient safety or patient care, whereas these links do exist for medical physicists responsible for the quality assurance and correct/safe application of ionizing radiation in healthcare.”;
- “I do not believe we are in the business of legislating but rather in the data collection business and educating the various legislative bodies.”;
- “I am not sure about the term *legislate*. If it means, ‘should CED/IFMBE be active in the legislative processes in their countries to make laws which benefit CE’ I would agree, with the caveat that this is very difficult. In addition to the justification of CE value to healthcare, the efforts would have to take into consideration the politics. It might be a step after certification and registration. Also, it is more likely a national effort rather than international.”;
- “No. *In my country* we neither legislate nor act as Notified Bodies. We can and should influence and IFMBE might be able to support this role, initially through lobbying but ideally through representation on appropriate bodies/committees.”;
- “Legislation that defines registration to practice may be the key. Whether we can legislate is the challenging question; progress is slow *in my country* as this would be a state-based requirement and, although we only have 7 states, this is completely challenging.”;
- “Legislation is only applicable when produced by national authorities. IFMBE can produce guidelines for best practices in CE/HTM.”;
- “We cannot legislate but we can propose recommendations for WHO in order to develop a global CE legislation.”;
- “No, but insist to be a health profession imposed by legislation.”;
- “Not sure we can and should”;
- “Yes, in a similar way as medical doctors (WHO, MOHs, ...) and others: we are health professionals similar to medical doctors.”;
- “No, I think we can stimulate proper legislation by providing guidelines and standards, but mandatory legislation is for governments.”;
- “No; however we can support legislative actions.”
- “Legislation, registration and certification should be done at national level/by country according to national regulations.”

The responses to the questions ‘Do/can we legislate?’, ‘Do we register?’, ‘Do we certify?’ and ‘Do we support accredited CE undergraduate programs?’ were positive for 41% (11/27 respondents), 74% (17/23), 83% (20/24) and 89% (16/18), respectively.

4 Discussion

Although the survey described above was spontaneously derived and informal, the fact that only a third of the IFMBE’s CED and HTAD leadership responded to the survey (even though e-mail reminders were sent) was unexpected given that (i) issues related to clinical engineering registration and/or certification have been discussed within IFMBE for about four decades [1, 5–7, 9] and (ii) clinical engineering in most countries is still far from being a fully recognized and regulated profession [1–9]. This does not align well with one of the mottos of the CED/IFMBE: “Together we can make it better”. However, despite the low response rate of the survey, there is a high degree of agreement (>73%) in response to the questions posed, except for the issue of CE legislation. This level of consensus indicates that there should be no further circling around the CE flame, but rather concrete practical steps taken towards achieving strategic goals.

5 Conclusion

Clinical engineering, however understood and practiced, should proactively and efficiently strive towards achieving well-defined strategic goals. It is hoped that of this survey, together with consensual white papers and position statements of the CED/IFMBE and other stakeholder organisations, will assist in identifying concrete and practical actions to both advance the professional recognition of CE practitioners globally and to guide the CE-related academic programmes and continuing professional development (CPD) initiatives, mindful of regional and national differences and priorities.

Acknowledgements The authors are grateful to all participating colleagues for their invaluable contribution to this survey.

Conflict of Interest The authors declare that they have no conflict of interest.

References

1. World Health Organization: Human Resources for Medical Devices, The Role of Biomedical Engineers. World Health Organization, Geneva (2017)
2. https://en.wikipedia.org/wiki/Clinical_engineering
3. American College of Clinical Engineering—ACCE at <http://accenet.org>
4. Association for Advancement of Medical Instrumentation—AAMI at <http://www.aami.org>
5. Clinical Engineering Division of the International Federation for Medical and Biological Engineering—CED/IFMBE at <http://cedglobal.org>
6. International Federation for Medical and Biological Engineering—IFMBE at <http://www.ifmbe.org>
7. International Federation for Medical and Biological Engineering—IFMBE: The IFMBE International Register of Clinical Engineers—Agreement on Mutual Recognition of Qualifications for Clinical Engineers (1981)
8. International Labour Organization (ILO) at <http://www.ilo.org>
9. International Federation for Medical and Biological Engineering—IFMBE: IFMBE CED White Paper—Certification/Registration of Clinical Engineering Practitioners (2018)

Designing a Healthcare Computer Aided Facility Management System: A New Approach

Ernesto Iadanza[✉], Alessio Luschi, Roberto Gusinu,
and Filippo Terzaghi

Abstract

This paper presents a custom decision-support information system designed to analyze and manage healthcare buildings, estate and assets in relation to the activity area of each room. The software drives its own SVG plans to retrieve structural information with a room-scale definition, built by DXF files inputted to the system itself. Each room is grouped in homogeneous areas according to the hospital's inner organization (Departments and Operative Units) with their own assets, technologies and environmental comforts, giving quantitative and qualitative results. The system output can be used by the top-management to assess parameters and improve the structure and organization.

Keywords

Hospital • Healthcare • CAFM • Managing • Support

1 Introduction

Modern hospital organizations are nowadays dealing with a big amount of data related to assets and personnel, that need to be organized and put in functional relations among them. Today hospitals must now undergo a big quantity of requirements in order to fulfill their clinical and medical

duties. These requirements are set by national and international institutions which force structures to respect given parameters in order to have sufficient hygienic, qualitative and organizational standards granted.

Clinical Engineering Services and Technical Departments must deal with these problems and find solutions to fully satisfy all sorts of technological, structural and organizational needs for a such a complex structure as a hospital. These structures developed, over the years, different technical tools to monitor the hospital by measuring quantitative, architectural, technological and people-related parameters.

Computer Aided Facility Management (CAFM) systems are decision-support tools based upon Integrated Healthcare Facility Management Models (IHFM) which provide indexes on those processes that can affect the performance of the healthcare structure. These tools can be very useful for the top-management for performance and risk evaluations, business management and development.

They provide access to stored information regardless of the workplace: data and plans can be acquired through web services, using a common browser over an internet or intranet network. These systems usually drive a Computer-Aided Design (CAD) engine to store info about space-units, assets, plants, employments and other aggregated data, and give visual outputs. Data are often stored in dedicated databases to which the maps are only linked. The main informative unit, i.e. the maximum degree of detail, may be the Homogeneous Functional Area (a set of rooms pooled together by destination of use) or the room itself.

This paper presents a Computer Aided Facilities Management System (CAFM). The main module of the system is designed to manage and analyze digital plans of hospital buildings, coded on specific layers. Unconventionally the plans are converted from DXF files into internal SVG maps, driven by the system itself. This allows the software to be unbounded to any external CAD system: the only requirement is to have a polyline which outbounds every single room, all of them laying on the same layer.

E. Iadanza (✉) · A. Luschi
Department of Information Engineering,
University of Florence, Florence, Italy
e-mail: ernesto.iadanza@unifi.it

A. Luschi
e-mail: alessio.luschi@unifi.it

R. Gusinu · F. Terzaghi
Azienda Ospedaliero Universitaria Senese, Siena, Italy
e-mail: dirsan@ao-siena.toscana.it

F. Terzaghi
e-mail: filippo.terzaghi@ao-siena.toscana.it

Therefore, the room is the most granular cell of information on which the system performs its analyses, offering a more full-scale methodology in comparison to an overall view that would not allow an accurate information on single space supplies.

Moreover, the core database can be linked to other existing databases, in order to use the system as a central control cockpit. In fact, information about staff organization, assets and health technologies are also available to the final users. The outputs can be used by the top-management as a decision-support tool in order to improve hospital's structure and organization and to reduce the major workflow risks.

2 Design and Implementation

The case study for the designed CAFM is the Hospital Campus of Le Scotte (Azienda Ospedaliero Universitaria Senese) in Siena, Italy. It is constituted by 12 pavilions hospitals spread on a large area of 207.820 m², with 800 beds and 8.100 rooms. Hospital spaces are grouped in 27 Departments: functional macrostructures working among more buildings, using different structures, technologies and rooms throughout the whole hospital area. Each Department has functional substructures with a lower level of aggregation called Operative Unit (OU).

The hospital represents a unique case-study due to the spatial dislocation of the single pavilions. They are located on a topography which is largely hilly, thus the inner paths and alleys which link together different buildings are not on the same constant level throughout the hospital area. In fact, it is very likely to have the first or second basement storey of a building at the same elevation of the ground floor of an adjoining pavilion. This implies a very complex spatial management of the whole premise.

The informative system is composed by a core-engine software which loads DXF maps, converts them into SVG path entities with their coordinates stored in a dedicated MSSQL Server 2008 Express R2 central database. After the initial conversion, the DXFs are no longer needed by the system, that becomes self-sufficient. This is an important aspect to focus on. Usually CAFM systems rely on DWG plans [1–3], using third-party on-premise proprietary (often closed-source and licensed) plugins or libraries to directly drive commercial CAD systems. Conversely, the aim of this project is to design a fully self-sufficient and independent system, which does not need any external CAD library to work properly. Planimetries can be obtained in any way (for example by external vendors or suppliers from a tendering procedure) and then loaded into the CAFM with no further restraints.

The developed application allows several functionalities such as space information, door-plates production and staff management and organization.

The system manages the following listed data in order to provide users with information about the analyzed rooms, thus operating like an internal space registration service:

- *Room Code*: a unique alphanumeric code to identify the building, the floor and the number of a given room;
- *Destination of Use*: chosen among a set of 36 available to straightly identify the carried-on activity;
- *Class*: is an additional optional specification to the Destination of Use to narrow the information;
- *Medical or Technical Department*;
- *Operative Unit*;
- *Number of beds* for relevant Destination of Use;
- *Surface* of the room;
- *Height* of the room;
- *Volume* of the room calculated from the last 2 parameters;
- *Personnel*: name, last name, telephone number and email of staff linked to a given room via the Room Code.

On top of the main core module, a dedicated web interface has been designed to let the end-user manage the aggregated data, in order to simply make faster decisions.

The web interface is fully HTML5 compliant, with a standard Javascript, jQuery and Bootstrap client framework which interacts via AJAX calls with RESTful Web APIs coded within Windows .NET 4.5 Framework installed on a local MS IIS Server (Fig. 1).

This web-application dynamically accesses information and floorplans about the hospital buildings, always without any on-premise CAD rendering engine installed local client computers. It allows users to visualize the last updated map of the requested floor of a building in real time by using AJAX and JQuery. Every time a click event on a room is performed, it triggers an asynchronous access to the server database to download the updated information without any callback to the page itself, with a consequential spare of computing time.

The engine provides the basic functions of a CAD engine such as multi-selection window, panning, zooming, printing, text placement and scaling, multiple selection by Destination of Use, Operative Unit or Department. Besides it gives further information on staff, assets and health technologies related to the selection.

Figures 2 and 3 summarize the described functionalities.

The CAFM also comes with a fully integrated search engine which offers a userfriendly web interface to perform simple and advanced search throughout the whole database,

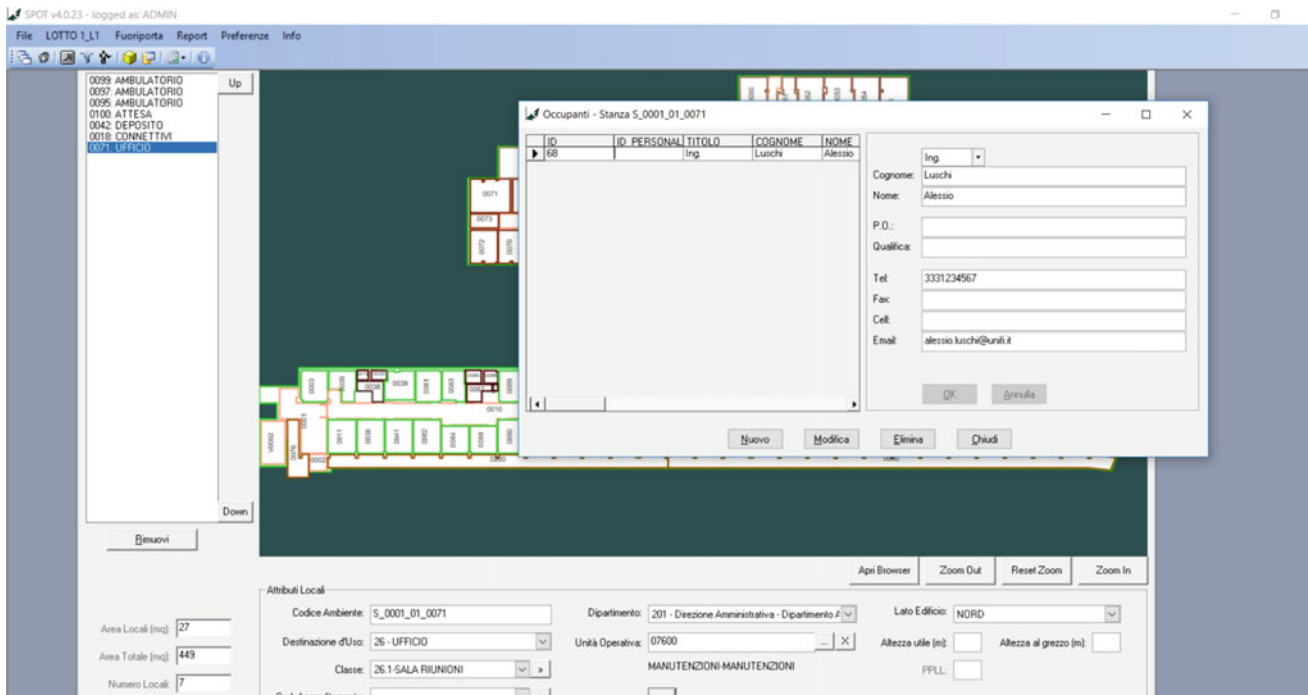


Fig. 1 Screenshot of the details window of the system with information about space, organization and staff

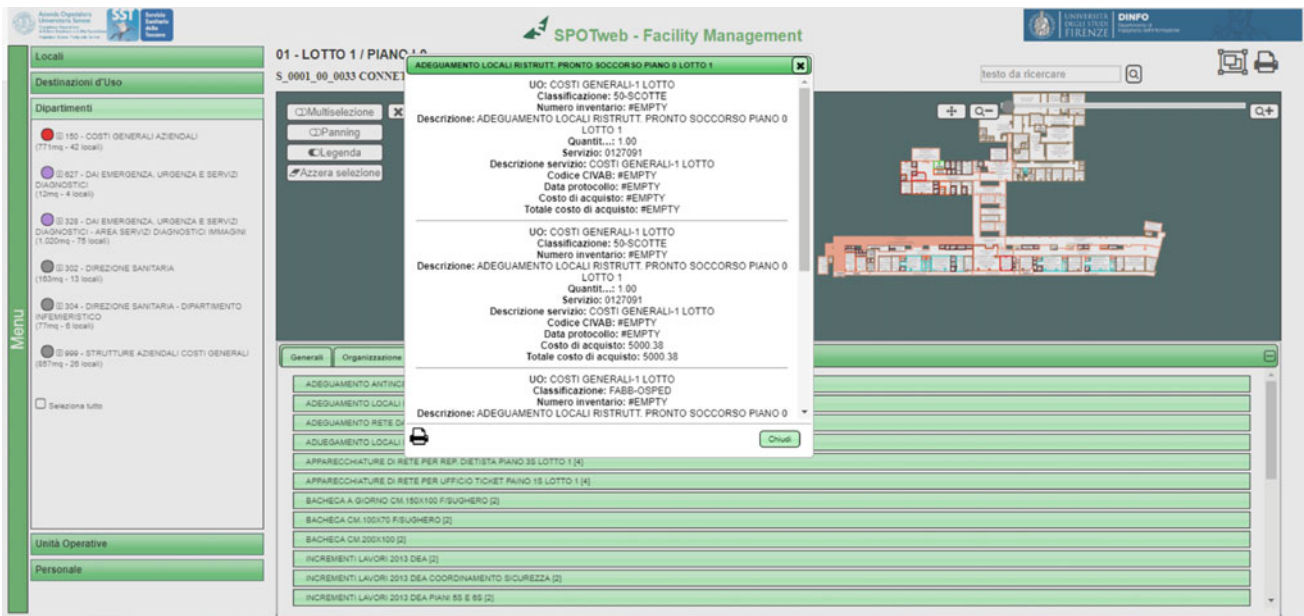


Fig. 2 Asset details for the selected room coded S_0001_00_0033

on each relevant field such as destination of use, staff names, assets, departments, operative units, room codes and more. It also offers a dynamic reporting functionality to print PDF reports based upon the search results (Fig. 4).

Finally, the whole system is provides with a very powerful functionality for managing the complex transfers

of entire departments. Indeed, due to the peculiar spatial organization of the hospital (described in the beginning of the paper), it is very useful for the top-management to visualize the whole hospital structure in terms of functional organization rather than spatial organization. For this reason, the system also offers the functionality to show all the

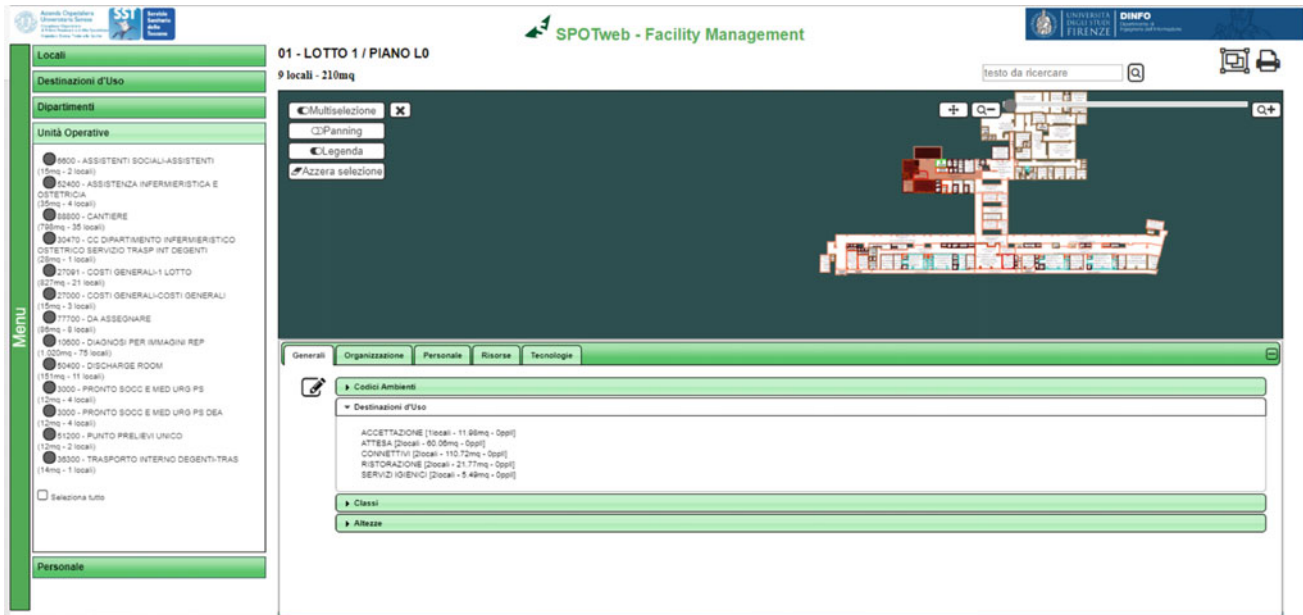


Fig. 3 Space details for a list of 9 selected rooms

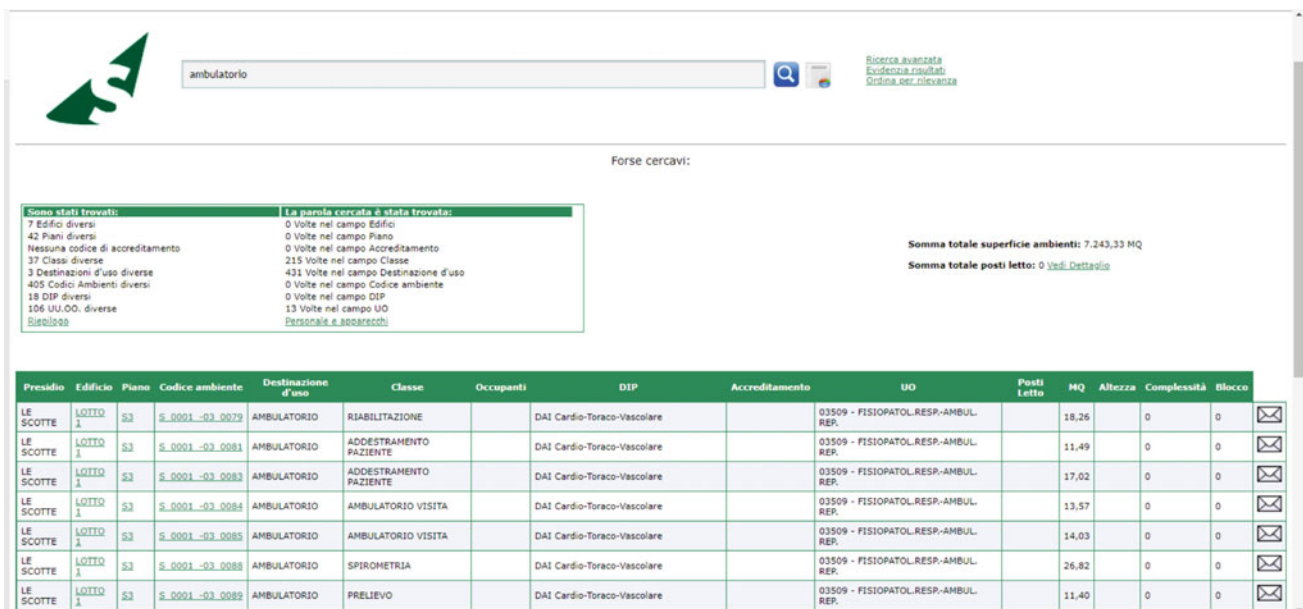


Fig. 4 Dedicated search engine application

Operative Units, grouped by floor and building, in a matrix shaped layout. Each cell represents a single OU, which can be moved across floors and buildings to evaluate new spatial configurations useful for transfer management. This

tool can easily answer the main question made the top-management in a transfer process: “does the target space meet the requirements of the new use it has to fulfill?” (Fig. 5).

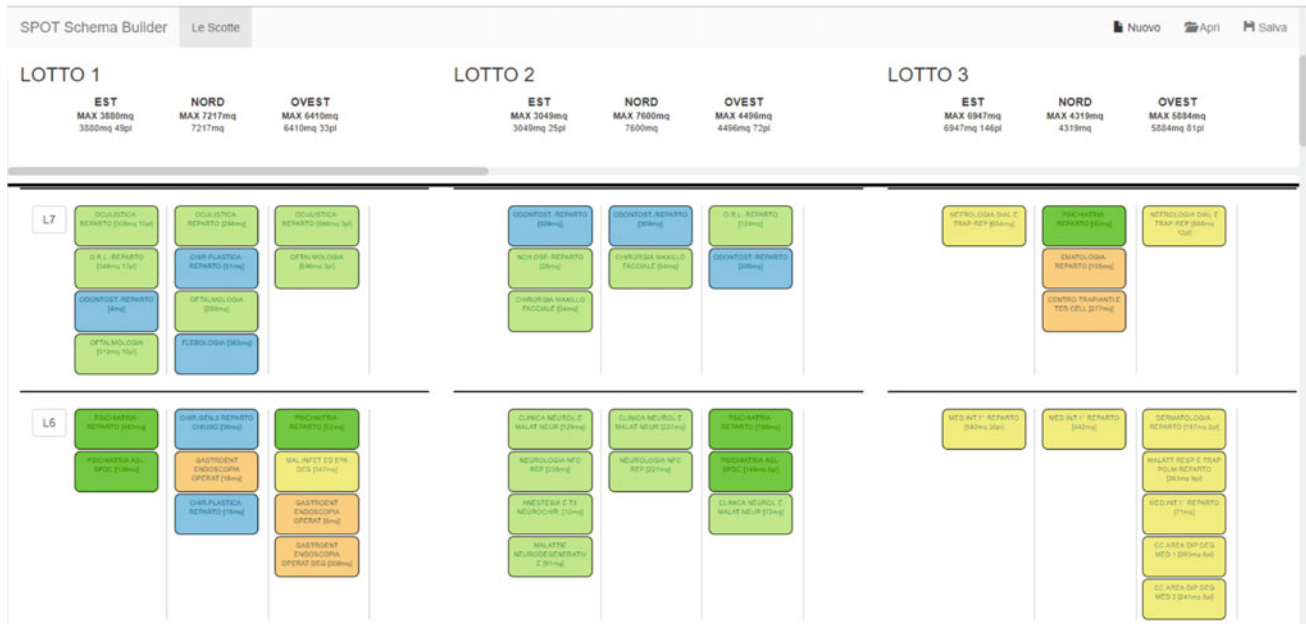


Fig. 5 Transfer management tool

3 Conclusions

The main aim of this work is to empower the knowledge sharing among different typologies of users, and to make it easier by the top-management to take decisions about transfer management and organization workflows. Moreover, spatial, technological and procedural data is resident inside the system so that it can be known by anyone who grants access to it, bringing information sharing to its maximum.

Besides, the system is very independent by the CAD system used to initially draw plans and schematics because it just needs an standard DXF file in order to load, code and convert the appropriate information. The CAFM is also independent by the used DBMS technology and can be interfaced with several databases like MS SQL Server, Oracle, MySQL, and more: data is read from maps, parsed by the software, and then stored in any type of database.

Future works aim to empower the system with other functionalities like bed management [4], legislative standards compliance [5] or to allow interoperability with healthcare decision support systems [6].

References

1. Iadanza, E., Marzi, L., Dori, F., Gentili, G.B., Torricelli, M.C.: Hospital health care offer. A monitoring multidisciplinary approach. In: World Congress on Medical Physics and Biomedical Engineering 2006. IFMBE Proceedings, vol. 14, pp. 3685–3688 (2007)
2. Luschi, A., Marzi, L., Miniati, R., Iadanza, E.: A custom decision-support information system for structural and technological analysis in healthcare. In: XIII Mediterranean Conference on Medical and Biological Engineering and Computing 2013. IFMBE Proceedings, vol. 41, pp. 1350–1353 (2014)
3. Luschi, A., Miniati, R., Iadanza, E.: A web based integrated healthcare facility management system. In: 6th European Conference of the International Federation for Medical and Biological Engineering. IFMBE Proceedings, vol. 45, pp. 633–636 (2015)
4. Iadanza, E., Luschi, A., Ancora, A.: Bed management in hospital systems. In: World Congress on Medical Physics and Biomedical Engineering 2018. IFMBE Proceedings, vol. 68/3, pp. 313–316 (2019)
5. Iadanza, E., Ottaviani, L., Guidi, G., Luschi, A., Terzaghi, F.: License: web application for monitoring and controlling hospitals' status with respect to legislative standards. In: XIII Mediterranean Conference on Medical and Biological Engineering and Computing 2013. IFMBE Proceedings, vol. 41, pp. 1887–1890 (2014)
6. Luschi, A., Monti, M., Iadanza, E.: Assisted reproductive technology center design with quality function deployment approach. In: World Congress on Medical Physics and Biomedical Engineering, June 7–12, 2015, Toronto, Canada. IFMBE Proceedings, vol. 51, pp. 1587–1590 (2015)

System for Monitoring Environmental Parameters in a Hospital Facility

Alessio Luschi, Riccardo Di Franco, Beatrice Turillazzi,
and Ernesto Iadanza 

Abstract

The paper presents a system for managing and monitoring environmental parameters in hospital facilities. It relies on existing data collected with a CAFM (Computer Aided Facility Management) system and allows granted users (such as CEO or Energy Manager) to monitor the ongoing energy consumption of a given activity area (Operating Rooms, Diagnostics, Intensive Care Units, Wards) in relation to the compliance to relevant threshold parameters. The system easily outputs aggregated data via PDF reporting.

Keywords

Environment • Energy • Hospital • Managing • CAFM

1 Introduction

A typical hospital facility consumes about 2.5 times the energy of an office. In the European Union (EU) there are about 15,000 hospitals which are responsible for the 5% of the total carbon-dioxide emissions in the whole EU. In this

A. Luschi (✉) · E. Iadanza
Department of Information Engineering, University of Florence,
Florence, Italy
e-mail: alessio.luschi@unifi.it

E. Iadanza
e-mail: ernesto.iadanza@unifi.it

R. Di Franco
Bachelor's Degree in Mechanical Engineering, University
of Florence, Florence, Italy
e-mail: riccardo.difranco@stud.unifi.it

B. Turillazzi
Department of Architecture, University of Bologna, Bologna, Italy
e-mail: beatrice.turillazzi@unibo.it

context the energy saving associated with a hospital gets a high relevance, and it comes clear that a well designed system to correctly manage the environmental impact of such a premise is crucial. These systems allow not only to minimize the cost of the energy demand, but also to save the amount of carbon-oxide introduced in the atmosphere.

In this scenario it appears clear that a hospital-oriented Computer Aided Facilities Management (CAFM) has to manage and provide performance indicators about the energy consumption and saving, in order to cut the costs for energy supply, giving useful information to the top management as a decision support system.

Thus, the designed application relies on a custom CAFM [1, 2] in order to assess and aggregate data which can be previously collected or directly fed in real-time by the system of energy sensors.

2 Methods

STREAMER is a research project which aims to halve the energy consumption and the CO₂-emissions for new or renewed hospital facilities in Europe in the next 10 years. It is co-financed inside the European Project named “Optimised design methodologies for energy-efficient buildings integrated in the neighborhood energy systems” [3].

The Hospital University Campus of Careggi, in Florence (Italy) is one of the four case studies for the STREAMER Project, so its CAFM system has been re-designed in order to correctly collect and store the energy parameters identified within the project.

First of all, one of the seven STREAMER typologies has been assigned to every single hospital space, to highlight its efficiency:

- *Comfort Class*
- *Hygienic Class*
- *Equipment Class*
- *Construction Class*

- *User Profile Class*
- *Access Security Class*
- *Bouwcollege Layer Class*.

Then, by combining the STREAMER typology, the destination of use and the activity area of the spaces, the following five energy classes have been identified:

- *Operating Rooms*
- *Intensive Care Units—Surgery Outpatient Clinics—High Speciality Diagnostics (MRI, CT, Angio-CT)—Laboratories*
- *Ward—Low Speciality Diagnostics (radiography, US)*
- *Outpatient Clinics*
- *Offices—Teaching Rooms—Alleys—Other*.

Each of the above energy classes has its own energy parameters: *Winter Temperature, Summer Temperature, Winter Humidity and Summer Humidity*.

Moreover, other environmental parameters have also been designed, more focused on compliance to legislative standards (for example *Air Ventilation*), which are used by external facility management applications within the hospital [4–6].

Each one of these parameters has its own minimum and maximum threshold value as reported in Table 1.

Once the data have been collected and stored inside the hospital's CAFM system [7], the main requirement is to

have an efficient managing system in order to update and monitor the parameters, query a single room (or a group of them) or a set of rooms with given attributes (i.e. all the rooms with at least one parameter—or a given parameter—outside the threshold range).

3 Results

The designed system is an HTML5 compliant web-application with a standard Javascript, jQuery and Bootstrap client framework which interacts via AJAX calls with RESTful Web APIs coded using Windows. NET 4.5 Framework.

The system analyzes a set of real values for the input parameters and matches them with the theoretical ones associated with the energy class of a given room. These input real values can be fed to the system directly inserting them in the database using a data entry form or creating a JSON file and transferring it through a dedicated REST Web API, using a HttpPost message. This functionality is designed to make the system fully integrable with any third-party sensors management system (SMS). In fact, by simply making the WebAPI accessible (via Intranet or VPN), the SMS could post the properly formatted actual values, implementing a conjunct real-time monitoring system.

The JSON string must have the following format:

```
{
  envParameters: [
    {
      ROOM_CODE: <room code according to the CAFM inner room list>,
      PAR_CODE: <parameter code (WINTERTEMP, SUMMERTEMP ...)>,
      TRIPLE: [<minValue>, <mediumValue>, <maxValue>],
      MU: <measurement unit>,
      DATE: <datetime of collection. Format YYYY-MM-DD HH:mm:ss>,
      OVERRIDE: <whenever the value overrides the current theoretical one>
    }
  ]
}
```

Table 1 Environmental parameters related to the destination of use of the rooms

Energy class	Winter temperature	Summer temperature	Winter humidity	Summer humidity
O.R.	22 °C ± 2 °C	22 °C ± 2 °C	50% ± 5%	50% ± 10%
ICU/high speciality diagnostics	21 °C ± 1 °C	23 °C ± 1 °C	50% ± 10%	50% ± 10%
Ward/low speciality diagnostics	21 °C ± 1 °C	25 °C ± 1 °C	50% ± 10%	50% ± 10%
Outpatient	21 °C ± 1 °C	25 °C ± 1 °C	50% ± 10%	50% ± 10%
Office/other	21 °C ± 1 °C	25 °C ± 1 °C	50% ± 10%	50% ± 10%

Fig. 1 Details section. Winter and summer temperatures together with winter and summer humidity are shown. Current values are displayed on the left column compared with the theoretical ones on the right side

Reali	Teorici
✖ Temperatura invernale °C : 15 15 15 09/04/2018 Aggiorna	Temperatura invernale °C : 18 22
✔ Temperatura estiva °C : 28 28 28 09/04/2018 Aggiorna	Temperatura estiva °C : - 26
⚠ Umidità invernale % : 40 50 60 06/04/2018 Aggiorna	Umidità invernale % : 35 45
⚠ Umidità estiva % : 45 50 55 06/04/2018 Aggiorna	Umidità estiva % : 50 60

Room_Code, *Par_Code* and *MU* are strings, *Triple* is an array of 3 strings, *Date* is a datetime object while *Override* is a Boolean value.

The comparison between the theoretical values and the real ones is performed using a dedicated window (Fig. 1).

In the upper section the system shows the analyzed room code, the Destination of Use of the room together with its Energy Class.

In the main central section, the environmental parameters are shown, divided by typologies. On the left the current values are shown with the date of collection, with the corresponding theoretical on the right.

The “compliant”, “not compliant” or “warning” icons represent the degree of compliance of the real value to its theoretical one:

- If the range of values for the collected parameter is fully contained inside the range for the theoretical ones, the icon will be a green tick mark;
- If it is only partially enclosed inside the range for the theoretical parameters, the icon will be a yellow warning sign;
- Otherwise, the icon will be a red alert cross.

By clicking the Update button, a modal window is opened to edit or input new values for the given row. The system allows a user to override an actual value for a given date (not necessarily the last collected one). This function is only available for a granted user, such the Energy Manager or Top Management Office member. User managing is entrusted to the System Administrator, which would add the allowed users to a grant list: the login password is the same of the local Intranet area, managed via LDAP (Lightweight Directory Access Protocol).

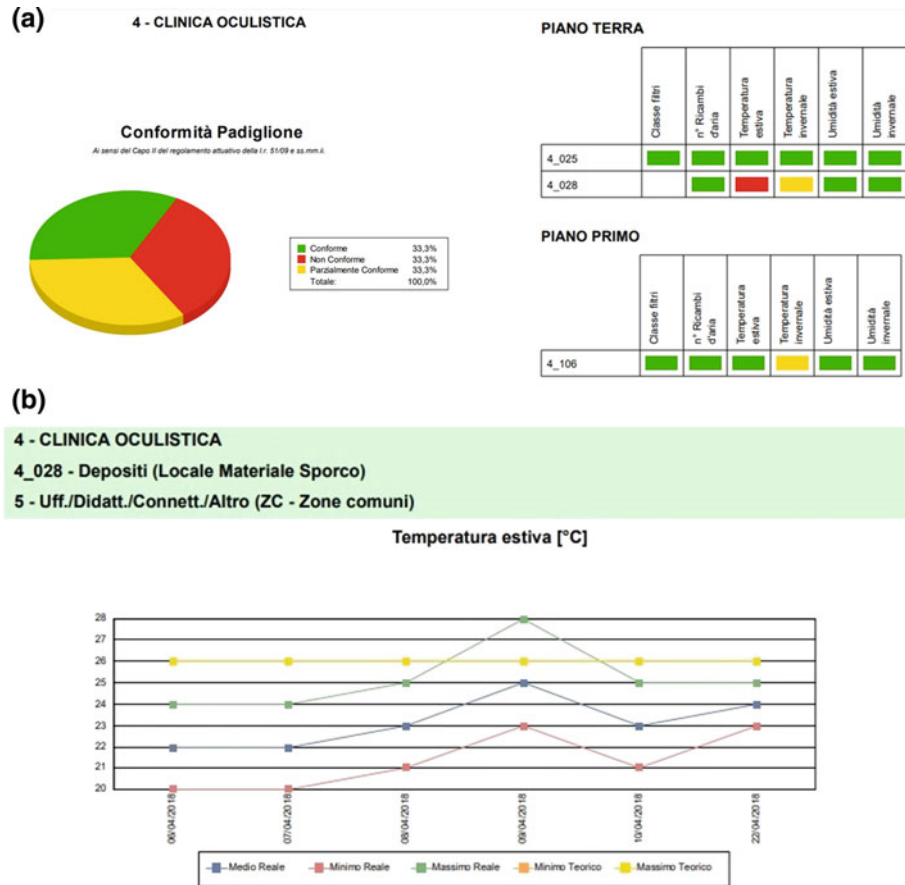
Fig. 2 Modal window with edit and override functionalities. Survey date and specification of the edited parameters are shown in the header. Minimum, maximum and average values are also displayed below together with the update date and a confirm checkbox

A granted user can also override a parameter (or all of them) without editing its value by clicking the Validate checkbox: this makes the real collected valued compliant to the theoretical range even if the values would not be (manual validation functionality) (Fig. 2).

The manual validation functionality allows a granted user to validate a parameter which slightly differ from the theoretical range, but which is assessed to represent a solid and consistent exception for the analyzed room.

The system can also produce a detailed report about the summary of the compliance of a room, a floor, a premise or the whole hospital to the energy parameters. A plot of the time evolution of the minimum, medium and maximum values of each parameter is also available (Fig. 3).

Fig. 3 a Report for the compliance of rooms grouped by floor and premise. The pie-chart on the left shows the percentage of compliance (green), non-compliance (red) and partially compliance (yellow) for the selected building. Tables for detailed compliance of each room to the analyzed parameters, grouped for floor, are also shown on the right side. **b** Report showing the time evolution of minimum (red), medium (blue) and maximum (green) values for each current parameter of a given room. Theoretical minimum (orange) and maximum's (yellow) evolution are also plotted



4 Conclusion

The proposed informative system has proven to be effective both for planning and verifying purposes. In fact, it can be used in development phases to design an efficient layout of energy saving according to the destination of use and activity area of different portions of the hospitals, as well as in a subsequent analysis, to verify the energy consumption in real-time or catch up, therefore allowing an effective intervention plan to improve efficiency wherever it would be needed.

References

- Luschi, A., Miniati, R., Iadanza, E.: A Web based integrated healthcare facility management system. In: 6th European Conference of the International Federation for Medical and Biological Engineering. IFMBE Proceedings, vol. 45, pp. 633–636 (2015)
- Iadanza, E., Marzi, L., Dori, F., Gentili, G.B., Torricelli, M.C.: Hospital health care offer. A monitoring multidisciplinary approach. In: World Congress on Medical Physics and Biomedical Engineering 2006. IFMBE Proceedings, vol. 14, pp. 3685–3688 (2007)
- Iadanza, E., Turillazzi, B., Terzaghi, F., et al.: The streamer European project. Case study: Careggi hospital in Florence. In: 6th European Conference of the International Federation for Medical and Biological Engineering. IFMBE Proceedings, vol. 45, pp. 649–652 (2015)
- Iadanza, E., Ottaviani, L., Guidi, G., Luschi, A., Terzaghi, F.: License: web application for monitoring and controlling hospitals' status with respect to legislative standards. In: XIII Mediterranean Conference on Medical and Biological Engineering and Computing 2013. IFMBE Proceedings, vol. 41, pp. 1887–1890 (2014)
- Iadanza, E., Luschi, A., Ancora, A.: Bed management in hospital systems. In: World Congress on Medical Physics and Biomedical Engineering 2018. IFMBE Proceedings, vol. 68/3, pp. 313–316 (2019)
- Luschi, A., Monti, M., Iadanza, E.: Assisted reproductive technology center design with quality function deployment approach. In: World Congress on Medical Physics and Biomedical Engineering, Toronto, Canada, 7–12 June 2015. IFMBE Proceedings, vol. 51, pp. 1587–1590 (2015)
- Luschi, A., E., Marzi, L., Miniati, R., Iadanza, E.: A custom decision-support information system for structural and technological analysis in healthcare. In: XIII Mediterranean Conference on Medical and Biological Engineering and Computing 2013. IFMBE Proceedings, vol. 41, pp. 1350–1353 (2014)

Adverse Drug Events (ADEs): A Novel RFID Device for a Safe and Strong Match Between Patients and Their Medications

Ernesto Iadanza[✉], Cesare Massaro, and Leonardo Vonci

Abstract

The Adverse Drug Events (ADEs) can be defined as errors in therapy that are not desirable, not intentional and foreseeable, that can cause or lead to an inappropriate use of the medication or to a danger for the patient. In this work it is shown the design, engineering and realization of a prototype device for the safe and secure administration of pharmacological therapy using RFID. In particular, the redesign of the prototype antenna is addressed, with a focus on its enhanced performance.

Keywords

ADE • RFID • Medication error • Patient • Electronic • Device

1 Introduction

The Adverse Drug Events (ADEs) can be defined as errors in therapy that are not desirable, not intentional and foreseeable, that can cause or lead to an inappropriate use of the medication or to a danger for the patient. An ADE is assessed basing on the type of drugs and on the clinical risk that could derive. With clinical risk we mean the probability that a patient is victim of ADE, i.e. he suffers damage or discomfort, attributable to medical care during his period of hospitalization (even if unintentional), that causes increase of length of stay, health worsening or even patient's death. It is worth to repeat that ADEs are preventable or avoidable events, due to errors in use of medication.

In literature ADEs are addressed under many aspects: healthcare, organizational, economic and social. The problem and the need for reduction of these events are very much felt in the health sector.

E. Iadanza (✉) · C. Massaro · L. Vonci
Department of Information Engineering, University of Florence,
Florence, Italy
e-mail: ernesto.iadanza@unifi.it

Scope of this work is the design, engineering and realization of a prototype device for the safe and secure administration of pharmacological therapy. The idea was creating an automated dispenser, called *DAVID* (Drugs Administration Versatile Integrated Device). This device, leveraging on RFID (Radio Frequency Identification) technologies, enables a secure association between drugs and patients, thus greatly reducing errors in the administration of therapy—therefore the clinical risk—in a healthcare structure.

We started by analyzing our previous prototype [1, 2] to spot and analyze the weak points and improve it.

First we faced the problem of the not satisfying range of the RFID antenna. This component needed a deep redesign to increase its reading/writing range, thus enabling a robust communication with all the involved tags (patient-tag, drug-tag and internal-tag).

A mechanical design has been performed, to obtain a physical model of the device. Using 3D modeling software, we have been able to provide the device with a welldefined shape, taking into account the size of all the components, their positions, their dimension and their function.

A revision of the server-side software (the one that programs the RFID tags with the patient's code and with his therapy) and of the internal firmware has been also performed.

The prototypal device has eventually been realized and tested, to verify its correct operation.

2 Materials and Methods

2.1 Previous Version: Problems to Solve

The *DAVID* system consists in an automated drugs dispenser based on passive-RFID (ISO 15693) technology, able to validate the actual association between drugs and patients as well as to enable the access to the drugs only in case of perfect match. As described in [1, 2], the device makes use of three different RFID tags as follows:

- Internal tag: used to store the patient's ID and his medications prescription
- Drug tag: the medication is RFID tagged and inserted into the DAVID drugs box
- Patient tag: the patient is wearing an RFID wristband with a unique patient's ID.

The DAVID's firmware is designed to ensure that the device will open (letting the patient access his medication) only if there is a correct match between patient and medication.

The previous antenna was a printed antenna providing an extremely reduced reading/writing range, requiring the tags to be in physical contact with it.

The device, to perform properly must be able to manage up to three tags at one time, some of which, for mechanical design reasons, will be a few centimeters away from the antenna. Therefore, it is our scope realizing an antenna able to reveal the tags and correctly communicate with them at these distances.

Another crucial issue is the mechanical design. The previously designed device needs many improvements. In the design stage many factors must be taken into account, such as: the components, the way of use, the users, the environment, etc.

Similarly, the previous software and firmware need a review, particularly about the code that is in charge of programming new tags and controlling the device operation. It is possible writing on the tags and feed their onboard memories with the pertinent data: the software must also take care of the data integrity by checking that writings and readings are correctly performed.

2.2 Tools

The design of the antenna has been performed using a radiofrequency (RF) spectrum analyzer to verify the exact tuning (13.56 MHz) of the antenna resonance frequency. We used an HP RF Network Analyzer at the Laboratory of Antennas and Microwaves of the Department of Information Engineering in Florence. This equipment is provided with several connector types and can operate within the range from 300 kHz to 3000 MHz.

The mechanical design of the device has been performed in Dassault Systèmes SolidWorks 2012, a software widely used for 3D design for its high precision and good interoperability with Computer Numerical Control (CNC) machines, for the physical realization of 3D models.

The realization of the prototype has been performed in collaboration with a company located in the city of Pistoia (UTS Ltd.), using:

- a numerical control milling machine with three-phase electro-spindle, power of 0.75 KW, useful worktop $700 \times 700 \times 300$ mm, equipped with three axes plus a fourth rotary axis, which uses an ISO GCode Standard programming language;
- a parallel, manual lathe with a power of 2 kW used for cylindrical roughing operations.

The following software tools have been used:

XAMPP 1.7.4 as Web Service for managing the database.

Eclipse Juno 4.2.1 from the Apache Software Foundation, used for developing the device server side software (named DrugTinServer).

HID OMNIKEY 5321 Smart Card Reader, RFID reader, managed through the DrugTinServer.

Texas Instruments TRF7960 Evaluation Board, to verify the correct read/write operations on the RFID tags.

2.3 Design of the New Antenna

As mentioned above, the previous printed antenna is not suitable for *DAVID* because of its very low range. Hence a new antenna has been designed, with the scope of obtaining a minimum reading/writing range of 4–5 cm (Fig. 1).

As a starting point, it has been selected an antenna consisting of 3 copper-wire coils with a diameter of 5 cm, provided with a capacitive trimmer that allows to regulate the resonance frequency. Using the RF spectrum analyzer, the resonance frequency has been measured. A frequency of 15.7 MHz has been obtained, therefore not compatible with the standard 13.56 MHz requirement.

Because the operation range of the circuit variable capacitor was not sufficient to cover the gap between the obtained and the desired frequency, it has been chosen to modify the number and the shape of the coils, thus sensibly varying the resonance frequency.

Two coils with a 7.5 cm diameter have been realized, achieving a frequency very close to the desired one. Then, by simply operating the variable capacitor with a screwdriver, the optimal 13.56 MHz resonance frequency has been obtained (Fig. 2).

The antenna has been then fixed to a plastic support, to simulate its placement inside the device, and placed on top of the electronic board (Fig. 3).

The presence of the electronic board and of the departing conductors, unavoidably creates magnetic fields that influence the antenna's resonance frequency. A subsequent tuning operation has been required, because also the smallest variation in the antenna position relative to the board create a sensible variation in the resonance frequency.

Fig. 1 Antenna's circuital diagram

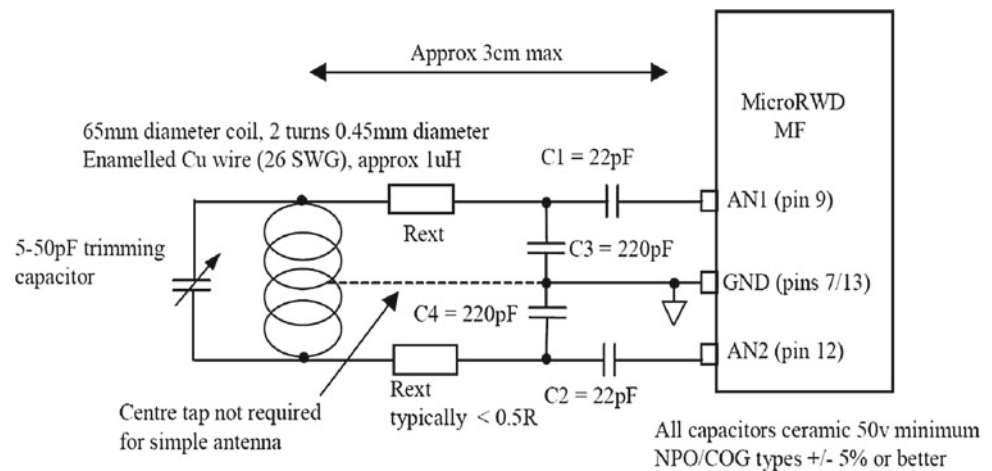
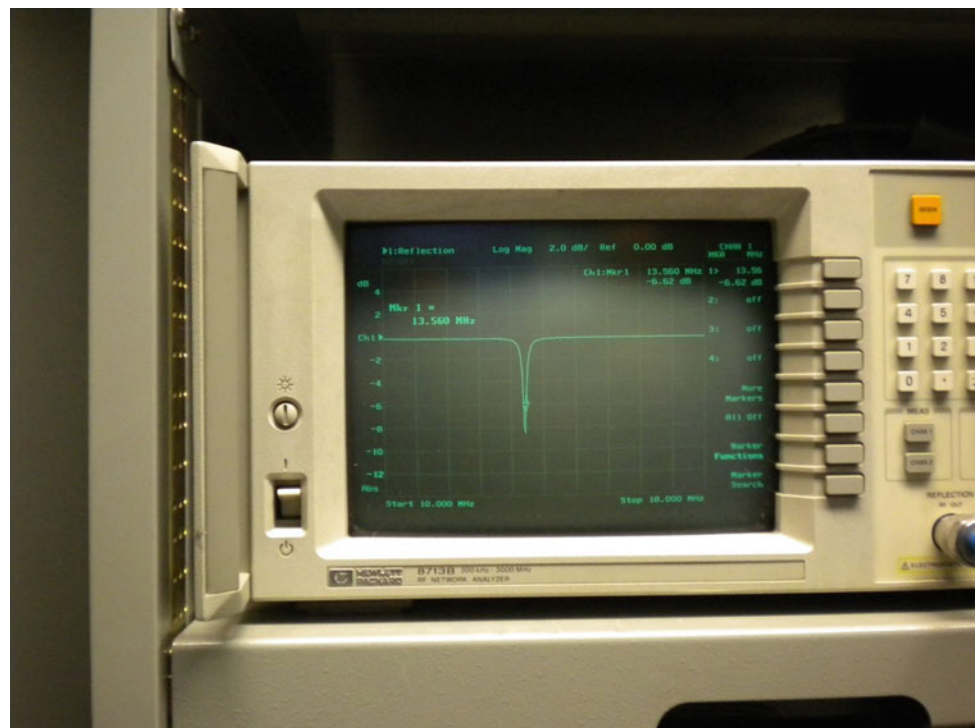


Fig. 2 Using the RF spectrum analyzer to measure the frequency



Once defined a relative distance from the board equal to 1.5 cm, the antenna has been precisely tuned at 13.56 MHz (Fig. 4).

Subsequently, as shown in Fig. 5, stepping down 4 dB from the position of the marker 2, that represents the cable attenuation of 1.36 dB, it has been calculated the bandwidth (BW) obtained as the difference between the values at the markers 5 and 5. The resulting bandwidth is very narrow: 142 kHz. Then, by considering the centerband value (CF) it has been possible to calculate the quality factor (Q) of this antenna, according to the relation $Q = CF/BW$, that resulted very high: 95.47.

Once the standard distance from the electronic board has been set (1.5 cm), some operation tests have been performed to verify the range and the actual functioning. It has been established how the antenna has an experimental operation range up to 5 cm and how it is able to manage the presence of the three RFID tags (internal, drug, patient) as required.

The tests have been performed using the following procedure, using a purposely developed custom software:

- Programming the internal tag with the data from a test patient with a certain prescription
- Programming the patient tag and the drug tag

Fig. 3 Antenna's positioning and connection to the RF analyzer probe

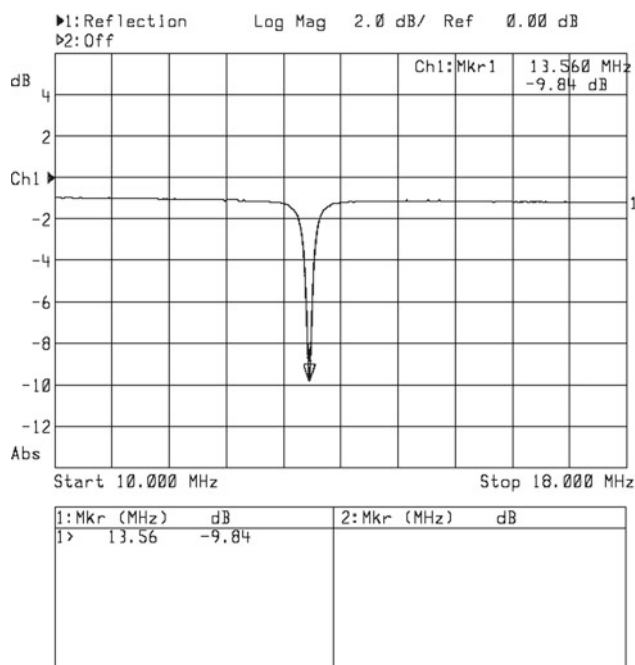
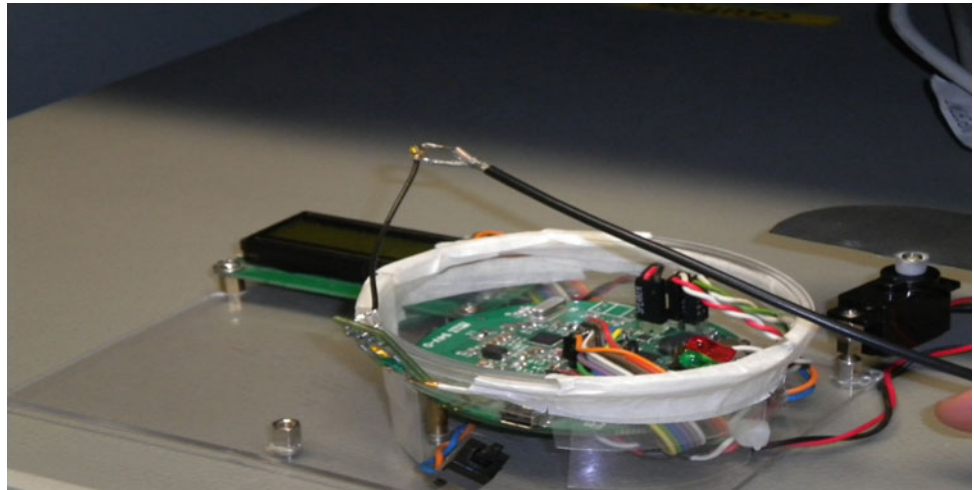


Fig. 4 Final tuning of the antenna at the resonance frequency of 13.56 MHz

- Positioning of the internal tag 1 cm above the antenna, to simulate its real positioning inside the device
- In case of correct identification of the internal tag, the drug tag is positioned on top of it, to verify the correct match between the two tags
- In case of positive match, the patient tag is then positioned under the circuit board, to verify if the antenna is able to read the three tags (the firmware will verify if the three tags match or not).

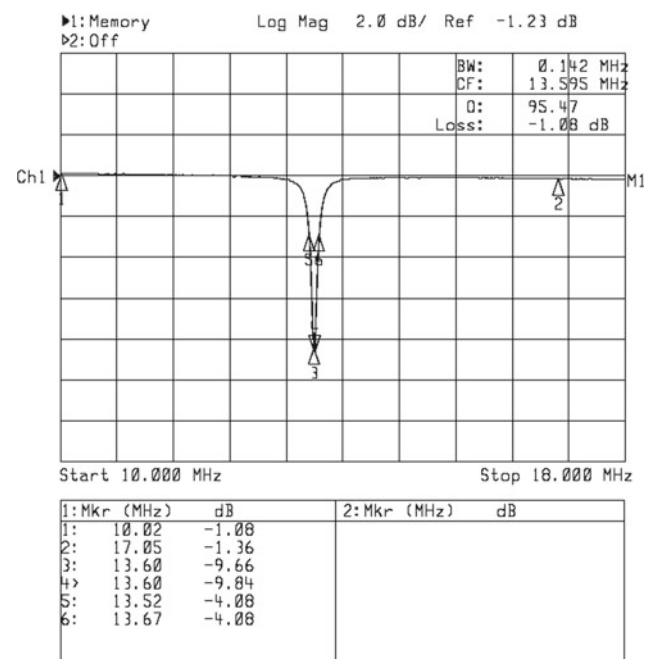


Fig. 5 Calculation of bandwidth (BW), centerband value (CF) and quality factor (Q)

Further tests have been performed using a patient tag programmed with a different ID from the one present in the internal tag, in order to check the correct operation of the device also in case of mismatch between internal tag and patient. This case simulates the device in the hands of the wrong patient.

After realizing the prototype, we decided to modify the shape of the antenna in order to simplify its fixing to device internal space reserved to the drugs (drugs box) by simply using double-sided adhesive strips.

3 Results

After the above described tests to verify the correct operation of the antenna, the following tag types have been used (see Figs. 6, 7):

- RFID tag Label 40 × 22 mm as internal tag
- RFID tag Label 40 × 22 mm as drug tag
- RFID Once Band as patient tag.

The variations in antenna's shape and positioning required to select the best positioning for the internal tag. Initially it had been hypothesized to place it on the bottom face of the drugs box, but the operation tests performed have highlighted how there emerged detection problems, because of the presence of the cables. It has then decided to place the tag on the back-side of the drugs box, as shown in Fig. 8, as a zone free from wiring. The correct tag detection has been verified.

The correct detection of the drug tag has been initially verified by only inserting the RFID tag into the *DAVID* drugs box. Then, to better simulate the real setting, the tag has been stuck onto a real sachet of medication with an internal metal coating. In this setting, we had a very poor detection. By using a different medication, in a plastic envelope without any metal coating, the detection was very good. This confirms that the cause of the bad functioning is

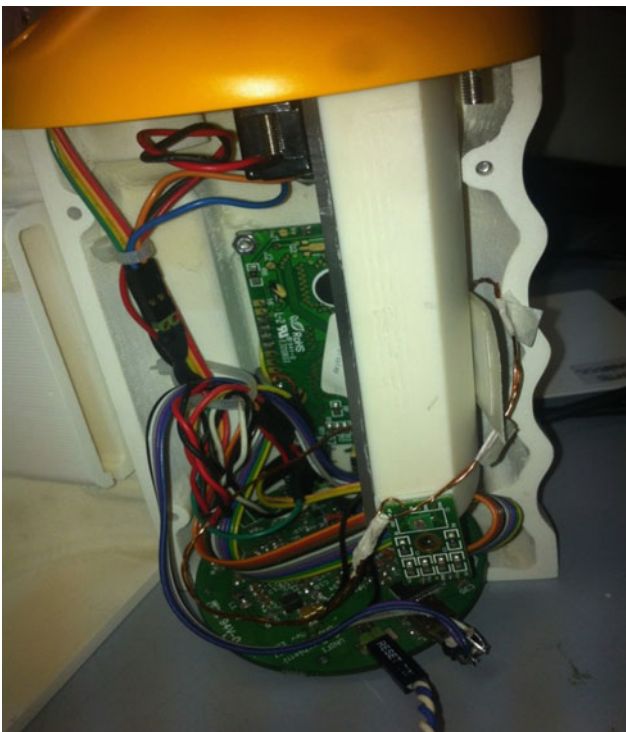


Fig. 6 Intern of the device



Fig. 7 RFID tags used as internal tag, drug tag and patient tag



Fig. 8 Positioning of the internal tag

the internal metal coating present in some medication packages.

The verification of the correct detection of the patient tag has been performed by approaching the patient's RFID bracelet to the device, previously programmed in order to verify its operation in case of correct association. Various tests have been performed, accosting the wristband to the



Fig. 9 Patient tag accosted to *DAVID* and correctly read

device from various angles. The position that guarantees the best functioning is shown in Fig. 9.

4 Conclusion

The problem of the correct identification of the patient in a healthcare structure, during the process of administering a medication, is still very actual and in search for a definitive solution [2–14].

RFID proved to be an affordable and very effective solution for the patient identification (through RFID wristbands) as well as for the correct association between patient and medication.

In this paper we presented an evolution of a custom device that goes in the direction of solving this problem, that every year is causing a lot of Adverse Drug Events (ADEs).

In particular, the process of redesigning and realizing a better performing antenna has been described.

The authors are currently addressing new techniques, such as 3D printing, in order to realize new half-sized prototype device to be tested in real healthcare settings.

References

1. Iadanza, E., et al.: An rFid smart container to perform drugs administration reducing adverse drug events. In: IFMBE Proceedings, vol. 37, pp. 679–682 (2011)
2. Iadanza, E., et al.: Drugs administration: how to reduce risks to patients. IFMBE Proceedings, 39 IFMBE, pp. 743–745 (2013)
3. Lesar, T.S., Briceland, L., Stein, D.S.: Factors related to errors in medication prescribing. *J. Am. Med. Assoc.* **277**(4), 312–317 (1997)
4. Senst, B.L., et al.: Practical approach to determining costs and frequency of adverse drug events in a health care network. *Am. J. Health-Syst. Pharm.* **58**(12), 1126–1132 (2001)
5. Stelfox, H.T., Palmisani, S., Scurlock, C., Orav, E.J., Bates, D.W.: The “To Err is Human” report and the patient safety literature. *Qual. Saf. Health Care* **15**(3), 174178 (2006)
6. Bisio, I., Sciarrone, A., Zappatore, S.: A new asset tracking architecture integrating RFID, Bluetooth low energy tags and ad hoc smartphone applications. *Pervasive Mob. Comput.* **31**, 79–93 (2016)
7. Gentili, G.B., Dori, F., Iadanza, E.: Dual-frequency active RFID solution for tracking patients in a children’s hospital. Design method, test procedure, risk analysis, and technical solution. *Proc. IEEE* **98**, 1656–1662 (2010)
8. Iadanza, E., Dori, F.: Custom active RFID solution for children tracking and identifying in a resuscitation ward. In: Proceedings of the 31st Annual International Conference of the IEEE Engineering in Medicine and Biology Society: Engineering the Future of Biomedicine, EMBC 2009 (2009)
9. Utku, S., Özcanhan, M.H., Unluturk, M.S.: Automated personnel-assets-consumables drug tracking in ambulance services for more effective and efficient medical emergency interventions. *Comput. Methods Programs Biomed.* **127**, 216–231 (2016)
10. Iadanza, E., Dori, F., Miniati, R., Corrado, E.: Electromagnetic interferences (EMI) from active RFID on critical care equipment. In: IFMBE Proceedings, vol. 29, pp. 991–994 (2010)
11. Bapat, A.C., Nimbhorkar, S.U.: Multilevel secure RFID based object tracking system. *Phys. Proc.* **78**, 336–341 (2016)
12. Iadanza, E., Marzi, L., Dori, F., Gentili, G.B., Torricelli, M.C.: Hospital health care offer. A monitoring multidisciplinary approach. In: IFMBE Proceedings, vol. 14, no. 1, pp. 3685–3688 (2007)
13. Iadanza, E., Chini, M., Marini, F.: Electromagnetic compatibility: RFID and medical equipment in hospitals. In: IFMBE Proceedings, 39 IFMBE, pp. 732–735 (2013)
14. Bianchi, L., et al.: Design of a RESTful web information system for drug prescription and administration. *IEEE J. Biomed. Health Inf.* **18**(3), 885–895 (2014)

Donation of Medical Devices in Low-Income Countries: Preliminary Results from Field Studies

Davide Piaggio, Daton Medenou, Roland C. Houessouvo, and Leandro Pecchia

Abstract

Most of the world population is being treated in low-income countries, where there are not only harsh environmental conditions but also a failure to meet international standards and minimum requirements of the medical devices and locations. This can jeopardize the safe and efficient functioning of the medical devices. This paper draws on 5 field studies that took place in Sub-Saharan Africa, presenting few examples of donated medical devices and discussing the possible steps in order to strive for a more universal free healthcare coverage.

Keywords

Medical devices • Medical locations • Donations • Low-resource settings • International standards • Minimum requirements

1 Introduction

Most of the world population does not benefit from the use of medical devices (MDs): in fact, less than 15% of the global population accounts for the use of over 75% of the MDs, suggesting inequitable access to healthcare in favor of higher resource settings [1].

Indeed, the people who need healthcare the most (i.e., the ones living in lower-resource settings) are also the ones who have less access to it. In order to tackle this, the United Nations (UN) promoted several sustainable development

goals (SDGs) in the 2030 Agenda for Sustainable Development, which strives for the achievement of inclusive and sustainable development for all, drawing on the principle of “leaving no one behind”. For biomedical engineering, the most relevant ones are *good health and wellbeing* (SDG3), *quality education* (SDG4), *clean water and sanitation* (SDG6), *industry, innovation and infrastructure* (SDG9) and *reduced inequality* (SDG10). The SDGs are one of the 6 leadership priorities of the World Health Organization (WHO), who defined them to give focus and direction to their work, aiming at promoting global health and wellbeing [2].

When it comes to SSA, 80% of the available medical devices are donated [3], and over 70% of them are broken or non-functional because of different reasons [1]. Williams and Kohler [4] confirm that these donations have, in many cases, become a financial burden for end-users, who have to reallocate their scarce resources in attempts to fix or get rid of the equipment. The paper [4] also explains that this situation is not only unfavorable for the end-users, but also for the donors: in fact, 62.5–87.54 cents are wasted out of every dollar spent on medical equipment.

During the past two years, we have been running 5 field studies in 3 Sub-Saharan countries (i.e., Benin, Ethiopia and South Africa). Such field studies helped us start understanding some of the reasons behind the non-use or the breakage of the MDs: the lack of spare parts, expertise, an efficient maintenance program, a management system, harsh environmental conditions, of unreliable and unstable electrical power sources, and failure to define and meet minimum requirements for MDs and medical locations [5–8].

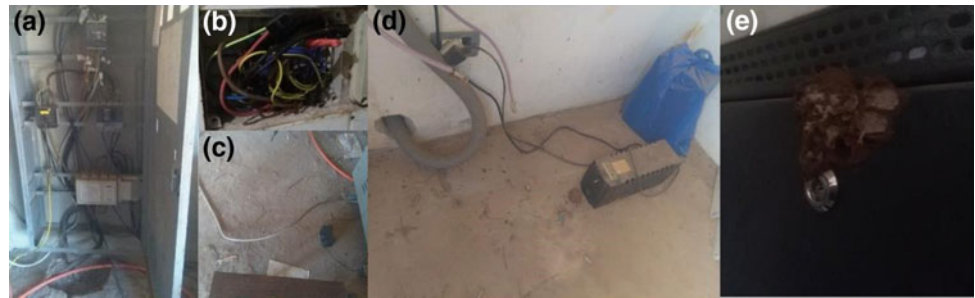
This paper presents the results from the 5 field studies along with a discussion on the possible future steps towards a more sensible and informed approach to the donation of MDs, both on the donors’ side and the end-users’ one.

D. Piaggio (✉) · L. Pecchia
University of Warwick, Coventry, CV47AL, UK
e-mail: d.piaggio@warwick.ac.uk

L. Pecchia
e-mail: l.pecchia@warwick.ac.uk

D. Medenou · R. C. Houessouvo
Department of Biomedical Engineering, Ecole Polytechnique
d’Abomey-Calavi, University of Abomey-Calavi, 01 BP 2009
Cotonou, Benin

Fig. 1 The conditions of the electrical panels, wiring and equipment



2 Methods

2.1 Case Studies, Focus Groups and Conferences

For the past 24 months, members of the Applied Biomedical Signal Processing and Intelligent eHealth (ABSPIE) Lab (University of Warwick, Coventry, UK) have been running 5 field studies, anticipated and followed by some focus groups to plan the following study and to sum up the results from the previous one. The field studies took place in Benin (2017 and 2018), Ethiopia (2018) and South Africa (2016 and 2017), the focus groups in the School of Engineering of the University of Warwick. Relevant literature was also taken into consideration.

Focus groups were held during relevant international events, including:

- The International Union for Physical and Engineering Sciences in Medicine (IUPESM) world congress, held in Prague, Czech Republic, on 3–8 June 2018;
- The first UBORA conference, held in Pisa, Italy, on 1–2 September 2018;
- The 4th World Health Organization (WHO) global forum on medical devices (4GFMD), held in Visakhapatnam, India, on 13–15 December 2018.

These events were great opportunities for exchanging ideas, opinions, receiving feedback and promoting part of the work of the ABSPIE Lab.

3 Results

3.1 General Conditions

The field studies, which were set in vocational hospitals, confirmed the severe conditions presented in the scarce literature. Although vocational hospitals may be representing only a part of the scenario, they still are a significant part of the healthcare system in these settings. High temperatures,

humidity, dust, vermin are some of the characteristics, along with inefficient electrical circuits and grounds (see Fig. 1). The pictures portray the conditions of the hospitals, including, for instance, dust over the wiring and equipment, which could become conductive and cause short circuits and damage to equipment in case of wet weather. Electric panels, power transformers, UPS, cables and electric cabins were not installed, maintained or services as expected [9]. Vermin is clearly apparent, with a wasps nest being on one of the pieces of equipment.

3.2 Minimum Requirements and International Standards

In higher-resource settings, medical locations and medical devices are regulated by international standards and minimum requirements. International scientific societies and technical commissions issue such standards and requirements in order to harmonize the state-of-the-art for medical location design (including but limited to electrical installations, rooms layouts, ventilation et cetera) and building and medical device design and production (see Fig. 2) [9]. While in most of the higher-resource settings the legislation promotes these standards and minimum requirements in different ways (e.g., in Italy they become law, while in the U.K. they only are strong recommendations), in most of the lower-resource settings there is a lack of standardization and a failure to meet such requirements [10].

The minimum requirements can be divided into structural, organizational and technological [11]. Examples of such standards could be the following (i.e., minimum requirements for activities of diagnostic imaging) taken from the Italian Legislative Decree n.484 [12]:

- Structural: a diagnostic imaging ward should have, among other things, a room for radiodiagnostics, with annexed spaces/changing room for users, a room/storage for clean materials and a room/storage for dirty materials and separate toilets for staff and users.
- Organizational: a diagnostic imaging ward should have, among other things, a number of healthcare operators

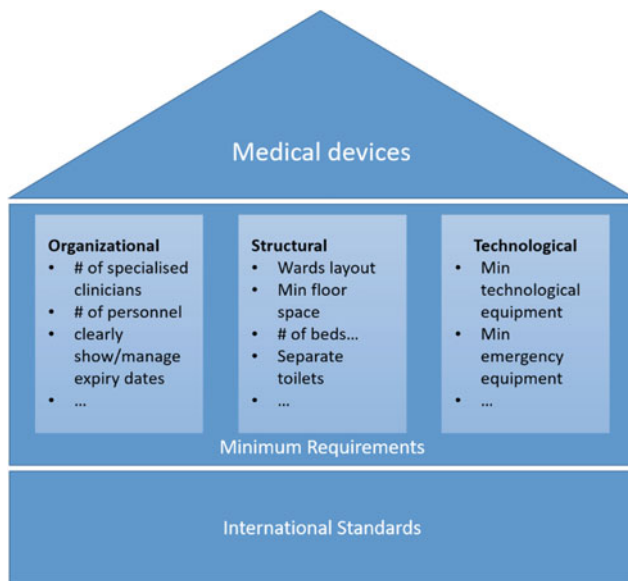


Fig. 2 The fundamental role of international standards and minimum requirements for the safe and efficient functioning of medical devices

and/or technicians appropriate for the complexity of the services offered and a quality control system.

- **Technological:** a diagnostic imaging ward should have, among other things, a high voltage generator (>30 kW) and a console table and a double focus rotating anode X-ray tube.

3.3 On Donations: X-Ray Machine and Oxygen Concentrator

This section provides two examples of donated medical devices along with related issues.

X-ray machine. Figure 3a, b, e show an X-ray machine that was donated to a hospital in Sub-Saharan Africa. The equipment was completely analogic and had been disassembled perfectly working in a European Hospital and sent

with 5 sheets of instructions (see Fig. 3d), written in a language non-locally spoken. The local technician had tried to assemble the parts, but he concluded that one of the non-fused terminal blocks was damaged (see Fig. 3c). Thus, he decided to send the supposedly broken part to Nigeria in order to replace it. Some members of the ABSPIE team were luckily on time to stop this process, retrieving the part. During the next field study, they came back with an experienced retired X-ray technician, who helped install the machine correctly collaborating with the local technician, promoting capacity building (see Fig. 4).

Oxygen concentrator. Figure 5 shows an oxygen concentrator that is a medical device used to deliver oxygen to patients who need it. The attention of some of the members of the ABSPIE group was caught by a nurse, who suspected that the oxygen concentrator they had was not working properly (i.e., when switching the switch from 1 to 2, the flow of oxygen was not doubling). After checking the device, the issue was identified with the filters.

This kind of MD is designed taking into consideration the above mentioned international standards and minimum requirements. In the case of the oxygen concentrator, this kind of device has two types of filters, external and internal. The external filters should have been washed weekly and had never been, while the internal filters should be changed after 4380 h of work and had already been working for 6501 h without having been changed [13]. These requirements are based on higher-income countries settings, where strict standards regarding medical locations are respected (e.g., the air in a surgical room has to be filtered at a 99.97% level [12]). This situation is utopic for many low-resource settings, where there is a lot of dust, and there is not filtering and not to 99.97%. Consequently, the minimum requirements regarding the filters of the oxygen concentrator should be even stricter or these devices should be redesigned to be more resilient.

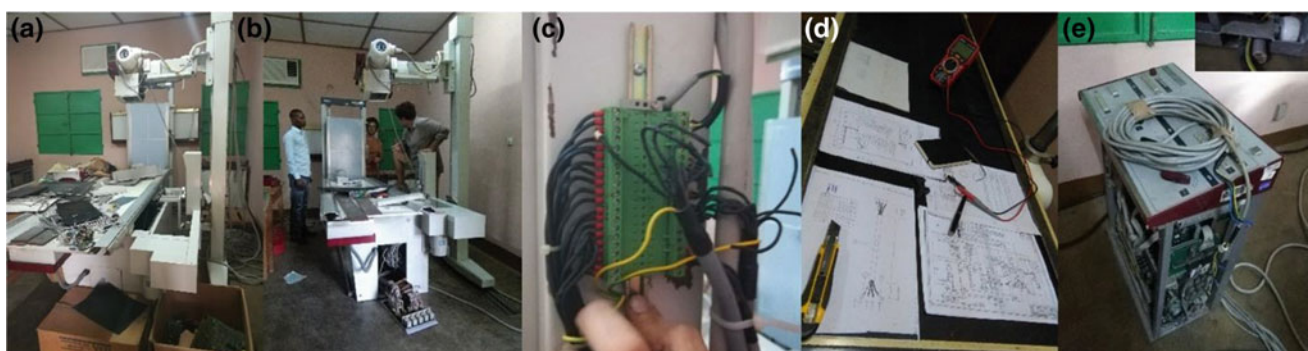


Fig. 3 a, b and e show the donated X-ray machine; c shows one of the non-fused terminal blocks; d shows the set of instructions



Fig. 4 Members of the ABSPIE team along with the local and the experienced technician assembling and testing the X-ray machine

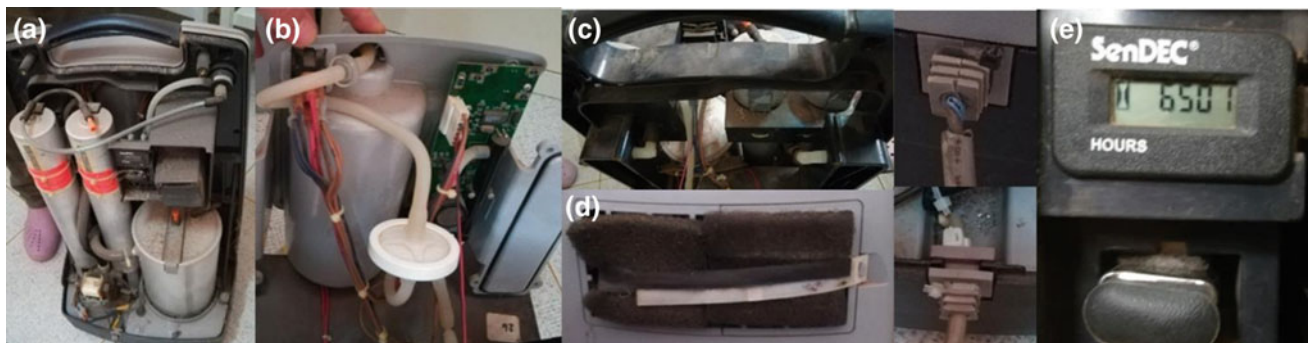


Fig. 5 a, b Oxygen concentrator and its components; c, d details of dust and filters; e display with numbers of hours that the device had been working

Figure 5 shows that the filters were full of dust (and most likely of bacteria), thus hindering the correct, safe and efficient functioning of the device and being a potential threat to patients' health.

4 Discussion and Conclusion

This paper aimed to report on our preliminary field experience on low-resource medical locations and on the donated MDs, which are often not working or working improperly. This is due to many reasons, first of which is the fact that 80% of the MDs market is ruled by higher-resource settings (namely the USA, Japan and Europe) [14], which define and set standards de facto that are not met in most of the lower-resource settings. Not only there should be a complete change in the way of designing medical devices towards a

user-driven and contextualized design, but also there should be a harmonization of the regulations of medical devices and locations between Europe and Africa. The ABSPIE group is also working on this front, cooperating internationally to promote this harmonization. The International Federation of Medical and Biological Engineering (IFMBE) African working group was funded at the IUPESM 2018 in Prague for this purpose.

Donations, as they are conceived now, should be made more carefully and could be regulated by the viability model proposed by Williams and Kohler [4], in order to avoid that donors waste resources and that the donations become a burden for the end-users. They should also be supported by a working local management system (paper-based or computerized) in order to keep track of the devices, their status, their maintenance schedule et cetera. Moreover, donations should always come along with installation and maintenance

support in order to avoid problems, like the ones that were mentioned above.

In conclusion, there is a clear need to regulate donations in a more sensible way and work towards new standards for medical devices to make them more resilient to harsh environments, such as the ones that can be found in lower-resource settings.

References

1. Arasaratnam, A., Humphreys, G.: Emerging economies drive frugal innovation. *World Health Organ. Bull. World Health Organ.* **91**(1), 6 (2013)
2. WHO: Sustainable development goals. [cited 2018 14/12/2018]. Available from: <https://sustainabledevelopment.un.org/?menu=1300>
3. Iadanza, E., Dyro, J.: *Clinical Engineering Handbook*. Elsevier, Amsterdam (2004)
4. Williams, D.B., Kohler, J.C.J.C.P.: Maximizing the value of donated medical equipment in resource-limited settings: the roles of donors and end-users. *CMBES Proceedings*, **39**(1) (2016)
5. Shah, M.T., et al.: Assessment of the availability of technology for trauma care in India. *World J. Surg.* **39**(2), 363–372 (2015)
6. LaVigne, A.W., et al.: Cervical cancer in low and middle income countries: addressing barriers to radiotherapy delivery. *Gynecol. Oncol. Rep.* **22**, 16–20 (2017)
7. Taylor, A., et al.: Innovating for global health: study of healthcare technology failure in southern Malawi. *Ann. Glob. Health* **82**(3), 600–601 (2016)
8. Rusatira, J.C., et al.: Enabling access to medical and health education in rwanda using mobile technology: needs assessment for the development of mobile medical educator apps. *JMIR Med. Educ.* **2**(1) (2016)
9. Pecchia, L.: Medical devices in low-resource settings. *SCOPE* **27**(4), 41–44 (2018)
10. De Maria, C., et al.: Safe innovation: on medical device legislation in Europe and Africa. *Health Policy Technol.* (2018)
11. Pecchia, L.: Health technology assessment of medical devices in low and middle income countries: study design and preliminary results. In *EMBEC & NBC 2017*, pp. 225–228. Springer, Berlin (2017)
12. Approvazione dell'atto di indirizzo e coordinamento alle regioni e alle province autonome di Trento e di Bolzano, in materia di requisiti strutturali, tecnologici ed organizzativi minimi per l'esercizio delle attività sanitarie da parte delle strutture pubbliche e private (1997)
13. Invacare. Invacare® Perfecto₂TM Oxygen Concentrator [cited 2018 12/12/2018]. Available from: https://www.invacare.com/doc_files/1143482.pdf
14. Zhang, W., Chatwin, C., Lui, R.: The Chinese medical device market: market drivers and investment prospects. *J. Commer. Biotechnol.* **22**(2), 33–39 (2016)

eVerlab: Software Tool for Medical Device Safety and Performance Inspection Management

Lejla Gurbeta, Almir Badnjević, and Emina Kurta

Abstract

This paper presents a unique software tool, eVerlab, for the management of medical device (MD) safety and performance inspection in healthcare institutions that are part of the Legal Metrology Framework. This is an online application, a functional tool for laboratory staff that perform MD inspections and for healthcare institutions staff enabling efficient management of MDs. It is composed of a Graphic User Interface (GUI) with the application of enabling the user to access its database. The software's database has imported records of real-time measurement measuring data which users have immediate access to. It creates the opportunity of users to review performance statuses of all medical devices in healthcare institutions. From the beginning of its application until today, the number of healthcare institutions registered in eVerlab and the number of verifications has significantly increased. Today, eVerlab software solution has 218 registered clients comprising over 3000 inspection reports of medical devices operating in Bosnia and Herzegovina. The database of the software solution provides the information necessary for a detailed analysis of performance variation, based on the historical behavior of different medical devices. The data collected and stored into the database can be used as input data to Machine Learning Algorithms for developing automated systems for the prediction of MD performances.

Keywords

Medical devices • Software solution • Inspection • Traceability • Machine learning • Expert system • Performance prediction

1 Introduction

Medical devices (MD) used for either diagnosis or treatment functions affect the lives of humans, enhancing the importance of quality control, reliability and recording faultiness for these devices [1]. Today, a typical healthcare institution consists of thousands of different medical devices manufactured by dozens of different companies [2]. With the objective of securing patient care and efficiency, the diversity creates a significant challenge [3]. What increases the weight of this challenge is the diversity behind manufacturers themselves [4]. In the case of all MDs, especially life-supporting MDs, device-specific management applications and services are critical to comprehend and follow. This is considered another difficult task due to the diversity of medical device manufacturers which have their own service protocols. Consistency can easily be lost, and the risk of incomplete maintenance/management can affect the lives of patients [5]. The International Bureau of Weights and Measure (BIPM) gives a detailed definition and description of all theoretical and practical aspects of measurement that can be referenced in medical device performance evaluation [6, 7] and by implementing the Legal Metrology Framework [8] MDs can be inspected for deviations of output values that are defined through international standards [9–12]. The complete safety status of a medical device (including post-market surveillance) is achieved in conjunction with clinical engineers continuously maintaining medical devices. Even though the medical device industry has advanced vastly, defects are still present and are the focus of ongoing research to engineers worldwide [13].

L. Gurbeta · A. Badnjević
Faculty of Engineering and Natural Sciences, International Burch
University, Sarajevo, Bosnia and Herzegovina
e-mail: lejla@verlab.ba

A. Badnjević
e-mail: almir@verlab.ba

L. Gurbeta · A. Badnjević
Medical Device Inspection Laboratory, Verlab Ltd., Sarajevo,
Bosnia and Herzegovina

E. Kurta (✉)
Sedia Biosciences Corporation, Portland, OR, USA
e-mail: ekurta@sediabio.com

Tracking inspections/maintenances and analysing performances of medical devices throughout time contributes to achieving sufficient post-market surveillance and MD management [14]. Traceability is critical and must meet a broad range of requirements, in the terms of determining its safety, reliability, risk and availability [15]. This is challenging considering it is a vast amount of measuring data, comprising a wide range of measurement parameters and the fact that the same amount of data is collected every year. This type of data today is termed Big Data, that researchers around the world find most efficient to store in digital databases. For this reason, a unique software solution eVerlab, for tracking inspection processes of medical devices exists [16]. Inspection Laboratory Verlab, created the software base with the goal of preventing loss of medical device database, missing records, delays or duplicate records. In practice, after every inspection process a complete set of documentation is created for the specific device [17]. Software solution, eVerlab, is easily accessible and a reliable online program updated on Verlab Inspection Laboratory's website. A detailed description of implementation of the software is given in the studies of Alic et al. [16, 17].

Further analysis and processing of Big Data is only possible with advanced computer techniques [18]. The most efficient techniques, in the context of determining MD performance classification and prediction, are Machine Learning Algorithms. Fundamentally, the real-time measurement data recorded in eVerlab software has the potential to serve as input data for the performance prediction of medical devices. Using this data, a Machine Learning Algorithm processes the vast amount of data to the extent where the performance status of a device is evaluated and therefore its maintenance management predicted. Creating such algorithms reduces conducting unnecessary, time-consuming and costly inspection processes done manually and provides comprehensive results to technical units of healthcare institutions.

A number of research studies in the past have had their focus on the management of medical diagnostic devices. In the study of Chaudhary et al. [19], the quality patient diagnosis, in terms of MDs, were evaluated in healthcare institutions in Chandigarh, India. They concluded that maintenance delays were one of the main factors affecting under-utilization of medical devices and quality patient diagnosis. Wallace et al. [20] also presented an analysis of failure modes of medical devices emphasizing important arguments. The generic problem pointed out in this study, is that the MDs tested did not have inspections against original design specifications. To prevent this from happening, consistent traceability analysis and inspection of any proposed changes of specification should be applied to all MDs [21].

This paper presents a detailed analysis of the software solution for tracking the inspection process of medical

devices, created in Bosnia and Herzegovina and evaluates its potential to be applied in Machine Learning techniques for performance prediction of various types of medical devices.

2 Methods

The software's database consists of documentation imported by the laboratory staff of Verlab, which is done after the completion of an inspection of a medical device. The software consists of a graphical user interphase (GUI) that demystifies the software program and enables the user to perform actions simply by clicking, tapping or navigating to visual indicators or icons [22].

Figure 1 represents the basic concept of eVerlab that provides the User the ability to access its database via GUI. Upon the User taking actions with visual indicators of GUI, its application methods leads to Inspection Reports specific to the User.

The types of medical devices whose inspection processes are tracked with this software are the following: anesthetic machines, defibrillators, dialysis machines, ECG devices, infusomats, neonatal and pediatric incubators, patient monitors, perfusors, respirators and therapeutic ultra-sounds [22]. For each device, during an inspection process, real-time measurement data is recorded and compared to standard measurement values specific to the device. MD performance can be classified as either accurate (meets safety requirements) or faulty (does not meet safety requirements) [23]. The resulting data is imported into software and is termed an Inspection Report [17].

3 Results

3.1 GUI System of eVerlab Software

Upon the accurate implementation and consistent application of eVerlab software in the past 4 years, successful inspection processes of MDs in healthcare institutions in Bosnia and Herzegovina have been conducted enabling efficient management of MDs as well as records of Big Data. An overview of accessing data records in eVerlab software is given in Fig. 2.

The comprehensive GUI system begins with a user log in (Fig. 3) and is followed by a search engine. This tool enables the user to access inspection information for a specific device, obtaining previously performed inspection data. The real-time measurement measuring data is stored in an Inspection Report Template with the complete set of parameter values and measurements that can be imported into Excel. The GUI system for all application processes are represented in Figs. 4, 5, 6 and 7.

Fig. 1 Block diagram of eVerlab software

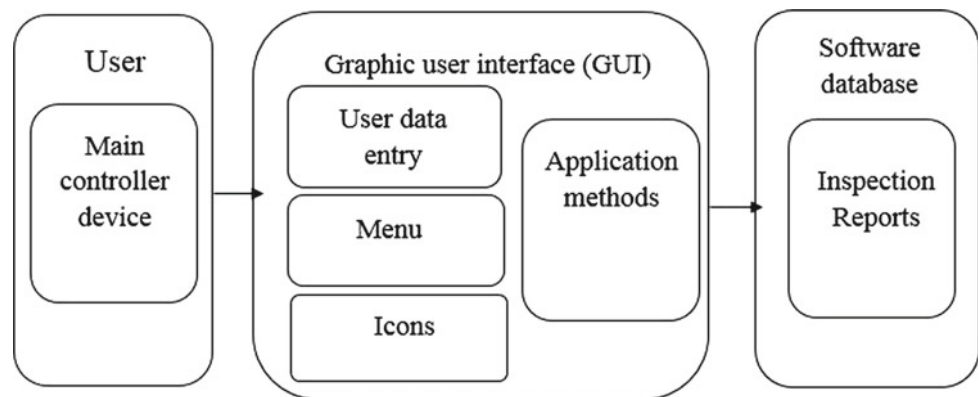


Fig. 2 Block diagram representing overview of eVerlab software application

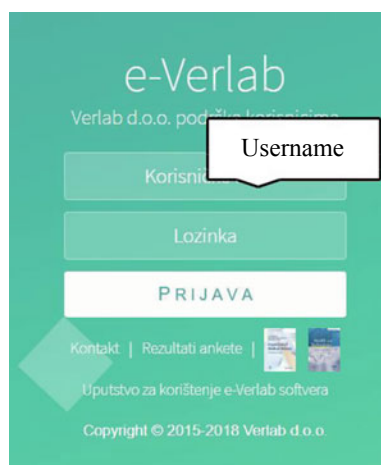
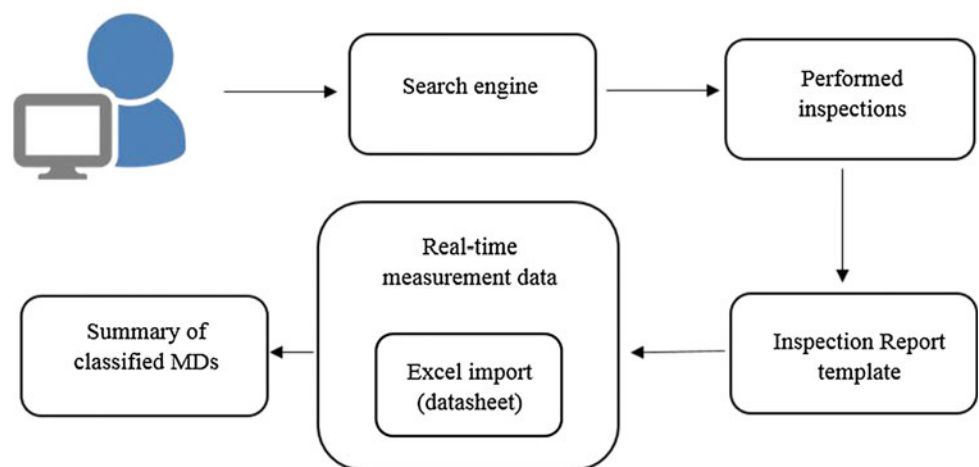


Fig. 3 Sign in for the application [22]

The search engine requires information on device group, manufacturer and date of inspection of the device. Figure 4 represents the form in which this information is implemented in the software.

Upon utilizing the search engine, the records of the specific device are located and presented to user. From here, the user can access all details of inspections, with previously performed and future (planned) inspections (Fig. 5).

The main database the user has access to is termed an Inspection Report. The Inspection Report is a real-time measured database which provides a precise analytical overview of medical devices in terms of their performance status, whether it is accurate or faulty. Report templates specific to a device group consist of the real-time measurement data recorded during inspection compared to nominal parameters set specific to each device as expected outputs. This template has a standard maximum deviation imported. The report provides the option of selecting YES or NO, whether the device is performing accurately or not. Figure 6 gives a representation of how this template is formulated in software GUI.

Figure 7 represents the detailed version of results of measurement. It comprises the date of inspections, manufacturer of device, device group and status of device (accurate/faulty).

Fig. 4 Laboratory staff login and search engine [22]

Verlab

Verifikacije

Biblioteka

Obavještenja

Ankete

Šifarnici

Narudžbe

Search engine with: Institute, Device group, Manufacturer, Device, Planned date, Verification status

Pretraga verifikacija

Ustanova: X

Grupa uređaja: X

Proizvođač: X

Uređaj: X

Planirani datum od: do

Stvarni datum od: do

Verifikacija ispravna:

Broj certifikata:

Broj naloga:

Pretraga Poništi

Ispravne ver.: 2020 2019 2018 2017 2016 2015 2011

Neispravne ver.: 2018 2017 2016 2015

Fig. 5 Resultant GUI upon using search engine with planned and performed inspections [22]

Planned inspections: Date, Institute, Device group, Manufacturer, Device, Serial Number.

Days remaining until inspection.

Planirane verifikacije

Datum uređaj Ser. br. Preostalo dana

Performed inspections: Date, Institute, Device group, Manufacturer, Device, Serial number, Inspection certificate.

Završene verifikacije

Datum	Ustanova	Grupa uređaja	Proizvođač	Uređaj	Ser. br.	Certifikat
-------	----------	---------------	------------	--------	----------	------------

Legenda | Verifikacije po bojama:

Planirani datum verifikacije istekao.

Planirani datum verifikacije između 1 i 15 dana u odnosu na trenutni datum.

Planirani datum verifikacije između 15 i 30 dana u odnosu na trenutni datum.

Verifikacija uređaja neispravna.

3.2 Future Application

A solution for the most efficient MD management and performance prediction is implementing the software's database to Machine Learning Algorithms [23]. Machine Learning Algorithms can most efficiently and in the shortest amount of time be used to predict MD performances [24]. In this way, maintenances can be planned without delay and negligence. eVerlab software has the data of inspecting medical devices in public and private healthcare institutions, during a four-year period. The resulting data can be used as input data to Machine Learning Algorithms.

The entire real-time measurement data from a specific device group can be collected and imported into Excel. An example of this is visible in Fig. 8. It shows data of only 26 inspections of defibrillators which is the number executed in less than a month. As visible, this is already a large number of data. In this way, a vast majority of data can be extracted in excel.

Specifically, obtaining the information of performance variation of only one type of MD from eVerlab software from this four year period, a dataset with more than 1000 variables could be collected and organized. Parameters of real-time measurement errors can be collected. The

Fig. 6 Report template in eVerlab for the defibrillator device group [22]

Nominal parameters		VERIFIKACIJA GREŠKE MJERILA			Allowed deviation
Izlazna energija					
Rb.	Xs [J]	Xm [J]	ΔX [J]	Dozvoljeno odstupanje [\pm J]	Usklađeno
1	10			1	Da ▼
2	30			5	Da ▼
3	50			5	
4	100			10	
Real-time measured values					
Rb.	Xs [J]	Xm [J]	δ [%]	Dozvoljeno odstupanje [\pm %]	Usklađeno
5	100			10	Da ▼
6	200			10	Da ▼
7	300			10	Da ▼
8	360			10	Da ▼

Fig. 7 Report of all inspections for period October–November in eVerlab database divided by device group [22]

DETALJNI REZULTATI MERENJA											
ANESTEZIOLOŠKA MAŠINA											
Broj ispitaja	Broj naloga	Datum ispitavanja	Status verifikacije	Zahtjev za verifikaciju	Metoda	Vrsta	Proizvođač	Uređaj	Serijski broj	Verifikacija ispravna	Spojevniji pregled
2279/18	2279/VL/18	2018-11-19	Završena	Naručbenica	Komparativna	Redovna	DAMECA	SIESTA	20504001	DA	DA
2282/18	2282/VL/18	2018-11-16	Završena	Naručbenica	Komparativna	Redovna	GE Datas Ohmeda	9100C	ME11120279	NE	DA
2281/18	2281/VL/18	2018-11-01	Završena	Naručbenica od 29.10.2018.	Komparativna	Redovna	GE Datas Ohmeda	ADU 55	40188337	DA	DA
2270/18	2270/VL/18	2018-10-26	Završena	Naručbenica od 18.10.2018.	Komparativna	Redovna	Dräger	PRIMAJS	AS44-0218	DA	DA
2271/18	2271/VL/18	2018-10-26	Završena	Naručbenica od 18.10.2018.	Komparativna	Redovna	GE Datas Ohmeda	ARANCE 55	AN8500414	DA	DA
2168/18	2168/VL/18	2018-10-08	Završena	Naručbenica od 08.10.2018.	Komparativna	Redovna	Mindray	WATO EX-85	KT95001640	DA	DA
2180/18	2180/VL/18	2018-10-08	Završena	Naručbenica od 08.10.2018.	Komparativna	Redovna	Stephan	ARV-U	S1081000688	DA	DA
			Završena	Naručbenica od 21.09.2018.	Komparativna	Redovna	Dräger	JULIAN	ARSD-0100	DA	DA
			Završena	Naručbenica od 21.09.2018.	Komparativna	Redovna	Dräger	PRIMAJS	ARZH-0241	DA	DA
			Završena	Naručbenica od 21.09.2018.	Komparativna	Redovna	Dräger	PRIMAJS	ARZH-0238	DA	DA

DEFIBRILATOR											
Broj ispitaja	Broj naloga	Datum ispitavanja	Status verifikacije	Zahtjev za verifikaciju	Metoda	Vrsta	Proizvođač	Uređaj	Serijski broj	Verifikacija ispravna	Spojevniji pregled
2278/18	2278/VL/18	2018-11-16	Završena	Ugovor od 11.10.2018.	Komparativna	Redovna	Scholer	DEFIARD 5000	101902007111	DA	DA
2212/18	2212/VL/18	2018-11-14	Završena	Naručbenica od 14.11.2018.	Komparativna	Redovna	Fukuda Denso	FC 560	30082447	DA	DA
2213/18	2213/VL/18	2018-11-14	Završena	Naručbenica od 14.11.2018.	Komparativna	Redovna	LIFE POINT	BIPHASICS	16086001	DA	DA

Fig. 8 Report on defibrillators imported into excel extracted directly from eVerlab [22]

Broj	Proizvođač	Model	Verifikacija	1. Zadana	1. Mjerna	1. Greška	2. Zadana	2. Mjerna	2. Greška	3. Zadana	3. Mjerna	3. Greška	4. Zadana	4. Mjerna	4. Greška
227070	Schiller	DEFIARD 5500					0.00	0.20	0.20	0.00	0.50	0.50	0.00	0.00	0.00
227070	FukudaDenki	FC 560					30.00	29.00	0.40	50.00	49.00	0.20	100.00	100.20	0.20
227070	LIFE POINT	BPMASICS					0.00	0.40	0.40	30.00	30.20	0.20	50.00	50.20	0.20
220090	NHOKICHEN	CARDOLIFE					0.00	0.50	0.50	30.00	28.30	1.50	50.00	48.50	1.50
227070	Schiller	DEFIARD 4000					0.00	0.20	0.20	30.00	30.40	0.40	50.00	50.50	0.50
227070	METRAV	PRMEDIC HD 100					30.00	30.20	0.20	50.00	50.40	0.40	100.00	101.40	1.40
227270	FukudaDenki	FC 560	30002440 DA	0.00	0.30	0.30	30.00	31.50	1.50	50.00	51.00	1.00	100.00	100.60	0.60
225470	Marquette	CARDIOSERV	10306264 DA	0.00	0.00	0.00	0.00	0.00	0.00	50.00	50.20	0.20	100.00	100.00	0.00
225770	Medica	BENHEART 03	EL-5702381 DA	0.00	0.00	0.00	0.00	0.00	0.00	46.40	3.60	0.00	100.00	92.70	7.30
224570	PRMEDIC	PRMEDIC DEFIN	05080 DA	20.00	0.00	0.00	0.00	0.00	0.00	103.10	3.10	0.00	100.00	102.70	2.70
224670	Siemens	THEVACARD 364	7275767E2209 DA	0.00	0.00	0.00	0.00	0.00	0.00	45.30	4.70	0.00	100.00	98.50	1.50
224770	HEARTSTREAM	AED/ILT	105000222 DA	0.00	0.40	0.40	0.00	0.00	0.00	0.00	0.00	0.00	0.00	0.00	0.00
224870	CARDIOSERV	GE-General	10195422 DA	0.00	0.40	0.40	30.00	30.00	0.00	50.00	50.30	0.30	100.00	100.10	0.10
223570	Medica	BENHEART 03	EL68020067 DA	0.00	0.40	0.40	0.00	0.00	0.00	3.40	0.00	0.00	100.00	93.10	6.90
220770	Medica	benheart 03	E2-85005011 DA	0.00	0.00	0.00	0.00	0.00	0.00	1.20	0.00	0.00	100.00	98.10	1.90
220090	NHOKICHEN	CARDOLIFE TEC	8106 DA	2.00	1.60	0.40	0.00	0.00	0.00	1.00	50.00	49.20	1.00	50.00	0.00
226570	Schiller	DEFIARD 4000	10009740202 DA	5.00	5.01	0.01	0.00	0.00	0.00	0.00	50.00	50.00	0.00	50.00	0.00
229570	Schiller	MINDEF 3	43300964 DA	2.00	2.30	0.30	0.00	0.00	0.00	1.90	30.00	28.50	1.50	50.00	48.50
220090	Medica	CARDIOSERV	10195571 DA	0.00	0.30	0.30	30.00	30.00	0.00	50.00	50.00	0.00	100.00	100.00	0.00
220270	CONTROL	PHYSIO	00002094 DA	5.00	5.10	0.10	0.00	0.00	0.00	0.70	0.30	0.00	0.00	0.00	0.00
226670	PRMEDIC	PRMEDIC DEFIN	719409207 DA	20.00	19.10	0.90	50.00	45.00	5.00	100.00	100.00	0.00	100.00	100.00	0.00
226770	GMA	RESCULIFE	1030395 DA	0.00	0.70	0.70	30.00	30.00	0.00	50.00	50.00	0.00	100.00	100.00	0.00
227070	NHOKICHEN	TEC	02437 DA	5.00	5.20	0.20	0.00	0.00	0.00	0.30	30.00	29.50	0.50	50.00	49.50
227270	NHOKICHEN	TEC	02201 DA	5.00	4.90	0.10	0.00	0.00	0.00	0.20	30.00	29.50	0.50	50.00	49.50
221470	NHOKICHEN	TEC/SSCK	05702 DA	5.00	5.20	0.20	0.00	0.00	0.00	0.20	30.00	28.40	1.60	50.00	48.40

information can be used as input for a chosen Machine Learning Algorithm which has the ability to process all of the information and predict performances of the medical device. This processed information can provide means of creating planned inspections for future maintenance of medical devices, also providing it in a way comprehensive and immediately available to all medical staff.

4 Conclusion

The consequences of failure of MDs have always been a major concern to biomedical engineers, due to the critical nature of these devices [25]. An inspection process which determines the performance of an MD must be done consistently and accurately in its post-market surveillance. Due to diversity of MD model types and manufactures, it is challenging to achieve consistency. Assessing on when to do an inspection process requires analysis of a large amount of data. Medical staff's comprehensive management and maintenance of MDs is of critical value, since they operate the machines daily. For this reason, a fast and reliable software solution for communication between clinical engineers and medical staff was created. Engineers of Inspection Laboratory Verlab have recognized the effectiveness of the implementation of a traceability software of all inspections and confirmed its effectiveness by successfully utilizing the eVerlab software solution to record performance characteristics of MDs in Bosnia and Herzegovina for the period of four years. Practically, based on the documented history records of these medical devices, performance variations of multiple types of medical devices can be elaborated. The sufficient guidance and simplicity of use lead to the successful use by multiple clients in Bosnia and the increase of clients and registered verifications year by year. All of the

data is documented in Inspection Reports with performance status of MD. The strategy for this prediction is applying inspection data to a Machine Learning Algorithm.

eVerlab software provides significant dataset and information for future research in Machine Learning algorithms for performance predictions of MDs. Collection of this data provides a strong basis for creating ANN and Fuzzy logic classifier systems in the medical industry, leading to faster, simpler and easily accessible determination on when a device needs to be inspected. These predictions prevent unnecessary, time-consuming inspection processes from being conducted.

Conflict of Interest Almir Badnjević, Lejla Gurbeta and Emina Kurta declare that they have no conflict of interest.

References

- Denger, C., Feldmann, R., Host, M., Lindholm, C., Shull, F.: A Snapshot of the State of Practice in Software Development for Medical Devices, 1st edn, pp. 1–3. IEEE (2007)
- Chong, C.-Y., Kumar, S.: Sensor networks: evolution, opportunities, and challenges. Proc. IEEE **91**(8), 1247–1256 (2003)
- Kaplan, A., Baim, D., Smith, J., Feigal, D., Simons, M., Jefferys, D., et al.: Medical device development. Circulation **109**(25), 3068–3072 (2004)
- Money, A., Barnett, J., Kuljis, J., Craven, M., Martin, J., Young, T.: The role of the user within the medical device design and development process: medical device manufacturers' perspectives. BMC Med. Inf. Decis. Mak. (2011)
- Cheng, M., World Health Organization.: Medical Device Regulations, p. 1. World Health Organization (2003)
- International Bureau of Weights and Measures. Available at: <http://www.bipm.org/>
- International Vocabulary of Metrology—Basic and General Concepts and Associated Terms (VIM), 3rd ed.
- Gurbeta, L., Badnjevic, A.: Medical devices in legal metrology framework. In: WHO Global Forum on Medical Devices, 09–12 May 2017, Geneva, Switzerland

9. Medical Device Directive 93/42/EEC at <https://eur-lex.europa.eu/LexUriServ/LexUriServ.do?uri=CONSLEG:1993L0042:20071011:en:PDF>
10. Medical Electrical Equipment ISO 60601, General requirements for basic safety and essential performance, IEC 60601-1-11:2010
11. Safety Testing of Medical Devices ISO 62353/2014
12. European Comission: Medical Devices. Guidance document at www.ec.europa.eu/health/medical-devices/files/meddev/2_1-1_04-1994_en.pdf
13. Gurbeta, L., Dzemic, Z., Bego, T., Sejdic, E., Badnjevic, A.: Testing of anesthesia machines and defibrillators in healthcare institutions. *J. Med. Syst.* **41**, 133 (2017). <https://doi.org/10.1007/s10916-017-0783-7>
14. Casey, V., Mc Caffery, F.: Med-Trace: Traceability Assessment Method for Medical Device Software Development, 1st ed, p. 1. In: European Systems and Software Process Improvement and Innovation Conference EuroSPI (2011)
15. Gurbeta, L., Izetbegović, S., Badnjević-Čengić, A.: Inspection and testing of infant incubators. In: Badnjević A., Cifrek M., Magjarević R., Džemić Z. (eds.) *Inspection of Medical Devices*. Series in Biomedical Engineering. Springer, Singapore (2018)
16. Gurbeta, L., Badnjevic, A., Pinjo, N., Ljumic, F.: Software package for tracking status of inspection dates and reports of medical devices in healthcare institutions of Bosnia and Herzegovina. In: XXV International Conference on Information, Communication and Automation Technologies (IEEE ICAT), pp. 1–5, 29–31 Oct 2015, Sarajevo, Bosnia and Herzegovina
17. Gurbeta, L., Badnjevic, A., Sejdinovic, D., Alic, B., Abd El-Ilah, L., Zunic, E.: Software solution for tracking inspection processes of medical devices from legal metrology system. In: XIV Mediterranean Conference on Medical and Biological Engineering and Computing (MEDICON), 31 Mar–02 Apr 2016, Paphos, Cyprus
18. Gong, A.: Data science and its relationship to big data and data-driven decision making. *Big Data* **1**(4), 194 (2013)
19. Chadhaury, P., Kaul, P.: Factors affecting utilization of medical diagnostic equipment: a study at a tertiary healthcare setup of Chandigarh (p. 1). India (2018)
20. Wallace, D., Kuhn, R.: *Failure Modes in Medical Device Software: An Analysis of 15 Years of Recall Data*, 8th edn, p. 351. World Scientific Publishing Company, USA (2001)
21. Gurbeta, L., Badnjevic, A.: Inspection process of medical devices in healthcare institutions: software solution. *Health Technology*, pp. 1–5 (2016). Retrieved from https://www.researchgate.net/publication/311499482_Inspection_process_of_medical_devices_in_healthcare_institutions_software_solution
22. Gurbeta, L., Almir, B.: Verlab Handbook: “Verlab solution for tracking inspection processes in healthcare”, pp. 1–10. Sarajevo, Bosnia and Herzegovina (2014)
23. Kurta, E., Kovacevic, Z., Gurbeta, L., Badnjevic, A.: Electromagnetic compatibility of medical devices: effects in everyday healthcare environment. In: 7th Mediterranean Conference on Embedded Computing MECO’2018, Budva, Montenegro
24. Murdoch, T., Detsky, A.: The inevitable application of big data to health care. *JAMA* (2013)
25. Krumholz, H.: Big data and new knowledge in medicine: the thinking, training, and tools needed for a learning health system. *Health Affairs* (2014)

Establishment of Measurement System for Hearing Aids at TÜBİTAK UME

Baki Karaböce, Hüseyin Okan Durmuş, and Emel Çetin

Abstract

Hearing devices in many different brands and types are used in our country. However, these hearing aids before being placed on the market do not pass mandatory/legal technical measurements. To verify that hearing aids work in a specified performance, measurements are always required to be done on the basis of scientific parameters and standards. For this purpose, the acoustic cabinet, microphone, ear simulator, analyzer and software-aided system was established in TÜBİTAK UME Medical Metrology Laboratory. The acoustic field generated by the sound source within the acoustic cabinet is analyzed with the reference microphone and ear simulator. In this set-up system, performance parameters such as acoustic impedance measurements in the range of between 100 Hz and 10 kHz, sensitivity, frequency response and noise insulation value are measured. In this paper, performance parameters' measurements of the sound pressure level of headphones that are designed specifically for musicians in Turkey are presented in 2.0 dB uncertainty.

Keywords

Hearing aid • Acoustical measurements • Acoustic cabin • Ear simulator • Metrology • Calibration

1 Introduction

According to VIM (International vocabulary of metrology—basic and general concepts and associated terms), metrology is the science of measurement and its application. Besides, metrology includes all theoretical and practical aspects of measurement whatever the measurement uncertainty and field of application [1]. Measurements play a key role to understanding and therefore controlling any process. Accurate measurement and control of the physical quantities are very critical to make meaningful extractions and statements. Acoustic measurements of hearing aids are also in this assessment.

Many different brands and types of hearing aids are used in our country. However, these hearing aids do not effectively pass a legal/mandatory technical measurement before being introduced to the market. According to our legislation, every product to be supplied to the market should have minimum safety conditions in terms of human health, life and property safety, animal and plant life and its health, environment and consumer protection [2]. Audits to ensure that the products in the market are legitimate and safe and precautions taken on the basis of these inspections directly affect the two major actors of the economy; the producers and consumers. While it is important for consumers not to include products that will adversely affect their health and safety, producers are also concerned about the prevention of unfair competition and the image of their products on the market [3].

On the other hand, when the literature has been examined, it has been seen that scientific and legal metrology studies related to healthcare services have also been studied seriously in Bosnia and Herzegovina. Bosnia and Herzegovina have appeared to be a proactive and the leading country in this field [4–9].

In the field of sales of hearing aids, domestic companies that sell hearing aids have complaints and searches that there is a serious irregularity in our market. In addition, there are reports that unhealthy hearing aids that may cause trauma to

B. Karaböce (✉) · H. O. Durmuş · E. Çetin
Medical Metrology Laboratory, TÜBİTAK National Metrology
Institute (UME), Kocaeli, Turkey
e-mail: baki.karaboce@tubitak.gov.tr

H. O. Durmuş
e-mail: huseyinokan.durmus@tubitak.gov.tr

E. Çetin
e-mail: emel.cetin@tubitak.gov.tr

the ear in the beginning find buyers in serious dimensions [10]. For this reason, it is necessary to make measurements/tests in accordance with scientific parameters and standards before being supplied to the market to verify that the hearing aids are working to the specified performance, and to be supplied to the market in this way.

Performance parameters of the sound pressure level measurements of the headphones, which is custom-built, having 6-speaker and produced for musicians in Turkey, for use in ear and belonging to a private company designed to be personalized and having Serial No: 102093 and MK 18 type was performed. The sensitivity of the device under test is 115 dB (1 kHz, 1 mW), frequency response is between 5 Hz and 22 kHz, impedance is 21 Ω (1 kHz) and noise isolation is -26 dB.

1.1 Measurement Infrastructure of UME Medical Metrology Laboratory for Hearing Aids Tests

Hearing aids are tested with hearing instrument analyzers using ear simulators and microphones in acoustic test cabinets. In the TÜBİTAK UME Medical Metrology Laboratory, Rohde & Schwarz UPV Audiovisual Analyzer [11] and 8020495 Model, Affinity 2.0 Interacoustics brand hearing instrument analyzers are used for this purpose. Acoustic measurements of hearing aids are performed using the apparatus shown in Fig. 1a and b.

The physical unit of the calibration is dB (Decibel). Sound Pressure Level; expressed in dB (Decibel) unit. In acoustic measurements of hearing aids, Normalized Response, Frequency Response and Sound Pressure Level are measured in dB. The range in which acoustic measurements of hearing aids are made is between 0 and 120 dB. Acoustic measurement traceability of hearing aids is provided through the devices shown in Table 1.

Tests of the basic properties of hearing aids are described in IEC 60118 Electroacoustics—Hearing Aids series and ANSI S3.22 Specification of Hearing Aid Characteristics standards. These are; Output Sound Pressure Level (SPL), Frequency Response, Output SPL Over Input SPL, Harmonic Distortion, Battery Current Drain and Automatic Gain Control (AGC) settings.

Odyoanalyzer R&S UPV allows measurements according to, IEC 60118-0:1983 (Hearing aids—Part 0: Measurement of the performance characteristics of hearing aids), IEC 60118-1:1995 (Hearing aids—Part 1: Hearing aids with induction pick-up coil input), IEC 60118-2:1983 (Hearing aids. Part 2: Hearing aids with automatic gain control circuits), IEC 60118-7:2005 (Electroacoustics—Hearing aids—Part 7: Measurement of the performance characteristics of hearing aids for production, supply and delivery quality

assurance purposes) and ANSI S3.22-2003 (Specification of Hearing Aid Characteristics) standards and provides a test system with the necessary acoustic accessories. Besides the measurements made on the basis of a certain standard, it is also possible to create/specify the desired tests by changing the existing parameters with this software. In addition to this, tests can be performed according to IEC 6011815 (Electroacoustics—Hearing aids—Part 15: Methods for characterising signal processing in hearing aids with a speech-like signal) using the optional R&S UPV-K71 as an extra speech signal.

The necessary equipment used in the calibration of hearing aids is as follows.

- Audio Analyzer R&S UPV
- Hearing Aid Test Box or Anechoic Box
- Measurement Microphone
- Low-Noise Measurement Microphone
- IEC 126 Coupler
- IEC 126 Coupler for 1/2" microphone
- IEC 711 Ear Simulator (optional)
- Acoustic Calibrator
- Microphone Power Supply

The following measurements can be made on the measurement system.

- Frequency Response Measurement
- Multi-Curve Measurement
- Saturation Sound Pressure Level Measurement
- Harmonic Distortion Measurement
- Measurement of Dynamic Behaviour
- Measurement of Input-Output Characteristics
- Measurement of Equivalent Input Noise
- Battery Current Measurement

2 Results and Discussion

In the measurements, the methods and device infrastructure defined in the IEC 60118-0 (Electroacoustics—Hearing Aids Part 0: Measurement of the performance characteristics of hearing aids) standard series [12] are used. For this purpose, acoustic cabin, microphone, ear simulator, analyzer and software supported system was established in TÜBİTAK UME Medical Metrology Laboratory. In the system; Rohde & Schwarz acoustic analyzer and application software, Brüel & Kjaer microphones, ear simulators and acoustic cabinet are used. In the case of lower frequency measurements, the “Full Anechoic Room” facilities installed in the UME are being used. The acoustic area created by the sound source within the acoustic cabinet is analyzed by reference microphone and ear simulator. In the installed system,

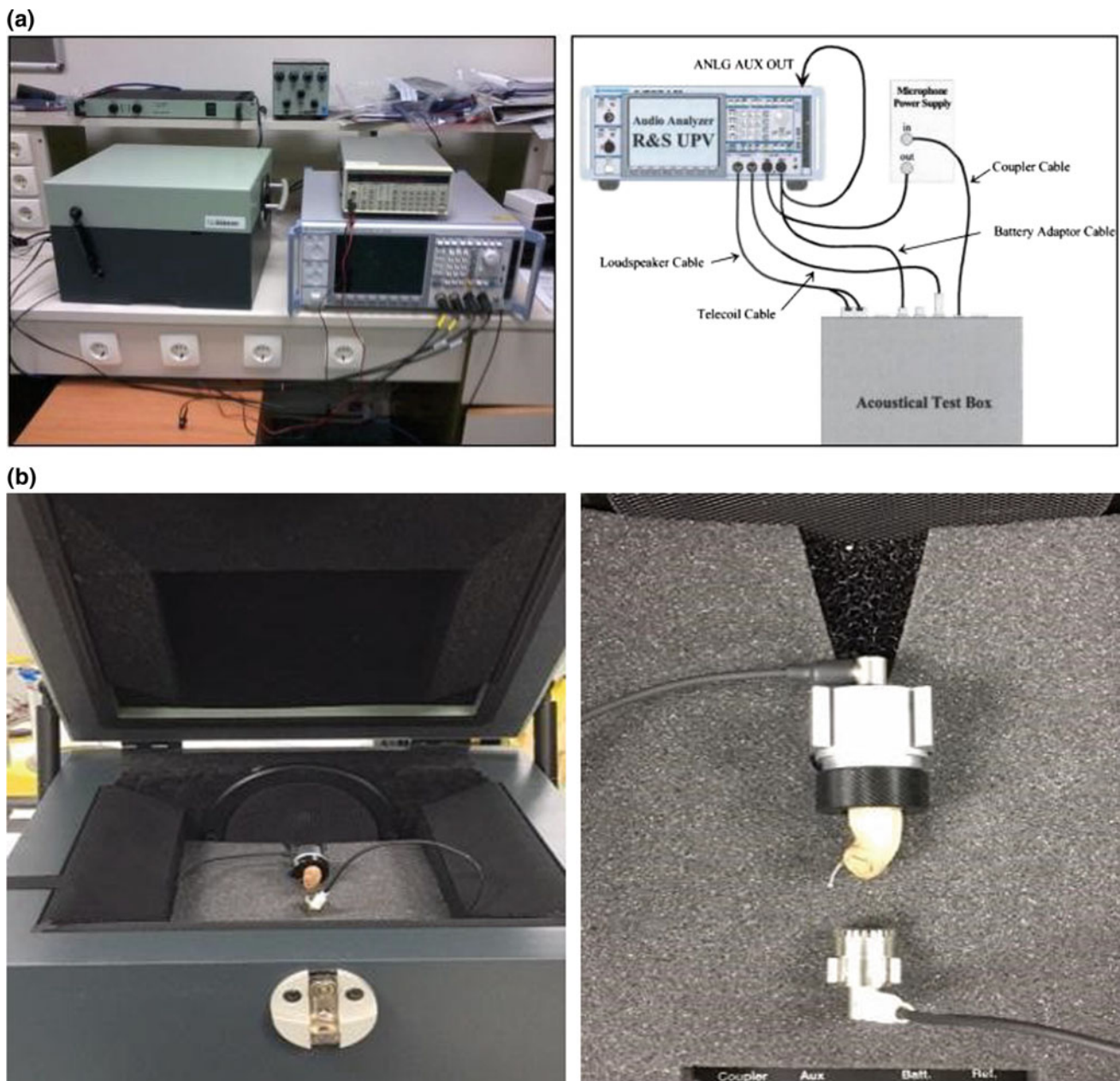


Fig. 1 a Hearing aids acoustic measurements calibration setup. b Mounting of hearing aid inside the cabin

Table 1 Instruments/devices used in calibration of acoustic measurements of hearing aids

Instrument name	Manufacturer	Type	Serial number	Calibration period
Ear simulator set	Brüel & Kjaer	4157	2874395	1 year
Condenser microphone	Brüel & Kjaer	4191	2884943	1 year

performance parameters such as acoustic impedance measurements, sensitivity, frequency response and noise isolation value in the range of 100 Hz–10 kHz are measured.

The performance measurements of the particular hearing aid instrument used as the musician headset shown in Fig. 2 were performed according to the method described in the

IEC 60118 standard. The earphones tested in the measurements are mounted on the Brüel & Kjaer 4157 ear simulator, which is located in the Brüel & Kjaer 4232 acoustic cabinet. The acoustic area created by the sound source in the acoustic cabin has also been analyzed with reference microphone and ear simulator.

Fig. 2 The special hearing aid tested

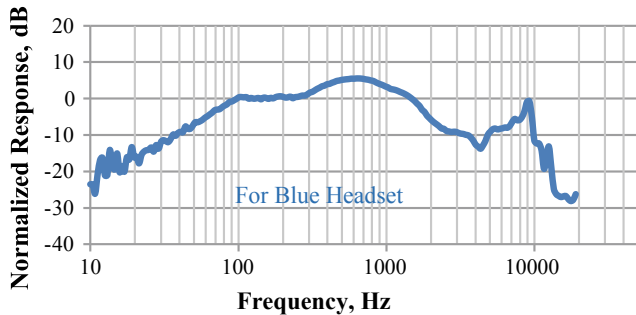


Fig. 3 Normalized frequency response of the musician's earphones for blue headset

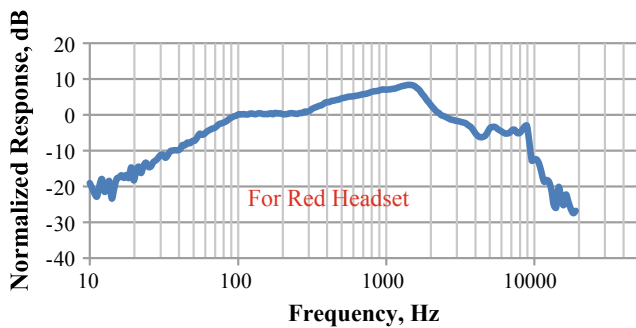


Fig. 4 Normalized frequency response of the musician's earphones for red headset

The performance measurement results of the special hearing aid instrument used as a musician headset are as shown in Figs. 3, 4, 5, 6, 7 and 8.

Normalized frequency response, frequency response and dynamic outputs of the right and left headsets are given in the graphs. Normalized frequency response is relative frequency response as per the selected frequency signal. Frequency response is sound pressure level measured in the acoustic coupler expressed as a function of frequency under specified test conditions. Dynamic output is dynamic behavior and it is the change of sound pressure level according to time. Based on these parameters, effective frequency ranges can be determined.

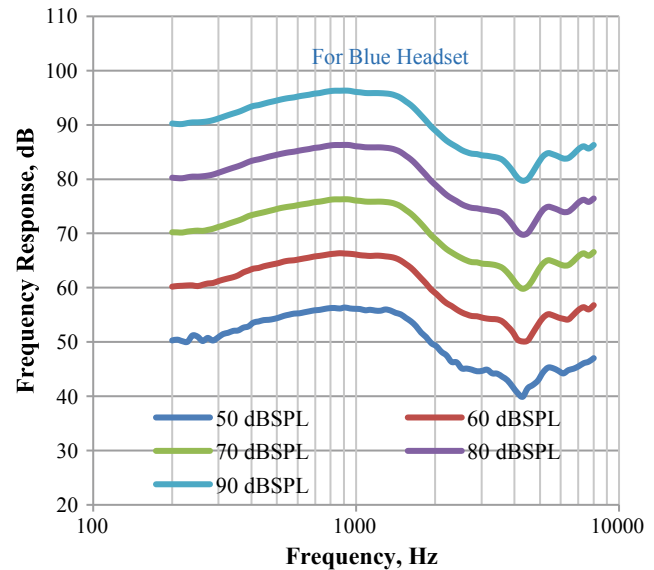


Fig. 5 Frequency response of the musician's earphones for blue headset

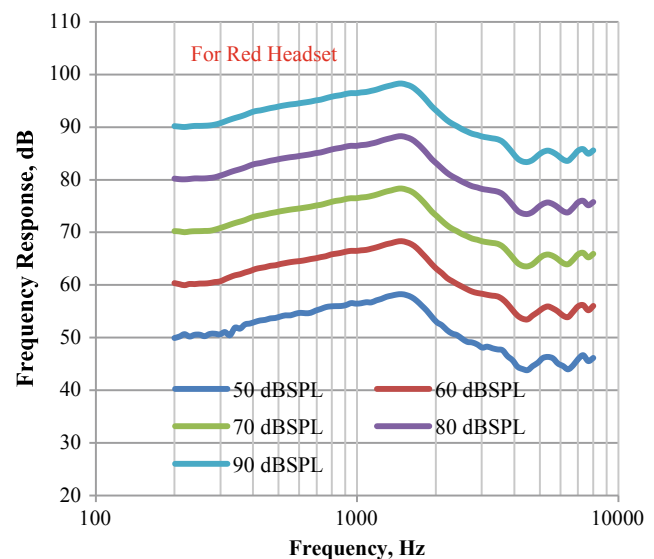


Fig. 6 Frequency response of the musician's earphones for red headset

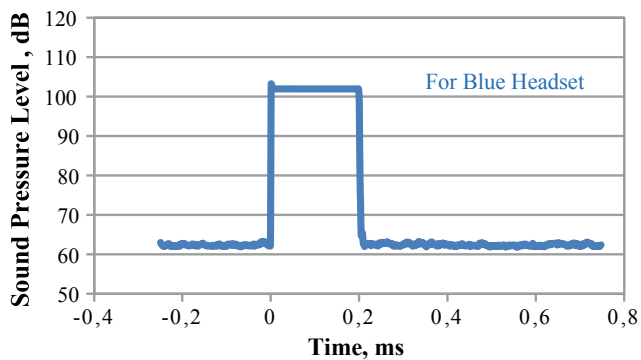


Fig. 7 Blue headset dynamic output (1 kHz)

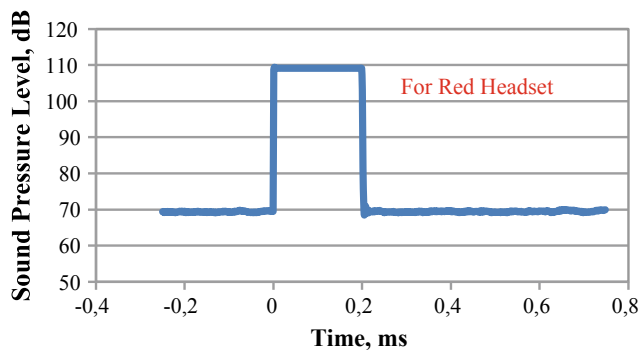


Fig. 8 Red headset dynamic output (1 kHz)

In addition, “Noise Insulation Value” and “Headphone Impedance Ratings” are also measured separately for Blue and Red headsets in dB. The noise insulation value was found to be 24.5 dB for the blue headset and 25.0 dB for the red headset. In other words, it can be said that the sound coming to the musician’s ear is reduced by 25 dB. The earphone impedance values for our work are measured as 23.92 Ω for “Blue Headset” and 23.41 Ω for “Red Headset”.

Low impedance headsets (less than approximately 25 Ω) work well with weakly amplified devices such as portable devices [13]. Therefore, it can be said that the tested device will work well during use.

3 Conclusion

In this paper, measurements of sound pressure level performance parameters and interpretations of measurements of a headphone that is designed specifically for musicians in

Turkey are presented in 2.0 dB uncertainty at the TUBITAK UME Medical Metrology Laboratory.

In order to make measurements of many brands and types of hearing aids, which their usage are increasing day by day in our country, according to scientific parameters and standards, to verify that the specified performance is working, and for the protection of the hearing health of our people, there are great benefits of hearing aids to go through a legal/mandatory technical measurement before being offered to the market.

References

1. <https://www.bipm.org/en/publications/guides/vim.html>
2. Turkish official paper: Regulation on Market Surveillance and Inspection of Products (Ürünlerin Piyasa Gözetimi ve Denetimine Dair Yönetmelik). Resmi Gazete Tarih: 17.1.2002, No: 24643
3. <http://www.kobi.org.tr/index.php/koblere-yoenelik-yararli-bilgiler/piyasa-goezetimivedenetimi>
4. Badnjević, A., Cifrek, M., Magjarević, R., Džemić, Z. (eds.): Inspection of Medical Devices. Series in Biomedical Engineering. Springer, Singapore
5. Badnjevic, A., Gurbeta, L., Jimenez, E.R., Iadanza, E.: Testing of mechanical ventilators and infant incubators in healthcare institutions. *Technol. Health Care* **25**(2), 237–250 (2017)
6. Gurbeta, L., Dzemic, Z., Bego, T., Sejdic, E., Badnjevic, A.: Testing of anesthesia machines and defibrillators in healthcare Institutions. *J. Med. Syst.* **41**, 133 (2017)
7. Badnjevic, A., Gurbeta, L., Boskovic, D., Dzemic, Z.: Medical devices in legal metrology. In: IEEE 4th Mediterranean Conference on Embedded Computing (MECO), Budva, Montenegro, pp. 365–367, 14–18 June 2015
8. Gurbeta, L., Vukovic, D., Džemic, Z., Badnjevic, A.: Legal metrology procedures for increasing safety and performance characteristics with cost benefits analysis: case study dialysis machines. In: Lhotska, L., Sukupova, L., Lacković, I., Ibbott, G. (eds.) World Congress on Medical Physics and Biomedical Engineering 2018. IFMBE Proceedings, vol. 68/2. Springer, Singapore (2018)
9. Gurbeta, L., Džemic, Z., Badnjevic, A.: Establishing traceability chain of infusion and perfusor pumps using legal metrology procedures in Bosnia and Herzegovina. In: Lhotska, L., Sukupova, L., Lacković, I., Ibbott, G. (eds.) World Congress on Medical Physics and Biomedical Engineering 2018. IFMBE Proceedings, vol 68/2. Springer, Singapore (2018)
10. <http://www.hurriyet.com.tr/ekonomi/12331020.asp>
11. R&S UPV-K7: Rohde & Schwarz software for hearing aids test operating manual
12. IEC 60118-0 (Electroacoustics—Hearing Aids Part 0: Measurement of the performance characteristics of hearing aids)
13. <https://www.turntablelab.com/pages/headphone-buying-guide-what-is-headphoneimpedance>

The Importance of Metrology in Medicine

Baki Karaböce, Hüseyin Okan Durmuş, and Emel Çetin

Abstract

Medical device calibration and test are one of the emerging, important and critical issues in the field of metrology. The traceability in medical devices and measurements are not powerful enough as much as the traceability in technical and military calibration and measurements. Patient safety is a must for the medical device industry and applications in the health sector. Therefore all measurement devices used in the medical field must be controlled periodically and all measurements must be standardized as a quality control regimen that guarantees the reliability of medical devices. Test, measurement, and calibration of bio-medical equipment are becoming increasingly significant for manufacturers when accuracy in diagnosis and effectiveness in treatment are required as well as patient safety. For this reason, it is expected that this article will provide a clear approximation of the correct measurements in the medical field as a guide to medical metrology studies.

Keywords

Measurements • Medical device • Medical metrology • Test • Control • Verification • Calibration • Traceability • Calibrators • Simulators • Analyzers • Phantoms • NMI • DI

1 Introduction

In the field of health, the diversity of devices used in imaging, diagnosis, and treatment has been increasing in recent years and its use is widespread [1–3].

Patient diagnosis and treatment are usually based on clinical findings, such as medical examinations and the results of statistical studies obtained from patients over the years. Medical measurements are important in establishing clinical findings and in establishing consistent statistical data from a large number of patients [4–6].

These systems range from a simple thermometer to computerized imaging systems, clinical measurement devices or computer-controlled, highly precise surgical robots. According to the findings and examination findings obtained with these systems, the treatment steps and methods are determined by the physician. Data obtained from measurement systems may be more important than findings from examinations. For example, a hernia that cannot be identified in the examination findings of a medical doctor can appear in MR (magnetic resonance) image. For this reason, medical devices are critical in the medical field.

2 Problems Related to Measurements and Importance of Medical Measurements

Based on the data obtained from medical devices, diseases are diagnosed and the path to be followed in treatment is determined. For example, if a diabetic patient has a high blood sugar level; it is highly likely that he or she will begin insulin therapy. Failure to measure glucose in the blood correctly will result in unnecessary treatment and/or delay in necessary treatment. Damage risk to life on the inaccurate measurement of glucose in the blood cannot be measured in addition to the high amount of expenses. Similar phenomenon exist in many health problems. For example, The National Institute of Standards and Technology (NIST) of

B. Karaböce (✉) · H. O. Durmuş · E. Çetin
Medical Metrology Laboratory, TÜBİTAK National Metrology
Institute (UME), Kocaeli, Turkey
e-mail: baki.karaboce@tubitak.gov.tr

H. O. Durmuş
e-mail: huseyinokan.durmus@tubitak.gov.tr

E. Çetin
e-mail: emel.cetin@tubitak.gov.tr

the United States has made a progress in cholesterol measurements between 1949 and 2000 years. More accurate or small uncertainty in cholesterol in the blood measurements will guarantee the fewer expenses and correct treatment as can be seen in Fig. 1 [7–9]. Definitive and standard methods and development of serum cholesterol standard reference materials (SRMs) will result in saving of treatment costs for misdiagnosed patients and additionally lives through timely and accurate diagnosis. In other words, measurements in the field of clinical metrology are of vital importance. Incorrect test results lead to incorrect treatment and/or money loss. For example, if you are healthy in the real situation, but the test shows that you are sick (False Positive), the wrong medicines and treatments will harm both your budget and you will lose your health. Or you are really sick in the real situation, but if the test says that you are healthy (False Negative) then your health will both get worse and your budget will also suffer more. So in both cases, that is, the wrong treatment and the loss of the budget will cost both you and the community very expensive.

Most of the devices in the hospitals are not calibrated through the metrological way. For example, it can be seen that the calibration requirement is fulfilled by switching on and off or zeroing or resetting the devices or attaching only labels. Some of the calibrations and tests are performed by non-accredited laboratories [10, 11]. The reasons can be listed as follows;

- Fulfillment of calibration makes possible to receive money from circulating capital fund of the hospital.
- The ignorance or carelessness of the medical doctors or the person concerned who request for calibration.
- There is no regular audit by authorities.

Calibrations of calibrators, simulators, analyzers, and phantoms which are used in the test, control, verification and calibration of medical devices are made by the distributors of those devices under the name of maintenance/repair/calibration in health institutes. This process is not correct metrologically and not within the scope of authority and accreditation. It has been determined that the vast majority of medical field devices are not metrologically calibrated or verified. The reasons for this can be listed as follows;

- Considering the frequency of use, measurement accuracy and health risk, it has been agreed to assign a calibration period for each device type. In general case, hospital's surgeons are not well aware of the importance of the test, control, verification and calibration of medical devices.
- Many manufacturers and distributors have no information about device calibration.
- The biomedical institute or departments of some universities are only more focused on consultancy and education but not calibration and measurement.

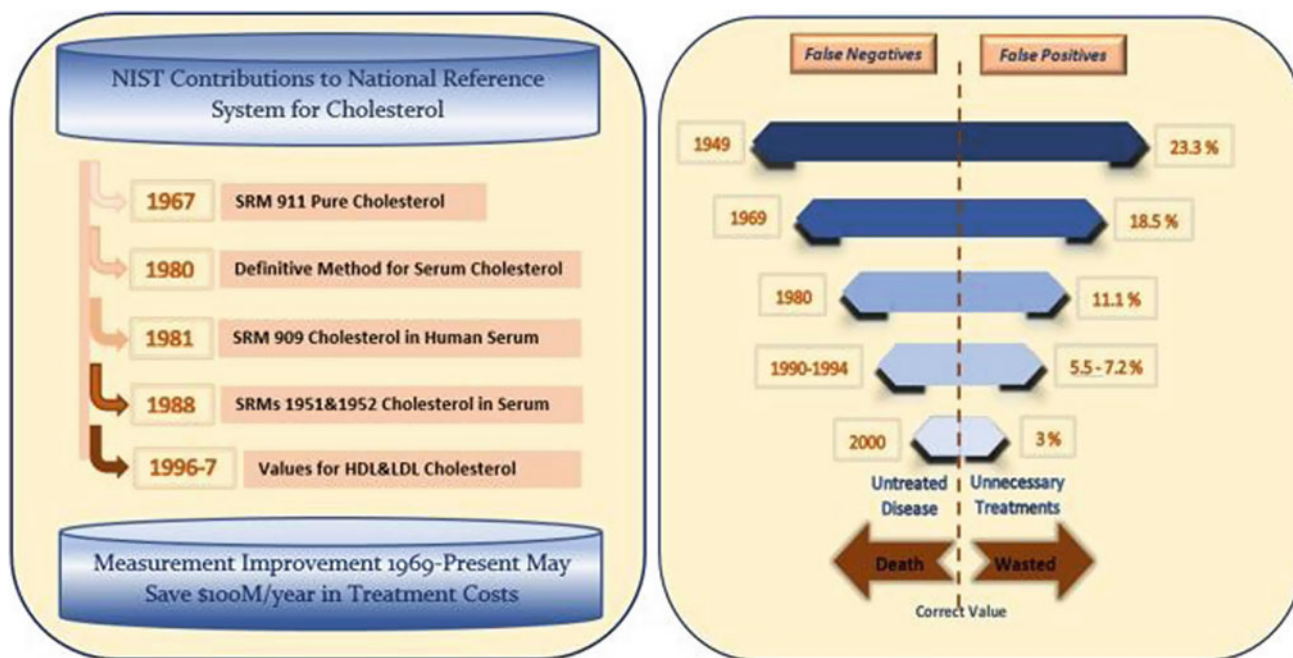


Fig. 1 Development of accuracy in glucose in the blood measurements [9]

The metrological reference values (produced for the country and by joining all necessary all international comparisons required for NMI's reference standards and reference materials used in the traceability of medical and clinical devices) are aimed to adapt to the international system.

3 Development of Medical Metrology Laboratory at TÜBİTAK UME, Turkey

The National Metrology Institute of Turkey (TÜBİTAK UME) has established for the aims of to ensure the traceability of measurement quantities relevant to medicine, to integrate the measurement quantities into the international metrology system through international comparisons and to ensure measurement unity by disseminating traceability to lower level laboratories within the country or abroad through calibration, measurement and test services as seen in Fig. 2. The other objective of the laboratory activities is to produce research projects in line with national priorities and the stakeholder demands.

As well as ensuring measurement traceability of the devices used in medicine and reliability studies, the Medical Metrology Laboratory has implemented projects such as calibrator design and production for medical devices and certified reference materials production for auto-analyzers [12]. In addition to this, the laboratory has also organized training programs for professionals that perform medical device calibrations.

Study areas of the TÜBİTAK UME Medical Metrology Laboratory include:

- Ensuring measurement traceability of the devices used in the health field
- Certified reference materials production for clinical measurements
- Calibrator design and production for medical devices
- Practical training programs for professionals perform in medical device calibrations
- Establishing systems and implementing projects for the application of ultrasonic techniques in the health field
- Conducting performance tests of hearing aids and headsets.

Calibration and Measurement Services include:

- Patient Simulator Calibrations
- Defibrillator/Pacer Analyzer Calibrations
- Electrical Safety Analyzer Calibrations
- Pulse-Oximetry Analyzer Calibrations
- Infusion Pump Analyzer Calibrations
- Gas Flow Analyzer Calibrations
- Electrosurgery Analyzer Calibrations
- Hearing Aid Performance Tests
- Measurement Systems for Ultrasonic Applications in the Health Field
- Standard Reference Materials (SRM).

A calibration scheme for Infusion pump analyzer can be seen in Fig. 3. An automated calibration set up is used to calibrate the flow and volume parameters of infusion pump analyzer with a written procedure and calibrated references.



Fig. 2 Calibration systems for simulators and analyzers at TÜBİTAK UME Medical Metrology Research Laboratory

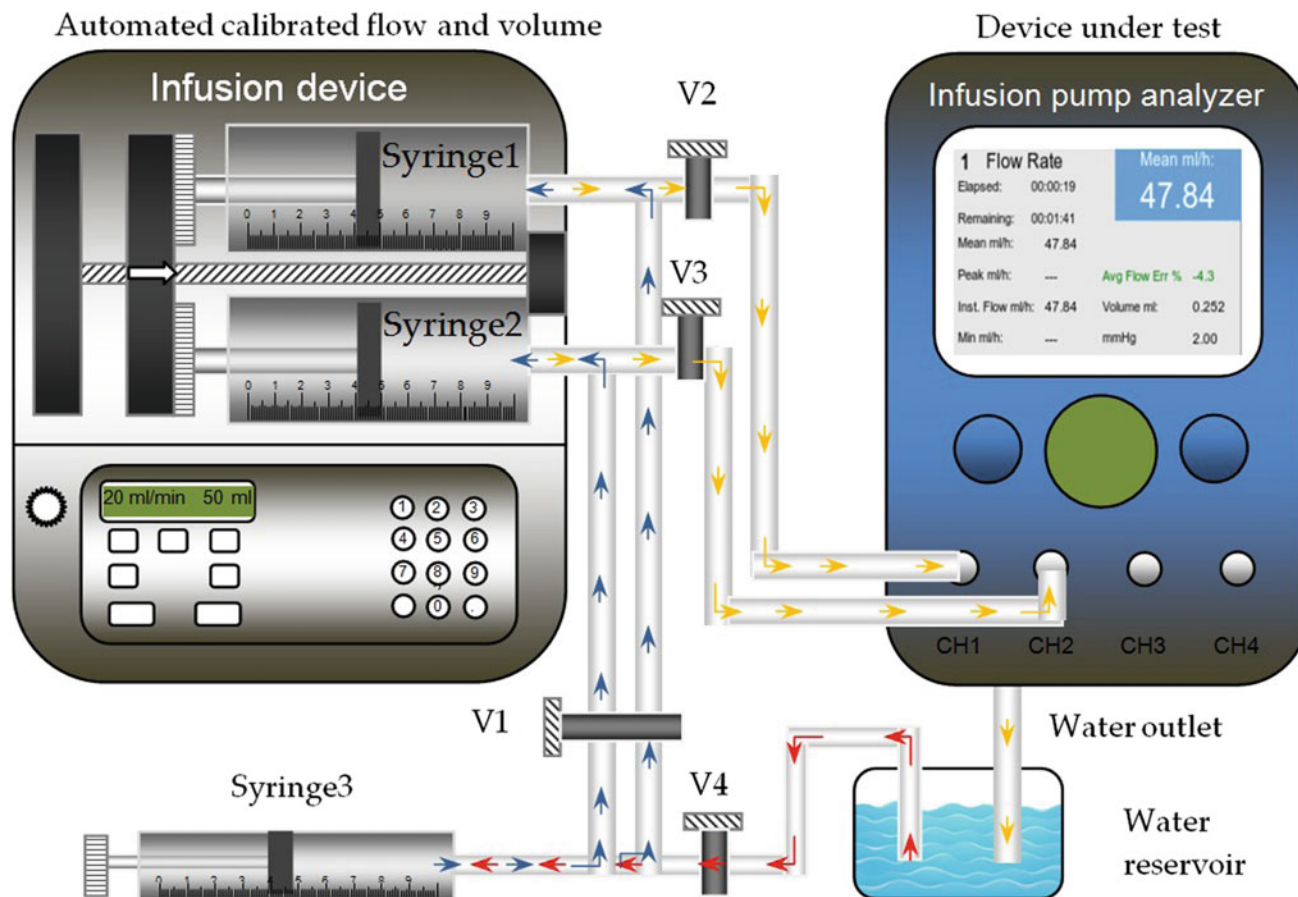


Fig. 3 Calibration scheme for infusion pump analyzer

Another calibration diagram for patient simulator can be seen in Fig. 4. A fully automated calibration set up is used to calibrate pressure, flow and electrical parameters of patient simulator with a written procedure and calibrated references.

4 Traceability in Medical Measurements

The traceability of a value attributed to a routine sample, calibrator or control material is generated by a series of comparative measurements in an increased hierarchical order named traceability chain [13]. All calibrations and measurements must be traceable to national or international standards that are based on SI or derived SI units as can be seen in Fig. 5.

5 Conclusions and Suggestions

Medical measurements are actually based on the research studies conducted by the work of national metrology institutes. A reliable measurement system can be created by

combining metrological instruments and quality assurance systems. Calibrations of the devices and systems used for transferring the measurement values, using of scientifically accepted measurement and calibration methods in measurements and control procedures required by legal metrology are metrological tools that must be used in the system. An objective and transparent system based on quality criteria can be established by using the internationally recognized standards of quality assurance [13].

Regular maintenance/repair as well as testing, measurement, verification and calibration must be carried out at regular intervals to ensure correct operation of medical devices during use. Some of the devices and apparatus used for testing, measuring, verifying and calibrating are commercially available. However, it is very important that institutions and organizations that provide services in the field of health as well as all areas should be able to monitor the devices used for diagnosis and treatment to national and/or international standards and to establish a measurement association within the country. It is necessary to carry out studies for the establishment and research of the necessary infrastructure for this traceability [14, 15].

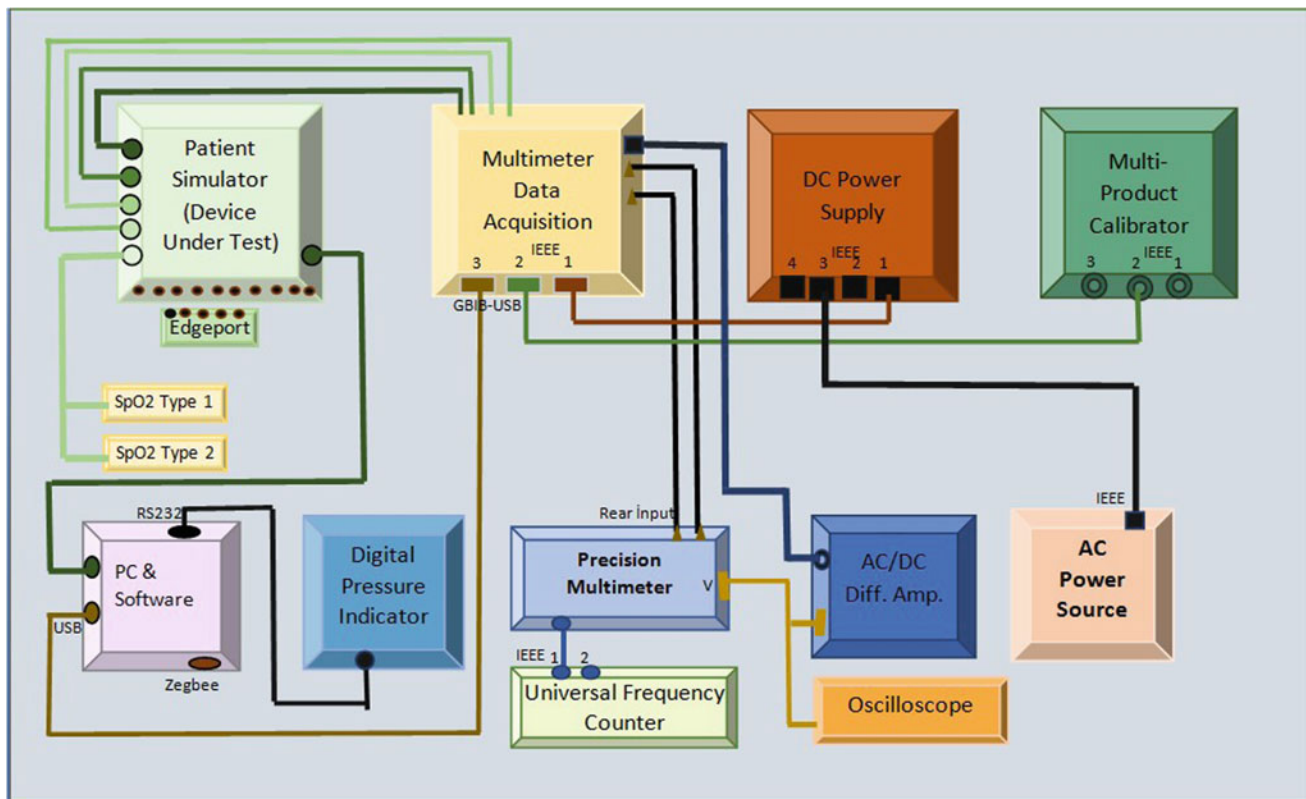


Fig. 4 Calibration diagram for patient simulator

To emphasize the importance of instrument calibrations used in the medical field and to ensure accurate calibration, a limited number of training programs are organized in some universities, public and private institutions. Trainings should be given to all interested persons, including hospital managers, calibration laboratory personnel and device users.

A regulation on testing, control and calibration of medical devices will create an appropriate environment in order to establish traceability of standards and reliability in medical measurements. In particular, audits should cover technical areas. For example, aspects such as calibration, compliance with a specific standard, traceability of the devices used should be controlled. It is foreseen that the accreditation institution and the pharmaceuticals and medical devices agency should act in coordination with the accreditation of the laboratories that perform medical device calibration.

Collaborative platforms for the collaboration of public institutions, universities and industrial organizations for the design and production of devices such as calibrators, phantoms, analyzers in the medical field are more widely and effectively used. Examination of written standards, medical and clinical devices, calibration/measurement systems within the feasibility project to be done and information obtained from interviews with related institutions, universities, hospitals and private laboratories must be compiled.

With this information, works to be done, calibration/measurement systems to be installed, plans of these calibrators, phantoms and reference materials which are considered of their design and production have to be given.

Official institutions, universities, biomedical calibration laboratories and private companies operate in specific areas of medical metrology, have variable approaches in this field [16–19]. Some private hospitals declaring that they are testing, checking, verifying and calibrating their own devices. Medical calibration units in the Ministry of Health in Turkey declare that they can test, control, verify and calibrate the medical devices in some hospitals within the capacities of their own portable system. But the traceability and reliability of medical devices is not provided by metrologically. Calibrations of instruments used in calibration (such as calibrator, simulator, analyzer and phantom) must be performed by authorized (accredited) and trained persons, using reference measurement standards, according to written standards or methods defined in the literature, if possible in controlled environments.

Some good examples can be given: the devices of the university hospital calibrate their laboratories with the systems in the relevant laboratories that they calibrate in their own systems. However, some of these devices are simulators, analyzers, etc. used in calibration to an organization

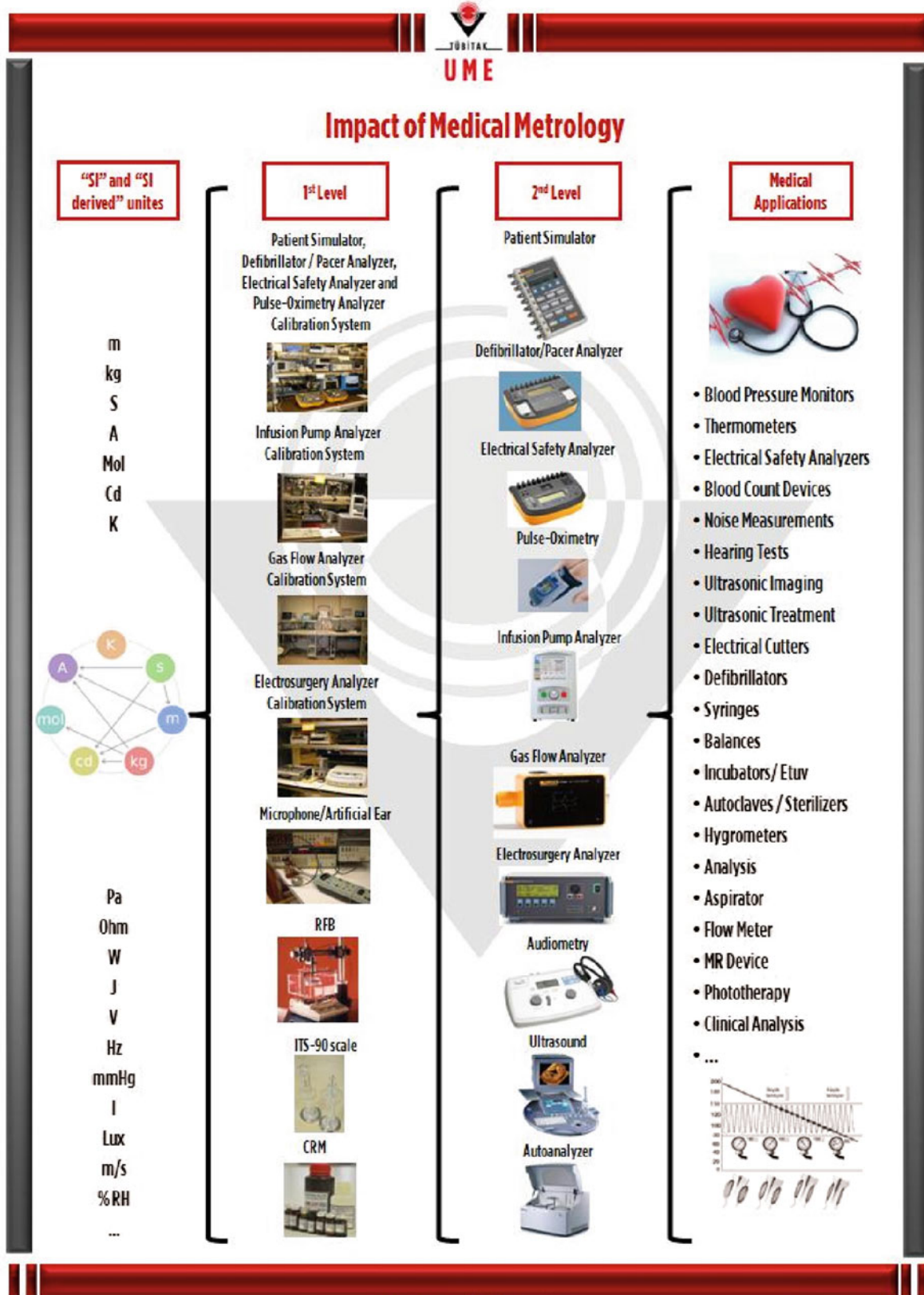


Fig. 5 Traceability chain in medical measurements

that does not have an accreditation certificate [20]. As you can see from the above information, they do their own calibrations, but the calibration should actually be done by independent third parties. When the situation is examined in terms of metrological traceability and reliability, it can be said that the calibration of the reference standards must be done by the accredited laboratories or the national metrology organization in the country.

Scheduled works in the field of medical metrology by National Metrology Institute (NMI) or Designated Institute (DI) can be listed as follows;

- Making preliminary study to ensure traceability in national and international standards for diagnostic and therapeutic devices which are serving in the field of health,
- Preliminary studies for the establishment of a measurement unity within the country for devices used in the health field,
- In the field of clinical metrology, investigation of required laboratory infrastructure for validation of measurement method used to verifying measurements, analyses and tests,
- In clinical metrology, planning for the production of reference materials used in chemical measurements,
- Creation of metrology awareness for universities, calibration laboratories and societies which are interested with this subject,
- Comparison and competence testing for the purpose of ensuring measurement unity between laboratories in the country.

Besides, training programs should be organized by the NMI and other organizations, universities and participation to these trainings should be encouraged.

Furthermore, most of the calibration companies do not have sufficient coverage in the accreditation certificate. Scope of certification of calibration companies must be carefully checked.

It has been stated that in the initial installation and licensing stages of ionizing radiation devices which are used in the health field, authorized agencies for ionizing radiation are taking part but later they don't do calibration and measurements. Safety of usage of medical device must be settled in order to avoid tomography, mammography, and X-ray devices produce higher doses from expected doses. Application of excess doses must be prevented in order to break kidney stones with few sessions in lithotripsy laboratories [21–23].

NMI must ensure the testing, control, verification and calibrations of medical devices in health institutes with reference standards. Calibrators, phantoms and reference

materials should be designed and manufactured in NMI. Trainings and workshops emphasizing the importance of medical device calibration should be organized.

In this article, the concept of medical metrology has been examined in detail. Medical metrology concept has been given in detail. Accuracy in medical measurements satisfies the more accurate diagnosis and treatment and less expenditure in health expenses. Even though metrology is an internationally linked activity, current situation shows that each NMI has some kind of studies in medical metrology field that are not harmonized between each other. International organizations (i.e. JCI [24], ECRI [25]) have individual guidelines for quality control of medical devices but don't directly aims to metrology traceability.

NMIs or DIs have to have a collaborative and multidisciplinary study in order to establish the traceability and equivalence of medical measurements in all over the world. Another important issue becomes to educate and train medical people who are engaged in use of medical devices and measurements.

References

1. Squara, P., Imhoff, M., Cecconi, M.: Metrology in medicine: from measurements to decision, with specific reference to anesthesia and intensive care. *Anesth. Analg.* **120**(1), 66–75 (2015). PMID 25625255
2. Tooker, J.: The importance of measuring quality and performance in healthcare. *MedGenMed.* **7**(2), 49 (2005). PMID 16369427
3. Zaitseva, E.: Importance measures in reliability analysis of healthcare system. In: *Human—Computer Systems Interaction: Backgrounds and Applications 2*. Part of the *Advances in Intelligent and Soft Computing* book series (AINSC), vol. 98. Springer International Publishing AG. Part of Springer Nature (2017)
4. Report: Medical Devices Industry And Market Prospects 2013-2023. Publication date 23/10/2013
5. Schreyögg, J., Bäuml, M., Busse, R.: Balancing adoption and affordability of medical devices in Europe. *Health Policy* **92**(2–3), 218–224 (2009). <https://doi.org/10.1016/j.healthpol.2009.03.016>
6. Zimmerman, M.: The importance of measuring outcomes in clinical practice. In: *US Psychiatric & Mental Health Congress 2014, Career, Major Depressive Disorder*, vol. 31, no. 10
7. National Institute of Standards and Technology, NIST. <http://www.nist.gov/medicaldevices-portal.cfm>
8. National Institute of Standards and Technology, NIST. http://www.nist.gov/el/isd/medical_devices.cfm
9. Semerjian, H.G., Watters, R.L.: Impact of measurement and standards infrastructure on the national economy and international trade. *Measurement* **27**, 179–196 (2000)
10. Ventola, C.L.: Challenges in evaluating and standardizing medical devices in health care facilities. *Pharm. Ther.* **33**(6), 348–359 (2008). PMID 19561797
11. Kiekens, K., Welkenhuyzen, F., Tan, Y., Bleys, P., Voet, A., Dewulf, W., Kruth, J-P.: A test object for calibration and accuracy assessment in X-Ray Ct metrology. In: *10th International Symposium on Measurement and Quality Control 2010*, 5–9 Sept

12. TÜBİTAK Ulusal Metroloji Enstitüsü, UME. <http://www.ume.tubitak.gov.tr/en/laboratuvarlarimiz/medical-metrology-laboratory>
13. Karaböce, B.: Metrological approach in medical measurements, National Metrology Institute of Turkey. In: 2nd International Conference on Medical Physics and Biophysics, Barcelona, Spain, 07–08 Nov 2016
14. Baura, G.D.: *Medical Device Technologies: A Systems Based Overview Using Engineering*, p. 512. Academic Press (2012)
15. Shirmohammadi, S., Barbé, K., Grimaldi, D., Rapuano, S., Grassini, S.: Instrumentation and measurement in medical, biomedical, and healthcare systems. *IEEE Instrum. Meas. Mag.* 6–12 (2016, October)
16. Bošnjaković, A., Džemić, Z.: Legal metrology: medical devices, CMBEBIH 2017 pp. 583–588. In: Badnjevic, A. (ed.) *CMBEBIH 2017, IFMBE Proceedings 62*. © Springer Nature Singapore Pte Ltd (2017). https://doi.org/10.1007/978-981-10-4166-2_88
17. Ferreira: The role of metrology in medical devices. Instituto Português da Qualidade, Portugal, OIML Bulletin Volume L II, Number 4 (2011, October)
18. Ferreira, M.: The role of metrology in the field of medical devices. *Int. J. Metrol. Qual. Eng.* 2(02), 135–140 (2011). <https://doi.org/10.1051/ijmqe/2011101>
19. Feldman, M.D., Petersen, A.J., Karliner, L.S., Tice, J.A.: Who is responsible for evaluating the safety and effectiveness of medical devices? The role of independent technology assessment. *J. Gen. Intern. Med.* 23(Suppl 1), 57–63 (2007)
20. Monteiro, E.C., Leon, L.F.: Metrological reliability of medical devices. *J. Phys. Conf. Ser.* 588, 012032 (2015)
21. Hermanek, P., Carmignato, S.: Establishment of metrological traceability in porosity measurements by X-ray computed tomography. In: *Conference: Developments in X-ray Tomography XI* (2017, September). <https://doi.org/10.1117/12.2276942>
22. Ainsley, C.G., Yeager, C.M.: Practical considerations in the calibration of CT scanners for proton therapy. *J. Appl. Clin. Med. Phys.* 15(3), 4721 (2014). <https://doi.org/10.1120/jacmp.v15i3.4721>. PMID 24892347
23. Villarraga-Gomez, H.: Understanding the metrology language for X-ray computed tomography. *Quality Magazine*, 17 Oct 2017
24. Joint Commission International—JCI. <https://www.jointcommissioninternational.org/>
25. Emergency Care Research Institute—ECRI. <https://www.ecri.org/Pages/default.aspx>

Part IX

Health Informatics, E-health and Telemedicine

Towards Pain-Fingerprinting: A Ubiquitous and Interoperable Clinical Decision Support System for Pain Assessment

Nuno Pombo and Nuno M. Garcia

Abstract

The subjectivity and the multidimensionality of pain raises several challenges in terms of its description, assessment and treatment. This study presents a Clinical Decision Support System for the pain condition based on the fusion of its different dimensions in order to produce an accurate and reliable assessment. The proposed system includes not only the value of the pain intensity but also several scores (e.g. regarding anxiety, or depression) obtained from the analysis of patients' behaviour related with the posted messages on social networks, such as Facebook, or Twitter. This study aims to introduce the paradigm for the pain assessment based on patients' behavioural scores to the detriment of its self-reporting of pain.

Keywords

Clinical decision support system • Pain assessment • Multidimensionality of pain • Pain intensity • Pain monitoring

1 Introduction

Pain is highly subjective and difficult to quantify because it is an individual and personal experience [1], which raises several challenges in terms of its description, assessment and treatment. In the last few years, computerized systems were increasingly developed to deliver clinical guidance related with the pain including education, reminders, feedback (in both directions between healthcare professionals and

patients), and disease control [2]. As pain is a multidimensional phenomenon [3–7] that can produce sensory, affective, and cognitive reactions that adversely affect the patients' emotional state, quality of life and well-being, congruently some of these systems also include scores and questionnaires to assess the pain on its different dimensions. From the clinical perception and knowledge perspective, the inclusion of additional information related with the several dimensions of pain rather than an isolated value (e.g. pain intensity) offers challenges and opportunities to enhance for example the data analysis, or the decision making [8]. However, from both health care professionals and patient perspective, this scenario may cause relevant constraints in terms of excessive information to collect, to analyse and process. On the one hand, this limitation may lead to incorrect and inaccurate analysis as a result of missing values in the collected data [9]. On the other hand, the exhaustive acquisition of data may be time consuming and troublesome. This study presents an innovative and disruptive system in which data are collected based on the patients' behaviour from daily life activities as opposite to the tedious and encyclopaedic approach based on a myriad of scores and questionnaires. The proposed system aims to provide an interoperable, ubiquitous, and patient-centred Clinical Decision Support System (CDSS) for pain assessment focused on the self-regulating principles for data acquisition, and analysis. The data collected on this system are based on the patients' behaviour related with the posted messages on social networks, such as Facebook, or Twitter. These applications have changed the profile of human interaction by enabling a faster and easier diffusion of the information, and by removing geographical and cost barriers.

The paper is organized as follows: this paragraph concludes Sect. 1; Sect. 2 includes the state of the art; Sect. 3 presents the proposed CDSS for pain assessment and Sect. 4 discusses the meaning and significance of the results, and concludes the paper proposing areas for continued research in this area.

N. Pombo (✉) · N. M. Garcia

Instituto de Telecomunicações, Universidade da Beira Interior,
Covilhã, Portugal
e-mail: ngpombo@di.ubi.pt

N. M. Garcia

Universidade Lusófona de Humanidades e Tecnologias, Lisbon,
Portugal

2 Background

The subjectivity of pain relies on physiological, neurological, and psychological aspects representing a multidimensional experience that raises several challenges to the acquisition of reliable data to support accurately the clinical decision making. As the self-report is considered the most accurate pain assessment method [10, 11], in which patients are asked to periodically rate their pain severity and related symptoms, then questionnaires and score are usually a privileged practice to collect data. The combination between the pain dimension, and questionnaires and scores on different CDSSs for pain assessment is shown in Table 1.

3 Proposed Approach

The proposed CDSS aims to reflect the multidimensional nature of pain. On the one hand, the monitoring system provides the pain intensity collected periodically using a mobile application [24]. On the other hand, the Online Cognitive Assessment Framework (OCAF) provides a score which is determined by combining all the messages posted on either Facebook, or Twitter. These messages are processed as follows: (1) an Application Programming Interface (API) obtains messages whose origin are the above mentioned social networks. (2) Then, using the Hidden Markov Model (HMM) the content of each message is segmented into words and expressions. (3) The next phase is related with the computed the distance, using the k-nearest neighbour (k-NN) algorithm [29], between the doublet word/phrases presented together in the message, and in the

expert-defined thesaurus. (4) Afterwards, the terminology score is adjusted through several dynamic thresholds. (5) Finally, this scaled value which represents the output of the OCAF is combined with the pain intensity collected using the monitoring app (Fig. 1).

The different modules that comprise the system are detailed below:

Message Acquisition: Aiming at to provide an interoperable service for the several healthcare stakeholders, including patients and HCP, this module is based on a web server that implements the APIs provided by Facebook, and Twitter in order to obtain, periodically, all the messages posted by the patient. Once collected, these messages, represented as a JSON file, are parser and inserted temporarily in a database for further analysis.

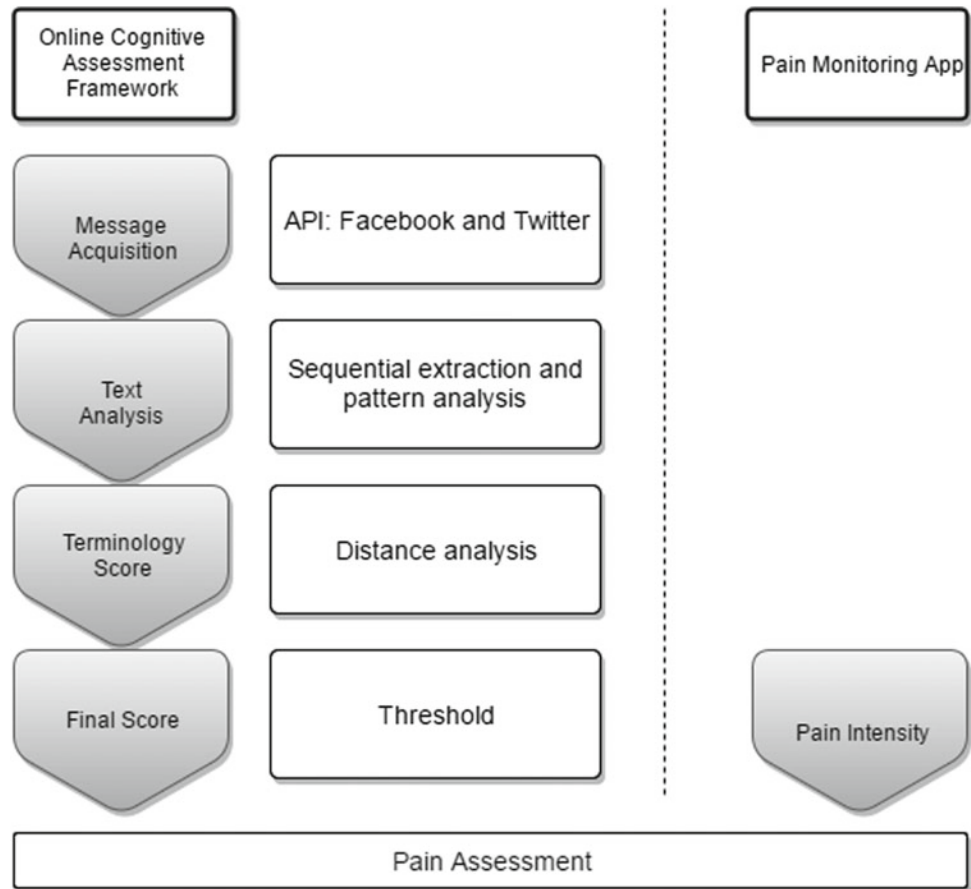
Text Analysis: This module aims to extract simple words, and expressions including abbreviations, and emoticons by means of an HMM which foundations are based on the conditional probability. Considerer two events A and B , the probability that A occurs given that B occurred is defined as:

$$P(A|B) = \frac{P(B|A) \cdot P(A)}{P(B)} \quad (1)$$

where, $P(B|A)$ is the probability that B occurs given that A occurred, $P(A)$ is the probability that A occurs, and $P(B)$ is the probability that B occurs. Thus, $P(A)$ means the prior probability, and $P(B|A)$ is the posterior probability. In line with this, since each event is considered as a variable which

Table 1 CDSSs for pain assessment its dimensions, questionnaires, and scores

Study/year	Pain dimension	Questionnaire and/or score
Axen [12, 13], 2011	Pain intensity	Numeric Rating Scale (NRS) [14]
Ljótsson [15], 2010	Anxiety	Visceral Sensitivity Index (VSI) [16]
	Depression	Montgomery Åsberg Depression Rating Scale-Self report (MADRS-S) [17]
	Disability	Sheehan Disability Scale (SDS) [18]
Marceau [19], 2010	Pain intensity	Brief Pain Inventory (BPI) [20]
	Catastrophizing	Pain Catastrophizing Scale (PCS) [21]
	Depression	Center for Epidemiological Studies Depression Scale (CES-D) [22]
	Disability	Oswestry Disability Index (ODI) [23]
Pombo [24], 2014	Pain intensity	NRS
Ruehlman [25], 2012	Anxiety, and depression	Depression Anxiety Stress Scale (DASS) [26]
	Catastrophizing	Profile of Chronic Pain Extended Assessment (PCP-EA) [27]
	Depression	CES-D
	Pain intensity, and interference	Profile of Chronic Pain: Screen (PCP-S) [28]

Fig. 1 The proposed architecture of the CDSS for pain assessment

exhibits a different state, then all the events may be mapped congruently with its casualities. This probabilistic causal network, constitutes a tool which combines graph theory with probability theory to represent relationships between variables (nodes in the graph) [30]. The joint probability distribution factorized as a product of several conditional distributions represents the dependency structure by a directed acyclic graph. Thus:

$$P(X_1, \dots, X_n) = \prod_{i=1}^n P(X_i | Pa(X_i^g)), \quad (2)$$

where, $Pa(X_i^g)$ are the parent nodes of X_i . In addition, the set of features may be considered as N observable states in which the set of arcs represents an observable sequence q_1, q_2, \dots, q_r . Thus, the probability distribution P may be considered as the probability of each state X whose element represents a transition probability matrix $T = (a_{ij})$ from state S_i to state S_j or $P(q_t = S_j | q_{t-1} = S_i)$ being q_t the state at time t . In simpler Markov models, the state is directly visible to the observer, and therefore the state transition probabilities are the only parameters. In a HMM, the state is not directly visible, but the output, dependent on the state, is visible.

Each state has a probability distribution over the possible output tokens. Hence, the probabilistic graphical model consisting of a set of observable (observations) and unobservable (states) random variables that describe the state of the modeled world at a particular time.

Terminology Score: This module aims to determine the similarity, e.g. distance, by comparing all the words and expressions with the content existing into the thesaurus. Each entry of the thesaurus is categorized in terms of pain dimension, such as anxiety, or depression, and is managed by experts (e.g. physicians) related with the phenomena of pain and its conditions. There are no restrictions for the content defined in the thesaurus, and therefore any dimension of pain may be included. The similarity is achieved using the k-NN, capitalizing its low-computation complexity for pattern recognition and its intuitive concept in which every data points of the same class should be closer in the feature space.

Given n training data defined by:

$$\{(x_1, y_1), \dots, (x_n, y_n)\} \quad (3)$$

where (x_i, y_i) represent data pair i for which x_i is the feature vector and y_i the corresponding target class. Thus, for a given data point x , the target class is determined as:

$$y_p = 1 - NN(x), \quad (4)$$

where:

$$p = \arg \min_i |x - x_i|^2. \quad (5)$$

Final Score: At last, the terminology score is adjusted in accordance with several defined thresholds. As occurs with the composition of the thesaurus, an expert is asked to determine different levels aiming at to reproduce a typical Likert-scale.

Pain Assessment: The obtained score is then combined with the pain intensity value provided by the mobile app aiming to provide a composed metric by the pair score-intensity and thus to capacity the CDSS for a composite analysis on pain.

4 Discussion and Conclusions

A timely, accurate and aggregated perspective of pain are prominent and challenging requirements on the design of CDSS for pain assessment. On the one hand, pain is highly subjectivity for each individual which may results in different and/or arbitrary self-assessment for equivalent clinical conditions. On the other hand, as pain is a multidimensional phenomenon it requires a multidisciplinary approach in order to fuse a variety of data with different meanings and granularities.

The proposed CDSS aims to combine, in a single solution, several dimensions of pain and use every dimensional score to enhance the overall metric, and therefore to promote a refined perception and assessment of pain. Towards this purpose, the presented system uses the knowledge of experts to design the thesaurus, composed with words and expressions related with each dimension of pain, and to define multiple thresholds. These activities are critical not only to assure the accuracy of the CDSS but also to enhance its ability to manage with multiple dimensions of pain, and therefore, to improve its adaptability and suitability for the decision making on different healthcare settings and scenarios. The main concept behind the presented study is to introduce CDSS for pain assessment based on behavioural scores to the detriment of self-report scores.

Finally, the roadmap for new versions of the CDSS includes complementary studies to address new algorithms for image processing in order to obtain a complementary textual description on the posted messages. Furthermore, this

feature may enable the inclusion of social networks focused on sharing images, such as Instagram.

Acknowledgements This work was supported by FCT project UID/EEA/50008/2013 (*Este trabalho foi suportado pelo projecto FCT UID/EEA/50008/2013*).

This article is based upon work from COST Action IC1303—AAPELE—Architectures, Algorithms and Protocols for Enhanced Living Environments and COST Action CA16226—SHELD-ON—Indoor living space improvement: Smart Habitat for the Elderly, supported by COST (European Cooperation in Science and Technology). More information in www.cost.eu.

Conflict of Interest Statement No conflicts of interest.

References

- Giordano, J., Abramson, K., Boswell, M.V.: Pain assessment: subjectivity, objectivity, and the use of neurotechnology. *Pain Physician* **13**, 305–315 (2010)
- Pombo, N., Garcia, N., Bousson, K., Spinsante, S., Chorbev, I.: Pain assessment—can it be done with a computerised system? A systematic review and meta-analysis. *Int. J. Environ. Res. Public Health* **13**, 415 (2016). <https://doi.org/10.3390/ijerph13040415>
- Ong, K.S., Seymour, R.A.: Pain measurement in humans. *Surgeon* **2**, 15–27 (2004)
- Melzack, R., Casey, K.L.: Sensory, motivational, and central control determinants of pain: a new conceptual model. In: *The Skin Senses*, pp. 423–443 (1968)
- Fernandez, E., Turk, D.C.: Sensory and affective components of pain: separation and synthesis. *Psychol. Bull.* **112**, 205–217 (1992)
- Holroyd, K.A., Talbot, F., Holm, J.E., Pingel, J.D., Lake, A.E., Saper, J.R.: Assessing the dimensions of pain: a multitrait-multimethod evaluation of seven measures. *Pain* **67**, 259–265 (1996)
- Kornbluth, I.D., Freedman, M.K., Holding, M.Y., Overton, E.A., Saulino, M.F.: Interventions in chronic pain management. 4. Monitoring progress and compliance in chronic pain management. *Arch. Phys. Med. Rehabil.* **89**, S51–S55 (2008)
- Pombo, N., Araújo, P., Viana, J.: Knowledge discovery in clinical decision support systems for pain management: a systematic review. *Artif. Intell. Med.* **60**, 1–11 (2014). <https://doi.org/10.1016/j.artmed.2013.11.005>
- Pombo, N., Rebelo, P., Araújo, P., Viana, J.: Combining data imputation and statistics to design a clinical decision support system for post-operative pain monitoring. *Procedia Comput. Sci.* **64**, 1018–1025 (2015). <https://doi.org/10.1016/j.procs.2015.08.621>
- Nekolaichuk, C.L., Bruera, E., Spachynski, K., MacEachern, T., Hanson, J., Maguire, T.O.: A comparison of patient and proxy symptom assessments in advanced cancer patients. *Palliat. Med.* **13**, 311–323 (1999). <https://doi.org/10.1191/026921699675854885>
- Pautex, S., Berger, A., Chatelain, C., Herrmann, F., Zulian, G.B.: Symptom assessment in elderly cancer patients receiving palliative care. *Crit. Rev. Oncol./Hematol.* **47**, 281–286 (2003)
- Axén, I., Bodin, L., Bergström, G., Halasz, L., Lange, F., Lövgren, P., et al.: Clustering patients on the basis of their individual course of low back pain over a six month period. *BMC Musculoskelet. Disord.* **12**, 99 (2011). <https://doi.org/10.1186/1471-2474-12-99>
- Axén, I., Bodin, L., Bergström, G., Halasz, L., Lange, F., Lövgren, P.W., et al.: The use of weekly text messaging over 6 months was

- a feasible method for monitoring the clinical course of low back pain in patients seeking chiropractic care. *J. Clin. Epidemiol.* **65**, 454–461 (2012). <https://doi.org/10.1016/j.jclinepi.2011.07.012>
14. Johnson, C.: Measuring pain. Visual analog scale versus numeric pain scale: what is the difference? *J. Chiropr. Med.* **4**, 43–44 (2005). [https://doi.org/10.1016/s0899-3467\(07\)60112-8](https://doi.org/10.1016/s0899-3467(07)60112-8)
 15. Ljótsson, B., Falk, L., Vesterlund, A.W., Hedman, E., Lindfors, P., Rück, C., et al.: Internet-delivered exposure and mindfulness based therapy for irritable bowel syndrome—a randomized controlled trial. *Behav. Res. Ther.* **48**, 531–539 (2010). <https://doi.org/10.1016/j.brat.2010.03.003>
 16. Labus, J.S., Bolus, R., Chang, L., Wiklund, I., Naesdal, J., Mayer, E.A., et al.: The Visceral Sensitivity Index: development and validation of a gastrointestinal symptom-specific anxiety scale. *Aliment. Pharmacol. Ther.* **20**, 89–97 (2004). <https://doi.org/10.1111/j.1365-2036.2004.02007.x>
 17. Svanborg, P., Asberg, M.: A new self-rating scale for depression and anxiety states based on the Comprehensive Psychopathological Rating Scale. *Acta Psychiatr. Scand.* **89**, 21–28 (1994)
 18. Sheehan, K.H., Sheehan, D.V.: Assessing treatment effects in clinical trials with the discan metric of the Sheehan Disability Scale. *Int. Clin. Psychopharmacol.* **23**, 70–83 (2008)
 19. Marceau, L.D., Link, C.L., Smith, L.D., Carolan, S.J., Jamison, R. N.: In-clinic use of electronic pain diaries: barriers of implementation among pain physicians. *J. Pain Symptom Manage.* **40**, 391–404 (2010). <https://doi.org/10.1016/j.jpainsymman.2009.12.021>
 20. Cleeland, C.S., Ryan, K.M.: Pain assessment: global use of the Brief Pain Inventory. *Ann. Acad. Med. Singapore* **23**, 129–138 (1994)
 21. Crombez, G., Bijttebier, P., Eccleston, C., Mascagni, T., Mertens, G., Goubert, L., et al.: The child version of the pain catastrophizing scale (PCS-C): a preliminary validation. *Pain* **104**, 639–646 (2003). [https://doi.org/10.1016/S0304-3959\(03\)00121-0](https://doi.org/10.1016/S0304-3959(03)00121-0)
 22. Radloff, L.S.: The CES-D Scale. *Appl. Psychol. Meas.* **1**, 385–401 (1977). <https://doi.org/10.1177/014662167700100306>
 23. Fairbank, J.C., Pynsent, P.B.: The Oswestry Disability Index. *Spine* **25**, 2940–2952 (2000)
 24. Pombo, N., Araújo, P., Viana, J., da Costa, M.D.: Evaluation of a ubiquitous and interoperable computerised system for remote monitoring of ambulatory post-operative pain: a randomised controlled trial. *Technol. Health Care* **22**, 63–75 (2014). <https://doi.org/10.3233/THC-130774>
 25. Ruhlman, L.S., Karoly, P., Enders, C.: A randomized controlled evaluation of an online chronic pain self management program. *Pain* **153**, 319–330 (2012). <https://doi.org/10.1016/j.pain.2011.10.025>
 26. Crawford, J.R., Henry, J.D.: The Depression Anxiety Stress Scales (DASS): normative data and latent structure in a large non-clinical sample. *Br. J. Clin. Psychol.* **42**, 111–131 (2003)
 27. Ruhlman, L.S., Karoly, P., Newton, C., Aiken, L.S.: The development and preliminary validation of the profile of chronic pain: extended assessment battery. *Pain* **118**, 380–389 (2005). <https://doi.org/10.1016/j.pain.2005.09.001>
 28. Ruhlman, L.S., Karoly, P., Newton, C., Aiken, L.S.: The development and preliminary validation of a brief measure of chronic pain impact for use in the general population. *Pain* **113**, 82–90 (2005). <https://doi.org/10.1016/j.pain.2004.09.037>
 29. Dudani, S.A.: The distance-weighted k-nearest-neighbor rule. *IEEE Trans. Syst. Man Cybern.* **SMC-6**, 325–327 (1976). <https://doi.org/10.1109/tsmc.1976.5408784>
 30. Larrañaga, P., Moral, S.: Probabilistic graphical models in artificial intelligence. *Appl. Soft Comput.* **11**, 1511–1528 (2011). <https://doi.org/10.1016/j.asoc.2008.01.003>

Identification of Alcohol Addicts Among High School Students Using Decision Tree Based Algorithm

Rijad Sarić, Dejan Jokić, and Edhem Čustović

Abstract

The paper aims to apply a decision tree based machine learning algorithm to predict possible alcohol addicts among high school students. The data mining process is performed on the real-world data collected in two high schools in Portugal. The dataset is originally designed for the estimation of high school student's performance where alcohol consumption is used as one of the parameters. In the implementation phase, KNIME analytics platform is applied to test the model. The significant part represents preprocessing of data where the new attributes are derived including class attribute labeled using alcohol addict matrix. Afterwards, the linear correlation is used to reduce the number of features. Data processing consists of dividing the dataset into training and test data, making artificial data for training phase and lastly analyzing the outputs of decision tree learner and predictor. Constructed decision tree determines the connections between certain attributes and student alcohol consumption. Finally, the overall accuracy of the model is measured using a confusion matrix.

Keywords

Machine learning • KNIME • Linear correlation • C4.5 decision tree algorithm

1 Introduction

Evidently, high-level of alcohol consumption has a serious effect on human body and mind for centuries. A large number of extensive medical investigations are discovered that alcohol may have more complex influence on health than e.g. smoking and physical inactivity. Moreover, alcohol as an organic solvent in high doses could seriously harm a large number of organs in the human body and in a longer period of time, such lifestyle increases the risk of developing alcohol addiction [1]. However, consuming alcohol in teenage when the brain is still developing represents the most dangerous situation since it affects adolescent mental as well as physical abilities. The negative effects of alcohol intake during this life phase are reflected in affecting many vital brain functionalities such as memory, learning abilities, reasoning, reactions, attention span and motivation. Various medical statistics related to the mentioned problem are shown that children who start drinking alcohol at age of thirteen would have poor school performance including deliberately skipping certain classes which in the worst-case scenario may lead to school exclusion. Also, consumers could become aggressive and violent having less self-control causing possible involvement in criminal acts or driving under alcohol [2, 3].

According to [4], alcohol dependence is more likely to be developed in case of young people who start drinking before age of fifteen than persons at older ages. Interestingly, the parents or siblings could influence child to start drinking. As research in [5] discovers that if at least one of the parents has got a history of alcoholism then there is a high probability that son or daughter is going to drink alcohol imitating the home alcohol-related behavior. Additionally, adolescents often choose peer groups whose behavior is very popular in society. Thus, if drinking alcohol symbolizes typical behavior and value within a peer group, it implies that every new member must satisfy that behavior in order to be accepted by the group.

R. Sarić (✉) · D. Jokić
Faculty of Engineering and Natural Sciences, International Burch
University, IBU, Ilidža, Bosnia and Herzegovina
e-mail: rijad.saric@stu.ibu.edu.ba

D. Jokić
e-mail: dejan.jokic@ibu.edu.ba

E. Čustović
School of Engineering and Mathematical Sciences, La Trobe
University, LTU, Melbourne, Australia
e-mail: e.custovic@latrobe.edu.au

In this paper, we applied a machine learning algorithm on the data about students from two Portuguese high schools to predict the possibility of becoming alcoholic as teenager. In essence, the decision tree algorithm is used for training the model for classifying alcohol addicts. The overall prediction process is conducted referring to the student alcohol consumption class which may be positive (P) or negative (N).

2 Background

According to [6, 7] during the last few decades level of education in Portugal has a significant increase due to the large EU Government investments towards educational systems. However, extensive statistical analysis of education in Portugal revealed high-level of student failures and school exclusion rates. In general, the largest number of high school students' failures was recorded in the core classes of mathematics and the native Portuguese language. Unsatisfactory grades in stated high school subjects could cause serious consequences since they also affect the fundamental knowledge of other subjects e.g. physics, chemistry, history or geography. The primary and secondary school education in Portugal consists of 12 years of mandatory schooling. Hence, it includes 9 years of primary education followed by 3 years of higher education. Furthermore, the grading system in Portugal is based on a 20-point grading scale, where zero represents the unsatisfactory grade, whereas twenty is an excellent score. The evaluation of student performance in a school year is split into three periods, and last evaluation concludes the final grade. The major goal of the conducted research in Portugal was to collect a significant amount of real-world data and estimate the key factors related to high-school student's poor performance in the core classes such as mathematics and Portuguese language.

Data collection was conducted by P. Cortez and A. Silva, University of Minho, in two secondary public schools, in the Alentejo region of Portugal. In order to create a reliable high school student database, the school reports including paper sheets with several attributes i.e. the final-period grade (G3) together with absences were used to complement gathered information. Besides, authors design a survey that consists of demographic, social, emotional and school-related questions. Two important questions were workday and weekend alcohol consumption. The traditional data collection was performed because most of the Portuguese schools' information systems rely on paper sheets despite the Government investments to ensure digital data manipulation. Eventually, after establishing the final version of the survey, the data were integrated into two datasets associated with mathematics (395 records) and

Portuguese language (649 records) subjects as in [7]. While analyzing the data some of the attributes were discarded due to incompleteness e.g. family income since only a few participants provided full answer regarding their family income, probably because of privacy issues. Therefore, the final number of attributes was thirty-three. In Table 1, the explanation of each dataset attribute is represented.

3 Data Preprocessing

Data pre-processing phase is necessary due to the noisy, incomplete, outlier and unreliable data. This process may be routine but also time-consuming. In general, it is estimated that data preparation accounts for 60–80% of the time spent on the machine learning process [8]. In this paper, KNIME [9] (Konstanz Information Miner) open-source platform for data processing, integration, analysis, exploration and application of different machine learning algorithms is used. This software provides a graphical representation of each data mining step together with knowledge discovery. KNIME is based on building workflows composed of data processing nodes. Each node has certain role and data are transferred using interconnections between nodes. Firstly, the dataset is imported and stored in internal tables. After that these tables are forwarded to other nodes responsible for data cleaning including dealing with missing values, creating derived attributes, removing outliers, partitioning tables into training and test data, etc. [10]. Finally, the predictive model with specific machine learning algorithm in our case C4.5 decision tree (ID3-extension) is used to correctly classify the data. The deep analysis of final outputs is available using view node or accuracy table.

Data pre-processing workflow in this case (see Fig. 1) begins with two file readers to separately import raw high school students' datasets. Then, numeric binning or precisely data discretization is simultaneously performed. Additionally, the rule engine node is utilized to create a new additional attribute named "Majorsub" which helps in categorizing students based on their core subject math or Portuguese language. Two attributes that represent weekend and workday alcohol consumptions are integrated into one attribute named "alco" using the alcohol addiction matrix. Afterwards, two datasets are merged into one (1044 data records) and all numeric values are converted into strings since the classification may provide better results dealing strictly with string values. In the end, the linear correlation is applied to find which data instances could be discarded before the data mining process using a correlation filter that requires the particular threshold value.

Table 1 The detailed description of attributes available in the dataset

Attribute	Description (domain)
Gender	Student's gender (binary: female or male)
Age	Student's age (numeric: from 15 to 22)
School	Student's school (binary: Gabriel Pereira or Mousinho da Silveira)
Address	Student's home address type (binary: urban or rural)
Pstatus	Parent's cohabitation status (binary: living together or apart)
Medu	Mother's education (numeric: from 0 to 4 ^a)
Mjob	Mother's job (nominal ^b)
Fedu	Father's education (numeric: from 0 to 4 ^a)
Fjob	Father's job (nominal ^b)
Guardian	Student's guardian (nominal: mother, father or other)
Famsize	Family size (binary: ≤ 3 or >3)
Famrel	Quality of family relationships (numeric: from 1 very bad to 5 excellent)
Reason	Reason to choose this school (nominal: close to home, school reputation, course preference or other)
Traveltime	Home to school travel time (numeric: 1 <15 min, 2 15–30 min, 3 30 min–1 h or 4 >1 h)
Studytime	Weekly study time (numeric: 1 <2 h, 2 2–5 h, 3 5–10 h or 4 >10 h)
Failures	Number of past class failures (numeric: n if $1 \leq n < 3$, else 4)
Schoolsup	Extra educational school support (binary: yes or no)
Famsup	Family educational support (binary: yes or no)
Activities	Extra-curricular activities (binary: yes or no)
Paidclass	Extra paid classes (binary: yes or no)
Internet	Internet access at home (binary: yes or no)
Nursery	Attended nursery school (binary: yes or no)
Higher	Wants to take higher education (binary: yes or no)
Romantic	With a romantic relationship (binary: yes or no)
Freetime	Free time after school (numeric: from 1 very low to 5 very high)
Goout	Going out with friends (numeric: from 1 very low to 5 very high)
Walc	Weekend alcohol consumption (numeric: from 1 very low to 5 very high)
Dalc	Workday alcohol consumption (numeric: from 1 very low to 5 very high)
Health	Current health status (numeric: from 1 very bad to 5 very good)
Absences	Number of school absences (numeric: from 0 to 93)
G1	First period grade (numeric: from 0 to 20)
G2	Second period grade (numeric: from 0 to 20)
G3	Final grade (numeric: from 0 to 20)

^a0 none, 1 primary education (4th grade), 2 5th to 9th grade, 3 secondary education or 4 higher education

^bTeacher, health care related, civil services (e.g. administrative or police), at home or other

3.1 Data Formation

The data discretization is performed on attributes age, absences, G1, G2, and G3 using KNIME numeric binner node specifying the number of intervals also known as bins for each column. The secondary education in Portugal is three years, so each student should graduate at the age of 17. However, our dataset contains student age values 15, 16, 17 and older. For the attribute age, 4 bins are defined as follows

10th, 11th, 12th, and older student for every student who is older than 17 (see Fig. 2a). Next, the 5 bins for the attribute absences are defined as no warning, e-mail warning, parent contact, last warning before exclusion and exclusion using specific ranges (see Fig. 2b). The last discretization is done on the grade attributes G1, G2 and G3 as the poor, week, sufficient, very good, and excellent (see Fig. 2c).

The Portugal high school students' dataset contains two attributes regarding alcohol intake and those are weekend

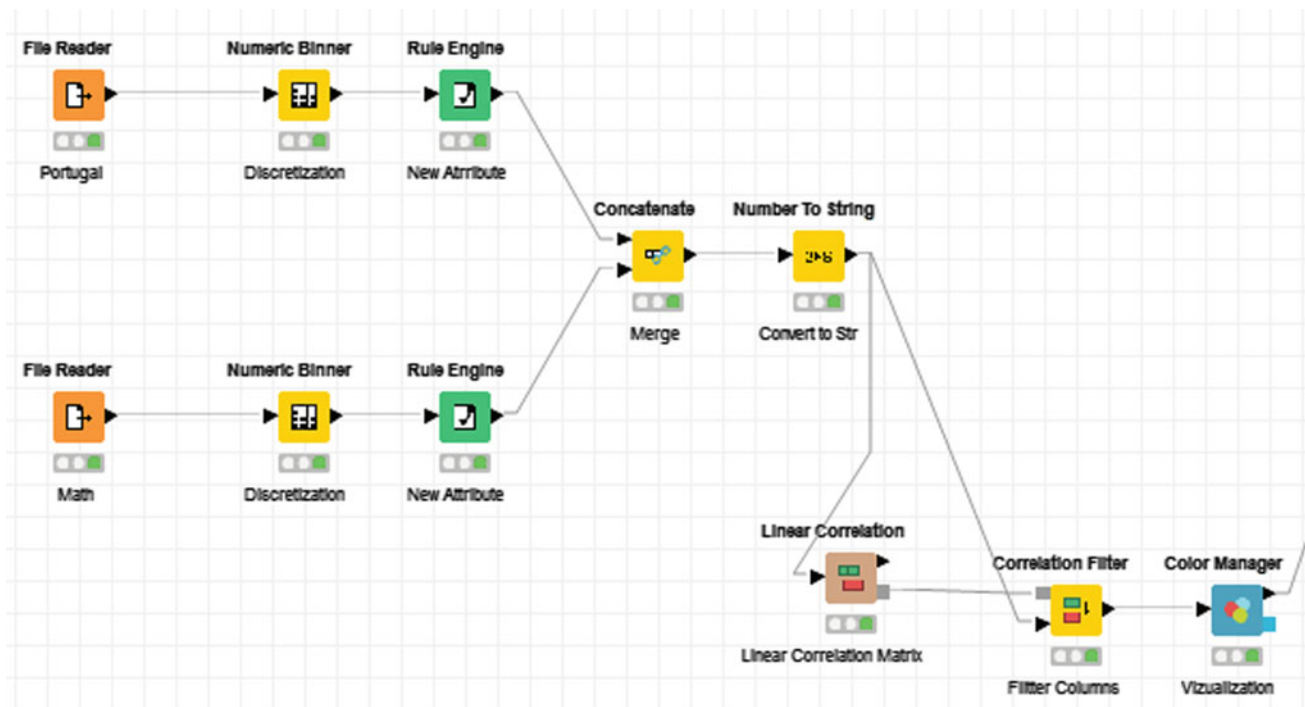


Fig. 1 The KNIME data-preprocessing workflow

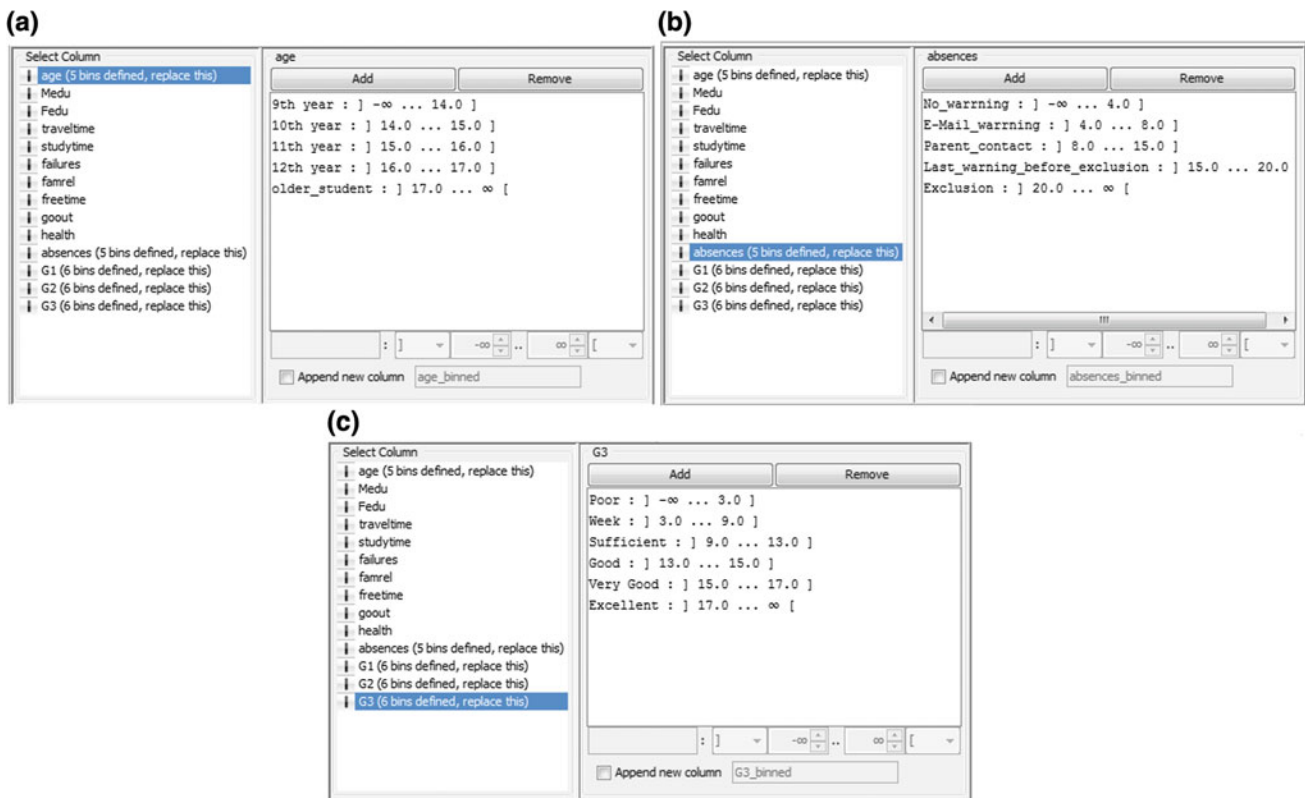


Fig. 2 The discretization of values for certain attributes presented in the dataset

Table 2 The matrix for a creating class attribute to label possible alcohol addicts

		Weekend				
		Very low	Low	Medium	High	Very high
Workday	Very low	N	N	N	N	N
	Low	N	N	N	N	P
	Medium	N	N	N	N	P
	High	N	N	P	P	P
	Very high	P	P	P	P	P

(Walc) and workday (Dalc) alcohol consumption. Consequently, a new attribute named “alco” related to alcohol drinking among high school students is derived and used as a class or target variable during the classification process. The new attribute is created according to an alcohol addict matrix considering values in both rows and columns. Hence, rows in the matrix represent workday alcohol consumption values, whereas columns stand for weekday alcohol consumption (see Table 2). For example, if workday alcohol consumption is low and weekday very high then a person is marked as possible alcohol addict including category positive (P). In contrast, if workday alcohol consumption is high and the weekend low a person is marked as non-alcohol addict with category negative (N). Thus, it is necessary to go over each data record available in the dataset to assign appropriate values based on the created matrix.

3.2 Linear Correlation

According to [11] linear correlation indicates the measurement between two random variables with the property of being bounded between -1 and 1. This property allows easily observing the linear dependence between two random variables. The linear correlation of two random variables x and y is given by the equation

$$\text{Corr}[X, Y] = \frac{\text{Cov}[X, Y]}{\text{stdev}[X]\text{stdev}[Y]} \tag{1}$$

where $\text{Cov}[X, Y]$ represents covariance between X and Y , and $\text{stdev}[X]$ or $\text{stdev}[Y]$ refers to the standard deviation of two random variables. Moreover, if $\text{Corr}[X, Y] < 0$ then X and Y are said to be negatively correlated. If $\text{Corr}[X, Y] \neq 0$ then X and Y are said to be linearly correlated. Finally, if $\text{Corr}[X, Y] = 0$ then X and Y are said to be uncorrelated.

KNIME linear correlation node calculates the linear correlation coefficient between two random variables. The correlation between the new (derived) attribute “alco” and all other attributes is particularly interesting to accomplish the main goal of successfully classifying possible alcohol addicts. Hence, the better insight would be provided by correlation matrix (see Fig. 3) where the entire linear

correlation distribution is illustrated. After, observing the linear correlation results between all attributes in the correlation matrix, the correlation filter is used to observe which columns could be eliminated before the next phase. KNIME correlation filter node determines which columns are redundant i.e. correlated and filters them out. After several attempts, the best threshold value for the correlation coefficient is determined as 0.404 suggesting that columns G1 and G2 should be eliminated for the further analysis. The stated suggestion is accepted since the attribute G3 (final grade) is enough to consider overall student performance during the school year as per Fig. 3. Thus, for the data mining phase, 31 out of 33 columns are selected. At the end of the data pre-processing phase, the node color manager is utilized to color two values of the class variable (P—blue, N—red). Certainly, this would help get a better visualization of classification result in decision tree root as well as leaf nodes.

4 Results and Discussion

After successful pre-processing of the data, the next phase represents trying different machine learning algorithms to obtain a meaningful and accurate prediction of alcohol addicts. In this paper, a decision trees machine learning algorithm is applied to classify the data. As [12] suggests the decision trees based algorithms are used for both classification and regression and they usually imitate the human level of reasoning, henceforth the data may be easily understood. In addition, the decision tree is composed of nodes which mark the attributes, branches that state the decision or rule and finally the outcomes denoted by leaves with categorical or continuous values.

The second part of the KNIME workflow starts with x-partitioner node intended to split the entire dataset into training and test. The dataset is commonly divided as 75% for model training and 25% for testing. Commonly, the training process should be performed on the majority of the data. However, the pre-processed dataset contains only 1044 data instances and henceforth SMOTE (Synthetic Minority Over-Sampling Technique) node is applied which over-samples the input data i.e. adding artificial rows in order to

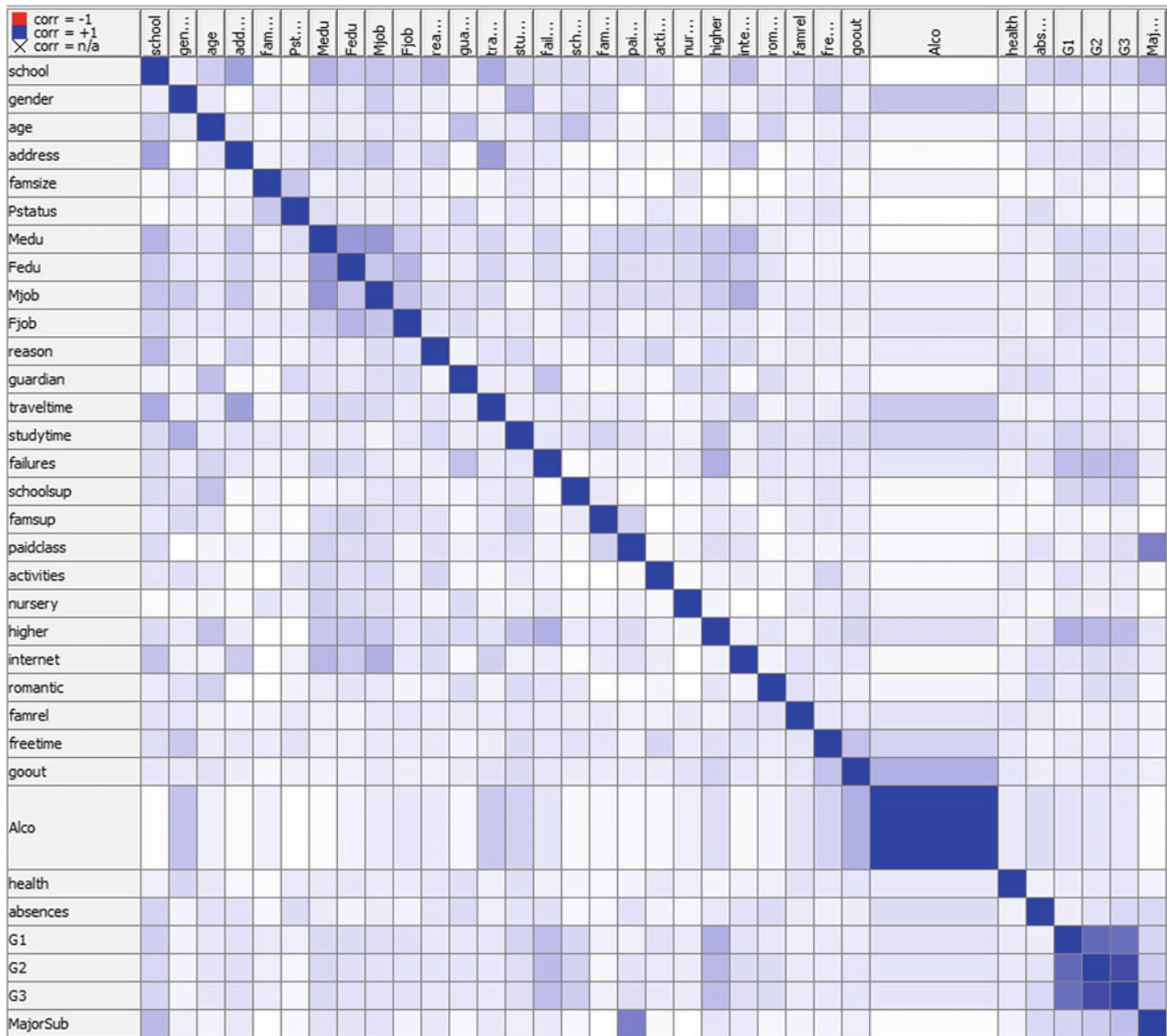


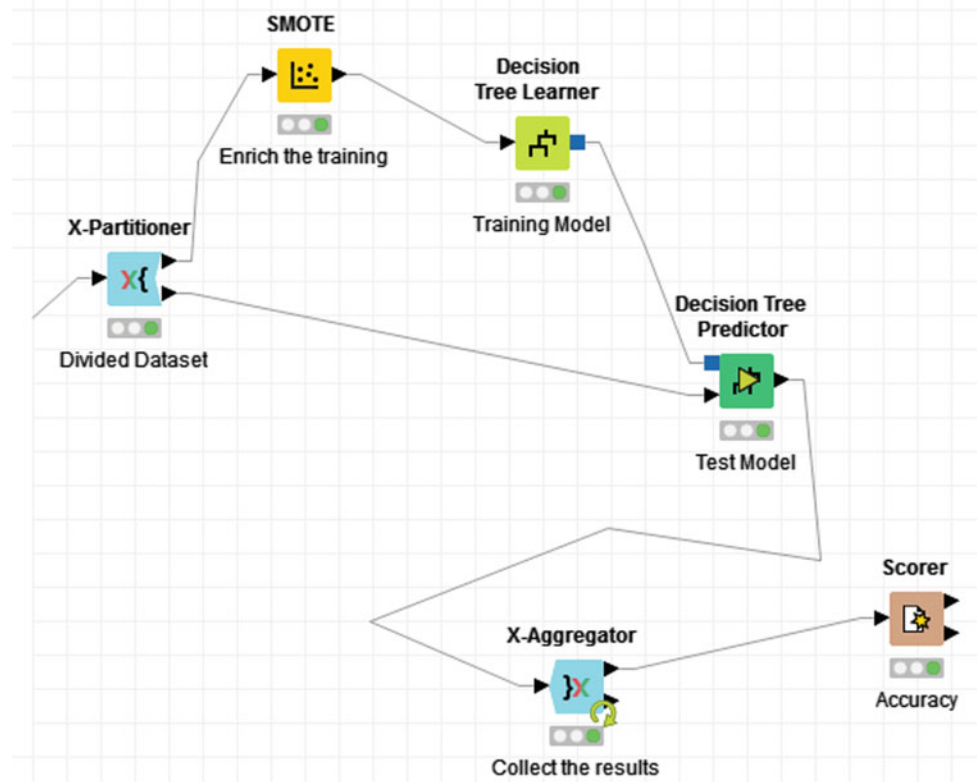
Fig. 3 Linear correlation matrix where the correlation between the main attribute alco and all other attributes is highlighted

enrich training data (see Fig. 4). Next, the decision tree learner node is added to train a model where the target attribute must be nominal. After that, the decision tree predictor node passes the test data through the decision tree model and predicts the class values in the new column named “alco_addict”. Lastly, the node x-aggregator is connected to collect the classification results from predictor comparing predicted and real classes. The overall accuracy of the model is measured using scorer node which provides a confusion matrix that represents correct as well as incorrect classification of the data as illustrated in Fig. 4.

4.1 Decision Tree Configuration

Decision tree learner node in KNIME is implemented mostly referring to the C4.5 packages for machine learning. C4.5 is actually an extension of Quinlan’s ID3 (Iterative Dichotomiser 3) and it is often used as statistical classifier [13]. KNIME decision tree predictor uses SPRINT classification algorithm that removes all of the memory restrictions. The algorithm is designed to allow many processes to execute at the same time to build a single consistent model. The most significant improvement of the algorithm represents the high level of parallelization [14].

Fig. 4 The data mining phase using KNIME workflow



Firstly, the parameters of the decision tree learner have to be configured in order to obtain appropriate results. The first parameter is the “class attribute” which must have nominal values. Then, the Gini index is selected for the quality measure as in the following equation

$$Gini = \sum_{i \neq j} p(i)p(j) \tag{2}$$

To increase the prediction quality and reduce the tree size the pruning method is utilized. This method proves to be an excellent choice since it avoids overfitting and boosts the general performance of the decision tree model. Next for the decision tree predictor node the new column is created named “alco_addict” which would have the predicted values with two possible categories P or N. The first version of the decision tree is not too deep but extremely wide, therefore reduce error pruning is deployed to obtain simplified version of the decision tree containing “goout” attribute as a root (see Fig. 5). Finally, the overall accuracy of the model equals approximately 93% referring to the confusion matrix with only 72 wrong classifiers (see Fig. 6).

Reduce error pruning technique helps in building a decision tree by not including all of the attributes available in the database. Analysis and testing the simplified version of the training decision tree reveals that the root attribute “goout”

has the highest impact on students’ alcohol consumption. As the values of attribute “goout” increase the number of alcohol addicts among high school students becomes greater. When “goout” reaches the value five, the tree has two branches male and female including root gender. As it is expected, there are a higher number of male alcohol addicts than female. The algorithm also classifies the alcohol addicts upon the health status of the high school student indicating that he or she with very good health are common alcohol consumers. Lastly, the algorithm marked some students who attend nursery school as possible alcohol addicts having normal health as well. Therefore, it is evident that “goout” is the key attribute that influences the lifestyle together with alcohol intake of high school students in Portugal.

Although no large number of investigations related to the prediction of possible alcohol addicts is published to date, some significant machine learning techniques are applied to the dataset in [7]. For instance, Palaniappan et al. [15] utilized the same dataset to predict alcohol consumption among high school students. The classification process is accomplished applying feed-forward Artificial Neural Network (ANN) using standard multilayer perceptron (MLP) and self-tuning MLP classifier (AutoMLP). Overall accuracy provided by AutoMLP equals 65%, whereas the ANN yields nearly 62% classification accuracy. Such low accuracy may be a

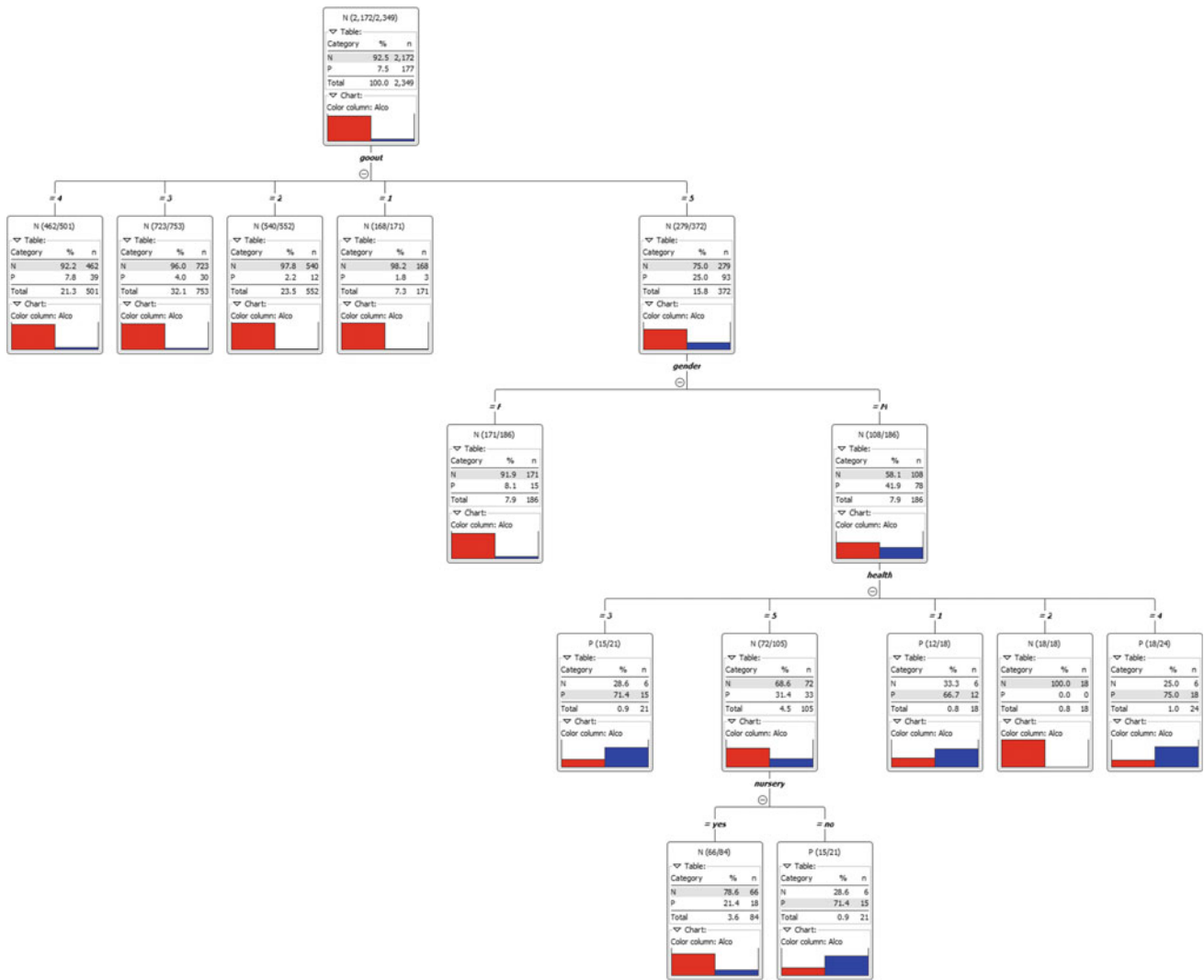


Fig. 5 Simplified decision tree training model for passing each data record through and validate the model accuracy

Alco \ Alco_addict	N	P
N	949	16
P	56	23

Correct classified: 972 Wrong classified: 72
 Accuracy: 93.103 % Error: 6.897 %
 Cohen's kappa (κ) 0.358

Fig. 6 KNIME confusion matrix for measure the accuracy of the entire classification model

consequence of inappropriate dataset purpose since it is primarily created to estimate student performance during a school year. However, the research conducted by Pagnotta and Amran [16] applied random forest algorithm by reducing the dataset to 14 features significant for prediction of alcohol

addicts among high school students. On the contrary, as a part of this paper, the C4.5 decision tree algorithm with a larger number of attributes succeeds to obtain a classification model of high accuracy. Besides, Afzali et al. [17] examine the outputs of seven machine learning algorithms using Australian and Canadian mid-adolescent data samples in order to predict different levels of alcohol consumption. The best predictive performance is achieved using elastic-net regularization which actually builds a model using a subset of predictors. In this study, the highest accuracy of alcoholic substance intake is obtained considering only psychopathology and personality clusters. Also, the prediction accuracy of elastic-net is evaluated and grouped as ever, monthly, weekly, and daily alcohol consumption. Based on everything that is presented above, it can be seen that systems like this could be useful for prevention and education of targeted groups and addition to systems developed for health practices [18–20].

5 Conclusion

In summary, it is clear that the adequate application of machine learning could reduce the alcohol addiction rate among teenagers and improve their lifestyle. Currently, several different types of research show how machine learning helps in selection of important features related to alcohol addiction issue. This research could be easily expanded using larger dataset related to this problem combining indicative features connected to alcohol intake. In this case, a large amount of data would help to make conclusions whether certain features affect the life of high school student to start with overdose alcohol use.

Statement of Conflicts of Interest and Informed Consent The authors whose names are listed on the title page of this paper declare that they have no conflict of interest.

References

- Grønbaek, M.: The positive and negative health effects of alcohol and the public health implications. *J. Int. Med.* **26**, 407–420 (2009)
- Moti, I.: Teenage drinking and the role of parents and guardians. *Drinkware Monitor*. [Online]. Available: <https://www.drinkaware.co.uk/media/1764/drinkaware-monitor-report-2016.pdf> (2016)
- Sindelar, H.A., et al.: Adolescent alcohol use and injury: a summary and critical review of the literature (2004)
- Beaglehole, R., Jackson, R.: Alcohol, cardiovascular diseases and all causes of death: a review of the epidemiologic evidence. *Drug Alcohol Rev.* **11**, 290 (1992)
- Marshall, E.J.: Adolescent alcohol use: risks and consequences. *J. Alcohol Alcohol.* **49**, 160–164 (2014)
- Eurostat: Early school leavers in Portuguese educational system. [Online]. Available: <https://ec.europa.eu/eurostat/> (2007)
- Cortez, P., Silva, A.: Using data mining to predict secondary school student performance. In: Portugal 5th International Future Business Technology Conference, Porto, Portugal, Feb 2008, pp. 5–12
- DataPreparator: What is data preparation? [Online]. Available: http://www.datapreparator.com/what_is_data_preparation.html (2010)
- Berthold, M.R., Cebron, N., Dill, F., Gabriel, T.R., Kotter, T., Meinl, T., Ohl, P., Sieb, C., Thiel, K., Wiswedel, B.L.: *KNIME: the Konstanz information miner*. In: *Studies of Classification, Data Analysis and Knowledge*. Springer (2007)
- Dwivedi, S., Kasliwal, P., Soni, S.: Comprehensive study of data analytics tools (RapidMiner, Weka, R tool, Knime). In: *Symposium on Colossal Data Analysis and Networking (CDAN)*, 18–19 Mar 2016, pp. 64–69
- Ratner, B.: The correlation coefficient: its values range between +1/−1, or do they? *J. Target. Meas. Anal. Market.* **17**, 139–142 (2009)
- Doo, H.: *Data Mining and its Application*, 1st edn, 336 pp. (2010). ISBN 9781844808915
- Quinlan, J.R.: Induction of decision trees. *Mach. Learn.* **1**, 81–106 (1986)
- Quinlan, J.R.: *C4.5: Programs for Machine Learning*. Morgan Kaufman (1993)
- Palaniappan, S., Hameed, N.A., Mustapha, A., Samsudin, N.: Classification of alcohol consumption among secondary school students. *JOIV: Int. J. Inform. Vis.* **1**, 224 (2017). <https://doi.org/10.30630/joiv.1.4-2.64>
- Pagnotta, F., Amran, M.H.: Using Data Mining to Predict Secondary School Student Alcohol Consumption. Department of Computer Science, University of Camerino (2016)
- Afzali, M.H., Sunderland, M., Stewart, S., Masse, B., Seguin, J., Newton, N., Teesson, M., Conrod, P.: Machine-learning prediction of adolescent alcohol use: a cross-study, cross-cultural validation (2018). <https://doi.org/10.1111/add.14504>
- Badnjevic, A., Gurbeta, L., Custovic, E.: An expert diagnostic system to automatically identify asthma and chronic obstructive pulmonary disease in clinical settings. *Nat. Sci. Rep.* **8**, 11645 (2018). <https://doi.org/10.1038/s41598-018-30116-2>
- Catic, A., Gurbeta, L., Kurtovic-Kozaric, A., Mehmedbasic, S., Badnjevic, A.: Application of Neural Networks for classification of Patau, Edwards, Down, Turner and Klinefelter Syndrome based on first trimester maternal serum screening data, ultrasonographic findings and patient demographics. *BMC Med. Genomics* **11**, 19 (2018). <https://doi.org/10.1186/s12920-018-0333-2>
- Gurbeta, L., Badnjevic, A., Maksimovic, M., Omanovic-Miklicanin, E., Sejdic, E.: A telehealth system for automated diagnosis of asthma and chronic obstructive pulmonary disease. *J. Am. Med. Inform. Assoc.* **25**(9), 1213–1217 (2018). <https://doi.org/10.1093/jamia/ocy055>

Identification of Real and Imaginary Movements in EEG Using Machine Learning Models

Joana Moreira, Mariana Moreira, Nuno Pombo, Bruno M. C. Silva, and Nuno M. Garcia

Abstract

The neural activity of the brain may be observed by means of an electroencephalogram (EEG) whose analysis and/or interpretation may lead to the recognition of human activities and behaviors. However, on imagined body movements the brain produces the same EEG patterns as the action performed. This study aims to differentiate real movements from imagined ones, through EEG signals. Three different models; Support Vector Machine, Logistic Regression, and K-Nearest neighbour were implemented to classify these events. The preliminary results, obtained from 15 participants, revealed that the Logistic Regression was the best classifier into the proposed model with accuracy rates varying from 36.8 to 90%. Finally, complementary studies should be addressed to optimize not only the accuracy but also to assure uniform accuracy among the different participants.

Keywords

EEG • Movement recognition • Logistic regression • Activity daily living

1 Introduction

The practice of the electroencephalography involves recording, analysis, and physiological interpretation of voltages on the human scalp [1]. This is possible because the neuronal activity in the brain induces electric fields that extend to the surface of the head [2], where they are detected by the electrodes and then recorded. Since the electroencephalogram (EEG) is a record of the oscillations of electric potential generated by brain sources [1], then its analysis can provide valuable information about the health and mental state of the individuals. Besides this proneness for medical diagnostic, the EEG also challenges for an interface between the human brain and the computer.

The brain computer interface (BCI) technology is used to help people who have severe motor disabilities in which people can activate or communicate with devices using brain waves. Therefore, EEGs analysis is timely, promising, and challenges for the creation of accurate classifiers that may efficiently support individuals in its daily life. The EEG recording were being implemented in several scenarios, as example in detection and classification of schizophrenia [3]. This application has however several open issues that challenges the EEG data analysis including the ability to differentiate real or imagined motor movement. Imagined body movement is registered by the EEG without body moment.

The interpretation of EEG signals related with imagined motions and daily living activities remains understudied and/or offers room for improvements. Furthermore, the importance of classifying real movement brain waves from imagined ones is crucial in the advance of the BCI.

Once, this paper proposes the application of machine learning models using EEG result data to differentiate either a real or an imagined motor movement. The main contribution of this study is to evidence a correlation between imagined and real movements demonstrated by means of a benchmark, using several classification models, from data collected from 15 participants.

J. Moreira · M. Moreira
Health Science Department, Universidade da Beira Interior,
Covilhã, Portugal

N. Pombo (✉) · B. M. C. Silva · N. M. Garcia
Instituto de Telecomunicações, Universidade da Beira Interior,
Covilhã, Portugal
e-mail: ngpombo@di.ubi.pt

N. M. Garcia
Universidade Lusófona de Humanidades e Tecnologias, Lisbon,
Portugal

B. M. C. Silva
Faculdade de Design, Tecnologia e Comunicação, Universidade
Europeia, IADE, Lisbon, Portugal

The paper is organized as follows: Sect. 2 introduces the rationale for the proposed system; in Sect. 3 the methods employed in the current work are presented, including details about data acquisition and signal processing; Sect. 4 describes the implemented classification models, whereas Sect. 5 presents results of the comprehensive experimental evaluation and finally Sect. 6 discusses the meaning and significance of the results, concludes the paper and proposes topics for continued research in this area.

2 Related Work

In the last years, an increasingly interest related with the research on BCI and acquisition of brain waves was observed [4]. Typically, these approaches use Electroencephalography (EEG), machine learning techniques and independent classifiers to measure BCI performance [5]. EEG has become a popular tool in brain research despite some known issues, including the offline analysis of neural signals.

Although BCI implementations have several challenges, such as, electrodes positioning, skin conductance, hair thickness, muscle movement and even mental fatigue, through fast signal processing the neurofeedback gained potential, especially on the study of motor imagined body movements [6]. This may improve significantly the quality of life for people with severe motor disabilities [7]. However, this technology can also be implemented in serious games, for example for rehabilitation purposes. The game industry represents new challenges for using EEG recordings [8], as illustrated in [9] which proposes a wearable EEG-based aiming at to control a computer game via brain waves. The obtained results evidenced the reliability of the system to control outside-world applications for general users or researchers.

Thus, the importance of achieving a reliable classifier for either imaginary and real movements has been addressed [10, 11]. The main principle is to render BCI efficiently to reproduce most of the particularities of the human brain. In addition, the study conducted by Kang et al. [12] whose purpose was to create a reliable predictor for early recovery of consciousness in comatose patients reported successful results with accuracies around 80%.

3 Data Acquisition

This study implements the data available in the PhysioNet database EEG Motor movement/imagery dataset [13]. The database contains data related with 109 participants. Each participant has a total of 14 records. The dataset characteristics are described as follows. First, (i) a target appears on either left or right side of the screen. The subject opens and

closes the corresponding fist until the target disappears. Then the subject relaxes; (ii) a target appears on either left or right side of the corresponding fist until the target disappears. Then the subject relaxes; (iii) a target appears on either top or bottom of the screen. The subject opens and closes either both fists (if the target is on the top) or both feet (if the target is on the bottom) until the target disappears. Then the subject relaxes; and finally (iv) a target appears on either top or bottom of the screen. The subject imagines opening and closing either both fists (if the target is on top) or both feet (if the target is on the bottom) until the target disappears. Then the subject relaxes.

In addition, the record observations include three codes (T0, T1 and T2), as described in Table 1.

The PhysioNet protocol exhibits several tasks including:

- **Task#1:** open and close left or right fist;
- **Task#2:** imagine opening and closing left or right fist;
- **Task#3:** open and close both fists or both feet;
- **Task#4:** imagine opening and closing both fists or both feet.

Nevertheless, in this study we only analyzed the participants' performing on Task#1 and Task#2 related with the T1 annotation. The repetitions of tasks varies between three and four in every record. However, these repetitions present the same duration, 4.1 s (T1), intercalated with a rest phase (T0) which also lasts for 4.1 s (T0). The participants included in our dataset were 2, 4, 5, 6, 8, 9, 10–18. On the contrary, participants 1, 3 and 7 were excluded, due to the fact that their records presented time variations related T0, and T1. The data were collected; using the BCI 2000, from 64-channel EEG, following the international 10–10 system (excluding electrodes Nz, F9, F10, FT9, FT10, A1, A2, TP9, TP10, P9, and P10), as presented in Fig. 1.

Hence, this model uses multiple brain waves representing unique features for the classification process. These brain waves are segmented into delta, theta, alpha, beta, and gamma waves. First, the delta waves, 4 Hz, occur in deep sleep, childhood and in serious organic brain disease. Second, the theta waves, 4–7 Hz, are present in childhood and during

Table 1 Record observations' description

Observation	Description
T0	Participant resting
T1	Corresponds to onset of motion (real or imagined) of <ul style="list-style-type: none"> • The left fist (in runs 3, 4, 7, 8, 11, and 12) • Both fists (in runs 5, 6, 9, 10, 13, and 14)
T2	Corresponds to onset of motion (real or imagined) of <ul style="list-style-type: none"> • The right fist (in runs 3, 4, 7, 8, 11, and 12) • Both feet (in runs 5, 6, 9, 10, 13, and 14)

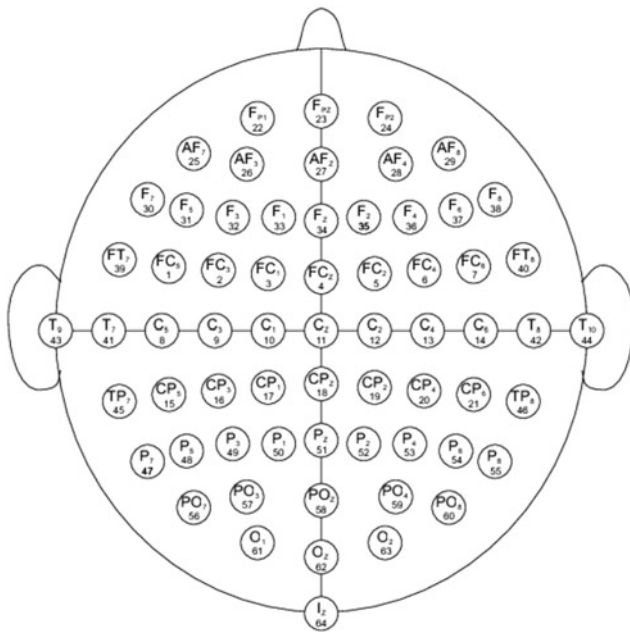


Fig. 1 EEG electrode placement system, 10–10 system courtesy used in PhysioNet protocol [13]

drowsiness and idling in adults. Third, the alpha waves, 8–12 Hz, are characteristic from a person awoken in a quiet, relaxed state. Fourth, the beta waves, 12–30 Hz, are affected by mental activity and occur during the alert/working state. Finally, the gamma waves, 30–100 Hz, appear in certain cognitive or motor functions. It should be noted this study is focused in three types of waves: theta, alpha and beta.

In addition, based on previous studies [14, 15], channels C3, C4, and Cz were selected due to the fact that they are suitable to collect the neural activity related with real and imaginary movements.

Thus, the power average was computed as presented in Eq. (1).

$$NPc3; \alpha = \frac{P_{c3; \alpha}}{P_{c3; \alpha} + P_{c3; \beta} + P_{c3; \theta}} \quad (1)$$

Following [6], to classify the movements from the recordings an array with the features of each recording was used and presented in Fig. 2.

Finally, the following classifiers were implemented aiming at to determine the real and the imaginary movements: Support Vector Machine, (SVM) [16], Logistic Regression (LR) [17], and K-Nearest neighbour (KNN) [18]. In addition, a 10-fold cross validation was implemented. The rationale for this methodology relies in the fact that when the data overfitting is observed, the training sample accuracy is likely to be unrealistically high, and consequently the predictive accuracy tends to be lower. A brief description of each classifier is provided below:

index	DATA
0	{NPc3;alpha;NPc3;beta;NPc3;theta}
1	{NPc4;alpha;NPc4;beta;NPc4;theta}
2	{NPcz;alpha;NPcz;beta;NPcz;theta}

Fig. 2 Array with the features extracted from each record

- *LR*: is used to analyze the relationship between predictors, and an outcome that is dichotomous responses including a real or imaginary movement [17]. The main purpose is to create a predictive model to describe data and to explain the relationship among dependent and independent variables.
- *SVM*: is based on the concept of decision planes defining decision boundaries. It attempts to determine the trade-off between minimizing the training set error and maximizing the margin to achieve the best generalization characteristics that may lead to trustworthy decisions [17]. As the decision plane is one that separates between a set of objects having different class memberships than the greatest possible margin may to model a robust system. The points closest to the separating hyperplane are known as support vectors.
- *KNN*: this classifier is based on an existing set of labeled data. Therefore, the class each piece of data should fall into is previously known. Thus, when a new piece of data (unlabeled data) is given, it is compared with the existing data, and is labeled in accordance with the most similar data. The most similar data is selected according to the similarity metrics including: Euclidean distance, or Manhattan distance.

4 Results

The preliminary results are presented in Table 2 containing both open and close movements of the left fist which was evaluated using different classifiers. The SVM was tested using Linear, Quadratic, Cubic, and Gaussian kernel. On the contrary, KNN was computed with multiple settings: Fine, Medium, Coarse, Cosine, Cubic and Weighted. This methodology enabled to determine all the classes from different granularities e.g. by means of variate numbers of neighbors.

The obtained results vary from the best accuracy rate, 90% with LR on the 11th participant, to the worst accuracy, 21.1% with the KNN cosine model in the 14th participant. On the one hand, the participant who obtained the best

Table 2 Detail of the preliminary results

Participants	Logistic regression (%)	SVM models					KNN models						
		Linear (%)	Quadratic (%)	Cubic (%)	Fine gaussian (%)	Medium gaussian (%)	Coarse gaussian (%)	Fine (%)	Medium (%)	Coarse (%)	Cosine (%)	Cubic (%)	Weighted (%)
#2	70	45	30	25	45	35	35	40	40	50	55	35	35
#4	59.1	72.7	40.9	31.8	40.9	36.4	36.4	54.5	50	45.5	59.1	50	45.5
#5	40	50	65	60	50	55	40	65	45	50	40	45	65
#6	57.1	52.4	71.4	76.2	66.7	76.2	57.1	61.9	52.4	52.4	33.3	52.4	71.4
#8	68.2	54.5	63.6	63.6	36.4	68.2	50	50	68.2	45.5	68.2	68.2	54.5
#9	85	80	80	75	70	75	55	65	80	55	65	75	80
#10	36.8	57.9	57.9	47.4	47.4	42.1	47.4	42.1	57.9	47.4	42.1	52.6	42.1
#11	90	80	80	75	60	75	70	65	85	55	70	80	80
#12	47.6	38.1	57.1	33.3	76.2	52.4	47.6	57.1	47.6	47.6	52.4	47.6	61.9
#13	75	41.7	54.2	70.8	33.3	37.5	41.7	45.8	41.7	41.7	25	41.7	37.5
#14	47.4	31.6	42.1	63.2	47.4	42.1	47.4	31.6	42.1	47.4	21.1	42.1	42.1
#15	57.1	47.6	57.1	38.1	52.4	57.1	47.6	28.6	52.4	52.4	61.9	52.4	57.1
#16	81	76.2	61.9	57.1	47.6	47.6	52.4	52.4	52.4	52.4	52.4	52.4	52.4
#17	66.7	71.4	61.9	52.4	61.9	76.2	57.1	66.7	61.9	52.4	76.2	61.9	71.4
#18	61.9	61.9	38.1	52.4	47.6	52.4	61.9	57.1	33.3	47.6	38.1	28.6	57.1
Mean (SD)	74 ± 16.3	64 ± 16.3	64 ± 20.4	59 ± 20.4	56 ± 9.6	60 ± 16.5	50 ± 12.2	57 ± 10.2	60 ± 18.7	53 ± 2.5	51 ± 16.5	57 ± 17.4	65 ± 18.3
Total basis	52.2	51	54.2	50.6	48.7	46.8	49.7	51.3	44.9	46.8	54.2	46.8	50

The bold value highlights the higher accuracy rate for each participant

accuracies in the models was the 11th participant with accuracies from 55 to 90%. Whereas, the participant who had the worst accuracies was the 10th with accuracies from 36.8 to 57.9%. In addition, the best result obtained with the KNN on the 11th participant in which was 85, 80, and 80% on the following settings respectively: Medium, Cubic, and Weighted. On the contrary, the SVM presents the higher accuracy on the 9th and 11th participants with 80% on both Linear and Quadratic models.

5 Discussion and Open Issues

Our experiments revealed that, independently of the selected classifier, the accuracy presents a fluctuation not only among different classifiers into the same participant, but also among the other participants. This phenomenon may be explained by the fact that each case differs with electrodes placements and/or with the manner of performing the imaginary motion. In addition, unlike the real motion performance, the imaginary activity if performed does not provide a visual and/or sensory feedback.

Alternatively, complementary studies should be addressed to optimize not only the accuracy but also to assure its homogeneity on the sample. Insufficient data normalization is a current constraint which resulted in the exclusion of some participants. In addition, complementary studies should be addressed to include Task#3, Task#4, and the related T2 observations.

Finally, the accuracy obtained for all the classifiers suggests that there is room for improvements related with both classification models, and features extracted from the selected channels.

6 Conclusions

This paper presents a computerized system to determine the correlation of imagined and real movements using EEG signals. The knowledge acquisition module was tested using several classification models such as: LR, SVM, and KNN. The preliminary results, obtained from 15 participants, revealed that the LR was the best classifier into the proposed model. On the one hand, LR revealed its suitability to interpret data with accuracy rates varying from 36.8 to 90%, in which the mean was $74\% \pm 16.3$. Another key point to remember, is the suitability of the proposed system to distinguish between imagined and real movements. Coupled with the data uniformization among all the participants, the overall performance of the system offers room for further studies.

Acknowledgements This work was supported by FCT project UID/EEA/50008/2013 (*Este trabalho foi suportado pelo projecto FCT UID/EEA/50008/2013*).

This article is based upon work from COST Action IC1303—AAPELE—Architectures, Algorithms and Protocols for Enhanced Living Environments and COST Action CA16226—SHELD-ON—Indoor living space improvement: Smart Habitat for the Elderly, supported by COST (European Cooperation in Science and Technology). More information in www.cost.eu.

References

1. Tong, S.: Quantitative EEG Analysis Methods and Applications. Artech House (2009)
2. Ullsperger, M., Debener, S.: Simultaneous EEG and fMRI: Recording, Analysis, and Application. Oxford University Press (2010)
3. Dvey-Aharon, Z., Fogelson, N., Peled, A., Intrator, N.: Schizophrenia detection and classification by advanced analysis of EEG recordings using a single electrode approach. *PLoS One* **10**, 1–12 (2015). <https://doi.org/10.1371/journal.pone.0123033>
4. He, B., Gao, S., Yuan, H., Wolpaw, J.R.: Brain–computer interfaces. In: He, B. (ed.) *Neural Engineering*. Springer, Boston, MA (2013). https://doi.org/10.1007/978-1-4614-5227-0_2
5. Vidaurre, C., Blankertz, B.: Towards a cure for BCI illiteracy. *Brain Topogr.* **23**, 194–198 (2010). <https://doi.org/10.1007/s10548-009-0121-6>
6. Choi, K.: Electroencephalography (EEG)-based neurofeedback training for brain–computer interface (BCI). *Exp. Brain Res.* **231** (3), 351–365 (2013). <https://doi.org/10.1007/s00221-013-3699-6>
7. Yong, X., Menon, C.: EEG classification of different imaginary movements within the same limb. *PLoS One* **10**(4), e0121896 (2015). <https://doi.org/10.1371/journal.pone.0121896>
8. Ahn, M., Lee, M., Choi, J., Jun, S.C.: A review of brain–computer interface games and an opinion survey from researchers, developers and users. *Sensors (Basel, Switzerland)* **14**(8), 14601–14633 (2014). <https://doi.org/10.3390/s140814601>
9. Liao, L.-D., Chen, C.-Y., Wang, I.-J., Chen, S.-F., Li, S.-Y., Chen, B.-W., et al.: Gaming control using a wearable and wireless EEG-based brain–computer interface device with novel dry foam-based sensors. *J. NeuroEng. Rehabil.* **9**, 5 (2012). <https://doi.org/10.1186/1743-0003-9-5>
10. Ramoser, H., Muller-Gerking, J., Pfurtscheller, G.: Optimal spatial filtering of single trial EEG during imagined hand movement. *IEEE Trans. Rehabil. Eng.* **8**, 441–446 (2000). <https://doi.org/10.1109/86.895946>
11. Hung, C.-I., Lee, P.-L., Wu, Y.-T., Chen, L.-F., Yeh, T.-C., Hsieh, J.-C.: Recognition of motor imagery electroencephalography using independent component analysis and machine classifiers. *Ann. Biomed. Eng.* **33**, 1053–1070 (2005). <https://doi.org/10.1007/s10439-005-5772-1>
12. Kang, X., Yang, F., Li, W., Ma, C., Li, L., Jiang, W.: Predictive value of EEG-awakening for behavioral awakening from coma. *Ann. Intensive Care* **5**, 52 (2015). <https://doi.org/10.1186/s13613-015-0094-4>
13. Goldberger, A.L., Amaral, L.A.N., Glass, L., Hausdorff, J.M., Ivanov, P.C., Mark, R.G., et al.: PhysioBank, PhysioToolkit, and PhysioNet: components of a new research resource for complex physiologic signals. *Circulation* **101**, e215–e220 (2000)
14. Neuper, C., Pfurtscheller, G.: Evidence for distinct beta resonance frequencies in human EEG related to specific sensorimotor cortical areas. *Clin. Neurophysiol.* **112**, 2084–2097 (2001). [https://doi.org/10.1016/S1388-2457\(01\)00661-7](https://doi.org/10.1016/S1388-2457(01)00661-7)

15. Deecke, L., Weinberg, H., Brickett, P.: Magnetic fields of the human brain accompanying voluntary movement: Bereitschaftsmagnetfeld. *Exp. Brain Res.* **48**, 144–148 (1982). <https://doi.org/10.1007/BF00239582>
16. Vapnik, V.N.: *The Nature of Statistical Learning Theory*, vol. 8. Springer (1995)
17. Harrell, F.E., Lee, K.L., Califf, R.M., Pryor, D.B., Rosati, R.A.: Regression modeling strategies for improved prognostic prediction. *Stat. Med.* **3**, 143–152 (1984). <https://doi.org/10.1002/sim.4780030207>
18. Dudani, S.A.: The distance-weighted k-nearest-neighbor rule. *IEEE Trans. Syst. Man Cybern.* **SMC-6**, 325–327 (1976). <https://doi.org/10.1109/tsmc.1976.5408784>

Development of a Diagnostic Support Software in the Clinicobiochemical Evaluation of Thyroid Disease Diagnosis

Arnela Tarakčija, Vedad Terzić, Almir Vardo, Sabrina Smajlović, Sabilja Zećiri, Selma Imamović, Tanja Dujić, Maja Malenica, and Tamer Bego

Abstract

The thyroid gland is one of the largest endocrine glands in the body and excretes two major hormones: thyroxine and triiodothyronine, known as T4 and T3, as well as calcitonin, a hormone important in calcium metabolism. Thyroid hormones are secreted into the bloodstream and are transported to every tissue in the body where they help energy utilization, maintain heat and regulate brain, heart, muscle function and functions of other organs. Primarily, the thyroid gland secretion is controlled by the thyroid stimulating hormone (TSH), secreted from the adenohypophysis. Increased hormone blood levels represent the hyperfunction of the gland or hyperthyroidism, and hormone deficiency is considered as a condition of hypofunction or hypothyroidism. An application has been developed based on an algorithm, and is used to determine the thyroid gland dysfunction. *HypoTir* application is based on the following parameters: TSH, fT4, T3 concentration, and presence of thyroid gland antibodies. The diagnostic performance of the application depends solely on the accuracy of the applied algorithm. For specific parameter values application displays a possible diagnosis. Further work and computational development in medicine is needed to provide faster, better and more efficient care as well as patient awareness and knowledge on existing illnesses.

Keywords

Thyroid diseases • TSH • fT4 • T3 • Thyroid antibodies • Algorithm • HypoTir • Application development

1 Introduction

The thyroid gland excretes thyroxine (T4), triiodothyronine (T3) and calcitonin, a hormone essential for calcium metabolism. Primarily, the thyroid gland secretion is controlled by the thyroid stimulating hormone (TSH), which is excreted from the adenohypophysis. Thyroid hormones help utilize energy, maintain heat and regulate brain, heart, muscle function and functions of other organs. They regulate metabolic processes that are essential for normal growth and development, but also participate in regulation of metabolic rate in adults [1, 2].

Disorders of the thyroid gland have been reported in over 110 countries around the world with 1.6 billion people being at risk and in need of iodine supplementation. Every disorder of the gland affects the whole organism and it is of great importance to determine the disorder and the etiology behind the disorder [3]. Therefore, it is necessary to perform gland function tests that include:

1. Blood tests
 - (a) blood hormone level (TSH, total T4 and T3, free T4)
 - (b) level of autoantibodies (thyroid peroxidase and thyroglobulin)
2. Tests that do not include blood testing
 - (a) tests with radioactive iodine
 - (b) scans.

Most commonly, the Thyroid gland disorders manifest themselves as hyperthyroidism and hypothyroidism. The term hyperthyroidism refers to any condition in which there are too many thyroid hormones present in the gland. In other

A. Tarakčija (✉) · V. Terzić · S. Smajlović · S. Zećiri · S. Imamović · T. Dujić · M. Malenica · T. Bego
Faculty of Pharmacy, University of Sarajevo, Sarajevo, Bosnia and Herzegovina
e-mail: arnela_t@outlook.com

A. Vardo
Faculty of Electrical Engineering, University of Sarajevo, Sarajevo, Bosnia and Herzegovina

words, the thyroid is hyperactive. Because of the negative feedback mechanism, the TSH is low or below the detection limit. The main causes of hyperthyroidism are: Graves' disease, thyroid nodules, thyroiditis, thyrotinomas, metastatic thyroid cancer, pituitary cell insensitivity for thyroid hormones, iodine excess, large dose of TSH and others. Some of the symptoms that are characteristic for hyperthyroidism are: tachycardia, tremor of the hands, sleep disturbance, irritability, weight loss, muscular weakness, bulging eyes (Graves' disease), accelerated heart rate (Plumer's disease) and others [4–6].

Hypothyroidism occurs when thyroid hormone production and secretion are reduced and due to the mechanism of negative feedback, TSH increases. The disease can be genetic or can develop during a patient's lifetime. It can occur in a subclinical form where the thyroid hormone levels are within the reference values, and TSH is slightly increased. Central hypothyroidism is caused by insufficient TSH stimulation of the thyroid gland, while a disorder of the gland is not present. The most common autoimmune thyroid disease with decreased thyroid function is Hashimoto syndrome which is characterized by the following symptoms: fatigue, cold intolerance, constipation, pale and dry skin, brittle nails, hair loss, weight gain, muscle weakness, prolonged menstrual bleeding, depression, loss of memory [7–10].

Other disorders that manifest themselves as hyper- or hypofunction of the gland are euthyroid sick syndrome, TSH secreting adenomas, thyroid hormones resistance and drug interferences [11, 12].

Historically, there have been many practical difficulties associated with the diagnosis of these disorders (which is a symptom of a variety of disorders and dysfunctions) due to the complex nature of the thyroid gland, pituitary and hypothalamus. According to ATA estimates, about 60% of people in the United States are unaware of their diagnosis [13]. Consequently, we have come up with an idea to develop an application in order to educate patients who are not familiar with the physiology and pathophysiology of thyroid gland. Accessibility to information has increased in the last decade and therefore, the possibility of educating patients. The aim of this study was to develop an application for personal computers and mobile devices that would diagnose and classify thyroid gland disorders while remaining patient friendly.

2 Methods and Materials

The results and conclusions of previously published scientific research papers and review studies were used as data source. In the experimental part of the study an application

called *HypoTir* was developed and its purpose is the classification of thyroid disorders based on parameters derived from the algorithm (see Fig. 1) used to determine thyroid dysfunction. The parameters listed in the shown algorithm are fT4, T3 and TSH concentration as well as the presence of thyroid antibodies. Based on the input data of biochemical parameters application succeeds to distinguish hypothyroidism from hyperthyroidism, even more specific, certain subtypes of these disorders.

An algorithm is a set of rules for problem solving. This is a schematic representation of the decision-making process composed of a flow chart with boundary paths that lead to some desired outcome. In health care, algorithms provide one strategy for translating CPG (Central pattern generator) based on evidence in practice. CPGs have been derived from rigorous systematic reviews of existing literature. Algorithms help health workers and patients make decisions about appropriate health care for certain clinical circumstances. They summarize the CPG using a step-by-step methodology tailored for the user that increases the ability to make a precise clinical decision based on the best evidence [14].

To create this application, the C# programming language was used in the Visual Studio programming environment. The graphical part of the application is programmed using Windows Forms.

The application can only be used on a Windows operating system with the Microsoft .NET Framework 4.5.2 installed (<https://www.microsoft.com/en-us/download/details.aspx?id=42642>).

Installing this framework is necessary because the programs made in the newer version of Windows Forms also require a newer 'background' for their execution.

The application was developed using two forms:

1. main forms
2. auxiliary forms.

The parameter values are entered in the main form, while the other form is reserved for the diagnosis. Based on the entered parameters, the second form changes the name of the disease and diagnosis.

3 Results and Discussion

The prevalence of thyroid gland dysfunction in adults in the general population ranges from 1 to 10% and is even higher in selected groups (Samuels 1998; Vanderpump 2000; Wang and Crapo 1997). The reasons for the variation include the place of examination, age and sex of the respondent and the way of assessment [16].

Thyroid Disorders Testing

[Click here for topics associated with this algorithm](#)

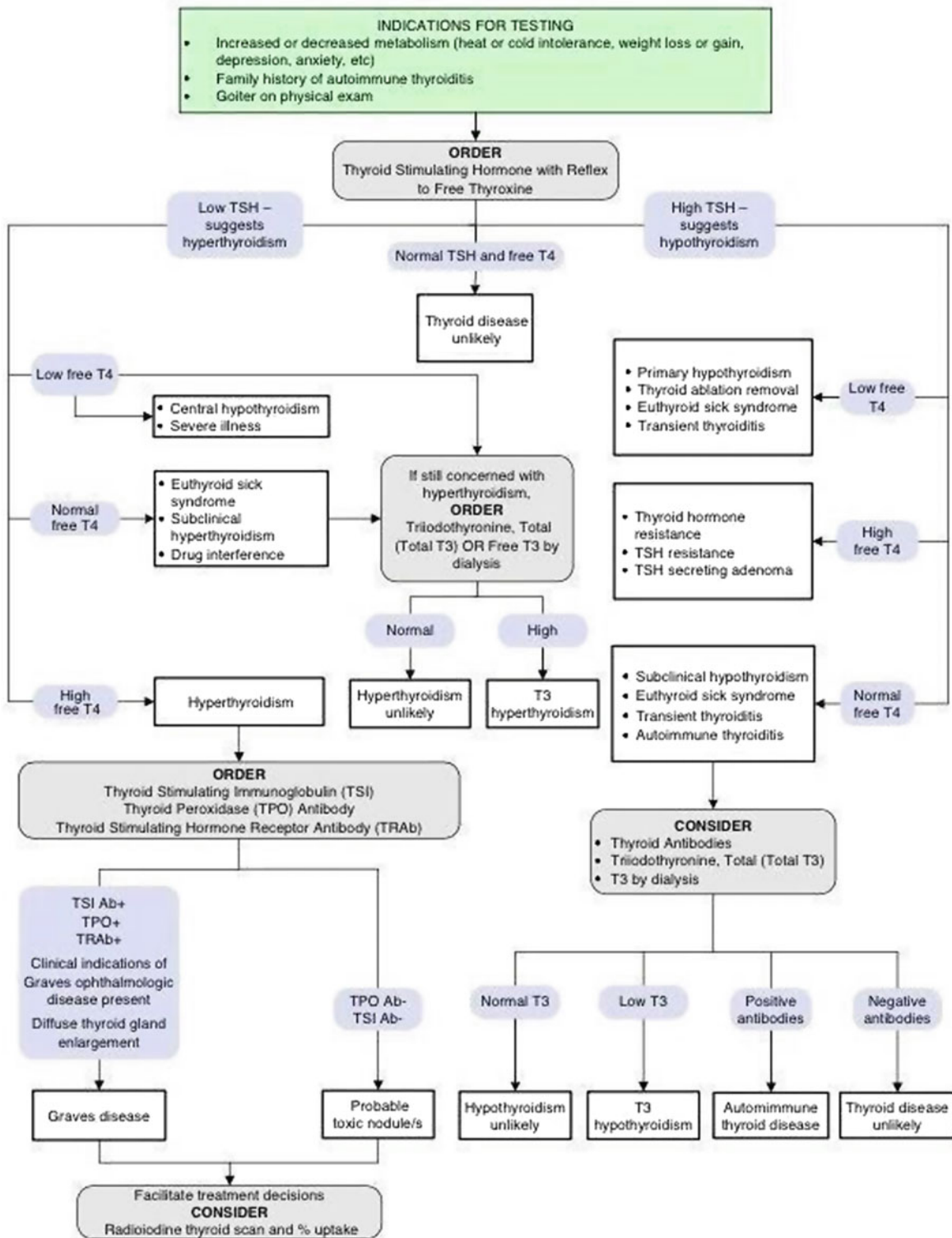


Fig. 1 Algorithm for diagnosis of thyroid disorders [15]

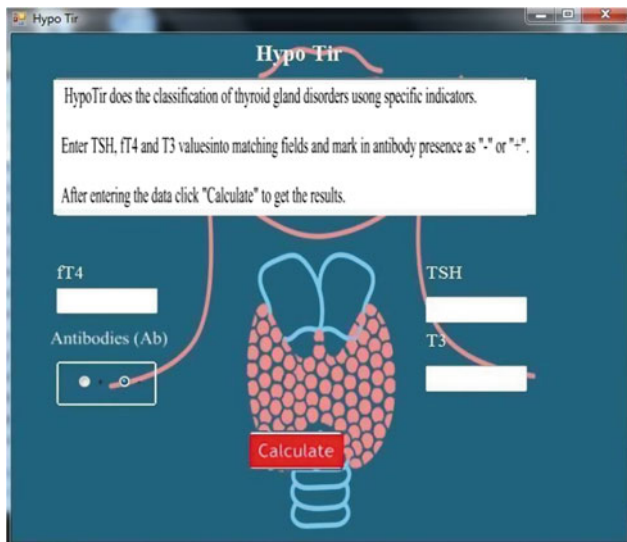


Fig. 2 Single-page screenshot of the *HypoTir* application showing graphical interface for implementing diagnostic tests. Directions for using the app are directly accessible at the top of the single interface page, as shown

Lack of information can lead to major problems in the treatment of some diseases. By using this application, patients can get information on the appropriate diagnosis with high degree of accuracy and precision. *HypoTir* application uses the following parameters: TSH, fT4, T3 concentration, and presence of thyroid gland antibodies. By using a specific combination of parameter values for each patient individually, the application according to mentioned algorithm displays possible diagnoses (Fig. 2).

The increase of TSH defines the thyroid gland hypofunction, while the other three parameters are responsible for the variability of the diagnosis (Table 1 and Fig. 3).

Low values of TSH defines the hyperfunction of the thyroid gland and the variability of the fT4, T3 and antibody parameters will allow the differentiation of the diagnosis. Antibodies usually indicate the presence of autoimmune diseases (Table 2).

If a patient enters normal values for TSH, fT4, T3, and doesn't mark the antibodies as positive, the following will be displayed (see Fig. 4): Thyroid gland disorder is unlikely.

HypoTir uses levels of hormones for each patient individually in order to diagnose the disease. A similar project called *ThyroSim*, a UCLA biocybernetics laboratory application, was developed to predict the effects of dietary supplements for the thyroid gland in patients with different absorption and secretion levels of T3 and T4 hormones. The application was developed with the intention of predicting concentrations of TSH, T4 and T3 after using supplements for the thyroid gland during a given period (max 100 days). It is useful for the prevention of possible thyrotoxicosis when using the supplements [17].

Jaganathan and Rajkumar, in the study of An Expert System for Optimizing Thyroid Disease Diagnosis, used multilayer perceptron (MLP), type of neuronal network, and C4.5 algorithms that function as decision trees [18]. The parameters used are the resin T3 uptake, the total serum T3, and the maximum absolute difference of TSH after injection of 200 μg TRH value and the basal value [17]. In a recent study (2015), besides the MLP and C4.5 algorithms, RBF-Radial Basis Function is used. A 98.15% accuracy rating over MLP with an improved F-score was achieved, which increased accuracy by more than 4.5%. The authors cite "The results of the studies show that the original combination of parameters is a reliable predictor of accurate patient classification" [19].

Table 1 *HypoTir* diagnosis with elevated TSH values

Parameter	Values				
TSH	Increased	Increased	Increased	Increased	Increased
fT4	Decreased	Increased	Normal	Normal	Normal
fT3	Decreased	Increased	Decreased	Decreased	Normal
Antibodies	Negative	Negative	Negative	Positive	Negative
Results	(I) Primary hypothyroidism (II) Euthyroid sick syndrome (III) Thyroid ablation removal (IV) Transient thyroiditis	(I) Thyroid hormone resistance (II) TSH resistance (III) TSH secreting adenoma	T3 hypothyroidism or euthyroid sick syndrome	Autoimmune thyroid disease (Hashimoto syndrome)	Low probability of hypothyroidism presence

Fig. 3 The *HypoTir* application with a demonstration of a diagnosis pop-up window. The window contains a probable diagnosis (up) and its short description (down)

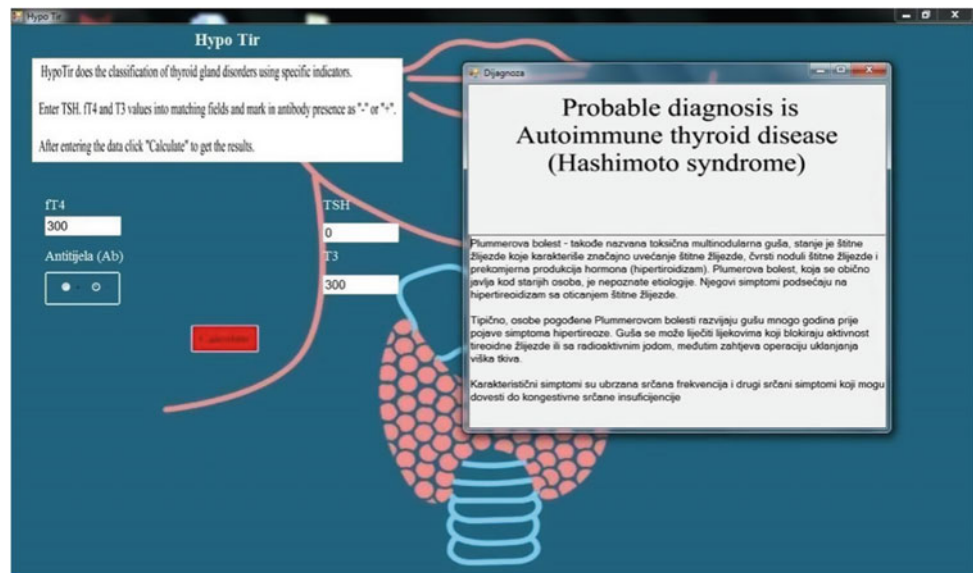
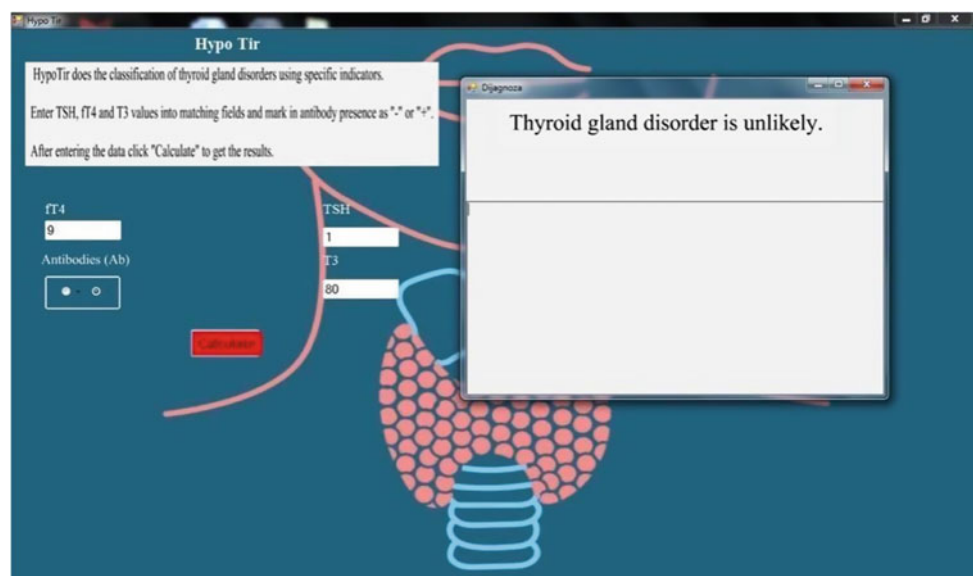


Table 2 *HypoTir* diagnosis with reduced TSH values

Parameter	Values				
TSH	Decreased	Decreased	Decreased	Decreased	Decreased
fT4	Decreased	Decreased	Decreased	Normal	Increased
fT3	Decreased	Normal	Increased	Normal	Increased
Antibodies	Negative	Negative	Negative	Negative	Positive
Results	Central hypothyroidism	Low probability of hyperthyroidism presence	T3 hyperthyroidism (thyrotoxicosis)	(I) Euthyroid sick syndrome (II) Subclinical hyperthyroidism (III) Drug interference	Graves' disease (with presence of ophthalmic disease and diffuse thyroid gland enlargement)

Fig. 4 *HypoTir* displaying results for patient with normal hormone and Ab values



Liu et al. in their study discussed the problem of classifying thyroid gland disorders using the Fuzzy K closest neighbor algorithm with the highest classification accuracy of 99.09% and the average accuracy of 98.82%. The same parameters used in earlier mentioned studies were taken into account [20].

Those studies were aimed at testing the accuracy and precision of the diagnostic capability of a specific program, but the diagnostic performance of *HypoTir* depends solely on the exactitude of the applied algorithm. Thus, if the algorithm diagnoses the disease with a certain accuracy, the application itself will have the same effect.

HypoTir classifies thyroid dysfunctions using the TSH, T3, fT4 blood values and antibody presence. The application is programmed to show disorders, with appropriate parameter combinations, after getting results of biochemical analysis. The user enters the values and gets a diagnosis with basic information about the disorder. Within the program, each parameter and disease are described briefly and easily, allowing the patient to gain insight into the parameters and the presented disorder. Programs of this type could be implemented into electronic health cards and can be extrapolated on other diseases. Patient education on the conditions and illnesses should enhance monitoring and treatment of diseases, thereby increasing the quality of life of patients and increasing the efficiency of medical doctors and pharmacist in successfully achieving a good quality treatment and consequently cure for the disease.

4 Conclusion

The prevalence of thyroid disease is relatively high in the adult population, so the need for improving diagnostics, monitoring and treatment as well as informing patients and medical experts is of great importance.

The future of research in medicine is largely dependent on symbiosis with other sciences, especially with computer science. There are many spheres that have not yet been explored, such as self-diagnosis and self-medication. Medicine, together with the IT sector, works to improve the quality of human life, so cooperation between them is not only desirable, but also necessary.

HypoTir diagnoses the disease in a simple way, based on the values of TSH, T3, fT4, and antibodies by an application being programmed to display appropriate disorders for the given combinations of values. This could ease the education and awareness of patients about the disorders they face.

References

1. American Thyroid Association Hypothyroidism. https://www.thyroid.org/wp-content/uploads/patients/brochures/Hypo_brochure.pdf?pdf=Hypothyroidism?pdf=Hypothyroidism. Last accessed 27 Nov 2018
2. Guyton, A.C., Hall, J.E.: Textbook of Medical Physiology, 11th edn. Elsevier Inc., Philadelphia (2006)
3. Khan, A., et al.: Thyroid disorders, etiology and prevalence. *J. Med. Sci.* **2**(2), 89–94 (2002)
4. American Thyroid Association Hyperthyroidism. https://www.thyroid.org/wp-content/uploads/patients/brochures/Hyper_brochure.pdf. Last accessed 04 Jan 2018
5. The National Institute of Diabetes and Digestive and Kidney Diseases. Hyperthyroidism (Overactive Thyroid). <https://www.niddk.nih.gov/health-information/endocrine-diseases/hyperthyroidism>. Last accessed 03 Jan 2018
6. WebMD Subclinical Hyperthyroidism. <https://www.webmd.com/women/tc/subclinical-hyperthyroidism-topic-overview>. Last accessed 12 Apr 2018
7. Fatourechi, V.: Subclinical hypothyroidism, an update for primary care physicians. *Mayo Clin. Proc.* **84**(1), 65–71 (2009)
8. Gupta, V., Lee, M.: Central hypothyroidism. *Indian J. Endocrinol. Metab.* **15**(2), 99–106 (2011)
9. The Mayo Clinic Staff Hashimoto's Disease. <https://www.mayoclinic.org/diseases-conditions/hashimotos-disease/symptoms-causes/syc-20351855>. Last accessed 07 Jan 2018
10. Endocrinology Advisor TSH Resistance. <http://www.endocrinologyadvisor.com/endocrinology-metabolism/tsh-resistance/article/595656/>. Last accessed 07 Jan 2018
11. De Groot, L.J.: Nonthyroidal illness syndrome. <http://www.thyroidmanager.org/wp-content/uploads/chapters/the-non-thyroidal-illness-syndrome.pdf>. Last accessed 06 Jan 2018
12. Drugs.com: Induced Thyroid Disorders. <https://www.drugs.com/cg/induced-thyroid-disorders.html>. Last accessed 03 Jan 2018
13. ATA General Information/Press Room. <http://www.thyroid.org/media-main/press-room/>. Last accessed 27 Nov 2018
14. Jablonski, A.M., et al.: The use of algorithms in assessing and managing persistent pain in older adults. *Am. J. Nurs.* **111**(3), 34–45 (2011)
15. ARUP Consult Thyroid Disorders Testing Algorithm. <https://arupconsult.com/algorithm/thyroid-disorders-testing-algorithm>. Last accessed 22 Dec 2017
16. Institute of Medicine of the National Academies: Medicare Coverage of Routine Screening for Thyroid Dysfunction, Prevalence and Consequences of Thyroid Dysfunction. The National Academies Press, Washington, DC (2003)
17. Han, S., et al.: THYROSIM app for education and research predicts potential health risks of over-the-counter thyroid supplements. *Thyroid* **26**(4) (2016)
18. Jaganathan, P., Rajkumar, N.: An expert system for optimizing thyroid disease diagnosis. *Int. J. Comput. Sci. Eng.* **7**(3) (2012)
19. Nallamuth, R., Palanichamy, J.: Optimized construction of various classification models for the diagnosis of thyroid problems in human beings. *Kuwait J. Sci.* **42**(2), 189–205 (2015)
20. Liu, D.Y., et al.: Design of an enhanced fuzzy k-nearest neighbor classifier based computer aided diagnostic system for thyroid disease. *J. Med. Syst.* **36**, 32–43 (2012)

Part X

**Artificial Intelligence and Machine Learning
in Healthcare**

Machine Learning Techniques for Performance Prediction of Medical Devices: Infant Incubators

Lemana Spahić, Emina Kurta, Sabahudin Ćordić, Merjem Bećirović, Lejla Gurbeta, Zivorad Kovacevic, Sebija Izetbegovic, and Almir Badnjevic

Abstract

This paper presents development of Expert System for prediction of performance of infant incubators based on real-time measured data. Temperature error, preventive maintenance intervals, number of additional parts and utilization coefficient were used as input information for the development of this system. Expert system is based on Artificial Neural Network (ANN) and Fuzzy logic (FL) classifier. Feed forward back-propagation artificial neural network with 12 neurons in hidden layer and sigmoid transfer function, using Bayesian regulation algorithm has shown best properties for prediction of the functionality of incubators based on performance output error. Fuzzy logic using Mamdani implication logic was developed as an extension of ANN and finally used for prediction of device performance. The developed expert system presented in this paper presents the first step in researching possibilities of usage such systems for upgrading medical device management strategies in healthcare institutions to answer challenges of increased sophistication of devices, but patient safety demands as well.

Keywords

Infant incubators • Artificial neural network • Fuzzy logic • Expert system • Medical devices • Inspection • Performance

L. Spahić (✉) · E. Kurta · S. Ćordić · M. Bećirović · L. Gurbeta · Z. Kovacevic · A. Badnjevic
Faculty of Engineering and Natural Sciences,
International Burch University, Sarajevo,
Bosnia and Herzegovina
e-mail: lemana.spahic@stu.ibu.edu.ba

S. Izetbegovic
University Clinical Center Sarajevo, Sarajevo,
Bosnia and Herzegovina

1 Introduction

Since 1891 and the invention of the first neonatal incubator, incubators are used worldwide present in the neonatal intensive care units (NICUs) of all hospitals [1]. In 1897, due to the increased death rate of pre-mature babies, the utilization of infant incubators became prominent worldwide [2]. Main applications of infant incubators include oxygenation of the baby and protection from harmful agents. During incubator use temperature, respiration, cardiac function (ECG) and brain activity (EEG), relative humidity, sound and skin temperature are monitored [3].

Every medical device has its benefits and risks, therefore patient safety can only be ensured when these risks and benefits are openly disclosed [4]. Ongoing sophistication of medical equipment occurs, with medical staff relying on their results for patient treatment and care. In spite of this, malfunctioning may still occur at any time. Therefore maintenance, safety and performance evaluation are critical for preventing malfunctions in all medical devices, including infant incubators [5].

One of the major priorities pertaining to maintenance of medical devices are their compliance to defined international standards. These standards establish a universal testing procedure for biomedical service [6]. In the case of infant incubators sensors for all parameters such as temperature, humidity, airflow and sound should be measured and tested [7]. Furthermore, certain test equipment for testing of wire resistance and chassis leakage exist [8]. An additional method for the inspections of medical devices is the implementation of legal metrology framework, implemented with the goal of compliance to EU Directives of new approach (New Approach Standardization) [9]. The legal metrology framework implemented in Bosnia and Herzegovina is presented in the work of Badnjevic et al. and others [9–14].

In the past researches have set their goal on developing software programs for the maintenance of medical device

systems. Previous research of Nichols and Linberg [15] and Linberg [16] presents successful disclosure of automated software updates to programmers. Advantages of such software is that they are based on newer methods, while older methods are limited to Excel spreadsheets and physical documentation [17–19]. With the beginning of the development of software programs and collecting big data from medical devices, machine learning algorithms in big data analytics became a prominent subject [20]. The effectiveness of this approach has resulted in developing clinically validated diagnostic techniques using artificial intelligence with the algorithms and techniques improving at a constant rate [21, 22].

Therefore, scientists in the past have conducted research deducing techniques for fast and accurate prediction of optimal usage of neonatal incubators. Amongst them Hagar et al. [23] focused on implementing different algorithms for intelligent incubator Length of Stay (LOS) prediction using data mining which proved to be an efficient technique. In the study of Sezdi [24] two distinct strategies were employed, preventive maintenance for older technology devices and predictive maintenance for newer high-tech devices. The results of the study had hidden medical equipment failures as a result of noncompliance with international standards. Furthermore, Chaudhary and Kaul [25] tested 30 medical diagnostic devices with the goal to determine their utilization coefficient (UC). Up to 23% of the devices were proven to be inadequately used.

Considering Artificial Neural Networks (ANNs) and fuzzy expert systems, the study of Virk et al. [26] provides a detailed analysis of developing expert systems for fault prediction of electronic components. Virk et al. [26] concluded that ANNs are highly efficient and used for prediction, along with fuzzy logic assisting in decision making and control purposes. Another successful fuzzy logic control system was conducted by Reddy et al. [27] in which fuzzy logic control which incorporates both incubator air temperature and infant's skin temperature to control the heating. The system resulted in a smooth fuzzy control with desired rise time. In addition, the study of Amer and Al-Aubidy [28] used ANN with back-propagation method to simulate the premature infant incubator control system. The sensor outputs of infant incubator were used as ANN inputs which identify the corresponding case and decide the suitable reaction upon previous training.

Expert systems and ANNs have the significant ability of changing and developing which makes them outstanding methodologies for creating systems which optimizes complex medical devices [29]. With the goal of determining the prediction of maintenance necessity of medical devices, experts work on fuzzy expert systems and ANNs which explicit advantages over manual testing procedures. One of

them includes fuzzy expert systems being faster and more accurate, contrary to time consuming and potentially inaccurate manual testing [30].

This paper presents implementing machine learning techniques for the development of an Expert System with the ability to predict the maintenance necessity of infant incubators. An artificial Neural Network (ANN) was tested in conjunction with Fuzzy Expert System.

2 Methods

Expert system presented in this paper is made for prediction of performance of infant incubators. Parameters used for prediction and the output of system are graphically presented in Fig. 1, and the procedure is explained in detail in following chapters.

2.1 Dataset Used for the Development of Expert System

For the development of Expert System presented in this paper, measurement data acquired during three-year period from 137 infant incubators used in healthcare institutions in Bosnia and Herzegovina were used (Table 1 and Fig. 2) Each incubator was inspected once a year and measurements of air temperature and relative humidity were collected by staff from appointed laboratory for inspection of medical devices with measuring function. All measurements were performed according to ISO 17020 [31] and with calibrated etalons [32].

The error is calculated with respect to preset value and after calculation the error is compared to the limits stated in Table 2.

As it can be seen from Table 2, the devices were all classified as either functional (accurate) or non-functional (faulty). A medical device equipment verified as accurate is a medical device which successfully complies to safety and measurement requirements, while a faulty medical device equipment is a medical device that during testing has failed to comply with the same requirements [6]. According to Gurbeta et al. [6] for infant incubators the requirements are, in the case of air temperature, that the error must be smaller than 0.8 °C and the device can be classified as accurate. For humidity, if the deviation is smaller than 10 than the device is classified as accurate. In all other cases the devices are classified as faulty.

The output of the ANN is the inspection status of the medical device. This output information is used as one of the input parameters for the development of fuzzy classifier. Additionally, the number of additional parts (parts that are most susceptible to damage in incubators), utilization

Fig. 1 Block diagram of the system

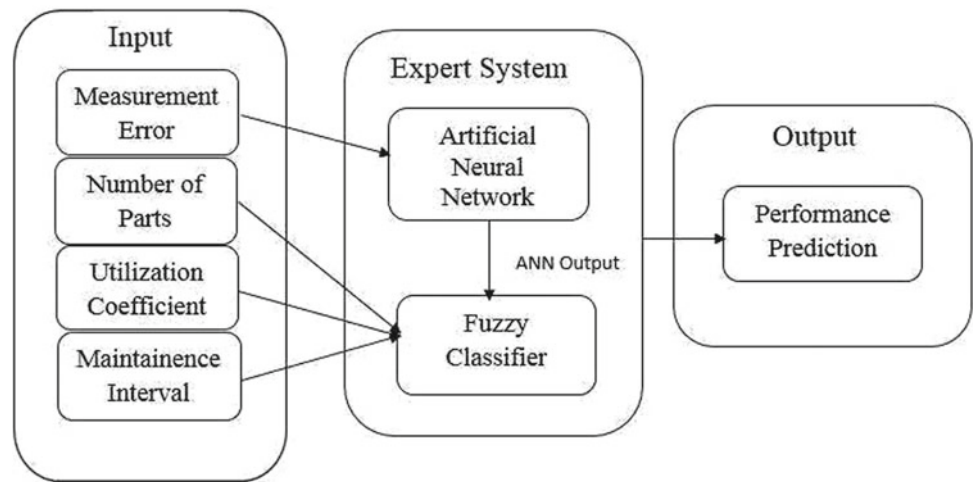


Table 1 Incubator inspection database

Period	Total number of devices	Accurate	Faulty
2015	22	14 (63.64%)	8 (36.36%)
2016	64	49 (76.56%)	15 (23.49%)
2017	54	38 (70.37%)	16 (29.63%)
Total	140	101 (72.14%)	39 (27.86%)

Fig. 2 Graphical representation of the ratio of accurate devices to faulty devices

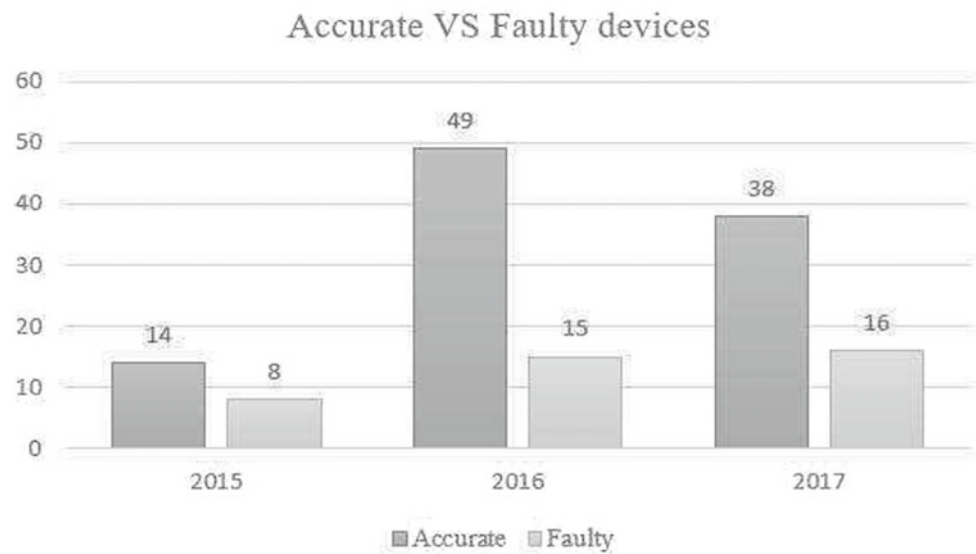


Table 2 Parameters used for calculating the error

Parameters	Values verified	Allowed deviation	Criteria	
			Error deviation	Classification
Air temperature	31°–37 °C	±0.8 °C	<0.8	Accurate
			>0.8	Faulty
Humidity	40–90%	±10%	<10	Accurate
			>10	Faulty

coefficient and yearly maintenance frequency were utilized for the development of fuzzy classifier.

2.2 Expert System for Prediction of Medical Device Performance

2.2.1 Artificial Neural Network Development

Artificial Neural Network has 5 inputs and 1 output. Inputs are the following: measurement error on 31 °C, measurement error on 32 °C, measurement error on 33 °C, measurement error on 34 °C, and measurement error on 37 °C. The dataset for training of ANN was divided in an 80/20 ratio, as recommended by experts which was also confirmed by experimental work [33–35] (Table 3).

Before choosing the architecture to be used in convergence with Fuzzy logic, multiple combinations of neuron numbers, training algorithms and neural network architectures were tested. Performance and training set confusion matrix precision with combinations of different neuron numbers and different training algorithms, with Trainlm and Trainbr employed in feed forward network and Trainbfg employed in recurrent network, are presented in Table 4.

In addition to being convenient for ANN development from small number of samples datasets, Bayesian regulation has an extensive ability to prevent overfitting [36, 37]. Figure 3 presents the architecture of the developed ANN.

2.2.2 Fuzzy Classifier for Maintenance Necessity Prediction

The fuzzy classifier used in the development of this expert system consisted of 4 input parameters and one output parameter. The input parameters used are:

1. Inspection status drawn from ANN output,
2. Number of additional parts/parts that are most susceptible to damage in incubators ranging from 0 to 6 by averaging the information from user manuals for different incubators [38, 39],
3. Utilization coefficient calculated statistically for Bosnia and Herzegovina [40] and
4. Yearly maintenance frequency in range from 1 to 3 times per year because the advised preventive maintenance for infant incubators is every 4–6 months [11].

Fuzzy inputs were all presented as trapmf membership function with general equation:

$$f(x; a, b, c, d) = \begin{cases} 1, & x \leq a \\ \frac{x-a}{b-a}, & a \leq x \leq b \\ 1, & b \leq x \leq c \\ \frac{d-x}{d-c}, & c \leq x \leq d \\ 0 & d \leq x \end{cases}$$

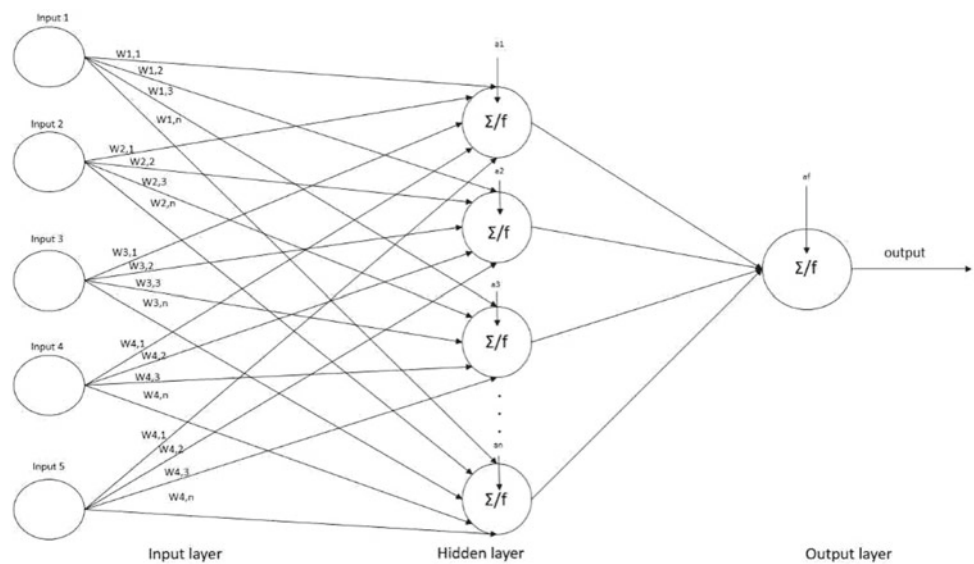
The overall accuracy of ANN-fuzzy model is dependent upon the if-then-action of the rules in fuzzy inference. In

Table 3 Data division for testing and validation

Training dataset		Subsequent validation (testing) dataset	
Classification group	Number of samples	Classification group	Number of samples
Accurate	85	Accurate	16
Faulty	25	Faulty	11
Σ	110	Σ	27

Table 4 Training set confusion matrix and performance as a measure of success of ANN prediction

Training algorithm	Number of neurons	Data division	Training	Performance
Trainlm	20	70–15–15	96.4	0.0279
Trainlm	12	70–15–15	97.3	0.0182
Trainlm	10	70–15–15	100	0.0150
Trainlm	8	70–15–15	98.2	3.69E–5
Trainbr	20	70–15–15	98.2	0.0134
Trainbr	12	70–15–15	100	8.39E–8
Trainbr	10	70–15–15	99.1	0.0110
Trainbr	8	80–10–10	99.1	0.0091
Trainbfg	20	80–10–10	100	1.55E–9
Trainbfg	12	80–10–10	100	6.8E–10
Trainbfg	10	80–10–10	100	4.24E–10
Trainbfg	8	80–10–10	100	1.52E–7

Fig. 3 Architecture of neural network

order to assure accurate prediction it is necessary to define precise combinations of input parameter membership functions. The membership functions are in minimum to maximum range with range adjustment for different parameters. Additional to the predicted ANN output, the fuzzy model enables control of final Expert System output on strictly defined rules so that fuzzy inference system will predict the correct maintenance necessity.

3 Results

A two-layer feed forward neural network in conjunction with Mamdani function fuzzy classifier was used for maintenance necessity prediction.

3.1 Testing Performance of Developed ANN

To evaluate the performance of developed ANN and the accuracy of prediction, mean square error was used as the measure of performance. Trial and error approach was

employed in order to determine the final combination of number of neurons and training algorithm.

The performance of the neural network architecture was determined by the computation of the following parameters:

- Specificity: (number of correct classified samples functional)/(number of total samples of functional).
- Sensitivity: (number of correct classified samples of functional class)/(number of total samples of functional class).
- Accuracy was determined by (number of correctly classified samples)/(total number of samples).

The ANN performance was tested with 20 samples for each of the architectures presented above. The results are presented in Table 5.

3.2 Testing Performance of Fuzzy Classifier

After setting the rules for all possible combinations, accuracy of Fuzzy prediction based on those rules was tested. All

Table 5 Confusion matrix of subsequent validation of developed ANN

	ANN		
	Accurate	Faulty	
Accurate	9	0	9
Faulty	0	11	11
	Specificity 100%	Sensitivity 100%	Accuracy 100%

Fig. 4 Graphical display of number of devices classified into linguistic categories. Yes (0–0.4), Maybe (0.31–0.88), and No (0.78–1)

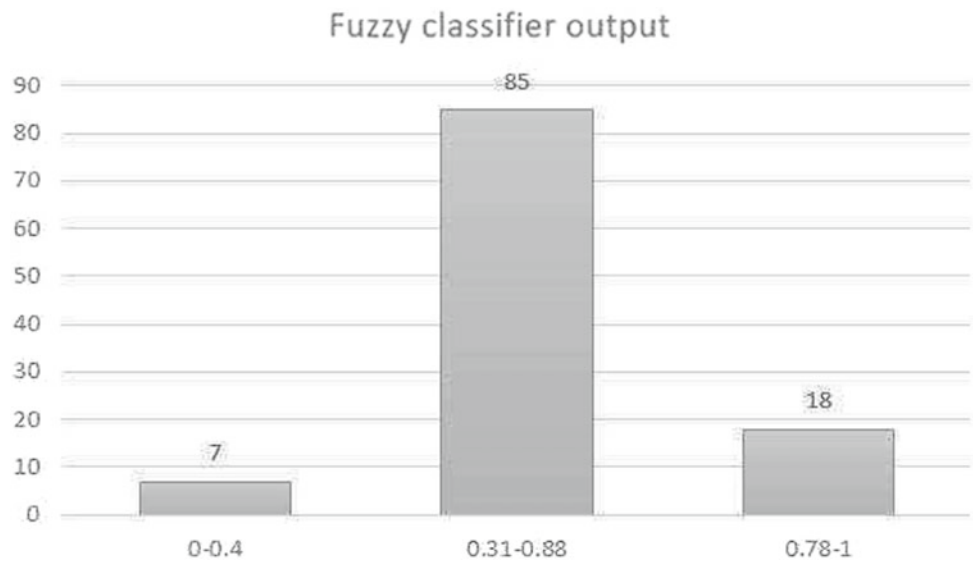


Fig. 5 Graphical display of average error gradient for 5 selected devices verified in consecutive years

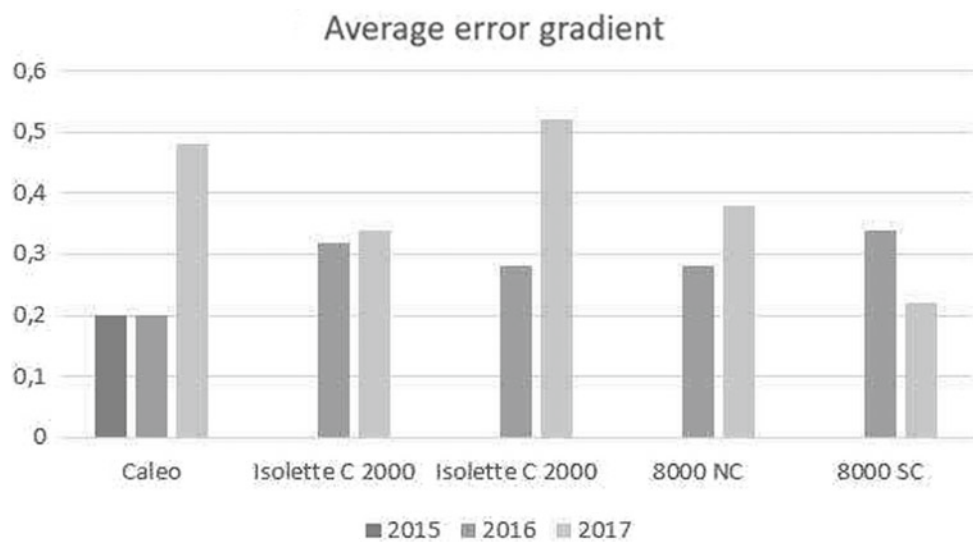


Table 6 Evaluation of developed expert system

ANN input					Inspection status	Number of parts	Utilization coefficient	Preventive maintenance frequency	System output
0.8	0.1	0.3	0.2	0.3	1	3	0.9	2	0.97
0.6	0.3	0.7	0.4	0.6	1	3	0.7	3	0.23
0.3	0.2	0.3	0.1	0.2	1	4	0.9	2	0.97
0.2	0.3	0.4	0.3	0.2	1	4	0.6	1	0.53
0.4	0.5	0.7	0.3	0.5	1	6	0.4	2	0.75

of the samples were classified in correct linguistic categories. Results are presented in Fig. 4.

The final developed Expert System was tested using 5 samples (Fig. 5) with provisionally assigned numbers of parts, utilization coefficients and maintenance frequencies (Table 6).

As it can be seen from Table 6, the developed expert system provides the results which are consistent with the inference logic used for rule definition in Fuzzy classifier.

4 Conclusion

Inspection of infant incubators is done based on parameters of environment temperature, humidity and skin temperature if the sensor is present. Although a high number of babies are born in Bosnia and Herzegovina, the country has only 140 verified incubators, with 36 of them malfunctioning. Because infant incubators are used to maintain the life of babies it is very important to have a tool that is able to predict whether the device needs maintenance and what is the exact level of that necessity.

Expert System developed in this paper was trained with 137 inspection samples from clinical centers and hospitals in Bosnia and Herzegovina. The samples are classified based on absolute error as accurate or faulty and then further including number of parts, utilization coefficient, and preventive maintenance frequency into three classes: incubators that need maintenance, incubators that maybe need maintenance (additional tests are needed), and incubators that do not need maintenance. Number of parts, utilization coefficient and preventive maintenance frequencies could not be punctually determined because that data is not presented in documentation. In order to have most accurate prediction, these data should be considered as relevant when doing inspection of medical devices.

Artificial Neural Network had 100% accuracy, meaning that inspection result was predicted correctly for all devices. Fuzzy classifier, correctly classified the samples in corresponding categories, based on syntax defined in rules. Concrete, reliable, realtime data would increase the reliability of the Expert System. However, this system has proven its efficiency in the field of maintenance prediction and can therefore be implemented in software solutions.

Expert System is a tool used in a lot of predictions including error and maintenance, but this paper presents a novel aspect of using Expert Systems in medical device performance evaluation. Overall system output is satisfying but further steps should be done in the field of data collection which would enable improvements.

Previous studies have shown that improved machine learning techniques are crucial in maintenance of medical devices today. The results obtained accurately prove the possibility of predicting maintenance necessity of the tested samples in both the ANN and Fuzzy Expert system. Similar results were obtained in one of the previous studies mentioned, in Sezdi [24], the system used detected 126 (22%) in 569 tested devices. The two systems created are, therefore, proven valuable in preventive maintenance. The expert system presented in this paper, along with the Expert System of Chaudhary and Kaul [25] had 100% accuracy of prediction of the devices used for testing. The studies and successful results provide useful insight in the many

applications Expert Systems and machine learning have in the maintenance of medical devices.

References

1. Antonucci, R., Porcella, A., Fanos, V.: The infant incubator in the neonatal intensive care unit: unresolved issues and future developments. *J. Perinat. Med.* **37**(6), 587–598 (2009)
2. Baker, J.P.: The incubator and the medical discovery of the premature infant. *J. Perinatol.* **20**(5), 321 (2000)
3. Tarigan, U., Ginting, R., Siregar, I.: Determining the need for improvement of infant incubator design with quality function deployment. In: *IOP Conference Series: Materials Science and Engineering*, vol. 309, no. 1, p. 012103. IOP Publishing (Feb 2018)
4. Webster, J.G.: *Medical Instrumentation Application and Design*. Wiley (2009)
5. Solecki, A.: [Ebook], 1st edn, pp. 2–6. Fluke Biomedical, USA. Retrieved from <https://www.hospimedica.com/whitepapers/6007329a-10-best-practices-incubators-wp-e.pdf> (2016)
6. Gurbeta, L., Izetbegović, S., Badnjević-Čengić, A.: Inspection and testing of infant incubators. In: Badnjević, A., Cifrek, M., Magjarević, R., Džemić, Z. (eds.) *Inspection of Medical Devices*. Series in Biomedical Engineering. Springer, Singapore (2018)
7. Badnjević, A., Cifrek, M., Magjarević, R., Džemić, Z. (eds.): *Inspection of Medical Devices*. Series in Biomedical Engineering. Springer, Singapore (2018)
8. Regulatory Controls: Fda.gov. Retrieved 18 Dec 2016, from <http://www.fda.gov/MedicalDevices/DeviceRegulationandGuidance/Overview/GeneralandSpecialControls/ucm2005378.htm> (2015)
9. Badnjevic, A., Gurbeta, L., Boskovic, D., Dzemic, Z.: Medical devices in legal metrology. In: *IEEE 4th Mediterranean Conference on Embedded Computing (MECO)*, pp. 365–367, Budva, Montenegro, 14–18 June 2015
10. Badnjevic, A., Gurbeta, L., Boskovic, D., Dzemic, Z.: Measurement in medicine—past, present, future. *Folia Med. Fac. Med. Univ. Sarajevo*. **50**(1), 43–46 (2015)
11. Badnjevic, A., Gurbeta, L., Jimenez, E.R., Iadanza, E.: Testing of mechanical ventilators and infant incubators in healthcare institutions. *Technol. Health Care* **25**(2), 237–250 (2017)
12. Gurbeta, L., Dzemic, Z., Bego, T., Sejdic, E., Badnjevic, A.: Testing of anesthesia machines and defibrillators in healthcare institutions. *J. Med. Syst.* **41**, 133 (2017). <https://doi.org/10.1007/s10916-017-0783-7>
13. Granulo, E., Becar, L., Gurbeta, L., Badnjevic, A.: Telemetry system for diagnosis of asthma and chronic obstructive pulmonary disease (COPD). In: *The 3rd EAI International Conference on IoT Technologies for HealthCare*, Vasteras, Sweden, 18–19 Oct 2016
14. Kurta, E., Kovacevic, Z., Gurbeta, L., Badnjevic, A.: Electromagnetic compatibility of medical devices: effects in everyday healthcare environment. In: *7th Mediterranean Conference on Embedded Computing MECO'2018*, Budva, Montenegro
15. Nichols, T., Linberg, K.: Apparatus and method to automatic remote software updates of medical device systems. Google Patents. Retrieved from <https://patents.google.com/patent/US6363282B1/en> (2002)
16. Linberg, K.: Apparatus and method for remote troubleshooting, maintenance and upgrade of implantable device systems. Google Patents. Retrieved from <https://patents.google.com/patent/US6442433B1/en> (2002)
17. Gurbeta, L., Badnjevic, A., Pinjo, N., Ljubic, F.: Software package for tracking status of inspection dates and reports of

- medical devices in healthcare institutions of Bosnia and Herzegovina. In: XXV International Conference on Information, Communication and Automation Technologies (IEEE ICAT), pp. 1–5, Sarajevo, Bosnia and Herzegovina, 29–31 Oct 2015
18. Gurbeta, L., Badnjević, A., Sejdinović, D., Alic, B., Abd El-Ilah, L., Zunic, E.: Software solution for tracking inspection processes of medical devices from legal metrology system. In: XIV Mediterranean Conference on Medical and Biological Engineering and Computing (MEDICON), Paphos, Cyprus, 31 Mar–02 Apr 2016
 19. Panda, A.: The Best Medicine: Why Healthcare Asset Tracking Software is Necessary to Save Lives, 1st edn, pp. 3–4. Texas (2017)
 20. Oxford: Home: Oxford English Dictionary. Retrieved from <http://www.oed.com/> (2018)
 21. Obermeyer, Z., Emanuel, E.: Predicting the future—big data, machine learning, and clinical medicine. *N. Engl. J. Med.* **375**(13), 1216–1219 (2016). <https://doi.org/10.1056/nejmp1606181>
 22. Foster, K., Koprowski, R., Skufca, J.: Machine learning, medical diagnosis, and biomedical engineering research—commentary. *Biomed. Eng. Online* **13**(1), 94 (2014). <https://doi.org/10.1186/1475-925x-13-94>
 23. Hagar, F., Taha, T., Mahmoud, M.: Applying Data Mining Technique for the Optimal Usage of Neonatal Incubator, 1st edn, pp. 1–11. Egypt (2012)
 24. Sezdi, M.: Two Different Maintenance Strategies in the Hospital Environment: Preventive Maintenance for Older Technology Devices and Predictive Maintenance for Newer High-Tech Devices [Ebook], 1st edn, p. 1. Hindawi Publishing Corporation, Istanbul (2016)
 25. Chaudhary, P., Kaul, P.: Factors affecting utilization of medical diagnostic equipment: a study at a tertiary healthcare setup of Chandigarh. *CHRISMED J. Health Res.* **2**, 316–323 (2015)
 26. Virk, S., Muhammad, A., Martinez-Enriquez, A.: Fault Prediction Using Artificial Neural Network and Fuzzy Logic [Ebook], 1st edn, p. 154. Mexican International Conference, Mexico (2008)
 27. Reddy, N., Hariharan, S., Mathur, G.: Toward a Fuzzy Logic Control of the Infant Incubator [Ebook], 1st edn, pp. 1–8. Research Gate, USA (2007)
 28. Amer, G., Al-Aubidy, K.: Novel Technique to Control the Premature Infant Incubator System Using Ann, 1st edn, p. 1. Science Direct, Jordan (2005)
 29. Liao, S.: Expert System Methodologies and Applications—A Decade Review From 1995 to 2004, 1st edn, p. 93. Science Direct. Retrieved from <https://www.sciencedirect.com/science/article/pii/S0957417404000934> (2004)
 30. Blomquist, M.: Systems and Methods for Automated Testing of Medical Equipment, 1st edn, p. 1. USA. Retrieved from <https://patents.google.com/patent/US5669877A/en> (1994)
 31. Official Gazette of B&H (OG BH), No. 75/14
 32. IMT Medical, PF 301, User Manual. <http://www.imtmedical.com/en-us/products/testingdevices/pf301/Pages/index.aspx#>. Accessed 8 June 2018
 33. Nielsen, M.: Neural Networks and Deep Learning. *Neuralnetworksanddeeplearning.com*. Retrieved 10 June 2017, from <http://neuralnetworksanddeeplearning.com/chap4.html> (2017)
 34. Alić, B., Gurbeta, L., Badnjević, A., Badnjević-Čengić, A., Malenica, M., Dujčić, T., Bego, T.: Classification of Metabolic Syndrome Patients Using Implemented Expert System. In: *CMBEBIH 2017*, pp. 601–607. Springer, Singapore (2017)
 35. Badnjević, A., Gurbeta, L., Cifrek, M., Marjanović, D.: Classification of asthma using artificial neural network. In: 2016 39th International Convention on Information and Communication Technology, Electronics and Microelectronics (MIPRO), pp. 387–390. IEEE (2016 May)
 36. Sarder, P., Schierding, W., Cobb, J.P., Nehorai, A.: Estimating sparse gene regulatory networks using a bayesian linear regression. *IEEE Trans. Nanobiosci.* **9**(2), 121–131 (2010)
 37. Liu, F., Zhang, S.W., Guo, W.F., Wei, Z.G., Chen, L.: Inference of gene regulatory network based on local Bayesian networks. *PLoS Comput. Biol.* **12**(8), e1005024 (2016)
 38. User Manual for DragerIsolette C8000. Retrieved from https://www.draeger.com/enus_us/Hospital/Products/Thermoregulation-and-Jaundice-Management/Neonatal-ClosedCare/Isolette-8000
 39. User Manual for DragerCaleo. Retrieved from https://www.draeger.com/en_uk/Hospital/Products/Thermoregulation-and-Jaundice-Management/Neonatal-Closed-Care/Caleo
 40. Federalni zavod za statistiku. Retrieved from <http://fzs.ba>

Prediction of Heart Diseases Using Majority Voting Ensemble Method

Dželila Mehanović, Zerina Mašetić, and Dino Kečo

Abstract

Heart disease is the one of the most serious problems in healthcare and affects large number of people. It is very important to detect it on time, otherwise it can cause serious consequences, such as death. In this paper, we applied artificial neural network, k-nearest neighbor and support vector machine algorithms to build model which will be used for prediction of heart disease. Multiple experiments using each of these algorithms are performed. Additionally, the ensemble learning is applied, and results are compared. Initially, the problem was approached as multiclass classification, however it was transformed into the binary classification problem, to simplify model since number of outputs is reduced from five to two. In both cases, the highest accuracies are obtained by majority voting which are 61.16% for multiclass classification and 87.37% for binary classification.

Keywords

Heart disease • Classification • ANN • SVM • KNN • Ensemble learning

1 Introduction

Since healthcare organizations are complex systems they generate vast amount of data that comes in different formats. Because of this, the key challenge is to build intelligent systems that will efficiently interpret generated data and support humans in decision making [1, 2].

To build such system, different solutions such as artificial intelligence methods, linked data, semantic web technologies and NoSQL datastores are combined. In recent years,

machine learning becomes popular for developing intelligent systems in healthcare. Machine learning algorithms are capable to approximate relationships between dataset variables in form of a function that is used for prediction and decision making. Application of machine learning models in healthcare systems improve efficiency and accuracy of the system overall [3].

Google employed machine learning to detect breast cancer by detecting patterns in the tissue with 87% accuracy, which is better than 73% accuracy achieved by human [4]. Scientists from Stanford developed algorithm for skin cancer detection using visual processing and deep learning inspired by neural networks [5]. In the [6] algorithm for detection of diabetic retinopathy using neural networks is presented.

One of the most common problems in healthcare is heart disease. Based on the latest statistics, number of people with heart disease is predicted to rise by 46% by 2030, which is more than 8 million adults with heart disease. According to World Health Organization [7], cardiovascular diseases (a group of disorders of the heart and blood vessels) are number one cause of death all over the world [8]. Statistical report of American Heart Association for 2017 [9] shows that about 92.1 million Americans are living with some cardiovascular disease.

Gi Beom Kim, in his paper [10] presents that according to database of Korean Health Foundation, about 50,000 of adults with heart disease live in South Korea and more than 4000 enter adulthood every year. At the current rate, it is estimated that about 70,000 of adults with heart disease will live there by the year 2020. Approximately 2200 people die of cardiovascular disease each day, which is one death on average every 40 s.

In recent researches [12–16] various machine learning algorithms have been applied to predict heart disease problems. Different techniques are employed to build reliable system which will produce useful results while lowering costs and diagnosis time. The goal of this paper is to build a model that will combine multiple classification algorithms to predict heart disease and to compare single algorithm models

D. Mehanović (✉) · Z. Mašetić · D. Kečo
International Burch University, Sarajevo 71000,
Bosnia and Herzegovina
e-mail: dzelila.mehanovic@stu.ibu.edu.ba

and ensemble model. Majority voting has been used as ensemble method for combining multiple machine learning algorithms [11].

The rest of paper is organized as follows: in Sect. 2 we summarize related works, in Sect. 3 we describe dataset and applied methods, in Sect. 4 we present results of our work and finally, we conclude our work with Sect. 5.

2 Literature Review

In the March 2017, Singh et al. [12] proposed web application that enables users to share their heart related problems and get diagnosis of disease using intelligent system online. Application takes inputs from user, process them and returns disease related to inputs from user. To avoid variance, dataset with 14 input attributes was split indiscriminately into two sets. Finally, implementation of model was performed using Naïve Bayes' classifier. As result, implemented application returns output to users based on prediction whether risk for heart disease is low, average or high.

Various data mining techniques were applied to predict heart disease. Devi et al. [13] analysed classification techniques for decision making in this field, especially Decision trees, Naive Bayes, Neural Networks and Support Vector Machines. They found out that application of hybrid data mining techniques can give promising results. Combining the outputs of each algorithm and comparing them helps to make prediction quicker and more accurate.

Datasets related to same disease problem may show different results applying same machine learning techniques. El-Bialy et al. [14] focused on integration of results of machine learning techniques applied on sets for heart diseases. They applied fast decision tree and C4.5 tree techniques, after which they compared features in trees resulted from different datasets. Common features among these datasets are collected to create new dataset which is used in later analysis. It is shown that accuracy of new dataset is higher than average accuracy of all separate datasets. Average accuracy of all datasets was 75.48% using fast decision tree and 76.30% using C4.5. Classification accuracy for newly collected dataset was 78.06 and 77.50% for fast decision tree and C4.5, respectively.

Venkatalakshmi and Shivsankar [15] presented prediction system for heart disease based on predictive mining. Experiments were carried out using Weka, open source tool for data mining, and data from UCI Machine Learning Repository. The goal was to compare performance of predictive data mining techniques such as Naive Bayes and Decision tree. Naive Bayes outperformed Decision Tree with accuracy of 85.03, while accuracy of Decision tree was 84.01.

In their research paper, Jabbar et al. [16] combined K-Nearest Neighbor and Genetic Algorithm on seven datasets to build heart disease classifier. The results of their study showed that accuracy is increased 5% using both, KNN and GA, rather than only KNN. Also, accuracy is decreasing as k-value goes on increasing. Although emphasis was on data related to Andhra Pradesh, city in India, it is shown that classifier gives high accuracy when it is applied on other heart disease datasets.

Table 1 shows summary of experiments mentioned above. It displays accuracy of heart disease classifiers obtained by several authors applying various methods.

Authors in [14, 15] used same dataset as we did, but unlike them, additionally, we want to apply multiclass classification to evaluate results. Besides that, our main goal is to explore gain achieved by application of ensemble learning.

3 Methodology

3.1 Dataset

As a part of this research, multiple machine learning models were developed using Heart Disease dataset from UCI Machine Learning Repository [17]. Original dataset contains 76 attributes, but all published works used only 14 of them, so we did same in our work. These attributes are selected as the most important for the reliable prediction. Data set contains 303 instances and it is publicly available.

The last attribute in dataset represents diagnosis of heart disease. Value 0 indicates absence of heart disease and values 1, 2, 3 and 4 indicate different levels of disease. Analyzing representation of each class individually, which are 54.12, 18.15, 11.88, 11.55 and 4.29% respectively, we can conclude that this dataset does not have skewed class problem.

Figure 1 shows visual representation of all attributes in dataset. It presents distribution of attributes in respect to particular class in dataset.

To split dataset, we applied two approaches. Firstly, we splitted data into training and testing set with ratio 66:34. Later, we applied 10-fold cross validation to compare results.

3.2 Feature Selection

After dataset was uploaded, we performed feature selection process which is used to identify attributes that are most relevant for prediction [18]. Two elevators were tried: GainRatioAttributeEval and InfoGainAttributeEval.

Table 1 Accuracy of various methods for heart disease classification in related work

#	Authors	Methods	Results
1	El-Bialy et al. [14]	Fast decision tree C4.5	78.06% 77.50%
2	Venkatalakshmi and Shivsankar [15]	Naive Bayes Decision tree	85.03% 84.01%
3	Jabbar et al. [16]	K-nearest neighbor and genetic algorithm	Accuracy is increased by 5% using both, KNN and GA, rather than only KNN

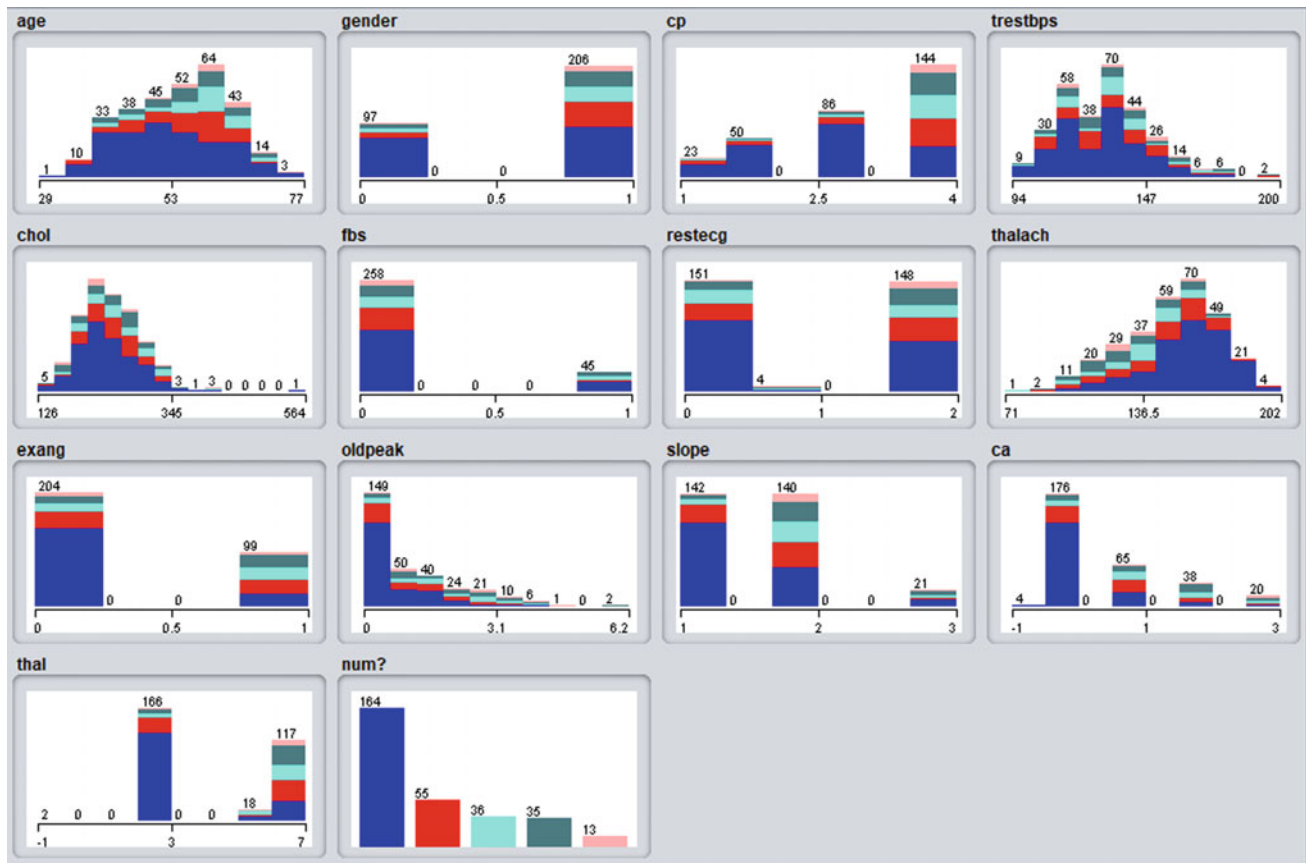


Fig. 1 Visual representation of attributes

According to the output of these two evaluators, several attributes were excluded from the further examination, as they showed no significant impact on an automated heart disease prediction process. Excluded attributes are resting blood pressure, serum cholesterol, fasting blood sugar and resting electrocardiographic result.

3.3 Classification

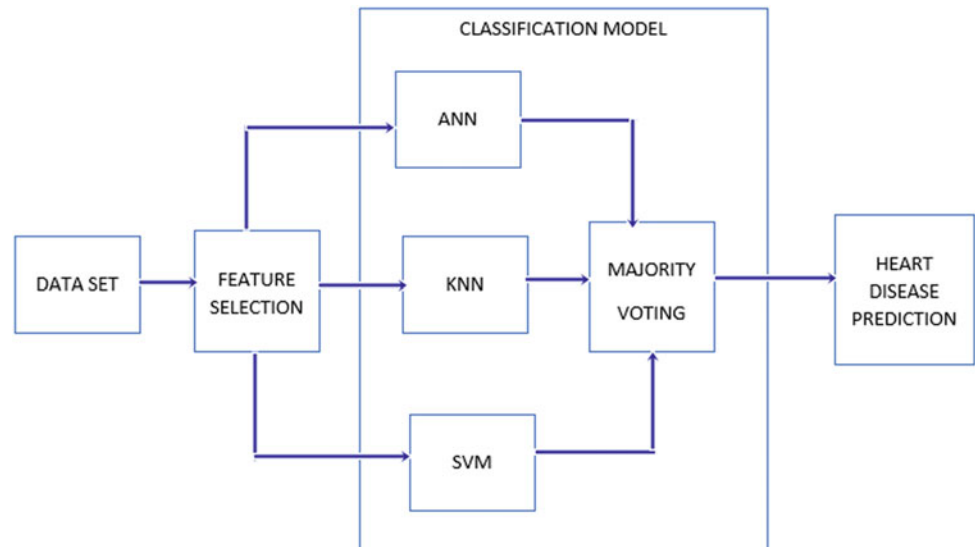
In our work, we applied ensemble learning to build model. Ensemble learning is used to combine several models to improve results. Multiple methods of ensemble learning

exist such as voting, stacking, bagging and boosting which are explained at [11] in detail. In our work we investigate majority voting. Each model included in majority voting makes its own prediction and final prediction is the one with highest number of votes.

We considered three classification algorithms: artificial neural network (ANN), support vector machine (SVM) and k-nearest neighbors algorithm (KNN). These algorithms are combined together and complement each other. Figure 2 shows the process of implementation.

Different combinations of parameters were used for each of these algorithms. Final model was built using the parameter values as provided in continuation.

Fig. 2 Process of model implementation



Artificial neural network contained 1 hidden layer and 0.4 learning rate. The value of training time was increased from default value of 500 to value of 5000. K-nearest neighbor was applied with value of k equal to 5. Also, we applied LinearNNSearch with Filtered Distance. Support vector machine was used with polynomial kernel and value of exponent equal to 1.5. The regularization factor was 3.0.

Described parameters were selected as the best combination for these algorithms according to obtained accuracy values.

Initial dataset had 5 output classes (class 0 for absence of disease and classes 1, 2, 3, 4 for presence) which are used for multiclass classification. Moreover, to compare results we applied binary classification with two classes (class 0 for absence and class 1 for presence of disease). Finally, for each of them we tested performance of ensemble learning.

4 Results

To measure performance of classifiers, we calculated the accuracy, the specificity and the precision.

The accuracy represents ratio of correctly classified samples and total number of samples [19].

$$ACC = \frac{TP + FN}{TP + FP + TN + FN} \quad (1)$$

The sensitivity or true positive rate (TPR) is ratio of true positives and actual positives ($TP + FN$) [19].

$$TPR = \frac{TP}{TP + FN} \quad (2)$$

The precision or positive predictive value (PPV) is ratio of true positives and predicted positives [19].

$$PPV = \frac{TP}{TP + FP} \quad (3)$$

From confusion matrix presented in Table 3, we can see types of mismatching between classes and notice that errors mostly occur between neighboring classes.

Table 2 and Fig. 3 show results obtained by multiclass classification and percentage split. The highest accuracy 61.16 is gained by majority voting, while ANN and KNN resulted in same accuracy 58.25, when applied separately.

From confusion matrix presented in Table 4, we can see that mismatch occurs between classes 0, 1, 2 and 3, not only between neighboring classes. But errors are reduced by increasing the distance between neighbored classes.

Table 3 and Fig. 4 show results obtained by multiclass classification and 10-fold cross validation. Again, majority voting achieved highest accuracy 58.41. In this case KNN outperformed ANN, while SVM still had the lowest accuracy.

If we compare results obtained by percentage split and cross validation for multiclass classification, we can observe that for the most of measurements percentage split results are higher than those of cross validation. Only ANN resulted in higher accuracy by cross validation than by percentage split.

In the next experiment, problem has been transformed into binary classification with output labels 0 and 1 where 0 presents absence and 1 presence of heart disease.

Table 4 and Fig. 5 show results obtained by binary classification and percentage split. It can be noticed that results are higher than those obtained by multiclass classification. Majority voting resulted in highest accuracy 87.37. Moreover, contrary to results of multiclass classification, KNN obtained lowest accuracy and SVM has highest accuracy, when applied without ensemble.

Table 2 Multi class classification results by percentage split

Algorithm	Sensitivity	Precision	Accuracy
ANN	0.58	0.50	58.25
KNN	0.58	0.66	58.25
SVM	0.53	0.56	53.39
Vote	0.61	0.68	61.16

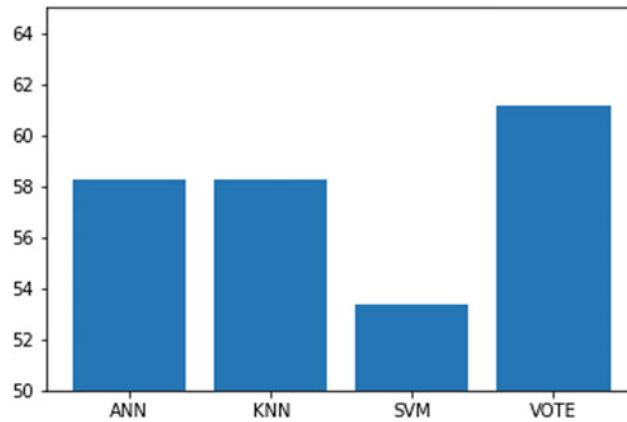


Fig. 3 Multi class classification results by percentage split

Table 3 Confusion matrix obtained by percentage split

	0	1	2	3	4
0	48	2	1	0	0
1	9	5	2	0	0
2	1	4	8	0	0
3	1	12	5	2	0
4	0	0	3	0	0

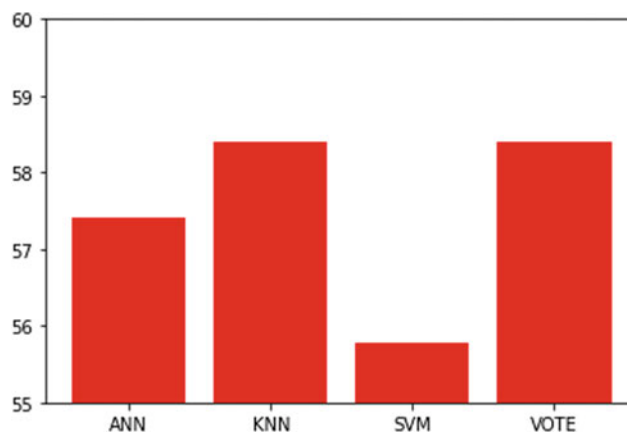
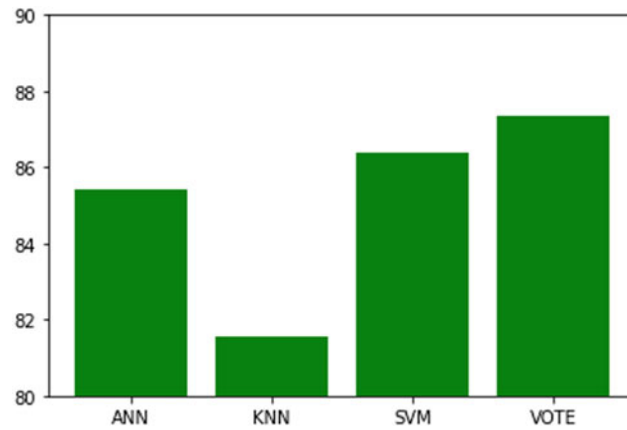


Fig. 4 Multi class classification results by 10-fold cross validation

Table 4 Multi class classification results by 10-fold cross validation

Algorithm	Sensitivity	Precision	Accuracy
ANN	0.57	0.52	57.42
KNN	0.58	0.52	58.41
SVM	0.55	0.48	55.77
Vote	0.58	0.52	58.41

**Fig. 5** Binary classification results by percentage split**Table 5** Confusion matrix obtained by 10-fold cross validation

	0	1	2	3	4
0	150	8	4	2	0
1	28	9	13	5	0
2	9	7	12	8	0
3	7	7	15	6	0
4	1	2	8	2	0

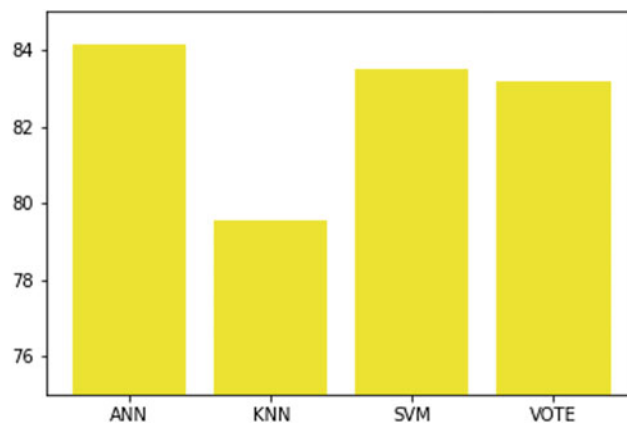
**Fig. 6** Binary classification results by 10-fold cross validation

Table 6 Binary classification results by percentage split

Algorithm	Sensitivity	Precision	Accuracy
ANN	0.85	0.85	85.43
KNN	0.81	0.81	81.55
SVM	0.86	0.86	86.40
Vote	0.87	0.87	87.37

Table 7 Binary classification results by 10-fold cross validation

Algorithm	Sensitivity	Precision	Accuracy
ANN	0.84	0.84	84.15
KNN	0.79	0.79	79.53
SVM	0.83	0.83	83.49
Vote	0.83	0.83	83.16

Table 5 and Fig. 6 show results obtained by binary classification and 10-fold cross validation. Unlike all previous cases, here majority voting did not achieve highest accuracy. Highest accuracy 84.15 is obtained by ANN. As with percentage split, KNN achieved lowest accuracy (Tables 6 and 7).

For binary classification, all results obtained by percentage split are higher than those obtained by cross validation.

Therefore, we may conclude that majority voting outperforms algorithms used separately and percentage split gives better results compared to 10-fold cross validation.

Conflict of Interest Declaration The authors declare that they have no conflict of interest.

5 Conclusion

In this paper we presented application of artificial neural network, k nearest neighbor and support vector machine on dataset with 14 attributes and 303 instances.

We evaluated difference between results obtained by algorithms applied separately and majority voting as ensemble learning. Problem is solved in two ways: as multiclass and binary classification, using two types of evaluation: percentage split and cross validation. We applied 66:34 percentage split and 10-fold cross validation.

In three of the four cases majority voting had highest accuracy equal to 61.15 for multiclass classification and 87.37 for binary classification. Only in binary classification with 10-fold cross validation single algorithm, ANN, outperformed ensemble learning method. This superiority of the ensemble learning over single algorithms could be explained by the fact that ensemble learning combines the best of all algorithms and gives single result. Also, results for binary classification are higher than those for multiclass classification. As the reason we could conclude number of classes that are available in decision making, since it is harder to 'learn' with five than with two outputs.

When it comes to data split, generally higher values of specificity, precision and accuracy are obtained by percentage split than by 10-fold cross validation.

References

- Luo, G.: MLBCD: a machine learning tool for big clinical data. *Health Inform. Sci. Syst.* **3** (2015)
- Belle, A., Thiagarajan, R., Reza Sorousmehr, S.M., Navidi, F., Beard, D.A., Najarian, K.: Big data analytics in healthcare. *Biomed Res. Int.* **2015** (2015)
- Corbett, E.: Real-world benefits of machine learning in healthcare. *Health Catalyst*. [Online]. Available: <https://www.healthcatalyst.com/clinical-applications-of-machine-learning-in-healthcare> (25 Apr 2017). Accessed 12 Mar 2018
- Krieger, L.M.: Google computers trained to detect cancer. *The Mercury News*. [Online]. Available: <https://www.mercurynews.com/2017/03/03/googlecomputers-trained-to-detect-cancer/> (03 Mar 2017). Accessed 13 Jan 2019
- Stanford University: Artificial intelligence used to identify skin cancer | Stanford News. *Stanford News*. [Online]. Available: <https://news.stanford.edu/2017/01/25/artificial-intelligence-used-identify-skin-cancer/> (25 Jan 2017). Accessed 13 Jan 2019
- Wang, P., et al.: Development and validation of a deep-learning algorithm for the detection of polyps during colonoscopy. *Nat. Biomed. Eng.* **2**(10), 741–748 (2018)
- WHO | World Health Organization (Mar 2018)
- WHO | Cardiovascular Diseases (CVDs) (May 2017)
- American Heart Association: Building healthier lives, free of cardiovascular diseases and stroke. [Online]. Available: <http://www.heart.org/HEARTORG/>. Accessed 23 Dec 2017
- Kim, G.B.: Psychosocial adjustment and quality of life of adolescents and adults with congenital heart disease. *Korean J. Pediatr.* **57**(6), 257–263 (2014)
- Ensemble Methods: Elegant Techniques to Produce Improved Machine Learning Results. *Toptal Engineering Blog*. [Online]. Available: <https://www.toptal.com/machine-learning/ensemble-methods-machine-learning>. Accessed 06 Mar 2018

12. Singh, G., Bagwe, K., Shanbhag, S., Singh, S., Devi, S.: Heart disease prediction using Naïve Bayes. *Int. Res. J. Eng. Technol. (IRJET)* **03**(04) (Mar 2017)
13. Devi, S.K., Krishnapriya, S., Kalita, D.: Prediction of heart disease using data mining techniques. *Indian J. Sci. Technol.* **9**(39) (2016)
14. El-Bialy, R., Salamay, M.A., Karam, O.H., Khalifa, M.E.: Feature analysis of coronary artery heart disease data sets. *Procedia Comput. Sci.* **65**, 459–468 (2015)
15. Venkatalakshmi, B., Shivsankar, M.V.: Heart disease diagnosis using predictive data mining. *Int. J. Innov. Res. Sci. Eng. Technol.* (2014)
16. Jabbar, M.A., Deekshatulu, B.L., Chandra, P.: Classification of heart disease using K-nearest neighbor and genetic algorithm. *Procedia Technol.* **10**, 85–94 (2013)
17. UCI Machine Learning Repository: Heart Disease Data Set. [Online]. Available: <http://archive.ics.uci.edu/ml/datasets/heart+Disease>. Accessed 16 Dec 2017
18. Brownlee, J.: An introduction to feature selection. *Machine Learning Mastery*. [Online]. Available: <https://machinelearningmastery.com/an-introduction-to-feature-selection/> (06 Oct 2014). Accessed 02 Sep 2018
19. Precision and Recall—Wikipedia. [Online]. Available: https://en.wikipedia.org/wiki/Precision_and_recall. Accessed 02 Sep 2018

Predicting the Outcome of Granulation and Tableting Processes Using Different Artificial Intelligence Methods

Nermina Sokolović, Majda Ajanović, Samir Badić, Miljana Banjanin, Mirna Brkan, Naida Čusto, Barbara Stanić, Merima Sirbubalo, Amina Tucak, and Edina Vranić

Abstract

Artificial intelligence methods offer a modern approach in solving different problems in the field of pharmacy, especially in the area of pharmaceutical technology. The main goal of this article is to present artificial intelligence methods that facilitate granulation and tableting processes. Artificial intelligence methods with the major impact in this area include artificial neural networks (ANN), cubist model, random forest method, k-NN and the combination of neuro-fuzzy logic (NFL) and gene expression programming (GEP). Besides giving a brief introduction to the methods listed above, the scientific goal of this paper is to present the on-going use they have in wet granulation process, roll compaction, solving the capping problems of the tablets, as well as helping with the scale-up process and quality improvement of ramipril tablets. In time to come, it is assumed that the diversity and pliability of the artificial intelligence methods can advance in the tablet making process, ensuring the much needed support in data analyzing and solving complex problems of tablet manufacturing that contain various input and output specification. It should always be duly noted, that even though artificial intelligence methods are far superior to the human brain when it comes to problem-solving and multitasking, these methods, and computer programming can never be the head of the operation, they could only mimic that.

Keywords

ANN • Neuro-fuzzy logic • GEP • Granulation processes • Process optimization • Quality improvement

1 Introduction

Artificial intelligence (AI) is being widely used in pharmaceutical researches due to ability to predict how process parameters or material properties affect the final product. The concept of artificial intelligence is designed to find the most adequate solution for an existing problem [1, 2]. AI presents a software or a machine, which is capable of solving a different kind of problems that are usually solved by humans using our natural intelligence [3].

Therefore, AI is of crucial importance in granulation processes. There are various models showing its influence in this field. Different machine-learning methods are suitable for optimizing granulation processes, as follows: Artificial neural network (ANN), Cubist, Random Forests (RF), k-Nearest Neighbors algorithm (k-NN) or Machine learning tools, such as Genetic Programming (GP) and Swarm Optimization (PSO) [1, 4].

1.1 ANN Model

Building a neural network is a highly complex task. ANN consists of three layers; input, hidden and output layer and all of them are connected. The main goal for the neural network is to learn the relationship between the independent and dependent variables, which is achieved through repeatedly presenting training set formulations to the neural network in many training cycles. The network performance is later assessed by determining the correlation between the actual values of dependent variables, and the values predicted by the neural network [5].

N. Sokolović (✉) · M. Ajanović · S. Badić · M. Banjanin · M. Brkan · N. Čusto · B. Stanić
Faculty of Pharmacy, University of Sarajevo, Zmaja Od Bosne 8, 71000 Sarajevo, Bosnia and Herzegovina
e-mail: 95nerminasokolovic@gmail.com

M. Sirbubalo · A. Tucak · E. Vranić
Department of Pharmaceutical Technology, Faculty of Pharmacy, University of Sarajevo, Zmaja Od Bosne 8, 71000 Sarajevo, Bosnia and Herzegovina

1.2 Cubist

This model can be expressed as a tree with linear regression functions. These functions are set at each node. *Cubist* model is based on two stages [2]:

- splitting criteria and
- pruning approach.

The output depends on the predictors used in the previous split [2].

1.3 Random Forest

This method uses many decision trees and then combines them in order to categorize different tasks. It can also be used for regression. In building this algorithm three steps are of crucial importance [2]:

- forming the subsamples,
- choosing several variables and
- the construction of the tree.

1.4 k-NN

It represents a technique that uses all existing cases and predicts the outcome by measuring similarity [2].

1.5 The Combination of Neuro-Fuzzy Logic (NFL) and Gene Expression Programming (GEP)

Systems have been developed neuro-fuzzy logic (NFL), which incorporates the neural network and the power of fuzzy logic. NFL has been useful in predicting the interactions between the formulation, analyzed process parameters and target product properties that we could not observe or conclude from the experimental data. GEP is able to provide highly predictive experimental equations. It presents a complex algorithm that involves computer programs (mathematical expressions, decision trees, and logical expressions) as neural networks, and encodes them into linear forms named chromosomes, susceptible to being mutated, transposed, or recombined. GEP technology uses many mathematical functions and later selects them by their ability to solve a specific problem [6, 7].

As progress is taking place in various fields of artificial intelligence and new ideas emerge every day, there is also a tendency to accelerate the development of pharmaceutical technology and granulation processes [1].

2 Predicting the Outcome of Granulation and Tableting Processes

Wet granulation is a method of size enlargement, which involves any process where agglomerates are formed using small particles, in which the original particles can still be distinguished (Fig. 1). Key steps in this process include mixing together dry compounds and adding binding substance in a liquid form that enables the formation of wet mass, which then flows through the high shear mixer in order to form granules of a certain size [8].

2.1 Wet Granulation Processes

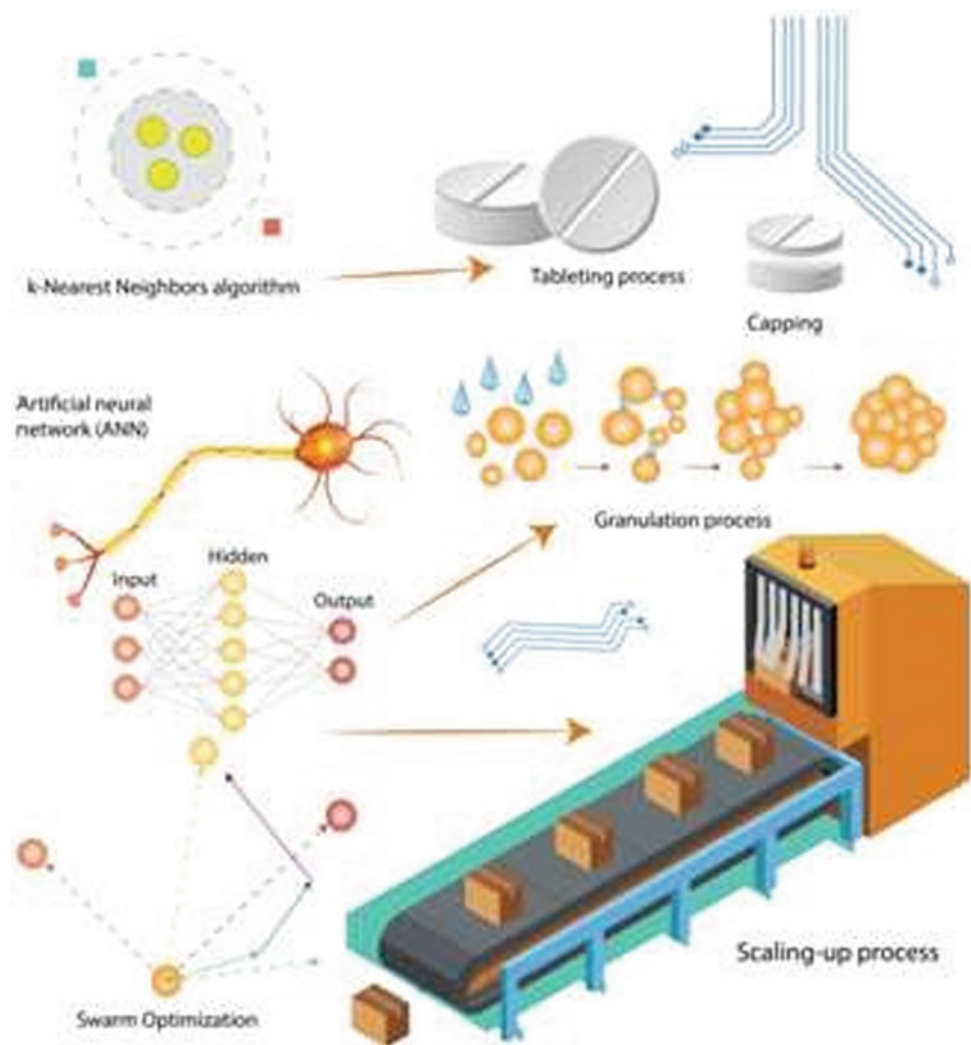
Manufacturing of solid-dosage pharmaceutical formulations is aspiring to be continuous, which means that every step is inter-connected. *Model predictive control* (MPS) represents an advanced control strategy [9]. The most significant unit operation in the production of tablets is granulation [10].

Twin-screw wet granulation (TSWG) represents a continuous granulation method, which has many advantages due to its process stability, flexible scale-up, short residence time, and controlled throughout [11]. There are different models and methods for mathematical modeling of this continuous process. *Population balance model* (PBM) is focused on granule characteristics and contrary, while the *discrete element method* (DEM) follows the motion of each individual particle. A hybrid model is a mixture of two listed methods in order to use advantages of each [9].

ANN model was designed to simulate different steps of this process. The experiment was performed on microcrystalline cellulose and water as a binder. Critical parameters were particle size distribution, liquid content, and porosity. The experiment was carried out using a twin-screw extruder. As input data feed flow rate, screw speed and its configurations, and liquid to solid ratio (L/S) were considered. Particle size distribution in terms of d-values (d10, d50, and d90) was expected as a response. Topology with 2 hidden layers containing 2 nodes per layer with non-linear activation function has shown the best results. As statistical parameters, they used a coefficient of determination and root-mean-squared error [9].

Once the ANN model was calibrated it was used to predict experimental data. It showed that increasing L/S forms larger granules, and since this is not always favourable, the liquid flow rate should be controlled. The coefficient of determination was statistically 0.99 except for training of d90. Developed ANN also has other advantages since it is very fast and it is more accurate than other mechanistic models. The results showed that this ANN model is competent to predict granule size distribution in

Fig. 1 Application of different artificial intelligence methods in predicting the outcome of various granulation and tableting processes



different conditions considering statistical and validation parameters [9].

Fluid bed granulation has a preference for combining many wet granulation operations into simple one. Main input parameters are product, inlet and outlet air temperature, consumption of liquid-binder, granulation liquid-binder spray rate, spray pressure, drying time, whilst main output properties include granule flow rate, granule size determined using light scattering method and sieve analysis, granule's Hausner ratio, porosity, and residual moisture. For the analysis of this process, different modeling techniques like *screening test*, *multiple regression analysis*, *self-organizing maps*, *artificial neural networks*, *decision trees*, and *rule induction* were used. In their comparison, it was found that nonlinear methods based on *artificial intelligence*, such as neural networks, are much better in generalization and prediction than conventional methods. It is very important to know all factors connected with the raw materials to provide and improve the quality of final product.

Korteby et al. [12] developed an ANN model with two hidden layers to predict the temperature distribution and the hydrodynamics during the fluidized bed granulation. Temperature initiates different hydrodynamic and thermodynamic processes that affect particle behavior. Predicting ability of this model was of $R^2 = 0.994$ and considering that it can be used as a predictive control tool to establish temperature profiles [12]. For the successful application of *artificial neural network* for data analysis, it is necessary to define network architecture like training methods, validation and testing of the network as well as network performance and reliability measurements [13].

As a modification of fluid bed granulation, a method using piezoelectric microphones was featured. Those piezoelectric microphones were embedded inside the fluid bed. ANN was also incorporated throughout the system to block any kind of interferences. Piezoelectric microphones emit signals corresponding to physical changes in the process of coating. This modification can be very useful in the

future if *Process analytical techniques* (PAT) develop a proper way of using information obtained from the passive acoustic methods [14].

2.2 Roll Compaction

Roll compaction is a dry granulation technique widely used in the pharmaceutical industry to prepare a sample prior to compression or encapsulation. It is mostly used for poor flowing materials and can also be used for materials which are moisture or heat sensitive. Broadly speaking roll compaction main function is to compress the powder into ribbons, which will then be milled to granules with a specific size distribution [5].

This method is most commonly used before tableting itself. Therefore, the properties of the final products, in this case, tablets are the main object. Nevertheless, in several studies, the properties of ribbons and granules were observed, and their significant impact on the final product has been noticed [15].

In order to demonstrate multiple dependence between formulation, process parameters, and quality of the final product, several approaches such as design of experiment (DoE) and quality by design (QbD) with intended goals have been included. However, these approaches did not provide relevant information due to the complexity of the processes in the pharmaceutical industry. Thus, computational intelligence (CI) can be easily bound with DoE approach and limit the obstacles. A great advantage of CI lays in the fact that there is no need for prior knowledge of processes. Rambali et al. [16], Weynberg et al. [17], Souihi et al. [18], have observed process parameters of roll compaction and came to different conclusions about how distinctive parameters affect mean granule size, as the most important granule characteristic [16–18].

Based on their research using DoE, principal factors affecting roll compaction are the compaction force, roll surface, roll speed, and screen size. Kazemi et al. [2] used CI methods to prove their usefulness in roll compaction/dry granulation and granule size distribution prediction. They have used five binary mixtures composed of microcrystalline cellulose and mannitol and have studied their influence on the quality of granules. Several methods were used: ANN, Cubist, Random Forest, k-NN etc. This analysis, using above mentioned models, has shown that size class, compaction force, true density, gap width, and intercept are the main parameters influencing roll compaction. Among all utilized models, Cubists have presented the best prediction on how these parameters will affect the process and ANN follows. In generally, CI methods have shown an advantage over conventional techniques in predicting the outcome. All the results rely only on this particular binary mixture [2].

The purpose of using Bio-inspired algorithms such as Grey Wolf Optimization (GWO), Bat Algorithm (BAT), Cuckoo Search (CS), Flower Pollination Algorithm (FPA), Social Spider Optimization (SSO), Genetic Algorithm (GA), and Particle Swarm Optimization (PSO) was to predict the porosity and hardness of the tablets. Pre-tableting granules were obtained by the roll compaction method. The properties of raw materials and excipients were already known, as the process variables. The results obtained by these algorithms were compared to the actual ones and it was shown that these CI algorithms were very good at predicting porosity and hardness of the tablets. GWO algorithm had the most accuracy in predicting tablet porosity while being equally efficient for pure powders, mixtures, and granules. Like any other bioinspired algorithm, it takes its roots in actual behavioral patterns of grey wolves. In their packs, every wolf has a predetermined and pre-designed position and movement to cover more areas and help them avoid their natural enemies. Turning their behavior into statistical model for predicting outcomes of the process with familiar input parameters a new evolutionary technique was applied in optimizing industrial processes. In this study input parameters, GWO predictor used were granule size upper limit, material, and compaction pressure. By using these algorithms in the future, the time for tablet production would be shortened and costs would be reduced [19].

2.3 Minimization of Capping

Capping represents one of the most serious problems during the tableting process, which affects the quality of tablets and mechanical strength. This problem leads to separation of the upper part of a tablet from the rest, and it appears in the case when the intensity of the elastic relaxation becomes bigger than the strength of the interparticulate bonding during the compression process (Fig. 1). The main goal was to estimate the influence of particle size and process parameters on the tablet capping tendency. In the prediction of capping coefficient (CC), artificial neural networks (ANN's) and fuzzy models were used [20].

It is important that inputs to the model, which are representing the powder's properties, are fixed to the values of the current batch, so the manufacturer can find an optimal setting for the tableting machine. When the model represents how the effects of the powder properties and tableting machine's settings affect the CC, the results in the CC can be minimized. The main advantage of experiments for modeling purposes is that they can significantly shorten the time for optimizing the machine and reduce the number of faulty tablets. However, these experiments are more cost-effective than the ones for optimization with trial and error. They can improve these procedures but cannot completely replace them [20].

2.4 Scaling-up Granulation Process

It is known that the scale-up granulation process is easier to achieve by maintaining geometric, dynamic and kinematic similarity. Dynamic and kinematic properties can only be controlled by impeller speed, which will further determine the force and collision energy between granules. In one specific experiment, artificial intelligence tools were used to predict the endpoint of the granulation process in high-speed mixer granulators through adequate predictions of the impeller power (Fig. 1) [6].

Neuro-fuzzy logic was used to predict critical variables for every step of the process, while GEP was used to obtain a transparent model that could properly predict the impeller power values as a function of the diameter and speed of the impeller, the amount of granulation liquid and the characteristics of the wet mass. This experimental model has worked for granulators of similar and dissimilar shapes and sizes (PMA 25L, 100L, 600L) and can be improved by adding additional information about the process [6].

2.5 Quality Improvement of Ramipril Tablets

For this quality by design approach, the drug ramipril was selected. Different ANN programs were used to improve understanding of the correlation between critical quality attributes and overall quality of the final product. These programs include INForm V.4 ANN (for neural networks), FormRules V.3.32 (for neuro-fuzzy logic) and INForm V.4 GEP [19].

Because of ramipril tablet's complex formulation and production process, special attention is required during the wet granulation process [22].

In that study, two lubricant types were selected, magnesium stearate (MgSt), and sodium stearyl fumarate (SSF). They were used in a two-level hierarchical experimental design consisting of 16 experiments, evaluating the effects of two formulation variables and three process variables (drying temperature, moisture, and sieve size) on the quality of ramipril, which was subjected to wet granulation process in high shear mixer prior to direct compression [19, 20]. ANN and genetic algorithms (GA) have been used to optimize formulation parameters for ramipril tablets. The main goal of studies that are focused on the relationship between formulation and process parameters and drug quality is to optimize the formulation parameters for a certain drug. Optimization is important because after it is done researchers can be sure that formulation is within the design space [21].

Variations in process formulations are necessary during pharmaceutical production. The main goal of the study, based on previous research, which is a correlation between

ramipril process, formulation parameters, and drug quality, is to present the flexibility of post-approval changes on ramipril tablets. The same software tools were used as in previous studies. Different factors that can affect drug stability do not necessarily change it as long as they are within Design Space. Results have shown that industry could continue activities within the Design Space. Information in this study is obtained using neural networks program [22].

3 Conclusion

Benefits of artificial intelligence in the pharmaceutical industry increased over the years. Nowadays, multitude methods of this kind appeared and their usefulness is not negligible. Many machine learning techniques, used in this particular paper, have demonstrated how pharmaceutical manufacturing becomes less complex by applying them.

CI has shown an advantage over conventional techniques in predicting the outcome of any granulation process. ANN has presented the best result in twin-screw wet granulation optimization, whilst Cubist was leading in predicting the outcome of roll compaction.

When it comes to granulation and tablet production, AI models are capable not only to predict the potential problem but they can also find a suitable solution for it. In this study, it has been shown how different AI methods in completely diverse ways are able to manage anything assigned. Optimization of process parameters or formulation is of crucial importance, and AI methods can help us easily understand the correlation between these two. Using these models can both save time and money. Thus far, artificial intelligence does not have sufficient potential without the natural one of us-humans. Nevertheless, considering the velocity of machine learning and computational intelligence development, this might change in the near future.

Conflict of Interest Authors have no conflicts of interest to disclose.

References

1. Hessler, G., Baringhaus, K.-H.: Artificial intelligence in drug design. *Molecules* **23**(10), 2520 (2018)
2. Kazemi, P., Khalid, M.H., Gago, A.P., Kleinebudde, P., Jachowicz, R., Szłęk, J., et al.: Effect of roll compaction on granule size distribution of microcrystalline cellulose-mannitol mixtures: computational intelligence modeling and parametric analysis. *Drug Des. Dev. Ther.* **11**, 241–251 (2017)
3. Shabbir, J., Anwer, T.: Artificial intelligence and its role in the near future. *CoRR* **14**(8), 1–11 (2015)
4. Barrett, S., Langdon, W.: Advances in the application of machine learning techniques in drug discovery, design and development. *Appl. Soft Comput.* 99–110 (2006)

5. Kesavan, J.G., Peck, G.E.: Pharmaceutical granulation and tablet formulation using neural networks. *Pharm. Dev. Technol.* **1**(4), 391–404 (1996)
6. Landin, M.: Artificial intelligence tools for scaling up of high shear wet granulation process. *J. Pharm. Sci.* **106**(1), 273–277 (2017)
7. Aksu, B., Yegen, G., Purisa, S., Cevher, E., Ozsoy, Y.: Optimisation of ondansetron orally disintegrating tablets using artificial neural networks. *Trop. J. Pharm. Res.* **13**(9), 1374 (2014)
8. Parikh, D.: *Handbook of Pharmaceutical Granulation Technology*, pp. 7–10. Informa Healthcare USA, New York (2010)
9. Shirazian, S., Kuhs, M., Darwish, S., Croker, D., Walker, G.: Artificial neural network modelling of continuous wet granulation using a twin-screw extruder. *Int. J. Pharm.* **521**(1–2), 102–109 (2017)
10. Shanmugam, S.: Granulation techniques and technologies: recent progresses. *BioImpacts* **5**(1), 55–63 (2017)
11. Liu, H., Galbraith, S.C., Ricart, B., Stanton, C., Smith-Goettler, B., Verdi, L., et al.: Optimization of critical quality attributes in continuous twin-screw wet granulation via design space validated with pilot scale experimental data. *Int. J. Pharm.* **525**(1), 249–263 (2017)
12. Korteby, Y., Mahdi, Y., Azizou, A., Daoud, K., Regdon, G.: Implementation of artificial network as a PAT tool for the prediction of temperature distribution within a pharmaceutical fluidized bed granulator. *Eur. J. Pharm. Sci.* **88**, 219–232 (2016)
13. Petrović, J., Chansanroj, K., Meier, B., Ibrić, S., Betz, G.: Analysis of fluidized bed granulation process using conventional and novel modeling techniques. *Eur. J. Pharm. Sci.* **44**(3), 227–234 (2011)
14. Carter, A., Briens, L.: An application of deep learning to detect process upset during pharmaceutical manufacturing using passive acoustic emissions. *Int. J. Pharm.* **552**(1–2), 235–240 (2018)
15. Kleinebudde, P.: Roll compaction/dry granulation: pharmaceutical applications. *Eur. J. Pharm. Biopharm.* **58**(2), 317–326 (2004)
16. Rambali, B., Baer, L., Jans, E., Massart, D.: Influence of the roll compactor parameter settings and the compression pressure on the buccal bioadhesive tablet properties. *Int. J. Pharm.* **220**(1–2), 129–140 (2001)
17. Weyenberg, W., Vermeire, A., Vandervoort, J., Remon, J.P., Ludwig, A.: Effects of roller compaction settings on the preparation of bioadhesive granules and ocular minitables. *Eur. J. Pharm. Biopharm.* **59**(3), 527–536 (2005)
18. N. Souihi, M. Josefson, P. Tajarobi, B. Gururajan, J. Trygg. Design space estimation of the roller compaction process. *Ind. Eng. Chem. Res.* **52**(35), 12408–12419 (2013)
19. Zawbaa, H., Schiano, S., Perez-Gandarillas, L., Grosan, C., Michrafy, A., Wu, C.: Computational intelligence modeling of pharmaceutical tableting processes using bio-inspired optimization algorithms. *Adv. Powder Technol.* **29**(12), 2966–2977 (2018)
20. Belič, A., Škrjanc, I., Božič, D.Z., Karba, R., Vrečer, F.: Minimisation of the capping tendency by tableting process optimisation with the application of artificial neural networks and fuzzy models. *Eur. J. Pharm. Biopharm.* **73**(1), 172–178 (2009)
21. Aksu, B., Paradkar, A., de Matas, M., Özer, Ö., Güneri, T., York, P.: A quality by design approach using artificial intelligence techniques to control the critical quality attributes of ramipril tablets manufactured by wet granulation. *Pharm. Dev. Technol.* **18**(1), 236–245 (2016)
22. Aksu, B., Sezer, A.D., Yegen, G., Kuşçu, L.: QbD implementation in biotechnological product development studies. In: Chen, T., Chai, S. (eds.) *Special Topics in Drug Discovery*, 1st ed., pp. 133–155. InTechOpen (2016)

Lactose Intolerance Prediction Using Artificial Neural Networks

Lemana Spahić, Emir Šehović, Alem Šećerović, Zerina Đozić,
and Lejla Smajlović-Skenderagić

Abstract

An Artificial Neural Network for lactose intolerance prediction is presented in this paper. The system input information were symptom related questions and answers from a condition-oriented questionnaire, that was filled by one hundred individuals from Bosnia and Herzegovina. Participants were genotyped on LCT 13910 C/T and LCT 22018 G/A polymorphisms, which are reliable predictors of lactose tolerance/intolerance, and that information was the output of the neural network. The ANN consisted of 6 input parameters, that feed the Bayesian regulation training algorithm with information. ANN performance evaluation was performed with 10 samples out of 100 genotyped samples and the results predict whether a person is lactose tolerant or lactose intolerant. The aim of the artificial neural network presented in this paper is to assist specialists in lactose intolerance prediction, avoiding unnecessary further laboratory and genetic testing in clinical practice.

Keywords

Lactose intolerance • Artificial neural network • Genotype • Diagnosis • Prediction

1 Introduction

Lactose is a disaccharide that is found in all mammalian milks and is very important for nutrition of newborn and infants. In order to be digested, lactose has to be hydrolyzed by enzyme

lactase (*lactase-phlorizin hydrolase*, or LPH) into simple sugars, glucose and galactose [1, 2]. Lactase is a trans-membrane glycoprotein of the small intestinal brush border membrane of enterocytes [3, 4] coded, in humans, with LCT gene located on the chromosome 2 [5], long (q) arm at position 21.3. This gene is 49.3 kb in length, consisted of 17 exons and is translated into a 6 kb transcript [6].

Lactase digestive activity reaches its peak in the first few months of life and decreases after the age of two years [7]. Deficient or absent lactase enzymatic activity in the small intestine results in inability of organism to digest lactose from milk and other dairy products. This condition is called lactose intolerance. Besides the congenital lactase deficiency, which is a very rare condition inherited in an autosomal recessive manner [8], identified by total lactose intolerance already at infant age, there are three other types of lactose intolerance: primary, secondary, and developmental lactase deficiency [9–12]. Developmental lactase deficiency and reduced lactase activity is found in infants born before 34 weeks of gestation [10]. Gray was among the first scientists to describe secondary lactase deficiency [13]. Secondary lactase deficiency could occur as a consequence of small intestinal injuries, caused by many different factors such as infections, surgery, chemotherapy, celiac disease, gastroenteritis, prolonged use of antibiotics and other [11]. The most common type of lactose intolerance, which appears in adulthood, is in most of cases characterized with low lactase activity (hypolactasia) leading to primary lactase deficiency [12].

Primary lactase deficiency prevalence in adults differs worldwide, varying from less than 5% to almost 100% of population [14]. Study that included data from 89 countries (approximately 84% of the world's population) found that lactose intolerance is present in 19–37% of western, southern, and northern European population and in 57–83% of Middle East population [15].

Primary adult lactose intolerance is related to the absence of lactase persistence alleles, producing “lactase non-persistence” phenotype [16]. On the contrary, certain number of individuals keep neonatal levels of lactase enzymatic

L. Spahić · E. Šehović · A. Šećerović · Z. Đozić ·
L. Smajlović-Skenderagić (✉)
International Burch University, Genetics and Bioengineering,
Francuske revolucije bb, 71 210 Ilidža, Sarajevo, Bosnia and
Herzegovina
e-mail: l.smajlovic.skenderagic@ibu.edu.ba

L. Spahić
e-mail: lemanaspahic@stu.ibu.edu.ba

activity throughout the adulthood due to the presence of lactase related alleles, producing “lactase-persistence” phenotype. Except for some allelic differences (silent mutations), lactase persistent and lactase non-persistent groups of individuals have identical coding sequences [6]. Lactase persistence/non-persistence phenotypes are connected with few single nucleotide polymorphisms, whose respective frequencies vary across different world regions and ethnic groups [16]. The most investigated polymorphism associated with lactase persistence is LCT 13910*C/T (rs4988235), that is found to be in almost full concordance with LCT 22018*G/A (rs182549) polymorphism [17]. Both LCT-13910 CC and LCT22018 GG genotypes are strong predictors of lactase non-persistence [18].

In lactose intolerant individuals, non-digested lactose passes from the intestines to the colon, where it serves as a bacterial substrate. Depending on the amount of lactose ingested, people with lactose intolerance can, shortly after consumption of milk and dairy products, experience discomfort and pain as a manifestation of different gastrointestinal symptoms. The most common symptoms of lactose intolerance are diarrhea, bloating, flatulence, nausea, gut distension, and abdominal pain [19].

Lactose intolerance can be distinguished from other disorders by different diagnostic tests such as: lactose tolerance test, hydrogen breath test, stool acidity test (children) or by genetic testing. First three types of diagnostic tests require ingestion of certain amounts of lactose, which can cause discomfort and could be painful for the patients. Genetic testing of lactose intolerance associated lactase polymorphisms is not widely available [20].

Machine learning is a field in artificial intelligence and is one of the most rapidly developing subfields of artificial intelligence research. Machine learning enables highly proficient intelligent data analysis. The inexpensive and relatively easy methods developed within the last two decades for collecting and storing data also contributed to making machine learning procedures easier and more consistent. Since the beginning, machine learning was used and implemented within the medical field [21]. Many hospitals and clinics worldwide are monitoring and collecting data which can later be used for machine learning purposes. The machine learning methodology is most convenient for very specific diagnostic problems [22].

Approximations of explanations of certain processes can be considered as the essence of machine learning. Approximations generally do not and cannot explain the whole process, therefore usage of other algorithms would be more convenient. The machine learning process takes into account that the patterns observed within the existing dataset will not change within the future datasets regarding the same problem. In medicine, machine learning programs used for predictions of medical diagnosis are mostly based on

concrete biological and physical parameters [23, 24]. However, sometimes, as is the case here, a target condition and symptom-oriented questionnaire can be used for creating the machine learning system [25].

The fundamental basis of machine learning is the optimization of prediction performance by utilizing previously collected data or previously gained experience. The machine learning models can be classified into two groups: predictive and descriptive. The predictive model makes future estimates based on the collected data, while the descriptive model obtains knowledge from the data. Sometimes, both of the models can be implemented into a single model [22].

ANNs are trained in such a way that the optimal weighting and bias values are acquired in order to obtain the desired mapping or clustering of data. In this manner, ANNs can find relationship within and between datasets without defining the exact mathematical principle behind it. The connection between the neurons in a neural network is what defines its architecture. There are two types of architectures: feedforward and feedback [26–28].

This paper presents the development and feasibility of an ANN for Lactose intolerance prediction. This diagnostic tool can assist specialists in clinical practice to make the diagnostic process significantly faster by avoiding unnecessary lactose tolerance and genetic testing.

2 Materials and Methods

2.1 Dataset

The dataset used in the development of this neural network was based on symptoms reported in lactose intolerance related questionnaire and obtained LCT 13910 C/T and 22018 G/A genotypes. Study included 100 unrelated participants from Bosnia and Herzegovina. Genetic analysis was done using PCR-RFLP methodology proposed by Bulchoes et al. [29]. The restriction digestion products were analyzed using agarose gel electrophoresis. LCT 13910 and 22018 related genotypes were determined according to the size of the digestion products.

The specific questionnaire was designed in order to investigate the occurrence and severity of main lactose intolerance symptoms, and to analyze symptoms with respect to obtained LCT 13910 and 22018 genotypes and self-reported lactose tolerance.

The questions that showed most correlation to the genotypes were:

1. Do you have close family members who experience health problems after consuming milk or dairy products?
2. Do you feel discomfort after consuming milk or dairy products?

3. Do you feel nausea after consuming milk or dairy products?
4. Do you feel flatulence after consuming milk or dairy products?
5. Do you feel pain in your stomach after consuming milk or dairy products?
6. Do you have diarrhea after consuming milk or dairy products?

The abovementioned questions and the answers in form of symptom intensity were the only parameters used as inputs of ANN. Their inputs are defined in Fig. 1, with Q1–Q6 each indicating a question respectively.

The dataset consisted of 100 samples whose distribution is presented in Table 1.

2.2 Development of Artificial Neural Network

Feedforward neural network architecture was constructed as it is best suited for solving problems related to classification.

The data division, for the purposes of artificial neural network training, was done in a 90/10 ratio, as confirmed by various trials. In order to prevent overfitting and due to its usefulness in pattern recognition, Bayesian regularization training algorithm was used. For each training iteration the train/test performance was calculated as Mean Square Error between the actual and predicted values (MSE).

Most prominently used training functions were used to test the performance of ANN in order to choose the appropriate architecture for further development. As it can be seen from Table 2, best performance was observed using Bayesian regularization training algorithm (Trainbr) with 20

neurons in the hidden layer. Bayesian regularization is an algorithm most prominently used with datasets consisting of small number of samples and therefore it was expected to be the most suitable algorithm for this particular dataset [30].

After determining the most suitable training algorithm, the network was further tested with different combinations of transfer functions in the hidden layer (Table 3). As it can be inferred from Table 3, the best performance was achieved with 20 neurons in the hidden layer with Tansig transfer function in the hidden layer and Logsig transfer function in the output layer, which are the defaults in Bayesian regularization.

3 Results and Discussion

The final result of the evaluation suggests that the most suitable architecture for Artificial Neural Network for Lactose Intolerance prediction is the one with Bayesian regularization training algorithm, default transfer functions and 20 neurons in the hidden layer.

The final model consists of 6 neurons in the input layer of the network, one for each input parameter in form of 6 questions from the questionnaire. The architecture of the network continues with 20 neurons and Tansig transfer function in the hidden layer, ending with Logsig transfer function in the output layer. The output layer has only one neuron, with the final output of either 0 or 1, lactose tolerant or lactose intolerant respectively.

Subsequent validation was performed using 10 samples from the initial dataset, which makes 10% of the overall dataset. Evaluation of ANN performance through specificity, sensitivity and accuracy parameters is displayed in Table 4. Specificity is calculated as a number of correctly classified

Fig. 1 Architecture of ANN for lactose intolerance prediction

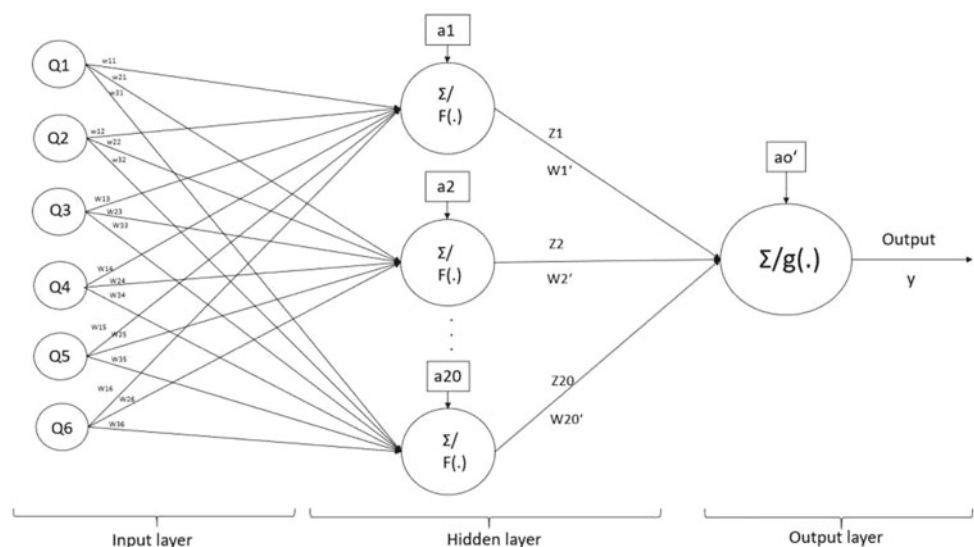


Table 1 Lactose tolerance dataset distribution

Training dataset		Subsequent validation dataset	
Sample group	Number of samples	Sample group	Number of samples
Lactose tolerant	50	Lactose tolerant	5
Lactose intolerant	40	Lactose intolerant	5
■	90	■	10

Table 2 ANN performance evaluation with different combinations of training algorithms and neuron numbers

Training algorithm	Number of neurons in hidden layer	ANN performance
Trainbr	5	3.9536 e-09
Trainbr	10	8.2886 e-09
Trainbr	20	9.9055 e-10
Trainbr	50	2.3298 e-09
Trainlm	5	0.0701
Trainlm	10	0.0719
Trainlm	20	0.0667
Trainlm	50	0.3767
Trainbfg	5	0.5468
Trainbfg	10	1.2571
Trainbfg	20	0.2979
Trainbfg	50	11.2636

Table 3 ANN performance evaluation with different transfer function combinations and different neuron numbers

Training algorithm	Number of neurons	Transfer functions	ANN performance
Trainbr	5	Tansig; logsig	3.9536 e-09
Trainbr	10	Tansig; logsig	8.2886 e-09
Trainbr	20	Tansig; logsig	9.9055 e-10
Trainbr	50	Tansig; logsig	2.3298 e-09
Trainbr	5	Purelin; purelin	0.0686
Trainbr	10	Purelin; purelin	0.0664
Trainbr	20	Purelin; purelin	0.0664
Trainbr	50	Purelin; purelin	0.0665
Trainbr	5	Logsig; logsig	0.0654
Trainbr	10	Logsig; logsig	0.0654
Trainbr	20	Logsig; logsig	0.0643
Trainbr	50	Logsig; logsig	0.0642

Table 4 Confusion matrix of subsequent validation dataset

	ANN		
	Lactose tolerant	Lactose intolerant	
Lactose tolerant	5	0	5
Lactose intolerant	0	5	5
	Specificity 100%	Sensitivity 100%	

Table 5 Confusion matrix for most of the k-folds of cross validation

	ANN		
	Lactose tolerant	Lactose intolerant	
Lactose tolerant	36	3	4
Lactose intolerant	4	47	6
	Specificity 92.3%	Sensitivity 92.2%	

samples of lactose tolerant group divided by the total number of lactose tolerant samples. Sensitivity is calculated as the number of correctly classified samples of lactose intolerant group divided by the total number of lactose intolerant samples. Accuracy is determined by the number of correctly classified samples divided by the total number of samples. All three analyzed parameters resulted with 100% for subsequent validation dataset, meaning that this neural network can correctly differentiate lactose tolerance and lactose intolerance.

k-fold cross validation method was implemented as an additional step in order to test the performance of ANN more thoroughly, according to the code presented in appendix. The dataset was subdivided into 10 classes for training and testing and the resulting accuracy varied slightly in multiple runs. The results obtained over trials of k-fold cross validation average to an accuracy level of 92.2% which is expected when taking the overall sample size into consideration. The most prominent resulting confusion matrix after cross validation is presented in Table 5.

4 Conclusion

An Artificial Neural Network for lactose intolerance prediction was presented in this paper. Training was done using 90 samples from a 100 samples dataset, 10 of which were used for subsequent validation. The ANN demonstrated very high specificity and sensitivity which indicates that successful and reliable ANNs based on Lactase non-persistence symptoms can be created.

Diagnosis of lactose intolerance is not a straightforward procedure and it usually involves analysis of initial symptoms and medical history combined with results of related biochemical and genetic testing. This ANN is an automatic diagnostic tool that is based solely on self-reported symptoms related to digestion of lactose. The final result is a tool, that if clinically optimized, is able to predict lactose intolerance without any laboratory testing.

Future perspectives of this work will include gathering more samples and performing LCT SNP related genotyping, which will further improve the scope of training parameters and enable the efficiency of the network when unexpected symptoms are reported. This work has the potential to be

used in healthcare and provide medical professionals with both time and cost-effective lactose intolerance diagnosis procedure.

References

1. Troelsen, J.T.: Adult-type hypolactasia and regulation of lactase expression. *Biochim. Biophys. Acta* **1723**, 19–32 (2005)
2. Rasinperä, H., Savilahti, E., Enattah, N.S., et al.: A genetic test which can be used to diagnose adult-type hypolactasia in children. *Gut* **53**, 1571–1576 (2004)
3. Danielsen, E.M., Skovbjerg, H., Norén, O., Sjöström, H.: Biosynthesis of intestinal microvillar proteins intracellular processing of lactase-phlorizin hydrolase. *Biochem. Biophys. Res. Commun.* **122**(1), 82–90 (1984)
4. Naim, H.Y., Sterchi, E.E., Lentze, M.J.: Biosynthesis and maturation of lactase-phlorizin hydrolase in the human small intestinal epithelial cells. *Biochem. J.* **241**(2), 427–434 (1987)
5. Kruse, T.A., Bolund, L., Grzeschik, K.H., Ropers, H.H., Sjöström, H., Noren, O., et al.: The human lactase-phlorizin hydrolase gene is located on chromosome 2. *FEBS Lett.* **240**(1–2), 123–126 (1988)
6. Boll, W., Wagner, P., Mantei, N.: Structure of the chromosomal gene and cDNAs coding for lactase-phlorizin hydrolase in humans with adult-type hypolactasia or persistence of lactase. *Am. J. Hum. Genet.* **48**(5), 889 (1991)
7. Troelsen, J.T., Olsen, J., Møller, J., Sjöström, H.: An upstream polymorphism associated with lactase persistence has increased enhancer activity. *Gastroenterology* **125**(6), 1686–1694 (2003)
8. Savilahti, E., Launiala, K., Kuitunen, P.: Congenital lactase deficiency. A clinical study on 16 patients. *Arch. Dis. Child.* **58**(4), 246–252 (1983)
9. Simoons, F.J.: Primary adult lactose intolerance and the milking habit: a problem in biologic and cultural interrelations. *Am. J. Dig. Dis.* **15**(8), 695710 (1970)
10. Antonowicz, I., Lebenthal, E.: Developmental pattern of small intestinal enterokinase and disaccharidase activities in the human fetus. *Gastroenterology* **72**(6), 1299–1303 (1977)
11. Heyman, M.B.: Lactose intolerance in infants, children, and adolescents. *Pediatrics* **118**(3), 1279–1286 (2006)
12. Vesa, T.H., Marteau, P., Korpela, R.: Lactose intolerance. *J. Am. Coll. Nutr.* **19**(sup2), 165S–175S (2000)
13. Gray, G.M., Walter, W.M., Colver, E.H.: Persistent deficiency of intestinal lactase in apparently cured tropical sprue. *Gastroenterology* **54**(4), 552–558 (1968)
14. Sahi, T.: Hypolactasia and lactase persistence historical review and the terminology. *Scand. J. Gastroenterol.* **29**(sup202), 1–6 (1994)
15. Storhaug, C.L., Fosse, S.K., Fadnes, L.T.: Country, regional, and global estimates for lactose malabsorption in adults: a systematic review and meta-analysis. *Lancet Gastroenterol. Hepato.* **2**(10), 738–746 (2017)
16. Kuokkanen, M., Enattah, N.S., Oksanen, A., Savilahti, E., Orpana, A., Järvelä, I.: Transcriptional regulation of the lactase-phlorizin

- hydrolase gene by polymorphisms associated with adult-type hypolactasia. *Gut* **52**(5), 647–652 (2003)
17. Mattar, R., Mazo, Carrilho.: Lactose intolerance: diagnosis, genetic, and clinical factors. *Clin. Exp. Gastroenterol* **113** (2012)
 18. Adler, G., Adler, M., Valjevac, A., Mackic-Djurovic, M., Kiseljakovic, E.: First Bosnian study of LCT -13910C > T and -22018G > A single nucleotide polymorphisms associated with adult-type lactose intolerance. *Folia Med. Fac. Med. Univ. Sarajevisis* **52**(1), 3–8 (2017)
 19. Wilt, T.J., Shaikat, A., Shamliyan, T., Taylor, B.C., MacDonald, R., Tacklind, J., et al.: Lactose intolerance and health. *Evid. Rep. Technol. Assess. (Full Rep.)* **192**(1), 410 (2010)
 20. Newcomer, A.D., McGill, D.B., Thomas, P.J., Hofmann, A.F.: Prospective comparison of indirect methods for detecting lactase deficiency. *N. Engl. J. Med.* **293**(24), 1232–1236 (1975)
 21. Michalski, R.S., Carbonell, J.G., Mitchell, T.M. (eds.): *Machine Learning: An Artificial Intelligence Approach*. Springer Science & Business Media (2013)
 22. Alpaydin, E.: *Introduction to Machine Learning*/Ethem Alpaydin (2010)
 23. Khan, J., Wei, J.S., Ringner, M., Saal, L.H., Ladanyi, M., Westermann, F., Meltzer, P.S.: Classification and diagnostic prediction of cancers using gene expression profiling and artificial neural networks. *Nat. Med.* **7**(6), 673 (2001)
 24. Baxt, W.G.: Use of an artificial neural network for data analysis in clinical decision making: the diagnosis of acute coronary occlusion. *Neural Comput.* **2**(4), 480489 (1990)
 25. Kononenko, I.: Machine learning for medical diagnosis: history, state of the art and perspective. *Artif. Intell. Med.* **23**(1), 89–109 (2001)
 26. Badnjevic A., Cifrek M., Koruga D.: Classification of chronic obstructive pulmonary disease (COPD) using integrated software suite. In: IFMBE XIII Mediterranean Conference on Medical and Biological Engineering and Computing (MEDICON), pp. 25–28. Sevilla, Spain (Sept 2013)
 27. Alic, B., Sejdinovic, D., Gurbeta, L., Badnjevic, A.: Classification of stress recognition using artificial neural network. In: IEEE MECO (2016)
 28. Alic, B., Gurbeta, L., Badnjevic, A., et.al.: Classification of metabolic syndrome patients using implemented expert system. In: CMBEBIH 2017. IFMBE Proceedings, vol 62, pp 601–607. Springer
 29. Bulhões, A., Goldani, H., Oliveira, F., Matte, U., Mazzuca, R., Silveira, T.: Correlation between lactose absorption and the C/T-13910 and G/A-22018 mutations of the lactase-phlorizin hydrolase (LCT) gene in adult-type hypolactasia. *Braz. J. Med. Biol. Res.* **40**(11), 1441–1446 (2007)
 30. Burden, F., Winkler, D.: Bayesian regularization of neural networks. In: *Artificial Neural Networks*, pp. 23–42. Humana Press (2008)

Comparative Study on Different Classification Techniques for Ovarian Cancer Detection

Jasna Nuhić, Lemana Spahić, Sabahudin Ćordić, and Jasmin Kevrić

Abstract

Diagnosing ovarian cancer is a medical challenge to clinical researchers. This study aims to develop a novel prototype of clinical management in diagnosis and management of patients with ovarian cancer. Various classification algorithms can be applied to cancer databases to devise methods that can predict cancer manifestation. Various methods, however, vary in terms of the level of accuracy, depending on the classification algorithm used. Identifying the most accurate classification algorithm is a challenging task, primarily due to limited data availability. In this paper, a comprehensive comparative analysis of nine different classification algorithms was conducted and their performances have been evaluated. The results indicate that all classifiers are relatively equal in accuracy, meaning that multiple classifying techniques can be used to support physicians in rendering more informed diagnostic decisions.

Keywords

Ovarian cancer • Classification • Machine learning • Attribute selection

1 Introduction

Cancer is malignancy and is caused by abnormal cell proliferation spreading to other tissue. It is not only a name for one particular disease but for a group of related diseases [1]. Cancer is not limited to a single location inside the body but starts as a grouping of mutated cells in a location in the body and spreads throughout it after those malignant cells multiply and enter the bloodstream. Another characteristic is that their cells are less specialized than normal cell due to their inability to mature into a cell type with specific function [2, 3].

Gene expression can be defined as the process by which a gene encoded by DNA is used for synthesis of a functional product that can be either a protein or some other functional product. Control of when and how often genes are expressed plays a crucial role in maintaining homeostasis in the organism [4].

Ovarian cancer accounts for 2.3% of all cancer deaths. In Europe, 65,538 new patients are diagnosed with ovarian cancer each year and 42,716, or 65%, end tragically [5]. In the United States of America, 22,440 women per year are diagnosed with ovarian cancer and 63% of patients die [6].

Diagnosing cancer is a very complex procedure that is susceptible to human and equipment error. First, a biopsy of problematic tissue is conducted and then it is subjected to cytological and molecular tests. These tests are performed in isolated environments in order to minimize potential errors, but errors can always happen [7]. The most effective way to reduce cancer deaths is to detect it earlier.

Rapid advancement of informational technology provided available and, in most cases, inexpensive devices to collect and store the data. In modern, well equipped, clinics data is gathered and shared in large information systems [8]. Nowadays, a vast number of clinical data and patient histories are available for ovarian cancer. With development of biomedical engineering, biomedical engineering researchers

J. Nuhić (✉)

Universitat Pompeu Fabra, Sarajevo,
Bosnia and Herzegovina
e-mail: jasna.nuhic01@estudiant.upf.edu

L. Spahić · S. Ćordić · J. Kevrić
International Burch University, Sarajevo,
Bosnia and Herzegovina
e-mail: lemana.spahic@stu.ibu.edu.ba

S. Ćordić
e-mail: sabahudin.cordic@stu.ibu.edu.ba

J. Kevrić
e-mail: jasmin.kevric@ibu.edu.ba

are examining the usage of machine learning techniques in supporting the diagnosis made by medical professionals.

Diagnosis is a relatively straightforward machine learning problem. In this process, a larger set of symptoms and conditions is considered for each patient in respect to classical diagnostic procedure, whereas medical professionals can consider only a limited number of parameters and give a diagnosis based on their interactions [9–11]. By using machine learning and data mining algorithms, medical professionals can establish better diagnoses, choose optimal medications for their patients, predict readmissions, identify patients at high-risk for poor outcomes, and in general improve patient's health while minimizing costs.

The realization of the complexity of certain decisions to treat particular diseases by scientists began 25 years ago when the importance of artificial intelligence became accentuated [12]. Use of data mining techniques will make diagnostic process more agile and also reduce health care costs and waiting times for the patients. The main advantage of using machine learning is the extraction of essential information from a large amount of data and its correlations [13].

Cancer is group of critical areas where classification has a crucial role and where data mining and machine learning are very powerful as tools in medical diagnosis. Therefore, machine learning techniques can help doctors make an accurate diagnosis of ovarian cancer and make the correct classification between cancerous and healthy tissue basing on gene expressions, as well as determining the cancer stage. The most important component in the diagnosis is evaluation of data taken from the patient and the specialist's decision, but artificial intelligence techniques provide support in rendering more informed decisions for medical professionals.

Ovarian cancer diagnosis prediction can be done by integrating big data and machine learning in order to aid prediction, diagnosis and therapy. Gene expression analysis performed by Millstein et al. identified 313 genes that are candidates for involvement in high grade ovarian cancer [14]. A support vector machine was used by Furey et al. to classify cancer tissue samples using gene expression microarrays and they found that most machine learning methods perform comparably on datasets utilized [15]. DNA methylation biomarkers were used as inputs of machine learning by Wei et al. and they have obtained significant results using various classification algorithms [16].

The major contributions of this paper are:

- comparison of different data mining algorithms on ovarian cancer datasets;
- identification of the best performing algorithm to predict ovarian cancer;
- extraction of useful, classified and accurate attributes for prediction of cancer;
- optimization of the task of correctly selecting the set of medical tests that a patient must perform to have the most accurate, the less expensive and time-consuming diagnosis possible;
- propose further investigation for the relevant genes determined in the paper to confirm their role in ovarian cancer detection; and
- obtain new discoveries in ovarian cancer mutation analysis.

This study's aim was to investigate different machine learning techniques. Several algorithms have been used and applied on the ovarian cancer dataset. The focus is on nine machine learning techniques: Naïve Bayes, Multilayer Perceptron, Simple Logistic, Nearest Neighbor, AdaBoost, Attribute Selected Classifier, Random Committee, PART, LMT and Random Forest. These various algorithms were tested using WEKA toolkit and their results analyzed.

2 Methods

2.1 Dataset

The Ovarian dataset used in this study was obtained from the Gene Expression Omnibus (GEO) database [17]. It consists of 148 samples of female patients. For each patient 83 gene expressions (attributes, features) were collected. Those gene expressions represent attributes, apart from the class attribute (patient having or not having ovarian cancer). Samples were taken invasively by biopsy of tissues of cancer suspicious patients. Gene expressions of those tissues were measured using qPCR, which is the gold standard for gene expression analysis [18, 19]. All diagnosis was performed and confirmed by medical professionals.

The number of samples corresponding to healthy and ovarian cancer groups is presented in Table 1. Of a total of 148 samples, 91 (i.e. 61.5%) had ovarian cancer while the remaining 57 (i.e. 38.5%) did not have ovarian cancer.

2.2 Classification Algorithms

Classification, or supervised learning, maps the data into predefined groups and classes. It is performed in two steps: model construction and model usage. Model construction is composed of a set of predetermined classes. The model is constructed by the training set. It is represented as classification rules, decision trees, or mathematical formulas [20].

Table 1 Data division of ovarian cancer database

Training dataset	
Classification group	Number of samples
Normal	57
Cancer	91
Σ	148

Attributes or unknown objects are classified by comparison of test sample with result from the model. In order to avoid over-fitting, the test set must be independent of the training set. The percentage of correctly classified test samples is known as the accuracy rate [20].

A total of nine classification algorithms were used in this comparative study and the Attribute Selected Classifier for attribute selection. The classifiers have been categorized into different groups such as Bayes, Functions, Lazy, Rules, Tree based classifiers, etc. A mix of algorithms have been chosen from these groups, according to the classification accuracy obtained. In order to obtain better and more robust accuracy, 10-fold cross validation was performed. The following sections briefly explain each of these algorithms.

(a) Naïve Bayes

The Naïve Bayes is widely used because of its clarity, elegance, and wholeness, which are reasons for its wide application range. It is combination of Naïve and Bayes, where Naïve stands for independence and Bayes for the Bayes rule. Independence assumes that the attributes are independent of each other [21].

Another assumption is that numeric attributes obey a Gaussian distribution, which is not always true. Therefore, sometimes other methods for estimating continuous distributions are preferred.

(b) Nearest Neighbor

Nearest Neighbor is a type of lazy learner classifiers with the main characteristic of storing instances during training. The learning process tends to be slow. The classification itself happens by a majority vote of its neighbours. Nearest Neighbour classifier proved to outperform many other classifiers in two-class problems [22].

(c) Multilayer Perceptron

Multilayer Perceptron (MLP) is a class of feed-forward artificial neural network (ANN) with one or more hidden layers between input and output layer. The advantage of such a structure is its ability to avoid overfitting and accomplish nonlinear multiple regressions reliably. MLP's

simple architecture can model most nonlinear problems while preserving low computational cost [21].

(d) Simple Logistic

Simple Logistic algorithm is a classifier for building linear logistic regression models that also copes quite well with overfitting. Simple logistic algorithms perform much better on dataset with small number of records. However, tree and ensemble tree classifiers can outperform it for larger datasets [21]. Such algorithms are explained further on.

(e) PART

PART is a type of rules classifiers and it uses the separate-and-conquer strategy to build a rule. By building a partial decision tree per iteration it does global optimization in order to produce accurate rule sets [22].

(f) LMT

LMT is a classifier from the decision trees group, used for building 'logistic model trees' (LMTs). LMTs are classification trees with logistic regression functions at the leaves. The LMT algorithm can deal with binary and multi-class target variables, numeric and nominal attributes and missing values. It ensures that only relevant attributes are included [23].

(g) AdaBoost

AdaBoost is a machine learning algorithm that is part of an ensemble methods called boosting where subsequent models attempt to fix the prediction errors made by prior models. It uses short decision tree models, called decision stumps since each has single decision point. The first model is normally constructed, but subsequent models are trained and added until no further improvements are possible [24].

(h) Random Committee

Random committee is form of ensemble learning approach. It is based on the assumption of improving performance by combining classifiers. Each classifier construction is denoted

by a different random number of seeds based on the same data. The output class is actually the average of predictions generated by each of these individual base classifiers [22].

(i) **Random Forest**

Random Forest is an ensemble of decision trees that consist of many decision trees. They are form of a nearest neighbor predictor with the output in terms of the mode of the class's output by individual trees. Random Forest usually yields fast and efficient models due to the possibility of usage without much modeling and handcrafting needed [22, 25].

(j) **Attribute Selected Classifier for Attribute Selection**

When Attribute Selected Classifier is used, the dimensionality of training and test data is reduced by attribute selection before being passed on to a classifier. That ability to select potentially relevant attributes is an essential data engineering component.

Three attribute selection systems used in this study are: locally produced correlation technique, wrapper method and Relief [26]. There are no restrictions for base classifiers.

Correlation based Feature Selection or CFS measures correlation between nominal attributes. It is an automatic algorithm that does not require specification of threshold or number of attributes to be selected. It is assumed that attributes are independent of each other, but strongly related to class. In case that attributes are dependent, there is great possibility for CFS to fail to select all the relevant attributes [25].

The two CFS algorithms used for attribute selection in this study are the CFS Subset Evaluation and the Correlation Attribute Selection. The CFS Subset Evaluation method evaluates the worth of a subset of attributes by considering the individual predictive ability of each attribute, as well as the degree of redundancy between them. The search method used for CFS Subset Evaluation method is Greedy Stepwise. It performs a greedy forward or backward search through the space of attribute subsets. Correlation Attribute Selection evaluation method reduces data by attributes selection before passing it on to a classifier. Search method used for it is Ranker. Ranker ranks attributes by their individual evaluations.

The Wrapper strategy uses an induction algorithm in order to estimate the merit of the attribute. Attribute wrappers are tuned to the specific interaction between an induction algorithm and its data. That makes them perform better than filters, but they tend to be much slower due to the re-run each time different induction algorithm is used [27].

3 Results and Discussion

For this study, 37 different classification algorithms were used to diagnose healthy and sick patients. The performance is defined as accuracy, which was determined as: (number of correctly classified samples)/(total number of samples) (Table 2).

For further application, the algorithms with best accuracy were chosen from each group of classifiers. From Bayes classification group, Naive Bayes classifier was chosen (with an accuracy of 89.25%). From the functions group, Multi-layer Perceptron and Simple Logistic classifiers were chosen (with an accuracy of 96.77%). From the Lazy group, Nearest Neighbor classifier was chosen (with an accuracy of 91.3978%). From META group, AdaBoost classifier (with an accuracy of 95.70%) and Random Committee classifier (with an accuracy of 93.55%) were chosen. From RULES group, PART classifier was chosen (with an accuracy of 91.40%). From the Tree group, LMT classifier (with an accuracy of 96.77%) and Random Forest classifier (with an accuracy of 95.67%) were chosen. No algorithm from MISC group is chosen due to its low accuracy. It should be noted that no more than two classifiers from one group were selected.

Table 3 compares and similar studies on ovarian cancer using different databases, but the same or similar algorithm. The performance is calculated by subtracting the result of another study from result obtained in this one. The positive performance indicates that this study outperformed the other, while negative indicate that it underperformed. Out of 13 comparisons, a positive result was obtained in 12 of them and one neutral. Nine of them were outperformed by 5 or more percent, which can be considered a significant difference. The case when it failed to outperform can be attributed to the difference between algorithms compared, since a genetic algorithm was not introduced in this study. Methodologically the most similar one is CV Parameter Selection, which was considered initially in testing phase for this study and later discarded due to its low accuracy.

Results with Attribute Selection

In order to extract relevant attributes, Attribute Selected Classifier was used. Three different evaluation methods were computed: Correlation-based Feature Selection (CFS) Subset Evaluation, Correlation Attribute Evaluation and Wrapper Subset Evaluation. All previously chosen classifiers were implemented as base classifier for each of evaluation methods. Different search methods were used, and pairs of evaluation and search methods are in Table 4.

Table 2 Accuracy results for classification algorithms

Classifying group	Classifying technique	Accuracy (%)
Bayes	Naïve Bayes	89.25
Functions	Multilayer perceptron	96.77
	Simple logistic	96.77
Lazy	Nearest neighbor	91.40
Meta	AdaBoost	95.70
	Random committee	93.55
Rules	PART	91.40
Trees	LMT	96.78
	Random forest	95.67

Table 3 Studies employing similar machine learning methodologies

Dataset	Results (x)	Results of this study (y)	y - x (%)
Extrauterine pelvic mass samples (biopsy) [28]	ANN sensitivity → 87.5%	MLP sensitivity → 96.7%	9.2
	ANN specificity → 92.7%	MLP specificity → 96.8%	4.2
	Small Naïve Bayes sensitivity → 94.7%	Naïve Bayes sensitivity → 100%	5.3
	Small Naïve Bayes specificity → 74.1%	Naïve Bayes specificity → 84.1%	10
	Large Naïve Bayes sensitivity → 96.6%	Naïve Bayes sensitivity → 100%	3.4
	Large Naïve Bayes specificity → 79.9%	Naïve Bayes specificity → 84.1%	4.2
Ultrasound description of adnexal pathology [29]	Logistic regression1 sensitivity → 92%	Simple logistic sensitivity → 97%	5
	Logistic regression1 specificity → 87%	Simple logistic specificity → 97%	10
	Logistic regression2 sensitivity → 92%	Simple logistic sensitivity → 97%	5
	Logistic regression1 specificity → 86%	Simple logistic specificity → 97%	11
Tumor markers and lipid associated sialic acid [30]	Multilayer perceptron accuracy → 90%	Multilayer perceptron accuracy → 97%	7
Gene expression profiling [31]	k-nearest neighbor accuracy → 71%	IBk accuracy → 91%	20
Proteomic spectrum data [32]	Genetic algorithm accuracy → 99%	CV parameter selection accuracy → 68%	-31

Table 4 Attribute selection evaluation and search method pairs

Attribute selection	
Evaluation method	Search method
CFS subset evaluation	Greedy stepwise
Correlation attribute evaluation	Ranker
Wrapper subset evaluation	Best first

In CFS Subset Evaluation and Correlation Attribute Evaluation methods, the same attributes were selected for each base classifier. Selected Classifiers are shown in Table 5. As we can see in Table 4, both methods selected 18 attributes. Out of those 36 selected attributes, genes 22, 23, 24, 30, 58 and 76 (the six of them), were selected by both methods, so there are 30 different relevant attributes according to CFS Subset Evaluation and Correlation Attribute Evaluation methods.

Accuracy of base classifiers applied for the CFS Subset Evaluation and Correlation Attribute Evaluation methods are shown in Table 6. For CFS Subset Evaluation method, the most successful were Nearest Neighbor and Random Forest classifiers with an accuracy of 94.6237%, while for Correlation Attribute Evaluation method AdaBoost was the best performing classifier with an accuracy of 95.6989%.

In the Wrapper Subset Evaluation method, different attributes were selected for each base classifier. Due to the space limitations, the selected classifiers are not presented in tabulated format, while their accuracy can be found in Table 6. The wrapper methods combined with different base classifiers gave different numbers of selected attributes each time performed. There are 30 different attributes selected at least once. Out of those 30 selected attributes genes 23 and 30, namely GYG1p1 and GSK3Bp3, were selected by five different base classifiers, which is the best result.

Four attributes were selected by all three methods, so they are the most relevant attributes for ovarian cancer classification. Those attributes are 22, 23, 24 and 30.

The genes selected by most machine learning techniques were: CALM 1/2/3, GYG1p1, PHKG2p3 and GSK3Bp3. The CALM gene (Calmodulin) encodes for calcium binding proteins that are subunits of phosphorylase kinase, meaning that they are included in cellular signaling [33–35]. GYG1p1 (Glycogenin 1) gene codes for proteins involved in glycosyltransferase that is a catalyst and involved in signaling [36]. PHKG2p3 (Phosphorylase Kinase catalytic subunit Gamma 2) is a gene coding for protein involved in glycogen storage and kinase activity and some variants are overexpressed in cancer [37]. GSK3Bp3 (Glycogen synthase kinase 3 beta) is an enzyme that catalyzes phosphorylation and is found to be upregulated in cancer [38].

4 Conclusion

In this study, nine classification techniques, namely Naïve Bayes, Multilayer Perceptron, Simple Logistic, Nearest Neighbor, AdaBoost, Random Committee, PART, LMT, and Random Forest were used to evaluate the percentage of accuracy, with and without attribute selection, for effective prediction techniques for ovarian cancer diagnostics.

Table 5 Results of attribute selection of CFS subset evaluation and correlation attribute evaluation methods for ovarian cancer database

Evaluator	Selected attributes																	
CF subset evaluator	10	16	17	22	23	24	30	33	35	36	39	41	58	62	68	76	77	82
Correlation attribute evaluator	4	3	21	79	22	24	58	5	30	80	23	76	20	25	56	54	26	19

Table 6 Attribute selection and simple classification results

Classifier	Accuracy (%)			
	CFS subset evaluation	Correlation attribute evaluation	Wrapper subset evaluation	No attribute selection
Naïve Bayes	89.25	87.10	89.25	89.25
Multilayer perceptron	92.47	82.80	93.55	96.77
Simple logistic	88.17	86.02	87.1	96.77
Nearest neighbor	94.62	93.55	97.85	91.40
AdaBoost	92.47	95.70	87.10	95.70
Random committee	92.47	90.32	89.25	93.55
PART	92.47	90.32	92.48	91.40
LMT	91.40	87.10	93.55	96.78
Random forest	94.62	93.55	91.4	95.67

In order to achieve the aforementioned objective, an ovarian cancer dataset was utilized. The attribute selection techniques were used to eliminate those attributes that have no significance in the classification process. Therefore, attribute selection technique is the most reliable and the most significant method to improve the accuracy of different classification techniques.

In this study, classification rules were compared to predict the best classifier to develop a new prototype for diagnosis with a predictable pattern for discovery of ovarian cancer. Experimental results show the effectiveness of the proposed method. The base for this is knowledge discovery and data mining. A classifier was identified to determine the nature of the disease, which is highly important for differentiating between healthy and ovarian cancer patients. When compared with previous similar studies using different databases, it clearly shows precedence of the use of GEO database. This study is useful in uncovering patterns hidden in the data that can help the clinicians and doctors in decision making.

All of the mentioned genes are members of signaling cascades and their mutation or dysfunction consequently leads to cancer development. Considering the fact that these genes have been determined as relevant by machine learning in this study can lead to further investigation from a biological perspective and experiments that would confirm the prediction. Not only would a positive outcome prove the efficacy of the used ML but could also lead to new discoveries in ovarian cancer mutation analysis.

References

- Moses, H.L., Nass, S.J. (eds.): *Cancer Biomarkers: The Promises and Challenges of Improving Detection and Treatment*. National Academies Press (2007)
- Kufe, D.W., Pollock, R.E., Weichselbaum, R.R., Bast, R.C., Gansler, T.S.: *Holland-Frei Cancer Medicine*. BC Decker Inc (2003)
- Frank, S.A.: *Dynamics of Cancer: Incidence, Inheritance, and Evolution*. Princeton University Press (2007)
- Watson, J.D., Baker, T., Bell, S., Gann, A., Levine, M., Losick, R.: *Molecular Biology of the Gene*. Pearson/Benjamin Cummings (2003)
- EUCAN Factsheets | Ovarian Cancer. Eco.iarc.fr. Retrieved 10 June 2017, from <http://eco.iarc.fr/eucan/CancerOne.aspx?Cancer=27&Gender=2> (2017)
- What Are the Key Statistics About Ovarian Cancer. Cancer.org. Retrieved 14 June 2017, from <https://www.cancer.org/cancer/ovarian-cancer/about/key-statistics.html> (2017)
- Schmidt, U., Begley, C.G.: Cancer diagnosis and microarrays. *Int. J. Biochem. Cell Biol.* **35**(2), 119–124 (2003)
- Sivagami, P.: Supervised learning approach for breast cancer classification. *Int. J. Emerg. Trends Technol. Comput. Sci.* **1**(4) (2012)
- Ghaheri, S. Shoar, M. Naderan, Hoseini, S.S.: The applications of genetic algorithms in medicine. *Oman Med. J.* **30**(6), 406 (2015)
- Fagella.: *7 Applications of Machine Learning in Pharma and Medicine*. Available at <https://goo.gl/1SIR5k> (2017)
- Magoulas, G.D., Prentza, A.: Machine learning in medical applications. In: *Machine Learning and Its Applications*. Springer, Berlin Heidelberg, pp. 300–307 (2001)
- Aloraini, A.: Different machine learning algorithms for breast cancer diagnosis. *Int. J. Artif. Intell. Appl.* **3**(6), 21 (2012)
- Bin Othman, M.F., Yau, T.M.S.: Comparison of different classification techniques using WEKA for breast cancer. In: *3rd Kuala Lumpur International Conference on Biomedical Engineering 2006*, pp. 520–523. Springer, Berlin, Heidelberg (2007)
- Millstein, J., Budden, T., Anglesio, M., Talhouk, A., Beeghly-Fadiel, A., Berchuck, A., Garcia, M.: A gene expression prognostic signature for overall survival in patients with high-grade serous ovarian cancer (2018)
- Furey, T.S., Cristianini, N., Duffy, N., Bednarski, D.W., Schummer, M., Haussler, D.: Support vector machine classification and validation of cancer tissue samples using microarray expression data. *Bioinformatics* **16**(10), 906–914 (2000)
- Wei, S.H., Balch, C., Paik, H.H., Kim, Y.S., Baldwin, R.L., Liyanarachchi, S., Karlan, B.Y.: Prognostic DNA methylation biomarkers in ovarian cancer. *Clin. Cancer Res.* **12**(9), 2788–2794 (2006)
- Shen, L., Zeng, Q., Guo, P., Huang, J., Li, C., Pan, T., Huang, T.: Dynamically prognosticating patients with hepatocellular carcinoma through survival paths mapping based on time-series data. *Nat. Commun.* **9**(1), 2230 (2018)
- VanGuilder, H.D., Vrana, K.E., Freeman, W.M.: Twenty-five years of quantitative PCR for gene expression analysis. *Biotechniques* **44**(5), 619–626 (2008)
- Derveaux, S., Vandessompele, J., Hellemans, J.: How to do successful gene expression analysis using real-time PCR. *Methods* **50**(4), 227–230 (2010)
- Aher, S.B., Lobo, L.M.R.J. Data mining in educational system using weka. In: *International Conference on Emerging Technology Trends (ICETT)*, vol. 3, pp. 20–25 (Mar 2011)
- Kumar, Y., Sahoo, G.: Analysis of Bayes, neural network and tree classifier of classification technique in data mining using WEKA (2012)
- Chetty, G., White, M., Akther, F.: Smart-phone-based data mining for human activity recognition. *Procedia Comput. Sci.* **46**, 1181–1187 (2015)
- Landwehr, N., Hall, M., Frank, E.: Logistic model trees. *Mach. Learn.* **59**(1–2), 161–205 (2005)
- Freund, Y., Schapire, R. E. (1996, July). Experiments with a new boosting algorithm. In *Icml* (Vol. 96, pp. 148–156)
- Nookala, G.K.M., Pottumuthu, B.K., Orsu, N., Mudunuri, S.B.: Performance analysis and evaluation of different data mining algorithms used for cancer classification. *Int. J. Adv. Res. Artif. Intell.* **2**(5), 49–55 (2013)
- Witten, I.H., Frank, E., Trigg, L.E., Hall, M.A., Holmes, G., Cunningham, S.J.: *Weka: practical machine learning tools and techniques with Java implementations* (1999)
- Kohavi, R., Gh, John: Wrappers for feature subset selection. *Artif. Intell.* **97**(1–2), 273–324 (1997)
- Antal, P., Verrelst, H., Timmerman, D., Moreau, Y., Van Huffel, S., De Moor, B., Vergote, I.: Bayesian networks in ovarian cancer diagnosis: potentials and limitations. In: *Computer-Based Medical Systems, CBMS 2000. Proceedings of 13th IEEE Symposium*, pp. 103–108. IEEE (2000)
- Kaijser, J., Bourne, T., Valentin, L., Sayasneh, A., Van Holsbeke, C., Vergote, I., Timmerman, D.: Improving strategies for diagnosing ovarian cancer: a summary of the International Ovarian Tumor Analysis (IOTA) studies. *Ultrasound Obstet. Gynecol.* **41** (1), 9–20 (2013)

30. Zhang, Z., Zhang, H., Bast, R.C.: An application of artificial neural networks in ovarian cancer early detection. In: Neural Networks, IJCNN 2000. Proceedings of the IEEE-INNS-ENNS International Joint Conference, vol. 4, pp. 107–112. IEEE (2000)
31. Ben-Dor, A., Bruhn, L., Friedman, N., Nachman, I., Schummer, M., Yakhini, Z.: Tissue classification with gene expression profiles. *J. Comput. Biol.* **7**(3–4), 559–583 (2000)
32. Stevens, E.V., Liotta, L.A., Kohn, E.C.: Proteomic analysis for early detection of ovarian cancer: a realistic approach? *Int. J. Gynecol. Cancer* **13**, 133–139 (2003)
33. CALM1 calmodulin 1 [Homo sapiens (human)]. Retrieved from <https://www.ncbi.nlm.nih.gov/gene/801> (2018)
34. CALM2 calmodulin 2 [Homo sapiens (human)]. Retrieved from <https://www.ncbi.nlm.nih.gov/gene/805>
35. CALM3 calmodulin 3 [Homo sapiens (human)]. Retrieved from <https://www.ncbi.nlm.nih.gov/gene/808> (2018)
36. GSK3B glycogen synthase kinase 3 beta [Homo sapiens (human)]. Retrieved from <https://www.ncbi.nlm.nih.gov/gene/2932> (2018)
37. PHKG2 phosphorylase kinase catalytic subunit gamma 2 [Homo sapiens (human)]. Retrieved from <https://www.ncbi.nlm.nih.gov/gene/5261> (2018)
38. GYG1 glycogenin 1 [Homo sapiens (human)]. Retrieved from <https://www.ncbi.nlm.nih.gov/gene/2992> (2018)

Normalized Neural Networks for Breast Cancer Classification

Emina Alickovic and Abdulhamit Subasi

Abstract

In almost all parts of the world, breast cancer is one of the major causes of death among women. But at the same time, it is one of the most curable cancers if it is diagnosed at early stage. This paper tries to find a model that diagnose and classify breast cancer with high accuracy and help to both patients and doctors in the future. Here we develop a model using Normalized Multi Layer Perceptron Neural Network to classify breast cancer with high accuracy. The results achieved is very good (accuracy is 99.27%). It is very promising result compared to previous researches where Artificial Neural Networks were used. As benchmark test, Breast Cancer Wisconsin (Original) was used.

Keywords

Breast cancer diagnosis • Supervised learning • Normalized neural networks • Multi layer perceptron • Breast cancer Wisconsin

1 Introduction

Cancer is a set of illnesses where body cells grow, alter, and multiply without control. As a rule, name of the cancer comes from the part of the body where it originated. Due to this, breast cancer refers to the unpredictable and often fast enlargement of cells that begin in the breast tissue. A cluster of rapidly separating cells may form a mass of extra tissue, called tumors. Tumors can either be cancerous (malignant)

or non-cancerous (benign). Malignant tumors travel through healthy body tissues and destroy them.

The term, breast cancer, refers to a malignant tumor that has developed from cells in the breast. It is the most common cancer among women in almost all parts of the world. But if it is discovered in the earlier stages, chance to cure it are very high. According to statistics, early stage detection and treatment results in a 98% survival rate but if it is detected in metastases this plummets to 27% [1].

In reality, one in eight women in the USA might expect to develop breast cancer during the life time [2]. Although in Bosnia and Herzegovina we do not have single register at government level, according to the reports of cantonal health care and hospital registers, breast cancer is the most common malign illness in our country [3]. Therefore, there is great need to develop a technique that will diagnose and classify breast cancer with high accuracy.

Till now, several different techniques have been used for breast cancer diagnosis. One of the most widely used techniques is mammography, but in literature, radiologists show significant differences in interpreting it [4]. Another widely used technique is Fine Needle Aspiration Cytology (FNAC) but its bad side is its modest accuracy rate (around 90%). Therefore, there is a need to develop another technique that will provide better performance for classification of breast cancer. The response to this need is usage of statistical techniques and artificial intelligence techniques. Here we define all data into two groups, either benign (that does not have cancer) or malignant group (strong evidence of having breast cancer). Due to this reason, breast cancer diagnosis can be discussed as classification problem [5–8].

Many researchers used different statistical and artificial intelligence techniques to predict and classify breast cancer techniques. Karabatak and Ince [9] used association rules and neural network to classify breast cancer pattern and they achieved the highest accuracy of 97.4%. Quinlan [10] used 10-fold cross-validation with the C4.5 decision tree method to reach accuracy of 94.74%. Goodman [11] used three different methods, optimized learning vector quantization

E. Alickovic
Department of Electrical Engineering, Linkoping University,
58183 Linkoping, Sweden
e-mail: emina.alickovic@liu.se

A. Subasi (✉)
Department of Information Systems, College of Engineering,
Effat University, Jeddah 21478, Saudi Arabia
e-mail: absubasi@effatuniversity.edu.sa

(LVQ), big LVQ, and artificial immune recognition system (AIRS) to obtained accuracies of 96.7, 96.8, and 97.2%, respectively. Setiono [12] used feed forward neural network rule extraction algorithm to obtain accuracy of 98.1%. Abbas [13] used Memetic Pareto ANN (MPANN) to achieve accuracy of 98%. Aličković and Subasi [14] employed genetic algorithms in order to eliminate insignificant features. Besides they used different data mining techniques for breast cancer detection. They obtained the highest classification accuracy using the Rotation Forest model with GA-based 14 features.

Artificial Neural Networks (ANNs) are computational models consisted of set of interconnected units called neurons. It is inspired by biological neural system, although functions of ANNs might be quite different from biological neural systems. Many researches on medical diagnosis of breast cancer with Wisconsin breast cancer dataset have been done by using Artificial Neural Networks (ANNs) in recent years, and most of these researches reported high classification accuracy.

In this research, we propose normalized Multi Layer Perceptron (MLP) neural network to classify types of breast cancer. This method consists of two stages. In the first stage, we normalized our dataset and then in the second stage we used Multi Layer Perceptron for classification. We use Wisconsin breast cancer (Original) dataset as benchmark test.

This paper is organized as follows. In Sect. 2, we give description of dataset used. In Sect. 3, theoretical background about Artificial Neural Networks, Multilayer Perceptron and Normalization is explained. In Sect. 4 we present out experimental results. In Sect. 5, we give final conclusion and possible future improvements.

2 Wisconsin Breast Cancer Database Overview

Breast cancer is one of the most spread cancers among women. Based on rates from 2005–2007, one in eight women is affected by this cancer during their lifetimes [15]. Breast cancer can also occur in man, although it is not that common. Although some of the risks such as aging, genetic risk factors, family history, menstrual periods, not having children, obesity, etc. that increase chances for development of breast cancer are known, it is not known how these risk factors causes cells to become cancerous. Many researches are being done currently to answer this question and understanding how certain alterations in DNA can cause normal breast cells to develop into cancerous is in a great progress [9].

Performance is evaluated based on the model using the Wisconsin breast cancer dataset (Original) to classify the types of breast cancer as either benign or malignant. This

dataset contains nine features summarized in Table 1 and each of these features is represented by some number between 1 and 10. These data is collected by Dr. William H. Wolberg at the University of Wisconsin—Madison and this dataset can be found on UCI Machine Learning Repository. Hospitals and it contains 699 records taken from 699 different persons and 241 (65.5%) records are malignant and 458 (34.5%) records are benign. Out of these 699 records, it contains 16 instances with missing attribute values. We tested out proposed method on set containing 683 data to prove efficiency of our method.

3 Theoretical Background

3.1 Artificial Neural Networks (ANNs)

ANN is an attempt to model information processing capabilities of nervous systems. It is a set of interconnected simple computation units called neurons. Link connecting neurons have weights. It performs useful computations through a process of learning, function that modifies these weights of the network to achieve desired high performances. The output of each neuron is computed by using an activation function such as sigmoid and step. ANNs are trained by experience, when applied an unknown input to the network it can generalize from past experiences and give new result [16–18]. There is an art when we design neural network because we need to pay attention to many parameters. When we design ANN, we first need to decide about ANN model, then we need to decide about number of layers and then about the number of neurons in each layer.

3.2 Multi Layer Perceptron (MLP)

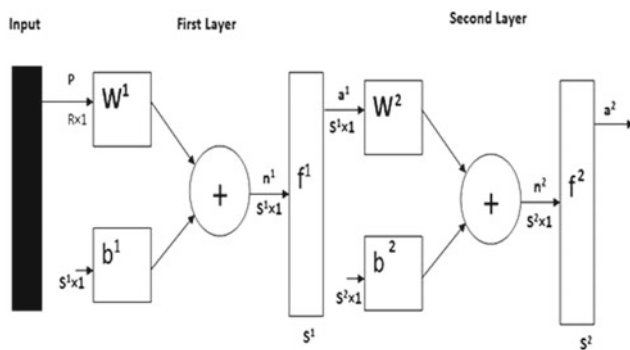
Multi Layer Perceptron is a neural networks consisting of input layer, one or more hidden layers and output layer. It is one of most widely used supervised learning neural network architecture. The input signal travels from beginning to end of the network in forward direction. So, for MLP networks, output of one layer is applied to be input of the following layer. Figure 1 illustrates the architecture of MLP. The output of the MLP network is given in Eq. (1), where M is the number of the layers in the network. MLPs have been applied to solve many diverse problems with high efficiency by training them in a supervised manner using error back propagation algorithm [18].

$$a_m^{m+1} = f_m^{m+1}(W_m^{m+1}a_m^m + b_m^{m+1}); m = 1, \dots, M-1 \quad (1)$$

Back propagation algorithm is a learning that consists of two passes (forward and backward pass) through an entire

Table 1 MLP architecture and training parameters

Architecture	
The number of layers	3
The number of neuron on the layers	Input: 9
	Hidden layer: 5
	Output layer: 1
The initial weights and biases	Random
Activation functions	Linear
Training parameters	
Learning rule	Levenberg–Marquardt
	Back propagation
Performance	0.01
Momentum	0.6
Learning Rate	0.2
Maximum number of epochs	100

**Fig. 1** Two-layer MLP network where P is an input vector, W is the weight vector, S1 and S2 are the number of neurons in the first and second Layer respectively, a is the output of the layer and f is transfer function

network. In the forward pass, input vector is applied to sensory nodes and as output it produces the actual response of the network. In this step, weights are all fixed. In the backward pass, the weights are adjusted in accordance with an error-correction rule. Error signal is produced by subtracting network response from a target (desired) response and this error signal is propagated through the network. Weights are adjusted to make network response close to desired response as much as possible [18].

3.3 Normalization

Training of ANNs could be made more proficient if particular preprocessing steps on the network inputs and targets are done. Network input processing functions converts inputs into a structure more appropriate for the network usage. The normalization process for the raw inputs has

large impact on data preparation to be more fitting for the training. If normalization was not used, training of the ANNs would have been very time-consuming. There are several different types of data normalization. Data minimization can be used to scale data in the same range, so each input attribute has minimized bias within ANN. It can also accelerate training time by starting the training process for all attributes within the equal range. Different techniques use different rules such as min max rule, sum rule, product rule, etc. [19]. In this paper, we will discuss two different normalization techniques: Min-Max Normalization and Mean and Standard Deviation Normalization.

- (a) *Min Max Normalization*: this method rescales attributes from one range to another. Often, features are rescaled to be in range [0 1] or [-1 1]. It is accomplished by using linear interpretation formulas such as Eq. (1).

$$x' = (x_{\max} - x_{\min}) \times \frac{(x_i - x_{\min})}{(x_{\max} - x_{\min})} + x_{\min} \quad (2)$$

When min-max normalization is applied, all attributes will be within the same new range. Good side of this normalization is preserving exactly all relationships in the data [19].

- (b) *Mean and Standard Deviation Normalization*: Another approach is to normalize mean and standard deviation of the training set. It normalizes inputs and targets in such a way that they will have zero mean and unity standard deviation. After training set is pre-processed by using normalization, then these new inputs are used to train network.

4 Experimental Results

In this section, evaluation of performance of our proposed model was done on Wisconsin breast cancer (Original) dataset. As it was already mentioned, this data set contains 699 records with 16 records having missing data. Our proposed model is given in Fig. 2.

As it can be seen in Fig. 2, we first normalized out training data using Mean and Standard Deviation Technique. Then this normalized data was used to improve Multi Layer Perceptron NN performances. By using Normalization technique together with Neural Networks, we developed a technique that is able to classify breast cancer types with very high accuracy rate. It is worth of mentioning here that we achieved significant improvement for classification by using first normalization and then MLP.

Simulation has been made by using MATLAB 2008. A variety of networks were developed and tested with random initial weights. The network is trained one hundred times. 80–20% was used. Eighty percent of records (546 records) were used for training and twenty percent of records (137 records) were used for testing. The training data set are used for learning the breast cancer pattern and then generate the decision rule(s). The testing data set which have not been used to train the system that are used to test the results.

Experimental results are taken as average of 100 runs and measured in term of classification accuracy Training parameters that gave us the highest accuracy can be seen in Table 1. While making experiments, different values of

parameters were used, and the results achieved can be seen in Table 2. As we can see from table two, the most important impact on performances of our system is the choice of transfer function. If we used any other function except linear, or combination of linear and other function. Accuracy rate is very poor. In average, it is around 75%. But, if we use linear transfer function, accuracy rate is extremely high. It is 99.27%, and this is one of the highest accuracies achieved in researches by using Artificial Neural Networks. So, by first normalizing data in preprocessing stage and after that using a linear transfer function we achieved improvement of classification rate for around 32%, what is a very significant improvement. From this we can see that the choice of appropriate function is crucial and the most important factor for correct classification of breast cancer records. When we used transfer functions other then only linear and change other parameters such as learning rate or momentum, we got certain change in average accuracy, but very small and accuracy achieved was very low. This can also be seen in Table 2.

After we selected only linear function for transfer function, we got enormous improvement in accuracy, 99.27%. So, from here we can conclude that although we select different values for training parameters, the most important factor is transfer function and as transfer function, we need to use only pure linear transfer functions in order to get the highest accuracy.

The results obtained in this research have been compared to results obtained by using neural networks from previous

Table 2 Classification accuracy obtained with proposed method using different parameters

Number of neurons in the layers	Transfer functions	Learning rate	Momentum	Training function	Number of epochs	Accuracy (%)
20–20–1	tansig–tansig–purelin	0.2	0.6	tarinlm	10	75.31
20–20–1	tansig–tansig–purelin	0.2	0.6	tarinlm	100	75.01
20–20–1	tansig–tansig–purelin	0.15	0.5	tarinlm	100	75.27
20–20–1	tansig–tansig–purelin	0.1	0.6	tarinrp	100	75.19
20–20–1	logsig–tansig–purelin	0.1	0.6	taringdm	50	73.36
20–20–1	logsig–tansig–purelin	0.2	0.6	tarinlm	50	75.26
20–1	logsig–purelin	0.2	0.6	tarinlm	50	75.79
20–1	tansig–logsig	0.15	0.6	tarinlm	50	75.18
20–1	tansig–purelin	0.15	0.5	tarinlm	50	75.36
20–1	purelin–tansig	0.15	0.6	taringdm	100	75.18
10–5–1	tansig–tansig–purelin	0.1	0.6	tarinlm	100	75.19
10–1	logsig–tansig–purelin	0.1	0.5	tarinrp	100	75.19
20–20–1	purelin–purelin–purelin	0.2	0.6	tarinlm	100	99.27
10–1	purelin–purelin	0.1	0.5	taringm	100	99.27
10–1	purelin–purelin	0.2	0.6	taringdm	50	99.27
10–1	purelin–purelin	0.2	0.6	tarinlm	50	99.27

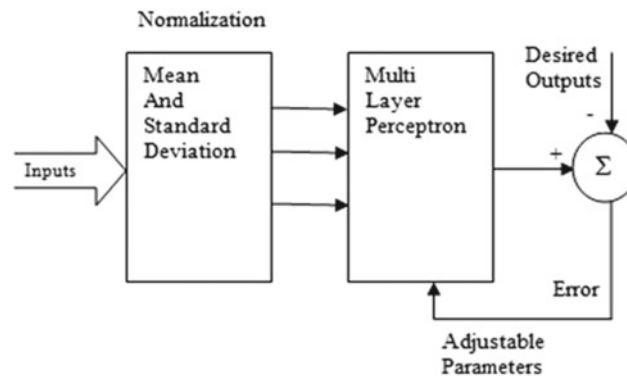


Fig. 2 Block diagram of proposed system for classification of breast cancer types

Table 3 Classification accuracy obtained with proposed method and classification accuracies obtained using neural networks in previous researches

Reference	Technique	Accuracy (%)
<i>Proposed method</i>	<i>Normalized multi layer perceptron</i>	99.27
Ubeyli [22]	Multilayer perceptron neural networks	91.92
Karabatak and Ince [9]	Association rules and neural networks	97.4
Setiono [12]	Feed forward neural network rule extraction algorithm	98.1
Ubeyli [22]	Recurrent neural network	98.15
Ubeyli [22]	Probabilistic neural network	98.61
Albrecht et al. [20]	Logarithmic simulated annealing with the perceptron algorithm	98.8
Marcano-Cedeño et al. [21]	AMMLP	99.26
Aličković and Subasi [14]	Rotation forest	96.78
Aličković and Subasi [14]	Rotation forest and GA	99.48

researches. We can see this comparison of the results done on the same dataset in Table 3. As it is shown in Table 3, this approach gave much better results than previous research done by using Artificial Neural Networks. One of the possible reasons why linear transfer function gave us the highest accuracy rate for Wisconsin breast cancer data set is the usage of normalization preprocessing.

5 Conclusion

Breast cancer is one the most widely spread cancers among women worldwide today. But, if it is diagnosed in its early stage, it can be cured very high chances. There are different methods used to diagnose and classify it, such as mammography etc. These methods have several drawbacks, and there is a need to find a better method. In recent years, artificial intelligence started to be in use in this area and it showed very good classification results. Our research is done

with purpose to contribute to better classification of breast cancer. Our method tested on Wisconsin breast cancer dataset that contains nine attributes showed very good classification accuracy of 99.27%. Method we used in our research is normalization technique combined with Multi Layer Perceptron neural network. A result achieved in this research is very promising compared to the earlier reported classification techniques for mining breast cancer data. This research demonstrated that normalization of data is also very important.

We believe that this technique can be useful and can help to physicians to make very accurate diagnostic decisions. In our future investigations, we will pay a lot of attention to evaluate our proposed technique on larger data sets and to apply this algorithm on other applications such as ECG, EEG, and Intrusion Detection and test the efficiency of this algorithm. Further studies of the data can yield more remarkable outcomes. This will also be the center of attention of our prospect work.

References

1. Cancer Facts and Figures| American Cancer Society. Available <https://www.cancer.org/research/cancer-facts-statistics/all-cancer-facts-figures/cancerfacts-figures-2009.html> (2009). Accessed 31 Jan 2019 [Online]
2. Breast Cancer Risk and Risk Factors. Breastcancer.org. Available https://www.breastcancer.org/symptoms/understand_bc/risk. Accessed 31 Jan 2019 [Online]
3. Mušanovic, M., Đapo, M.: RANA detekcija raka dojke. Zavod zdravstvenog Osiguranja Kantona Sarajevo, Ministarstvo Zdravstva Kantona Sarajevo (2009)
4. Elmore, J., Wells, M., Carol, M., Lee, H., Howard, D., Feinstein, A.: Variability in radiologists' interpretation of mammograms. *N. Engl. J. Med.* **22**, 1493–1499 (1994)
5. Anderson, T.W.: An introduction to multivariate statistical analysis. Wiley, New York (1984)
6. Dillon, W.R., Goldstein, M.: Multivariate Analysis Methods and Applications. Wiley, New York (1984)
7. Hand, D.J.: Discrimination and Classification. Wiley, New York (1981)
8. Johnson, R.A., Wichern, D.W.: Applied Multivariate Statistical Analysis, 5th edn. Upper Saddle River, Prentice-Hall, NJ (2002)
9. Karabatak, M., Ince, M.C.: An expert system for detection of breast cancer based on association rules and neural network. *Expert Syst. Appl.* **36**, 3465–3469 (2009)
10. Quinlan, J.R.: Improved use of continuous attributes in C4. *J. Artif. Intell. Res.* **4**, 77909 (1996)
11. Goodman, D., Boggess, L.: Artificial immune system classification of multiple-class problems. In: Intelligent Engineering Systems Through Artificial Neural Networks, Fuzzy Logic, Evolutionary Programming Complex Systems and Artificial Life, vol. 12, pp. 179–184 (2002)
12. Setiono, R.: Generating concise and accurate classification rules for breast cancer diagnosis. *Artif. Intell. Med.* **18**, 205–217 (2000)
13. Abbas, H.A.: An evolutionary artificial neural network approach for breast cancer diagnosis. *Artif. Intell. Med.* **25**, 265–281 (2001)
14. Aličković, E., Subasi, A.: Breast cancer diagnosis using GA feature selection and rotation forest. *Neural Comput. Appl.* **28**(4), 753–763 (2017)
15. National Cancer Institute, Cancer Statistics. Available <http://www.seer.cancer.gov/statfacts/html/breast.html>. Last visited on 19 May 2011 [Online]
16. Bishop, C.M.: Neural Networks for Pattern Recognition. Clarendon Press, Oxford (1996)
17. Hanbay, D., Turkoglu, I., Demir, Y.: An expert system based on wavelet decomposition and neural network for modeling Chua's circuit. *Expert Syst. Appl.* <https://doi.org/10.1016/j.eswa.2007.03.002> (2007)
18. Haykin, S.: Neural networks, a comprehensive foundation. Macmillan College Publishing Company Inc, New York (1994)
19. Jayalakshmi, T., Santhakumaran, A.: Statistical normalization and back propagation for classification. *Int. J. Comput. Theor. Eng.* **3**(1), 1793–8201 (2011)
20. Albrecht, A.A., Lappas, G., Vinterbo, S.A., Wong, C.K., Ohno-Machado, L.: Two applications of the LSA machine. In: Proceedings of the 9th International Conference on Neural Information Processing, pp. 184–189. <https://doi.org/10.1109/ICONIP.2002.1202156> (2002)
21. Marcano-Cedeño, A., Quintanilla-Domínguez, J., Andina, D.: WBCD breast cancer database classification applying artificial metaplasticity neural network. *Expert Syst. Appl.* **38**, 9573–9579 (2011)
22. Ubeyli, E.D.: Implementing automated diagnostic systems for breast cancer detection. *Expert Syst. Appl.* **33**, 1054–1062 (2007)

Part XI
Pharmaceutical Engineering



Landscape of *CYP3A5* Variants in Central-Eastern and South European Populations

Grażyna Adler, Izabela Uzar, Anastazja Kazlova, Amina Valjevac, Emina Kiseljakovic, Emir Mahmutbegovic, Nermin N. Salkic, Mateusz A. Adler, Nevena Mahmutbegovic, Maciej Grabowski, and Ewa Rębacz-Marón

Abstract

The detoxification mechanisms occurring in the cells and tissues of the body are necessary to maintain homeostasis. The CYP enzymes family support these mechanisms, take a part in the pharmacokinetics of drugs and neutralizing xenobiotics. The predominant sub-family of CYP enzymes are *CYP3A5* coded by gene *CYP3A5*. The distribution of *CYP3A5* variants varies in different ethnic groups, while the absence of functional *CYP3A5*, linked to diminished enzymatic function, is most frequent. Knowledge about distribution of *CYP3A5* variants in different ethnic groups is important to establish the clinical relevance of screening for these variants and to optimize and individualize pharmacotherapy. The aim of the study was to establish the distribution of variants

1* and **3* of *CYP3A5* gene and compare our results with those from other Central-Eastern and South European populations. The studied population consisted of 469 healthy adults: Belarusians, Bosnians and Poles (241 female and 228 male) mean age 50.68 (± 16.09) y. DNA was extracted from buccal swabs, and for the **1* and **3* variants of *CYP3A5* gene, the PCR-RFLP was performed. The frequency of the *CYP3A5*3* variant in Belarusians, Bosnians and Poles was 98.44, 97.89 and 94.56%, followed by the **1* variant: 1.56, 2.11 and 5.44%, respectively. We showed that Central-Eastern and South European populations are characterized by high variability of *CYP3A5* variants. This may be taken into consideration in the prognosis of pharmacotherapy efficacy in the studied populations.

G. Adler (✉) · M. Grabowski
Department of Studies in Antropogenetics and Biogerontology,
Pomeranian Medical University, 71-210, Szczecin, Poland
e-mail: gra2@op.pl

G. Adler
Department of Gerontobiology, Pomeranian Medical University,
Żołnierska 48, 71-210 Szczecin, Poland

I. Uzar
Department of General Pharmacology and Pharmacoeconomics,
Pomeranian Medical University, Szczecin, Poland
e-mail: uzari@wp.pl

A. Kazlova · E. Rębacz-Marón
Department of Vertebrate Zoology and Anthropology,
University of Szczecin, Szczecin, Poland
e-mail: anastasiyakazlova19941103@gmail.com; rebae@univ.szczecin.pl

E. Rębacz-Marón
e-mail: rebae@univ.szczecin.pl

A. Valjevac
Laboratory for Molecular Medicine, Center for Genetics,
Medical Faculty, University of Sarajevo, Sarajevo, 71000,
Bosnia and Herzegovina
e-mail: aminavaljevac@gmail.com

E. Kiseljakovic
Department of Medical Biochemistry, Faculty of Medicine,
University of Sarajevo, Cekalusa 90, 71000 Sarajevo,
Bosnia and Herzegovina
e-mail: eminacengic@hotmail.com

E. Mahmutbegovic
Institution of Health Protection of Women and Motherhood
Canton Sarajevo, 71000 Sarajevo, Bosnia and Herzegovina
e-mail: emirmahmutbegovic@hotmail.com

N. N. Salkic
Department of Gastroenterology and Hepatology, University
Clinical Centre Tuzla, Tuzla, Bosnia and Herzegovina
e-mail: snermin@gmail.com

M. A. Adler
Warsaw School of Economics, 02-554 Warsaw, Poland
e-mail: matadler@o2.pl

N. Mahmutbegovic
Neurology Clinic, Clinical Center of University of Sarajevo,
Sarajevo, Bosnia and Herzegovina
e-mail: nevenaradulovic@hotmail.com

Keywords

Distribution • Cytochrome P450 • *CYP3A5* gene • Variants

1 Background

Ethnicity and geographic location are important factors linked to genetic differences. Recently, the progress in the human genome analysis expands the knowledge about different response to drugs linked to variants of genes, encoding protein factors and enzymes. Pharmacogenetics is important to establish the clinical relevance of gene variants and in order to optimize and individualize pharmacotherapy. The CYP enzyme family (known as cytochrome P450 monooxygenase enzymes, P450s) consists of more than 50 isozymes. While, CYP3A is the subfamily, which consists of the isozymes CYP3A4, CYP3A5, CYP3A7 and CYP3A43. Human CYP3A5 enzyme (known as cytochrome P450 family 3 subfamily A member 5) is a protein encoded by the *CYP3A5* gene localized in a cluster on chromosome 7q21-q22.1. Previously, many of preclinical and clinical studies have provided evidence on relationship of the *CYP3A5* variants and their effects on drugs absorption, distribution and elimination, as well as risk of diseases [1–4]. To date, at least 10 of its variants have been reported, from **1B* to **1I* [5, 6]. The *CYP3A5*1* is the wild type variant with normal level of gene expression and enzyme activity [7]. While, variant **3* has diminished the enzyme activity [8]. Homozygous subjects for *CYP3A5*3* appear to be defective in CYP3A5 due to the creation of a cryptic splice site, which results in the incorporation of the intronic sequence in the mature mRNA and the production of a truncated protein as a result of premature termination of translation [8].

On the one hand, CYP3A family is estimated to participate in the metabolism of 40 to 60% of all clinically administered medicines; cancer chemotherapeutics and the immunosuppressants cyclosporine A and tacrolimus, also cholesterol-lowering drugs, HIV protease inhibitors, calcium channel blockers, antiepileptics, and some antibiotics [8]. On the other hand, researchers suggest that the carrying of the *CYP3A5*3* variant may increase the risk of acute and chronic leukemia, colorectal cancer and may also be associated with the risk of schizophrenia [3, 4, 9, 10]. The *CYP3A5*3* variant is common but its frequency shows large discrepancies; in Caucasians is about 90%, in Chinese, 70% and African Americans about 50% [8, 11, 12].

2 Aim

The aim of our study was to establish the distribution of variants **1* and **3* of *CYP3A5* gene in Belarusian, Bosnian and Polish population and to compare our results with those from other Central-Eastern and South European populations.

3 Materials and Methods

For the purpose of the study, we chose 469 apparently healthy subjects; 64 Belarusians, 166 Bosnians and 239 Poles, mean age 39.19 (± 12.45) y, 49.16 (± 16.02) y and 54.81 (± 15.38), respectively. Twins and subjects with any serious illness (including: hepatic, pulmonary, renal, and cancer) were excluded from the study. It was conducted according to the standards of the Declaration of Helsinki (1975, revised 2000), and the protocol of the study was approved by the local bioethical committee.

Genomic DNA was extracted from buccal swabs according to the manufacturer's instructions (QIAGEN, Hilden, Germany). DNA amplification was performed using a LabCycler device (SensoQuest GmbH, Göttingen, Germany) followed by previously described PCR-RFLP techniques [13] (see Table 1). For quality control purposes, approximately 10% of the samples were re-genotyped in a blinded fashion and the same results were obtained.

4 Statistical Analysis

Genotype and allele frequencies were obtained by direct counting. A χ^2 test was used to verify that genotype prevalence and allele frequencies were in agreement with Hardy-Weinberg equilibrium. All tests were performed using R CRAN statistical software (version 3.4.2) (R Core Team 2017). $P < 0.05$ was considered statistically significant for all analyses.

5 Results

The frequencies of variants **1* and **3* of *CYP3A5* gene in Belarusians, Bosnians and Poles were 1.56 and 98.44%, 2.11 and 97.89%, 5.44 and 94.56%, respectively.

The results of the study demonstrated that the prevalence of genotypes AG (**1*3*) of *CYP3A5* gene in Belarusians, Bosnians and Poles was 3.13% ($n = 2$), 4.2% ($n = 7$) and 10.88% ($n = 26$), respectively. There were no homozygotes

Table 1 Characteristics of *CYP3A5* variants, PCR-RFLP conditions

<i>CYP3A5</i> allele	Ref. sequence/nucleotide change	Amino acid change	Functional consequence	Primer sequence 5' → 3'	Restriction enzyme	Fragment sizes (bp) wild type/variant allele
*1	Wild type	None	Normal function	cat gac tta gta gac aga tga c ggt cca aac agg gaa gaa ata	<i>SspI</i>	148, 125, 20
*3	776746/6986 A > G	Splicing defect	Loss of function	cat gac tta gta gac aga tga c ggt cca aac agg gaa gab ata	<i>SspI</i>	168, 125

Mismatch with the *CYP3A5* sequence was bolded; bp-base pair; the PCR product representing *3 allele was cleaved by *SspI* into 168 bp and 125 bp fragments; the wild type *1 allele was cleaved by the same enzyme into 148, 125 and 20 bp

AA (*1*1) in both, Belarusian, Bosnian and Polish population. The results conformed to the expected Hardy-Weinberg equilibrium ($\chi^2 = 0.016$; $p = 0.899$, $\chi^2 = 0.077$; $p = 0.781$ and $\chi^2 = 0.374$; $p = 0.791$, respectively).

The distribution for *1 and *3 variants of *CYP3A5* gene in Central-Eastern and South European populations has been fairly well documented [14–24]. In this and the published studies for Central-Eastern and South populations, the distribution of *1 variant varied from less than 5.0% in Belarusians, Bosnians, Kosovars and Croats (this study, [17, 20]) through up to 6.0% in Bulgarians, Greeks, Russians and Poles, to up to about 9.0% in Italians, Spaniards and Macedonians (this study, [16, 18, 19, 21, 23, 24]). The peak value 12.5%, was obtained in Portuguese [22] (see Table 2).

It is worth noting, that the results previously obtained by us for the population of Polish newborns ($n = 200$) are almost identical to those obtained in this study in healthy adults ($n = 166$); 6.0 and 94.0% versus 5.44 and 94.56%, for *1 and *3, respectively (this study, [15]). On the other hand, our results for the Bosnian population as compared to the results by Semiz et al. [14] were different; 2.11 and 97.89% versus 6.0 and 94.0%, for *1 and *3, respectively.

6 Discussion

There is growing evidence that polymorphic variants of genes encoding for drug metabolizing enzymes and transporters impact directly their function linked to efficacy

Table 2 Distribution of *CYP3A5* variants in Central-Eastern and South European populations

Country/population (n)	Frequency of variant of <i>CYP3A5</i> (%)		Ref.
	*1	*3	
Belarus, Belarusians, 64	1.56	98.44	This study
Bosnia and Herzegovina, Bosnians, 166	2.11	97.89	
Poland, Poles, 239	5.44	94.56	
Bosnia and Herzegovina, Bosnians, 140	6.00	94.00	[14]
Poland, Poles, 200 ^a	6.00	94.00	[15]
Bulgaria, Bulgarians, 112	5.36	94.64	[16]
Croatia, Croats, 2637	4.50	95.50	[17]
Greece, Greeks, 283	5.65	94.35	[18]
Italy, Italians, 50	7.00	93.00	[19]
Kosovo, Kosovars, 234	1.71	98.29	[20]
Macedonia, Macedonians, 174	9.20	90.80	[21]
Portugal, Portuguese, 135	12.50	87.50	[22]
Russia, Russians, 443	5.40	94.60	[23]
Spain, Spaniards, 177	9.00	91.00	[24]

^aNeonatal population; unmarked—healthy adults; *1—allele with normal level of gene expression and enzyme activity; *3—allele with reduced enzyme activity

and/or side effects of medication. The United States Food and Drug Administration (FDA) and the European Medicines Agency (EMA) have listed about 120 drugs, in which there is an evidence to support the influence of genomic biomarkers over-dosing, safety risk and/or efficacy [25, 26]. The human CYP3A subfamily has considerable variability in its expression linked to polymorphism of genes, while population variability is high [27]. Variation in CYP3A expression is important for substrates with narrow therapeutic indices, e.g. cancer chemotherapeutics and the immunosuppressants.

The analysis, combining literature data with our own, showed that distribution of variant *1 in Central-Eastern and South European populations is uneven and vary from the lowest value 1.56% in Belarusians to the highest value 12.5% in Portuguese (this study, [22]).

In some of the Balkans populations we noticed significant differences in the distribution of variant *1 CYP3A5 gene. When we compared the distribution of this variant in Macedonians (9.2%) with results in Bosnians (2.11%), Croats (4.5%) and Kosovars (1.71%) it was significantly higher ($p = 0.0010$; 0.0086 and 0.0012 , respectively) (this study, [17, 20, 21]).

The same comparison was made between Greeks (5.65%) and Kosovars (1.71%), ($p = 0.0372$) and between Croats (4.5%) and Kosovars (1.71%), ($p = 0.0638$) [17, 18, 20].

The significantly higher distribution of *1 variant was also found between: Kosovars (1.71%) and Russians (5.4%), Poles (6.0%), Spaniards (9.0%) and Portuguese (12.5%), ($p = 0.0364$; $p = 0.035$; $p = 0.0015$ and $p < 0.0001$, respectively) [15, 20, 22–24]. Furthermore, the distribution of *1 variant was significantly higher in Portuguese (12.5%) than in Poles (5.44%), Russians (5.4%), Bosnians (2.11%) and Belarusians (1.56%), ($p = 0.0264$; $p = 0.0086$; $p = 0.0008$; $p = 0.0241$, respectively) (this study, [22, 23]). Otherwise, in Croats (4.5%) the distribution of *1 variant of CYP3A5 gene was less frequent than in Spaniards (9.0%) and Portuguese (12.5%) ($p = 0.0113$ and $p < 0.0001$, respectively) and between Greeks (5.65%) compared to Portuguese and Spaniards compared to Bosnians ($p = 0.0252$; $p = 0.0116$) (this study, [17, 18, 22, 24]).

To sum up, the frequency of *1 variant of CYP3A5 gene obtained in our study ranks among lower values—between the values for others Central-Eastern and South European populations. Unfortunately, we did not find the data for few Central-Eastern and South European populations, which in our opinion would be interesting for a bigger picture of the distribution of examined *1 and *3 alleles.

7 Conclusion

We showed that Central-Eastern and South European populations are characterized by high variability of CYP3A5 variants. This may be taken into consideration in the prognosis of pharmacotherapy efficacy in the studied populations.

Acknowledgements This work was funded in part by the Pomeranian Medical University, Szczecin, Poland (decision reference number WNoZ-307-02/S/18).

Declaration of Interest The authors declared no potential conflicts of interest with respect to the research, authorship, and/or publication of this article.

References

1. Zhou, S.F.: Polymorphism of human cytochrome P450 2D6 and its clinical significance. *Clin. Pharmacokinet.* **48**(11), 689–723 (2009)
2. Zhang, Y.P., Zuo, X.C., Huang, Z.J., Cai, J.J., Wen, J., Duan, D. D., et al.: CYP3A5 polymorphism, amlodipine and hypertension. *J. Hum. Hypertens.* **28**(3), 145–149 (2014)
3. Wang, B.S., Liu, Z., Xu, W.X., Sun, S.L.: CYP3A5*3 polymorphism and cancer risk: a meta-analysis and meta-regression. *Tumour Biol.* **34**(4), 2357–2366 (2013)
4. Du, J., Zhang, A., Wang, L., Xuan, J., Yu, L., Che, R., et al.: Relationship between response to risperidone, plasma concentrations of risperidone and CYP3A4 polymorphisms in schizophrenia patients. *J. Psychopharmacol.* **4**(7), 1115–1120 (2010)
5. Lee, S.J., van der Heiden, I.P., Goldstein, J.A., van Schaik, R.H. N.: A new CYP3A5 variant, CYP3A5*11, is shown to be defective in nifedipine metabolism in a recombinant cDNA expression system. *Drug Metab. Dispos.* **35**(1), 67–71 (2007)
6. Shuichi, Fukuen, Tsuyosh, Fukuda, Hiromi, Maune, Ikenaga, Yuka, Isamu, Yamamoto, Tadanobu, Inaba, et al.: Novel detection assay by PCR-RFLP and frequency of the CYP3A5 SNPs, CYP3A5 *3 and *6, in a Japanese population. *Pharmacogenetics* **12**(4), 331–334 (2002)
7. Roy, J.N., Lajoie, J., Zijenah, L.S., Barama, A., Poirier, C., Ward, B.J., et al.: CYP3A5 genetic polymorphisms in different ethnic populations. *Drug Metab. Dispos.* **33**(7), 884–887 (2005)
8. Kuehl, P., Zhang, J., Lin, Y., Lamba, J., Assem, M., Schuetz, J., et al.: Sequence diversity in CYP3A promoters and characterization of the genetic basis of polymorphic CYP3A5 expression. *Nat. Genet.* **27**(4), 383–391 (2001)
9. Kronbach, T., Fischer, V., Meyer, U.A.: Cyclosporine metabolism in human liver: identification of a cytochrome P-450III gene family as the major cyclosporinemetabolizing enzyme explains interactions of cyclosporine with other drugs. *Clin. Pharmacol. Ther.* **43**(6), 630–635 (1988)
10. Aoyama, T., Yamano, S., Waxman, D.J., Lapenson, D.P., Meyer, U.A., Fischer, V., et al.: Cytochrome P-450 hPCN3, a novel cytochrome P-450 IIIA gene product that is differentially expressed in adult human liver. cDNA and deduced amino acid

- sequence and distinct specificities of cDNA-expressed hPCN1 and hPCN3 for the metabolism of steroid hormones and cyclosporine. *J. Biol. Chem.* **264**(18), 10388–10395 (1989)
11. Chou, F.C., Tzeng, S.J., Huang, J.D.: Genetic polymorphism of cytochrome P450 3A5 in Chinese. *Drug Metab. Dispos.* **29**(9), 1205–1209 (2001)
 12. Shih, P.S., Huang, J.D.: Pharmacokinetics of midazolam and 1'-hydroxymidazolam in Chinese with different CYP3A5 genotypes. *Drug Metab. Dispos.* **30**(12), 1491–1496 (2002)
 13. van Schaik, R.H., van der Heiden, I.P., van den Anker, J.N., Lindemans, J.: CYP3A5 variant allele frequencies in Dutch Caucasians. *Clin. Chem.* **48**(10), 1668–1671 (2002)
 14. Semiz, S., Dujčić, T., Ostanek, B., Prnjavorac, B., Bego, T., Malenica, M., et al.: Analysis of CYP3A4*1B and CYP3A5*3 polymorphisms in population of Bosnia and Herzegovina. *Med. Glas. (Zenica)* **8**(1), 84–89 (2011)
 15. Adler, G., Łoniewska, B., Parczewski, M., Kordek, A., Ciechanowicz, A.: Frequency of common CYP3A5 gene variants in healthy Polish newborn infants. *Pharmacol Rep.* **61**(5), 947–951 (2009)
 16. Atanasova, S.Y., von Ahsen, N., Toncheva, D.I., Dimitrov, T.G., Oellerich, M., Armstrong, V.W.: Genetic polymorphisms of cytochrome P450 among patients with Balkan endemic nephropathy (BEN). *Clin. Biochem.* **38**(3), 223–228 (2005)
 17. Ganoci, L., Božina, T., Mirošević Skvrce, N., Lovrić, M., Mas, P., et al.: Genetic polymorphisms of cytochrome P450 enzymes: CYP2C9, CYP2C19, CYP2D6, CYP3A4, and CYP3A5 in the Croatian population. *Drug Metab. personalized Ther.* **32**(1), 11–21 (2017)
 18. Arvanitidis, K., Ragia, G., Iordanidou, M., Kyriaki, S., Xanthi, A., Tavridou, A., et al.: Genetic polymorphisms of drug-metabolizing enzymes CYP2D6, CYP2C9, CYP2C19 and CYP3A5 in the Greek population. *Fundam. Clin. Pharmacol.* **21**(4), 419–426 (2007)
 19. Turolo, S., Tirelli, A.S., Ferrareso, M., Ghio, L., Belingheri, M., Groppali, E., et al.: Frequencies and roles of CYP3A5, CYP3A4 and ABCB1 single nucleotide polymorphisms in Italian teenagers after kidney transplantation. *Pharmacol Rep.* **62**(6), 1159–1169 (2010)
 20. Krasniqi, V., Dimovski, A., Bytyqi, H.Q., Eftimov, A., Šimičević, L., Božina, N.: Genetic polymorphisms of CYP2C9, CYP2C19, and CYP3A5 in Kosovar population. *Arh. Hig. Rada. Toksikol.* **68**(3), 180–184 (2017)
 21. Kapedanovska Nestorovska, A., Jakovski, K., Naumovska, Z., Hiljadnikova Bajro, M., Sterjev, Z., Eftimov, A., et al.: Distribution of the most common genetic variants associated with a variable drug response in the population of the Republic of Macedonia. *Balkan J. Med. Genet.* **17**(2), 5–14 (2014)
 22. Oliveira, E., Marsh, S., van Booven, D.J., Amorim, A., Prata, M.J., McLeod, H.L.: Pharmacogenetically relevant polymorphisms in Portugal. *Pharmacogenomics* **8**(7), 703–712 (2007)
 23. Mustafina, O.E., Tuktarova, I.A., Karimov, D.D., Somova, R.S., Nasibullin, T.R.: CYP2D6, CYP3A5, and CYP3A4 gene polymorphism in Russian, Tatar, and Bashkir populations [Article in Russian]. *Genetika* **51**(1), 109–119 (2015)
 24. Gervasini, G., Vizcaino, S., Gaisba, C., Carrillo, J.A., Benitez, J.: Differences in CYP3A5 genotype distribution and combination with other polymorphisms between Spaniards and other Caucasian populations. *Ther. Drug Monit.* **27**(6), 819–821 (2005)
 25. <http://www.ema.europa.eu>. Access Aug 2018
 26. <http://www.fda.gov>. Access Aug 2018
 27. Zanger, U.M., Schwab, M.: Cytochrome P450 enzymes in drug metabolism: regulation of gene expression, enzyme activities, and impact of genetic variation. *Pharmacol. Ther.* **138**(1), 103–141 (2013)

Development of Inhalable Dry Gene Powders for Pulmonary Drug Delivery by Spray-Freeze-Drying

Edina Vranić, Merima Sirbubalo, Amina Tucak, Jasmina Hadžiabdić, Ognjenka Rahić, and Alisa Elezović

Abstract

There is considerable potential for pulmonary gene therapy as a treatment for a number of conditions for which current treatment is inadequate. Delivering genes directly to the lungs by dry powder inhalers (DPIs) have attracted much attention due to better stability of genes. Formulating genes as powders for aerosol delivery is a challenge as it requires not only flowability and dispersibility of the powders but also maintaining gene stability and biological activity during manufacturing and delivery. In this review, we aim to provide an overview about the potentials of spray-freeze-drying (SFD) for the development of inhalable dry gene powders for pulmonary drug delivery. We will discuss the main steps involved within the production process (i.e., spraying, freezing and drying) and introduce different SFD methods which can successfully be used for the production of porous particles whose physical and aerosol characteristics are considered to be ideal for use in pulmonary drug delivery.

Keywords

Pulmonary drug delivery • Gene therapy • Dry gene powders • Spray-freeze-drying

1 Introduction

In recent years, the lungs have been studied as a very attractive target for drug delivery [1]. Pulmonary drug delivery offers several advantages over injectable, transdermal or oral methods of delivery. Inhalables provide a

non-invasive method of delivering drugs into the bloodstream, they enable effective drug targeting to the lungs for relatively common respiratory tract diseases and provide very rapid absorption similar to the intravenous route because of an enormous surface area and a relatively low enzymatic, controlled environment for the systemic absorption of medications. Delivering drug to the lungs can also help avoid gastrointestinal tract problems such as poor solubility, low bioavailability, gut irritability, unwanted metabolites, food effects and dosing variability [2, 3].

Gene therapy has as its central principle the addition of gene function through gene transfer. It has been the subject of a great deal of information, and misinformation, over the past decades [4]. However, there is considerable potential for pulmonary gene therapy as a treatment for a number of conditions for which current treatment is inadequate [5]. Gene delivery in humans requires carriers that will transfer genes into the nuclei of target cells. These carriers (viral or non-viral systems) first must be safe for human use, they must be efficient in transfection, and protect the genes from degradation before arriving at the target cell. Both viral and non-viral gene delivery systems have been used in the lungs, however, both have limitations associated with their biological properties [5]. Viral vectors are highly effective delivery agents, but their high immunogenicity has led researchers to seek safer alternatives [6]. Very popular non-viral delivery systems are biodegradable and biocompatible poly (D,L-lactide-co-glycolide) (PLGA) polymers, cationic liposomes, polyethyleneimine (PEI) etc. They are much safer than viral delivery systems, but their transfection efficiency *in vivo* is limited [7].

Pulmonary administration is a powerful tool for achieving effective pulmonary gene therapy against several lung diseases, such as cystic fibrosis, α 1-antitrypsin deficiency, and lung cancer [8]. These diseases could be treated by high-level and long-term expression of the corresponding gene of interest [6]. The lungs possess inherent advantages for gene therapy since they are easily accessible via the airways, offer a large surface area for transfection and reduce

E. Vranić (✉) · M. Sirbubalo · A. Tucak · J. Hadžiabdić · O. Rahić · A. Elezović

Department of Pharmaceutical Technology, Faculty of Pharmacy, University of Sarajevo, Zmaja od Bosne 8, 71 000 Sarajevo, Bosnia and Herzegovina
e-mail: evranic@yahoo.com

the risk of systemic side effects. The most important thing in pulmonary gene therapy is to deliver a therapeutic gene to the lungs. To achieve this goal, several intravenous formulations have been developed. However, delivery to the lungs via intravenous injection is limited since genes are rapidly degraded by endonucleases in the systemic circulation. Another problem is nontargeted distribution, subsequently leading to poor therapeutic effects and adverse effects [8, 9]. Delivering genes directly to the lungs by nebulizers, pressurized metered-dose inhalers (pMDIs), or dry powder inhalers (DPIs) can solve these problems. Among these aerosol inhalation systems, DPIs have attracted much attention due to their low cost, portability, no propellant, and ease of handling [10]. Dry powder formulation also offers the better stability of genes by minimizing the exposure to high shear stress (during nebulization) and avoids the compatibility issues with propellants (in metered dose inhaler (MDI) [11]. Particle engineering methods that are suitable for preparing inhaled powder formulation of genes are spray drying, spray-freeze-drying and supercritical fluid technology [12]. Spray-freeze-drying (SFD) is powderization technique used to produce highly porous low-density powders, with high dispersibility and reachability to the lungs.

2 Spray-Freeze-Drying (SFD)

Spray-freeze-drying is biopharmaceutical powder production method, which has been attracting increasing interest in various areas of research [13]. The process has been widely used in pharmaceutical research, as well as food science and technology [14]. This technology can enhance the apparent solubility of poorly water-soluble drugs [15–18]. It is used as an approach that facilitates the development of dosage forms for alternative delivery pathways (pulmonary, nasal routes and delivery to the epidermis by needle-free injection) [19]. Some research groups have used SFD for preprocessing the protein/peptide ingredient prior to encapsulation in poly (lactic-co-glycolic acid) (PLGA) microspheres [20, 21]. It is also used very successfully to improve the storage stability of protein/peptide active ingredients [13, 22]. Spray-freeze-drying is preferred over classical spray-drying or freeze-drying for many reasons. First, it is possible to produce very porous powders with controlled particle-size distributions, and the technology offers the possibility to process thermosensitive active ingredients.

The term “spray-freeze-drying” (SFD) refers to processes with three steps in common: dispersion of bulk liquid solutions into droplets, droplet freezing, and sublimation drying of the frozen material. Schematic diagram of the spray-freeze-drying process is shown in Fig. 1. The first step in SFD is the dispersion of bulk liquid and the formation of droplets by using various types of nozzles and droplet stream

generation systems. In the next step, droplets are being frozen either by transfer of thermal energy from the liquid to a cold gas, another immiscible liquid or a solid in contact with the droplet surface or by the diffusion of energy rich volatiles into the surroundings at low vapor pressure. The final step of the process is sublimation drying in which mobile solvent molecules separate from the surface of the frozen solid when they have acquired sufficient energy. This final step is significantly different from sublimation drying of frozen solutions in vials during freeze-drying because the specific surface area of frozen droplets exceeds the ratio of the surface area available for the escape of solvent molecules [19].

Spray-freeze-drying covers different production methods: atmospheric freezing, spray-freezing into vapor over a liquid cryogen (SFV), spray-freezing into liquid cryogen (SFL), spray-freezing onto solid surfaces (thin film freezing, TFF) [13, 19]. Spray freezing into vapor over liquid cryogen (SFV) was first reported in 1948 and was performed by Benson and Ellis to investigate the surface area of protein particles [23]. The liquid feed was atomized into the vapor over a cryogenic liquid, such as liquid nitrogen or propane using either two-fluid or ultrasound nozzles. The droplets begin to freeze during the time of flight through the cold vapor phase and completely freeze upon contact with the cryogenic liquid phase itself [13]. Spray-freezing into liquid cryogen (SFL) is one of the most commonly used spray-freeze-drying techniques and it involves the atomization of a drug solution mostly via a two-fluid or an ultrasonic nozzle into a spray chamber filled with a cryogenic liquid [24]. The spraying process can be performed beneath or above the surface of the cryogenic liquid, depending on the position of the nozzle. Upon contact with the cryogenic liquid, the droplets solidify rapidly (in milliseconds) because of the high heat-transfer rate. After the spray freezing process is completed, the whole content can be lyophilized, with conventional freeze-drying. The frozen solvent is removed, as in the case of freezing with cryogenic liquids, by vacuum or atmospheric freeze-drying. The large surface area of the frozen powder and loose porous structure of the powder allow relatively fast and homogeneous drying compared with a standard lyophilization process [25].

Spray-freeze-drying is highly promising technology for the production of porous particles whose physical and aerosol characteristics are considered to be ideal for use in pulmonary drug delivery. The particles produced by SFD are typically amorphous and homogeneous. Spray freeze-dried particles can be engineered to the desired respiratory size range (below 5 μm) or even down to nano-scale [25]. The large porous particles have relatively small aerodynamic diameters usually smaller than 5 μm and large geometrical diameters usually larger than 10 μm .

Spray-freeze-drying has become very popular for processing of biologicals such as therapeutic proteins,

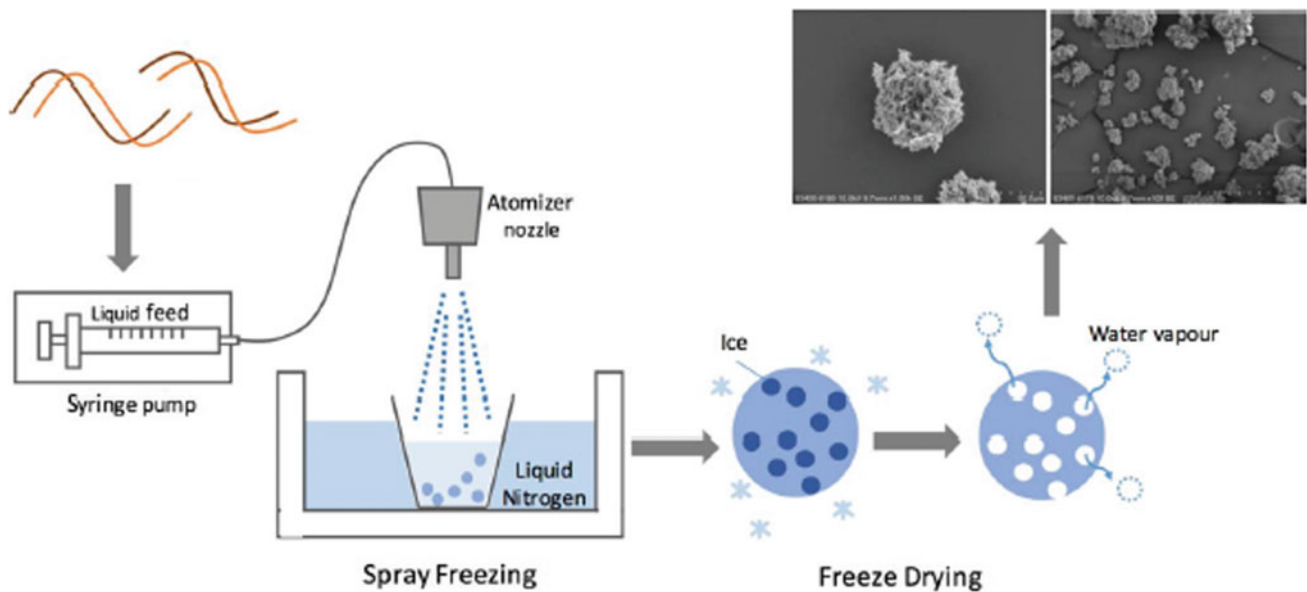


Fig. 1 Schematic diagram of the spray-freeze-drying process [11]

monoclonal antibodies, and vaccines because of its ability to produce highly porous particles at sub-ambient temperatures with or without excipients. Spray-freeze-drying has been used to formulate a significant number of thermolabile and highly potent therapeutic proteins/peptides into dry powder inhalation products, including recombinant-derived humanized anti-IgE monoclonal antibody [26], recombinant human deoxyribonucleases [26], insulin [27], small interfering RNA (siRNA) [11] and plasmid DNA pSG5lacZ [28]. It is important to mention that the application of SFD is not limited to the production of porous materials; the technique is equally capable of producing high-density particles. It is also worth noting that the application of SFD is not only limited to aqueous solutions because most volatile organic solvents can be processed [25]. Despite all, SFD methods have many disadvantages. Almost all SFD methods are still highly experimental and only scaled for laboratory purposes [13]. Methods are not as well established due to their high complexity and high cost.

3 Development of Dry Gene Powders by SFD

Formulating genes as powders for aerosol delivery is a challenge as it requires not only flowability and dispersibility of the powders but also maintaining gene stability and biological activity during manufacturing and delivery [29]. Development of inhalable aerosol systems for pulmonary gene delivery is critical for clinical use. The main problem in the formulation is destabilization of the gene or delivery system caused by several stresses: heating, freezing, spraying and shearing stress in the nozzle [8, 9]. These forms of

physical stress during the preparation might cause a critical loss of the gene. Therefore, a stable preparation of dry gene powder is necessary to achieve the clinical application of pulmonary gene therapy. Critical factors that can affect inhalability of the particles are also morphology and particle size of prepared powders [11]. To allow efficient lung deposition, prepared powders must have optimal particle size. Only particles that exhibited aerodynamic diameter between 1 and 5 μm can reach the deep lung. Aerodynamic diameter is affected by the geometric diameter as well as the density of the particles. Particles with a geometric diameter of 1–5 μm usually have poor flowability and dispersibility due to the strong cohesion force. On the other hand, porous particles with large geometric size tend to have small aerodynamic size because of the low density. These types of particles are desirable for inhalation due to the good flowability and dispersibility. In general, aerosol particles with aerodynamic diameters between 1 and 5 μm can achieve good lung deposition and the choice of inhaler device, therefore plays an important role in determining the success of aerosol delivery [1, 25].

Very porous particles produced by spray-freeze-drying has made this technology an attractive method for preparing inhaled powders. Porous particles with large physical size and low density exhibit small aerodynamic size, which can promote high flowability. In addition, porous particles have high specific surface area, thereby enhancing dissolution rate in the lungs. The porosity of the particles could be controlled by altering the solute concentration of the feed solution for spray-freeze-drying [11].

In one of the first studies, Maa et al. successfully used spray-freeze-drying to produce protein powders containing

recombinant human desoxyribonuclease (rhDNase) and anti-IgG monoclonal antibody (anti-IgG Mab) for dry powder inhalation. Maa et al. revealed that a dry powder produced by SFD had superior inhalation characteristics compared to dry powders prepared by spray drying. Spray-freeze-drying can also guarantee the high-level recovery of produced dry powders, even if the initial amount of the formulation is small, which is very important for the study of dry gene powders on a laboratory scale since the employed genes are relatively expensive [26].

Kuo and Hwang first reported about the dry gene powders prepared by SFD. However, its gene transfection characteristics in vivo have remained unknown [30]. Mohri et al. successfully prepared inhalable dry plasmid DNA (pDNA) powders by SFD. They examined the stability of pDNA obtained through SFD and the morphology of prepared dry pDNA powders. All powders had spherical and highly porous particles about 20–40 μm in diameter. The ternary structure of pDNA was evaluated by electrophoresis to investigate the integrity of pDNA in the powders prepared by SFD. In the preparation without chitosan, the pDNA was almost completely degraded through SFD. However, the addition of chitosan improved the destabilization of pDNA caused by the physical stress during SFD. Chitosan has been reported to show high tolerability in the body. Unfortunately, on the other hand, it has been reported that the transfection efficiency of chitosan is low compared to that of polyethyleneimine (PEI), a non-biodegradable polycation [9]. Kuo and Hwang also reported the destabilization of pDNA through SFD and a protective effect of polyethyleneimine, a polycation, but not mannitol, supporting their results in part [30].

Okuda et al. also used SFD to prepare inhalable dry gene powders. In order to achieve higher gene transfection efficiency, authors have synthesized poly(aspartamide) derivatives with an ethylenediamine unit as a side chain (poly{N[N-(2-aminoethyl)-2-aminoethyl]aspartamide} (PAsp(DET)) and their block copolymers with poly(ethylene)glycol (PEG-PAsp(DET)) as vectors. These novel biodegradable polycations have superior efficiencies with minimal cytotoxicity compared to PEI. The final product had spherical and porous structures with a 5–10 μm diameter, and they showed that the integrity of plasmid DNA could be maintained during powder production. Both PAsp(DET)- and PEG-PAsp(DET)-based dry gene powders could achieve higher gene transfection efficiencies in the lungs compared with chitosan-based dry gene powders [8].

Liang et al. demonstrated in their study that dry gene powder could be stably prepared by SFD without the loss of plasmid DNA integrity and that the powder exhibited a gene expressing effect in the lungs of mice following pulmonary administration [31]. For clinical application, however, a higher gene transfection efficiency in the lungs is necessary.

In their last study, Liang et al. employed spray-freeze-drying to prepare dry powder of small interfering RNA (siRNA) to treat lung diseases. Mannitol and herring sperm DNA were used as bulking agent and model of small nucleic acid therapeutics, respectively. The gel retardation and liquid chromatography assays showed that the siRNA remained intact after spray-freeze-drying even in the absence of delivery vector. The powder formulation exhibited a high emitted fraction (EF) of 92.4% and a modest fine particle fraction (FPF), of around 20%. Authors successfully demonstrated that spray-freeze-drying can be used to produce naked siRNA formulation with intact integrity [11].

4 Conclusion

Spray-freeze-drying is powderization technique used to produce a highly porous low-density powders. The powders produced by SFD are considered more suitable for inhalation compared with those produced by conventional techniques. Spray-freeze-drying involves multiple steps: liquids are first sprayed into a cryogen such as liquid nitrogen and the droplets, which are frozen immediately, are then transferred into a freeze dryer to allow the sublimation of ice, resulting in the formation of highly porous powders. Spray-freeze drying has shown to be a feasible method if good particle size control, spherical particle shape and a high product yield are essential. The porous particles produced by spray-freeze-drying has made this technology an attractive method for preparing inhaled gene powders. Many authors reported the use of spray-freeze-drying technology to produce dry powder of gene complexes that are suitable for inhalation. These dry powders produced by SFD could very successfully reach to intrapulmonary region and exhibit gene expression in the lungs. Since the aerosol performance of a powder formulation is also affected by the design of inhaler, a careful selected inhaler device could improve the delivery efficiency.

Conflict of Interest The authors have no conflicts of interest to disclose.

References

1. Labiris, N., Dolovich, M.: Pulmonary drug delivery. Part I: Physiological factors affecting therapeutic effectiveness of aerosolized medications. *Br. J. Clin. Pharmacol.* **56**(6), 588–599 (2003a)
2. Patton, J., Byron, P.: Inhaling medicines: delivering drugs to the body through the lungs. *Nat. Rev. Drug Discov.* **6**(1), 67–74 (2007)
3. Swarbirck, J., Boylan, J.: *Encyclopedia of Pharmaceutical Technology*, 3rd edn, pp. 1279–1287. M. Dekker, New York (2000)

4. West, J., Rodman, D.M.: Gene therapy for pulmonary diseases. *Chest* **119**(2), 613–617 (2001)
5. Jenkins, R.G., McAnulty, R.J., Hart, S.L., Laurent, G.J.: Pulmonary gene therapy. Realistic hope for the future, or false dawn in the promised land? *Monaldi Arch. Chest. Dis.* **59**, 17–24 (2003)
6. Bivas-Benita, M., Romeijn, S., Junginger, H.E., Borchard, G.: PLGA–PEI nanoparticles for gene delivery to pulmonary epithelium. *Eur. J. Pharm. Biopharm.* **58**(1), 1–6 (2004)
7. Roth, J.A., Cristiano, R.J.: Gene therapy for cancer: what have we done and where are we going? *J. Natl. Cancer Inst.* **89**(1), 21–39 (1997)
8. Okuda, T., Suzuki, Y., Kobayashi, Y., Ishii, T., Uchida, S., Itaka, K., Kataoka, K., Okamoto, H.: Development of biodegradable polycation-based inhalable dry gene powders by spray freeze drying. *Pharmaceutics* **7**(3), 233–254 (2015)
9. Mohri, K., Okuda, T., Mori, A., Danjo, K., Okamoto, H.: Optimized pulmonary gene transfection in mice by spray-freeze dried powder inhalation. *J. Control. Release* **144**(2), 221–226 (2010)
10. Labiris, N., Dolovich, M.: Pulmonary drug delivery. Part II: The role of inhalant delivery devices and drug formulations in therapeutic effectiveness of aerosolized medications. *Br. J. Clin. Pharmacol.* **56**(6), 600–612 (2003b)
11. Liang, W., Chan, A., Chow, M., Lo, F., Qiu, Y., Kwok, P., Lam, J.: Spray freeze drying of small nucleic acids as inhaled powder for pulmonary delivery. *Asian J. Pharm.* **13**(2), 163–172 (2017)
12. Pfeifer, C., Hasenpusch, G., Uezguen, S., Aneja, M.K., Reinhardt, D., Kirch, J., Schneider, M., Claus, S., Friess, W., Rudolph, C.: Dry powder aerosols of polyethylenimine (PEI)-based gene vectors mediate efficient gene delivery to the lung. *J. Control. Release* **154**, 69–76 (2011)
13. Schiffter, H.: Spray-freeze-drying in the manufacture of pharmaceuticals. *Eur. Pharm. Rev.* **3**, 1–7 (2007)
14. Ishwarya, S.: Spray-freeze-drying: a novel process for the drying of food and bioproducts. *Trends Food Sci. Technol.* **41**, 161–181 (2015)
15. Rogers, T.L., Overhoff, K.A., Shah, P., Yacaman, M.J., Johnston, K.P.: Micronized powders of a poorly water soluble drug produced by a spray-freezing into liquid-emulsion process. *Eur. J. Pharm. Biopharm.* **55**, 161–172 (2003)
16. Kondo, M., Niwa, T., Okamoto, H., Danjo, K.: Particle characterization of poorly water-soluble drugs using a spray-freeze drying technique. *Chem. Pharm. Bull.* **57**(7), 657–662 (2009)
17. Leuenberger, H.: Spray-freeze-drying—the process of choice for low water soluble drugs. *J. Nanoparticle Res.* **4**, 111–119 (2002)
18. Hu, J., Johnston, K., Williams, R.: Rapid dissolving high potency danazol powders produced by spray freezing into liquid process. *Int. J. Pharm.* **271**(1–2), 145–154 (2004)
19. Wanning, S., Süverkrüp, R., Lamprecht, A.: Pharmaceutical spray freeze drying. *Int. J. Pharm.* **488**(1–2), 136–153 (2015)
20. Costantino, H., Johnson, O., Zale, S.: Relationship between encapsulated drug particle size and initial release of recombinant human growth hormone from biodegradable microspheres. *J. Pharm. Sci.* **93**(10), 2624–2634 (2004)
21. Leach, W., Simpson, D., Val, T., Anuta, E., Yu, Z., Williams, R., Johnston, K.: Uniform encapsulation of stable protein nanoparticles produced by spray-freezing for the reduction of burst release. *J. Pharm. Sci.* **94**(1), 56–69 (2005)
22. Wang, S.H., Kirwan, S.M., Abraham, S.N., Staats, H.F., Hickey, A.J.: Stable dry powder formulation for nasal delivery of anthrax vaccine. *J. Pharm. Sci.* **101**(1), 31–47 (2012)
23. Benson, S., Ellis, D.: Surface areas of proteins. I. Surface areas and heats of absorption I. *J. Am. Chem. Soc.* **70**(11), 3563–3569 (1948)
24. Rogers, T.L., Johnston, K.P., Williams III, R.O.: Solution based particle formation of pharmaceutical powders by supercritical or compressed fluid CO₂ and cryogenic spray-freezing technologies. *Drug Dev. Ind. Pharm.* **27**, 1003–1015 (2001)
25. Chow, A., Tong, H., Chattopadhyay, P., Shekunov, B.: Particle engineering for pulmonary drug delivery. *Pharm. Res.* **24**(3), 411–437 (2007)
26. Maa, Y.F., Nguyen, P.A., Sweeney, T., Hsu, C.C.: Protein inhalation powders: spray drying versus spray freeze drying. *Pharm. Res.* **16**, 249–254 (1999)
27. Bi, R., Shao, W., Wang, Q., Zhang, N.: Spray-freeze-dried dry powder inhalation of insulin-loaded liposomes for enhanced pulmonary delivery. *J. Drug Target.* **16**(9), 639–648 (2008)
28. Yu, Z., Garcia, A.S., Johnston, K.P., Williams III, R.O.: Spray freezing into liquid nitrogen for highly stable protein nanostructured microparticles. *Eur. J. Pharm. Biopharm.* **58**, 529–537 (2004)
29. Lam, J., Liang, W., Chan, H.: Pulmonary delivery of therapeutic siRNA. *Adv. Drug Deliv. Rev.* **64**(1), 1–15 (2012)
30. Kuo, J.H., Hwang, R.: Preparation of DNA dry powder for non-viral gene delivery by spray—freeze-drying: effect of protective agents (polyethyleneimine and sugars) on the stability of DNA. *J. Pharm. Pharmacol.* **56**, 27–33 (2004)
31. Liang, W., Kwok, P.C.L., Chow, M.Y.T., Tang, P., Ma-son, A.J., Chan, H.K., Lam, J.K.W.: Formulation of pH responsive peptides as inhalable dry powders for pulmonary delivery of nucleic acids. *Eur. J. Pharm. Biopharm.* **86**, 64–73 (2014)



Antimicrobial Activity of Selected Wild Mushrooms from Different Areas of Bosnia and Herzegovina

Mirsada Salihović, Aida Šapčanin, Selma Špirtović-Halilović, Irma Mahmutović-Dizdarević, Anesa Jerković-Mujkić, Elma Veljović, Ekrem Pehlić, Fuad Gaši, and Sabilja Zećiri

Abstract

The aim of this study was to examine the antimicrobial activity of selected wild mushrooms from different areas of Bosnia traditionally used in the diet. These are the first tests of antimicrobial activity of fungi extracts growing in Bosnia and Herzegovina. Wild mushrooms *Boletus edulis* Bull. (1782) and *Cantharellus cibarius* Fr. (1821) were collected from different areas of Bosnia and Herzegovina. Nine microbial strains were tested: four Gram-positive bacteria (*Staphylococcus aureus* ATCC 25923; Methicillin-resistant *Staphylococcus aureus*: MRSA ATCC 33591; *Bacillus subtilis* ATCC 6633; and *Enterococcus faecalis* ATCC 29212), four Gram-negative bacteria (*Salmonella abony* ATCC 6017; *Pseudomonas aeruginosa* ATCC 9027; *Escherichia coli* ATCC 25922; Extended Spectrum Beta-Lactamase producing *E. coli*: ESBL *E. coli* ATCC 35218), and one yeast *Candida albicans* ATCC 1023, through the agar well diffusion method. Investigated wild mushrooms performed antibacterial activity against three strains of Gram-positive bacteria: *S. aureus*, MRSA and *B. subtilis*. Antibacterial activity of the examined extract depends on the locality on which mushrooms grow. The broader spectrum of antibacterial activity was observed in case of

C. cibarius extracts, and largest inhibition zones with this mushroom species were recorded against *S. aureus* (18.11 ± 0.20 mm) and *B. subtilis* (18.10 ± 0.17 mm). Extracts of *B. edulis* exhibited the largest inhibition zones against MRSA (20.03 ± 0.08 mm). In comparison to the standard antibiotic, tested extracts showed significant inhibition of this multidrug-resistant pathogen.

Keywords

Antimicrobial activity • Wild mushrooms

1 Introduction

The discovery of penicillin was followed by the discovery and commercial production of many other antibiotics. Large amounts of antibiotics used for human therapy, as well as for farm animals and even for fish in aquaculture, resulted in the selection of pathogenic bacteria resistant to multiple drugs. Indeed, some strains have become resistant to practically all of the commonly available agents. For example, the methicillin-resistant *Staphylococcus aureus* (MRSA) is resistant not only to methicillin but usually also to aminoglycosides, macrolides, tetracycline, chloramphenicol, and lincosamides. Such strains are also resistant to disinfectants, and MRSA can act as a major source of hospital-acquired infections. An old antibiotic, vancomycin, was resurrected for treatment of MRSA infections. However, transferable resistance to vancomycin is now quite common in *Enterococcus* and found its way finally to MRSA in 2002, although such strains are still rare [1].

The problem of multi-drug resistant microorganisms has reached an alarming level all over the world, finding new antibiotics has become an urgent need for the treatment of microbial infections. The use of natural products has been extremely successful in the discovery of new medicine [2].

M. Salihović (✉) · A. Šapčanin · S. Špirtović-Halilović · E. Veljović · S. Zećiri
Faculty of Pharmacy, University of Sarajevo, Sarajevo, Bosnia and Herzegovina
e-mail: mirsada.salihovic@ffsa.unsa.ba

I. Mahmutović-Dizdarević · A. Jerković-Mujkić
Faculty of Science, University of Sarajevo, Sarajevo, Bosnia and Herzegovina

E. Pehlić
Faculty of Biotechnical Sciences, University of Bihać, Bihać, Bosnia and Herzegovina

F. Gaši
Faculty of Agriculture and Food Sciences,
University of Sarajevo, Sarajevo, Bosnia and Herzegovina

The literature describes the antimicrobial activity of various types of mushrooms [3–5]. In fact, mushrooms could be a source of natural antibiotics.

Mushrooms could be defined as macrofungi with distinctive fruiting bodies and reproductive structures, and recently they have been identified as a major source of biologically active natural products. About 10,000 known species belonging to the class basidiomycetes, of which about 5000 species are edible and almost 2000 species have medicinal properties [6]. In addition to their high nutrition content, mushrooms are rich in bioactive metabolites such as lecithin, polysaccharide, phenolic and polyphenolic compounds, polyketides, terpenoids, glycopeptides, saponin and ergosterol with high medicinal value [7–9]. Many antimicrobial compounds are isolated from mycelium and fruiting bodies of mushrooms. These secondary metabolites function just like antibiotics, and mushrooms need these antibiotics and vitamins to vegetate and reproduce [10].

The extracts of *Laetiporus sulphureus*, *Ganoderma lucidum* and *Lentinus edodes* have already demonstrated antibacterial activity [5, 11, 12]. Furthermore, *Fistulina hepatica*, *Ramaria botrytis*, and *Russula delica* extracts were promising against multi-resistant microorganisms namely MRSA, *Escherichia coli* and *Proteus mirabilis* [13].

Until now, only the compounds from microscopic fungi have been present in the market as antibiotics.

The abovementioned facts served as the basis for the study of selected wild mushrooms and their antimicrobial activity. The aim of this study was to examine the antimicrobial activity of selected wild mushrooms from different areas of Bosnia and Herzegovina traditionally used in the diet. These are the first tests of antimicrobial activity of fungi extracts growing in Bosnia and Herzegovina.

2 Materials and Methods

Wild mushrooms *Boletus edulis* Bull. (1782) and *Cantharellus cibarius* Fr. (1821) were collected from different areas of Bosnia and Herzegovina (Table 1).

In vitro antimicrobial activity of lyophilized mushrooms was evaluated against four Gram-positive (*Staphylococcus aureus* ATCC 25923; Methicillin-resistant *Staphylococcus aureus*: MRSA ATCC 33591; *Bacillus subtilis* ATCC 6633; and *Enterococcus faecalis* ATCC 29212), four Gram-negative bacteria species (*Salmonella abony* ATCC 6017; *Pseudomonas aeruginosa* ATCC 9027; *Escherichia coli* ATCC 25922; Extended Spectrum Beta-Lactamase producing *E. coli*: ESBL *E. coli* ATCC 35218), and one yeast *Candida albicans* ATCC 1023. For antimicrobial assays, lyophilized material was dissolved in 5% dimethyl sulfoxide (DMSO) to the final concentration of 1 mg/mL. Antimicrobial effects of investigated wild mushrooms were determined by agar well diffusion method [14]. Standard antibiotic Ampicillin (10 µg; HiMedia Laboratories Pvt. Ltd., India), and antimycotic Nystatin (100 units; Oxoid Ltd., England) were used as positive control, while DMSO was used as negative control. Bacterial species were cultured overnight at 37 °C in Mueller Hinton medium (*Fluka Biochemica*; Buchs, Switzerland), while *C. albicans* in Sabouraud Glucose Agar (*Fluka Biochemica*; Buchs, Switzerland). According to Wayne [15], the sterile saline solution was used for inoculums adjusting to the final density of 0.5 McFarland standards ($\sim 1.5 \times 10^8$ CFU/mL). Microbial inoculums were spread over the entire surface of plates with growth medium and left for 15 min at room temperature to achieve a total absorption. Dissolved material of wild mushrooms and control samples (100 µl) were then

Table 1 Geographic origin of investigated wild mushrooms

Sample code	Mushrooms species	Locality	Coordinates
1	<i>Boletus edulis</i> Bull. (1782); Boletaceae	Bužim	45.05°N, 16.05°E
2		Cazin	44.97°N, 15.94°E
3		Olovo	44.13°N, 18.58°E
4		Ključ	44.53°N, 16.77°E
5		Foča	43.51°N, 18.78°E
6	<i>Cantharellus cibarius</i> Fr. (1821); Cantharellaceae	Gračanica	44.71°N, 18.31°E
7		Podvinjci	44.06°N, 18.23°E
8		Rudo	43.62°N, 19.37°E
9		Ključ	44.53°N, 16.77°E
10		Foča	43.51°N, 18.78°E

Leg. et det.: M. Salihović, 2017

transferred into the wells of inoculated agar plates. Plates with bacteria were incubated for 18–24 h at 37 °C, and those containing fungi were incubated for 24–48 h at 37 °C. Antimicrobial activity of tested mushrooms was evaluated based on inhibition zones diameter (mm). All tests were performed in three replications and the mean values (\pm SD) were calculated.

3 Results and Discussion

Overall results showed that investigated wild mushrooms extracts exhibited various antibacterial activity against three strains of Gram-positive bacteria: *S. aureus*, MRSA and *B. subtilis* (Table 2; Fig. 1). Extract of *B. edulis* collected at the locality Ključ caused the largest inhibition zones, especially

in the case of MRSA (20.03 ± 0.08 mm). It is known that fruiting bodies of *B. edulis* are an important source of carbohydrates (mannose, rhamnose, glycans), lectins (boledulin A, B, C), organic acids (malic, oxalic, quinic, ketoglutaric acids), amino acids (glutamine, alanine, serine, proline) and microelements. Polysaccharides isolated from *B. edulis* are responsible for many biological activities [16]. Furthermore, extracts of *C. cibarius* collected in almost every site were also effective against MRSA (Table 2). Standard antibiotic Ampicillin, used as positive control, did not show any inhibition of this MDR pathogen.

DMSO as solvent control showed no inhibition.

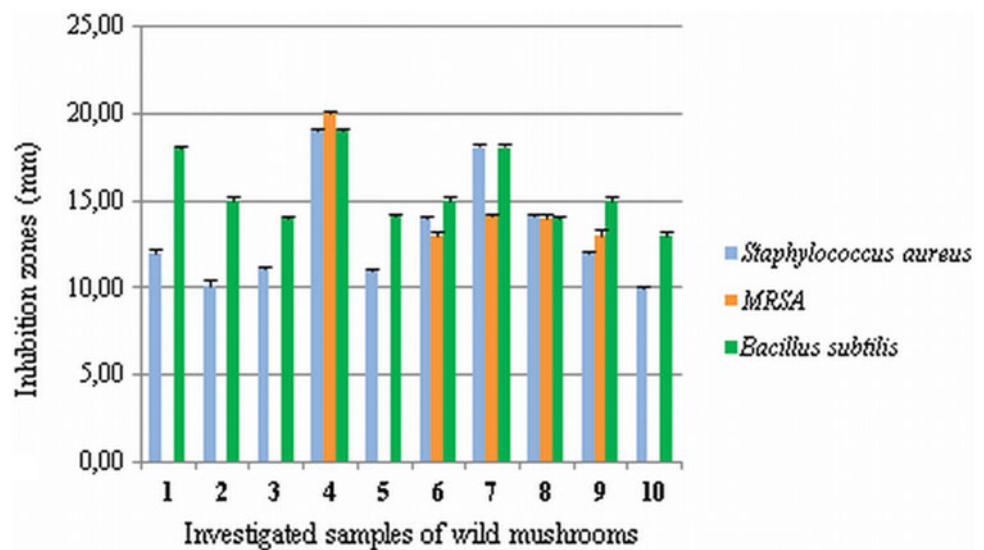
Considering the geographic origin of *C. cibarius*, generated results indicate that the most potent extracts were made from the plant material collected in the locality Podvinjci (Table 2). Study of Aina et al. [6] revealed the antimicrobial

Table 2 Inhibition zones (mm) obtained through the agar well diffusion method

Investigated sample	Bacterial species with achieved growth inhibition		
	<i>Staphylococcus aureus</i>	MRSA	<i>Bacillus subtilis</i>
1	12.01 \pm 0.21	NI	18.06 \pm 0.13
2	10.12 \pm 0.33	NI	15.06 \pm 0.14
3	11.08 \pm 0.13	NI	13.96 \pm 0.18
4	19.03 \pm 0.08	20.03 \pm 0.08	19.03 \pm 0.16
5	10.96 \pm 0.16	NI	14.08 \pm 0.19
6	14.05 \pm 0.13	13.03 \pm 0.17	15.07 \pm 0.13
7	18.11 \pm 0.20	14.11 \pm 0.12	18.10 \pm 0.17
8	14.11 \pm 0.10	14.05 \pm 0.23	14.06 \pm 0.13
9	12.00 \pm 0.11	12.96 \pm 0.38	15.04 \pm 0.17
10	9.96 \pm 0.16	NI	13.00 \pm 0.21
Positive control (Ampicillin; 10 μ g)	33.03 \pm 0.09	NI	47.98 \pm 0.23

The results are the mean \pm SD ($n = 3$). NI = No inhibition zone. DMSO = NI
Sample numbers 1–10 corresponds to the designations listed in Table 1

Fig. 1 Detected zones of inhibition (mm) caused by the activity of *B. edulis* and *C. cibarius* extracts (Sample numbers 1–10 corresponds to the designations listed in Table 1)



and antioxidant potency of extracts derived from *C. cibarius*, consequently suggesting its potential use in the pharmaceutical industry in making drugs with little or no side effect as it is produced from a natural source when compared to synthetic drugs. Constituent phytochemicals and nutraceuticals such as pleuromutilin and chanterellins present in *C. cibarius* have a synergistic effect in its antimicrobial and antioxidant activities [17].

Growth inhibition of *E. faecalis*, Gram-negative bacteria, and *C. albicans* was not recorded in this investigation. Different antimicrobial effects of investigated mushroom extracts could be explained by the differences in the microbial cell wall structure [18, 19]. The cell wall of Gram-positive bacteria is composed of several layers of peptidoglycans, and Gram-negative bacteria cell wall consists of one peptidoglycan layer and an outer membrane containing phospholipids and lipopolysaccharides, whereas the fungal cell wall contains chitin and other polysaccharides [20].

4 Conclusion

Investigated extracts of wild mushrooms collected in different areas of Bosnia and Herzegovina have a significant antibacterial property illustrated primary against Gram-positive bacteria. The interesting finding was the possibility of tested extracts to inhibit the growth of MDR pathogen. In the era characterized by the search for any new sources of antibiotics, these results of MRSA inhibition are invaluable. Further investigations should be focused on the evaluation of chemical composition and pharmacological activities of both *B. edulis* and *C. cibarius*. Such studies are necessary to broaden the therapeutic applications of these popular edible mushrooms.

Acknowledgements This work was supported by the Federal Ministry of Education and Science in Bosnia and Herzegovina and was carried out within the framework of the project “Chemical composition and antioxidative potential of wild edible mushrooms from Bosnia and Herzegovina” (Grant no. 0101-8183-3/17, dated 01.12.2017).

References

- De Lencastre, H., Oliveira, D., Tomasz, A.: Antibiotic resistant *Staphylococcus aureus*: a paradigm of adaptive power. *Curr. Opin. Microbiol.* **10**, 428–435 (2007)
- Harvey, A.: Strategies for discovering drugs from previously unexplored natural products. *Drug Discov. Today* **5**, 294–300 (2000)
- Šiljegović, J.D., Stojković, D.S., Nikolić, M.M., Glamočlija, J.M., Soković, M.D., Čirić, A.M.: *Zbornik Matice srpske za prirodne nauke* **120**, 299–305 (2011)
- Solak, M.H., Kalmis, E., Saglam, H., Kalyoncu, F.: *Phytother. Res.* **20**, 1085–1087 (2006)
- Turkoglu, A., Duru, M.E., Mercan, N., Kivrak, I., Gezer, K.: Antioxidant and antimicrobial activities of *Laetiporus sulphurous* (Bull.) Murrill. *Food Chem.* **101**, 267–273 (2007)
- Aina, D.A., Jonathan, S.G., Olawuyi, O.J., Ojelabi, D.O., Durowoju, B.M.: Antioxidant, antimicrobial and phytochemical properties of alcoholic extracts of *Cantharellus cibarius*—a Nigerian mushroom. *N. Y. Sci. J.* **5**(10), 114–120 (2012)
- Pereira, E., Barros, L., Martins, A., Ferreira, I.C.: Towards chemical and nutritional inventory of Portuguese wild edible mushrooms in different habitats. *Food Chem.* **130**, 394–403 (2012)
- Hillaimaharani, K.A., Sharmila, K., Thangaraju, P., Karthick, M., Kalaiselvam, M.: Studies on antimicrobial and antioxidant properties of oyster mushroom *Pleurotus florida*. *J. Pharm. Sci. Res.* **4**, 1540–1545 (2013)
- Poyraz, B., Güneş, H., Tül, B., Baş Sermently, H.: Antibacterial and antitumor activity of crude methanolic extracts from various Macrofungi species. *Biyol. Bilim. Araşt. Derg.* **8**(1), 5–10 (2015)
- Özcan, Ö., Ertan, F.: Beta-glucan content, antioxidant and antimicrobial activities of some edible mushroom species. *Food Sci. Technol.* **6**(2), 47–55 (2018)
- Gao, Y.H., Tang, W.B., Gao, H., Chan, E., Lan, J., Li, X., Zhou, S.: Antimicrobial activity of the medicinal mushroom *Ganoderma*. *Food Rev. Int.* **21**, 211–229 (2005)
- Hatvani, N.: Antibacterial effect of the culture fluid of *Lentinus edodes* mycelium grown in submerged liquid culture. *Int. J. Antimicrob. Agents* **17**, 71–74 (2001)
- Alves, M.J., Ferreira, I.C.F.R., Martins, A., Pintado, M.: Antimicrobial activity of wild mushrooms extracts against clinical isolates resistant to different antibiotics. *J. Appl. Microbiol.* **113**, 466–475 (2012)
- Balouiri, M., Sadiki, M., Ibsouda, S.K.: Methods for in vitro evaluating antimicrobial activity: a review. *JPA* **6**(2), 71–79 (2016)
- Wayne, P.: Clinical and laboratory standards institute. Performance standards for antimicrobial susceptibility testing, p 17 (2007)
- Zavastin, D.E., Bujor, A., Tuchilus, C., Mircea, C.G., Gherman, S. P., Aprotosoiaie, A.C., Miron, A.: Studies on antioxidant, antihyperglycemic and antimicrobial effects of edible mushrooms *Boletus edulis* and *Cantharellus cibarius*. *J. Plant Dev.* **23**, 87–95 (2016)
- Barros, L., Venturini, B.A., Baptista, P., Estevinho, L.M., Ferreira, I.C.F.R.: Chemical composition and biological properties of Portuguese wild mushroom: a comprehensive study. *J. Agric. Food Chem.* **56**, 3856–3862 (2008)
- Dulger, B., Gonuz, A., Gucin, F.: Antimicrobial activity of the macrofungus *Cantharellus cibarius*. *Pak. J. Biol. Sci.* **7**(9), 1535–1539 (2004)
- Zavastin, D.E., Bujor, A., Tuchilus, C., Mircea, C.G., Gherman, S. P., Aprotosoiaie, A.C., Miron, A.: Studies on antioxidant, antihyperglycemic and antimicrobial effects of edible mushrooms *Boletus edulis* and *Cantharellus cibarius*. *J. Plant De.* **23**, 87–95 (2016)
- Kosanić, M., Ranković, B., Rančić, A., Stanojković, T.: Evaluation of metal concentration and antioxidant, antimicrobial, and anticancer potentials of two edible mushrooms *Lactarius deliciosus* and *Macrolepiota procera*. *J. Food Drug Anal.* **24**(3), 477–484 (2016)

Effects of ^{99m}Tc on the Redox Properties of L-Thyroxine

Safija Herenda, Anera Kazlagić, Edhem Hasković, and Denis Hasković

Abstract

This paper presents the redox properties of hypothyroid drug L-thyroxine without and in the presence of sodium pertechnetate (^{99m}Tc) by an electrochemical method on glassy-carbon (GC) electrodes using a cyclic voltammetry technique. The cyclic voltammetry method was used to investigate the effects of various concentrations of L-thyroxine without and in the presence of ^{99m}Tc radiopharmaceuticals, the effect of the number of scan cycles, as well as the effect of ^{99m}Tc activity on the appearance of cyclic voltammograms. The results show that with the increase of the concentration of L-thyroxine, the increase of the peak current in the reduction area is notable. Obtained results show that the application of different concentrations of ^{99m}Tc on the drug exhibits the inhibitory properties of used radiopharmaceutical in the treatment of hypothyroidism.

Keywords

L-thyroxine • Sodium pertechnetate • Cyclic voltammetry

1 Introduction

Hypothyroidism represent a reduced function of the thyroid gland, in other words the absence of the thyroid gland hormone effect in the cells. For treating this disease, the most commonly used drug is L-thyroxine. Most people who consume this medicine, are frequently exposed to scintigraphy method, in the purpose of diagnosing the disease, whereby their radiopharmaceutical is injected intravenously.

Scintigraphy method allows the localization of radiopharmaceutical collection sites, and information on the state of the thyroid gland with the help of the gamma-ray is obtained [1, 2].

The role of thyroid hormones is to regulate growth and development, boost basal metabolism and accelerate carbohydrate metabolism.

The thyroid hormone is produced as an extract of the thyroid gland of the pig or is prepared as a sodium salt (levothyroxin from L-thyroxine and liothyronine from the triiodothyronine). Daily doses for the replacement of thyroid hormone levothyroxins are about 120 μg [3]. For the normal production of human thyroid hormones, daily intake of iodine in the body is required in the amount of 100–200 μg [4].

Levothyroxine sodium (abbreviated L-thyroxine) is used to treat hypothyroidism. It is a synthetic thyroid hormone, which has the same effect as natural thyroid hormones. It increases the metabolism of lipids, proteins and carbohydrates, regulates the consumption of oxygen and body temperature, acts on the bloodstream and the nervous system. It is used to compensate for natural hormone in hypothyroidism. Strongly binds to plasma proteins, and effects only occur after a few days and last for quite a long time after cessation of treatment. L-thyroxine is unevenly absorbed from the gastrointestinal tract.

In this paper, the kinetics of L-thyroxine were performed without and in the presence of radiopharmaceuticals.

S. Herenda · A. Kazlagić (✉)

Department of Chemistry, Faculty of Science, University of Sarajevo, Zmaja od Bosne 33-35, 71000 Sarajevo, Bosnia and Herzegovina
e-mail: anera.kazlagic@outlook.com

E. Hasković

Department of Biology, Faculty of Science, University of Sarajevo, Zmaja od Bosne 33-35, 71000 Sarajevo, Bosnia and Herzegovina

D. Hasković

Organizational Unit Clinical Chemistry and Bio-Chemistry, Clinical Center of the University of Sarajevo, Bolnička 25, 71000 Sarajevo, Bosnia and Herzegovina

The radiopharmaceutical used in the test was ^{1m}Tc , in the form of a solution of sodium pertechnetate, and the tests were performed in vitro. The redox properties of ^{99m}Tc can be monitored using the electrochemical method, because it has stable oxidation states in aqueous solutions [5]. In the following text, ^{99m}Tc ($^{99m}\text{TcO}_4^-$) instead of the full name sodium pertechnetate was labeled ^{99m}Tc .

2 Materials and Method

Material: Sodium pertechnetate labeled ^{99m}Tc ($t_{1/2} = 6.01$ h, $A_0 = 2$ mCi, commercial generator Dr. Abdulah Nakas General Hospital Sarajevo), KH_2PO_4 and Na_2HPO_4 , Fisher Chemical (Wien, Austria); L-thyroxine (Favistan, Bosnalijek, Sarajevo, B&H). All other compounds used in this study were commercially available as the highest purity reagents.

Method: The instrument used for the measurement is the potentiostat/galvanostat PAR 263A in the classical three-electrode system, where the glassy carbon electrode was used as the working electrode, the reference electrode is a saturated Ag/AgCl electrode, while Pt-electrode was used as counter electrode. Cyclic voltammetry is commonly used as a technique for the study of kinetics of different types of drugs. By using this technique, it is also possible to establish an irreversible controlled diffusion reaction by monitoring the effect of pH, the impact of the scan rate and the effect of concentration [6–8]. Electrochemical techniques such as cyclic voltammetry offer high sensitivity, precision, low cost and accuracy [9]. In the previous research [10–14] for determination of kinetic parameters and behavior of drugs in in vitro conditions, an electrochemical method was used. In order to determine the effect of different L-thyroxine concentrations and its kinetic characteristics, a cyclic voltammetry technique was used, with the default potential range being -1.5 to 0.7 V, and a scanning speed of 50 mV. The studies were conducted with and without ^{99m}Tc , in a phosphate buffer solution which pH was 7.

3 Results and Discussion

In order to test the effect of different L-thyroxine concentrations in phosphate buffer (pH 7), we used the cyclic voltammetry method in the range of potentials from -1.5 to 0.7 V and at a scanning speed of 50 mV/s. From cyclic voltammograms, the values of current peaks at different

concentrations $[\text{L-thyroxine}] = 0.1386, 0.2226, 0.2623, 0.3007$ and 0.3735 μM were measured. In the area of reduction, at the potential of -0.800 V, with increasing drug concentration in the solution, an increase in the current peak is evident from Fig. 1.

Graphic representation of this data gives a curve (Fig. 2) showing a linear increase in current with increased concentration of L-thyroxine.

In order to investigate the effect of radiopharmaceutical on L-thyroxine, whether if it inhibits or activates the drug concentration, ^{99m}Tc solution was added (Fig. 3). Figure 3 shows that the ^{99m}Tc addition affects the activity of the drug. The obtained current values are greater than the current values of the reaction without the presence of radiopharmaceuticals, and from the enclosed, it can be seen that with the addition of the ^{99m}Tc solution, the currents increase and the chemical reaction rate constant, accordingly, are less. Therefore, we can conclude that ^{99m}Tc acts as an inhibitor.

In order to test whether the drug layer on the surface of the GC electrode was correctly applied, 30 scan cycles of GC/L-thyroxine electrode in phosphate buffer was recorded

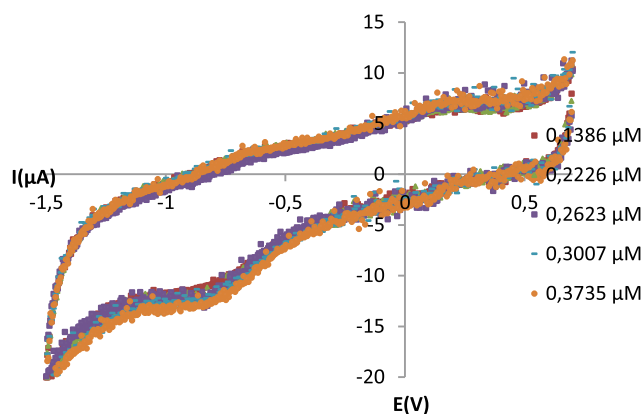


Fig. 1 Cyclic voltammogram of GC electrode in presence of various concentration of L-thyroxine

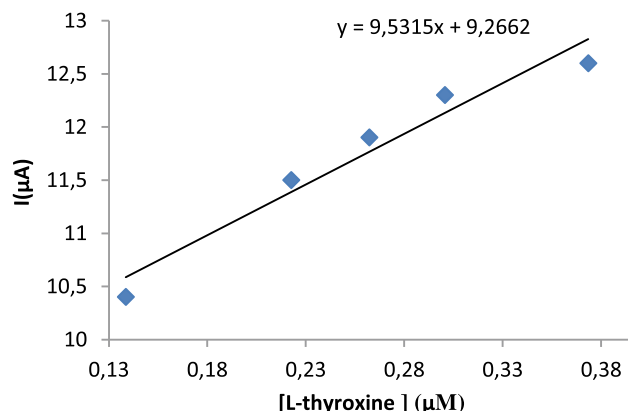


Fig. 2 Graphical representation of current as the function of concentration of Lthyroxine

^{1m}Tc ($^{99m}\text{TcO}_4^-$) instead of the full name sodium pertechnetate was labeled ^{99m}Tc .

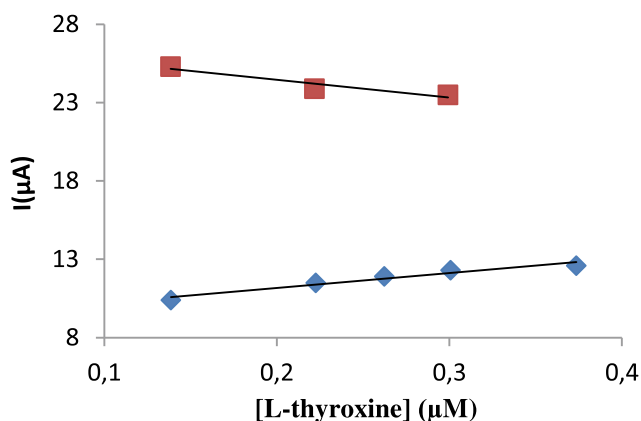


Fig. 3 Current as function of drug concentration L-thyroxine, without and with the addition of ^{99m}Tc solution: (diamond) without ^{99m}Tc , (square) with ^{99m}Tc

at a scan rate of 50 mV s^{-1} . The recording showed that there are no deviations in the appearance of the curve for every cycle, as can be seen in Fig. 4, where the values of the currents in the anode oxidation field are presented, at a potential of 0.4455 V .

Since the current is directly proportional to the thickness of the surface film, the deviation of the curve towards larger or smaller values with the increase in the number of cycles indicates the uneven distribution of the drug on the surface of the electrode. In Fig. 4 it can be clearly seen that by the diffusion process the L-thyroxine layer is aligned equally throughout the surface of the GC electrode.

To test the effect of the ^{99m}Tc solution on the L-thyroxine drug, ^{99m}Tc solution was added at a different time interval, while the initial activity of ^{99m}Tc was 2 mCi . In Fig. 5, three voltammograms of L-thyroxine in the presence of ^{99m}Tc were shown, where recordings were performed in the potential range from -1.5 V to 0.7 V at a constant scan rate of 50 mV/s . The concentration of L-thyroxine was constant $0.2991 \mu\text{M}$. As ^{99m}Tc gradually decays with time, the reduction of the reduction peak appears disproportionately, which is in accordance with the law on radioactive decay.

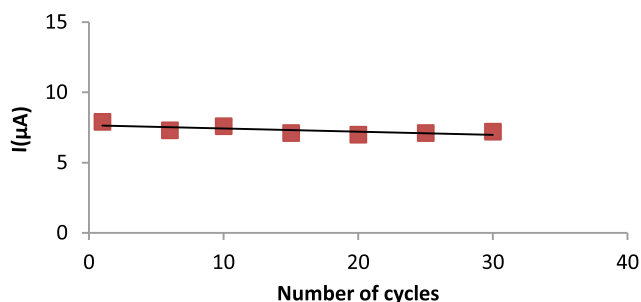


Fig. 4 Dependence of oxidation peak from the number of cycles on GC/Lthyroxine electrode in phosphate buffer

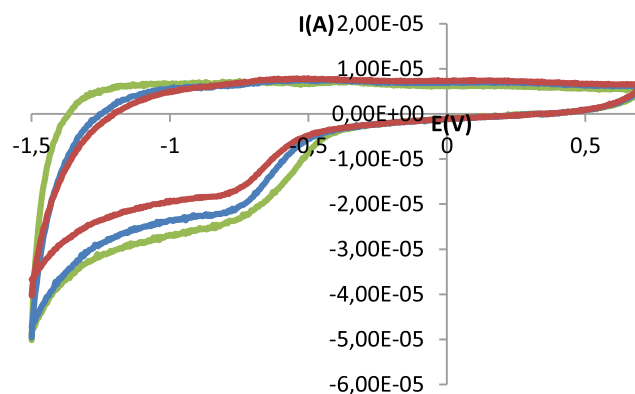


Fig. 5 Cyclic voltammograms for the L-thyroxine concentration of $0.2991 \mu\text{M}$, before and after the indicated time were: initial recording (green line); recording after 3 h (blue line); recording after 4 h and 45 min (red line)

As time elapses, decrease of reduction peaks is observed. The activity of the radionuclide decreases with time, which can be seen according to the data in Table 1. The activity was calculated based on the formula of the law of decay.

4 Conclusions

Considering the results obtained by cyclic voltammetry, it is possible to make a few conclusions:

By increasing the concentration of a drug, an increase in the current point in the reduction area is observed. It was thus established that the concentration of the investigated drug has a significant effect on its kinetic characteristics.

Increase in current strength goes up to a certain limit when saturation occurs, and any further drug addition makes no sense because there are no significant shifts or volumes on the voltammogram.

The influence of different cycles on the appearance of voltammogram in the presence of the selected drug concentration is also investigated. 30 cycles have been recorded. Since the diagram shows that there is almost no deviation at different recording cycles, it has been found that recording cycles have no significant effect on the appearance of cyclovoltammogram.

By comparing the obtained currents depending on the concentration of drug Lthyroxine without and with ^{99m}Tc , we come to the conclusion that ^{99m}Tc acts as an inhibitor. Accordingly, due to inhibitory properties, ^{99m}Tc affects the organism in such a way that it slows down the growth of cancer cells.

Research showed that for the L-thyroxine, ^{99m}Tc activity has a significant effect on the voltammogram form.

Table 1 Change in radionuclide activity with time change

t (h)	A (mCi)
0	2.00
3.00	1.41
4.75	1.16

The radioactive decomposition process is an exponential process and from the table data (Table 1) a decrease in ^{99m}Tc activity with time change t can be seen, which directly affects the shift of a current point.

Which chemical reaction exactly happens between the drug in the blood of a patient undergoing radiopharmaceutical diagnosis, or how it reacts with ^{99m}Tc , can not be detected by this method. For the purpose of detecting the details of complex chemical reactions, it would be desirable to use a more precise, or more suitable technique for that purpose (e.g., Raman's spectroscopy or SEM).

Conflict of Interest The authors declare that there are no conflicts of interest regarding the publication of this paper.

References

- Vellabhajosula, S.: *Molecular Imaging: Radiopharmaceuticals for PET and SPECT*. Springer, New York (2009)
- Welch, M., Redvanly, C.S.: *Handbook of Radiopharmaceuticals: Radiochemistry and Applications*, 88–89. Wiley, NY (2003)
- Zulić, I., Mulabegović, M.N.: *Farmakologija, klinička farmakologija, toksikologija*. Printing and Publishing House "Jež", Sarajevo (1995)
- Wartofsky, L.: *Bolesti štitnjače u: Harrison Principi interne medicine*, ur: Ž. Ivančević i sur. Placibo (1997)
- Serrano, P.N.: *Electrochemistry of technetium analogs rhenium and molybdenum in room temperature ionic liquid*. UNLV theses, Dissertations, Professional Papers, and Capstones (2011)
- Skoog, D.A., West, D.M.: *Osnove analitičke kemije*, VI izdanje (englesko); I izdanje (hrvatsko), Zagreb (1999)
- Elqudaby, H.M., Gehad, G.M., El Din, G.M.G.: *Electrochemical behaviour of trimebutine at activated glassy carbon electrode and its direct determination in urine and pharmaceuticals by square wave and differential pulse voltammetry*. *Int. J. Electrochem. Sci.*, 856–857 (2013)
- Gopu, G., Manisankar, P., Muralidharan, B., Vedhi, C.: *Stripping voltammetric determination of analgetics in their pharmaceuticals using nano-riboflavin-modified glassy carbon electrode*. *Int. J. Electrochem.*, 1–2 (2011)
- Engin, C., Yilmaz, S., Saglikoglu, G., Yagmur, S., Sadikoglu, M.: *Electroanalytical investigation of paracetamol on glassy carbon electrode by voltammetry*. *Int. J. Electrochem. Sci.*, 1917–1918 (2015)
- El-Shanawany, A.A., El-Adl, S.M., El Haleem, D.S., El Wanees, S.: *Electrochemical characterization and determination of the anticancer drug flutamide*. *Ann. Chemschen Forshung* **2**, 29–40 (2014)
- Muralidharan, B., Gopu, G., Vedhi, C., Manisankar, P.: *Voltammetric determination of analgesics using a montmorillonite modified electrode*. *Appl. Clay Sci.*, 206–207 (2007)
- Sanad, M.H.: *Novel radiochemical and biological characterization of ^{99m}Tc -histamine as a model for brain imaging*. *J. Anal. Sci. Technol.*, 1–2 (2014)
- Chen, P., McCreery, R.L.: *Control of electron transfer kinetics at glassy carbon electrodes by specific surface modification*. *Anal. Chem.* **68**, 3958–3965 (1996)
- Orazem, M.E., Tribollet, B.: *Electrochemical Impedance Spectroscopy*, vol. 48. Wiley, NY (2011)



Novel Aspects of Drug Delivery: Wireless Electronic Devices

Berina Tatlić, Lejla Šejto, Merima Sirbubalo, Amina Tucak, and Edina Vranić

Abstract

A novel system of delivery presents many advantages such as sustained delivery, higher bioavailability, improved medication compliance, and therapeutic outcomes, patient monitoring, and minor side effects. One of the improved ways of drug delivery is electronic capsules which can deliver drugs to a specific site in the gastrointestinal tract and can also be used for patient monitoring. Wireless transdermal patches are a novel electronic drug delivery system, which is portable, disposable and worn on the skin surface to deliver medications on the transdermal level. Electronic transdermal drug delivery has made a major contribution to clinical practice due to improving the efficiency of drug delivery over the conventional route. The improvement can provide a solution for getting rid of the bondage of batteries as well as the restrictions of inconvenient wires, on self-powered systems. The greatest achievement of wireless transdermal patches is the ability to further improve transdermal drug delivery for certain drugs that could not be administered using conventional transdermal patches. Electronic drug delivery systems such as capsules, on the other side, can be used not only to deliver drugs to a specific site in the gastrointestinal tract but can also record data and report the state of patients gastrointestinal tract, and after excretion, this information can be studied and used to present them graphically.

Keywords

Electronic drug systems • Transdermal delivery • Wireless • Patch • Pill

B. Tatlić (✉) · L. Šejto
Faculty of Pharmacy, University of Sarajevo, Sarajevo, Bosnia and Herzegovina
e-mail: berina.tatlic@gmail.com

M. Sirbubalo · A. Tucak · E. Vranić
Department of Pharmaceutical Technology, Faculty of Pharmacy, University of Sarajevo, Sarajevo, Bosnia and Herzegovina

© Springer Nature Switzerland AG 2020
A. Badnjevic et al. (eds.), *CMBEBIH 2019*, IFMBE Proceedings 73,
https://doi.org/10.1007/978-3-030-17971-7_82

1 Introduction

Electronic drug delivery systems (EDDS) have recently become highly popular as they are effective in administering drugs at an exact time and maintaining effective doses; however, as effective as they are, their uses are limited as EDDS can't be applied to every body part. This method of drug delivery is painless. When the drug formulation is applied to intact skin it will be delivered systemically. The research has been conducted on transdermal drug delivery system. A transdermal way is considered to be one of the most convenient forms of drug delivery. This novel system of drug delivery presents many advantages over traditional delivery systems such as sustained delivery, higher bioavailability, improved medication compliance, and therapeutic outcomes, patient monitoring and minor side effects caused by drugs. Electronic drug delivery systems can reduce side effects by delivering targeted drug particular sites in the parts of the body that are difficult to reach. This way of treating the disease can also be a noninvasive alternative to parenteral routes. Transdermal route suffers from limitations due to low permeability governed by the skin. Further in this paper we will discuss more about novel electronic drug delivery systems, specifically wireless transdermal patches and electronic capsules, their working mechanisms and advantages over conventional drug delivery [1–5].

2 Smart Pills

An electronic capsule is a drug delivery system which can deliver one drug or several different types of drugs to a specific site in the gastrointestinal tract (GIT) where it may normally be difficult to do, and can also be used for patient monitoring. It is made from a durable material resistant to GIT secretions and contains a pump, drug reservoir, battery, pH and temperature sensors, a wireless receiver and a

microprocessor. Patient monitoring is achieved through constant measurements of pH levels and temperature [1, 6]. Since the capsule is made from materials resistant to GIT secretions, drug effects will be delayed until it reaches its designated place in the GIT, where the dose will be fully released, which allows easier prediction of therapeutic effects. EDDS have certain other advantages compared to conventional pharmaceutical forms—they are portable, interactive and wirelessly controlled via a computer or a smart-phone which allows drug in question to be administered by the patient. There are, some disadvantages to these devices—their manufacturing is extremely pricey, there is difficulty in achieving necessary biocompatibility and there are certain dangers when it comes to devising failure while the device is in use [1].

2.1 IntelliCap®

The IntelliCap® capsule (Fig. 1), developed by Dieter Becker et al. and manufactured by Medimetrics, is an electronic wireless drug delivery system which can be administered orally and is capable of delivering real-time information on physiological conditions such as pH value and temperature. This allows the researchers to be able to locate the capsule at any point in time by the typical physiological pH profiles in humans. When using this device, certain individual patient factors such as body weight are used in combination with pharmacodynamics of the drug to develop the best release profile possible [1, 8, 9].

The capsule itself is, in fact, a pump (Fig. 2). The power source needs to be small but has a long-lasting power

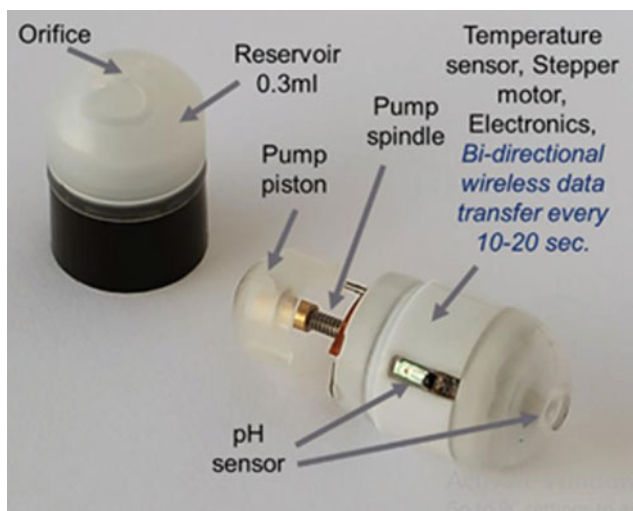


Fig. 1 Photograph of the IntelliCap® capsule (short version) [7]

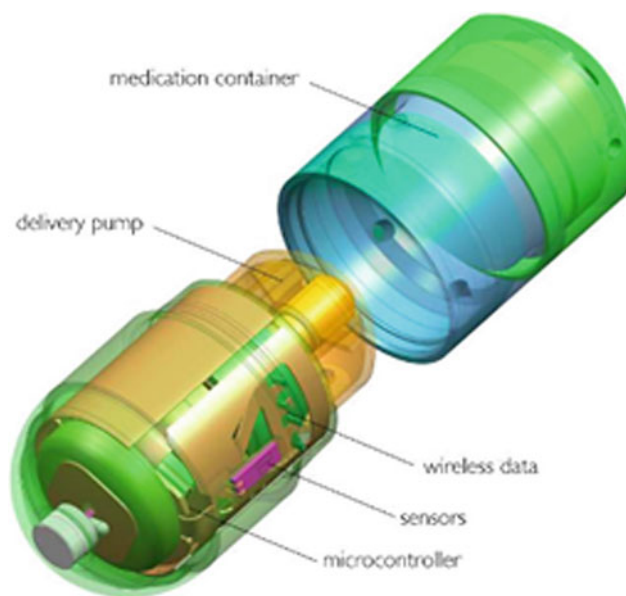


Fig. 2 IntelliCap® structure [1]

supply. Researchers from MIT have recently developed a device that when ingested, powers up using gastric acid, but since this device has been only tested on pigs, it has not yet been tested on humans or approved for human use. Sensors are used to collect environmental data of the capsule or device [7].

These can be pH sensors, pressure sensors, temperature sensors etc. and they must be made of biocompatible materials, so the device lasts as long as possible inside the body. Drug reservoirs are filled with a drug solution which flows through a system of channels modulated by valves and pumps. Electromagnetic propulsion technology with flow rates of 0.1–1000 ml/h supposedly improves the flow of drug solutions through and out of the device. The microprocessor is the most important part of this device. It is recommended to use processors with low power requirements in implantable and orally administered devices [7].

2.2 SmartPill®

SmartPill® is “an ingestible capsule that measures pressure, pH and temperature as it travels through the GI tract to assess GI motility” [1]. Other than assessing GIT motility, pH, and temperature, Smart-Pill can be used to determine a gastric emptying time, colonic transit time, total intestinal time and pressure. The capsule is minimally invasive and works via wireless technology. It should be ingested following a meal, after which measure values for pH, temperature and pressure

are transmitted to a receiver carried by the patient. This process is done until the capsule is excreted. Then the receiver is used to download recorded data to the SmartPill[®] software which expresses this information graphically and allows it to be used for diagnostic purposes [10].

2.3 Uses of SmartPill[®] and IntelliCap[®] So Far

The IntelliCap[®] system has been so far used in several studies as a tool to uncover the properties of drugs. In one of those studies, conducted in 2014 by Mauer et al., the IntelliCap[®] system was used to prove the ileocolonic release of ColoPulse[®] tablets.

The main goal was to prove in vivo that there was a connection between gastrointestinal pH and the release of the active substance in the ileocolonic area. Dual-label isotope strategy was used to study release from ColoPulse[®] tablets in 16 individuals who were healthy volunteers. They were each given a ColoPulse[®] specific-release tablet containing ¹³C-urea and a different, uncoated ¹⁵N₂-urea tablet, which had an immediate release. After five minutes an IntelliCap[®] capsule was swallowed, followed by pH measurement until the elimination was completed (through the faecal route). It is important to note that release from ColoPulse[®] tablets occurred after a pH intestinal value of 7 was reached, regardless of how long it took the tablet to reach a said area, and this information was confirmed using the IntelliCap[®] system [8].

Also in 2014, two different studies used the IntelliCap[®] system in fasting human subjects with the goal of investigating pH and temperature profiles in the gastrointestinal tract. In this case, it was possible to measure gastric emptying time, intestinal transit time and how long it took the capsule to reach the colonic region, by measuring pH and temperature changes along the way. A high fluctuation of the pH values was discovered, ranging from pH 1.7 to pH 4.7. The values increased during the intestinal transit—to pH 5.9–6.3 in the proximal part and pH 7.4–7.8 in the distal parts of the small intestine. However, in the colonic region, those fluctuations were higher, varying from pH 5 to pH 8. These results can increase the comprehension of drug release from solid pharmaceutical forms taken orally while the patient is fasting [9].

The SmartPill[®] device has been approved for use by FDA since 2006 and has since been used in many studies and trials. In 2012, it was used to assess GIT function in patients with spinal cord injuries [1, 10]. In another study, it was used in combination with PillcamSB2 for patients suspected of having Crohn's disease [11].

3 Electronic Transdermal Patches

A novel electronic drug delivery system that is called electronic transdermal patches (Fig. 3) is portable, disposable and worn on the skin surface to deliver medications on the transdermal level. More functions are being integrated into devices that people can wear wherever they go. The main reason for developing such a delivery system is because convenient ways that need batteries can cause problems such as frequently charging as well as inconvenient to carry them. The improvement of self-powered systems provides a solution for wearable smart electronics to get rid of the bondage of batteries as well as the restrictions of inconvenient wires. These systems combine enhanced energy harvester and wireless transmission technology. The electronic transdermal patch usually contains sensors, memory, electronic circuits, and drug delivery components. They use data collected to determine when to deliver the drug which is stored within the patch. All of the stored data can be made available for downloading on the external source for patient monitoring and management [12, 13].

Design of the transdermal patches are usually contained of a reservoir where the drug is stored, that is enclosed on one side with an impermeable backing and has an adhesive that is in contact with skin on the other side. A reservoir can be liquid- or gel-based and the drug can be dissolved in those, which can simplify formulation and permit the use of liquid chemical enhancers such as ethanol. Hydrogel formulations are considered desirable because they can provide an electroconductive base with an added advantage of ease of application to adapt to the contours of the body.

Design of the transdermal patches characteristically is composed of four layers [13]:

- an impermeable backing membrane,
- a drug reservoir,

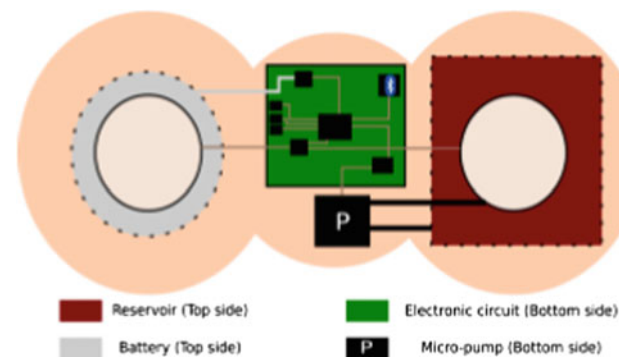


Fig. 3 Bottom view of the proposed patch ($12 \times 4 \text{ cm}^2$) [21]

- a semipermeable membrane (rate-limiting membrane) and
- an adhesive layer.

Other designs can incorporate drugs into a solid polymer matrix which simplifies manufacturing because matrix systems can have three layers by eliminating semipermeable membrane or just two layers if the drug is directly incorporated into the adhesive [13].

3.1 Physical Penetration Enhancement

The most of the transdermal patches that have been used in clinical are from:

- First generation of patches and in comparison with oral drug delivery, transdermal patches should be able to provide better bioavailability because of the need for not so frequent dosing of small, lipophilic, low-dose drugs.
- Second generation of transdermal delivery systems have some better preferences due to their ability to recognize that for the better expansion of drug is very important to enhance skin permeability. They have an advanced clinical practice. Because it has improved delivery of the small molecule [3, 4].

The ideal enhancer should increase the permeability of the skin in the way that it would break the integrity of the *stratum corneum*. The enhancers that can be used are chemical, iontophoresis, and non-cavitation ultrasound [3].

- Third generation has made an impact on drug delivery because its effects are targeted directly to the *stratum corneum*. This can enable stronger disruption of its barrier and due to that a more efficient transdermal delivery of the macromolecules while still protecting other tissues with novel enhancers such as electroporation, cavitation ultrasound, and microneedles. And the main reason for enabling this advances to be made is that to make all aggressive approaches medically acceptable [15–20].

3.2 Active Methods for Drug Transport

There are certain technologies that are used to modify the barrier properties of the *stratum corneum*. The two major means of electrically-facilitated transdermal drug delivery systems are iontophoresis and electroporation. In electroporation, cells are temporarily exposed to high intensities of electric pulses that will lead to the formation of aqueous pores in the lipid bilayers of the *stratum corneum* which will

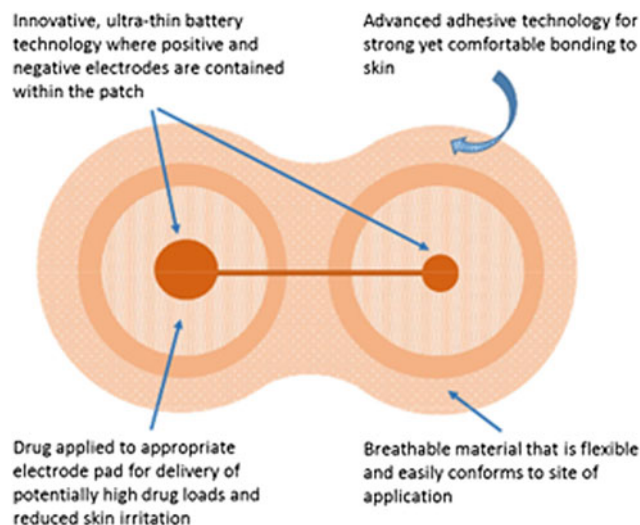


Fig. 4 WEDD[®] transdermal patch [1]

allow the diffusion of drugs across the skin. On the other side, iontophoresis involves the application of physiologically acceptable electrical currents (0.1–1.0 mA/cm²) to drive charged permeants into the skin through electrostatic effects and make ionic drugs pass into the body through the skin by its potential gradient. Iontophoresis has a minor effect on skin structure when compared to electroporation [14].

Ionsys[®] (Alza Corporation, Mountain View, CA, USA) was a second iontophoretic system that was approved by FDA in 2006. This was a fully integrated single-use iontophoretic system for the systemic delivery of fentanyl for fast relief of postoperative pain that is also patient controlled. But it was suspended by European Medicines Agency in 2009. Due to patch corrosion in one of the branches which could potentially lead to self-activation of the system with toxic over-dose [1, 13].

Wearable Electronic Disposable Drug (WEDD) (Fig. 4) is an example of noninvasive electronic transdermal drug delivery developed by Travanti Pharma a Teikoku Pharma Affiliate company and it is a portable and Disposable patch which uses low levels of currents to deliver medication transdermally. Combined with an ultrathin battery these electrodes are incorporated into the patch to give a single, self-contained disposable unit [1].

4 Conclusion

Over the past couple of decades, EDDS have become a highly popular way of administering drugs because of how efficient, reliable and simple to use they are. Wireless transdermal patches have the ability to further improve transdermal drug delivery by allowing for certain drugs to be administered that

could not be administered using traditional dermal patches. Their effect can further be improved by modifying the properties of the stratum corneum by using iontophoresis and electroporation. As opposed to patches, EDDS in the form of capsules or tablets can be used not only to deliver drugs to specific locations in the GIT, but also to record and report on the state of a patients' GIT (such as temperature, pH value, pressure etc.) and have recently seen a rise in development and production. Their advantage is the simplicity of usage upon ingestion, the device begins to send information to a wireless receiver. After excretion, this information can be gathered, presented graphically and studied.

Conflict of Interest Authors have no conflicts of interest to disclose.

References

- Vadlapatla, R., Wong, E.Y., Gayakwad, S.G.: Electronic drug delivery systems: an overview. *J. Drug Deliv. Sci. Technol.* **41**, 359–366 (2017)
- Sung, S.H., Kim, Y.S., Joe, D.J., Mun, B.H., You, B.K., Keum, D. H., et al.: Flexible wireless powered drug delivery system for targeted administration on cerebral cortex. *Nano Energy* (2018)
- Talbi, Y., Campo, E., Brulin, D., Fourniols, J.Y.: Controllable and reusable patch for transdermal iontophoresis drug delivery. *Electron. Lett.* **54**(12), 739–740 (2018)
- Prausnitz, M.R., Langer, R.: Transdermal drug delivery. *Nat. Biotechnol.* **26**(11), 1261–1268 (2008)
- Lin, S., Yuk, H., Zhang, T., Parada, G.A., Koo, H., Yu, C., et al.: Stretchable hydrogel electronics and devices. *Adv. Mater.* **28**, 4497–4505 (2016)
- Narayanan, A.V., Charyulu, R.N.: Pharmaco-electronics and electropharmaceuticals: the arts and science of electronic drug delivery. *Res. J. Pharm. Technol.* **10**, 3544–3548 (2017)
- Becker, D., Zhang, J., Heimbach, T., Zou, H., Shimizu, J., Wanke, C.: Novel orally swallowable IntelliCap[®] device guarantee success in MR development by quantitative determination of regional drug absorption in man. *AAPS PharmSciTech* **15**(6):1490–1497 (2014 Dec)
- Maurer, J.M., Schellekens, R.C.A., van Rieke, H.M., Wanke, C., Jordanov, V., Stellaard, F., et al.: Gastrointestinal pH and Transit time profiling in healthy volunteers using the IntelliCap system confirms Ileo-Colonic Release of ColoPulse tablets. *PLoS ONE* **10** (7), 1–17 (2015)
- Koziolek, M., Grimm, M., Becker, D., Jordanov, V., Zou, H., Shimizu, J., et al.: Investigation of pH and temperature profiles in the GI tract of fasted human subjects using the IntelliCap[®] system. *J. Pharm. Sci.* **104**(9), 2855–2863 (2015)
- Williams, R.E. III, Bauman, W.A., Spungen, A.M., Vinnakota, R. R., Farid, R.Z., Galea, M., et al.: SmartPill Technology Provides Safe and Effective Assessment of Gastrointestinal Function in Persons With Spinal Cord Injury, 81–84. *International Spinal Cord Society* (2012)
- Yung, D., Plevris, J., Koulaouzidis, A.: PTU-010 a combination of Pillcam[®]SB2 and SmartPill[®] in the investigation of patients referred for assessment of known or suspected small-bowel Crohn's disease & their association with faecal calprotectin levels; Case Series. *Gut* **65**(Suppl 1), A56.2–A57 (2016)
- Shi, M., Wu, H., Zhang, J., Han, M., Meng, B., Zhang, H.: Self-powered wireless smart patch for healthcare monitoring. *Nano Energy* **32**, 479–487 (2017)
- Prausnitz, M.R., Langer, R.: Transdermal drug delivery. *Nat. Biotechnol.* **26**(11), 1261–1268 (2008)
- Alkilani, A., McCrudden, M.T., Donnelly, R.: Transdermal drug delivery: innovative pharmaceutical developments based on disruption of the barrier properties of the stratum corneum. *Pharmaceutics* **7**(4), 438–470 (2015). CMBEBIH2019, 082, v2 (final): 'Novel aspects of drug delivery: Wireless electronic devices'
- Guy, R.H., Hadgraft, J. (eds.): *Transdermal Drug Delivery*. Marcel Dekker, New York (2003)
- Williams, A.: *Transdermal and Topical Drug Delivery*. Pharmaceutical Press (2003)
- Prausnitz, M.R., Mitragotri, S., Langer, R.: Current status and future potential of transdermal drug de-livery. *Nat. Rev. Drug Discovery* **3**, 115–124 (2004)
- Bronaugh, R.L., Maibach, H.I. (eds.): *Percutaneous Absorption*. Marcel Dekker, New York (2005)
- Morgan, T.M., Reed, B.L., Finnin, B.C.: Enhanced skin permeation of sex hormones with novel topical spray vehicles. *J. Pharm. Sci.* **87**, 1213–1218 (1998)
- Arora, A., Prausnitz, M.R., Mitragotri, S.: Micro-scale devices for transdermal drug delivery. *Int. J. Pharm.* **364**(2), 227–236 (2008)

Quantification of Active Substances in Some Drugs Using by Derivative UV/Vis spectroscopy

A. Etminan, A. Uzunović, A. Topčagić, S. Žero, M. Dizdar, L. Klepo, D. Čulum, H. Džudžević-Čančar, and I. Tahirović

Abstract

UV/Vis spectroscopy is usually used in identification of active substances in drugs. The aim of this study was to test the application of the derivative UV/Vis spectroscopy in determination of the active substances content (ASC) in some drugs. Acetylsalicylic acid (ASA), meloxicam (M) and naproxen (N) were the selected ASC that were analyzed in different drug samples. The all analyses were carried out on the Perkin-Elmer Lambda 25 spectrophotometer in triplicate. The pure ASA, M and N were used as standards, and the calibration curve method was used to determine the ASC in the samples. The absorption spectrums were recorded in the visible (Vis) region 400–800 nm for ASA, and in ultraviolet (UV) 200–400 nm region for M and N. After recording the absorption spectrums, a third-order derivations were made using UV WinLab software. The obtained ASC was within acceptable limits with declared values (d.v.) for the two drugs: [meloxicam in Melox (Nobel), and naproxen in Nalgesin S (Krka)]. The observed deviations were <10% (the measured meloxicam content was 92.27%, and for naproxen was 90.06%) of the d.v., which is in line with the *U.S. Pharmacopoeia (U.S.Ph.)*. In the case of Aspirin protect 100 (Bayer), the content of ASA was 89.56% of the d.v., which is slightly lower than that prescribed by the *U.S.Ph.* (deviation $\pm 5\%$ of the d.v.).

Based on the obtained results, it can be concluded that UV/Vis derivative spectroscopy is a suitable method for determining of the ASC in some drugs.

Keywords

Acetylsalicylic acid • Meloxicam • Naproxen • Derivative UV/Vis spectroscopy

1 Introduction

Quantification of the active substances content (ASC) in drugs is a very important part of the quality control in pharmaceutical companies. Analytical methods based on measurements of UV absorption or visible light are the most popular methods commonly used in laboratories. The basic disadvantage of UV/Vis spectroscopy is its low selectivity. One of the simplest methods for increasing selectivity is the absorption spectrum's derivation. By doing so, spectral interferences are eliminated, which results in an increase in the sensitivity of the method [1].

Standard calibration solutions must be as close as possible to the samples as a whole, and must include as wide concentration range of samples as possible [2]. In order to achieve experimental measurements that are representative of the concentration of the analyte in the sample, it is necessary to keep all variables constant, or with minimal changes within very narrow intervals [3]. In drug analysis, the problem of basic absorption is encountered when the amount of the active substance is low in relation to the total amount of tablet. In the case of tablets, this is strongly expressed if the absorption maximum is found in the UV area [4].

The derivative spectrum can be obtained by optical, electronic or mathematical methods. Optical and electronic techniques were used on early UV/Vis spectrophotometers, but were largely suppressed by mathematical techniques [5]. The application of derivative spectroscopy has recently

A. Etminan · A. Topčagić · S. Žero · M. Dizdar · L. Klepo · D. Čulum · I. Tahirović (✉)
Faculty of Science, Department of Chemistry, University of Sarajevo, Zmaja od Bosne 35, Sarajevo, Bosnia and Herzegovina
e-mail: itah@pmf.unsa.ba

A. Uzunović
Agency for Medicinal Products and Medicinal Devices of Bosnia and Herzegovina, Maršala Tita 9, Sarajevo, Bosnia and Herzegovina

H. Džudžević-Čančar
Faculty of Pharmacy, University of Sarajevo, Zmaja od Bosne 8, Sarajevo, Bosnia and Herzegovina

increased, primarily thanks to the development of computer technology [6]. The UV/Vis spectroscopy is an appropriate method for routine analysis of ASC in raw materials due to its speed, simplicity of performance, and does not require expensive instruments [7].

The main aim of this study was to examine the possibility of using derivative spectroscopy to analyze the content of active substances in some drugs. An analysis of three different active substances is planned: acetylsalicylic acid, meloxicam, and naproxen from different manufacturers.

2 Methods

Absorption spectrums were recorded in visible (Vis) region (400–800 nm) for ASA, and in ultraviolet (UV) region (200–400 nm) for meloxicam and naproxen. Using computer software, third-order derivatives (D3) of the absorption spectrums were obtained and the ASC in tablet samples were calculated. Calibration curve method was used to determine the ASC in the samples.

2.1 Samples

Acetylsalicylic acid (ASA), meloxicam (M) and naproxen (N) were the selected active substances that were analyzed in different drug samples: Aspirin protect 100 (Bayer), Melox (Nobel) and Nalgesin S (Krka).

The pure active substances were used as standards: acetylsalicylic acid 100%, SIGMA ALDRICH Trace CERTR by MERCK, meloxicam 99.92% by Derivados Quimicos, and naproxen sodium 99.7% by Krka.

2.2 Instrumentation

The analyses were carried out on the Perkin-Elmer Lambda 25 spectrophotometer in triplicate. Analytical balance (Mettler Toledo AB 104) was used to weight the mass of the pure standards.

3 Results and Discussion

While preparing the samples, it was especially important to choose a suitable solvent, since in some preliminary trials there were interferences for some samples, so spectrum capture could not be performed adequately. Also, prepared solutions were not stable, and had to immediately be subjected to measurement after their preparation, as there was

significant deviation in absorbance if the measurements were made after several hours, and also calibration curve would not be linear.

3.1 Quantification of Acetyl-Salicylic Acid (ASA)

After preparing stock standard solution of ASA by dissolving a certain amount of pure standard powder in 1 M NaOH, working solutions were prepared by taking different aliquots of that solution, and the volumetric flasks filled up to the mark with a solution of Fe(III) chloride. In this way, the working solutions with different concentrations (in range of 0.01–0.06 mg/mL) were obtained. The absorption spectrums of ASA working solutions were then recorded in the visible region compared to 1 M NaOH as a blank test. Subsequently, using computer software, third-order derivatives (D3) of the absorption spectrums were obtained, and the values of the D3 of the absorbances read at 434.15 nm are shown in Table 1.

Then a calibration curve was constructed, $D3 = f[\gamma_{(mg/mL)}]$, with equation: $y = 0.0681x + 0.0003$; $R^2 = 0.9974$.

Aspirin tablet solution was prepared in the same manner as standard solutions of pure ASA. Absorption spectrums were then recorded under the same operating conditions as with the ASA standard (Fig. 1)

Subsequently, using the computer software, derivatives of the third-order of values from the recorded spectrums were performed, and the results were obtained as shown in Table 2.

Maximum values of D3 were read at 434.15 nm. Mean value was 89.56 ± 3.42 mg, and a deviation was -10.44% compared to the declared value.

3.2 Quantification of Naproxen (N)

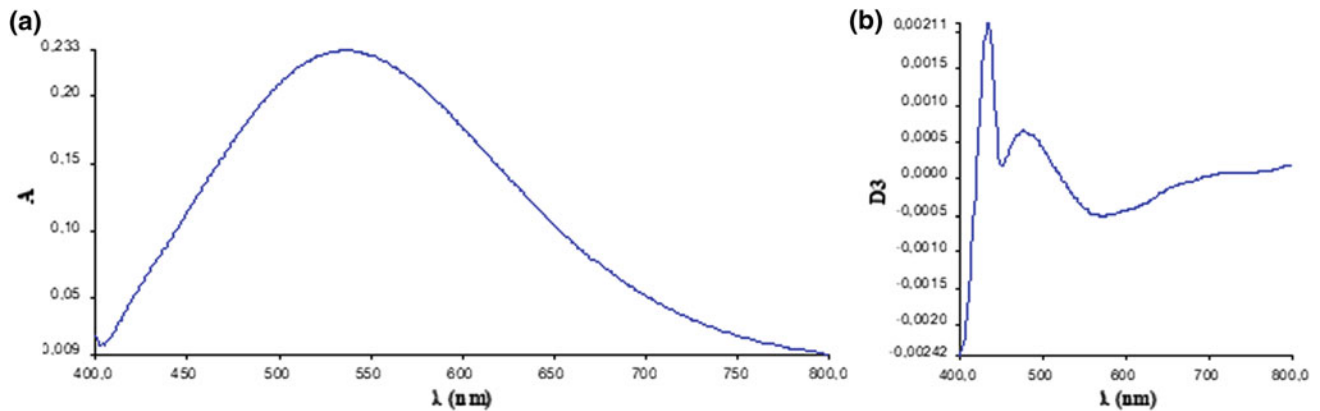
Stock standard solution of N was prepared by dissolving a certain amount of pure standard powder in methanol. Working solutions were prepared in the concentration range of 0.01–0.1 mg/mL by taking different aliquots of stock solution and filling the volumetric flask to the mark with distilled water. The absorption spectrums of N working solutions were then recorded in the UV region compared to methanol as a blank test.

Subsequently, using computer software, third-order derivatives (D3) of the absorption spectrums were obtained, and the values of the D3 of the absorbances read at 316.46–319.51 nm are shown in Table 3.

Then a calibration curve was constructed, $D3 = f[\gamma_{(mg/mL)}]$, with equation: $y = 1.2139x - 0.0006$; $R^2 = 0.9997$.

Table 1 Derivations of the third-order of the absorption spectrums of ASA standard solutions

No.	γ_{ASA} (mg/mL)	D3
1.	0.01	0.00094
2.	0.02	0.00178
3.	0.03	0.00237
4.	0.04	0.00312
5.	0.06	0.00438

**Fig. 1** Absorption (a) and derivative (b) spectrum of Aspirin protect 100 tablet**Table 2** Derivations of the third-order of absorption spectrums of an Aspirin protect 100 tablet sample

No.	D3	m_{ASA} (mg)
1.	0.00211	88.67
2.	0.00207	86.67
3.	0.00221	93.33

Table 3 Derivations of the third-order of the absorption spectrums of N standard solutions

No.	γ_N (mg/mL)	D3
1.	0.01	0.01264
2.	0.02	0.02348
3.	0.03	0.03487
4.	0.04	0.04777
5.	0.10	0.12112

Nalgessin S tablet solution was prepared in the same manner as standard solutions of pure N. Absorption spectrums were then recorded under the same operating conditions as with the N standard (Fig. 2).

Subsequently, using the computer software, derivatives of the third-order of values from the recorded spectrums were performed, and the results were obtained as shown in Table 4.

Maximum values of D3 were read at 316.46 nm. Mean value was 247.67 ± 11.50 mg, and a deviation was -9.94% compared to the declared value.

3.3 Quantification of Meloxicam (M)

After preparing stock standard solution of M by dissolving a certain amount of pure standard powder in 0.1 M NaOH,

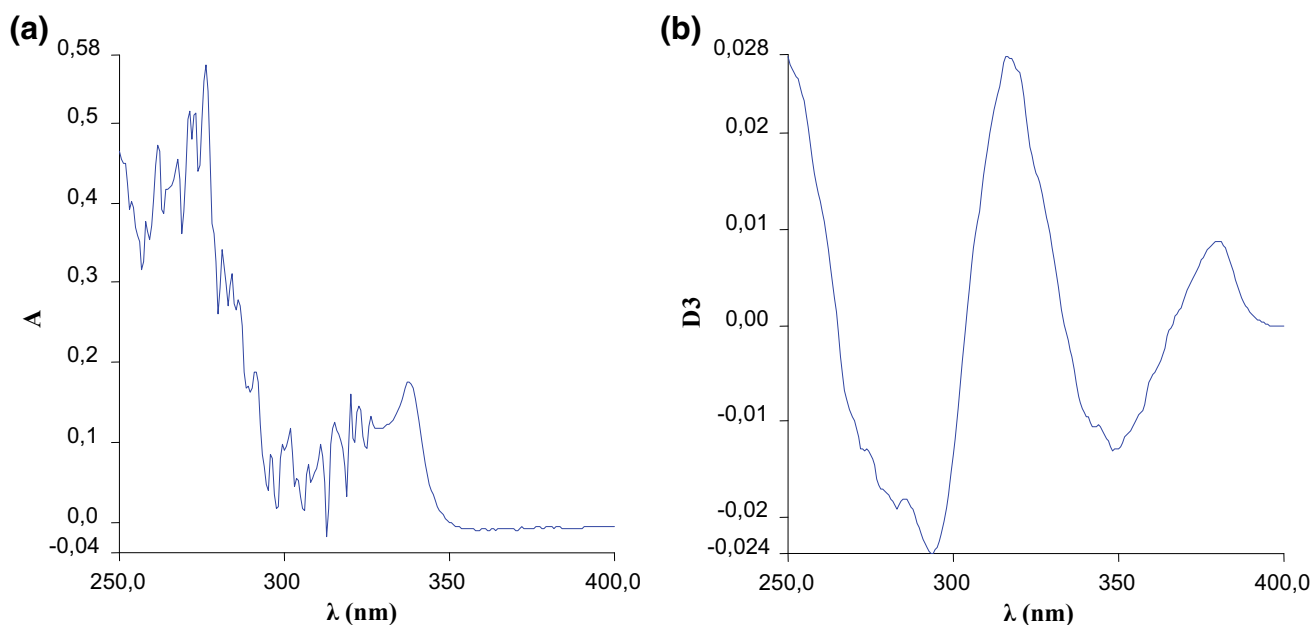


Fig. 2 Absorption (a) and derivative (b) spectrum of Nalgesin S tablet

Table 4 Derivations of the third-order of absorption spectrums of the Nalgesin S tablet sample

No.	D3	m_N (mg)
1.	0.02805	236
2.	0.02950	248
3.	0.03084	259

Table 5 Derivations of the third-order of the absorption spectrums of M standard solutions

#	γ_M (mg/mL)	D3
1.	0.005	0.01422
2.	0.015	0.03736
3.	0.020	0.04964
4.	0.025	0.06187
5.	0.030	0.07284

different aliquots were taken and the volumetric flask filled to the mark with distilled water. In this way, the working solutions with different concentrations (in range of 0.005–0.03 mg/mL) were obtained. The absorption spectrums of M working solutions were then recorded in the UV region compared to 0.1 M NaOH as a blank test.

Subsequently, using computer software, third-order derivatives (D3) of the absorption spectrums were obtained, and the values of the D3 of the absorbances read at 343.90–345.12 nm are shown in Table 5.

Then a calibration curve was constructed, $D3 = f[\gamma_{(mg/mL)}]$, with equation: $y = 2.361x + 0.002$; $R^2 = 0.9997$.

Meloxicam tablet solution was prepared in the same manner as standard solutions of pure M. Absorption spectrums were then recorded under the same operating conditions as with the M standard (Fig. 3).

Subsequently, using the computer software, derivatives of the third-order of values from the recorded spectrums were performed, and the results were obtained as shown in Table 6.

Maximum values of D3 were read at 345.73 and 343.90 nm. Mean value was 6.92 ± 0.71 mg, and a deviation was -7.73% compared to the declared value.

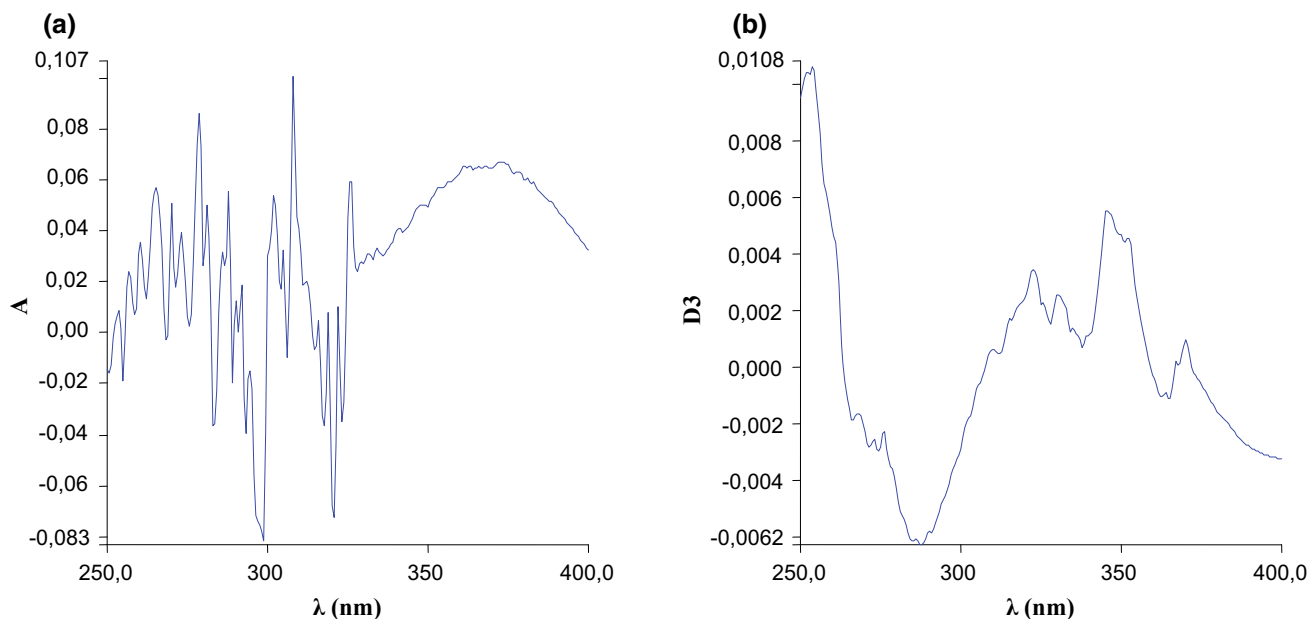


Fig. 3 Absorption (a) and derivative (b) spectrum of Melox tablet

Table 6 Derivations of the third-order of absorption spectrums of the Melox tablet sample

#	D3	m_M (mg)
1.	0.00549	6.75
2.	0.00527	6.30
3.	0.00594	7.70

4 Conclusions

This study covered three drugs of various manufacturers whose active substances were acetylsalicylic acid, meloxicam, and naproxen. Using the method of derivative UV/Vis spectroscopy, the mass of the active substances in the tablets were determined.

Based on the obtained results, it can be concluded that the mass of the active substance obtained by the experiment does not differ significantly from the weight indicated on the declaration for two drugs [Melox (Nobel), and Nalgesin S (Krka)]—the observed deviations were <10% (the measured meloxicam content was 92.27% of the declared value, and for naproxen was 90.06% of the declared value), which is in accordance with the *US Pharmacopeia (U.S.Ph.)*.

In the case of Aspirin protect 100 (Bayer), the content of acetylsalicylic acid as an active substance was 89.56% in relation to the declared value, which is slightly lower than the value prescribed by the *U.S.Ph.* (deviation of $\pm 5\%$ compared to the declared content).

Therefore, based on the obtained results, it can be concluded that the method of derivative UV/Vis spectroscopy is

suitable for the quantitative determination of active substances in some drugs.

References

1. Karpinska, J.: Basic principles and analytical application of derivative spectrophotometry. Edited by Jamal Uddin, Intech, 254–268 (2012)
2. Skoog, D.A., West, D.M., Holler, F.J.: Osnove analitičke kemije. Školska knjiga, Zagreb, 542–561 (1999)
3. Memić, M.: Spektrometrijske metode analize, odabrana poglavlja, Prirodno – matematički fakultet Univerziteta u Sarajevu, 9–50, 90–94 (2012)
4. Nikolin, B.: Analitika lijekova, 31–41. Sarajevo-Publishing (1998)
5. Owen, A.J.: Uses of Derivative Spectroscopy. Agilent Technologies (1995)
6. Thomas, M.J.K., Ando, D.J., Denney, R.C., Sinclair, R.: Ultraviolet and Visible Spectroscopy, 143–160. University of Greenwich. Wiley, NY (1996)
7. Ojeda, B.C., Rojas, S.F.: Recent applications in derivative ultraviolet/visible absorption spectrophotometry: 2009–2011. *Microchem. J.* (2012)

In Vitro Evaluation of Transdermal Patches Containing Capsaicin Marketed in Bosnia and Herzegovina

A. Uzunovic, M. Dacic, Z. Ademovic, S. Osmancevic, S. Pilipovic, and A. Sapcanin

Abstract

Capsaicin has been applied topically to treat some peripheral painful states, such as rheumatoid arthritis, cancer pain and diabetic neuropathy. Due to the pre-systemic metabolism of intragastric capsaicin and very rapid elimination half-life made topical application of capsaicin advantageous. The aim of this study was to evaluate differences in the dissolution characteristics of capsaicin transdermal patches commercially available on the local market (formulation I, II and III). USP Apparatus 5 (Paddle Over Disc) is used for transdermal patch release testing at fixed rotation speed (50 rpm). The 9 cm² patch was exposed to 500 mL of phosphate buffer solution pH 4.0, 5.0 and 7.4. All dissolution studies were carried out at 32 ± 0.5 °C and samples were collected at various time intervals (60, 240, 480 and 720 min) and analyzed for capsaicin content using optimized and validated high-performance liquid chromatography (HPLC). The mobile phase consisted of acetonitrile:water (50:50 v/v). pH change in the release media showed no significant difference in capsaicin release profile for formulation I and II. For formulation III, the resulting results vary considerably with pH change. Although

several apparatus and procedures have been used to study in vitro release characteristics of transdermal patches, USP Apparatus 5 could be considered as a discriminatory test that would be able to detect the differences in the dissolution rate of all tested capsaicin patches at short sampling intervals (1–12 h).

Keywords

Capsaicin • Transdermal patches • Dissolution • USP Apparatus 5

1 Introduction

Transdermal patches are flexible pharmaceutical forms of various sizes that contain one or more active drug substances. It is placed on the skin to deliver a specific dose of the drug through the skin to the bloodstream. Transdermal administration has certain advantages over oral and parenteral administration and for some drugs it is also the most convenient way to deliver drug. Compared to oral drug administration, the transdermal route of administration eliminates drug interactions with food as well as its chemical degradation in the gastrointestinal tract. Therefore, transdermal patches increasingly occupy an important place in pharmaceutical research and development [1]. However, many drugs cannot be transported through the skin and the rate of penetration and permeation of the drug in or through the skin depends on age, race, skin application and skin diseases. However, the main limiting factor for the delivery of drugs through the skin is barrier characteristics of the outer layer of the skin (epidermis) [2]. Capsaicin (8-metil-N-vanillyl-trans-6-nonenamide) has been used in traditional medicine since ancient times and since 1980, topical capsaicin preparations for pain therapy have been used. Capsaicin is natural alkaloid which belongs to the group of capsaicinoids. It is secondary metabolite of hot peppers. Capsaicin binds to vanilloid receptor subtype 1

A. Uzunovic · S. Pilipovic
Agency for Medicinal Products and Medical Devices, Titova 9,
Sarajevo, Bosnia and Herzegovina

M. Dacic (✉)
Faculty of Pharm and Health, Slavka Gavrančića 17c, Travnik,
Bosnia and Herzegovina
e-mail: nelami@hotmail.com

Z. Ademovic · S. Osmancevic
Faculty of Pharmacy, University of Tuzla, Univerzitetska 9, Tuzla,
Bosnia and Herzegovina

A. Sapcanin
Faculty of Pharmacy, University of Sarajevo, Zmaja od Bosne 8,
Sarajevo, Bosnia and Herzegovina

M. Dacic
Institute for Biomedical Diagnostics and Research Genom,
Slavka Gavrančića 17c, Travnik, Bosnia and Herzegovina

(TRPV1). By binding to the TRPV1 receptor, the capsaicin molecule produces similar sensations to those of excessive heat or abrasive damage [3]. However, the clinical use of capsaicin is limited due to the strong hot sensation of capsaicin. In addition, the metabolism of the first passage is noticed in rats and mice [4] and the half-life of capsaicin administered intravenously in rats was very short (7.06 min) [5]. Also, very low solubility in water results in a complicated procedure for designing pharmaceutical formulations [6]. Capsaicin is used in topical therapies and applied to the skin causes a feeling of burning and hyperemia or increased circulation in the treated area, which helps relieve rheumatic pain [7]. Clinical studies performed with topical administration of lower concentrations of capsaicin (0.025 or 0.075%) showed poor or moderate efficacy in the treatment of musculoskeletal or neuropathic symptoms [8, 9]. Clinical studies with high doses of capsaicin patches (5–10%) for treatment of postherpetic neuralgia have shown a significant reduction of pain from the 2–12 week of the study [10]. Topical application of capsaicin also showed a favorable safety profile. After absorption, capsaicin is rapidly eliminated in the liver via the cytochrome P450, with a half-life of 1.54 h [11]. Thanks to the positive results of clinical studies, the European Union has issued approval for the use of this patch for the treatment of peripheral neuropathy in non-diabetic patients.

In vitro drug release test from transdermal patches is a widespread method for measuring and determining the release variability between products and these test are required by regulatory bodies. For the dissolution rate test, a paddle over a disc, a paddle over the cell and a rotating cylinder method may be used, which depends on the composition, size and shape of the patch. The paddle over disk method is considered the USP standard method for testing the release rate of the active drug substance from the transdermal patches. This method is simple, does not require special equipment and is most similar to the methods used to determine the rate of dissolution of the active substance from other dosage forms such as tablets or capsules.

The aim of this study was to develop and optimize a discriminatory in vitro method for determining the capsaicin

dissolution rate from transdermal patches commercially available on the local market (formulation I, II and III). Variable parameters were pH of the dissolving medium, which mimics in vivo physiological pH values in the range of 4.0–7.4 and sampling time within the range of 1–12 h, which is the time period in which capsaicin released from the transdermal patches usually achieves optimal therapeutic effects.

2 Materials and Methods

2.1 Chemicals

Capsaicin (USP reference standard) was purchased from Sigma-Aldrich, Germany, KH_2PO_4 , H_3PO_4 , KOH, NaOH and acetonitrile from Fluka, Switzerland.

2.2 Transdermal Patches

Formulation I contains 0.018 mg of capsaicin/cm², formulation II contains 0.036 mg of capsaicin/cm² and formulation III contains 0.145 mg of capsaicin/cm².

2.3 Dissolution Apparatus

USP Apparatus 5 (Paddle Over Disc) is used to measure the capsaicin dissolution rate from transdermal patches. The rate of dissolution of capsaicin from the transdermal patches is measured using a 125 μm stainless steel mesh disc that holds the patch straight at the bottom of the dispenser vessel. The area from which capsaicin is released is turned upward. During the test, a distance of 25 ± 2 mm is maintained between the disk surface and the paddle. Each of the six dissolution vessels was filled with 500 mL of dissolution medium with different pH values (4.0, 5.0 and 7.4) at 32 ± 0.5 °C. Surface area of patches was 9 cm². Rotation of paddle was fixed at 50 rpm. Samples (5 mL of dissolution media) were collected at various time intervals (1, 4, 8 and 12 h).

2.4 High Performance Liquid Chromatography (HPLC)

Capsaicin was determined by High-Performance Liquid Chromatography (HPLC, Shimadzu, Japan) system consisting of solvent delivery system, an autosampler, pump and UV-VIS detector. The performed separation method for analysis is previously described [12]. Capsaicin was detected at 222 nm. The separation was carried out with a Pronto-SILC18 column (4.0×155 mm, $3 \mu\text{m}$) at room temperature using mobile phase was acetonitrile:water 50:50 v/v. The injection volume was $10 \mu\text{l}$ and flow rate 0.9 mL/min . Samples for HPLC analysis were filtered through membrane filter prior to injection.

2.5 Statistical Analysis

The similarity of the dissolution profiles can be compared by model-independent approach calculating factor of similarity (f_2) [13]. Evaluation of f_2 factors is based on the following conditions: minimum of three time points, time points are the same for two formulations, relative standard deviation or coefficient of variation must be less than 20% for the first point and less than 10% for the second and last point. Generally, for curves to be considered similar, f_2 values should be close to 100 (50–100).

3 Results and Discussion

In the first step, the HPLC method for the identification and determination of capsaicin in transdermal patches was validated (specificity, linearity and repeatability of the method). Standard calibration curve for capsaicin is shown in Fig. 1.

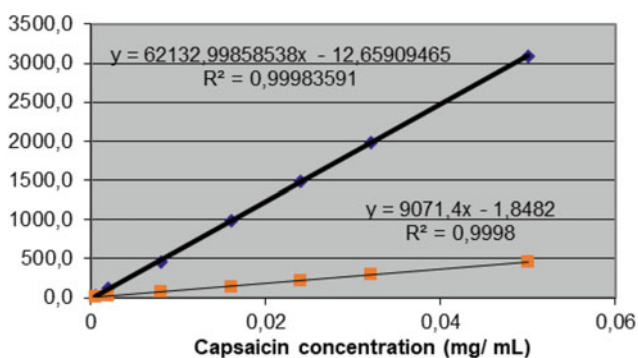


Fig. 1 Standard calibration curve for capsaicin (surface and height at 222 nm)

Based on the retention time for capsaicin (2.18 min) in the standard solution and samples confirmed the specificity of the analytical procedure using the test conditions. Linearity was confirmed using different concentration (0.0005–0.05 mg/mL) of standard solutions of capsaicin. Using the correlation coefficient (r), linearity ($r \geq 0.995$) was confirmed. The repeatability of the method is confirmed based on the values for a relative standard deviation (RSD) $\leq 2.0\%$ obtained by measuring the intensity of absorbance [mAU] and the height of the capsaicin 0.05 mg/mL solution in 10 parallel measurements.

Table 1 shows the in vitro release results of capsaicin from all three transdermal patches tested under the following conditions: pH medium 4.0, speed of paddle rotation 50 rpm and sampling time of 1, 4, 8 and 12 h.

pH change in the release media showed no significant difference in capsaicin release profile for formulation I and II. For formulation III, the resulting results vary considerably with pH change. The amount of released capsaicin from formulation III is higher at experimental conditions compared to formulations I and II, confirming that in vitro model was discriminatory (comparison I–III by calculating factor of similarity (f_2): $86.61 < f_2 < 98.19$ and comparison II–III calculating factor of similarity (f_2): $89.14 < f_2 < 98.42$). This result was expected as formulation III contains much higher amount of capsaicin compared to other two formulations. On the other hand, the similarity in capsaicin release profiles in Formulas I and II was confirmed (comparison III: $99.29 < f_2 < 99.98$).

4 Conclusions

USP Apparatus 5 (Paddle Over Disc method) is considered the USP standard method for testing the release of active substance from transdermal patches. The paddle rotation speed was chosen in accordance with the pharmacopoeia requirements (50 rpm). At pH 4.0, 5.0 and 7.4 the capsaicin release rate from three transdermal patches was measured after 1–12 h.

The results showed that the developed discriminatory in vitro method allows determination of the rate of capsaicin release from transdermal patches, thereby contributing to the quality control of commercially available patches.

Table 1 In vitro results of capsaicin release from formulations I, II and III at conditions pH 4.0, 5.0 and 7.4 at 50 rpm, release time 1, 4, 8 and 12 h

Released capsaicin [mg/cm^2] \pm SD (n = 6)				
Time (h)	pH	Formulation I $\bar{x}_{n=6} \pm \text{SD}$	Formulation II $\bar{x}_{n=6} \pm \text{SD}$	Formulation III $\bar{x}_{n=6} \pm \text{SD}$
Interval 0–1 h	pH 4.0	0.24 \pm 0.03	0.47 \pm 0.02	1.53 \pm 0.09
	pH 5.0	0.08 \pm 0.01	0.10 \pm 0.01	0.19 \pm 0.01
	pH 7.4	0.10 \pm 0.01	0.09 \pm 0.01	0.22 \pm 0.03
Interval 0–4 h	pH 4.0	0.30 \pm 0.02	0.57 \pm 0.03	1.85 \pm 0.11
	pH 5.0	0.09 \pm 0.01	0.11 \pm 0.01	0.37 \pm 0.02
	pH 7.4	0.16 \pm 0.01	0.17 \pm 0.01	0.47 \pm 0.02
Interval 0–8 h	pH 4.0	0.41 \pm 0.03	0.65 \pm 0.06	1.99 \pm 0.15
	pH 5.0	0.26 \pm 0.03	0.36 \pm 0.04	0.87 \pm 0.07
	pH 7.4	0.28 \pm 0.03	0.26 \pm 0.03	1.19 \pm 0.13
Interval 0–12 h	pH 4.0	0.44 \pm 0.02	0.67 \pm 0.07	2.13 \pm 0.18
	pH 5.0	0.53 \pm 0.05	0.57 \pm 0.05	1.26 \pm 0.11
	pH 7.4	0.62 \pm 0.05	0.53 \pm 0.05	1.79 \pm 0.15

References

1. Prausnitz, M.R., Mitragotri, S., Langer, R.: Current status and future potential of transdermal drug delivery. *Nat. Rev.* **3**, 115–124 (2004)
2. Cevc, G.: Lipid vesicles and other colloids as drug carriers on the skin. *Adv. Drug Deliv. Rev.* **56**, 675–711 (2004)
3. Knotkova, H., Pappagallo, M., Szallasi, A.: Capsaicin (TRPV1 agonist) therapy for pain relief: farewell or revival? *Clin. J. Pain* **24**, 142–154 (2008)
4. Donnerer, J., Amann, R., Schuligoi, R., Lembeck, F.: Absorption and metabolism of capsaicinoids following intragastric administration in rats. *Arch. Pharmacol.* **342**, 357–361 (1990)
5. Kawada, T., Watanabe, T., Katsura, K., Takami, H., Iwai, K.: Formation and metabolism of pungent principle of Capsicum fruits. XV. Microdetermination of capsaicin by high-performance liquid chromatography with electrochemical detection. *J. Chromatography* **329**, 99–105 (1985)
6. Rollyson, W.D., Stover, C.A., Brown, K.C., Perry, H.E., Stevenson, C.D., McNeese, C.A., Ball, J.G., Valentovic, M.A., Dasgupta, P.: Bioavailability of capsaicin and its implications for drug delivery. *J. Control Release* **196C**, 96–105 (2014)
7. Reyes-Escogido, M.L., Gonzalez-Mondragon, E.G., Vazquez-Tzompantzi, E.: Chemical and pharmacological aspects of capsaicin. *Molecules* **16**, 1253–1270 (2011)
8. Zhang, W.Y., Li Wan Po, A.: The effectiveness of topically applied capsaicin. A meta-analysis. *Eur. J. Clin. Pharmacol.* **46**, 517–522 (1994)
9. Mason, L., Moore, R.A., Derry, S., Edwards, J.E., McQuay, H.J.: Systematic review of topical capsaicin for the treatment of chronic pain. *BMJ* **328**, 991–997 (2004)
10. Backonja, M., Wallace, M.S., Blonsky, E.R., Cutler, B.J., Malan Jr., P., Rauck, R., Tobias, J.: NGX-4010, a high-concentration capsaicin patch, for the treatment of postherpetic neuralgia: A randomised, double-blind study. *Lancet Neurol.* **7**, 1106–1112 (2008)
11. Babbar, S., Marier, J.F., Mouksassi, M.S., Beliveau, M., Vanhove, G.F., Chanda, S., Bley, K.: Pharmacokinetic analysis of capsaicin after topical administration of a high-concentration capsaicin patch to patients with peripheral neuropathic pain. *Ther. Drug Monit.* **31**, 502–510 (2009)
12. Al Othman, Z.A., Ahmed, Y.B.H., Habila, M.A., Ghafar, A.A.: Determination of capsaicin and dihydrocapsaicin in capsicum fruit samples using high performance liquid chromatography. *Molecules* **16**, 8919–8929 (2011)
13. Prajapati, S.T., Patel, C.G., Patel, C.N.: Formulation and evaluation of transdermal patch of repaglinide. *ISRN Pharm.* **5**, 1–9 (2011)

UV-VIS Determination of Acetylsalicylic Acid in Aspirin Tablets Using Different Solvents and Conditions

M. Dacić, A. Uzunović, A. Kunić, S. Pilipović, and A. Šapčanin

Abstract

Acetylsalicylic acid is the salicylic drug which is commonly used like analgesic, antipyretic and anti-inflammatory drug. There are a lot of methods for analysis, but we decided for UV-VIS spectroscopy. In this paper are correlation results from UV-VIS determination of acetylsalicylic acid in six aspirin tablets from different manufacturers in Bosnia and Herzegovina using two different methods and changing parameters in first one. Standards and samples are prepared at the same way. First method was done using 1 M NaOH for degradation of acetylsalicylic acid and development of colors with 0.02 M FeCl_3 in 0.03 HCl (optimal pH = 1.6). For this analysis we made (multiple times) five standards with different concentrations (50–250%), changing pH of FeCl_3/HCl solution (0.60, 1.60, 1.95). Then, we changed the concentration range of standards: 50–250, 80–120, 80–160%. The best absorbance results were at 530 nm using FeCl_3/HCl solution at pH 1.60, so we analyze samples using that solutions. The second method was dissolving standards and samples in concentrated ethanol and measuring absorbance at 227 nm. Both method gave good results and can be used for pharmaceutical research.

Keywords

Acetylsalicylic acid • UV-VIS spectroscopy • Absorbance

1 Introduction

Acetylsalicylic acid is the prototypical analgesic used in the treatment of mild to moderate pain. It has anti-inflammatory and antipyretic properties and acts as an inhibitor of cyclooxygenase which results in the inhibition of the biosynthesis of prostaglandins. Aspirin also inhibits platelet aggregation and is used in the prevention of arterial and venous thrombosis [1].

Acetylsalicylic acid appears to produce analgesia by virtue of both a peripheral and CNS effect. Peripherally, acetylsalicylic acid acts by inhibiting the synthesis and release of prostaglandins. Acting centrally, it would appear to produce analgesia at a hypothalamic site in the brain, although the mode of action is not known. Acetylsalicylic acid also acts on the hypothalamus to produce antipyresis; heat dissipation is increased as a result of vasodilatation and increased peripheral blood flow. Acetylsalicylic acid's antipyretic activity may also be related to inhibition of synthesis and release of prostaglandins [2].

There are a lot of methods which are used for determination of acetylsalicylic acid, like HPLC, UV-VIS determination, volumetric etc. For this paper, we decided to use UV-VIS spectroscopy because of simplicity and low costing.

UV-visible spectroscopy is a technique that readily allows one to determine the concentrations of substances and therefore enables scientists to study the rates of reactions, and determine rate equations for reactions, from which a mechanism can be proposed [3].

For the analysis, we took six acetylsalicylic acid tablets from local market. In this paper this tablet will be designated as Sample 1–6.

M. Dacić · A. Kunić (✉)
Faculty of Pharm and Health, Slavka Gavrančića 17c, Travnik,
Bosnia and Herzegovina
e-mail: mineladaca@gmail.com

A. Uzunović · S. Pilipović
Agency for Medicinal Products and Medical Devices, Titova 9,
Sarajevo, Bosnia and Herzegovina

A. Šapčanin
Faculty of Pharmacy, University of Sarajevo, Zmaja od Bosne 8,
Sarajevo, Bosnia and Herzegovina

2 Materials and Methods

2.1 Standard Preparation

2.1.1 Method with FeCl₃/HCl Solution

The method is based at the procedure described at Maksimović [4]. For standards preparation, we use USP Acetylsalicylic acid Reference Standard (500 mg) CAT No. 1044006. At the analytical balance (Mettler Toledo, ±0.01 mg) was measured 10.31 mg of standard in the volumetric flask of 10 ml and added 1 ml 1.0 M NaOH, then heated to boiling and boiled five minutes. The flask was cooled and added distilled water to the mark. That was the stock solution which we used for making diluted standards in volumetric flask of 10 ml. We made three different series of five standards with different concentrations and different pH. There was pipetted appropriate amount of stock standards in the volumetric flask of 10 ml depend of concentration and diluted with 0.02 M FeCl₃ in 0.03 M HCl (for three series of standards used FeCl₃/HCl solution had three different pH). pH of FeCl₃/HCl solution was set using NaOH and HCl, depend of required values of pH, which was: 0.60, 1.60 and 1.95.

2.1.2 Method with Ethanol

For standards preparation, we used the same Acetylsalicylic acid Reference Standard. At the analytical balance (Mettler Toledo, ±0.01 mg) was measured 5.00 mg of standard in volumetric flask of 10 ml and added ethanol to the mark. After dissolving, we pipetted 0.4, 0.5, 0.6, 0.7 and 0.8 ml of stock solution in volumetric flask of 10 ml and added distilled water to the mark, so we had five diluted standards with concentrations: 20, 25, 30, 35 and 40 µg/ml (80, 100, 120, 140, 160% respectively).

2.2 Sample Preparation

2.2.1 Method with FeCl₃/HCl Solution

From each batch, we took 20 tablets using random selection and measure the tablets mass for calculating average mass of the tablet. Then, the tablets were crumbled and weight the mass of tablet powder that suits the weight of 50.00 mg acetylsalicylic acid in volumetric flask of 100 ml. In flask was added 5 ml 1 M NaOH and heated to the boiling and boiled five minutes. When the flask was cooled, we added distilled water to the mark and mixing. Solution was filtered and 0.25 ml of filtrate was pipetted in volumetric flask of 10 ml and added FeCl₃/HCl solution (pH = 1.60) to the mark. That was the solution for measuring the absorption at 530 nm with FeCl₃/HCl as reference solution.

2.2.2 Method with Ethanol

There was measured the mass of the tablet powder that suits the weight of 5.00 mg acetylsalicylic acid in volumetric flask of 10 ml and added ethanol to the mark. After dissolving, we filtrated the solution and pipette 0.50 ml of filtrate in volumetric flask of 10 ml and dilute with distilled water to the mark. That was the solution for measuring the absorption at 227 nm with distilled water as reference solution.

UV-VIS spectroscopy. Analysis was carried out using a double beam UV-VIS spectrophotometer Shimadzu, UV-1800, using quartz cells and Shimadzu software at 227 and 530 nm.

Quantitation. The calibration curve was used with different concentrations. The concentration ranges of the standard curves were 10–50, 40–60 and 20–40 µg/ml. For quantitation acetylsalicylic acid in tablets was used curve with concentration range 20–40 µg/ml.

Recovery study. In order to verify the accuracy and precision of the analytical procedure, recovery studies were carried out by calculating the amount of the measured mass (m_m) through the determined mass (m_d) of acetylsalicylic acid (Formula 1).

$$R\% = m_m/m_d * 100 \quad (1)$$

There was calculated standard deviation and relative standard deviation which was under 2.0 in some of analyses, so accuracy and precision was satisfactory recording USP parameters [5]. The problem was in absorbance response at the lower pH, which is the reason why we used the FeCl₃/HCl solution with the pH = 1.60 (better absorbance response).

3 Results and Discussion

3.1 Method with FeCl₃/HCl Solution

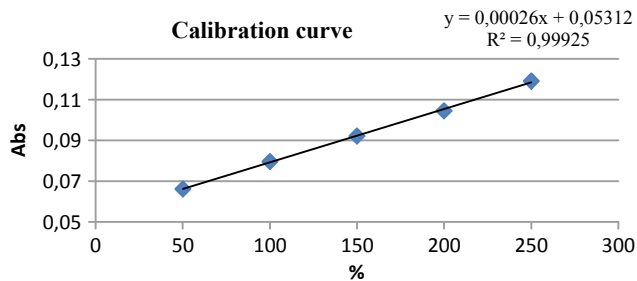
Calibration Curves

At the beginning we used FeCl₃/HCl solution with pH 0.60 to development the colors of standards with concentration range 50–250%. Table 1 are results of determined amount of acetylsalicylic acid in standards.

From the recovery we can realize that the method isn't good, because we didn't find the amount which we added. At Fig. 1 is showed calibration curve of correlation of concentration-absorbance.

Table 1 Correlation of added and measured mass of acetylsalicylic acid standards at concentration range 50–250%, pH = 0.60

%	$\mu\text{g/mL}$	Added (mg)	Measured (mg)	R (%)
50	9.994	24.985	41.535	166.240
100	19.988	49.970	49.970	100.000
150	29.982	74.955	57.862	77.196
200	39.976	99.940	65.588	65.628
250	49.970	124.925	74.716	59.809

**Fig. 1** Calibration curve %-absorbance at the concentration range 50–250%, pH = 0.60

Correlation coefficient (R^2) is 0.99925 so the linearity is good, but we can see that absorbance is weak and all standards had absorbance below 0.11 so at the pH 0.60 there doesn't arise the tetraaquasalicylic iron (III) complex which is responsible for color development.

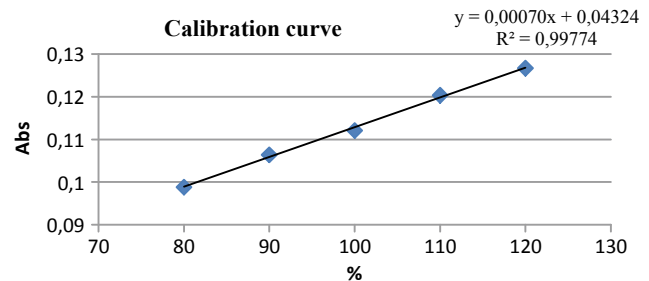
In the following text are results of measured standards at different concentrations and with different pH values.

All results of standards which have pH 0.60 had lower absorbance and recovery wasn't satisfying (see Table 2 and Fig. 2). Standards with pH 1.60 had the best absorbance values, so we decided to use FeCl_3/HCl with pH 1.60 (see Table 3 and Fig. 3) which is recommended by Maksimović [4]. Standards with pH 1.95 had good measured absorbance (see Table 4 and Fig. 4), but the correlation coefficient was 0.98583 so the curve linearity isn't satisfactory for pharmaceutical researching where has to be >0.995 [5].

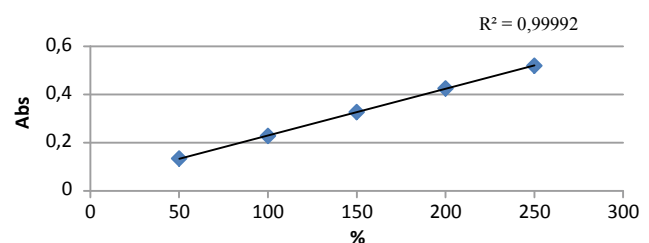
For the final concentrations, we made standards with concentration range 80–160%, pH 1.60 (see Table 5 and Fig. 5).

Table 2 Correlation of added and measured mass of acetylsalicylic acid standards at concentration range 80–120%, pH = 0.60

%	$\mu\text{g/mL}$	Added (mg)	Measured (mg)	R (%)
80	39.976	39.976	44.065	110.230
90	44.973	44.973	47.424	105.449
100	49.970	49.970	49.970	100.000
110	54.967	54.967	53.643	97.592
120	59.964	59.964	56.476	94.182

**Fig. 2** Calibration curve %-absorbance at the concentration range 80–120%, pH = 0.60**Table 3** Correlation of added and measured mass of acetylsalicylic acid standards at concentration range 50–250%, pH = 1.60

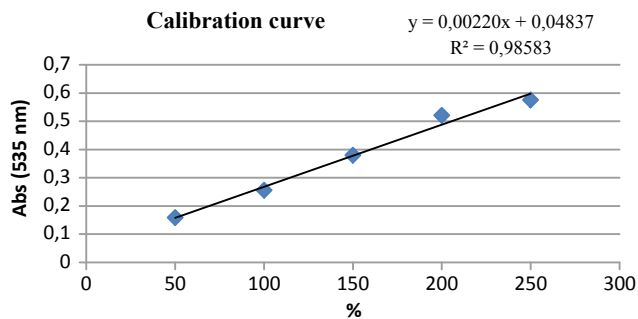
%	$\mu\text{g/mL}$	Added (mg)	Measured (mg)	R (%)
50	10.31	5.155	6.066	117.663
100	20.62	10.310	10.310	100.000
150	30.93	15.465	14.788	95.624
200	41.24	20.620	19.224	93.227
250	51.55	25.775	23.501	91.177

**Fig. 3** Calibration curve %-absorbance at the concentration range 50–250, pH = 1.60

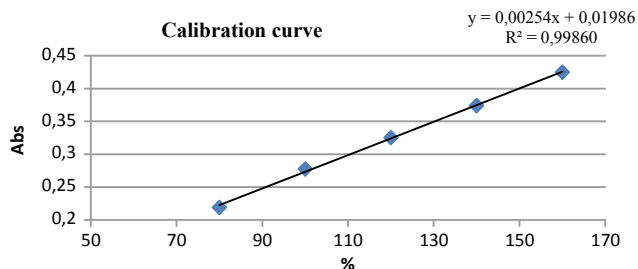
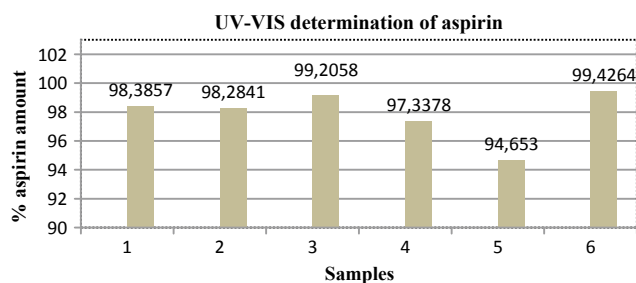
Recovery's for this standards (Table 5) has values 95.53–100% and SD and RSD is lower than 2.00 so we can use this curve for pharmaceutical researching.

Table 4 Correlation of added and measured mass of acetylsalicylic acid standards at concentration range 50–250%, pH = 1.95

%	µg/mL	Added (mg)	Measured (mg)	R (%)
50	10.31	5.155	6.397	124.097
100	20.62	10.310	10.310	100.000
150	30.93	15.465	15.314	99.023
200	41.24	20.620	21.004	101.865
250	51.55	25.775	23.213	90.059

**Fig. 4** Calibration curve %-absorbance at the concentration range 50–250, pH = 1.95**Table 5** Correlation of added and measured mass of acetylsalicylic acid standards at concentration range 80–160%, pH = 1.60

%	µg/mL	Added (mg)	Measured (mg)	R (%)
80	20.620	8.248	8.130	98.570
100	25.775	10.310	10.310	100.000
120	30.930	12.372	12.076	97.607
140	36.085	14.434	13.874	96.117
160	41.240	16.496	15.759	95.531
			AVG	97.565
			SD	1.8148
			RSD	1.860

**Fig. 5** Calibration curve %-absorbance at the concentration range 80–160%, pH = 1.60**Fig. 6** Results of measured % of acetylsalicylic acid in aspirin tablets

Sample Results

For this paper, we analyzed six tablet samples from six different manufacturers. Results are in Fig. 6.

For pharmaceutical determination, the amount of acetylsalicylic acid in aspirin tablets have to be 90–110% (EU Pharmacopoeia, Monograph of aspirin tablets and USP, Aspirin tablets monograph) [6, 7]. The measured amounts were 94.65–99.43% so all analyzed tablets has satisfying amount of acetylsalicylic acid.

3.2 Method with Ethanol

Calibration Curves

We made one calibration curve following the method which is described earlier. Results are in Table 6.

In Table 6 are results which shows that recovery, SD and RSD for acetylsalicylic acid standards, which are prepared in ethanol, has excellent values, so we used calibration curve from this results for determination acetylsalicylic acid in tablets (see Fig. 7).

From the R^2 , which is 0.99989, we can realize that the linearity is good for pharmaceutical researching, so we use this curve for analyzing samples.

Table 6 Correlation of added and measured mass of acetylsalicylic acid standards

%	µg/mL	Added (mg)	Measured (mg)	R (%)
80	20	4	3.981	99.517
100	25	5	5.000	100.000
120	30	6	5.942	99.041
140	35	7	6.951	99.297
160	40	8	7.939	99.232
			AVG	99.417
			SD	0.367
			RSD	0.370

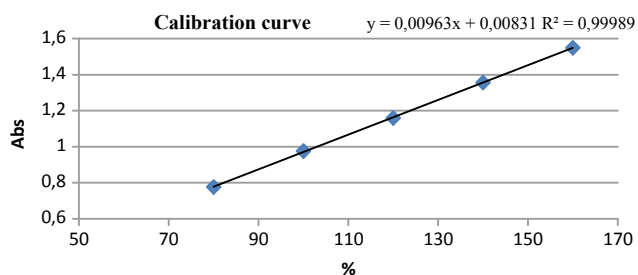


Fig. 7 Calibration curve %-absorbance at the concentration range 80–160%

Table 7 Sample results

Sample	Measured (mg/tbl)	Manufacturer declaration (mg)	%
1	104.407	100	104.407
2	97.299	100	97.299
3	99.004	100	99.004
4	97.367	100	97.367
5	98.553	100	98.553
6	97.425	100	97.425

Sample Results

The same samples, which were analyzed with first method, are analyzed with method with ethanol too. Results are in Table 7.

Measured amount range for this tablets was 98.30–104.41%, which is within the EU and USP pharmacopoeias range of 90–110%, so this method can be use for determination of acetylsalicylic acid too. The problems which we had doing this method was related with quantitative solving tablets. There is very important to have the same all conditions in preparing standards and samples. Temperature,

minutes in ultrasonic bath etc. are crucial factor for solving samples, so have to be same to get good results.

4 Conclusion

There was analyzed acetylsalicylic acid at six tablet samples with two different methods. The conditions and preparing was different, but both methods gave good results. Method with FeCl_3/HCl solution are sensitivier so all parameters has to be right to get good results, so it is a little beat difficultier than a method with ethanol. With second method is easier to analyze samples but at first step, the most important thing is to make UV-VIS spectar of standard and make conclusion at which wavelength is the best absorbance response for standards, so you can use that wavelength for samples. Results are good in both methods, so they can be used for pharmaceutical researching.

References

1. PubChem, Open Chemistry Database, <https://pubchem.ncbi.nlm.nih.gov/compound/aspirin#section=Top>. Last accessed 12.11.2018
2. DrugBank, <https://www.drugbank.ca/drugs/DB00945>. Last accessed 12.11.2018
3. RSC, Advanced the Chemical Sciences. http://www.rsc.org/learnchemistry/content/filerepository/CMP/00/001/304/UV-Vis_Student%20resource%20pack_ENGLISH.pdf. Last accessed 12.11.2018
4. Maksimović, M., Čavar, S., Vidić, D.: Praktikum iz osnova organske hemije, 73–83. Faculty of Sciences, Sarajevo (2009)
5. UV-VIS spectroscopy, USP—Physical tests (857) UV-VIS spectroscopy, page: 40. <https://hmc.usp.org/sites/default/files/documents/HMC/GCs-Pdfs/c857.pdf>. Last accessed 14.11.2018
6. EU Pharmacopoeia, Monograph of aspirin tablets
7. USP monograph of aspirin tablets, https://www.uspnf.com/sites/default/files/usp_pdf/EN/USPNF/iras/aspirin_tablets.pdf. Last accessed 15.11.2018

Lysozyme-Enzybiotic with Valuable Effects in Prevention and Treatment of Postoperative Complications in Adult Patients After Bilateral Tonsillectomy

Begović Begler, Vehabović Midhat, Amila Šahinpašić, and Una Glamočlija

Abstract

Introduction: Enzybiotics are enzymes with antimicrobial and immunomodulatory activity. The aim of this study was to investigate the effectiveness and safety of enzybiotic lysozyme in combination with pyridoxine for the prevention and treatment of postoperative complications after bilateral tonsillectomy. **Materials and Methods:** The study was designed as randomized controlled, parallel-group, open, prospective, multicenter clinical study in adult patients after bilateral tonsillectomy. 160 patients were randomized to the lysozyme + pyridoxine or control group. Efficacy was evaluated by: Visual analog scale (for pain), clinical signs (for wound healing and postoperative complications), and the need for treatment (with analgesics and systemic antimicrobials). Safety was evaluated by reporting adverse effects. **Results:** Lysozyme + pyridoxine was superior to control with respect to the pain reduction (starting already from the first day of treatment), the reduction of local fibrin deposits and the need for analgesics. No statistically significant difference was seen regarding local bleeding (less than 15% patients in both groups) and infection (less than 5% patients in both groups). Systemic antibiotics were used by 16 patients (19.1%) in lysozyme + pyridoxine group and 24 patients (31.6%) in control group (no statistical difference, $P > 0.050$). **Conclusion:** Lysozyme + pyridoxine showed beneficial effects in respect of suppression of pain with subsequent lower need for analgesics, as well as in the

faster process of healing of postoperative scar. Moreover, next to its suitability for application, lysozyme + pyridoxine lozenges showed excellent tolerability and safety profile.

Keywords

Tonsillectomy • Postoperative treatment • Lysozyme + pyridoxine • Pain • Wound healing

1 Introduction

Enzybiotics are microorganism-degrading enzymes found in various natural sources. Although discovered a century ago, they were in the shade of antibiotics. Today, when the world is faced with antibiotics resistance, enzybiotics gain attention due to specific properties that can be utilized in therapy [1, 2]. Lysozymes are among the most studied enzybiotics. They have muramidase activity (hydrolyzing β -1,4 glycosidic bonds between N-acetylmuramic acid and N-acetyl-D-glucosamine residues of the bacterial cell wall peptidoglycans) resulting in killing gram-positive bacteria (which have a thick layer of extracellularly exposed peptidoglycans). Non-enzymatic mechanism of lysozyme (increase in bacterial membrane permeability) is responsible for activity against gram-negative bacteria (which have peptidoglycan layer buried between inner and outer membranes) [3]. Lysozyme enhances activity of antibiotics and enables reduction of their doses. It is used in case of poor tolerance of other antibacterial agents [4]. Lysozyme has key role in human immunity, property which have been comprehensively reviewed in several papers [5–8]. Additionally, lysozyme possess analgesic effects [9].

There are preparations containing combination of lysozyme with pyridoxine (an inactive form of vitamin B6). Biologically active form of pyridoxine, pyridoxal phosphate, is a coenzyme in more than 100 enzymatic reactions relevant

B. Begler
University Clinical Center Sarajevo, 71000 Sarajevo,
Bosnia and Herzegovina

V. Midhat · A. Šahinpašić · U. Glamočlija (✉)
Bosnalijek dd, 71000 Sarajevo, Bosnia and Herzegovina
e-mail: una.glamoclija@bosnalijek.com

U. Glamočlija
School of Medicine, University of Mostar, 88000 Mostar,
Bosnia and Herzegovina

for virtually all physiological functions, including the humoral and cellular immunity [10]. Combination of lysozyme and pyridoxine has antiseptic effects and it is used for the treatment of the oral cavity and pharynx mucosa. It is effective in aphthous stomatitis, gingivitis, herpetic lesions, and erosions of the mucosa of various etiologies [11, 12]. Lysozyme + pyridoxine possess fungistatic, antiviral (including HIV-1) and antitumor activity [13].

Due to the antimicrobial, anti-inflammatory and analgesic activity, lysozyme + pyridoxine combination may be advantageous in the postoperative treatment of tonsillectomy patients. Tonsillectomy is among the most common surgeries performed by otolaryngologists. Fever and pain are expected outcomes. About 20% of adult patients' experience complications such as bleeding from the scar and infection [14, 15]. Aim of this study was to investigate the effectiveness and safety of lysozyme + pyridoxine in the prevention and treatment of postoperative complications in adult patients after bilateral tonsillectomy.

2 Materials and Methods

Study design and patients The study was designed as randomized, controlled, parallel-group, open, prospective, multicenter clinical study. Using a random choice method (1:1), adult patients of both genders, older than 16 years, who underwent bilateral tonsillectomy were randomized into one of the two groups (lysozyme + pyridoxine and control group).

Methods Patients assigned to the lysozyme + pyridoxine group were treated with the Lysobact® compressed lozenge (active substances: lysozyme hydrochloride 20.0 mg and pyridoxine hydrochloride 10.0 mg; Bosnalijek dd, Sarajevo, Bosnia and Herzegovina). Initial dose was applied 24 h after the operation (3×2 lysozyme + pyridoxine lozenges), and therapy was continued until the eighth postoperative day (4×2 lysozyme + pyridoxine lozenges daily). Lysozyme + pyridoxine lozenges were placed under the tongue and kept for 10 min until completely dissolved. In the control group lysozyme + pyridoxine was not used in the postoperative treatment of patients.

Data collection Patients self-assessed the pain using the Visual analog scale (VAS) 1–10 scoring (three times a day, from first until eight postoperative day). Wound healing was estimated daily on control checks (on postoperative days 1–8 and 14) by the review of postoperative scar and fibrin deposits, bleeding from the scar and infection. The use of analgesics and systemic antimicrobial treatment were evaluated. Adverse effects reports were used for the safety evaluation.

Data analysis MedCalc Statistical Software version 18.10 for Windows, was used for statistical analysis of the data. Student t-test was used for comparison of two independent samples (for numeric variables whose distribution was normal) and Mann-Whitney U Test was used for comparison of two independent samples (for numeric variables whose distribution was not normal). *P*-values less than 0.05 were considered statistically significant.

3 Results

160 patients (from four clinical study centers) were enrolled into the study. 84 patients (64% women) were enrolled to the lysozyme + pyridoxine group and 76 patients (59% women) to the control group. There was no significant difference in patients' age between groups ($P = 0.079$): mean and standard deviation in lysozyme + pyridoxine group 25.52 ± 6.35 and in the control group 27.39 ± 6.90 . Median (interquartile range) of the duration of disease related to tonsils was similar between groups ($P = 0.180$): 5 (3–10) years in lysozyme + pyridoxine and 7 (5–10) years in the control group (Fig. 1).

The median number of tonsillitis per year was similar between groups ($P = 0.073$): 5 (4–6) in lysozyme + pyridoxine and 6 (5–6.75) in control group (Fig. 2).

Patients self-assessed their feeling of pain using VAS scoring. Median of all VAS scores was significantly lower in lysozyme + pyridoxine than control group ($P < 0.000$) (Fig. 3).

Lysozyme + pyridoxine group had significantly lower median VAS score already from the first day of treatment ($P = 0.018$) until the end of the study (Fig. 4).

Percentage of patients who used analgesics is shown in Fig. 5.

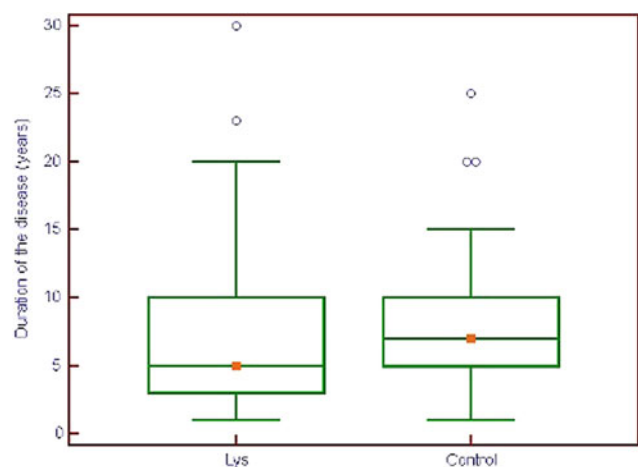


Fig. 1 Duration of the disease related to tonsils in Lys (lysozyme + pyridoxine) and control group

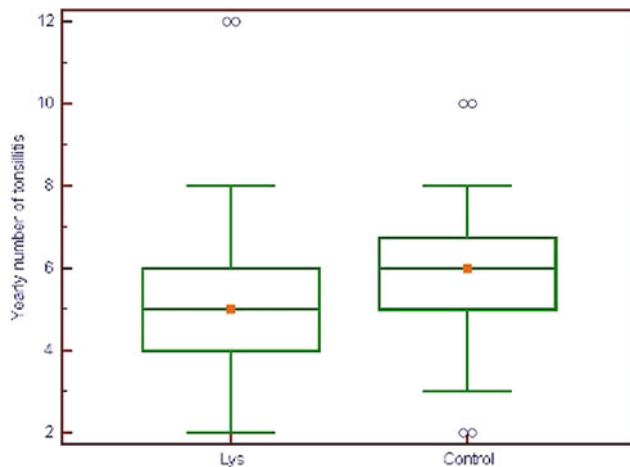


Fig. 2 Yearly number of tonsillitis in Lys (lysozyme + pyridoxine) and control group

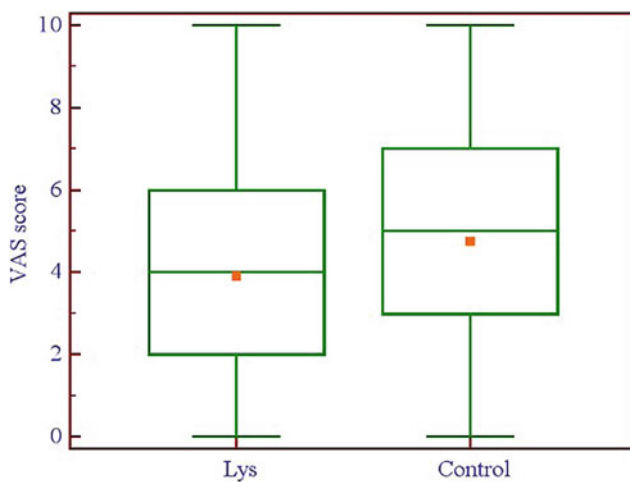


Fig. 3 Average of all visual analog scale score measurements in Lys (lysozyme + pyridoxine) and control group

The reduction of fibrin deposits was monitored on the control checkups. Already on the first day of lysozyme + pyridoxine administration, a significant difference in fibrin deposits was reported between groups ($P = 0.010$).

The odds ratio of postoperative bleedings from scars (OR = 1.49, 95% CI: 0.54–4.05, $P = 0.439$) was not statistically significant, with 11 patients with bleeding (13.1%) in lysozyme group and 7 patients with bleeding (9.2%) in control group.

Number of patients with postoperative infections was similar between groups: three patients (3.6%) in lysozyme + pyridoxine group and five patients (6.6%) in control group ($P = 0.390$).

No difference between groups was observed in the number of patients who used systemic antibiotics ($P > 0.050$): 16 patients (19.1%) in lysozyme + pyridoxine group and 24 patients (31.6%) in control group.

No adverse effects of lysozyme + pyridoxine have been reported.

4 Discussion

Lysozyme + pyridoxine lozenges were effective and safe in the postoperative treatment of patients after bilateral tonsillectomy. The treatment group was superior to control in pain reduction (starting already from the first day of treatment), the consequent lower need for analgesics and the reduction of local fibrin deposits. There is a lack of data about lysozyme + pyridoxine treatment in adult patients after tonsillectomy. This study showed beneficial effects without adverse reactions indicating that this treatment could be applied in clinical practice.

The main treatment goals in patients after tonsillectomy are reduction of pain and infection and promotion of healing. Lysozyme + pyridoxine had beneficial activity in all of them. VAS score for pain reduction was statistically lower in lysozyme + pyridoxine group, starting from the first day of administration until the end of the study. Accordingly, lower use of analgesics was reported in lysozyme + pyridoxine treated patients (Fig. 5). Analgesic activities of lysozyme have already been recognized. Bianchi proposed that lysozyme can be used in treatment of herpes zoster and cancer pain [16, 17]. Lysozyme digested with artificial gastric juice produces fragments which also have antinociceptive activity [18]. Besides direct analgesic effect, pain reduction was result of faster wound healing in lysozyme + pyridoxine group (observed from the first day of treatment). Treated group had the gradual lowering of fibrin deposits followed by better healing of postoperative scar. Previous reports showed the beneficial effect of lysozyme on wound healing. Lysozyme shortened the healing time and reduced inflammatory reaction of skin wounds in guinea pigs. Cationic properties and influence on wound pH may result in observed effects [19]. Lysozyme healing properties are also observed in chronic crural ulcerations patients [20]. In this study, lysozyme + pyridoxine compared to control group had lower percentage of patients with infection (3.6 vs. 6.6%) and systemic antimicrobial treatment (19.1 vs. 31.6%), but this difference was not statistically significant. Antimicrobial activity of lysozyme is well known [3, 4], and small number of patients could result in no statistically significant difference connected to this activity (infection percentage and need for systemic antimicrobial treatment).

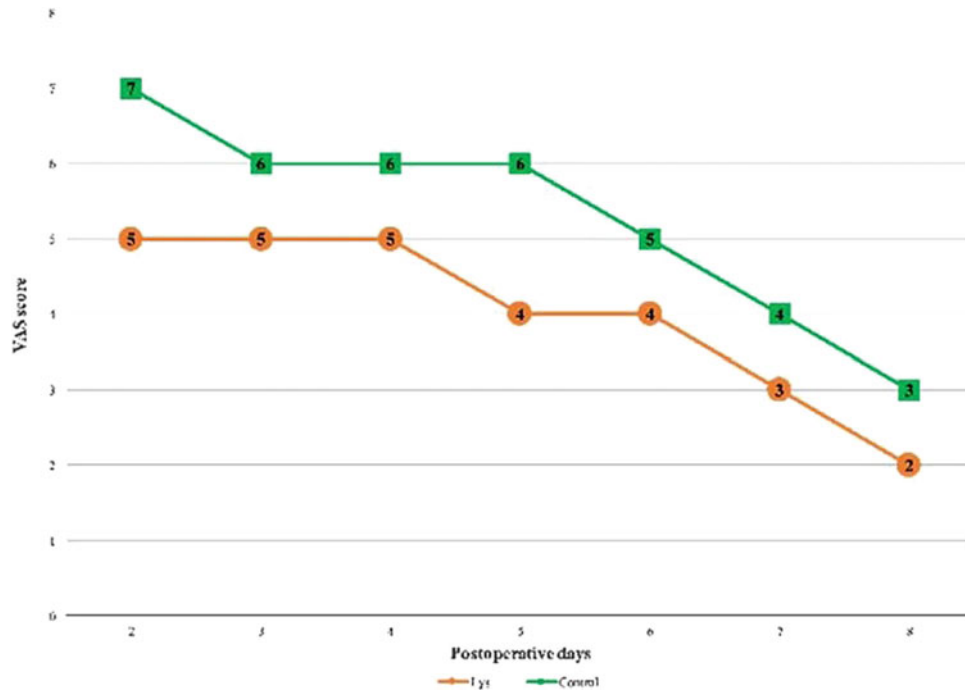


Fig. 4 Median VAS score values in Lys (lysozyme + pyridoxine) and control group

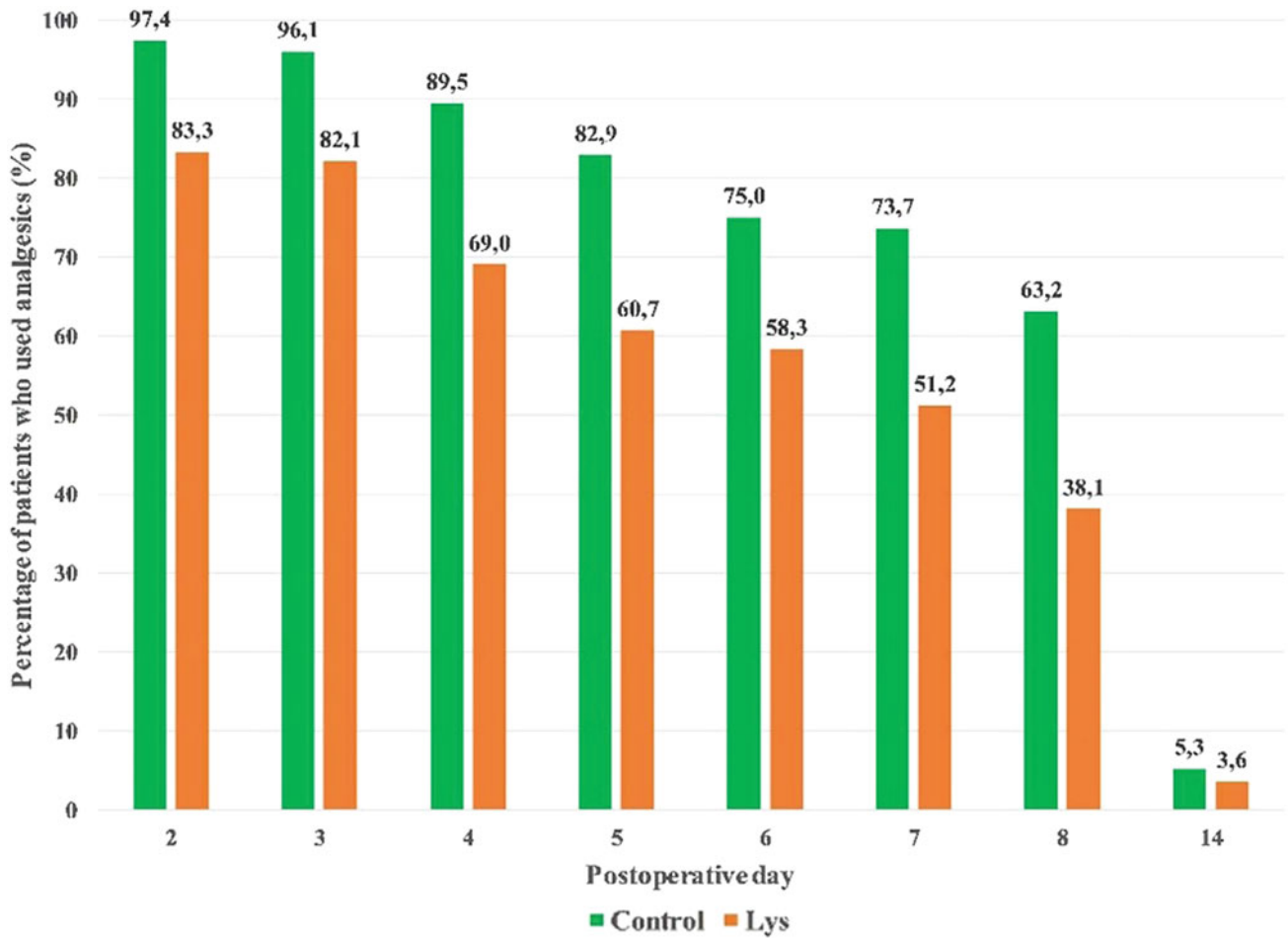


Fig. 5 Percentage of patients who used analgesics in lysozyme + pyridoxine (Lys) and control group

Small number of patients experienced postoperative bleedings from scars (11 (13.1%) in lysozyme + pyridoxine group and 7 (9.2%) in control group). Although the difference was not statistically significant, this result should be evaluated in the study involving higher number of patients. There are studies which have shown that lysozyme doesn't have significant effect on bleeding during tonsillectomy [21, 22].

Limitations of this study were small number of patients, no blinding and no comparator treatment in control group. Similar placebo or comparator controlled studies on higher number of patients should be conducted in order to confirm obtained results.

5 Conclusion

Lysozyme + pyridoxine was effective in the postoperative treatment of patients after bilateral tonsillectomy. It reduced pain (lowered the need for analgesics) and improved the process of healing of postoperative scar. It showed excellent tolerability and safety profile. Future larger randomized controlled studies with placebo and active control should be performed to confirm our results.

Conflict of Interest The authors declare that Bosnalijek dd (a company which produces Lysobact® compressed lozenge) supported this study.

References

1. Veiga-Crespo, P., Ageitos, J.M., Poza, M., Villa, T.G.: Enzybiotics: a look to the future, recalling the past. *J. Pharm. Sci.* **96**(8), 1917–1924 (2007)
2. Sudhakar, G.K., Venkatesh Kamath, B., Aravind, P.: Enzybiotics-a review. *Int. J. Pharm. Sci. Res.* **3**(4), 69–71 (2013)
3. Ragland, S.A., Criss, A.K.: From bacterial killing to immune modulation: recent insights into the functions of lysozyme. *PLoS Pathog.* **13**(9), e1006512 (2017)
4. Pellegrini, A., Thomas, U., Fellenberg, R., Wild, P.: Bactericidal activities of lysozyme and aprotinin against gram-negative and gram-positive bacteria related to their basic character. *J. Appl. Bact.* **72**, 180–187 (1992)
5. Fabian, T.K., Hermann, P., Beck, A., Fejerdy, P., Fabian, G.: Salivary defense proteins: their network and role in innate and acquired oral immunity. *Int. J. Mol. Sci.* **13**, 4295–4320 (2012)
6. Gorr, S.U.: Antimicrobial peptides in periodontal innate defense. *Front Oral Biol.* **15**, 84–98 (2012)
7. Nakatsuji, T., Gallo, R.L.: Antimicrobial peptides: old molecules with new ideas. *J. Invest. Dermatol.* **132**, 887–895 (2012)
8. Wiesner, J., Vilcinskas, A.: Antimicrobial peptides. The ancient arm of the human immune system. *Virulence* **1**, 440–464 (2010)
9. Carrillo, W., Spindola, H., Ramos, M., Recio, I., Carvalho, J.E.: Anti-inflammatory and anti-nociceptive activities of native and modified hen egg white lysozyme. *J. Med. Food* **19**(10), 1–5 (2016)
10. Thorne Research Inc.: Vitamin B6 (pyridoxine; pyridoxal 5'-phosphate) monograph. *Altern. Med. Rev.* **6**, 87–92 (2001). <http://www.altmedrev.com/publications/6/1/87.pdf>
11. Topic, B., Malic, M., Arifhodzic, F., Zivojinović, V.: Lyso-B in the management of the aphthous stomatitis. *Stom. Vjes.* **2–3**, 129–133 (1979)
12. Lazic, D., Kekic, Lj., Petkovic, D.: Medical treatment of oral mucous membrane lesions with Lysobact. *Stom. Vjes.* **2–3**, 134 (1980)
13. Chandrasekar Lakshmi, K., Sankarapandian, S., Nagalingeswaran, K., Kindo, A., Ganesan, N.: Oral candidal carriage, salivary lysozyme levels, and their relationship with CD4 count in HIV-infected patients. *J. Investig. Clin. Dent.* **7**(1), 81–86 (2016)
14. Seshamani, M., Vogtmann, E., Gatwood, J., Gibson, T.B., Scanlon, D.: Prevalence of complications from adult tonsillectomy and impact on health care expenditures. *Otolaryngol. Head Neck Surg.* **150**(4), 574–581 (2014)
15. Cooper, L.: Post-tonsillectomy management: a framework. *Aust. Fam. Physician* **45**(5), 289–291 (2016)
16. Bianchi, C.: Is Fleming's lysozyme an analgesic agent? An experimental reappraisal of clinical data. *Eur. J. Pharmacol.* **71**(2–3), 211–221 (1981)
17. Bianchi, C.: Is Fleming's lysozyme an analgesic agent? Experiments on mice. *Clin. Exp. Pharmacol. Physiol.* **10**(1), 45–52 (1983)
18. Bruzzese, T., Cedro, A., Fanciano, C.A., Basilico, L., Angeli, A., Ferrari, F., Patrini, G., Giagnoni, G.: Antinociceptive properties of lysozyme fragments. *Boll. Chim. Farm.* **128**(1), 33–37 (1989)
19. Gasior-Chrzan, B.: Effect of ovalbumin lysozyme on healing of standard skin wounds in guinea pigs. *Przegl. Dermatol.* **75**(6), 431–434 (1988)
20. Gasior-Chrzan, B.: Clinical trial of lysozyme treatment of crural ulcers in humans. *Przegl. Dermatol.* **75**(6), 435–438 (1988)
21. Kubo, T., Takemoto, I., Aruga, H., Nonoguchi, H., Ashida, K., Matsunaga, T., Yatomi, T., Hori, T., Higuchi, N.: Effect of leftose syrup on hemorrhage during otolaryngological surgery. *Pract. Otol. Kyoto* **77**(11), 2453–2459 (1984)
22. Yura, K., Kawahara, T., Koshimune, A., Watanabe, Y., Miyaguchi, M., Mori, N., Sakai, S.: Influence of lysozyme (leftose®) on bleeding during tonsillectomy and adenoidectomy in children. *Pract. Oto-Rhino-Laryngol.* **84**(1), 121–127 (1991)

Use of Hollow Microneedle Drug Delivery Systems in Treatment of Diabetes Mellitus

Anesa Sušić, Zekira Hrnjica, Ilma Kajgana, Minela Mujezinović, Alma Hasanbegović, Jelena Brčkalo, Amina Tucak, Merima Sirbubalo, and Edina Vranić

Abstract

Use of microneedles as drug delivery systems provides a number of benefits to patients. Easier and simple drug use, reduced side effects, and incontinence are some of them. Microstock patch has been developing for the last few decades and they represent minimally invasive way for administration drugs in organism through the skin (transdermal administration). One of the approaches “poke with patch” uses microneedles to make holes (Hollow microneedles) and then apply a transdermal (TD) patch to the skin surface. TD drug delivery can improve compliance, minimize peaks, provide continuous drug administration and troughs in plasma levels during the day. These systems can take the place of more risky and invasive injection-based drug delivery (such as insulin injection). Objective of this paper is to research and present the application of hollow microneedles in treating diabetes and to compare it with conventional application of the drug. The drugs that we processed are metformin, insulin and exendin. Metformin is effective for treating diabetic patients therapeutically and preventively, maximizing the use of the current diabetes patch device. The main lack of conventional application of insulin is the fact that the application itself isn't optimal for a patient. TDI showed significant improvement at level of absorption and bioavailability of the drug. New findings indicate that Exendin-4 diabetes microneedles can potentially replace the currently used subcutaneous

(SC) injections because they can effectively reduce blood-glucose levels in patients with type 2 diabetes and are convenient to use.

Keywords

Microneedles • Diabetes • Metformin • Insulin • Exendin

1 Introduction

Diabetes is a chronic disease characterized by low pancreas ability to produce enough insulin (a hormone regulating blood sugar or glucose) or when the body can not effectively use the insulin it produces. According to the World Health Organization report, the global prevalence of diabetes has almost doubled since 1980, with an increase of 4.7–8.5% in the adult population [1].

Ogurtsova et al. in one global study included data sources from 111 countries and results showed that there were 415 million people with diabetes aged 20–79 years. That number was predicted to rise to 642 million by 2040 [2].

Oral ingestion and hypodermic injections as the most common forms of drug administration possess several limitations (e.g. pain, absorption and metabolism issues and side effects).

Microneedles can enable collection of the same information or drug delivery with less trauma to the tissue (or even eliminating it). Microneedles represent a unique technological approach to enhance drug permeation across the stratum corneum [3].

Microneedle technologies have been subject to intensive research and development efforts. The number of publications describing microneedles as minimal invasive devices for DD has grown exponentially [4].

In form of the patent, the first concept to make micropores in the skin came by Gerstel and Place from Alza Research in the early 1970s. It took about 25 years for

A. Sušić (✉) · Z. Hrnjica · I. Kajgana · M. Mujezinović · A. Hasanbegović · J. Brčkalo
Faculty of Pharmacy, University of Sarajevo, Zmaja od Bosne 8, 71000 Sarajevo, Bosnia and Herzegovina
e-mail: anesasusic@ffsa.unsa.ba

A. Tucak · M. Sirbubalo · E. Vranić
Department of Pharmaceutical Technology, Faculty of Pharmacy, University of Sarajevo, Zmaja od Bosne 8, 71000 Sarajevo, Bosnia and Herzegovina

Microchip fabrication technology to converge with newer ways to make the possibilities for the mass production of microneedle arrays. With the onset of new microfabrication techniques available in the microchip industry, came various three-dimensional designs with greater aspect ratios of solid and hollow microneedles [5].

Current applications of microneedles include the delivery of macromolecules such as vaccines, proteins, and peptides including insulin for diabetics [6].

2 Transdermal Application: Hollow Microneedles

Transdermal drug delivery (TDD) has proven to be of great therapeutic use. It can improve compliance and provide continuous drug administration. This system can take place of more risky and invasive injection-based DD (such as insulin injection) [7].

Microneedles represent a unique technological approach to enhance drug permeation across the stratum corneum. There are specific strategies and designs of microneedles for TDD. One of the approaches “poke with patch” uses microneedles to make holes (Hollow microneedles) and then apply a transdermal patch to the skin surface. Hollow microneedles are traditionally used to allow liquid formulations through the SC and act like micron scale syringes. Compared to solid, the hollow microneedles have an added advantage as they can permit the administration of a larger drug dose [4].

They facilitate active fluid flow through the needle bore and into the skin. This can lead to much faster rates of delivery that can be modulated over time. These microneedles offer the possibility of transporting drugs for more rapid rates of delivery by pressure-driven flow or diffusion. There are only a few hollow microneedles that have been fabricated and limited work has been published on their possible use to deliver compounds into the skin [8].

Microneedles technologies have been subject to intensive research and development efforts. Their usage improves the surface contact with the skin and facilitates penetration of therapeutic molecules into the skin. There are many advantages of microneedle technologies, such as pain-free delivery; minimal introduction of pathogens through microneedle-induced holes; they do not cause bleeding; eliminate transdermal dosing variability of small molecules; potential for self-administration; the potential to overcome and reduce instances of accidental needle-stick injuries and the risk of transmitting infections. Microneedles are easy and safe to use and they can be produced with high precision, accuracy, and low cost. They also avoid the first-pass effect.

Some studies, in addition to the ease of microneedles waste disposal, have combined the microneedle systems with a pump or pressurized gas.

Microneedles sharp tips are short enough to limit contact with skin nerves and in that way prevent pain sensation. Because they are narrow enough, microneedles do not induce minimal trauma and also reduce the opportunities for infections to develop the following insertion. This method is minimizing disadvantages of conventional injection needles and transdermal patches. Microneedles can be manufactured using polymers (poly-L-lactic acid, polyglycolic acid, polycarbonate, ect.), metal or silicon. Biocompatible and biodegradable polymers can be safely applied to the skin and are generally cost-effective. Microneedles can deliver a wide range of drugs ranging from small molecular weight (e.g. ibuprofen) to high molecular weight (e.g. ovalbumin compounds).

A number of challenges with microneedles include scale-up manufacture to industrial levels which will require considerable planning and standardization. The issues which should be considered are issues surrounding product sterility; the potential for accidental reuse of certain microneedle modalities; appropriate packaging and manufacturing aspects and the potential for undesired immunological effects. The choice of appropriate biomaterials for preparation of microneedle is limited due to lack of mechanical strength, poor control of DD, and limitation of drug loading dose [4].

Microneedles can only be inserted into the skin if they have the correct shape and adequate physical properties. They need to be applied with the required force to avoid breaking or bending before insertion, because some fragments can be left in the skin. Microneedles can cause skin irritation and in some cases allergy [9].

3 Transdermal Delivery of Metformin

Metformin is used for treating and protecting people at a prediabetes stage as one of the most effective drugs. Commonly administered orally, microneedles loaded with metformin distribute it directly into the metabolic circulation. This prevents some of the complications with the slow absorption in the digestive system [10].

Metformin that is directly introduced through the skin reaches metabolic circulation more than when it is metabolized through digestion. TDD systems require more studies on human patients in the future [11].

The hydrophobic layer prevents moisture from damaging the microneedles after insertion into the skin, as well as preventing premature release of metformin. The heater

embedded in the patch triggers when it detects elevated glucose levels, warming the microneedles then the transitional temperature of tridecanoic acid of ~ 41 °C is exceeded, exposing the underlying polymer to interstitial water thus releasing the drug. Adjusting the quantity of metformin being liberated in this way can be done stepwise in a titratable fashion by adjusting the number of microneedles in the device. Experiments on genetically diabetic mice demonstrate without a doubt the drug release on thermal activation of dissolving polymers results in substantial lowering of blood sugar levels in the test subjects over the next few hours.

The present design makes it unlikely to deliver the daily adult dose of metformin without the use of an unacceptably large patch and/or unfeasibly large amounts of microneedles. An essential criterion as with all TDD applications, passive or facilitated in some way, is that the potency of the drug is high and the daily dosage no more than a few milligrams [12].

Hydrogel-forming microneedles swell in the skin allowing diffusion of metformin contained in a reservoir layer. Containing no drug themselves this process enables microneedles to deliver the drug to the dermal microcirculation. Migdadi et al. study showed that hydrogel-forming microneedles could find use to enhance TDD of a great range of therapeutic substances. This could be a technology that could be used for TDD of many drugs with high oral doses.

In Table 1 is shown a comparison of plasma profiles ($\mu\text{g}/\text{mL}/\text{h}$) after oral administration of metformin Cl to TD microneedles administration at different periods on the rat model. Laboratory rats of an average weight of 224.5 g (± 16.57 g) were administered with 100 g of metformin HCL transdermally.

Plasma concentrations were lower after TDD in comparison to oral administration of metformin HCl. Metformin HCl in the rat model yielded targeted plasma concentration reaching human therapeutic concentration after being delivered [13].

The relative TD bioavailability of metformin HCl when using hydrogel-forming microneedles was estimated as 0.6 of its oral bioavailability. The TD bioavailability of metformin HCl when using hydrogel-forming microneedles was

estimated as 0.3 meaning that 30% of the drug loading would be delivered within 24 h. The dose of metformin HCl used in this study is much lower than the oral human dose. Steady-state concentration was achieved in the plasma profile of metformin HCl within 24 h. Results of the in vivo experiment using hydrogel-forming microneedles arrays suggest potentially successful TDD of metformin HCl [13].

4 Transdermal Delivery of Insulin

Insulin is widely used to control blood glucose levels in people with diabetes since its extraction and identification in 1921 by Banting and associates. From the moment of insulin discovery, so far it has been continuously working on the improvement of insulin production, purification, the creation of new pharmaceutical formulations and methods of delivery, with a view to the patient's compliance [14].

Non-invasive insulin delivery systems have the potential to overcome the most important problems with regard to the effective treatment of diabetic patients, replacing traditional treatment. Pain in the application site, needle phobia, and therapeutic compliance [15]. It is also a worrying statistic that nearly 65% of patients with type 1 or 2 diabetes are not sure of their ability to administer insulin on their own [16]. In order to overcome this disadvantage, noninvasive routes such as oral, buccal, pulmonary, nasal, and TD are suggested. TDD is an attractive alternative to the SC delivery route for different drugs and vaccines but is usually limited by an extremely low throughput of the outer layer of the skin, the stratum corneum (SC) of 10–15 m. The Microneedle Field (MNA) has shown tremendous potential to effectively deliver the drugs intradermally and transdermally, especially when relatively small drug volume is required [17, 18].

In the past decade, many studies have been conducted aimed at assessing pharmacokinetic and pharmacodynamic variability in insulin behavior in relation to the use of various insulin preparations [19–27]. Rigorously controlled conditions, identical doses of the same preparations may have been shown to result in different pharmacokinetic and pharmacodynamic responses in the same patients [28].

Table 1 Plasma profile after application of metformin HCl using hydrogel forming microneedles in comparison with plasma profile after application of metformin HCl in oral control group on the rat model [13]

Model	Type of microneedles	Drug	Plasma profile after application ($\mu\text{g}/\text{mL}/\text{h}$)	Plasma profile ($\mu\text{g}/\text{mL}/\text{h}$) after oral administration (100 mg/kg)—control group (h)
Rat (weight 224.5 \pm 16.57 g)	Hydrogel forming microneedles	Metformin HCl (100 mg)	1 h 0.62 \pm 0.51	1 4.97 \pm 2.57
			3 h 3.76 \pm 2.58	2 6.25 \pm 2.94
			4 h 3.21 \pm 0.69	4 1.42 \pm 1.37
			24 h 3.77 \pm 2.09	24 \approx 0

Gupta et al. performed the first reported clinical study that was based on comparing TD drug use and use of microsystems with SC drug administration. The results of this study showed significant differences in insulin absorption, with hollow micro-administration being superior. The results also suggest that the use of insulin by microneedles can increase patient compliance, especially in children and adolescents who often miss insulin injections due to fear, pain, anxiety, and discomfort associated with SC needles and catheters. It has been concluded that the TD route of use is much more successful than the traditional way of applying insulin, as increased patient compliance and improved health outcomes as well as pharmacokinetics itself [28].

Kochba et al. performed a clinical study in 14 patients, this study shows a superior pharmacological profile of the hollow microneedles compared to the SC injection of the same insulin using a conventional needle. Insulin delivery showed a shorter absorption time, worsened exposure and reduced interpatient variability in time absorption. In addition, the time to reach maximum concentrations, by 50%, is considerably shorter after using hollow microneedles compared to SC injection. Finally, late AUC levels of glucose were higher in TD applications, which potentially limited the late hypoglycemic event [29].

Review of insulin delivery systems published in 2018, reports improvement in developing glucose responsive systems to constitute smart insulin patch. Creating forms based on a microgel, micelles and microcapsules with core-shell structures, which are thermo- and hypoxia-sensitive, possibly could be borrowed to microneedles system for accurate insulin delivery. It's believed that those forms act like glucose sensitive, so it's suspected that they could imitate the function of β -cell [30].

5 Transdermal Delivery of Exendin

Exendin-4 is the first glucagon-like peptide-1 (GLP-1) receptor agonist to be approved for therapeutic use in humans. This peptide has 39 amino acids originally isolated from the saliva of the Gila monster. It shares approximately 53% sequence homology with the mammalian gut hormone, GLP-1 [31]. Due to changes in the amino acid sequence, exendin-4 is resistant to degradation against the enzyme dipeptidyl peptidase-4 (DPP-4) and has a longer half-life than native GLP-1 [32]. As a GLP-1 receptor agonist, exendin-4 shows numerous anti-diabetic actions, including glucose-dependent stimulation of insulin secretion, suppression of glucagon secretion, reduction of motility and food intake and improvement in pancreatic endocrine function [33].

Ex-4 is generally administered by SC injection on a daily basis, which may result in pain, needle phobia, infection, and inconvenience to the patient. Daily injections create a large amount of needle waste, which may result in needle-stick injury, blood-borne virus transmission, and needle recycling costs [34].

Microneedles fabricated from hyaluronic acid (HA) were developed, evaluated their characteristics and assessed the improvement on TDD of relatively high molecular weight drugs. The novel microneedles fabricated from hyaluronic acid is found to have several advantages over previous microneedles. Firstly, as a major component of skin, hyaluronic acid reasonably expected to overcome the safety issues when applied to silicon and metal microneedles. Moreover, its high water-soluble characteristic makes it easy and suitable for mass production, in contrast to other published methods that require more complex multistep fabrication schemes.

The exendin-4 tip-loaded microneedles provided rapid exendin-4 administration. They showed comparable acute effects on glucose tolerance, insulin secretion, and plasma concentration profiles, as compared with subcutaneous injection, in type 2 diabetic GK/Slc rats. To sum up, HA microneedles are a useful alternative method to improve the TDD, especially drug with relatively high molecular weight without seriously damaging the skin. They might be effective and safe dosage form for transdermal delivery in the clinical setting.

In conclusion, these findings indicate that the novel soluble microneedles fabricated with HA were very useful alternative method to DD from the skin to the systemic circulation without serious skin damage. Therefore, the HA microneedles might be effective and safe dosage form for TDD of insulin and exendin-4 in clinical applications for the treatment of diabetes [35].

In a study conducted by Lahiji, Jang et al. they used the most recent technique for dissolving microneedles fabrication, in which the activity of encapsulated compounds is highly conserved during the fabrication process. They analyzed the thermal, chemical, and physical factors that can affect the activity of Ex-4 dissolving microneedles. They optimized the fabrication conditions for Ex-4 dissolving microneedles for fabrication of Ex-4 dissolving microneedles. The *in vivo* delivery comparison of SC injection and Ex-4 dissolving microneedles suggested that they possess efficiency similar to that of SC in reducing the levels of blood glucose. In conclusion, they have successfully developed and fabricated Ex-4 dissolving microneedles by optimizing the thermal, chemical, and physical factors involved in their fabrication; these factors (temperature during fabrication, pH, and concentration of the polymer)

were highly instrumental in maintaining the activity of encapsulated Ex-4. Their findings indicate that Ex-4 dissolving microneedles can potentially replace the currently used SC injections because they can effectively reduce blood-glucose levels in patients with type 2 diabetes and are convenient to use [36].

6 Conclusion

The use of microneedles for TDD is still a relatively new concept since it's only been in use since the 1990s. So far this method of delivery has been studied in drugs that otherwise have a significant risk of adverse reactions by their usual methods. Since fluctuation of blood glucose can have dangerous effects and controlling the doses of medicines that regulate glucose levels can be tricky, antidiabetic medication has been the subject of many such studies. Studies in the early 2000s on diabetic rats showed promise for an applicable microchip patch for insulin delivery. More recent studies have confirmed this and have shown that the main benefit is the faster onset of the insulin's effect. It is also possible to formulate hydrogel-forming microneedles for the delivery of metformin. The dose required to get the same blood concentrations as with the oral application is significantly lower. Tests for metformin delivery have been promising in rats and show a potential for a future micro patch formulation that could maintain constant therapeutic doses for 24 h. Recent studies have also shown that exendin-4 can also be delivered transdermally using microneedles fabricated from hyaluronic acid. Studies show that this delivery method could be just as effective and less costly than the conventional subcutaneous injections. Overall, the method of using microneedles for TDD of antidiabetic medication has been shown to have numerous advantages for patients. The greatest benefits are realized where subcutaneous injections could be replaced. Although some further research is needed to determine the conditions under which some of the medications could best be used in humans, this method of drug distribution is promising to significantly reduce medical costs and the incidence of adverse effects in patients.

Conflict of Interest The authors have no conflicts of interest to disclose.

Reference

- Global report on diabetes [Internet]: World Health Organization. Available from <http://www.who.int/diabetes/global-report/en/>. 7 Nov 2018
- Ogurtsova, K., da Rocha Fernandes, J., Huang, Y., Linnenkamp, U., Guariguata, L., Cho, N., Cavan, D., Shaw, J., Makaroff, L.: IDF diabetes atlas: global estimates for the prevalence of diabetes for 2015 and 2040. *Diabetes Res. Clin. Pract.* **128**, 40–50 (2017)
- Khanna, P., Strom, J.A., Malone, J.I., Bhansali, S.: Microneedle-based automated therapy for diabetes mellitus. *J. Diabetes Sci. Technol.* **2**(6), 1122–1129 (2008)
- Alkilani, A., McCrudden, M., Donnelly, R.: Transdermal drug delivery: innovative pharmaceutical developments based on disruption of the barrier properties of the stratum corneum. *Pharmaceutics* **7**(4), 438–470 (2015)
- Cleary, G.W.: Microneedles for drug delivery. *Pharm. Res.* **28**(1), 1–6 (2011)
- Cheung, K., Das, D.: Microneedles for drug delivery: trends and progress. *Drug Deliv.* **23**(7), 2338–2354 (2014)
- Wermeling, D., Banks, S., Hudson, D., Gill, H., Gupta, J., Prausnitz, M., Stinchcomb, A.: Microneedles permit transdermal delivery of a skin-impermeant medication to humans. *Proc. Natl. Acad. Sci.* **105**(6), 2058–2063 (2008)
- Prausnitz, M.: Microneedles for transdermal drug delivery. *Adv. Drug Deliv. Rev.* **56**(5), 581587 (2004)
- Serrano-Castañeda, P., Escobar-Chavez, J., Rodriguez-cruz, I., Melgoza, L., Martinez-Hernandez, J.: Microneedles as enhancer of drug absorption through the skin and applications in medicine and cosmetology. *J. Pharm. Pharm. Sci.* **21**(1), 73 (2018)
- Yu, W., Jiang, G., Zhang, Y., Liu, D., Xu, B., Zhou, J.: Nearinfrared light triggered and separable microneedles for transdermal delivery of metformin in diabetic rats. *J. Mater. Chem. B* **5**, 9507–9513 (2017)
- Lee, H., Choi, T., Lee, Y., Cho, H., Ghaffari, R., Wang, L., Choi, H., Chung, T., Lu, N., Hyeon, T., Choi, S., Kim, D.: A graphene-based electrochemical device with thermoresponsive microneedles for diabetes monitoring and therapy. *Nat. Nanotechnol.* **11**, 566–572 (2016)
- Guy, R.: Managing diabetes through the skin. *Nat. Nanotechnol.* **11**, 493–494 (2016)
- Migdadi, E.M., Courtenay, A.J., Tekko, I.A., McCrudden, M.T.C., Kearney, M.C., McAlister, E., McCarthy, H.O., Donnelly, R.F.: Hydrogel-forming microneedles enhance transdermal delivery of metformin hydrochloride. *J. Control. Release* **285**, 142–151 (2018)
- Roxhed, N., Samel, B., Nordquist, L., Griss, P., Stemme, G.: Painless drug delivery through microneedle-based transdermal patches featuring active infusion. *IEEE Trans. Biomed. Eng.* **55**, 1063–1071 (2008)
- Pearson, T.: Practical aspects of insulin pen devices. *J. Diabetes Sci. Technol.* **4**, 522–531 (2010)
- Ross, S., Scoutaris, N., Lamprou, D., Mallinson, D., Douroumis, D.: Inkjet printing of insulin microneedles for transdermal delivery. *Drug Deliv. Transl. Res.* **5**, 451–461 (2015)
- Sousa, F., Castro, P., Fonte, P., Sarmiento, B.: How to overcome the limitations of current insulin administration with new noninvasive delivery systems. *Ther. Deliv.* **6**, 8394 (2015)
- Tucak, A.: Mikroiglama posredovana dostava lijekova kroz kožu-formulacijski aspekti [Završni rad integriranog studija prvog i drugog ciklusa]. Univerzitet u Sarajevu (2017)
- Resnik, D., Možek, M., Pečar, B., Janež, A., Urbančič, V., Iliescu, C., Vrtačnik, D.: In vivo experimental study of noninvasive insulin microinjection through hollow si microneedle array. *Micromachines* **9**, 40 (2018)
- Zhou, C., Liu, Y., Wang, H., Zhang, P., Zhang, J.: Transdermal delivery of insulin using microneedle rollers in vivo. *Int. J. Pharm.* **392**, 127133 (2010)
- Norman, J., Brown, M., Raviele, N., Prausnitz, M., Felner, E.: Faster pharmacokinetics and increased patient acceptance of intradermal insulin delivery using a single hollow microneedle in children and adolescents with type 1 diabetes. *Pediatr. Diabetes* **14**, 459–465 (2013)

22. Ito, Y., Nakahigashi, T., Yoshimoto, N., Ueda, Y., Hamasaki, N., Takada, K.: Transdermal insulin application system with dissolving microneedles. *Diabetes Technol. Ther.* **14**, 891–899 (2012)
23. Gill, H., Denson, D., Burris, A., Prausnitz, M.: Effect of microneedle design on pain in human volunteers. *Clin. J. Pain* **24**, 585–594 (2008)
24. Pettis, R., Harvey, A.: Microneedle delivery: clinical studies and emerging medical applications. *Ther. Delivery* **3**, 357–371 (2012)
25. Jung, H.: Microneedle: the future of pharmaceutical and cosmeceutical delivery systems. *J. Phar. Drug Deliv. Res.* **06** (2017)
26. Lee, J., Prausnitz, M.: Drug delivery using microneedle patches: not just for skin. *Expert Opin. Drug Deliv.* **15**, 541–543 (2018)
27. Ma, G., Wu, C.: Microneedle, bio-microneedle and bioinspired microneedle: a review. *J. Control. Release* **251**, 11–23 (2017)
28. Gupta, J., Felner, E., Prausnitz, M.: Rapid pharmacokinetics of intradermal insulin administered using microneedles in type 1 diabetes subjects. *Diabetes Technol. Ther.* **13**, 451–456 (2011)
29. Kochba, E., Levin, Y., Raz, I., Cahn, A.: Improved insulin pharmacokinetics using a novel microneedle device for intradermal delivery in patients with type 2 diabetes. *Diabetes Technol. Ther.* **18**, 525–531 (2016)
30. Jin, X., Zhu, D., Chen, B., Ashfaq, M., Guo, X.: Insulin delivery systems combined with microneedle technology. *Adv. Drug Deliv. Rev.* **127**, 119–137 (2018)
31. Doyle, M.E., Egan, J.M.: Mechanisms of action of glucagonlike peptide 1 in the pancreas. *Pharmacol. Ther.* **113**, 546–593 (2007)
32. Gallwitz, B.: New therapeutic strategies for the treatment of type 2 diabetes mellitus based on incretins. *Rev. Diabetic Stud.* **2**, 61–69 (2005)
33. Kolterman, O.G., Buse, B., Fineman, M.S., Gaines, E., Heintz, S., Bicsak, T.A., Taylor, K., Kim, D., Aispoma, M., Wang, Y., Baron, A.D.: Synthetic exendin-4 (exenatide) significantly reduces postprandial and fasting plasma glucose in subjects with type 2 diabetes. *J. Clin. Endocrinol. Metab.* **88**, 3082–3089 (2013)
34. Li, J., Zeng, M., Shan, H., Tong, C.: Microneedle patches as drugs and vaccine delivery platform. *Curr. Med. Chem.* **24**, 2413–2422 (2017)
35. Liu, S.: The development of novel microneedle arrays fabricated from hyaluronic acid, and their application in the transdermal delivery of diabetes drugs. *Mol. Pharm.* **13**, 272–279 (2016)
36. Lahiji, S., Jang, Y., Huh, I., Yang, H., Jang, M., Jung, H.: Exendin-4-encapsulated dissolving microneedle arrays for efficient treatment of type 2 diabetes. *Sci. Rep.* **8** (2018)

Toxicity of Azo Dyes in Pharmaceutical Industry

Armina Gičević, Lamija Hindija, and Alma Karačić

Abstract

Azo compounds represent about two thirds of all synthetic dyes. Their usage in pharmaceutical industry has many purposes. One of the most important is coloring of pharmaceutical agents which improves their easy identification. Azo dyes often used in manufacturing of pharmaceuticals are: E102 Tartrazine, E110 Sunset Yellow FCF, Ponceau 4R (Cochineal Red A), Azorubine (Carmoisine), Amaranth, E133 Brilliant Blue and E129 Allura Red. Many azo dyes show carcinogenic and mutagenic activity, and they can provoke allergic reactions. Generally, toxicity of ingredients grows with the increase of benzene rings in their structure. Carcinogenicity of azo dyes directly depends on the structure of molecule and on mechanism of degradation. Products of degradation of azo dyes are mostly aromatic amines with different structures and they can also have carcinogenic properties. Carcinogenicity of many azo dyes is due to their cleaved products such as benzidine. Benzidine is known as carcinogen for the human urinary bladder. Except of carcinogenic and mutagenic activity, azo dyes can alter biochemical markers and they can provoke allergic reactions.

Keywords

Azo dyes • Toxicity • Carcinogenicity • Allergic reactions • Pharmaceutical industry

A. Gičević (✉)

Department of Pharmaceutical Analysis, Faculty of Pharmacy, University of Sarajevo, Zmaja od Bosne 8, 71000 Sarajevo, Bosnia and Herzegovina
e-mail: armina.gicevic@ffsa.unsa.ba

L. Hindija

Department of Pharmaceutical Technology, Faculty of Pharmacy, University of Sarajevo, Zmaja od Bosne 8, 71000 Sarajevo, Bosnia and Herzegovina

A. Karačić

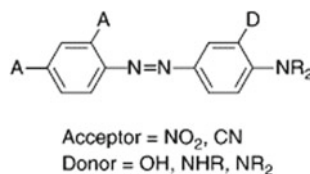
Sarajevo, Bosnia and Herzegovina

1 Introduction

A color additive is a chemical compound that reacts with another substance and causes the formation of a color. The pharmaceutical industry uses various inorganic and organic dyes. The usage of dyes in pharmaceutical industry has commercial, psychological and practical purposes. Different colors of drugs also can help patients to distinguish different strengths of the same drug which can reduce risk of an overdose or underdose [1].

Most dyes/coloring agents used in the pharmaceutical industry belong to one of the following groups: azo dyes, quinoline dyes, triphenylmethane dyes and xanthine dyes [2].

Azo compounds represent about two thirds of all synthetic dyes. They are the most widely used and structurally diverse class of organic dyes in commerce. Their chemical formula is $R-N=N-R'$, where $-N=N-$ represents the azo group and the R or R' is either aryl or alkyl compound [3].



Structural formula of azo dyes. Source http://www.chm.bris.ac.uk/webprojects2002/price/classify.htm?fbclid=IwAR1QTaIRivGOTikJQc7-S61nV_Z_nzGSyDcYCwSw86d702K71L3RwNRresc

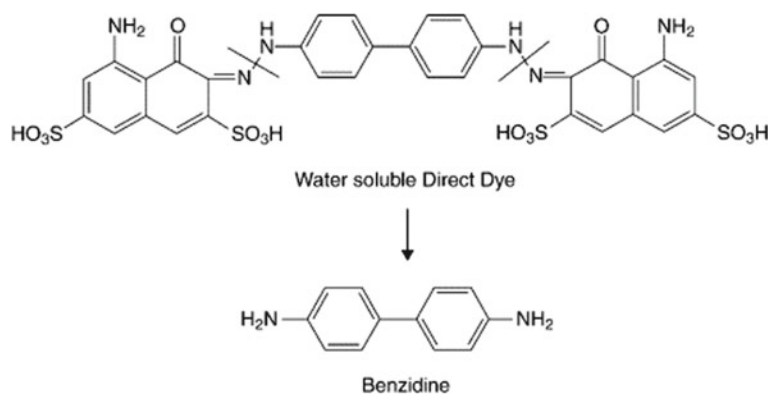
Azo dyes often used in manufacturing of pharmaceuticals are: E102 Tartrazine, E110 Sunset Yellow FCF, Ponceau 4R (Cochineal Red A), Azorubine (Carmoisine), Amaranth, E133 Brilliant Blue and E129 Allura Red.

Many azo dyes show carcinogenic and mutagenic activity, and they can provoke allergic reactions. Generally, toxicity of ingredients grows with the increase of benzene rings in their structure. Carcinogenicity of azo dyes directly depends on the structure of molecule and on mechanism of degradation. Products of degradation of azo dyes are mostly

aromatic amines with different structures and they can also have carcinogenic properties [1].

Some azo dyes can be carcinogenic without being cleaved into aromatic amines. However, the carcinogenicity of many azo dyes is due to their cleaved product such as benzidine. Benzidine induces various human and animal tumors. Another azo dye component, p-phenylenediamine, is a contact allergen. Reduction of azo dyes can be accomplished by human intestinal microflora, skin microflora, environmental microorganisms, to a lesser extent by human liver azoreductase, and by nonbiological means [3].

cytotoxicity and genotoxicity of the TRZ dye in human leukocyte cultures and performed theoretical studies to predict its toxicity *in silico*. They concluded that mutagenic and cytotoxic effect were dose dependent [5]. Gao et al. were evaluating the toxic effect of tartrazine on the learning and memory functions in mice and rats. Animals were administered different doses of tartrazine for a period of 30 days and were evaluated by open-field test, step-through test, and Morris water maze test, respectively. Furthermore, the biomarkers of the oxidative stress and pathohistology were also measured to explore the possible mechanisms involved.

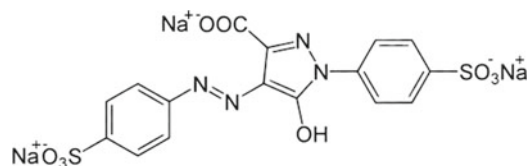


Conversion of water soluble direct dye to benzidine. Source <https://ars.els-cdn.com/content/image/3-s2.0-B978184569695500167-f16-04-9781845696955.gif>

p-Phenylenediamine is one of the primary intermediates in the azo dyes. Poisoning with p-phenylenediamine causes angioneurotic edema, intravascular hemolysis, rhabdomyolysis with acute renal failure. 1-Amino-2-naphthol, which is one of the components of an important group of 1-amino-2-naphthol-based azo dyes, has been reported to be a carcinogen. Gottlieb et al. proved that the metabolite of Sunset Yellow 1-amino-2-naphthol-6-sulphonate was not mutagenic, which could be due to the decrease in membrane permeability of this compound. Benzidine is a product of the reduction of Congo Red, and the sulfonated benzidine is a product of the reduction of Acid Orange 6. Benzidine is known as carcinogen for the human urinary bladder. The addition of a sulfonic acid group to benzidine reduces the mutagenicity [4].

2 Tartrazine

Tartrazine (TRZ) is a lemon-yellow dye which is widely used in pharmaceuticals and also cosmetics and food manufacturing. Few studies have addressed the toxicology of TRZ in human cells or tissues. Floriano et al. evaluated the



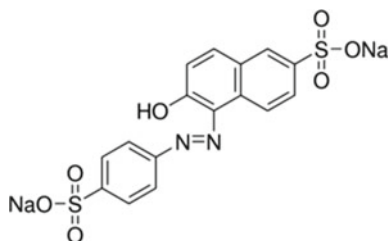
Structural formula of Tartrazine. Source https://www.researchgate.net/figure/Chemical-structure-of-Tartrazine_fig1_321634795?fbclid=IwAR0JZGNHfNbNmEH8D3Qp1uvpauQIh0J1yAhB4kdbSMrGW-6wM7MfBwWFfu6o

The results indicated that tartrazine extract significantly enhanced active behavioral response to the open field, increased the escape latency in Morris water maze test and decreased the retention latency in step-through tests. The decline in the activities of catalase, glutathione peroxidase (GSH-Px), and superoxide dismutase (SOD) as well as a rise in the level of malonaldehyde (MDA) were observed in the brain of tartrazine-treated rats, and these changes were associated with oxidative damage. The dose levels of tartrazine in the present study produced a few adverse effects in learning and memory functions in animals. The mechanisms might be attributed to the promotion of lipid peroxidation

products and reactive oxygen species, inhibition of endogenous antioxidant defense enzymes and damage of brain tissue [6].

Tartrazine has been associated with anaphylactoid reactions, angioedema, asthma, urticaria and hyperkinesia in patients with hyperactivity and eosinophilia. Because of the cross-sensitivity of azo dyes with aspirin sodium benzoate and indomethacin, azo dye excipients should be avoided in patients with history of hypersensitivity or allergy to these drugs.

3 Sunset Yellow



Structural formula of Sunset yellow. Source https://www.sigmaaldrich.com/content/dam/sigma-aldrich/structure3/090/mfcd00036437.eps/_jcr_content/renditions/mfcd00036437-medium.png

Sunset yellow (FD&C 6), another azo dye, has also been associated with the same adverse effects as seen with tartrazine. The incidence of cross-sensitivity to aspirin varies between 2 and 20% in patients with asthma, therefore, it is prudent not to prescribe preparations containing azo dyes to such patients.

Because of the adverse events reported with specific dyes, the FDA has (since 1980) mandated labeling when tartrazine is used in a product. The American Academy of Pediatrics has published a list of drugs/nutritional supplements that do not contain any dyes; physicians treating patients with a history of hypersensitivity reactions may find this reference helpful [2].

Khayyat et al. have done a study where they investigated the possible toxic effects of two types of widely used food and drug colorants, Sunset Yellow and Allura Red, by assessing the physiological, histopathological and ultra-structural changes in the liver and kidney. Also, they investigated the genotoxic effect of both dyes on white blood cells. Thirty adult male albino rats were divided into three groups of 10 animals each: control (received water), Sunset Yellow-treated (2.5 mg/kg body weight) and Allura Red-treated (7 mg/kg body weight). The doses were applied orally for 4 weeks. The results indicated an increase in the biochemical markers of hepatic and renal function (aspartate aminotransferase—AST, alanine aminotransferase—ALT,

urea, uric acid and creatinine) in animals administered with the azo dyes. They also observed a noticeable increase in MDA and a marked decrease in total antioxidant levels in azo dye-treated animals compared to controls. Conversely, both dyes adversely affected the liver and kidney of albino rats and altered their histological and fine structure, with downregulation of Bcl2 and upregulation of COX2 expression. Comet assay results showed that Sunset Yellow and Allura Red cause histopathological and physiological aberrations in the liver and kidney of male Wistar albino rats. Moreover, Sunset Yellow but not Allura Red induced a potential genotoxic effect [7] (Fig. 1).

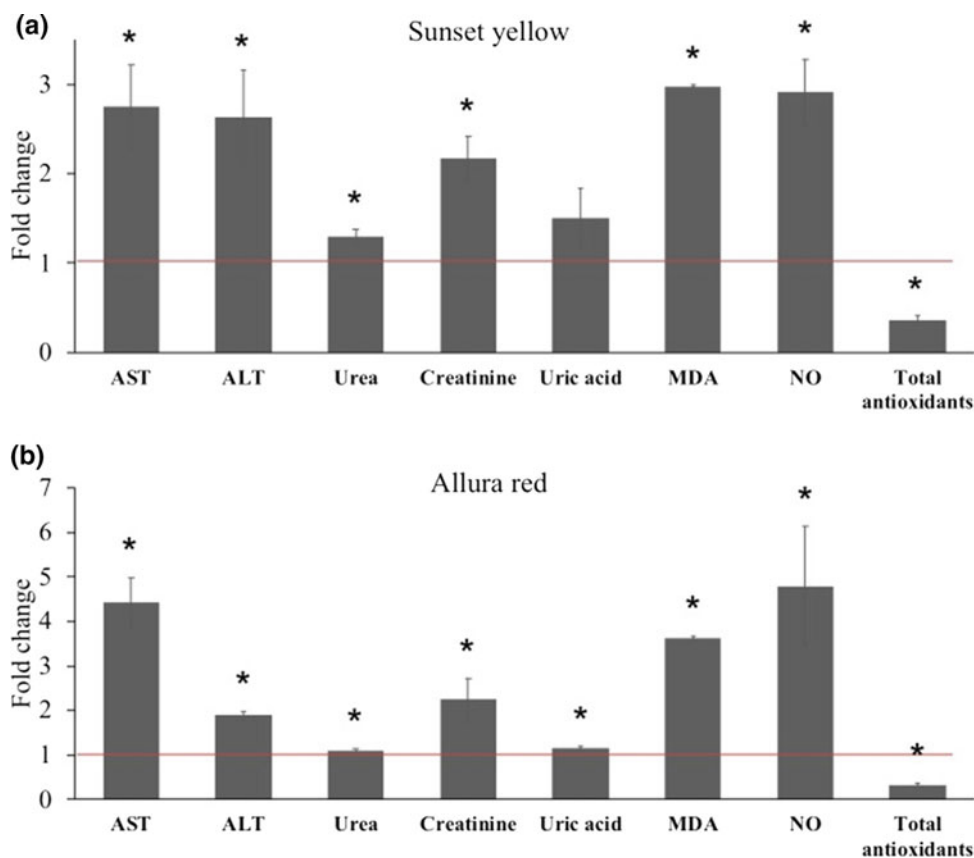
Qu et al. investigated the toxicity of Sunset yellow combined with sodium sulfite and mechanisms of damage in HepG2 cells using High Content Analysis (HCA). They used the CCK-8 assay to determine cell viability. They concluded that this combination led to the growth decrease of HepG2 cells in a dose-dependent manner. Sunset yellow and sodium sulfite had IC50 values of 1.06, and 0.30 g/L at 24 h, respectively. HCA showed that both Sunset yellow and sodium sulfite had synergistic effects on cell number, membrane permeability, mitochondrial membrane potential, intracellular calcium level, oxidative stress, and high dose group DNA damage [8].

Ali et al. were examining the combination of Sunset yellow (SY) and sodium benzoate (NaB). Genotoxic effects of different combinations of SY and NaB were assessed in vivo in female rats. Different combinations of SY and NaB were dissolved in water and administered daily to six animals groups for 12 weeks. Different combinations of SY and NaB induced an increase in the frequency of tailed nuclei (DNA damage) in liver cells. In addition, administration of SY plus NaB resulted in an abnormal distribution of serum proteins. The results showed that the combination of SY and NaB could have genotoxic potential [9].

Genotoxic and cytotoxic effects of curcumin and sunset yellow were tested by Haverić et al. using the chromosome aberration analysis and cytokinesis-block micronucleus cytome assay in human lymphocyte culture. Tested concentrations of sunset yellow significantly associated with frequencies of structural aberrations, chromatid-type aberrations, total aberrant cells and micronuclei showing considerable dose dependent clastogenic activity. In higher analyzed concentrations, curcumin significantly increased only nuclear buds frequency, suggesting its potential genotoxicity, while sunset yellow showed dose-dependent genotoxic potential. Obtained results point toward favorization of natural coloring agents [10].

Amin et al. conducted a study to evaluate the toxic effects of tartrazine and carmoisine on renal, hepatic function, lipid profile, blood glucose, body-weight gain and biomarkers of oxidative stress in tissue. Tartrazine and carmoisine were administered orally in two doses, one low and the other high

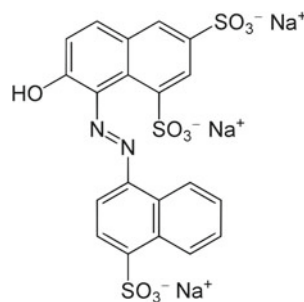
Fig. 1 Effect of sunset yellow and allura red on biochemistry parameters and oxidative biomarkers in male rats [7]



dose for 30 days followed by serum and tissue sample collection for determination of ALT, AST, alkaline phosphatase, urea, creatinine, total protein, albumin, lipid profile, fasting blood glucose in serum and estimation of GSH, catalase, SOD and MDA in liver tissue in male albino rat. It was concluded that tartrazine and carmoisine affect adversely and alter biochemical markers in vital organs e.g. liver and kidney not only at higher doses but also at low doses [11].

Cemek et al. got unique results for concentrations of trace and major elements in rats' liver, kidney and brain tissues exposed to tartrazine and carmoisine, especially for iron and zinc contents. They suggested that anemia in mice may be related to iron deficiency. Also by consuming carmoisine at both low and high doses resulted with a reduction of zinc content in kidneys, because zinc is chelated by consumed dyes. Although low dose tartrazine caused to reduce liver zinc content, high dose tartrazine cause to same effect in kidney. Aluminium and barium are essential trace elements and the levels of these elements in brain are reduced by consuming high and low doses of tartrazine. Also there is a significant increase of calcium levels in liver tissue with high doses of carmoisine [12].

4 Ponceau 4R

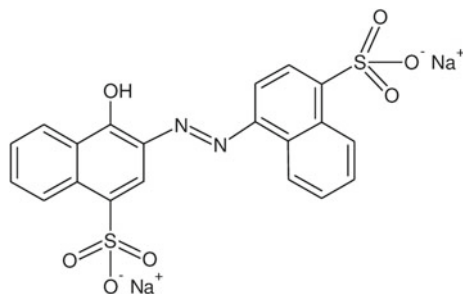


Structural formula of Ponceau 4R. Source https://file.medchemexpress.com/product_pic/hy-d0193.gif

Ponceau 4R may increase hyperactivity in affected children and adversely affect those that are sensitive to aspirin [1].

Rowe et al. investigated the use of six dyes (Tartrazine, Quinoline Yellow, Sunset Yellow, Azorubine, Ponceau 4R and Allura Red). The study results connected these dyes to behaviour issues in children. Nonetheless, after reviewing the outcomes of the study, the European Food Standards Agency came to the conclusion that no legislative change or amendment was in fact required [13].

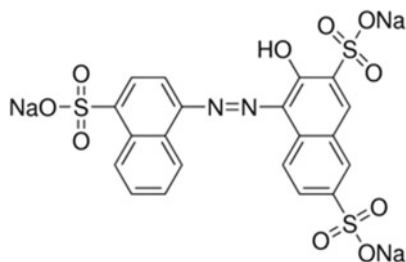
5 Azorubine



Structural formula of Azorubine. Source https://www.sigmaaldrich.com/content/dam/sigma-aldrich/structure5/145/mfcd00003978.eps/_jcr_content/renditions/mfcd00003978-medium.png

Azorubine has shown no evidence of mutagenic or carcinogenic properties. Like Ponceau 4R, it may have an adverse effect on the activity and attention in children. Azorubine may rarely cause skin and respiratory reactions in susceptible individuals, even at the approved dose [14].

6 Amaranth



Structural formula of Amaranth. Source https://www.sigmaaldrich.com/content/dam/sigma-aldrich/structure5/178/mfcd00004076.eps/_jcr_content/renditions/mfcd00004076-medium.png

Amaranth in certain concentrations can induce dose-related DNA damage in the colon of mice after oral administration. Except genotoxicity amaranth can, as some

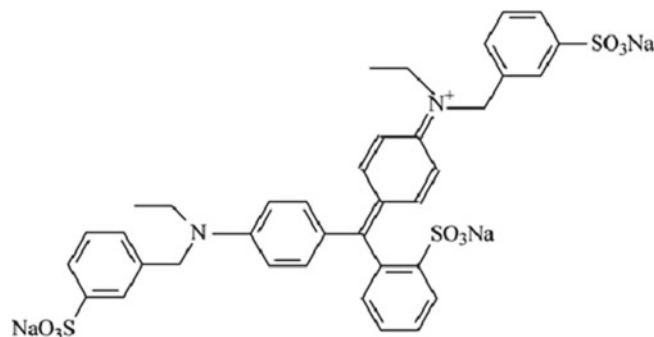
other azo dyes, also cause allergic or asthmatic reactions for sensitive people, as well as frequent headaches and children's hyperactivity [1].

Also, in another study conducted by Sasaki et al., on the genotoxicity of food dyes, such as Amaranth, it was observed that DNA damage occurred on the colon, bladder, stomach, and gastrointestinal organs even at the lowest dose. Mpountoukas et al. investigated the potential genotoxic, cytotoxic and cytostatic effects in human peripheral blood cells for Amaranth in vitro. According to the results, it was identified that food dyes have a toxic effect on human lymphocyte cells and cause an increase in the sister chromatid exchange 1.7 times compared to the control group, and show effects of direct binding on DNA. Similar results were found in a study that was carried out by Shimada et al. DNA damage was noticed in rat colon after applying 10 mg kg^{-1} of azo food dyes. It appeared that the DNA damage was induced in pregnant female and male rats fed with Amaranth orally [15].

7 Brilliant Blue

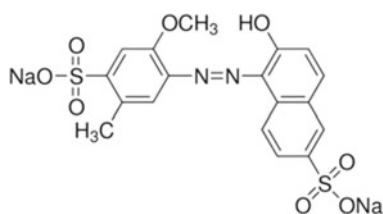
Brilliant Blue has the capacity of inducing an allergic reaction in individuals with pre-existing moderate asthma [1].

Remy et al. study was conducted to evaluate the retinal toxicity of Brilliant Blue G (BBG) following intravitreal injection in rat eyes and examine the biocompatibility and the staining properties in humans. No significant reduction in retinal ganglion cell numbers and no morphological alterations were noted. A sufficient staining of the internal limiting membrane (ILM) was seen in patients with macular hole, while the staining pattern in epiretinal membranes (ERM) cases was patchy, indicating that parts of the ILM were peeled off along with the ERM in a variable extent. No toxic effects attributable to the dye were noted during patient follow-up. No retinal toxicity or adverse effects related to the dye were observed in animal and human studies. The long-term safety of this novel dye will have to be evaluated in larger patient series and a longer follow-up [16, 17].



Structural formula of Brilliant blue. Source https://www.researchgate.net/figure/Chemical-structure-of-Brilliant-Blue-R-BBR-dye_fig11_271563974

8 Allura Red



Structural formula of Allura red. Source https://www.sigmaaldrich.com/content/dam/sigma-aldrich/structure/5/051/mfcd00059526.eps/_jcr_content/renditions/mfcd00059526-medium.png

Allura Red may cause allergic reactions (e.g. urticaria, asthma), especially when administered in mixes with other synthetic color additives [1].

Rajan and Anandan conducted a study where the emphasis was made on knowing the effect of these common agents, in particular with reference to artificial food color Allura red (FD&C # 40)—orange red food dye on DNA damage using catfish 0 + 2—as a model organism. The methodology was to understand direct damage of nucleus by micronuclei test and chromosomal damage by alkaline single-cell gel electrophoresis (COMET) assay. The freshwater catfish *Clarias batrachus* was used for specificity genotoxic indicators micronucleus assay and COMET assays. The blood sample was tested for genotoxicity and the results revealed DNA damage through alkaline single-cell gel electrophoresis (comet) and micronuclei assays. Hence it was concluded that the usage of food color containing Allura red (FD&C # 40)—orange red food dye may be toxic at a genetic level if the usage is prolonged [18].

In the study conducted by Uysal et al. the toxic effects of four different synthetic dyes (Ponceau 4R, Sunset Yellow, Amaranth, Tartrazine) on 72 ± 4 h larvae of Oregon

(R) wild type of *Drosophila melanogaster* were investigated. The effects of the dyes on longevity were studied separately in female and male populations. The study determined that the maximum mean life span of the female and male *D. melanogaster* populations decreased with increasing concentrations of dyes. Based on the results obtained from the larval mortality and life span experiments, the order of toxicity for dyes was: Tartrazine > Amaranth > Sunset Yellow \geq Ponceau 4R [15].

9 Conclusion

One of the most often used coloring agents in pharmaceutical industry are azo dyes. However, they show some severe side effects, such as carcinogenic and mutagenic activity.

Some of them promote lipid peroxidation products and reactive oxygen species, inhibit endogenous antioxidant defense enzymes which result in the brain tissue and adverse effects in learning and memory functions. They may cause histopathological and physiological aberrations in liver and kidneys and change membrane permeability, mitochondrial membrane potential and intracellular calcium level. Some combinations lead to structural chromosome aberrations, chromatid-type aberrations, total aberrant cells and micronuclei. For sensitive people, they can cause allergic or asthmatic reactions, as well as frequent headaches and children's hyperactivity. It also has toxic effects on human lymphocyte cells, increases the sister chromatid exchange and shows effect of binding on DNA directly.

To prevent the abuse of synthetic dyes, the permissible type and usage of synthetic dyes are strictly regulated in many countries. It is very important to be aware that consequences of inadequate dosage and combination of azo dyes can cause serious health issues. Also, pharmaceutical industry should consider surcease or decreased use of

conventional dyes and start using newer, safer dyes such as Brilliant blue for which is proved that has less side effects.

Conflict of Interest The authors have no conflicts of interest to disclose.

Reference

1. Šuleková, M., Smrčová, M., Hudák, A., Heželová, M., Fedorová, M.: Organic colouring agents in the pharmaceutical industry. *Folia Vet.* **61**(3), 32–46 (2017)
2. Pawar, S., Kumar, A.: Issues in the formulation of drugs for oral use in children: role of excipients. *Paediatr. Drugs* **4**(6), 371–379 (2002)
3. Chung, K.T.: Azo dyes and human health: a review. *J. Environ. Sci. Health C Environ. Carcinog. Ecotoxicol. Rev.* **34**(4), 233–261 (2016)
4. Feng, J., Cerniglia, C.E., Chen, H.: Toxicological significance of azo dye metabolism by human intestinal microbiota. *Front Biosci. (Elite ed.)* **4**, 568–586 (2012)
5. Floriano, J.M., da Rosa, E., do Amaral, Q.D.F., Zuravski, L., Chaves, P.E.E., Machado, M.M., et al.: Is tartrazine really safe? In silico and ex vivo toxicological studies in human leukocytes: a question of dose. *Toxicol Res. (Camb.)* **7**(6), 1128–1134 (2018)
6. Gao, Y., Li, C., Shen, J., Yin, H., An, X., Jin, H.: Effect of food azo dye tartrazine on learning and memory functions in mice and rats, and the possible mechanisms involved. *J. Food Sci.* **76**(6), 125–129 (2011)
7. Khayyat, L.I., Essawy, A.E., Sorour, J.M., Soffar, A.: Sunset yellow and Allura red modulate Bcl2 and COX2 expression levels and confer oxidative stress-mediated renal and hepatic toxicity in male rats. *PeerJ.* **6**, e5689 (2018)
8. Qu, D., Gu, Y., Feng, L., Han, J.: High content analysis technology for evaluating the joint toxicity of sunset yellow and sodium sulfite in vitro. *Food Chem.* **233**, 135–143 (2017)
9. Ali, M.Y., Hassan, G.M., Hassan, A.M.S., Mohamed, Z.A., Ramadan, M.F.: In vivo genotoxicity assessment of sunset yellow and sodium benzoate in female rats. *Drug Chem. Toxicol.* 1–10 (2018)
10. Haverić, A., Haverić, S., Hadžić, M., Lojo-Kadrić, N., Ibrulj, S.: Genotoxicity and cytotoxicity analysis of curcumin and sunset yellow in human lymphocyte culture. *Cell. Mol. Biol. (Noisy-le-grand)* **64**(3), 87–91 (2018)
11. Amin, K.A., Abdel Hameid, H., Abd Elstar, A.H.: Effect of food azo dyes tartrazine and carmoisine on biochemical parameters related to renal, hepatic function and oxidative stress biomarkers in young male rats. *Food Chem. Toxicol.* **48**(10), 2994–2999 (2010)
12. Cemek, M., Büyükkuroğlu, M.E., Sertkaya, F., Alpdağtaş, S., Hazini, A., Önül, A., et al.: Effects of food colour additives on antioxidant functions and bioelement contents of liver, kidney and brain tissues in rats. *J. Food Nutr.* **2**(10), 686–691 (2014)
13. Rowe, R.C., Sheskey, P.J., Quinn, M.E.: *Handbook of Pharmaceutical Excipients*, 6th edn. Pharmaceutical Press and American Pharmacists Association, USA (2009)
14. EFSA: Scientific opinion on the re-evaluation of Azorubine/Carmoisine (E 122) as a food additive. <https://www.efsa.europa.eu/en/efsajournal/pub/1332>. Accessed 12 Dec 2018
15. Uysal, H., Genc, S., Ayar, A.: Toxic effects of chronic feeding with food azo dyes on drosophila melanogaster oregon R. *Sci. Iran. C* **24**(6), 3081–3086 (2017)
16. Remy, M., Thaler, S., Schumann, R.G., May, C.A., Fiedorowicz, M., Schuettauf, F., et al.: An in vivo evaluation of brilliant blue G in animals and humans. *Br. J. Ophthalmol.* **92**, 1142–1147 (2008)
17. Bastaki, M., Farrel, T., Bhusari, S., Pant, K., Kulkarni, R.: Lack of genotoxicity in vivo for food colour additive allura red AC. *Food Chem. Toxicol.* **105**, 308–314 (2017)
18. Rajan, A.P., Anandan, S.: Investigation of carcinogenic and mutagenic property of food colour using catfish *Clarias Batrachus* by using alkaline single-cell gel electrophoresis (comet) assay and micronucleus assay. *Int. J. Med. Res. Pharmacol. Sci.* **4**(7), 29–34 (2017)

Genes Associated With Free Fatty Acid Levels and Dyslipidemia in Type 2 Diabetes Patients

S. Mandal

Abstract

Type 2 diabetes mellitus (T2D) is a complex metabolic disorder associated with disturbances not only in carbohydrates and proteins but also with impairment of lipid metabolism. It is largely influenced by complex interactions of environmental and genetic factors, or both. High prevalence and increasing number of patients with T2D in the world, represent constant challenge for better elucidation of pathophysiological processes that lead to development of disease. In this paper, I have tried to summarize the results of my research and new findings from recent analyses of genome-wide association studies (GWAS) which helped us in the identification of common and rare genetic variants associated with insulin resistance (IR), dyslipidemia, Metabolic syndrome (MetS) and Type 2 diabetes. Many variants of certain genes are directly involved in glucose metabolism; however, functional and additional studies are suggested in order to be able to understand the contribution of other variants associated with impaired lipid and lipoprotein metabolism. New technologies such as metabolomics, proteomics, genomics, a more recently, lipidomics clearly point out directions in identification and detection of good/best biological gene candidates involved in fatty acid and lipoprotein metabolism. Mutational sequencing for these genes i.e. genetic regions associated with T2D, obesity, dyslipidemia and IR, could serve as a protective measure for not only insulin sensitivity but also, insulin secretion, obesity and other glycemic traits.

Keywords

Gene variation • Free fatty acid • Dyslipidemia • Type 2 diabetes

S. Mandal (✉)
 Department of Natural Sciences in Pharmacy, Faculty of Pharmacy, University of Sarajevo, Sarajevo, Bosnia and Herzegovina
 e-mail: mandalshakira@yahoo.co.uk

1 Introduction

Type 2 *Diabetes mellitus* (T2D) is a complex and chronic metabolic disease characterized by defective production or action of insulin and high glucose and lipid levels in the blood. As a result of alterations in lipid metabolic pathways, circulating plasma free fatty acids (FFAs) and lipoproteins concentration rises. It is well known that the long chain fatty acids (polyunsaturated fatty acid, PUFA), very important biomolecules and main constituents of cell membrane play a key role in the cell function and therefore regulate the β -cells functionally, with effects on insulin sensitivity and secretion. Elevated concentration of FFAs (especially saturated fatty acids) in plasma is associated with impaired insulin sensitivity and secretion, as well as glucose intolerance. Chronic elevation of FFAs can lead to β -cell dysfunction, which in turn lead ultimately leads to hyperglycemia [1–3].

A disturbance in the regulation of free fatty acid metabolism is a key event responsible for insulin resistance (IR) and Type 2 diabetes. According to the glucose-fatty acid cycle of Randle et al., preferential oxidation of free fatty acids over glucose plays a major role in insulin sensitivity and leads to metabolic disturbances of diabetes [4]. However, other underlying mechanisms are now being described in order to explain the molecular basis of insulin resistance. Finally, modulation of transcription factors by free fatty acids through their binding to peroxisome proliferator-activated receptors and nuclear receptors could also contribute to impaired glucose and insulin metabolisms [5–10].

1.1 Genetics of Type 2 Diabetes

Type 2 diabetes is heterogeneous disorder and it is caused by more than 500 genes; but still, it is not known all genes that are responsible for T2D. This metabolic disease is caused not only by single gene, such as MODY type of diabetes, it the case of diabetes when mutations happen on hepatocyte

Table 1 Genes that is associated with risk of T2D

Gene/nearest gene	Traits	Ref.
TCF7L2	Impaired insulin secretion, FG, T2D, HOMA-B	[12, 37]
IRS1	Insulin production, IR, FG, dyslipidemia	[11, 16, 37]
IGF2	T2D	[12, 21, 32]
KNCJ11	Hyperinsulinemia, T2D, increased glucagon level	[13, 25]
HNF4A	Hyperinsulinemia, T2D	[23, 28]
GCKR	FG, T2D	[12, 17]
SLC2A2	T2D, decreased HOMA-B	[28, 37]
<i>FADS1/2</i>	FG, decreased HOMA-B	[14, 24, 28]
CETP	FG, HOMA-IR, T2D	[10, 30]

FG—fasting glucose, HOMA-B—homeostatic model assessment for B-cell, HOMA-IR—homeostatic model assessment for IR

nuclear factor (*HNF1A*) and/or on glucokinase (*GCK*). It is important to mention that MODY is sometimes misdiagnosed as type 2 diabetes. Nowadays, it is known that T2D represent strong heritable and polygenic disease which caused by interaction of many various gene and, also some environmental factors (lifestyle, diet, etc.). Mechanisms and processes which underlying and involved in these interactions is still poorly understood and completely elucidate [11–14]. Some of genes that are known that are T2D related genes are *CAPN10* (*CAPN10* encodes a cysteine protease) and *TCF7L2*. It has a role in intracellular remodeling, post-receptor signaling and in some other intracellular functions. Also, there are more specific candidate gene studies which focus on genes that are involved in glucose metabolism, insulin secretion, post-receptor signaling and lipid metabolism. According to the recent studies in Table 1 presented some of new discovered genes that are linked with the T2D development [15–17].

1.2 Genetics of Fatty Acids

Fatty acids (FA) as a lipid represent biomolecules that are having very important roles in human physiology: (i) there are a source of energy and main structural components for cell membranes; (ii) and signal molecules, involved in gene expression of lipids, carbohydrates and proteins. Also, there are influenced on cell growth and differentiation. Specific fatty acid especially free non-esterified fatty acids (NEFA) affect on gene expression is influenced by their different structure and metabolism and interact with genome through several mechanisms. Various types of FFA regulate the activities of some transcription factors such as *PPAR*, *LXR*, *HNF4* and *SREBP*. They are having a direct impact on gene transcription by binding to some transcription factor, as well on some specific enzyme mediated pathways (such as

cyclooxygenase, lipoxygenase, protein kinase C, or sphingomyelinase signal transduction pathways). Involving in changes of metabolic processes in membrane lipid composition, fatty acids affect to G-protein receptors or tyrosine kinase-linked receptors signaling. Genes that directly influence on fat storage are *GRB14*, *PPARG*, *HMGAI*, *FTO*, *LPINI*, etc [18–21].

1.3 Fatty Acids and Type 2 Diabetes

Free fatty acids play important roles in skeletal muscles, liver, heart and pancreas. In diabetes, lipid and carbohydrate metabolism are regulated improperly by insulin. It is important to mention that free fatty acids provide energy and they also have role as signaling molecules in many processes including insulin secretion. This mechanism is not clear yet but they compete with glucose for energy source and oxidation [4]. In conditions with increased free fatty acids concentration in body it will be lead to insulin resistance. Also, the mechanisms by which free fatty acids make some changes in glucose transport or some phosphorylation activity are still not known [22–28]. Association of certain genes and fatty acids with glucose level and insulin sensitivity in T2D was presented in Table 2.

1.4 Type 2 Diabetes and Dyslipidemia

T2D patients usually have disturbance in lipid and lipoprotein concentrations and they are developing a dyslipidemia (high total cholesterol (TC), high triglycerides (TG), elevated low-density lipoprotein (LDL), and decreased high-density lipoprotein (HDL). The cause of dyslipidemia may be genetic, environmental, or both. Patients with diabetic dyslipidemia have increased expression of genes such

Table 2 Genes associated with FFA levels and T2D

Gene/nearest gene	Traits	Ref.
GRB14	T2D, decreased, IS, increased HOMA-B	[12, 28]
PPAR γ	T2D	[12, 20, 30]
HMGA1	T2D	[13, 18, 32]
CAPN10	T2D	[16]
LXR	LDL, VLDL	[14, 22, 31]
HNF4	T2D, decreased β -cell function	[14, 23, 28]
SREBP	T2D, FG, FI	[14, 22, 31, 36]
<i>FADS1/2</i>	T2D, FG	[14, 24, 28, 39]
<i>LPIN1</i>	T2D	[39]
ALG14	T2D	[28]
LPGAT1	T2D	[28]
GCK	FG, glycemic control, T2D, HOMA-B	[16, 17, 24]
HNF1AN	T2D, reduced β -cell function	[21, 28]
THADA	T2D	[15, 20, 37]
FTO	BMI, T2D, dyslipidemia	[12, 23]

BMI—body mass index, LDL—low density lipoprotein, VLDL—very low density lipoprotein, FI—fasting insulin

Table 3 Genes associated with dyslipidemia in T2D

Gene/nearest gene	Traits	Ref.
LDLR	Total cholesterol	[14, 20]
PCSK9	FG, total cholesterol	[17, 29]
<i>FADS1/2</i>	TG, HDL, LDL	[14, 24, 36, 39]
MTHFR	FG, reduced β -cell function	[23, 28]
CETP	TG, FI	[12, 14, 36]
GCKR	TG, VLDL, HDL, LDL	[14, 24]
FABP2	T2D, HDL, LDL	[10, 23]
FTO	T2D, dyslipidemia	[12, 23]

TG—triglyceride, HDL—high density lipoprotein

as IL10 and IFNA genes. T2D is characterized with changes in metabolism in lipids as well as with insulin deficiency and dysfunction of β -cells. Dyslipidemia i.e. impaired lipid metabolism is involved in glycemic control and plasma lipid elevation. It is known that diabetic patients with dyslipidemia have higher risk for macro- and microvascular complications and atherosclerosis. Also, T2D patients with dyslipidemia have high mortality level of cardiovascular diseases which are caused by metabolic abnormality and by changes in serum lipids and lipoproteins [29–37]. Genes FADS1 and FADS2 linked with polygenic dyslipidemia which contributes cumulative effects of multiple common variants of certain gene or nearest gene (showed in Table 3).

2 Materials and Methods

In this paper, were presented the summarized results of my research as well as the results of other authors, obtained from previous and newly studies of GWAS analyses. These findings provide the most comprehensive view to data of the genetic contribution to type 2 diabetes with respect to free fatty acids and dyslipidemia association with common and rare variants of certain or nearest gene/s.

New technologies such as metabolomics, proteomics, genomics, a more recently, lipidomics bring a good opportunity to development of new trends and clear directions in

identification and detection of good biological gene candidates involved in fatty acid and lipoprotein metabolisms for their association with dyslipidemia in T2D. “Omics” technologies uses modern analytical methods and techniques in the analysis the large number of metabolites in different biological samples in order to understanding of cellular processes and pathophysiological mechanisms of T2D and, also, the development of new pharmacological target in therapy. Application techniques include: GC-MS, LC-MS/MS, flow injection analysis, NMR, MRS, ESR, etc.

3 Results

The results of recent genetic test and identification studies, as well data from three large scale of genome-wide association studies: DIAbetes Genetic Replication And Meta-analysis (DIAGRAM), the Meta-Analyses of Glucose and Insulin-related traits Consortium (MAGIC), and Meta-analysis using canonical correlation analysis (Meta-CCA) for glycemic and other traits were presented. The characteristics of these studies are summarized in Tables 1, 2 and 3.

4 Discussion

The main objectives of the present work are summarize results of my research and new findings from recent analyses of genome-wide association studies (GWAS) which were helped to us to the identification of common are rare genetic variants of associated with insulin resistance (IR), dyslipidemia, Metabolic syndrome (MetS) and Type 2 diabetes. Many variants of certain genes e.g. PPAR γ , LXR, HNF4, GRB, FTO, SLC27A4 and SREBP, are directly involved in glucose metabolism (Table 1).

However, functional and additional studies are suggested the contribution of the other variants influenced by impaired lipid and lipoproteins metabolism as consequence of elevated free fatty acids (FFA). Some specific gene such as *LPINI*, *ALG14*, *FADS1/2*, *LPGATI*, *GCKR*, *HNF1AN*, and *PDK2L1* variations were identified which affected de novo lipogenesis (synthesis and metabolism of fatty acid as well cellular signaling and metabolic pathways) and were significantly associated with concentrations of C16:0, C18:0, C16:1 and C18:1, as a major saturated and unsaturated fatty acids (Table 2). In addition, it is shown that *FADS1* variant is associated with T2D markers and other triats. Importantly, here was reported for the first-time our findings of association of *FADS1* polymorphism rs174550 with levels of selected (different chain length and degree of saturation) of free fatty acids: lower levels of C14:0 and C18:0, and positive association with C18:1 [39]. Also, in the same study,

FADS1 variant was correlated with markers of dyslipidemia (Table 3). Our previous study with *LPINI* suggested the association of this gene with C14:0, C14:1, and C20:3 [38]. Finally, here was reported for the first time analysis of *FADS1* polymorphism rs174550 and their association with FFAs in the sample of BH population.

5 Conclusions

Metabolome and GWASs analysis has allowed identification and detection of numerous genetic variants that associate with T2D and dyslipidemia. Also, they was shown which polymorphism of certain genes associated with specific FFAs in T2D patients with dyslipidemia. Importantly, previous and future findings from GWAS analysis demonstrated of links between genetic variants associated with lipids and T2D in order to applied in further identification as well for precise diagnose and individual therapy treatment of diseases such as dyslipidemia, MetS and Type 2 diabetes.

References

1. Pankow, J.S., Duncan, B.B., Schmidt, M.I., Ballantyne, C.M., Couper, D.J., Hoogeveen, R.C., Golden, S.H.: Fasting plasma free fatty acids and risk of type 2 diabetes. *Diabetes Care* **27**, 77–82 (2004)
2. Boden, G.: Free fatty acids as target for therapy. *Curr. Opin. Endocrinol. Diabetes* **11**(5), 258–263 (2004)
3. Cnop, M.: Fatty acids and glucolipotoxicity in the pathogenesis of type 2 diabetes. *Biochem. Soc. Trans.* **36**(3), 348–352 (2008)
4. Randle, P.J., Garland, P.B., Hales, C.N., Newsholme, E.A.: The glucose fatty-acid cycle. Its role in insulin sensitivity and the metabolic disturbances of diabetes mellitus. *Lancet*. **1**(7285), 785–789 (1963)
5. Boden, G.: Free fatty acids and insulin secretion in humans. *Curr. Diab. Rep.* **5**, 167–170 (2005)
6. Boden, G.: Obesity, insulin resistance and free fatty acids. *Curr. Opin. Endocrinol. Diabetes Obes.* **18**(2), 139–143 (2011)
7. Ragheb, R., Medhat, A.M.: Mechanisms of fatty acid-induced insulin resistance in muscle and liver. *J. Diabetes Metab.* **2**, 127–132 (2011)
8. Oh, Y.S., Bae, G.D., Baek, D.J., Park, E.-Y., Jun, H.-S.: Fatty acid-induced lipotoxicity in pancreatic beta-cells during development of type 2 diabetes. *Front. Endocrinol.* **9**(384), 1–10 (2018)
9. Wolf, G.: Role of fatty acids in the development of insulin resistance and type 2 diabetes mellitus. *Nutr. Rev.* **66**(10), 597–600 (2008)
10. Lobo, S., Wiczler, B.M., Smith, A.J., Hall, A.M., Bernlohr, D.A.: Fatty acid metabolism in adipocytes: functional analysis of fatty acid transport proteins 1 and 4. *J. Lipid Res.* **48**, 609–620 (2007)
11. So, W.Y., Ng, M.C.Y., Lee, S.C., Sanke, T., Lee, H.K., Chan, J.C. N.: Genetics of type 2 diabetes mellitus. *HKMJ* **6**(1), 69–76 (2000)
12. Brown, A.E., Walker, M.: Genetics of insulin resistance and the metabolic syndrome. *Curr. Cardiol. Rep.* **18**(75), 1–8 (2016)
13. Fall, T., Xie, W., Poon, W., Yaghootkar, H., Mägi, R., Knowles, J. W., Lyssenko, V., et al.: Using genetic variants to assess the

- relationship between circulating lipids and type 2 diabetes. *Diabetes* **64**, 2676–2684 (2015)
14. Georgiadi, A., Kersten, S.: Mechanisms of gene regulation by fatty acids. *Adv. Nutr.* **3**, 127–134 (2012)
 15. Huang, M.C., Chang, W.T., Chang, H.Y., Chung, H.F., Chen, F.P., Huang, Y.F., et al.: FADS gene polymorphisms, fatty acid desaturase activities, and HDL-C in type 2 diabetes. *Int. J. Environ. Res. Public Health* **28**(6), E572 (2017)
 16. Kommoju, U.J., Maruda, J., Kadarkarai Samy, S., Irgam, K., Kotla, J.P., Reddy, B.M.: Association of IRS1, CAPN10, and PPARG gene polymorphisms with type 2 diabetes mellitus in the high-risk population of Hyderabad India. *J. Diabetes* **6**(6), 564–573 (2014)
 17. Moore, K.J., Goldberg, I.J.: The emerging roles of PCSK9: more than a one trick pony. *Arter. Thromb. Vasc. Biol.* **36**(2), 211–212
 18. Kong, H., Liu, Y., Zheng, L., Wang, Q., Zhang, Y.: One of the crucial proteins to influence type 2 diabetes: the high mobility group A1. *Biosci. Biotech. Res. Comm.* **9**(4), 580–586 (2016)
 19. Boucher, J., Kleinridders, A., Kahn, C.R.: Insulin receptor signaling in normal and insulin-resistant states. *Cold Spring Harb. Perspect. Biol.* **6**, 1–23 (2014)
 20. Smith, C.E., Ordovás, J.M.: Fatty acid interactions with genetic polymorphisms for cardiovascular disease. *Curr. Opin. Clin. Nutr. Metab. Care* **13**(2), 139–144 (2010)
 21. Hayakawa, J., Wang, M., Wang, C., Han, R.H., Jiang, Z.-Y., Han, X.: Lipidomic analysis reveals significant lipogenesis and accumulation of lipotoxic components in ob/ob mouse organs. *PLEFA* **136**, 161–169 (2017)
 22. Jump, D.B.: Dietary polyunsaturated fatty acid regulation of hepatic gene transcription. *Scand. J. Nutr.* **46**(2), 59–67 (2002)
 23. Abbas, S., Raza, S.T., Ahmed, F., Ahmad, A., Rizvi, S., Mahdi, F.: Association of genetic polymorphism of PPAR γ -2, ACE, MTHFR, FABP-2 and FTO genes in risk prediction of type 2 diabetes mellitus. *J. Biomed. Sci.* **20**(80), 1–8 (2013)
 24. Rousseaux, J., Duhamel, A., Dumont, J., Dallongeville, J., Molnar, D., Widhalm, K., et al.: The n-3 long-chain PUFAs modulate the impact of the GCKR Pro446Leu polymorphism on triglycerides in adolescents. *J. Lipid Res.* **56**, 1774–1780 (2015)
 25. Billings, L.K., Florez, J.C.: The genetics of type 2 diabetes: what we learned from GWAS? *Ann. N. Y. Acad. Sci.* **1212**, 59–77 (2010)
 26. Prasad, R.B., Groop, L.: Genetics of type 2 diabetes—pitfalls and possibilities. *Genes* **6**, 87–123 (2015)
 27. Goh, G.Y.S., Winter, J.J., Bhansali, F., Doering, K.R.S., Lai, R., Lee, K., et al.: NHR-49/HNF4 integrates regulation of fatty acid metabolism with a protective transcriptional response to oxidative stress and fasting. *Aging Cell* **17**, 1–14 (2018)
 28. Wu, J.H.Y., Lemaitre, R.N., Manichaikul, A., Guan, W., Tanaka, T., Foy, M., et al.: Genome-wide association study identifies novel loci associated with concentrations of four plasma phospholipid fatty acids in the de novo lipogenesis pathway. *Circ. Cardiovasc. Genet.* **6**, 171–183 (2017)
 29. Schofield, J.D., Liu, Y., Rao-Balakrishna, P., Malik, R.A., Soran, H.: Diabetes dyslipidemia. *Diabetes Ther.* **7**, 203–219 (2016)
 30. Taskinen, M.-R., Borén, J.: New insights into the pathophysiology of dyslipidemia in type 2 diabetes. *Atherosclerosis* **239**, 483–495 (2015)
 31. Simopoulos, A.: The FTO gene, browning of adipose tissue and omega-3 fatty acids. *J. Nutrigen. Nutrigenomics* **9**, 123–126 (2016)
 32. Bełtowski, J.: Liver X receptors (LXR) as therapeutic targets in dyslipidemia. *Cardiovasc. Ther.* **6**, 297–316 (2008)
 33. Schoenborn, V., Heid, I.M., Vollmert, C., Lingenhel, A., Adams, T.D., Hopkins, P.N., et al.: The ATGL gene is associated with free fatty acids, triglycerides, and type 2 diabetes. *Diabetes* **55**, 1270–1275 (2006)
 34. Zhu, J., Sun, Q., Zong, G., Si, Y., Liu, C., Qi, Q., et al.: Interaction between a common variant in FADS1 and erythrocyte polyunsaturated fatty acids on lipid profile in Chinese Hans. *J. Lipid Res.* **54**, 1477–1483 (2013)
 35. Bardini, G., Rotella, C.M., Giannini, S.: Dyslipidemia and diabetes: reciprocal impact of impaired lipid metabolism and beta-cell dysfunction on micro- and macrovascular complications. *Rev. Diab. Stud.* **9**(2–3), 82–93 (2012)
 36. Chen, Y.-C., Xu, C., Zhang, J.-G., Zeng, C.-P., Wang, X.-F., Zhou, R., et al.: Multivariate analysis of genomic data to identify potential pleiotropic genes for type 2 diabetes, obesity and dyslipidemia using Meta-CCA and gene-based approach. *PLoS ONE* **13**(8), 1–16 (2018)
 37. Scott, R.A., Scott, L.J., Mägi, R., Marullo, L., Gaulton, K.J., Kaakinen, M., et al.: An expanded genome-wide association study of type 2 diabetes in Europeans. *Diabetes* **66**, 2888–2902 (2017)
 38. Bego, T., Mandal, S., Dujic, T., Mlina, B., Semiz, S., Malenica, M., et al.: Association of LPIN1 gene variants with fatty acids in Bosnian population with metabolic syndrome. *Biochim. Clin. (Special Supplement)* **37** (2013)
 39. Lokvancic, H., Mandal, S., Adilovic, M., Sterner, M., Gremesperger, G., Ahqvist, E., et al.: Association of FADS1 genetic variation with free fatty acid levels and type 2 diabetes-related traits. *Diabetologia* **61**(Suppl:1), 559 (2018)

Part XII
Genetic Engineering

Correlation of Leukemia Genes Overexpression and Point Mutations in Different Tissues

Fatima Mrkulić, Lejla Gurbeta, Enisa Omanović-Miklićanin, Tamer Bego, Berina Hasanefendić, and Almir Badnjević

Abstract

Chromosomal aberrations are a hallmark of leukemia. The prognostication of acute lymphocytic leukemia (ALL), chronic lymphocytic leukemia (CLL), acute myeloid leukemia (AML), and chronic myeloid leukemia (CML) has vastly expanded with chromosomal analyses over the years. Current treatment strategy has been refined by discovery of genes and its mutations which are involved in disease causation and progression. These genes are named biomarkers or prognostic markers and they give information about favorable and unfavorable prognosis of the patients. This paper aims to summarize the most common mutated genes in all four types of leukemia and to find correlation of their expression and point mutations in certain tissues, using COSMIC database. Highest number of point mutations in leukemia genes was found in hematopoietic and lymphoid tissues and it was three times higher than in other tissues which could be explained by relatedness of genes with specific leukemia. Mostly overexpressed gene was CEBPA whereas NOTCH1 gene had the highest number of point mutations. Further research about new prognostic markers

is crucial because they can significantly improve development of new therapeutic targets thereby increasing patient outcome and quality of life.

Keywords

Leukemia • Gene • Biomarker • Gene expression • Prognostication

1 Introduction

Leukemia is a type of blood cancer occurring when the bone marrow makes abnormal white blood cells (WBCs). WBCs play a key role in the immunity by protecting our body from bacteria, viruses and fungi as well as from abnormal cells and foreign substances [1–3]. Leukemia is called acute or chronic based upon how fast it gets severe. Acute leukemia gets worse very quickly while chronic leukemia develops very slowly. The four mayor types of leukemia are acute lymphocytic leukemia (ALL), chronic lymphocytic leukemia (CLL), acute myeloid leukemia (AML), and chronic myeloid leukemia (CML). Leukemia commonly occurs in men than in women. Its mortality rate is usually higher in whites than in people of other racial and ethnic groups [4, 5]. First understanding of leukemia genetics was brought by cytogenetic analyses [4].

1.1 Acute Lymphocytic Leukemia

Acute lymphocytic leukemia is the most common malignancy in children [6–8]. However, ALL also occurs in older adults (20%) [7]. Males are more prone to the disease than females with a sex ratio 1.4:1, respectively.

Chromosomal aberrations in ALL include chromosomal translocations resulting in gene fusions, copy number alterations (CNA) and point mutations. Good-risk or favorable marker for survival of the patients (children and adults) is

F. Mrkulić · L. Gurbeta (✉) · E. Omanović-Miklićanin · A. Badnjević
Department of Genetics and Bioengineering, International Burch University, Sarajevo, Bosnia and Herzegovina
e-mail: gurbetalejla@gmail.com

L. Gurbeta · A. Badnjević
Verlab Ltd., Sarajevo, Bosnia and Herzegovina

E. Omanović-Miklićanin
Faculty of Agriculture and Food Sciences, University of Sarajevo, Sarajevo, Bosnia and Herzegovina

T. Bego
Faculty of Pharmacy, University of Sarajevo, Sarajevo, Bosnia and Herzegovina

B. Hasanefendić
University Clinical Center Sarajevo, Sarajevo, Bosnia and Herzegovina

chromosomal translocations t(12;21)(p13;q22) resulting in gene fusion ETV6-RUNX [7, 9]. High-risk or unfavorable markers are chromosomal translocations: KMT2A (MLL) with adjacent genes, BCR-ABL1 and TCF3-PBX1. Interestingly, early studies of children with TCF3-PBX1 reported poor prognosis whereas recent studies have reported improved outcome [10–14].

1.2 Chronic Lymphocytic Leukemia

Chronic lymphocytic leukemia is the most common adult leukemia in the western countries [15–17]. Risk factors include sex and age since incidence is two-times higher in men than in women and disease occurrence increases with age (range: 70–72 years) [18, 19].

Genetic aberrations in CLL include chromosomal alterations (deletions and trisomies) and mutations as well as alterations in the expression of miRNA and epigenetic modifications [20, 21]. Overall NOTCH1, SF3B1 and BIRC3 are detected in 15.9, 12.2 and 8.6% of all CLL cases, respectively [22].

1.3 Acute Myeloid Leukemia

Acute myeloid leukemia is a blood cancer which affects myeloid lineage of hematopoiesis [22]. It occurs predominantly in older adults (>65 years old) but children AML cases have also been reported [23, 24].

Somatic mutations such as point mutation accounted for 73% whereas translocations were observed in 55% of patients with AML [25, 26]. Molecular markers in AML includes NPM1, CEBPA and FLT3 gene whose app. frequency in denovo AML is 35, 7 and 20–25%, respectively [25]. CEBPA is favorable prognostic marker as well as NPM1 in contrast with FLT3 gene whose deleterious effect resulted in decreased overall survival [23, 26–28].

1.4 Chronic Myeloid Leukemia

Chronic myeloid leukemia is a typical cytogenetic disease with an incidence of 1–2 cases per 100,000 adults. In children CML is a very rare disease. Median age at diagnosis is usually 57–60 years with a male/female ratio of 1.2–1.7 [29].

Pathogenesis of CML is observed by the fusion of the Abelson murine leukemia (ABL) gene on chromosome 9 and the breakpoint cluster region (BCR) gene on chromosome 22. This fusion leads to the expression of an oncoprotein, BCR-ABL also called Philadelphia chromosome [30]. CML is the first leukemia in which targeted approach worked successfully with the development of tyrosine kinase inhibitors (TKIs).

2 Methods

The purpose of this study was to evaluate the relationship between leukemia gene overexpression and point mutations in the tissues. The research was performed using catalogue of somatic mutations in cancer (COSMIC database) from which all expressional and mutational data were collected [29]. Most common mutated genes in all four types of leukemia were chosen to conduct an analysis of how many samples were overexpressed in certain tissues and how many samples were mutated (point mutation) in certain tissues (Table 1). Also, to examine the connection between number of overexpressed and mutated samples of a gene in certain tissues.

Tissue overexpression and point mutation data was collected from twenty following tissues: adrenal gland, breast, central nervous system, cervix, endometrium, hematopoietic and lymphoid, kidney, large intestine, liver, lung, oesophagus, ovary, pancreas, prostate, skin, soft tissue, stomach, thyroid, upper aerodigestive tract and urinary tract. They were chosen based on the criteria that leukemia genes were mostly overexpressed in them.

3 Results

3.1 Overexpression Pattern in Tissues

Highest overall overexpression of all abovementioned and chosen leukemia genes was observed in breast tissue followed by endometrium, liver and upper aerodigestive tract (Fig. 1). Lowest overall overexpression of leukemia genes was in adrenal gland (Fig. 1). Mostly overexpressed gene was CEBPA which is mutated in acute myeloid leukemia

Table 1 Type of leukemia and genes of interest used for analysis of tissue overexpression and point mutations

Leukemia	Gene
ALL	PBX1
	ETV6
	TCF3
CLL	NOTCH1
	SF3B1
	BIRC3
AML	NPM1
	CEBPA
	FLT3
CML	BCR
	ABL1

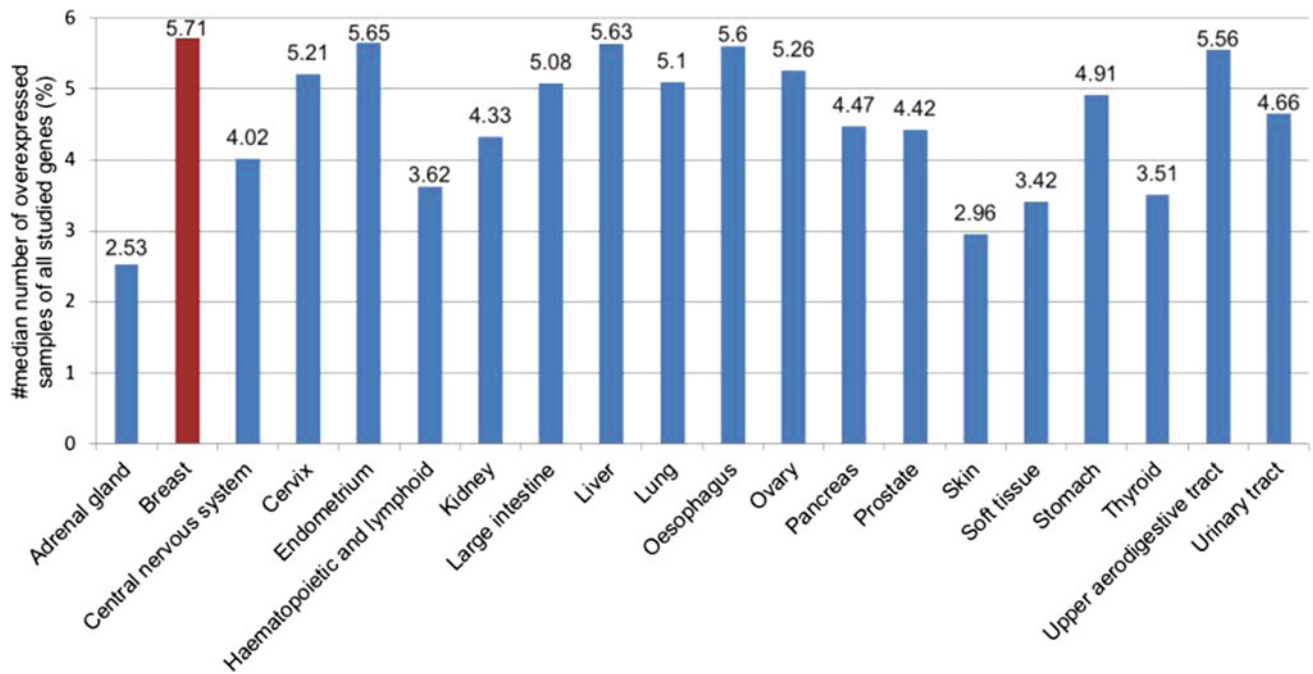


Fig. 1 Median number of overexpressed samples of all studied genes in twenty chosen tissues

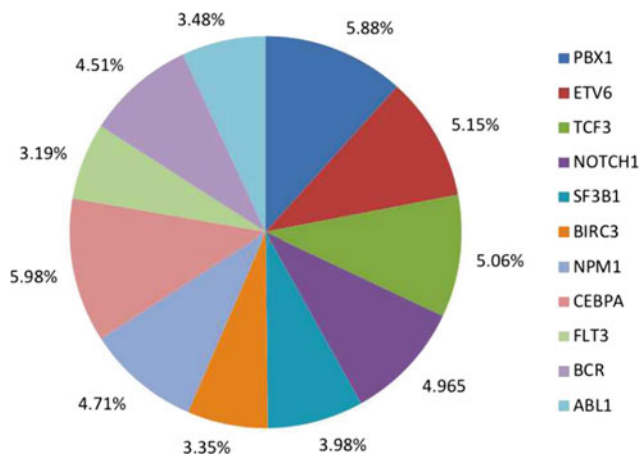


Fig. 2 Median number of overexpressed samples in leukemia genes

(AML) (Fig. 2). Least overexpressed gene was FLT3 which also belongs under AML category (Fig. 2).

3.2 Point Mutation Pattern in Tissues

The highest number of point mutations among all studied leukemia genes was observed in haematopoietic and lymphoid tissues, whereas point mutations were not seen in adrenal gland tissue (Fig. 3). Mostly mutated gene was NOTCH1 which belongs under the chronic lymphocytic leukemia (CLL) category (Fig. 4). On the other hand, PBX1 gene was not mutated at all (Fig. 4).

ALL, CLL and CML genes have been noticed to have a higher number of point mutations specifically substitution missense mutations whereas insertion frameshift/inframe mutations in these genes were less present or not present at all (Fig. 5). On the contrary, AML genes have a high number of insertion frameshift/inframe mutations and very low number of substitution missense mutations (Fig. 5).

Identification of disrupted genes and their pathways provides new targets which could facilitate treatment design. Genetic alterations drive the progression of normal cells into cancerous cells leading to metastatic disease. Acute lymphocytic leukemia (ALL), acute myeloid leukemia (AML), chronic lymphocytic leukemia (CLL) and chronic myeloid leukemia (CML) metastasize mostly to lymphatic system [31, 32]. Therefore, the highest number of point mutations observed in haematopoietic and lymphoid tissues could be explained by migratory patterns of leukemia [31].

Since the highest overexpression in this study was recorded to be in breast tissue and leukemia gene point mutations in haematopoietic and lymphoid tissues in three times higher amount than in other tissues, overexpression and point mutations does not relate to each other. Moreover, some of these genes induce breast cancer development either by fusion with breast cancer genes or on their own which could be explanation for their high expression pattern in breast tissue [33].

Out of all genes CEBPA gene was seen to be the mostly expressed in all tissues. The reason for this may be due to its function which involves regulation of differentiation of

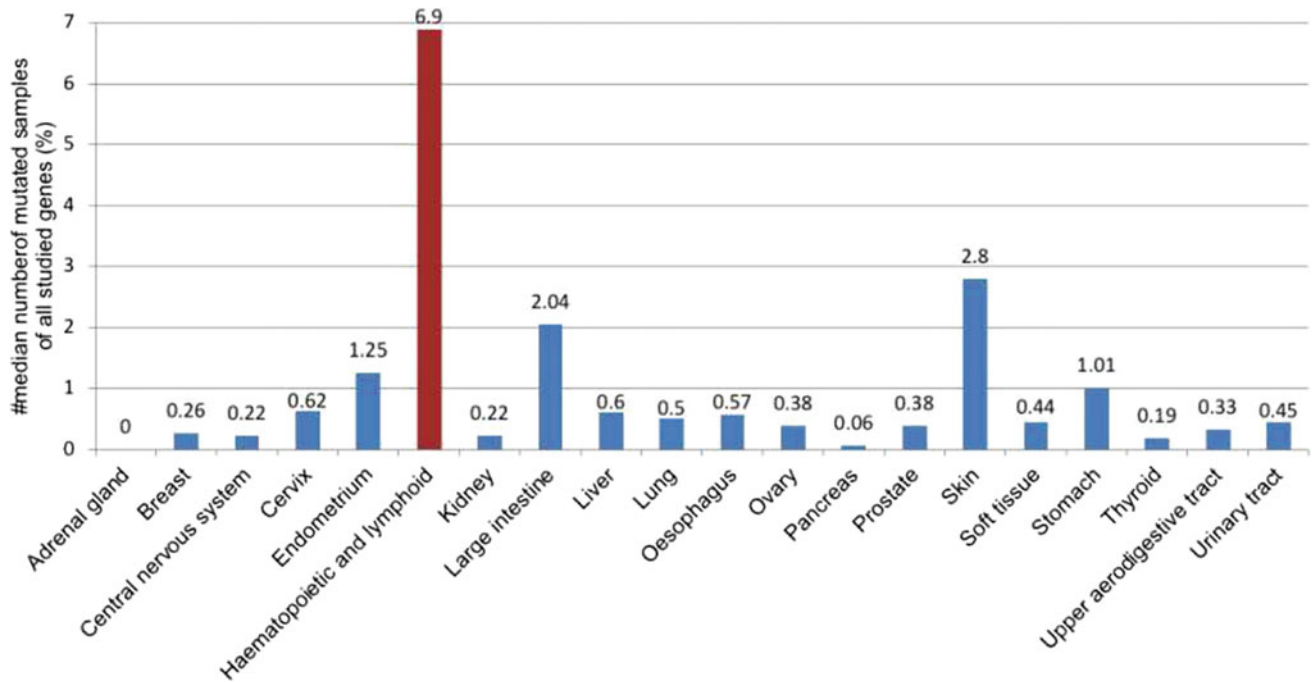


Fig. 3 Median number of mutated samples (point mutations) of all studied genes in twenty chosen tissues

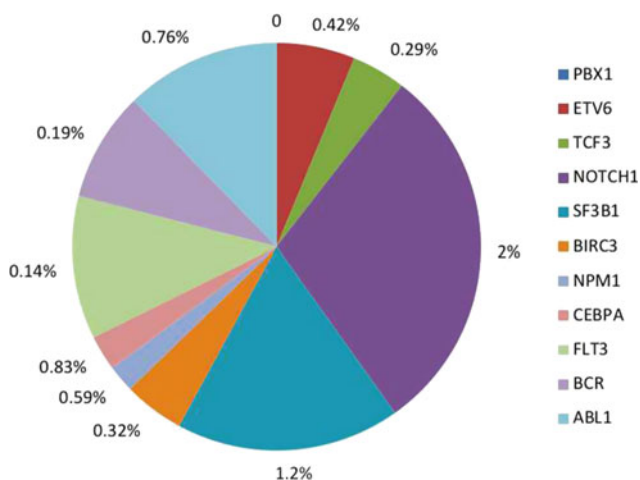


Fig. 4 Median number of mutated samples (point mutations) in leukemia genes

blood cells during hematopoiesis because blood circulates all over the body and covers all tissues [34].

Highest incidence of point mutations was in NOTCH1 gene which is responsible for cell fate decision therefore playing a key role in cell development. Many papers have recorded point mutations in NOTCH1 gene since it coexists among all leukemia types [35–47].

Insertion frameshift/inframe mutations are considered to be the most deleterious of all types of point mutations. Incidence of these mutations has been recorded to be the

highest in NPM1, CEBPA and FLT3 genes (AML) [48, 49]. Overall survival of AML patients is the shortest of all other leukemia types which can be correlated with the type of point mutation and its effect on patient survival.

Interestingly, of these three genes patient with CEBPA gene mutations has the highest survival in AML which correlates with presented result that CEBPA has the lowest percentage of insertion frameshift/inframe mutation [49–53]. Poor prognostic marker of AML is FLT3 gene where patients with the mutations in FLT3 gene have a short survival rate [54–57]. This as well correlates with presented result in which FLT3 gene has the highest number of insertion frameshift/inframe mutations.

4 Conclusion

Our understanding of leukemia has undergone a dramatic change by discovery of biomarkers. Our knowledge and perception of leukemia is constantly evolving with the emergence of new molecular techniques. Genetic alterations in ALL, CLL, AML and CML such as point mutations give information about patient prognosis whether favorable (longer survival) or unfavorable (shorter survival) one. Ongoing preclinical and clinical studies are very important since they can unravel newer prognostic markers based on which newer therapeutic targets could be developed and patient outcome and quality of life increased.

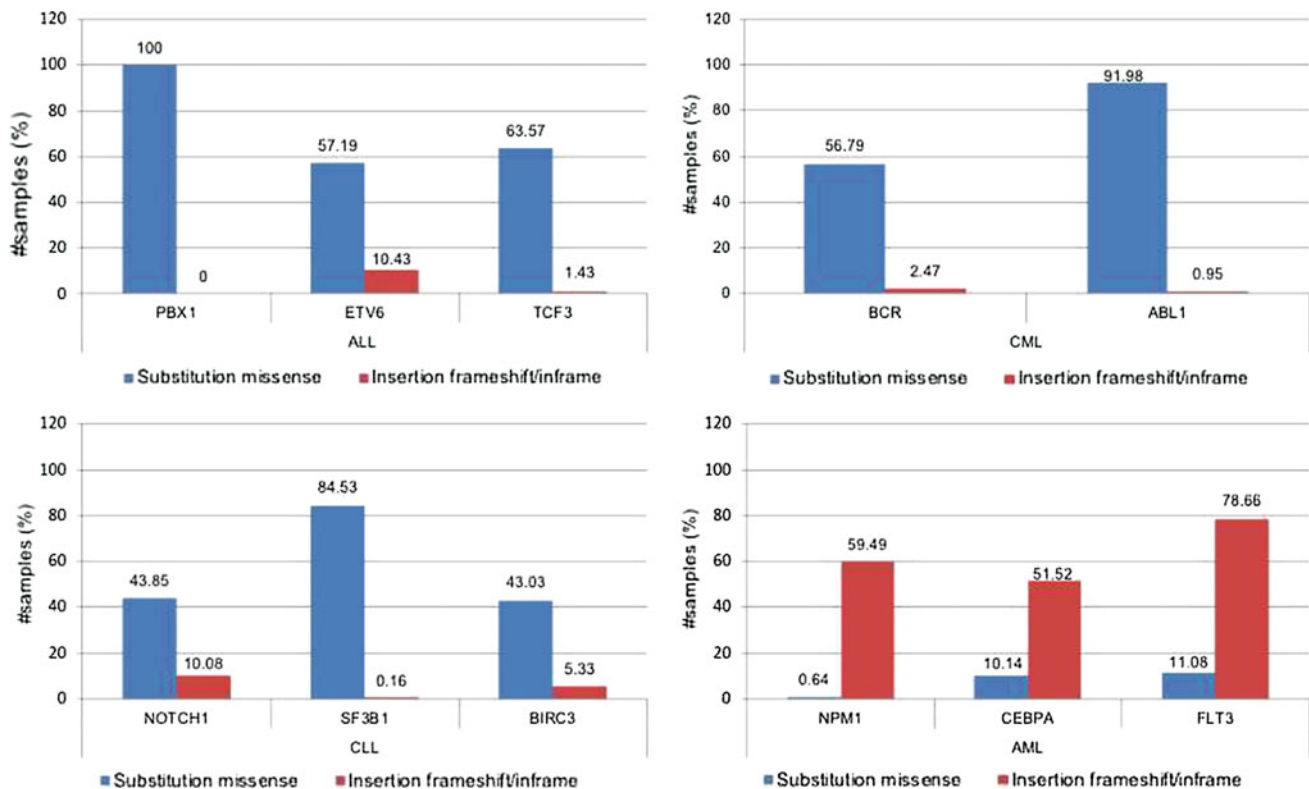


Fig. 5 Correlation of two types of point mutations (substitution missense and insertion frameshift/inframe) among leukemia genes

References

- Weinberg, R.: *The Biology of Cancer*, 1st edn. Garland Science, Taylor & Francis Group, LLC, New York City (2007)
- Gilliland, D.G., Jordan, C.T., Felix, C.A.: The molecular basis of leukemia. *Hematol. Am. Soc. Hematol. Educ. Program* **2004**(1), 80–97 (2004). <https://doi.org/10.1182/asheducation-2004.1.80>
- Badnjevic, A., Beganovic E, Music, O.: Facts about solution based and cartridge based devices for blood gas analyses. In: *IEEE 18th International Conference on System, Signals and Image Processing*, pp. 1–5, Sarajevo, Bosnia and Herzegovina, 16–18 June 2011
- Jemal, A., Siegel, R., Ward, E., et al.: Cancer statistics, 2008. *CA Cancer J. Clin.* **58**, 71–96 (2008). <https://doi.org/10.3322/ca.2007.0010>
- Badnjevic, A., Gurbeta, L., Boskovic, D., Dzemic, Z.: Measurement in medicine—past, present, future. *Folia Med. Fac. Med. Univ. Sarajevisis J.* **50**(1), 43–46 (2015)
- Janczar, S., Janczar, K., Pastorczak, A., et al.: The role of histone protein modifications and mutations in histone modifiers in pediatric B-cell progenitor acute lymphoblastic leukemia. *Cancers* **9**(1), 2 (2017). <https://doi.org/10.3390/cancers9010002>
- Moorman, A.V.: New and emerging prognostic and predictive genetic biomarkers in B-cell precursor acute lymphoblastic leukemia. *Haematologica* **101**(4), 407–416 (2016). <https://doi.org/10.3324/haematol.2015.141101>
- Yokota, T., Kanakura, Y.: Genetic abnormalities associated with acute lymphoblastic leukemia. *Cancer Sci.* **107**(6), 721–725 (2016). <https://doi.org/10.1111/cas.12927>
- Roberts, K.G., Mullighan, C.G.: Genomics in acute lymphoblastic leukaemia: insights and treatment implications. *Nat. Rev. Clin. Oncol.* **12**(6), 344–357 (2015). <https://doi.org/10.1038/nrclinonc.2015.38>
- Raimondi, S.C., Behm, F.G., Roberson, P.K., et al.: Cytogenetics of pre-B-cell acute lymphoblastic leukemia with emphasis on prognostic implications of the t(1;19). *J. Clin. Oncol.* **8**(8), 1380–1388 (1990). <https://doi.org/10.1200/JCO.1990.8.8.1380>
- Kager, L., Lion, T., Attarbaschi, A., et al.: Incidence and outcome of *TCF3-PBX1*-positive acute lymphoblastic leukemia in Austrian children. *Haematologica* **92**(11), 1561–1564 (2007). <https://doi.org/10.3324/haematol.11239>
- Moorman, A.V., Ensor, H.M., Richards, S.M., et al.: Prognostic effect of chromosomal abnormalities in childhood B-cell precursor acute lymphoblastic leukaemia: results from the UK medical research council ALL97/99 randomised trial. *Lancet Oncol.* **11**(5), 429–438 (2010). [https://doi.org/10.1016/S1470-2045\(10\)70066-8](https://doi.org/10.1016/S1470-2045(10)70066-8)
- Garg, R., Kantarjian, H., Thomas, D., et al.: Adults with acute lymphoblastic leukemia and translocation (1;19) abnormality have a favorable outcome with hyperfractionated cyclophosphamide, vincristine, doxorubicin, and dexamethasone alternating with methotrexate and high-dose cytarabine chemotherapy. *Cancer* **115**(10), 2147–2154 (2009). <https://doi.org/10.1002/cncr.24266>
- Beldjord, K., Chevret, S., Asnafi, V., et al.: Oncogenetics and minimal residual disease are independent outcome predictors in adult patients with acute lymphoblastic leukemia. *Blood* **123**(24), 3739–3749 (2014). <https://doi.org/10.1182/blood-2014-01-547695>
- Kipps, T.J., Stevenson, F.K., Wu, C.J., et al.: Chronic lymphocytic leukaemia. *Nat. Rev. Dis. Primers* **3**, 17008 (2017). <https://doi.org/10.1038/nrdp.2017.8>
- Rai, K.R., Jain, P.: Chronic lymphocytic leukemia (CLL)—then and now. *Am. J. Hematol.* **91**(3), 330–340 (2016). <https://doi.org/10.1002/ajh.24282>

17. Jeyakumar, D., O'Brien, S.: The next generation of targeted molecules for the treatment of chronic lymphocytic leukemia. *Oncol.* (Williston Park) **30**(11), 1008–1015
18. Cerhan, J.R., Slager, S.L.: Familial predisposition and genetic risk factors for lymphoma. *Blood* **126**(20), 2265–2273 (2015). <https://doi.org/10.1182/blood-2015-04-537498>
19. Lichtenstein, P., Holm, N.V., Verkasalo, P.K., et al.: Environmental and heritable factors in the causation of cancer—analyses of cohorts of twins from Sweden, Denmark, and Finland. *N. Engl. J. Med.* **343**(2), 78–85 (2000). <https://doi.org/10.1056/NEJM200007133430201>
20. Quesada, V., Conde, L., Villamor, N., et al.: Exome sequencing identifies recurrent mutations of the splicing factor SF3B1 gene in chronic lymphocytic leukemia. *Nat. Genet.* **44**(1), 47–52 (2011). <https://doi.org/10.1038/ng.1032>
21. Te Raa, G.D., Derks, I.A., Navrkalova, V., et al.: The impact of SF3B1 mutations in CLL on the DNA-damage response. *Leukemia* **29**(5), 1133–1142 (2015). <https://doi.org/10.1038/leu.2014.318>
22. Chiaretti, S., Marinelli, M., Del Giudice, I., et al.: NOTCH1, SF3B1, BIRC3 and TP53 mutations in patients with chronic lymphocytic leukemia undergoing first-line treatment: correlation with biological parameters and response to treatment. *Leuk. Lymphoma* **55**(12), 2785–2792 (2014). <https://doi.org/10.3109/10428194.2014.898760>
23. Ferrara, F., Schiffer, C.A.: Acute myeloid leukaemia in adults. *Lancet* **381**(9865), 484–495 (2016). [https://doi.org/10.1016/S0140-6736\(16\)61727-9](https://doi.org/10.1016/S0140-6736(16)61727-9)
24. Sanz, M.A., Iacoboni, G., Montesinos, P., et al.: Emerging strategies for the treatment of older patients with acute myeloid leukemia. *Ann. Hematol.* **95**(10), 1583–1593 (2016). <https://doi.org/10.1007/s00277-016-2666-2>
25. Chaudry, S.F., Chevassut, T.J.T.: Epigenetic guardian: a review of the DNA methyltransferase DNMT3A in acute myeloid leukaemia and clonal haematopoiesis. *Biomed. Res. Int.* **2017**, 5473197 (2017). <https://doi.org/10.1155/2017/5473197>
26. Papaemmanuil, E., Gerstung, M., Bullinger, L., et al.: Genomic classification and prognosis in acute myeloid leukemia. *N. Engl. J. Med.* **374**, 2209–2221 (2016). <https://doi.org/10.1056/NEJMoa1516192>
27. Matsuo, H., Kajihara, M., Tomizawa, D., et al.: Prognostic implications of *CEBPA* mutations in pediatric acute myeloid leukemia: a report from the Japanese pediatric leukemia/lymphoma study group. *Blood Cancer J.* **4**(7), e226 (2014). <https://doi.org/10.1038/bcj.2014.47>
28. Metzeler, K.H., Herold, T., Rothenberg-Thurley, M., et al.: Spectrum and prognostic relevance of driver gene mutations in acute myeloid leukemia. *Blood* **128**(5), 686–698 (2016). <https://doi.org/10.1182/blood-2016-01-693879>
29. Höglund, M., Sandin, F., Simonsson, B.: Epidemiology of chronic myeloid leukaemia: an update. *Ann. Hematol.* **94**(Suppl 2), S241–S247 (2015). <https://doi.org/10.1007/s00277-015-2314-2>
30. Jabbour, E., Kantarjian, H.: Chronic myeloid leukemia: 2014 update on diagnosis, monitoring, and management. *Am. J. Hematol.* **89**(5), 547–556 (2014). <https://doi.org/10.1002/ajh.23691>
31. Forbes, S.A., Beare, D., Boutselakis, H., et al.: COSMIC: somatic cancer genetics at high-resolution. *Nucleic Acids Res.* **45**(D1), D777–D783 (2017). <https://doi.org/10.1093/nar/gkw1121>
32. Badnjevic, A., Gurbeta, L., Boskovic, D., Dzemic, Z.: Medical devices in legal metrology. In: *IEEE 4th Mediterranean Conference on Embedded Computing (MECO)*, pp. 365–367, Budva, Monténégro, 14–18 June 2015
33. Trendowski, M.: The inherent metastasis of leukaemia and its exploitation by sonodynamic therapy. *Crit. Rev. Oncol. Hematol.* **94**(2), 149–163 (2015). <https://doi.org/10.1016/j.critrevonc.2014.12.013>
34. Tian, Z., Hwang, T., Kuang, R.: A hypergraph-based learning algorithm for classifying gene expression and array CGH data with prior knowledge. *Bioinformatics* **25**(21), 2831–2838 (2009). <https://doi.org/10.1093/bioinformatics/btp467>
35. Chapiro, E., Russell, L., Radford-Weiss, I., et al.: Overexpression of *CEBPA* resulting from the translocation t(14;19)(q32;q13) of human precursor B acute lymphoblastic leukemia. *Blood* **108**(10), 3560–3563 (2006). <https://doi.org/10.1182/blood-2006-03-010835>
36. Gianfelici, V.: Activation of the NOTCH1 pathway in chronic lymphocytic leukemia. *Haematologica* **97**(3), 328–330 (2012). <https://doi.org/10.3324/haematol.2012.061721>
37. Weng, A.P., Ferrando, A.A., Lee, W., et al.: Activating mutations of NOTCH1 in human T cell acute lymphoblastic leukemia. *Science* **306**(5694), 269–271 (2004). <https://doi.org/10.1126/science.1102160>
38. Boskovic, D., Badnjevic, A.: Opportunities and challenges in biomedical engineering education for growing economies. In: *IEEE 4th Mediterranean Conference on Embedded Computing (MECO)*, pp. 407–410, Budva, Monténégro, 14–18 June 2015
39. Palomer, T., McKenna, K., O'Neil, J., et al.: Activating mutations in NOTCH1 in acute myeloid leukemia and lineage switch leukemias. *Leukemia* **20**(11), 1963–1966 (2006). <https://doi.org/10.1038/sj.leu.2404409>
40. Badnjevic, A., Gurbeta, L.: Development and perspectives of biomedical engineering in south east european countries. In: *IEEE 39th International Convention on Information and Communication Technology, Electronics and Microelectronics (MIPRO)*, Opatija, Croatia, 30 May–03 June 2016
41. Aljedai, A., Buckle, A.M., Hiwarkar, P., Syed, F.: Potential role of notch signalling in CD34+ chronic myeloid leukaemia cells: cross-talk between notch and BCR-ABL. *PLoS ONE* **10**(4), e0123016 (2015). <https://doi.org/10.1371/journal.pone.0123016>
42. Wouters, B.J., Jordà, M.A., Keeshan, K., et al.: Distinct gene expression profiles of acute myeloid/T-lymphoid leukemia with silenced *CEBPA* and mutations in NOTCH1. *Blood* **110**(10), 3706–3714 (2007). <https://doi.org/10.1182/blood-2007-02-073486>
43. Zhu, Y.M., Zhao, W.L., Fu, J.F., Shi, J.Y.: NOTCH1 mutations in T-cell acute lymphoblastic leukemia: prognostic significance and implication in multifactorial leukemogenesis. *Blood* **12**(10), 3043–3049 (2006). <https://doi.org/10.1158/1078-0432.CCR-05-2832>
44. Mansour, M.R., Linch, D.C., Feroni, L., Goldstone, A.H., Gale, R. E.: High incidence of Notch-1 mutations in adult patients with T-cell acute lymphoblastic leukemia. *Leukemia* **20**, 537–593 (2006). <https://doi.org/10.1038/sj.leu.2404101>
45. Badnjevic, A., Cifrek, M., Gurbeta, L., Feric E.: Classification of chronic obstructive pulmonary diseases based on neuro-fuzzy software. In: *Chronic Obstructive Pulmonary Disease (COPD): Clinical Symptoms, Emerging Treatment Strategies and Impact on Quality of Life*. Nova Science Publisher (2016). ISBN: 978-1-63484-500-7
46. Abdel-ilah, L., Veljović, E., Gurbeta, L., Badnjević, A.: Applications of QSAR study in drug design. *Int. J. Eng. Res. Technol. (IJERT)* **6**(06) (2017)
47. Kozic, A., Gurbeta, L., Omanovic-Miklicanin, E.: The influence of erythropoietin (EPO) on cancer cells and its role in the cancer treatment. *Int. J. Eng. Res. Technol. (IJERT)* **6**(07) (2017)
48. Leroy, H., Roumier, C., Huyghe, P., et al.: *CEBPA* point mutations in hematological malignancies. *Leukemia* **19**(3), 329–334 (2005). <https://doi.org/10.1038/sj.leu.2403614>
49. Heath, E.M., Chan, S.M., Minden, M.D., Murphy, T., Shlush, L.I., Schimmer, A.D.: Biological and clinical consequences of NPM1 mutations in AML. *Leukemia* **31**(4), 798–807 (2017). <https://doi.org/10.1038/leu.2017.30>

50. Wouters, B.J., Löwenberg, B., Erpelinck-Verschueren, C.A.J., et al.: Double CEBPA mutations, but not single CEBPA mutations, define a subgroup of acute myeloid leukemia with a distinctive gene expression profile that is uniquely associated with a favorable outcome. *Blood* **113**(13), 3088–3091 (2009). <https://doi.org/10.1182/blood-2008-09-179895>
51. Badnjevic, A., Beganovic, E., Gvozdenovic, V., Sehic, G.: Automated closed loop controller of inspired oxygen system for improved mechanical ventilation in newborns. In: IEEE 34th International Convention on Information and Communication Technology, Electronics and Microelectronics (MIPRO), pp. 145–149, Opatija, Croatia, 23–27 May 2011
52. Veljovic, E., Spirtovic-Halilovic, S., Muratovic, S., Osmanovic, A., Badnjevic, A., et al.: Artificial neural network and docking study in design and synthesis of xanthenes as antimicrobial agents. In: CMBEBIH 2017. IFMBE Proceedings, vol. 62, pp. 617–626. Springer, Singapore (2017). https://doi.org/10.1007/978-981-10-4166-2_93
53. Fasan, A., Haferlach, C., Alpermann, T., et al.: The role of different genetic subtypes of CEBPA mutated AML. *Leukemia* **28** (4), 794–803 (2014). <https://doi.org/10.1038/leu.2013.273>
54. Tiesmeier, J., Müller-Tidow, C., Westermann, A., Czwalińska, A., Hoffmann, M.: Evolution of FLT3-ITD and D835 activating point mutations in relapsing acute myeloid leukemia and response to salvage therapy. *Leukemia Res.* **28**(10), 1069–1074 (2004). <https://doi.org/10.1016/j.leukres.2004.02.009>
55. Catic, A., Gurbeta, L., Kurtovic-Kozaric, A., Mehmedbasic, S., Badnjevic, A.: Application of neural networks for classification of Patau, Edwards, Down, Turner and Klinefelter syndrome based on first trimester maternal serum screening data, ultrasonographic findings and patient demographics. *BMC Med. Genomics*, Jan 2018
56. Badnjevic-Cengic, A., Kovacevic, P., Dragic, S., Momcicevic, D., Badnjevic, A., Gurbeta, L., Hasanefendic, B.: Serum nitric oxide levels in patients with acute myocardial infarction with ST elevation (STEMI). *Respir. J.* **5**(1–2) (2015)
57. Andersson, A., Johansson, B., Lassen, C., Mitelman, F., Billstrom, R.: Clinical impact of internal tandem duplications and activating point mutations in FLT3 in acute myeloid leukemia in elderly patients. *Eur. J. Haematol.* **72**(5), 307–313 (2004). <https://doi.org/10.1111/j.1600-0609.2004.00225.x>

Craniometric Analysis of the Foramen Magnum for Gender Determination in Bosnian Human Skulls

Zurifa Ajanović and Aida Sarač-Hadžihalilović

Abstract

The human skull shows certain morphological differences between male and female that can be used in the sex determination of skeletal remains. One of these differences is in the size and shape of the foramen magnum, which is important for sex determination especially in burned cadavers because the area around the foramen magnum is covered by a greater amount of soft tissue which protects bones. The aims of this study were to determine the prediction of sex determination based on craniometric analysis of foramen magnum of the human skulls. *Material and method:* The research was conducted on 100 human degenerated and macerated adult skulls of known sex and known age (50 male skulls, 50 female skulls) selected by randomization of 211 human skulls (139 male and 72 female skulls) belonging to the Osteological Collection of the Department of Anatomy, Medical Faculty, University of Sarajevo. For analysis of the size of foramen magnum we used the craniometric method where we measured two linear diameters of foramen magnum and where we calculated the area of foramen magnum using two formulas published by Radinsky and Teixeira which are based on the sagittal and transverse diameter. *Results:* ROC curve revealed that the predictability of sagittal diameter of foramen magnum in sex determination of skull was 73%, the predictability of transverse diameter of foramen magnum in sex determination of skull was 65.3%, and the predictability of area of foramen magnum in sex determination of skull was 70.9% when this area is calculated using Radinsky formula, and 71.2% when this area is calculated using Teixeira formula. *Conclusion:* All diameters of the foramen magnum and area of the foramen magnum

showed sexual dimorphism. Sagittal diameter showed the highest effect for gender determination (73%), followed by area (FM \approx 71%) and the least effect was shown by transverse diameter with 65.3% accuracy.

Keywords

Gender determination • Foramen magnum • Craniometric analysis • Skull

1 Introduction

The human skull shows certain morphological differences between male and female that can be used in the sex determination of skeletal remains. One of these differences is in the size and shape of the foramen magnum, which is important for sex determination especially in burned skulls because the area around the foramen magnum is covered by a greater amount of soft tissue which protects bones [1].

Foramen magnum is a greater opening on the occipital bone through which the cavity of the skull communicates with the vertebral canal and through which the intracranial part of the central nervous system (brain) continues to the extracranial part (spinal cord) [2].

The shape and size of foramen magnum are distinguished between male and female skulls and can be used to determine the sex of skeletal remains. The foramen magnum region is protected by soft tissue and foramen magnum is most commonly preserved in post-mortem residues [3].

Differences between male and female include characteristics that are related to reproduction role, to endocrine system, their physical and physiological characteristics, effect related to behavior, all those can vary within a single population and between different populations [2].

Authors around the world studied differences in the size and shape of the foramen magnum because there is a difference between populations.

Z. Ajanović (✉) · A. Sarač-Hadžihalilović
Department of Anatomy, Medical Faculty, University of Sarajevo,
Čekaluša 90, Sarajevo, Bosnia and Herzegovina
e-mail: zurifa.ajanovic@gmail.com

A. Sarač-Hadžihalilović
e-mail: aida024@bih.net.ba

In Brazilian population sex determination using foramen magnum was studied by Suazo et al. [4] on a sample of 211 human skulls, and Manoel et al. [5] on a sample of 215 human skulls (139 males and 76 females).

In Indian population, Jain et al. [6] in their study which included 68 human skulls (38 male and 30 female) concluded that all linear diameters of foramen magnum were larger in male skulls than in female skulls.

In same population, Kanchan et al. [7] conducted a study on 118 human skulls (69 male and 49 female) where they measured sagittal and transverse diameter of foramen magnum and calculated the surface of the foramen magnum. They concluded that the length (sagittal diameter), breadth (transverse diameter) and area of foramen magnum were found to be larger in males than in females.

In north India ethnic group, Yadav [8] in his research conducted on 96 human skulls (50 males and 46 females), concluded that all linear diameters are larger in male than the same diameters in female skulls.

On a sample from British population, Gapert [3], using a multivariate binary logistic regression, concluded that determination of sex can be performed using foramen magnum with 70.3% accuracy.

The aims of this study were to determine the prediction of sex determination based on craniometric analysis of foramen magnum of Bosnian adult human skulls.

2 Materials and Methods

The research was conducted on 100 human degenerated and macerated adult skulls of known sex and known age (50 male skulls, 50 female skulls) selected by randomization of 211 human skulls (139 male and 72 female skulls) belonging to the Osteological Collection of the Department of Anatomy, Medical Faculty, University of Sarajevo.

For analysis of the size of foramen magnum we used the craniometric method where we measured two linear diameters of foramen magnum and where we calculated the area of foramen magnum using two formulas published by Radinsky and Teixeira which are based on the sagittal and transverse diameter.

We measured sagittal diameter and transverse diameter using sliding caliper graduated to the last 0.01 mm.

Sagittal diameter (anteroposterior diameter, or vertical, or length of the foramen magnum) represents distance between basion and opisthion and that is the longest diameter of the foramen magnum in midsagittal plane. Basion is the anthropometric point where the midsagittal plane intersects with anterior border of the foramen magnum, while opisthion is anthropometric point where the midsagittal plane intersects with posterior border of the foramen magnum.

Transverse diameter (width) of the foramen magnum is the longest diameter of the foramen magnum in transversal plane. That is the distance between two most lateral points on lateral borders of the foramen magnum.

The area of foramen magnum was calculated using formulas published by Radinsky [9] and Teixeira [10]:

1. Radinsky formula is:

$$FM = 1/4 \times \pi \times H \times W$$

$\pi = 3.14$; H = sagittal diameter; W = transverse diameter.

2. Teixeira formula is:

$$FM = \pi \times ((H + W)/4)^2$$

$\pi = 3.14$; H = sagittal diameter; W = transverse diameter.

2.1 Statistical Analysis

Statistical analysis was performed using SPSS computer software for Windows (Statistical Package for Social Sciences, version 19.0) and Microsoft Excel (version 11).

Descriptive statistics are expressed as minimum and maximum value, and the difference of arithmetic mean between the two groups was tested by Student t test and ROC curve.

3 Results

The mean sagittal diameter in this research is 36.0 mm and mean transverse diameter is 31.0 mm. The sagittal diameter ranges from minimum value of 28.0 mm to maximum value of 42.0 mm. Transverse diameter ranges from minimum value of 23.0 to maximum value of 37.0 (Table 1).

The mean area of foramen magnum calculated using Radinsky formula is $857.7 \pm 130.9 \text{ mm}^2$, while the mean area of foramen magnum calculated using Teixeira formula is $865.4 \pm 129.7 \text{ mm}^2$. The area of foramen magnum calculated using Radinsky formula ranges from minimum value of 571.5 mm^2 to maximum value of 1219.9 mm^2 . The area of foramen magnum calculated using Teixeira formula ranges from minimum value of 572.3 mm^2 to maximum value of 1224.8 mm^2 (Table 2).

The significance for sex determination using sagittal and transverse diameter and areas of foramen magnum was

Table 1 Descriptive statistics of diameters (mm) and areas (mm²) of the foramen magnum

	All (n = 100)	Minimum–maximum
Sagittal diameter (mm)	36.0 (34.0–38.0)	28.0–42.0
Transverse diameter (mm)	31.0 (28.0–32.0)	23.0–37.0
Area (R) (mm ²)	857.7 ± 130.9	571.5–1219.9
Area (T) (mm ²)	865.4 ± 129.7	572.3–1224.8

Data are presented as median (25th and 75th percentiles); mean ± SD; n—number of cases

Table 2 Descriptive statistics of diameters (mm) and areas (mm²) of foramen magnum in both sexes

	Female (n = 50)	Male (n = 50)	p value
Sagittal diameter (mm)	35.0 (33.0–37.0)	37.0 (35.0–39.0)	<0.0005
Transverse diameter (mm)	29.5 (27.0–32.0)	31.0 (29.0–33.0)	0.008
Area (R) (mm ²)	809.0 ± 97.1	906.3 ± 142.6	<0.0005
Area (T) (mm ²)	816.2 ± 95.7	914.5 ± 141.1	<0.0005

Data are presented as median (25th and 75th percentiles); mean ± SD; n—number of cases; p—probability

Table 3 Optimal cut-off, area under the curve (AUC), 95% confidence interval (95% CI), probability (p) of sagittal and transverse diameter for differentiation between male and female crania

Variable	Cut-off values	AUC	(95% CI)	p value
<i>Male versus female crania</i>				
Sagittal diameter (mm)	37.5	0.730	0.632–0.829	<0.0005
Transverse diameter (mm)	30.5	0.653	0.545–0.760	0.008

tested using Student t test. The analysis of sagittal diameter in both sexes revealed $p < 0.0005$ and analysis of transverse diameter in both sexes revealed $p = 0.008$.

The analysis of area of foramen magnum calculated using Radinsky formula revealed $p < 0.0005$, and analysis of area of foramen magnum calculated using Teixeira formula revealed $p < 0.0005$.

All of diameters of foramen magnum (sagittal and transverse diameter) showed statistically significant effect for gender determination.

Area of foramen magnum showed statistically significant effect for gender determination when calculated using both formulas (Radinsky and Teixeira) (Table 3).

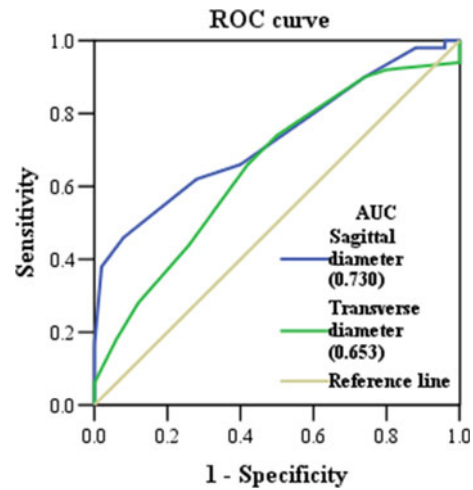


Fig. 1 Receiver operating characteristic (ROC) curve of sagittal and transverse diameter for differentiation between male and female crania

Table 4 Optimal cut-off, area under the curve (AUC), 95% confidence interval (95% CI), probability (p) of area using Radinsky’s (R) and Teixeira’s (T) formula for differentiation between male and female crania

Variable	Cut-off values	AUC	(95% CI)	p value
<i>Male versus female crania</i>				
Area (R) (mm ²)	887.8	0.709	0.606–0.812	<0.0005
Area (T) (mm ²)	894.2	0.712	0.610–0.815	<0.0005

The ROC curve of diameters of foramen magnum is shown in Fig. 1. The area under the curve shows prediction for gender determination using linear diameters. This area for sagittal diameter is 0.730 and for transverse diameter this area is 0.653. The predictability of sagittal diameter is 73% and is higher than the predictability of transverse diameter which is 65.3% accuracy (Table 4).

The ROC curve of areas of foramen magnum calculated using Radinsky and Teixeira formula is shown in Fig. 2. The area under the curve shows prediction for gender determination using areas of foramen magnum. This area for area of foramen magnum calculated using Radinsky formula is 0.709 and for area of foramen magnum calculated using Teixeira formula this area is 0.712. The predictability of area calculated using Teixeira formula is 71.2% and is higher than the predictability of the area of foramen magnum calculated using Radinsky formula which is 70.9% accuracy.

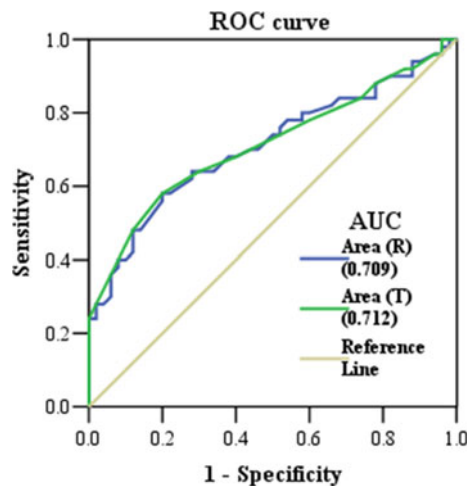


Fig. 2 Receiver operating characteristic (ROC) curve of area using Radinsky's and Teixeira's formula for differentiation between male and female crania

4 Discussion

The present study shows the predictability for gender determination of both diameters of foramen magnum and area of foramen magnum.

The significance for sex determination using sagittal and transverse diameter and areas of foramen magnum was tested using Student t test. The analysis of sagittal diameter in both sexes revealed $p < 0.0005$ and analysis of transverse diameter in both sexes revealed $p = 0.008$.

The analysis of area of foramen magnum calculated using Radinsky formula revealed $p < 0.0005$, and analysis of area of foramen magnum calculated using Teixeira formula revealed $p < 0.0005$.

All diameters of foramen magnum (sagittal and transverse diameter) showed statistically significant effect for sex determination.

Area of foramen magnum showed statistically significant effect for sex determination when calculated using both formulas (Radinsky and Teixeira).

The predictability of sagittal diameter is 73% and is higher than the predictability of transverse diameter which is 65.3% accuracy. The predictability of area calculated using Teixeira formula is 71.2% and is higher than the predictability of area of foramen magnum calculated using Radinsky formula which is 70.9% accuracy.

Numerous authors studied sexual dimorphism of foramen magnum in their ethnic group because size and shape of skeletal remains are different between different populations.

In Bosnian population we analyzed sex determination using linear diameters of skulls [11] and using morphoscopic predictors [12].

In this study we analysed gender determination using linear diameters of foramen magnum of Bosnian adult human skulls and we compared our results with results of other authors.

In the study conducted by Kamath et al. on a sample from south India population all dimensions and area of foramen magnum showed sex predictability. The sex predictability is the highest for area (70.3%), followed by sagittal diameter (69.6%), while transverse diameter is the lowest with 66.4%. Area is the first in the group, followed by sagittal diameter, while transverse diameter is the lowest. In our study, sagittal diameter shows the highest effect for sex determination (73%), followed by area (FM \approx 71%), and the lowest effect is shown by transverse diameter with 65.3% accuracy [1].

In the research which was conducted by Babu et al. [13] on human skulls from Indian population, all diameters showed statistically significant effect for sex determination and the first in group is the sagittal diameter with 86.5%, followed by area with 81.6 and 82.2%, while transverse diameter is the lowest with 65.4% accuracy which is similar to our results.

Gapert [3], on a sample from the British population (158 human skulls, 82 male and 76 female), using a multivariate binary logistic regression, concluded that the determination of sex can be performed using foramen magnum with 70.3% accuracy and using a univariate logistic regression for sex determination of foramen magnum with 65.8% accuracy.

Suazo et al. [4] studied sex differences of foramen magnum on 211 human skulls of Brazilian population. They measured the sagittal and vertical diameter of foramen magnum and they concluded that the all diameters were longer in male skulls than the same diameters in female skulls.

Manoel et al. [5] on a sample of 215 human skulls (139 male and 76 female) from Brazilian population, concluded that the width (transverse diameter) of the foramen magnum showed statistically significant effect in the determination of sex, where length of the foramen magnum (anteroposterior diameter) did not show statistically significant effect for sex determination.

5 Conclusion

All diameters of the foramen magnum (sagittal and transverse diameter) show sexual dimorphism. Area of the foramen magnum, which was calculated using Radinsky and Teixeira formulas, shows sexual dimorphism. Sagittal diameter shows the highest effect for gender determination (73%). Transverse diameter shows the lowest effect for gender determination (65.3%). Area of the foramen magnum

shows significant effect for gender determination with 70.9% using Radinsky formula and 71.2% using Teixeira formula.

Acknowledgements We would like to express special appreciation to **Assistant Professor Dr. Amela Dervišević**, Department of Human Physiology, Medical faculty, University of Sarajevo for statistical expertise.

References

1. Kamath, V.G., Asif, M., Shetty, R., Avadhani, R.: Binary logistic regression analysis of foramen magnum dimensions for sex determination. *Anat. Res. Int.* **2015**, 1–9 (2015)
2. Sarač-Hadžihalilović, A.: *Anatomically-Anthropological Significance of the Skull*, English edn. Faculty textbook, Medical Faculty University of Sarajevo (2017)
3. Gapert, R., Black, S., Last, J.: Sex determination from the foramen magnum: discriminant function analysis in an eighteenth and nineteenth century British sample. *Int. J. Leg. Med.* **123**, 25–33 (2009)
4. Suazo, G.I.C., Russo, P.P., Zavando, M.D.A., Smith, R.L.: Sexual dimorphism in the foramen magnum dimensions. *Int. J. Morphol.* **27**(1), 21–23 (2009)
5. Manoel, C., Prado, F.B., Caria, P.H.F., Groppo, F.C.: Morphometric analysis of the foramen magnum in human skulls of Brazilian individuals: its relation to gender. *Braz. J. Morphol. Sci.* **2**(26), 104–108 (2009)
6. Jain, S.K., Choudhary, A.K., Mishra, P.: Morphometric evaluation of foramen magnum for sex determination in a documented north Indian sample. *J. Evol. Med. Dent. Sci.* **42**(2), 8093–8098 (2013)
7. Kanchan, T., Gupta, A., Krishan, K.: Craniometric analysis of foramen magnum for estimation of sex. *Int. J. Med. Health Pharm. Biomed. Eng.* **7**(7), 166–168 (2013)
8. Yadav, Y., Goswami, P.: A study of length and width of foramen magnum in North India. *Int. J. Sci. Res.* **6**(3), 371–372 (2014)
9. Radinsky, L.: Relative brain size, a new measure. *Science* **155**, 836–838 (1967)
10. Teixeira, W.R.G.: Sex identification utilizing the size of the foramen magnum. *Am. J. Forensic Med. Pathol.* **3**(3), 203–206 (1982)
11. Ajanović, Z., Sarač-Hadžihalilović, A., Gojak, R.: Determination of sex by discriminant function analysis of linear diameters in Bosnian human skulls. *IFMBE Proc.* **62**, 88–94 (2017)
12. Ajanović, Z., Sarač-Hadžihalilović, A., Gojak, R., Dervišević, L.: Morphoscopic predictors for sexual dimorphism of skulls. *Folia Med. Fac. Med. Univ. Saraeviensis* **51**(2), 86–91 (2016)
13. Babu, R.Y.P., Kanchan, T., Attiku, Y., Dixit, P.N., Kotian, M.S.: Sex estimation from foramen magnum dimensions in an Indian population. *J. Forensic Leg. Med.* **3**(19), 162–167 (2012)
14. Uysal, S., Gokharman, D., Kacar, M., Tuncbilek, I., Kosa, U.: Estimation of sex by 3D CT measurements of the foramen magnum. *J. Forensic Sci.* **50**, 1310–1314 (2005)
15. Abdel-Karim, R., Housseini, A., Hashish, R.: Adult sex estimation using three dimensional volume rendering multislice computed tomography of the foramen magnum and occipital condyles: a study in Egyptian population. *Int. J. Adv. Res.* **3**, 1212–1215 (2015)

Liver Enzymes as Biomarkers for Hepatotoxicity of Statins in Patients with Dyslipidemia

N. Velickova, M. Nateva, and S. Stojanovska

Abstract

Various chemical agents or pharmaceuticals as drugs administered into the body in increased concentrations for a long time may have hepatotoxic or carcinogenic effect. In human biomonitoring are used different biomarkers, which can confirm the presence of various chemical agents in the body and their effects on cells or molecules. The aim of the study is to biomonitoring of the hepatotoxic effects of statins (atorvastatin and rosuvastatin) as a chemical agents or drugs in therapy of patients with dyslipidemia, using biochemical biomarkers as liver enzymes. Materials and methods: Follow-up laboratory tests (AST, ALT, GGT, ALP, cholesterol, and triglycerides) were evaluated with biochemical analyzer Cobas Integra 400 Plus, after 6 months of treatment with statins. The study included 28 subjects, aged 28–84 years (the mean 63.7), 15 women and 13 men, mainly patients with confirm dyslipidemia. Results: The observation of total serum transferases confirmed that 20 of the subjects (71.42%) have a normal serum transferases (AST and ALT) but 8 of the subjects (28.58%) (Groups 1 and 2) have a abnormal level of serum transferases. Subjects in Group 1 (5 subjects with atorvastatin therapy) have an abnormal level of serum transferases (AST and ALT), the mean value of AST was 43.6 U/L and for ALT 73.6 U/L. Subject in Group 2 (3 subjects with rosuvastatin therapy) has >10 times more of the level of AST and ALT (the mean value of AST was 580.3 U/L, and ALT 1802.3 U/L). In the Group 2 we reported older patients (with the

ages after 60) with long time therapy with rosuvastatin (more than 6 months) who demonstrated significant elevation of ALT according with other chronic diseases as a cardiovascular diseases, diabetes mellitus type 2, acute pancreatitis and in alcohol abusers. Conclusions: We want to emphasize the importance of biomonitoring of liver enzymes as biomarkers which associates hepatotoxicity. Statins therapy (on patients with dyslipidemia) combined with other metabolic drugs and inhibitors, might increase the risk of liver injury. Individual differences, such as sex, age, sensitivity and immune ability, affect the degree of hepatotoxicity of various drugs (in our study statins) as a chemical agents present in the body.

Keywords

Statins • Dyslipidemia • Liver enzymes • Hepatotoxicity • Biomonitoring

1 Introduction

Biological monitoring is a set of activities which can confirm the toxic effects of different substances present in the body. Most of these activities use the qualitative (cytological and histopathological) or quantitative methods (by determining the concentrations of different substances and their metabolites in biological media such as blood, urine, serum, specific tissues, etc.). In addition, biomonitoring can confirm or exclude the cytotoxic or genotoxic effect of various physical and chemical agents present in the body, especially in the conditions of its chronic exposure. It means that various chemical agents or pharmaceuticals as drugs administered into the body in increased concentrations for a long time may have toxic or carcinogenic effect. In human biomonitoring are used different biomarkers, which can confirm the presence of various chemical agents in the body and their effects on cells or molecules. The term “marker” define any substance or change in the cells or tissues that can

N. Velickova (✉)

Faculty of Medical Sciences, University “Goce Delcev”, Stip,
Republic of Macedonia
e-mail: nevenka.velickova@ugd.edu.mk

M. Nateva

Clinical Center “Mother Teresa”, PHI University Clinic of Clinical
Chemistry, Skopje, Republic of Macedonia

S. Stojanovska

PHI Health Care—“Academician Prof. Dr. Dimitar Arsov”, Kriva
Palanka, Republic of Macedonia

be identified or measured. The most commonly used biological medium for human biomonitoring is blood. A number of physical and chemical agents present in our environment represent a potential health risk for each exposed individual, simultaneously increasing the risk of disease present in the society. The degree of hepatotoxic effects on each exposed individual depends on the degree of exposure to the given factor, the method of elimination or the sensitivity to its toxic effects, the years of exposure and the genetically-determined differences between the individuals. Human biomonitoring in correlation with the development of molecular biology, biochemistry and genetic screening, allows detecting of cellular or pathophysiological changes in the organism as a result of reaction of the organism exposed to certain physical, chemical or biological agents. By applying biochemical and cytogenetic methods, the detection, screening and quantification of certain biomarkers can be directly evaluated. Thus, with indirect biomonitoring of different agents (in our study, chemical or pharmaceutical agents, such as statins) and measurement of the levels of liver enzymes as a biomarkers can confirm the hepatotoxicity of the statins on the cells.

Dyslipidemia should be diagnosed with complete lipid status including total cholesterol (TC), low-density lipoprotein cholesterol (LDL-C), triglycerides (TG) and highdensity lipoprotein cholesterol (HDL-C). Other metabolic disturbances and other diseases should be excluded by measuring glucose, alanine and aspartate transferases (ALT and AST), creatinine and thyroid stimulating hormone. On patients with dyslipidemia, complete lipid status should be checked 6–8 weeks after initiation of therapy according to any change to drug therapy, such as dose change, change of compound, or starting combination therapy.

Statins (3-hydroxy-3-methylglutaryl coenzyme A [HMGCoA] reductase inhibitors) can lower cholesterol in the blood, as a result on the inhibition of 3-hydroxy-3-methylglutaryl coenzyme A reductase. However, for the other side it causes pathophysiological changes in muscle tissue (increasing the serum creatine kinase values), and hepatic tissue (increasing the values of liver enzymes), and other cytological changes as important biomarkers for the hepatotoxic effect of statins. Scientific studies indicate that statins have cytotoxic effects in the organism, if they are used in high doses and for long time [1, 2]. The biochemical side effects of statins (simvastatin, atorvastatin, pravastatin, rosuvastatin, fluvastatin, lovastatin, and pitavastatin) are explained with their possibility to cause a reduction in intracellular cholesterol levels, leading to increased LDL receptor expression on hepatocyte membranes with a subsequent reduction in the circulating levels of apoB-containing. In addition, they can inhibit an enzyme that is essential not only for cholesterol biosynthesis, but also for the synthesis of other nonsterol precursors essential

for normal cellular function [3]. Some of the studies [4–6] confirm the multiple effects of statins such as antiinflammatory effects, antioxidant effects, antiproliferative and immunomodulatory effects, plaque stability, normalization of sympathetic outflow, and prevention of platelet aggregation are due to reduction of circulating isoprenoids and hence inactivation of signalling proteins. These multiple lipid-independent effects of statins termed as statin pleiotropy.

Rosuvastatin as a member of the drug class of statins is a synthetic lipid-lowering agent for oral administration and it is sparingly soluble in water and methanol as well as slightly soluble in ethanol. In one of the nonclinical toxicology trials (104-week study in rats) [7, 8] is observe that rosuvastatin produces carcinogenicity (2, 20, 60 or 80 mg/kg/day by oral gavage). The frequency of uterine stromal polyps was significantly increased in females at 80 mg/kg/day. In these studies, increased incidence of carcinogenicity with administration of rosuvastatin was shown at a higher dose or long time exposure. Also, in other studies of human biomonitoring is confirmed that rosuvastatin induces cytotoxicity, clastogenicity and DNA effects in human lymphocytes in vitro. Obese individuals may have higher levels of serum transferases than their lean counter parts [9]. Treatment with statins tends to increase serum transferases. This effect is dose-dependent and meta-analyses of randomized placebo controlled trials demonstrate that low to moderate doses of statins are not associated with clinically significant elevations in transferases ($>3 \times \text{ULN}$) [10, 11]. The risk of these complications is increased in elderly patients with chronic diseases and in alcohol abusers [7]. Furthermore, statins cause hepatotoxic effect which is observed in several percent of treated patients, usually in the first weeks of the therapy [12–14]. This is a fundamental research that can be found in further clinical practice because the project goal is biomonitoring of the hepatotoxic effects of statins (chemical agents used in patients with dyslipidemia), as an effective therapy for lowering the concentration of cholesterol in the blood, using biochemical biomarkers as liver enzymes.

2 Materials and Methods

The biomonitoring of the hepatotoxic effects are conducted by evaluating the biochemical markers, mainly liver enzymes (serum transferases) as important indicators or parameters for evaluating the hepatotoxic effect of certain chemical agents, in our study, statins. All participants will be informed of the nature and purpose of the research. Only those participants who give written consent are included in the study. Tests were conducted in accordance with the Declaration of Helsinki and with the principles of good clinical practice. Recruitment and diagnostic tests were

conducted in the University Clinic of Clinical Chemistry, Clinical Center “Mother Teresa” in Skopje.

The study was performed in the years 2017–2018. Inclusion criteria are as follows: *Hyperlipidemia treated with statins for minimum of 6 months*. The following biochemical parameters using standard automated technique were assessed: blood cells count and levels of bilirubin, aspartate (AST) and alanine (ALT) aminotransferase, total and LDL and HDL cholesterol, triglycerides, glucose, amylase, lipase, urea and creatinine. They were evaluated with biochemical analyzer *Cobas Integra 400 Plus (Roshe Diagnostics)* after 6 months of treatment with statins.

The principle for AST evaluation include that AST catalyzes the reaction between Laspartate and 2-oxoglutarate. The oxaloacetate formed is deducted by NADH in a reaction catalyzed by malate dehydrogenase (MDH) to form L-malate and NAD. The rate of the NADH oxidation is directly proportional to the catalytic AST activity. It is determined by measuring the decrease in absorbance at 340 nm.

The principle for ALT evaluation include that ALT catalyzes the reaction between Lalanine and 2-oxoglutarate. NADH reduces the pyruvate formed in a reaction catalyzed by lactate dehydrogenase (LDH) to form L-lactate and NAD⁺. The rate of the NADH oxidation is directly proportional to the catalytic ALT activity. It is determined by measuring the decrease in absorbance at 340 nm.

The study included 28 subjects, aged 28–84 years (mean 63.7), 15 women and 13 men, mainly patients with confirmed dyslipidemia.

3 Results and Discussion

Dyslipidemia in the subjects is define with observation of complete lipid status including total cholesterol (TC) (the mean = 5.68 mmol/L), low-density lipoprotein cholesterol (LDL-C) (the mean = 2.49 mmol/L), triglycerides (TG) (the mean = 3.22 mmol/L) and highdensity lipoprotein cholesterol (HDL-C) (the mean = 1.24 mmol/L). All of the subjects used the therapy with statins (atorvastatin and rosuvastatin) for minimum of 6 months with daily dose of statins 5–40 mg.

The observation of total serum transferases confirmed that 20 of the subjects (71.42%) have a normal serum transferases (AST and ALT) but 8 of the subjects (28.58%) have a abnormal level of serum transferase (Table 1).

10 of the subjects with atorvastatin therapy have a normal level of AST (the mean values = 20.5 ± 4.2 U/L) and ALT (the mean value = 22.3 ± 9.4 U/L). Also, 10 of the subjects with rosuvastatin therapy have a normal level of AST (the mean value = 22.9 ± 4.8 U/L), and for ALT (the mean values = 21.2 ± 10.5 U/L) (Table 2).

Table 1 The total number and percentage of subject with normal and abnormal level of serum transferases

Liver enzymes	Group-1 (atorvastatin)		Group-2 (rosuvastatin)		Total	
	N	%	N	%	N	%
Normal	10	66.7	10	76.92	20	71.42
Abnormal	5	33.3		23.18	8	28.58
Total	15	100	13	100	28	100

Table 2 Number of subjects with atorvastatin and rosuvastatin therapy with normal level of AST and ALT

No. of subjects with atorvastatin therapy (normal level of serum transferases)	AST	ALT	No. of subjects with rosuvastatin therapy (normal level of serum transferases)	AST	ALT
1	22	15	1	17	20
2	16	16	2	31	49
3	21	18	3	16	17
4	21	22	4	28	24
5	17	12	5	21	14
6	16	22	6	23	15
7	28	40	7	28	24
8	19	14	8	21	20
9	27	31	9	22	13
10	18	33	10	22	16
Mean \pm S.D.	20.5 ± 4.2	22.3 ± 9.4	Mean \pm S.D.	22.9 ± 4.8	21.2 ± 10.5

Table 3 Number of subjects with atorvastatin and rosuvastatin therapy with abnormal level of AST and ALT

(Group 1) No. of subjects with atorvastatin therapy (abnormal level of serum transferases)	AST (10–34) U/L	ALT (10–45) U/L	(Group 2) No. of subjects with rosuvastatin therapy (>10 time of level of serum transferases)	AST U/L 10–34	ALT U/L 10–45
1	47	87	1	700	4319
2	38	69	2	154	93
3	49	112	3	887	995
4	44	50			
5	40	50			
Mean ± S.D.	43.6 ± 4.6	73.6 ± 26.4	Mean ± S.D.	580.3 ± 380.9	1802.3 ± 2225.7

But, subjects (5) in Group 1 (4 men + 1 woman) with atorvastatin therapy, have a abnormal level of serum transferase (AST and ALT) and 3 of the subjects in Group 2 (2 men + 1 woman) with rosuvastatin therapy have >10 times more of the level of serum transferases (AST and ALT).

In the Group 1 of subjects (with atorvastatin therapy) the mean values for AST was 43.6 U/L and for ALT 73.6 U/L. In the Group 2 of subjects (with rosuvastatin therapy) the mean value for AST was 580.3 U/L, and for ALT 1802.3 U/L (Table 3).

In the Group 2 we report older patients (with the ages after 60) with long time therapy with rosuvastatin (more than 6 months) who demonstrated significant elevation of ALT according with other chronic diseases as a cardiovascular diseases, diabetes mellitus type 2, acute pancreatitis and in alcohol abusers. That confirmed our expectation that in the subjects who have been treated for a long time with statins, can induce the following changes: increased the values of certain serum transferases as important biochemical biomarkers for the hepatotoxicity of these drugs. Also, the values of serum transferases (AST and ALT) are much more high in subjects with other chronic disease. For that reasons the decision about the statins daily doses and therapy, should be based on an individual assessment of the patients because they have hepatotoxic effect if they are retained in the body for a long time, especially in high dose. We assume that hepatotoxicity of statins will be different in different subjects according to their age, duration of therapy, sensitivity and other physiological parameters. Previous published studies confirmed that the risk of side effects increases with age and liver and kidney dysfunction and polypharmacy with the resulting increase in the potential for drug interactions [15, 16]. The same results are observe in patients with chronic therapy with clopidogrel [17]. Neuvonen et al. [18] and Lau et al. [19] suggested that atorvastatin, but not pravastatin, decreased the inhibitory effect of clopidogrel on platelet aggregation [18, 19]. As an inactive prodrug,

clopidogrel is metabolized mainly by CYP3A4 and CYP3A5 isozymes (cytochrome P450 (CYP) isozymes), whereas atorvastatin could reduce the effects of clopidogrel by inhibiting the CYP3A-dependent formation of its active metabolites [18]. A population-based cohort study investigated the interactions between CYP3A4-metabolized statins and clopidogrel [17]. According to these results they conclude that combination of atorvastatin and clopidogrel may induce hepatic injury via competitive activation and excessive consumption of CYP3A4. Pharmacokinetics of pravastatin is clearly different from atorvastatin. The duration from atorvastatin exposure to the onset of hepatic toxicity can be variable [19]. The significant ALT elevations it's not immediately after taking statins. When we compare the conclusions of studies before [15–19] all of them confirmed that elevation of serum transferases is often self-limiting and may be related to the alteration of the hepatocyte cell membrane with liver enzyme leakage rather than direct injury to the liver cells. Main of these previously published studies supports the use of statin treatment in patients with high cardiovascular risk whose elevated aminotransferase levels have no clinical relevance or are attributable to known stable chronic liver conditions. For that reason the decision should be based on an individual assessment of risks and benefits.

4 Conclusions

The doses of statins should be adjusted and monitored more responsible. Monitoring of liver enzymes should be done before the start of treatment with statins in patients with dyslipidemia. During treatment, the focus should be done not only on clinical symptoms but on the preclinical symptoms that may alert muscle or liver complications. With results of our study we want to emphasize the importance of biomonitoring of liver enzymes as biomarkers which

associated hepatotoxicity. Statins therapy (on patients with dyslipidemia) combined with other metabolic drugs and inhibitors, might increase the risk of liver injury. Individual differences, such as sex, age, sensitivity and immune ability, affect the degree of hepatotoxicity of various drugs (in our study statins) as a chemical agents present in the body.

References

- Wiklund, O., Pirazzi, C., Romeo, S.: Monitoring of lipids, enzymes, and creatine kinase in patients on lipid-lowering drug therapy. *Curr. Cardiol. Rep.* **15**, 397 (2013)
- Liu1, Y., Cheng1, Z., Ding1, L., Fang1, F., Cheng1, K.-A., Fang1, Q., Shi, G.P.: Atorvastatin-induced acute elevation of hepatic enzymes and the absence of cross-toxicity of pravastatin. *Int. J. Clin. Pharmacol. Ther.* **48**(12), 798–802 (2010)
- MacDonald, J.S., Halleck, M.M.: The toxicology of HMG–CoA reductase inhibitors: prediction of human risk. *Toxicol. Pathol.* **32**, 26–41 (2004)
- Cannon, C.P., Braunwald, E., McCabe, C.H., et al.: Intensive versus moderate lipid lowering with statins after acute coronary syndromes. *N. Engl. J. Med.* **350**, 1495–1504 (2004)
- LaRosa, J.C., Grundy, S.M., Waters, D.D., et al.: Intensive lipid lowering with atorvastatin in patients with stable coronary disease. *N. Engl. J. Med.* **352**, 1425–1435 (2005)
- Pedersen, T.R., Faergeman, O., Kastelein, J.P., et al.: High-dose atorvastatin vs usual-dose simvastatin for secondary prevention after myocardial infarction: the IDEAL study: a randomized controlled trial. *JAMA* **294**, 2437–2445 (2005)
- US Food and Drug Administration (FDA). *PhRMA/FDA/ASSLD drug induced hepatotoxicity white paper post marketing considerations* (2000). <http://www.fda.gov/downloads/Drugs/ScienceResearch/ResearchAreas/ucm091462.pdf>. Accessed 2 Feb 2010
- Ali Berber, A., C elik, M., Aksoy, H.: Genotoxicity evaluation of HMG CoA reductase inhibitor rosuvastatin. *Drug. Chem. Toxicol.* **37**(3), 316–321 (2014)
- Kiortsis, D.N., Nikas, S., Hatzidimou, K., Tsianos, E., Elisaf, M. S.: Lipid-lowering drugs and serum liver enzymes: the effects of body weight and baseline enzyme levels. *Fundam. Clin. Pharmacol.* **17**(4), 491–494 (2003)
- de Denus, S., Spinler, S.A., Miller, K., Peterson, A.M.: Statins and liver toxicity: a metaanalysis. *Pharmacotherapy.* **24**, 584–591 (2004)
- Wlodarczyk, J., Sullivan, D., Smith, M.: Comparison of benefits and risks of rosuvastatin versus atorvastatin from a meta-analysis of head-to-head randomized controlled trials. *Am. J. Cardiol.* **102**, 1654–1662 (2008)
- Thapar, M., Russo, M., Bonkovsky, H.L.: Statins and liver injury. *J. Gastroenterol. Hepatol.* **9**(9), 605–606 (2013)
- Cadranel, J.F., Seddik, M., Loric, S., Jeanne, S.: Statins: hepatotoxicity and monitoring. *Presse Medicale.* **38**(5), 717–725 (2009)
- Jose, J.: Statins and its hepatic effects: newer data, implications, and changing recommendations. *J Pharm.Bioallied Sci.* **8**(1), 23–28 (2016)
- Marcum, Z.A., Vande, J.P., Linnebur, S.A.: FDA drug safety communications: a narrative review and clinical considerations for older adults. *Am. J. Geriatr. Pharmacother.* **10**, 264–271 (2012)
- Walker, D.B., Jacobson, T.A.: Initiating statins in the elderly: the evolving challenge. *Curr. Opin. Endocrinol. Diabetes Obes.* **15**, 182–187 (2008)
- Blagojevic, A., Delaney, J.A., L evesque, L.E., et al.: Investigation of an interaction between statins and clopidogrel after percutaneous coronary intervention: a cohort study. *Pharmacoevidemiol. Drug Saf.* **18**, 362–369 (2009)
- Neuvonen, P.J., Niemi, M., Backman, J.T.: Drug interactions with lipid-lowering drugs: mechanisms and clinical relevance. *Clin. Pharmacol. Ther.* **80**, 565–581 (2006)
- Lau, W.C., Waskell, L.A., Watkins, P.B., et al.: Atorvastatin reduces the ability of clopidogrel to inhibit platelet aggregation: a new drug–drug interaction. *Circulation* **107**, 32–37 (2003)

Impact of Antibiotic Misuse on Genetics Alterations of Bacteria

Emina Aruković, Dina Fetahović, and Belma Pehlivanović

Abstract

Antibiotic resistance is a live issue when it comes to public health and emerging infectious diseases. Opinion of many experts in this field is that misuse or overuse of antibiotics have contributed to fast development of antibiotic resistance. This paper is focused on genetics alterations of bacteria caused by misuse of antibiotics. The acquisition of resistance can occur by horizontal or vertical transmission, so we described the mechanisms of resistance, as well as evolution of resistance genes. We explained mutagenesis induced by antibiotics, as well as recombination and lateral transfer mechanisms. At the end we got to multiple drug resistant bacteria, as a most urgent threat to a public health. Many strains of bacteria become resistant, or in many cases multi-resistant to many therapeutic drugs because of their ability to adapt to the environment and to develop different mechanisms of resistance to most old and new antimicrobial agents. Some strains have become resistant to practically all of the commonly available agents.

Keywords

Antibiotic resistance • Mutagenesis • Antibiotic misuse • Multiresistance • PCR

1 Introduction

In modern world, the misuse of antibiotics is described as a global threat to public health due to occurrence of antibiotic-resisting bacteria and less effective antibiotic therapies. Antibiotic therapies are effective if patients follow the pharmacotherapeutical guidelines, apply antibiotics according to prescriptions and avoid self-medication. Usually, misuse of antibiotic therapy refers to non-completed therapies, skipping of doses, overuse of doses or using antibiotics for wrong treatment such as viral infections. Factor associated with antibiotic therapy misuse also included patient's knowledge and attitudes toward antibiotic consumption, expectations from the therapy, physician's knowledge and experience, and pharmaceutical marketing. All those factors lead to occurrence of antibiotic resistance which has become a serious global health problem. It is estimated that only in Europe 25,000 people die each year as a result of multidrug-resistant bacterial infections and that this costs the European Union economy €1.5 billion annually [33].

Antibiotic resistance is well known and documented problem which can occur naturally and can affect anyone, of any age, in any country, but the acceleration of the process is directly connected to misuse of antibiotics. Back in 1945 Sir Alexander Fleming warned that the inappropriate use of penicillin can cause the development of resistant mutant forms of *Staphylococcus aureus* that could cause more serious infections. Only a few years after the widespread of penicillin, the significant numbers of strains of *Staphylococcus aureus* have become resistant to this drug [19]. Unfortunately, in past years no improvement has been made to prevent and control antibiotics resistance, in fact every day there are more cases reported that certain bacteria have developed resistance to different antibiotics. The list of bacteria developing resistance is impressive, from sulfonamide and penicillin-resistant *Staphylococcus aureus* in the

E. Aruković (✉) · D. Fetahović · B. Pehlivanović
Faculty of Pharmacy, University of Sarajevo, Zmaja od Bosne 8,
71000 Sarajevo, Bosnia and Herzegovina
e-mail: emina.arukovic@ffsa.unsa.ba

D. Fetahović
e-mail: dina.fetahovic@ffsa.unsa.ba

B. Pehlivanović
e-mail: belma.pehlihanovic@ffsa.unsa.ba

1930s and 1940s [28] to *penicillin resistant Neisseria gonorrhoeae* (PPNG) [17], and beta-lactamase producing *Haemophilus influenzae* in the 1970s, [19, 20] *methicillin resistant Staphylococcus aureus* (MRSA) and the resurgence of multi-drug resistant (MDR) *Mycobacterium tuberculosis* in the late 1970s and 1980s, [21, 27].

The aim of this paper is to present mechanisms of antibiotic resistance, both genetic and biological mechanisms, as well as horizontal and vertical processes in occurrence of antibiotic resistance. Paper will also describe all of the alterations on bacterial genome induced by antibiotic misuse.

2 Mechanisms of Antibiotic Resistance

Bacteria have developed resistance to every antibiotic used so far and there are several pathways that describe mechanisms of antibiotic resistance, but all of them can be summarized into 3 main mechanisms that include (a) enzymatic degradation of antibacterial drugs (b) alteration of bacterial proteins that are antimicrobial targets and (c) changes in membrane permeability to antibiotics. Antibiotic destruction/transformation is described as one of the oldest and most common mechanism of resistance that effect major antibiotic classes such as beta-lactams (penicillin, cephalosporins, monobactams). Bacteria produce one or more enzymes that are capable of chemically degrading antibiotics and making them pharmacologically inactive [16]. Some bacteria may modify the receptors or intracellular targets of antibiotics. Such receptor modification includes modifications in the structural conformation of penicillin-binding protein or ribosomal alterations that can render aminoglycosides, or DNA modifications resulting in resistance to fluoroquinolones [29]. Antibiotic active efflux was first described for tetracyclines and is relevant for those antibiotics that act inside bacteria in period of active development of transport mechanisms [15]. Antibiotic resistance can also occur by spontaneous gene mutation where some bacteria can acquire resistance to antimicrobial agents by either genetic mutation or by accepting antimicrobial resistance genes from other bacteria. The genes that codify this resistance (the “resistant genes”) are normally located in specialized fragments of DNA known as transposon (sections of DNA containing “sticky endings”), which allow the resistance genes to easily move from one plasmid to another. When such genetic mutations occurs they cause changes in bacterial DNA which can be then transferred with mechanisms of conjugation, transformation and transduction [29].

3 Genetics of Resistance

3.1 Antibiotic-Induced Mutagenesis

For a very long time bacteria was considered as passive microorganisms, and that some of them are just “lucky” antibiotic resistant forms. After a numerous research works and projects scientists gathered enough information to prove that bacteria have mechanisms that promote genetic variation under certain conditions [7]. Antibiotic-induced mutagenesis supposedly occurs because of development of single-stranded DNA, and consequently the SOS response is activated [7]. SOS response is a reply to DNA injury in which mutagenesis and DNA repair are induced [23]. Quinolones, even though they have a mutagenic effect on bacteria, are widely used family of DNA damaging antibiotics, and numerous studies have shown that subinhibitory concentrations of quinolones rise the frequency of resistance mutants in some bacteria [7]. B-Lactams are the most widely used antibiotics in clinical medicine, so the resistance may become a severe problem because they are used to treat a broad range of infections [4]. B-lactams have also been demonstrated to be a good triggers for the activation of SOS response in bacteria [24].

3.2 Antibiotic-Induced Recombination and Lateral Transfer

The genetic variability is produced primarily by mutagenesis and secondarily by recombination, which shuffles preexisting mutations [6]. There are several factors that make recombination more likely to occur. The first factor is physical proximity, which is more likely to exist between members of the same community, because many species of bacteria show significant geographical and ecological structuring [31]. A second factor is the homology dependence of recombination: in many bacterial species, the probability of acceptance of a recombination event decreases exponentially with genetic distance between the donor and recipient of DNA [22]. Lastly, if the major environmental change is lacking, the import of distantly related genetic material is more likely to reduce the competency of the recipient and consequently be removed by negative selection [31]. Recombination requires the genetic recombination genes *recB*, *recC*, *recD* and *recA*, which are part of the bacterial RecBCD recombination system. These proteins generally require near-perfect homology between the two complementary DNA strands [18]. Horizontal gene transfer

(HGT) among and within bacterial populations can occur by the three mechanisms: transformation (uptake of free DNA), conjugation (plasmid-mediated transfer) and transduction (phage-mediated transfer) [31]. While vertical inheritance of single resistance mutations does take place, it is an incomplete picture of the genetic basis of antibiotic resistance in the real world. Bacteria can transfer genes of all kinds, among closely and distantly related bacteria by horizontal gene transfer. HGT typically involves many genes being transferred, which are physically connected on the strand of DNA that is transferred. In general, bacterial chromosomes carry a stable set of genes required for their basic life processes, but many bacteria have specialized systems for linking together and expressing diverse genes so that they are readily transferable by the systems that effect HGT. This system, called an integron, figures prominently in antibiotic resistance [30].

3.3 Evolution of Antibiotic Resistance Genes

The history of antibiotic resistance genes can be divided into the 'preantibiotic' and 'antibiotic' periods, which can also be defined as the macro- and microevolutionary periods. Whilom is characterized by a history of revision in natural ecosystems, mostly through mutations, with a limited contribution of HGT to the processes. What is not known is if these processes have been involved in providing an antibiotic resistance or some other functions [4]. The beginning of mass production of antibiotics over half a century ago represented a major breakthrough in the medical treatment of infectious diseases [7]. Hardly anyone could foresee the huge variety of modes that bacteria use to evolve, especially their ability of interchanging genes, which is now well known as horizontal gene transfer. This capacity of bacteria is the reason why, in spite of the success of antibiotics in curing diseases, the emergence of multidrug-resistant bacteria is currently a major worldwide concern [14]. Probably the best-documented case of the ancient evolution of antibiotic resistance genes comes from the analysis of *b*-lactamases. The primary resistance mechanism is enzymatic inactivation through the cleavage of the *b*-lactam ring by *b*-lactamases [3]. Scientists proven that antibiotic resistance is a natural phenomenon that predates the modern selective pressure of clinical antibiotic use. They reported targeted metagenomics analyses of rigorously authenticated ancient DNA from 30,000-year-old Beringian permafrost sediments and identified a highly diverse collection of genes encoding resistance to β -lactam, tetracycline and glycopeptide antibiotics [9].

4 Detecting Antibiotic Resistance Genes

Variety of mechanisms cause antibiotic resistance: first is a presence of an enzyme that inactivates the antimicrobial substance, then the presence of some alternative enzyme for the enzyme that is inhibited by the antimicrobial agent, then a mutation in the antimicrobial agent's target. After that there can be a posttranscriptional or posttranslational modification of the antimicrobial agent's target, reduced uptake of the antimicrobial substance, an active efflux of the antimicrobial agent and overproduction of the target of the antimicrobial agent [10]. Nucleic acid-based detection technology/systems are rapid and sensitive methods to detect the presence of resistance genes. This technology is divided into hybridization systems and amplification systems, although many amplification technologies are also partly based on hybridization technology [10]. Hybridization is based on the fact that a cytosine forms base pairs with a guanine and an adenine forms base pairs with either a thymidine (in DNA) or a uracil (in RNA). In hybridization, the DNA in a sample is single stranded and allowed to combine with a single-stranded probe. Probes can be labeled with a radioactive isotopes, antigenic substrates, enzymes or chemiluminescent compounds [10].

PCR includes cycles of heating the sample for denaturing and elongation of the primers by a thermostable DNA polymerase. Actually, each round of amplification doubles a number of DNA target molecules, but the process is rarely 100% efficient because of the presence of inhibitors, and in later rounds of amplification DNA polymerase may become less efficient [10]. In PCR-single-strand conformation polymorphism (PCR-SSCP), the PCR amplification product is divided into two single-stranded molecules and subjected to non-denaturing polyacrylamide gel electrophoresis. Under nondenaturing conditions, the single-stranded DNA (ssDNA) molecule has a secondary structure that is determined by the nucleotide sequence, buffer conditions, and temperature. The mobility of the ssDNA molecule depends on its size and secondary structure. ssDNAs at different positions in the gel indicate a difference in sequence [10]. The technique was originally described for the detection of mutations in oncogenes and allelic variants in human genes [26]. PCR has been used to detect vancomycin [11] and gentamicin [13] resistance genes. Primers for *tetM*, one of the known tetracycline resistance genes, were used to analyse unamended garden soils by PCR, but there was no detection of related tetracycline resistance genes [1]. PCR is an excellent tool to detect potential antibiotic resistance genes. PCR-SSCP is capable of detecting more than 90% of all

single-nucleotide changes in a 200-nucleotide [12]. Plenty of molecular techniques can be used for diagnostic of genes mutations, but no universal technique, which is optimal for detection of nucleic acids, exists. The choice of a specific technique depends on the information required or the target.

5 Multiple Drug Resistance

Massive use of the antibiotics led to an increase resistance of bacteria. The presence of antibiotic-resistant bacteria is of great medical concern due to the treatment of infectious diseases [32]. Antibiotic misuse had led many of the bacterial pathogens linked with epidemics of human disease to evolve into multidrug-resistant (MDR) forms [8]. Penicillin was discovered in 1928 and was followed by discovery and commercial production of many other antibiotics. Due to that, we now take for granted that any infection can be cured by antibiotic therapy [32]. In the interview that Sir Alexander Fleming gave for The New York Times in 1945, he cautioned that misuse of penicillin could lead to the selection of resistant forms of *Staphylococcus aureus* that could cause more serious infections in the host or in other people that the host was in contact with. One year after, the massive use of penicillin had led to significant number of strains of this bacterium. Many strains of bacteria become resistant, or in many case multi-resistant to many therapeutic agents because of their ability to adapt to their environment and to develop different mechanisms of resistance to most old and new antimicrobial agents [2]. Some strains have become resistant to practically all of the commonly available agents. Among the gram-positive organisms, methicillin-resistant *Staphylococcus aureus* (MRSA) and *E. faecium* represent the biggest therapeutic obstacle. The evolution of MRSA illustrates the genetic adaptation of an organism into a first-class multidrug-resistant pathogen. *S. aureus* first developed resistance to β -lactam antibiotics such as penicillin and methicillin, and by 2003, more than 50% of *S. aureus* isolates reacquired in U.S. hospitals were MRSA [5]. Those isolates are usually resistant to all β -lactam compounds by production of a modified penicillin-binding protein, PBP2a, and to most aminoglycosides and fluoroquinolones by unrelated resistance mechanisms. Hospital-acquired MRSA remain still unresistant to glycopeptides. In addition, novel molecules promising for treating MRSA infections such as linezolid, quinupristin, dalfopristin, tigecycline, daptomycin, and ceftobiprole. *S. aureus* developed low level resistance to vancomycin, which was associated with a thickening of the pathogen's cell walls. So far, the biggest threat is the spread of vancomycin-resistant MRSA isolates. The vancomycin resistance determinant was a plasmid-mediated VanA

determinant from *E. faecium* strains that were concomitantly identified from the same patients. Lack of previous or additional reports of vancomycin-resistant MRSA isolates may be because of lack of detection or to lack of stability of the plasmid-mediated vancomycin-resistant determinants in *S. aureus*. However, a recent report indicates that a single plasmid transfer from VRE to MRSA may be sufficient for expression of resistance. There are therapeutic options for treating vancomycin resistant MRSA such as linezolid, quinupristin, dalfopristin, tigecycline, ceftobiprole and daptomycin but the clinical efficacy of the best antibiotic combinations still remains to be determined, since we still have not faced outbreaks with those isolates [25]. Alarming situation is increased number of *E. faecium* infections, since the majority of *E. faecium* isolated in U.S. critical care units is now resistant to vancomycin and to ampicillin with some strains having developed resistance to the newer antibiotics as well [5]. Positive side is that some molecules still retain some activity against vancomycin resistant *Enterococci* (VRE), such as linezolid, quinupristin, dalfopristin, tigecycline and daptomycin, with linezolid only being given orally. Quinupristin/dalfopristin is not effective against *E. faecalis*. Recently, the new antibiotic molecule was reported. It is called Platensimycin, originated from *Streptomyces platenensis*, and showed activity against VRE and MRSA [25]. Among the gram negative bacteria the biggest challenge are multidrug resistance *Pseudomonas aeruginosa* and *Acinetobacter*. This list is recently extended to members of the *Enterobacteriaceae* family, including hospital-associated strains of *Klebsiella*, *Escherichia coli*, and *Enterobacter*. This resistant gram-negative organisms were, until recently, sensitive on carbapenems, such as imipenem. Some strains have now developed effective ways to demolish effect of this antibiotics, including the production of β -lactamases that destroys the carbapenems; changes in outer-membrane porins that block the entry of these antibiotics; and active pumping of the antibiotic out of the cell using complex "efflux pumps." The situation is further complicated by the fact that the "permeability" barrier and efflux mechanisms also affect other classes of antibiotics (e.g., quinolones, aminoglycosides, and tigecycline). For some gram-negative bacteria polymyxins are only choice in therapy, although their toxicity (mainly renal) is still a problem, and reports of resistance are rising [5].

6 Conclusion

Antimicrobial resistance is a threat to the world we know, because of illnesses that were once easily treatable with antibiotics to become untreatable, leading to the epidemics. It is hard to say that someone could predict how many

methods bacteria use to evolve, especially their ability of interchanging genes. Faced with this gloomy picture, 21st century scientists must turn to compounds developed decades ago and previously abandoned because of toxicity or test everything they can think of and use whatever looks active in controlling this threat.

Conflict of Interest Authors declare that they have no conflict of interest.

References

1. Agero, Y., Sengelov, G., Jensen, L.B.: Development of a rapid method for direct detection of tet(M) genes in soil from Danish farmland. *Environ. Int.* **30**, 117–122 (2004)
2. Alanis, A.J.: Resistance to antibiotics: are we in the post-antibiotic era? *Arch. Med. Res.* **36**, 697–705 (2005)
3. Aminov, R.I., Mackie, R.I.: Evolution and ecology of antibiotic resistance genes. *FEMS Microbiol. Lett.* **271**, 147–161 (2007)
4. Aminov, R.I.: The role of antibiotics and antibiotic resistance in nature. *Environ. Microbiol.* **11**(12), 2970–2988 (2009)
5. Arias, C.A., Murray, B.E.: Antibiotic-resistant bugs in the 21st century—a clinical super-challenge. *N. Engl. J. Med.*, **360**(5), 439–443 (2009)
6. Bjedov, I., et al.: Stress-induced mutagenesis in bacteria. *Science* **300**, 1404–1409 (2003)
7. Couce, A., Blázquez, J.: Side effects of antibiotics on genetic variability. *FEMS Microbiol. Rev.* **33**, 531–538 (2009)
8. Davies, J., Davies, D.: Origins and evolution of antibiotic resistance. *Microbiol. Mol. Biol. Rev.* **74**(3), 417–433 (2010)
9. D'Costa, V.M., et al.: Antibiotic resistance is ancient. *Nature* **477**, 457–461 (2011)
10. Fluit, A.C., Visser, M.R., Schmitz, F.J.: Molecular detection of antimicrobial resistance. *Clin. Microbiol. Rev.*, **14**(4), 836–871 (2001)
11. Guardabassi, L., Agero, Y.: Genes homologous to glycopeptide resistance vanA are widespread in soil microbial communities. *FEMS Microbiol. Lett.* **259**, 221–225 (2006)
12. Hayashi, K.: PCR-SSCP: a method for detection of mutations. *Genet. Anal. Tech. Appl.* **9**, 73–79 (1992)
13. Heuer, H., et al.: Gentamicin resistance genes in environmental bacteria: prevalence and transfer. *FEMS Microbiol. Ecol.* **42**, 289–302 (2002)
14. Hoiby, N.: Ecological antibiotic policy. *J. Antimicrob. Chemother.* **46**, 59–62 (2000)
15. Hooper, D.C.: Efflux pumps and nosocomial antibiotic resistance: a primer for hospital epidemiologists. *Clin. Infect. Dis.* **40**, 1811–1817 (2005)
16. Jacoby, G.A., Munoz-Price, L.S.: The new β -lactamases. *N. Engl. J. Med.* **352**, 380–391 (2005)
17. Jaffe, H.W., et al.: Infections due to penicillinase-producing *Neisseria gonorrhoeae* in the United States: 1976–1980. *J. Infect. Dis.* **144**, 191–197 (1981)
18. Jolivet-Gougeon, A., et al.: Bacterial hypermutation: clinical implications. *J. Med. Microbiol.* **60**, 563–573 (2011)
19. Levy, S.B.: From tragedy the antibiotic era is born. In: Levy, S.B. (ed.) *The Antibiotic Paradox: How the Misuse of Antibiotics Destroys Their Curative Powers*, 2nd edn, pp. 1–14. Perseus Publishing, Cambridge, MA (2002)
20. Lind, I.: Epidemiology of antibiotic resistant *Neisseria gonorrhoeae* in industrialized and developing countries. *Scand. J. Infect. Dis.* **69**(Suppl), 77–82 (1990)
21. Lowy, F.D.: Medical progress: *Staphylococcus aureus* infections. *N. Engl. J. Med.* **339**, 520–532 (1998)
22. Majewski, J.: Sexual isolation in bacteria. *FEMS Microbiol.* **199**, 161–169 (2001)
23. Michel, B.: After 30 years of study, the Bacterial SOS response still surprises us. *PLoS Biol.* **3**(7), 1174–1176 (2005)
24. Miller, C., et al.: SOS response induction by β -lactams and bacterial defense against antibiotic lethality. *Science* **305**, 1629–1631 (2004)
25. Nordmann, P., et al.: Superbugs in the coming new decade; multidrug resistance and prospects for treatment of *Staphylococcus aureus*, *Enterococcus* spp. and *Pseudomonas aeruginosa*. *Curr. Opin. Microbiol.* **10**, 436–440 (2007)
26. Orita, M., et al.: Rapid and sensitive detection of point-mutations and DNA polymorphisms using the polymerase chain reaction. *Genomics* **5**, 874–879 (1989)
27. Pablos-Mendez, A., et al.: Global surveillance for antituberculosis-drug resistance, 1994–1997. *N. Engl. J. Med.* **338**, 1641–1649 (1998)
28. Rammelkamp, M.: Resistances of *Staphylococcus aureus* to the action of penicillin. *Proc. R Soc. Exp. Biol. Med.* **51**, 386–389 (1942)
29. Sefton, A.M.: Mechanisms of antimicrobial resistance. *Drugs* **62**, 557–566 (2002)
30. Summers, A.O.: Genetic linkage and horizontal gene transfer, the roots of the antibiotic multi-resistance problem. *Anim. Biotechnol.* **17**(2), 125–135 (2006)
31. Thomas, C.M., Nielsen, K.M.: Mechanisms of, and barriers to, horizontal gene transfer between bacteria. *Nat. Rev. Microbiol.* **3**, 711–721 (2005)
32. Volkmann H., et al.: Detection of clinically relevant antibiotic-resistant genes in municipal wastewater using real-time PCR (TaqMan). *J. Microbiol. Meth.* **56**, 277–286 (2004)
33. Walker, D., Fowler, T.: Annual Report of the Chief Medical Officer: Infections and the Rise of Antimicrobial Resistance, vol. 2 (2011)

Diagnosis of Skin Disease Based on Fingerprint

Selena Kurtić and Zvezdan Stojanović

Abstract

The main scientific goal of this paper is that on the basis of the collected photos, files and documents, we can make one large database that will help us successfully in future use in medical sciences (dermatology), for early detection and diagnosis of the patient's disease. In this research, we used techniques for fingerprint recognition. These techniques can be divided into three phases, pre-processing, extraction of minutiae and comparison of minutiae. Based on the theoretical expose that has been written and MATLAB code that performs all of these actions. With the help of MATLAB code we were able to make a comparison with the desired image of a fingerprint and get to know whether the test person has any of these skin diseases.

Keywords

Fingerprint • Fingerprint scanner • Skin disease • Dermatology

1 Introduction

Fingerprint recognition is a complex problem for identifying samples and designing the algorithm needed for extraction, matching and re-recognition. There is a misconception that automatic finger recognition has completely solved the problem because it was one of the first measurements used by the machine to solve the problem fifty years ago. On the

S. Kurtić (✉)
Internacionalna Poslovno-Informaciona Akademija, Tuzla, Bosnia and Herzegovina
e-mail: selena@ipi-akademija.ba

Z. Stojanović
Slobomir P Univerzitet, Doboj, Bosnia and Herzegovina
e-mail: zvezdan.stojanovic@spu.ba

Z. Stojanović
Evropski Univerzitet Brčko, Brčko, Bosnia and Herzegovina

contrary, fingerprint recognition is still a challenging and important problem of sample recognition.

The basic research methods to be used in the research are:

1. Analysis of the collection of existing literature on the topic of work (content analysis)
2. Analysis of sources of medical knowledge about skin diseases, which will be analyzed and consolidated into one whole and archive medical documents (General scientific methods: statistical, comparative)
3. Field work (photography, description of occurrence and process visible on patients)
4. A comparative analysis of all the mentioned data sources for harmonization and making relevant conclusions (General scientific methods: statistical, comparative)
5. A comprehensive synthesis of the studied material and the conversion of the archival image with the help of a Matlab program that will compile the desired scanned fingerprint to find out whether the investigated person has any of the aforementioned diseases.

2 Research Objectives

From this scientific goal comes the general social aim of the research. Medicine will advance, and speed and diagnosis costs as well as the speed of treatment and recovery of patients will accelerate. Ranks in the laboratories in which the analyzes were performed, based on the samples taken (blood, wound, tissue, etc.) would be reduced. Samples will be taken only for checking and accuracy—confirmation in cases where something suspicious is due to the urgency of treatment.

In the process of obtaining a fingerprint image, the skin texture on the finger is scanned. Skin is an outstanding organ in the body, which is able to perform various vital functions. It can be shaped in different shapes, stretched, and hardened.

There are many skin disorders, which can affect your palms and fingers. These diseases can be divided into two groups. In the first group, palms and fingers are mostly affected. In the second group, skin lesions may be diffuse, including wide areas. Skin diseases can also be distinguished by the type or localization of histopathological changes in the epidermis and dermis. In the further work, a description of the photographs together is followed. This clearly shows that skin diseases can cause many problems in the biometric system.

We got fingerprints with patients suffering from various skin disorders. For this study, it is also necessary to analyze the effect of skin disease on a particular fingerprinting method, considering the methods of obtaining it: A classic forensic fingerprinting method by using a dactyloscopy of ink and carton, purely by taking fingerprints by chemical processing fingerprinting using a special dactyloscopic paper and electronic stamping Finger (using a fingerprint scanner).

The most common skin diseases are psoriasis, atopic eczema, vulgaris and pulpitis sicca, so we used those images for further processing. The likelihood of other skin diseases is lower. However, the quality of other skin diseases we collected was not similar to these images. In most cases, these prints were almost without papillary lines (edges) or were not recognizable; that is, these prints are not suitable for further processing (detection of sample algorithms, for example, biometric patterns can not be detected for further processing and analysis).

3 Minutiae

A wide variety of systems requires reliable features of a validation scheme or identification of a person's identity. The aim of such programs is to provide the service to a legitimate user, not to anyone. Examples of these systems are secure access to buildings, computer systems, laptops, cell phones and ATMs.

In the world of computer security, biometrics refers to an authentication technique that relies on measurable physiological and individual features that can be automatically verified. In other words, everything that has unique personal attributes that can be used for personal identification purposes, including fingerprint, eye mesh, and voicemail.

4 Sample Sampling and Image Processing

In order to better analyze and recognize fingerprints, it is important that samples be taken as high as possible. Unspecified patterns may occur due to, for example, dry and cracked skin, or because the print lines are too shallow to obtain high-quality prints, so the print lines will be discontinued or will not be detected in the image.

There are various image enhancement methods to get the fingerprint lines as best as possible. The general image enhancement methods can be divided into pixel operations (e.g. negative images, histogram modeling, binary limitation, contrast stretching) and spatial operations (e.g. filtering, spatial removal, spatial averaging). To reduce the noise level in the image, which improves fingerprint detection, we use Gaussian blur filter.

$$Gx = 12 * \pi * \sigma^2 e^{-x^2/2\sigma^2} \quad (1)$$

In a two-dimensional space where x is the distance from the apical axis, y of the axis of the ordinates, and σ is the standard deviation of the Gauss distribution:

$$Gx, y = 12 * \pi * \sigma^2 e^{-x^2 + y^2/2\sigma^2} \quad (2)$$

Values $G(x, y)$ are located in concentric circles, with Gauss distribution from the center point. The values from that distribution make up the matrix with which we count the convolution with the image. The new value of each pixel in the picture is determined by the mean pixel values in its neighborhood using Gauss's distribution. The original pixel gains the highest value that is determined by the Gaussian function, and the adjacent lesser values increase their distance from the original. The filter result is a dim image (blurred) because the high frequency signals are muted (Figs. 1, 2 and 3).

Increasing the standard deviation will result in larger image sharpness and thicker edges.

To remove an unsharp masking image in the image, remove the low frequency component proportional to the non-sharp part of the image.

The filter result is a sharper image.

To convert the page image to a black and white picture, we use binary limitation. Image binarization is performed by selecting the threshold and if the pixel value in the image is smaller than that pixel gains the value of zero (black) otherwise it takes 255 (white). The threshold value can be

Fig. 1 The ideal print



Fig. 2 Realization of the process saved by column



Fig. 3 Realization of processes stored by columns



Fig. 4 Ideally sharpened and segmented image



determined by histogram. As the histogram of the image is bimodal, meaning that it has two bushes, the segmentation threshold is taken as the mean value (Fig. 4).

There are two main methods of recognizing fingerprints: recognition based on the minutia (local structure) and the recognition of the total sample (global structure).

Since fingerprints are viewed from the perspective of a computer in fact digital images, it is necessary to consider which parts of the system comprise a system for automated

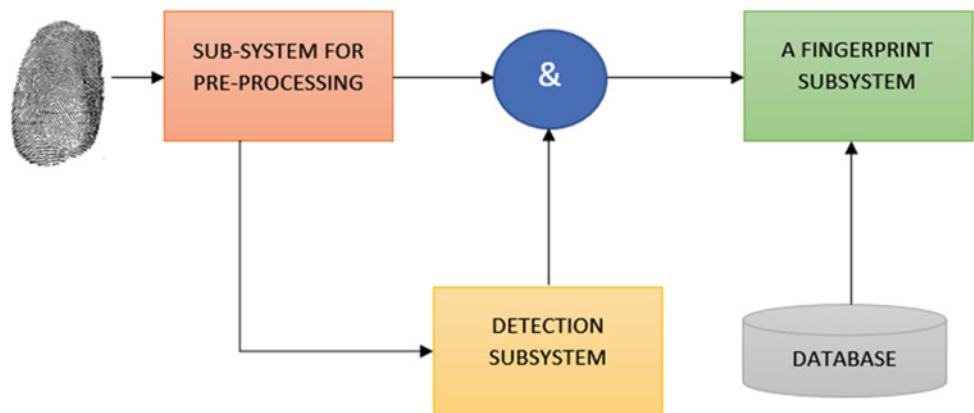
fingerprint processing. Such a system consists of the following three subsystems and is shown in Fig. 5.

1. Pre-processing subsystem—its task is to normalize the image by lighting, contrast and size, rotation of the print, and neutralizing the background. Preprocessing is performed prior to the fingerprint recognition itself.
2. The fingerprint subsystem shall be responsible for determining whether a particular presentation of data contains one or more prints and determining where exactly they are in the picture.
3. A subsystem for recognizing the print job—the task is to determine the identity of the person, i.e. to link the prints and names with an acceptable low level of incorrect identification of the person and with a great tolerance to various forms of one and the same print.

In addition to the aforementioned subsystems, there is a database in which fingerprints are stored on which recognition is made. Processing or recognition is done in a few steps:

1. Remove excessive information
2. Determining the main features
3. Comparison with the sample from the database (Fig. 5)

Fig. 5 Fingerprint recognition system



Fingers are subject to external influences such as environmental influences such as dirt, water, etc. These impacts have to be removed to make the papilla lines clean and well visible. It is therefore necessary to normalize an image by light, contrast, and size, rotation of the print, and neutralize the background for the entire subsystem for preprocessing. Also used are so-called filament filters that reject all lines in the image that are not in the direction of papillary lines. The last stage before determining the characteristic points is tapering. Thinning reduces the spread of the papillary line to one pixel. This reduces excessive information without changing the fingerprint curvature. The phase of determining the characteristic points is followed by determining the endings of the line and their branching (in the minutiae). It is necessary to take into account that there are some characteristic points that arise as a result of external influences during the fingerprinting process. They are eliminated using the experience gained on the basis of previous inputs. After this elimination follows the determination of attributes for each characteristic point, which implies information on the end of the papillary line or branch type, its location (x, y), and the direction of the papillary line. The last step is to

create a graph of characteristic points. The number of characteristic points generally ranges from 10 to 100 points.

5 Fingerprint Recognition System

The fingerprint recognition system consists of a device, a minutiae extractor, and a detector (Fig. 6).

The aim of designing a renaming system is to work in the worst conditions and get the best results.

6 Exposition

In the pictures (Figs. 7 and 9), shown below, we can see how the minutiae of the original fingerprint image with a diagnosed skin disease is pronounced. We will see two cases.

1. First, we look at the case when we do not match the minutiae, or when we searched the fingerprint database with a single skin disease and we did not match. None of the patients in our database have any such illness (Fig. 8).

Fig. 6 Simplified fingerprint recognition system

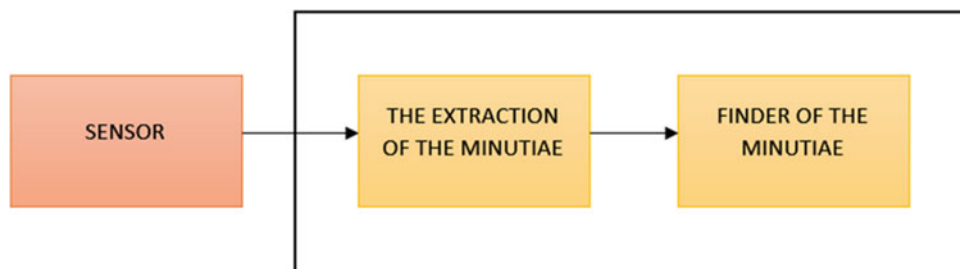
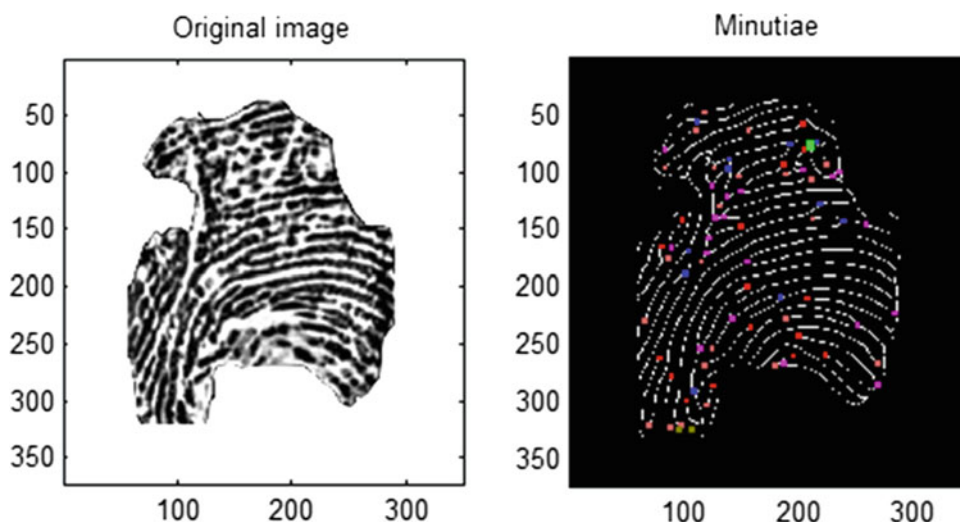


Fig. 7 Minutiae of the original fingerprint image with a diagnosed skin disease



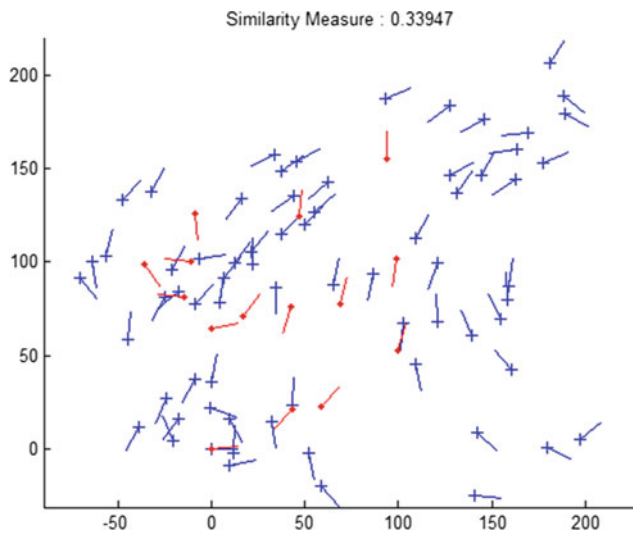


Fig. 8 Similarity measure: 0.33947

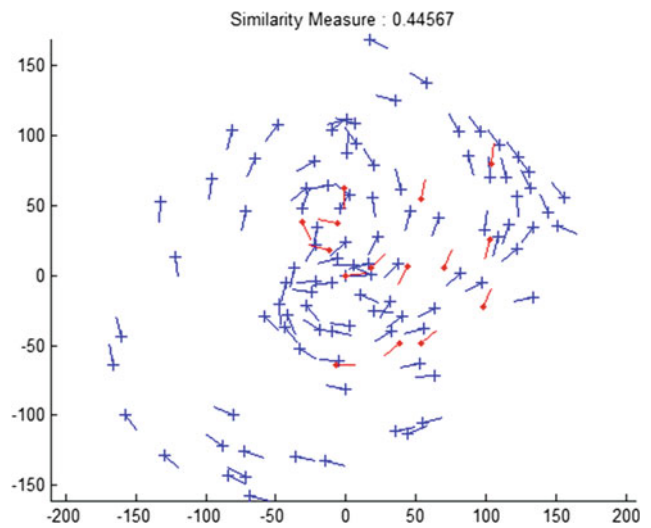


Fig. 10 Similarity measure: 0.44567

In this case we compared a fingerprint from a person with mild psoriasis.

- The second case we have observed is when we have a match between the minutiae, or when we have a fingerprint scan of the warts (verruca vulgaris) found on several of our patients from the fingerprint database (Figs. 9 and 10).

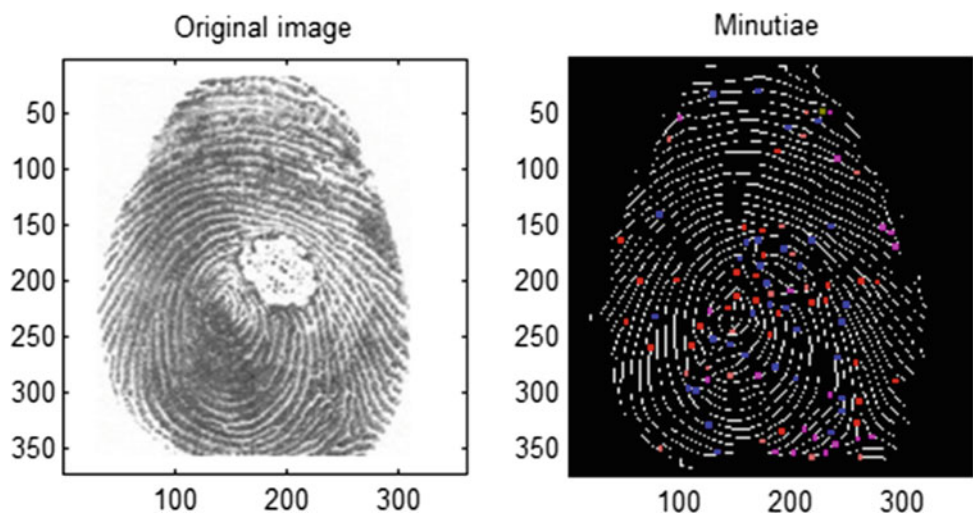
7 Conclusion

In this paper, we have come up with the most common skin diseases most commonly encountered in medical institutions for treating them. From previous practice, we have found

that the process of diagnosing some skin disease is very long, often erroneous. During this scientific-research work, we have come to the conclusion that through the proper classification, selection, analysis by comparison, the image of skin diseases, which we covered by the project, can be very rapid diagnosis of skin disease in patients. With very little resources, we have reduced the cost of diagnosing skin diseases (it is not necessary to take skin samples and send to pathology to diagnose the disease). We used combination of methods and if greater certainty is needed in determining the diagnosis, one method can be checked with the other.

A MATLAB code has been written that tracks all the mentioned fingerprint recognition steps and for checking the print match. This is how we can show how easy it is to understand the fingerprint processing and to demonstrate the key problem of fingerprinting.

Fig. 9 Minutiae of the original fingerprint image with a diagnosed skin disease



References

1. Lee, H., Kim, E., Park, M.: A genetic feature weighting scheme for pattern recognition. *Integr. Comput. Aided Eng.* **14**(2), 161–171 (2007)
2. Mohammed, A.A., Minhas, R., Wu, Q.M.J., Sid-Ahmed, M.A.: An efficient fingerprint image compression technique based on wave atoms decomposition and multistage vector quantization. *Integr. Comput. Aided Eng.* **17**(1), 29–40 (2010)
3. Maltoni, D., Maio, D., Jain, A., Prabhakar, S.: *Handbook of Fingerprint Recognition*, 2nd edn (2009)
4. Sambasiva Rao, G., NagaRaju, C., Reddy, L.S.S., Prasad, E.V.: A novel fingerprints identification system based on the edge detection. *Int. J. Comput. Sci. Netw. Secur.* **8**, 394–397 (2008)
5. Girgisa, M.R., Sewisyb, A.A., Mansour, R.F.: Employing generic algorithms for precise fingerprint matching based on line extraction. *Graph. Vis. Image Process. J.* **7**, 51–59 (2007)
6. Raju Sonavane, Sawant, B.S.: Noisy fingerprint image enhancement technique for image analysis: a structure similarity measure approach. *J. Comput. Sci. Netw. Secur.* **7**(9), 225–230 (2007)
7. Wei, L.: Fingerprint classification using singularities detection. *Int. J. Math. Comput. Simul.* **2**(2), 158–162 (2008)
8. Tong, X., Liu, S., Huang, J., Tang, X.: Local relative location error descriptor-based fingerprint minutiae matching. *J. Pattern Recognit. Lett.* **29**, 286–294 (2008)
9. Ji, L., Yi, Z.: Fingerprint orientation field estimation using ridge protection. *J. Pattern Recognit.* **41**, 1491–1503 (2008)
10. Jain, A.K.: *Fundamentals of Digital Image Processing*. Prentice Hall, Englewood Cliffs (1989)
11. Sonka, M., Hlavac, V., Boyle, R.: *Image Processing, Analysis and Machine Vision*. Brooks Cole (1998)
12. Gonzalez, R., Woods, R.: *Digital Image Processing*. Addison Wesley Publishing (2002)
13. Aushermann, D.A., Fairchild, R.C., Moyers, R.E., Hall, W.D., Mitchel, R.H.: A proposed method for the analysis of dermatoglyphics patterns. *Proc. SPIE* **40** (1973)
14. Babler, W.J.: Embryologic development of epidermal ridges and their configuration. *Birth Defects Orig. Art. Ser.* **27**(2) (1991)
15. Bazen, A.M., Gerez, S.H.: Elastic minutiae matching by means of thin-plate spline models. In: *Proceedings of International Conference on Pattern Recognition* (16th), vol. 2, pp. 985–988 (2002)

Epigenetics: How Does It Affect Cancer?

Letícia Vieira da Silva, Bruno Oliveira Rezende,
Hiara Lopes Pinheiro Teixeira, Bianca da Silva Duque,
and Gisele Aparecida Fófano

Abstract

Purpose: Cancer may have several pathways of formation, including changes in genes. Thus, this article points out the genes related to specific and nonspecific types of tumors, as well as the importance of this data for the health care area. **Methodology:** This is a Literature Review made from the PubMed database. The research randomly used 200 articles from 2013 to 2018 with the keywords “epigenetics” and “cancer”, of which only 24 were selected since the others did not present the description of the gene related to the tumor. **Results:** 25 articles were selected, most of them focused on hepatocellular carcinoma. Among the tumors derived from systems, those from the gastrointestinal tract were more likely to be studied related to genes. It might be inferred that certain genes, such as HOTAIR and ASXL-1, appear in the table more than once, which shows that these molecules have carcinogenic abilities in any tissue. **Conclusion:** The epigenetic field is responsible for every advance on medical pathways to treat and discover cancer. This knowledge of cancer origin might lead to the creation of most effective drugs and the genes showed on this review may be specific targets for medicines in the future.

Keywords

Genetic alteration • Tumor origin • Cancer diagnosis • Oncogenetic

1 Introduction

By 2017, neoplasms were responsible for more than 9 million deaths worldwide [1]. The genesis may be from intrinsic DNA alterations, such as methylation, shade modification, nucleosome remodeling and RNA mediated changes [2].

Thus, epigenetic studies rise, which aim not only to discover new therapeutic targets in the pathways of neoplasia formation, but also to improve the effectiveness that already have [3]. In addition, they offer new ways to analyze the prognosis of the disease, which help in determining when the treatment should be aggressive [4].

Every change in DNA is called Epigenetic, which can become hereditary, responsible for modifying the activity and expression of genes. These changes might happen normally, through aging or by outwards non-natural methods, such as stress. However, when the variations exceed the limits supported by the cell, then the neoplasms are born [4].

In view of the above, this article aims to show the main changes associated with cancer, according to studies found in literature and, when available, the specific genes associated to disease and the relevancy of this information to improve cancer treatment.

2 Methodology

This article is an integrative review. Articles were used from the PubMed database using the descriptors “epigenetics” and “cancer”. The inclusion criteria were papers that described types or cancer spots and had the gene identification, besides the keywords in their abstract or title.

The search of “epigenetics” and “cancer” resulted on 27,672 articles. Articles from 2013 to 2018 were included using the “5-year”, filter available on the site itself. This addition decreases the number to 14,231. 200 articles were consulted and only 24 could be used in this research.

L. V. da Silva (✉) · B. O. Rezende · H. L. P. Teixeira ·
B. da Silva Duque · G. A. Fófano
Medicine Department, Faculdade Governador Ozanam Coelho,
Ubatuba, Brazil
e-mail: leticiavieiradasilva@gmail.com

3 Results

See Table 1.

4 Discussion

4.1 Epigenetic and Its Modulating Factors

Initially, epigenetics was presented as an independent cellular change of DNA but linked to the phenotype. Nowadays, the meaning of DNA modulation is controlled by

diverse events [2]. So, it is an ambiguous concept by itself because what is restricted to the physical aspects is not passed to their heirs, but what changes DNA usually takes years or generations to manifest. In this sense, epigenetics, in this article, refers to outward factors able to alter the expression and the genes, leaving the wider concept.

To understand the genetic alterations, it is necessary to understand what causes or avoids them. Among the reasons, they may include chemical substances such as pesticides, industrial products [27], while in the protection field there is Resveratrol, which is able to prevent the expression of genes that cause lung cancer [12]. Knowing that many of the

Table 1 Epigenetic modifications related to cancer

Author	Gene	Cancer type
Markman et al. [5]	BRD4	Mucoepidermoid carcinoma
Haifeng et al. [6]	EPHB2; EPHB4	Colorectal cancer
Lascano et al. [7]	DNMT; HDAC inhibitors	Tumors
Cheng [8]	CIMP	Hepatocellular carcinoma
Taheri et al. [9]	Yamanaka factors (Oct3/4, Klf-4, Sox-2, c-Myc)	Melanoma
Lin et al. [10]	CDC25A/E2F7/CCNE1	Hepatocellular carcinoma
Huliák et al. [11]	Myofibroblasts, H3K9, H4K16	Gastrointestinal tumors
Fudhaili et al. [12]	Protein 36	Non-small cell lung cancer
Zhang et al. [13]	Zeb1	Tumors
Law et al. [14]	E-Cadherin, FBP1, IGFBP3, XAF1 e CREB3L3	Hepatocellular carcinoma
Asada and Kitamura [15]	ASXL1	Myeloid neoplasm
Indraccolo et al. [16]	Mismatch repair (MMR)	Glioblastoma
He et al. [17]	APC2	Colorectal cancer
Lu et al. [18]	Histone H3; Lysin 4; WDR5	Cancer of bladder, colon, breast, prostate, stomach; pancreatic ductal adenocarcinoma, neuroblastoma ...
Merino et al. [19]	DHRS3	Breast cancer
Chin et al. [20]	PD-L1 Inc RNA HOTAIR	Glioblastoma multiforme
Beggs et al. [21]	SFRP1, SFRP2, SRP4, SRP5, WIF1, TUBB6, SOX7, APC1A, APC2, MINT1, RUNX3	Colitis malignition
Ryser et al. [22]	IS, HLA-A, HLA-B, HLA-C, ITH	Genomic intratumoral heterogeneity (ITH)
Mochizuki et al. [23]	EZH2	Neck tumors
Li and Luo [24]	DNMT1, DNMT3A, HDAC1, EZH2, HOTAIR	Leukemia
Stelloo et al. [25]	H3K27ac, H3K4me3, H3K27me3	Prostate cancer
Tegeder et al. [26]	SMARCB1/INI1	Teratoma
Chi et al. [27]	H3K4me2 chromatin	Endometrium cancer
Inoue et al. [28]	ASXL1	Myeloid neoplasm

Authorship: The authors, 2018

Subtitles: The word "Tumors" was used for genetic changes that can lead to any carcinogenesis in that region, with that specific cell type contained in the table

changes will become hereditary [27] one must understand epigenetics as something inserted day-to-day and not as a distant field of research.

Environmental factors might also alter the expression of cell molecules and have epigenetic changes to occur. Exposure to artificial light during the night, for example, deregulates the melatonin cycle and causes loss of its protective properties, thereby increasing the possibility of prostate and breast cancer [29], i.e., this exposure might act as a trigger for gene modification, described by Stello et al. [25], in the molecules H3K27ac, H3K4me3, H3K27me3.

The alterations may not only be mediated by extrinsic controllable factors, but also be naturally occurring over time. It is called the “molecular clock hypotheses”, and this explains that all the cells resemble the original ones. However, they become polymorphic over time, moving away from the original lineage, and this is mainly due to errors in DNA methylation after replication [22].

Therefore, if the cells proliferate a lot or substances act on them, the greater the chance of errors to occur, the cells might move away from the maternal phenotype and, therefore, the risk of becoming malignant causing cancer may increase. An interesting aspect among the results was the appearance of malignancy of colitis related to specific cellular alterations. According to Beggs et al. [21], these occur due to the presence of cytokines in the environment inflamed by intestinal diseases. Another aspect that may be emphasized is that the inflammation leads to tissue destruction, which forces it to enter into a repair process and may contribute more to carcinogenesis.

Among the types of cancer more commonly found in this study individually, hepatocellular carcinoma received greater attention between the articles surveyed. In 2017, there were almost 820,000 deaths from liver cancer [1] regardless of the reason for its emergence. This type of cancer is just less deadly than cancers of the gastrointestinal tract and respiratory system [1]. When cancers are separated by systems, the gastrointestinal presents more studies, and the epidemiology justifies it, once this system have the highest number of cancers with high mortality.

4.2 Details of Epigenetics

The study of epigenetics should be taken carefully since it is possible to find dominant processes for each of the tumors, carcinogenesis and epigenetics itself—they are not linear and unique processes. The gene, ASXL1, for instance, is more found than once in the table, being associated with myeloid neoplasia [15, 28], although it is not the only target that modulates this disease, once DNMT1, DNMT3A, HDAC1, EZH2, and HOTAIR are also capable of altering it and induce hematopoietic cell carcinogenesis [24]. HOTAIR

prefers chronic myeloid leukemia and it states, although it is not restricted to these [24], that ASXL1 does not appear to have a preferred pattern [28]. Thus, there are different alterations which may generate similar clinical problems and, in the analysis of the Myeloid Syndromes, they should be investigated.

Observing the table, it is noticeable that different sites of alterations might lead to the same outcome, and this is not limited to hematopoietic neoplasms. Even with this vast knowledge, research should not be restricted to changes already known to be linked to the patient’s specific types of neoplasia. One example would be HOTAIR itself, studied by Li and Luo [24], which also relates to non-small cell lung cancer and breast cancer.

In addition, the same pathway, when activated in different organs, may lead to other carcinogenic processes. As described by Inoue et al. [28], the ASXL1 gene is one of those responsible for recruiting and modulating H3K4, influencing some carcinogenesis processes. Therefore, the affected tissues can lead to different types of cancer, while ASXL1 is related to neoplasia of the sanguine system. The portion activated by it is also involved in prostate and endometrial cancer, as shown in Table 1.

However, it is an infeasible search for all genes indiscriminately. Then, research demonstrating the main responsible for neoplasia should be used to define the most common alterations in order to be applied as prophylaxis, diagnostic confirmation, follow-up therapeutic and prognostic analysis. In the case of non-confirmation with these ones, the researcher should proceed to larger processes, as a second follow-up line, such as HOTAIR.

4.3 Epigenetics as Prophylaxis

Epigenetic changes, such as the ones described in the table, might be transformed into useful biomarkers for both diagnosis and prophylaxis. This, according to Beggs et al. [21], when added to endoscopy, may help in the diagnosis of those at higher risk of developing neoplasia. For this, methylation would be the best marker, especially for neoplasia derived from the inflammatory process.

4.4 Epigenetics as Diagnosis and Prognosis

Levels of genetic or protein expression may indicate the presence or progression of a disease. Breast cancer, for example, begins with a reduction of the DHRS3 protein and, in the metastatic form, has lower levels [19], demonstrating its function as a marker for both progression and diagnosis of the cancer, since it may be done by analyzing the deviation of these protein levels.

WDR5 might be expressed in prostate cancer, and in this case, it indicates the feature of resistance to castration and proliferates quickly. It may also be presented in neoplasia of bladder, colon and stomach; through the induction of the MYC oncoprotein, it might lead to breast cancer and neuroblastoma, and all with a low survival rate [18]. Thus, it is important to use this marker, as it determines a more aggressive treatment than the non-carriers of this mutation.

4.5 Epigenetics as Therapy

Drugs, such as PUGNAc, O-GlcNAcase inhibitor, are evidence of the advancement in the fields of epigenetics. This drug, used in mice, was able to regulate the expression of ASXL1, stabilizing the protein of the same name and was able to increase the survival of the transplanted mice [28].

Moreover, according to Chin et al. [20], changes induced by epigenetics are potentially reversible. Thus, 5-Azacytidine, an epigenetic inhibitor drug that prevents DNA methylation, proves to be useful for patients with neoplasia in the hematopoietic system, since this is the most frequent alteration and, ultimately, more active genes. In addition, cancer patients such as prostate, breast and lung cancer may benefit from Vorinostat, which pre-date histone deacetylation [20]. Because they have the same pathway of Genesis, possibly those with endometrial cancer will also benefit from this drug.

Regarding breast cancer, something even more specific would be the combination of entinostat (E), ATRA (A) and doxorubicin (D) (EAD), having cells to become more differentiated and tumors reduced in size. However, the current finding is that AD is the best way to increase the expression of the DHRS3 gene, which is responsible for decreasing cancer growth [19]. For the definition of up-to-date treatments, epigenetics emerges again, as it leads to the discovery of protein and genetic pathways that are altered by the carcinogenic process and which return to normality by the use of the drug, functioning as a double-pathway.

5 Conclusion

The epigenetic field is responsible for many advances on medical pathways to treat and discover cancer. There are a lot of genes in the human body and uncountable cells, all of them can suffer from chemical products, light or aging and start a carcinomatous process. This knowledge of cancer origin may lead to most effective drugs and the genes showed on this review might be specific targets for them in the future.

References

1. Global Health Data Exchange [Homepage on internet]. GBD Results Tool [access at 16 Dec 2018]. Available on: <http://ghdx.healthdata.org/gbd-results-tool>
2. Dawson, M.A., Kouzarides, T.: Cancer epigenetics: from mechanism to therapy. *Cell* **150**(1), 12–27 (2012)
3. Chiappinelli, K.B., Zahnow, C.A., Ahuja, N., Baylin, S.B.: Combining epigenetic and immune therapy to combat cancer. *Cancer Res.* **76**(7), 1683–1689 (2016)
4. Ohm, J.E.: Environmental exposures, the epigenome, and African American women's health. *J. Urban Health.* 1–7 (2018)
5. Markman, R.L., Webber, L.P., Nascimento, Filho, C.H.V., et al.: Interfering with bromodomain epigenome readers as therapeutic option in mucoepidermoid carcinoma. *Cell Oncol. (Dordr).* 1–13 (2018)
6. Haifeng, L., Xingfang, J., Ning, S., et al.: Notch signaling promotes serrated neoplasia pathway in colorectal cancer through epigenetic modification of EPHB2 and EPHB4. *Cancer. Manag. Res.* **10**, 6129–6141 (2018)
7. Lascano, S., Lopez, M., Arimondo, P.B.: Natural products and chemical biology tools: alternatives to target epigenetic mechanisms in cancers. *Chem. Rec.* **18**(12), 1854–1876 (2018)
8. Gan-xun, L., Ze-yang, D., Yu-wei, W., et al.: Integrative analysis of DNA methylation and gene expression identify a six epigenetic driver signature for predicting prognosis in hepatocellular carcinoma. *J. Cell. Physiol.* 1–9 (2018)
9. Taheri, H., Cagin, U., Yilmazer, A.: Reprogramming of human melanocytes and melanoma cells with yamanaka factors. In: *Methods in Molecular Biology* vol 1916, 249–261 (2018)
10. Lin, C., Yuan, G., Hu, Z., et al.: Bioinformatics analysis of the interactions among lncRNA, miRNA and mRNA expression, genetic mutations and epigenetic modifications in hepatocellular carcinoma. *Mol. Med. Rep.* 1356–1364 (2018)
11. Huliák, I., Bodai, L., Czepán, M., et al.: Genetic, epigenetic and transcriptional comparison of esophagus tumor associated and adjacent normal myofibroblasts. *Oncol. Rep.* [on internet] [access at 17 Dec 2018]; **41**(2), 839–52 (2018). Available at: <http://www.spandidos-publications.com/or/41/2/839>
12. Fudhaili, A., Yoon, N.A., Kang, S., et al.: Resveratrol epigenetically regulates the expression of zinc finger protein 36 in non small cell lung cancer cell lines. *Oncol. Rep.* [on internet] [access at 2018 Dec 17]; **41**(2), 1377–1386 (2018). Available at: <https://www.spandidos-publications.com/or/41/2/1377>
13. Zhang, Y., Xu, L., Li, A., Han, X.: The roles of ZEB1 in tumorigenic progression and epigenetic modifications. *Biomed. Pharmacother.* **110**, 400–408 (2018)
14. Law, C.T., Wei, L., Tsang, F.H., et al.: HELLS regulates chromatin remodeling and epigenetic silencing of multiple tumor suppressor genes in human hepatocellular carcinoma. *Hepatology* [on internet] [access at 2018 Dec 14] (2018). Available at: <https://aasldpubs.onlinelibrary.wiley.com/doi/pdf/10.1002/hep.30414>
15. Asada, S., Kitamura, T.: Aberrant histone modifications induced by mutant ASXL1 in myeloid neoplasms. *Int. J. Hematol.* 1–8 (2018)
16. Indraccolo, S., Lombardi, G., Fassan, M., et al.: Genetic, epigenetic and immunologic profiling of MMR-deficient relapsed glioblastoma. *Clin. Cancer Res.* 1892 (2018)
17. He, Y., Sun, L.Y., Wang, J., et al.: Hypermethylation of APC2 Is a predictive epigenetic biomarker for Chinese colorectal cancer. *Dis. Markers.* 8619462 (2018)

18. Lu, K., Tao, H., Si, X., Chen, Q.: The histone H3 lysine 4 presenter WDR5 as an oncogenic protein and novel epigenetic target in cancer. *Front. Oncol.* **8**, 502 (2018)
19. Merino, V.F., Cho, S., Nguyen, N., et al.: Induction of cell cycle arrest and inflammatory genes by combined treatment with epigenetic, differentiating, and chemotherapeutic agents in triple-negative breast cancer. *Breast Cancer Res.* **20**, 145 (2018)
20. Chin, C., Lunking, E.S., de la Fuente, M., Ayadi, N.G.: Immunotherapy and epigenetic pathway modulation in glioblastoma multiforme. *Front Oncol.* **8**, 521 (2018)
21. Beggs, A.D., Mehta, S., Deeks, J.J., et al.: Validation of epigenetic markers to identify colitis associated cancer: results of module 1 of the ENDCAP-C study. *EBioMed.* (2018) pii: S2352-3964(18)30538-3
22. Ryser, M.D., Yu, M., Grady, W., Siegmund, K., Shibata, D.: Epigenetic heterogeneity in human colorectal tumors reveals preferential conservation and evidence of immune surveillance. *Sci. Rep.* **8**(1), 17292 (2018)
23. Mochizuki, D., Misawa, Y., Kawasaki, H., et al.: Aberrant epigenetic regulation in head and neck cancer due to distinct EZH2 overexpression and dna hypermethylation. *Int. J. Mol. Sci.* **19**(12), 3707 (2018)
24. Li, Z., Luo, J.: Epigenetic regulation of HOTAIR in advanced chronic myeloid leukemia. *Cancer Manag. Res.* **10**, 5349–5362 (2018)
25. Stelloo, S., Nevedomskaya, E., Kim, Y., et al.: Integrative epigenetic taxonomy of primary prostate cancer. *Nat. Commun.* **9**(1), 4900 (2018)
26. Tegeder, I., Thiel, K., Erkek, S., et al.: Functional relevance of genes predicted to be affected by epigenetic alterations in atypical teratoid/rhabdoid tumors. *J. Neuro-Oncol.* 1–13 (2018)
27. Chi, S., Liu, Y., Zhou, X., et al.: Knockdown of long non-coding HOTAIR enhances the sensitivity to progesterone in endometrial cancer by epigenetic regulation of progesterone receptor isoform B. *Cancer Chemother. Pharmacol.* 1–11 (2018)
28. Inoue, D., Fujino, T., Kitamura, T.: ASXL1 as a critical regulator of epigenetic marks and therapeutic potential of mutated cells. *Oncotarget.* **9**(81), 35203–35204 (2018)
29. Zubidat, A.E., Fares, B., Fares, F., Haim, A.: Artificial light at night of different spectral compositions differentially affects tumor growth in mice: interaction with melatonin and epigenetic pathways. *Cancer Control.* **25**(1), 1073274818812908 (2018)

Screening of Heavy Metal Occurrence in Edible Plants from Bosnian Market

Aida Sapcanin, Aida Hasanovic, Mirsada Salihovic, Ekrem Pehlic, and Selma Špirtović-Halilović

Abstract

Occurrence of heavy metals in edible plants cannot be underestimated as these foodstuffs are important components of human diet. Intake of heavy metal-contaminated edible plants may pose a risk to the human health. The presence of heavy metals such as As, Cd, Pb, Zn, Co, Fe and Se was determined by using an atomic absorption spectrophotometry (AAS) method in the samples of the following edible plants obtained from the Bosnian markets: 1—*Cichorium intybus* L. var. *foliosum* Hegi, 2—*Allium schoenoprasum* L., 3—*Allium porrum*, 4—*Plantago major*, 5—*Cucurbita maxima*, 6—*Asparagus officinalis*, 7—*Brassica oleracea* var. *Sabauda*, 8—*Beta vulgaris*, 9—*Brassica oleracea* var. *Acephala*, 10—*Solanum lycopersicum* var. *Cerasiforme*, 11—*Cynara scolymus*, 12—*Brassica rapa* subsp. *Rapa*, 13—*Plantago lanceolata*, 14—*Raphanus sativus*, 15—*Eruca sativa*, 16—*Valerianella locusta*, 17—*Beta vulgaris* subsp. *Vulgaris*, 18—*Atriplex hortensis*, 19—*Anthyllis vulneraria*, 20—*Brassica oleracea* *Gongylodes*, 21—*Brassica oleracea* var. *Italica*, 22—*Capsicum frutescens*, 23—*Physalis peruviana*, 24—*Phoenix dactylifera*, 25—*Aronia melanocarpa*, 26—*Prunus cerasus*, 27—*Rubus fruticosus*, 28—*Rubus idaeus*, 29—*Prunus domestica*, 30—*Vitis vinifera* cvs. *Cardinal*, 31—*Ficus*, 32—*Vaccinium myrtillus*, 33—*Vitis vinifera*, 34—*Mespilus germanica*, 35—*Vaccinium vitis-idaea*, 36—*Prunus domestica*, 37—*Juniperus communis*, 38—*Ocimum basilicum*, 39—

Rosmarinus officinalis, 40—*Achillea millefolium*, 41—*Salvia officinalis*, 42—*Ocimum basilicum Purpurascens*, 43—*Foeniculum vulgare*, 44—*Hypericum perforatum* and 45—*Valerianella locusta*. Essential elements, Zn, Fe, Co and Se were detected in the examined plant samples, while toxic heavy metals Pb and Cd were detected in some plants. Average consumption of these plants can provide the recommended daily intake of the essential nutrients and the consumption of such plants will not expose the consumer to the effects of toxic elements. However, there is a constant need to have routine monitoring of occurrence of potentially toxic elements in edible plant material in order to prevent possible heavy metal poisoning in long-term consumption of plants which contain such elements even only in traces.

Keywords

Edible plants • Essential elements • Toxic elements • Healthy diet • Food safety

1 Introduction

Contamination of different species of edible plants with heavy metals must not be underestimated as plants represent a very important component of human diet. Food safety is a global concern that covers a variety of different areas of everyday life. Edible plants are a source of vitamins, minerals and fibre and their antioxidant properties are also beneficial for human body. For this reason, intake of plant-based food contaminated with heavy metals can contribute to development of health-related risks in child and adult populations. Furthermore, food quality control is generally concerned with the occurrence of heavy metal contamination [1–3]. International guidelines for food quality control have lowered the threshold for maximum quantity of heavy metal allowance in food. It has been done due to increased threats caused by presence of these metals

A. Sapcanin (✉) · M. Salihovic · S. Špirtović-Halilović
Department of Natural Science in Pharmacy, Faculty of Pharmacy,
University of Sarajevo, Zmaja od Bosne 8, 71 000 Sarajevo,
Bosnia and Herzegovina
e-mail: ida@bih.net.ba

A. Hasanovic
Faculty of Medicine, University of Sarajevo, Cekalusa 90, 71 000
Sarajevo, Bosnia and Herzegovina

E. Pehlic
Faculty of Biotechnical Sciences, University of Bihac, Luke
Marjanovića bb, 77 000 Bihac, Bosnia and Herzegovina

in human diet and their contribution to food contamination [2]. Plants absorb heavy metals from the soil or through their exposure to polluted air [4–9]. Different studies have shown that heavy metals represent one of the major contaminating agents in fruit and vegetables [1, 7–13]. Heavy metals can accumulate on plant surfaces, which can occur either from the traffic emission of polluting gases, or the pollutants are transmitted through the air during plant growth, transport, or placement of plant products in open markets [5]. Long-term consumption of heavy metals through food chain inevitably leads to chronic accumulation of these metals in kidneys and liver, causing disorder in various biochemical processes which, consequently, leads to cardiovascular, neurological or bone diseases [14–16]. Therefore, there is a continuous need to have routine monitoring of occurrence of potentially toxic elements in edible plant material so that any possible heavy metal poisoning occurring after long-term consumption of plants which contain such elements even only in traces can be prevented.

2 Materials and Methods

2.1 Collection of Samples and Preparation for Further Analysis

For the purpose of the analysis of the occurrence of essential and toxic heavy metals in edible plants, samples have been collected from the Bosnian-Herzegovinan market (origin: ecofarms, or foreign commercial suppliers). The following edible plants were analysed: 1—*Cichorium intybus* L. var. *foliosum* Hegi, 2—*Allium schoenoprasum* L., 3—*Allium porrum*, 4—*Plantago major*, 5—*Cucurbita maxima*, 6—*Asparagus officinalis*, 7—*Brassica oleracea* var. *Sabauda*, 8—*Beta vulgaris*, 9—*Brassica oleracea* var. *Acephala*, 10—*Solanum lycopersicum* var. *Cerasiforme*, 11—*Cynara scolymus*, 12—*Brassica rapa* subsp. *Rapa*, 13—*Plantago lanceolata*, 14—*Raphanus sativus*, 15—*Eruca sativa*, 16—*Valerianella locusta*, 17—*Beta vulgaris* subsp. *Vulgaris*, 18—*Atriplex hortensis*, 19—*Anthyllis vulneraria*, 20—*Brassica oleracea* *Gongylodes*, 21—*Brassica oleracea* var. *Italica*, 22—*Capsicum frutescens*, 23—*Physalis peruviana*, 24—*Phoenix dactylifera*, 25—*Aronia melanocarpa*, 26—*Prunus cerasus*, 27—*Rubus fruticosus*, 28—*Rubus idaeus*, 29—*Prunus domestica*, 30—*Vitis vinifera* cvs. *Cardinal*, 31—*Ficus*, 32—*Vaccinium myrtillus*, 33—*Vitis vinifera*, 34—*Mespilus germanica*, 35—*Vaccinium vitis-idaea*, 36—*Prunus domestica*, 37—*Juniperus communis*, 38—*Ocimum basilicum*, 39—*Rosmarinus officinalis*, 40—*Achillea millefolium*, 41—*Salvia officinalis*, 42—*Ocimum basilicum Purpurascens*, 43—*Foeniculum vulgare*, 44—*Hypericum*

perforatum and 45—*Valerianella locusta*. The samples were collected into polyethylene bags previously decontaminated with distilled water, and then immediately brought to the laboratory. The samples were cut into smaller pieces and dried in the oven at 80 °C and then powdered in the mortar. The dried powdered samples were kept in closed glass containers at room temperature until further analysis.

2.2 Preparation of Samples for the AAS Analysis

About 5 g of dried powdered sample was blended with 23 mL of 6M HNO₃ and kept at 80 °C for about 8 h until the process of absorption ended. Then, the sample was cooled down to room temperature, filtered through Whatman filter paper and dissolved in a normal container of 25 mL using de-ionised water filled up to the level [17]. The sample was then analysed using the method of an atomic absorption spectrophotometry (Perkin Elmer A 800) to determine contents of Zn, Fe, Co, Se, Cd, Pb and As.

3 Results and Discussion

The analysis demonstrated the heavy metals capacity for bioabsorption and bioaccumulation. Absorption and accumulation of different heavy metals in plants depend on bioavailability and contents of metals in the soil, on the genetic characteristics of the plant, and on other environmental factors. Table 1 shows the content of essential elements Zn, Fe, Co and Se in the analysed plant extracts.

Zinc content in the analysed edible plants ranged from 0.001 to 0.062 mg/L; iron ranged from 0.001 to 0.188 mg/L; cobalt ranged from 0.005 to 0.105 mg/L; and selenium ranged from 0.200 to 14.124 mg/L. The highest level of iron and selenium was registered in the plant *Ocimum basilicum*; the highest level of cobalt was registered in the plant *Ocimum basilicum Purpurascens*, and the highest level of zinc was registered in the plant *Plantago lanceolata*. The aforementioned plants were obtained from eco-farms. The edible plants investigated in this study were found to contain adequate concentrations of essential element nutrients necessary for proper body development.

Table 2 shows the content of the toxic heavy metals As, Pb and Cd in plant extracts.

The content of cadmium was detected in *Physalis peruviana*, *Brassica oleracea* var. *Italica*, *Phoenix dactylifera*, *Foeniculum vulgare* and *Valerianella locusta* plants, while the highest content of lead was detected in the plant *Hypericum perforatum*. The aforementioned plants were obtained from foreign commercial suppliers. Cadmium is

Table 1 Content (mg/L) of essential heavy metals Zn, Fe, Co i Se in plant extracts

Plant sample	Latin name	Zn (mg/L)	Fe (mg/L)	Co (mg/L)	Se (mg/L)
1.	<i>Cichorium intybus</i> L. var. <i>foliosum</i> Hegi	0.009	0.014	0.009	1.052
2.	<i>Allium schoenoprasum</i> L.	0.024	0.016	0.015	1.101
3.	<i>Allium porrum</i>	0.007	0.011	0.009	0.998
4.	<i>Plantago major</i>	0.015	0.019	0.010	0.982
5.	<i>Cucurbita maxima</i>	0.008	0.001	0.009	1.023
6.	<i>Asparagus officinalis</i>	0.023	<0.001	0.010	1.316
7.	<i>Brassica oleracea</i> var. <i>Sabauda</i>	0.012	<0.001	0.007	1.244
8.	<i>Beta vulgaris</i>	0.011	0.022	0.007	1.111
9.	<i>Brassica oleracea</i> var. <i>Acephala</i>	0.012	0.004	0.012	1.560
10.	<i>Solanum lycopersicum</i> var. <i>Cerasiforme</i>	0.006	<0.001	0.006	1.076
11.	<i>Cynara scolymus</i>	0.006	<0.001	0.005	0.990
12.	<i>Brassica rapa</i> subsp. <i>Rapa</i>	0.011	0.004	0.015	1.453
13.	<i>Plantago lanceolata</i>	0.062	0.036	0.081	7.379
14.	<i>Eruca sativa</i>	0.008	<0.001	0.017	1.639
15.	<i>Valerianella locusta</i>	0.017	0.072	0.019	1.735
16.	<i>Valerianella locusta</i>	0.010	0.010	0.018	1.575
17.	<i>Beta vulgaris</i> subsp. <i>Vulgaris</i>	0.016	0.065	0.028	2.107
18.	<i>Atriplex hortensis</i>	0.026	0.011	0.030	2.101
19.	<i>Anthyllis vulneraria</i>	0.011	0.013	0.029	2.342
20.	<i>Brassica oleracea</i> <i>Gongylodes</i>	0.012	<0.001	0.034	2.433
21.	<i>Brassica oleracea</i> var. <i>Italica</i>	0.015	0.007	0.031	1.984
22.	<i>Capsicum frutescens</i>	<0.001	0.001	0.023	1.350
23.	<i>Physalis peruviana</i>	0.009	<0.001	0.025	1.495
24.	<i>Phoenix dactylifera</i>	0.011	<0.001	0.038	1.833
25.	<i>Aronia melanocarpa</i>	<0.001	0.002	0.018	0.200
26.	<i>Prunus cerasus</i>	<0.001	0.004	0.041	0.557
27.	<i>Rubus fruticosus</i>	0.004	0.047	0.031	0.271
28.	<i>Rubus idaeus</i>	<0.001	0.003	0.045	0.438
29.	<i>Prunus domestica</i>	<0.001	0.002	0.033	0.332
30.	<i>Vitis vinifera</i> cvs. <i>Cardinal</i>	0.004	0.291	0.052	0.407
31.	<i>Ficus</i>	0.003	0.022	0.054	0.328
32.	<i>Vaccinium myrtillus</i>	<0.001	0.000	0.056	0.617
33.	<i>Vitis vinifera</i>	0.001	0.007	0.059	1.179
34.	<i>Mespilus germanica</i>	0.002	0.010	0.054	2.574
35.	<i>Vaccinium vitisidaea</i>	<0.001	0.002	0.067	2.866
36.	<i>Prunus domestica</i>	0.001	0.001	0.057	2.274
37.	<i>Juniperus communis</i>	<0.001	0.003	0.060	2.730
38.	<i>Ocimum basilicum</i>	0.015	0.188	0.017	14.124
39.	<i>Rosmarinus officinalis</i>	0.001	0.004	0.011	4.729
40.	<i>Achillea millefolium</i>	0.001	0.004	0.070	2.699
41.	<i>Salvia officinalis</i>	<0.001	0.002	0.062	2.404
42.	<i>Ocimum basilicum</i> <i>Purpurascens</i>	0.004	0.366	0.105	3.921
43.	<i>Foeniculum vulgare</i>	0.006	0.027	0.082	3.193
44.	<i>Hypericum perforatum</i>	0.005	0.040	0.089	3.051
45.	<i>Valerianella locusta</i>	0.004	0.050	0.093	3.385

Table 2 Content (mg/L) of toxic heavy metals As, Pb i Cd in plant extracts

Plant sample	Latin name	Cd (mg/L)	Pb (mg/L)	As (mg/L)
1.	<i>Cichorium intybus</i> L. var. <i>foliosum</i> Hegi	<0.001	<0.001	<0.001
2.	<i>Allium schoenoprasum</i> L.	<0.001	<0.001	<0.001
3.	<i>Allium porrum</i>	<0.001	<0.001	<0.001
4.	<i>Plantago major</i>	<0.001	<0.001	<0.001
5.	<i>Cucurbita maxima</i>	<0.001	<0.001	<0.001
6.	<i>Asparagus officinalis</i>	<0.001	<0.001	<0.001
7.	<i>Brassica oleracea</i> var. <i>Sabauda</i>	<0.001	<0.001	<0.001
8.	<i>Beta vulgaris</i>	<0.001	<0.001	<0.001
9.	<i>Brassica oleracea</i> var. <i>Acephala</i>	<0.001	<0.001	<0.001
10.	<i>Solanum lycopersicum</i> var. <i>Cerasiforme</i>	<0.001	<0.001	<0.001
11.	<i>Cynara scolymus</i>	<0.001	<0.001	<0.001
12.	<i>Brassica rapa</i> subsp. <i>Rapa</i>	<0.001	<0.001	<0.001
13.	<i>Plantago lanceolata</i>	<0.001	<0.001	<0.001
14.	<i>Eruca sativa</i>	<0.001	<0.001	<0.001
15.	<i>Valerianella locusta</i>	<0.001	<0.001	<0.001
16.	<i>Valerianella locusta</i>	<0.001	<0.001	<0.001
17.	<i>Beta vulgaris</i> subsp. <i>Vulgaris</i>	<0.001	<0.001	<0.001
18.	<i>Atriplex hortensis</i>	<0.001	<0.001	<0.001
19.	<i>Anthyllis vulneraria</i>	<0.001	<0.001	<0.001
20.	<i>Brassica oleracea</i> <i>Gongylodes</i>	<0.001	<0.001	<0.001
21.	<i>Brassica oleracea</i> var. <i>Italica</i>	0.001	<0.001	<0.001
22.	<i>Capsicum frutescens</i>	<0.001	0.016	<0.001
23.	<i>Physalis peruviana</i>	0.001	<0.001	<0.001
24.	<i>Phoenix dactylifera</i>	0.002	<0.001	<0.001
25.	<i>Aronia melanocarpa</i>	<0.001	0.014	<0.001
26.	<i>Prunus cerasus</i>	<0.001	0.030	<0.001
27.	<i>Rubus fruticosus</i>	<0.001	0.023	<0.001
28.	<i>Rubus idaeus</i>	<0.001	0.031	<0.001
29.	<i>Prunus domestica</i>	<0.001	0.020	<0.001
30.	<i>Vitis vinifera</i> cvs. <i>Cardinal</i>	<0.001	0.034	<0.001
31.	<i>Ficus</i>	<0.001	0.022	<0.001
32.	<i>Vaccinium myrtillus</i>	<0.001	0.025	<0.001
33.	<i>Vitis vinifera</i>	<0.001	0.026	<0.001
34.	<i>Mespilus germanica</i>	<0.001	0.026	<0.001
35.	<i>Vaccinium vitisidaea</i>	<0.001	0.036	<0.001
36.	<i>Prunus domestica</i>	<0.001	0.032	<0.001
37.	<i>Juniperus communis</i>	<0.001	0.037	<0.001
38.	<i>Ocimum basilicum</i>	<0.001	0.212	<0.001
39.	<i>Rosmarinus officinalis</i>	<0.001	0.073	<0.001
40.	<i>Achillea millefolium</i>	<0.001	0.044	<0.001
41.	<i>Salvia officinalis</i>	<0.001	0.223	<0.001
42.	<i>Ocimum basilicum</i> <i>Purpurascens</i>	<0.001	0.058	<0.001
43.	<i>Foeniculum vulgare</i>	0.001	0.065	<0.001
44.	<i>Hypericum perforatum</i>	<0.001	0.375	<0.001
45.	<i>Valerianella locusta</i>	0.001	0.082	<0.001

one of the most mobile elements among all toxic heavy metals. Because of its high mobility, cadmium is readily taken up by plants from the soil and transferred to the aerial parts of the plant, where it can accumulate to a high level. Because of its high mobility in soil, the bioaccumulation of cadmium in plant-based food is usually high compared to the other trace elements [18]. Most importantly, edible plants may be inadvertently contaminated with chemicals of environmental concern and potentially toxic heavy metals through environmental pollution, industrial activity or the absorption of heavy metals from contaminated soils, industrial effluent, or contaminated irrigation water [19].

4 Conclusions

The plants collected from eco-farms contained more essential metals compared to the plants obtained from the foreign commercial suppliers. Toxic heavy metals were registered in the plants obtained from the foreign commercial suppliers.

In general, an average consumption of plants selected for this study can provide the daily recommended quantities of essential elements and at the same time will not expose the consumer to the effects of toxic elements. Nevertheless, there is a continuous need for routine monitoring of toxic elements in edible plant material to prevent any possible heavy metal poisoning in case of long-term consumption of such food, even when these elements are present only in traces. Furthermore, it is necessary to perform a mathematical-statistical analysis of potential health risks consumption of such plants could pose to children and adults in case of future long-term consumption of the selected plant species.

Acknowledgements This work was supported by the Federal Ministry of Education and Science in Bosnia and Herzegovina and was carried out within the project "Investigation of the antioxidative status of different plants used in everyday nutrition and obtained from Bosnian markets" (Grant no. 0101-7552-17/15, dated 14.12.2015).

Declaration of Conflicting Interests The author(s) declared no potential conflicts of interest with respect to the research, authorship, and/or publication of this article.

References

- Marshall: Enhancing food chain integrity: quality assurance mechanism for air pollution impacts on fruits and vegetables systems. Crop Post Harvest Program, Final Technical Report (R7530). <http://www.sussex.ac.uk/spru/1-4-7-1-11-1.html> (2004)
- Radwan, M.A., Salama, A.K.: Market basket survey for some heavy metals in Egyptian fruits and vegetables. *Food Chem. Toxicol.* **44**, 1273–1278 (2006)
- Khan, S., Cao, Q., Zheng, Y.M., Huang, Y.Z., Zhu, Y.G.: Health risk of heavy metals in contaminated soils and food crops irrigated with waste water in Beijing. *China. Environ. Pollut.* **152**(3), 686–692 (2008)
- Khairiah, T., Zalifah, M.K., Yin, Y.H., Aminath, A.: The uptake of heavy metals by fruit type vegetables, grown in selected agricultural areas. *Pak. J. Biol. Sci.* **7**(2), 1438–1442 (2004)
- Jassir, M.S., Shaker, A., Khaliq, M.A.: Deposition of heavy metals on green leafy vegetables sold on roadsides of Riyadh city, Saudi Arabia. *Bull. Environ. Contam. Toxicol.* **75**, 1020–1027 (2005)
- Kachenko, A.G., Singh, B.: Heavy metals contamination in vegetables grown in urban and metal smelter contaminated sites in Australia. *Water Air Soil Pollut.* **169**, 101–123 (2006)
- Singh, S., Kumar, M.: Heavy metal load of soil, water and vegetables in periurban Delhi. *Environ. Monitor. Assess.* **120**, 71–79 (2006)
- Sharma, R.K., Agrawal, M., Marshall, F.M.: Heavy metals (Cu, Cd, Zn and Pb) contamination of vegetables in Urban India: a case Study in Varanasi. *Environ. Poll.* **154**, 254–263 (2008)
- Sharma, R.K., Agrawal, M., Marshall, F.M.: Atmospheric depositions of heavy metals (Cd, Pb, Zn, and Cu) in Varanasi city India. *Environ. Monit. Assess.* **142**(1–3), 269–278 (2008)
- Singh, K.P., Mohon, D., Sinha, S., Dalwani, R.: Impact assessment of treated/untreated wastewater toxicants discharged by sewage treatment plants on health, agricultural, and environmental quality in wastewater disposal area. *Chemosphere* **55**, 227–255 (2004)
- Sinha, S., Gupta, A.K., Bhatt, K., Pandey, K., Rai, U.N., Singh, K.P.: Distribution of metals in the edible plants grown at Jajmau, Kanpur (India) receiving treated tannery wastewater: relation with physiochemical properties of the soil. *Environ. Monit. Assess.* **115**, 1–22 (2006)
- Sharma, R.K., Agrawal, M., Marshall, F.M.: Heavy metals contamination in vegetables grown in wastewater irrigated areas of Varanasi, India. *Bull. Environ. Contam. Toxicol.* **77**, 311–318 (2006)
- Sharma, R.K., Agrawal, M., Marshall, F.M.: Heavy metals contamination of soil and vegetables in suburban areas of Varanasi, India. *Ecotox. Environ. Saf.* **66**, 258–266 (2007)
- Joint FAO/WHO Expert Committee on Food Additives: Summary and conclusions. In: 53rd Meeting, Rome, June 1–10 (1999); Jorhem, L., Sundstroem, B.: Levels of lead, cadmium, zinc, copper, nickel, chromium, manganese and cobalt in foods on the Swedish market, 1983–1990. *J. Food Comp. Anal.* **6**, 223–241 (1993)
- Jarup, L.: Hazards of heavy metal contamination. *Br. Med. Bull.* **68**, 167–182 (2003)
- Feig, D.I., Reid, T.M., Loeb, L.A.: *Reactive oxygen species in tumorigenesis*. *Cancer Res.* **54**(Suppl.), 1890–1894 (1994)
- Allen, S.E., Grimshaw, H.M., Rowland, A.P.: Chemical analysis. In: Moore, P.D., Chapman, S.B. (eds.) *Methods in Plant Ecology*. Blackwell Scientific Publication, Oxford, London, pp. 285–344 (1986)
- Lebeau, T., Bagot, D., Jezequel, K., Fabr, B.: Cadmium biosorption by free and immobilized microorganisms cultivated in a liquid soil extract medium: effects of Cd, pH, and techniques of culture. *Sci. Total Environ.* **291**, 73–83 (2002)
- Tangahu, B.V., Abdullah, S.R.S., Basri, H., Idris, M., Anuar, N., Mukhlisin, M.: A review on heavy metals (As, Pb, and Hg) up-take by plants through phytoremediation. *Int. J. Chem. Eng.* Article ID: 939161 (2011)

Genetic Polymorphism β -Lactoglobulin Gene in Dubska Pramenka Sheep Breed

Amela Masala, Ivona Alilović, Husein Ohran, Szilvia Kusza, Teufik Goletic, Amina Hrkovic-Porobija, and Aida Hodzic

Abstract

Polymorphism exists in β -lactoglobulin (LGB) milk encoding gene in dairy animals, resulting in presence of different protein isoforms in milk. There is a link between genetic polymorphism in dairy proteins with technological properties of milk, milk yield and allergic reactions in humans. This study was conducted to identify LBG protein isoforms and their frequencies in population of Dubska Pramenka sheep breed. A total of 90 blood samples were genotyped using PCR-RFLP analysis. Genotypes were determined by PCR amplification followed by digestion with *RsaI* for identification of A and B alleles and using *MspI* for C allele identification. Two genetic variants (A and B) and three genotypes (AA, AB and BB) were identified. The presence of allele C in this study was not noticed. Gene frequencies of

LGB A were 13; LGB B were 61; LGB AB were 61. There is no data on the genetic influence on the quality and quantity of milk from Dubska pramenka sheep, and there is need for further studies.

Keywords

LBG • Dubska pramenka sheep • PCR-RFLP

1 Introduction

Genetic polymorphism plays an important role in animal breeding. This is nature's mechanism that leads to more than one isoform of a single protein [34]. It is important in many fields of animal breeding, especially in food industry, regarding the quantity and quality of meat and dairy products [11]. The possible relationships between LGB polymorphism and the yield, composition and cheese-making ability of milk have been studied [3, 8, 9, 18, 21, 25, 33, 36]. Information on lactoprotein genotypes becomes important in selection programs to improve the frequency of beneficial alleles for milk technological properties [17].

Additionally, it is estimated that 3% of the infants are sensitive to milk proteins [22]. Since milk is a biological fluid that contains all nutritional requirements for a particular mammalian newborn [10], it is necessary to develop a selection method for dairy species to reduce or eliminate the protein fractions that cause milk allergies [22].

The principal proteins in sheep and goat milk are about the same as in cow milk. The average protein content in sheep milk is 5.8% which consist of two groups, caseins and whey proteins [30].

β -lactoglobulin (LBG) is the major whey protein in the milk of ruminants and it also exists in the milk of some nonruminants (pigs, horses, dogs, cats, dolphins, whales) [22]. It is absent from the milk of rodents, rabbits and camels [24]. Though LBG is isolated 60 years ago, its biological role is largely unknown [26]. Since lactoglobulin binds to

A. Masala
Inspekt-RGH d.o.o. Sarajevo, Hamdije Kreševljakovića 18/I,
71000 Sarajevo, Bosnia and Herzegovina
e-mail: amelamasala92@gmail.com

I. Alilović (✉) · H. Ohran · A. Hrkovic-Porobija · A. Hodzic
Department of Chemistry, Biochemistry and Physiology, Faculty
of Veterinary Medicine, University of Sarajevo, Zmaja od Bosne
90, 71000 Sarajevo, Bosnia and Herzegovina
e-mail: ivona.bozic@vfs.unsa.ba

H. Ohran
e-mail: husein.ohran@vfs.unsa.ba

A. Hrkovic-Porobija
e-mail: amina.hrkovic@vfs.unsa.ba

A. Hodzic
e-mail: aida.hodzic@vfs.unsa.ba

S. Kusza
Animal Genetics Laboratory, University of Debrecen,
Böszörményi str 138, 4032 Debrecen, Hungary
e-mail: kuszasz@hotmail.com

T. Goletic
Department for Poultry Breeding, Production and Health
Protection, Veterinary Faculty, University of Sarajevo, Zmaja od
Bosne 90, 71000 Sarajevo, Bosnia and Herzegovina
e-mail: teufik.goletic@vfs.unsa.ba

retinol, fatty acids and other hydrophobic substances, it is possible to play a role in the digestion of milk fat and their resorption in newborns [14]. This protein is expressed in the mammary glands during pregnancy and lactation [1]. Aschaffenburg and Drewry [5] first reported on LGB genetic polymorphism. Gen coding for LGB protein is sequenced in sheep, goats, and cattle [15]. It is located on the third chromosome of the sheep [16]. Three polymorphic genetic variants (A, B and C) have been described. The genetic variants A and B differ by a tyrosine–histidine substitution in aminoacid position 20 [29]. The genetic variant C is a sub-type of variant A, differ at the aminoacid position 148 (arginine–glutamine substitution), and it was identified by Erhardt [12]. The sheep LBG allele A and B are present in almost all sheep breeds, while allele C is quite rare, limited to several specific breeds [3].

The Dubska Pramenka sheep breed is the main sheep breed reared in Bosnia and Herzegovina. It originates from the village of Dub, Municipality of Travnik [37]. Given the purpose of production, it is classified as three-purpose sheep (for milk, meat and wool), since it was crossbred with foreign fine-wooled types of sheep and with some breeds developed for meat production [37]. It is an indigenous sheep breed with cultural, historical and economical significance. The Dubska Pramenka sheep is traditionally used for milk production and the production of various dairy products. In order to meet the requirements of the economic market, it is necessary to determine the genes associated with the quantity and composition of the produced milk.

To the best of our knowledge, no other study concerning the LBG genetic polymorphism in Dubska Pramenka sheep exists up to this moment. This study is conducted to determine type and frequency of sheep milk protein alleles in Bosnia and Herzegovina, regarding the distribution of three variants of the LBG gene in native Dubska Pramenka sheep breed, using the PCR–RFLP technique. Also, no data on the genetic influence on the quality and quantity of milk from Dubska Pramenka sheep, and there is need for further studies.

2 Materials and Methods

The present study was carried out at 90 Dubska Pramenka unrelated sheep from Gračanica ($n = 30$) and mountain Vlašić (Dub $n = 30$, Karaula $n = 30$). Blood samples were collected from *V. jugularis* into 5 ml tubes containing EDTA (BD Vacutainer blood collection tube) and stored at -20 until DNA extraction.

The genomic DNA was isolated from blood samples using extraction method described by Zsolnai and Orban [39]. PCR amplifications were performed in reaction mixtures of 12.5 μL containing 4.75 μL H_2O , 6.25 μL of RED Taq Ready Mix (MgCl₂, dNTP, Taq DNK Polymerase),

0.5 μL of each primer, and 0.5 μL of genomic DNA (SIGMA ALDRICH Co LLC). The 120-bp fragment of the LBG gene was amplified using LBG1 (5'-CAACTCAAGGTCCTCTCCA-3') and LBG2 (5'-CTTCAGTCTCTCCACGTACA-3') primers (SIGMA ALDRICH Co LLC). PCR cycling consisted of initial denaturation at 95 °C for 10 min, followed by 35 cycles each with denaturation at 93 °C for 15 s, annealing at 60 °C for 15 s, extension at 70 °C for 30 s, and a final extension at 72 °C for 10 min. PCR products were checked by electrophoresis on 2% Agarose gel (SeaKem LE Agarose, Lonza) in TAE buffer (AccuGENE). As molecular weight marker, 100 bp ladder was used, then stained with ethidium bromide, and visualized under UV light.

For genotyping, the 12.5 μL PCR product of LBG was digested with *RsaI* for identification of A and B alleles (Feligini et al. 1998), and using *MspI* for C allele identification [4]. In both cases, 12.5 μL of PCR product were digested with 0.5 μL of *RsaI* and 0.5 μL of *MspI* restriction enzyme in a 15.5 μL total reaction volume for 4 h at 37 °C. PCR-RFLP products were quantified by electrophoresis, as previously mentioned. The amplified and digested segments are the following polymorphic nucleotide sequences: allele A 17, 37, and 66 bp; allele B 17 and 103; allele C A-75 and C-105 bp.

3 Results

The PCR-RFLP method was used for LBG genotyping of 90 samples of Dubska Pramenka sheeps. Detection of the genetic polymorphism of the LBG gene was performed by digestion of the PCR products of 120 bp with *RsaI* and *MspI* restriction enzyme, and three genotypes with two alleles were detected. The presence of C allele was not detected.

Direct counting was used to estimate genotype and allele frequencies of LBG genetic variants. A chi-square test (χ^2) was performed to check whether the populations were in Hardy–Weinberg equilibrium. Popgene version 1.31 [38] was used for all calculations and χ^2 analyses.

Table 1 showed the genotypes and allele frequencies in the entire examined population of the Dubska Pramenka sheep breed for LBG.

Table 2 showed the presence of different genotypes in three different farms (Gračanica, Dub and Karaula) (Fig. 1).

4 Discussion

The development of molecular genetics has brought significant changes in the detection of protein polymorphisms for which a relationship with production characteristics has been established. As an example, polymorphic lactoproteins may

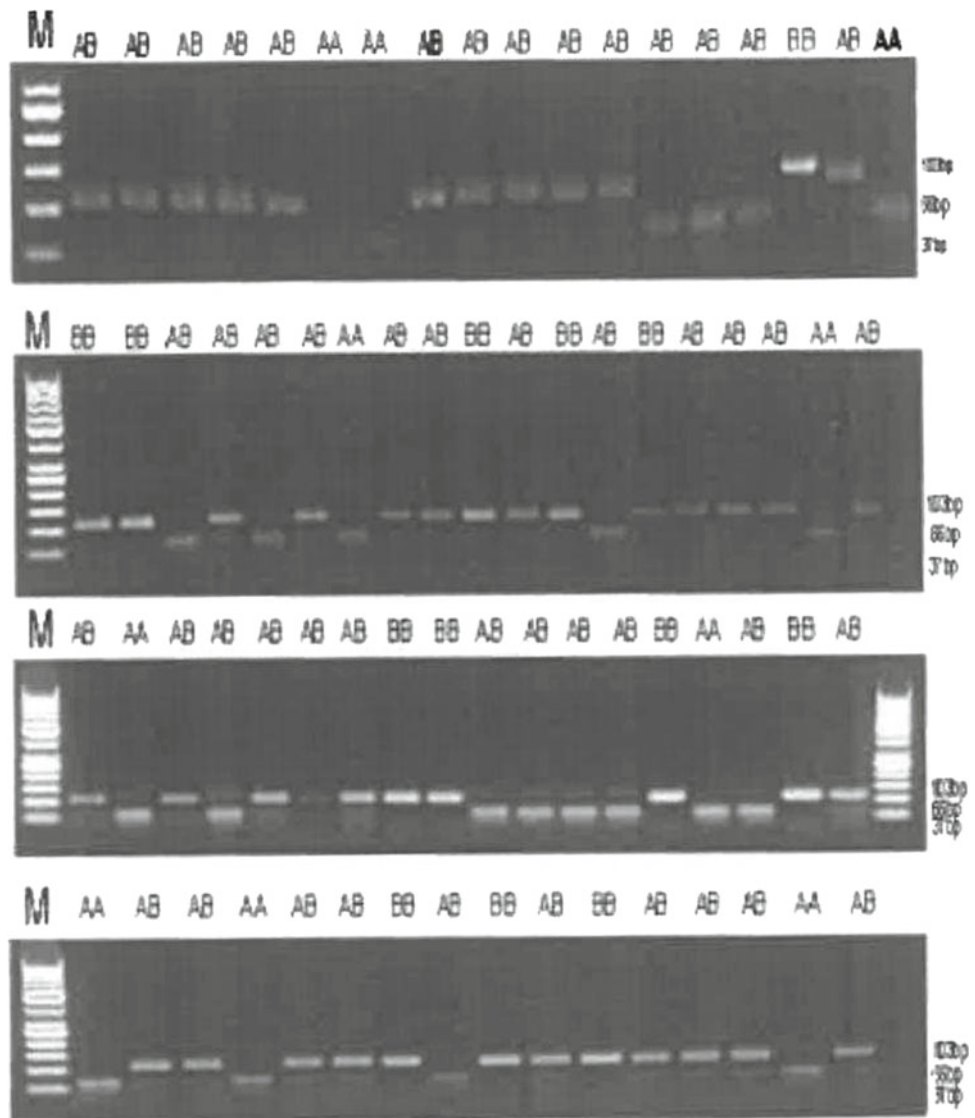
Table 1 The genotypes and allele frequencies in the entire examined population of the Dubska Pramenka sheep breed for β -lactoglobulin

		Genotype frequency			Allel frequency		X ²
Dubka Pramenka sheep breed	n = 90	AA	AB	BB	A	B	
	Observed values	13	61	16	0.48	0.52	11.57
	Expected values	22.5	45	22.5			Df = 2

Table 2 The presence of different genotypes in three different farms (Gračanica, Dub and Karaula)

Farm	Genotypes		
	AA (%)	AB (%)	BB (%)
Karaula	10	73	17
Dub	23	70	7
Gračanica	10	60	30

Fig. 1 PCR amplification of LGB gene in Dubska Pramenka sheep and digestion by *RsaI* restriction enzyme



be used, for which numerous studies have determined that they are related to the usefulness of milk in technological processing, particularly in cheese production.

In our study of Dubska Pramenka sheep breed for LGB, two genetic variations, A and B, with frequencies 0.48 and 0.52 were determined, while allele C was not found in the examined population.

The domination of A allele was also proved in the East Friesian breed, as well as in Slovakian Valaska and Tsigai sheep [27] and in Lithuanian Native Coarse-wooled and Blackface sheep [20]. According to other authors, the LGB A allele was more frequent than the B allele in the Cokanski breed, Iranian Karakul, the Finnish Landrace, the Russian Karakul, the Ghezel, the Hungarian Racka, the Pag island sheep, the Manchega and the Hyfer Border Leicester breeds [3, 17, 19, 28, 35, 31]; (Lopez-Galvez et al. 1994).

The β -LG B allele was found to be more frequent than A in the Romanov [23], Tajik [2], Sarda [6], Lacha [32], and Chios [23] breeds.

The low incidence of C allele was also observed in Merino, Massase, Merinoland, Kivircik, Gokceada and Sakiz sheep breeds in the research by Recio et al. [32], Erhardt et al. (1989), Elmaci et al. [11].

Amigo et al. [3] stated that LGB A could be the original form of ovine LGB.

Numerous studies point to the link between LGB genotype and milk quality. Carolie et al. [7] and Faraghi et al. [13] reported the positive influence of B allele on the amount of milk fat in Sarda sheep breed, while Lopez-Galvez et al. (1993) reported that the genotype AA had better properties in cheese production in comparison to the genotype BB or AB in Manchega sheep breed.

In our study, the most common genotype in Dubska Pramenka sheep breed, was the AB, that was determined in 68% of the examined population. Based on the obtained heterozygous data, it can be concluded that the examined Dubska Pramenka sheep breeds were not kept in a closed environment without selection.

The location Karaula had the highest heterozygosity, which was 73% of the AB LGB genotype, then the Dub site with 70% and Gračanica with 60%. The genotype BB was slightly smaller, which was 17% in the locality Karaula, in the locality Dub 7%, and in Gračanica where this genotype was most represented by 30%. The genotype that was least represented in two of three sites was AA, which was 10% in the Karaula site, Dub 23%, and Gračanica 10%.

Taking into account the farmer's data on the amount of milk that the examined sheep have, it is possible to explain the presence of certain genotypes and their correlation with the amount of milk. Based on these data, it is justified to assume that a lower percentage of heterozygousness, but

also a high percentage of certain genotypes, results in lower milk yield. On the other hand, a group characterized by good milk quality determines the presence of AB genotype LGB and the low presence of genotype BB.

Why is such a high percentage of alleles A and B LGB, also genotype AB of examined dairy sheep populations in the Mediterranean and Bosnia and Herzegovina, is still an open question. Continuous non-selective selection of sheep breeds made by farmers themselves and the potential superiority of AB genotype LGB for milk and cheese production could be an explanation for this phenomenon [8].

According to Staiger (2007) suggestion the milk production is not significantly different between genotypes, but the BB genotype was associated with less milk production in East Friesian sheep. It follows from this that sheep with only one copy of A alleles produce 40 g of milk per day more than sheep that do not have a single copy of the A allele.

References

1. Ali, S., Clark, A.J.: Characterization of the gene encoding ovine beta-lactoglobulin: similarity to the genes for retinol binding protein and other secretory proteins. *J. Mol. Biol.* **199**(3), 415–426 (1988)
2. Aliev, G.A., Koloteva, R.S.: Geneticheskoe raznobrazje beta-lactoglobulina V koloke ovets. *Animal Breed. Abstr.* **43**, 400 (1975)
3. Amigo, L., Recio, I., Ramos, M.: Genetic polymorphism of ovine milk proteins: its influence on technological properties of milk. *Int. Dairy J.* **10**(3), 135 (2000)
4. Anton, I., Zsolnai, A., Fesus, L., Kukovics, S., Molnár, A.: Survey of β -Lactoglobulin and α S1-Casein polymorphisms in Hungarian dairy sheep breeds and crosses on DNA level. *Arch. Anim. Breed.* **42**(4), 387–392 (1999)
5. Aschaffenburg, R., Drewry, J.: Occurrence of different beta-lactoglobulins in cow's milk. *Nature* **176**(4474), 218 (1995)
6. Bolla, P., Caroli, A., Mezzelani, A., Rizzi, R., Pragnacco, G., Fraghi, A., Casu, S.: Milk protein markers and production in sheep. *Anim. Genet.* **20**, 78–79 (1989)
7. Caroli, A., Bolla, P., Spanu, A.: Effect of beta lactoglobulin genotype of milk yield in the Sardinian sheep. In: *Proceeding 11th Congress National Animal Science and Production Association*, Udine, Italy, pp. 181–182 (1995)
8. Cubric-Curic, V., Feligini, M., Lukac-Havranek, J., Curik, I., Enne, G.: Genetic polymorphism of b-lactoglobulin in native sheep from the island of Pag. *Food Technol. Biotechnol.* **40**(1), 75–78 (2002)
9. Dario, C., Carnicella, D., Bufano, G.: Effect of B-946-lactaglobulin genotypes on ovine milk composition in altamura breed. *Archivos de zootecnia* **54**(205), 105–108 (2005)
10. El-Agamy, E.I.: The challenge of cow milk protein allergy. *Small Ruminant Res.* **68**(1–2), 64–72 (2007)
11. Elmaci, C., Oner, Y., Balcioglu, S.: Genetic polymorphism of β -lactoglobulin gene in Native Turkish sheep breeds. *Biochem. Genet.* **44**(7–8), 379–384 (2006)

12. Erhardt, G.: Evidence for a third allele at the β -lactoglobulin (β -Lg) locus of sheep milk and its occurrence in different breeds. *Anim. Genet.* **20**(3), 197–204 (1989)
13. Faragi, A., Carta, A., Pilla, F.: Beta-lactoglobulin polymorphism in sarda dairy sheep. In: *Proceeding of 74th Annual Meeting of the European Association for Animal Production*, p. 42 (1996)
14. Fogolari, F., Ragona, L., Licciardi, S., Romagnoli, S., Michelutti, R., Ugolini, R., Molinari, H.: Electrostatic properties of bovine β -lactoglobulin. *Proteins Struct. Funct. Bioinf.* **39**(4), 317–330 (2000)
15. Folch, J.M., Coll, A., Sanchez, A.: Complete sequence of the caprine β -Lactoglobulin gene1. *J. Dairy Sci.* **77**(12), 3493–3497 (1994)
16. Hayes, H.C., Petit, E.J.: Mapping of the β -lactoglobulin gene and of an immunoglobulin M heavy chain-like sequence to homoeologous cattle, sheep, and goat chromosomes. *Mamm. Genome* **4**(4), 207–210 (1993)
17. Ivankovic, A., Dovc, P.: Polymorphisms of beta-lactoglobulin and alpha s1-casein genes in the pag islad sheep. *Acta Agriculturae slovenica (Slovenia)* (2004)
18. Jurate, K., Gediminas, V., Jolanta, M., Ilma, T.: Genetic polymorphism of b-lactoglobulin in Lithuanian Blackface and Lithuanian Native Coarsewooled sheep. *Veterinarija ir zootechnika* **29**(51) (2005)
19. Kerekes, A., Baranyi, M., Nagy, S., Kovacs, P., Bosze, Z.S.: Beta-lactoglobulin genetic polymorphisms in Hungarian Awassi and Racka sheep. *Anim. Welfare Ethol. Hous. Syst.* **4**, 437–444 (2008)
20. Kučinskiene, J., Vagonis, G., Maleviciute, J., Maleviciute, J., Tapio I.: Genetic polymorphism of b-lactoglobulin in Lithuanian blackface and Lithuanian native Coarsewooled sheep. *Veterinarija ir Zootechnika* **51**(29), 90–92 (2005)
21. Kumar, A., Rout, P.K., Roy, R.: Polymorphism of β -lacto globulin gene in Indian goats and its effect on milk yield. *J. Appl. Genet.* **47**(1), 49–53 (2006)
22. Kusza, S., Sziszkosz, N., Nagy, K., Masala, A., Kukovics, S., András, J.: Preliminary result of a genetic polymorphism of β -lactoglobulin gene and the phylogenetic study of ten balkan and central european indigenous sheep breeds. *Acta Biochim. Pol.* **62**(1) (2015)
23. Macha, J., Novackova, I.: Geneticky Polimorfismus beta-laktoglobulinu V mlece ovci. *Zivocisma viroba* **19**, 883–888 (1974)
24. Martin, P., Szymanowska, M., Zwierzchowski, L., Leroux, C.: The impact of genetic polymorphisms on the protein composition of ruminant milks. *Reprod. Nutr. Dev.* **42**(5), 433–459 (2002)
25. Mele, M., Conte, G., Serra, A., Buccioni, A., Secchiari, P.I.E.R.: Relationship between beta-lactoglobulin polymorphism and milk fatty acid composition in milk of Massese dairy ewes. *Small Ruminant Res.* **73**(1–3), 37–44 (2007)
26. Mercier, J.C., Vilotte, J.L.: Structure and function of milk protein genes. *J. Dairy Sci.* **76**(10), 3079–3098 (1993)
27. Michalcova, A., Krupova, Z.: Influence of b-lactoglobulin C genotypes on composition of milk and milk production traits of the Slovak ovine breeds. *Acta fytotechnica et zootechnica Mimoriadne číslo, Slovaca Universitas Agriculturae Nitriae*, pp. 438–446 (2009)
28. Mohammadi, A., Nassiry, M., Elyasi, G., Shodja, J.: Genetic polymorphism of b-lactoglobulin in certain Iranian and Russian sheep breeds. *Iran. J. Biotechnol.* **4**(4), 265–268 (2006)
29. Muioli, B., D'andrea, M., Pilla, F.: Candidate genes affecting sheep and goat milk quality. *Small Ruminant Res.* **68**(1–2), 179–192 (2007)
30. Park, Y.W., Juárez, M., Ramos, M., Haenlein, G.F.W.: Physico-chemical characteristics of goat and sheep milk. *Small Ruminant Res.* **68**(1–2), 88–113 (2007)
31. Rampilli, M., Cecchi, F., Giuliotti, L., Cattaneo, G.M.: The influence of B-Ig genetic polymorphism on protein distribution and coagulation properties in milk of Massese breed ewes. In: *Proceedings IDF Seminar “Milk protein polymorphism”*, Brussels, pp. 311–315 (1997)
32. Recio, I., Fernandez-Fournier, A., Martin-Alvarez P.J., Ramos, M.: Beta-lactoglobulin polymorphism in ovine breeds: influence on cheese-making properties and milk composition. *Lait* **77**, 259–265 (1997)
33. Staiger, E.A., Thonney, M.L., Buchanan, J.W., Rogers, E.R., Ottenacu, P.A., Mateescu, R.G.: Effect of prolactin, β -lactoglobulin, and κ -casein genotype on milk yield in East Friesian sheep. *J. Dairy Sci.* **93**(4), 1736–1742 (2010)
34. Tahira, I., Mahmood, A., Saqlain, M., Hanif, N.Q., Raja, G.K.: Study of β -lactoglobulin milk protein variants in buffalo. *Pak. J. Zool.* **46**(2), 549–552 (2014)
35. Thomas, A.S., Dawe, S.T., Walker, R.A.: Milk protein polymorphisms in Hyfer and Border Leicester X Merino sheep. *Milchwissenschaft* **44**, 686–688 (1989)
36. Triantaphyllopoulos, K.A., Koutsouli, P., Kandris, A., Papachristou, D., Markopoulou, K.E., Mataragka, A., Massouras, T., Bizelis, I.: Effect of β -lactoglobulin gene polymorphism, lactation stage and breed on milk traits in Chios and Karagouniko sheep breeds. *Ann. Anim. Sci.* **17**(2), 371–384 (2017)
37. Vazić, B., Rogić, B., Pihler, I., Drinić, M., Savić, N.: Morphometric characterization and body measurement correlation in Dubska Pramenka sheep. *Contemp. Agric.* **66**(1–2), 38–43 (2017)
38. Yeh, F.C., Young, R.C., Boyle, T.: Microsoft Window-based freeware for population genetic analysis (POPGENE, ver. 1.31). University of Alberta (1999)
39. Zsolnai, A., Orbán, L.: Accelerated separation of random complex DNA patterns in gels: comparing the performance of discontinuous and continuous buffers. *Electrophoresis Int. J.* **20**(7), 1462–1468 (1999)

Part XIII
Student Competition Session

Prostate Tissue Classification Based on Prostate-Specific Antigen Levels and Mitochondrial DNA Copy Number Using Artificial Neural Network

Lemana Spahić and Sabahudin Ćordić

Abstract

Prostate cancer is the most prominent cancer in men and one of the leading morbidity causes when referred to cancer. Prostate cancer usually affects men older than 65 but young men can also acquire cancer in specific conditions. Over the years, vast amounts of data about Prostate-Specific Antigen (PSA) levels were collected and together with novel mitochondrial DNA (mtDNA) copy number data can be used for risk assessment and prostate cancer diagnosis. This paper presents development of an Artificial Neural network (ANN) for classification between normal and prostate cancer patients based upon Prostate-Specific Antigen (PSA) levels and Mitochondrial DNA (mtDNA) copy number. For the development of Neural Network, samples of PSA level and mtDNA copy number were used. State of prostate was classified based on 352 samples as normal or cancerous with 175 samples being normal according to biopsy results and 177 being cancerous according to biopsy results. Among all tested architectures, the two-layer feedforward ANN with Logsig transfer function showed the best performance. An addition of k-fold cross validation method yielded better results with sensitivity was 100%, specificity 98.8% and overall accuracy of the system in subsequent validation was 99.4%.

Keywords

Artificial neural network • Cancer • Prostate • Classification

1 Introduction

Cancer is referred to as malignancy and presents an abnormal cell proliferation with spread to other tissues. It is not only a name for one particular disease but for a group related disease [1]. Cancer is not limited to a single location inside the body, but it can start anywhere in the body and its cells differ from normal cells primarily by their unstoppable proliferation. Another characteristic is that their cells are less specialized than normal cell [2, 3].

Prostate is an organ located just below the bladder and in front of the rectum in males. The size of prostate is subjected to age dependent changes with younger men having smaller prostate and older men having an enlarged prostate [4]. The onset of prostate cancer is marked by cells in the prostate gland growing uncontrollably. Almost all accountable prostate cancers are in the group of adenocarcinomas and they develop from the gland cells. If not classified as adenocarcinomas, prostate cancers can be: sarcomas, small cell carcinomas, transitional cell carcinomas, and neuroendocrine tumors. Some of these cancers are quicker in growth in spread, but most of them are slow [5–7].

Prostate cancer is the most common cancer in men in America, with estimated 19% of all cancer incidences belonging to prostate cancer with 8% of overall cancer morbidity. Statistics for 2017 indicated that about 161,360 new cases with 26,730 deaths would occur [8]. Europe, a continent that harbors 9% of all the world population, bares the burden of 25% all cancer cases. Prostate cancer statistics for 2018 indicate that 21.3% of all cancers in men attributed to prostate cancer with a morbidity rate of 10% [9]. Generally, prostate cancer develops in older men, about 60% of cases are diagnosed in men older than 65, rarely below 40 years old, and the average age of diagnosis is around 66. The morbidity rate in America is 2.44% meaning that 1 in 41 men will die if diagnosed with prostate cancer [10].

Prostate-Specific antigen (PSA) is defined as a substance produced by the prostate gland [11]. If the levels of PSA are

L. Spahić (✉) · S. Ćordić
Faculty of Engineering and Natural Sciences, Department of Genetics and Bioengineering, International Burch University, Francuske Revolucije bb, Sarajevo, Bosnia and Herzegovina
e-mail: lemanaspahic@gmail.com

S. Ćordić
e-mail: sabahudin.cordic@stu.ibu.edu.ba

Table 1 ANN studies and their accuracy

Paper	Dataset	Accuracy
Snow et al. [31]	PSA level samples from 1787 men with prostate cancer	87% accuracy for biopsy prediction 90% accuracy for cancer recurrence prediction
Djavan et al. [32]	PSA concentration level database and radical prostatectomy database	Prediction ANN sensitivity: 67%, specificity: 100% and accuracy: 100%
Stephan et al. [33]	1188 samples of PSA from men diagnosed with either prostate cancer or being prostate tumours	Sensitivity in range: 90–95% Specificity in range 90–95% Overall accuracy 78–84%
Takeuchi et al. [34]	Magnetic resonance imaging and 12-core biopsy samples from 334 men	5–10% higher accuracy when compared to logistic regression analysis

elevated, that is a strong indication of prostate cancer, prostatitis or enlarged prostate. PSA levels above the borderline value, which is taken to be four, are mostly first indicators that further examination is needed in order to diagnose or exclude prostate cancer [11].

Mitochondria is a cellular organelle in charge of producing energy, and is also referred to as the energy factory of each cell [12]. Mitochondrial DNA (mtDNA) copy number has been found to alter the expression of genes and therefore lead to genetic susceptibility to tumor-specific malignancies [13]. Decreased mtDNA content in peripheral blood leukocytes was found to be correlated with aggressive and fast progressing prostate cancer [14, 15].

Diagnosis of cancer is a very complex and sensitive procedure and susceptible to human errors and equipment errors. It is done by first taking a biopsy sample of suspicious tissue and then subjecting it to cytological and molecular tests. These tests are performed in isolated environments in order to decrease error possibility to minimum, but errors can always happen [16]. Nowadays, vast number of clinical data and patient histories are available for this disease. With the development of biomedical engineering researchers have examined the usage of machine learning techniques in supporting the diagnosis made by medical professionals.

Diagnosis is a relatively straightforward machine learning problem. In this process, a larger set of symptoms and conditions can be taken into account for each patient in respect to classical diagnostics procedure, where medical professionals can take into account only a limited number of parameters and give a diagnosis based on their interactions [17–19]. By using neural network systems medical professionals can establish better diagnoses, choose optimal medications for their patients, predict readmissions, identify patients at high-risk for poor outcomes, and in general improve patients' health while minimizing costs.

Besides application in aerospace and automotive industry, finance and economy, Artificial Neural Networks (ANNs) were used for years in order to classify different diseases [20–28]. Some research groups have already used Artificial Neural Network (ANN) for cancer diagnostic prediction and

classification of cancer types. Research done by Tan et al. was based on datasets from whole genome RNA expression together with 52 prostate tumor tissues and 50 normal tissues using ensemble machine learning with different prediction methods yielding different accuracies: 67.65, 73.53 and 67.65% [29]. Zupan et al. [30] made classifiers using 1055 localized prostate cancer samples and obtained accuracies for default classifier 68.1%, naïve Bayes classifier 70.8%, decision tree induction 68.8% and for Cox 69.7%. The above mentioned studies indicate that various types of machine learning are in use for prostate cancer prediction. Table 1 shows Artificial Neural Network studies based on prostate cancer and their accuracies.

This paper presents the development of neural network architecture for classification between cancer and normal prostate tissue basing on PSA levels and mtDNA copy number. Developed neural network architecture can be useful in laboratories for confirming the established diagnosis.

2 Materials and Methods

2.1 Dataset

The dataset for development of neural network was obtained from the research done by Zhou et al. [35].

For each patient multiple parameters such as age, PSA level, daily fat intake, smoking history, family history, BMI, and mtDNA copy number were obtained. However, only PSA level and mtDNA copy number was proven to be directly related to prostate cancer development. The number of samples corresponding to normal and prostate cancer group is presented in Table 2. For development of neural network this dataset was divided into two groups. One group was used for training of ANN and the other for testing the performance of the developed system. Number of samples per each group is presented in Table 2. Samples were divided into these two groups in 90/10 ratio because a portion of training data will also be used in the validation process

Table 2 Data division for testing and validation

Training dataset		Subsequent validation (Testing) dataset	
Classification group	Number of samples	Classification group	Number of samples
Normal	175	Normal	19
Cancer	177	Cancer	19
Σ	352	Σ	38

during ANN development, and in order to encompass as many cases as possible in training.

Training dataset contained 352 samples. Out of those 175 (49.716%) were samples of normal tissue and 177 (50.284%) were cancer affected tissue. For subsequent validation 38 samples were used. Out of those, 19 (50%) were normal tissue samples and 19 (50%) were cancer diseased tissue.

2.2 Development of Artificial Neural Network

ANNs consists of processing units, neurons connected parallel. Each connection between neurons is weighted and the activation is determined by summation of these weighted connections. The activation of neuron is determined by its transfer function that can be linear or nonlinear. ANNs are trained so connection weights and biases are determined in order to produce the desired mapping of data. In this way, ANNs are able to capture relationship between the data without defining exact mathematical model. The connection of neurons in neural network defines its architecture which can be feedforward and feedback. In this paper feedforward neural network will be developed since this architecture is sufficient for solving problems of classification [21, 26, 28]. When it comes to data division in the Artificial Neural Network Architecture, data was divided in 80/20 ratio as recommended by experts and confirmed by experimental work [24, 28].

Bayesian regulation training algorithm was used because of its prominent feature of preventing overfitting and it is found to be very useful in pattern recognition problems [36, 37].

At each training iteration train/test performance was evaluated by total confusion matrix, error gradient and Mean

Square Error between the predicted and actual values (MSE), where n is total number of samples:

$$MSE = \frac{1}{n} \sum_{i=1}^n (X_{predicted} - X_{actual})^2$$

In this paper, neural network architecture with linear and nonlinear transfer functions in hidden layer is examined. Also, different number of neurons was used in hidden layer in order to get best possible performance. Network was trained for 5, 10, 20, 25 and 30 neurons in order to evaluate the most suitable number of neurons for accurate prediction of Prostate cancer using this particular dataset.

3 Results

The purpose of the design phase was to develop optimal neural network architecture for solving the problem of classification between normal and cancerous prostate tissue based on PSA levels and mtDNA copy number. The neural network performance using different transfer functions and different number of neurons in hidden layer is presented in Table 3.

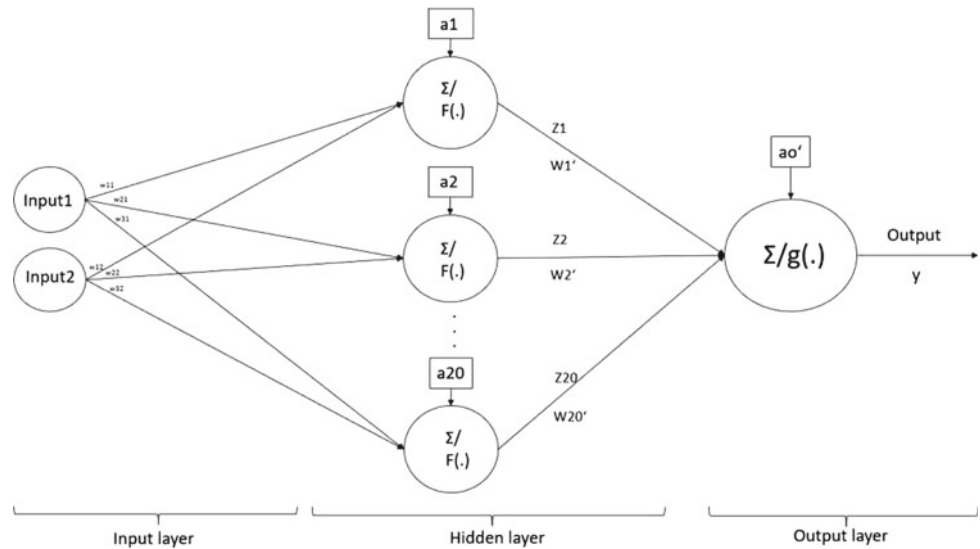
As it can be seen from Table 3. Performance was the best at 0.0086 and that performance was obtained with 20 neurons with Logsig activation function in the hidden layer. Therefore Logsig activation function with 20 neurons in the hidden layer was used as the basis for neural network architecture development. The architecture is presented in Fig. 1. The architecture presents 2 input layer parameters that go through hidden layer to a single output. Each of the input parameters interacts with each neuron in hidden layer. Each neuron from hidden layer gives output to neuron in the output layer.

The performance of the neural network architecture was determined by the computation of the following parameters:

Table 3 Performance of ANN with different number of neurons

Transfer function in hidden layer	Performance with different number of neurons				
	5	10	20	25	30
Logsig	0.0088	0.0087	0.0086	0.0090	0.0095
Transig	0.0101	0.0091	0.0100	0.0095	0.0094
Purelin	0.0147	0.0137	0.0137	0.0137	0.0142
Hardlim	0.1980	0.1372	0.0726	0.1113	0.0613

Fig. 1 Neural network architecture



Specificity: (number of correct classified samples normal class)/(number of total samples of normal class). Sensitivity: (number of correct classified samples of cancer class)/(number of total samples of cancer class). Accuracy was determined by (number of correctly classified samples)/(total number of samples). The ANN performance was tested with 38 samples and the results are presented in Table 4.

Results shown in Table 4 indicate that cancerogenic tissue can be detected with 94.7% accuracy using this neural network. This result suggests that out of 19 patients tested that indeed have cancer, all 19 will be classified as positive. Out of 19 patients that show some indications but do not

have cancer, 18 of them will be classified as normal by this neural network. These results lead to sensitivity of 100% and specificity of 94.7%.

An additional step in Neural network development was employment of K-fold cross validation. After performing K-fold cross validation with respect to the code presented in the appendix, the performance of the ANN varied significantly when compared to the previously presented method. Because k-fold cross validation is suitable for use in cases when a complex dataset with relatively small number of samples is present, three different training algorithms with different number of neurons were tested (Table 5).

Table 4 Confusion matrix

	ANN		
	Normal	Cancer	
Normal	18	1	19
Cancer	0	19	19
	Specificity 94.7%	Sensitivity 100%	

Table 5 Performance of ANN with K-fold cross validation with different number of neurons and different training algorithms combination

Training algorithm	Number of neurons	Performance
Trainlm	20	0.006
Trainlm	10	0.0398
Trainlm	5	0.0227
Trainbr	20	0.0425
Trainbr	10	0.0454
Trainbr	5	0.0389
Trainbfg	20	0.2224
Trainbfg	10	0.1809
Trainbfg	5	0.2063

The best performance was observed using Levenberg Marquardt training algorithm with again 20 neurons in the hidden layer. Sensitivity, specificity and accuracy parameters were 100, 98.8 and 99.4% respectively. Therefore it can be said that this method yields the best results in terms of both performance and confusion matrix outcomes.

4 Conclusion

This paper presents an Artificial Neural Network as a diagnostic tool for cancer. The neural network was trained with dataset containing 352 samples, where 177 of them had cancer in prostate tissue and 175 had normal tissue. Data was divided in training and validation sets, 352 samples and 38 samples respectively.

Since diagnostic methods used for cancer diagnosis are histology and immunohistochemistry based, these non-invasively obtained parameters can be used as ANN inputs and the output of ANN would indicate the doctor if biopsy is indeed necessary, and therefore invasive procedures would be avoided if possible.

When compared to the papers presented in the introductory section, this neural network generally shows better performance or performance equal to previously published research. Introduction of mtDNA copy number as a relevant indicator of Prostate Cancer is a novel approach that can be further developed in conjunction with this ANN. The results shown in this paper are advantageous when compared to previously developed neural networks for prostate cancer diagnosis because of employment of mtDNA copy numbers as relevant cancer indicators.

In the future, authors will tend to develop a user interface for implementation of the neural network described in this paper. By doing that, this type of diagnostics will be available for usage by medical professionals.

References

- Moses, H.L., Nass, S.J. (eds.): *Cancer Biomarkers: The Promises and Challenges of Improving Detection and Treatment*. National Academies Press (2007)
- Kufe, D.W., Pollock, R.E., Weichselbaum, R.R., Bast, R.C., Gansler, T.S.: *Holland-Frei Cancer Medicine*. BC Decker Inc., (2003)
- Frank, S.A.: *Dynamics of Cancer: Incidence, Inheritance, and Evolution*. Princeton University Press (2007)
- Gundem, G., Van Loo, P., Kremeyer, B., Alexandrov, L.B., Tubio, J.M., Papaemmanuil, E., et al.: The evolutionary history of lethal metastatic prostate cancer. *Nature* **520**(7547), 353 (2015)
- Gupta, M.D.: *Prostate Cancer Basics* (2014)
- Russo, G., Mischi, M., Scheepens, W., De la Rosette, J.J., Wijkstra, H.: Angiogenesis in prostate cancer: onset, progression and imaging. *BJU Int.* **110**(11c), E794–E808 (2012)
- Carter, B.S., Bova, G.S., Beaty, T.H., Steinberg, G.D., Childs, B., Isaacs, W.B., Walsh, P.C.: Hereditary prostate cancer: epidemiologic and clinical features. *J. Urol.* **150**(3), 797–802 (1993)
- Siegel, R.L., Miller, K.D., Jemal, A.: *Cancer statistics, 2017*. *CA Cancer J. Clin.* **67**(1), 7–30 (2017)
- What Are the Key Statistics About Prostate Cancer.: *Cancer.org*. Retrieved 26 August 2018, from <https://www.cancer.org/cancer/prostate-cancer/about/key-statistics.html> (2017)
- Ferlay J., et al.: Cancer incidence and mortality patterns in Europe: estimates for 40 countries and 25 major cancers in 2018. *Eur. J. Cancer* (2018). <https://doi.org/10.1016/j.ejca.2018.07.005>
- Partin, A.W., Kattan, M.W., Subong, E.N., Walsh, P.C., Wojno, K.J., Oesterling, J.E., et al.: Combination of prostate-specific antigen, clinical stage, and Gleason score to predict pathological stage of localized prostate cancer: a multiinstitutional update. *Jama* **277**(18), 1445–1451 (1997)
- Chen, X.J., Butow, R.A.: The organization and inheritance of the mitochondrial genome. *Nat. Rev. Genet.* **6**(11), 815 (2005)
- Hu, L., Yao, X., Shen, Y.: Altered mitochondrial DNA copy number contributes to human cancer risk: evidence from an updated meta-analysis. *Sci. Rep.* **6**, 35859 (2016)
- Moore, A., Lan, Q., Hofmann, J.N., Liu, C.S., Cheng, W.L., Lin, T.T., Berndt, S.I.: A prospective study of mitochondrial DNA copy number and the risk of prostate cancer. *Cancer Causes Control* **28**(6), 529–538 (2017)
- Tu, H., et al.: Mitochondrial DNA copy number in peripheral blood leukocytes and the aggressiveness of localized prostate cancer. *Oncotarget* **6**, 41988–41996 (2015)
- Schmidt, U., Begley, C.G.: Cancer diagnosis and microarrays. *Int. J. Biochem. Cell Biol.* **35**(2), 119–124 (2003)
- Ghaehri, A., Shoar, S., Naderan, M., Hoseini, S.S.: The applications of genetic algorithms in medicine. *Oman Med. J.* **30**(6), 406 (2015)
- Fagella: 7 Applications of Machine Learning in Pharma and Medicine. Available at: <https://goo.gl/1SIR5k> (2017)
- Magoulas, G.D., Prentza, A.: Machine learning in medical applications. In: *Machine Learning and its Applications*. Springer, Berlin, pp. 300–307 (2001)
- Badnjevic, A., Cifrek, M., Koruga, D., Osmankovic, D.: Neuro-fuzzy classification of asthma and chronic obstructive pulmonary disease. *BMC Med. Inf. Decis. Making J* (2015)
- Badnjevic, A., Cifrek, M., Koruga, D.: Classification of Chronic Obstructive Pulmonary Disease (COPD) using integrated software suite. In: *IFMBE XIII Mediterranean Conference on Medical and Biological Engineering and Computing (MEDICON)*, 25–28 September 2013. Sevilla, Spain (2013)
- Badnjevic, A., Cifrek, M.: Classification of asthma utilizing integrated software suite. In: *6th European Conference of the International Federation for Medical and Biological Engineering (MBEC)*, 07–11 September 2014. Dubrovnik, Croatia (2014)
- Badnjevic, A., Koruga, D., Cifrek, M., Smith, H.J., Bego, T.: Interpretation of pulmonary function test results in relation to asthma classification using integrated software suite. In: *IEEE 36 International Convention on Information and Communication Technology, Electronics and Microelectronics (MIPRO)*, pp. 140–144, 21–25 May 2013. Opatija, Croatia (2013)
- Badnjevic, A., Gurbeta, L., Cifrek, M., Marjanovic, D.: Classification of Asthma using Artificial Neural Network, *IEEE MIPRO* (2016)
- Aljovic, A., Badnjevic, A., Gurbeta, L.: Artificial Neural Networks in the Discrimination of Alzheimer's Disease using Biomarkers Data, *IEEE MECO*, 12–16 June 2016. Bar, Montenegro (2016)
- Alic, B., Sejdinovic, D., Gurbeta, L., Badnjevic, A.: Classification of Stress Recognition using Artificial Neural Network, *IEEE MECO* (2016)

27. Fojnica, A., Osmanovic, A., Badnjevic, A.: Dynamical Model of Tuberculosis-Multiple Strain Prediction based on Artificial Neural Network, IEEE MECO. Bar, Montenegro (2016)
28. Alic, B., Gurbeta, L., Badnjevic, A., et.al.: Classification of metabolic syndrome patients using implemented expert system, CMBEBIH 2017. In: IFMBE Proceedings, vol. 62, pp. 601–607. Springer, Berlin (2017)
29. Tan, A.C., Gilbert, D.: Ensemble machine learning on gene expression data for cancer classification. In: Proceedings of New Zealand Bioinformatics Conference, 13–14 February 2003. Te Papa, Wellington, New Zealand (2003)
30. Zupan, B., Demšar, J., Kattan, M.W., Beck, J.R., Bratko, I.: Machine learning for survival analysis: a case study on recurrence of prostate cancer. *Artif. Intell. Med.* **20**(1), 59–75 (2000)
31. Snow, P.B., Smith, D.S., Catalona, W.J.: Artificial neural networks in the diagnosis and prognosis of prostate cancer: a pilot study. *J. Urol.* **152**(5), 1923–1926 (1994)
32. Djavan, B., Remzi, M., Zlotta, A., Seitz, C., Snow, P., Marberger, M.: Novel artificial neural network for early detection of prostate cancer. *J. Clin. Oncol.* **20**(4), 921–929 (2002)
33. Stephan, C., Cammann, H., Semjonow, A., Diamandis, E.P., Wymenga, L.F., Lein, M., et al.: Multicenter evaluation of an artificial neural network to increase the prostate cancer detection rate and reduce unnecessary biopsies. *Clin. Chem.* **48**(8), 1279–1287 (2002)
34. Takeuchi, T., Hattori-Kato, M., Okuno, Y., Iwai, S., Mikami, K.: Prediction of prostate cancer by deep learning with multilayer artificial neural network. *bioRxiv*, 291609 (2018)
35. Zhou, W., Zhu, M., Gui, M., Huang, L., Long, Z., Wang, L., Chen, H., Yin, Y., Jiang, X., Dai, Y., Tang, Y., He, L., Zhong, K.: Peripheral blood mitochondrial DNA copy number is associated with prostate cancer risk and tumor burden. *PLoS ONE* **9**(10), e109470 (2014)
36. Sarder, P., Schierding, W., Cobb, J.P., Nehorai, A.: Estimating sparse gene regulatory networks using a bayesian linear regression. *IEEE Trans. Nanobiosci.* **9**(2), 121–131 (2010)
37. Liu, F., Zhang, S.W., Guo, W.F., Wei, Z.G., Chen, L.: Inference of gene regulatory network based on local bayesian networks. *PLoS Comput. Biol.* **12**(8), e1005024 (2016)

Influence of Artificial Microgravity on Human Arterial Vessels

S. Akulov, A. Fedotov, I. Makarov, A. Sidorov, and A. Kosheleva

Abstract

The aim of this work is to study the alterations occurred in human cardiovascular system under artificially simulated microgravity. Artificial gravity produced by short-arm centrifuge along the head-to-feet axis induces gravity gradients and causes hemodynamic alterations. We have used differential arterial blood pressure measurements, pulse wave contour analysis, and accelerated photoplethysmography (APPG) to determine the impact of artificially simulated microgravity on human vascular system. The group of 50 healthy male volunteers was studied in a short-arm human centrifuge at normal gravity gradient of 1 Gz during 10 min at supine position lying at the nacelle. Blood pressure and APPG parameters registered before, during and after exposure of artificial gravity.

Keywords

Artificial gravity • Short-arm centrifuge • Cardiovascular system • Accelerated photoplethysmography • Ankle-brachial pressure index

1 Introduction

Artificial gravity along the head-to-feet axis on a short-arm centrifuge induces gravity gradients. This physiological condition of significantly higher gravitational acceleration at the feet than at the heart level is specific and likely induces blood sequestration in the lower limbs [1].

S. Akulov (✉) · A. Fedotov · A. Kosheleva
Samara University, Moskovskoe Highway 34, Samara,
443086, Russia
e-mail: sakulov1981@mail.ru

I. Makarov · A. Sidorov
Samara State Medical University, 89 Chapayevskaya Street,
Samara, 443099, Russia

This phenomenon could be very useful in functional diagnostics of cardiovascular system as well as in therapy for patients with different pathologies such as peripheral artery disease, obliterating atherosclerosis of vessels in lower extremities and others vascular diseases.

The study of the artificial gravity influences on cardiovascular system may be important for space medicine, e.g. creating diagnostic and therapeutic instruments for astronauts suffering from cardiovascular deconditioning and negative effects of zero-gravity during long-term space flights.

A number of research has examined human tolerance to high gravitational acceleration at different conditions and several physiological parameters were investigated such as heart rate variability (HRV), arterial blood pressure (ABP), cardiac output, stroke volume, respiratory sinus arrhythmia, etc. [2–4].

However there is an obvious lack of the research about influence of artificial gravity factors on cardiovascular system, especially on the conditions of arterial vessels. This work is devoted to study the effects of artificially simulated microgravity on human vascular system based on ABP measurements, calculating ankle-brachial pressure index (ABPI) for estimating hemodynamics in the lower limbs as well as using pulse wave contour analysis and accelerated photoplethysmography for assessing arterial stiffness.

2 Materials and Methods

For generating artificial gravity we have used short-arm human centrifuge with variable rotation rate and outer radius of 2.4 m that can produce gravitational acceleration up to $g = 6$ at the feet of the subject and therefore different gravity gradients along head-to-foot direction (Gz) (Fig. 1). The heart level of the subject was situated at approximately 1 m from the center of rotation. The subjects were located in the

Fig. 1 Short-arm human centrifuge used in the study



centrifuge nacelle, which is perpendicular to the gravitational acceleration vector g and collinear to centrifugal acceleration vector.

The rotation rate of the short-arm centrifuge was set at 30 rates per minute (rpm) to obtain gravity gradient at the heart level of $G_z = 1$ and simulate artificial gravity for cardiovascular system. The study has included 3 consecutive sessions: initial session was at rest, lying in nacelle without rotation; the next session was under gravity gradients of $G_z = 1$ at supine position and the end session after exposure, lying in nacelle without rotation. Each session of the study was lasted for 10 min.

During this study short-arm human centrifuge and the necessary diagnostic instrumentation was located at the Regional Hospital in Samara. The Ethical Committee has approved the study that was conducted in accordance with the 1964 Declaration of Helsinki on experiments on human subjects. The aims, protocol and methods of this study were thoroughly described to the volunteers, and they signed an informed consent form.

For participating in this study 30 male young subjects (age: 21 ± 3.6 years old, weight: 68 ± 7.2 kg, height: 171 ± 11 cm) without clinical evidence of heart diseases were selected. All volunteers were tested in the afternoon at least 2 h after last main meal and according to experimental conditions they were asked not to take caffeine and nicotine containing products during 4 h before the experiment.

To record distal pulse waves and arterial blood pressure we have used special 4-channel biomedical acquisition system ("New Devices Ltd", Samara, Russian Federation) that contains unobtrusive wearable sensors, electronic circuits for analog and digital biosignal pre-processing and Bluetooth module for transmitting data to the PC at the control room for further advanced processing and calculating HRV and vascular indices via custom written software tool in MATLAB R2014b (Mathworks[®], USA).

Digital pulse wave and arterial blood pressure were continuously and simultaneously recorded during the experiments with the sampling frequency of 250 Hz and 24 bits resolution of analog-to-digital conversion. Pulse waves were recorded with the photoplethysmography (PPG) probe located at the cuticle of forefinger of the right hand. Differential arterial blood pressure was measured with two cuffs placed on the left arm and on the left ankle by using oscillometric method.

For extracting single pulse waveforms from the entire recording adaptive detector was employed [5]. This detector is characterized by small errors in detecting maximums and onsets of pulse waves, contaminated by various types of artifacts and noise of different origin and intensity.

To decrease the uncertainties of pulse wave signal processing and vascular indices we preliminary applied digital interpolation to the biosignals by using cubic splines, thus the sampling frequency was selected at 2000 Hz.

To estimate the alterations in the human vascular system under artificially simulated microgravity we have used ankle-brachial pressure index (ABPI) [6], digital pulse wave contour analysis and accelerated photoplethysmography based on calculating the second derivative of the digital pulse wave.

As ABP parameters we have used systolic arterial pressure (*SAP*), diastolic arterial pressure (*DAP*), pulse arterial pressure (*PAP*) calculated as difference between *SAP* and *DAP*, and mean arterial pressure (*MAP*) calculated as follows:

$$MAP = DAP + PAP/3$$

Photoplethysmography is a simple method for detecting the arterial pulsations (pulse waves) generated by the elastic nature of the peripheral vascular arteries and heart contractions [7].

The shape of pulse waves is mainly formed by the interaction between the left ventricle of the heart and large vessels of the systemic circulation, and reflects the composition of forward and reflected pulse waves [8]. Noninvasive estimation of arterial stiffness could be realized by contour analysis of the digital pulse waveforms [9]. The basic hemodynamic parameter that affects the pulse waveform is arterial stiffness, which in turn, is an effective and reliable prognostic marker of atherosclerosis and endothelial dysfunction [10].

Using traditional indices for contour analysis of the pulse wave for patients with severe arterial stiffness is associated with a number of obstacles and difficulties, the main of which is the complication of detecting the reflected wave maximum (so called dicrotic peak) and the further definition of its amplitude and temporal position.

Figure 2 shows typical pulse waveforms in the time domain, the amplitude of the pulse wave is given in arbitrary units. Typical waveforms demonstrate obvious morphological features of the pulse wave signal and emphasize distinctions between healthy and young individual and elderly person with significantly decreased arterial stiffness. Figure 3 illustrates the amplitude spectrum of the corresponding replicated pulse waveforms from Fig. 2.

With developing severe dysfunctions in the arterial system, the bimodal shape of pulse wave disappears, and the dicrotic peak becomes indistinguishable, which leads to significant difficulties in using classic indices for pulse wave contour analysis.

To obtain reliable index for pulse wave morphology assessment we perform Fast Fourier Transform for the sequence formed by consecutive replication of a single pulse waveform with removed dc component. The expression for

the amplitude spectrum of the pulse wave could be determined as follows:

$$X(k) = \sum_{n=0}^{N-1} x(n) \cdot e^{-j\frac{2\pi}{N}nk}$$

where $x(n)$ is a sample of the pulse wave in time domain; n is sample's number in the time domain; k is sample's number in the frequency domain; N is a total number of samples in the considered sequence of pulse waves; $X(k)$ is a sample of the pulse wave in the frequency domain.

Analysis of the obtained spectral characteristics for different types of pulse waveforms has shown significant differences in the structure of the amplitude spectrum. For numerical evaluation of these spectral differences we suggest the use of spectral harmonic index (*SHI*) defined as the amplitude ratio of the first harmonic (As_1) to the second harmonic (As_2):

$$SHI = \frac{As_1}{As_2}$$

We have also calculated pulse wave transmission time (PWTT) between big toe of the right leg and forefinger of the right hand to indirectly estimate the elasticity of arterial blood vessels, according to well known Moens-Korteweg equation [11]. The accelerated photoplethysmography (APPG) has been developed to allow more accurate recognition of the inflection points on the original PPG wave, i.e. dicrotic notch. APPG waveform includes 4 systolic waves (a, b, c, d) and 1 diastolic wave (e) (Fig. 4). To obtain APPG signal from originally recorded PPG signal we have applied the following operation for second derivative:

$$APPG(n) = PPG(n+2) - 2PPG(n) + PPG(n-2)$$

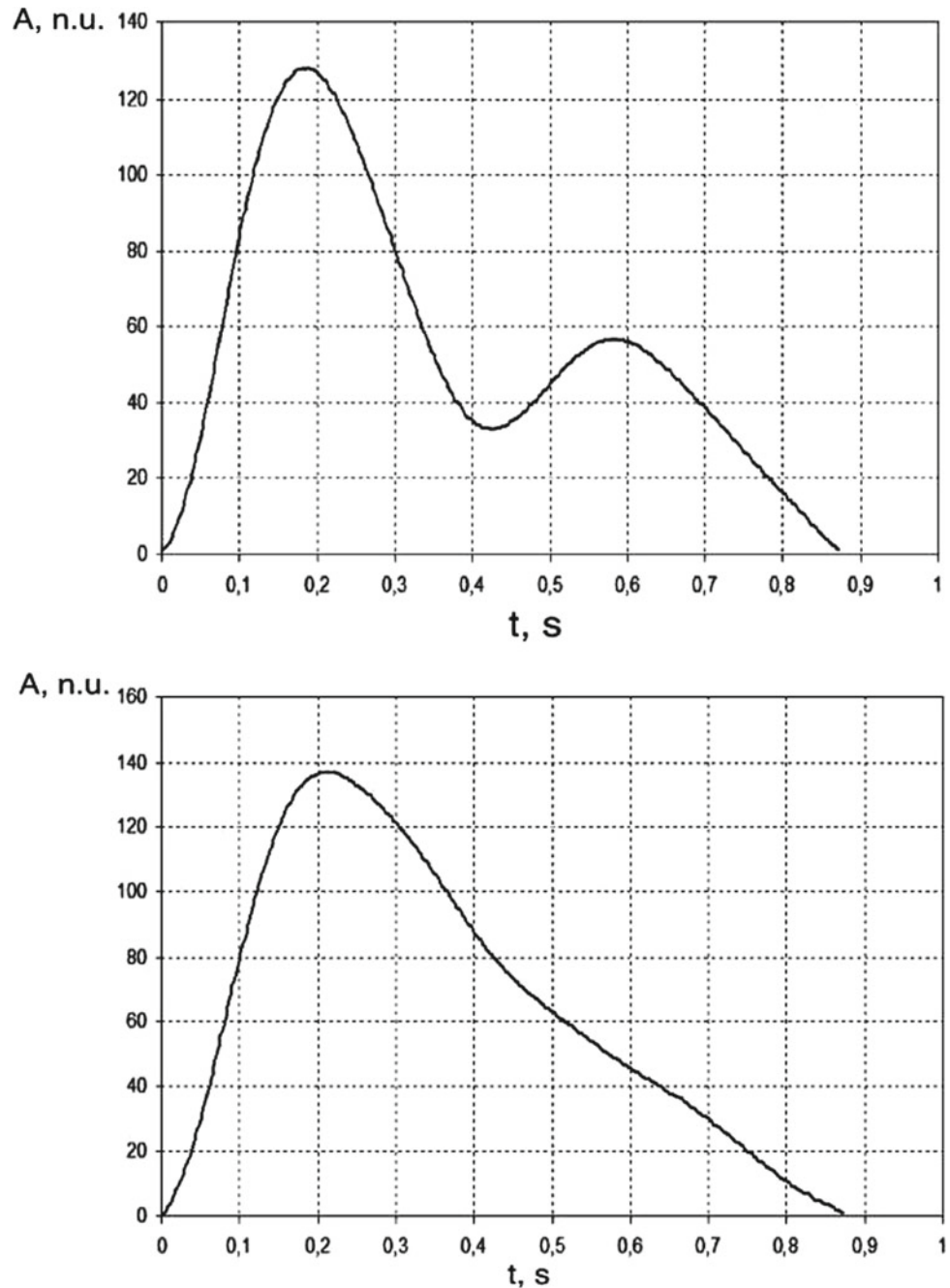
In this work as vascular index we have used the ratio of the height of early negative wave b to that of the initial positive wave a in APPG, so called b/a ratio. This ratio has demonstrated very good correlation with vascular aging and could be considered as promising vascular index and non-invasive assessment of arterial stiffness [12].

3 Results

All experimental data in the tables below are presented as $M \pm SD$ (M is the mean value of the HRV or vascular index and SD is the standard deviation).

Tables 1 and 2 contain the results of calculating ABP values and vascular indices, respectively, at rest, for 1 Gz gravity gradient at the heart level and after exposure.

Fig. 2 Typical pulse waveforms: top trace is for healthy and young individual; bottom trace is for elderly person with decreased arterial stiffness



Figures 5 and 6 depicts box-and-whisker plots for considered ABP values and vascular indices, respectively.

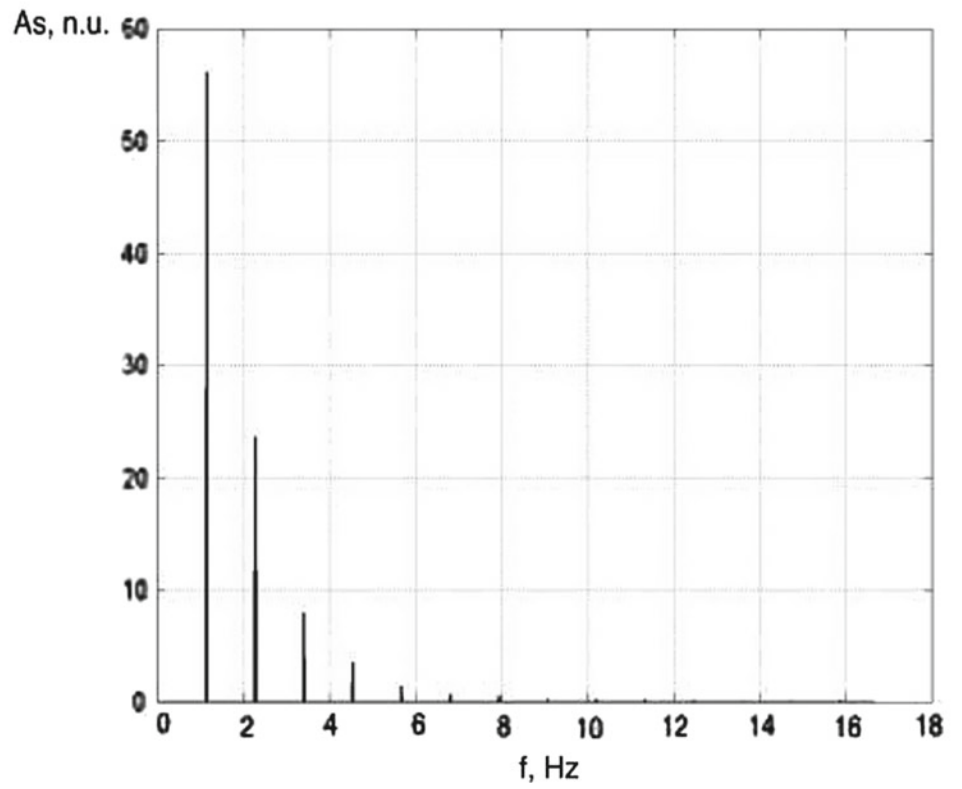
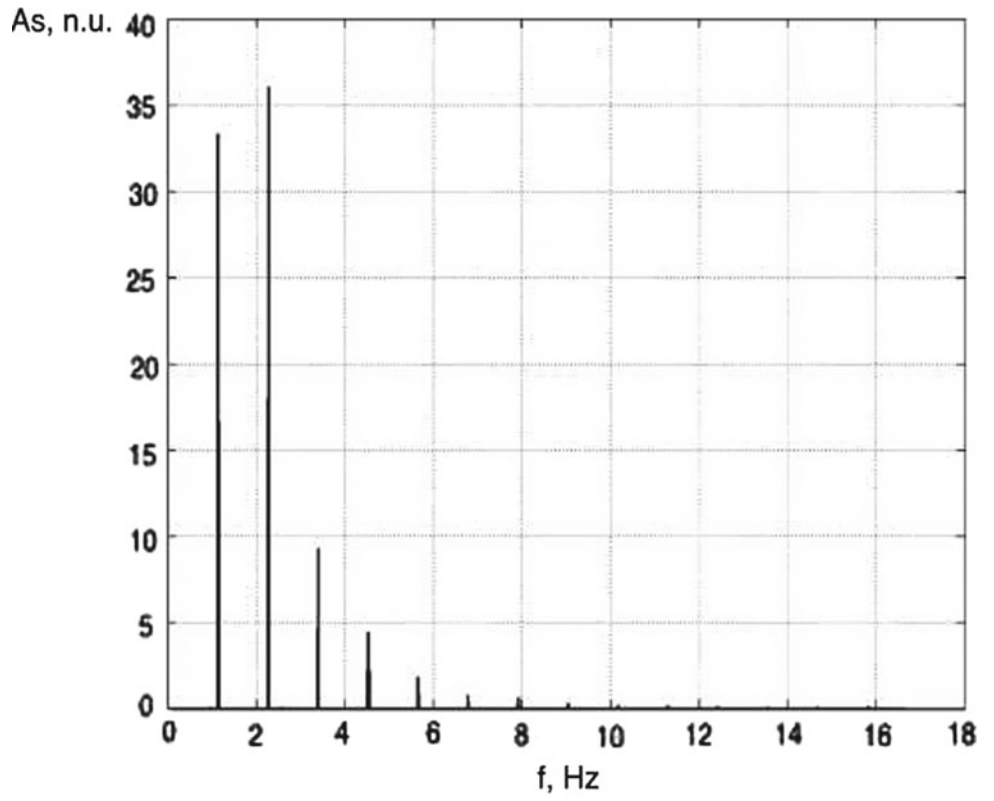
4 Discussion

As a result of the research it was revealed that vascular indices, such as ankle-brachial pressure index and b/a ratio, calculated from accelerated PPG signal, significantly alternates with gravity gradients along head-to-foot direction.

The nature of changes in both vascular indices indicates about improvement in the human vascular system. It is well known that ABPI decreases with the development of vascular diseases, while negative b/a ratio of accelerated photoplethysmogram increases with ageing and with the progression of atherosclerosis [6, 11]. Therefore, authors suggest noticeable possibilities of using gravity therapy for patients with vascular diseases.

Our research has shown that ABP values for the left arm do not change significantly at the conditions of artificial

Fig. 3 The amplitude spectrum for replicated pulse waveform from Fig. 2



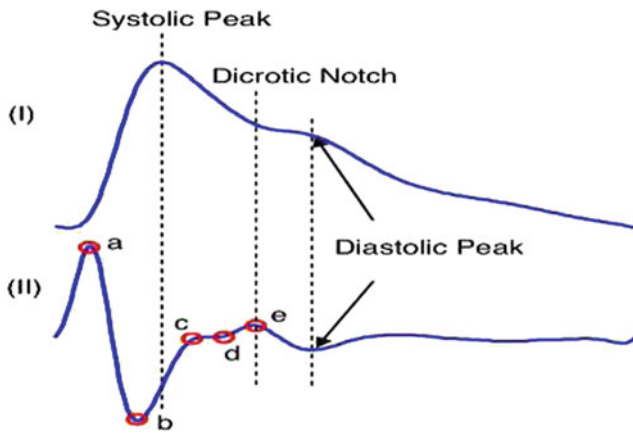


Fig. 4 From top to bottom: the typical PPG waveform for young male (curve I); second derivative of PPG waveform (curve II) [10]

gravity. However, considerable changes are observed for ABP at the left ankle. Thus the effects of artificial gravity are crucial for arterial vessels in lower extremities.

The minor changes in pulse arterial pressure measured at the left ankle and at the left arm could be explained in terms of gradual cardiovascular adaptation from one session to another, especially for young participants at our study.

5 Conclusion

Our research has shown a great promise of using artificial gravity for patients with vascular diseases treatment.

Further research will be related to study the group of elder volunteers with various cardiovascular diseases in order to estimate the influence of artificial gravity on alterations of vascular indices and arterial blood pressure.

Table 1 Arterial blood pressure values for two levels of gravity gradient at the heart level

Index	Rest	Gz = 1	After exposure
<i>ABP values for the left arm</i>			
SAP, mmHg	118.29 ± 12.01	123.76 ± 9.01	116.75 ± 10.64
DAP, mmHg	70.35 ± 6.91	79.22 ± 6.87	71.29 ± 7.67
MAP, mmHg	86.33 ± 7.63	94.07 ± 6.64	86.44 ± 7.81
PAP, mmHg	47.94 ± 9.82	44.55 ± 8.06	45.45 ± 8.52
<i>ABP values for the left ankle</i>			
SAP, mmHg	134.92 ± 15.77	251.33 ± 15.54	133.41 ± 16.59
DAP, mmHg	70.06 ± 10.67	176.71 ± 21.89	71.41 ± 12.22
MAP, mmHg	92.42 ± 13.56	201.58 ± 18.43	92.08 ± 12.45
PAP, mmHg	91.68 ± 11.11	74.63 ± 16.47	62.02 ± 12.81

Table 2 Vascular indices for two levels of gravity gradient at the heart level

Index	Rest	Gz = 1	After exposure
<i>Vascular indices for the left arm</i>			
b/a	-0.98 ± 0.11	-1.13 ± 0.11	-0.99 ± 0.12
SHI	1.95 ± 0.41	1.62 ± 0.61	1.98 ± 0.43
FF	1.47 ± 0.15	1.37 ± 0.16	1.51 ± 0.15
<i>Vascular indices for the left ankle</i>			
b/a	-1.12 ± 0.14	-1.19 ± 0.21	-1.09 ± 0.17
SHI	1.95 ± 0.59	1.64 ± 1.21	1.72 ± 0.55
FF	1.39 ± 0.09	1.32 ± 0.13	1.42 ± 0.11
PWTT, s	0.137 ± 0.041	0.105 ± 0.059	0.134 ± 0.029
ABPI	1.14 ± 0.12	2.04 ± 0.14	1.15 ± 0.14

Fig. 5 Box-and-whisker plots for ABP values

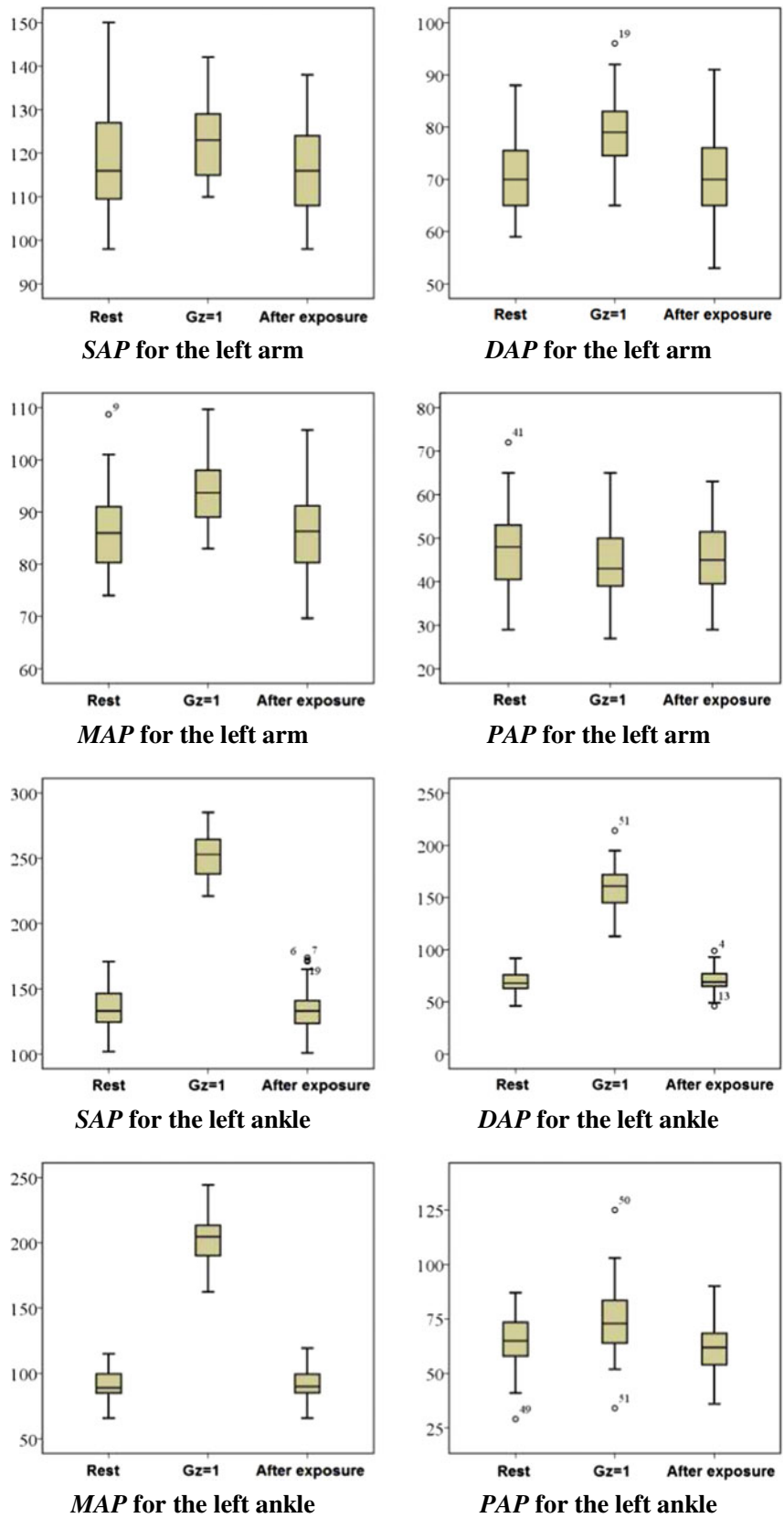
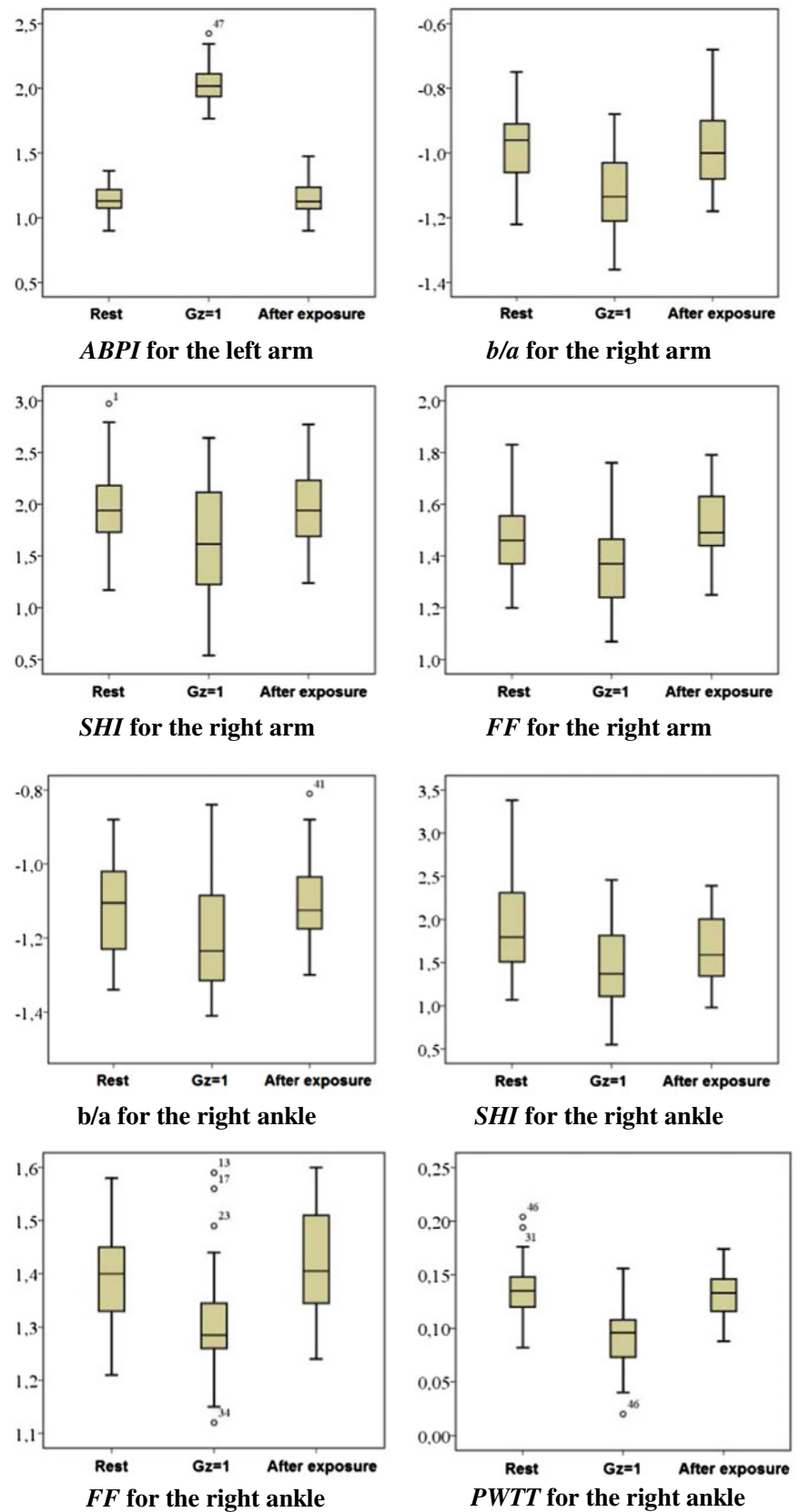


Fig. 6 Box-and-whisker plots for considered vascular indices



Acknowledgements The reported study was funded by RFBR according to the research project №. 17-48-630406.

Conflict of Interest The authors declare that they have no conflict of interest.

References

1. Zander, V., Anken, R., et al.: Short radius centrifuges—a new approach for life science experiments under hyper-g conditions for applications in space and beyond. *Recent Pat. Space Technol.* **3**, 74–81 (2013)
2. Migeotte, P.F., et al.: Respiratory sinus arrhythmia on the ESA-short-arm human centrifuge. *IEEE Eng. Med. Biol. Mag.* **28**(6), 86–91 (2009)
3. Fontollet, T., et al.: Effects of gravitational acceleration on cardiovascular autonomic control in resting humans. *Eur. J. Appl. Physiol.* **115**(7), 1417–1427 (2015)
4. Burton, R.R., Smith, A.H.: *Adaptation to Acceleration Environments*. Wiley Online, pp. 943–970 (2011)
5. Fedotov, A.A.: Amplitude–time method for detecting characteristic pulse wave points. *Biomed. Eng.* **46**(6), 241–245 (2013)
6. Al-Qaisi, M., et al.: Ankle brachial pressure index (ABPI): An update for practitioners. *Vasc. Health Risk Manag.* **5**, 833–841 (2009)
7. Allen, J.: Photoplethysmography and its application in clinical physiological measurement. *Physiol. Meas.* **28**, 1–39 (2007)
8. Weber, T.: Arterial stiffness, wave reflections, and the risk of coronary artery disease. *Circulation* **109**, 184–189 (2004)
9. Millasseau, S.C., et al.: Contour analysis of the photoplethysmographic pulse measured at the finger. *Hypertension* **8**, 1449–1456 (2006)
10. Millasseau, S.C., et al.: Determination of age-related increases in large artery stiffness by digital pulse contour analysis. *Clin. Sci.* **103**, 371–377 (2002)
11. Takazawa, T., et al.: Assessment of vasoactive agents and vascular aging by the second derivative of photoplethysmogram waveform. *Hypertension* **32**, 365–370 (1998)
12. Elgendi, M., et al.: Detection of *a* and *b* waves in the acceleration photoplethysmogram. *BioMed. Eng. OnLine* **13**, 139 (2014)

Using the Distance in Logistic Regression Models for Predictor Ranking in Diabetes Detection

Ghazaal Sheikhi and Hakan Altınçay

Abstract

Logistic regression is widely used to model the relationship between a response variable and multiple independent variables. In practice, the most important variables for each problem domain are generally well known. However, a wealth of ongoing studies has been exploring additional variables for improving the prediction performance using an enriched model. In this article, a new method for ranking binary independent variables is suggested based on the distance between two decision boundaries. The boundaries correspond to the cases when value of the variable is zero or one. It is shown that, using age and body mass index as the base variables for diabetes prediction, the distances mentioned above are effective for ranking additional variables, leading to better scores than several conventionally used approaches.

Keywords

Logistic regression • Feature selection • Binary predictors • Decision boundary • Diabetes prediction

1 Introduction

Type 2 diabetes detection corresponds to the task of determining whether a given medical record belongs to a person who has diabetes. Logistic regression (LR) models are widely used for computing the probability of having diabetes as a function of various risk factors [1–3]. LR-based models

are experimentally shown to provide comparable or better area under the receiver operating characteristic (AUC) scores compared with many other well-known schemes such as support vector machines [4]. An LR model comprises a set of weights assigned to a pre-defined list of predictors and an offset value. These weights are also important for the experts in the domain. When all predictors are held constant, the weight of a predictor corresponds to the change in the *logit* value due to one unit change in the predictor [5].

Consider the LR model including three predictors x_1 , x_2 and x_3 defined as

$$\log\left(\frac{p}{1-p}\right) = \beta_0 + \beta_1x_1 + \beta_2x_2 + \beta_3x_3 \quad (1)$$

Assume that the model is developed for diabetes detection. For a given sample $x_j = [x_{1j}, x_{2j}, x_{3j}]$, p represents the probability that the sample is from a patient having diabetes. $\frac{p}{1-p}$ is called odds and $\log(\text{odds})$ is named as *logit*.

The complexity of the model depends on the number of predictors. In general, simpler models using a smaller subset of predictors are preferred due to their interpretability for the experts in the domain. Moreover, over-fitting may occur as the dimensionality increases, mainly due to employing redundant or correlated predictors that unnecessarily increase the model complexity. Because of these reasons, feature or predictor ranking (or selection) is extensively studied. For instance, in wrapper approaches such as forward selection, the predictors are included to the model as long as the model improves. As an alternative approach, filters such as Chi-square (χ^2), Odds-ratio (OR), Student *t* test (*t*Test), Correlation Coefficient (CC), Gini Index (GI) and Information Gain (IG) have been widely used for this purpose [6–8]. In practice, the relative performance of these schemes depends on the characteristics of the data and number of predictors that need to be determined.

In diabetes detection, both categorical and continuous predictors are used for generating models. For example,

G. Sheikhi (✉) · H. Altınçay
Department of Computer Engineering, Eastern Mediterranean University Famagusta, via Mersin 10, Northern Cyprus, Turkey
e-mail: ghazaal.sheikhi@cc.emu.edu.tr

H. Altınçay
e-mail: hakan.altincay@emu.edu.tr

AGE and body mass index (BMI) are the most important continuous predictors. Gender and family history are binary and, level of education is categorical [9, 10]. The categorical predictors having more than two values are converted to dummy variables, each of which is binary. Consequently, the LR-based models used for diabetes detection are in terms of continuous and binary predictors. In other words, diabetes model development corresponds to finding the best set of binary predictors to be utilized together with AGE and BMI.

Assume that in (1), x_1 and x_2 represent these continuous predictors and, let x_3 be replaced by a candidate binary predictor denoted by x_i . When x_i is zero, *logit* is a linear expression of x_1 and x_2 . Let $x = [x_1, x_2]$ and $g_i(x)$ denote the expression of *logit* when $x_i = 0$. Then, $g_i(x) = \beta_0 + \beta_1 x_1 + \beta_2 x_2$. When $x_i = 1$, the expression for *logit* can be computed by adding β_i , i.e. $g_i(x) + \beta_i$ [5]. It should be noted that $g_i(x) = 0$ and $g_i(x) + \beta_i = 0$ are parallel lines on $(x_1; x_2)$ plane and, the perpendicular distance between these lines depends on the distribution of samples having $x_i = 0$ and $x_i = 1$. If the samples in these two groups overlap, it is expected to obtain $\beta_i \approx 0$, meaning that x_i is a redundant feature. If the distance is large, x_i should be considered as an important predictor since one decision boundary cannot generalize both groups of samples. To the best of our knowledge, the aforementioned distance has not been previously considered for ranking predictors.

In this study, it is aimed to evaluate the importance of each binary predictor by taking into account the distance between decision boundaries obtained when the predictor value is zero and one. The scores assigned to predictors are used for ranking them. Majority of the filter approaches take into account the number of positive and negative samples for which the predictor has a non-zero value. For example

$$OR(x_i) = \frac{A \times D}{B \times C} \quad (2)$$

where A and C respectively denote the number of positive and negative samples for which $x_i = 1$. Similarly, B and D correspond to the number of positive and negative samples where $x_i = 0$. As an alternative strategy, for each x_i , the distance between $g_i(x) = 0$ and $g_i(x) + \beta_i = 0$ obtained on $(x_1; x_2)$ plane can be used to scale six filter-based selection schemes mentioned above.

The rest of the paper is organized as follows. Section 2 presents a brief review of LR models. In Sect. 3, using distance as a ranking metric is explained. The experiments

and the results are presented in Sect. 4. Finally, Sect. 5 concludes the paper and provides potential future work.

2 A Brief Review of LR Models

Let S_{i0} and S_{i1} respectively denote the training samples having $x_i = 0$ and $x_i = 1$. Consider the relationship between a binary response variable and three predictors as given in (1) computed using the whole set of training samples, i.e. $S_{i0} \cup S_{i1}$. The *logit*(p) is equal to $g_i(x)$ and $\hat{g}_i(x) = g_i(x) + \beta_i$ respectively when $x_i = 0$ and $x_i = 1$ as given below [5]:

$$\text{logit}(p) = \begin{cases} g_i(x) & \text{when } x_i = 0 \\ \hat{g}_i(x) & \text{when } x_i = 1 \end{cases} \quad (3)$$

The model can be represented using two parallel lines namely, $g_i(x) = 0$ and $\hat{g}_i(x) = 0$. The decision boundary for samples in S_{i0} is $g_i(x) = 0$ and for samples in S_{i1} , it is $\hat{g}_i(x) = 0$. Consider the samples in S_{i0} that are on $g_i(x) = 0$. For those samples, *logit*(p) is equal to zero. This means that $p = 0.5$ on the decision boundary. On the positive side of $g_i(x)$, $p > 0.5$ and on the negative side $p < 0.5$. Consider an arbitrary sample $x \in S_{i0}$. The perpendicular distance from x to $g_i(x) = 0$ can be calculated as [11]

$$d_{i0} = \frac{g_i(x)}{\sqrt{\beta_1^2 + \beta_2^2}} \quad (4)$$

Similarly, the distance from x to $\hat{g}_i(x) = 0$ is

$$d_{i1} = \frac{g_i(x) + \beta_i}{\sqrt{\beta_1^2 + \beta_2^2}} \quad (5)$$

Hence, the distance between $g_i(x)$ and $\hat{g}_i(x)$ denoted by r can be computed as

$$r = d_{i1} - d_{i0} = \frac{\beta_i}{\sqrt{\beta_1^2 + \beta_2^2}} \quad (6)$$

Since $g_i(x)$ and $\hat{g}_i(x)$ are computed using both S_{i0} and S_{i1} , it can be argued that the LR-based model is a compromise solution since the decision boundaries corresponding to the estimated model are not optimal for any group of samples. As an example, the decision boundary that would be obtained using only S_{i0} or only S_{i1} might have different slopes from $g_i(x) = 0$.

3 Using R_i for Predictor Ranking

In this study, we assume that the optimal decision boundaries of S_{i0} and S_{i1} are in parallel and hence can be accurately represented using the linear model given in (1). In such cases, a given predictor can be ranked in terms of the distance between $g_i(x)$ and $\hat{g}_i(x)$, i.e. r_i . When $r_i \approx 0$, it can be argued that the predictor is redundant. When $r_i \gg 0$, this means that the samples in S_{i0} and S_{i1} highly differ in terms of *logit* values. Hence, r_i can be used as a measure for ranking binary predictors as given in Algorithm 1.

Algorithm 1. Feature ranking using r_i

Require: Candidate predictors: $x_i, i > 2$
for each predictor x_i **do**
 Compute the expression *logit*(p) using x_1, x_2 and x_i
 Compute r_i using (6)
end for
 Rank the predictors using r_i

As an alternative approach, r_i is used to scale the aforementioned filter methods, namely χ^2 , OR, *t*Test, CC, GI and IG. The algorithm used to scale χ^2 is presented in Algorithm 2. It can be applied to all filters by replacing χ^2 by the desired filter. It should be noted that both algorithms can be easily generalized to the cases when more than two continuous predictors are employed. In such cases, $g_i(x)$ corresponds to a hyper plane.

Algorithm 2 Feature ranking using $r_i \times \chi_i^2$

Require: Candidate predictors: $x_i, i > 2$
for each predictor x_i **do**
 Compute the expression *logit*(p) using x_1, x_2 and x_i
 Compute r_i using (6)
 Compute $r_i \times \chi_i^2$
end for
 Rank the predictors using $r_i \times \chi_i^2$

4 Experimental Results

4.1 Datasets

In order to evaluate proposed algorithm, an electronic health record (EHR) and three national health survey data sets are

used. By processing this information, five diabetes data sets are prepared incorporating two continuous predictors (AGE and BMI) and several binary variables. It should be noted that all direct indicators of diabetes were removed from the data. Two data sets named as KAGGLE1 and KAGGLE2 are extracted from Kaggle EHR which contains de-identified electronic health records of 9948 people in the United States. It is collected by Practice Fusion from 2009 to 2012 and then published by Kaggle for a competition. The records include information about demography, anthropometry, symptoms, diagnoses, prescribed medications for specific diagnoses and results of laboratory tests. In KAGGLE1 data set, in addition to AGE and BMI, 21 binary features are defined based on gender, family history of diabetes, smoking status and diagnoses. Each diagnosis predictor is defined as whether a patient is diagnosed with a specific disease category from the broadest ICD9 disease coding. KAGGLE2 is formed by replacing diagnosis predictors with medication predictors determined as whether a specific medication is prescribed for endocrine nutritional and metabolic diseases, and immunity disorders. There are 28 binary predictors in KAGGLE2 besides AGE and BMI.

The remaining three data sets are extracted from the survey of National Center for Health Statistics (NCHS) conducted in different years. This survey represents demographic and biologic characteristics of a cross-sectional population in the United States. This data is collected annually by interviewing the selected population at home using questionnaires and then examining them at Mobile Exam Center. The collected data is published on a two-years basis. In this study, NHANES 2005–2006, NHANES 2007–2008 and NHANES 2009–2010 survey data are selected to form NHANES1, NHANES2 and NHANES3 diabetes data sets, respectively. There are 13 binary predictors in these data sets extracted from gender, ethnicity, education level, family history of diabetes, high blood sugar, hypertension and physical activity.

4.2 Results

The experimental phase is devised as follows. Each ranking algorithm is firstly applied to compute the ranking scores of all binary predictors. Then, feature subsets are formed by appending top ranked binary predictors to continuous features in a step-wise manner. In other words, the first subset consists of AGE, BMI and the first-ranked binary predictor while the other binary predictors are gradually added to the subset one by one according to their ranks. Finally, each feature subset is examined by a logistic regression model generated to detect diabetes. Five-fold cross validation is applied and subset performance is quantified by mean AUC value. The proposed distance metric is utilized for ranking

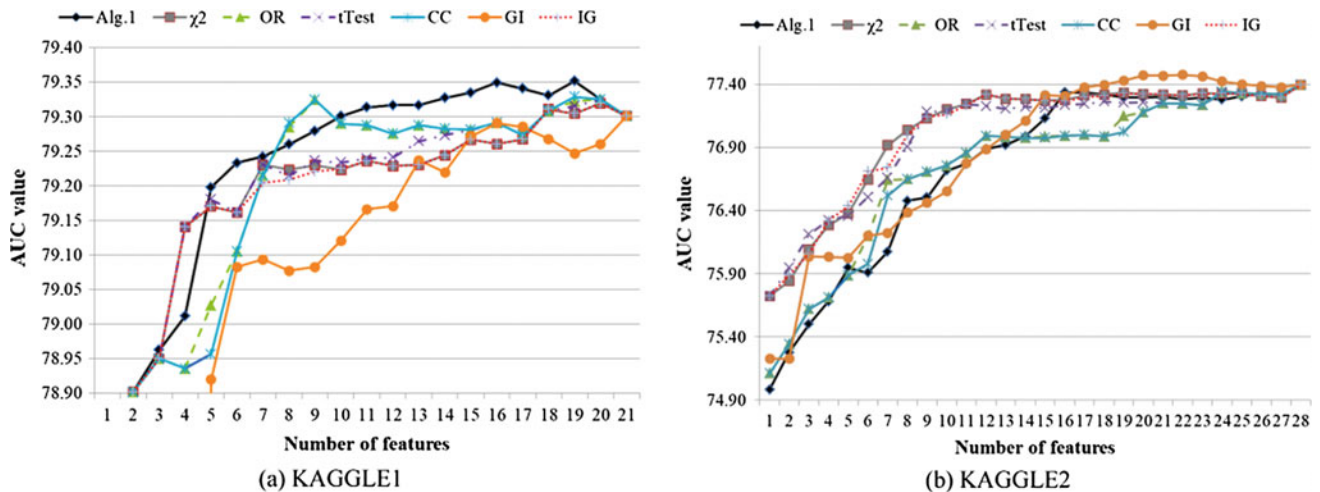


Fig. 1 Experimental results on KAGGLE1 and KAGGLE2

predictors as explained in Algorithm 1. Similarly, six well-known filter approaches namely, χ^2 , OR, t Test, CC, GI and IG are applied in ranking phase for comparison. AUC curves achieved using Algorithm 1 and six filter approaches are illustrated in Fig. 1 for KAGGLE1 and KAGGLE2. Note that AUC values are expressed as percentage.

Figure 2 presents the average AUC scores for different number of binary feature on NHANES1, NHANES2, and NHANES3. It can be seen that better curves are generally obtained on NHANES datasets. However, the proposed algorithm is poor on KAGGLE2. The reason is the estimated models are highly reliable and useful for ranking predictors only in cases when cardinalities of the two sample sets, S_{i0} and S_{i1} are close to each other. In other words, the predictors must not be sparse, while KAGGLE2 is highly sparse.

The features are also ranked by scaled versions of the filter methods as explained in Algorithm 2. In Fig. 3, AUC curves of OR and scaled OR are presented for KAGGLE1 and NHANES1. It can be seen in the figures that further improvements can be achieved. However, in order to make a more objective comparison, AUC values are firstly averaged among all tested subsets. Then, the best filter is assumed as the one with maximum average AUC. The best filter is then considered as the reference to conduct Wilcoxon signed-ranks test. Wilcoxon's p -value is computed to measure if the reference curve is significantly better than other curves ($p < 0.05$). In Table 1, these average AUC values and their related p -values are presented. For the reference

filter, p -value is denoted by 1.00. The cases where there is no significant difference in AUC values are shown in bold. In the last column, the number of data sets for which the ranking method is among the winners is reported. It can be inferred from Table 1 that Algorithm 1 is among the best on four datasets and, Algorithm 2 can be utilized to enhance the conventional filters, particularly OR.

5 Conclusions

In this study, two algorithms are studied for ranking binary predictors when used together with continuous predictors. The experimental results have shown that the proposed algorithms are among the top-ranked schemes on majority of the datasets. The proposed algorithms are based on computing the prediction models for two groups of samples, S_{i0} and S_{i1} . However, in practice, one of these groups may be small. This means that the value of a predictor may be non-zero only for a small set of samples. In such cases, the estimate for the coefficient of that predictor may not be reliable. Another assumption of the proposed metric is that the decision boundaries of the two groups are in parallel. However, the best-fitting boundaries might have a non-zero angle. As a future work, we are planning to improve the proposed algorithms by modifying them to consider the number of samples and the angles between best-fitting models of each subset of samples.

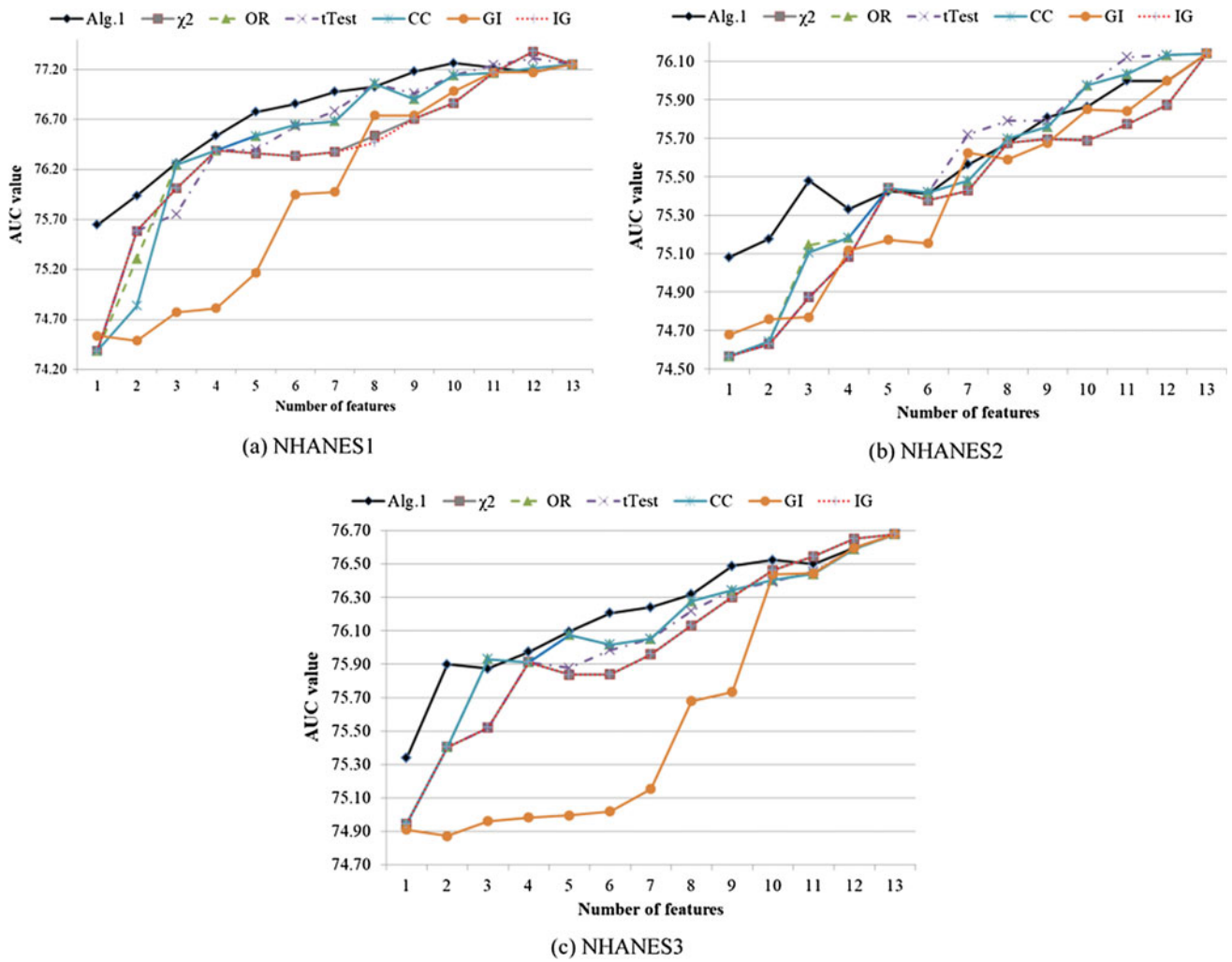


Fig. 2 Experimental results on NHANES1, NHANES2 and NHANES3

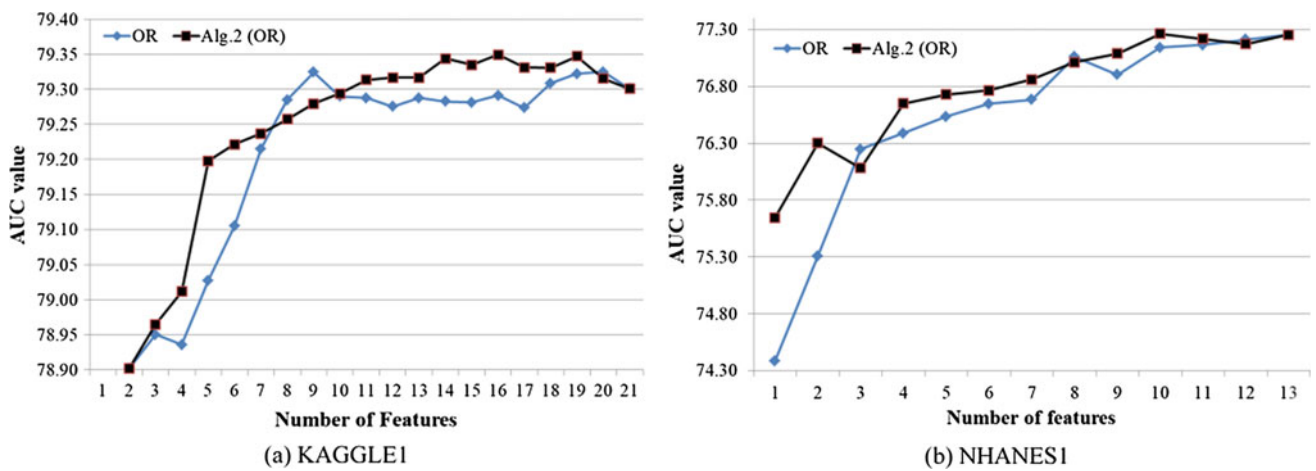


Fig. 3 Experimental results for OR and Alg.2 (OR) on a KAGGLE1 and b NHANES1

Table 1 Average AUC scores with p-values computed using Wilcoxon signed-ranks test

Filter	KAGGLE1	KAGGLE2	NHANES1	NHANES2	NHANES3	#Wins
Alg.1	79.16 (1.00)	76.74 (0.00)	76.78 (1.00)	75.61 (1.00)	76.21 (1.00)	4
χ^2	79.12 (0.00)	77.03 (1.00)	76.41 (0.00)	75.40 (0.00)	76.01 (0.00)	1
OR	79.13 (0.00)	76.76 (0.00)	76.53 (0.00)	75.51 (0.17)	76.08 (0.01)	1
tTest	79.13 (0.00)	76.99 (0.01)	76.53 (0.01)	75.51 (0.53)	76.03 (0.00)	1
CC	79.12 (0.00)	76.74 (0.00)	76.50 (0.00)	75.51 (0.17)	76.08 (0.01)	1
GI	78.70 (0.00)	76.85 (0.03)	75.98 (0.00)	75.41 (0.00)	75.57 (0.00)	0
IG	79.12 (0.00)	77.02 (0.81)	76.41 (0.00)	75.40 (0.00)	76.01 (0.00)	1
Alg.2 (χ^2)	79.16 (0.35)	76.99 (0.10)	76.69 (0.04)	75.54 (0.03)	76.10 (0.04)	2
Alg.2 (OR)	79.16 (0.57)	76.78 (0.00)	76.77 (0.53)	75.59 (0.44)	76.20 (0.17)	4
Alg.2 (tTest)	79.12 (0.00)	76.97 (0.38)	76.56 (0.01)	75.52 (0.00)	76.10 (0.02)	1
Alg.2 (CC)	79.10 (0.00)	76.77 (0.00)	76.55 (0.01)	75.48 (0.00)	76.16 (0.01)	0
Alg.2 (GI)	79.13 (0.02)	76.96 (0.01)	76.58 (0.31)	75.57 (0.57)	75.92 (0.00)	2
Alg.2 (IG)	79.00 (0.00)	76.28 (0.00)	76.32 (0.02)	75.56 (0.83)	76.14 (0.54)	2

Acknowledgements We would like to offer special thanks to Kamran Kamaei for his assistance in preparing NHANES data sets.

References

- Ramezankhani, A., Pournik, O., Shahrabi, J., Azizi, F., Hadaegh, F., Khalili, D.: The impact of oversampling with SMOTE on the performance of 3 classifiers in prediction of type 2 diabetes. *Med. Decis. Making* **36**(1), 137–144 (2016)
- Lee, B.J., Ku, B., Nam, J., Pham, D.D., Kim, J.Y.: Prediction of fasting plasma glucose status using anthropometric measures for diagnosing type 2 diabetes. *IEEE J. Biomed. Health Inf.* **18**(2), 555–561 (2014)
- Wang, C., Li, L., Wang, L., Ping, Z., Flory, M.T., et al.: Evaluating the risk of type 2 diabetes mellitus using artificial neural network: an effective classification approach. *Diabetes Res. Clin. Pract.* **100**(1), 111–118 (2013)
- Güvenir, H.A., Kurtcephe, M.: Ranking instances by maximizing the area under ROC curve. *IEEE Trans. Knowl. Data Eng.* **25**(10), 2356–2366 (2013)
- James, G., Witten, D., Hastie, T., Tibshirani, R.: *An Introduction to Statistical Learning: With Applications in R*, ser. Springer Texts in Statistics. Springer, Berlin (2013)
- Saeyns, Y., Inza, I., Larranaga, P.: A review of feature selection techniques in bioinformatics. *Bioinformatics* **23**(19), 2507–217 (2007)
- Hira, Z.M., Gillies, D.F.: A review of feature selection and feature extraction methods applied on microarray data. *Adv. Bioinf.* **2015** (2015)
- Huang, Y., McCullagh, P., Black, N., Harper, R.: Feature selection and classification model construction on type 2 diabetic patients' data. *Artif. Intell. Med.* **41**(3), 251–262 (2007)
- Lindstrom, J., Tuomilehto, J.: The diabetes risk score: a practical tool to predict type 2 diabetes risk. *Diabetes Care* **26**(3), 725–731 (2003)
- Robinson, C.A., Agarwal, G., Nerenberg, K.: Validating the CANRISK prognostic model for assessing diabetes risk in Canada's multiethnic population. *Chronic Dis. Injuries Can.* **32**, 19–31 (2011)
- Duda, R.O., Hart, P.E., Stork, D.G.: *Pattern Classification*. John Wiley and Sons (2001)

Expert System for Performance Prediction of Anesthesia Machines

Lejla Hadžić, Arnela Fazlić, Osman Hasanić, Nudžejma Kudić, and Lemana Spahić

Abstract

This paper presents an Expert System for prediction of Anesthesia machines performance and inspection requirements. It consists of Artificial Neural Network and Fuzzy classifier. The system takes 12 inputs as follows: three for measured values of volume, three for measured gas concentration, three for visual inspection of the device, average utilization time of the anesthesia machine, preventive maintenance intervals and number of additional parts. For development of the system 197 samples were used. All samples were acquired during real-time study in healthcare institutions in Bosnia and Herzegovina during the period of three years. Two-layer feedforward back propagation network with 23 neurons in hidden layer and hyperbolic tangent sigmoid transfer function was trained with 158 samples. Out of 39 validation samples, the developed network was accurate in 97.44% cases. Fuzzy rules are defined according to recommendations. Validation of developed expert system was performed using 39 samples out of which expected results were obtained for 38 samples while for 1 sample false prediction of performance status of anesthesia machine was recorded.

Keywords

Anesthesia machine • Inspection • Classification • Performance status • Artificial neural network • Fuzzy classifier • Expert system

1 Introduction

One of the milestones achieved in medicine that has affected every patient is the invention of anesthesia and anesthesia machines. Robinson and Toledo defined anesthesia machine as an apparatus that helps deliver general anesthesia to patients during surgery which eliminated main factor that caused fear of surgeries: pain [1]. Dorsch and colleagues characterized anesthesia machines as essential devices in operating rooms which by administration of anesthetic gases leave the patients with clinical picture defined by lack of response to stimuli, inability to maintain airway protection and spontaneous breathing, amnesia in regards to operation proceedings and cardiovascular changes [2].

Considering its importance in surgical procedures and operating rooms various national associations of Anesthesiologists have recommended the minimum safety features for machines used in their countries or by their members [3–5].

Safety features for anesthesia machines that are mandatory and those that are desirable are specified by many international standards [6, 7]. Due to the complex nature of anesthesia machines as well as variations in design among manufacturers, a single checklist cannot test the integrity and safety of all existing anesthesia machines [8]. An elaborate and in-depth check of anesthesia machine should be done after servicing of the device, while machine check should be done daily prior to usage. Between each anesthetic conduct minor check procedure should be conducted [9]. Checking procedures of anesthesia machines should be user friendly and less time consuming while ensuring a thorough check of

L. Hadžić · A. Fazlić · O. Hasanić · N. Kudić · L. Spahić (✉)
Department of Genetics and Bioengineering, International Burch
University, Sarajevo, Bosnia and Herzegovina
e-mail: lemanaspahic@stu.ibu.edu.com

L. Hadžić
e-mail: lejla.hadzic@stu.ibu.edu.ba

A. Fazlić
e-mail: fazlicarnelabjk@yahoo.com

O. Hasanić
e-mail: osman.hasanic@stu.ibu.edu.ba

N. Kudić
e-mail: kudic.nudzejma@gmail.com

all components of the machine [10]. Safety features are sub-divided into the several categories based on gas supplies (from the central pipeline to the machine as well as cylinders), flow meters, vaporizers, fresh gas delivery (breathing systems and ventilators), scavenging and monitoring [11].

Better understanding of the basics of anesthesia machine and checking each component of the machine for proper functioning prior to use, regular inspections and maintenance are essential to minimize hazards [12]. Studies from all over the world suggest that anesthesia can cause severe adverse effects if not properly maintained and used [13–15]. Despite of existence of strict safety measures, various incidents in operating rooms are observed due to anesthesia machine malfunction [15]. Medical safety is ensured by combined application of measuring standards and reference standards which reduces the potential hazard to patient and medical personnel to a minimum. Therefore, requirements for technical service and calibration of medical devices and software control should be included into standardization [16, 17]. One of the most important steps for regulation and standardization of healthcare system of one country, such as Bosnia and Herzegovina, is introduction of medical devices into legal metrology system. Unbiased control of medical devices is conducted, with documented traceability to international standards [18–20].

Study performed by Gurbeta et al. that aimed to investigate the electrical safety of Anesthesia machines and to perform independent inspection of efficiency of preventive and corrective maintenance. It showed that 13.84% of tested anesthesia machines performance is not in accordance with requirements and should be either serviced or the device has to be removed from use [21].

Exploration of use of artificial intelligence (AI) in healthcare sphere by medical researchers, informatics specialists and digital entrepreneurs exist for decades. Machine learning is used for diagnosis, prediction and classification of many prevalent diseases that significantly decrease quality of life such as Alzheimer's disease [22, 23], asthma [24–26], diabetes [27, 28] and cardiovascular diseases [29, 30] as well as some frequent genetic disorders such as Down, Patau, Edwards syndrome and Klinefelter syndrome [31]. In the sphere of anesthesia and anesthesia machines Caelen et al., developed machine learning techniques that enabled closed-loop control of anesthesia [32], while model for estimating the depth of anesthesia was developed by Zhang and Roy. The developed model demonstrated good performance in discriminating awake and asleep states for three common anesthetic regimes [27]. Also, machine learning is

successfully used for development of system for prediction of preoperative anesthetic risk which is of prime importance for safe operation [33].

At the end of the last century development of various software based on artificial intelligence for control of anesthesia and monitoring its alarms was performed [34–36].

However, there is an absence of systems based on artificial intelligence aiming to predict performance status of anesthesia machine and inspection requirements that would increase the quality and safety of care.

Creation of big data structures enabled individual data characteristic for each anesthesia machine inspected in Bosnia and Herzegovina according to legal metrology framework established for medical devices with measuring function [37] in period from 2015 to 2017 was obtained by courtesy of Verlab Ltd. Sarajevo. This provides a possibility for prediction of device performance status and inspection requirement to increase the safety and accuracy of diagnosis and treatment, and thus the quality of service to patients and the reliability of the device, which is essential for medical practitioners. This paper presents a machine learning system based on Artificial Neural Network and Fuzzy logic which yields prediction of anesthesia machine performance status and indication of necessity for anesthesia machine maintenance.

2 Methods

Block diagram of developed Expert System based on Artificial Neural Network and Fuzzy classifier for prediction of Anesthesia machine performance status is represented in Fig. 1.

2.1 Dataset for Development of Expert System for Prediction of Anesthesia Machine Performance Status

Database consisted of 197 samples. Each sample contains visual inspection results for the device, and measurements of volume and anesthesia gas concentrations. Each device was inspected once a year, for three consecutive years in healthcare institutions in Bosnia and Herzegovina. All measurements were acquired by experts from appointed laboratory for inspection of medical devices with measuring function. These measurements were conducted by procedures in accordance to ISO 17020 [21, 38].

Fig. 1 Block diagram of the developed Expert System based on Artificial Neural Network and Fuzzy classifier

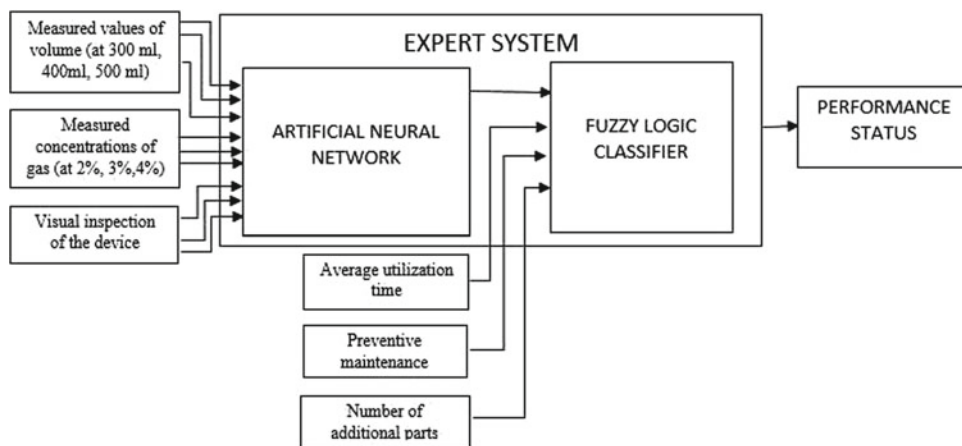


Table 1 Analysis of dataset

Total number	Accurate	Faulty
197	173	24
	87.8%	12.2%

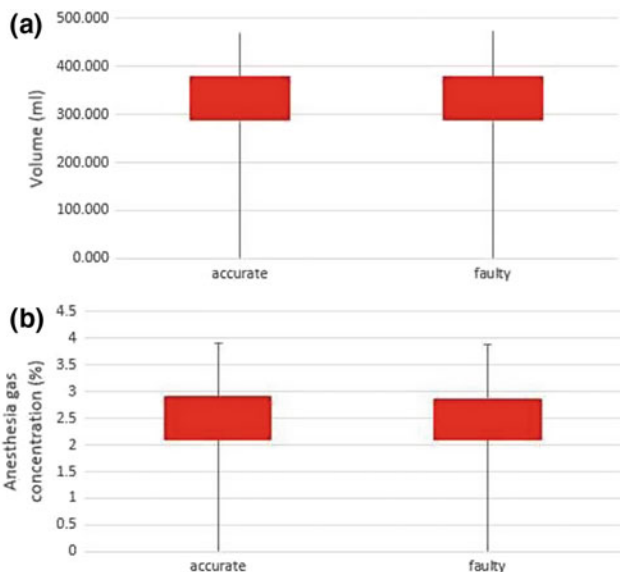


Fig. 2 a Mean value of volume measurements in case of accurate and faulty device. b Mean value of gas concentration measurements in case of accurate and faulty device

Table 1 gives an overview of the dataset by two classes, functional (accurate)—devices which comply to legal technical and measurement requirements and nonfunctional (faulty)—devices which do not comply to legal technical and measurement requirements [39].

Statistical analysis of available data was performed where mean value for volume measurement in case of accurate and faulty device was determined and represented in Fig. 2a and mean value for measurement of gas concentration in case of

accurate and faulty device was determined and represented in Fig. 2b.

Additionally, quartiles of data for each six measurements were determined and represented in Fig. 3. Figure 3a represents quartiles for three measurements of volume (300, 400 and 500 mL) while Fig. 3b represents quartiles determined for three measurements of gas concentration (2, 3 and 4%).

2.2 Development of Artificial Neural Network

Artificial Neural Network was developed in order to perform prediction of performance status of anesthesia machine based on measurements of patient related output parameters that are volume and anesthesia gas concentration. Based on these measurements, anesthesia machine can have high probability for failure and therefore needs to be inspected more than once a year, pr low probability for failure thus period for inspection can remain once a year.

Division of dataset on training data used for ANN development and validation data for testing of performance of designed ANN was performed. Data was divided using trial and error method during the process of network training [40]. The best performance of Artificial Neural Network was obtained for division of training data represented to 80% for training, 15% for validation and 5% for testing.

Two-layer feedforward network with hyperbolic tangent sigmoid transfer function in hidden layer (Table 2) and a softmax neuron in the output layer showed the best performance.

Fig. 3 **a** Representation of quartiles for three measurements of volume (red-quartile 1, blue-quartile 2). **b** Representation of quartiles for three measurements of gas concentration (red-quartile 1, blue-quartile 2)

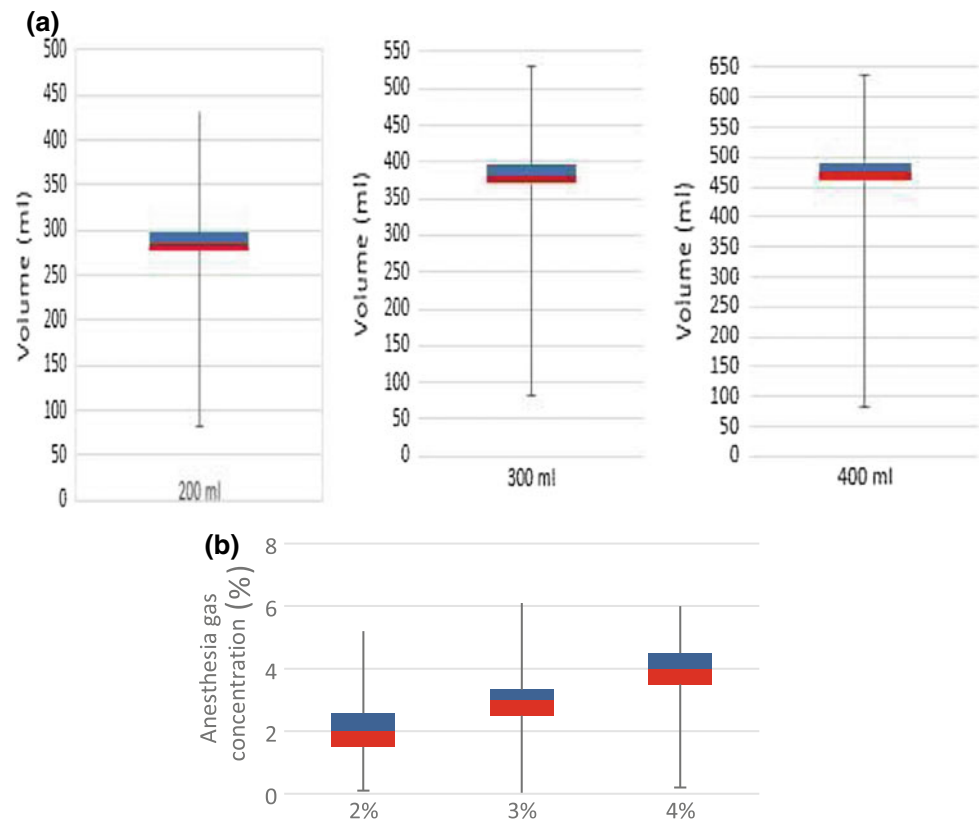


Table 2 Network development

Network architecture	Feedforward	Performance
Number of neurons	10	0.2760
	15	0.1202
	20	0.1188
	23	3.7467e-07
	25	0.1169
Transfer function	logsig	7.8103e-07
	tansig	3.7467e-07
	hardlim	3.5323e-06
	purelin	0.2042

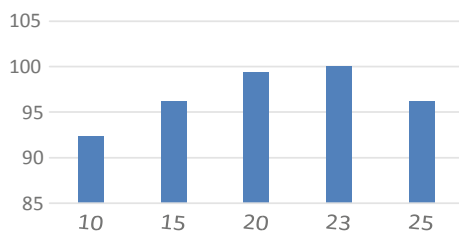
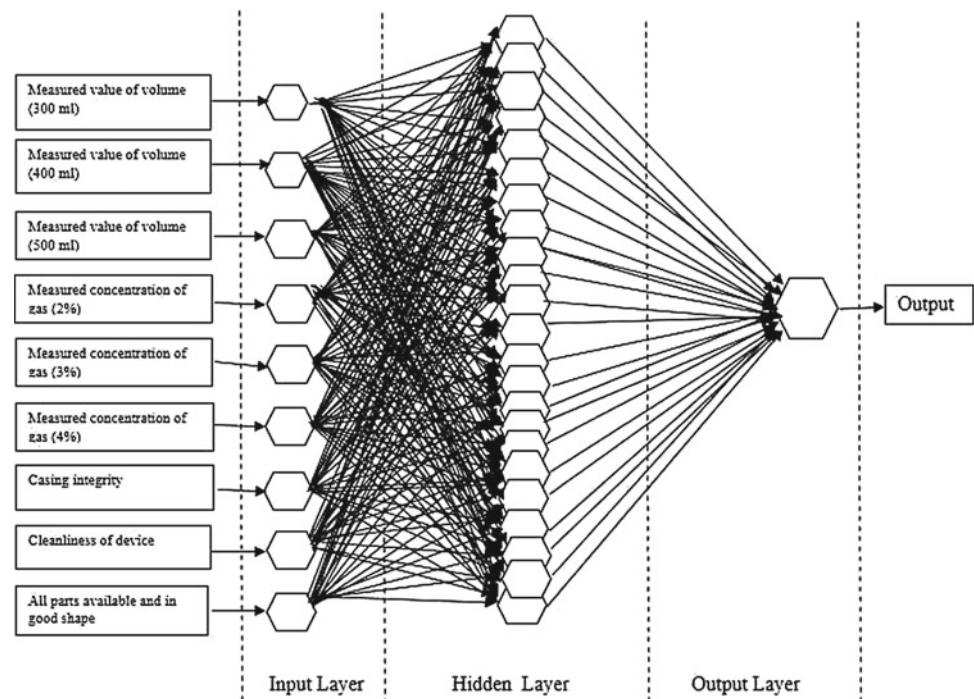


Fig. 4 Graphical display of output accuracy of networks with 10, 15, 20, 23 and 25 neurons in hidden layer

During the process of network training number of neurons was selected using trial and error method in order to generate functional Artificial Neural Network with desired performance (Table 2). Appropriate number of neurons was chosen according to the Mean Square Error (MSE) [18]. Training of the network with 158 samples with 10, 15, 20, 23 and 25 neurons in hidden layer has been performed and output accuracy of each is represented in Fig. 4.

According to data represented in Table 2 and Fig. 4 the best performance and accuracy were obtained for network

Fig. 5 An illustration of the architecture of the developed network with 23 neurons in hidden layer



with 23 neurons. Network inputs constitute the input layer which is followed by a hidden layer which consists of parallelly connected neurons. Weighted summation of the inputs is performed by each neuron [27], then passed to hyperbolic tangent sigmoid transfer function.

The path of changing the input in desired output using 23 neurons in hidden layer is displayed in the architecture of the network (Fig. 5). Interaction of each input parameter with each of the 23 neurons in hidden layer if followed by passing of the signal from each neuron from hidden layer to neuron in output layer where processing of the signal is performed by this neuron and desired output of the network is given.

2.3 Development of Fuzzy Classifier

Fuzzy classifier has four inputs that are as follows: output of Artificial Neural Network and information about the average utilization time of the anesthesia machine, preventive maintenance intervals and the number of parts prone to degradation over time. Average utilization time of anesthesia machine was estimated considering the work of Leong and colleagues which categorized surgical operations into several groups in dependence of their duration [41]. Since anesthesia machine is crucial device in each operating room, in our study we created a modified approach for estimation of anesthesia machine utilization considering basic premises offered in the work of Chaudhary and Kaul [42]. Preventive maintenance intervals are specified as combination of maintenance intervals suggested by Dräger [43],

manufacturer of more than half investigated anesthesia machines in Bosnia and Herzegovina, and Universal Anesthesia Machine Maintenance Manual [44]. Number of additional parts is estimated according to recommendations from Universal Anesthesia Machine Maintenance Manual [44]. Membership function border and inclusion values for aforementioned inputs are defined by the equations in the Appendix 2.

Fuzzy rules, 13 of them, were defined using the following logic: short utilization time of anesthesia machine gives low chance (due to its usage) to turn faulty, frequent maintenance intervals ensure proper functioning of device and higher the number of additional parts higher the possibility that anesthesia machine will need inspection. Outputs are generated based on fuzzy rules, and they give information on performance status of the device and indicate if inspection is required.

Output is classified as low, medium and high in order to enable more combinations of rules to be created, while in the final step all output values higher than 0.5 are taken as indication that inspection is required, while all output values lower than 0.5 are taken as indication that inspection is not required (Membership function relations in Appendix 2).

3 Results

During the training, the highest output accuracy was achieved with 23 neurons, therefore further testing of the network with 39 samples was performed and results of

Table 3 Performance of ANN

	Classified as high probability for maintenance required	Classified as low probability for maintenance required
Actual high probability for maintenance required 11	TP = 10	FN = 1
Actual low probability for maintenance required 28	FP = 0	TN = 28
	10	29
	Sensitivity = 90.91%	Specificity = 100%

classification of anesthesia machines for inspection requirement are represented in Table 3. It was expected that the output of Artificial Neural Network will be 28 devices with low probability for inspection required and 11 devices with high probability for inspection required.

It is shown that out of 11 samples that are expected to be classified as devices with high probability for inspection required, the network classified 10 samples correctly while 1 sample turned to be a false negative. Out of 28 samples that were expected to be classified as devices with low probability for maintenance requirement, 28 showed the low probability for maintenance requirement while 0 samples have been false positive.

After performing K-fold cross validation according to the code in Appendix 1, the performance of the ANN deteriorated exponentially which is highly unlikely to happen with respect to the dataset which is very convenient for ANN to interpret. Therefore we did not present the results from cross validation as it did not provide any benefit to the system.

According to these results, sensitivity and specificity of the network were calculated and are presented in Table 3. Results shown in Table 3 indicate, that when device with high probability for inspection requirement undergoes a test using this neural network, there is 90.91% chance that this device will be classified as a device with high probability for inspection required. Percentage of specificity indicates that when device with low probability for inspection required conducts a test with this network, there is 100% of chance that device will be classified as device with low probability for inspection required.

This Artificial Neural Network is trained so that it finally shows accurate results in 97.44% of cases. Considering the situation in healthcare system in Bosnia and Herzegovina regarding anesthesia machines and the fact that for development of this system we have dealt with small number of samples that are quite similar it is to be expected that network will not have accuracy on desired top level.

Therefore, additional data for anesthesia machines has to be obtained and those data presented to developed network in order to increase its classification performance.

Validation of fuzzy classifier was performed by adjusting parameters for ANN output, average utilization time of

device, maintenance and number of additional parts on and observing the output of fuzzy classifier. Obtained results were satisfying. Finally, developed expert system for prediction of performance status of device and indication if device will need inspection was tested using 39 samples for which data of their inspection is analyzed through three years (2015–2017). This is followed by selection of parameters for average utilization time of the anesthesia machine, preventive maintenance intervals and number of additional parts. Selection was performed in way that most frequent combinations of parameters that reflect healthcare system in Bosnia and Herzegovina are covered. Expected results are obtained for 38 samples while for 1 sample, that was classified by ANN as a false negative developed expert system gave false prediction of performance status and therefore false indication of inspection requirement.

Out of 39 samples tested by this expert system four anesthesia machines, whose type is the most frequent in healthcare institutions included in this study, are selected and result of their testing represented in Table 4. Output of ANN network, parameters for utilization, preventive maintenance and number of additional parts which are used as inputs to fuzzy classifier are represented on the left side of Table 4. Using predetermined rules expert system predicted performance status and gave indication for inspection requirement. In this study performance status is defined in a manner that value of 1 indicates that inspection is required, while value of 0 indicates that inspection of the device is not required. Since data of anesthesia machines inspected during three years is analyzed, approach used to give a final decision on inspection requirements based on performance status of last two inspections if possible, if not performance status of the last inspection of device is used as crucial determinant.

4 Conclusion

In this paper development of Expert System consisted of Artificial Neural Network and Fuzzy classifier for prediction of Anesthesia machine performance status and inspection requirement is presented. For development of Artificial

Table 4 Result of subsequent testing

Verification						2015/2016/2017						
2015	2016	2017	AUT	PMI	NAP	Performance status			Indication for maintenance			FI
0	1	1	0.1	3	1	1	0	0	Yes	No	No	No
1	1	0	0.9	6	5	1	1	1	Yes	Yes	Yes	Yes
1	0	1	0.18	2	1	0	1	0	No	Yes	No	No
0	1	0	0.85	7	4	1	1	1	Yes	Yes	Yes	Yes

AUT average utilization time of the anesthesia machine, *PMI* preventive maintenance intervals, *NAP* number of additional parts, *FI* final indication

Neural Network 197 samples consisting of information about measured values of volume, gas concentration and visual inspection of the device were used. Two-layer feed-forward backpropagation network with 23 neurons in hidden layer and hyperbolic tangent sigmoid transfer function was trained with 158 samples. Testing of developed neural network was performed with 39 samples for validation. Out of 39 samples, developed network was accurate in 97.44% of cases for prediction of Anesthesia machine performance status. Output of Artificial Neural Network was used as an input to Fuzzy classifier as well as additional information about average utilization time of the anesthesia machine, preventive maintenance intervals and number of additional parts. Fuzzy rules are defined according to recommendations. Obtained outputs are used to predict the performance status of medical device and give indication for device maintenance. Although artificial intelligence has already been used for control of anesthesia and monitoring alarms, systems based on artificial intelligence aimed to predict performance status of anesthesia machine and inspection requirements still have not been developed. Therefore, expert system developed in this study gives an opportunity for unbiased prediction of performance status according to which adequate and well-timed device inspection, if required, can be performed. This approach enables fast and reliable control of anesthesia machine status and increase the quality and safety of care. Since this approach is developed under the conditions and available data from Bosnia and Herzegovina additional work and upgrades in sense of additional data from neighboring countries would increase precision and reliability of developed system. Therefore significant contribution in prevention of anesthesia machine failure by prediction of device performance status will be achieved and possibility for well-timed inspection will be enabled.

Appendix 1: K-Fold Cross Validation

```

k = 10;
cv = cvpartition(length(input1),'kfold',k);
for i = 1:k
trainIdxs{i}= find(training(cv, i));
testIdxs{i}= find(test(cv, i));
trainMatrix{i} = [input1(trainIdxs{i}) input2(trainIdxs{i})
output(trainIdxs{i})];
validMatrix{i} = [input1(testIdxs{i}) input2(testIdxs{i})
output(testIdxs{i})];
end

net = patternnet(____);
net.trainFcn = 'trainbfg';
net.divideFcn = "";
net.trainParam.epochs = 30;
net.trainParam.max_fail = 500;
net.trainParam.min_grad = 0.000000000000001;
for i = 1:k
[net,tr] = train(net,trainMatrix{i}(:,1:2)',trainMatrix{i}
(:,3)');
end

```

Appendix 2: Membership Functions

$$\mu_{\text{low}}(\text{utilization}) = \begin{cases} 1, & 0 < ut < 0.1 \\ \frac{0.25-ut}{0.15}, & 0.1 \leq ut \leq 0.25 \\ 0, & ut > 0.25 \end{cases}$$

$$\mu_{\text{medium}}(\text{utilization}) = \begin{cases} 0, & 0 < ut < 0.25 \\ \frac{ut-0.2}{0.15}, & 0.2 \leq ut \leq 0.35 \\ 1, & 0.35 < ut < 0.55 \\ \frac{1.55-ut}{0.1}, & 0.55 \leq ut \leq 0.65 \\ 0, & ut > 0.65 \end{cases}$$

$$\mu_{\text{high}}(\text{utilization}) = \begin{cases} 0, & 0 < ut < 0.6 \\ \frac{ut-0.6}{0.25}, & 0.6 \leq ut \leq 0.85 \\ 1, & 0.85 < ut < 1 \end{cases}$$

$$\mu_{\text{high}}(\text{maintenance}) = \begin{cases} 1, & 0 < m < 2.5 \\ \frac{4-m}{1.5}, & 2.5 \leq m \leq 4 \\ 0, & m > 4 \end{cases}$$

$$\mu_{\text{medium}}(\text{maintenance}) = \begin{cases} 0, & 0 < m < 3 \\ \frac{m-3}{1}, & 3 \leq m \leq 4 \\ \frac{8-m}{1.5}, & 6.5 \leq m \leq 8 \\ 0, & m > 8 \end{cases}$$

$$\mu_{\text{low}}(\text{maintenance}) = \begin{cases} 0, & 0 < m < 7 \\ \frac{m-7}{2}, & 7 \leq m \leq 9 \\ 1, & 9 < m < 12 \end{cases}$$

$$\mu_{\text{small}}(\text{additional parts}) = \begin{cases} 1, & 0 < ap < 1 \\ \frac{2-ap}{1}, & 1 \leq ap \leq 2 \\ 0, & ap > 2 \end{cases}$$

$$\mu_{\text{medium}}(\text{additional parts}) = \begin{cases} 0, & 0 < ap < 1.75 \\ \frac{ap-1.75}{0.5}, & 1.75 \leq ap \leq 2.25 \\ 1, & 2.25 < ap < 3.25 \\ \frac{3.75-ap}{0.5}, & 3.25 \leq ap \leq 3.75 \\ 0, & ap > 3.75 \end{cases}$$

$$\mu_{\text{high}}(\text{additional parts}) = \begin{cases} 0, & 0 < ap < 3.5 \\ \frac{4.5-ap}{1}, & 3.5 \leq ap \leq 4.5 \\ 1, & ap > 4.5 \end{cases}$$

$$\mu_{\text{high}}(\text{ANN probability}) = \begin{cases} 1, & 0 < ann < 0.35 \\ \frac{0.55-ann}{0.2}, & 0.35 \leq ann \leq 0.55 \\ 0, & ann > 0.55 \end{cases}$$

$$\mu_{\text{low}}(\text{ANN probability}) = \begin{cases} 0, & 0 < ann < 0.45 \\ \frac{ann-0.45}{0.2}, & 0.45 \leq ann \leq 0.65 \\ 1, & ann > 0.65 \end{cases}$$

$$\mu_{\text{low}}(\text{output}) = \begin{cases} 1, & 0 < out < 0.2 \\ \frac{0.35-out}{0.15}, & 0.2 \leq out \leq 0.35 \\ 0, & out > 0.35 \end{cases}$$

$$\mu_{\text{medium}}(\text{output}) = \begin{cases} 0, & 0 < out < 0.3 \\ \frac{out-0.3}{0.1}, & 0.3 \leq out \leq 0.4 \\ 1, & 0.4 < out < 0.6 \\ \frac{0.7-out}{0.1}, & 0.6 \leq out \leq 0.7 \\ 0, & out > 0.7 \end{cases}$$

$$\mu_{\text{high}}(\text{output}) = \begin{cases} 0, & 0 < out < 0.65 \\ \frac{out-0.65}{0.15}, & 0.65 \leq out \leq 0.8 \\ 1, & out > 0.8 \end{cases}$$

References

1. Robinson, D.H., Toledo, A.H.: Historical development of modern anesthesia. *J. Invest. Surg.* **25**(3), 141–149 (2012)
2. Dorsch, J.S., Dorsch, S.E., Welch, J.P.: Understanding anesthesia equipment. *Anesthesiol. J. Am. Soc. Anesthesiol.* **64**(1), 135 (1986)
3. Subrahmanyam, M., Mohan, S.: Safety features in anaesthesia machine. *Indian J. Anaesth.* **57**(5), 472 (2013)
4. Gaba, D.M.: Anaesthesiology as a model for patient safety in health care. *BMJ: Br. Med. J.* **320**(7237), 785 (2000)
5. Kim, T.W., Nemergut, M.E.: Preparation of modern anesthesia workstations for malignant hyperthermia-susceptible patients a review of past and present practice. *Anesthesiol. J. Am. Soc. Anesthesiol.* **114**(1), 205–212
6. ISO/TC 121: Anaesthetic and Respiratory Equipment. Retrieved from <https://www.iso.org/obp/ui/#iso:std:iso:5358:ed-2:v1:en>
7. ISO/TC 121/SC 1: Breathing Attachments and Anaesthetic Machines. (08 December 2016). Retrieved from <https://www.iso.org/committee/51986/x/catalogue/> (2016)
8. Goneppanavar, U., Prabhu, M.: Anaesthesia machine: checklist, hazards, scavenging. *Indian J. Anaesth.* **57**(5), 533 (2013)
9. Ehrenwerth, J., Eisenkraft, J.B., Berry, J.M.: *Anesthesia Equipment E-Book: Principles and Applications*. Elsevier Health Sciences (2013)
10. Patil, V.P., Shetmahajan, M.G., Divatia, J.V.: The modern integrated anaesthesia workstation. *Indian J. Anaesth.* **57**(5), 446 (2013)
11. Jain, R.K., Swaminathan, S.: Anaesthesia ventilators. *Indian J. Anaesth.* **57**(5), 525 (2013)
12. Pouzeratte, Y., Sebbane, M., Jung, B., Delay, J.M., Eliet, J., Eledjam, J.J., et al.: A prospective study on the user-friendliness of four anaesthesia workstations. *Eur. J. Anaesthesiol.* **25**(8), 634–641 (2008)
13. Kawashima, Y., Takahashi, S., Suzuki, M., Morita, K., Irita, K., Iwao, Y., et al.: Anesthesia-related mortality and morbidity over a 5-year period in 2,363,038 patients in Japan. *Acta Anaesthesiol. Scand.*, **47**(7), 809–817 (2003)
14. Li, G., Warner, M., Lang, B.H., Huang, L., Sun, L.S.: Epidemiology of anesthesia related mortality in the United States, 1999–2005. *Anesthesiol. J. Am. Soc. Anesthesiol.* **110**(4), 759–765 (2009)
15. Mehta, S.P., Eisenkraft, J.B., Posner, K.L., Domino, K.B.: Patient injuries from anesthesia gas delivery equipment a closed claims update. *Anesthesiol. J. Am. Soc. Anesthesiol.* **119**(4), 788–795

16. do Céu Ferreira, M.: The role of metrology in the field of medical devices. *Int. J. Metrol. Qual. Eng.* **2**(2), 135–140 (2011)
17. Gurbeta, L., Vukovic, D., Džemic, Z., Badnjevic, A.: Legal metrology procedures for increasing safety and performance characteristics with cost benefits analysis: case study dialysis machines. In: *World Congress on Medical Physics and Biomedical Engineering*, pp. 55–59. Springer, Singapore (2018)
18. Badnjević, A., Gurbeta, L., Bošković, D., Džemić, Z.: Medical devices in legal metrology. In: *2015 4th Mediterranean Conference on Embedded Computing (MECO)*, pp. 365–367. IEEE (2015)
19. Gurbeta, L., Džemic, Z., Badnjevic, A.: Establishing traceability chain of infusion and perfusor pumps using legal metrology procedures in Bosnia and Herzegovina. In: *World Congress on Medical Physics and Biomedical Engineering*, pp. 45–49. Springer, Singapore (2018)
20. Badnjević, A., Cifrek, M., Magjarević, R., Džemić, Z. (eds.): *Inspection of Medical Devices*. Series in Biomedical Engineering. Springer, Singapore
21. Gurbeta, L., Džemic, Z., Bego, T., Sejdic, E., Badnjevic, A.: Testing of anesthesia machines and defibrillators in healthcare institutions. *J. Med. Syst.* **41**(9), 133 (2017)
22. Aljović, A., Badnjević, A., Gurbeta, L.: Artificial neural networks in the discrimination of Alzheimer's disease using biomarkers data. In: *5th Mediterranean Conference on Embedded Computing (MECO)*, pp. 286–289. IEEE (2016)
23. Zhang, Y., Dong, Z., Phillips, P., Wang, S., Ji, G., Yang, J., Yuan, T.F.: Detection of subjects and brain regions related to Alzheimer's disease using 3D MRI scans based on eigenbrain and machine learning. *Front. Computat. Neurosci.* **9**, 66 (2015)
24. Badnjević, A., Gurbeta, L., Cifrek, M., Marjanovic, D.: Classification of asthma using artificial neural network. In: *39th International Convention on Information and Communication Technology, Electronics and Microelectronics (MIPRO)*, pp. 387–390. IEEE (2016)
25. Badnjević, A., Gurbeta, L., Cifrek, M., Marjanović, D.: Diagnostic of asthma using fuzzy rules implemented in accordance with international guidelines and physicians experience. In: *39th International Convention on Information and Communication Technology, Electronics and Microelectronics (MIPRO)*, pp. 375–380. IEEE (2016)
26. Prasadl, B.D.C.N., Prasad, P.E.S.N.K., Sagar, Y.: An approach to develop expert systems in medical diagnosis using machine learning algorithms (asthma) and a performance study. *Int. J. soft Comput. (IJSC)* **2**(1), 26–33 (2011)
27. Sejdinović, D., Gurbeta, L., Badnjević, A., Malenica, M., Dujic, T., Čaušević, A., et al.: Classification of prediabetes and type 2 diabetes using artificial neural network. In: *CMBEBIH 2017*, pp. 685–689. Springer, Singapore (2017)
28. Mani, S., Chen, Y., Elasy, T., Clayton, W., Denny, J.: Type 2 diabetes risk forecasting from EMR data using machine learning. In: *AMIA Annual Symposium Proceedings*, vol. 2012, p. 606. American Medical Informatics Association (2012)
29. Alić, B., Gurbeta, L., Badnjević, A.: Machine learning techniques for classification of diabetes and cardiovascular diseases. In: *6th Mediterranean Conference on Embedded Computing (MECO)*, pp. 1–4. IEEE (2017)
30. Sitar-Taut, D.A., Pop, D., Zdrengea, D., Sitar-Taut, A.V.: Using machine learning algorithms in cardiovascular disease risk evaluation. *J. Appl. Comput. Sci. Math.* **3**(5), 29–32 (2009)
31. Catic, A., Gurbeta, L., Kurtovic-Kozaric, A., Mehmedbasic, S., Badnjevic, A.: Application of neural networks for classification of Patau, Edwards, Down, Turner and Klinefelter Syndrome based on first trimester maternal serum screening data, ultrasonographic findings and patient demographics. *BMC Med. Genomics* **11**(1), 19 (2018)
32. Caelen, O., Bontempi, G., Coussaert, E., Barvais, L., Clément, F.: Machine learning techniques to enable closed-loop control in anesthesia. In: *19th IEEE International Symposium on Computer-Based Medical Systems, 2006. CBMS 2006*, pp. 696–701. IEEE (2006)
33. Karpagavalli, S., Jamuna, K.S., Vijaya, M.S.: Machine learning approach for preoperative anaesthetic risk prediction. *Int. J. Recent Trends Eng.* **1**(2), 19 (2009)
34. Watt, R.C., Maslana, E.S., Mylrea, K.C.: Alarms and anesthesia: challenges in design of intelligent systems for patient monitoring. *IEEE Eng. Med. Biol. Mag.* **12**(4), 34–41 (1993)
35. Mylrea, K.C., Orr, J.A., Westenskow, D.R.: Integration of monitoring for intelligent alarms in anesthesia: neural networks—can they help? *J. Clin. Monit.* **9**(1), 31–37 (1993)
36. Seagull, F.J., Sanderson, P.M.: Anesthesia alarms in context: an observational study. *Hum. Factors* **43**(1), 66–78 (2001)
37. Badnjević, A., Gurbeta, L., Bošković, D., Džemić, Z.: Medical devices in legal metrology. In: *4th Mediterranean Conference on Embedded Computing (MECO)*, pp. 365–367. IEEE (2015)
38. Verification of anesthetic machines: Retrieved from <http://www.verlab.ba/en/US/Usluge/VerifikacijaAnestezioloskihMasina#> (n.d.)
39. Regulation on metrological and technical requirements for respirators and anesthesia machines: Retrieved from: http://www.met.gov.ba/dokumenti/PRAVILNIK%20O%20MJERITELJSKIM%20I%20TEHNICKIM%20ZAHTJEVIMA%20ZA%20RESPIRATOR%20I%20ANESTEZIOLOSKE%20MASINE_BOSANSKI.pdf (2018)
40. Schalkoff, R.J.: *Artificial Neural Networks*, vol. 1. McGraw-Hill, New York (1997)
41. Leong, G., Wilson, J., Charlett, A.: Duration of operation as a risk factor for surgical site infection: comparison of English and US data. *J. Hosp. Infect.* **63**(3), 255–262 (2006)
42. Chaudhary, P., Kaul, P.: Factors affecting utilization of medical diagnostic equipment: a study at a tertiary healthcare setup of Chandigarh. *CHRISMED J. Health Res.* **2**(4), 316 (2015)
43. Anesthesia Machines: Retrieved from: https://www.draeger.com/enus_us/Hospital/Productselector/AnaesthesiaWorkstations/Anaesthesia-Machines
44. Universal Anesthesia Machine (UAM): Retrieved from <https://www.gradianhealth.org/our-products/uam/>

Smoking and Caffeine Consumption as Stress Coping Mechanisms in Medical Students

Lejla Šabić and Adnan Mujanović

Abstract

Introduction: Managing working and personal life can result in conflicting demands for young medical students. An increasing number of students report concerns about the amount of stress in their life. This study was conducted to examine smoking and caffeine consumption and their relationship with stress as stress coping mechanisms among medical students. We aimed to estimate the prevalence of stress and its association with cigarette and caffeine substances induced behaviors. Substances found in cigarettes and caffeinated drinks (nicotine, caffeine, etc.) can trigger different neurological and endocrinological pathways which result in release or inhibition of other neuroactive substances, such as dopamine or adenosine, or hormones like cortisol. **Methods:** The data was collected from the original questioner created by the authors of this paper, which consisted of questions exploring stress symptoms, food, drink and tobacco related behavior patterns. **Results:** The statistical analysis of the collected data shows slightly different smoking patterns in male and female participants, but significant disproportion in genders when it comes to caffeinated drinks. The study concludes that there is a significant stress impact on caffeine and cigarette consumption, and thus affecting general health of the average medical student. **Conclusion:** It is necessary to provide and familiarize students with different stress-coping programs, which will in term have no, or less, side effects on their health and make the academic environment more suitable for coping with stress.

Keywords

Stress • Smoking • Caffeinated drinks • Medical students • Cortisol

1 Introduction

Medical students are exposed to various stressors [1] that may produce a variety of stress coping mechanism such as smoking [2, 3] and consumption of high levels of caffeinated beverages [4]. In order to maintain a remarkable grade-point-average (GPA) students often have to work beyond their mental threshold and physical strength. Therefore, medical students are more prone to consume caffeine than others among college students [5]. Also, college life is an important transition period during which young adults set out to explore tobacco use, either as a stress reliever, or a result of peer pressure and social acceptance [6]. Some surveys have reported that the prevalence of cigarette smoking continues to rise among students of medicine [7, 8].

Energy drinks are fortified beverages with added nutritional supplements [9, 10]. These beverages contain large doses of methylxanthines (some of which include caffeine) and other stimulants such as taurine, inositol, niacin, panthenol and herbs [11]. Caffeine is structurally similar to adenosine, and its amount can range from a modest 50 mg to an alarming 505 mg per one packaging [12]. With time, energy drinks became more than just drinks, the young population consumed them to increase their cognitive function, especially before exams or an assignment deadline. The marketing of these drinks relies chiefly on that the natural ingredients in energy drinks supply may increase energy, alertness, improve athletic performance and concentration time [13–15].

Although nicotine found in tobacco is already classified as a highly addictive substance, caffeine is classified, by the Food and Drug Administration, as “generally recognized as

L. Šabić · A. Mujanović (✉)
Faculty of Medicine, University of Tuzla, Tuzla,
Bosnia and Herzegovina
e-mail: adnan.mujanovic5@gmail.com

safe” [16]. The symptoms of both caffeine and nicotine withdrawal include nervous irritability, tremors, muscle twitching, sensation disturbances, tachypnea, palpitation, flushing, arrhythmias, diuresis, gastrointestinal disturbances and patients may have generalized anxiety or depression [17]. More serious side effects of caffeine loss include tachycardia and arrhythmias, in addition to electrolyte imbalances such as hypokalemia, hypomagnesaemia and hypophosphatemia [18]. All these adverse effects raise the needs for closer scrutiny and possible regulation [19]. On the other hand, it has been clinically proven that cigarette smoking causes lung cancer, chronic obstructive lung disease, atherosclerotic cardiovascular diseases, peptic ulcer disease, intrauterine growth retardation, spontaneous abortion, antepartum hemorrhage, female infertility, sexual dysfunction in men, and many other diseases [20].

Previous studies conducted worldwide among college students demonstrated that energy drink consumption is a common practice, and that there is a prevalence of smoking in that same target group. However, only limited number of research studies has been done to determine coloration between smoking and caffeine consumption with stress levels among medical college students. In addition, there is no adequate data that report associated factors as part of stress coping mechanisms. Thus, such study is urgently needed.

2 Methods and Materials

2.1 Participants

The sample consisted of 300 participants. Participants were students from the Medical faculty of University of Tuzla, ranging from their freshman to their senior years covering all preclinical and clinical years.

2.2 Materials and Procedure

The questioner was created by the authors of this paper for a specific use in this study. All of the participants were informed why were they taking the poll and what will the results be used for. The survey was anonymous and voluntary, meaning no one was forced to fill it against their will. The survey consisted of 23 items which were divided into 4 categories. First category included 5 items which represented general information (gender, age, study year, relationship and household status). Second category was based on a 4-level Likert-type scale (1-lowest to 4-highest), to evaluate their psychological state through their general opinions about themselves. This category included 6 items. Third category was also based on a 4-level Likert-type scale

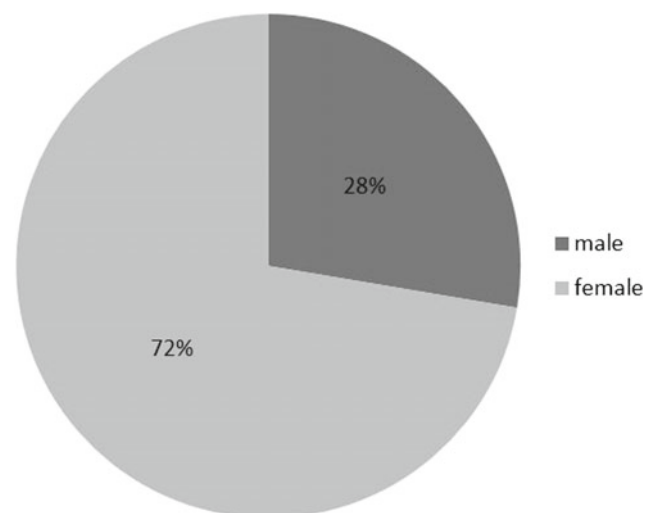
(never, rarely, sometimes and often) but here we evaluated intrapersonal stress results, such as, changes in dietary regimes or caffeine and cigarette intake. This category included 8 items. Finally, the forth category was based on closed question types, offering the participants the options of “Yes” or “No” for an answer. This category included 4 items and was evaluating students’ academic stress results. Participants were assured of the confidentiality and anonymity of their answers. The poll was distributed at the beginning of the finals exam period and was conducted over the course of one month.

3 Results

The majority of the students that took part in the study were female (72.34%) as presented in Graph 1. In Table 1 shows the structure of the sample by gender and college year. The average age of the sample was 24 years ($M = 24.28 \pm SD = 2.69$) and there was no significant statistical difference between the groups (by gender or college years) in terms of age ($p = 0.36$).

Results of the psychological symptoms of stress and by gender, as shown in Table 2, are higher in female than male participants. The most common high intensity symptom for both genders is “loss of sleep” (20.48% of male and 28.11% if female participants). Furthermore, ineffective coping with stress is significantly correlated with females ($r = 0.96$; $p < 0.01$) as well as a significant correlation between young women experiencing significantly more the highest intensity psychological symptoms compared to young men ($t = 3.76$; $p < 0.01$).

Food and drink intakes in high stressed situations are presented in Table 3. The most relevant to this study is the



Graph 1 Sample design by gender

Table 1 Gender and year of study distribution of the sample

Study year	N	%	M	%	F	%
I	35	11.67	9	3.00	26	8.67
II	91	30.33	24	8.00	67	22.33
III	37	12.33	10	3.33	27	9.00
IV	33	11.00	9	3.00	24	8.00
V	40	13.33	7	2.33	33	11.00
VI	64	21.33	24	8.00	40	13.33
Total		100		100		100

Table 2 Psychological symptoms by gender $t = 3.76$; $p < 0.01$; $r = 0.96$; $p < 0.01$

Psychological symptoms	Frequency (%)							
	Male				Female			
	Disagreed	Partly agree	Partly disagree	Agreed	Disagreed	Partly agree	Partly disagree	Agreed
Problems with concentration	60.24	19.28	15.66	4.82	50.23	31.80	12.90	5.07
Loss of sleep	37.35	25.30	16.87	20.48	24.42	34.10	12.90	28.11
Decision fatigue	60.24	16.87	19.28	2.41	53.00	28.11	13.36	7.37
Loss of pleasure in everyday activities	62.65	21.69	7.23	8.43	51.15	26.73	11.06	14.75
Decreased confidence	60.24	14.46	12.05	12.05	55.30	23.96	5.99	14.75
Feeling worthless	83.13	8.43	1.20	4.8	75.58	9.68	6.45	6.91

Table 3 Frequency of food and drink related behavior

Food or drink	Frequency (%)			
	Often	Rarely	Sometimes	Never
Fruits and vegetables	148(49.93)	42(14.00)	103(34.33)	6(2.00)
Fast food	84(28.00)	64(21.33)	132(44.00)	19(6.33)
Sweets and snacks	105(35.00)	63(21.00)	110(36.67)	21(7.00)
Water and juice	241(80.33)	15(5.00)	43(14.33)	1(0.33)
Caffeinated drinks	161(53.67)	55(18.33)	70(23.33)	13(4.33)
Alcohol	13(4.33)	92(30.67)	63(21.00)	131(43.67)
Cigarettes	40(13.33)	27(9.00)	47(15.67)	186(62.00)
Drugs	13(4.33)	129(43.00)	52(17.33)	105(35.00)

frequency of consumption when it comes to caffeinated drinks and cigarettes.

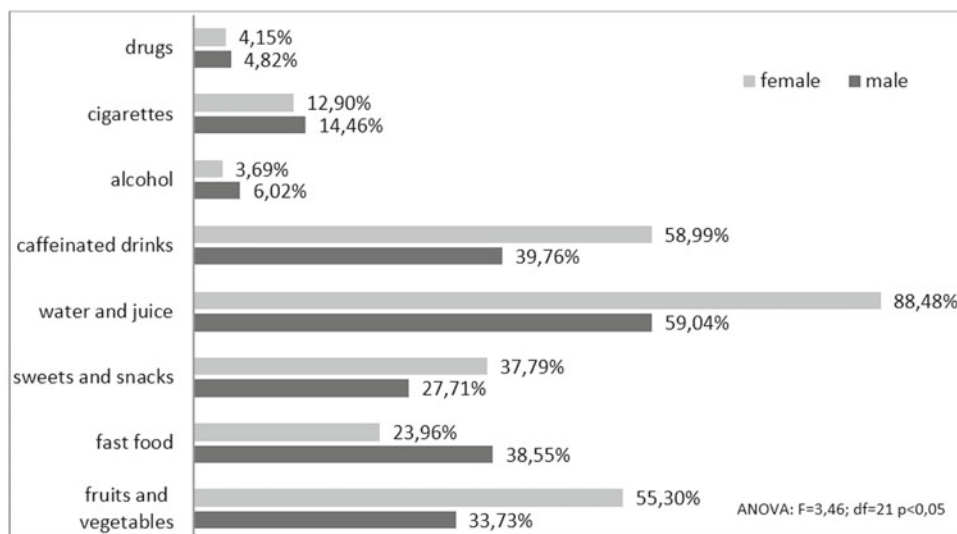
Graph 2 shows which of the often-consumed foods or drinks are preferable to opposite genders.

Both genders consume mostly water and juice (88.48% female and 59.04% female students). In addition, the analysis has shown that male students tend to eat more fast food

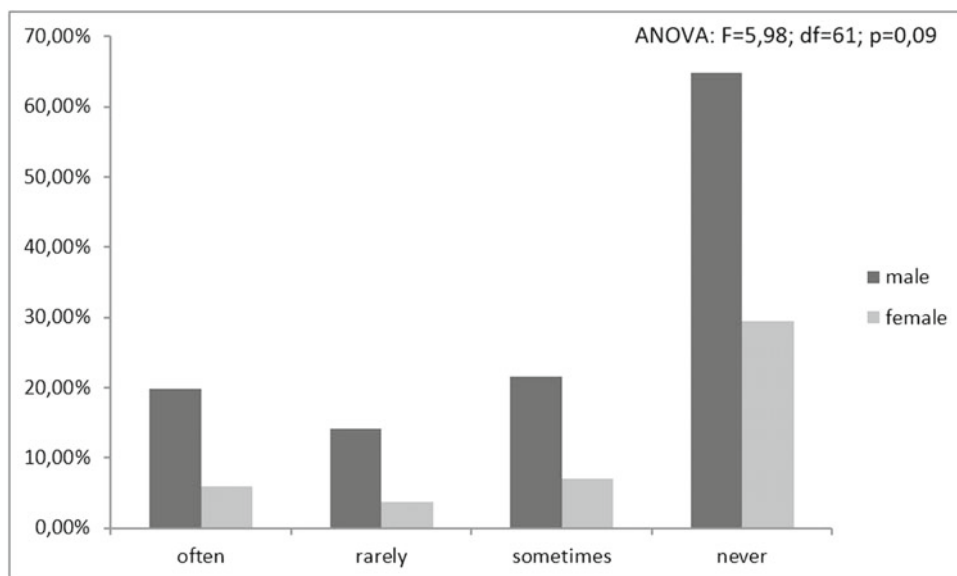
when in high stress situations whereas female students tend to consume more caffeinated drinks (ANOVA: $F = 3.46$; $df = 21$; $p < 0.05$) (Graph 3).

The analysis has shown that cigarette intake in stressed situations is increased, but also that there is not a major statistical difference in cigarettes consumption between the genders (ANOVA: $F = 5.98$; $df = 61$; $p = 0.09$).

Graph 2 Frequently consumed food and drinks by gender when stressed



Graph 3 Cigarette consumption by gender when stressed



4 Discussion

This study was based on the premise that medical students are exposed to high levels of stress and that these levels of stress cause increased smoking and caffeine consumption as stress coping mechanisms among medical students which can, combined with different sleep patterns, anxiety, lower self-esteem and depression, lead to a very unhealthy life style.

There are many benefits and disadvantages of caffeine intake. Benefits included increased arousal and decreased fatigue, but there were many disadvantages. Some of which were: restlessness, increased heart rate, increased blood pressure, anxiety, addiction for long time of high doses, and

hallucination. High percentage of students (77.6%) is aware of the effect on the cardiac system, with the increased heart rate. However, only a small fraction of students (8.8%) was aware that caffeine consumption in high doses for a long time can lead to hallucination. Also, it is found that some consumers (15.5%) tried to quit consumption but they couldn't and developed some symptoms like difficulty in concentration, feeling nervous, anxious, irritable, and felt the urge to consume caffeine [21].

Students of health sciences in Mekelle University showed significantly high prevalence rates of smoking, especially in their second year. The study showed that about half of the current smokers started smoking after joining the university and hence the number of smokers was increased in the second year. However, the lower prevalence of smoking

after the second year may be due to comparatively greater awareness and knowledge of the health risks of cigarette smoking amongst students in their higher years [22].

The relationship between caffeine and cigarette consumption has already been asserted many times. Study done with undergraduate students from Western New York, United States reported that energy drink consumption was associated with smoking [23]. The association of energy drinks with other potential negative health and behavioral outcomes suggests that use of these products may represent a marker for other activities that may negatively affect adolescent development, health and well-being [24].

Most of the students in this study were in their early to mid-twenties. They were questioned in a high-stress period. Based on the results of this study, we can distinguish slightly different stress related behavior patterns in male and female students. In similar situations as their male colleagues, young women become more indecisive and in comparison, to their male colleagues they react more intensively. Other than that, female students consume higher doses of caffeinated drinks during stressful situations like final exams. On the other hand, their male counterparts tend to cope with stress by eating high fat foods. Also, when it comes to smoking, male students have a slightly higher prevalence of daily cigarette consumption, unlike female students, even though there isn't any major statistical difference.

Although, this study is related to behavior patterns in caffeine and cigarette consumption, there is a basis for further studies of stress related behavior on other aspects of students' lives, like their dietary regimes, psychological coping mechanisms and how these stressful situations may or may not help them in their further, even more stressful careers.

The results presented here, although preliminary, underline important areas for future research related to stress and caffeine and cigarette consumption, when it comes to medical students. These young people have to manage their daily life affairs and all college demands all while trying to maintain a healthy lifestyle. High demanding college program mixed with poor time management and constant fatigue, can lead students to use these for mentioned stress coping mechanism, which than tend to have a negative impact on their immune system, hormonal and neurological level.

Although the sample in this study consisted of medical students, the results indicate that students have already compromised their health and wellbeing even though they have not yet faced the true challenges of their profession nor have been employed yet in their branch of work. Therefore, if they don't change their unhealthy habits and lifestyle, it will have a negative impact in their future when they finish college, start working and start living a family lifestyle.

Author Contributions Assistant professor, Azra Kurtić mentored and finalized the review for this paper. Major aspect of her contribution was helping the authors with the statistical analysis of the results. She helped the authors every step along the way in a process of writing this paper, as well as gave her feedback on the early drafts.

References

1. Ibrahim, N., Al-Kharboush, D., et al.: Prevalence and predictors of anxiety and depression among female medical students in King Abdulaziz University, Jeddah, Saudi Arabia. *Iran. J. Public Health* **42**(7), 726–736 (2013)
2. Al-Turki, Y.A.: Smoking habits among medical students in Central Saudi Arabia. *Saudi Med. J.* **27**, 700–703 (2006)
3. Abdulghani, H.M., Alrowais, N.A., et al.: Cigarette smoking among female students in five medical and nonmedical colleges. *Int. J. Gen. Med.* **6**, 719–727 (2013)
4. Bawazeer, N.A., AlSobahi, N.A.: Prevalence and side effects of energy drink consumption among medical students at Umm Al-Qura University, Saudi Arabia. *Int. J. Med. Students* **1**(3), 104–108 (2013)
5. Al-Turki, Y., Alenazy, B., et al.: Caffeine Habits among medical students in King Saud University. *Int. J. Sci. Res.* **5**(2), 754–764 (2016)
6. Kegler, M.C., Kingsley, B., et al.: The functional value of smoking and non-smoking from the perspective of American Indian youth. *Fam Community Health* **22**, 31–42 (1999)
7. Clauson, K.A., Shileds, K.M., et al.: Safety issues associated with commercially available energy drinks. *J. AM. Pharm. Assoc.* **48** (3): e55–63; quiz e64-7 (2008)
8. McGraw, M.M.: Are energy drinks safe? *Nursing* **43**(3), 68 (2013)
9. Rigotti, N.A., Lee, J.E., Wechsler, H.: US College students' use of tobacco products: results of a national survey. *JAMA* **284**, 699–705 (2000)
10. Rigotti, N.A., Regan, S., et al.: Tobacco use by Massachusetts public college students: long term effect of the Massachusetts Tobacco Control Program. *Tob. Control* **11**:ii20–ii24 (2002)
11. Nahla, K.R.I., Rahila, I., et al.: Energy drinks consumption amongst medical students and interns from three colleges in Jeddah, Saudi Arabia. *J. Food Nutr. Res.* **2**(4), 174–179 (2014)
12. Smit, H.J., Rogers, P.J.: Effects of low doses of caffeine on cognitive performance, mood and thirst in low and higher caffeine consumers. *Psychopharmacology* **152**(2), 167–173 (2000)
13. Reissig, C.J., Strain, E.C., Griffiths, R.R.: Caffeinated energy drinks—a growing problem. *Drug Alcohol Depend.* **99**(1–3), 1–10 (2009)
14. Kamran, B.: Consumption's Pattern and knowledge of athletes about energy drink in South of Iran (Shiraz). *J. Nutr. Food Sci.* **2** (3), 1–7 (2012)
15. Aslam, H.M., Mughal, A., et al.: Assessment of pattern for consumption and awareness regarding energy drinks among medical students. *Arch. Public Health* **71**(1), 31 (2013)
16. American Psychiatric Association.: *Diagnostic and statistical manual of mental disorders*, vol. 22, 4th edn, pp. 150–179. Washington, DC (2000)
17. Bonnet, M.H., Balkin, T.J., et al.: The use of stimulants to modify performance during sleep loss: a review by the sleep deprivation and stimulant task force of the American Academy of sleep medicine. *Sleep* **28**(9), 1163–1187 (2005)
18. Heckman, M.A., Weil, J., Gonzalez de Mejia, E.: Caffeine (1,3,7-trimethylxanthine) in foods: a comprehensive review on consumption, functionality, safety, and regulatory matters. *J. Food Sci.* **75**(3), 77–87 (2010)

19. Hidiroglu, S., Tanriover, O., et al.: A survey of energy-drink consumption among medical students. *J. Pak. Med. Assoc.* **63**(7), 842–845 (2013)
20. Thompson, B., Coronado, G., et al.: Prevalence and characteristics of smokers at 30 Pacific Northwest colleges and universities. *Nicotine Tob. Res.* **9**(3), 429–438 (2007)
21. Silverman, K., Mumford, G.K., Griffiths, R.R.: Enhancing caffeine reinforcement by behavioral requirements following drug ingestion. *Psychopharma* **114**, 424–432 (1994)
22. Eticha, T., Kidane, F.: The prevalence of and factors associated with current smoking among college of health sciences students, Mekelle University in Northern Ethiopia. *PLoS ONE* **9**(10), e111033 (2014)
23. Miller, K.E.: Energy drinks, race and problem behaviors among college students. *J. Adolesc. Health* **43**(5), 490–497 (2008)
24. Azagba, S., Langille, D., Asbirdge, M.: An emerging adolescent health risk: caffeinated energy drink consumption patterns among high school students. *Prev. Med.* **62**, 54–59 (2014)

Review of Biosensors in Industrial Process Control

Emina Kišija, Dina Osmanović, Jasna Nuhić, and Selma Cifrić

Abstract

This paper presents an overview of biosensors used for industrial process control. The review was performed on twenty selected papers. Two widely used biosensors were analyzed: the biosensor for glycerol detection and the biosensor for detection of antibiotic residue in milk. In the case of glycerol detection, using whole bacterial cells of *Gluconobacteroxydans* showed highest sensitivity. In addition, an amperometric biosensor with gold electrode based on enzyme glycerol dehydrogenase with added diaphorase immobilized in polycarbamoyl sulfonate hydrogel showed appreciable results. For antibiotic detection, the parallel affinity sensor array, based on antibody binding, showed the best performance characteristics, with the detection limit of 0.12 µg/L for certain antibiotics.

Keywords

Industrial process control • Glycerol • Fermentation • β-lactam • Amperometric • Electrodes

E. Kišija (✉)

Electrical and Electronics Engineering, Faculty of Engineering and Natural Sciences, International Burch University, Sarajevo, Bosnia and Herzegovina

e-mail: emina.kisija@stu.ibu.edu.ba

D. Osmanović · S. Cifrić

Genetics and Bioengineering, Faculty of Engineering and Natural Sciences, International Burch University, Sarajevo, Bosnia and Herzegovina

e-mail: dina.osmanovic@stu.ibu.edu.ba

S. Cifrić

e-mail: selma.cifric@stu.ibu.edu.ba

J. Nuhić

Multidisciplinary Research in Experimental and Health Sciences, Faculty of Health and Life Sciences, Universitat Pompeu Fabra, Barcelona, Spain

e-mail: jasna.nuhic01@estudiant.upf.edu

1 Introduction

Biosensors are used for monitoring of a wide range of bioprocesses in industry. Mello and Kubota [1] presented advantages of using biosensors compared to traditional methods. Biosensors are more specific and provide results quicker than other analytical methods such as chromatography, electrophoresis, and titration. In contrast to biosensors, those methods are slow and expensive, require well-trained operators and many steps of sample preparation [1].

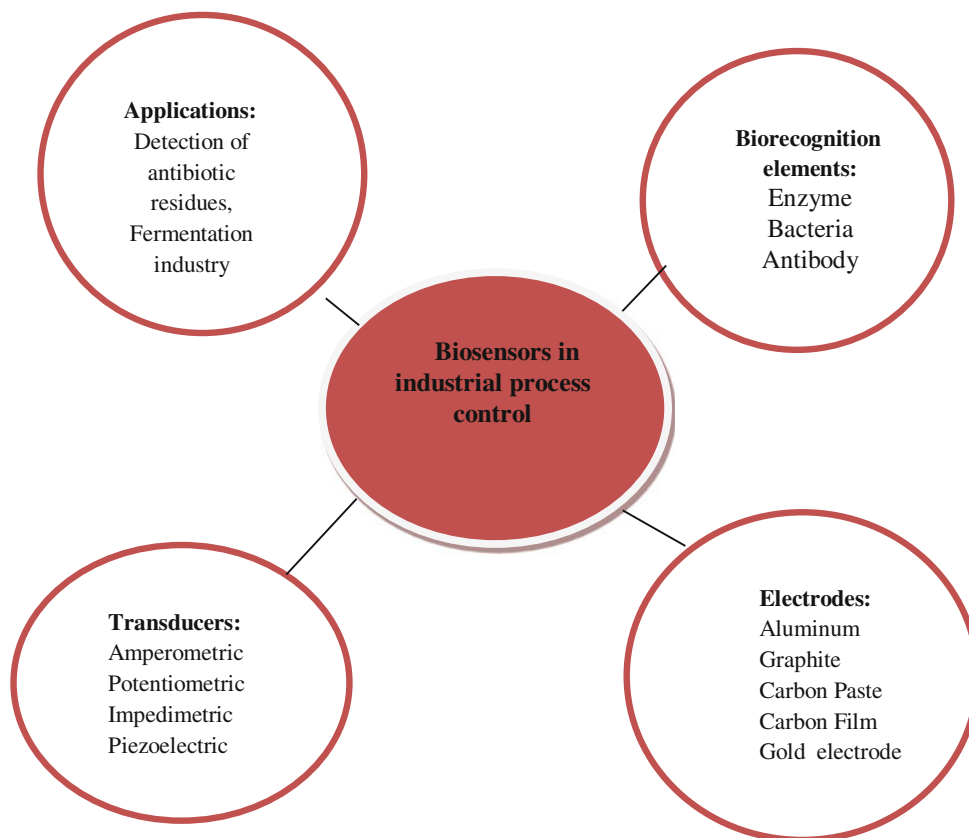
Most of them are used for monitoring of glucose, ethanol, lactate, penicillin and acetic acid in different industries, such as fermentation industry, penicillin production, cell cultivation and bioprocess monitoring. Because of their specificity, enzymes are very desirable biological components. Immobilized enzymes are attached to insoluble material, which enables the enzyme to stick in the place during reactions and be more resistive to changes of, for example, pH level or temperature. In this process, enzymes can be easily separated from the material and used again. There are several types of immobilization: adsorption, covalent bonding, entrapment and cross-linking. Adsorption technique of immobilizing an enzyme onto a biosensor transducer is one of the most straightforward methods, while covalent bonding is the most widely used.

Cell-based and organelle-based biosensors are also used, as well as immunological biosensors. Many different transducers are employed for biosensors applications, but most of them are based on electrochemical detectors. Most common techniques are: amperometric, potentiometric and conductometric [2].

An overview of applications of this type of biosensors, as well as biorecognition elements and transducers, mentioned in this paper, are presented in Fig. 1.

According to Lepenaide et al. [3], it is very important to control the amount of glycerol in different industries such as medicine, clinical chemistry, pharmaceuticals, food and

Fig. 1 Application, types of transducers and types of biorecognition elements in industrial process control biosensors



beverage production. Supervision of glycerol is prescribed by law and performed on a daily basis.

Another very important process that must be controlled is milk production. As stated by Ferrini et al. [4], the presence of antibiotic residues, used for cattle treatment, can cause allergenic or toxicological response in consumers, as well as resistance to antibiotics or many other problems in the food. That is why control of antibiotic presence in milk is performed within all European Union countries by food producers and authority [5].

2 Methods

This paper provides an overview of methods used for glycerol and β -lactam detection in milk (Fig. 1). To facilitate data, we searched the following databases: MEDLINE, PubMed, Embase and Scopus. Twenty published papers were identified and used to write this review.

The criteria for paper selection were:

- the paper is written in English
- the entire paper is available
- the paper was published between 2000 and 2018
- the paper's focus is detection of glycerol or antibiotics
- the results contain statistical data.

Eleven papers were used for the review of biosensors for glycerol detection. Six of them were used to compare different enzymes and microbial cells as biorecognition elements, while five for comparing electrodes used in amperometric transduction of signals. Nine papers were used to review biosensors for β -lactam detection: five to make the comparison between different detection types using antibodies, and four to compare transduction measurement methods.

3 Results

3.1 Biosensors for Glycerol Detection

Different types of biosensors for glycerol detection are shown in Tables 1 and 2. The average sensitivity of all presented biosensors, based on different biorecognition elements, was calculated using the formula $\frac{1}{n} \sum_{i=1}^n a_i$ and the result is $1,691,286 \text{ nA mM}^{-1}$. Sensitivities of all biosensor except the one using *Gluconobacteroxydans* are shown in Fig. 2. The reason why sensitivity of this sensor cannot be seen in the figure is that it was too high when compared to others. A biosensor that uses *Gluconobacteroxydans* cells is found to be a significant outlier with the sensitivity of $755,000 \text{ nA mM}^{-1}$ ($P < 0.05$). This means that this

sensitivity is high above the average. Glycerol dehydrogenase provided the lowest sensitivity of 90 nA mM^{-1} . An average lower limit for a linear range is 6.44×10^{-4} . A significant outlier ($P < 0.05$) is found to be 5×10^{-3} which is the beginning of the linear range for enzyme using Gluconobacteroxydans. This means that this biosensor has the linear range which starts at significantly higher concentration of glycerol compared to other biosensors for glycerol detection. The average upper limit for linear range is 7.6×10^{-3} . There are no significant outliers in the upper limit which means that no upper linear range is significantly different from the others. The widest linear range is found in the case of the enzymatic biosensor that uses glycerol dehydrogenase. Storage stability is very variable in the case of the analyzed biorecognition elements. The lowest stability is provided by glycerol oxidase immobilized in glutaraldehyde vapor, being 10% of the original value in one day. The immobilized glycerol dehydrogenase—diaphorase showed the best storage stability of 90% after 2 months, 70% after 7 months and 66% after 11 months. Katrlík et al. [7] described immobilization of these enzymes using the polycarbonyl sulfonate (PCS) prepolymer immobilization technique with intention to create enzyme membranes with good stability parameters.

According to the literature, electrochemical transducers are used for glycerol detection because of their sensitivity, reliability and cost-effectiveness. The amperometric measurement approach showed the best results. Therefore, various electrodes are analyzed to decide which one of them provides best results for glycerol detection: aluminum, rods of spectroscopic graphite, carbon paste electrode (CPE), gold electrode (AUE) and carbon film electrode (CFE). Characteristics of electrodes with different enzymes, glutamate dehydrogenase (GDH) or glycerol phosphate oxidase (GPO) are listed in Tables 3 and 4, for efficiency comparison.

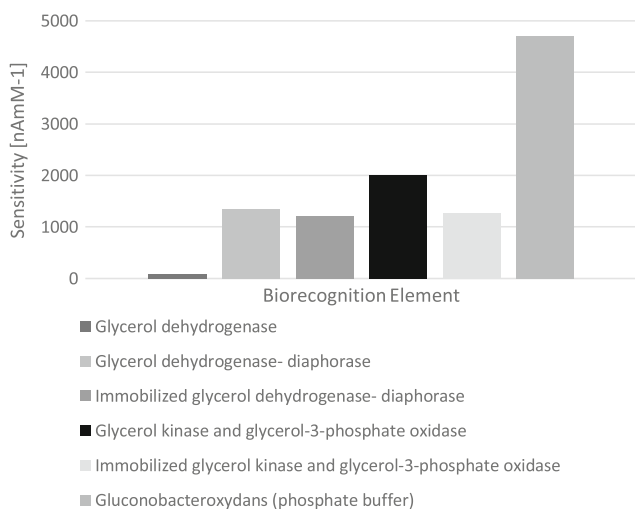
Different values for detection limit of five electrodes from selected papers [8, 14–17] were obtained and shown in Fig. 3. The mean value of limits of detection is $\bar{X} = 1.366 \mu\text{M}$. As can be seen, the gold electrode (Aue) provided the lowest limit of detection of $0.43 \mu\text{M}$ which is $0.936 \mu\text{M}$ below the mean value. This means that using Aue allows smaller amount of glycerol to be detected than is the case with other electrodes, which is indicative of high sensitivity. Rods of spectroscopic graphite also showed sufficient sensitivity of 32 mA/Mcm^2 , but its stability is unsatisfactory. There is an enormous loss in just 20 h, while using Aue, after 51 days, only 13% loss of original value is measured, implying to the great storage stability. The same can be

Table 1 Characteristics of biorecognition elements for glycerol detection

Biorecognition element	Sensitivity (nA mM^{-1})	Linear range (M)	References
Glycerol dehydrogenase	90	9.97×10^{-7} to 1.0×10^{-4}	Álvarez-González et al. [6], Katrlík et al. [7]
Glycerol dehydrogenase-diaphorase	1350	1.0×10^{-6} to 2.0×10^{-5}	Katrlík et al. [7], Gamella et al. [8]
Immobilized glycerol dehydrogenase-diaphorase	1215	–	Katrlík et al. [7]
Glycerol kinase and glycerol-3-phosphate oxidase	2000	1.0×10^{-6} to 1.0×10^{-5}	Katrlík et al. [7], Gamella et al. [8]
Immobilized glycerol kinase and glycerol-3phosphate oxidase	1270	–	Katrlík et al. [7]
Gluconobacteroxydans (pre-hydrolyzed samples analysis)	755×10^3	up to 2×10^{-3}	Tkáč et al. [9]
Gluconobacteroxydans (phosphate buffer)	4700	2×10^{-6} to 5×10^{-4}	Tkáč et al. [10]
Gluconobacteroxydans (thermometric flow injection analysis)		5×10^{-3} to 40×10^{-3}	Navrátil et al. [11]
Glycerol oxidase immobilized by electro-chemical polymerization in EDT		5×10^{-5} to 25.6×10^{-3}	Goriushkina et al. [12]
Glycerol oxidase immobilized by electro-chemical polymerization in Resydrol		5×10^{-5} to 4×10^{-4}	Goriushkina et al. [12]
Glycerol oxidase immobilized in glutaraldehyde vapor		5×10^{-5} to 2×10^{-4}	Goriushkina et al. [12]

Table 2 Characteristics of biorecognition elements for glycerol detection

Biorecognition element	Storage stability	Additional information	References
Glycerol dehydrogenase	–	Detection limit: 4.3×10^{-4} mM.	Álvarez-González et al. [6], Katrlík et al. [7]
Glycerol dehydrogenase-diaphorase	87% after 51 days	Sufficient for 120 measurements	Katrlík et al. [7], Gamella et al. [8]
Immobilized glycerol dehydrogenase-diaphorase	90% after 2 months; 70% after 7 months; 66% after 11 months	–	Katrlík et al. [7]
Glycerol kinase and glycerol-3-phosphate oxidase	70% of initial sensitivity after 16 h	Sufficient for 138 measurements	Katrlík et al. [7], Gamella et al. [8]
Immobilized glycerol kinase and glycerol-3-phosphate oxidase	91% after 2 months, 73% after 5 months	–	Katrlík et al. [7]
Gluconobacteroxydans (pre-hydrolyzed samples analysis)	50% after 7 days	Detection limit: 0.02 mM— 8×10^{-4} mM	Tkác et al. [9]
Gluconobacteroxydans (phosphate buffer)		Response time: 22 s	Tkác et al. [10]
Gluconobacteroxydans (thermometric flow injection analysis)	90% after a month		Navrátil et al. [11]
Glycerol oxidase immobilized by electrochemical polymerization in EDT	75% in 15 days, 14%—in 40 days	Detection limit: 0.05 mM	[12]
Glycerol oxidase immobilized by electrochemical polymerization in Resydrol	38% in 2 weeks, 13%—in 40 days	Detection limit: 0.05 mM	Goriushkina et al. [12]
Glycerol oxidase immobilized in glutaraldehyde vapor	10% in 1 day	Detection limit: 0.05 mM	Goriushkina et al. [12]

**Fig. 2** Sensitivity of biosensors for glycerol detection based on different biorecognition elements

concluded for carbon paste electrode: it provided the widest linear range and great sensitivity, but storage stability is poor.

3.2 Biosensors for β -Lactam Detection

The average detection limit based on different biorecognition elements for β -lactam detection was calculated. Since, in different papers, detection limits are given in different units,

we converted them under the assumption that density of the milk is 1 kg/L, although its true value varies with temperature and homogenization [13]. Biosensors based on different biorecognition elements are presented in Table 5. The average detection limit is 8.62 $\mu\text{g}/\text{kg}$. For the biosensors whose detection limit is presented as a range between two values, the average value is calculated from the data in the original papers. The significant outlier ($P < 0.05$) is detected to be 50 $\mu\text{g}/\text{kg}$, which is the detection limit of cephalixin using biosensor based on penicillin-binding protein. Detection limits are shown in Fig. 4.

In the case of the di-peptide assay and tri-peptide assay for β -lactam detection, the detection limit of the di-peptide assay is lower for 0.3 $\mu\text{g}/\text{kg}$. As can be seen, a parallel affinity sensor array (PASA) has the lowest detection limit.

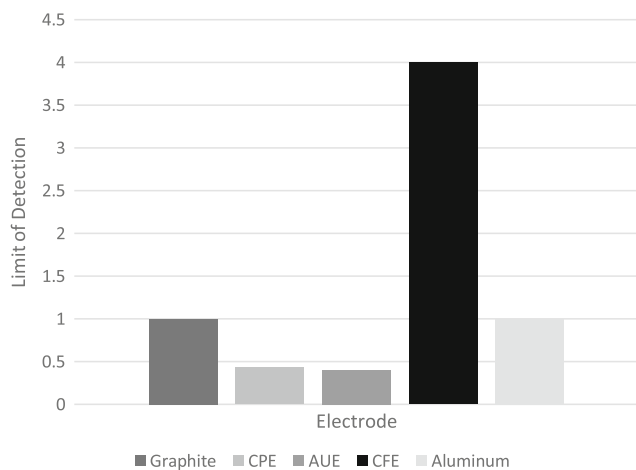
Based on different transducers, several biosensors are used for Penicillin G detection: impedimetric, amperometric, potentiometric and piezoelectric immunosensor (Table 6). The impedimetric immunosensor showed better performance than the amperometric and potentiometric because its linear range is the greatest and limit of detection is 3.0×10^{-15} M, which is very small when compared to the others. The mean value of limits of detection of these three methods is $\bar{X} = 0.1 \times 10^{-6}$, following that this immunosensor has an impressive sensitivity, since its limit is much lower than the average. The potentiometric sensor shows lower percentage recoveries in milk samples that contain greater penicillin concentrations (Fig. 5). It can be seen that, for the

Table 3 Characteristics of electrodes for glycerol detection

Electrode	Enzyme	Linear range (M)	Detection limit (M)	References
Aluminum	GDH	5×10^{-6} to 2×10^{-3}	1×10^{-6}	Eftekhari [14]
Rods of spectroscopic graphite	GDH	1×10^{-6} to 200×10^{-6}	1×10^{-6}	Niculescu et al. [15]
Carbon paste	GDH	9.97×10^{-7} to 10×10^{-4}	4.3×10^{-7}	Švancara et al. [16]
Gold electrode	GDH	1×10^{-6} to 2×10^{-5}	4×10^{-7}	Gamella et al. [8]
Carbon film	GPO	10×10^{-6} to 147×10^{-6}	4×10^{-6}	Emilia Ghica and Brett [17]

Table 4 Characteristics of electrodes for glycerol detection

Electrode	Enzyme	Potential	Sensitivity [mA/Mcm ²]	Stability	References
Aluminum	GDH	0.4 [V vs. SCE]	–	–	Eftekhari [14]
Rods of spectroscopic graphite	GDH	0.2 [V vs. Ag/AgCl]	32	After 20 h, 20% loss	Niculescu et al. [15]
Carbon paste	GDH	0.15 [V vs. Ag/AgCl]	–	After the third day, 20% loss	Švancara et al. [16]
Gold electrode	GDH	0.15 [V vs. Ag/AgCl]	20.7	After 51 days, 13% loss	Tkác et al. [8]
Carbon film	GPO	−0.15 [V vs. SCE]	10.1 ± 0.05	–	Emilia Ghica and Brett [17]

**Fig. 3** Limit of detection for glycerol biosensors based on different electrodes

concentration of 5 mg/L of penicillin G, recovery is 110%, for 10 mg/L, 60% and for the concentration of 20 mg/L, recovery is only 30%.

A piezoelectric immunosensor is used for detection of three antibiotics: Penicillin G, ampicillin and the group of penicillins (Table 6). For all of them, satisfying results were obtained. Limits of detection are close in value but the lowest is provided for penicillin G (PEG) detection. Linear range is of similar value for all, but the widest range is

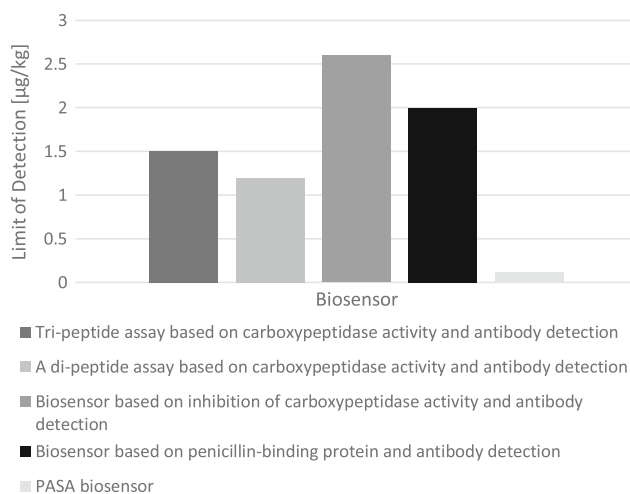
provided for ampicillin detection. Recovery is the best for the group of penicillins, being 94% for 10 mg/L.

4 Conclusion

For, glycerol detection biosensor the average sensitivity, calculated from the data presented in Table 1, is $1,691,286 \text{ nA mM}^{-1}$. The biosensor which uses *Gluconobacteroxydans* cells as a biorecognition element is not included in this calculation because its sensitivity is $755,000 \text{ nA mM}^{-1}$, which is high above the average. In the case of enzymatic biosensors, glycerol dehydrogenase/diaphorase biosensor showed better characteristics, when compared to glycerol kinase/glycerol-3-phosphate oxidase biosensor. The biosensor that is based on glycerol dehydrogenase and diaphorase, after immobilization into PCS gel, is the best enzymatic sensor that can be used for glycerol detection regarding storage stability. It can be stored up to 11 months as the level of sensitivity decreases to only 66% of the initial value. Glycerol dehydrogenase showed the widest linear range of 9.97×10^{-7} to $1.0 \times 10^{-4} \text{ M}$. After comparing several electrodes used in the amperometric measurement approach to measure their efficiency (Table 3 and 4), it can be observed that detection limit is the lowest for gold electrode (Fig. 2), being $0.43 \text{ }\mu\text{M}$. Low detection limits indicate the great sensitivity.

Table 5 Review of biosensors in β -lactam detection

Biosensor	Detection limit [$\mu\text{g}/\text{kg}$]	Additional information	References
Tri-peptide assay based on carboxypeptidase activity and antibody detection	1.5	0% false negative 27% false positive; could not detect cloxacillin	Gustavsson [5]
A di-peptide assay based on carboxypeptidase activity and antibody detection	1.2	0% false negative 27% false positive; could not detect cloxacillin	Gustavsson [5]
Biosensor based on inhibition of carboxypeptidase activity and antibody detection	2.6	Repeatability: 7.3–16% Recovery range: 108–118%	Gustavsson et al. [18]
Biosensor based on penicillin-binding protein and antibody detection	2–50	–	Cacciatore et al. [19]
Hybrid biosensor	–	Accuracy: 97–106% False positive less than 5%	Ferrini et al. [4]
PASA biosensor	0.12–31.8	–	Knecht et al. [20]

**Fig. 4** Detection limits of biosensors for β -lactam detection based on different biorecognition elements

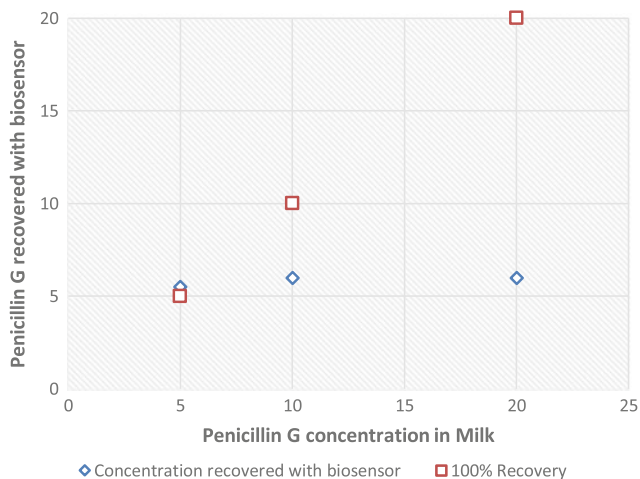
Furthermore, Aue has shown the best storage stability of 87% after 51 days. These benefits make gold electrode, using amperometric measurement type, the most desirable for this kind of detection.

For β -lactam detection, the average limit of detection of six different biosensors is 8.62 $\mu\text{g}/\text{kg}$ and PASA showed the smallest possible value of 0.12 $\mu\text{g}/\text{kg}$. Also, it is the first immuno-based biosensors array that allows simultaneous detection of different antibiotics, which makes it suitable for

use in industrial process control. Of four analyzed transducers for penicillin G detection, the impedimetric immunosensor provided the greatest sensitivity since its limit of detection is 3.0×10^{-15} M. Potentiometric biosensors are useful when there is a low concentration of penicillin in the milk sample, while recovery is not satisfactory when concentration of penicillin in milk is high (Fig. 5). The Piezoelectric immunosensor is used for detection of three different antibiotics, showing satisfying results for all of them.

Table 6 Efficiency of biosensors for antibiotics detection

Biosensor	Antibiotics	Detection limit	Linear range	Recovery	References
Impedimetric	Penicillin G	3.0×10^{15} M	1.0×10^{-13} to 1.0×10^8 M	For 5 nmol/L—76%	Thavarungkul et al. [21]
Amperometric	Penicillin G	1.82×10^9 M	5.2×10^{-9} to 41.6×10^{-9} M	For 2 nmol/L—96.4%	Wu et al. [22]
Potentiometric	Penicillin G	0.3×10^{-6} M	7.5×10^{-6} to 146×10^{-6} M	For 5 mg/L—110% For 10 mg/L—60%	Ismail et al. [23]
Piezoelectric	Penicillin G	0.8×10^{-6} g/L	2.5×10^{-6} to 250×10^{-6} g/L	For 10 mg/L—90%	Karaseva and Ermolaeva [24]
	Ampicillin	3.9×10^{-6} g/L	2.5×10^{-6} to 500×10^{-6} g/L	For 10 mg/L—87%	Karaseva and Ermolaeva [24]
	Group of penicillin's	1.7×10^{-6} g/L	1×10^{-6} to 250×10^{-6} g/L	For 10 mg/L—94%	Karaseva and Ermolaeva [24]

**Fig. 5** Penicillin G recovery with the potentiometric biosensor

References

- Mello, L.D., Kubota, L.T.: Review of the use of biosensors as analytical tools in the food and drink industries. *Food Chem.* **77** (2), 237–256 (2002)
- Brooks, S.L., Higgins, I.J., Newman, J.D., Turner, A.P.F.: Biosensors for process control. *Enzyme Microb. Technol.* **13** (12), 946–955 (1991)
- Lapenaite, I., Ramanaviciene, A., Ramanavicius, A.: Current trends in the enzymatic determination of glycerol. *Crit. Rev. Anal. Chem.* **36**(1), 13–25 (2006)
- Ferrini, A.M., Mannoni, V., Carpico, G., Pellegrini, G.E.: Detection and identification of β -lactam residues in milk using a hybrid biosensor. *J. Agric. Food Chem.* **56**(3), 784–788 (2008)
- Gustavsson, E.: Biosensor analysis of lactams in milk using the carboxypeptidase activity of a bacterial penicillin-binding protein. *J. AOAC Int.* **89**(3), 832–837 (2006)
- Álvarez-González, M.I., Saidman, S.B., Lobo-Castañón, M.J., Miranda-Ordieres, A.J., Tuñón-Blanco, P.: Electrocatalytic detection of NADH and glycerol by NAD⁺ modified carbon electrodes. *Anal. Chem.* **72**(3), 520–527 (2000)
- Katrlík, J., Mastihuba, V., Voštiar, I., Šefčovičová, J., Štefuca, V., Gemeiner, P.: Amperometric biosensors based on two different enzyme systems and their use for glycerol determination in samples from the biotechnological fermentation process. *Anal. Chim. Acta* **566**(1), 11–18 (2006)
- Gamella, M., Campuzano, S., Reviejo, A.J., Pingarrón, J.M.: Integrated multienzyme electrochemical biosensors for the determination of glycerol in wines. *Anal. Chim. Acta* **609**(2), 201–209 (2008)
- Tkáč, J., Švitel, J., Novák, R., Šturdík, E.: Triglyceride assay by amperometric microbial biosensor: Sample hydrolysis and kinetic approach. *Anal. Lett.* **33**(12), 2441–2452
- Tkáč, J., Navrátil, M., Šturdík, E., Gemeiner, P.: Monitoring of dihydroxyacetone ' production during oxidation of glycerol by immobilized *Gluconobacteroxydans* cells with an enzyme biosensor. *Enzyme Microb. Technol.* **28**(4–5), 383–388 (2001)
- Navrátil, M., Tkáč, J., Švitel, J., Danielsson, B., Šturdík, E.: Monitoring of the bioconversion of glycerol to dihydroxyacetone with immobilized *Gluconobacteroxydans* cell using thermometric flow injection analysis. *Process Biochem.* **36**(11), 1045–1052 (2001)
- Goriushkina, T.B., Shkotova, L.V., Gayda, G.Z., Klepach, H.M., Gonchar, M.V., Soldatkin, A.P., Dzyadevych, S.V.: Amperometric biosensor based on glycerol oxidase for glycerol determination. *Sens. Actuators B Chem.* **144**(2), 361–367 (2010)
- Rutz, W.D., Whitnah, C.H., Baetz, G.D.: Some physical properties of milk. I. Density. *J. Dairy Sci.* **38**(12), 1312–1318 (1955)
- Eftekhari, A.: Glycerol biosensor based on glycerol dehydrogenase incorporated into polyaniline modified aluminum electrode using hexacyanoferrate as mediator. *Sens. Actuators B Chem.* **80**(3), 283–289 (2001)
- Niculescu, M., Mieliauskiene, R., Laurinavicius, V., Csöregi, E.: Simultaneous detection of ethanol, glucose, and glycerol in wines using pyrroloquinoline quinone-dependent dehydrogenases based biosensors. *Food Chem.* **82**(3), 481–489 (2003)
- Švancara, I., Vytřas, K., Barek, J., Zima, J.: Carbon paste electrodes in modern electroanalysis. *Crit. Rev. Anal. Chem.* **31** (4), 311–345 (2001)

17. Emilia Ghica, M., Brett, C.M.: Development and applications of a bienzymatic amperometric glycerol biosensor based on a poly (neutral red) modified carbon film electrode. *Anal. Lett.* **39**(8), 1527–1542 (2006)
18. Gustavsson, E., Bjurling, P., Sternesjö, Å.: Biosensor analysis of penicillin G in milk based on the inhibition of carboxypeptidase activity. *Anal. Chim. Acta* **468**(1), 153–159 (2002)
19. Cacciatore, G., Petz, M., Rachid, S., Hakenbeck, R., Bergwerff, A. A.: Development of an optical biosensor assay for detection of β -lactam antibiotics in milk using the penicillin-binding protein 2x. *Anal. Chim. Acta* **520**(1–2), 105–115 (2004)
20. Knecht, B.G., Strasser, A., Dietrich, R., Märtlbauer, E., Niessner, R., Weller, M.G.: Automated microarray system for the simultaneous detection of antibiotics in milk. *Anal. Chem.* **76**(3), 646–654 (2004)
21. Thavarungkul, P., Dawan, S., Kanatharana, P., Asawatreratanakul, P.: Detecting penicillin G in milk with impedimetric label-free immunosensor. *Biosens. Bioelectron.* **23**(5), 688–694 (2007)
22. Wu, H., Fan, S., Zhang, W., Chen, H., Peng, L., Jin, X., et al.: Amperometric immunosensor based on covalent immobilization of new methylene blue and penicillin polyclonal antibody for determination of penicillin G in milk. *Anal. Methods* **6**(2), 497–502 (2014)
23. Ismail, F., Adeloju, S.B., Moline, A.N.: Fabrication of a single layer and bilayer potentiometric biosensors for penicillin by galvanostatic entrapment of penicillinase into polypyrrole films. *Electroanalysis* **26**(12), 2607–2618 (2014)
24. Karaseva, N.A., Ermolaeva, T.N.: Piezoelectric immunosensors for the detection of individual antibiotics and the total content of penicillin antibiotics in foodstuffs. *Talanta* **120**, 312–317 (2014)

The Assessment of Drug Interactions and Safety of Administration with Regard to Special Population Groups by a Developed Computer Program

Vanja Piljak, Belma Muftić, Sukejna Redžepi, Mirza Dedić, and Nermina Žiga

Abstract

Diabetes mellitus is a chronic disease that occurs due to a deficit in the secretion of insulin, or due to inadequate insulin action. Taking into consideration that diabetes mellitus is a chronic disease, thus it is unavoidable that a large number of diabetics, aside from their diabetes medicine, will be using other medication, which can cause interactions between the two types of drugs when they are combined. The aim of this project is to create a computer program which will aid a pharmacist during the process of dispensing diabetes medication, enabling him to check possible drug interactions and the safety of using certain types of drugs when drug pharmacodynamics and pharmacokinetics may be altered. Using C# and the MVC pattern, a program was developed which allows the examination of interactions between different drugs. By choosing the drugs of interest, the designed computer program is able to recognize if the given drug combination is safe, dangerous, or if it requires caution during administration. The program is also able to evaluate if the given diabetes medication is safe to use in special populations where drug pharmacodynamics and pharmacokinetics are altered. The application provides information that is easily and instantly available which can have a significant impact whilst working in pharmacy where the pharmacist needs to quickly make a decision regarding the safety of administration of a certain drug.

Keywords

Insulins • Oral antidiabetics • Drug interactions • Special populations • C# • The MVC pattern

1 Introduction

According to the World Health Organization, diabetes mellitus is a chronic disease that occurs due to a deficit in the secretion of insulin, or due to inadequate insulin action. Diabetes mellitus is characterized by hyperglycaemia, high blood sugar, which is followed up by symptoms such as polyuria, polydipsia, and an unexplainable weight loss [1]. Uncontrolled diabetes will lead to blood vessel damage as well as nerve damage in many organic systems, which will cause the development of many typical complications such as: diabetic neuropathy, nephropathy, retinopathy, etc. [2]. Likewise, it is important to point out that diabetics have a greater predisposition of amputation of the lower extremities compared to non-diabetics, and that pregnancy in females with diabetes is classified as a high risk pregnancy [1].

According to the International Diabetes Federation, in 2017 there were 425 million registered people with the diagnosis of diabetes mellitus, and in the mentioned year, four million of the 425 million have died of diabetes mellitus [3]. If the rising trend in diagnosed diabetes continues, it is estimated that by 2040 we will have approximately 642 million people diagnosed with diabetes, or in other words, one in 11 adults will be affected by diabetes mellitus [4].

Classification of diabetes mellitus:

Type 1 diabetes mellitus:

- Autoimmune;
- Idiopathic (unknown cause).

Type 2 diabetes mellitus:

- With an insulin resistance;

V. Piljak (✉) · S. Redžepi · M. Dedić · N. Žiga
Faculty of Pharmacy, University of Sarajevo, Sarajevo, Bosnia and Herzegovina
e-mail: vanja.piljak@hotmail.com

B. Muftić
Faculty of Electrical Engineering, University of Sarajevo, Sarajevo, Bosnia and Herzegovina

- With a defect in insulin secretion.
- Other specific types [5].

Diabetes type 1 (T1D) in most cases is the result of an autoimmune process, where beta cells of the pancreas are destroyed, which leads to an almost complete deficiency in insulin secretion. Due to the lack of insulin secretion, T1D requires a constant insulin administration, most commonly in the form of an insulin pen, or in the form of an insulin pump [2]. Literary data shows that the rate of occurrence of T1D in children and adolescents is rising by 3, and 5% in preschool children. It is estimated that every year, 70,000 children under the age of 15 are affected by T1D in the world, which is almost 200 children every day [6].

Diabetes type 2 (T2D) is a metabolic disorder that results in hyperglycaemia because of the inadequate effect of insulin on the body, also known as insulin resistance. Unlike type 1 diabetes, T2D is preventable by enforcing a healthy diet as well as regular physical activity. Pharmacological treatment includes the use of oral antidiabetic drugs and insulin [2]. The number of diagnosed with T2D is becoming a growing problem taking into consideration the growing number of older people in the entire population of the world, as well as the growing number of overweight people, due to the unhealthy lifestyle and diet. Today T2D is not only present in the older population, but in children and adolescents as well, due to the above mentioned obesity and inadequate lifestyle decisions. Studies show that the incidence of T2D in children will grow in the next 15 years by 50%, which is a worrying fact [7].

Taking into consideration that diabetes mellitus is a chronic disease, it is unavoidable that a large number of diabetics, aside from the diabetes medicine, will be using other medication, which can cause interactions between the two types of drugs when they are combined. Drug interactions are especially significant during polymedication, and it is most common in patients who are affected by a number of chronic diseases, which is the case in many geriatric patients. The use of one drug (A) can change the effect of another drug (B), in accordance with one of the two generally accepted mechanisms:

- By modifying the pharmacological effect of drug B without changing its concentration in bodily fluids (pharmacodynamics interaction);
- By changing the concentration of drug B at its site of action (pharmacokinetic interactions) [8].

The main objective of this project is to create a computer program which will aid a pharmacist during the process of dispensing diabetes medication, enabling him to check

possible drug interactions and the safety aspect of using certain types of drugs when drug pharmacodynamics and pharmacokinetics may be altered which occurs in certain kind of special populations, e.g. children, or in patients with certain medical conditions, e.g. renal and hepatic failure.

2 Methodology

All of the registered insulins and oral antidiabetics were collected from the official drug register in Bosnia and Herzegovina. The collected data is about the interaction between different drugs, as well as special populations and clinical conditions which require caution with the intake of the medication, or where the medicament in question is contraindicated with the given conditions. For each medicament the data was collected from the “Summary of Product Characteristics” (SmPC), and based on those, the Excel tables were created. The data was sorted into three Excel sheets regarding contraindicated drug combinations, drug combinations which require caution, and drug administration to special populations, after which the application development started.

The programming language used for the implementation of the application which tests the chosen medication for diabetes for interaction with another drug is C#, where a *Windows Forms* project was created which serves as a user interface. For the development, the MVC¹ pattern was used, where the model is the drug itself, as well as the appropriate descriptions for interactions, view is the *Windows Forms window*, and the *controller* is the *Excel* reader class.

While the program is starting, only basic information about the drugs is loaded from the reaction tables in order to avoid any delay due to the reading of the files. The resulting reaction will be read after the two chosen medicaments are sent as parameters to the function *reakcijaLijekova*. Beside the mentioned reaction, the program also needs to read what effect does the drug have on certain populations (e.g. children), thus returning the ones which have the label “caution” or “dangerous” as the description of the diabetes medicament. Since the position of the drug in the table is memorized, the latency of the program is minimized as it is not needed to go through all of the tables in order to find the requested drug, but can rather access it right away. Furthermore, in order to minimize the input error, the program is designed so that user can go through the alphabetically-sorted list of available drugs, but it also offers the possibility to enter the name of the drug, and select it. With this, the input validation is avoided, and the users have knowledge of which drugs are in the system.

¹MVC—Model View Controller.

Fig. 1 a Safe combination,
b dangerous combination,
c cautious combination



After the safety of the combination of the two selected drugs is determined, one of the following three results will be displayed, depending on the resulting reaction (Fig. 1):

Other than the mentioned way, it is also possible to choose just the diabetics medicament (where the second field should be blank), after which only the description will be loaded. It is important to point out that, in the case that no interaction between two drugs is found, the program will consider that as a safe combination.

The diagram below shows the overall structure of the program. As mentioned, the MVC pattern is used, and the appropriate packages are displayed, each of which contains one or more classes. The model contains classes which describe the drugs and the interactions between two given drugs, whereas the controller uses the models to store the data (i.e. the Excel tables) it reads. Since the program can be translated into English, there is a translation table from which the appropriate translation of a word/phrase is read. Lastly, the view is the window itself, and when a request from the user comes, it uses the controller to form a response, which is explained and shown further on (Fig. 2).

The activity diagram below displays how the program is checking the interaction between two given drugs. The first

step is registering the two chosen drugs which the user selected, after which the press on the button “Check” triggers the program. Since the data is arranged in three sheets (the first being dangerous interactions, second cautious, and third special populations), the first sheet is being read through, in order to check if the interaction is dangerous. If it is not, then the second sheet is opened with the intent to find the second medicament, but if it is not found, it is safe to conclude that the two drugs are not in any kind of dangerous or cautious interaction. The last step is to read through the third sheet, where only the populations where it is not recommended to use the drug or the ones pharmacist needs to be cautious about are loaded as the return data. In the end, the data is fed to the program and displayed to the user (Fig. 3).

3 Results and Discussion

When the application is opened, two options are presented, “Medicament 1” and “Medicament 2”. Option “Help” contains a short tutorial on the use of the application. The program also offers the option to change the language from

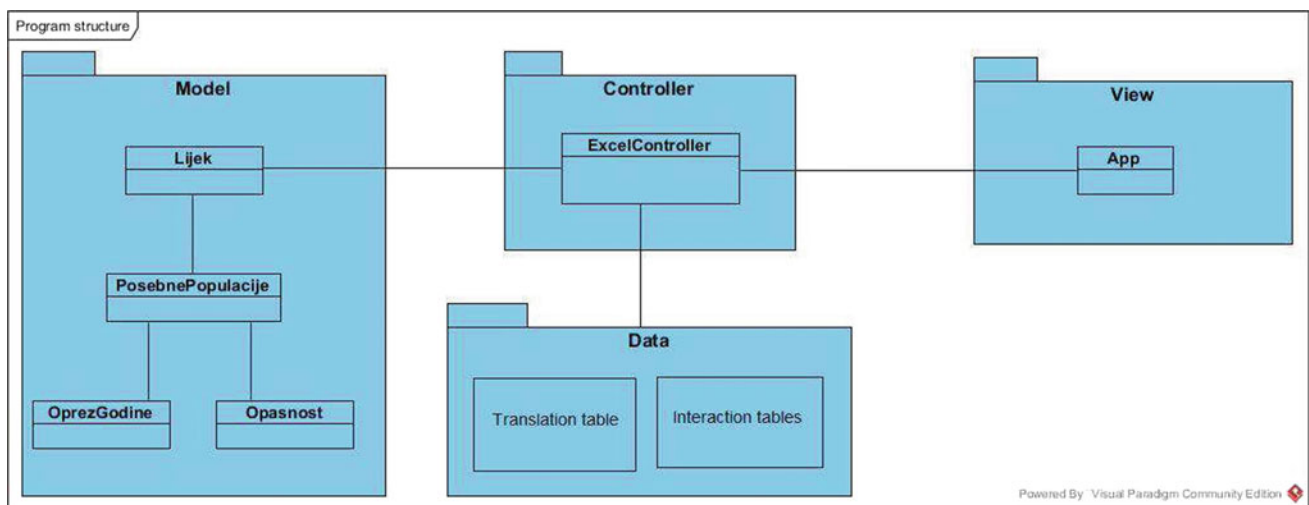


Fig. 2 Program structure

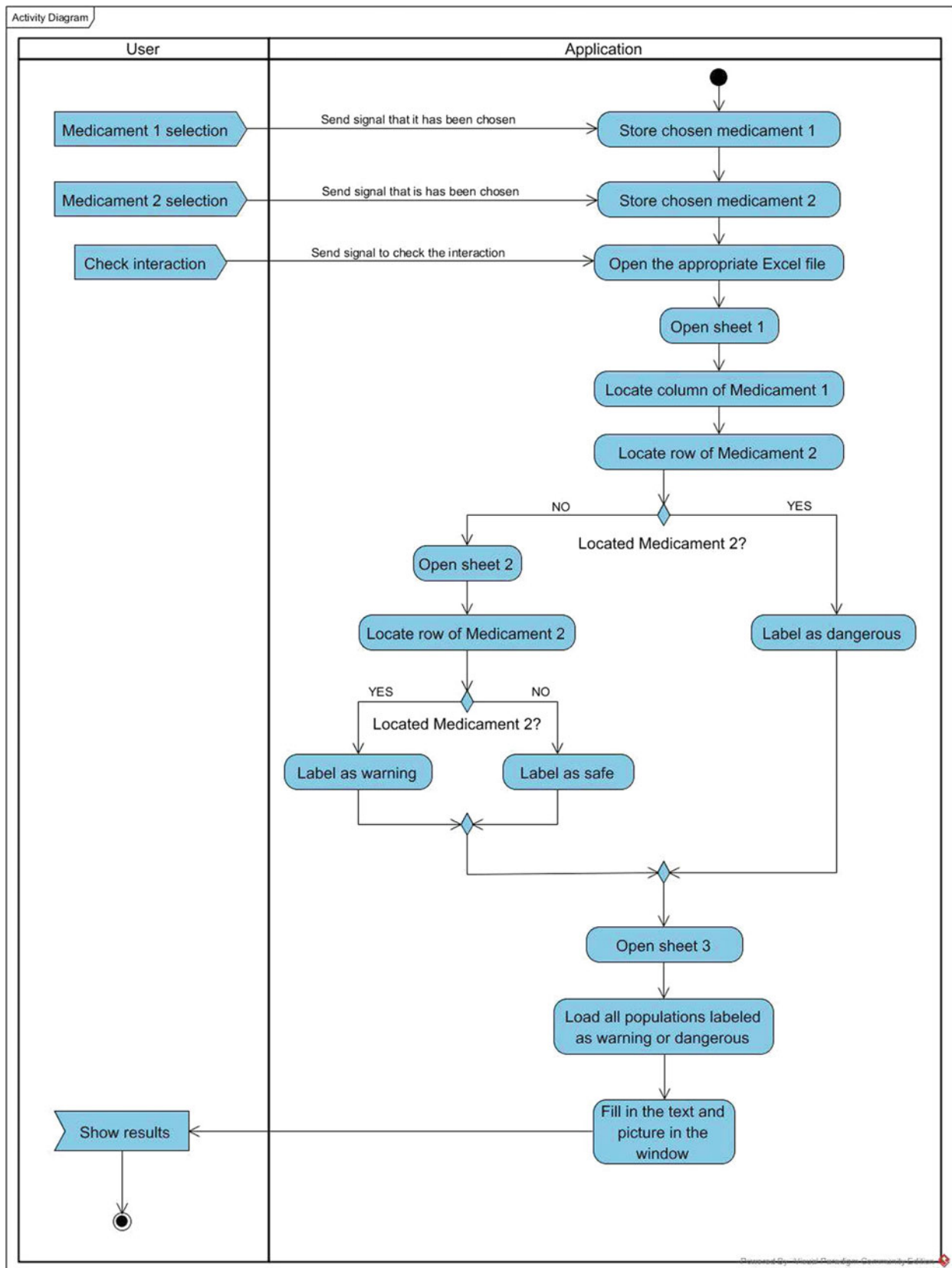
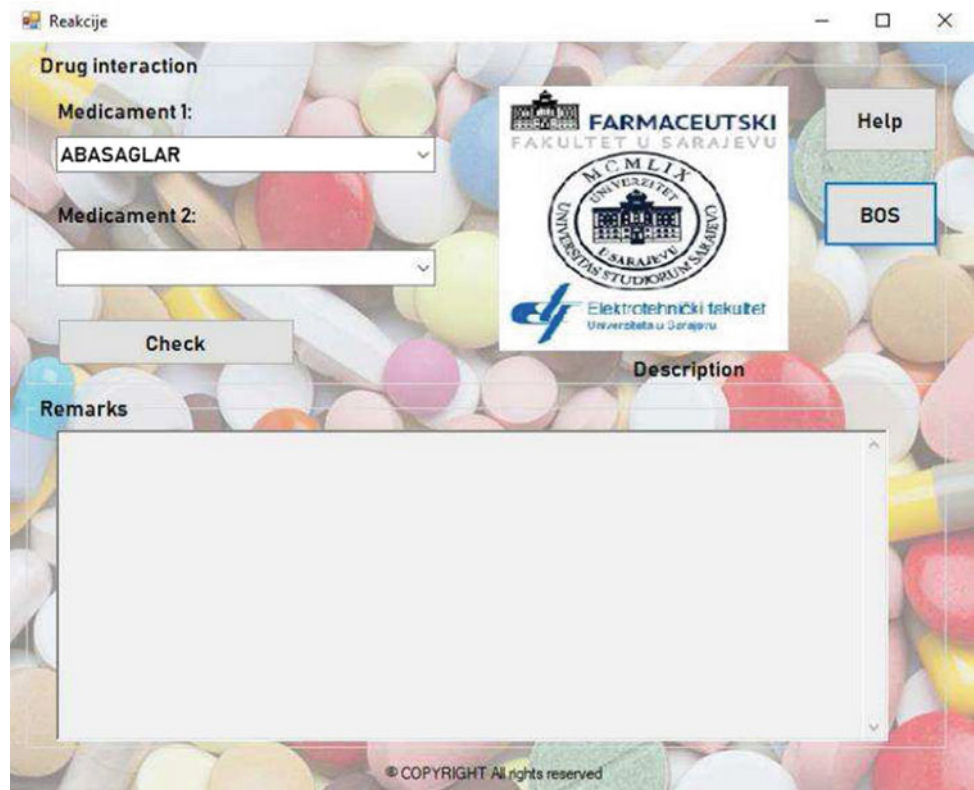


Fig. 3 Activity diagram

Fig. 4 The appearance of the program when it is opened



Bosnian to English. Figure 4 displays the appearance of the program when it is opened.

The “Medicament “1 field opens a list from which the user can choose brand names of insulins and oral antidiabetics which are currently registered in the country of Bosnia and Herzegovina. The name of the medicine can be typed in or chosen from the list.

The field “Medicament 2” offers a variety of drugs under generic names which can potentially react with some of the registered insulins and oral antidiabetics. Drugs which do not interact with any of the insulins or antidiabetics are not offered in the list. If a drug is suspected to interact with one of the insulins or oral antidiabetics, but is not found in the list, it can be concluded that the drug does not cause an interaction with any of the insulins or oral antidiabetics, and is safe to use.

After the two medications which are suspected to cause an interaction are chosen, pushing the button “Check” will show the result of the combination of the two medications, i.e. is the combination safe (“OK”), contraindicated (“Dangerous”), or if it should be administered with caution (“Warning”). The program also, shows under the section “Remarks” information for administering chosen insulin or oral antidiabetic to special population groups, such as pregnant women, or to patients with certain medical conditions. Figure 5 shows one of the possible interaction results mentioned above.

In the example above, the combination of “Glifor” and cimetidine leads to an interaction which is not dangerous, but requires an amount of caution during administration of these drugs, e.g. a change in the terms of dosage of “Glifor” might be required and the patient should be advised about possible changes in blood glucose levels when these drugs are taken together. Likewise, based on the information from the section “Remarks”, it is now possible to check the safety of using “Glifor” in certain population groups. For example, if the drug is labelled as “dangerous” for a certain population group, e.g. pregnant women, the drug should not be dispensed to those patients.

Depending on which two medications are chosen, one of the results may also be “OK”, which means that the combination of the two drugs is safe to use. Figure 6 shows an example of such results when the drug “Glucophage” (metformin) is combined with simvastatin. It must be emphasized that the “OK” result refers only to the combination of these two medicines, whilst the use of “Glucophage” with certain special population categories, such as pregnant women, is still dangerous.

The program can also show the “Dangerous” warning for a certain combination of drugs which are contraindicated and can lead to severe health problems. Figure 7 shows an example of that result when the insulin “Apidra” is combined with pioglitazone which can lead to heart failure.

Fig. 5 Result “Warning” for the combination of the two chosen drugs

Reakcije

Medicament 1:
GLIFOR

Medicament 2:
CIMETIDIN

Check

Help

BOS

WARNING

Remarks

Elderly: WARNING
 Children under 10 years: DANGEROUS
 Pregnancy: DANGEROUS
 Nursing women: DANGEROUS
 Renal insufficiency: WARNING
 Hepatic insufficiency: DANGEROUS
 Dehydration/shock: DANGEROUS
 Heart failure: WARNING
 Diabetic ketoacidosis: DANGEROUS
 Alcoholism: DANGEROUS
 Creatinine clearance (CrCl <45ml/min): DANGEROUS

© COPYRIGHT All rights reserved

Fig. 6 Result “OK” for the combination of the two chosen drugs

Reakcije

Medicament 1:
GLUCOPHAGE

Medicament 2:
SIMVASTATIN

Check

Help

BOS

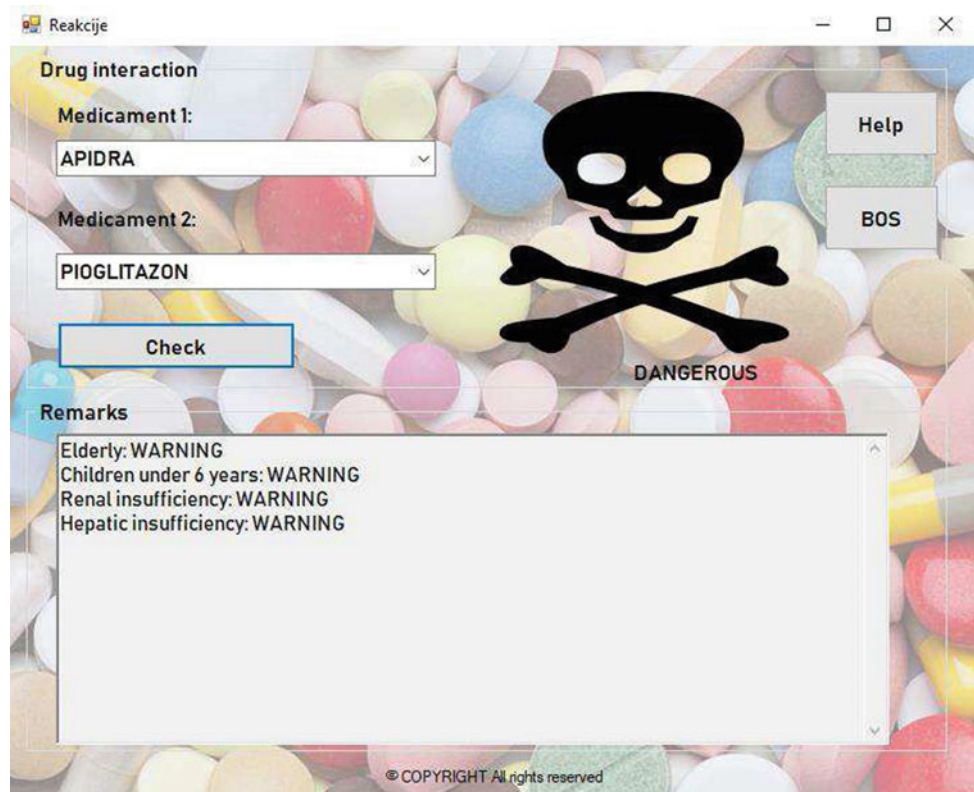
OK

Remarks

Elderly: WARNING
 Children under 10 years: DANGEROUS
 Pregnancy: DANGEROUS
 Nursing women: DANGEROUS
 Renal insufficiency: WARNING
 Hepatic insufficiency: DANGEROUS
 Dehydration/shock: DANGEROUS
 Heart failure: WARNING
 Diabetic ketoacidosis: DANGEROUS
 Alcoholism: DANGEROUS
 Creatinine clearance (CrCl <45ml/min): DANGEROUS

© COPYRIGHT All rights reserved

Fig. 7 Result “Dangerous” for the combination of the two chosen drugs



In case the pharmacist does not need the information on interactions, but only information on the effects of the diabetes medicine on special population groups and patients with certain medical conditions, it is sufficient to choose the desired medication in field “Medicament 1” and to choose the check button, while leaving the field “Medicament 2” blank. Figure 8 shows an example with the drug “Siofor”.

While using this application, possible problems have been identified, which will be worked on in the hopes of improving the program and making the overall application easier to use. One of these problems is the “OK” sign which can lead a pharmacist into believing that a medicine is safe to use, when in fact the “OK” sign refers only to the combination of the two medicines which is safe to use. The diabetes medication alone can still be dangerous for certain populations and medical conditions. This problem can be resolved in several ways: by providing the consumer with detailed instructions on how the program should be used, or by changing the program format so that the two sections, i.e. the interactions and the special population groups, are clearly divided.

Taking into consideration that the drug interaction information has been taken from the “Summary of Product Characteristics” (SmPC) for every diabetes medication

individually, in certain summaries the interactions of the given diabetes medication were sometimes referred to the entire pharmacological or chemical group of drugs, and as such they were inserted in the program. For example, Medicament 2 option encompasses the names of the entire groups of drugs (e.g. ACE inhibitors), and they are not found as individual drugs of those groups which makes the input of those medicines into the program more difficult, i.e. the user has to look for the entire group instead of the individual drug while checking the possible drug interactions. Also, some insulins and oral antidiabetics do not interact with all the drugs within the particular group. Since the program is the pilot version, this will be resolved in the future by inputting the data for each drug from these groups individually into the data base.

The program currently works only with medication used for treating diabetes. In further work, the program will be upgraded to include other drug groups, and this is planned to be achieved by expanding the data base by collecting and inputting data regarding other drug groups.

It is important to emphasize that this is a work in progress and that the application shown above is the pilot version and further work will be dedicated to the application in the hopes of resolving the current identified problems.

Fig. 8 Display of information on the effects of chosen diabetes medication on special populations and patients with certain medical conditions



4 Conclusion

This application provides significant information regarding the drug interactions and the administration of diabetes medication to special populations and medical conditions that have an altered drug pharmacokinetics and pharmacodynamics. The information is instantly and easily available which has a great impact whilst working in a pharmacy taking into consideration that a pharmacist needs to relatively quickly make a decision regarding the safety of administration of a certain drug. But it must be emphasized that this program exists only to guide the pharmacist, and the decision on administration of a certain drug should in the end only be up to the pharmacist. Moreover, the program can also be used by any other health professionals, such as medical physicians, dentists, nurses, etc.

Currently, the application works only with diabetes drugs that have been registered in Bosnia and Herzegovina, but if an electronic drugs registry were to be introduced it would be possible to expand the program to work with all the other drugs that have been registered in Bosnia and Herzegovina. In that case, the program would need to use a drug data base or API² instead of the *Excel* reader for more efficient program execution. The second step would be integration with the existing system, where based on reading the drug

prescription the program could determine whether two drugs have a contraindicated reaction. Also, integration with the electronic medical records of patients could also be of use in terms of checking if the medication affects the therapy which the patient is already using, which would greatly reduce the possible negative effects of the interaction between the two medicines.

Conflict of interest declaration The authors whose names are listed immediately below certify that they have no affiliations with or involvement in any organization or entity with any financial interests (such as honoraria, educational grants, membership, employment, stock ownership or other equity interest), or non-financial interest (such as personal or professional relationship) in the subject matter or materials discussed in this work.

References

1. Chobain, A.V., Bakris, G.L., Black, H.R.: The seventh report of the joint national committee on prevention, detection, evaluation, and treatment of high blood pressure: the JNC 7 report. *JAMA* 289 (2003)
2. Heljić, B., Dilić, M., Čengiće, M., Čengiće, F., Lončarević, N.: *Diabetes mellitus-klinički aspekti*, Jež, Sarajevo (2002)
3. International Diabetes Atlas: *Diabetes by Region*, 8th edn. [Online]. http://diabetesatlas.org/IDF_Diabetes_Atlas_8e_interactive_EN/. Access: 14.07.2018 (2007)

4. Strategija borbe protiv dijabetesa u FBiH 2014–2024: Federalno ministarstvo zdravstva (2014)
5. World Health Organization: Definition, Diagnosis and Classification of Diabetes Mellitus and its Complications. Report of a WHO Consultation, Part 1: Diagnosis and Classification of Diabetes Mellitus (1999)
6. Adler, A.I., Stratton, I.M., Neil, H.A.: Association of systolic blood pressure with macrovascular and microvascular complications of type 2 diabetes: prospective observational study. *BMJ* **321**, 412–419 (2000)
7. Popović, P.S., Heljić, B.: Vodič za dijabetes. Sarajevo: Klinički centar Banja Luka, Institut za naučnoistraživački rad i razvoj Kliničkog Centra Univerziteta u Sarajevu (2008)
8. Rang, H.P., Dale, M.M., Ritter, J.M., Moore, P.K.: Farmakologija - Prvo srpsko izdanje, 5th edn, p. 718. Belgrade, Data status (2005)

Implementing the Calculation of the Appropriate Drug Dose for Children Using the Programming Language C#

Sukejna Redžepi, Belma Muftić, Vanja Piljak, Nermina Žiga, and Mirza Dedić

Abstract

Drug dosage is the amount of a drug or medicinal substance, which needs to be administered to a patient in the form of a single dose or in the form of multiple doses, in order to achieve desirable therapeutic effect. Determining the adequate dose for a child represents a challenge, since the drug pharmacokinetics are different in the bodies of children, compared to those in adults, therefore children usually require lower doses of medication compared to adults. There are numerous formulas to calculate the appropriate drug dose for children, based on the child's age, weight, etc. The aim of this project is to design a computer program that will calculate the drug dosage for children quicker, and requiring less effort. Using the programming language C#, a user interface was developed. The application enables calculating the dose for children based on the adult dosage and the age or weight of a child requiring the medication, and it also regards children under the age of one as a special group and enables the calculation of the dose for those children specifically. The application simplifies the work of a pharmacist in a drugstore in terms of dispensing medication for children and it can be also used by paediatricians while prescribing drugs for children.

Keywords

Drug dosage • Child dosage • Dose calculation formulas • C# programming language

1 Introduction

Posology is the study concerned with dosage. Drug dosage implies the determination of the amount of drug or medicinal substance, which needs to be administered to a patient in the form of one single dose or in the form of multiple doses, for the sake of achieving desirable therapeutic effect, considering the fact that the given dose makes the poison or the cure in this case [1]. The quantity of the drug administered to a patient within 24 h in the form of one single dose, or multiple doses for the purpose of treatment is called a dosage [2]. Several types of doses can be differentiated:

- The physiological or ineffective dose (dosis physiologica) is the quantity of drug which has no effect, but is still present in the organism.
- The therapeutic or effective dose (dosis terapeutica) is the optimal quantity of drug with which a therapeutic effect is achieved and is always greater than the ineffective dosage.
- The effective dosage (ED50) is the quantity of drug effective in 50% of the human population [3].
- The toxic dose (dosis toxica) is the quantity of drug which leads to toxic effects in the organism.
- The lethal dosage (dosis letalis) is the quantity of drug which leads to the death of an organism. Minimal lethal dose (dosis letalis minima) is the minimum quantity of drug, which still causes death. Medium lethal dosage (dosis letalis media) is the quantity of drug which usually causes death [2].

In the majority of cases, a single dose of drug is not enough to cure the cause of illness and therefore the dose has to be repeated so that the drug therapeutic concentrations can be maintained at the drug's site of action. The dosage frequency is different for different drugs and therefore two more types of doses can be differentiated:

S. Redžepi (✉) · V. Piljak · N. Žiga · M. Dedić
Faculty of Pharmacy, University of Sarajevo, Sarajevo,
Bosnia and Herzegovina
e-mail: sukejnars@gmail.com

B. Muftić
Faculty of Electrical Engineering, University of Sarajevo,
Sarajevo, Bosnia and Herzegovina

- The maximum singular dose (*dosis maxima singula*) is the largest therapeutic dose of a drug which can be administered all at once without harmful consequences.
- The maximum daily dose (*dosis maxima pro die*) is the largest quantity of drug, which taken in a time interval of 24 h does not cause toxic effects [2].

Doses which are listed in the pharmacopoeia for certain substances are related to the adult, i.e. normally developed person, therefore when dosing drugs for children, certain adjustments must be made. The differences between the dosage required for children, and the dosage required for adults is due to many factors which include changes in pharmacokinetic parameters, age, body, weight, surface area, and genetic predisposition [4]. There are numerous formulas for calculating the dosage for children from an adult dose, based on weight, age and surface area of the child's body [5].

Dilling-Martinet's rule (dose according to the child's age) [5]

$$\text{Child dose (CD)} = \frac{\text{age of the child}}{20} \times \text{adult dose (AD)}$$

Thiemich-Feer's rule (dose according to the child's body weight) [5]

$$\text{Child dose (CD)} = \frac{\text{weight of the child}}{70} \times \text{adult dose (AD)}$$

Augsberger's formulas [5]

$$\begin{aligned} \text{Child dose (CD)} &= 4 \times \text{age of the child} + 20 \\ &= \% \text{ adult dose (AD)} \end{aligned}$$

$$\begin{aligned} \text{Child dose (CD)} &= 1.5 \times \text{weight of the child} + 10 \\ &= \% \text{ adult dose (AD)} \end{aligned}$$

Young's formula [2]

$$\text{Child dose (CD)} = \frac{\text{age of the child}}{\text{age of the child} + 12} \times \text{adult dose (AD)}$$

Bolognini's formula [5]

$$\text{Child dose (CD)} = \frac{1}{20 - \text{months of the child}} \times \text{adult dose (AD)}$$

The main reason age influences the effect of drugs is the fact that the elimination of drugs is less efficient in newborns and older people, therefore the drugs have a stronger and longer effect in those age groups. Glomerular filtration rate (GFR) of infants calculated according to surface area of the body is just around 20% of the adult's value, and the tubular function is decreased as well. Therefore, infants have a

longer half-life of drug elimination from the plasma than adults [6]. Immaturity of kidneys of prematurely born children can also have a great effect on the drug elimination. Hence, it is necessary to decrease the dosage or to increase the interval between two consecutive drug doses [7].

In children's practice the drugs need to be prescribed in liquid form, if possible. Insoluble powders need to be mixed with a liquid and pills need to be crushed and administered with a liquid as well. Drugs with an unpleasant taste should not be mixed with food, because they can cause long-term reluctance towards taking that specific food, and hence sugar and syrups should be used to correct the drug's taste and smell. The majority of drugs can be administered in children through the rectum, after a previous enema for cleansing, or in the form of a suppository [5].

The purpose of developing a computer program that can calculate doses for children is to allow paediatricians and pharmacists faster and easier calculation of the accurate dosage for children while prescribing and dispensing drugs. Although computer programs that can calculate paediatric dose are not a new concept in medicine, currently in Bosnia and Herzegovina such a system is not in use in regular clinical practice.

2 Methodology

The programming language C# was used for the development of an application which calculates the right drug dosage for children, where a Windows Forms project was developed as the user interface. Since the calculations for this project do not need any special classes, no particular pattern was used.

The user is required to insert the drug dosage for an average man (where it is indicated that the dosage is in milligrams), after which the user needs to insert one of the following three possibilities:

1. The age of the child (in years)
2. The weight of the child (in kilograms)
3. The age of the child not older than one year (in months).

It is possible to insert decimal numbers for any of the above mentioned values, while characters (except for the dot and the comma) are forbidden. However, if the input field contains more than one comma or dot, a message will pop up notifying that an error occurred with the information where it had occurred, and on that location the resulting value will not be calculated. In case the error is within the field for the dosage of an average adult, no resulting value will be calculated. Furthermore, if there is no value for the dosage for adults, or if all three child values are empty, a message will be shown to notify the user.

When the values are inserted correctly, the resulting field (or fields) where there is an input will calculate the right drug dosage for the child according to the following formulas (according to the previously mentioned options respectively):

$$\text{Child dose [mg]} = \frac{\text{age of the child [years]}}{20} * \text{adult dose [mg]}$$

$$\text{Child dose [mg]} = \frac{\text{weight of the child [kg]}}{70} * \text{adult dose [mg]}$$

$$\text{Child dose [mg]} = \frac{1}{20 - \text{age of child [months]}} * \text{adult dose [mg]}$$

The field with the resulting child dose cannot be modified, which prevents the possibility of unwanted input. A help button is available in the program, which explains to the user how to use the application. Furthermore, the program offers the resetting of some or all fields with the appropriate button(s). What is important to point out is that the program does not depend on any particular drug, but requires the single dose of the active substance for the given medicament, based on which it calculates the child dose.

3 Results and Discussion

Once the pharmacist starts the application, a window will open on the computer desktop, which represents the starting form of the program. The starting appearance of the program is shown on Fig. 1 in which it can be seen that the application is composed of several spaces in which the corresponding data is entered, necessary for performing the program's function for which it is intended. The program offers the option to change the language from Bosnian to English.

In the lower right corner of the program there is the option "Help", which essentially gives instructions to the user on what data is sufficient to enter in order to receive the corresponding results, alongside with what requires attention to be paid on. By clicking on the mentioned option, a window is opened, shown on Fig. 2.

The first step, during the dose calculations, is entering the individual dosage for an adult of a specific active substance of drug, i.e. the carrier of pharmacological activity. The dosage is entered in the space marked as "Adult dose" (in milligrams). The next step is entering one of the mandatory data requirements related with the child, e.g. age in the space "Age of child". After entering the data, by clicking on the option "Calculate" (in the lower right corner), in the space

Fig. 1 Display of the starting program appearance

Fig. 2 Display of instructions for opening the program

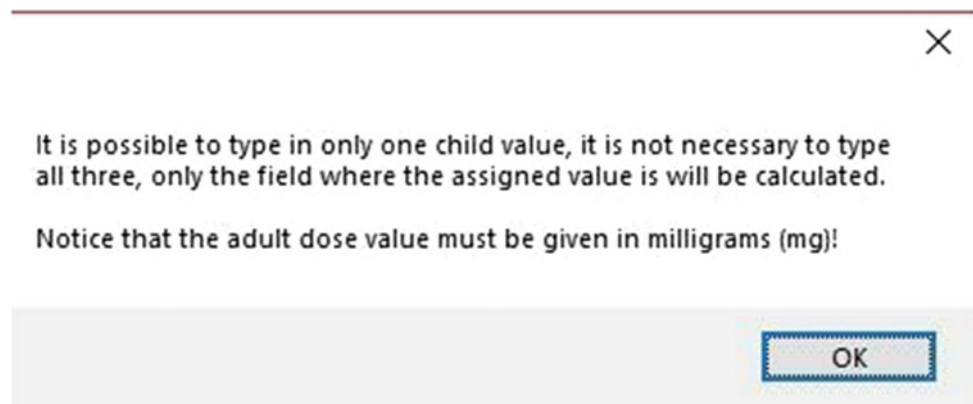
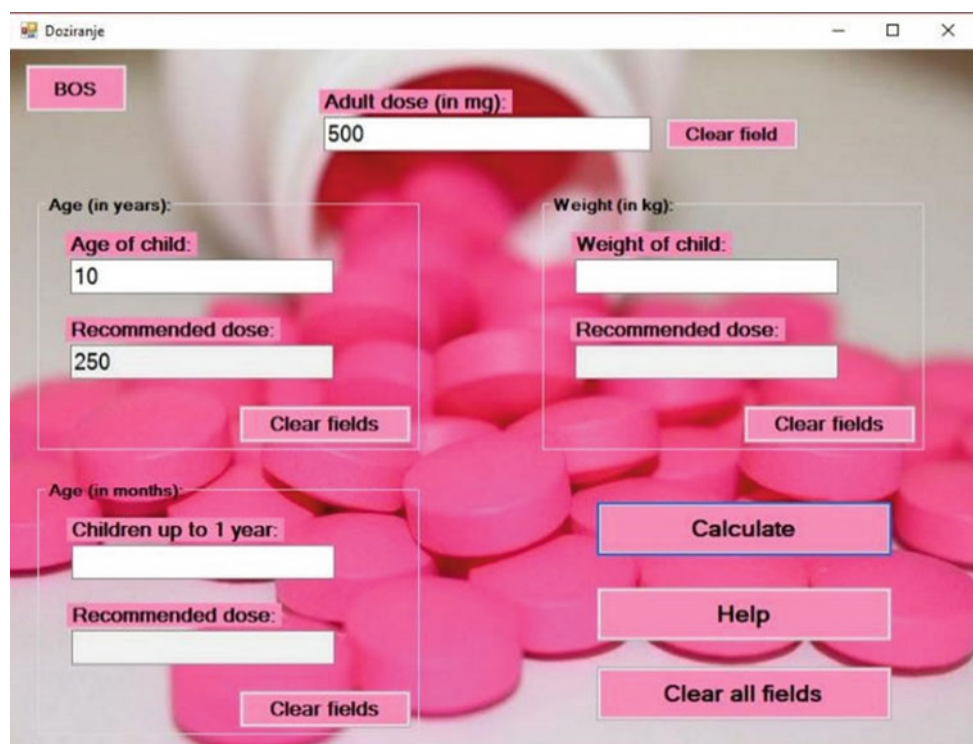


Fig. 3 Display of entering and calculating the dosage for a child based on the age entered



“Recommended dose” a number is shown representing the suitable drug dosage for the treatment of the child of a specific age. The above-mentioned text is visually shown in Fig. 3.

Also, instead of data based on the child’s age, the dosage can be calculated based on the child’s weight as well. Calculations are done almost the same, as it was described in the previous example, with the difference that the weight data is entered in the space “Weight of child”.

Visual display of this calculation is shown in the Fig. 4.

Children younger than the age of one are going to be regarded as a special group and therefore the program enables dosage calculation specifically for children within this group. The procedure of entering data is the same as in the previous two examples, with the fact that instead of data

about the age and the weight of the child, the age of the baby in months, not years, is entered in the space “Children up to 1 year”.

Mentioned procedure is shown on the Fig. 5.

The program also allows simultaneously getting data about the recommended drug dosage for a child based on age, weight, as well as number of months. What needs to be done in this case is to enter data of an individual adult’s dosage of the drug, then data about age, weight and the age of the infant in months, and click on the option “Calculate”, after which in the three fields recommended drug doses are simultaneously presented based on the entered data. It is also important to mention that the entered data for the age, weight and number of months, doesn’t have to relate to the same child, i.e. the data can relate respectively to three different

Fig. 4 Display of entering and calculating the dosage for a child based on child's weight data

The screenshot shows a software window titled "Doziranje" with a background image of pink pills. A pink button labeled "BOS" is in the top left. The "Adult dose (in mg):" field contains the value "500" and has a "Clear field" button next to it. There are three input sections, each with a "Clear fields" button below it:

- Age (in years):** Includes "Age of child:" and "Recommended dose:" fields.
- Weight (in kg):** Includes "Weight of child:" (containing "22") and "Recommended dose:" (containing "157.143") fields.
- Age (in months):** Includes "Children up to 1 year:" and "Recommended dose:" fields.

 At the bottom right, there are three buttons: "Calculate" (highlighted with a blue border), "Help", and "Clear all fields".

Fig. 5 Display of entering and calculating the dosage of a child under the age of one, based on the age in number of months

This screenshot is similar to Fig. 4, but with different data entered. The "Adult dose (in mg):" field still contains "500". The "Weight (in kg)" section is empty. The "Age (in months)" section has "6" entered in the "Children up to 1 year:" field, and the "Recommended dose:" field below it contains "35.714". The "Calculate" button remains highlighted with a blue border.

Fig. 6 Display of the simultaneously entered and calculated dosage for a child based on data for age, weight and number of months

The screenshot shows a software application window titled "Doziranje" with a background image of pink pills. The interface is divided into three main sections for calculation, each with a "Clear fields" button:

- Adult dose (in mg):** Input field contains "500".
- Age (in years):**
 - Age of child: Input field contains "10".
 - Recommended dose: Input field contains "250".
- Weight (in kg):**
 - Weight of child: Input field contains "22".
 - Recommended dose: Input field contains "157.143".
- Age (in months):**
 - Children up to 1 year: Input field contains "6".
 - Recommended dose: Input field contains "35.714".

At the bottom right, there are three buttons: "Calculate", "Help", and "Clear all fields".

children. What is important is that the calculations for these three children are done for the same drug and the same individual dose.

Visual representation of the simultaneous calculations for all three cases is shown in Fig. 6.

It is important to state that the program cannot calculate the dosage for a child over one year of age by using Bolognini's formula (field "Age (in months)") which is intended entirely for calculations of the dosage for the children younger than one year.

The research conducted in Singapore examining the effect of computer calculated doses on medication error rates showed that the medication error rate decreased by 15.6% when the dose was calculated by a computer. The research showed that the medication error was quite common in outpatient, emergency department and discharge prescriptions and that the computer calculated doses can significantly reduce errors [8]. The developed program for calculation of drug dose for children can be implemented in various parts of the healthcare system in Bosnia and Herzegovina, such as hospitals, family practices, and pharmacies. The program would enable paediatricians and pharmacists easier and faster calculation of the drug dose for children, allowing more efficient process of prescribing and dispensing medications to children.

4 Conclusion

Based on the application's working principle stated above, it can be seen that its main purpose is to simplify the work of a pharmacist in a drugstore in terms of dispensing medicine for children, in accordance with their, still insufficiently developed, capability to metabolize the medicine. Of course, besides pharmacists, the application would be beneficial to paediatricians, making it much easier for them to prescribe drugs for children. Information, necessary for the application's functioning (age, weight or months of a child), is very easily accessible, taking into account that the doctor needs to state them in the prescription.

The main characteristic of this application is that it allows dosage calculation for children based only on the data of a singular dose of a specific medicine and on the information about age or weight of a child, or the baby's age in months. In other words, in order for a child's dosage to be calculated, it is not necessary to know the trade name of the medicine, but only the singular dose. What may be a disadvantage of the application is that it requires the manual insertion of the singular dose necessary for the calculations. However, if integrated with an e-register, it would be possible to select the wanted drug, and the program would retrieve the data for

that drug in order to perform the calculations. In that case, access to the database of the e-register would be needed. Another possibility is to send an API (Application Programming Interface) request; however, both ways would get the needed data, but also minimize the possibility of an ignorance error due to the lack of knowledge of the right dosage.

It is important to emphasize the project is in early stages of the development, and that the currently developed application will be further evaluated in a pilot study to determine its practicality, accuracy and efficiency in clinical practice.

Conflict of Interest Declaration The authors whose names are listed right below certify that they have no affiliation with or involvement in any organization or entity with any financial interests (such as honoraria, educational grants, membership, employment, stock ownership or other equity interest), or non-financial interest (such as personal or professional relationship) in the subject matter or materials discussed in this work.

References

1. Schnaare, R.L., Prince, S.J.: Metrology and Pharmaceutical Calculations. In: Felton, L. (ed.) Remington: Essentials of Pharmaceutics, 1st edn, pp. 114–115. Pharmaceutical Press, London (2013)
2. Ansel, H.C.: Pharmaceutical Calculations, 13th edn. Lippincott Williams & Wilkins, pp. 103–121 (2010)
3. Rang, H.P., Dale, M.M., Ritter, J.M., Moore, P.K.: Farmakologija - Prvo srpsko izdanje, 5th edn, pp. 713–714. Data status, Belgrade (2005)
4. Khan, M.A., Reddy, I.K.: Pharmaceutical and Clinical Calculations, 2nd edn, pp. 269–271. CRC Press, Boca Raton (2000)
5. Jugoslovenska farmakopeja IV, 4th edn. Zavod za ispitivanje i kontrolu lijekova SRH, Zagreb, pp. 373–374 (1984)
6. Ritter, J.M., Lewis, D.L., Ferro, A.: Clinical Pharmacology and Therapeutics, 5th edn, pp. 53–54. Hodden Education, London (2008)
7. Walker, R., Edwards, C.: Clinical Pharmacy and Therapeutics, 2nd edn, p. 342. Churchill Livingstone, New York (1999)
8. Kirk, R.C., Li-Meng Goh, D., Packia, J., Min Kam, H., Ong, B.K.: Computer calculated dose in paediatric prescribing. In: PubMed. <https://www.ncbi.nlm.nih.gov/pubmed/16119974> (2005). Accessed 17 Jan 2019



ORÁO: RESTful Cloud-Based Ophthalmologic Medical Record for Chromatic Pupillometry

Ernesto Iadanza, Rachele Fabbri, Alessio Luschi, Francesca Gavazzi, Paolo Melillo, Francesca Simonelli, and Monica Gherardelli

Abstract

Chromatic pupillometry represents a pioneering approach to the evaluation of inherited ocular diseases in childhood and a pilot study has been designed to evaluate its clinical utility. The physicians involved in the project belong to two different University centres: the data they gather must be collected in an electronic medical record reachable via web. Therefore, a specified medical record has been designed. It has been realized as a .NET application with RESTful architecture. The user-interfaces have been built with the aim to reduce the risk of error and with particular attention to usability, according to standards. Each web page of the medical record has been made as user-friendly as possible. Thanks to these characteristics, the physicians have a good attitude toward the use of the electronic medical record as a way to improve the progression of the pilot study.

Keywords

Chromatic pupillometry • Healthcare • EMR • RESTful • Usability

1 Introduction

The Italian Ministry of Education, Research and University funded the project *Toward new methods for early diagnosis and screening of genetic ocular diseases in childhood* (PRIN 2015), aiming to detect new methods for the study of

E. Iadanza (✉) · R. Fabbri · A. Luschi · F. Gavazzi · M. Gherardelli
Department of Information Engineering, University of Florence, Florence, Italy
e-mail: ernesto.iadanza@unifi.it

P. Melillo · F. Simonelli
Eye Clinic, Multidisciplinary Department of Medical, Surgical and Dental Sciences, University of Campania Luigi Vanvitelli, Naples, Italy

Inherited Retinal Diseases (IRDs). Chromatic pupillometry is the method used to study and evaluate the cones and rods functionality. Its application in paediatric ophthalmology represents a pioneering approach for IRDs diagnosing and monitoring. A pilot study has been designed to evaluate the clinical feasibility of the pupillometric protocol and the usefulness of chromatic pupillometry. The study is multi-centric: 60 cases and 20 controls have been recruited and examined by the project clinical partners. The cases are IRD-affected children, while controls consist in healthy subjects. The age range spans between 8 and 16 years [1]. The Department of Information Engineering (DINFO), University of Florence, has been involved in the project because of his previous experiences in developing RESTful web applications and Clinical Decision Support Systems (CDSS) [2–4]. An Electronic Medical Record (EMR) has been designed and realized to collect examination data of cases and controls both from the recruiting centres of Milan and Naples.

In this paper ORÁO,¹ the EMR realized for the above-mentioned project, is presented. A particular attention has been posed in describing the interfaces of the platform and the features that make them usable and reduce safety issues.

2 Platform Project

The EMR has been deployed as an .NET application, with Model View Controller (MVC) architectural code pattern. This cloud-based platform is hosted on the server farm of the DINFO, one of the project partners. A key design requirement for this platform is to have a cloud-based application, because of the multicentricity of the study. Data recorded by physicians are stored in a database which provides query

¹From the ancient greek verb *ὀράω*, meaning *I see*. **ORÁO** is the acronym of *Ophthalmologic medical Record for chromAtic pupillOmetry*.

functionalities for clinical evaluations concerning the pupillometric protocol and the pilot study itself.

The design of the platform is described in the following sections.

2.1 User Interface Design

The platform, named ORÁO, has been designed to facilitate the implementation of the visit workflow, specifically designed for this project, minimizing the overall impact on the staff. The healthcare providers must perceive it as a way to improve the quality of their work, instead of one more technology solution they are forced to deal with.

The platform must have a dedicated web page for every stage of the visit, from collecting patient personal data to single exams and procedures. The examination data collecting form has been designed starting from the specifications given by the clinical partners who participated in conceiving the pilot study. A list of input fields that every examination page should contain, as well as the type of each input field (short or long text, date, file, multiple choice, boolean, decimal or integer), has been implemented including potential maximum values that cannot be overstepped.

Usability is defined as “the extent to which a product can be used by specified users to achieve specified goals with effectiveness, efficiency, and satisfaction in a specified context of use” [5]. It means that it is possible to reduce safety risks with an usability-oriented design of the interfaces in the platform. Thus, techniques and standards for ensuring high levels of usability must be adopted to provide an optimal user-interface experience by the physicians [6, 7].

2.2 Pilot Study Design

The pilot study establishes a baseline visit and a 28 ± 7 days follow-up. Examinations consist of participant’s personal data collection, registration of ophthalmologic clinical and instrumental data and pupillometry. The pupillometric protocol designed in the pilot study is performed by multi-chromatic pupillometer DP-2000 by NeurOptics (see Figs. 1 and 2). It is able to stimulate one or both eyes with different user-selected light intensities and colors. Then the pupil profile and light stimulus characteristics are transferred from the device to a data file with extension *.DAT* for external analysis. The pupillometer works at a sampling frequency of 30 Hz. Light stimulation has four different chromatic options: red (622 nm), green (528 nm), blue (463 nm) and white.

After an initial period of ten minutes of dark-adaptation, the patient is stimulated under three different conditions: low intensity stimulus with dark background, high intensity

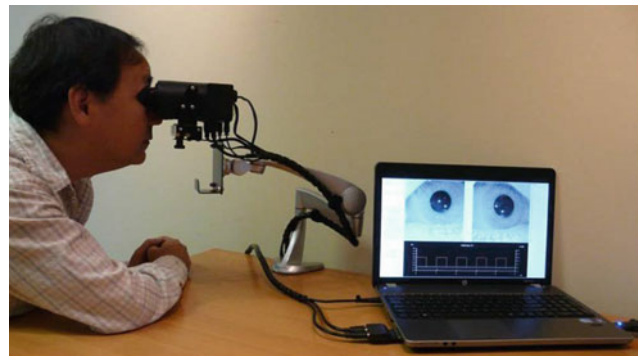


Fig. 1 DP-2000 multi-chromatic pupillometer, by NeurOptics

stimulus with dark background and high intensity stimulus with blue background, the latter is performed after 3 min for eyes adaptation to light. Every stimulus is repeated three times for light colors of red and blue, for a total of eighteen stimuli (see Table 1).

Different light color, intensities and background color stimulate the various light-sensitive retinal cells. These cells respond to the light stimulation by changing the pupil diameter. Physicians must analyze pupil time trend to evaluate the function of the retinal cells. The pupillometer measures and records the pupil response to the light stimulations expected by the pupillometric protocol. The output of the pupillometer DP-2000 is, as stated above, a *.DAT* file composed by various sections. Section *<merged-pupil-data>* contains data regarding the pupil diameter response; in particular, columns 2, 4 and 8 respectively collect time, right-diameter and left-diameter sampled values of all the acquisitions, according to the pupillometric protocol of the pilot study. This values must be properly elaborated to be presented to the physicians in a suitable way: when the specialist studies the pupil response, he/she must choose the stimulus index and view the relative graph of right and left pupil diameter time trend. Moreover, in another section of the *.DAT* file, there are parameters of medical interest, collected in a table. This information must be extracted and made available in the platform interface for the end-users.

2.3 RESTful Cloud-Based Platform

Since the pilot study is multicentric, ORÁO must be remotely reachable via web. For the same reason, the platform must be provided with a central database for clinical data storage and data must be available and visible by all scholars involved in the study. A Virtual Machine (VM) has been created on the above cited server farm at the DINFO in order to respond to the previous characteristics. The VM hosts the web server running the application as well as the database engine.

Fig. 2 A particular of the pupillometer DP-2000, showing the camera and its support arm

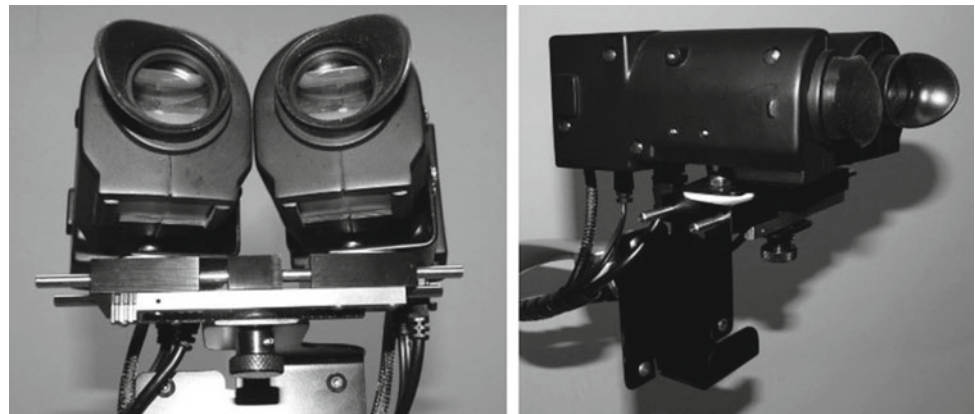


Table 1 Pupillometric protocol

Stimuli index		Light intensity	Background color
Red stimuli	Blue stimuli		
0–2	3–5	Low	Dark
6–8	9–11	High	Dark
12		Blue background adaptation	
13–15	16–18	High	Blue
19		No stimulus for technical reasons	

The user, after a login step, must be able to view data stored in the database using the platform interface, edit the existing records and input new information. The physicians of the recruiting centres of Naples and Milan involved in the study must be provided with the possibility to export a .CSV file containing pupillometric data, in order to evaluate the progression of the pilot study. The platform must be implemented with a RESTful architecture. It facilitates data exchange between server and clients. It also permits an easy future integration of third-party applications with the developed Application Programming Interfaces (APIs).

3 Results

The web application has been realized in MS Visual Studio 2017² using Visual Basic .NET (VB.NET) and ASP.NET framework 4.5.2. The pages have been implemented using Twitter Bootstrap v.3.3.7³ framework, an open source toolkit for web development with HTML 5.0, CSS 3, and Javascript (JS). The database is realized using the Relational Database Management System (RDBMS) engine Microsoft SQL Server Express 2008 R2. APIs have been implemented in .NET.

At their first use of the EMR, physicians are requested to sign up by choosing an email address and a password. Then

the access has to be approved by the administrator of the platform. Once the user is allowed to access, he/she is able to log in and use the EMR to register, modify and examine patients' data. From the homepage of the platform (see Fig. 3), users are able to enter personal data of a new patient or to access to clinical data of patients already registered in the database. The top navigation menu, displayed in every page of the application, gives the user the possibility to:

- Register personal data of a new patient coming for the baseline examination, by clicking on the button *New patient*;
- Select an already registered patient from the *Patients list*, which contains name, last name, birth date, fiscal code and gender;
- *Search patients* by name, last name, birth date, fiscal code or any combination of them.

When a physician selects a patient, he/she is redirected to a page showing all the patient follow-ups identified by the date of their registration. Each one of them is also associated to a green or white background color (see Fig. 4): if follow-up date has a green background, it means that it is consolidated and no more editable, but only viewable. Once the user has selected the date of the follow-up he wants to open, he is redirected to a page where he can choose the ophthalmologic examination he desires to register, edit or view.

²<https://visualstudio.microsoft.com>.

³<https://getbootstrap.com>.

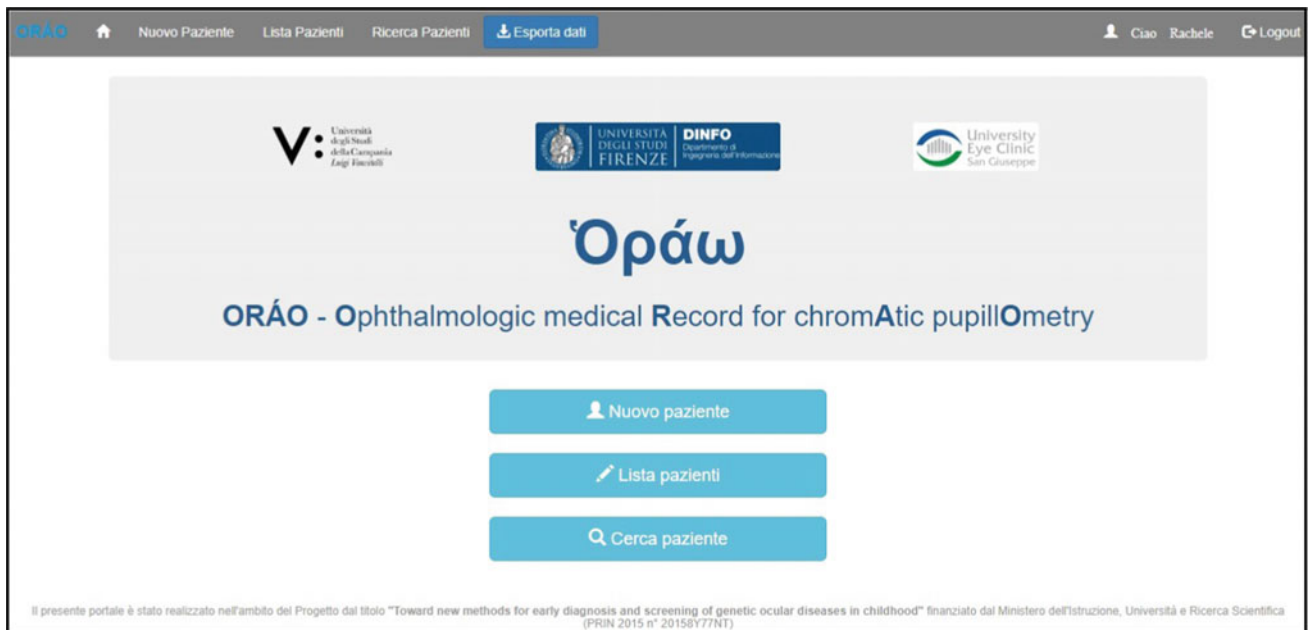


Fig. 3 ORÁO homepage

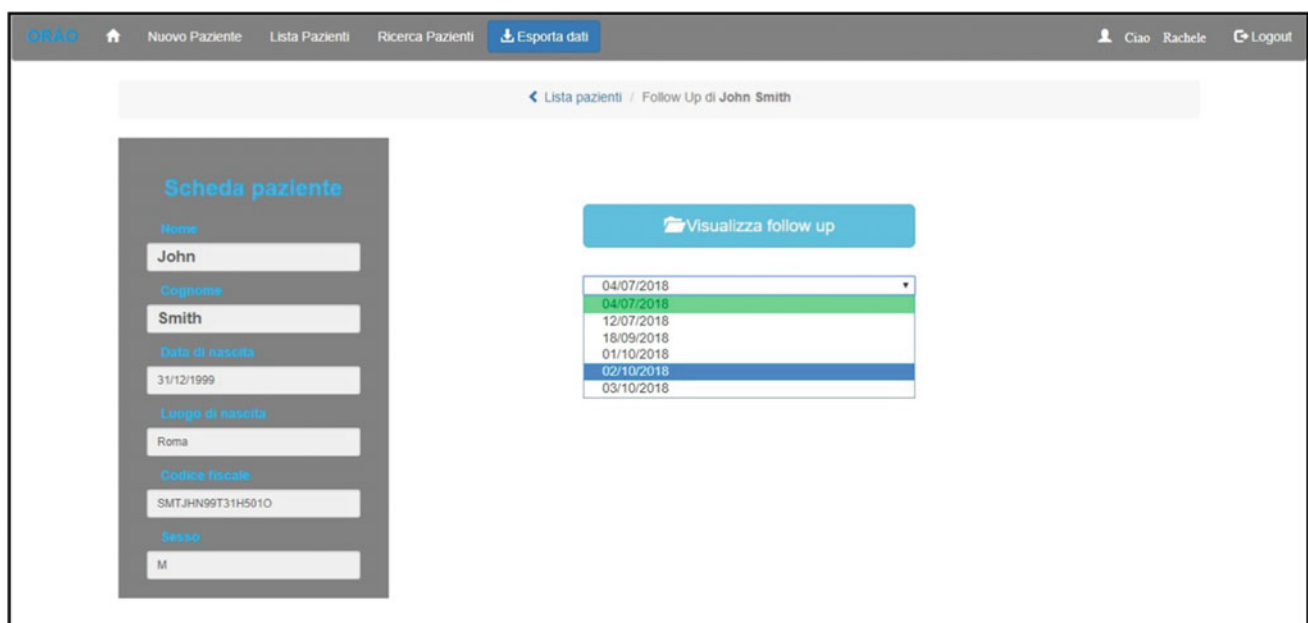


Fig. 4 Example of the list of follow-ups registered for the selected patient. It is possible to notice the difference between consolidated and editable follow-up dates

There are two types of examinations: binocular and monocular examinations. In the monocular examinations interface, input fields are layered on two columns. The right column's input fields are intended to collect data about left eye. As it is possible to see in Fig. 5, on the upper level of the column it is clearly indicated the corresponding eye (right and left). This is the typical approach used by

ophthalmologists and it is also adopted here as a mean for risk reduction. Monocular examinations can be clinical and instrumental. For binocular examinations (see Fig. 6), anamnesis, binocular investigation and genetic report can be saved inside each follow-up.

Both monocular and binocular views have on the left side a menu containing personal data of the patient being

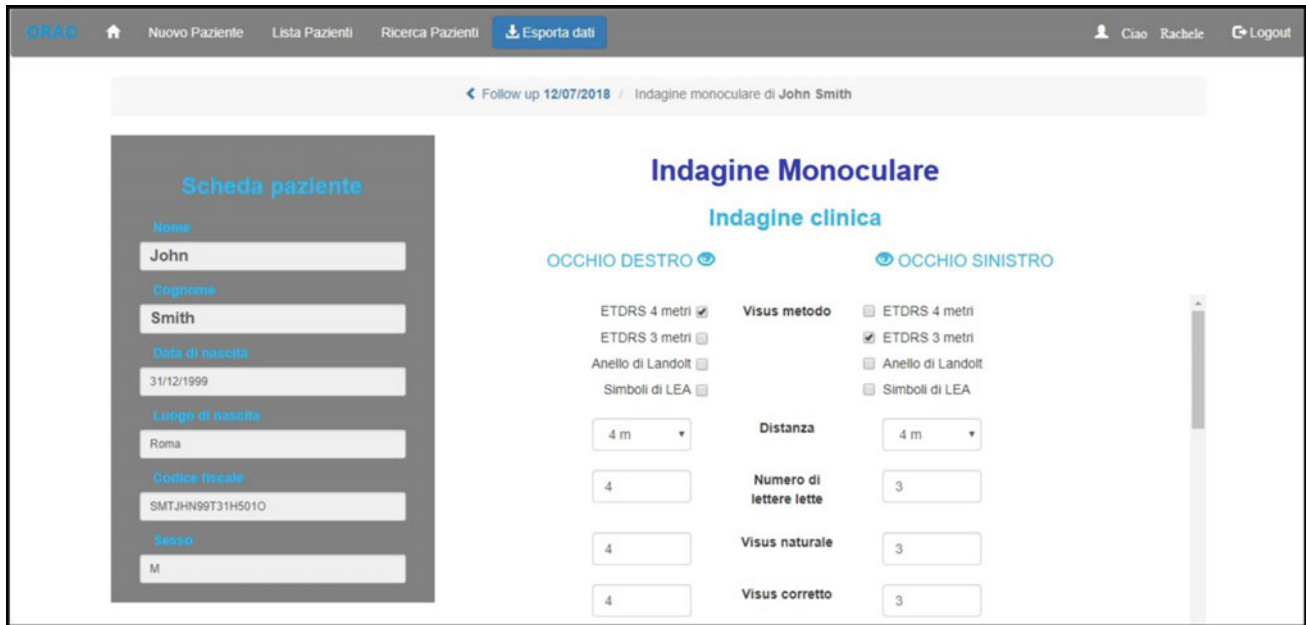


Fig. 5 Example of the interface of a monocular examination page

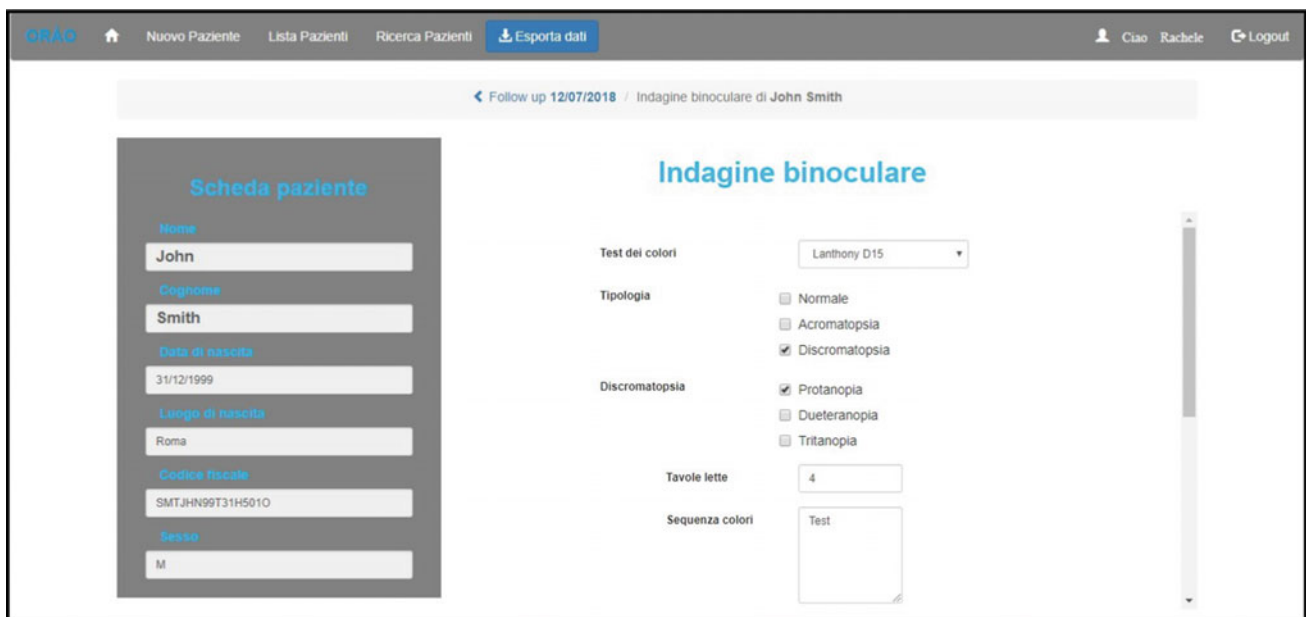


Fig. 6 Example of the interface of a binocular examination page

examined. Furthermore, on the top of the examination form the follow-up date is shown and patient’s name and last name are repeated and highlighted.

Pupillometry interface The pupillometry interface (see Fig. 7) has been designed to properly show the pupil diameter response to each stimulus, as stated by the pupillometric protocol. In this page, users are requested to upload the .DAT file containing the pupillometric output of the examined patient. Then the file is read and data are

elaborated in order to present clinical information in a way that is suitable to physicians’ studies. Users must also choose the index of the stimulus they need to view.

Afterwards, the graphic of the right and left pupil stimulus response is shown as a function of time. Moreover a table containing parameters of interest, measured during the stimulation, is provided. Moving the mouse pointer over the graphic, the user is able to read both the right and left pupil diameter values. Furthermore, a summary of technical

Pupillometria

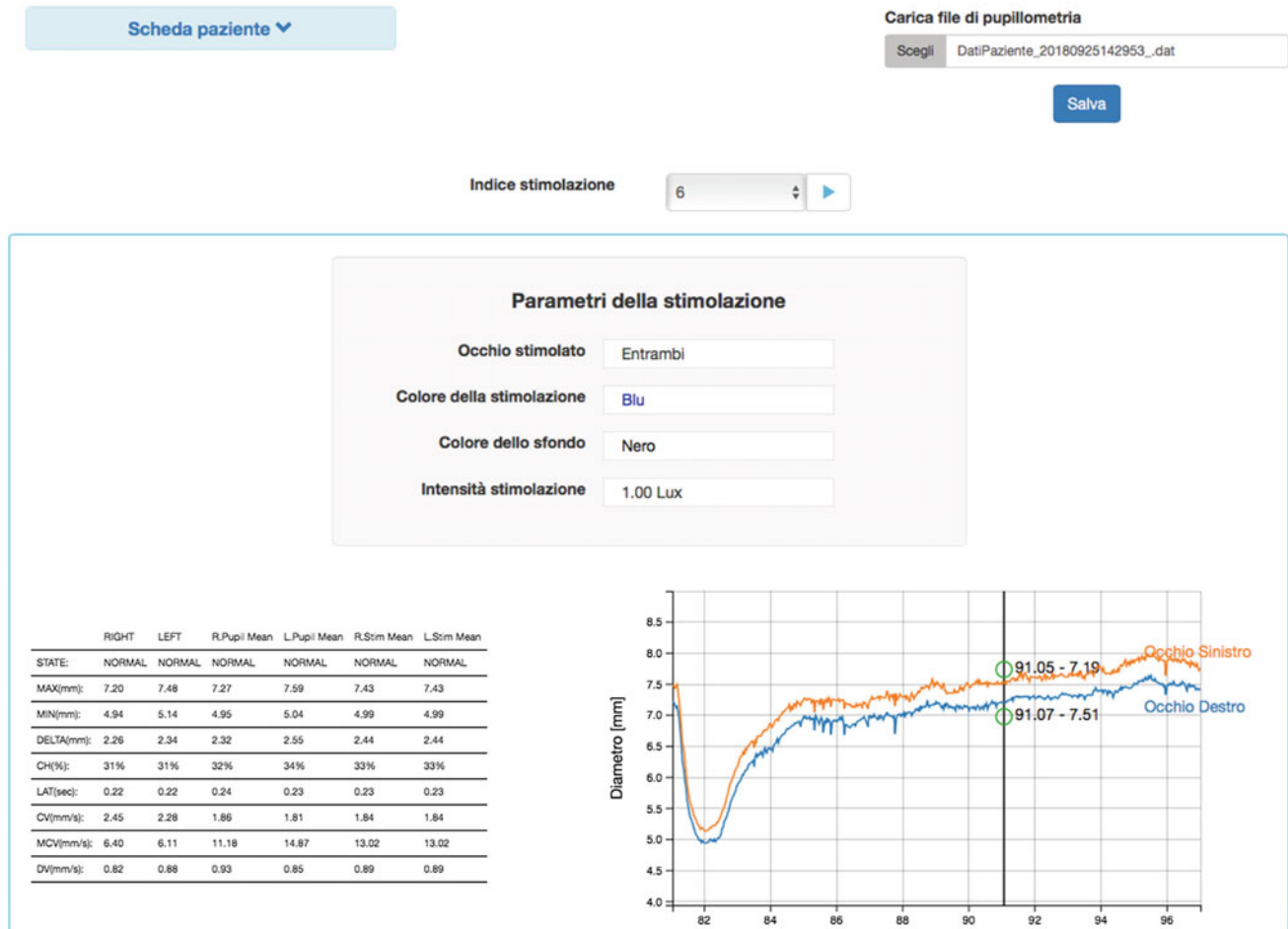


Fig. 7 Pupillometry page: the graphic of pupil diameter time trend and the table with the parameters measured during the stimulations

characteristics for every stimulus is shown: stimulated eye (right, left or both), stimulus color, light intensity and background color.

Pupillometric data elaboration In the .DAT file of the pupillometer, there are two sections data are read from. In one section all the acquired values are collected together, belonging to the various stimulations expected by the pupillometric protocol; in the other section, every stimulus index (from 0 to 19) is associated to the first and last sample acquisition index (see Fig. 8).

1. The user uploads the .DAT file he/she wants to study and chooses the stimulus index (from 1 to 20) from a menu in the pupillometry interface (see Fig. 9).
2. The index chosen by the user is read from the interface (client-side) and used to extract the corresponding first and last sample numbers from the .DAT file (server-side).

3. Once the first and last sample numbers are identified, all the values in between are stored inside a matrix. They correspond to time, right and left pupil diameter acquired by the pupillometer during the stimulation.
4. The matrix is elaborated thanks to the JS library D3⁴ (Data Driven Document). The D3 library allows to create the final graph presented in the pupillometry application interface.

In the x-axis, time is measured in seconds while diameters values are expressed in millimetres. Dynamic labels have been created with D3 aiming to make the graph as readable as possible: while user moves the mouse pointer over the figure, punctual values of right and left pupil diameter are shown.

⁴<https://d3js.org>.

```

<RIGHT-PUPIL-ANALYSIS>
20
0 0 34 513 2 1 1.000000
1 0 514 993 2 1 17.000000
2 0 994 1474 2 1 33.000000
3 1 1475 1954 2 1 49.000000
4 1 1955 2434 2 1 65.000000
5 1 2435 2915 2 1 81.000000
6 2 2916 3845 2 1 97.000999
7 2 3846 4776 2 1 128.000992
8 2 4777 5706 2 1 159.000992
9 3 5707 6637 2 1 190.000992
10 3 6638 7567 2 1 221.000992
11 3 7568 8498 2 1 252.000992
12 4 8499 9398 2 1 283.001007
13 5 14803 15732 2 1 493.002014
14 5 15733 16663 2 1 524.002014
15 5 16664 17593 2 1 555.002014
16 6 17594 18524 2 1 586.002014
17 6 18525 19454 2 1 617.002014
18 6 19455 20385 2 1 648.002014
19 7 20386 21285 2 1 679.002014
<\RIGHT-PUPIL-ANALYSIS>
    
```

Fig. 8 Figure shows how every stimulus index is associated to the corresponding start and end sample in the .DAT file, output of the DP-2000 pupillometer. The first column contains stimulus indexes, while the third and fourth columns collect respectively the first and last acquisition index

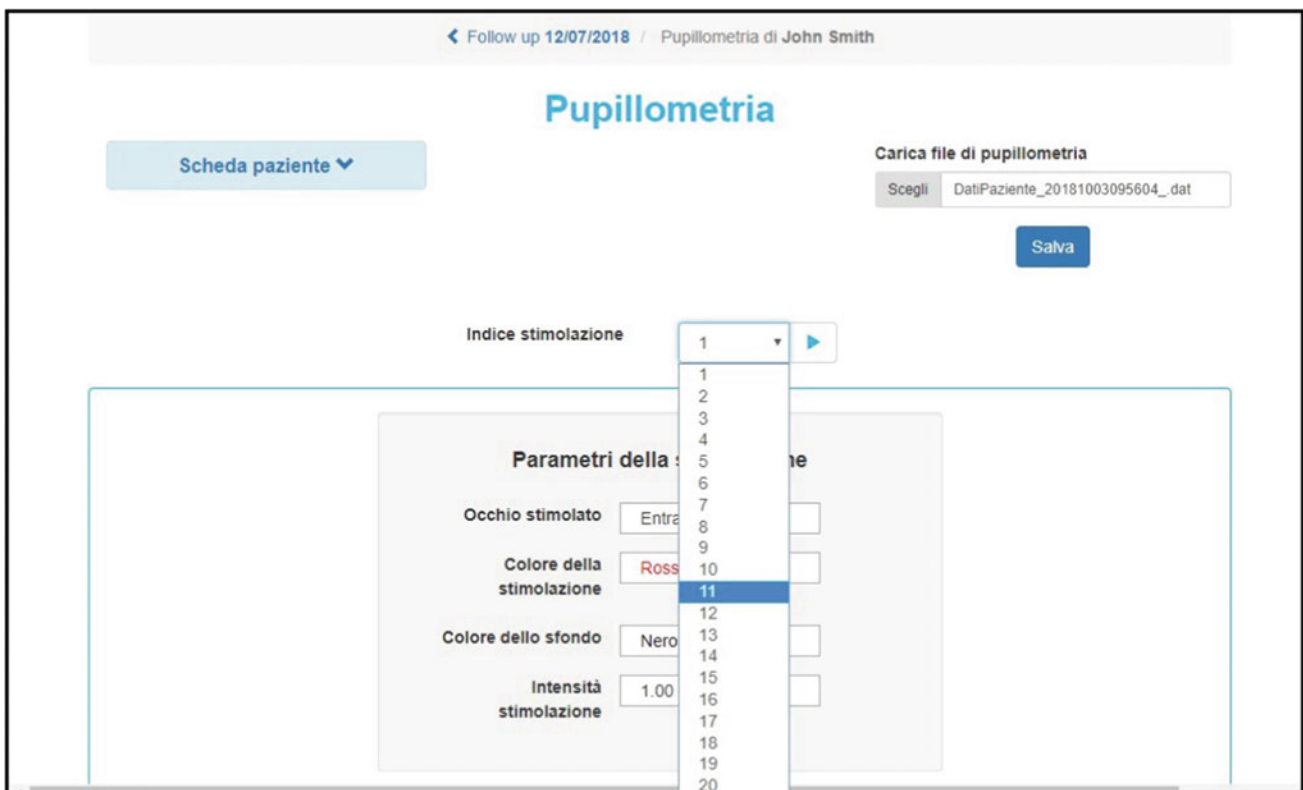


Fig. 9 Figure shows how user is expected to choose stimulus index from the drop down menu in the interface

4 Discussion

In this paper, ORÁO, a cloud-based EMR for ophthalmologic examinations, has been presented. It has been designed to match the characteristics of the pupillometric protocol as well as the specifications given by the physicians involved in the pilot study. High attention has been given to the usability of interfaces, introducing elements and redundancies with the aim of reducing safety issues, originated by the use of the platform.

As described above, in the top area of all the platform web pages a menu providing direct links both to the previous page and to the current page is displayed.

This element is very important to provide the end-user with a full awareness of the selected functionality during his/her navigation through the platform. It also facilitates a better understanding of the EMR structure.

Since the purpose of EMR is to collect clinical patient data, the main safety issues deal with the possibility to make mistakes while saving data. If this should happen, the physician could make a diagnosis mistake of false-positives or false negatives because of wrong saved data, or data attributed to a wrong patient. Some elements have been introduced in the interface of ORÁO to avoid this scenario. For example, the above mentioned personal data menu which appears on the left side of the examinations form, together with the bold patient name and last name in the top side of the examinations pages, aim to provide the end user with the awareness of the selected patient during the whole process. For the same reasons, the follow-up date is always shown next to the patient name and last name in the upper menu.

In the follow-up page, users must choose the date of the follow-up they want to open. Follow-ups may be consolidated, as stated above, or editable. The user is able to distinguish these two types from the menu containing the dates, thanks to the different background color. Green corresponds to a consolidated one, while white means that edits are allowed. Other elements that contribute to make the interface as usable as possible are the feedback messages. When the user performs an incorrect action, which could possibly have

irreversible consequences, a message is shown informing about the danger. The messages are as clear as possible, written in the user language to make them widely understandable. The issues concerning data storage on the web, such as safety and privacy, have not been addressed yet because the clinical study is in a preliminary phase. The appropriate measures will be taken as soon as possible, during the next evolution of the pilot study.

Acknowledgements We would like to thank professor Paolo Nesi and his Distributed Systems and Internet Technologies Lab (DISIT) for their support in providing the cloud infrastructure. The authors declare that they have no conflict of interest.

References

1. Melillo, P., et al.: Toward a novel medical device based on chromatic pupillometry for screening and monitoring of inherited ocular disease: a pilot study. In: IFMBE Proceedings, vol. 68/3, pp. 387–390. Springer (2019)
2. Guidi, G., Pettenati, M.C., Miniati, R., Iadanza, E.: Heart failure analysis dashboard for patient's remote monitoring combining multiple artificial intelligence technologies. In: Proceedings of the Annual International Conference of the IEEE Engineering in Medicine and Biology Society, EMBS, art. no. 6346401, pp. 2210–2213 (2012)
3. Guidi, G., Melillo, P., Pettenati, M.C., Milli, M., Iadanza, E.: Performance assessment of a clinical decision support system for analysis of heart failure. In: XIII Mediterranean Conference on Medical and Biological Engineering and Computing 2013. IFMBE Proceedings, vol. 41, pp. 1354–1357. Springer (2014)
4. Bianchi, L., Paganelli, F., Pettenati, M.C., Turchi, S., Ciofi, L., Iadanza, E., Giuli, D.: Design of a RESTful Web information system for drug prescription and administration. IEEE J. Biomed. Health Inform. 1–11 (2013)
5. W. ISO. 9241—Part 11: Ergonomics of Human-System Interaction. Usability: Definitions and Concepts. Technical Report, International Organization for Standardization (Mar 2018)
6. IEC/ISO. IEC 62366-1: 2015 Medical Devices—Part 1: Application of Usability Engineering to Medical Devices (2015)
7. Zahabi, M., Kaber, D.B., Swangnetr, M.: Usability and safety in electronic medical records interface design: a review of recent literature and guideline formulation. Hum. Factors 57(5), 805–834 (2015)

A Language Independent Decision Support System for Diagnosis and Treatment by Using Natural Language Processing Techniques

Merve Kevser Gökgöl and Zeynep Orhan

Abstract

Global mobility including all countries in the world, is growing at a rate faster than the world's population, which is surpassed 244 million people in 2015. The explosive growth in the importance, interest and the study of international migration urges new developments for accessible, efficient and affordable global public health systems. In order to actualize such improvements and eliminate the undesirable consequences of wrong or late diagnosis in global public healthcare, we propose an intelligent healthcare diagnostics engine. Current diagnosis systems have obstacles about easy user access by worldwide health seekers. In this study, it is aimed to reach patients using different languages while providing an opportunity to enter symptoms in their everyday language text, besides medical expressions of symptoms. Language independency is provided on the background of user interface by using translate functions in TextBlob, python. Named entity recognition (NER) techniques, based on natural language processing (NLP), are applied to develop language independent predictive model. Extracted terms are implied as an input of the model and analyzed for degree of matching symptoms for the corresponding diagnosis. The accuracy at a range of 20 and 100% has been accomplished based on the degree of matching of patient's enquiry with database of the system, for languages other than English.

Keywords

Global public healthcare • Natural language processing • Text matching • Medical diagnosis

M. K. Gökgöl (✉)

Department of Information Technologies, International Burch University, Sarajevo, Bosnia and Herzegovina
e-mail: mervekevser@gmail.com

Richmond Park International Secondary School, Sarajevo, Bosnia and Herzegovina

Z. Orhan

Istanbul, Turkey
e-mail: zorhan@gmail.com

1 Introduction

Access to health services is one of the basic human rights for everyone, regardless of nation, ethnicity or any other personal specifications. The World Health Assembly Resolutions (61.17 and 70.15) urge the member states to consider promoting and developing the globally accessible systems [1]. International migration in the world, is growing faster than the world's population rate. In all countries human mobilization is over 244 million people according to data recorded in 2015 [2]. In order to approach developments of global healthcare systems online healthcare systems should be affordable and accessible by everyone. The United Nations (UN)-led networks offered potential to address global health vulnerability, however, such networks have generally lacked adequate financing, enforcement and reporting mechanisms [2].

In the United States (U.S.), some group of investigators developed web-based communication and disease management system that provides clinical information and facilities between patients with asthma and their providers, while another group of researchers working on immediate information exchange system in case of emergency situations [3]. Furthermore, the Integrated Delivery System Research Network (IDSRN) was developed in the U.S. in cooperation with a network of nine partners that encompass a wide variety of healthcare organizational settings to more than 55 million people [3]. However, current studies do not offer an access to quality, effective and affordable healthcare services for global healthcare seekers, regardless of user language.

The simple medical and health aspects of providing health prevention, promotion and treatment services may be complicated by cultural, social and linguistic factors that are different from those in the host populations. The potential of information technology in medical diagnostics is still in the process of being actualized.

Natural Language Processing (NLP) systems have a potential to ease access to coded data by providing a solution where clinical information is automatically extracted and analyzed. The information is then accessed reliably for different applications such as decision support systems, quality assurance, literature search and outcome analysis. NLP based systems can provide a complete, easy to review, summary of all information available to the patient while giving alerts about the possible risks.

Healthcare data is massive, since it includes patient centric data, resource management data and transformed data. Treatment records of millions of patients can be stored and computerized. Therefore, NLP techniques helps us in answering several important and critical questions in healthcare. Some of the questions are: Is current clinical diagnostic systems are available in wide-range use? How efficiently contributing current methods to clinical decision support at the point of detection and care? In this study we proposed satisfying answers for these questions and more.

A human interpreter must translate and dissect the greater part of the components inside the content and see how each word may impact the setting of the content. This requires broad ability in sentence structure, syntax (sentence structure), semantics (implications), in the source and target dialects, and additionally skill in the space. Human and Machine Translation each have their offer of limitations and difficulties. For instance, no two individual interpreters will create indistinguishable interpretations of a similar content in a similar syntax match, and it might take a few rounds of updates to meet the user's prerequisites.

In this study, Python is used to enable the data powerfully and to obtain quick, efficient, qualitative and accurate solutions. Another reason why Python is preferred for this study is, its sentence structure and semantics are straightforward, and it has great string taking care of usefulness.

In order to extract information from the corresponding data set input text should be preprocessed. Text preprocessing is the process of converting a well-defined text corpus into its component words and sentences. While word segmentation breaks up the sequence of characters in a text by locating the word boundaries, the points where one word ends and another begins [4].

This process of information extraction (IE), turns the unstructured information embedded in texts into structured data, for example for populating a relational database to enable further processing [5]. The initial phase in most IE assignments is to locate the best possible names or named entities specified in a content. The undertaking of named entity recognition (NER) is to discover each specify of a named element in the content and mark its' compose. What constitutes a named entity type is application specific; these commonly include people, places, and organizations but also

more specific entities from the names of genes and proteins [6] to the names of college courses.

2 Clinical Decision Making

Clinical decision support systems (CDSSs) have significance in order to reduce medical errors and increase health care quality, efficiency and patient satisfaction. Studies have shown that well executed clinical decision system (CDS) can reduce adverse events from drug-drug interactions [7, 8] and medication errors [9]; decrease unnecessary laboratory testing [10] cardiovascular risk in patients with type 2 diabetes [11]; improve practitioner performance [12]; improve public health outcomes associated with outbreaks of foodborne illness [13] and produce cost savings associated with hospital-based pharmacy interventions [14]. When it comes to deploying a web-based system, standards will be essential for success on a large scale and in addition to enabling scale and spread across multiple technology platforms, standards are necessary to create systems that are sustainable, maintainable, and updatable which will also reduce the maintenance costs [15].

3 Named Entity Recognition (NER) and Symptom extraction methods

There are numerous studies in recent years that have successfully accumulated rapidly to incorporate a large amount of unstructured data in various biomedical natural language processing problems.

Even sophisticated NLP systems are built on the foundation of recognizing words or phrases as medical terms that represent the domain concepts (named entity recognition) and understanding the relations between the identified concepts [16]. Preparing of clinical data frequently begins with spelling diagnosis and setting particular extension of shortened forms.

NER capable to identify predefined entities as well as the domain of entities or the entity types from informal texts [17]. For general entities several NLP studies, such as assigning entities to relevant Wikipedia abstracts or corresponding nodes in knowledge base, have been performed [18]. In biomedical studies, NER is challenging because many biological and medical terms, such as names of symptoms or names of plants, have multiple synonyms and they are often referred by using abbreviations [19]. To resolve these ambiguities, several NER and standardization-normalization studies have been led for a few biological entities (symptoms, diseases and disorders) and chemical entities (drugs and compounds) [20]. Although machine

learning (ML) approaches have been used for normalization, most normalization tools rely on the accuracy of domain-specific dictionary rules [21]. MetaMap was developed to improve the retrieval of relevant MEDLINE citations [22]. This program maps biological elements to idea identifiers in the Unified Medical Language System (UMLS) Metathesaurus [23]. On the other hand, DNorm [24], utilizes pairwise figuring out how to standardize-normalize disease names; it appoints in the content to appropriate disease names in a controlled vocabulary, where a mention and a concept name are referred as a vector.

3.1 Syntactic and Semantic Similarity

Syntax similarity is a measure of the degree to which the word sets of two given sentences are similar. A similar of 1% (or 100%) would mean a total overlap between vocabularies, whereas 0 means there is no common words.

For extended texts, specific NLP applications of semantic analysis may include information retrieval, IE, text summarization, data-mining, and machine translation and translation aids [4]. Semantic analysis is also pertinent for much shorter texts, right down to the single word level, for example, in understanding user queries and matching user requirements to available data.

4 Methodology

In this section the sources of the data that were used in this task is defined, the preprocessing steps we have performed on the data, the format of the data and the method that was used for evaluating the participating systems are analyzed.

This research was designed to develop a broad, comprehensive, robust, open-source NLP system to extract and process semantically viable information to support the heterogeneous clinical domain. The research was based on extracting symptoms entered to the system by patient using NER method of NLP.

At first, in order to prepare the data for preprocessing, patient's entry text is divided into sentences. Similarity score is computed for every pair of sentences in the texts and filled into a similarity matrix.

4.1 Data Collection and the Structure of the Data

We have considered two sources for disease data. Mayo Clinic website [25] contains highly detailed information about diseases: Disease overview, symptoms, when to see a

doctor, causes, risk factors, complications and so on. The second data we collected is AZ Symptoms website's data [26]. In the second source, disease definitions, symptoms, causes, prevention, risk factors and complications information are included for 120+ diseases. The main reason why we use this dataset is, symptom information is more likely to match an average person's daily language when explaining the sickness. Sample set of symptoms for eye cancer: bleeding eyes, brown or black spot on the white or iris of the eye, protruding eyes.

Each symptom and other data valued words including severity, duration, location, cause, accompanied by any other symptoms, change in intensity are also extracted from written expression (as an individual expression or sentence structure of symptoms) accordingly. Structure of collected data categorized in four main branches; symptoms, diseases, tests (medical examinations) and corresponding treatments as described in Table 1.

Once tables are created symptoms are analyzed as input and they are trained by the process to detect possible diagnoses, tests and treatments. Disease data table as indicated in Table 2 consists of ID, Name, Description, Symptoms ID, Tests ID, Treatments ID, Risks, Causes, Preventions and Complications. Data content of symptoms, tests and treatments are represented with numerical values in different databases and they are embedded to system to analyze strength of the relationship.

As indicated in Table 3 symptoms are identified by ID value, name, locations (neck, knee, eye, low back), level of the symptom which is also indicated with numerical values (sharp, low, high, sudden, mild, etc,...) and causes, and possible conditions for a patient to visit the doctor.

A Table of tests (medical examinations) which is given in Table 4, describes details about essential examinations' ID, name, definition, why it is required (why is done), preparation, expectation, risks and results.

Recommended treatments for the most related symptoms are demonstrated in Table 5. Treatments are classified with their ID numbers, names and definitions.

4.2 Implementation

Using the corresponding data sets Python is used to develop the most efficient and appropriate model. TextBlob [27] is a python library used for input and output processing, and for string matching which actually classifies input symptoms as a disease. Two sets are used for classification, one including only symptoms, and the other the matching diseases. Details about diseases such as treatments and tests are recommended, are stored in MySQL [28] database.

Disease symptoms are preprocessed and saved as a variable. These steps are both applied to the disease dataset

Table 1 General structure of database table

Symptoms	Diseases	Tests	Treatments
ID	ID	ID	ID
Name	Name	Name	Name
Location ID	Description	Definition	Definition
Level ID	Symptoms ID	Why_is_done	
Causes	Test ID	Preparation	
See_doctor	Treatment ID	Expectation	
	Risks	Risks	
	Causes	Results	
	Prevention		
	Complications		
	Gender		
	Age		

Table 2 A sample disease table in database

ID	24
Name	Leukemia
Description	Leukemia is cancer of the body's blood-forming tissues, including the bone marrow and the lymphatic system
Symptoms ID	21,69,114,119,133,168,173,0,0,0,0,0,0
Test ID	8,94,104
Treatment ID	113,114,115,116,117
Risks	Factors that may increase your risk of developing some types of leukemia include: Previous cancer treatment. People who've had certain types of chemotherapy and radiation therapy for other cancers have an increased risk of developing certain types of leukemia Genetic disorders. Genetic abnormalities seem to play a role in the development of leukemia. Certain genetic disorders, such as Down syndrome, are associated with an increased risk of leukemia Exposure to certain chemicals. Exposure to certain chemicals, such as Benzene which is found in gasoline and is used by the chemical industry, also is linked to an increased risk of some kinds of leukemia Smoking. Smoking cigarettes increases the risk of acute myelogenous leukemia. Family history of leukemia. If members of your family have been diagnosed with leukemia, your risk for the disease may be increased
Causes	Scientists don't understand the exact causes of leukemia. It seems to develop from a combination of genetic and environmental factors
Prevention	None
Complications	None
Gender	Not gender restricted
Age	Not age restricted

and user text. Semantic similarity between user symptoms and symptom dataset is analyzed. Additional to semantic similarity checking, the syntax of the query is also significant to estimate similarity with disease symptoms, therefore, each query is syntactically compared with disease symptoms. For this purpose, FuzzyWuzzy [29] library's string similarity function is used. Fuzzy string matching uses Levenshtein Distance to calculate the differences between

sequences. Mathematically, the Levenshtein distance between two strings a , b (of length $|a|$ and $|b|$ respectively) is given by $\text{lev}_{a,b}(|a|,|b|)$ where

$$\text{lev}_{a,b}(i,j) = \begin{cases} \max(i,j) & \text{if } \min(i,j) = 0 \\ \min \begin{cases} \text{lev}_{a,b}(i-1,j) + 1 \\ \text{lev}_{a,b}(i,j-1) + 1 \\ \text{lev}_{a,b}(i-1,j-1) + 1_{(a_i \neq b_j)} \end{cases} & \text{otherwise.} \end{cases} \quad (1)$$

Table 3 A sample table of symptoms in database

ID	3
Name	Abdominal pain
Location ID	Stomachache, tummy ache, gut ache and bellyache
Level ID	49,9
Causes	Abdominal pain that steadily worsens over time, often accompanied by the development of other symptoms, is usually serious. Causes of progressive abdominal pain include: Cancer, Crohn's disease, Enlarged spleen (splenomegaly). Gallbladder cancer, Hepatitis (liver inflammation), Kidney cancer. Lead poisoning, Liver cancer, Non-Hodgkin s lymphoma, Pancreatic cancer. Stomach cancer, Tubo-ovarian abscess (pus-filled pocket involving a fallopian tube and an ovary). Uremia (buildup of waste products in your blood)
See_doctor	Have someone drive you to urgent care or the emergency room if you have: severe pain, fever, bloody stools, persistent nausea and vomiting, weight loss, skin that appears yellow. Severe tenderness when you touch your abdomen, swelling of the abdomen

Table 4 A sample from test table in database

ID	5
Name	Bilirubin test
Definition	Bilirubin testing checks for levels of bilirubin in your blood
Why is done	Bilirubin testing is usually done as part of a group of tests to check the health of your liver. Bilirubin testing may be done to: Investigate jaundice, elevated levels of bilirubin can cause yellowing of your skin and the whites of your eyes (jaundice). A common use of the test is to measure bilirubin levels in newborns, determine whether there might be blockage in your liver's bile ducts, help detect or monitor the progression of other liver disease, such as hepatitis, help detect increased destruction of red blood cells, help follow how a treatment is working, help evaluate suspected drug toxicity
Preparation	None
Expectation	Bilirubin testing is done using a blood sample. Usually, the blood is drawn through a small needle inserted into a vein in the bend of your arm. The needle is attached to a small tube, in which your blood is collected. You may feel a quick pain as the needle is inserted into your arm and experience some short-term discomfort at the site after the needle is removed
Risks	None
Results	Normal results for a bilirubin test are 1.2 milligrams per deciliter (mg/dL) of total bilirubin for adults, and usually 1 mg/dL for those under 18. Normal results for direct bilirubin are generally 0.3 mg/dL

Table 5 A sample table of treatments in database

ID	1
Name	Open abdominal surgery
Definition	If you have an abdominal aortic aneurysm, surgery is generally recommended if your aneurysm is about 1.9–2.2 in. (about 5–5.5 cm) or larger. Open abdominal surgery to repair an abdominal aortic aneurysm involves removing the damaged section of the aorta and replacing it with a synthetic tube (graft), which is sewn into place. This procedure requires open abdominal surgery, and it will generally take you a month or more to fully recover

where $1 (a_i \neq b_j)$ is the indicator function equal to 0 when $a_i = b_j$ and equal to 1 otherwise, and $lev_{a,b} (i, j)$ is the distance between the first i characters of a and the first characters of b . This function (Eq. 1) provides a similarity score in range 0 and 100, that denotes two strings are equal by similarity index.

Following step is the matching obtained symptoms with diseases. In this phase, each user symptom has a similarity

score for each symptom in all diseases. Top N results with highest similarities are chosen from this list. The final N results are finally matched with diseases. According to these results, matched diseases are ordered in terms of the percentage of matched symptoms in disease's symptoms. TestsIDs for the predicted disease are processed and details of pre-established connections are represented in the language of input. Figure 1 summarizes each step of application.

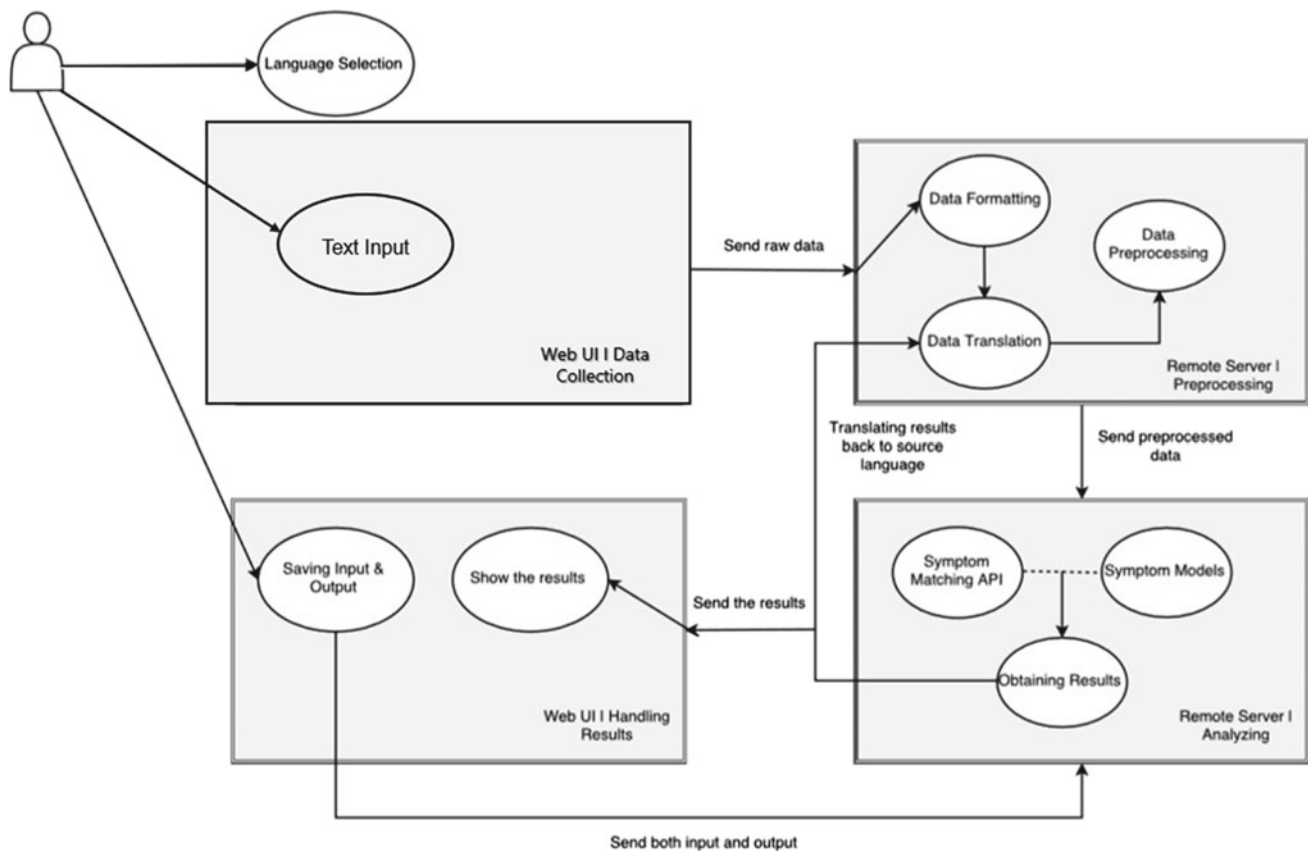


Fig. 1 Diagram representation of a Language Independent Healthcare Decision Support System (LI-HDSS)

After the training process, the system is tested for various diagnoses and patients, then the percentage risk of possible disease is indicated in output information. Corresponding to this, treatments and recommendations (any medical examinations, tests) are driven.

5 Results and Conclusion

A comprehensive database including 4280 different symptoms and the corresponding 880 diseases are processed in the implementation. If a disease has 10 symptoms and 5 symptoms from that disease match with the user symptoms, that disease is predicted with 5/10 means 50% confidence. From highest to lowest, predicted diseases are printed on the screen with matched symptoms made bold as shown in Table 6. In order to exclude irrelevant results, a minimum threshold of 20% is set. After testing and comparing results with the database of Mayo Clinic [25] and AZ symptoms [26] database the LIHDSS has been accomplished the accuracy at a range of 20 and 100% depending on degree of matching of patient's enquiry with dataset of the system. Possible output value is ranked according to number of matching symptoms. A sample user enquiry provided in

Table 6 represents two possible decisions in the expected range of accuracy. First result is given with 75%, which states 3 matched symptoms out of 4 while second possible result is given by 35% with 1 matching symptom.

A Language Independent Healthcare Decision Support System (LI-HDSS) is developed to convert the clinical data into significant and effective information for global healthcare seekers. Different inputs are tested to assess the abilities supported by TextBlob [27] library. Output is based on the result obtained FuzzyWuzzy [29] library regardless of some spelling mistakes that user might have done while giving the input. The project may provide a significant help in clinical decision process which gives effective results even with patients own words as symptoms. In order to achieve this, the behavior of different classifiers is tested in the context of the problem. NER techniques, based on NLP, are applied to develop language independent predictive model. The impact of outcomes, assessing performance in reduction of time from diagnosis to treatments, improves the quality of public healthcare and reduce the cost due to prevention of misdiagnosis. Due to the rapid change and growth in Healthcare decision support system, it is possible to say that we work on a quite dynamic system. In order to obtain better prediction, symptom database might be updated frequently by adding

Table 6 A sample user input and result

<p>Jason</p> <hr/> <p>User input: Ağır öksürüyorum. Farklı bir renkte balgam var. Sürekli yorgunum. Ateşim var. Bazen titreme geliyor. Göğsümde ağrı var</p> <p>Results:</p> <ul style="list-style-type: none"> • Acute bronchitis: % 75 Matched symptoms: <ul style="list-style-type: none"> – Persistent, deep cough that can produce yellowish, green, or gray sputum – Fever – Pain in the chest aggravated by a cough Other symptoms: <ul style="list-style-type: none"> – Wheezing or becoming short of breath <hr/> <ul style="list-style-type: none"> • Frostbite: % 33 Matched symptoms: <ul style="list-style-type: none"> – Bluish gray or white skin that feels hard, cold and numb Other symptoms: <ul style="list-style-type: none"> – Numbness and prickling sensation – Swollen, painful, blistered and red skin
--

more possible symptoms, diseases, tests and treatments. Further contribution of this study is to develop an online or offline diagnostic engine which will provide as accurate classification as possible regardless of spelling mistakes. LI-HDSS provides more accurate result with higher degree of matching, if patient's enquiry is provided more detailed.

References

1. UN-General Assembly 71st session, 63rd plenary meeting, official records. **63**, 1–25 (2016)
2. World Health Organization, UN Migration Agency: Report of the 2nd global consultation on migrant health. Heal. Migrants (2017)
3. Ortiz, E., Clancy, C.M.: AHRQ update use of information technology to improve the quality of healthcare in the United States (2001)
4. Klein, E., Loper, E.: Natural Language Processing With Python (2009 Jan)
5. Indurkha, N., Damerou, F.J.: Handbook of Natural Language Processing (2010)
6. Martin, J.H., Jurafsky, D.: Speech and language processing: an introduction to natural language processing, computational linguistics, and speech recognition. *Comput. Linguist.* **26**(4), 638–641 (2017). University of Colorado, Boulder. Prentice Hall, Upper Saddle River, NJ
7. Smithburger, P.L., Buckley, M.S., Bejian, S., Burenheide, K., Kane-Gill, S.L.: A critical evaluation of clinical decision support for the detection of drug-drug interactions. *Expert Opin. Drug Saf.* **10**(6), 871–882 (2011)
8. Sönnichsen, A., Trampisch, U.S., Rieckert, A., Piccoliori, G., Vögele, A., Flamm, M., Johansson, T., Esmail, A., Reeves, D., Löffler, C.: Polypharmacy in chronic diseases-reduction of inappropriate medication and adverse drug events in older populations by electronic decision support (PRIMA-eDS): study protocol for a randomized controlled trial. *Trials* **17**(1), 57 (2016)
9. Fritz, D., Ceschi, A., Curkovic, I., Huber, M., Egbring, M., Kullak-Ublick, G.A., Russmann, S.: Comparative evaluation of three clinical decision support systems: prospective screening for medication errors in 100 medical inpatients. *Eur. J. Clin. Pharmacol.* **68**(8), 1209–1219 (2012)
10. Felcher, A.H., Gold, R., Mosen, D.M., Stoneburner, A.B.: Decrease in unnecessary vitamin d testing using clinical decision support tools: making it harder to do the wrong thing. *J. Am. Med. Inf. Assoc.* **24**(4), 776–780 (2017)
11. Cleveringa, F.G., Gorter, K.J., van den Donk, M., Rutten, G.E.: Combined task delegation, computerized decision support, and feedback improve cardiovascular risk for type 2 diabetic patients: a cluster randomized trial in primary care. *Diabet. Care* **31**(12), 2273–2275 (2008)
12. Garg, A.X., Adhikari, N.K., McDonald, H., Rosas-Arellano, M.P., Devereaux, P.J., Beyene, J., Sam, J., Haynes, R.B.: Effects of computerized clinical decision support systems on practitioner performance and patient outcomes: a systematic review. *JAMA* **293**(10), 1223–1238 (2005)

13. Wu, W.Y., Hripcsak, G., Lurio, J., Pichardo, M., Berg, R., Buck, M.D., Morrison, F.P., Kitson, K., Calman, N., Mostashari, F.: Impact of integrating public health clinical decision support alerts into electronic health records on testing for gastrointestinal illness. *J. Public Health Manag. Pract.* **18**(3), 224–227 (2012)
14. Calloway, S., Akilo, H.A., Bierman, K.: Impact of a clinical decision support system on pharmacy clinical interventions, documentation efforts, and costs. *Hosp. Pharm.* **48**(9), 744–752 (2013)
15. Tcheng, J.E., et al.: CLINICAL DECISION Summary of a Meeting Series. National Academy of Medicine (U.S.), Washington (2017)
16. Cohen, P.R., Perrault, C.R.: Elements of a plan-based theory of speech acts. *Cogn. Sci.* **3**(3), 2177–2212 (1979)
17. Demner-Fushman, D., Chapman, W.W., McDonald, C.J.: What can natural language processing do for clinical decision support? *J. Biomed. Inf.* **42**(5), 760–772 (2009)
18. Kawamoto, K.: Improving clinical practice using clinical decision support systems: a systematic review of trials to identify features critical to success. *BMJ* **330**(7494), 765 (2005)
19. Hachey, B., Radford, W., Nothman, J., Honnibal, M., Curran, J.R.: Evaluating entity linking with wikipedia. *Artif. Intell.* **194**, 130–150 (2013)
20. Leaman, R., Khare, R., Lu, Z.: Challenges in clinical natural language processing for automated disorder normalization. *J. Biomed. Inform.* **57**, 28–37 (2015)
21. Rocktäschel, T., Weidlich, M., Leser, U.: Chemspot: a hybrid system for chemical named entity recognition. *Bioinformatics* **28**(12), 1633–1640 (2012)
22. Cho, H., Choi, W., Lee, H.: A method for named entity normalization in biomedical articles: application to diseases and plants. *BMC Bioinf.* **18**(1), 1–12 (2017)
23. Aronson, A.R.: Effective mapping of biomedical text to the UMLS Metathesaurus: the MetaMap program. *Proceedings. AMIA Symposium*, p. 17 (2001)
24. Leaman, R., Doğan, R.I., Lu, Z.: DNorm: disease name normalization with pairwise learning to rank. *Bioinformatics* **29**(22), 2909–2917 (2013)
25. Diseases and Conditions—disease and condition information from Mayo Clinic experts (n.d.). Retrieved October 10, 2018, from <https://www.mayoclinic.org/diseases-conditions/index>
26. Medical Symptoms. (n.d.). Retrieved October 10, 2018, from <http://www.azsymptoms.com/>
27. Loria, S.: TextBlob: simplified text processing (2018). Retrieved October 10, 2018, from <https://textblob.readthedocs.io/en/dev/>
28. MySQL (2018). Retrieved November 10, 2018, from <https://www.mysql.com/>
29. Seatgeek: Seatgeek/fuzzywuzzy (2018 Aug 20). Retrieved October 10, 2018, from <https://github.com/seatgeek/fuzzywuzzy>

Fabrication of Rectal and Vaginal Suppositories Using 3D Printed Moulds: The Challenge of Personalized Therapy

Sarah Krezić, Esved Krhan, Emir Mandžuka, Nikolina Kovač, Danira Krajina, Amina Marić, Sajra Komić, Azra Nikšić, Amina Tucak, Merima Sirbubalo, and Edina Vranić

Abstract

In this research, we aimed to combine three areas of science; pharmacy and bioengineering, as well as the small part of information technology, in an effort to solve the evergrowing problem of personalized drugs, in this case, suppositories. Various studies have shown that the person's preferences and adherence to medicine are influenced by the characteristics of the product, in the case of suppositories, mainly by shape. We have obtained all of the existing information regarding vaginal and rectal abnormalities, which we have incorporated into computer software, making it possible to suggest the most adequate and appropriate shape of suppositories for each patient. Considering the high price of personalized drugs and the emergence of new trends in bioengineering, we have come to the idea of including three-dimensional printing, which has recently had a breakthrough in these areas of science and also proved to be a very powerful new tool for future development in pharmaceuticals. We have managed to make different moulds for rectal and vaginal suppositories, despite the fact that there are no studies on the topic of three-dimensional printing of moulds for suppositories. We also created a software tool for predicting the optimal shape of the suppositories.

Keywords

Suppositories • Personalized medication • 3D-printing • Informational technologies

1 Introduction

Drugs can be administered in different forms, through different routes of application, and one of these is in the form of rectal and vaginal suppositories. This way of the application can be useful when other routes of administration are inadequate or unsuitable. Suppositories represent a solid pharmaceutical form which is used for drug delivery through vaginal and rectal routes of administration. They can be used either to achieve a local or systemic therapeutic effect. A large number of rectal suppositories are used for indications such as incontinence or topical relief, while vaginal suppositories are mostly used to treat vaginal yeast infections and bacterial vaginosis [1].

Bioprinting is a subcategory of additive manufacturing (AM), also known as three-dimensional (3D) printing. It is defined as the printing of structures using viable cells, bio-materials and biological molecules [2]. The AM process uses digital blueprints to deposit material, allowing for the incorporation of complex geometric features during building, including intricate internal structures that could not otherwise be created [3]. Within many discoveries in the pharmaceutical and biomedical market, three-dimensional printing (3DP) is believed to be the most revolutionary and powerful. It serves as a technology for the development of new dosage forms, tissue and organs engineering as well as disease modelling. The term three-dimensional printing was defined by International Standard Organization (ISO) as—fabrication of objects through the deposition of a material using a print head, a nozzle, or another printer technology [4]. The novel approaches in the formulation of solid dosage forms for individualized therapy are particularly focused and include transdermal drug delivery as well as biomedical applications of additive manufacturing techniques including drugs, implants, surgical models, bioprinted materials and biorobotics [5].

S. Krezić (✉) · E. Krhan · E. Mandžuka · N. Kovač · D. Krajina · A. Marić · S. Komić · A. Nikšić
Faculty of Pharmacy, University of Sarajevo, Zmaja od Bosne 8, 71000 Sarajevo, Bosnia and Herzegovina
e-mail: sarahkrezić@ffsa.unsa.ba

A. Tucak · M. Sirbubalo · E. Vranić
Department of Pharmaceutical Technology, Faculty of Pharmacy, University of Sarajevo, Zmaja od Bosne 8, 71000 Sarajevo, Bosnia and Herzegovina

Advantages of 3D printing are that the Active Pharmaceutical Ingredient (API) can be distributed in the dosage form as per requirement to achieve a defined release pattern. Complex and feasible geometries of the dosage form can be created for better efficiency. 3D printing helps to achieve formulations flexibility with complex release profiles. It encourages innovations in pharmaceuticals such as polypill and Fixed Dose Combination (FDC) with different and preset release behaviour of the individual drug. It creates opportunities for advancing in newer and better drug delivery. Additional advantages are cost efficiency, high yield, liberty in designing and manufacturing and also extended collaboration [6].

Taking into account the above, we consider that the use of 3D printing with the polylactic acid as basic material could be a new, more practical, affordable and economically acceptable way of preparing different solid pharmaceutical formulations, in our case specifically suppositories, for precise and more personalized drug delivery for particular patient categories,¹ including pediatric population, geriatric population and patients with certain specific diseases. One of the most used materials in 3D-printing of biomaterials is Polylactic Acid (PLA). The main reason supporting this fact is its ability to metabolize into non-toxic and non-carcinogenic degradation products. It can be metabolized and effectively excreted by the human body [8]. The process of making PLA material involves renewable sources such as starch and sugar cane. This fact makes it a better option in bioengineering, considering the fact that other plastic materials are nonrenewable and could be toxic for the human body.

2 Materials and Methods

2.1 Materials

PLA filament (Ultimaker, Netherlands) was used to fabricate the suppository moulds, while Witepsol H 15 (Farmadent, Slovenia) was used for suppositories formulation.

2.2 Design of Suppositories

The program used for the design of 3D printed moulds is named CURA or Solidworks to be more specific. This method represents the combination of Solidworks program

¹Personalized medicine refers to customization of medical treatment to the needs, characteristics and preference of individual patients. This concept started long back when the clinicians used to observe similar symptoms in different ailments with different causes and curable through different treatment approaches [7].

with Ultimaker 3D printer containing the integration plugin which enables the user to convert files directly. This way the functions of Ultimaker Cura have been greatly improved. With the help of this program, after inscribing the necessary dimensions, we managed to design the models which were to be used in our project (Fig. 1).

2.3 Printing Process

For the operation of 3D printing, we used the Ultimaker 2+ printer (Figs. 2 and 3). The printing process was done at the Faculty of Mechanical Engineering University of Sarajevo. The characteristics of Ultimaker 2+ that we set for the process of printing of suppositories included PLA as—Chosen material with the infill density of 22%.

The nozzle size was 0.4 mm and the height of the layer was 0.1 mm. The printing speed was maintained at 50 mm/s and the amount of fan speed was 100%. The Ultimaker 2+ consists of two parts which were heated during the process: extruder with 210 °C and the build plate heated at only 60 °C.

2.4 Suppository Fabrication

Following the process of printing was the process of stuffing the moulds with appropriate materials. For that purpose, we have only used the base substance (Witepsol H 15) without incorporating the active ingredient. The process involved melting the base substance in the water bath on the temperature of 70 °C until the melting occurred. The follow-up step of the process was stuffing the moulds with previously melted substance. Prior to this was lubricating the inner surface of the moulds with liquid paraffin in order to avoid difficulties that may occur during the pull out of the suppositories from the moulds. The finishing step involved cooling the suppositories in a cold, dry place for the period of 1 h, which was followed by taking the finishing product out of the moulds.

2.5 Customization of Computer Software

The software is made to offer the optimal shape and formulation of the suppositories for each patient, based on the following data: age, gender, weight, existing conditions, and previous experience with rectal and/or vaginal suppositories administration.

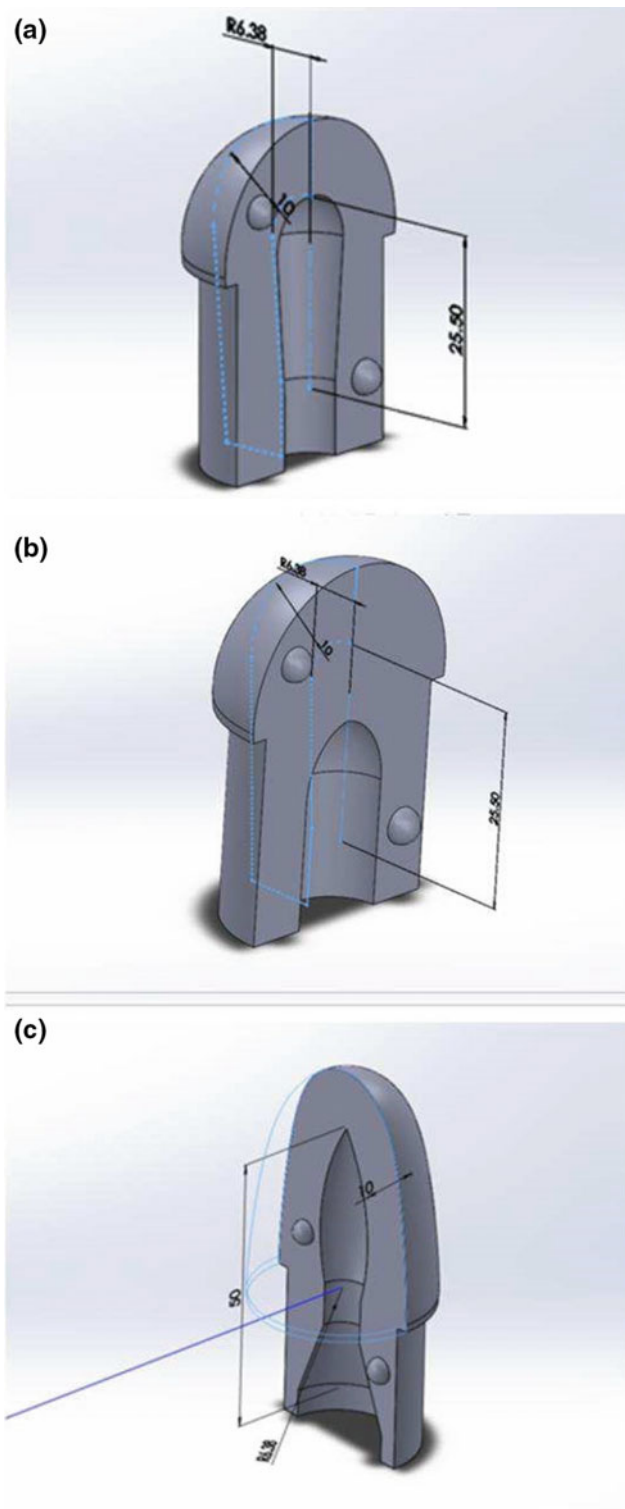


Fig. 1 Different shapes and sizes of suppositories designed in CURA, solidworks in combination with Ultimaker: **a** torpedo-shaped; **b** bullet-shaped and **c** rocket-shaped

3 Results and Discussion

Personalized medicines have lately emerged as a new reliable method in treating patients considering the genetic differences and specific conditions every patient has. Today, speaking of personalized medicines we think of selecting the right medicine and dosing based on patient's genetic variations in order to minimize side effects and ensure more successful outcomes [9]. Different studies have investigated the impact of shape and size of suppositories on patient adherence to therapy and outcomes [10–12].

According to recent studies, the shape of vaginal suppositories affects women's willingness-to-try. One study included 99 sexually-active women who were given the option to choose between one of the second generation prototypes including round oval, long oval, teardrop, bullet and tampon, with each of them having a constant volume of 3 mL respectively [10]. Suppositories were made to prevent the transmission of diseases such as Chlamydia, herpes and HIV. The willingness-to-try values varied by shape, with long, oval and bullet having significantly higher values of willingness-to-try than other shapes.

Different shapes of suppositories, aside from some of them being more preferred for their shape, are also crucial in some specific conditions where common types of suppositories would not be suitable [11].

Female genital abnormalities might cause difficulties in the life of every woman which is the main reason why more and more women today decide to undergo cosmetic surgery. There are many procedures termed as female genital surgery such as labiaplasty, clitoral hood reduction, vaginal rejuvenation and they have shown themselves to improve not just aesthetic aspects of genitalia but also functional [12]. These conditions can cause changes in the appearance and size of vaginal opening which can be a reason why some women are not comfortable with conventional shape suppositories highlighting the need for making personalized suppositories for such patients [11].

Considering the facts that support the use of different shapes of a suppository for treating different conditions we have developed an application that we hope will help each patient to request upon the most suitable shape, making their treatment completely optimized.

By using an application we designed, our patients will be given the best option regarding the shape and size of suppositories, taking into account their age, weight, special conditions and comorbidities, cultural aspects, previous experience with such products and other characteristics in order to meet their requirements.

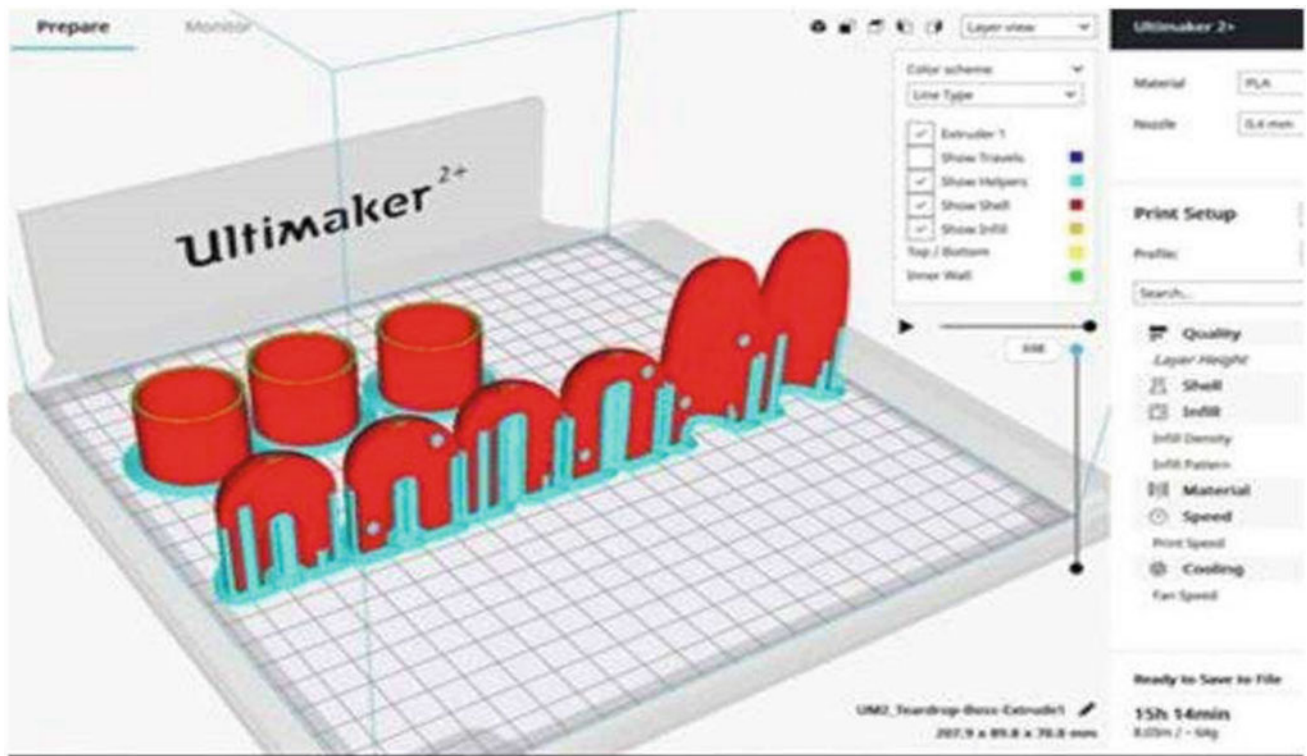


Fig. 2 The set-up of the established properties presented in Ultimaker 2+, with two different steps of the printing process

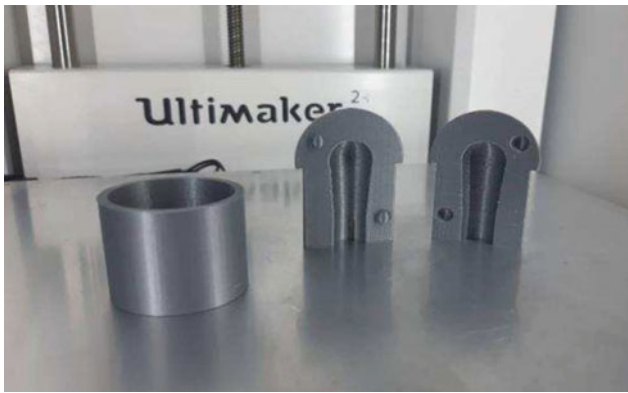


Fig. 3 Suppository moulds during the process of printing in the Ultimaker 2+

The moulds were printed using PLA. The stuffing was made using solid fat (Witepsol), that started leaking throughout the moulds, with emphasize on the cavities between the linking parts, which are to connect two sides of the mould itself (Fig. 4).

There are a few solutions to this problem, one of which is the modification of the mould design. The modification to the design should be made in a way to minimize the cavities between the linking parts of the moulds, essentially meaning that the moulds should be made in a different way, out of one singular part, if possible, which would omit the parts and the cavities altogether. Another solution would be to enfold the moulds with an impermeable material so that this added coat enables retention of the stuffing inside the moulds and prevents it from leaking. Leaking of the stuffing could lead to very serious defects of the rectal and vaginal suppositories, regarding their quality, efficiency and safeness, so it needs to be taken seriously and prevented by all means.

Since we were in the process of making the medicines with the moulds, we had no other choice, but to go with the enfolding the moulds with a suitable material, to prevent the problem of leaking. We wrapped the moulds into aluminium foil, which was to be our first coat, and then afterwards, the moulds with the foil, again enfolded, this time into paper napkins. Since these moulds need to be pinned on the stand for them to dry, and the stands that we used are made of iron, the coat made of napkins served as the reducer of the pressure administered to the moulds by the stand rings. The moulds were set in the stand rings in a way that potentiated the performance of pressure by the rings to be beyond the linking area of two parts of the mould.

Today, there are endless variations of the 3D printers, as well as the possibilities of applying different strategies when it comes to creating a 3D-printed object. If provided with a few different, up-to-date 3D-printing machines, one can take into account the problem that we encountered and resolve it in a unique, advanced and efficient way.

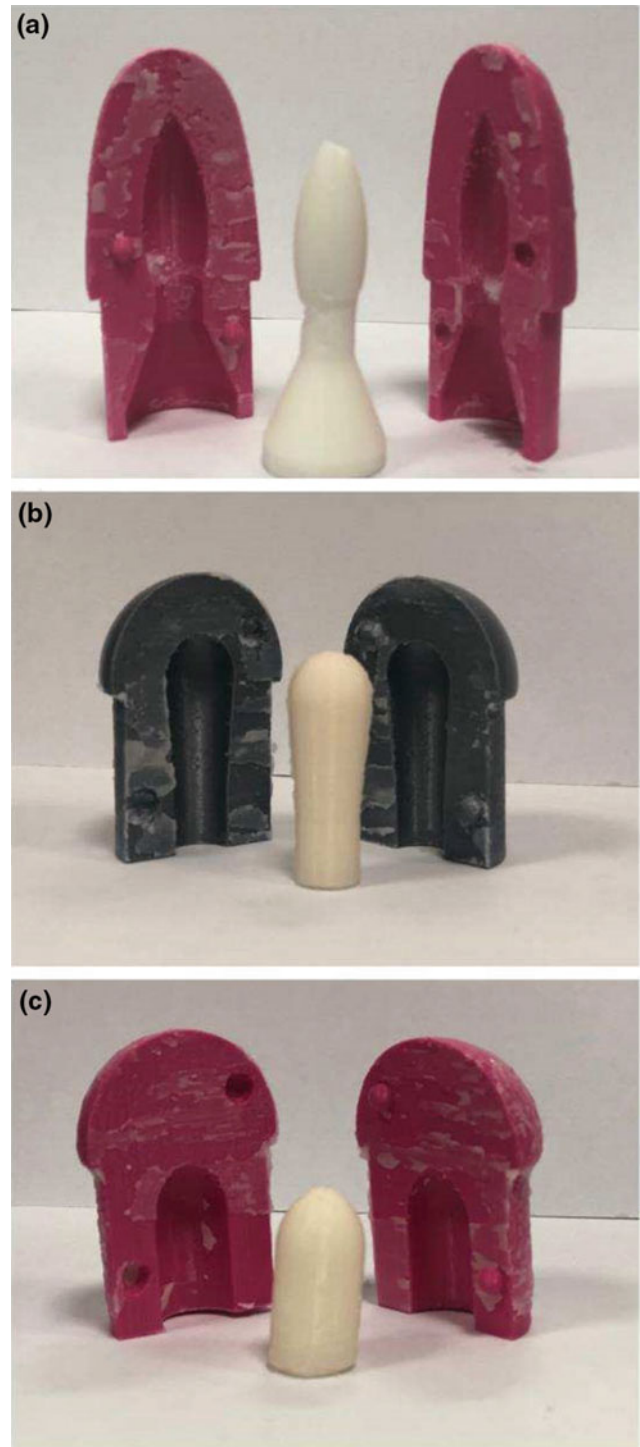


Fig. 4 The shape of suppositories obtained after the use of 3D printed moulds: **a** rocketshaped; **b** torpedo-shaped; **c** bullet-shaped

We have developed a software that will allow the adaptation of the rectal and vaginal suppositories to individual characteristics of the patients. It is simple computer software that can be installed in pharmacies and would be very easy to use. The software contains basic information about the

patient (age, gender, weight, existing conditions, previous experience with rectal and vaginal suppository administration). Based on all of the data entered, the software offers the optimal shape and formulation of the rectal and vaginal suppositories for a particular patient. This way, the proposed form of the preparation would fully correspond to the condition of the patient, following the minimization of discomfort and difficulty in drug application. It should be noted that this is an initial and trial version of the program that could be further improved and adapted to use in pharmacies and hospitals, depending on the results of the initial application.

4 Conclusion

The aim of this research was the production of personalized moulds for rectal and vaginal suppositories. People are individually highly distinguished, therefore, each individual has different needs regarding drug formulation and preparation. For some population groups or some particular age group, rectal or vaginal applications are extremely unpleasant or ineffective.

We have worked on the development of 3D moulds for personalized formulation and preparation of medicines, as well as the development of the software that would make the selection of rectal and vaginal suppositories easier, using a database that contains information about age, sex, weight, special conditions and prior experience. These moulds would provide an adequate dose and shape for children, elderly people, persons with certain diseases and others.

This method of production would also enable better doctor-patient and patient-pharmacist relations, mutual trust, better absorption and efficiency of the active substance, avoidance of substances that can be irritating for a particular patient, and a number of other benefits.

Personalized moulds provide a good option for further research, as well as a new technique in the production of suppositories. It is important to note that this was experimental research conducted by a group of students and is exclusively based on information gathered from clinical trials and scientific articles. There were no studies investigating the impact of vaginal and rectal abnormalities on the shape of suppositories, therefore, we were unable to obtain convincing evidence, if the shapes of suppositories that we

made, would actually be the most appropriate, based on individual needs. Further research on this specific topic is required in order to create quality evidence that would support the use of the proposed method.

Acknowledgements Authors are thankful to Maida Osmanlić for her kind help in the process of designing and printing the moulds and Dino Ćosić for his help in the making of computer software.

Conflict of Interest The authors have no conflicts of interest to disclose.

References

1. Ham, A.S., Buckheit, Jr., R.W.: Designing and developing suppository formulations for anti-HIV drug delivery. *Ther. Deliv.* **8**(9), 805–817 (2017)
2. Kačarević, Ž.P., Rider, P.M.: An introduction to 3D bioprinting: possibilities, challenges and future aspects. *Materials* **11**(11), 2199 (2018)
3. Ricles, L.M., Coburn, J.C., Di Prima, M., Oh, S.S.: Regulating 3D-printed medical products. *Sci. Transl. Med.* **10**(461), eaan6521 (2018)
4. Jamróz, W., Szafraniec, J., Kurek, M., Jachowicz, R.: 3D Printing in pharmaceutical and medical applications—recent achievements and challenges. *Pharm. Res.* **35**(9), 176 (2018)
5. Tappa, K., Jammalamadaka, U.: Novel biomaterials used in medical 3D printing techniques. *J. Func. Biomater.* **9**(1), 17 (2018)
6. Shende, P., Agrawal, S.: Integration of 3D printing with dosage forms: a new perspective for modern healthcare. *Biomed. Pharmacother.* **107**, 146–154 (2018)
7. Rogowski, W., Payne, K., Schnell-Inderst, P., Manca, A., Rochau, U., Jahn, B., et al.: Concepts of ‘personalization’ in personalized medicine: implications for economic evaluation. *Pharmacoeconomics* **33**(1), 49–59 (2018)
8. Konta, A., García-Piña, M., Serrano, D.R.: Personalised 3D printed medicines: which techniques and polymers are more successful? *Bioengineering* **4**(4), 79 (2017)
9. Vogenberg, F.R., Barash, C.I., Prusel, M.: Personalized medicine—part 1: evolution and development into theranostics. *Pharm. Ther.* **35**(10), 560–576 (2010)
10. Li, Z., Zaveri, T., Ziegler, G.R., Hayes, J.E.: Shape of vaginal suppositories affects willingness-to-try and preference. *Antiviral Res.* **97**(3), 280–284 (2013)
11. Yuanyua, S., Xucong, R., Lia, H., Kathuriab, H., Guang, D., Lifeng, K.: Fabrication of nondissolving analgesic suppositories using 3D printed moulds. *Int. J. Pharm.* **513**(1–2), 717–724 (2016)
12. Magon, N., Alinsod, R.: Female cosmetic genital surgery: delivering what women want. *J. Obstet. Gynecol. India* **67**(1), 15–19 (2016)

Coated 3D Printed PLA Microneedles as Transdermal Drug Delivery Systems

Mirela Camović, Amila Bišćević, Iman Brčić, Kana Borčak, Sadžida Bušatlić, Nejra Čenanović, Anida Dedović, Alen Mulalić, Maida Osmanlić, Merima Sirbubalo, Amina Tucak, and Edina Vranić

Abstract

Microneedles facilitate transdermal drug delivery by piercing microscale pores through the *stratum corneum*. They usually penetrate only through the *stratum corneum* thus the nociceptors of the skin will not be stimulated. Therefore, as an alternative approach, microneedles provide a minimally invasive method for drug delivery. Additive manufacturing which is called three-dimensional (3D) printing revolutionized the field of pharmaceutical and biomedical sciences due to their capabilities for fast and cost-effective prototyping of complex structures. Biodegradable 3D printed PLA microneedles are an emerging class of novel transdermal drug delivery systems. Aims of this study were to fabricate 3D printed microneedles and investigate for the first time the ability to coat different drug formulations on 3D printed microneedles. We demonstrated that 3D printing combined with the post-fabrication etching step could make ideally sized and shaped microneedles. Dip coating method revealed to be the best coating method for 3D printed microneedles because of its simplicity and ability to create a uniform load over the printed microneedles. We have also shown that 3D printed microneedles could successfully penetrate and break off into porcine skin.

Keywords

3D printing • PLA microneedles • Transdermal drug delivery • Coating

1 Introduction

Transdermal drug delivery has been used since 1981 as an alternative route of oral and parenteral administration of drugs in order to minimize and avoid limitations associated with them [1–4]. Transdermal systems are often a desirable form of drug delivery, because this route avoids the degradation of drugs in the GI tract and first-pass metabolism, which in the end reduces the frequent administration of drugs and the plasma level “peaks and valleys” often caused by oral dosing and therefore the risk of side effects [1]. This process is, however, limited by the outer layer of the skin, the *stratum corneum*, to small (<400–500 Da), lipophilic ($\log P$ 1–3) and potent molecules with elimination half-life <10 h and low oral bioavailability [5, 6].

Microneedles (MNs) are micrometre-sized needles [7] (solid or hollow) with a length of 50–900 μm , and a diameter of less than 300 μm which create microchannels and penetrate up to 70–200 μm through only outermost layers of skin, superficial enough not to reach the nerve receptors in reticular dermis [8–10]. Therefore, as an alternative approach, microneedles provide a minimally invasive method for forming micro-scale channels into the skin for delivering various components in safe, painless and cost-effective manners [5, 6]. These microchannels help topically applied drug molecules to bypass the SC which is the major limitation for transdermal permeation [4], and makes them a better candidate for drug delivery compared to conventional transdermal patches, or hypodermic needles that are often painful [11]. They have a number of benefits including reduced risk of infection, ease of disposal, minimal invasiveness, and the ability to increase the transcutaneous flux of drugs [7].

M. Camović (✉) · A. Bišćević · I. Brčić · K. Borčak · S. Bušatlić · N. Čenanović · A. Dedović · A. Mulalić
Faculty of Pharmacy, University of Sarajevo, Zmaja od Bosne 8, 71000 Sarajevo, Bosnia and Herzegovina
e-mail: mirela.camovic@hotmail.com

M. Osmanlić
Faculty of Mechanical Engineering, University of Sarajevo,
Wilsonovo šetalište 9, 71000 Sarajevo, Bosnia and Herzegovina

M. Sirbubalo · A. Tucak · E. Vranić
Department of Pharmaceutical Technology, Faculty of Pharmacy,
University of Sarajevo, Zmaja od Bosne 8, 71000 Sarajevo,
Bosnia and Herzegovina

Microneedles are classified into four categories: solid, coated, hollow, hydrogelforming and dissolvable microneedles [7], usually made of various materials such as ceramic [12], metal [13], silicon [14], glass, polymers [15], hydrogels [16], etc. While, metal microneedles are expensive, more brittle and non-biodegradable, polymer-based microneedles are considerably cheaper, soluble and hence safer for drug delivery [17]. Furthermore, there is a chance of breaking metal microneedles after inserting them into the skin and thus leaving behind pieces of metal that raise safety concerns [18]. Although polymer microneedles are made up of cheap and relatively strong material, their tips are inevitably blunt due to the low modulus and yield strength of polymers [11].

Although micro molding is the most commonly used fabrication method for dissolving and gel-forming MNs, there are serious concerns regarding biocompatibility, possible skin irritation and even sterilization issues of the fabrication material [19]. This process involves the creation of master template(s) followed by casting all subsequent microneedles, but template production becomes problematic in order to make any modifications [20]. Other methods include direct photolithography [21], drawing lithography [22], lithography [23], mold-based etching [24] and solvent casting [25]. A relatively new microfabrication technique for producing microneedles is 3D printing.

Additive manufacturing which is called three-dimensional (3D) printing represents a fabrication method where 3D objects are made by fusing or depositing proper materials (ceramics, liquids, metal, plastic, powders or even living cells) layer by layer from a digital model designed by employing design software [26, 27]. It is launched in the 1980s and has revolutionized the field of pharmaceutical and biomedical sciences due to their capabilities for fast and cost-effective prototyping of complex structures [28].

Generally, the application of 3D printing in pharmacy and medicine could provide many benefits including [26, 29]:

- achieving unparalleled flexibility,
- cost-effectiveness,
- enhanced collaboration,
- increased productivity,
- manufacturing capability of pharmaceutical drug products,
- the customization and personalization of medical products, drugs and equipment,
- the democratization of design and manufacturing,
- time-saving.

3D printers for printing plastic materials include fused deposition modelling (FDM), selective laser sintering (SLS) and stereolithography (SLA). In FDM, a molten thermoplastic polymer filament is extruded by two rollers through a high-temperature nozzle which solidifies onto a build plate [30]. FDM methods are versatile, safe cost-effective and can be used for printing renewable, biodegradable, thermoplastic material with a relatively low melting point, such as polylactic acid (PLA) and polyvinyl alcohol, which is approved for use in dissolvable stitches by the Food and Drug Administration (FDA). However, the biggest limitation is low resolution when it comes to manufacturing fine structures like microneedles [27, 31].

Aims of this study were to fabricate 3D printed microneedles, etch their arrays to obtain ideally sized and shaped needles and then test their ability to penetrate and break off into porcine skin. We also wanted to investigate for the first time the ability to coat different drug formulation on 3D printed microneedles (Fig. 1).

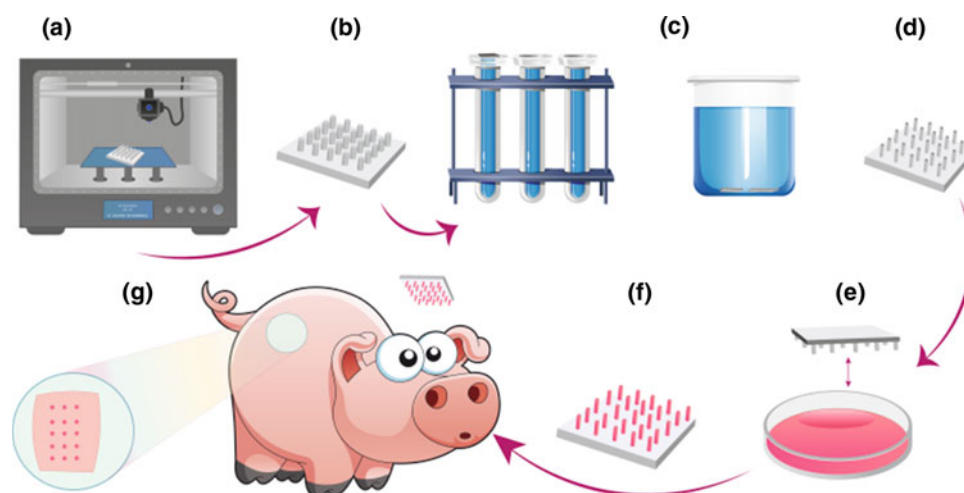


Fig. 1 Schematic illustration of **a** 3D printing of microneedles by using FDM, **b** 3D printed microneedles as fabricated, **c** chemically etched microneedles using 5M KOH, **d** etched microneedles after washing with water, **e** loading drug using “dipping method”, **f** coated microneedles, **g** fracture test of microneedles in porcine skin

2 Materials and Methods

2.1 Materials

PLA filament (Ultimaker); KOH (Sigma Aldrich); PEG 1000 (A.C.E.F); gelatin (RUF); lidocaine hydrochloride ampulla (Galenika a.d.); amoxicillin capsule (Hemofarm a.d.); methyl red (Sigma Aldrich); carmine red (Sigma Aldrich). All other reagents and chemicals used were of analytical grade or pharmacopeial grade.

2.2 Printing 3D Microneedles

Microneedles were printed on Ultimaker 2+ machine. Printer Ultimaker 2+ is reliable, efficient and easy to use. Thanks to the support of a wide range of materials, it is suitable for a wide variety of applications, from prototypes to custom tools. It is an excellent comprehensive 3D printer that provides consistent results. It is optimized to work with Optimized mode for: PLA, ABS, CPE, CPE+, PC, Nylon, TPU 95A. It can objects in sizes from 600 microns to 20 microns. The printing/construction speed is 24 mm³/s, and the travel speeds up to 300 mm/s. In our work White and Orange PLA (Ultimaker) were used as materials for printing. The printing

process was performed at Faculty of Mechanical Engineering, University of Sarajevo. The program which was used for 3D printing is named CURA. Microneedles were designed using Solidworks software package.

We printed microneedles in two different sizes. For white 3D microneedles (Fig. 2c, d) (lengths 2.0 mm, widths 0.6 mm) nozzle size was 0.25 mm, layer height was 0.1 mm, infill density was 22%, print speed was 30 mm/s, with cooling by fan. Fan speed was 100%, extruder temperature was 210 °C, while built plate temperature was 60 °C. For orange 3D microneedles (Fig. 2a, b) (lengths 1.45 mm, widths 0.465 mm) thicknesses was 0.1 mm, nozzle size was 0.25 mm, layer height was 0.1 mm, infill density was 22%, print speed was 30 mm/s, tip size was 0.075 mm, fan speed was 100%, extruder temperature was 210 °C, while built plate temperature was 60 °C.

2.3 Etching 3D Printed Microneedles

After fabrication microneedles were placed in prepared 5M KOH solution for 4 h, such that only the peaks were sunk. Microneedles were washed several times with distilled water and were returned to the test tube so that only the peaks were submerged. After 4 h, microneedles were completely

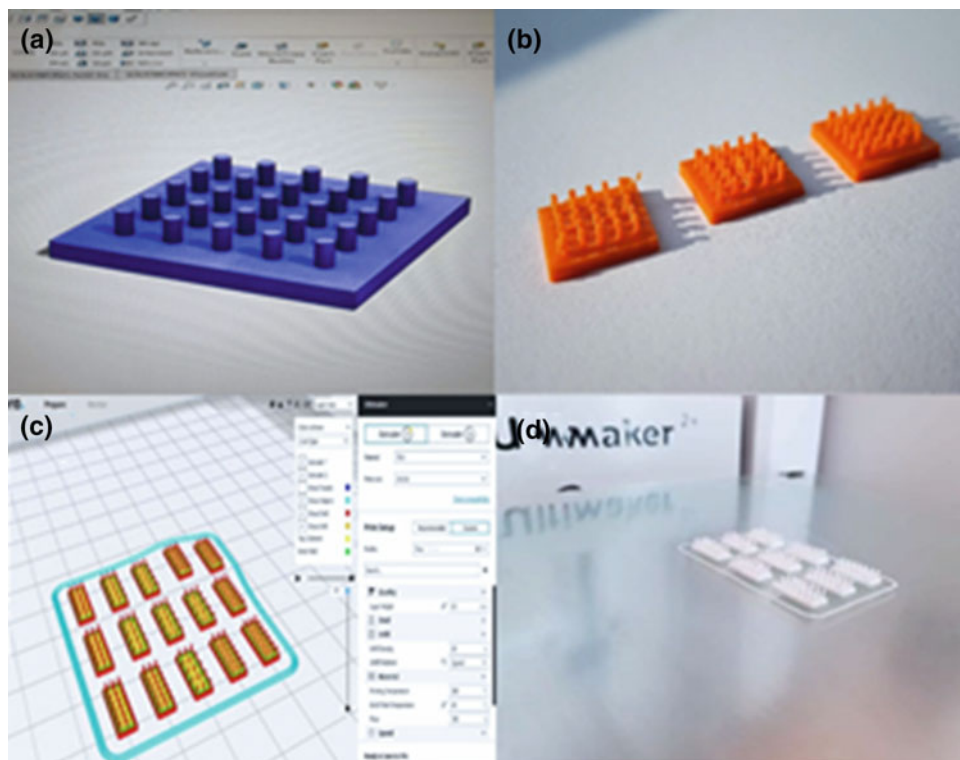


Fig. 2 The procedure of 3D MNs printing **a** preparation for printing orange 3D PLA MNs, **b** printed orange 3D PLA MNs, **c** preparation for printing white 3D PLA MNs, **d** printed white 3D MNs

Table 1 Coating formulations and methods for 3D printed MNs

Formulation (composition)	Method
CF1: 1 g solid PEG + 2 mL lidocaine + carmine red	Dip coating
CF2: 20 μ L liquid PEG + methyl red	With micropipette
CF3: 3.5 mL liquid PEG + 3.5 mL lidocaine + 0.3 g gelatine + carmine red	Dip coating
CF4: 1 g solid PEG + 0.1 g amoxicillin + carmine red	Dip coating
CF5: 4 mL liquid PEG + 4 mL lidocaine + carmine red	Pump spraying

CF—coating formulations

submerged in KOH solution for additional 5 h [20]. After a total of 9 h of etching microneedles in KOH solution, they were finally washed with distilled water and observed by an optical microscope (Meiji ML2000).

2.4 Coating 3D Printed Microneedles

Three different coating methods and five different coating formulations were used. The formulations are listed in Table 1. Carmine red and methyl red were used as indicators to facilitate ocular inspections of MNs coatings.

Coating formulations (CF1, CF3, CF4) were poured into the simple dip coating device developed in-house that comprises a plate with grooves. Single microneedles were dipped in molten liquid formulations CF1, CF3 and CF4 for 1 min. A hot plate was used as the heat source. Microneedles were first dipped into the formulations and then withdrawn. The liquid layer was then allowed to dry at room temperature to form a solid film coating. In second method 20 μ L of coating formulation (CF2) was dripped with a pipette on to the microneedles arrays by hand and set to dry under ambient conditions for 24 h. Coating formulation (CF5) was applied to the microneedles by pump spray, and set to dry.

2.5 Transdermal Application of Microneedles in Vitro

Porcine skin was cut into 2 \times 1 cm slabs and used for microneedle fracture testing into the skin in vitro. Subcutaneous fatty tissue was separated from the *stratum corneum* of the porcine skin with scalpel and skin was then washed with saline solution to enhance penetration. After that, porcine skin was nailed to hard surface. Microneedles were each manually inserted into porcine skin for 30 s and then removed. After removing the microneedles, the skin surface was examined by magnifier to determine microneedles

penetration into the skin. Carmine red was used as the indicator to facilitate ocular inspections of penetration.

3 Results and Discussion

3.1 Preparation and Coating 3D Printed MNs

Microneedles can be fabricated from all kind of materials such as metals, polymers, glass, silicon and ceramics. However, the key is to manufacture the microneedles with proper shape and proper physical properties to be able to penetrate the skin without breaking [20, 32]. Conducted studies concluded that microneedles with lengths up to 1450 μ m, widths of 465 μ m, thicknesses of 100 μ m, and tip sizes of less than 75 μ m cause less pain than a 26-gauge hypodermic needle [20]. However, 3D printers that have been used to produce microneedles are unlikely to produce microneedles with these features. Therefore, it is necessary to use post-fabrication etching step to obtain ideally sized and shaped microneedles. We made microneedles array etching by following up the procedures of Luzuriaga et al. [20]. Microneedles arrays decreased their thickness and width after they were completely immersed in 5M KOH solution for 9 h.

The etching rate of the microneedles was evaluated via optical microscopy (Fig. 3c, d). To produce more defined microneedles arrays we tried to submerge only the needle tips in 5M KOH solution for 24 h, but we found out that base solution completely destroyed our microneedles. We also tried to etch them in HCl, but after 12 h nothing changed.

Exploring microneedles coating methods we discovered many different coating methods for microneedles made from all kind of materials [31–34] but we did not find any coating methods for 3D printed PLA microneedles. Thus, our biggest challenge in this study was to develop suitable coating formulation for uniform and thick coatings on 3D printed microneedles. We wanted to find a composition that could create a uniform load over the needles. The coating process should: make a uniform coating as opposed to a patchy coating to provide reproducibility and dosage control, limit deposition only onto microneedles and not on the base substrate for tight dosage control and minimizing drug loss during coating, avoid high temperatures to maintain drug integrity, use aqueous coating solution to prevent denaturing of proteins and other biological molecules, achieve high drug loading per microneedle to maximize drug dosage, provide good adhesion of the coating to the microneedle to prevent wiping off on the skin during insertion and have rapid, or otherwise controlled, dissolution kinetics in the skin for bolus, or sustained, release) [32]. Among many coating methods in various conducted studies dip coating method

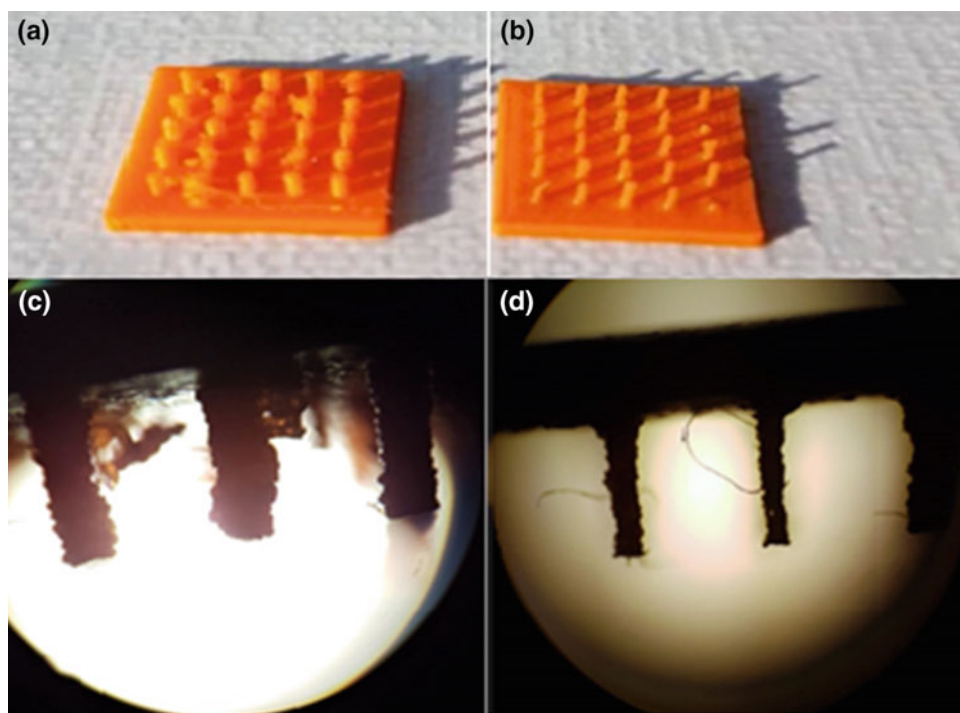


Fig. 3 Macroscopic and microscopic (zoom 4×) MNs view **a** as fabricated MNs macroscopic view, **b** etched MNs macroscopic view, **c** as fabricated MNs microscopic view, **d** etched MNs microscopic view

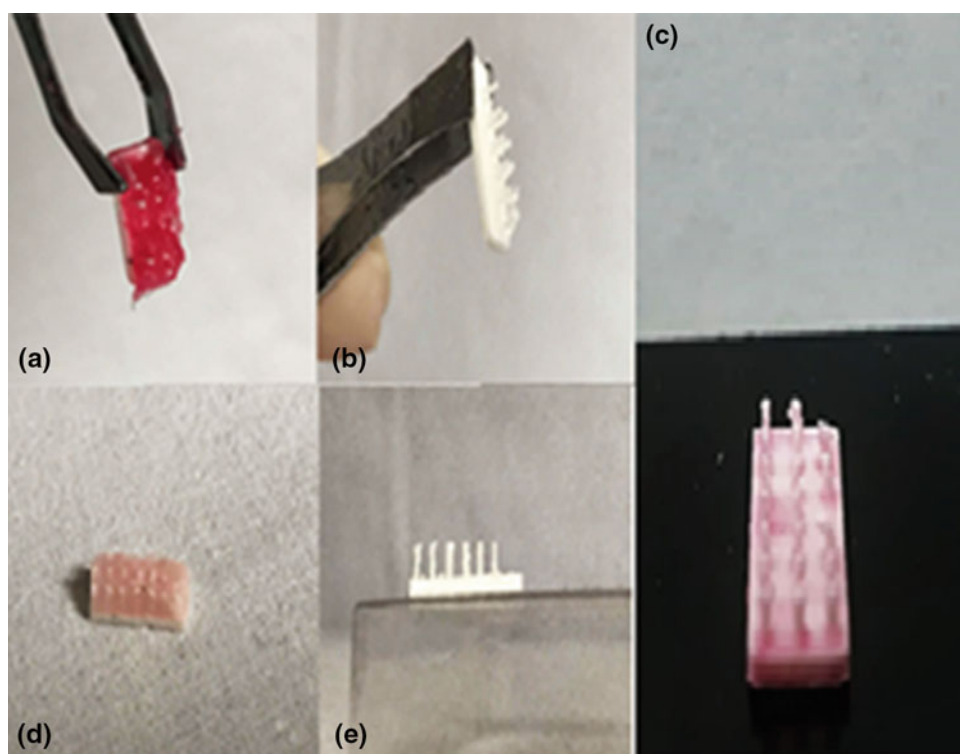


Fig. 4 Coating methods **a** CF1, **b** CF2, **c** CF3, **d** CF4, **e** CF5

revealed to be the best coating method for ceramic microneedles because of its simplicity and its ability to coat complex shapes [32]. In our work we examined three different coating methods and five different coating formulations for 3D printed microneedles coating. The problem with CF2 was that formulation could not sustain on the model because of its low viscosity. The CF5 method was performed by spraying the formulation by pump. As result microneedles were not coated due to its low viscosity. Dip coating method (CF1, CF3, CF4) showed to be the most successful for coating with small variations between different compositions. During coating investigation we have encountered a lot of problems. The first problem was to achieve successfully coating on microneedles avoiding to coat the base as in case CF1. Another problem was the maintenance of the mixture on the microneedles like in the CF2 and CF5 where we could not remain our formulation on microneedles. In CF1 and CF4 coating was not successful because of too much amount of formulation that remained on the microneedles. CF3 showed to be the most successful method with the optimized amounts of the substance. In this formulation we selected gelatin as the viscosity enhancer and as a result we have had an adequately and uniform applied mixture on the microneedle arrays (Fig. 4).

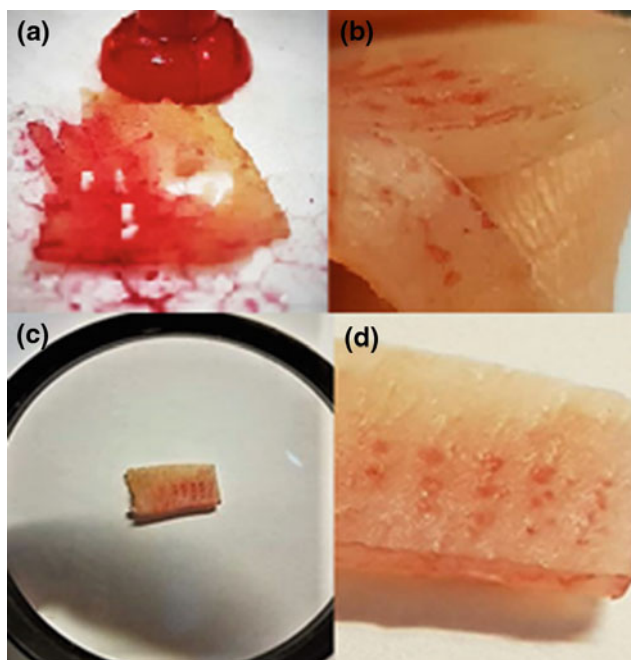


Fig. 5 **a** Etched MNs application, **b** cross section of porcine skin after etched MNs insertion, **c**, **d** application of non-etched MNs (under the magnifier)

3.2 In Vitro Transdermal MNs Application

Because patients resort to less painful and less demanding drug applications, transdermal administration by microneedles is part of non-invasive drug administration methods. Microneedles are also estimated to offer not more or even lesser risk of infection compared to hypodermic needles and studies have shown that the skin recovers its barrier properties within 2 h after microneedles removal when no occlusion was applied to the skin [20]. After making, etching and coating 3D printed microneedles we performed in vitro fracture testing into porcine skin. We used porcine skin because of the functional and structural resemblance with human skin. The thickness of porcine skin differs greatly depending on the location (pig epidermis: 30–140 μm ; human epidermis: 50–120 μm) [35]. The test on the skin was carried out with etched microneedles and non-etched ones obtaining pressure by our fingers. Conducted studies concluded that microneedles in length 1400 μm inserted by pressure into the porcine skin resulted in 84% of the microneedles breaking away from the array and remaining incorporated in the skin [20]. We have shown that 3D printed microneedles could successfully penetrate and break off into porcine skin. We established that after applying etched microneedles they penetrate the *stratum corneum* but if we apply stronger pressure, their firing occurs (Fig. 5a). Therefore, we found out that the sharp microneedles (which were dipped 9 h in 5M KOH solution) have shown instability and fragility under the pressure.

We also tested how as non-etched microneedles behave when applied to the skin and realized by looking through magnifier that they successfully pierced the skin and do not break off (Fig. 5c, d). Cross-section of porcine skin has determined that microneedles pierced the skin (Fig. 5d). We realized that non-etched microneedles have shown more stability under the same pressure.

4 Conclusion

We believe that this non-invasive method of transdermal drug delivery will replace, in major part, other methods of drug application such as hypodermic needles. In summary, we demonstrated that 3D printing combined with the post-fabrication etching step could make ideally sized and shaped microneedles for transdermal drug delivery. This study provides the first examination of the design and control of PLA microneedle coating formulations. We have demonstrated that the distribution and uniformity of the

coatings applied to 3D printed microneedles, varied with different compositions. However, more suitable coating methods are still needed to enable a uniform coating located on the needles only. Factors like coating viscosity may affect the coating distribution on the microneedles. There is still a lot of research needed before optimized coating method can be presented. For example, it is necessary to study the significance of surfactants and viscosity enhancers in producing uniform coatings on 3D printed microneedles. We also managed to prove the penetration of 3D printed microneedles in the porcine skin. After several attempts, we came to the conclusion that non-etched microneedles have shown much easier penetration. With this conclusions we would, hopefully open the door for further research in this area and improve transdermal drug delivery devices.

Acknowledgements We would appreciate Assistant Professor Jasmina Hadžić, Assistant Professor Ognjenka Rahić and Assistant Professor Alisa Elezović at the Department of Pharmaceutical Technology for helpful advices, and Teaching and Research Assistant Emina Aruković, DVM for preparation of porcine skin.

Conflict of Interest Authors have no conflicts of interest to disclose.

References

- Teo, A.L., Shearwood, C., Ng, K.C., Liu, J., Mochhala, S.: Transdermal microneedles for drug delivery applications. *Mater. Sci. Eng. B* **132**(1–2), 151–154 (2006)
- Paudel, K.S., Milewski, M., Swadley, C.L., Brogden, N.K., Ghosh, P., Stinchcomb, A.L.: Challenges and opportunities in dermal/transdermal delivery. *Ther. Deliv.* **1**(1), 109–131 (2010)
- Vranić, E., Tucak, A., Vrabac, Dž., Rahić, O., Elezović, A., Hadžić, J.: Microneedle-assisted delivery of NSAIDs. In: Badnjević, A. (eds.) *CMBEBIH 2017. IFMBE Proceedings*, vol. 62, pp. 311–316. Springer, Singapore (2017)
- Alexander, A., Dwivedi, S., Ajazuddin, Giri, T.K., Saraf, S., Saraf, S., et al.: Approaches for breaking the barriers of drug permeation through transdermal drug delivery. *J. Control Release* **164**, 26–40 (2012)
- Gill, H.S., Prausnitz, M.R.: Coating formulation for microneedles. *Pharm. Res.* **24**(7), 1369–1380 (2007)
- Hadgraft, J., Du Plessis, J., Goosen, C.: The selection of non-steroidal anti-inflammatory agents for dermal delivery. *Int. J. Pharm.* **207**(1–2), 31–37 (2000)
- Ita, K.: Transdermal delivery of drugs with microneedles: strategies and outcomes. *J. Drug Deliv. Sci. Tech.* **29**, 16–23 (2015)
- Yadav, D.J., Vaidya, K.A., Kulkarni, P.R., Raut, R.A.: Microneedles: promising technique for transdermal drug delivery. *Int. J. Pharm. Bio Sci.* **2**(1), 684–708 (2010)
- Roxhed, N., Samel, B., Nordquist, L., Griss, P., Stemme, G.: Painless drug delivery through microneedle-based transdermal patches featuring active infusion. *IEEE Trans. Biomed. Eng.* **55**(3), 1063–1071 (2008)
- Henry, S., McAllister, V.D., Mark, G.A., Prausnitz, P.M.: Microfabricated microneedles: a novel approach to transdermal drug delivery. *J. Pharm. Sci.* **87**, 922–925 (1998)
- Olatunji, O., Das, D.B., Nassehi, V.: Modelling transdermal drug delivery using microneedles: effect of geometry on drug transport behaviour. *J. Pharm. Sci.* **101**(1), 164–175 (2012)
- HariPriya, K., Chandra, K.S., Ajay, B.K.: Characterization of microchannels created by metal microneedles: formation and closure. *J. List* **13**(3), 473–481 (2011)
- Wilke, N., Mulcahy, A., Ye, S.-R., Morrissey, A.: Process optimization and characterization of silicon microneedles fabricated by wet etch technology. *Microelectron. J.* **36**(7), 650–656 (2005)
- Hartmann, X.H.M., van der Linde, P., Homburg, E.F.G.A., van Breemen, L.C.A., de Jong, A.M., Luttgé, R.: Insertion process of ceramic nanoporous microneedles by means of a novel mechanical applicator design. *Pharmaceutics* **7**(4), 503–522 (2015)
- Zhang, Y., Jiang, G., Hong, W., Gao, M., Xu, B., Zhu, J., et al.: Polymeric microneedles integrated with metformin-loaded and PDA/LA-coated hollow mesoporous SiO₂ for NIR-triggered transdermal delivery on diabetic rats. *ACS Appl. Bio Mater.* (2018) (In press)
- Donnelly, R.F., McCrudden, M.T.C., Alkilani, A.Z., Larraneta, E., McAlister, E., Courtenay, A.J., et al.: Hydrogel-forming microneedles prepared from “super swelling” polymers combined with lyophilised wafers for transdermal drug delivery. *PLoS One* **9**(10), 111–547 (2014)
- Park, J.H., Allen, M.G., Prausnitz, M.R.: Biodegradable polymer microneedles: fabrication, mechanics and transdermal drug delivery. *J. Control Release* **104**(1), 51–66 (2005)
- Martanto, W., Moore, J.S., Cous, T., Prausnitz, M.R.: Mechanism of fluid infusion during microneedle insertion and retraction. *J. Control Release* **12**, 357–361 (2006)
- McCrudden, M.T., McAlister, E., Courtenay, A.J., González-Vázquez, P., Singh, T.R., Donnelly, R.F.: Microneedle applications in improving skin appearance. *Exp. Dermatol.* **24**(8), 561–566 (2015)
- Luzuriaga, M., Berry, D., Reagan, J., Smaldone, R., Gassensmith, J.: Biodegradable 3D printed polymer microneedles for transdermal drug delivery. *Lab. Chip* **18**(8), 1223–1230 (2018)
- Dardano, P., Calìo, A., Palma, V.D., Bevilacqua, M.F., Matteo, A.D., Stefano, L.D.: A photolithographic approach to polymeric microneedles array fabrication. *Materials* **8**, 8661–8673 (2015)
- Choi, Y., Lee, S.G., Jeong, J.H., Lee, K.M., Jeong, K.H., Yang, H., et al.: Nanostructured lipid carrier-loaded hyaluronic acid microneedles for controlled dermal delivery of a lipophilic molecule. *Int. J. Nanomed.* **1**, 289 (2013)
- Ceysens, F., Chaudhri, B.P., Hoof, C.V., Puers, R.: Fabrication process for tall, sharp, hollow, high aspect ratio polymer microneedles on a platform. *J. Micromech. Microeng.* **23**, 075–023 (2013)
- Kim, H., Theogarajan, L.S., Pennathur, S.A.: Repeatable and scalable fabrication method for hollow silicon microneedles. *J. Micromech. Microeng.* **28**, 035–007 (2018)
- Wang, Q.L., Zhu, D.D., Liu, X.B., Chen, B.Z., Guo, X.D.: Microneedles with controlled bubble sizes and drug distributions for efficient transdermal drug delivery. *Sci Rep.* **6**, 28755 (2016)
- Ventola, C.L.: Medical applications for 3D printing: current and projected uses. *P&T* **39**(10), 704–711 (2014)
- Pedde, R.D., Mirani, B., Navaei, A., Styan, T., Wong, S., Mehrali, M., et al.: Emerging biofabrication strategies for engineering complex tissue constructs. *Adv. Mater.* **29**, 1–27 (2017)
- Jassim-Jaboori, A., Oyewumi, M.O.: 3D printing technology in pharmaceutical drug delivery: prospects and challenges. *J. Biomol. Res. Ther.* **04**(4), 4 (2015)

29. Goole, J., Karim, A.: 3D printing in pharmaceuticals: a new tool for designing customized drug delivery systems. *Int. J. Pharm.* **499**(1–2), 376–394 (2016)
30. Economidou, S.N., Lamproua, D.A., Douroumisb, D.: 3D printing applications for transdermal drug delivery. *Int. J. Pharm.* **544**(2), 415–424 (2018)
31. Gill, H.S., Prausnitz, R.: Coated microneedles for transdermal delivery. *J. Control Release* **117**(2), 227–237 (2007)
32. Gidlof, Z.: Coating of bioceramic microneedles, Degree Thesis, Umeå University, Pharmacology and Clinical Neuroscience, Umeå (2017)
33. Haj-Ahmad, R., Khan, H., Arshad, M.S., Rasekh, M., Hussain, A., Walsh, S., Li, X., Chang, M.W., Ahmad, Z.: Microneedle coating techniques for transdermal drug delivery. *Pharmaceutics* **7**(4), 486–502 (2015)
34. Chen, J., Qiu, Y., Zhang, S., Yang, G., Gao, Y.: Controllable coating of microneedles for transdermal drug delivery. *Drug Dev. Ind. Pharm.* **41**(3), 415–422 (2013)
35. Banski, K.L., Mittermayr, R., Herdon, D.N., Norbury, W.B., Masters, O.E., Hofmann, M.: A porcine model of full-thickness burn, excision and skin autografting. *Burns* **34**(8), 1119–1127 (2009)

Development of a Diagnostic Support Software in the Clinicobiochemical Evaluation of Secondary Amenorrhea Diagnosis

Nikolina Begović, Amina Džiho, Lamija Aliman, Igor Đukić, Arnela Tarakčija, Vedad Terzić, Neven Meseldžić, Selma Imamović, Tanja Dujić, Maja Malenica, and Tamer Bego

Abstract

Amenorrhea is defined as the absence of menstrual bleeding and it is classified as primary, as the absence of menarche and secondary, usually longer than six to twelve months. The causes of secondary amenorrhea are pathological changes of female reproductive organs and hypothalamic-pituitary axis which, due to complex pathophysiology, are difficult to differentiate. Amenorrhea is associated with other disorders such as anxiety and depression, osteoporosis, cardiovascular diseases, endometrial cancer and infertility. Therefore, the importance of accurate diagnosis and consequent treatment is indisputable. For the purpose of accurate diagnosis, there has been developed an application based on the selected algorithm used for the evaluation of secondary amenorrhea. Algorithm allows healthcare workers and patients to make a decision on health protection based on the best evidence and to minimize costs and time frame of testing, as well. During the preparation of AmnSec application, there were used reference intervals on the following biochemical parameters: prolactin, TSH, FSH, testosterone, DHEAS and presence of virilization. The combination of default values offers the possible cause of secondary amenorrhea while the diagnostic success of the application entirely depends on the accuracy of the algorithm that the application is based on. The development of this type of application makes it easier for patients to access valid information by simply using their personal computers or mobile phones. Further work and the progress of the information sector in medicine is needed

to provide more efficient, faster and better care and higher quality information for patients as the axis of improving health and life quality.

Keywords

Secondary amenorrhea • PCOS • Algorithm • Application development • Prolactin

1 Introduction

Female menstrual cycle includes ritmical model of changes that happens on monthly basis on female reproductive organs, primarily ovarians, under control of female endocrine system, and all of that to prepare the body for potential pregnancy. Releasing the gonadotropine-releasing hormone (GnRH) is the first step in menstrual cycle and it works on pituitary to release follicle-stimulating hormone (FSH) and luteinizing hormone (LH) and these hormones will act on ovaries to produce estrogen, progesterone and androgens. Any defect at any level of this physiological cycle can cause some kind of disorder or permanent absence of menstrual cycle (amenorrhea) [1, 2].

Amenorrhea is defined as the absence of menstrual bleeding and it is classified as primary and secondary. Primary amenorrhea is defined as the absence of menses within five years of secondary sex characteristics development. Secondary amenorrhea is defined as the absence of menstrual bleeding for an arbitrary period, usually longer than six to twelve months. Causes of secondary amenorrhea can be various pathological changes on endometrial level (e.g. Asherman syndrome), ovaries (e.g. Turner syndrome, PCOS), hypophysis (e.g. Neoplasm, Sheehan syndrome, drugs) and hypothalamus (e.g. FHA) [3].

Besides it can be result of various pathological changes, prolonged amenorrhea can be associated with significant medical morbidity which differs depending on whether the amenorrhea is estrogen-deficient or estrogen-replete.

N. Begović (✉) · A. Džiho · L. Aliman · A. Tarakčija · V. Terzić · N. Meseldžić · S. Imamović · T. Dujić · M. Malenica · T. Bego
Faculty of Pharmacy Sarajevo, University of Sarajevo, Sarajevo,
Bosnia and Herzegovina
e-mail: nikolina.begovic@yahoo.com

I. Đukić
Faculty of Technical Sciences, University of Novi Sad,
Novi Sad, Serbia

Estrogen-deficient amenorrhea is associated with reduced bone mineral density and increased osteoporosis risk, while estrogen-replete amenorrhea can lead to dysfunctional uterine bleeding in the short term and predispose to endometrial carcinoma in the long term [4]. Also, it can be related to complicated depression and/or anxiety disorders, cardiovascular diseases and infertility. Major risk factors that could increase the risk of amenorrhea include family history (inherited predisposition for the problem), eating disorders (anorexia), and athletic overtraining [5].

Diagnostic approach to patients with secondary amenorrhea consists of anamnesis, physical examination and laboratory evaluation for identification of causes of amenorrhea. Anamnesis include family history-taking and evaluation of a lifestyle, including exercise patterns, changes in weight, chronic illness, medication use, chemotherapy or radiation exposure, and stress impact [6]. When the physical examination is normal (the majority of cases), the initial investigation should exclude pregnancy and estimate serum hormone concentrations. Laboratory evaluation tests include: thyroid function test (TSH), ovary function test (FSH), prolactin test (low levels of the hormone prolactin may be a sign of pituitary gland tumor), and male hormone test (excessive testosterone secretion is suggested most often by hirsutism and rarely by increased muscle mass or other signs of virilization). Hormone challenge tests are being used to trigger menstrual bleeding. Result from this test can indicate the lack of estrogen. Imaging tests such as ultrasound, computed tomography scan (CT scan) and magnetic resonance imaging (MRI) may be recommended afterwards. If other testing reveals no specific cause, a hysteroscopy may be advised [7, 8].

The prevalence of secondary amenorrhea that is not caused by pregnancy, lactation or menopause is 3–4% [3]. Considering the complex nature of not only the diagnosis of secondary amenorrhea, but the clinical picture of the disease that causes it as well, and the complexity of the female reproductive system, understanding secondary amenorrhea itself along with causal-link is very difficult. The number of studies in the field of secondary amenorrhea diagnostics that point to the importance of a systematic approach to establishing a diagnosis of this disorder is immense. Various research has been carried out in the field of diagnostics by using algorithms, quizzes and applications, but continuous improvement is indispensable.

Thus, an idea about application that will assist in better understanding of secondary amenorrhea was born. Algorithmic approach while preparing the application for evaluation of laboratory tests minimizes the risk of diagnostic error, as well as costs and time frame of test itself. Development of this type of application would also enable patients better access through their mobile phones or computers.

2 Methods and Materials

The results and conclusions of previously published scientific research papers and review studies were used as data source. In the experimental part of the study an application called AmnSec was developed and its purpose is the classification of secondary amenorrhea causes based on parameters derived from the algorithm (see Fig. 1). The parameters listed in the shown algorithm are TSH, FSH, prolactin, testosterone and dehydroepiandrosterone sulfate (DHEAS).

An algorithm is a set of rules for problem solving. This is a schematic representation of the decision-making process composed of a flow chart with boundary paths that lead to some desired outcome. In health care, algorithms provide one strategy for translating CPG (Central pattern generator) based on evidence in practice. CPGs have been derived from rigorous systematic reviews of existing literature. Algorithms help health workers and patients make decisions about appropriate health care for certain clinical circumstances. They summarize the CPG using a step-by-step methodology tailored for the user that increases the ability to make a precise clinical decision based on the best evidence [9].

A native application with focus on JavaScript programming language was made. To make this application, 1 JavaScript framework and 1 library were used. First framework is ElectronJS [11], which enables an API to make native app using only web technologies such as: JS, HTML and CSS. For the UI part, library called ReactJS [12], which provides interaction was used. For app visuals, CSS toolkit Bootstrap [13] was used and some CSS were costume written. Every input is validated, so it is not possible to determine patients' cause with empty fields or values bellow 0. Following reference values were used: TSH 0.5–5 mIU/L, PRL 4–30 ng/mL, FSH 5–20 IU/L, testosterone 8–60 ng/dL, DHEAS 250–300 ng/dL (0.7–0.8 μ mol/L) as well as virilism presence [14, 15]. The application is easy to use, after entering specific values, a click on "Calculate" will open second window containing possible secondary amenorrhea cause.

3 Result and Discussion

Patients' lack of information can lead to major problems in the treatment of some disease. By programming an application, patients can receive information on the appropriate diagnosis with a lesser probability of error. During the preparation of the AmnSec applications, the following parameters were used: TSH, prolactin, FSH and testosterone/DHEAS concentrations and the presence of virilization (see Fig. 2).

Fig. 1 Algorithm for the detection of the cause of secondary amenorrhea [10]

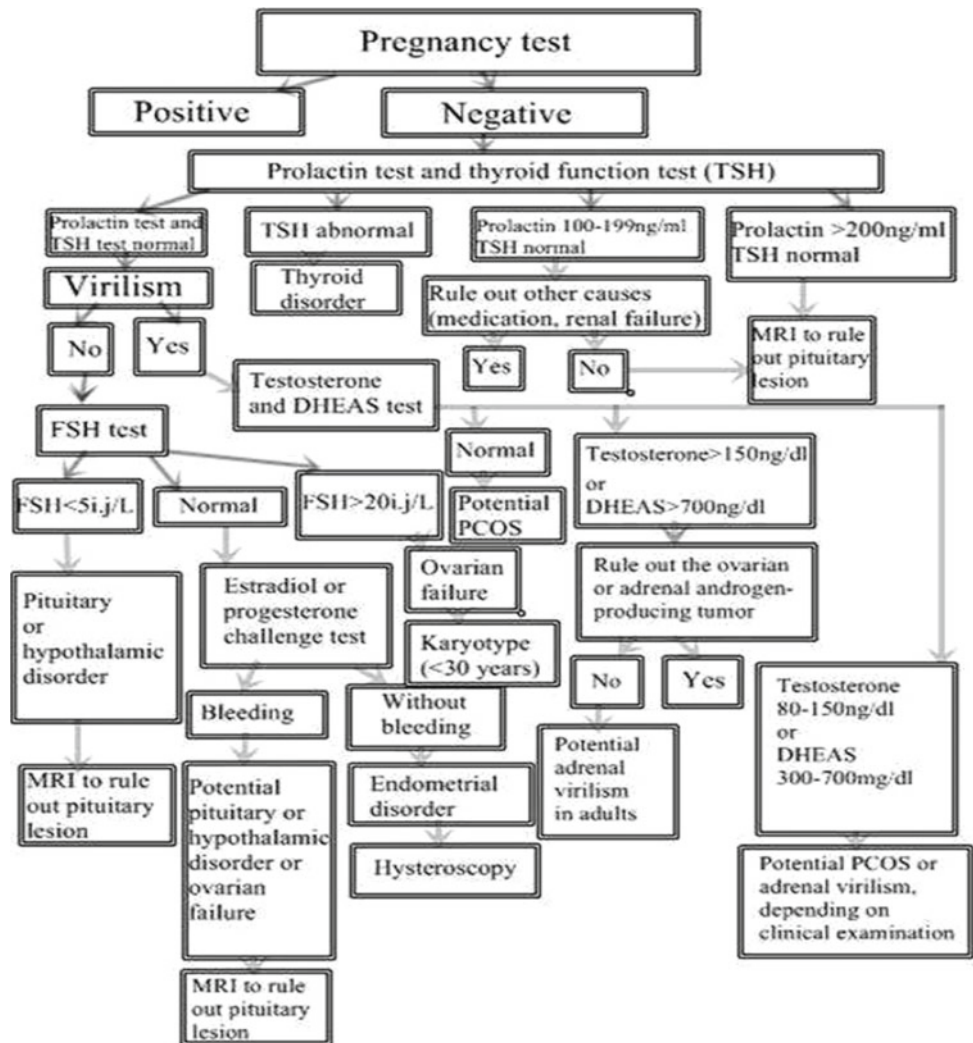
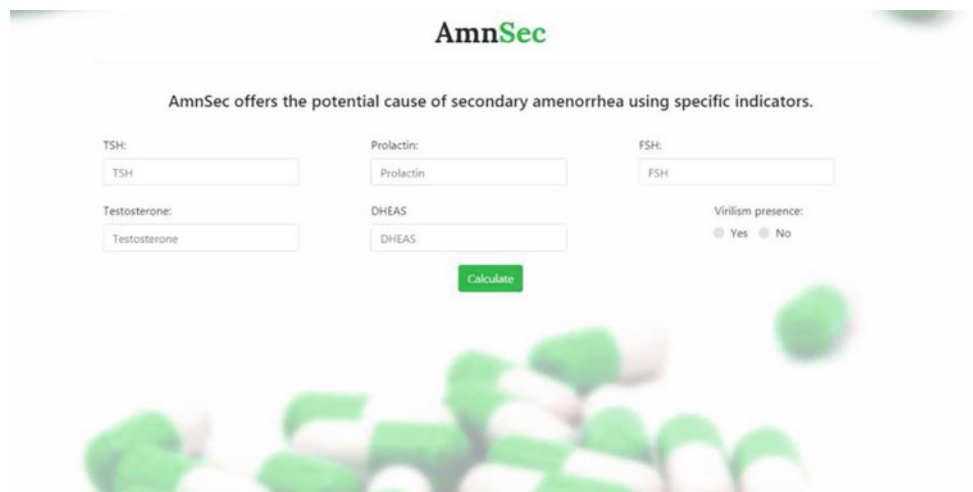


Fig. 2 Single-page screenshot of the AmnSec application showing graphical interface for implementing diagnostic tests



By using a specific combination of parameter values for each patient individually, the application, according to said algorithm, displays possible diagnoses (see Table 1).

If first value insertion does not indicate the possible diagnose, the AmnSec application cause pop-up window with further test requirements. Depending on following

Table 1 Possible AmnSec diagnoses in patients with secondary amenorrhea

TSH	Prolactin	Virilism	FSH	Testosterone/DHEAS	Disorder
Abnormal	–	–	–	–	Thyroid disorder
N	≥ 200	–	–	–	Potential pituitary lesion
N	100,199	–	–	–	Rule out other causes (medications, renal failure); if so—potential pituitary lesion
N	N	No	>20	–	Ovarian failure Karyotype should be done if the woman is less than 30 years of age
N	N	No	N	–	Estradiol or progesterone challenge test required (to induce bleeding) Bleeding—potential pituitary/hypothalamic disorder or ovarian failure Without bleeding—Endometrial disorders (for example Asherman syndrome)
N	N	No	<5	–	Pituitary or hypothalamic disorder
N	N	Yes	–	>150/>700	Ovarian or adrenal androgen producing tumor Potential adrenal virilism in adults
N	N	Yes	–	N	Potential PCOS
N	N	Yes	–	80–150/300–700	Potential PCOS or adrenal virilism depending on clinical examination

N normal value; – value of the parameter does not affect the diagnostics

input, application offers possible diagnose. If a user inputs values that do not match the ones shown in Table 1, the application as a result displays: “Additional examination required”.

By using a decision tree similar algorithm, the symptoms or biochemical parameters can be used in a step-by-step process to obtain a final diagnosis. Research of Priyanka et al. [16] is an example of using an algorithm for determining secondary amenorrhea using symptoms and biochemical parameters to determine the cause of this disorder. 100 examinees were used in the study, where it is shown that a systematic approach to diagnosis by taking anamnesis and physical examination can avoid unnecessary tests.

A similar approach, using a diagnostic scheme for differential diagnosis of the etiology of primary and the secondary amenorrhea was also analyzed by Nakano et al. [17]. The study included a group of 40 patients (seven normal control subjects and thirty-three amenorrheic patients) subjected according to the scheme including progestin test, a cyclic estrogen and progestin test, a luteinizing hormone-releasing hormone (LH-RH) loading test, and a gonadotropin loading test. The character of their response to test facilitated the etiologic diagnosis of amenorrhea, accelerating the differential diagnosis and treatment of amenorrhea induced by an endocrine disturbance in the hypothalamic-pituitary-ovarian-uterine axis. Such studies confirm the credibility of the algorithmic approach while their comparison with AmnSec suggests the advantages of using the application in terms of finding the most probable

diagnosis by simply entering parameter values instead of analyzing each of the parameters individually.

The use of computer technology as a diagnostic aid for a disease is already a well established practice and numerous examples are available to the general public for examination. Mendelian [18], an interactive information web site, provides information to patients and physicians about diagnosing rare diseases as well as gene disorders that cause these diseases. The very attractive and interesting appeal and simpleness of the website helps the patient to understand the diagnosed disease through various interactive quizzes with appropriate information for diagnosed disease. AmnSec uses values of the hormone level taking into account the reference values for the secondary amenorrhea diagnosis and on the basis of the various combinations of these values offers the possible cause of secondary amenorrhea.

DDxHuB—Differential diagnosis Hub [19], is a system which intends on distinguishing a particular disease or health condition from others that present similar symptoms and lab test results. Unlike AmnSec, which uses specific and simple access in secondary amenorrhea diagnosis, this system uses serum concentrations of large numbers of parameters. Also, it considers patients’ lifestyle (e.g. smoking). Thus, that makes DDxHuB more detailed but complicated for use, as well. On the other hand, it provides clearer diagnosis along with disease description for patients.

Delimaris et al. [5] they have developed similar educational software (ERS) which serves as an auxiliary tool for students and laborators in the education of clinical-biochemical

evaluation of amenorrhea. In this software, the diagnostic path does not follow the algorithm; instead the evaluation of the amenorrhea is performed on the basis of variation of the descriptive values of three parameters (high/normal/low levels of FSH, LH and prolactin). AmnSec monitors six parameters following the usual diagnostic pathway and requires a more extensive approach to amenorrhea evaluation, which is required due to the complexity of this disorder. Because of the algorithm used in programming our application, LH as a biochemical parameter is not used in the diagnosis of the disorder, which is considering the high costs and impracticality of hormone sampling a advantage of the diagnostic tool.

4 Conclusion

The prevalence of secondary amenorrhea that is not caused by pregnancy, lactation or menopause, is relatively high in women of reproductive age, resulting from, not only female reproductive organs, but also the hypothalamus-pituitary axis disorders.

Considering diagnostics complexity of the secondary amenorrhea and causative disorders with a comprehensive approach requirement, the idea of application development that provides a simple evaluation of the causes of secondary amenorrhea is highly significant. The application is based on an algorithm that tracks several parameters (prolactin, TSH, virilization, FSH, testosterone and DHEAS) and depending on their specific values provides the possible cause of secondary amenorrhea.

AmnSec offers an easier access to information and better understanding of secondary amenorrhea for patients, which contributes to forming more rational attitude to the disorder they face with. It is a result of the cooperation of medical sciences and IT technology, which is the basis of future development of diagnostics, more efficient, faster and more convenient care, evaluation of results and informing patients. Therefore, it improves overall health and life quality.

References

1. Thiagarajan, D.K., Jeanmonod, R.: Physiology, Menstrual Cycle. StatPearls Publishing (2018)
2. Nawaz, G., Rogol, A.D.: Amenorrhea. StatPearls Publishing (2018)
3. Lobo, R.A., et al.: Comprehensive Gynecology, 7th edn. Elsevier, Amsterdam (2017)
4. Golden, N.H., Carlson, J.L.: The pathophysiology of amenorrhea in adolescent. *Menstrual Cycle Adolesc. Health* **1135**(1), 163–178 (2008)
5. Delimaris, I., Delimaris, K.: Development of an educational research software with advisory role in the clinicobiochemical evaluation of amenorrhea. *Prog. Health Sci.* **4**(1), 83–87 (2014)
6. Master-Hunter, T., Heiman, D.L.: Amenorrhea, evaluation and treatment. *Am. Fam. Phys.* **73**(8), 1374–1382 (2006)
7. The Practice Committee of the American Society for Reproductive Medicine: Current evaluation of amenorrhea. *Fertil. Steril.* **90**(3), 219–225 (2008)
8. Mayo Clinic Amenorrhea, <https://www.mayoclinic.org/diseases-conditions/amenorrhea/diagnosis-treatment/drc-20369304>. Last accessed 2018/11/29
9. Jablonski, A.M., et al.: The use of algorithms in assessing and managing persistent pain in older adults. *Am. J. Nurs.* **111**(3), 34–45 (2011)
10. MSD Priručnik simptoma bolesti, <http://www.msd-prirucnici.placebo.hr/msdsimptomi/amenoreja>. Last accessed 2018/12/09
11. Electron—Build cross platform desktop apps with JavaScript, HTML, and CSS. <https://electronjs.org/>. Last accessed 2018/12/10
12. React—A JavaScript library for building user interfaces. <https://reactjs.org/>. Last accessed 2018/12/10
13. Bootstrap—The most popular HTML, CSS, and JS library in the world. <https://getbootstrap.com/>. Last accessed 2018/12/10
14. Laboratory Reference Ranges, <https://education.endocrine.org/system/files/ESAP%202015%20Laboratory%20Reference%20Ranges.pdf>, last accessed 2018/12/09
15. Mayo Clinic Laboratories Test Catalog, <https://www.mayocliniclabs.com/testcatalog/Clinical+and+Interpretive/602753>, last accessed 2018/12/09
16. Pryanka, S., et al.: Secondary amenorrhea: causes, management and outcome using algorithmic approach. *IOSR J. Dent. Med. Sci.* **16**(5), 87–91 (2017)
17. Nakano, R., et al.: A schematic approach to the work-up of amenorrhea. *Fertil. Steril.* **28**(3), 229–236 (1977)
18. Mendelian: Fixing Diagnosis for Rare Diseases. <https://www.mendelian.co/>. Last accessed 2018/12/09
19. DDxHub—Differential Diagnosis Hub. <https://blood-test.biz/>. Last accessed 2019/01/16

Acid-Resistant Capsules with Sugar Microneedles for Oral Delivery of Ascorbic Acid

Mirela Camović, Amila Bišćević, Iman Brčić, Kana Borčak, Sadžida Bušatlić, Nejra Čenanović, Anida Dedović, Alen Mulalić, Merima Sirbubalo, Amina Tucak, and Edina Vranić

Abstract

Oral delivery is one of the most common ways of drug administration because of its simplicity. However, this method of delivery can be limited for many drugs like peptides or proteins. Scientists have been trying to enable oral delivery of this kind of structures for decades. Because intestine does not have sharp pain receptors like skin, the insertion of microneedles would not be painfully. Modelled by previous research, we tried to formulate sugar microneedles that contain active substance (ascorbic acid) and incorporate them into the acid-resistant capsules. We have chosen sugar because of its ability to dissolve into the intestine. 3D printed microneedles were used as a model for the preparation of different silicon molds. These molds were used for sugar microneedles. Different types of sugar showed different types of performance, for example, a combination of two sugars resulted to be the best in our case. Our next step after successfully produced sugar microneedles is focused on their ability to dissolve into the intestine. Using acidic and basic medium we have examined the behavior of the sugar microneedles formulation that we put into acid-resistant capsules.

Keywords

Oral drug delivery • Sugar microneedles • Silicon molds • Acid-resistant capsules

1 Introduction

Oral drug delivery is one of the most common ways of using medicines that prefer both doctors and patients. However, this administration may be limited due to poor absorption, as well as degradation of certain drugs. It especially poses a challenge for biological drugs (e.g. insulin, nucleic acid and monoclonal antibodies) that are highly susceptible to proteases, endonucleases, bacteria and pH that prevails in the gastrointestinal tract (GIT). Therefore, these medications require application by parenteral injections. In an attempt to provide oral delivery of earlier mentioned macromolecules as well as other sensitive drugs, microneedle-based technology has been developed [1].

The microneedles (MNs) are solid or hollow tubes whose length is 50–900 μm and the outer diameter is generally smaller than 300 μm . In order to respond to different therapeutic requirements, and to optimize the drug's degree or site of delivery, MNs may have a different shape, size and density per unit of support or adhesive membrane surface. MNs are manufactured from metals [2], silicones [3], polymers [4], glass and other materials [5].

Making drug delivery safe is one of the most common aspects of research. Using natural sugars as ingredients can be a good way of improving drug delivery. Due to its safeness for human health and its profile to digest in the biological system, sugar may be used as excipients for drug delivery [6–8]. Existing methods for drug delivery by sugars are passive drug targeting by which pharmaceutical material is delivered to targeted tissues or organs with lesion utilizing transport properties of material coated with or containing sugars; and active drug targeting by which pharmaceutical material is delivered selectively to targeted cells utilizing the selective sensitivity of the cells to the molecular structure of sugars [9].

Conducted studies have shown that biodegradable MNs have been fabricated from sugars such as sucrose, trehalose [10], and maltose [9, 11]. In many studies, maltose as a safe

M. Camović (✉) · A. Bišćević · I. Brčić · K. Borčak · S. Bušatlić · N. Čenanović · A. Dedović · A. Mulalić
Faculty of Pharmacy, University of Sarajevo, Zmaja od Bosne 8, 71000 Sarajevo, Bosnia and Herzegovina
e-mail: mirela.camovic@hotmail.com

M. Sirbubalo · A. Tucak · E. Vranić
Department of Pharmaceutical Technology, Faculty of Pharmacy, University of Sarajevo, Zmaja od Bosne 8, 71000 Sarajevo, Bosnia and Herzegovina

excipient may be utilized as a drug delivery system [11]. The studies so far were based on transdermal drug delivery [9, 11] but we tried to go a step forward and tried oral drug delivery with sugar MNs. This way of delivering drug is less painfully and has more efficient absorption. In addition, it is safe due to ingestible materials such as sugars.

The MNs are poured with selective pH-sensitive coatings (sugar) and inserted into the gastro-resistant capsules. The delivery of the drug takes place from the inner core of the capsule to the target tissue [12]. In this study, we used 3D printed MNs that were imprinted in silicone. Silicone served as a mold for pouring sugar. We tested four types of sugar: maltose, sucrose, fructose and glucose.

It is necessary for this form to show acceptable bioavailability and to safely pass through the GIT. For capsules containing MNs, it has been proven that they can safely pass through and get out of the GIT [1]. Patients would not feel any pain while taking the drug because there are no pain receptors in the GIT [13]. Advantages of the application of MNs are [11]: fast drug delivery to the systemic circulation, the absence of pain, and it is not invasive delivery. MNs defect: weighing the precision of the dosage.

2 Materials and Methods

2.1 Materials

Protesil putty (Vannini Dental Industry, Italy); ProtesilCatalyst gel (Vannini Dental Industry, Italy); HydroXtreme putty soft base (Swiss Tec); HydroXtreme putty soft catalyst (Swiss Tec); Protesil light (Vannini Dental Industry) have been used for preparation of silicone molds. Glucose (DM Drogerie Markt, Germany); Fructose (Bio Una, Serbia); Maltose (Himedia Laboratories Pvt, India); Sucrose (DM Drogerie Markt, Germany); ascorbic acid (DM Drogerie Markt, Germany) have been used for sugar MNs formulations. DRcaps #1 natural transparent (CAPSUGEL, Switzerland)

were kindly donated by CAPSUGEL. 3D printed PLA MNs (ULTIMAKER +2) were used for silicone mold preparation. All other reagents and chemicals used were of analytical grade or pharmacopeial grade.

2.2 Mold Making

5 g of silicone HydroXtreme putty soft base and HydroXtreme putty soft catalyst were used for M1 mold (Fig. 3a). We used 5 g of silicone that was made of Protesil putty and Protesil-Catalyst gel to make M2 mold (Fig. 3b). 5 g of Protesil catalyst gel and Protesil light were used for M3 mold (Fig. 3c). As a template for making molds, we used 3D printed MNs. At room temperature, 3D printed MNs were plunged into this amount of silicone and then removed after 3 min. In this way, prepared molds were ready to be filled with sugar for forming MNs.

2.3 Forming Sugar Microneedles

For the production of the sugar MNs, we used four types of sugar: glucose, fructose, sucrose and maltose. We were looking for the best possible formulation by mixing sugars in different proportions. A certain amount of sugar has been measured on an analytical scale, and then transferred to the metal paten. Sugar was melted on the electric heater in order to obtain the appropriate consistency to make the filling of sugar in the molds easier. After about 3 min, they were ready to be pulled out of molds. We tried nine combinations of sugars and ascorbic acid (Table 1):

1. 1 g of sucrose and 0.15 g ascorbic acid,
2. 1 g fructose and 0.15 g ascorbic acid,
3. 1 g glucose and 0.15 g ascorbic acid,
4. 1 g fructose with 1 g maltose and 0.3 g ascorbic acid,
5. 1 g fructose with 1 g glucose and 0.3 g ascorbic acid,

Table 1 Results of sugar combinations for making MNs

MNs	Sugar (g)	Ascorbic acid (g)	Result
F1	1 g sucrose	0.15 g	Unsuccessfully
F2	1 g fructose	0.15 g	Successfully
F3	1 g glucose	0.15 g	Successfully
F4	1 g fructose and 1 g maltose	0.3 g	Successfully
F5	1 g fructose and 1 g glucose	0.3 g	Successfully
F6	1 g glucose and 1 g maltose	0.3 g	Successfully
F7	0.5 g fructose, 0.5 g glucose and 0.5 g maltose	0.3 g	Successfully
F8	1 g fructose and 1 g glucose	0.3 g	Successfully
F9	0.5 g fructose, 0.5 g glucose, 0.5 g maltose and 0.5 g sucrose	0.3 g	Unsuccessfully

F = formulation

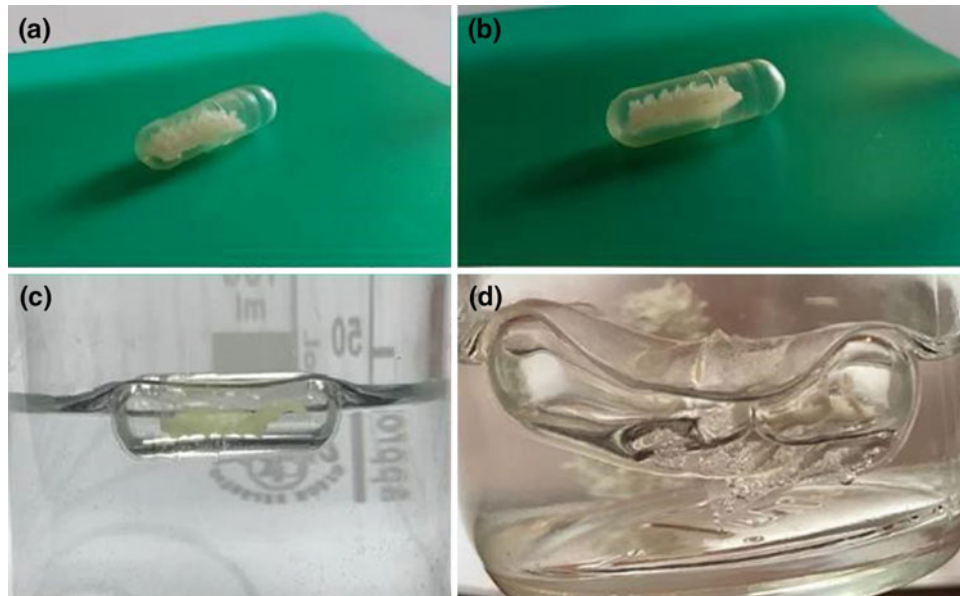


Fig. 1 Experiment in acidic and base medium **a1** acid resistant capsule with sugar MNs, **a2** capsule into the acidic medium and **b1** acid resistant capsule with sugar MNs, **b2** capsule into the basic medium

6. 1 g maltose with 1 g glucose and 0.3 g ascorbic acid,
7. 0.5 g fructose with 0.5 g glucose and 0.5 g maltose and 0.3 g ascorbic acid,
8. 1 g fructose with 1 g maltose and 0.3 g ascorbic acid,
9. 0.5 g maltose with 0.5 g glucose, 0.5 g fructose, 0.5 g sucrose and 0.3 g ascorbic acid.

2.4 Experiment with Acidic and Basic Medium

Acid resistant DRcaps #1 capsules with different sugar MNs were dipped in HCl to test their ability to stay intact in acidic medium (Fig. 1a1). After that, we prepared a phosphate buffer containing disodium hydrogen phosphate, sodium chloride and sodium dihydrogen phosphate. The pH of this buffer was 6.8. We wanted to test in which time they would be dissolved. In the water bath at 37 °C, we put seven lab glasses with prepared buffer. In each was a capsule with a different type of sugar MNs (Fig. 1b2).

3 Results and Discussion

3.1 Formulation of Different Types of Sugar Microneedles

Many studies have shown that maltose was the most suitable type of sugar for MNs formulation [13]. However, in our working conditions, we were unable to achieve high temperature needed to completely dissolve maltose, and we tried to dissolve it at 100 °C, which did not produce a positive

result. There occurred caramelization, and burning of maltose. With sucrose, the problem was consistency, because it became dry and hard very fast. Therefore, we did not use these two sugars for further research. Glucose and fructose showed the best results because of its easy melting, mixing and filling the molds. Their consistency was very fluently compared to other combinations. After this experiment, we focused on possible combinations between fructose, glucose, and maltose. We decided to experiment with maltose because of many other positive results by recent studies [9, 11].

Sucrose MNs with ascorbic acid (F1) was unsuccessfully molded with molds M1, M2, and M3. The problem with this formulation was high consistency which did not allow us to manipulate with it. It got hardened too fast so the sugar did not penetrate the mold deep enough (Fig. 2a).

Fructose MNs with ascorbic acid (F2) were successfully molded with M1 and M2. This formulation was the easiest to handle because the sugar melted very fast and had very low consistency, which allowed us to make well-shaped MNs (Fig. 2b).

Glucose MNs with ascorbic acid (F3) were successfully molded with M2 (Fig. 2c) Glucose melted rapidly and easy. Compared to F2 this formulation gave not so precise MNs. But the formulation was in liquid shape long enough to enable us to fill the models. Glucose and fructose (F4) were one of the best formulations we got. This formulation presented to be the most promising because of its low consistency and time of hardening. Mixing those two sugars gave us better results than using them separately. The consistency was very low which allowed the sugar to penetrate deep into the mold and get us precise MNs (Fig. 2e).

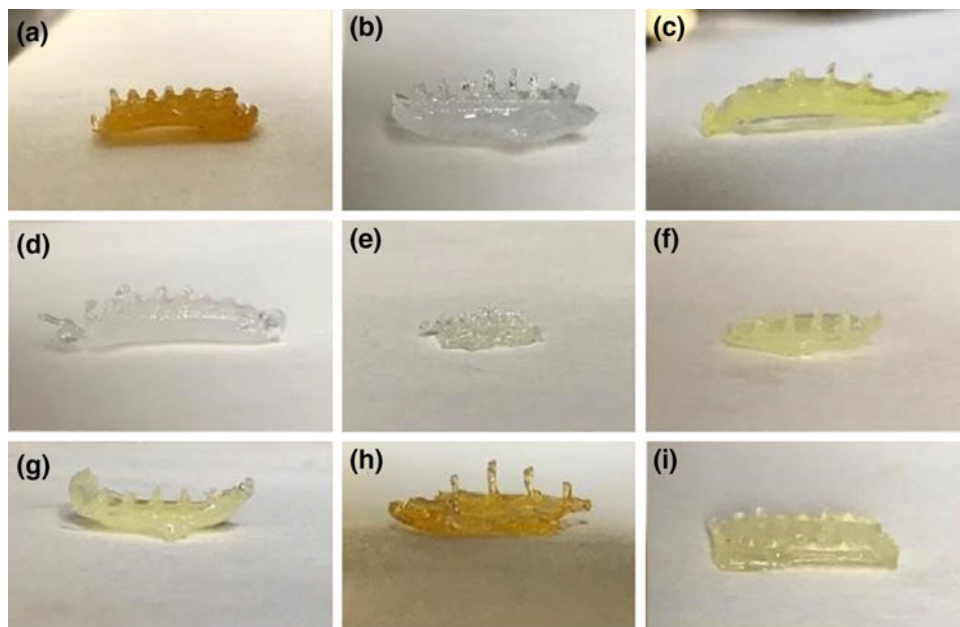


Fig. 2 Different types of sugar formulation MNs **a** sucrose, **b** fructose, **c** glucose, **d** fructose and maltose, **e** fructose and glucose, **f** glucose and maltose, **g** fructose, glucose and maltose, **h** fructose and glucose, **i** fructose, maltose, glucose and sucrose

Maltose in combination with one of these sugars (glucose and fructose) proved to be also a good method because we managed to melt maltose and make MNs of it. Separately we could not melt maltose at above 100 °C, but combining it with other sugars we were able to melt it and get a liquid formulation with good hardening time which allowed us to make a homogenous formulation (Fig. 2d, f, g, i).

Combination of maltose, glucose and fructose (F7) resulted to be also very promising method. Melting these three sugars, we realized that its structure has good features regarding its consistency or stability during filling and appearance (Fig. 2g).

3.2 Results of Using Different Types of Molds

Mold M1 (Fig. 3a) was similar to mold M2. The only difference was that mold M2 was more flexible for use. M2 (Fig. 3b) has been shown to be very stable so we were able to make very precise MNs but the problem with this mold was hard retrieval of MNs. M3 (Fig. 3c) resulted to be the easiest to use. Due to its flexible characteristics, we could easily take the MNs out, but the MNs did not look as good as in previous molds (M1 and M2).

3.3 Results of an Experiment in Acidic and Base Medium

After preparing our sugar MNs from a different type of sugars, we decided to use this experiment so we can test if our sugar MNs will stay intact till they arrive at the intestine. All sugar MNs were inserted into the acid resistant DRcaps #1 capsules and were dipped into an acidic medium with HCl. After 1 h our capsules stayed intact so we confirmed that this formulation will pass through the stomach. After that, we used phosphate buffer which was poured into the 7 lab glasses. We incubated them in the heated bath at 37 °C, to imitate the human organism. After 7 min F2 and F7 began melting. In the period of 40 min, all formulation of sugar MNs dissolved. We assume that the acid resistant DRcaps #1 capsules will reach the GI tract and the coating will dissolve, revealing the sugar MNs (middle). Then the

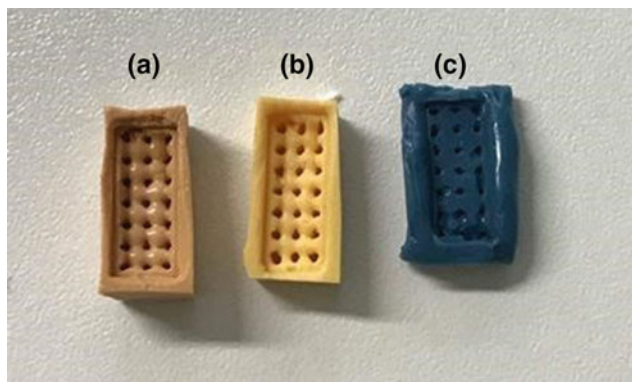


Fig. 3 Type of molds **a** M1 mold, **b** M2 mold, **c** M3 mold

sugar MNs will be compressed through peristalsis releasing the drug through the needles.

4 Conclusion

Sugar MNs for oral drug delivery is a promising replacement for peptides and proteins, which nowadays can only be used parenterally. Considering that all materials we used (molds, sugars, acid resistant capsules and 3D printed MNs) are cheap, accessible and easy to make (3D printed MNs and molds) we came to the conclusion that this way of technology will take a major part in future for oral delivery of macromolecules. This way of drug delivery technology brings also many questions, like what kind of effects will sugar MNs produced for a specific group of patients (patients with diabetes and insulin resistance). We assume that we can overcome this problem by making MNs with a combination of different sugars. If we want to do the complete characterization of this formulation, it would be necessary to do the dissolution test by Pharmacopoeial standards. We recognized there are many challenges ahead of us but we stayed focused on our mission.

Acknowledgements We would like to express our special gratitude to the CAPSUGEL® team from Zagreb for the generous donation. Appreciation to dentist Haris Izberović, DMD for help with making silicon molds in his laboratory and Maida Osmanlić for help with designing 3D printed microneedles.

Conflict of Interest Authors have no conflicts of interest to disclose.

References

1. Traverso, G., Schoellhammer, C., Schroeder, A., Maa, R., Lauwers, G., Polat, B., et al.: Microneedles for drug delivery via the gastrointestinal tract. *J. Pharm. Sci.* **104**(2), 362–367 (2014)
2. Ita, K.: Transdermal delivery of drugs with microneedles: strategies and outcomes. *J. Drug Deliv. Sci. Tech.* **29**, 1623 (2015)
3. Hartmann, X.H.M., van der Linde, P., Homburg, E.F.G.A., van Breemen, L.C.A., de Jong, A.M., Luttge, R.: Insertion process of ceramic nanoporous microneedles by means of a novel mechanical applicator design. *Pharmaceutics* **7**(4), 503–522 (2015)
4. Zhang, Y., Jiang, G., Hong, W., Gao, M., Xu, B., Zhu, J., et al.: Polymeric microneedles integrated with metformin-loaded and PDA/LA-coated hollow mesoporous SiO₂ for NIR-triggered transdermal delivery on diabetic rats. *ACS Appl. Bio Mater.* 2018 (In press)
5. Vučen, S., Pajić, N., Savić, S., Vuleta, G.: Mikroigle-fizički pojačivači (trans) dermalne isporuke lijekova. *Arhiv za farmaciju* **64**, 295–321 (2014)
6. Duverger, E., Carpentier, V., Roche, A.C., Monsigny, M.: Sugardependent nuclear import of glycoconjugates from the cytosol. *Exp. Cell Res.* **207**(1), 197–201 (1993)
7. Takakura, Y., Hashida, M.: Macromolecular carrier systems for targeted drug delivery: pharmacokinetic considerations on biodistribution. *Pharm. Res.* **13**, 820 (1996)
8. Mogusala, N.R., Devadasu, V.R., Venisetty, R.K.: Fabrication of microneedle molds and polymer based biodegradable microneedle patches: a novel method. *Am. J. Drug Deliv. Ther.* **2**(2), 2349–7211 (2015)
9. Miyano, T., Tobinaga, Y., Kanno, T., Matsuzaki, Y., Takeda, H., Wakui, M., et al.: Sugar micro needles as transdermic drug delivery system. *Biomed. Microdevice* **7**(3), 185–188 (2005)
10. Martin, C.J., Allender, C.J., Brain, K.R., Morrissey, A., Birchall, J. C.: Low-temperature fabrication of biodegradable sugar glass microneedles for transdermal drug delivery applications. *J. Controlled Release* **158**(1), 93–101 (2012)
11. Nguyen, H.X., Banga, A.K.: Fabrication, characterization and application of sugar microneedles for transdermal drug delivery. *Ther. Deliv.* **8**(5), 249–264 (2017)
12. MIT Technology Licensing Office: Microneedle Pill for Enhanced Oral Delivery of Protein and Nucleic Acid Drugs. Available at <https://tlo.mit.edu/technologies/microneedle-pill-enhanced-oral-delivery-protein-and-nucleic-acid-drugs> (2018). Accessed 9 Dec 2018 [online]
13. Trafton, A.: New drug-delivery capsule may replace injections. MIT News Office. Available at <http://news.mit.edu/2014/microneedles-drug-delivery-capsule-1001> (2014). Accessed 9 Dec 2018 [online]

Effect of Commercially Available Synthetic Insulin on the Biofilm Formation in *S. aureus* and *E. coli* Bacterial Strains

Jasmin Novalić and Berina Bektić

Abstract

Biofilms are microorganisms that play a huge role in various fields of study. Bacterial ability for biofilm formation can be examined in the presence of different host substances which may affect the biofilm formation capability in different ways. Synthetically used hormones are substances used by patients in order to supply their hormonal deficit. One of the most widely used synthetically-produced hormones is insulin. The hormone is used for treatment of diabetes patients. In our study we examined the antibacterial effect of several V/V solutions of commercially available insulin as well as the biofilm forming capacity for the following bacterial strains: *Staphylococcus aureus* ATCC 25923, *Escherichia coli* ATCC 25922, a clinical strain of *Escherichia coli* and a clinical strain of methicillin-resistant *Staphylococcus aureus* (MRSA). The results of our study showed that insulin detemir does not have any antibacterial capabilities for the four tested bacterial strains. The results also indicate that *Staphylococcus aureus* ATCC 25923 mixed with a V/V insulin detemir diluted suspension at all tested concentrations (from 10% to 10⁻⁸%) elevated biofilm formation while the other three tested strains showed no change in biofilm formation upon addition of insulin. This refers to a utilization process of the insulin detemir suspension from the three mentioned bacterial strains. From this it is evident that the effect different drugs have on the biofilm forming capacity of bacteria is significant in ordinating therapy for patients who take the drug of choice on a regular basis.

Keywords

Biofilms • Hormones • Bacteria • Insulin

1 Introduction

When the adequate growth conditions and requirements are obtained, the presence of bacterial species is indisputable all over the Earth [1]. An extensive percentage of these bacteria (over 99.9%) are highly capable of the formation of biofilms, either on biological or non-biological surfaces. In that case, the biofilm serves as the bacteria's natural state of being [2], which implies the fact that bacteria, encompassed by all other microorganisms, possess the greatest colonization ability [3]. Considering the fact that the resistance against antimicrobials is elevated [5–7], biofilms developed a high level of concern among the Science World, therefore the interest for biofilm examination has tremendously expanded [4].

Because of the activating effect that several antibiotic substances have on the formation of biofilms, the urgency of researches that incorporates different antimicrobial as well as anti-biofilm effect of different substances [8] is created in order to clear up the issue. All individuals, who are due to everyday life circumstances exposed to major infections, are unprotected to a large number of foreign substances which increase the biofilm formation capacity. An example of such substances are synthetically hormones for different kinds of therapies. The most predominant and ubiquitous of those hormones is insulin [9]. The usual procedure implemented to maintain control of the levels of glucose in humans blood system, for those who are not able to metabolize glucose by themselves, is via treatment with basal insulin which is taken with any meal [10]. Insulin detemir is a type of basal insulin. Along with an another type of long-acting (basal) insulin, called insulin glargine, insulin detemir is the only insulin accepted for utilization as a basal therapy for type 1 and type 2 diabetes patients [10, 11].

The goal the following study was to determine any change in the capability of the biofilm formation for of the following pathogenic bacterial strains: *Staphylococcus aureus* ATCC 25923, *Escherichia coli* ATCC 25922, a clinical strain of

J. Novalić (✉) · B. Bektić
 Department of Genetics and Bioengineering,
 International Burch University, Sarajevo, Bosnia and Herzegovina
 e-mail: jasminnovalic@yahoo.com

Escherichia coli and a clinical strain of methicillin-resistant *Staphylococcus aureus* (MRSA) in surrounding with a synthetically produced insulin hormone (insulin detemir) suspension which is regularly used in commercial, clinical or personal purposes.

2 Methods

2.1 Bacterial Strands

The organisms that were tested constituted cultures of: *Staphylococcus aureus* ATCC 25923, *Escherichia coli* ATCC 25922, a clinical strain of *Escherichia coli* and clinical strain of methicillin-resistant *Staphylococcus aureus* (MRSA) in Lauria Bertani (LB) Broth enhanced by 50% glycerol and kept at a temperature of -80°C . The recovery of those bacterial strains from glycerol was performed by plating on Blood Agar medium, optimal for the bacterial growth after which an incubation step happened. The incubation was done at 37°C and took a whole night followed by another overnight incubation step in Tryptic Soy Broth (TSB) enhanced by 1% glucose.

2.2 Hormonal V/V Solutions

The tested hormonal solution included:

1. Insulin suspension; generic name: Insulin detemir; brand name: Levemir; commercially available suspension; ready for use ($C_{\text{initial}} = 100 \text{ iU/ml}$, 14.2 mg/ml). The tested hormonal solution was diluted in a sterile environment in a highly concentrated ethanol solution (96%) as a V/V solution as follows: 10; 1; 10^{-1} ; 10^{-2} ; 10^{-3} ; 10^{-4} ; 10^{-5} ; 10^{-6} ; 10^{-7} ; $10^{-8}\%$.

2.3 Antibacterial Testing

E. coli ATCC 25922 in liquid medium broth, where the density of the bacterial solution was regulated to 0.5 McFarland standard for the determination of turbidity of bacterial suspensions was inoculated into the hormonal V/V solution of insulin detemir, diluted in 96% ethanol, ranging from 10 to $10^{-8}\%$ of the initial insulin detemir concentration. After the overnight incubation process, the load of every tube was inoculated onto a Plate Count Agar and afterwards incubated overnight again. The assessment of bactericidal action of the tested hormonal solutions was analyzed in line with the presence of bacterial development on Plate Count Agar.

2.4 Testing of the Effect of Hormonal V/V Solution on *Staphylococcus aureus* ATCC 25923, *Escherichia coli* ATCC 25922, a Clinical Strain of *Escherichia coli* and a Clinical Strain of Methicillin-Resistant *Staphylococcus aureus* (MRSA)

The capability of the biofilm formation was tested by applying the Tissue culture Plate Method (TCP). Five microlitres of the bacterial culture, which was incubated overnight and grown in Tryptic Soy Broth and enriched with 1% glucose with a density of 0.315 (Abs.) at OD 600. were combined to a final V/V hormonal suspension with a concentration of $90 \mu\text{l}$. At the time of a 48 h incubation time, the cultures were tapped and washed with Phosphate Buffer Saline solution. The solution was left to dry. Afterwards, the wells were filled with $125 \mu\text{l}$ of 0.1% crystal violet solution, and then cleaned after the incubation process lasted. The biofilms which were formed were all read at OD 600 on ELISA plate reader.

Samples which contained only Tryptic Soy Broth and examined V/V hormonal suspension were tested in quadruplets and gave values for the negative controls which were subtracted from the average value of the wells filled with the tested bacterial strains inoculated in observed V/V hormonal suspensions in Tryptic Soy Broth.

Wells which weren't inoculated, also in quadruplet were utilized for obtaining results for the values of the negative control. Biofilm forming capability of the tested bacterial strains was further calculated per formulas: non-adherent $\text{OD} < \text{ODc}$, weak $\text{ODc} < \text{OD} \leq 2\text{ODc}$, moderate $2\text{ODc} < \text{OD} \leq 4\text{ODc}$ and strong $4\text{ODc} < \text{OD}$.

The calculation of ODc, the cut off value, was done by the following formula:

$$3 \times STDEV \text{ neg. control} + AVGOD \text{ of negative control} \quad (1)$$

3 Results

3.1 Antibacterial Activity of Insulin Detemir V/V Solutions in Tested Bacterial Strains

The growth of bacteria was noticed in all bacterial strains combined with the V/V solutions of the hormonal suspension at all concentrations tested in this study (Table 1).

3.2 Biofilm Formation Activity and Capability

A change in biofilm category for *S. aureus* ATCC 25923 upon addition of insulin V/V solution from NA to W occurred at the concentrations: 1 and $10^{-3}\%$.

Table 1 Antibacterial activity of tested bacterial strains combined with the V/V solution of insulin detemir

V/V solution concentration (%)	<i>Staphylococcus aureus</i> ATCC 25923,	Clinical strain of <i>Escherichia coli</i> ,	<i>Escherichia coli</i> ATCC 25922,	Methicillin resistant <i>Staphylococcus aureus</i> (MRSA)
10	Growth	Growth	Growth	Growth
1	Growth	Growth	Growth	Growth
10 ⁻¹	Growth	Growth	Growth	Growth
10 ⁻²	Growth	Growth	Growth	Growth
10 ⁻³	Growth	Growth	Growth	Growth
10 ⁻⁴	Growth	Growth	Growth	Growth
10 ⁻⁵	Growth	Growth	Growth	Growth
10 ⁻⁶	Growth	Growth	Growth	Growth
10 ⁻⁷	Growth	Growth	Growth	Growth
10 ⁻⁸	Growth	Growth	Growth	Growth

A change in biofilm category for *S. aureus* ATCC 25923 upon addition of insulin V/V solution from NA to M occurred at the concentrations: 10⁻⁵, 10⁻⁶, 10⁻⁷, 10⁻⁸%.

No change occurred in biofilm category upon addition of insulin at all other tested insulin concentrations for methicillin-resistant *Staphylococcus aureus* (MRSA) *Escherichia coli* ATCC 25922 and Clinical strain of *Escherichia coli*. (see Table 2)

4 Discussion and Conclusion

Biofilms represent communities of microorganisms with the greatest colonization abilities between all other microorganism species, because of their omnipresence in nature [13].

Biofilms, among all other specifications and abilities, are also accountable for a large number of diseases [14]. Regardless of the mentioned fact, the testing of the bacterial capability on biofilm formation is not very present in everyday practice [15]. The number of diabetes patients grows rapidly, so does the usage of commercially available insulin [16]. The asperity and time consumption of insulin action during the time of infections are not known, because the grade of insulin resistance has not been compared to any other cases, also resistant to this hormone. The reasons for the resistance to insulin while acute infections occur are also unclear [17].

The overall approach for the examination of biofilm formation capability of various bacterial strains was to measure the bacterial residues on the wells after a 48 h

Table 2 The effect of different concentrations of the V/V solutions of insulin detemir on the biofilm production potential of the four tested bacterial strains

V/V solution concentration of Insulin detemir C _{initial} = 100 iU/ml	<i>Staphylococcus aureus</i> ATCC 25923		Clinical strain of <i>Escherichia coli</i>		<i>Escherichia coli</i> ATCC 25922		Methicillin resistant <i>Staphylococcus aureus</i> (MRSA)	
	Mean Abs.	Biofilm	Mean Abs.	Biofilm	Mean Abs.	Biofilm	Mean Abs.	Biofilm
(-) Control	0.107	N/A	0.107	N/A	0.107	N/A	0.017	N/A
(+) Control	1.6895	S	0.357	N/A	0.36929	N/A	0.30875	N/A
10	0.35425	N/A	0.2775	N/A	0.05525	N/A	0.0115	N/A
1	0.1975	W	0.0635	N/A	0.00975	N/A	0.05175	N/A
10 ⁻¹	0.13575	N/A	0.01575	N/A	0.0255	N/A	0.021	N/A
10 ⁻²	0.127	N/A	0.0215	N/A	0.0195	N/A	0.017	N/A
10 ⁻³	0.20425	W	0.01075	N/A	0.02325	N/A	0.0035	N/A
10 ⁻⁴	0.24375	N/A	0.005	N/A	0.054	N/A	-0.03475	N/A
10 ⁻⁵	0.315	M	0.03275	N/A	0.06275	N/A	-0.004	N/A
10 ⁻⁶	0.3385	M	0.0315	N/A	0.04975	N/A	-0.00725	N/A
10 ⁻⁷	0.43475	M	0.0565	N/A	0.0585	N/A	-0.00425	N/A
10 ⁻⁸	0.9215	M	0.05775	N/A	0.02325	N/A	-0.024	N/A

N/A non-adherent; W weak; M medium; S strong

incubation time mixed with a V/V insulin detemir hormonal suspension. The measurement was performed on the ELISA plate reader. The *S. aureus* bacterial strain showed possession of the ability of biofilm formation in various host tissues [18]. The results of our study showed no antibacterial effect for all the V/V solutions of the hormonal suspension at all concentrations tested in this study (from 10 to 10⁻⁸%). *Staphylococcus aureus* ATCC 25923 bacterial strain in an environment with a present insulin detemir hormone solution showed the ability of biofilm formation. Based on the data obtained, the largest biofilm forming ability was shown at a hormonal concentration of 10⁻⁸%. That refers that a moderate type of biofilm was formed, when 1.42 × 10⁻⁹ mg/ml hormonal suspension of insulin detemir was present. A change in biofilm category for *S. aureus* ATCC 25923 upon addition of insulin V/V solution from non-adherent to weak occurred at the concentrations: 1% and 10⁻³%. A change in biofilm category for *S. aureus* ATCC 25923 upon addition of insulin V/V solution from non-adherent to moderate occurred at the concentrations: 10⁻⁵, 10⁻⁶, 10⁻⁷ and 10⁻⁸%.

The three other tested bacterial strains: *Escherichia coli* ATCC 25922, a clinical strain of *Escherichia coli* and methicillin-resistant *Staphylococcus aureus* (MRSA) haven't shown any change in biofilm category in the presence of a hormonal suspension of insulin detemir. At several tested insulin hormone concentrations, the results showed that methicillin-resistant *Staphylococcus aureus* (MRSA) gives no change in biofilm forming category.

The negative results of *Escherichia coli* ATCC 25922, a clinical strain of *Escherichia coli* and methicillin-resistant *Staphylococcus aureus* (MRSA) are indicating that those bacterial strains utilized insulin. Even though the study of the insulin degradation has been examined for a long time, meaningful conclusions are present since only 1980s [19].

The limitation of our study was the number of bacterial samples analyzed, which leads to more representative results in correlated to the results from referent bacterial strains. According to other literature, the hypothesis that biofilm formation is dependent of the concentration of the same substance was proved [20].

The observing of biofilms is a very under-examined field of study with a high development rate since a large number of unexamined substances which can affect the formation of biofilms are existing. Altogether, this study has stressed that synthetically basal insulin hormone used by diabetes patients can lead to higher biofilm formation rate in patients infected with *Staphylococcus aureus* bacterial strain. Therefore, the

more studies should be done to test the effect different substances have on the biofilm forming capacity of bacteria, considering that biofilms represent the natural state of bacteria.

References

1. Fenchel, T., Finlay, B.J.: The ubiquity of small species: patterns of local and global diversity. *BioScience* **54**(8), 777–784 (2004). [https://doi.org/10.1641/0006-3568\(2004\)054%5b0777:TUOSSP%5d2.0.CO;2](https://doi.org/10.1641/0006-3568(2004)054%5b0777:TUOSSP%5d2.0.CO;2)
2. Vu, B., Chen, M., Crawford, R. J., Ivanova, E.P.: Bacterial extracellular polysaccharides involved in biofilm formation. *Molecules* **14**(7), 2535–2554 (2009). <http://www.mdpi.com/1420-3049/14/7/2535>
3. Estela, C.R.L., Alejandro, P.R.: Biofilms: a survival and resistance mechanism of microorganisms. In: Antibiotic resistant bacteria—a continuous challenge in the new millennium. InTech (2012). https://scholar.google.com/scholar?hl=en&as_sdt=0%2C5&q=Biofilms%3A+a+survival+and+resistance+mechanism+of+microorganisms&btnG=
4. Merritt, J.H., Kadouri, D.E., O'Toole, G.A.: Growing and analyzing static biofilms. *Curr. Protoc. Microbiol.* **22**(1), 1B-1 (2011). <https://currentprotocols.onlinelibrary.wiley.com/doi/abs/10.1002/9780471729259.mc01b01s22>
5. Mah, T.F.C., O'toole, G.A.: Mechanisms of biofilm resistance to antimicrobial agents. *Trends Microbiol.* **9**(1), 34–39 (2001)
6. Xu, K.D., McFeters, G.A., Stewart, P.S.: Biofilm resistance to antimicrobial agents. *Microbiology* **146**(3), 547–549 (2000)
7. Høiby, N., Bjarnsholt, T., Givskov, M., Molin, S., Ciofu, O.: Antibiotic resistance of bacterial biofilms. *Int. J. Antimicrob. Agents* **35**(4), 322–332 (2010)
8. Lesouhaitier, O., Clamens, T., Rosay, T., Desriac, F., Louis, M., Rodrigues, S., Gannesen, A., Plakunov, V.K., Bouffartigues, E., Tahrioui, A., Bazire, A.: Host peptidic hormones affecting bacterial biofilm formation and virulence. *J. Innate Immun.* **5**, 1–5 (2018 Nov)
9. Klosowska, K., Plotkin, B.: Human insulin modulation of *Escherichia coli* adherence and chemotaxis. *Am. J. Infect. Dis.* **2**(4), 197–200 (2006)
10. Goldman-Levine, J.D., Lee, K.W.: Insulin detemir—a new basal insulin analog. *Ann. Pharmacother.* **39**(3), 502–507 (2005)
11. Barnett, A.H.: Insulin glargine in the treatment of type 1 and type 2 diabetes. *Vasc. Health Risk Manag.* **2**(1), 59 (2006)
12. Chopra, S.S.: Industry funding of clinical trials: benefit or bias? *JAMA* **290**(1), 113–114 (2003 Jul 2)
13. Anderl, J.N., Franklin, M.J., Stewart, P.S.: Role of antibiotic penetration limitation in *Klebsiella pneumoniae* biofilm resistance to ampicillin and ciprofloxacin. *Antimicrob. Agents Chemother.* **44**(7), 1818–1824 (2000)
14. Müller, F.M.C., Seidler, M., Beauvais, A.: *Aspergillus fumigatus* biofilms in the clinical setting. *Med. Mycol.* **49**(Supplement_1), S96–S100 (2011)
15. Mackintosh, D., Coleman, K., Davies, A.J.: Mitogenic activity of insulin in the culture of a trypanosome: duration and dose response. *Cell Biol. Int.* **27**(1), 75–78 (2003)

16. Geerlings, S.E., Meiland, R., Hoepelman, A.I.: Pathogenesis of bacteriuria in women with diabetes mellitus. *Int. J. Antimicrob. Agents* **19**(6), 539–545 (2002)
17. Yki-Järvinen, H.A.N.N.E.L. E., Sammalkorpi, K., Koivisto, V.A., Nikkilä, E.A.: Severity, duration, and mechanisms of insulin resistance during acute infections. *J. Clin. Endocrinol. Metabol.* **69**(2), 317–323 (1989)
18. Boles, B.R., Horswill, A.R.: Agr-mediated dispersal of *Staphylococcus aureus* biofilms. *PLoS Pathogens* **4**(4), e1000052 (2008)
19. Becker, A.B., Roth, R.A.: Insulysin and pitrilysin: insulin-degrading enzymes of mammals and bacteria. In: *Methods in Enzymology*, vol. 248, pp. 693–703. Academic Press (1995)
20. Rachid, S., Ohlsen, K., Witte, W., Hacker, J., Ziebuhr, W.: Effect of subinhibitory antibiotic concentrations on polysaccharide intercellular adhesin expression in biofilm-forming *Staphylococcus epidermidis*. *Antimicrob. Agents Chemother.* **44**(12), 3357–3363 (2000)

Use of Biosensors in Diabetes Monitoring: Medical and Economic Aspects

Haris Hadžović, Minela Alić, Anida Dedović, Anesa Sušić, Berina Tatlić, Zerina Zorlak, Nermina Žigić, Maja Malenica, and Tamer Bego

Abstract

Over the past ten years, technology has been developed to the point, where it can enable continuous and efficient monitoring of blood glucose levels for patients with diabetes mellitus. The biggest step forward was demonstrated by biosensors, which, with a non-invasive approach, provide healthcare workers with the information required for good titration of insulin doses. We looked at the benefits of using biosensors in diabetes monitoring in terms of medical aspect and economic justification of replacing traditional test strips with biosensors. In this paper, we have shown potential benefits in terms of improving diabetes control, patient benefits, and how the medical benefit is collerating with the economic viability of biosensors use. On the territory of Bosnia and Herzegovina test strips for glucose control are still in use. This paper includes an analysis of the costs of traditional monitoring and monitoring using biosensors. We also reviewed the monitoring of diabetes in neighboring countries such as Croatia, Slovenia, Montenegro, and Serbia in order to compare them with the current situation in Bosnia and Herzegovina.

Keywords

Biosensors • Diabetes mellitus • Glucose monitoring • Economy

1 Introduction

Diabetes mellitus is one of the biggest health issues in the world's health care system. According to the World Health Organisation, the global prevalence of diabetes mellitus has

risen from 4.7 to 8.5% among adults since 1980 [1]. Diabetes mellitus is a disease resulting in abnormal metabolism of carbohydrates and a rising level of glucose in blood causing a condition called hyperglycemia. The Body's ability to produce or respond to the hormone insulin is impaired due to pancreatic cell damage or the complete absence of insulin excretion. Worldwide it is a leading cause of heart disease, stroke, blindness, kidney failure, and lower limb amputation. A conventional way of measuring glucose levels in blood is via a glucometer. This method is becoming less effective and very uneconomic [2, 3].

In order to maintain normal blood glucose levels, biosensors began to be increasingly used for continuous monitoring of the level of glucose in the blood. Biosensors are analytical devices containing a biological sensory element. They show sensitivity and specificity with complex analytical measurements making them easier to run. Glucose biosensors account for approximately 85% of the world's market for biosensors [4, 5]. Great economic prospects are associated with the management of diabetes, in order to provide a reliable and tight glycemic control. Glucose oxidases (Gox) based amperometric enzyme electrodes, have played a major role in the simple and easy-to-use, blood sugar measurement and are expected to play a similar role in continuous glucose monitoring. Many different approaches have been explored in the glucose enzyme electrodes working mechanisms. Such devices offer great promise in addition to diabetes control and also for other important applications [6–8]. Despite many impressive advances in the design and use of glucose biosensors, there are still major challenges in achieving clinically accurate continuous glycemic monitoring. Monitoring of diabetes mellitus is the first example of individualized medicine [5, 9].

Furthermore, this research will discuss electrochemical biosensors for measurements of glucose levels in blood, their configuration and also challenges that are faced for the improvement of their mechanism of action and further development.

H. Hadžović (✉) · M. Alić · A. Dedović · A. Sušić · B. Tatlić · Z. Zorlak · N. Žigić · M. Malenica · T. Bego
Faculty of Pharmacy, University of Sarajevo, Zmaja od Bosne 8,
71 000 Sarajevo, Bosnia and Herzegovina
e-mail: harishadzovic@ffsa.unsa.ba

In Bosnia and Herzegovina, biosensors are not approved as opposed to EU members such as Croatia and Slovenia. For a detailed overview of the glucose monitoring status in the region see Appendix 1 [10–13].

2 Glucose Monitoring

2.1 Traditional Glucose Monitoring

In the traditional glucose monitoring mode, a glucometer (electronic device), a glucose strip and a lancet (a skin cleanser) are used.

For patients with Type 1 diabetes, insulin-dependent patients, it is recommended to measure blood glucose several times a day. Health workers, according to the current health status of the patient, his gender, age, and physical activity, determine the time to measure blood glucose. The recommendations are as follows:

- Before each meal
- 1/2 after meals
- At midnight
- Before physical activity
- During and after physical activity
- If a patient believes that blood glucose is oscillating
- When a patient is ill or under stress [14].

According to the NICE guidelines type 1 diabetes mellitus patients should measure their blood glucose levels 4–10 times a day [15].

2.2 Biosensors

Biosensors are analytical devices used for quantification of an analyte by biorecognition (binding of an analyte on a bioelement) and then they convert this biological response into a measurable signal [16]. The main parts of these devices are:

1. Biorecognition element—detects bioelements (enzymes, antibodies ...). It can be:
 - Metabolic—measures the change in the concentration of one of the substrates or products;
 - Affinity—measures the binding of analyte and bioelement;
 - Catalytic—measures the change in the auxiliary substrate [17].
2. Transducer—translates physical or chemical signals into an electrical signal. It can be:

- Electrochemical—measures the motion of the electrons when a certain potential is applied (potentiometric, voltammetric, amperometric);
 - Optical—it can be colorimetric (measures absorption of light) and photometric (measures fluorescence or illumination with a photomultiplier or photodiode detector);
 - Piezoelectric—change in frequency is proportional to absorbed material mass [18].
3. A signal processing system that reads and interprets the result.

The immobilization techniques used for connecting the biorecognition element and transducer/sensor are:

- Physical interaction (adsorption);
- Matrix immobilization;
- Membrane immobilization;
- Covalent bonding.

CGM systems (continuous glucose monitoring) measures glucose in blood and in subcutaneous tissue, but due to possible thromboembolism and contamination of electrodes with proteins and coagulation factors, measurements in blood are not usually performed. It measures glycemic changes during the day, which allows the prediction of hypo/hyperglycemia, also it can be connected to an insulin pump and thus having the function of an artificial pancreas. The disadvantage is that it is invasive and causes tissue inflammation that directly affects the results [19, 20].

In practice, several methods of minimally invasive measurement are used:

- enzymatic transcutaneous electrodes (CGMS MiniMed)
- Microdialysis (GlucoDay Menarini)
- Reverse iontophoresis (GlucoWatch Cygnus) [21].

Biosensors available on the market.

The development of biosensors for measuring blood glucose levels has contributed to a much easier way of life for diabetes mellitus patients. Biosensors available on the market differ in terms of mechanism and additional features that are increasingly being built in and improved, e.g. measuring ketones.

In this paper, we have looked at some of the most prominent biosensors in the market, produced by Roche, Abbot, Bayer, AgaMAtrix, and Medtronic.

Their mechanism is based on the measurement of hexokinase, glucosidase or glucose-1-dehydrogenase. Nowadays there are apps that allow patients to continuously

monitor their blood glucose level, via connecting modern devices with biosensor readers.

FreeStyle Libre Flash is a product of the Abbot Company and is usually intended for an adult population. The device consists of a small sensor, which is carried on the back of the upper arm to continuously monitor glucose levels. The sensor does not require patients to perform a finger prick for acquiring a sample. Patients can place a handheld reader near the device to see their current levels of glucose. These readings can be used to monitor your therapy and possibly adjust the dose. The price of a biosensor is most commonly 59€ and lasts for about 14 days [22].

Ascensia Elite is a product of the Bayer Company. It is a small device that provides blood sugar control with the ability to memorize 20 test results. To make sure that the patient has used the device correctly there is a sound signal that confirms that the procedure was done properly. In terms of reliability, sensory capillary technology ensures the ultimate accuracy that lasts. The product features: Individual closed test strips, 14 days/memory, easy setup of test strips. The price depends on the generation and model of the biosensor and ranges from 40 to 120€. Modern biosensors reach a price of 399€ [23, 24].

Guardian™ Sensor 3 CGM (5 Pack) is a product of Medtronic. The sensor continuously transfers small amounts of glucose from the interstitial fluid into your skin and translates it into an electronic signal. The Guardian Sensor 3 is intended for use with the Medtronic MiniMed® 670G system to continuously monitor glucose levels for patients with diabetes. It is intended to be used by patients aged 14 years and older and to be used by the MiniMed 670G system to automatically adjust basal insulin levels. It is indicated for use as an additional device to supplement, not replace, information obtained from standard blood glucose monitoring devices. The sensor is intended for a single use and requires a prescription. The Guardian Sensor 3 lasts for 7 days of continuous use. It costs 485.8€. It is the most accurate sensor with a MARD rating of 8.7% 2 using CONTOUR®NEXT LINK 2.4 Meter. It is easy to insert, with a flexible design that moves with your body for ultimate comfort [25]. For information about more available biosensors see Appendix 2 [26–33].

3 Materials and Methods

We compared the cost of conventional monitoring of blood glucose (SMBG) with concurrent monitoring using a flash sensor for patients with type 1 diabetes mellitus. For price comparison, a number of daily measurements needs to be set. With conventional monitoring the price changes with the

number of daily tests. For an accurate estimate of the economic efficiency of these methods, we used different scenarios with different numbers of daily measurements. The number of daily glucose controls ranges from 4 to 10 and above, and we have taken 4 values for our calculation [15].

We did a cost-minimization analysis, which means that we have compared the cost of resources spent on monitoring in both cases for one patient for one year. Cost minimization analysis is used in pharmacoeconomic studies to identify cheaper treatment options if they are equally effective [34]. The results of this analysis are presented tabular and graphically. The equivalence of the effectiveness of these two methods is questionable, in terms of the number of daily measurements, as well as the potential complications that lead to additional costs due to inefficient glucose monitoring. We have indicated the potential additional costs and their incidence for both methods. For our analysis, we used the in Croatia already available, FreeStyle Libre flash glucose monitoring system from the Abbott Laboratories manufacturer as a biosensor and a set of 40 glucose strips and lancets that can be purchased in apothecaries in Bosnia and Herzegovina.

4 Results

Number of daily measurements:

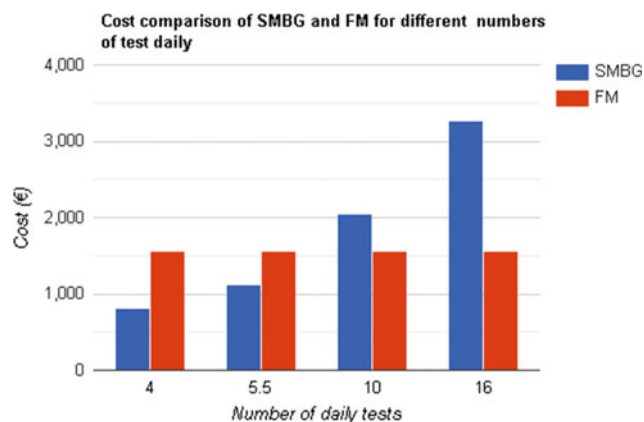
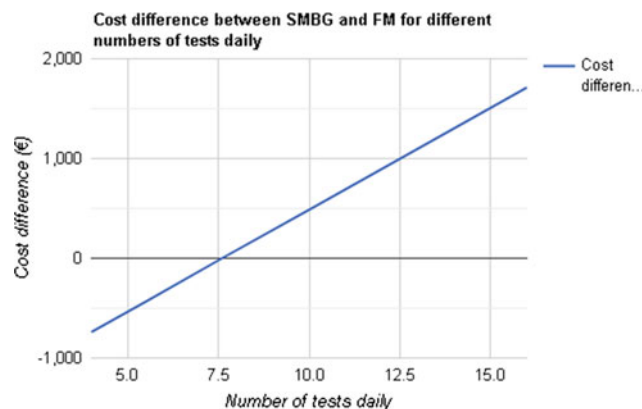
In practice, patients with T1DM measure their blood sugar between 4 and 10 or more times a day, this number depends on the condition of the patient and is determined by a doctor [15]. In the IMPACT study, which we refer to for the clinical benefit of flash monitoring compared to SMBG, the number of daily measurements averaged 5.5 [35]. Patients with more frequent hypoglycemia incidences are suggested to perform more frequent measurements up to 10 times per day according to the NICE guidelines [15]. In the IMPACT study as well as in the real-world database, flash monitoring users measure glucose up to 16 times per day (The database is refers to T1DM and T2DM) [36]. For the cost calculation for one patient per year, the following numbers of daily measurements were taken: 4, 5.5, 10 and 16 times a day [36] (Tables 1 and 2).

Table 1 Price of flash monitoring for one patient per year

Number of daily blood glucose measurements	4/5.5/10/16 (€)
Sensor	59.9
Sensor per year	1557.4
Flash monitoring per year	1557.4

Table 2 Price of self-monitoring of blood glucose for one patient per year

Number of daily blood glucose measurements	4 (€)	5.5 (€)	10 (€)	16 (€)
Lancet (piece)	0.1	0.1	0.1	0.1
Strip (piece)	0.46	0.46	0.46	0.46
Lancet per year	146	200.75	365	584
Strips per year	671.6	923.45	1679	2686.4
SMBG per year	817.6	1124.2	2044	3270.4
SMBG py—FM per year	−739.8	−433.2	+486.6	+1713

**Fig. 1** Cost comparison of SMBG and FM for different numbers of tests daily**Fig. 2** Cost difference between SMBG and FM for different numbers of tests daily

Resource prices for glucose monitoring:

The FreeStyle biosensor price is 59.9€, and the price of its reader is the same. Biosensor readers, as well as the glucometer for SMBG are not included in the calculation because there is no exact lasting period for them. We will assume that the patient uses one biosensor for 14 days (26 biosensors per year) according to data from the manufacturer [37]. For SMBG, prices of 40 glucose strips of 18.4€ were used, which can be purchased in pharmacies in Bosnia and Herzegovina and lancets which are paid per piece and the price of one is 0.07–0.13€. For our calculation, we used 0.1€ as the price for one lancet.

The tables show prices in relation to the number of daily measurements. For flash monitoring regardless of the number of daily measurements the price remains the same, while the price of SMBG increases with the number of measurements (Fig. 1).

5 Discussion

The results show that the price of flash monitoring is much higher in the first two cases. These first two cases are very common in practice and from this, it can be concluded that biosensors aren't affordable for most patients. Biosensors are

cheaper if the average number of daily measurements is above 7.6 (Fig. 2).

Although at first, biosensors look like a much more expensive alternative, they generally improve health care for diabetes. So it's not enough to just do a cost minimization analysis, but a cost-effectiveness analysis as well. Because glucose monitoring and diabetes carry different complications that add additional potential costs. As one of the effectiveness parameters, we can take how many daily measurements we get for a certain price. In the case of flash monitoring the price remains the same, regardless of the number of measurements, while the price of SMBG is growing. We conclude that biosensors according to this parameter are more effective, and the difference in price is best seen at 16 measurements per day.

The clinical benefit of flash monitoring system for patients with type 1 diabetes mellitus was demonstrated in the randomized clinical IMPACT trial. The study was conducted with patients with T1DM who intensively consume insulin (flash monitoring group—120, SMBG group—121), at 23 sites in Germany, Austria, Spain, Sweden, and the Netherlands for 6 months. The average age of respondents was 43.7 years (18–80). It has been shown that the SMBG group has more frequent episodes of hypoglycemia [35].

On average in the SMBG group, patients measured glucose 5.5 daily and had frequent episodes of hypoglycemia

Table 3 Difference in healthcare resources spent between the FM and the SMBG group during the IMPACT trial

Health care resources used for 6 months	Flash monitoring	SMBG
Emergency department visits	2	3
Ambulance callouts	2	5
Hospitalizations	2	3
Days in hospital	4	11

with a drop in glucose below 3.9 mmol/ml: 1.3 symptomatic hypoglycemia per week and 1.74 biochemical hypoglycemia per week. On average in a hypoglycemic state, a patient using SMBG was for 3 h and 25 min a day. Flash monitoring has the potential to reduce the incidence of hypoglycemia and during the study the patients using biosensors were in a hypoglycemic state for 2.03 h daily [38]. Patients using traditional monitoring experience severe hypoglycemia (glucose < 2.5 mmol/ml) 3.2 times a year, but patients using flash monitoring only 1.65 times a year. Severe hypoglycemia in 11.8% of cases requires medical assistance or hospitalization [39]. Hospitalization for T1DM patients averages 5.46 days [40]. In a UK study savings of £207.3 (234.075€) were estimated for the treatment of severe hypoglycemia, for biosensor users compared to SMBG [36]. These savings are per patient and can be added to groups of patients who measure glucose 4 and 5.5 times a day. This is an estimate for the UK health care standards and cannot be used as data for our research.

During the 6 months of the IMPACT trial, patients in the flash monitoring group spent 4 days in a hospital, while patients from the SMBG group spent 11 days. They also had more ambulance callouts as well as more frequent hospitalizations and more emergency department visits [36] (Table 3).

In Table 3, it can be seen that different complications occur more often in the SMBG group of patients. All these complications carry additional health insurance costs. Due to the small number of these situations, we cannot make an extra calculation, but we can definitely conclude that the additional costs when using the biosensor is smaller. According to our estimates with these potential costs the difference in price is minimal.

Biosensors make it easier for the patient to monitor glucose, there's no need for unnecessary finger pricks while

measuring and creates a new level of comfort in monitoring this parameter. Because of the easy way to measure the level of adherence of the patients with the number of daily measurements increases naturally. The reader has a memory of 90 days, which means that during a medical examination the doctor has an insight into the condition of the patient in the last 90 days and does not have to rely on the responsibility and sincerity of the patient as far as glucose control is concerned. This reduces the incidence of the abovementioned situations that lead to increased additional costs. Glucose strips for insulin-dependent patients are refunded by the Cantonal Health Insurance Institute, while all customers are buying lancets. This suggests that one glucose monitoring set is not 100% refunded by the institute. We calculated that lancets represent 22.22% of the SMBG price. Accordingly, we may suggest that biosensor monitoring is commercialized in a similar way, so that a part of the price is paid by the patients, and partly by the Department.

In 2016 the Sarajevo Cantonal Health Insurance Institute issued 49 884 packages of glucose strips which cost them 756,190.2€ [41]. Considering this we see that diabetes carries a huge economic burden for this country. With the commercialization of biosensors, we could see some economic improvements for the Institute.

6 Conclusion

Based on the conducted research, we can safely assert that biosensor application is justified from a medical and an economic aspect. A greater level of adherence for patients while monitoring diabetes is achieved which results in better titration of doses. Research has shown that biosensors are more cost-efficient than conventional monitoring for patients who test glucose levels more than 7.6 times a day. The position of Bosnia and Herzegovina in comparison with EU countries for diabetes monitoring is considerably lower, considering that patients from Croatia and Slovenia have the possibility of monitoring glucose using biosensors through their Institutes of Health Insurance. There is no drastic difference in relation to countries that are not in the EU (Serbia and Montenegro) where conventional monitoring is still being conducted.

Conflict of Interest The authors have no conflicts of interest to disclose.

Appendix 1

Country	Monitoring type	Monitoring with biosensors	Models and manufacturers of biosensors	Health Insurance Institute participation
Bosnia and Herzegovina	SMBG	–	–	Health Insurance Institute provides strips for diabetes type 1 patients, while lancets are sold to the patients
Montenegro	SMBG	–	–	<p>Glucometer—insured diabetic patients on insulin therapy</p> <p>Diagnostic strips for device</p> <p>Diabetic children and adolescents till the age of 18 on insulin therapy, depending on number of prescribed daily dosages, get up to 200 strips</p> <p>Diabetic insured patients from the age 18 on insulin therapy, depending on number of prescribed daily dosages, get between 25 and 100 strips</p> <p>Lancets for blood sampling from the finger</p>
Croatia	SMBG and biosensors	In use since year 2018	<p>1. FreeStyle Libre flash glucose monitoring system—reader and sensor (manufacturer Abbot)</p> <p>2. Medtronic MiniMed MiniLink Real time transmitter, Medtronic MiniMed Guardia 2 link transmitter and Enlite sensor (manufacturer Medtronic MiniMed)</p>	<p>Children from the age 4 till the age 18</p> <p>Pregnant patients</p> <p>Blind patients</p> <p>Diabetes type 1 patients on intense insulin therapy (4 or more daily dosages), with detected hypoglycemia in hospital care in Zagreb, Clinic Sestre Milosrdnice, Dubrava, University clinic for diabetes, endocrinology and metabolic diseases Vuk Vrhovac, Clinic in Split, Osijek and Rijeka</p>
Serbia	SMBG	–	–	<p>Strips for children that use 4 or more daily dosages of insulin, also for pregnant patients—150 strips a month or 450 for 3 months</p> <p>For children on 2–3 insulin daily dosages—100 strips a month</p> <p>Children with diabetes type 2 that are not on insulin therapy—50 strips a month</p> <p>Adults on 1, 2 or 3 insulin daily dosages—50 strips for 3 months</p> <p>Adults on 4 or more insulin daily dosages—100 strips a month</p> <p>Blind and visually impaired patients with diabetes mellitus—device for glucose measurement with strips</p>
Slovenia	SMBG and biosensors	In use since year 2014	Dexcom CGM	<p>Children under 7</p> <p>Pregnant patients</p> <p>Bad regulation of diabetes mellitus</p>

Appendix 2

Manufacturer	Name of biosensor	Mechanism	Main characteristics relevant for patients	Work memory	Special remarks	Price
Bayer	Ascensia Elite	Enzymatic system that measures glucose in blood	Sound signal implies that procedure was done properly	14 days 20 measurements	Additional ketones tracking Point of care testing	40€
	Elite XL	Enzymatic system that measures glucose in blood		100 measurements	Self-testing	120€
	Esprit	Capillary blood glucose, referenced to whole blood	Sensory capillary technology provides the best accuracy Longlasting battery	120 measurements	Laboratory testing Duration of test 30 s	399€
	Esprit 2	Capillary blood glucose, referenced to whole blood				
	Contour	Microfill sensors	New Fast Accurate, reliable	240 measurements	0.6 µl of sample	>399€
Life scan	One Touch Fast Take	Electrochemical	Comfortable, fast	15 s	Calibrated for whole blood	87.2–261.5€
	One Touch Profile	Electrochemical	Comfortable, simple, fast	15 s		
	One Touch Ultra	Electrochemical	Fast, with software, safe, accurate	5 s	1 µl of sample	
Rosche	TM Accu-Chek	Combination of sensor enzymatic strips Electrochemical	Fast, with software, safe, accurate	100 measurements 15 s 2 steps	1 µl of sample	87.2€
Dexcom	Dexcom PLATINUM G4 i PLATINUM G5	Glucose level measured by sensory needle	Modern, with software, fast, accurate, reliable, simple, discrete	7 days	High precision for hypo/hyperglycemia, used for diagnosis confirmation	717.3–1534€
Integrity application	Glucotrack	Ultrasonic, electromagnetic, thermal technology based in work unit	Safe, reliable, painless, simple for use	6 months	Unlimited testing as needed Offline analysis and USB port for data	1743.1€ (work unit 104, 587€)

References

1. UNECE. In: Unece.org. https://www.unece.org/trans/danger/publi/ghs/ghs_welcome_e.html. Accessed 11 Dec 2018
2. Armour, J., Lucisano, J., Gough, D.: *Diabetes* **39**, 1519 (1990)
3. Genuth, S., Alberti, K.G., Bennett, P., et al.: Expert committee on the diagnosis and classification of diabetes mellitus. Follow-up report on the diagnosis of diabetes mellitus. *Diabetes Care* **26**, 3160–3167 (2003)
4. Wang, J.: Electrochemical glucose biosensors. *Chem. Rev.* **108**(2), 814–825 (2008)
5. Aston, W.J., Turner, A.P.F.: Biosensor and biofuel cells. In: Russel, G.E. (ed.) *Biotechnology and Genetic Engineering Reviews*, vol. 1, pp. 89–120. Intercept, Newcastle upon Tyne (1984)
6. Wang, J.: *Electroanalysis* **13**, 983 (2001)
7. Newman, J.D., Turner, A.P.F.: *Biosens. Bioelectron.* **20**, 2388 (2005)
8. Willner, I., Katz, E., Willner, B.: *Electroanalysis* **9**, 965 (1997)
9. Scarano, S., Mascini, M., Turner, A.P.F., Minunni, M.: *Biosens. Bioelectron.* **25**, 957–966 (2010)
10. Hrvatski zavod za zdravstveno osiguranje. In: Hzzo.hr. <http://www.hzzo.hr>. Accessed 24 Nov 2018
11. Остваривање права на помагала за лечење и контролу шећерне болести. In: Rfzo.rs. <https://www.rfzo.rs/index.php/arhiva-vesti/965-prava-napomagala-sb>. Accessed 24 Nov 2018
12. Fzocg.me. <http://fzocg.me/documents/Lista%20medtehnopomagala%20januar%202018.pdf>. Accessed 24 Nov 2018
13. Pravice sladkornih bolnikov iz obveznega zdravstvenega zavarovanja. In: Zzss.si. <http://www.zzss.si/zzss/internet/zzss.nsf/vrstagradiva/68F89572FE81D5D3C1256F5A0058A8CA?OpenDocument>. Accessed 24 Nov 2018
14. Life With Diabetes | Diabetes Management Blog | Accu-Chek. In: Accu-chek.com. <https://www.accucheck.com/life-withdiabetes/management-tips>. Accessed 12 Dec 2018
15. National Institute for Health and Care Excellence: Type 1 diabetes in adults: diagnosis and management. Available from <https://www.nice.org.uk/guidance/ng17> (Aug 2015). Accessed 12 Dec 2018
16. Singh, S.: Applications of enzyme biosensors in diabetes. *Int. J. Tech. Res. Appl.* **4**(1), 1 (2018)
17. Touhami, A.: Biosensors and nanobiosensors: design and applications. In: *Nanomedicine*, chap. 15, pp. 271–277. One Central Press (2014)
18. Cordeiro, L.P.L.: Amperometric Enzyme-Based Biosensors: Refined Bioanalytical Tools for In Vivo Biomonitoring, pp. 22–23. University of Groningen (2018)
19. Martinkova, P., Pohanka, M.: Biosensors for blood glucose and diabetes diagnosis: evolution, construction, and current status. *Anal. Lett.* **48**(16), 2516–2517 (2015)
20. Yoo, E., Lee, S.Y.: Glucose biosensors: an overview of use in clinical practice. *Sensors* **10**(5), 4558–4576 (2011)
21. Prašek, M., Jakir, A.: Inzulinske pumpe i kontinuirano mjerenje glukoze. *Medix* **15**(80/81), 172–173 (2009)
22. FreeStyle Libre | Glucose Monitoring System—Diabetes Care. In: <https://www.freestylelibre.co.uk/libre/>. Accessed 13 Dec 2018
23. Ascensia | About Us—Our Products. In: Ascensia.com. <https://www.ascensia.com/about-us/our-products/>. Accessed 13 Dec 2018
24. Bayer Esprit—Manual. In: [manualsdir.com](http://www.manualsdir.com/manuals/49875/bayer-esprit.html). <http://www.manualsdir.com/manuals/49875/bayer-esprit.html>. Accessed 13 Dec 2018
25. Medtronicdiabetes.com. <https://www.medtronicdiabetes.com/sites/default/files/library/download-library/userguides/Guardian%20Sensor%203%20User%20Guide.pdf>. Accessed 2 Dec 2018
26. Amsldiabetes.com.au. <http://amsldiabetes.com.au/wpcontent/uploads/2017/04/Dexcom-G4-G5-Price-List.pdf>. Accessed 3 Dec 2018
27. MiniMed Insulin Pump Therapy | Medtronic Diabetes. In: Medtronicdiabetes.com. <https://www.medtronicdiabetes.com/home>. Accessed 3 Dec 2018
28. Newman, J., Turner, A.: Home blood glucose biosensors: a commercial perspective. *Biosens. Bioelectron.* **20**(12), 2435–2453 (2005)
29. Diabetes. <http://www.diabetes.org/diabetes-statistics/nationaldiabetes-fact-sheet.jsp>. Accessed 3 Dec 2018
30. Forrow, N., Bayliff, S.: A commercial whole blood glucose biosensor with a low sensitivity to hematocrit based on an impregnated porous carbon electrode. *Biosens. Bioelectron.* **21**(4), 581–587 (2005)
31. ManualsLib. In: [Manualslib.com](https://www.manualslib.com/). <https://www.manualslib.com/>. Accessed 6 Dec 2018
32. Directory of Instruction Manuals and User Guides | manualsdir.com. In: [Manualsdir.com](http://www.manualsdir.com/). <http://www.manualsdir.com/>. Accessed 10 Dec 2018
33. Ilić, M.: Načini praćenja glukoze. *Jugoslav Med. Biohem.* **22** (Suppl 1), 0354–3447 (2008)
34. Antman, E.M., Califf, R.N., Choudhry, N.K.: *Cardiovascular Therapeutics: A Companion to Braunwald's Heart Disease*, vol. 4, pp. 1–32 (2008)
35. Bolinder, J., Antuna, R., Geelhoed-Duijvestijn, P., Kroger, J., Weitgasser, P.: Novel glucose-sensing technology and hypoglycaemia in type 1 diabetes: a multicentre, non-masked, randomised controlled trial. *Lancet* **388**, 2254–2263 (2016)
36. Hellmund, R., Weitgasser, R., Blissett, D.: Cost calculation for a flash glucose monitoring system for UK adults with type 1 diabetes mellitus receiving intensive insulin treatment. *Diabetes Res. Clin. Pract.* **183**, 193–200 (2018)
37. Sensor | FreeStyle Libre von Abbott. In: [Freestylelibre.de](https://www.freestylelibre.de/libre/produkte/sensors.html). <https://www.freestylelibre.de/libre/produkte/sensors.html>. Accessed 13 Dec 2018
38. UK Hypoglycaemia Study Group: Risk of hypoglycaemia in types 1 and 2 diabetes: effects of treatment modalities and their duration. *Diabetologia* **50**, 1140–1147 (2018)
39. Foos, V., Varol, N., Curtis, B.H., Boye, K.S., Grant, D., Palmer, J. L., et al.: Economic impact of severe and non-severe hypoglycemia in patients with type 1 and type 2 diabetes in the United States. *J. Med. Econ.* **18**, 420–432 (2015)
40. McEwan, P., Larsen Thorsted, B., Wolden, M., Jacobsen, J., Evans, M.: Healthcare resource implications of hypoglycemia-related hospital admissions and inpatient hypoglycemia: retrospective record-linked cohort studies in England. *BMJ Open Diabetes Res. Care* **4**, 122 (2016)
41. ANON: Skupstina.ks.gov.ba. http://skupstina.ks.gov.ba/sites/skupstina.ks.gov.ba/files/izvjestaj_zzo_0.pdf. Accessed 12 Dec 2018

Therapeutic Aspects and Diagnosis of the Attention Deficit Hyperactivity Disorder—ADHD in Adults

Samuell Ferreira, Rubens Zeron, Guilherme Carvalho, Lara Gandra, Victoria Carestiato, Alice Bastos, Juliana Silva, and Adnan Mujanović

Abstract

Attention Deficit Hyperactivity Disorder (ADHD) is characterized by difficulties in modulating attention and hyperactivity/impulsivity. It is a very common disorder in childhood compromising school performance, hampering interpersonal relationships and causing low self-esteem that can continue in adult life and bring even more damage to the execution of routine activities in patients lives. The most commonly used treatment for ADHD is through psychostimulant drugs, however, association with other therapies is important to ameliorate the symptoms of hyperactivity. There by the treatment should be multidisciplinary, where several professionals with the family should be accompanying and treating individuals with ADHD. The objective of this study was to highlight the importance of early diagnosis and the contribution of knowledge acquisition on the nuances in the diagnosis of ADHD in adults even during medical training and multidisciplinary therapeutic procedures to improve the symptoms of adult patients with ADHD. It is concluded that the pharmacological treatment is quite effective, mainly regarding the use of methylphenidate as psychostimulant, presenting a very satisfactory profile of side effects. In some individuals with the disorder, pharmacological treatment is not sufficient because the symptoms persist or there are comorbidities. In these cases, multidisciplinary treatment with psychopharmaceuticals, psychotherapies, school and family follow-up is necessary to alleviate symptoms, leading individuals with ADHD to participate in activities common to all in the family and in society, thus preventing conduct disorders and

delinquency. Therefore, the early diagnosis of ADHD with a correct treatment institution is essential for a better prognosis of the patient.

Keywords

Attention deficit disorder • Hyperactivity • Treatment • Adult

1 Introduction

Attention Deficit Hyperactivity Disorder (ADHD) is characterized by difficulties to modulate attention and hyperactivity/impulsivity also being related by some authors to conduct disorders [1]. It is a very common disorder in childhood compromising school performance, hampering interpersonal relationships and causing low self-esteem. The diagnosis of ADHD in childhood is made through information collected from parents and teachers and also through clinical observation of the child, in addition to the adult patient family participation and also the self report, exclusive in some patients which may cause difficulties to diagnose. Symptoms must be present for at least six months, impair school or social functioning and begin before the age of twelve. Diagnosis requires at least six symptoms in the context of inattention or hyperactivity/impulsivity [2] the necessary number of symptoms to diagnose ADHD in adults is still a matter of conflict between authors.

For a better understanding of the thinking process of an individual with ADHD, it is known that he does not direct his attention only to an object, due to his great sensitivity to external stimulation, he traces a tangle of associations that come very close to abstraction. It can be said then that a hyperactive patient has a very large abstraction capacity that leads to a very high intellectual and creative potential [3].

When the diagnosis is made early, the lower the psychological consequences over the years in people with the disorder. The most commonly used treatment for ADHD is

S. Ferreira (✉) · R. Zeron · G. Carvalho · L. Gandra · V. Carestiato · A. Bastos · J. Silva · A. Mujanović
Itaperuna, Brazil
e-mail: samuelferreira1@hotmail.com

R. Zeron
e-mail: rzeeron@gmail.com

pharmacotherapy, however, association with other therapies is important to ameliorate the symptoms of hyperactivity. Thus, the treatment should be multidisciplinary, where several professionals with the family should be accompanying and treating individuals with ADHD.

These inquiries point to a reflection on the moment in which one lives and is faced with the erroneous labeling of agitated and impatient patients of hyperactive stigmatizing them from their infancy and often for the rest of their lives. The aim of this study was to highlight the importance of early diagnosis and the contribution of multidisciplinary therapeutic procedures to ameliorate the symptoms of individuals with ADHD.

2 Methods and Materials

It had as a methodological approach to qualitative research, with the purpose of providing fundamental theoretical contribution to the construction of the final work. Studies were identified by searching electronic databases (MEDLINE, COCHRANE, LILACS, BVS). No restrictions for language or year of publication were applied. Search terms included were “Attention Deficit Disorder”; “Hyperactivity”; “ADHD”; “Treatment” and “Adult”. Two reviewers performed eligibility assessment and selection of screened records independently in an unblinded. Disagreements were resolved by consensus. In case of duplicated publications, the most complete and recent was selected. Information was extracted from studies: Conceptualization, particulars and diagnosis; Comorbidities; Multidisciplinary treatment and follow-up of the ADHD and Drugs prescribed in the treatment of ADHD.

3 Results

3.1 Attention Deficit and Hyperactivity Disorder—ADHD

3.1.1 Conceptualization, Particulars and Diagnosis

Nervous system that would result in a malfunctioning of the mechanism responsible for controlling attention and filtering of external stimulation [4].

It is essential that the clinical diagnosis be made by a professional specialized in mental health, be it doctor or psychologist, through neurological examinations. More complex neuropsychological tests and much more modern examinations are already being used, such as single-photon emission tomography that is very promising for the future [2].

Magnetic resonance imaging (MRI) brain scanning has been used to examine the brain structure in children with ADHD. In a study published in the USA in 1994, the anterior part of the brain of eighteen boys with ADHD was compared to eighteen boys without the disorder. It was found that the face and rostral body, two frontal regions of the brain part, were significantly smaller in boys with ADHD. This finding indicates that boys with ADHD have a deficiency in this region of the brain that inhibits responses, which seems to be the main problem with those with ADHD. Another difference observed in the brain was that while in children without the disorder an area called the right caudate nucleus is usually larger than the left, in children with ADHD the two nuclei were the same size. The researchers also found that blood flow in the brain in children with ADHD was lower in the region of the caudate nucleus and especially reduced in the right side [5].

Until recently, it was believed that ADHD was a disorder that disappeared with age, as the nervous system completed its maturation. Today we know that this is not true. Some studies show that ADHD persists in adult life in about 50–70% of cases [3].

3.1.2 Comorbidities

The presence of comorbidity is an extremely common situation in individuals with ADHD and should be actively checked during the diagnostic phase [2].

Research shows a high rate of comorbidity between ADHD and disruptive behavior disorders (behavioral disorder and oppositional defiant disorder), which is around 30–50%. The rate of comorbidity is also significant with the following diseases: depression (15–20%); anxiety disorders (around 25%) and learning disorders (10–25%) [6].

In children and adolescents there is a frequent association of other psychiatric disorders mainly conduct, opposition and challenge disorders, mood disorders, anxiety disorders, tics and learning disabilities. About 8–30% of children present with anxiety and mood disorders (bipolar and depression), with a 10–92% incidence of learning difficulties. These are developmental specific disorders such as dyslexia, dysorthographia, dysgraphia, motor and language difficulties. The prognosis in these cases is more difficult [7].

Comorbidities are more frequent in patients with associated conduct disorder. These adults are very anxious, especially because of the difficulty they have in staying in a job, in marriage and tending to alcoholism, smoking and drug abuse. Thus, in the diagnosis of children with ADHD, care should be taken not to rule out other symptoms as secondary [6].

It is not difficult to find reasons why a child with ADHD may be depressed, anxious or aggressive. Precarious social skills, problems with parents, poor school performance and

other related aspects of ADHD can be instituted as causal factors. Although these should not be ignored, the possibility that the child suffers from another psychiatric disorder that may respond to appropriate pharmacotherapy should not be underestimated [6].

3.2 Treatment of ADHD

3.2.1 Multidisciplinary Treatment and Follow-up of the ADHD

The multidisciplinary treatment is the most suitable for caring for people with ADHD, encompassing psychological and pharmacological, psychosocial and psychoeducational interventions, since ADHD presents innumerable associated problems in different areas of life, regarding, not only the primary symptoms of disorder, but also coexisting or secondary as a major consequence.

Educators should be aware of conflict incompetence versus disobedience versus ADHD, and learn to discriminate between the three types of problems. It is necessary to develop a repertoire of interventions to be able to act efficiently in the school environment of a student with ADHD. These interventions minimize the negative impact of the child's temperament. A second repertoire of interventions should be developed to educate and improve the eminent abilities of the child with ADHD [8]. In adulthood, it depends on the patient, the appearance of symptoms may vary according to the demand of the required activities, the patient's behavior in relation to his/her interpersonal relationship, impulsive direction, excessive workaholics, organization and support of care over time highlights aspects of inattention in adult patients.

Before any treatment, a physical examination should be done to rule out other causes for the individual's behavior, such as chronic middle ear infection, sinusitis, visual, auditory or neurological problems.

In addition to pharmacological treatment there is the psychotherapy indicated for the treatment of ADHD which is entitled "Cognitive Behavioral Therapy (CBT)". There is as yet no scientific evidence that other forms of psychotherapy aid in the symptoms of ADHD.

3.2.2 Drugs Prescribed in the Treatment of ADHD

Several drugs have already been studied in the treatment of ADHD, and there is more solid evidence of efficacy with the use of psychostimulants and antidepressants (especially tricyclics).

Heterocyclic antidepressants have demonstrated efficacy in the treatment of ADHD, with results published in numerous studies over the past 30 years. In general, smaller doses are used and the therapeutic effect seems to occur

more in the behavioral sphere than in the cognitive sphere, which makes them drugs of second choice in relation to stimulants [7]. The profile of potentially serious adverse events may also limit their use.

Medications are more widely propagated and ardently discussed in relation to treatment for ADHD. Hundreds of studies have indicated that stimulants, certain antidepressants and clonidine (a drug used to treat hypertension in adults) can be very useful for people with ADHD. Stimulants, the most commonly used drugs, have been shown to be quite effective in improving behavior, academic performance, and social adjustment. The patient's response may, however, depend on the presence of other problems (in fact, medications do not help all patients) [6].

Table 1 presents the medications most used in the treatment of ADHD: the drugs of first choice and those of second choice.

The decision to use medication in the child with ADHD is based on fulfilling the diagnostic criteria. The symptoms of ADHD should be persistent and cause functional impairment at home, at school or in social setting. Clinical examination and anamnesis should not reveal contraindications to treatment. In the adult the conduct will also depend on the fulfillment of the diagnostic criteria, but it should not be totally linked to the filling of scales. The experience in diagnosing the disorder in this population is of extreme importance and the clinical history evidencing the degree of impairment of the disorder in the patient's life will be decisive.

The use of psychostimulants, such as methylphenidate, with or without associated psychotherapy, was the best strategy for the treatment of ADHD according to Gomes et al. [5]. There is a considerable amount of data attesting to the safety and efficacy of methylphenidate. The clinical efficacy of methylphenidate has been proven in more than 1500 clinical studies in the last 40 years [10].

The pharmacological properties of methylphenidate have been well characterized in several preclinical studies. According to ANVISA [11] methylphenidate has been used for more than 50 years in the treatment of ADHD. Its effectiveness in the treatment of ADHD is well established. Published studies show that methylphenidate significantly improves daytime sleepiness and cataplexy.

According to Gomes et al. [5] the consumption of methylphenidate favors concentration in the tasks to be performed, promoting greater stability.

4 Discussion

Although ADHD affects a large number of school children and adolescents, and in a very high percentage of the cases studied, they remain in the adult's life, ADHD continues to

Table 1 Medications used in the treatment of ADHD

Medicines recommended in consensus of specialists		
Chemical name	Dose	Approximate duration of the effect
<i>First choice: stimulants (in alphabetical order)</i>		
Lisdexanfetamine	30, 50 or 70 mg in the morning	12 h
Methylphenidate (short duration)	5–20 mg 2–3 times a day	3–5 h
Methylphenidate (extended duration)	18, 36 or 54 mg in the morning	12 h
	20, 30 or 40 mg in the morning	8 h
<i>Second choice: if the first stimulant has not obtained the expected result, one should try the second stimulant</i>		
<i>Third choice</i>		
Atomoxetine (1)	10, 18, 25, 40 and 60 mg once a day	24 h
<i>Fourth choice: antidepressives</i>		
Imipramine (antidepressant)	2.5–5 mg per kg of body weight divided into 2 doses	
Nortriptyline (antidepressant)	1–2.5 mg per kg of body weight divided into 2 doses	
Bupropion (antidepressivo)	150 mg twice a day	
<i>Fifth choice: if the first antidepressant did not achieve the expected result, the second one should be tried</i>		
<i>Sixth choice: alpha-agonists</i>		
Clonidine (antihypertensive drug)	0.05 mg at bedtime or twice daily	12–24 h
<i>Other drugs</i>		
Modafinil (medicine for sleep disorder)	100–200 mg by day at breakfast	

Other medicines that do not yet exist in Brazil:

Focalin—a “derivative” of methylphenidate (actually a part of the molecule itself)

Daytrana—an adhesive (to put on the skin) of methylphenidate

Dexedrine—an amphetamine (Dextroamphetamine); there is the short-acting and long-acting formulation

Adderall—a mixture of amphetamines; there is the short-acting and long-acting formulation

Source Brazilian Association of Deficit of Attention—ABDA [9]

be little known by parents, education professionals and even by health professionals. Disinformation is the main challenge to be overcome, so that early diagnosis of the disease and appropriate treatment can be achieved, drastically reducing family, school, behavioral and psychological conflicts. Therefore, many consequences of ADHD such as depression, behavioral disorders and relationship problems can be easily minimized or even avoided.

The causes that lead to hyperactivity are very varied and probably dependent on diversified factors. In most cases, it is difficult to determine a precise etiology since no brain damage is detected as in other mental disorders, and these are not always well understood, which can make the individual potentially incapable, if not subjected to an appropriate intervention.

Besides the pharmacological treatment, it is important the multidisciplinary treatment with psychotropic drugs, psychotherapies, school and family support. Multidisciplinary treatment contributes to attenuating the symptoms by bringing individuals with ADHD to participate in activities common to all in the family and in society, thus preventing conduct disorders and delinquency.

Conflict of Interest None.

References

- Farré-Riba, A., Narbona, J.: EDAA: Escala para la evaluación del trastorno por déficit de atención con hiperactividad. TEA, Madrid (2001)
- American Psychiatric Association: DSM-5. Manual diagnóstico e estatístico de transtornos mentais, 5 edn. (2014). ISBN 9788582710883
- Silva, A.B.B.: Mentis inquietas: entendendo melhor o mundo das pessoas distraídas, impulsivas e hiperativas. Napedes, Rio de Janeiro (2003)
- Bastos, F.L., Thompson, T.A., Martinez, O.C.A.: Uma revisão do distúrbio de Déficit de Atenção/Hiperatividade. Apresentado no 1º Encontro Brasileiro de Neurologia, Outubro de 2000
- Gomes, M., Palmira, A., Barbirato, F., Rohde, L.A., Mattos, P.: Conhecimento sobre o transtorno de déficit de atenção/hiperatividade no Brasil. J. Bras. Psiquiatr. **56**(2), 94–101 (2007)
- Antoniuk, S.A.: Transtorno de Déficit de Atenção e Hiperatividade Conceitos e dilemas. J. Paranaense Pediatr. **3**(1) (2002)
- Popper, C.: Antidepressants in the treatment of attention-deficit/hyperactivity disorder. J. Clin. Psychiatry **58**(suppl 14), 14–29 (1997)
- Smith, C.: Dificuldades de Aprendizagem de A a Z, 1 edn. Ed. Artes Médicas (2001)

9. Brazilian Association of Deficit of Attention—ABDA. <https://tdah.org.br/depressao-e-tdah-parte-i/> (2016). Accessed 20 Aug 2018
10. Connor, D.F.: Preschool attention deficit hyperactivity disorder: a review of prevalence, diagnosis, neurobiology, and stimulant treatment. *J. Dev. Behav. Pediatr.* **23**, S1–S9 (2002)
11. Ritalina ® e Ritalina ® LA (coridrato de metilfenidato); Novartis Biociência SA; comprimidos 10 mg, papsulas 10, 20, 30 ou 40 mg. Anvisa. http://www.anvisa.gov.br/datavisa/ila_bula/firmVisualizarBula.asp?pNuTransacao=24848562016&pIdAnexo=4017454 (2016). Accessed 20 Aug 2018

Predicting the Severity of a Mammographic Tumor Using an Artificial Neural Network

Laila Mušić and Nusreta Gabeljić

Abstract

Mammography is a medical imaging technique which utilizes low-energy X-rays specifically for imaging of breast tissue. Being able to classify mammographic tumors as benign or malignant in the early diagnostic stages can help decrease the amount of subsequent examinations, thus decreasing the associated inappropriate diagnostics (such as false-positives and false-negatives). The following paper describes a method using an artificial neural network in order to predict the severity of a mammographic tumor as either benign or malignant, in order to enhance the overall digital diagnostic procedure of mammographic screening. A feedforward neural network architecture was developed using a data set provided by Institute of Radiology at University Erlangen-Nuremberg. K-fold cross validation was utilized in artificial neural network training, and the effect of varying quantities of neurons in the hidden layer was evaluated by assessing the system output. The single-layer, feedforward neural network architecture created, with 80 neurons in hidden layer, achieved the best performance. The overall structure resulted a sensitivity of 85.0%, specificity of 81.0%, and accuracy of 82.9% in classifying mammographic tumors as benign or malignant.

Keywords

Mammography • Artificial neural network (ANN) • Artificial intelligence • Tumor classification • Breast cancer • Benign tumor • Malignant tumor

1 Introduction

Breast cancer starts when cells in the breast begin to grow out of control [2]. Firstly, these cells form a tumor that can often be seen on an X-ray or felt as a lump [2]. There are two kinds of tumors: malignant and benign. The tumor is malignant cancerous if the cells can invade surrounding tissues or spread (metastasize) to distant areas of the body while benign do not spread. Cells in almost any part of the body has ability to become cancer and can spread to other areas. It's also important to understand that most breast lumps are benign and not cancer (malignant) [2]. Non-cancerous breast tumors are abnormal growths, but they do not spread outside of the breast and luckily they are not life threatening [2]. But unfortunately, some benign breast lumps can increase a woman's risk of getting breast cancer [2].

A mammogram is an X-ray image of the breast. Mammography is an imaging modality that uses low energy X-rays specifically for imaging of breast tissue [16]. Mammography practice utilizes standardized views of the breasts to for the assessment of breast lesions [16]. Mammography is the most effective method for breast cancer screening available today [12]. Mammograms can be used to check for breast cancer in women who have no signs or symptoms of the disease [8]. All abnormal mammograms should be followed up with additional testing (diagnostic mammograms, ultrasound, and/or biopsy) to determine whether cancer is present [8].

To detect early cancer in asymptomatic women, screening mammography is used [8, 16]. It is also used as a screening tool for the detection of early breast cancer in asymptomatic women [16]. Screening mammograms usually involve two or more X-ray images, of each breast [8]. The diagnostic mammogram can also be used to evaluate changes found during a screening mammogram or to view breast tissue using special techniques when it is difficult because of special circumstances, such as the presence of breast

L. Mušić (✉) · N. Gabeljić
International Burch University, Sarajevo, Bosnia and Herzegovina
e-mail: laila.music@stu.ibu.edu.ba

N. Gabeljić
e-mail: nusreta96@hotmail.com

implants [8]. Diagnostic mammography takes an image of the breast for diagnosis of a previously identified suspicious breast lesion [16]. Surveillance mammography assesses recurrence of malignancy in women with known breast cancer [16].

With the help of X-ray images, it is possible to detect of tumors which cannot be felt [8]. Early detection of breast cancer is so important because it allows early treatment and an increase in survival rates [8, 16]. With screening mammography, early detection of a malignant tumor is possible before the tumor spreads [8]. There are significant results of randomized clinical trials and other studies showing that screening mammography play role in reduction of the number of deaths from breast cancer among women between age of 40 and 74, especially for women older than 50 years [8].

The benefits of screening mammography need to be balanced against its harms, which are basically inappropriate diagnostics, including false-negative results and false-positive results, and radiation exposure [8]. False-negative results means that mammograms results appear normal even though breast cancer is present in reality [8]. Taking everything into account, screening mammograms miss about 20% of breast cancers that are actually present at the time, leading to delays in treatment and a false sense of security for affected women [8]. It is reported that mammography has a false-negative (missed cancer) rate of at least 10% [3].

This is partly due to dense tissue obscuring the cancer and the appearance of cancer on mammograms having a large overlap with the appearance of normal tissue [3]. Reasons for false negative results and not seeing the cancer include error of the one who is observing them, but more frequent reason is when the cancer is hidden by other dense tissue in the breast, and even after retrospective review of the mammogram, the cancer cannot be seen. Furthermore, lobular cancer, one form of breast cancer, has a growth pattern that produces shadows on the mammogram that are indistinguishable from normal breast tissue [3]. According to statistics false-negative results occur more often among younger women than among older women because younger women are more likely to have dense breasts [8].

False-positive results occur when radiologists see an abnormality (that is, a potential “positive”) on a mammogram but no cancer is actually present [8]. Research shows that false-positive mammograms may affect women’s well-being and behavior [23]. Some women who receive false-positive results may be more likely to return for routine screening or perform breast self-examinations more frequently. However, some women who receive false-positive results become anxious, worried, and distressed about the possibility of having breast cancer, feelings that can last for many years. False-positive mammogram results can lead to anxiety and other forms of psychological distress in affected

women [8]. The additional testing required to rule out cancer can also be costly and time consuming and can cause physical discomfort. The chance of having a false-positive result increases with the number of mammograms a woman has [8]. Low positive predictive value of breast biopsy resulting from mammogram interpretation leads to approximately 70% unnecessary biopsies with benign outcomes [12]. To reduce the high number of unnecessary breast biopsies, several computer-aided diagnosis (CAD) systems have been proposed in the last years [12].

Being able to classify mammographic tumors as benign or malignant in the early diagnostic stages can help decrease the amount of subsequent examinations, thus decreasing the associated inappropriate diagnostics (such as false-positives and false-negatives).

2 Materials and Methods

2.1 Dataset

This data set provided by the Institute of Radiology at University Erlangen-Nuremberg is sufficient enough to be used in application to predict the severity of a mammographic tumor, via artificial neural network [4, 12]. The data, which was collected from full field digital mammograms in 2003–2006, includes a BIRADS assessment, the age of the patient, three BI-RADS attributes, and the conclusive, factual severity of the tumor (i.e. malignant or benign) [4, 12].

BI-RADS (Breast Imaging Reporting and Database System) is a system founded by the American College of Radiology; it is a consistent method when it comes to describing mammogram results, and is inclusive of seven standardized categories, as well as four breast density categories [8]. The aforementioned categories, ranked from the least amount of breast density to the highest, are as follows: (0) Need additional imaging evaluation, (1) Negative, (2) Benign finding, (3) Probably benign, (4) Suspicious abnormality, (5) Highly suggestive of malignancy, (6) Known biopsy-proven malignancy [8].

Each sample in the given dataset (of 961 total samples) has a related BI-RADS assessment ranging from 1 (definitely benign) to 5 (highly suggestive of malignancy), assigned in a double-review process by physicians [4, 12]. Assuming that all cases with BI-RADS assessments greater or equal a given value (varying from 1 to 5), are malignant and the other cases benign, sensitivities and associated specificities can be calculated [4, 12]. 830 total samples were taken from the 961 in the already-present dataset due to some samples having missing attributes.

There are six attributes for each sample: 1 goal field attribute, 1 non-predictive attribute, and 4 predictive

attributes [4, 12]. More descriptively, the attributes are as follows: (1) BI-RADS assessment (ordinal): 1–5, (2) Age (integer): patient’s age in years, (3) Shape: mass shape: round = 1, oval = 2, lobular = 3, irregular = 4 (nominal), (4) Margin (nominal): mass margin: circumscribed = 1, microlobulated = 2, obscured = 3, ill-defined = 4, speculated = 5 (nominal), (5) Density (ordinal): mass density high = 1, iso = 2, low = 3, fat-containing = 4, (6) Severity (binominal): benign = 0, malignant = 1 [4, 9, 12].

2.2 Artificial Neural Network

A feedforward neural network architecture due to its efficiency proven by previous works, its primary advantages being an effective training algorithm and a better understanding of the system behavior [1, 7, 10, 13, 14]. The advantages of this type of neural network include [1, 7, 10]. The 830 samples were separated into a group of 820 samples for use with the ANN and 10 samples to test the data with [12]. The artificial neural network consisted of two layers: (1) Input Layer (six inputs and a hidden layer), (2) Output Layer (one output neuron) [1, 14].

The backpropagation Levenberg-Marquardt algorithm was used for training, because it advantageously utilizes the steepest descent method with the Newton method [1, 7, 11, 15]. The Levenberg-Marquardt (LM) algorithm is an iterative system that finds the minimum of a function that is expressed as the sum of squares of nonlinear functions [6, 11]. This algorithm obtained its operating stability from the steepest descent method, and adopted its accelerated convergence in the minimum vicinity from the Newton method [1, 7].

In determining the optimal number of neurons in the hidden layer, the trial method was used [1, 10]. The number of neurons was increased from 2 to 100, and neural network performance was evaluated respectively. As seen in Fig. 1, the optimal neural network performance parameters were to use a k-value (i.e. neuron amount) of 80, using 90% of the input data for training, 5% for validation, and 5% for testing the neurons. Due to database size and nonlinearity of the provided data for neural network, k-fold cross validation type training was implemented [1, 10, 13, 14]. At each training iteration, the train/test performance was evaluated as Mean Square Error between the predicted and actual values (MSE), where n is total number of samples [1].

3 Results

As the network is trained, the weights of the system are continually adjusted in order to reduce the difference between the output of the system and the desired response of

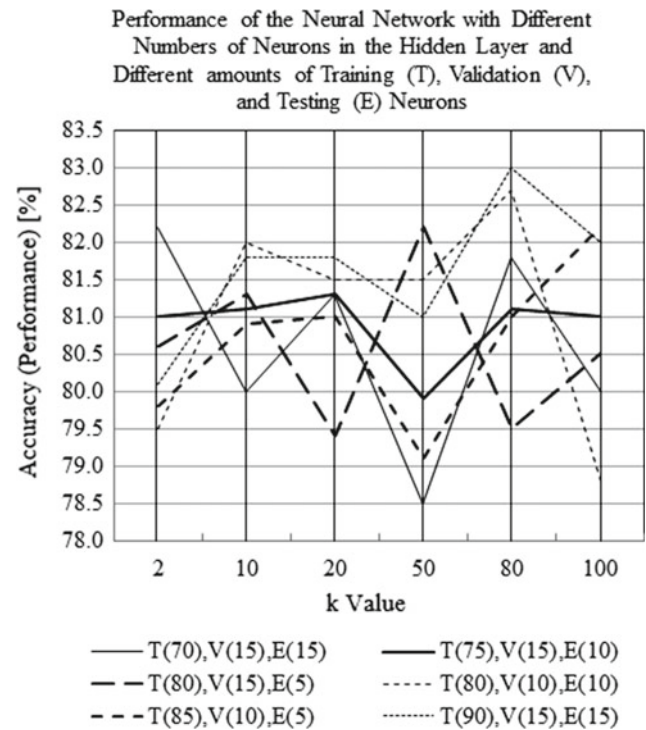


Fig. 1 Neural network performance

the system. The number of neurons in the hidden layer was chosen to be 80 (since this neural network architecture caused in optimum performance for training and validation) (Fig. 2).

Classification success rate after neural network training was 82.90% correct classification of the mammographic tumors with accurate specificity and sensitivity.

Confusion Matrix for the Artificial Neural Network's Mammographic Tumor Classification

<i>True positive</i> 340 41.5%	<i>False positive</i> 58 41.5%	Positive predictive value $Ppv = Tp / (Tp + Fp)$ $340 / (340 + 58)$ 85.4%
<i>False negative</i> 82 10.0%	<i>True negative</i> 340 41.5%	Negative prediction value $Npv = Tn / (Tn + Fn)$ $340 / (82 + 340)$ 80.6%
Sensitivity $= Tp / (Tp + Fn)$ $340 / (340 + 82)$ 80.6%	Specificity $= Tn / (Tn + Fp)$ $340 / (58 + 340)$ 41.5%	Accuracy $= (Tp + Tn) / (Tp + Tn + Fp + Fn)$ $(340 + 340) / (340 + 340 + 58 + 82)$ 82.9%

Fig. 2 Confusion matrix

4 Conclusion

The National Cancer Institute is supporting the development of several new technologies to detect breast tumors [8]. This research ranges from methods being developed in research labs to those that are being studied in clinical trials [8].

The system developed here provides a valuable diagnostic and treatment decision support tool for physicians, helping to lower the overall percentages of false-positives and false-negatives factored in mammographic screening procedures [14]. The National Cancer Institute is supporting the development of several new technologies to detect breast tumors [8]. This research ranges from methods being developed in research labs to those that are being studied in clinical trials [8].

Classification success rate after neural network training was 82.9%, which contributes to the positive development and increased accuracy of digital mammography scanning methods. The benefit of using neural network to classify mammographic tumors should be utilized by physicians in order to improve the quality, accuracy, and potentially the speed of digital mammography.

References

1. Abraham, A.: Artificial neural networks. In: Sydenham, P., Thorn, R. (eds.) *Handbook of Measuring System Design*. Wiley, London (2005)
2. American Cancer Society. What is breast cancer? <https://www.cancer.org/cancer/breastcancer/about/what-is-breast-cancer.html> (21 Sep 2017). Retrieved 13 Dec 2018
3. Cochrane Nordic Center. Mammography-leaflet; screening for breast cancer with mammography [pamphlet]. The Nordic Cochrane Center. <http://www.cochrane.dk/screening/mammography-leaflet.pdf> (2005)
4. Elter, M., Schulz-Wendtland, R., Wittenberg, T.: The prediction of breast cancer biopsy outcomes using two CAD approaches that both emphasize an intelligible decision process (dissertation, 2007). *Med. Phys.* **34**(11), 4164–4172 (2007)
5. Lourakis, M.: A brief description of the Levenberg-Marquardt algorithm implemented by Levmar. Doctoral Dissertation, Foundation for Research and Technology—Hellas (2005) [Abstract]. https://www.researchgate.net/publication/239328019_A_Brief_Description_of_the_Levenberg-Marquardt_Algorithm_Implemented_by_levmar (11 Feb 2005). Retrieved 23 Dec 2018
6. Marquardt, D.: An algorithm for least-squares estimation of nonlinear parameters (doctoral dissertation, 1963). *SIAM J. Appl. Math.* **11**(2), 431–441 (1963). <https://doi.org/10.1137/0111030>
7. National Cancer Institute: Mammograms. <https://www.cancer.gov/types/breast/mammograms-fact-sheet> (7 Dec 2016). Retrieved 13 Dec 2018
8. National Cancer Institute (Dictionary of Cancer Terms). Definition of spiculated mass (2018). <https://www.cancer.gov/publications/dictionaries/cancer-terms/def/spiculatedmass>. Retrieved 13 Dec 2018
9. Rouse, M.: Expert System (Petersen, S. Contr.). <https://searchenterpriseai.techtarget.com/definition/expert-system> (2018). Retrieved 23 Dec 2018
10. Sapna, S., Tamilarasi, A., Pravin Kumar, M.: Backpropagation learning algorithm based on Levenberg Marquardt algorithm. Unpublished Doctoral Dissertation. College of Engineering, Tamil Nadu, India
11. Schulz-Wendtland, R.: Mammographic mass data (Elter, M. Donor). https://archive.ics.uci.edu/ml/machinelearning-databases/mammographic-masses/mammographic_masses.names (Oct 2007). Retrieved 13 Dec 2018
12. Subaşı, A., Yılmaz, M., Özçelik, H.R.: Classification of EMG signals using wavelet neural network (doctoral dissertation, 2006). *J. Neurosci. Methods* **156**(1–2), 360–367 (2006). doi:10.1016/PMID: 16621003
13. Šahinbegovic, H., Mušić, L., Alić, B.: Distinguishing physical actions using an artificial neural network. In: XXVI International Conference on Information, Communication and Automation Technologies (ICAT), Sarajevo, Bosnia and Herzegovina, 26–28 Oct 2017
14. The Mathworks, Inc.: Levenberg-Marquardt backpropagation <https://www.mathworks.com/help/deeplearning/ref/trainlm.html;jsessionid=96ec0f3d4f26067224703e6bd3ee> (n.d.). Retrieved 23 Dec 2018
15. World Health Organization (WHO). Diagnostic imaging: mammography https://www.who.int/diagnostic_imaging/imaging_modalities/dim_mammography/en/ (04 Aug 2015). Retrieved 13 Dec 2018

Author Index

A

Ademovic, Z., 559
Adler, Grażyna, 527
Adler, Mateusz A., 527
Adnan, Mujanović, 681
Ajanović, Majda, 499
Ajanović, Zurifa, 605
Akulov, S., 655
Alickovic, Emina, 91, 519
Alić, Minela, 761
Alilović, Ivona, 641
Aliman, Lamija, 743
Altınçay, Hakan, 665
Amidžić, Ljiljana, 37
Antoniou, A., 205
Antunes, Alexandre, 13
Aruković, Emina, 617
Assunção, Pedro, 13, 51
Avdić, Monia, 273
Avramović, Aleksej, 185

B

Babic, Ankica, 341
Babić, Zdenka, 185
Badić, Samir, 499
Badnjević, Almir, 149, 429, 483, 597
Badnjevic-Cengic, Alma, 149
Banjanin, Miljana, 499
Baraković, Sabina, 387
Bastos, Allice, 769
Bećirović, Merjem, 483
Beganović, Adnan, 119, 125, 131, 137, 143, 155
Beganović, Nejra, 43
Begić, Nedim, 293
Begler, Begović, 569
Bego, Tamer, 149, 475, 597, 743, 761
Begović, Nikolina, 743
Bektić, Berina, 755
Bešlić, Nermina, 131
Bišćević, Amila, 735, 749
Bocchi, Leonardo, 61, 201, 309
Bologna, Francesca, 309
Borčak, Kana, 735, 749
Borodzicz, Sonia, 3
Boskovic, Dusanka, 81, 87
Botonjić Karahusić, Aida, 293
Braga-Pontes, Cátia, 13

Brčić, Iman, 735, 749
Brčkalo, Jelena, 575
Brkan, Mirna, 499
Bušatlić, Sadžida, 735, 749
Busuladžić, Mustafa, 143

C

Çalışkan, Gülizar, 213, 219
Camović, Mirela, 735, 749
Carestiato, Victoria, 769
Carić, Bojana Radošević, 325
Carreira, Bruno, 13
Carvalho, Guilherme, 769
Čenanović, Nejra, 735, 749
Cerić, Šejla, 131
Çetin, Emel, 437, 443
Cifrić, Selma, 173, 687
Čiva, Lejla M., 119, 137
Ćordić, Sabahudin, 483, 511, 649
Correia, Pedro, 13
Čulum, D., 553
Cunha, Francisco, 51
Čusto, Naida, 499
Čustović, Edhem, 459
Cybulski, Gerard, 3

D

Dacić, M., 559, 563
da Silva Duque, Bianca, 629
da Silva, Letícia Vieira, 629
Daskalaki, A., 105
Dedić, Mirza, 695, 705
Dedić, Remzo, 287
Dedović, Anida, 735, 749, 761
Dedović, Edis, 99, 143
Dermitzakis, A., 105
Di Franco, Riccardo, 413
Dinarević, Enida Cero, 387
Dizdar, M., 553
Djorovic, Smiljana, 337
Đozić, Zerina, 505
Dragojevic, Boris, 87
Dujčić, Tanja, 475, 743
Đukić, Igor, 743
Durmuş, Hüseyin Okan, 437, 443
Džiho, Amina, 743

Džudžević-Čančar, H., 553

E

Elezović, Alisa, 167, 533
 Elibol, Murat, 213, 219, 267
 Ender, Ferenc, 303
 Etminan, A., 553

F

Fabbri, Rachele, 713
 Faria, Sérgio, 51
 Fazlić, Arnela, 671
 Fedotov, A., 655
 Felici, Andrea, 201
 Ferreira, Samuel, 769
 Fetahović, Dina, 617
 Filipi, Janja, 185
 Filipović, Nenad, 315, 331, 337, 379
 Fófano, Gisele Aparecida, 629
 Fonseca-Pinto, Rui, 13, 51
 Francia, Piergiorgio, 61

G

Gabeljić, Nusreta, 775
 Gajić, Slavica, 185
 Galić, Kristina, 119
 Gandra, Lara, 769
 Garcia, Nuno M., 453, 469
 Gaši, Fuad, 539
 Gavazzi, Francesca, 713
 Gavrilović, Zvezdana, 235
 Gazdić-Šantić, Maja, 125, 131, 137
 Gazibegović-Busuladžić, Azra, 143
 Gharehbaghi, Arash, 341
 Gherardelli, Monica, 713
 Gičević, Armina, 581
 Gillanders, Ross, 185
 Glackin, James, 185
 Glamočlija, Una, 569
 Gökgöl, Merve Kevser, 395, 721
 Goletic, Teufik, 641
 Gomes, Dulce, 13
 Grabowski, Maciej, 527
 Guarino, Maria P., 13
 Gurbeta, Lejla, 149, 429, 483, 597
 Gürlek, Ceren, 267
 Gusinu, Roberto, 407

H

Hadžabić, Jasmina, 167, 533
 Hadziabdic, Naida, 75
 Hadžić, Lejla, 671
 Hadžović, Haris, 761
 Hajdarpašić-Saračević, Aida, 371
 Halilović, Sabina, 75
 Halonen, Heidi T., 21
 Hamidović, Medina, 303
 Hasanbegović, Alma, 575
 Hasanefendić, Berina, 579
 Hasanić, Osman, 671
 Hasanović, Aida, 321, 635
 Hasanović, Jakub, 321

Hasković, Denis, 543
 Hasković, Edhem, 543
 Herenda, Safija, 543
 Hindija, Lamija, 581
 Hodzic, Aida, 641
 Houessouvo, Roland C., 423
 Hrkovic-Porobija, Amina, 641
 Hrnjica, Zekira, 575
 Hukeljić, Behija Berberović, 149
 Hukić, Mirsada, 273
 Husić, Đenana, 251
 Husić, Jasmina Baraković, 387
 Hyttinen, Jari A.K., 21

I

Iadanza, Ernesto, 407, 413, 417, 713
 Ibrahimpašić, Tarik, 179
 Ignjic, Tatjana, 111
 Ihalainen, Teemu O., 21
 Ilić, Dušan I., 245
 Ilves, M., 7
 Imamović, Selma, 475, 743
 Izetbegovic, Sebiija, 483

J

Januário, Filipa, 13
 Jašić, Rahima, 125, 131, 137
 Jelačić, Zlata, 287
 Jerković-Mujkić, Anesa, 539
 Jokić, Dejan, 43, 179, 459
 Jovanović, Vedran, 185
 Jukic, Samed, 75

K

Kajgana, Ilma, 575
 Karaböce, Baki, 437, 443
 Karačić, Alma, 581
 Karagoz, Irfan, 159
 Karaman, Nermina, 99
 Kazlagić, Anera, 257, 543
 Kazlova, Anastazja, 527
 Kečo, Dino, 491
 Kevrić, Jasmin, 67, 75, 193, 511
 Kezić, Nikola, 185
 Kilic, Azra Music, 349
 Kiseljakovic, Emina, 527
 Kišija, Emina, 173, 687
 Klepo, L., 553
 Kolarević, Goran, 111
 Komić, Sajra, 729
 Köse, Ayşe, 267
 Kosheleva, A., 655
 Kostić, Tino, 293
 Kovacevic, Zivorad, 483
 Kovač, Nikolina, 729
 Krajina, Danira, 729
 Krasić-Arapović, Antonela, 119
 Krezić, Sarah, 729
 Krhan, Esved, 729
 Kudić, Nudžejma, 671
 Kulaglič, Ajla, 371
 Kunić, A., 563
 Kurta, Emina, 429, 483

Kurtić, Selena, 623
Kusza, Szilvia, 641

L

Lalić, Katarina, 325
Lasić, Ivan, 119, 137
Lasić, Valentina, 119
Leitão, Catarina, 13
Lejla, Šabić, 681
Lekkala, J., 7
Lepara, Orhan, 81
Lučić, Miloš A., 245
Lučić, Silvija, 245
Luschi, Alessio, 407, 413, 713
Lylykangas, J., 7

M

Mahmutbegovic, Emir, 527
Mahmutbegovic, Nevena, 527
Mahmutović-Dizdarević, Irma, 539
Makarov, I., 655
Mäkelä, E., 7
Maksimović, Mirjana, 235
Malenica, Maja, 475, 743, 761
Malliori, A., 105
Mandal, S., 589
Mandžuka, Emir, 729
Marić, Amina, 729
Marković, Bojan, 357
Martinho, Ricardo, 13
Masala, Amela, 641
Mašetić, Zerina, 273, 491
Massaro, Cesare, 417
Medenou, Daton, 423
Medvedec, M., 403
Mehanović, Dželila, 491
Melillo, Paolo, 713
Mercan, Mine, 395
Meseldžić, Neven, 743
Meydan, Cafer, 213
Mīdhat, Vehabović, 569
Milosevic, Zarko, 315
Moreira, Joana, 469
Moreira, Mariana, 469
Mrkulić, Fatima, 597
Muftić, Belma, 695, 705
Mujanović, Adnan, 769
Mujezinović, Minela, 575
Mulalić, Alen, 735, 749
Mušić, Laila, 775
Mustafić, Lejla Divović, 149
Muštra, Mario, 185
Mutaf, Tuğçe, 213, 219

N

Nateva, M., 611
Naumović, Milica, 225
Niewiadomski, Wiktor, 3
Nikolić, Dalibor, 315, 331
Nikolic, Milica, 379
Nikšić, Azra, 729
Novalić, Jasmin, 755
Nuhic, Jasna, 67, 173, 511, 687

O

Odobašić, Lejla, 273
Ohran, Husein, 641
Oliveira, Luis, 13
Omanović-Miklićanin, Enisa, 257, 597
Öncel, Suphi Şurişvan, 213, 219, 267
Oral, İzel, 267
Orhan, Zeynep, 395, 721
Osmancevic, S., 559
Osmanlić, Maida, 735
Osmanovic, Ahmed, 75
Osmanović, Dina, 173, 687
Osmić, Hasan, 99

P

Pallikarakis, N., 105, 205
Paraš, Smiljana, 37
Pavicar, Bojan, 111
Pecchia, Leandro, 423
Pehlić, Ekrem, 539, 635
Pehlivanović, Belma, 617
Pennati, Diletta, 309
Perrella, Antonia, 61
Perva, Omer, 149
Petrović, Biljana V., 155
Piaggio, Davide, 423
Pilipovic, S., 559, 563
Piljak, Vanja, 695, 705
Pires, Gabriel, 13
Poluta, M., 403
Pombo, Nuno, 453, 469
Popović, Nataša, 225
Praskalo, Jovica Ž., 155

R

Rahić, Ognjenka, 167, 533
Ramić, Samir, 251
Ramović, Amar, 251
Ranogajec, Zeljko, 111
Rantanen, V., 7
Raspudić, Vesna, 281
Rautiainen, M., 7
Reşbacz-Marón, Ewa, 527
Redžepi, Sukejna, 695, 705
Redžić, Mahira, 137
Rezende, Bruno Oliveira, 629
Rijo, Rui, 13
Risojević, Vladimir, 185
Roganović, Sonja, 225
Rotas, K., 205

S

Sabo, Tibor, 357
Sacconi, Leonardo, 309
Šadija, Amara, 131
Sadowiec, Marta, 3
Šahinpašić, Amila, 569
Sakanovic, Semir, 193
Salihović, Mirsada, 539, 635
Salkic, Nermin N., 527
Šapčanin, Aida, 321, 539, 559, 563, 635
Sarač-Hadžihalilović, Aida, 605
Sarić, Rijad, 43, 459

- Saveljić, Igor, 315, 331, 337
 Sayed, Ahmed El, 273
 Scortecci, Costanza, 309
 Šećerović, Alem, 505
 Seco, Maria Alexandra, 13
 Sefić-Pašić, Irmina, 125
 Šehić, Adnan, 125
 Šehović, Emir, 371, 505
 Šejto, Lejla, 547
 Sen, Li, 245
 Sepehri, Amir A., 341
 Šetrajčić, J.P., 239
 Šetrajčić-Tomić, A.J., 239
 Shekhi, Ghazaal, 665
 Sidorov, A., 655
 Silva, Bruno M.C., 469
 Silva, Juliana, 769
 Simić, Mitar, 185
 Simonelli, Francesca, 713
 Sirbubalo, Merima, 167, 499, 533, 547, 575, 729, 735, 749
 Skopljak-Beganović, Amra, 125, 131, 137
 Škrbić, Ranko, 245
 Sljivo, Sanda, 81
 Smajlović, Sabrina, 475
 Smajlović-Skenderagić, Lejla, 371, 505
 Sokolović, Nermina, 499
 Sorelli, Michele, 61, 201, 309
 Spahić, Lemana, 371, 483, 505, 511, 649, 671
 Špirtović-Halilović, Selma, 539, 635
 Springer, Andreas, 303
 Stanić, Barbara, 499
 Stojanović, Zvezdan, 623
 Stojanovska, S, 611
 Stojnić, Vladan, 185
 Subasi, Abdulhamit, 29, 91, 519
 Surakka, V., 7
 Sušić, Anesa, 575, 761
 Sustersic, Tijana, 379
 Syrimpeis, V., 205
- T**
 Tahirović, I., 553
 Tarakčija, Arnela, 475, 743
 Tarchi, Pietro, 309
 Tatlić, Berina, 547, 761
 Távora, Luís, 51
 Teixeira, Hiara Lopes Pinheiro, 629
 Telalovic, Jasminka Hasic, 349
 Terzaghi, Filippo, 407
 Terzić, Vedad, 475, 743
- Tiribilli, Eleonora, 309
 Topčagić, A., 553
 Topčagić, Muhamed, 99
 Tubić, Biljana, 357
 Tucak, Amina, 167, 499, 533, 547, 575, 729, 735, 749
 Turillazzi, Beatrice, 413
 Turnbull, Graham, 185
- U**
 Uzar, Izabela, 527
 Uzunović, A., 553, 559, 563
- V**
 Valchinov, E., 205
 Valjevac, Amina, 527
 Vardo, Almir, 475
 Vegar-Zubović, Sandra, 125, 131, 137
 Vehkaoja, A., 7
 Velickova, N, 611
 Veljović, Elma, 539
 Venesvirta, H., 7
 Verho, J., 7
 Vojinović, Nataša, 37
 Vonci, Leonardo, 417
 Vrana, Nihal Engin, 379
 Vranić, Edina, 167, 499, 533, 547, 575, 729, 735, 749
 Vučenović, S.M., 239
 Vujnović, Saša, 245
 Vuković, Blaženko, 325
- W**
 Wojciechowska, Małgorzata, 3
- Y**
 Yaman, Emine, 29
 Yarkent, Çağla, 267
- Z**
 Zećiri, Sabilja, 475, 539
 Zeron, Rubens, 769
 Žero, S., 553
 Žiga, Nermina, 695, 705
 Žigić, Nermina, 761
 Zorlak, Zerina, 251, 761
 Żyliński, Marek, 3